Lecture Notes in Mechanical Engineering

Yafang Han *Editor*

Advances in Materials Processing

Proceedings of Chinese Materials Conference 2017

Springer

Lecture Notes in Mechanical Engineering

Lecture Notes in Mechanical Engineering (LNME) publishes the latest developments in Mechanical Engineering—quickly, informally and with high quality. Original research reported in proceedings and post-proceedings represents the core of LNME. Also considered for publication are monographs, contributed volumes and lecture notes of exceptionally high quality and interest. Volumes published in LNME embrace all aspects, subfields and new challenges of mechanical engineering. Topics in the series include:

- Engineering Design
- Machinery and Machine Elements
- Mechanical Structures and Stress Analysis
- Automotive Engineering
- Engine Technology
- Aerospace Technology and Astronautics
- Nanotechnology and Microengineering
- Control, Robotics, Mechatronics
- MEMS
- Theoretical and Applied Mechanics
- Dynamical Systems, Control
- Fluid Mechanics
- Engineering Thermodynamics, Heat and Mass Transfer
- Manufacturing
- Precision Engineering, Instrumentation, Measurement
- Materials Engineering
- Tribology and Surface Technology

More information about this series at http://www.springer.com/series/11236

Yafang Han
Editor

Advances in Materials Processing

Proceedings of Chinese Materials Conference 2017

Springer

Editor
Yafang Han
Chinese Materials Research Society
Beijing
China

ISSN 2195-4356 ISSN 2195-4364 (electronic)
Lecture Notes in Mechanical Engineering
ISBN 978-981-13-0106-3 ISBN 978-981-13-0107-0 (eBook)
https://doi.org/10.1007/978-981-13-0107-0

Library of Congress Control Number: 2018938381

© Springer Nature Singapore Pte Ltd. 2018, corrected publication 2018
This work is subject to copyright. All rights are reserved by the Publisher, whether the whole or part of the material is concerned, specifically the rights of translation, reprinting, reuse of illustrations, recitation, broadcasting, reproduction on microfilms or in any other physical way, and transmission or information storage and retrieval, electronic adaptation, computer software, or by similar or dissimilar methodology now known or hereafter developed.
The use of general descriptive names, registered names, trademarks, service marks, etc. in this publication does not imply, even in the absence of a specific statement, that such names are exempt from the relevant protective laws and regulations and therefore free for general use.
The publisher, the authors and the editors are safe to assume that the advice and information in this book are believed to be true and accurate at the date of publication. Neither the publisher nor the authors or the editors give a warranty, express or implied, with respect to the material contained herein or for any errors or omissions that may have been made. The publisher remains neutral with regard to jurisdictional claims in published maps and institutional affiliations.

Printed on acid-free paper

This Springer imprint is published by the registered company Springer Nature Singapore Pte Ltd.
part of Springer Nature
The registered company address is: 152 Beach Road, #21-01/04 Gateway East, Singapore 189721, Singapore

Preface

This is the proceedings of the selected papers presented at Chinese Materials Conference 2017 (CMC2017) held in Yinchuan City, Ningxia, China, on July 06–12, 2017.

The Chinese Materials Conference (CMC) is the most important serial conference of Chinese Materials Research Society (C-MRS) and is held each year since early 1990s. Chinese Materials Conference 2017 had 37 symposia covering four fields of energy and environmental materials, advanced functional materials, high-performance structural materials, and design, preparation, and characterization of materials. More than 5500 participants attended the conference, and the organizers received more than 700 technical papers. By recommendation of symposium organizers and after peer-reviewing, 434 papers are published in the present proceedings, which are divided into four volumes of

Part 1: Advances in Energy and Environmental Materials
Part 2: High Performance Structural Materials
Part 3: Advances in Materials Processing
Part 4: Advanced Functional Materials

This is the volume for Part 3 including 123 papers selected from 6 symposia of E01: surface science and engineering technology for materials; E02: advanced preparation and processing technologies of materials; E04: solidification science and technology; E05: service behavior and structure safety for oil pipes and equipment; E06: materials genomes; Z: materials simulation, computation, and design.

The editors would like to give the thanks to the symposium chairs and all the paper reviewers of this volume, and the thanks should be also given to Mrs. Yiming Jia and Mr. Yongzheng Zhang for their hard work of compilation and typesetting for each paper in this volume.

Beijing, China
March 2018

Yafang Han

Contents

Plasma Nitriding of 2024 Al Alloy Deposited with Ti Film: Effects of N_2–H_2 Ratio on Microstructure Evolution and Mechanical Properties 1
Fanyong Zhang, Mufu Yan, Chen Lu and Fuxing Yin

Microstructure and Welding Performance of Sn–Ag–Cu Material 15
Zhigang Kong and Yilin Zhou

Enhanced Corrosion Resistance of 6063 Aluminum in Surface Modification Using γ-Aminopropyl Triethoxysilane 21
Linlin Zhang, Jinwei Wang, Jixue Zhou, Haihua Zhuang, Jianhua Wu, Baichang Ma and Shouqiu Tang

Effect of Dual-Sided Laser Peening Modes on Residual Stress Distribution of Aero-engine Titanium Blades 29
Peixuan Ouyang, Liangju He, Peijie Li and Guangbao Mi

Preparation and Wear Behavior of Enamel Coating on Ti–6Al–4V ELI Titanium Alloy 47
Qiuyuan Feng, Yongqiang Zhang, Zhihong Dong, Pinghui Zhang, Jian Wang, Dingchun Wang, Qi Gao, Xiao Peng and Fuhui Wang

Effect of Fiber Content on Surface Performance of Potassium Titanate Whiskers and Carbon Fiber-Reinforced Phenolic Composites 61
Rui Wang, Meifeng He, Junhao Huo, Baozhong Fan and Fang Liu

Influence of Surface Buffer Layer Thickness and Deposition Rate on the Release Rate of Silver Ions in Ag–TiOx Nanocomposites 75
Jian Xiong and Luying He

Analysis on the Major Environmental Factors Affecting the Weather Resistance of Polyester Coating 83
Xin Xu, Quan Jiang and Yannan Shi

Structural Analysis and Optical Properties of Sol-gel Derived $CuCoMnO_x$ Spinel Composite Oxide Coatings 95
Jie Min and Weiyang Guo

Effect of Cooling Rate on Solidification Structure of Zinc–Aluminum–Magnesium Alloy 105
Guanghui Liu, Guangrui Jiang and Haiquan Wang

Effect of Nanosecond Pulse Laser Shock Peening on the Microstructure and Performance of Welded Joint of 316L Stainless Steel 113
Yuqin Li, Y. H. Li, X. D. Wang, W. S. Xu, F. D. Qiao and S. J. Wang

The Effect of Mechanical Shot Blasting in Producing the Surface Ultrafined Grain Layer on Large-Size Titanium Plate 127
Quantong Yao, Guanglan Zhang, Ying Gao and Weiping Tong

Research on Influence of Abrasive Particles on Lubricating Performance of the Emulsion for Cold Rolling Strip 135
Yan Li, Yiqing Chen, Peng Gao, Bin Zhong, Fangfang Ai, Lin Li and Yu Xiao

Properties of Carbon Nanotubes (CNTs) Reinforced Copper Matrix Composites by Ultrasonic Welding 145
Zhengqiang Zhu, Mingfeng Li, Qiankun Xiao and Yifu Zhang

Effect of Print Method Based on SLM Technology on the Microstructure and Property of 316L Stainless Steel 157
Zhenghua Huang, Wenjun Qi, Yongxin Zhou, Chunjie Xu, Zhongming Zhang, Jianye Liu and Gaofeng Hu

Precipitation Behavior of 1.3%Si Non-oriented Silicon Steels During Strip Casting Process 165
Feng Fang, Xiang Lu, Mengfei Lan, Yuanxiang Zhang, Yang Wang, Guangming Cao, Guo Yuan, Yunbo Xu and Guodong Wang

Influence of Initial Microstructure on the Hot Working Flow Stress of ZK60 Mg Alloy 175
Yunteng Liu, Di Zhang, Tao Lin, Jixue Zhou, Yu Liu, Changwen Tian and Yuansheng Yang

Effects of Post-welded Heat Treated on the AZ31B Magnesium Alloy Joint Welded by Automatic TIG Welding 183
Hongtao Liu, Wenyi Cheng, Ruochao Wang, Jixue Zhou, Yanfei Chen, Jinwei Wang and Yuansheng Yang

High Temperature Hot Deformation Behavior and Constitutive Model Construction of High Quality 51CrV4 Spring Steel 191
ZhiGang Wang, FeiMing Xie, ChaoBin Lai, HongWei Li, Qing Zhang and Diqiang Luo

Effect of Process Parameters on the Interface Microstructure and Thickness of Silver Cladding Copper Wires Prepared by Core-Cladding Continuous Casting 201
Feng Yi, Xuefeng Liu and Yue Pan

Modelling and Analysis of the Relationship Between Process Parameters and Cross Section Geometry of Tin Single Tracks in Liquid Metal Flow Rapid Cooling Additive Manufacturing 217
Ang Li, Xuefeng Liu, Bo Yu, Yang Yan and Baoqiang Yin

Dependence of Microstructure, Relative Density and Hardness of 18Ni-300 Maraging Steel Fabricated by Selective Laser Melting on the Energy Density 229
Jie Tian, Zhenghua Huang, Wenjun Qi, Yajiang Li, Jianye Liu and Gaofeng Hu

Influence Law of Process Parameters on the Continuity and Dimensional Uniformity of 7075 Aluminum Alloy Single Tracks Manufactured by Selective Laser Melting 243
Xuefeng Liu, Ang Li, Baoqiang Yin, Bo Yu and Yang Yan

Void Evolution Law and Its Control in Steel Ingot Forging 257
Xin-li Wen, Qing-quang Zhang and Chao-lei Zhang

Comparison of the High Cycle Fatigue Behavior of Ti–6Al–4V Produced Respectively by EBM and Hot-Rolling 269
Yunxi Liu, Wei Chen, Zhiqiang Li, Zheyuan Chen and Gang Yao

Microstructure and Texture of Hot Rolled Plate and Finished Product in Fe–3%Si Common Grain-Oriented Silicon Steel 279
Rong Zhu, Lifeng Fan, Feng Guo and Jianzhong He

Effect and Mechanism of Cold-Hot Roll Bonding Process on Interfacial Bonding Properties of Aluminum/Steel Laminated Composite Plate 287
Xuefeng Liu, Xing Ming, Dandan Zhang and Zhangzhi Shi

Analysis of Large Inclusions in the Working Layer of Centrifugally Cast High-Chromium Steel Composite Roll 307
Hongliang Fan, Aimin Zhao, Wei Pei, Shaoheng Sun, Wei Liu and Bing Zhang

Optimization of 6005 Aluminum Alloy Components 315
Gang Sun, Pengwei Li, Qingmei Ma, Pilin Cui, Xiangjie Wang, Bo Huang and Jianzhong Cui

Role of Annealing Time in Thin-Gauge Non-oriented Silicon Steels Processed by Strip Casting 325
Haitao Jiao, Wei Xiong, Jiapeng Yang, Yuangxiang Zhang, Feng Fang, Chenggang Li, Guangming Cao, Yunbo Xu and Yongmei Yu

Temperature Distribution Laws During Selective Laser Melting Process of Nickel Base Alloy GH4169 335
Bin Liu, Le Tan, Zhanyong Zhao, Hao Zhang, Jing Li, Peikang Bai, Jianhong Wang and Yahui Cheng

Microstructure, Residual Stress and Corrosion Resistance in Electrodeposited Copper Foils 345
Yanhong Hua, Zhihua Nie, Guojie Huang, Yanfeng Li, Haofeng Xie and Dongmei Liu

Effect of Co Addition on Microstructure and Properties of Cu–Ni–Si Alloy 353
Jiang Li, Guojie Huang, XuJun Mi, LiJun Peng, HaoFeng Xie and Yonglin Kang

Effect of Controlled Rolling and Cooling on Microstructure and Properties of Cold Heading Steel Containing Boron and Titanium 361
Shipeng Ruan, Aimin Zhao, Lijun Wang, Guangjie Han and Peng Zhang

Preparation of TiAl Based Metallic Fibers 367
Yongchuan Yu, Shuling Zhang and Weiye Chen

Microstructure and Microhardness of a Laser Additive Forming Repaired Steam Turbine Blade 379
Xiangdong Zhang, Tianwei Liu, Shugang Wang and Chi Jiang

Regeneration Technology of Coated Sand for Selective Laser Sintering 387
Rui Pan, Bingrong Zhang and Jianxiang Liu

Technic Study on Polycrystalline Cubic Boron Nitride Tools Dry Cutting Harden GCr15 Based on the Finite Element Analysis and the Orthogonal Experiment 397
Yunhai Jia, Shaoning Lv and Lixin Zhu

Microstructures and Tensile Behaviors of Stainless Steel Clad Plate . . . 405
CuiXin Chen, MingYang Liu, BaoXi Liu, FuXing Yin, YanChun Dong, Wei Fang and Xin Zhang

Transformation Behavior During Isothermal Partitioning Process in Micro-alloyed Q&P Steel 413
Fei Peng, Yunbo Xu, Xingli Gu, Yuan Wang, Xunda Liu and Yongmei Yu

Effects of Heat Treatment on Microstructures and Mechanical Properties of Stainless Steel Tubes for Rivet Parts 423
Sirui Cheng, Qingyun Zhao, Hong Huang and Fenglei Liu

Effect of Post-weld Heat Treatment on Microstructure and Mechanical Properties of 309L/E5015 Fusion Zone of Bimetal Lined Pipe Weld 435
Dongming Liu, Yuheng Ning, Tao Jiang and Xu Sun

Efficient Water-Based Rust Inhibitor for Surface Treatment of Iron and Steel 445
Kunkui Wu, Jinfeng Bai, Yang Liu and Yan Zhang

Effects of Fiber Laser Welding Speeds on Microstructures and Properties of E36 Steel Butt Joints 453
Yan Gao, Li Cui, Changshi Gu and Dingyong He

Preparation and Mechanical Properties of 42CrMo/40CrNiMo Dissimilar Steel Joints Prepared by Diffusion Bonding 463
Jie Wang, Fuqi Zhang, Guanzhong Yang, Bin Wang and Minmin Xia

Effect of Cold Drawing on Microstructure and Mechanical Properties of 410 Martensite Stainless Steel Wire 477
Haonan Yu, Renbo Song, Yao Tan, Tianyi Wang and Lun Li

Microstructural Properties and Hardening Mechanism of Explosion Hardening of Mn13Cr2 Steel Surface 487
Qinan Ba, Renbo Song, Yifan Feng and Lun Li

Effects of Solution Temperature on Microstructure and Properties of Fe–Mn–Al–C Ferrite-Based Steel 495
Xuan Li, Renbo Song, Naipeng Zhou, Jiajia Li and Lun Li

Interfacial Peel Strength and Microstructure of Titanium/Aluminium Foil Manufactured by Ultrasonic Consolidation Process 505
Yujie Han, Yaoqi Wang, Hongliang Hou and Yanling Zhang

Deep Densification of ZrB_2 by Hot Pressing 517
Tao Gui, Lei Yang, Yuyang Liu, Xue Bai, Xingming Wang and Bo Song

Effect of Welding Thermal Cycle on Mechanical Properties and Corrosion Resistance of A7N01-T5 Aluminum Alloy 529
Cui Huang, Shufang Zhang, Jie Hu and Xiaomin Wang

Experimental Investigation of Selective Laser Melting AlSi10Mg Alloy 543
Wei Pan, Yangjie Tang, Yantao Liu, Yongzhong Zhang and Pengyue Wu

Corrosion Behavior Evolution of A7N01 Aluminum Alloys with Different Heat Treatments in the IGC Solution 551
Jie Hu, Cui Huang and Xiaomin Wang

Microstructures of Conventionally As-Cast Mg–Zn–Y Alloys 569
Qian Li, Zhenghua Huang, Yongxin Zhou, Chunjie Xu, Yangde Li and Weirong Li

Influence of Process Parameters by Enclosed Cooling Slope Channel on Microstructures of Semi-solid ZCuSn10P1 Alloy 583
Yongkun Li, Rongfeng Zhou, Lu Li, Fan Xiao, Yehua Jiang and Dehong Lu

Metal Flow Law of Variable Diameter Metal Wire During Die Drawing 595
Kaisong Li and Xuefeng Liu

Dielectric and Impedance Studies on $(K_{0.5}Na_{0.5})NbO_3$-Based Ceramics 609
Yafei Yan, Minhong Jiang, Jiageng Song, Chongyan Hao, Qi Jin, Shengnan Han, Lin Li, Jinwei Zhang and Xiaoyu Yao

Solidification Structure of Metastable Immiscible Cu–Fe Alloy Under Different Cooling Rates 621
Shichao Liu, Hang Li, Jinchuan Jie, Guomao Yin and TingJu Li

Microstructure and Properties of Nickel-Based Superalloy Prepared by Two-Phase Zone Directional Solidification 629
Xue-Feng Liu, Zhang-Ke Wang, Ang Li and Bao-Qiang Yin

Rheological Stress Behavior of B10 Copper-Nickel Alloy During Hot Deformation Process 643
Jianing Zhang, Dongmei Liu, Qiangsong Wang, Fang Liu and Shuyu Yang

Microstructure and Mechanical Properties of Aluminum Clad Steel Plates by Cold Rolling and Annealing Heat Treatment 655
Fuxing Yin, Jiule Ma, Baoxi Liu, Jining He, Fanyong Zhang, Mingyang Liu and Yanchun Dong

Analysis of Stripe Defects on the Cold Rolled Aluminum Strip Surface 667
Yan Li, Lei Xia, Yiqing Chen, Peng Gao, Bin Zhong, Fangfang Ai and Lin Li

Effect of Multi-pass Submerged Friction Stir Processing on Microstructure Evolution and Mechanical Properties of AZ61 Magnesium Plate 673
Xicai Luo, Datong Zhang, Wen Zhang and Cheng Qiu

Effect of Rolling Process on Microstructure and Magnetic Properties of 50W800 Electrical Steel 681
Ruifeng Dong, Rui Zhang, Lifeng Fan and Rong Zhu

Evaluation on the Dimensional Stability of Filled and Un-Filled Models of Investment Casting Pattern Materials 689
Liqiang Zeng, Yi Li, Zengjun Wang, Jiaqi Lu and Hua Li

Relationship of Oil Composition and Lubricating Characteristics in Cold Rolling Aluminum Strips 697
Yongtao Zhao, Jianlin Sun, Guangzhao Yuan and Chenglong Wang

Finite Element Simulation for Hot Continuous-Rolled TC4 Alloy Seamless Pipe 705
Jiaxin Shi, Wei Yu, Entao Dong and Jun Wang

Vibration Effects on Weld Bead Characteristic of FV520B Stainless Steel Remanufactured with Surfacing Deposition Technology 717
Jian Liu, Sheng Zhu, Zhihai Cai and Ping Zhang

Evolution of Oxide Structures of Low-Alloy Steel Surface During Short-Time Oxidation at High Temperature 725
Jun Wang, Wei Yu, Entao Dong and Jiaxin Shi

Joining 304 Stainless Steel and TC4 Alloy Using Ag Foil Interlayer by Plasma Activated Sintering 735
Mei Rao, Jian Zhang, Jiayu He, Guoqiang Luo, Shulong Liu, Qiang Shen and Lianmeng Zhang

Resistance Spot Welding Process and Properties of Hot Dip Galvanized DP590 High Strength Steel 743
Ruxia Liu, Mei Rao, Shulong Liu, Jian Zhang and Guoqiang Luo

Surface Integrity of Nickel-Base Superalloy Materials by Electric Hot Machining 751
Jikun Yu, Shimin Geng, Shuo Liu, Xin Liu, MingYu Wu and Hongyou Zhang

Analysis of the Spring-Back Properties of the TRIP/TWIP Steel Containing 0.035% RE 761
Lihui Wang, Hongchuan Zhu, Xiangdong Liu, Libo Pan and Tao Gong

Polishing on Cubic Boron Nitride Abrasive Materials of Bearing Hollow Roller 769
Hongyou Zhang and Mingyu Wu

Preparation of Large Size Monolayer MoS_2 by a Two-Step Heating Process by CVD 777
Fengjiao Lv, Yi Zeng, Bo Liu, Bin Tang and Qing Chen

Influences of Initial Composition and Solid Back Diffusion on the Solidification Path of Al–Fe–Si Alloys 785
Guang Wei Zhao, Chong Ding, Xi Cong Ye and Cai Hua Huang

Influence of Mold Temperature on Microstructure and Shrinkage Porosity of the A357 Alloys in Gravity Die Casting 793
Longfei Li, Daquan Li, Junzhen Gao, Yongzhong Zhang and Yonglin Kang

Solidification Behavior and Mechanical Property of a Highly Undercooled Al–Si Alloys 803
Bo Dang, Zengyun Jian and Junfeng Xu

Different Interfaces of Primary Transition and Eutectic Transition 811
Junfeng Xu, Dandan Fan, Bo Dang and Zengyun Jian

Application of CAFÉ Method on Microstructure Simulation of Semi-solid Al–7%Si Alloy 819
Wenying Qu, Fan Zhang, Daquan Li, Min Luo, Zhiyu Yang and Yongzhong Zhang

Effects of Cooling Rate and Grain Refiner on Semi-solid Rheocasting Slurries of Al–Zn–Mg Alloy 829
Min Luo, Daquan Li, Wenying Qu, Xiaokang Liang and Jianzhong Fan

Microstructures and Mechanical Properties of 584 mm 7055 Alloy Billet by Direct Chill Casting Under Annular Electromagnetic Stirring Coupled with Intercooling 839
Yajun Luo, Zhifeng Zhang, Minwei Gao, Bao Li and Chunsheng Chen

Effects of Al–Ti–B–RE Grain Refiner on Microstructure of A357 Alloy 847
Chuanzheng Zhang, Yuelong Bai, Zhifeng Zhang, Bao Li and Chunsheng Chen

Effect of Cobalt on Microstructure and Mechanical Properties of Invar Alloy 855
Cuixin Chen, Baojun Ma, Sainan Miao and Baoxi Liu

Effect of Melt Treatment on Fe-Rich Phase in Al–25Si–2Fe–2Mn Alloy 865
Fan Xiao, Lu Li, Rongfeng Zhou, Yongkun Li, Yehua Jiang and Dehong Lu

An Overview of Phase Diagram and Thermodynamic Parameters of Pt–Au–Sn System 881
Jieqiong Hu, Ming Xie, Song Chen, Aikun Li, Saibei Wang and Yongtai Chen

Failure Mechanisms of Ti–Al_3Ti Metal-Intermetallic Laminate Composites 893
Yuan Meini, Li Yao, Li Lizhou, Chen Hehe and Huang Bin

Microstructures and Properties of High Performance Cast Irons Applied in Automobile Flywheels 905
Xianfei Ding, Hong Huang, Xiaozheng Li, Warkentin Matthias, Shiyao Huang and Qiang Feng

P110T Casing Material's Relation of Creep and Relaxation for the Sealing Surface of Premium Connection in High Temperature Gas Well 917
Ying Zhang, Zhanghua Lian, Mi Zhou and Tiejun Lin

Aluminum Alloy Pipe Design and Mechanical Property Analysis 931
Shangyu Yang, Chun Feng, Yaorong Feng and Lihong Han

Experimental Validation of Constraint Effects on Toughness Test of Pipeline Girth Welds 941
Lin Chen, Jianwu Liu, Ling Wang and Dengzun Yao

Material Identification and Safety Evaluation of Defective 15Cr1Mo1V Steel 951
Xianxi Xia, Guodong Zhang, Fei Xue and Qinzheng Ma

Permeation Characteristic and Mechanism of CO_2 in High Density Polyethylene 963
Houbu Li, Dongming Yang, Dongna Zhang, Yuanyuan Zhu, Pengli Ge, Dongtao Qi and Zhihong Zhang

Dropout Failure Analysis for Long Round Thread Connection at Mill End 975
Zhiyong Pan, Yaorong Feng, Lihong Han, Jianjun Wang, Xianren Kuang, Peng Yang, Chengli Song, Han Ding and Shen Cong

Coupling Effect of Transient Temperature-Pressure on Casing String During Volume Fracturing in Shale Gas Wells 985
Yan Xi, Jun Li, Yang Yu, Zongyuan Li and Bowen Mei

Application of Titanium Alloy Tubing in HPHT Gas Wells to Reduce Vibration and Buckling 1001
Qiang Zhang, Zhanghua Lian, Taihe Shi and Yisheng Mou

Stress Analysis of Tubing Thread of the Gas Seal Test in Deep Gas Well 1015
Yisheng Mou, Zhanghua Lian, Qiang Zhang and Taihe Shi

Assessment Methods for the Dented Pipe of Grade X80 1029
Qiaofei Sun, Lei Guo, Dahai Zheng, Leilei Wang and Yi Liu

Influence of Cement Defection on Casing Stress Under Cyclic Loading During Multi-stage Hydro-Fracturing 1039
Xueli Guo, Jun Li, Yang Yu and Gonghui Liu

Simulation Analysis of the Strain Behaviour of X80 Girth Weld Joint 1055
Shixin Wang, Zhiwen Li, Zhenglong Li, Zhaojun Zhang and Changchai Han

Toughness Scatter About FCAW-S Girth Weld for X80 Pipeline Steel 1065
Youxiao Xu, Feng Wang, Lin Chen, Ziyun Wei and Weichen Song

Graphene Modified Epoxy Coating Tubing Applied in the Water Injection Wells 1075
Caihong Lu, Chun Feng, Lijuan Zhu, Long Jiang, Guhui Gao, Lihong Han and Yaorong Feng

Corrosion Behavior of Ni–P Alloy Coated Carbon Steel Tubing in Water Injection Wells 1083
Lijuan Zhu, Chun Feng, Caihong Lu, Long Jiang, Juntao Yuan, Tao Tian and Xin Xu

Ultrafast Precipitation Kinetics in an Ultrafine-Grained Al–Cu Alloy Used for Oil Drill Pipes 1093
Long Jiang, Chun Feng, Lihong Han, Yaorong Feng, Caihong Lu, Lijuan Zhu, Hang Wang, Gang Liu and Jun Sun

Creep Behavior and Mechanism of Casing in Thermal Well Under Cyclic Steam Stimulation at Medium Temperature 1103
Hang Wang, Lihong Han, Shangyu Yang, Tao Tian, Long Jiang and Wei Chen

Evaluating the Compatibility of PA11 Pipe with Oil Field Media Based on Tensile Tests 1113
Nan Ding, Meng Zhang, Houbu Li, Xiang Zhang, Ke Cai and Bin Wei

Impact Fracture Behavior of Large-Diameter X80 Line Pipes 1125
Hui Feng, Hao Ding, Yiming Zhang and He Li

Hydrostatic Experimental Study and Failure Mechanism of Glass Fiber Reinforced Thermoplastic Pipes Used for Oilfields 1133
Guoquan Qi, Dongtao Qi, Nan Ding and Xiaodong Shao

Girth Welding on Oil and Gas Pipeline Projects in China 1143
Yongli Sui

Cigarette Butts Water Extracts as Corrosion Inhibitor in Oil Field Acidizing Fracture Using Different Metal Chlorides Intensifiers 1155
Xunji Li, Juantao Zhang, Wenwen Song, Zeliang Chang, Yan Han and Rui Cai

Prospect and Latest Development of Pipeline Integrity Management in China 1167
Shaohua Dong, Yinuo Chen and Zongqi Liu

Sulfate Reducting Bacteria Corrosion Component Study of N80 Steel in Simulating Oilfield Produced Water 1187
Wenwen Song, Juantao Zhang, Xunji Li, Bin Li, Fagen Li and Anqing Fu

Application of Grain Boundary Diffusion Method into High-Throughput Synthesis Materials Chip for Sintered Nd–Fe–B Magnets 1195
Xing Yu, Guang Feng, Yifei Zhu, Lei Zhao, Yunhai Jia and Haizhou Wang

Structures and Properties of Near-Rapidly Solidified Fe–12Mn–9Al–1.2C Dual-Phase Lightweight Steel Containing 3 wt% Ni 1207
Jianlei Zhang, Wei He, Yang Yang, Yunhu Zhang, Lian Duan, Zhiping Luo, Changjiang Song and Qijie Zhai

Constitutive Model of Wrought Superalloy GH4066 in Hot Deformation Process 1217
Yanju Wang, Jiaying Jiang, Chonglin Jia, Xingwu Li and Yongjun Guan

Gradient Speed Control Method to Reduce the Residual Stress on a Turbine Disk in Forging Process 1229
Yanju Wang, Jiaying Jiang, Yong Zhang, Yongjun Guan and Xingwu Li

Microstructure Evolution in Solidified Al–Si Hypereutectic Alloys Under the Impact of an Electric Current Pulse 1237
Yunhu Zhang, ZhiShuai Xu, Honggang Zhong, Chen Xiangru, Changjiang Song and Qijie Zhai

First-Principles Calculations, Thermodynamic Calculations and Kinetic Calculations of Ultra High Strength Aluminum Alloys of Al–Zn–Mg–Cu–Zr 1245
Jinsan Wang, Jinxin Zang and Xiang Xiao

Thermodynamic Description of the Al–Mg–Y System 1255
Kaiming Cheng, Jixue Zhou, Jingrui Zhao, Shouqiu Tang and Yuansheng Yang

Finite Element Simulation of Hot Spinning for GH4169 Superalloy Thin-Walled Shell 1265
Bangqi Yin, Degui Liu, Xiangyi Xue, Yang Wu, Hongchao Kou and Jinshan Li

First-Principles Study of Au-Doping Effects in $Hg_{1-x}Cd_xTe$ (x = 0.25, 0.5, 0.75) 1279
Xueli Sun, Dechun Li, Zhaogen Zhong, Shengzhi Zhao, Kejian Yang, Xiangyang Li, Reng Wang and Ji Liu

Preparation and Numerical Simulation of Structural Parameters of Ni–Fe Bimetallic Porous Anode Support for Solid Oxide Fuel Cells . . . 1291
Xin Gu, Jie Yu, Wenhui Ma, Guoqiang Lv, Dingwen Kang and Guangjie Xie

Thermodynamic Calculation of Phase Diagrams for the Rare Earth Binary Alloys: RE–Nd (RE = La, Ce, Pr, Y) Systems 1305
Kaicheng Yang, Lei Xu, Maohua Rong, Qingrong Yao and Jiang Wang

Erratum to: Effect of Process Parameters on the Interface Microstructure and Thickness of Silver Cladding Copper Wires Prepared by Core-Cladding Continuous Casting E1
Feng Yi, Xuefeng Liu and Yue Pan

Plasma Nitriding of 2024 Al Alloy Deposited with Ti Film: Effects of N_2–H_2 Ratio on Microstructure Evolution and Mechanical Properties

Fanyong Zhang, Mufu Yan, Chen Lu and Fuxing Yin

Abstract 2024 Al alloys were firstly deposited with pure Ti film (~5.0 μm in thickness) using magnetron sputtering, then plasma nitrided for 8 h at 490 °C under N_2–H_2 gas mixtures with different N_2 content (15, 40 and 50%). The Ti–N and Ti–Al diffusion reactions were activated simultaneously on the surface of Al alloy to obtain duplex coatings. The results showed that the duplex coatings were composed of nitride/aluminide layers ($TiN_{0.3}/Al_3Ti/Al_{18}Ti_2Mg_3$ layers). With increasing the N_2 content in the gas mixture, the peak ratio $I_{(002)}/I_{(100)}$ of the outer $TiN_{0.3}$ phase increased and the nitride particles grew larger. The surface hardness of coatings increased with the increasing N_2–H_2 ratio, reaching the maximum value of 630 HV under 50%N_2 + 50%H_2. The coatings obtained under gas mixture with high N content showed larger fluctuation at the initial stage during friction tests. All the obtained coatings showed the similar friction coefficient (~0.30) at the stable stage, much lower than the untreated Al alloy (~0.45). The sample nitrided under 50%N_2 + 50%H_2 exhibited the lowest wear rate, 60% lower than that of the uncoated one. The nitrided samples exhibited predominant abrasive wear and adhesive wear.

F. Zhang · F. Yin
Research Institute for Energy Equipment Materials, Hebei University of Technology, Tianjin 300130, China
e-mail: fany_zhang@163.com

F. Yin
e-mail: hbgdhjn@163.com

F. Zhang · F. Yin
Tianjin Key Laboratory of Materials Laminating Fabrication and Interface Control Technology, Hebei University of Technology, Tianjin 300130, China

M. Yan (✉) · C. Lu
National Key Laboratory for Precision Hot Processing of Metals, School of Materials Science and Engineering, Harbin Institute of Technology, Harbin 150001, China
e-mail: prsm_604@163.com

C. Lu
e-mail: zfy19861010@163.com

© Springer Nature Singapore Pte Ltd. 2018

Y. Han (ed.), *Advances in Materials Processing*, Lecture Notes in Mechanical Engineering, https://doi.org/10.1007/978-981-13-0107-0_1

Keywords 2024 Al alloy · Plasma nitriding · Intermetallic coating
Microstructure · Wear resistance

Introduction

Aluminum alloys have numerous industrial applications due to their attractive properties such as light weight, high specific strength and favorable mechanical formability [1]. However, the widely spread use of Al alloys has been limited by their low hardness and poor wear resistance [2]. In the past years, several methods such as plasma nitriding, plasma electrolytic oxidation, plasma spray, ion implantation and laser surface alloying are employed to enhance the surface mechanical properties of Al alloys [3–7]. Nevertheless, these methods usually produce single ceramic or intermetallic coatings. Recently, duplex coatings containing both ceramics and intermetallics have attracted increasing attentions due to their enhanced properties.

Plasma nitriding is a well-known surface modification method to obtain nitride coatings. Recently, duplex treatment combining plasma nitriding and other established surface modification technologies are used to produce composite coatings for ferrous alloys, i.e., chromizing followed by plasma nitriding [8, 9], aluminizing followed by nitriding [10], plasma nitriding followed by physical vapor deposition (PVD) of titanium, chromium or zirconium [11]. For nonferrous components, Zhang et al. [12] have reported a TiN/Ti_3Al composite coating produced by laser nitriding Al coated Ti6Al4V alloy, with increased hardness and modulus. The corrosion resistance and surface hardness of NiAl coating were improved due to the formation of hard AlN particles during plasma nitriding [13]. Thus, it would be worthy to explore nitride layers on the surface of Al alloys by combining plasma nitriding and other surface technologies.

In previous studies, the surface mechanical properties of Al alloys could be enhanced by surface alloyed with transition metal elements such as Ti, Cr and so on [14, 15]. Since titanium can react with both nitrogen and aluminum, it is a suitable candidate for producing Ti–N and Ti–Al layers on the surface of Al alloys. In our previous studies [16, 17], duplex surface treatment via depositing Ti film followed by plasma nitriding was carried out on the surface of Al alloy to produce Ti–N/Ti–Al layers with enhanced mechanical properties. The as-obtained Ti–N layer played an important role in improving the surface mechanical properties of Al alloys, while the Ti–Al intermetallic layer acted as the transition layer to decrease the mismatch between the nitride layer and the Al substrate. Thus, in the present study, the effects of nitriding atmosphere (N_2–H_2 ratio) on the microstructure evolution as well as the corresponding mechanical properties of the duplex layers were investigated.

Experimental Details

Materials

2024 Al alloy was used for surface treatment, with chemical composition of 3.81 Cu, 1.40 Mg, 0.40 Mn, 0.40 Fe, 0.14 Zn, 0.22 Si, Ti < 0.05, Cr < 0.05 (in wt %), and Al balance. The specimens (20 mm in diameter and 4 mm in height) were ground up to 2000 grid with silicon carbide paper, polished with diamond pastes to a mirror-like finish and ultrasonically cleaned in acetone.

Coating Process

The duplex surface treatment involves two sequential procedures. Firstly, pure Ti films were deposited onto the 2024 Al alloy disk by using a closed field unbalanced magnetron sputtering ion plating system (UDP-450, Teer Coatings Ltd, UK) with a high quality Ti target (99.999%, 330 mm × 134 mm × 8 mm). Secondly, the Ti-coated Al alloy samples were plasma nitrided in a nitriding unit (LDMC-30, 30 kW) [18]. The nitride chamber was evacuated to below 8 Pa by a rotary pump before applying the glow discharge. Then, the nitriding treatments were carried out at 490 °C for 8 h under the gas mixture (N_2 + H_2) with different volume content of N_2 (15, 40 and 50%). The corresponding nitride samples were defined as PN15, PN40 and PN50, respectively. The voltage and the working pressure during nitriding were 650 V and 230 Pa, respectively. After the treatment, the samples were cooled down slowly inside the chamber with a nitrogen gas flow.

Characterization

X-ray diffraction technique was used by employing Cu–Kα radiation (λ = 0.15406 nm) to identify the phases in the modified surface layers. The working voltage is 40 kV and the scanning speed is 3°/min. The microstructure of the surface layer was studied using a scanning electron microscope (SEM, FEI QUANTI 200F), with the energy dispersive X-ray spectrometer (EDS). The surface hardness of the as coated sample was measured using a Vickers microhardness tester (HV-1000) at the indentation load 10 g for 15 s. Five measurements were taken for each test and the mean value was used.

The dry sliding wear tests were conducted using a pin-on-disc wear testing machine (POD-1). During wear tests, the cylindrical pins of the 2024 Al alloy (before and after treatment) were rotated against a stationary hardened chromium steel (Rc64) ball of 5 mm diameter at the speed of 200 r/min (0.1 m/s) for 1200 s. The normal contact load was 2 N. All tests were performed in air, without lubrication

(temperature 20 °C, humidity 60% RH). The worn surfaces and wear debris of selected samples were characterized using SEM equipped with energy dispersive X-ray. The weight loss was measured by an electronic balance with minimum measuring range of 0.1 mg. Weight wear rate W_L, was calculated according to the following equation: $W_L = \Delta M / L \times n$, where ΔM (g) is the weight loss, L (N) is the contact load and n (r) is the total number of turns.

Results and Discussions

Microstructure Evolution

The XRD patterns of the pure Ti film and samples plasma-nitrided at 490 °C for 8 h under different atmosphere are shown in Fig. 1. The as-deposited Ti film crystallized in the HCP structure (α-Ti) and The top surface layer of the nitrided samples are mainly composed of $TiN_{0.3}$. The $TiN_{0.3}$ phase keeps the similar preferred orientation of (002) with that of the as-deposited Ti film. In addition, the peak ratio $I_{(002)}/I_{(100)}$ increases with increasing the volume fraction of N_2 in the atmosphere. The peaks of aluminides ($Al_{18}Ti_2Mg_3$) were observed, indicating the Ti–Al reaction during plasma nitriding. However, the Al peaks come form the diffraction of Al alloy substrate because of the thin thickness of the nitride layer.

Figure 2 shows the SEM observations on the surface morphology of Ti film and the as-obtained layers at different nitriding atmosphere. As can be seen from Fig. 2a, the as-obtained Ti film exhibits the petaloid feature, crystallizing in the range of about 200 nm. The Ti film is found to be uniform with minor small voids. After plasma nitriding, the voids between the primary Ti particles disappear and the

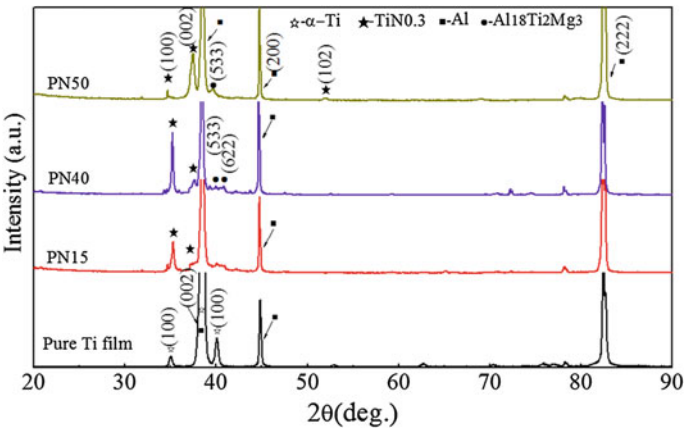

Fig. 1 XRD patterns of pure Ti film and surface layers of Ti coated 2024 Al alloy nitrided under different nitriding atmosphere at 490 °C for 8 h

surfaces become smooth with the formation of ultrafine sphere-like particles (Fig. 2b–d). These particles are in the nanoscale, forming along the larger original Ti particles, with the size of about 50, 75 and 90 nm for PN15, PN40 and PN50, respectively. With increasing the volume fraction of N_2 in the mixture gas, these nitride particles grow larger and the nitride surfaces become much denser.

Figure 3 displays the EDS results of the nitride surfaces obtained under the gas mixture of 15%N_2 + 85%H_2 and 50%N_2 + 50%H_2. The nitrogen content of the surface obtained under 15%N_2 + 85%H_2 is about 18.82 at.%, whereas it increases up to 22.43 at.% for the surfaces prepared under 50%N_2 + 50% H_2. Combined with the XRD results, it can be inferred that increasing the volume fraction of N_2 facilitates the reaction between active N atoms and α-Ti, thus contributing to the formation of $TiN_{0.3}$.

Figure 4 shows the backscattered electron (BSE) images of the cross section structure of the pure Ti film and the nitrided samples. As can be seen from Fig. 4a, the Ti film shows uniform structure without voids in the interface. The thickness of the Ti film is ~5.0 μm. As seen in Fig. 4b–d, obvious diffusion layer are observed between the Ti film and the Al alloy substrate after plasma nitriding. The as-obtained surface coating is composed of three sublayers and the thickness of the outer nitride layer is 3.6, 3.0 and 4.8 μm, respectively. The thickness of the middle layer is 0.5, 1.0 and 0.5 μm. The thickness of inside layer is 3.6, 6.0 and 2.0 μm.

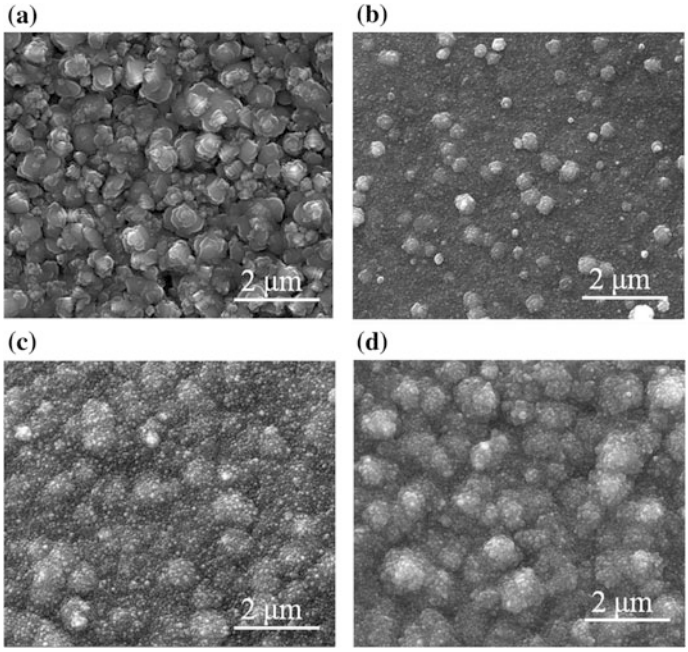

Fig. 2 Surface morphologies of Ti coated 2024 Al alloy nitrided under different nitriding atmosphere at 490 °C for 8 h: **a** pure Ti film, **b** PN15, **c** PN40 and **d** PN50

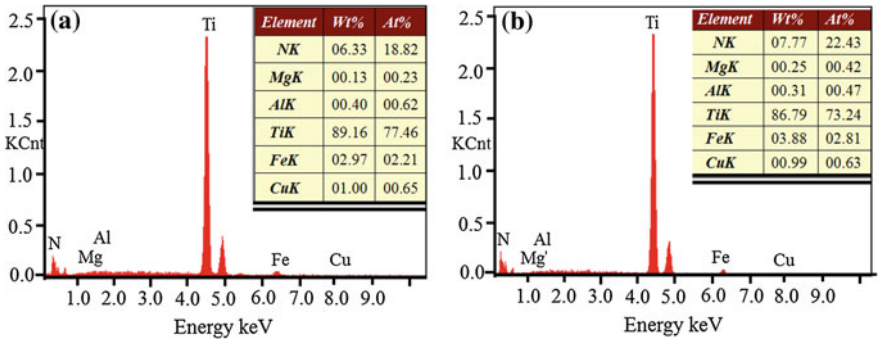

Element	Wt%	At%
NK	06.33	18.82
MgK	00.13	00.23
AlK	00.40	00.62
TiK	89.16	77.46
FeK	02.97	02.21
CuK	01.00	00.65

Element	Wt%	At%
NK	07.77	22.43
MgK	00.25	00.42
AlK	00.31	00.47
TiK	86.79	73.24
FeK	03.88	02.81
CuK	00.99	00.63

Fig. 3 EDS analysis of surface of Ti coated 2024 Al alloy nitrided under different nitriding atmosphere at 490 °C for 8 h: **a** PN15, **b** PN50

In summary, the sample nitrided (PN40) show the maximum thickness of the as-obtained coating.

Figure 5 shows the corresponding elements distribution of the treated samples. Obviously, intense inter-diffusion occurs between the Ti film and Al alloy substrate. Three distinct stages can be observed in the elements curves, which is in agreement

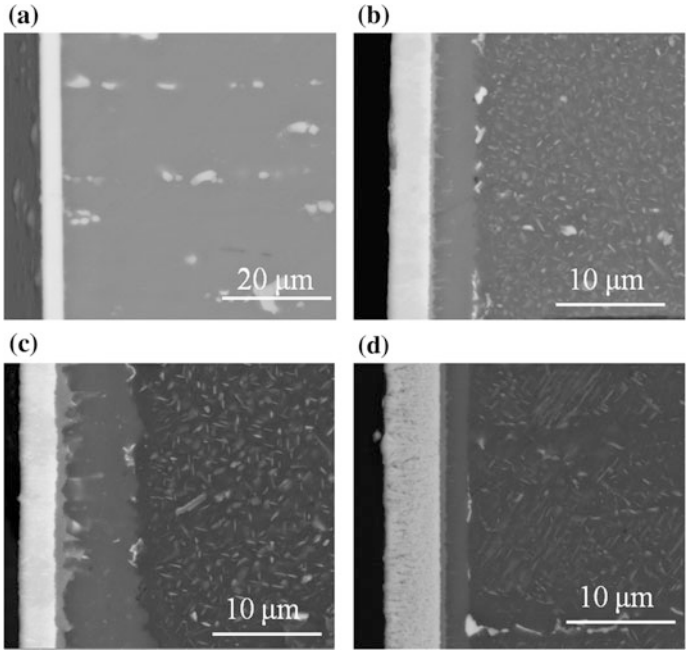

Fig. 4 Cross-sectional morphologies of Ti coated 2024 Al alloy nitrided under different nitriding atmosphere at 490 °C for 8 h: **a** pure Ti film, **b** PN15, **c** PN40 and **d** PN50

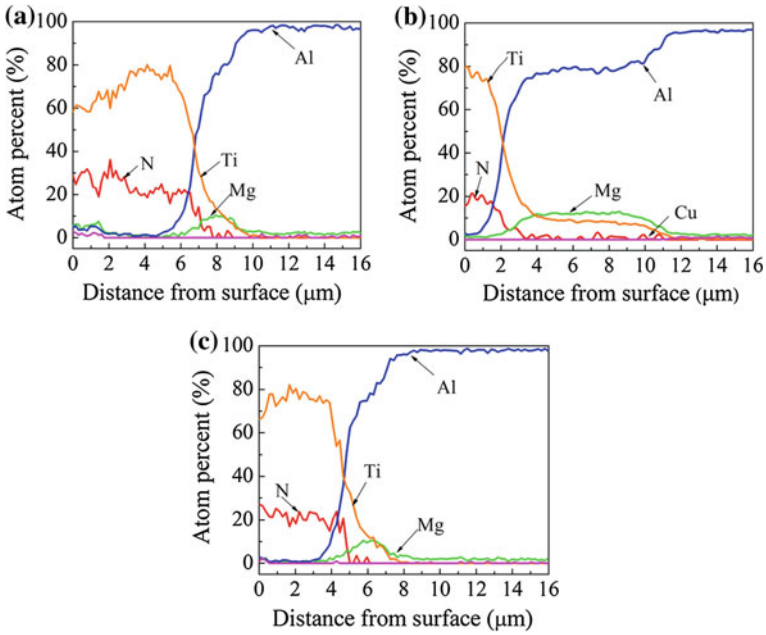

Fig. 5 Elements distributions of cross-section of Ti coated 2024 Al alloy nitrided under different nitriding atmosphere at 490 °C for 8 h: **a** PN15, **b** PN40 and **c** PN50

with the three sublayers in Fig. 4b–d. In the first stage, the atomic ratio between nitrogen and titanium is about 0.34, close to that of $TiN_{0.3}$. Combined with the XRD results in Fig. 1, it can be inferred that the outside white layer mainly consist of $TiN_{0.3}$ phase. In the second stage, the atomic ration of (Al + Mg)/Ti is close to 3, indicating the Mg doped Al_3Ti phase. Interestingly, the Mg atoms aggregate at the interface to form the third stage. The atom ratio of Al: Mg: Ti is close to 18: 2: 3, indicating that the inside layer is made of $Al_{18}Ti_2Mg_3$ phase.

Actually, the layer growth involves the competition of Ti–N reaction and Ti–Al reaction. At low volume fraction of N_2 in the mixture gas (15%), the diffusion rate of N atoms in α-Ti is slower than that of Al in α-Ti, attributing to the formation of thick Ti–Al layer. When increasing the volume fraction of N_2 up to 40%, both of the Ti–N and Ti–Al reaction accelerate, while the Ti–Al reaction plays a dominant role thus leading to the fast growth of aluminide layer. However, when the volume fraction of N_2 increases to 50%, more active N atoms are ionized from the N_2–H_2 mixture gas, resulting in the fast growth of Ti–N layer. Thus, the solution of N in the Ti inhibits the Ti–Al diffusion, leading to the decrease of the aluminide layer.

Mechanical Properties

Figure 6 displays the surface hardness of the untreated, Ti-coated and nitride samples under different gas mixture. Obviously, the surface hardness of the Al

alloys is significantly increased after plasma nitriding. The surface hardness is enhanced with increasing the volume fraction of N_2 in the gas mixture. The nitrided samples (PN50) reaches the maximum value of 630 HV, which is about 6 times higher than that of the untreated 2024 Al alloy substrate.

As for the hardness of coatings, the preferred orientation is a dominant factor due to geometrical strengthening based on the dislocation theory. Generally, the highly preferred orientation on the close-packed plane with movable slip system could yield much higher hardness. In the present study, (002) plane is the close-paced plane for the $TiN_{0.3}$ with hexagonal structure. As mentioned in the XRD results, the peak ratio $I_{(002)}/I_{(100)}$ of the $TiN_{0.3}$ phase increased with the increasing volume fraction of N_2. Thus, the samples nitrided under 50%N_2 + 50%H_2 have the high hardness.

Dry sliding wear test is used to evaluate the wear behavior of the untreated and the nitrided samples under different gas mixture. Figure 7 shows the coefficients of friction (COF) vs sliding time curves of the tested samples. The friction curve of the untreated Al alloy exhibits large fluctuations, indicating typical characteristic of severe adhesive wear for soft materials. After plasma nitriding, the friction curves of the nitrided samples is composed of two stages, i.e., the initial stage of severe wear and stable wear stage. At the initial stage, the rather high values of COFs might result from the high contact force due to the severe adhesion between the counter face and the $TiN_{0.3}$ layer. At the stable wear stage, the hard $TiN_{0.3}$ and aluminide particles could play a role of abrasive medium, leading to the decrease of the fluctuations of friction curves for the coated samples. Obviously, the samples nitrided under different gas mixture exhibit the similar COF values (0.30), lower than the untreated one (0.45). According to the above illustration, it can be inferred that the wear behavior of the nitrided samples mainly depends on the outer $TiN_{0.3}$ layer.

Figure 8 shows the wear rate of the untreated and nitrided samples under different gas mixture. Obviously, the nitride/aluminide coatings decrease the wear rate of Al alloys remarkably. In addition, the wear rate of samples decreases with the increasing volume fraction of N_2 in the gas mixture. As for the sample nitrided under 50% N_2 + 50%H_2, it shows the lowest wear rate of 0.6×10^{-7} g r^{-1} N^{-1}, which decreases about 60% compared with that of the untreated Al alloy (1.5×10^{-7} g r^{-1} N^{-1}).

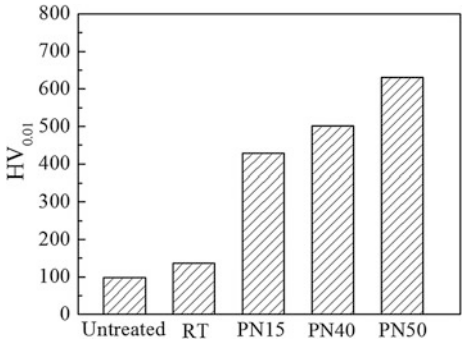

Fig. 6 Surface hardness of the 2024 Al alloy before and after plasma nitrided under different nitriding atmosphere

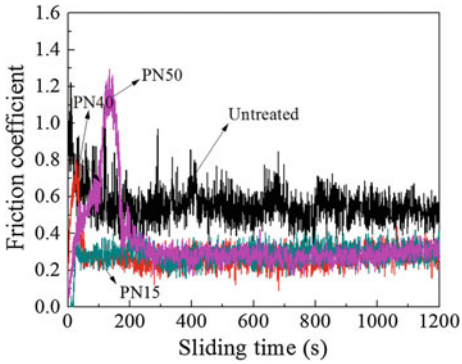

Fig. 7 Frictional coefficient curves of the uncoated and nitrided 2024 Al alloy with a GCr15 ball under 2 N for 1200 s

Actually, in the present study, the wear resistance of the samples could be improved by increasing the surface hardness of the outer $TiN_{0.3}$ layer.

Figure 9 displays the SEM morphologies of the wear surfaces of the untreated and nitrided samples under different gas mixture. Obviously, the width of the wear track decreases with increasing the volume fraction of N_2 in the gas mixture, which is in agreement with the results of wear rate. As seen from Fig. 9a, large grooves and material smearing are observed on the wear surface of the untreated Al alloy. Such is the typical characteristics of the severe adhesion wear between the steel count face and the soft Al alloy substrate. As for the nitrided surfaces, apparent ploughing with craters is visible on the wear surfaces in Fig. 9b–d. Such typical features of abrasive wear are attributed to the abrasive particles detached from $TiN_{0.3}/Al_3Ti/Al_{18}Ti_2Mg_3$ layers under the cyclic contact force.

As can be seen from Fig. 10, the wear debris of the untreated Al alloy shows large flake-like particles with stratified structure (Fig. 10a), while the nitrided samples exhibits much smaller debris with the mixture of large sheets and small particles in Fig. 10b–c. In addition, the wear debris of the samples nitrided under $50\%N_2 + 50\%H_2$ becomes much finer compared with the samples nitrided under $15\%N_2 + 85\%H_2$. Actually, some flake-like particles in Fig. 10b–c might result from the adhesive wear between the steel counter face and the surface layers.

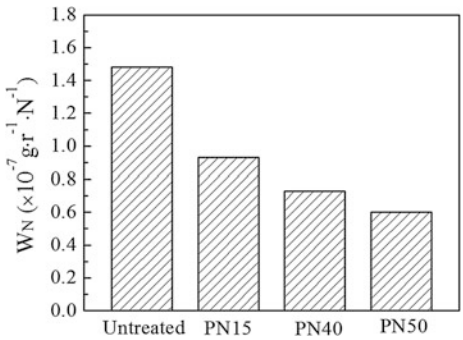

Fig. 8 Wear rate of uncoated and nitrided 2024 Al alloy with a GCr15 ball under 2 N for 1200 s

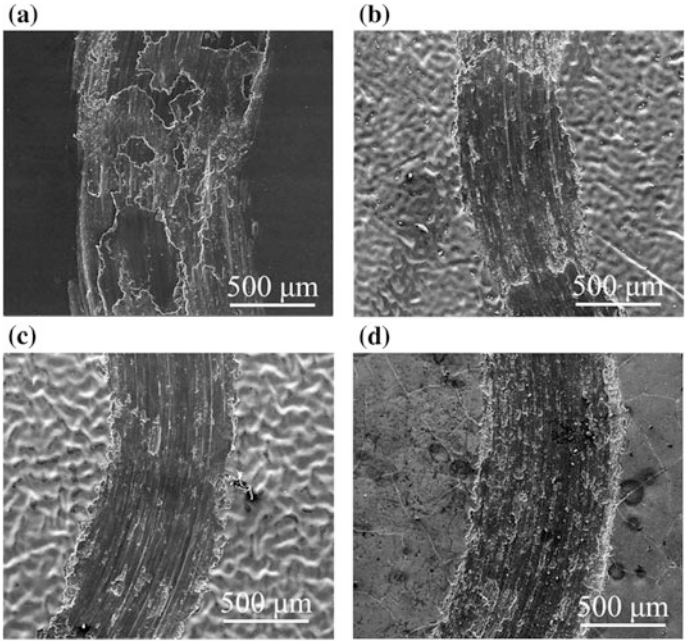

Fig. 9 Worn surfaces of 2024 Al alloy nitrided under different atomsphere at 490 °C for 8 h: **a** untreated, **b** PN15, **c** PN40 and **d** PN50

Figure 11 shows the magnified SEM images of the wear debris and the corresponding EDS analysis is summarized in Table 1. The wear debris in Fig. 11a exhibit the sharp-angled feature, while the debris in Fig. 11b look cotton-shaped. Thus, it can be inferred that spalling or detaching mostly occurs for the case in Fig. 11a, while the accumulative rolling of the hard particles to form the fine particles in Fig. 11b. According to Table 1, the wear debris contain high amount of O, indicating the oxidation during the wear test. The high amount of Ti and N indicates the nitride particles for the marked Area A and C. The high amount of Al and Ti indicates the aluminide particles for the marked area B and D. Therefore, based on the above analysis, the nitrides samples exhibit mainly abrasive wear accompanied with the adhesive wear and oxidation wear.

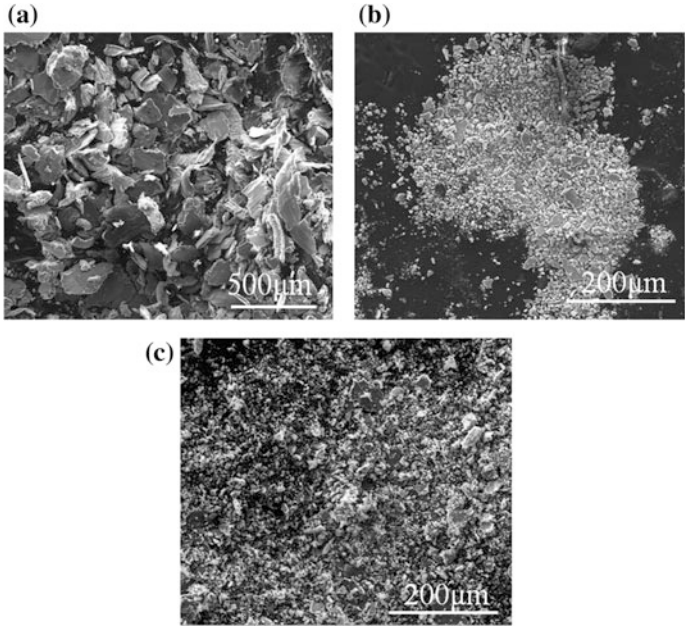

Fig. 10 Wear debris of 2024 Al alloy nitrided under different atomsphere at 490 °C for 8 h: **a** untreated, **b** PN15 and **c** PN50

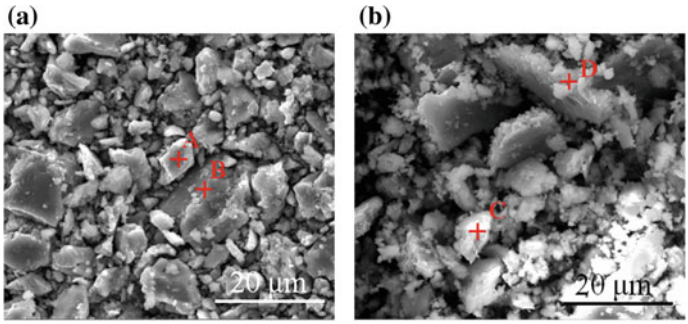

Fig. 11 Magnified SEM images of wear debris in Fig. 10b–c: **a** PN15 and **b** PN50

Table 1 EDS results of wear debris in Fig. 11

Elements (at.%)	N	O	Mg	Al	Ti	Fe	Cu
A	17.60	10.38	4.42	33.05	34.08	0.27	0.21
B	2.46	1.51	11.73	75.75	8.23	–	0.32
C	21.22	22.66	1.46	9.64	44.50	0.30	0.22
D	6.51	27.44	1.93	27.91	35.51	0.32	0.38

Summary

In this study, the duplex surface treatments via depositing Ti film followed by plasma nitriding have been employed on the surface of 2024 Al alloy. The effects of nitriding atmosphere on the microstructure evolution, hardness and wear behavior of the as-obtained surface layer have been investigated. The following conclusions can be drawn:

(1) Nitride/aluminide multilayer coatings have been fabricated by plasma nitriding Ti-coated 2024 Al alloys. The as-obtained coatings are composed of the outer $TiN_{0.3}$ layer and inside intermetallic layer (Al_3Ti and $Al_{18}Ti_2Mg_3$). The outer $TiN_{0.3}$ phase exhibites the (002) preferred orientation. The peak ratio $I_{(002)}/I_{(100)}$ of the outer $TiN_{0.3}$ phase increases with increasing N_2 content in gas mixtures. Plasma nitriding leads to dense nitride surface on 2024 Al alloy. High content of N_2 in gas mixtures results in the formation of larger nitride particles. The samples nitrided under 40%N_2 + 60%H_2 reaches the maximum thickness of multilayer coating.

(2) The surface hardness of 2024 Al alloy is improved remarkably by nitride/aluminide multilayer coatings and increases with the elevated volume fraction of N_2 in gas mixtures. The samples nitrided under 50%N_2 + 50%H_2 reaches the maximum hardness of 630 HV. The N_2–H_2 ratio has no obvious effect on friction coefficient of nitride/aluminide coatings. The stable COFs of coatings is about 0.32, much lower than the untreated Al alloy (0.45). The wear rate of coatings decreases with the elevated N–H ratio. The wear mechanism of the nitrided 2024 Al alloy exhibites the mixture feature of abrasive wear and adhesive.

Acknowledgements The authors gratefully acknowledge the National Natural Science Foundation of China (Grant No. U1537201), Natural Science Foundation of Tianjin (Grant No. 16JCQNJC03500), Natural Science Foundation of Hebei Province (Grant No. E2017202066) for the financial support of this research work.

References

1. H. Tang, Z. Cheng, J. Liu et al., Preparation of a high strength Al-Cu-Mg alloy by mechanical alloying and press-forming. Mater. Sci. Eng., A **550**(31), 51–54 (2012)
2. F. Khodabakhshi, A. Simchi, A.H. Kokabi, Surface modifications of an aluminum-magnesium alloy through reactive stir friction processing with titanium oxide nanoparticles for enhanced sliding wear resistance. Surf. Coat. Technol. **309**, 114–123 (2017)
3. M. Moradshahi, T. Tavakoli, S. Amiri et al., Plasma nitriding of Al alloys by DC glow discharge. Surf. Coat. Technol. **201**(3), 567–574 (2006)
4. F.F. Wei, W. Zhang, T. Zhang et al., Effect of variations of Al content on microstructure and corrosion resistance of PEO coatings on Mg Al alloys. J. Alloy. Compd. **690**, 195–205 (2017)

5. G. Hou, Y. An, X. Zhao et al., Improving interfacial, mechanical and tribological properties of alumina coatings on Al alloy by plasma arc heat-treatment of substrate. Appl. Sur. Sci. **411**, 53–66 (2017)
6. A. Fateme, H. Savaloni, Surface nanostructure modification of Al substrates by N^+ ion implantation and their corrosion inhibition. T. Nonferr. Metal. Soc. **27**(3), 701–710 (2017)
7. H.C. Man, S. Zhang, T.M. Yue et al., Laser surface alloying of NiCrSiB on Al6061 aluminium alloy. Surf. Coat. Technol. **148**(2), 136–142 (2001)
8. V.H. Baggio-Scheid, G. de Vasconcelos, M.A.S. Oliveira, Duplex surface treatment of chromium pack diffusion and plasma nitriding of mild steel. Surf. Coat. Technol. **163–164**, 313–317 (2003)
9. F. Haftlang, A. Habibolahzadeh, M.H. Sohi, Comparative tribological studies of duplex surface treated AISI 1045 steels fabricated by combinations of plasma nitriding and aluminizing. Mater. Des. **60**, 580–586 (2014)
10. F. Haftlang, A. Habibolahzadeh, M.H. Sohi, Improving electrochemical properties of AISI 1045 steels by duplex surface treatment of plasma nitriding and aluminizing. Appl. Sur. Sci. **329**, 240–247 (2015)
11. Z.D. Liu, X.C. Zhang, F.Z. Xuan, Z.D. Wang, S.T. Tu, Process technological aspects of the production and properties of in situ combined plasma-nitrided and PVD hard-coated high alloy tool steels. Mater. Des. **37**, 268–273 (2012)
12. Z.D. Liu, X.C. Zhang, F.Z. Xuan et al., In situ synthesis of TiN/Ti_3Al intermetallic matrix composite coatings on Ti6Al4V alloy. Mater. Des. **37**, 268–273 (2012)
13. N. Daemi, F. Mahboubi, H. Alimadadi, Effect of plasma nitriding on electrodeposited Ni-Al composite coating. Mater. Des. **32**, 971–975 (2011)
14. H.C. Man, S. Zhang, F.T. Cheng, Improving the wear resistance of AA 6061 by laser surface alloying with NiTi. Mater. Lett. **61**, 4058–4061 (2007)
15. A. Almeida, M. Anjos, R. Vilar et al., Laser alloying of aluminium alloys with chromium. Surf. Coat. Technol. **70**(2–3), 221–229 (1995)
16. F.Y. Zhang, M.F. Yan, Microstructure and mechanical properties of multiphase layer formed during depositing Ti film followed by plasma nitriding on 2024 aluminum alloy. Appl. Sur. Sci. **301**, 410–417 (2014)
17. F.Y. Zhang, M.F. Yan, Surf. Coat. Technol. **253**, 268–276 (2014)
18. M.F. Yan, R.L. Liu, Influence of process time on microstructure and properties of 17-4PH steel plasma nitrocarburized with rare earths addition at low temperature. Appl. Sur. Sci. **256**, 6065–6071 (2010)

Microstructure and Welding Performance of Sn–Ag–Cu Material

Zhigang Kong and Yilin Zhou

Abstract The research on the lead-free solder materials has been a hot topic in electronic packaging industry. Among the lead-free solder materials, Sn–Ag–Cu alloys is potential substitutes for conventional Sn–37Pb solder. The alloys have advantages of good wetting property, superior interfacial properties and high creep resistance. In this article, the organization and welding performance of Sn–Ag–Cu Material were investigated. The experimental results showed that the microstructure of Sn–Cu solder contained a large number of Cu_6Sn_5 phase, while the main phase in Sn–Ag–Cu alloys was Ag_3Sn intermetallic compound which was floc and β-Sn primary crystals, but no Cu_6Sn_5 phase existed.

Keywords Lead-free solder · Organization · Welding performance IMC

Introduction

With the increasing focus on environmentally benign development of electronic packages, Pb-free alloys have received a great deal of attention. The harmful effects of Pb on the environment and human health accelerated the research and development toward a full transition to Pb-free solder technology [1, 2]. And therefore the reliability of electronic products based in the lead-free solder alloy is always an important issue for concerning. Since Sn–Cu based solder alloy has good weldability it has been used as a high temperature solder for production and the attention has been paid on the Sn–Cu alloy [3, 4]. All the Pb-free solders are potential substitutes for conventional Sn–37Pb solder. Among them the most promising ones are undoubtedly Sn–Ag–Cu ternary alloys, which have advantages of good wetting property, superior interfacial properties, high creep resistance and low coarsening rate [5, 6].

Z. Kong (✉) · Y. Zhou
Research Laboratory of Electrical Contacts and Connectors, Beijing University of Post and Telecommunications, Beijing 100876, China
e-mail: zgkong@bupt.edu.cn

© Springer Nature Singapore Pte Ltd. 2018

Y. Han (ed.), *Advances in Materials Processing*, Lecture Notes in Mechanical Engineering, https://doi.org/10.1007/978-981-13-0107-0_2

Sn–Ag–Cu alloy with a small amount Ag addition in Sn–Cu alloy is ternary alloy. It has been found that the addition of Ag can reduce the melting temperature and improve the mechanical properties of the solder. The experimental results show that the formation of intermetallics between lead-free solder and substrate compound (IMC: Intermetallic Compound) layer is one of the important issues to affect the reliability of solder joints. Moreover, in the case of electronic products, IMC layer will change [7–9]. The interface between the amount of the thickness of the interconnect metal compound is a sign of a good weld. However IMC phase has intrinsic brittleness the thick layer of IMC will result in reducing mechanical properties of the solder joint. This will have a direct impact on the reliability of the interconnection. Therefore studying the morphology and distribution of IMC within solder interface area is very important.

In this paper, Sn–Ag–Cu alloy was selected as the solder Cu and Au/Ni/Cu as the substrate respectively, and the welding process, the formation and growth behaviors of the intermetallic phases at the interfaces of these solder joints were investigated. The effect of aging parameters on the growth of the IMC, and hence on solder joint quality was discussed.

Experimental Procedure

After welding, the samples cut from the cross-section of the interface were prepared for microstructure observation. The etchant consisting of 90% C_2H_5OH–7% HNO_3–3%HCl was used to reveal the cross-sectional microstructure. The morphology and composition of the tested specimens were examined by scanning electron microscope (SEM) and energy dispersive spectroscopy (EDS). At least five measurements for each compositional analysis were performed to obtain the average value.

Three solder alloys, Sn–Cu, Sn–Ag3–Cu0.5 (96.5 wt% Sn, 3.0 wt% Ag and 0.5 wt% Cu) and two substrates of pure Cu and 0.5Au–1.5Ni–Cu (gold plating 0.5 μm, nickel plating 1.5 μm) were selected in the present investigation).

Results and Discussion

Microstructure of the Alloy

Figure 1 shows the microstructure of the lead-free solder Sn–Cu alloy As shown in Fig. 1 that a large number of white granular particles in homogeneously distributed in the alloy. According to the binary Sn–Cu eutectic phase diagram, Sn–Cu solder alloy is mainly composed of primary β-Sn crystalline and eutectic, the white particles precipitated in the eutectic is η-(Cu_6Sn_5), and the eutectic structure is located in the gap among the β-Sn dendrites.

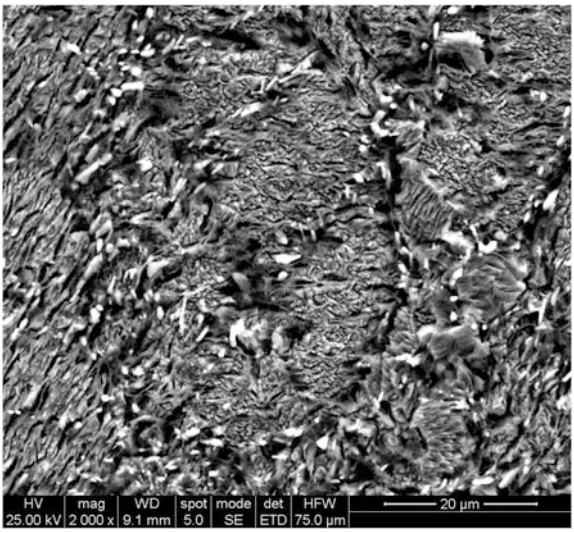

Fig. 1 SEM morphologies of Sn–Cu0.7 solder alloy

Figure 2 is the SEM morphology of Sn–Ag3–Cu0.5 solder. It can be seen that the microstructure contained a large number of floc structure. EDS analysis results (as shown in Table 1) showed that the element Cu didn't existed in the floc structure, and the flocculent phase was Ag_3Sn Intermetallic phase. It was found that the addition of Ag increased the Ag_3Sn formation trend. When Ag content was less than 3.2 wt%, Ag_3Sn was not easy to be detected. The Sn–Ag eutectic composition is Sn–3.5Ag, and the eutectic phase formed by β-Sn phase and fine Ag_3Sn [10, 11]. It has been observed that the uniformly dispersed fine Ag_3Sn in Sn can improve the mechanical properties of the solder [12].

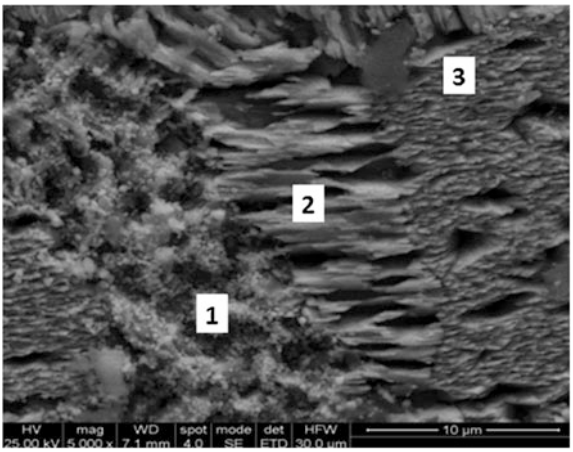

Fig. 2 SEM morphologies of Sn–Ag3–Cu0.5 alloy

Welding Performance

Figure 3 shows the microstructure of Sn–Ag3–Cu0.5/Cu joint interface. It can be found that η-Cu_6Sn_5 immediately formed when the liquid molten solder contacts with the solid phase Cu, and there are holes between Cu_6Sn_5 phase and the Cu substrates. These small holes between IMC and Cu substrate are very small at initial, generally difficult to be observed. So they are often ignored, but they will grow under the stress which caused from the contact failure.

Figure 4 shows the microstructure of Sn–Ag3–Cu0.5/0.5Au–1.5Ni–Cu solder interface area. Au layer on the Ni layer was very thin, and will be very easy to completely dissolve the solder when touching the liquid solder. Au in the solder first formed metallic compound $AuSn_4$ which is not the very stable structure [13, 14]. Subsequently, Ni will be diffused to solder to form Ni–Sn IMC [15]. Since the Ni layer is very thin, as the reaction proceeds Cu layer will join to the reaction after Ni layer depleted, which will provide a lot of Cu elements to generate (Cu, Ni)$_6Sn_5$ intermetallic compound, and hence Ag_3Sn diffuse between solder and substrate interface to become thick, partial formation of the lumps. The results show that the lead-free solder composition greatly influence the interconnect interface IMC tissue component, and tiny differences in Ag solder will bring great impact on IMC formation process and the tissue components. Thus, the IMC produced during the interface reaction will be different which is depended on the Ag content.

Table 1 Composition of Sn–Ag3–Cu0.5 alloy

Element (wt%)	Sn	Ag	Cu
1	79.95	19.86	0.19
2	98.88	0.95	0.06
3	97.64	1.64	0.72

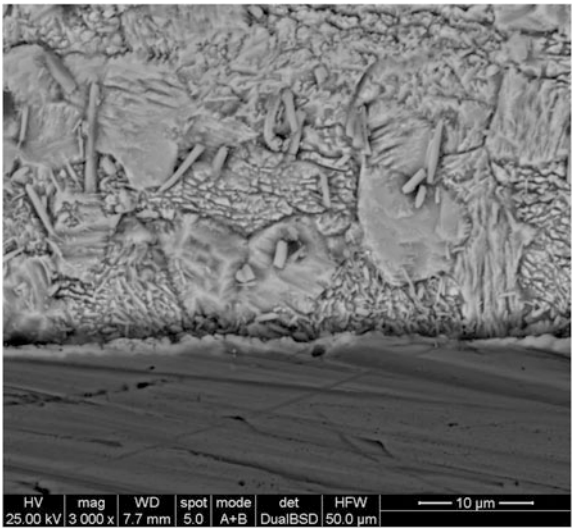

Fig. 3 Interface of Sn–Ag3–Cu0.5/Cu solder joint

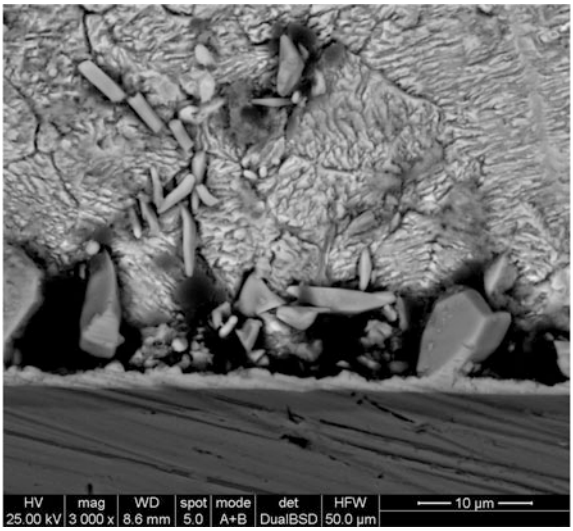

Fig. 4 Interface of Sn–Ag3–Cu0.5/0.5Au–1.5Ni–Cu solder joint

Summary

1. Sn–Cu solder contains a large number of Cu_6Sn_5 phases, while Sn–Ag–Cu contains IMC Ag_3Sn phase and β-Sn primary crystals with the solder organization of floc like without Cu_6Sn_5 phase.
2. For the Sn–Ag–Cu solder, different solder substrates have different welding properties. For Cu solder substrate, there is a small hole in the welding interface. For the gold plated substrates, there are a large number of the IMC graphic, in the welding interface, which may reduce the reliability of electrical connection.

Acknowledgements The study is financially supported by the National Natural Science Foundation of China (No. 61674017).

References

1. C.M. Gourlay, K. Nogita, S.D. McDonald, A rheological assessment of the effect of trace level Ni additions on the solidification of Sn–0.7Cu. Scripta Mater. **54**, 1557–1562 (2010)
2. C.M. Gourlay, J. Read, K. Nogita, The maximum fluidity length of solidifying Sn–Cu–Ag–Ni solder alloys. J. Electron. Mater. **37**, 51–60 (2012)
3. H.L. Pang, B.S. Xiong, T.H. Low, Low cycle fatigue study of lead free 99.3Sn–0.7Cu solder alloy. Int. J. Fatigue **26**, 865–872 (2004)
4. J.W. Yoon, Y.H. Lee, D.G. Kim, Intermetallic compound layer growth at the interface between Sn-Cu-Ni solder and Cu substrate. J. Alloys. Compd. **381**, 151–157 (2004)
5. H.K. Sung, J.M. Kim, S. Yoo, Curr. Appl. Phys. **13**, 103–107 (2013)
6. E.H. Amalu, W.K. Lau, N.N. Ekere, Microelectron. Eng. **88**, 1610–1617 (2011)

7. H. Naoyuki, U. Tokuteru, T. Yorinobu, Effects of Zn addition and aging treatment on tensile properties of Sn–Ag–Cu alloys original research article. J. Alloys Compd. **527**, 226–232 (2012)
8. K. Nogita, J. Read, T. Nishimura, Microstructure control in Sn-0.7mass%Cu alloys. Mater. Trans. **46**, 2419–2425 (2005)
9. K. Fakpan, Y. Otsuka, Y. Mutoh, Creep-fatigue crack growth behavior of Pb-contained and Pb-free solders at room and elevated temperatures. J. Proc. Eng. **10**, 1238–1243 (2011)
10. H. Nishikawa, J.Y. Piao, T. Takemoto, Microstructure of interface between Sn–Cu solder with Ni and Cu plate. J. JPN. I. MET. **70**, 427–433 (2011)
11. H. Nishikawa, J.Y. Piao, T. Takemoto, Interfacial reaction between Sn-0.7Cu solder and Cu substrate. J. Electron. Mater. **35**, 1127–1132 (2006)
12. D. Ma, W.D. Wang, S.K. Lahiri, Scallop formation and dissolution of Cu-Sn intermetallic compound during solder reflow. Appl. Phys. **91**, 3312–3317 (2012)
13. F. Ochoa, X. Deng, N. Chawla, Effects of cooling rate on creep behavior of a Sn-3.5 Ag alloy. J. Electron. Mater. **33**, 1592–1607 (2004)
14. J.X. Wang, S.B. Xue, D.S. Fang, Trans. Nonferrous Met. Soc. China **16**, 1374–1378 (2006)
15. K.S. Kim, S.H. Huh, K. Suganuma, Effects of intermetallic compounds on properties of Sn-Ag-Cu lead-free soldered joints. J. Alloys Compd. **352**, 226–236 (2009)

Enhanced Corrosion Resistance of 6063 Aluminum in Surface Modification Using γ-Aminopropyl Triethoxysilane

Linlin Zhang, Jinwei Wang, Jixue Zhou, Haihua Zhuang, Jianhua Wu, Baichang Ma and Shouqiu Tang

Abstract The corrosion protection of 6063 aluminum with film of 3-aminopropyl triethoxysilane was studied in this paper. Electrochemical tests in neutral 3.5% (wt %) NaCl solution, scanning electronic microscopy (SEM), energy dispersive spectroscopy (EDS), and confocal laser scanning microscope (CLSM) were performed. The result showed that the silane films could offer unexceptionable corrosion resistance to metal. A highly crosslinked and dense interfacial layer formed on the surface of the metal, which makes the substrate and the coating firmly combined to reduce the corrosion current density and inhibit the occurrence of corrosion. The film with bridging group had excellent hydrophobicity which can heavily restrict corrosion product proceeds at the interface.

Keywords Silane treatment · Corrosion resistance · Silane film Aluminum alloy

L. Zhang · J. Wang · J. Zhou (✉) · S. Tang
Shandong Key Laboratory for High Strength Lightweight Metallic Materials (HLM), Advanced Materials Institute, Shandong Academy of Sciences, Jinan 250014, China
e-mail: zhoujx@sdas.org

L. Zhang
e-mail: zhlinlin@sdas.org

J. Wang
e-mail: wjinw@sdas.org

S. Tang
e-mail: tangshq@sdas.org

H. Zhuang · J. Wu · B. Ma
Shandong Engineering Research Center for Lightweight Automobiles Magnesium Alloys, Advanced Materials Institute, Shandong Academy of Sciences, Jinan 250014, China
e-mail: 1021656314@qq.com

J. Wu
e-mail: jianhw@sdas.org

B. Ma
e-mail: mabch@sdas.org

© Springer Nature Singapore Pte Ltd. 2018

Y. Han (ed.), *Advances in Materials Processing*, Lecture Notes in Mechanical Engineering, https://doi.org/10.1007/978-981-13-0107-0_3

Introduction

In the traditional metal-finishing industries, many protection methods have been applied to enhance the corrosion resistance of the aluminum. Chromium conversion treatment has been extensively used for aluminum to achieve good corrosion resistance, because of its good protective effect and mature technology [1]. Nevertheless, on account of the excellent performance of the films were connected with hexavalent chromium, which has been reported to be carcinogenic, and unable to meet the needs of green technology [2, 3]. Recently, many organosilane surface treatments have been investigated for metals pretreatment and it was found that the silane coating is more environmentally friendly [4]. The silane surface technology of metal has been regarded as one of the promising alternatives for chromates in recent years. Silanes are organofunctional hybrid organic-inorganic chemicals, with the general structure of $Y(CH_2)nSi(OX)_3$, which OX is hydrolyzable alkoxy group, for example, methoxy (OCH_3) or ethoxy (OC_2H_5); and Y is organofunctional group such as amino (NH_2) which is responsible for a good adhesion between metal and paint [5–7]. However, silane film is not only can improve adherence between substrate and paint coating but also as a pretreatment can improve the barrier properties and filiform corrosion resistance to protect metal efficiently against corrosion [8, 9].

In a dilute silane solution (e.g. 2–5 vol.%), water or water/alcohol mixture complete the hydrolysis of alkoxy groups into hydrophilic silanols (SiOH) over a period of time. When the quantity of hydrophilic silanols (SiOH) is enough, dip metals into the dilute silane solution for a while, followed by drying in high temperature heat curing. It is generally assumed that these hydrophilic silanols (SiOH) groups are readily absorbed onto the metal surface in the dilute silane solution, and via drying, silane molecules bond firmly to metal by covalent metallo-siloxane bonds (MeOSi), which is obtaining through the condensation reaction between hydrophilic silanols group (SiOH) and the metal hydroxyls group (MeOH) [10, 11].

The reaction of hydrolysis and condensation balances taking place in the solution according to the following schematic equations:

$$\text{–Si–O–R} + H_2O \rightarrow \text{–Si–OH} + \text{R–OH}. \tag{1}$$

$$\text{R–Si–OH} + \text{R–Si–OH} \leftrightarrow \text{R–Si–O–Si–R} + H_2O. \tag{2}$$

$$\text{R–Si–O–Si–R} + \text{R–OH} \leftrightarrow \text{R–Si–O–R} + \text{R–Si–OH}. \tag{3}$$

Reactions above show the importance of the presence of water in the condensation reactions that are taking place between the silane and the metallic surface, and which will take place on the aluminum surface according to the following reactions:

$$3R\text{–}Si\text{–}OH + (OH)_3 \equiv Al \rightarrow (R\text{–}Si\text{–}O)_3 \equiv Al + 3H_2O. \quad (4)$$

$$3R\text{–}Si\text{–}O\text{–}CH_3 + (OH)_3 \equiv Al\ (R\text{–}Si\text{–}O)_3 \equiv Al + 3CH_3OH. \quad (5)$$

The complete characterization of the silane layers is researched, which is formed on aluminum alloy under silane condition. These silane coatings will be used as pretreatment of aluminum alloys to enhance the resistance of the alloy and the increase the interface bonding strength.

Experimental Methods

The silane used was γ-aminopropyl triethoxysilane, with an approximate purity of 98%. Hydrolysis was performed in the presence of deionized water and ethanol (ethanol/deionized water/silane 40/55/5), the pH of the alkaline silane solution was adjusted to 8 with the addiction of acetic acid to control the self condensation tendency. Constant stirring during all the hydrolysis process, that was studied up to 4 h.

6063 aluminum alloy panels were used as substrate for this work, the composition of it given in Table 1. They were abraded with abrasive papers starting from 800 to 2000 grit size, rinsed with deionized water, and then followed by acetone degreasing. The alkaline surface activation was performed through 1 min dipping in 5 g/L NaOH solution at 60 °C, which can provide an alkaline etching and a chemical activation of the surface, leading to the formation of a high surface density of hydroxyl group on the metal sample to combine with the Al–OH bonds in the silane solution. The substrates were then rinsed in deionized water and bloe-dried with compressed air.

Dipping the aluminum alloy substrate into the hydrolyzed silane solution for 2 min, and then cured at 180 °C for 40 min to obtain a dried film. The silaned substrates were analyzed by means of electronic microscopy (SEM), energy dispersive spectroscopy (EDS) and confocal laser scanning microscope.

Results and Discussion

The surface morphology of the silane films was characterized by Electronic microscopy (SEM) were showed in Fig. 1a, contrasting with the aluminum alloy's surface morphology without silane films showed in Fig. 1b. Continuous coverage is

Table 1 The composition of 6063 aluminum alloy

Elements	Cu	Si	Fe	Mn	Mg	Zn	Cr	Ti	Al
Content	0.1	0.2–0.6	0.35	0.1	0.45–0.9	0.1	0.1	0.1	Remain

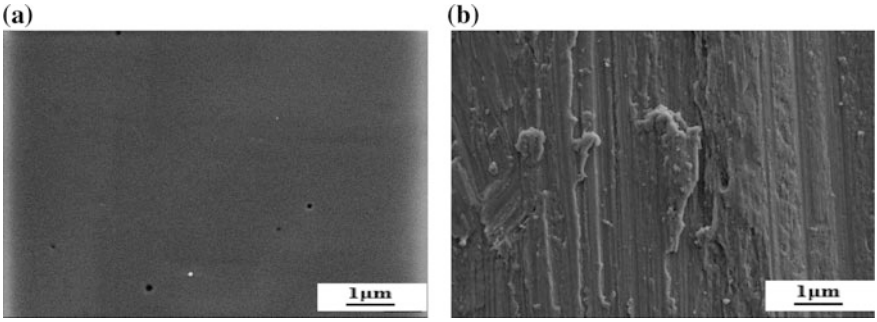

Fig. 1 SEM images of silane coating on Aluminum alloy substrate. **a** The substrate with silane treatment. **b** The substrate without silane treatment

found on dip-coated film (Fig. 1a), which leads to high uniformity. Contrasting with the surface morphology of the aluminum alloy without silane films (Fig. 1b) which is uneven and non-uniformity, the film deposited on the aluminum alloy substrate have no scratch, more dense and the surface is very smooth, as well as the surface pores filled by silane films can significantly reduce the pore depth. The surface of aluminum alloy was covered by a continuous, uniform film, which was benefit for subsequent coating's adhesion.

In Fig. 2 energy spectrum (EDS) analysis of the silane substrate was studied, as we could see, 30.20% Si elements contained in the film, illustrating the surface of aluminum alloy was generated with a layer of colorless transparent silane film. At the same time, it could be seen silane film consist of C, O, Si and other elements.

In Fig. 3 the potentiodynamic polarization curves of the silane film were reported. In order to quantitative analysis of the sample's corrosion resistance,

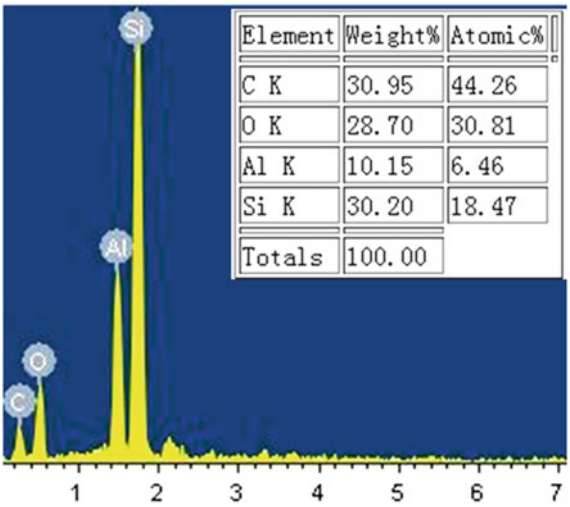

Element	Weight%	Atomic%
C K	30.95	44.26
O K	28.70	30.81
Al K	10.15	6.46
Si K	30.20	18.47
Totals	100.00	

Fig. 2 EDS analysis of the silane substrate

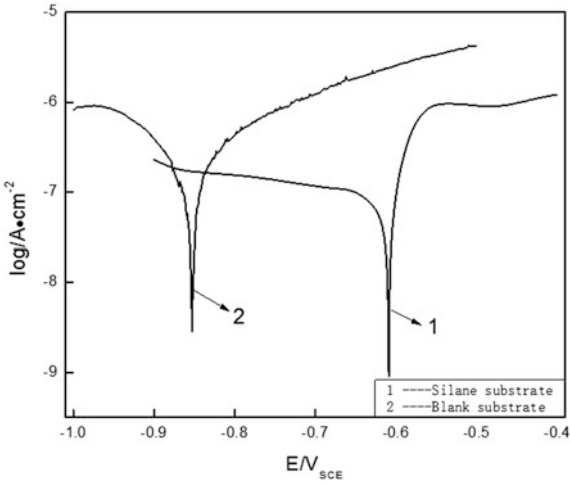

Fig. 3 The potentiodynamic polarization curves of the substrates

Table 2 The fitting data of potentiodynamic polarization curves

Substrate	E_{corr} (V)	I_{corr} (A cm^{-2})
Silane substrate	−0.608	9.290×10^{-8}
Blank substrate	−0.852	1.164×10^{-6}

simulating the data of Fig. 3, showed in Table 2. In Fig. 3 we obtained that the substrate with silane treatment had a lower corrosion density, achieved to 9.290×10^{-8} A cm^{-2}, as well as had a more positive corrosion voltage, up to −0.608 V. However, the blank substrate had a higher corrosion density, and also had a more negative corrosion voltage, that we studied respectively up to 1.164×10^{-6} A cm^{-2} and −0.852 V. As far as we know, the substrate had lower corrosion current density and more positive corrosion voltage, the corrosion resistance of the substrate is better. So, the substrate with silane treatment had a better corrosion resistance.

In Fig. 4 three-dimensional figure of the silane film was present by confocal laser scanning microscope (CLSM). We could intuitive see the surface morphology of the silane film. In the three-dimensional figure, the darker position represented the lower height. Rugged peak made the silane film and the substrate fit together, not only keep the substrate forming corrosion resistance, but also strengthen the binding force. The silane film as an intermediary to the combination of substrate and coating firmly together.

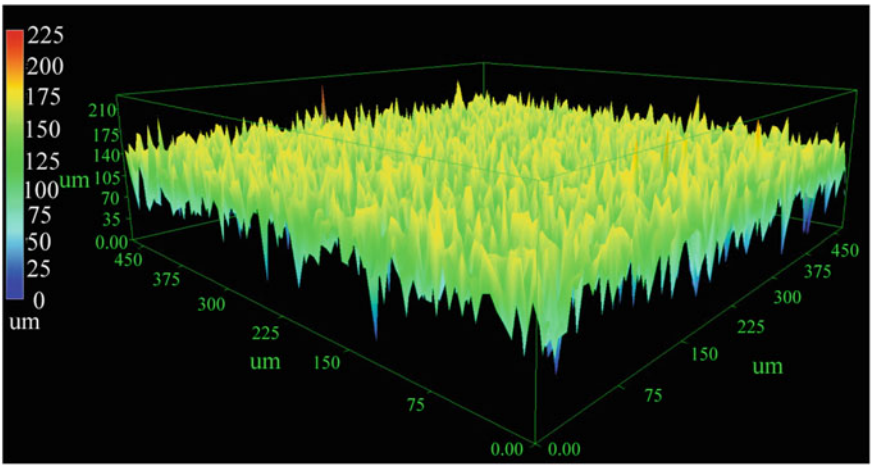

Fig. 4 The three-dimensional figure of the silane film by confocal laser scanning microscope (CLSM)

Summary

According to this study, it is possible to deposit silane layer on aluminium substrates and therefore to pretreat multi-metal systems. To obtain the better deposition it is necessary to cure at high temperature (180 °C) for 40 min, the silane layer producing a very protective coating.

SEM images and EDS images indicate that continuous coverage is found by silane treatment, The aluminum alloy was covered by a continuous, uniform film, which consisted of C, O, Si and other elements. The potentiodynamic polarization curves show that the substrate with silane treatment has a great corrosion resistance. CLSM image shows that the silane film and the substrate can fit together by rugged peak.

Acknowledgements This research was financially supported by National Key Research and Development Plan (2017YFB0103904) and the Natural Science Foundation of Shandong Province (ZR2017PEE007).

References

1. Y.Y. Yue, Z.X. Liu, T.T. Wang et al., Effect of phosphate-silane pretreatment on the corrosion resistance and adhesive-bonded performance of the AZ31 magnesium alloys, J. Prog. Org. Coat. **76**, 835–843 (2013)
2. M. Pantoja, B. Díaz-Benito, F. Velasco et al., Analysis of hydrolysis process of γ-methacryloxypropyltrimethoxysilane and its influence on the formation of silane coatings on 6063 aluminum alloy. J. Appl. Surf. Sci. **255**, 6386–6390 (2009)

3. A. Eshaghi, A. Eshaghi, Effect of chromate conversion coatings on the adhesion and corrosion resistance of painted 5083 aluminum alloy. J. Mater. Sci. **48**, 171–175 (2012)
4. M. Trueba, S.P. Trasattti, Pyrrole-baed silane primer for corrosion protection of commercial Al alloys. PartII: corrosion performance in neutral NaCl solution. J. Prog. Org. Coat. **66**, 265–275 (2009)
5. D. Zhu, W.J. van Ooij, Corrosion protection of AA 2024-T3 by bis-[3-(triethoxysilyl) propyl] tetrasulfide in sodium chloride solution. Part 2: mechanism for corrosion protection. J. Sci. Direct. **45**, 2177–2197 (2003)
6. A.P. Romano, M. Fedel, F. Deflorian et al., Silane sol–gel film as pretreatment for improvement of barrier properties and filiform corrosion resistance of 6016 aluminium alloy covered by cataphoretic coating. J. Prog. Org. Coat. **724**, 695–702 (2011)
7. W.J. Van Ooij, T. Child, Protecting metals with silane coupling agents. J. Chemtech. **28**, 26–35 (1998)
8. G. Pan, D.W. Schaefer, Wim J. van Ooij et al., Morphology and water resistance of mixed silane films of bis[3-(triethoxysilyl) propyl] tetrasulfide and bis-[trimethoxysilylpropyl] amine. J. Sci. Direct. **515**, 2771–2780 (2006)
9. W.J. Van Ooij, D. Zhu, M. Stacy et al., Corrosion protection properties of organofunctional silanes-an overview. J. Tsinghua Sci. Technol. **10**, 639–664 (2005)
10. L. Calabrese, L. Bonaccorsi, A. Capri, E. Proverbio, Adhesion aspects of hydrophobic silane zeolite coatings for corrosion protection of aluminum substrate. J. Prog. Org. Coat. **77**, 1341–1350 (2014)
11. N. Asadi, R. Naderi, M. Saremi, Determination of optimum concentration of cloisite in an eco-friendly silane sol-gel film to improve corrosion resistance of mild steel. J. Appl. Clay Sci. **95**, 243–251 (2014)

Effect of Dual-Sided Laser Peening Modes on Residual Stress Distribution of Aero-engine Titanium Blades

Peixuan Ouyang, Liangju He, Peijie Li and Guangbao Mi

Abstract For thin-walled structure components, dual-sided laser peening modes greatly affect surface integrity of the components. In this study, simplified compressor blade made of TC17 titanium alloy was chosen as the studied object. The effect of simultaneous and non-simultaneous dual-sided laser peening on residual stress distributions along surface and depth were studied through numerical simulation. The influencing mechanisms of dual-sided laser peening modes on residual stress distribution along depth were investigated by means of wave propagation theory. This study is instructive in parameter choosing for laser peening of thin-walled structure components based on better understanding the effect of dual-sided laser peening modes on residual stress distribution.

Keywords Titanium blades · Simultaneous dual-sided laser peening
Non-simultaneous dual-sided laser peening · Residual stress distribution
Wave propagation

P. Ouyang · P. Li (✉)
State Key Laboratory of Tribology, Department of Mechanical Engineering,
Tsinghua University, Beijing 100084, China
e-mail: lipj@mail.tsinghua.edu.cn

P. Ouyang
e-mail: oypx12@mails.tsinghua.edu.cn

L. He
School of Aerospace, Tsinghua University, Beijing 100084, China
e-mail: helj@mail.tsinghua.edu.cn

P. Ouyang · G. Mi (✉)
AECC Beijing Institute of Aeronautical Materials, Beijing 100095, China
e-mail: miguangbao@163.com

© Springer Nature Singapore Pte Ltd. 2018

Y. Han (ed.), *Advances in Materials Processing*, Lecture Notes in Mechanical Engineering, https://doi.org/10.1007/978-981-13-0107-0_4

Introduction

Laser shock peening (LSP) is considered as an advanced technology with vast applied prospects, such as aviation [1], nuclear [2, 3], automobile [4] and medical industries [5]. It imparts compressive residual stresses (CRS) in metal surfaces by means of laser-generated pressure pulses in order to make treated materials more resistant to fatigue [6], corrosion [7, 8] and wear [9]. Compared with traditional surface enhancement techniques, such as shot peening, LSP could produce lower surface roughness, much deeper penetration of CRS and better controllability in applying the process [10, 11]. As a result, LSP has a distinct advantage in improving the fatigue life and resistance of foreign object damage (FOD) for fans and compressor blades made of titanium alloys.

One of the keys to improving the fatigue life is the distribution of LSP-induced residual stress state since it greatly affects the occurrence of fatigue crack initiation and propagation. X-ray diffraction (XRD) and strain gage hole drilling method are widely used for quantifying residual stress fields in LSP-treated components [12–14]. However, the residual stress along depth of thin-walled components tends to relax during measurement, thus these measuring methods are not quite suitable for blades. Besides, the experimental measurement of residual stress field not only requires that LSP treatment must be actually applied to the components but also costs a lot of time and money to gain the whole residual stress field of the components. Therefore, numerical simulation of laser peening process provides detailed residual stress state overcoming the aforementioned shortcomings and has become trend [15, 16].

Dual-sided laser peening is applied to blades since thin-walled components are prone to deform when applying pressure pulses on only one side. There are two common modes to realize dual-sided laser peening. One is simultaneous dual-sided peening, and the other one is that the upper surface is peened firstly and right after the bottom surface is peened, which is also called "non-simultaneous dual-sided peening". General Electric Company has published patents both about simultaneous and non-simultaneous dual-sided peening [17, 18]. However, it is still confusing that which one of the two modes is better for laser peening of blades. Some hold the opinion that simultaneous dual-sided peening has advantage over the non-simultaneous mode due to less deformation and less spalling near the surface, while some hold the opposite point that simultaneous dual-sided peening is worse than the non-simultaneous mode owing to spalling in the mid-depth. Making a clear knowledge of the stress field distribution state could help better understand merits and demerits of the two peening modes. Zhang et al. studied the stress wave transmission in plates with different thickness in order to understand the residual stress distribution induced by simultaneous dual-sided peening [19]. Nevertheless, the comparison of residual stress distributions caused by simultaneous and non-simultaneous dual-sided peening has not been studied.

With this motivation, the goal of this work is to study the effect of various dual-sided peening modes on the residual stress distribution of TC17 blades by

numerical simulation and explain the differences by means of shock wave transmission theory, which contributes to better understanding the merits and demerits of the two peening modes.

Laser Shock Peening Process

Figure 1 shows the schematic of LSP process. A nanosecond laser with high power density (several GW/cm^2) passes through a layer of transparent material (typically water) and then interacts with an opaque overlay (typically aluminum foil or black tape) on the metal surface, following the evaporation of the opaque overlay and the generation of plasma. The confinement of the transparent material on the plasma leads to the generation of powerful shock waves (1–10 GPa) into the target surface. Plastic deformation occurs generating residual compressive stress on the surface and through the depth of the target when the magnitude of pressure wave exceeds the Hugoniot elastic limit (HEL) of the target materials. Since the opaque overlay protects the target surface from direct laser ablation and thermal effect propagation, laser shock peening is considered as a pure mechanical process.

Finite Element Modeling

Material Model

Laser shock peening is a high-strain-rate process on the order of 10^5–10^7 s^{-1}. At such high strain rate, plastic deformation behavior of materials is related to strain hardening, strain rate effect and thermal softening, which is significantly different from static and quasi-static loading conditions. The Johnson-Cook model

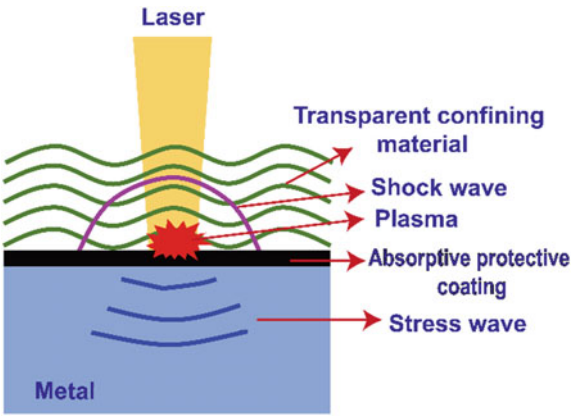

Fig. 1 Schematic of laser shock peening process

Table 1 Input parameters for TC17 titanium alloy

Material	ρ (kg/m^3)	E (GPa)	v	A (MPa)	B (MPa)	n	C	$\dot{\varepsilon}_0$
TC17	4680	112	0.34	1100	590	0.41	0.0152	0.001

(J-C model) is considered as a mature constitutive model [20] and was adopted in this study to model the LSP process. Since LSP process is regarded as a pure mechanical process without thermal effect, the temperature term in J-C model can be removed, as shown in Eq. 1,

$$\sigma = \left(A + B\varepsilon_p^n\right)(1 + C\ln\frac{\dot{\varepsilon}}{\dot{\varepsilon}_0}) \tag{1}$$

where σ is the equivalent von Mises stress, ε_p is the equivalent plastic strain, $\dot{\varepsilon}$ and $\dot{\varepsilon}_0$ represent the experimental and the reference strain rate respectively. *A, B, n* and *C* are the material constant. Constant *A* represents the yield stress at 0.2% offset strain, constant *B* and *n* represent the strain hardening effect. The expression in the second bracket represents the strain rate effect through constant *C*. The constants in J-C model and other input parameters for TC17 titanium alloy used herein are given in Table 1 [21, 22].

Pressure Model

The pressure loading of LSP process is modeled as a transient pressure with a specific spatial profile whose characteristics depend on the laser parameters. For Gaussian laser pulse, the pressure-time history of LSP process was reasonably simplified into a triangular ramp [23]. It was reported that the pressure pulse is 2–3 times of the laser pulse, hence the pressure pulse was set to 50 μs for a 20 μs laser used in this study. The peak pressure was given by Fabbro's model [24],

$$P(\mathrm{GPa}) = 0.01\sqrt{\frac{\alpha}{2\alpha+3}} \times \sqrt{Z(\mathrm{g}\cdot\mathrm{cm}^{-2}\cdot\mathrm{s}^{-1})} \times \sqrt{I_0(\mathrm{GW/cm}^2)} \tag{2}$$

where α is the fraction of absorbed laser energy used for increasing the plasma thermal energy, I_0 is the incident power intensity, and Z is the reduced shock impedance between the target and the liquid medium,

$$2/Z = 1/Z_{\mathrm{liquid}} + 1/Z_{\mathrm{target}} \tag{3}$$

where Z_{liquid} and Z_{target} are the acoustic impedances of liquid medium and target respectively. In this study, the peak pressure was 4 GPa. Therefore, the pressure-time history of the LSP process is as shown in Fig. 2.

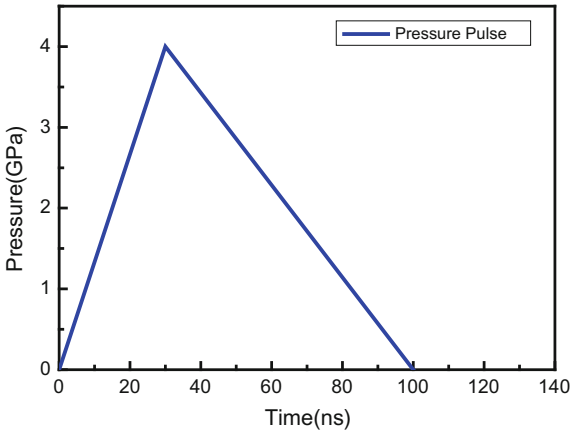

Fig. 2 Pressure-time history of the LSP process

Solution Procedure

The LSP process was simulated by FEM commercial code Abaqus. The component is a simplified compressor blade made. Figure 3a shows the whole component geometry, the upper surface of which is curved and the bottom surface of which is flat. To save computational expense, half of the component was studied as shown in Fig. 3b. The constraint conditions include axial symmetry on ZOY surface and encastre of the block far away from the thin-walled structure. The LSP-treated area is the border region of the blade, the exact size of which is 70 mm (length) × 8 mm (width) × 1–2 mm (thickness). The LSP-treated area has finer elements (0.3 mm by 0.3 mm by 0.02 mm) than the untreated area, as shown in Fig. 3b. There are totally 505,412 C3D8R elements and 536,479 nodes in the model. The border

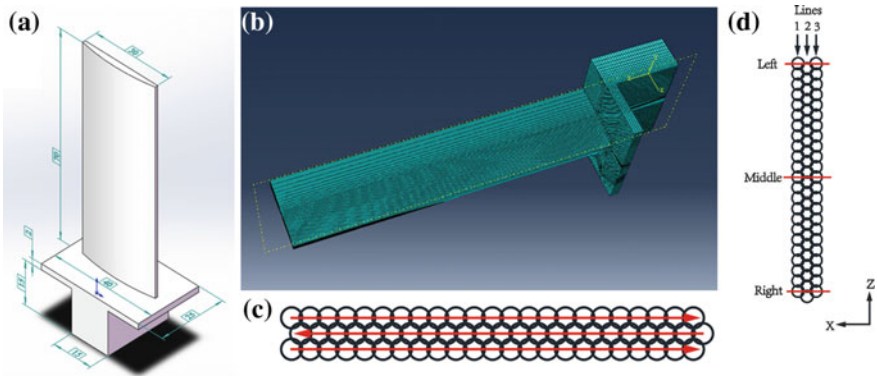

Fig. 3 **a** Whole component geometry of the simplified compressor blade; **b** meshing on the half of the component; **c** the peening path with overlapping rate of 13.4%; **d** the name of the interested regions for further analysis

region was peened according to a common zigzag path with the laser spot of 3.5 mm and overlapping of 13.4%, as shown in Fig. 3c. It contains 69 shots for each surface of the component. Figure 3d gives the names of the lines in the path and the positions of the interested regions.

Typically, laser peening process is firstly simulated using an explicit solution until plastic deformation completes, then the system is imported to an implicit solution to reach equilibrium [23, 25]. However, this "explicit-implicit" procedure becomes difficult to execute for 3D finite element simulations with a large number of laser shots. It needs to import the model between explicit and implicit solutions for every shot. To reduce the computational time, a modified explicit procedure was adopted in this study. The explicit solver runs with domain-parallelization and 50us was adopted as the stabilized time for each shot.

Results and Discussion

Residual Stress Distribution on the LSP-Treated Surface

The uniformity of residual stress distribution on the LSP-treated surface is vital for the fatigue properties of the components. Hence the residual stresses along the three lines (Line 1, 2 and 3 as shown in Fig. 3d) on the upper and bottom surfaces were studied. Figures 4 and 5 show the residual stress distributions on the surfaces treated by simultaneous and non-simultaneous dual-sided laser peening, respectively. (a), (b) and (c) respectively represent the residual stress distributions of line 1, 2 and 3. In these figures, black profiles represent data from the upper surface of the blade, and red profiles represent data from the bottom surface of the blade. As shown in Fig. 4, the residual stresses of the upper and bottom surfaces for every line nearly complete overlap. It indicates that there is a good symmetry in residual stress of upper and bottom surfaces for simultaneous dual-sided laser peening. However, for non-simultaneous dual-sided laser peening, it shows a worse symmetry in residual stress of upper and bottom surfaces than the simultaneous mode, as shown in Fig. 5. Counted from Figs. 4 and 5, the average residual stress and

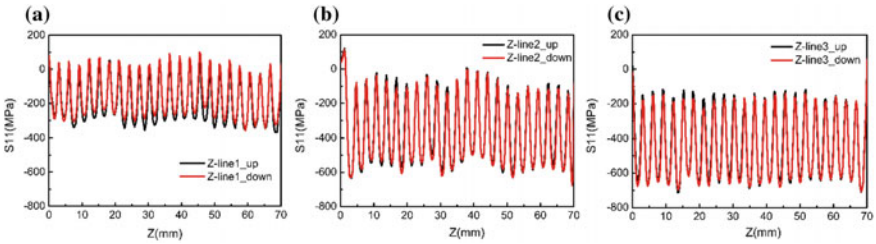

Fig. 4 Residual stress distribution on the upper and bottom surfaces treated by simultaneous dual-sided laser peening. **a** for line 1; **b** for line 2; **c** for line 3

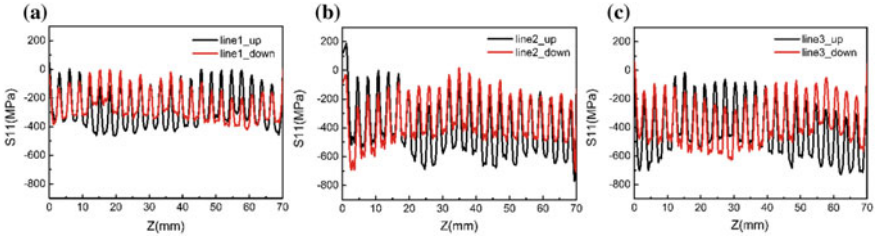

Fig. 5 Residual stress distribution on the upper and bottom surfaces treated by non-simultaneous dual-sided laser peening. **a** For line 1; **b** for line 2; **c** for line 3

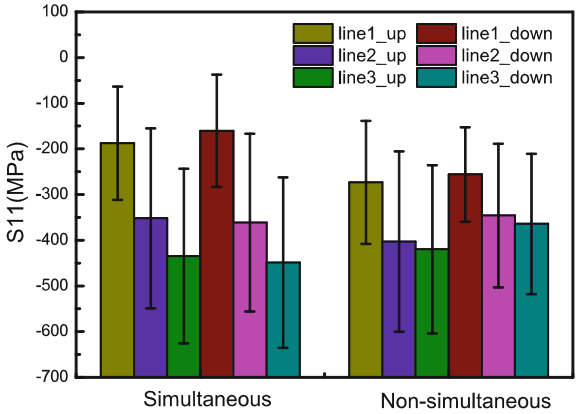

Fig. 6 Average residual stress and relevant standard deviation of every line on the surfaces for two dual-sided laser peening modes

relevant standard deviation of every line for two dual-sided laser peening modes are shown in Fig. 6. It makes clear that simultaneous dual-sided laser peening produces symmetrical residual stress distribution on the upper and bottom surfaces, while the non-simultaneous mode produces higher residual compressive stress on the upper surface than that on the bottom surface. The similar result has been reported that the RCS on the early peening surface was higher than that on the late peening surface. Both for these two modes, the RCS is increased with the peening turns of the lines, the reason for which is not only edge effect but also that the residual compressive stress of the earlier peening area is relieved by the counterbalanced tensile stress induced by the later peening. The large standard deviations of all the lines in Fig. 6 were caused by the less RCS of the overlapping area between two spots, indicating that the overlapping rate of 13.4% is not suitable for the Gaussian laser pulse used in this study.

Residual Stress Distribution Along Depth

Fatigue crack initiation is inseparably linked with the residual stress distributions not only on the treated surface, but also along the depth of the component. Hence the residual stress along the depth at different positions was also studied. Line 1 and Line 3 were selected for study due to large thickness differences. As shown in Fig. 3d, the centers of the far left, middle and far right shots for each line were chosen as the interested position. The residual stress distributions along the depth at the interested positions are shown in Fig. 7, among which, (a) corresponds to the simultaneous dual-sided laser peening and (b) corresponds to the non-simultaneous mode. For each line in each mode, the residual stresses along the depths of the far left, middle and far right shots have good stability. For the simultaneous dual-sided laser peening, the residual stress along the depth of line 1 shows a regular pattern of compressive-tensile-compressive-tensile-compressive-tensile-compressive stress, while the residual stress along the depth of line 2 shows a compressive-tensile-compressive-tensile-compressive stress pattern. For the non-simultaneous dual-sided laser peening, the residual stresses along the depth of both line 1 and line 2 show a regular pattern of compressive-tensile-compressive stress. The depths of the CRS layers are listed in Table 2. For the simultaneous dual-sided laser peening, the depths of CRS layer on the upper and bottom surfaces are close, while for the non-simultaneous mode, the depths of CRS layer on the upper and bottom surfaces have great difference. For line 1, the CRS layer depth of the upper surface is less than that of the bottom surface, while for line 3, the CRS layer depth of the upper surface is greater than that of the bottom surface. The difference of the two dual-sided peening modes in residual stress distribution along depth would influent the fatigue fracture behavior, thus the mechanisms affecting the residual stress distribution along depth for these two modes should be studied. The following section is trying to elaborate the influence mechanisms.

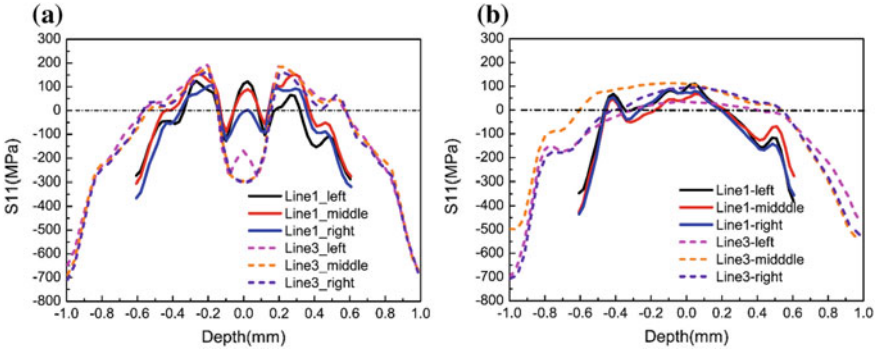

Fig. 7 Residual stress distribution along the depth at the left, middle and right region of line 1 and line 2. **a** Simultaneous dual-sided laser peening; **b** non-simultaneous dual-sided laser peening

Table 2 Depth of compressive residual stress layer for two dual-sided laser peening modes

Peening modes		Left		Middle		Right	
		Upper	Bottom	Upper	Bottom	Upper	Bottom
Simultaneous	Line 1	272	289	177	232	251	246
	Line 3	439	423	469	423	439	423
Non- simultaneous	Line 1	156	394	156	394	156	425
	Line 3	703	607	395	461	627	461

Mechanism of Dual-Sided Laser Peening Modes on Residual Stress Distribution Along Depth

The residual stress distribution along depth is related to plastic deformation, which depends on the shock wave transmission inside the blade. Hence, in order to better understand the residual stress distributions along depth, the shock wave transmission along depth and the corresponding plastic strain for single-spot laser peening on the blade with different thickness were studied. The middle region of line 1 and line 3 were chosen. Since the residual stress distribution patterns along depth of line 1 and line 3 are similar for non-simultaneous dual-sided laser peening, only the middle spot of line 3 was studied for the non-simultaneous peening mode. For the simultaneous peening mode, both the middle spots of line 1 and line 3 were studied.

Figure 8 shows the stress wave transmission along depth for the simultaneous dual-sided laser peening on the middle region of line 3. At 0 μs, two compressive waves start to transmit into the blade from the upper and bottom surfaces. The crests of the two compressive waves reach the upper and bottom surfaces at 40 μs and then gradually decrease during propagation, as shown in Fig. 8a. When the stress waves are stronger than Hugoniot elastic limit (HEL) of TC17 titanium alloy, plastic deformation occurs. Owing to the energy consumption caused by elastic and plastic deformation, the compressive waves are gradually weakened and the plastic deformation amount gradually decreases during wave propagation. The two compressive waves begin to meet at 180 μs and the wave crests completely overlap at 230 μs, leading to the strongest compressive stress (Fig. 8a) and the largest tensile strain of X direction (PE11) in the mid-depth (Fig. 9a). Then the two wave crests separate from each other and continue to transmit along their original transmitting directions, leaving gradually reduced compressive stress and stable plastic strain in the mid-depth (Figs. 8b and 9b). At 410 μs, the compressive waves reach the free surfaces of the blade and are reflected to propagate back into the blade as tensile waves [26], as shown in Fig. 8b. In 430–450 μs, owing to the effect of the reflected tensile waves, compressive plastic deformation along X direction occurs in the region of 0.1–0.3 mm away from each side of the blade, which is embodied in the reduction of PE11 as shown in Fig. 9b. At 540 μs, the two tensile wave crests begin to meet and complete overlap at 590 μs, bringing about strong tensile stress and a reduction in tensile plastic strain of X direction in the mid-depth, as shown in

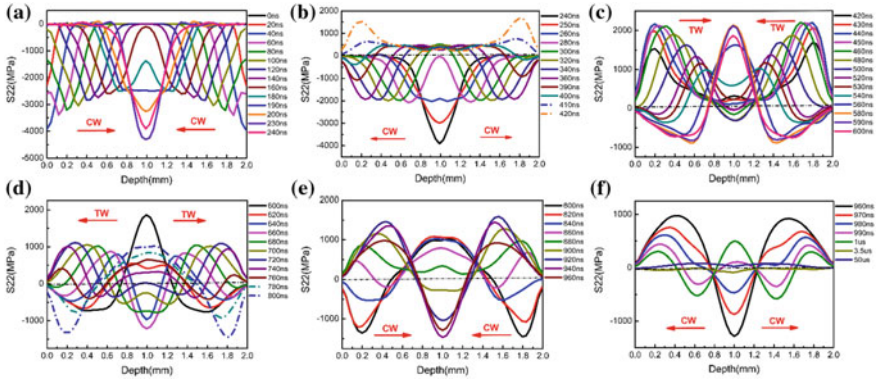

Fig. 8 Stress wave transmission along depth for simultaneous dual-sided laser peening on the middle region of line 3

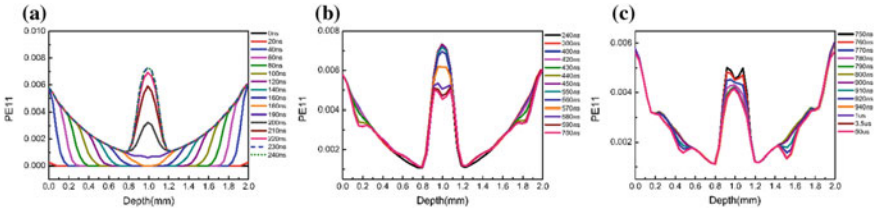

Fig. 9 Plastic strain of X direction (PE11) along depth for the simultaneous dual-sided laser peening on the middle region of line 3

Figs. 8c and 9b. After complete overlapping, the tensile waves separate and propagate along the original direction, leaving that the stress in the mid-depth first decreases and then increases to balance the propagating tensile wave. In 760–780 μs, the tensile stress in the mid-depth reduces tensile plastic strain in the mid-depth (Fig. 9c). At 780 μs, the tensile waves reach the free surfaces and begin to transmit back as compressive waves. The reflecting compressive waves transmit into the blade and meet at 940 μs in the middle position, as shown in Fig. 8e. In 910–940 μs, the strong counterbalancing tensile stresses following the propagating compressive wave result in the reduction of PE11, as shown in Figs. 8e and 9c. After passing through the overlapping region, the compressive waves turn very weak and the springback process starts after 1us. After several microseconds, the stress along depth turns to be stabilized, forming the so-called residual stress. This is the whole process of stress wave propagation and the corresponding plastic strain evolution in the middle region of line 3 with thickness of 2 mm. The residual stress profile is related to the plastic strain profile.

For line 1 with the thickness of 1.2 mm, the propagation mechanism of simultaneous dual-sided laser peening is a bit more complicated than that for line 3 with the thickness of 2 mm due to different energy dissipation rates in the component

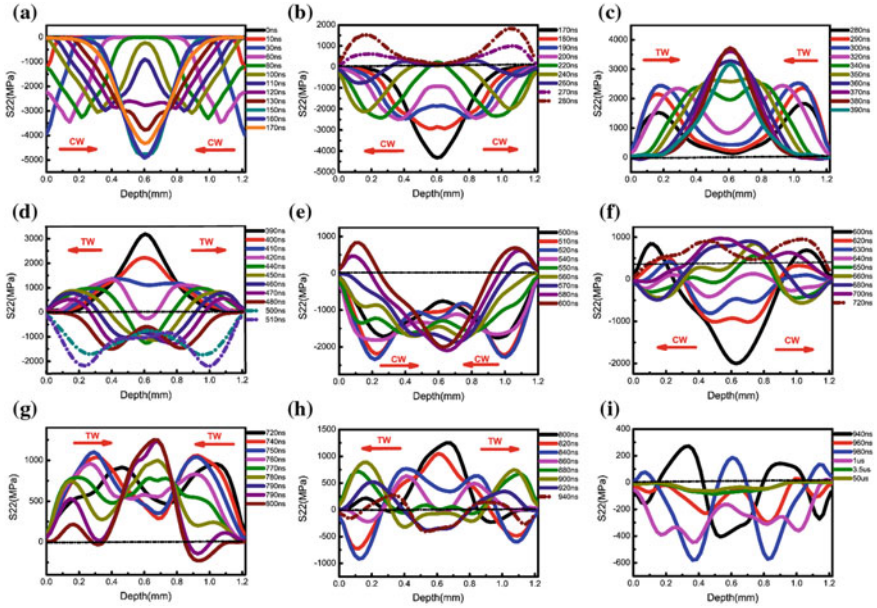

Fig. 10 Shock wave transmission along depth for simultaneous dual-sided laser peening on the middle region of line 1

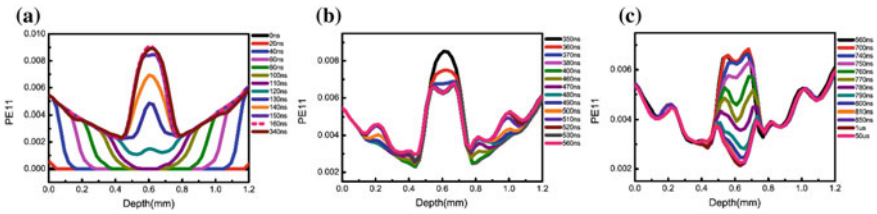

Fig. 11 Plastic strain of X direction (PE11) along depth for the simultaneous dual-sided laser peening on the middle region of line 1

with different thickness. The compressive waves transmit inside and the wave crests first overlap completely at 160 μs (Fig. 10a), corresponding to the maximum tensile plastic strain of X direction (PE11) in Fig. 11a. Then the compressive waves move away from the central position and reach the free surfaces at 260 μs (Fig. 10b). The compress waves are reflected and begin to propagate back as tensile waves at 270 μs. The crests of the two tensile waves start to meet at 360 μs and completely overlap at 380 μs (Fig. 10c), resulting in the reduction of tensile plastic strain PE11 in the mid-depth (Fig. 11b). After overlapping, the tensile waves continue to move along the original propagating directions. In 460–480 μs, the counterbalancing compressive waves following the tensile wave crests cause increased plastic strain of X direction, as shown in Fig. 11b. At 480 μs, the tensile waves reach the free

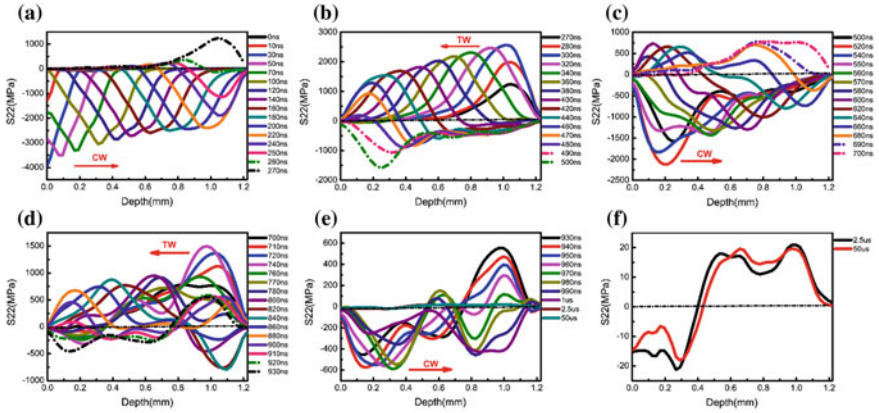

Fig. 12 Shock wave transmission along depth on the middle region of line 1 for first-surface laser peening

surfaces and are reflected to propagate back inside as compressive waves at 500 μs (Fig. 10d).The reflected compressive waves at 510 μs still have sufficiently high pressure to induce plastic deformation of the material in the regions of 0.1–0.3 mm away from the free surfaces (Fig. 11b). The compressive waves meet in the mid-depth again at 580 μs (Fig. 10e), and subsequently reach the free surfaces and are reflected to tensile waves at 700 μs (Fig. 10f). The reflected tensile waves propagate inside again and the increasing tensile stress in the middle region due to wave superposition lead to the decreased tensile plastic strain, as shown in Fig. 11c. The tensile waves meet at 800 μs and reach the free surfaces at 920 μs. Two very weak compressive waves generated by reflection of the tensile waves transmit into the blade in 940–960 μs, after when the tensile waves are weak enough to be ignored and the springback process starts. At several microseconds, the springback process completes and the stress state keeps stabilized at 50 μs.

For non-simultaneous dual-sided laser peening along the depth of line 1, wave propagation in the blade is different with that for the simultaneous mode. For the upper-sided laser peening, the compressive wave transmits inside and reach the opposite side at 260 μs (Fig. 12a), resulting in the gradually reduced tensile strain of X direction (PE11) along the depth (Fig. 14a). Then the compressive wave is reflected by the free surface and transmits back into the target as tensile wave at 270 μs (Fig. 12a), causing compressive plastic strain of X direction (Fig. 14a). The tensile wave transmits back and reach the upper surface at 480 μs, then is reflected to propagate towards the bottom surface as compressive wave at 490 μs. During the period of 570–620 μs, the counterbalancing tensile wave following the compressive wave reduces tensile strain of X direction, as shown in the region of 0–0.2 mm away from the upper surface (Fig. 14b). At 690 μs, the compressive wave reaches the bottom surface and transmit back as a tensile wave at 700 μs. The tensile wave propagates inside and causes the reduction of tensile strain in 760 μs (Fig. 14c).

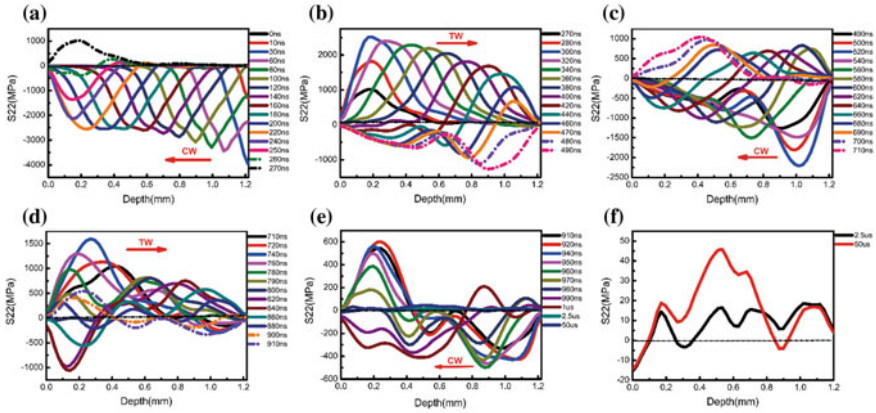

Fig. 13 Shock wave transmission along depth on the middle region of line 1 for second-surface laser peening

Then the tensile wave reaches the upper surfaces at 920 μs and is reflected to transmit back as a compressive wave. The compressive wave turns very weak at 1 μs, followed by the springback process. At 50 μs, the blade is considered to be stabilized (Fig. 12f) and the bottom-sided laser peening is carried out.

In Fig. 13a, the stress profile at 0 μs refers to the stabilized stress profile at 50 μs of the upper-sided laser peening process. Similar with the upper-sided laser peening process, the compressive wave transmits towards the upper surface and reach it at 260 μs, leaving gradually reduced tensile strain based on the existing strain caused by the upper-sided laser peening. Then the compressive wave is reflected and transmits back into the target as a tensile wave at 270 μs. The reflecting tensile wave relaxes the tensile strain of X direction at 290–300 μs (Fig. 14d). It reaches the bottom surface at 480 μs, and then transmits back towards the upper surface as a compressive wave. At 560–600 μs, the counterbalancing tensile wave following the compressive wave relaxes the tensile strain as shown in Fig. 14e. The compressive wave reaches the upper surface and reflects back as a tensile wave at 700 μs. The tensile wave propagates and reaches the upper surface again at 920 μs. Subsequently, the tensile wave is reflected to transmit back as a compressive wave. However, the compressive wave turns very weak after 1 μs, and the springback process begins to occur. At last, the stress state keeps stabilized at 50 μs.

As previously discussed, the transmitting waves (S22) influence the plastic strain of X direction (PE11), while the plastic strain (PE11) could well reflects the residual stress (S11), hence, the types of the transmitting waves and the corresponding typical plastic strain and residual stress of X direction for the three laser peening processes are summarized in Table 3. For the simultaneous dual-sided peening mode, since the thickness of component corresponding to line 1 is less than line 3, the shock wave could transmit more cycles in the region of line 1, which causes more plastic deformation and tensile residual stress in the mid-depth. However,

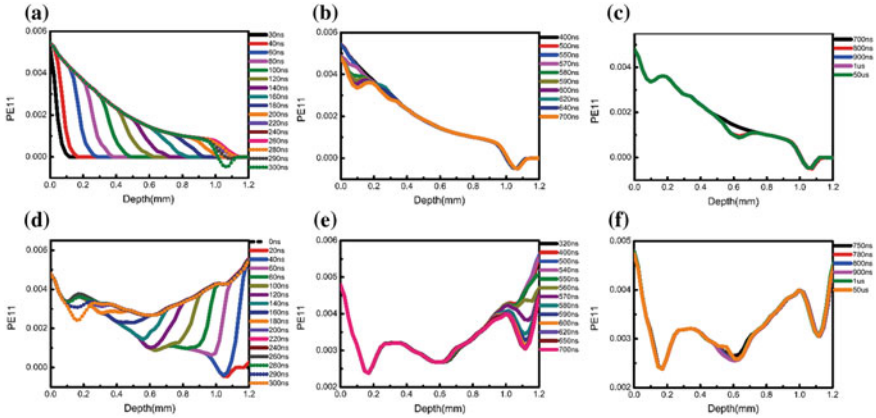

Fig. 14 Plastic strain of x direction (PE11) along depth for the non-simultaneous dual-sided laser peening on the middle region of line 1

Table 3 Typical plastic strain evolution with the shock wave propagation and the corresponding residual stress for two dual-sided laser peening modes

	Line1_ simultaneous		Line3_ simultaneous		Line1_non-simultaneous			
PE11	CW	0-270ns	CW	0-410ns	CW	0-260ns	CW	0-260ns
	TW	280-480ns	TW	420-780ns	TW	270-480ns	TW	270-480ns
	CW	500-720ns	CW	780- ns	CW	490-680ns	CW	480-690ns
	TW	720-940 ns	--	--	TW	700-910 ns	TW	700-880 ns
S11	50us		50us		50us		50us	

tensile residual stress is not welcomed in the mid-depth since it is prone to generate fatigue crack as stress concentration region. Hence, for simultaneous dual-sided laser peening of thin components, smaller shock wave pressure should be adopted in order to prevent a number of wave propagation and the inducing tensile residual stress in the mid-depth. For the non-simultaneous dual-sided peening mode, since there is no interference of wave in the mid-depth, the residual stress in the

mid-depth tends to be more smooth than that for the simultaneous mode, which benefits the fatigue property of the component. However, there is also a key problem for the non-simultaneous dual-sided peening mode. The reflecting tensile waves would induce great tensile residual stress and spalling at the region close to the opposite surface. Hence, proper shock wave pressure or foils for absorbing wave should be applied in the non-simultaneous dual-sided laser peening.

Conclusion

In this study, we studied the residual stress distribution on treated surfaces and along the depth of the simplified compressor blade caused by simultaneous and non-simultaneous dual-sided laser peening by means of numerical simulation. The mechanisms of dual-sided laser peening modes on the residual stress distribution along depth were further studied trough shock wave transmission theory. The main conclusions are listed in the following:

(1) Simultaneous dual-sided laser peening produces more symmetric residual stress on the upper and bottom surfaces than non-simultaneous mode. However, the overlapping of 13.4% induces great residual stress differences between the centers of the spots and the overlapping regions, which is prone to induce fatigue crack initiation in the stress concentration regions. Hence, the overlapping of 13.4% is not suitable for Gaussian laser pulse.
(2) The residual stress along depth shows different patterns for the two dual-sided laser peening modes. For the simultaneous mode, the residual stress along depth shows compressive-tensile-compressive-tensile-compressive-tensile-compressive pattern for line 1 with thickness of 1.2 mm, and shows compressive-tensile-compressive-tensile-compressive patter for line 3 with thickness of 2 mm. For the non-simultaneous mode, the residual stresses along depth for both line 1 and line 3 show a regular pattern of compressive-tensile-compressive stress. The difference in residual stress distribution could be explained by the shock wave propagation theory, such as the interaction of waves and the reflection by free surfaces.
(3) The residual stress distribution along the depth depends on not only the dual-sided laser peening modes but also the thickness of components and the shock wave pressure. Dual-sided laser peening mode makes a more marked difference in the residual stress distribution than the thickness and the shock wave pressure.

Acknowledgements This study was financially supported by the National Natural Science Foundation of China (Grant No. 51471155) and Aviation Innovation Foundation of China (Grant No. 2014E62149R). The authors appreciate Dr. Wang (Qiang Wang) and Dr. Luo (Xuekun Luo) for supporting information about the sample geometry and LSP parameters.

References

1. S. Zabeen, M. Preuss, P.J. Withers, Evolution of a laser shock peened residual stress field locally with foreign object damage and subsequent fatigue crack growth. Acta Mater. **83**, 216–226 (2015)
2. Y. Sano, N. Mukai, M. Obata, Laser peening without coating: process, effects and applications. The Tenth International Conference on Shot Peening, Tokyo, Japan, 2008
3. M.R. Hill, Assessment of tensile residual stress mitigation in alloy 22 welds due to laser peening. J. Eng. Mater-T. ASME **126**, 465–473 (2004)
4. P. Ganesh, R. Sundar, H. Kumar et al., Studies on fatigue life enhancement of pre-fatigued spring steel specimens using laser shock peening. Mater. Design **54**, 734–741 (2014)
5. M.P. Sealy, Y.B. Guo, Fabrication and characterization of surface texture for bone ingrowth by sequential laser peening biodegradable orthopedic magnesium-calcium implants. J. Med. Devices **5**, 011003 (2011)
6. C. Correa, L.R. de Lara, M. Díaz et al., Effect of advancing direction on fatigue life of 316L stainless steel specimens treated by double-sided laser shock peening. Int. J. Fatigue **79**, 1–9 (2015)
7. J.Z. Lu, K.Y. Luo, D.K. Yang et al., Effects of laser peening on stress corrosion cracking (SCC) of ANSI 304 austenitic stainless steel. Corros. Sci. **60**, 145–152 (2012)
8. U. Trdan, J. Grum, SEM/EDS characterization of laser shock peening effect on localized corrosion of Al alloy in a near natural chloride environment. Corros. Sci. **82**, 328–338 (2014)
9. Y.B. Guo, R. Caslaru, Fabrication and characterization of micro dent arrays produced by laser shock peening on titanium Ti–6Al–4 V surfaces. J. Mater. Process. Technol. **211**, 729–736 (2011)
10. P. Peyre, X. Scherpereel, L. Berthe et al., Surface modifications induced in 316L steel by laser peening and shot-peening. Influence on pitting corrosion resistance. Mater. Sci. Eng., A **280**, 294–302 (2000)
11. C.S. Montross, T. Wei, L. Ye et al., Laser shock processing and its effects on microstructure and properties of metal alloys: a review. Int. J. Fatigue **24**, 1021–1036 (2002)
12. A. King, A. Steuwer, C. Woodward et al., Effects of fatigue and fretting on residual stresses introduced by laser shock peening. Mater. Sci. Eng., A **435**, 12–18 (2006)
13. C.A. Lavender, S.T. Hong, M.T. Smith et al., The effect of laser shock peening on the life and failure mode of a cold pilger die. J. Mater. Process. Technol. **204**, 486–491 (2008)
14. C. Rubio-González, G. Gomez-Rosas, J.L. Ocaña et al., Effect of an absorbent overlay on the residual stress field induced by laser shock processing on aluminum samples. Appl. Surf. Sci. **252**, 6201–6205 (2006)
15. R.A. Brockman, W.R. Braisted, S.E. Olson et al., Prediction and characterization of residual stresses from laser shock peening. Int. J. Fatigue **36**, 96–108 (2012)
16. N. Hfaiedh, P. Peyre, H. Song et al., Finite element analysis of laser shock peening of 2050-T8 aluminum alloy. Int. J. Fatigue **70**, 480–489 (2015)
17. M.E. Graham, J.D. Jackson, Dual laser shock peening, U.S. Patent 6,479,790 (2002)
18. S.R. Mannava, P.K. Wright III, F.H. Azad, et al, Single sided laser shock peening, U.S. Patent 6,559,415 (2003)
19. X. Zhang, H. Li, S. Duan et al., Modelling of residual stress field induced in Ti–6Al–4 V alloy plate by two sided laser shock processing. Surf. Coat. Tech. **280**, 163–173 (2015)
20. M.A. Meyers, Dynamic Behavior of Materials (Wiley, 1994)
21. B.L. Wang, Study on the mechanical properties of titanium alloy TC17 and characteristics in machining, Doctoral dissertation of Shangdong University, 2013
22. X. You, X.F. Nie et al., Parameter identification of constitutive model at high strain rate for TC17 titanium alloy under shock wave induced by nanosecond pulsed lasers. Chinese J. Lasers **43**, 102–109 (2016)
23. K. Ding, L. Ye, Simulation of multiple laser shock peening of a 35CD4 steel alloy. J. Mater. Process. Technol. **178**, 162–169 (2006)

24. R. Fabbro, J. Fournier, P. Ballard et al., Physical study of laser-produced plasma in confined geometry. J. Appl. Phys. **68**, 775–784 (1990)
25. P. Peyre, I. Chaieb, C. Braham, FEM calculation of residual stresses induced by laser shock processing in stainless steels. Model. Simul. Mater. Sci. Eng. **15**, 205 (2007)
26. T.X. Yu, X.M. Qiu, *Impact Dynamics*, 1st edn. (Tsinghua University Press, 2011)

Preparation and Wear Behavior of Enamel Coating on Ti–6Al–4V ELI Titanium Alloy

Qiuyuan Feng, Yongqiang Zhang, Zhihong Dong, Pinghui Zhang, Jian Wang, Dingchun Wang, Qi Gao, Xiao Peng and Fuhui Wang

Abstract An enamel coating was prepared on the surface of Ti–6Al–4V extra low interstitial (ELI) titanium alloy by using slurry sintering process. The surface three-dimensional morphology, wear track morphology, microhardness and the tribological behavior of alloy with and without enamel coating and adhesion strength between the coating and base alloy were characterized by means of atomic force microscopy (AFM), scanning electron microscopy (SEM), microhardness test, friction and wear testing machine and thermal shock method, respectively. The morphologies of the coating and base alloy before and after wear were comparatively analyzed, and wear mechanism was discussed. The results show that the microstructure of enamel coating was compact and combines well with the base alloy. The thickness of enamel coating was about 30 μm, and the coating was uniform and smooth. Compared to base alloy, the hardness of enamel coating improved obviously. Under the condition of dry friction and wear, the wear mass loss and wear rate of alloy with enamel coating was little, only one quarter and about 29.6% of that for alloy without enamel coating. The alloy with enamel coating shows excellent wear-resistance. Wear mechanism of Ti–6Al–4V ELI titanium alloy is adhesive and abrasive wear, while the enamel coating shows abrasive wear.

Keywords Titanium alloy · Enamel coating · Microhardness · Friction and wear Wear mechanism

Q. Feng (✉) · Y. Zhang · P. Zhang · J. Wang · D. Wang · Q. Gao
Institute of Baoti, Baoti Group Ltd., Baoji, 721014 Shannxi, China
e-mail: fengqiuyuan2003@163.com

Z. Dong · X. Peng
Laboratory for Corrosion and Protection, Institute of Metal Research, Chinese Academy of Sciences, Shenyang, 110016 Liaoning, China

F. Wang
School of Materials Science and Engineering, Northeastern University, Shenyang, 110819 Liaoning, China

© Springer Nature Singapore Pte Ltd. 2018

Y. Han (ed.), *Advances in Materials Processing*, Lecture Notes in Mechanical Engineering, https://doi.org/10.1007/978-981-13-0107-0_5

Introduction

Thanks to their excellent properties such as little density, higher specific strength, better corrosion resistance and non-magnetic, titanium and titanium alloys have extensively application prospects in the fields of aviation and aerospace, chemical industry, ships, ocean engineering, metallurgy, automobile, sports, architecture and medical treatment. They are praised as 21th metal materials and have the reputations of "space metal", "ocean metal". However, it is known that titanium alloys have poor wear resistance and easy to adhesion due to their low hardness. Therefore, the service performance and life period are restricted in a certain extent [1]. It is an effective approach treated on titanium and titanium alloys surface to improve their wear resistance by using surface modification technology [2]. The frequently-used surface treatment technologies are electroplating [3], nitriding/carburizing [4, 5], metallic cementation [6, 7], micro-arc oxidation [8, 9], plasma spraying [10], vapor deposition [11], ion implantation [12], laser deposit [13, 14], enamel coating [15], and so on.

Among these technologies, enamel coating can improve the anti-oxidation and corrosion resistance of titanium alloys due to their higher chemical stability and thermal expansion coefficient close to titanium alloys. Owing to the merits of simply preparation process and low cost, the enamel coating can be hopefully obtained practical application [16]. In the last few years, relative studies have indicated that the enamel coating is a good candidate as high temperature coating for Ti-based alloys, Ti_3Al and TiAl intermetallics due to its high thermal stability oxidation and better compatibility with the base alloy. The effect of enamel coating on the oxidation and hot corrosion resistance of Ti–24Al–14Nb–3V was investigated by Guan et al. [17], through the measurement, they found that the enamel coating remarkably improved the oxidation resistance of Ti–24Al–14Nb–3V because the coating has good chemical stability, and thermal expansion coefficient of coating matches well with the base alloy. The enamel coating was prepared on the surface of Ti60 alloy and the effects of coating on the isothermal oxidation behavior of alloy had been researched by Xiong et al. [18]. The results showed that the formation of dense and uniform coating on Ti60 alloy can protect the base alloy and decrease the diffusion rate of oxygen in the coating.

After mixed SiO_2, Al_2O_3 and other powder to prepare enamel slurry and coated them on metal material surface, and then sintered at high temperature, the obtained enamel coating possess higher hardness [19] and can improve the wear resistance of titanium alloys and other metal materials. Unfortunately, seldom research concerning the tribological properties of enamel coating had been carried out. There are many methods to prepare the enamel coating, such as slurry sintering method, spraying method and electrophoresis method, etc. Among these methods, slurry sintering method had been applied widely due to its simple process and lower cost [20]. In the present study, enamel coating was prepared on the surface of Ti–6Al–4V ELI titanium alloy using slurry sintering method at first, and then the friction

and wear behavior of coating was priority investigated. Finally, the wear mechanism of Ti6Al4V ELI titanium alloy with and without enamel coating was discussed in detail.

Experimental Materials and Methods

Experimental Materials

The selected substrate material is Ti–6Al–4V ELI titanium alloy, which the chemical composition is composed of Ti89.52%, Al6.12%, V4.2% and the rest 0.16%. The main properties: thermal expansion coefficient is 9.1–10.0 × 10^{-6}/°C, elastic modulus at room temperature is 109 GPa, and the tensile strength, yield strength, elongation and reduction of area are 845, 785 MPa, 11.5 and 16.5%, respectively. Φ30 mm × 10 mm disc samples were cut from a 10 mm thick Ti–6Al–4V ELI titanium alloy rolling plate using wire-electrode cutting. The samples were polished by 200, 400, 600, 800, and 1000# waterproof abrasive paper from rough to fine, and then ultrasonic cleaned for reservation. Considering the match relationship between the coating and base alloy, the chemical composition of enamel powders were fixed (by mass fraction) and shown in Table 1.

Preparation of Enamel Coating

The enamel coating was prepared by using traditional enamel preparation process, the coating and sintering procedures are as flows: enamel powders preparation → slurry preparation → pretreatment of substrate → slurry painting → drying → sintering.

1. Preparation of enamel powders: enamel powders were selected and weighed according to the fixed ratio. After entirely mixed uniform, they were placed into aluminum oxide crucible to melt at high temperature in box-type electric resistance furnace. After melting, the molten slurry was quenched to be enamel glazes. Finally, the enamel glazes were crushed and ball-milling for 100 h, and then they were sieved. The grain size of glazes was less than 10 μm.

Table 1 Chemical composition of enamel powder (wt%)

SiO_2	Al_2O_3	ZrO_2	ZnO	B_2O_3	CaO	Na_2O	Others
58.26	7.98	5.29	9.00	4.66	3.66	3.40	7.75

2. Slurry preparation: After sieving, the alcohol with fixed ratio was added into glaze powders and blended uniform by ball-milling for 4 h. In the end, the glaze powders were made to be enamel slurry. The alcohol acted as solvent and assistant grind agent.
3. Pretreatment of substrate: Taking consider that the adhesion strength between the coating and base alloy relate to the surface condition of alloy, therefore, the oil contamination and oxidation film on the surface of alloy must to be cleaned up, and make the surface to form homogeneous rough surface. Before coating, the surface of alloy was treated by abrasive blasting. The pressure and time of abrasive blasting was 0.4 MPa and 30 s. After abrasive blasting, the surface roughness R_a of substrates reached to 0.2 μm. The samples were cleaned using ultrasonic and degreased for 10 min in ethyl alcohol. Finally, the cleaned samples were put into acetone for reservation.
4. Slurry painting: The enamel slurry was uniformly sprayed on the surface of base alloy by using spraying method. The pressure of spraying was 0.2 MPa. The thickness of coating was controlled by adjusting the spraying time. After spraying, the samples were put into drying oven and dried at 100 °C for 120 min.
5. Sintering: The dried samples were placed on fire-resistance brick, and loaded in SX-4-10 box-type resistance furnace to dry 10 min at 900 °C. After that, the samples were taken out from the furnace to cool down in air. The apparent of enamel coating was compact, smooth and bright and shows good surface quality.

Characterization of Enamel Coating

The surface tridimensional morphology of enamel coating was analyzed by using atomic force microscopy (AFM). Standard Vickers microhardness measurements were conducted with a 200 g load held for 10 s with five measurements made for each alloy and enamel coating (Wilson-Wolpert Tukon®2100B).

Sliding wear behavior was evaluated by an all-purpose tribometer (MUT-3) in dry condition. The contact form of friction counterpart was ball-plane spot contact and reciprocating linear motion form and the counterpart was GCr15 steel ball of diameter 9.5 mm under a normal load of 10 N. The reciprocate stroke, frequency and wear time are 10 mm, 5 Hz and 30 min, respectively. At least three tests were conducted for each alloy with and without coating at room temperature and relative humidity ($\sim$60%). The friction coefficient was obtained by automatic calculation from the friction force measured with sensor. Before and after wear, the samples were cleaned by ultrasonic in acetone and dried, and then weighed using electronic balance with 0.001 mg precision. According to the difference of mass before and after wear, the wear mass loss can be calculated.

Following the sliding tests, the worn surface morphologies of substrate and coating were observed by using scanning electron microscopy (SEM, JSM-6360LV), and the wear width was measured to calculate wear rate. The linear scanning analysis on the interface between enamel coating and base alloy were analyzed by using energy dispersive X-ray analysis (EDAX) attached to SEM. The thermal expansion coefficient of base alloy and enamel coating were measured using thermal expansion instrument (DIL402C, made in German).

The adhesion strength and match extent of thermal expansion coefficient between enamel coating and base alloy were evaluated by using thermal shock test. The procedures of thermal shock test are as follows: the samples with enamel coating were placed into muffle furnace for holding 5 min at 750 °C. After the samples were heated homogeneously, they were taken out from the muffle furnace, and put into cold water quickly. When the samples cooled down entirely, they were placed into muffle furnace to heat at 750 °C again, and cooled down again, it will be repeated continuously for 50 times. Finally, the samples were observed whether the coating cracking or spallation from the base alloy or not.

Wear rate is an important qualification because it can judge the wear property of material based on the volume of material loss, it can be defined as:

$$K = V/SF. \tag{1}$$

In this formula, K is wear rate, $mm^3\ N^{-1}\ m^{-1}$; V is wear volume, mm^3; S is sliding distance, m; F is the product of load, N. The wear volume can be calculated by using the following formula [21]:

$$V = \frac{\pi}{3}\left(r - \sqrt{r^2 - \frac{d^2}{4}}\right)^2 \cdot \left[3r - \left(r - \sqrt{r^2 - \frac{d^2}{4}}\right)\right] \tag{2}$$

In this formula, V is wear volume, mm^3; r is the radius of steel ball, mm; d is the width of grinding crack, mm.

Results and Discussion

The Surface Tridimensional Morphology of Enamel Coating

Figure 1 shows the surface tridimensional morphology of enamel coating. From this Figure, it can be seen that the enamel coating is composed of granular enamel powders. The microstructure of enamel coating takes on uniform and compact. Meanwhile, the particles of oxide in coating are very small. The surface roughness of enamel coating is about 0.4 μm, which will have an effect on fiction and wear of coating.

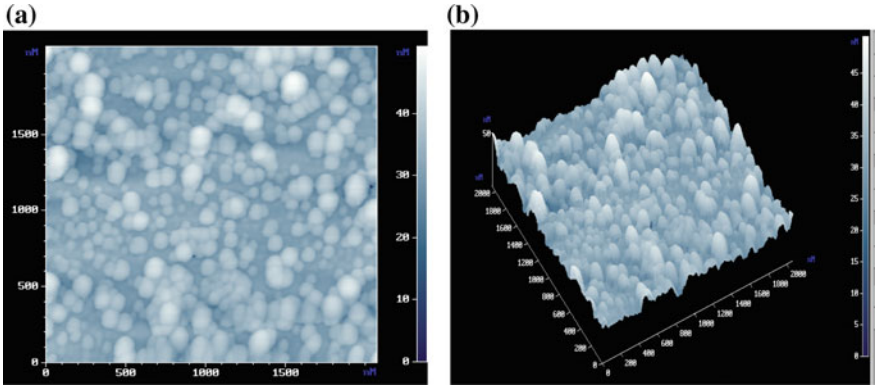

Fig. 1 AFM images of the enamel coating **a** surface; **b** AFM image

Cross Sectional Morphology of the Coating

Figure 2 gives the cross section of sample with enamel coating and the EDAX energy spectrum analysis result of line scanning on the interface of coating and base alloy.

From Fig. 2a, it had been measured that the average thickness of enamel coating is about 30 μm. The enamel coating consists of a gray matrix with fine particles. It can be clearly seen that the enamel coating is very dense, uniform, and adhesion well with the base alloy. However, few voids formed in the coating due to volatility of gas during the enamel powders were sintered.

From Fig. 2b, it can be seen that the elements on the interface of coating and substrate are Al, Si, Zr, Ca, Ti, V and Zn. Among these elements, Al, V and Ti are

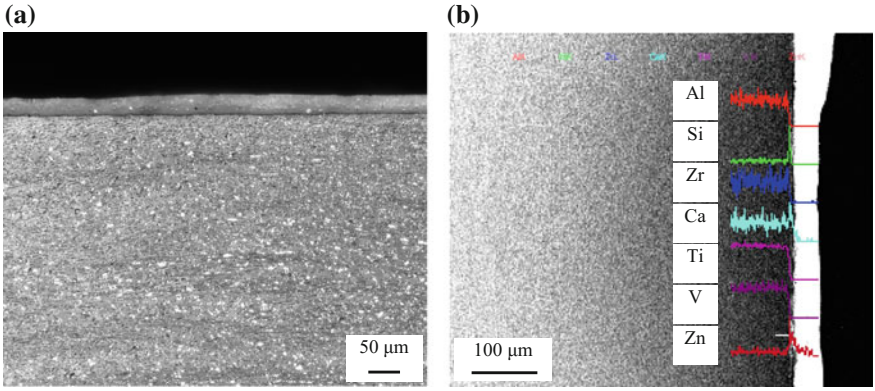

Fig. 2 Optical Microscope (OM) cross-sectional morphology of the enamel coating (**a**) and linear scanning analysis on the interface between coating and base alloy (**b**)

the main components of base alloy, while Si, Zr, Ca and Zn elements are the main components of enamel, which indicate that the inter-diffusion occurred on the interface of base alloy and coating. The reason can be attributed to enamel coating preparation procedure. During preparation the enamel coating, the samples had been sintered at 900 °C, owing to higher temperature, atoms moved violently and inter-diffusion occurred on the interface between base alloy and coating, which favors coating to combine well with substrate. The research of Mi et al. [22] showed that oxygen in enamel coating and matrix component generated interface reaction to form oxide during preparation the enamel coating. Meanwhile, owing to the close thermal expansion coefficient between enamel coating and base alloy, their compatibility may be ensured. Tao et al. [23] thought that the reason of adhesion strength between coating and base alloy can be attributed to Si and Al elements in enamel coating inward penetrating into alloy, in which a chemical reaction and inter-diffusion occurred on the interface of coating and base alloy to form a chemical adhesive.

By means of measuring, the thermal expansion coefficient of selected enamel coating and Ti–6Al–4V ELI titanium alloy is 9.2×10^{-6}/°C and 9.1×10^{-6}/°C at room temperature, the values are very close, which indicates that the thermal expansion coefficient of coating and alloy material matches very well, therefore, the binding force between coating and base alloy are also excellent. Furthermore, through adding special additive and tailoring the ingredients and structure of enamel, it could make enamel powders infiltration with substrate during sintering at appropriate temperature, resulting in coating adhesion well with alloy [16]. The perfect adhesion of coating and alloy can remarkably improve the friction and wear property of material [24]. Therefore, application enamel coating is an effective approach to improve the wear resistance of base alloy.

Adhesion Strength of the Coating

The enamel coating has no cracking and spallation from base alloy after continuous 50 time's circulation thermal shock testing at 750 °C and then quenching in water. The result indicated that the enamel coating has excellent anti-thermal shock property, which illustrated excellent adhesion strength between coating and base alloy. Moreover, because thermal expansion coefficient of coating and alloy matches well, the coating combines well with base alloy. When enamel coating subjected major thermal shock, there has no stress concentration in coating during cold and hot alternate circulation, hence, no cracking and spallation phenomenon occurred in enamel coating. Tao et al. [23] obtained the similar result when they researched anti-thermal shock property of enamel coating and Ti–6Al–4V titanium alloy.

Friction Behavior of the Coating

Figure 3 shows that coefficient of friction of sample with and without enamel coating changes with time in dry friction condition.

From this figure, it can be found that the friction coefficient of Ti–6Al–4V ELI titanium alloy without enamel coating takes on upward trend at initial friction stage, which illustrate that the alloy exist pre- grinding phase.

At initial friction stage, the friction force is small because the roughness of couple grinds surface is minor. Therefore, the coefficient of friction of alloy is small too. Along with proceeding of wear, the roughness of couple grinds surface increase leading to friction force increasing, so, the coefficient of friction increases as well. After passing by pre-grinding phase, the roughness of couple grinds surface drives to stable. When wear goes into stable phase, friction becomes stationary. The coefficient of friction of alloy fluctuates heavily during medium term friction. Finally, it stabilizes at 0.4 during later period of friction (Fig. 3a).

Compared to alloy without enamel coating, the coefficient of friction of alloy with enamel coating fluctuates heavily at initial running-in stage, it decreases at about 0.7 during medium term friction and finally tends to stable (Fig. 3b). The reason can be contributed that the surface roughness of enamel coating is higher. Because the enamel coating was sintered using enamel powders, the surface roughness is rather larger (R_a = 0.4 μm, two times higher than that of base alloy). Thus, the coefficient of friction of coating fluctuates heavily at initial stage, and the running-in time is relatively long. With the friction time increasing, the coefficient of friction of alloy with enamel coating tends to stable, and gets into steady wear phase.

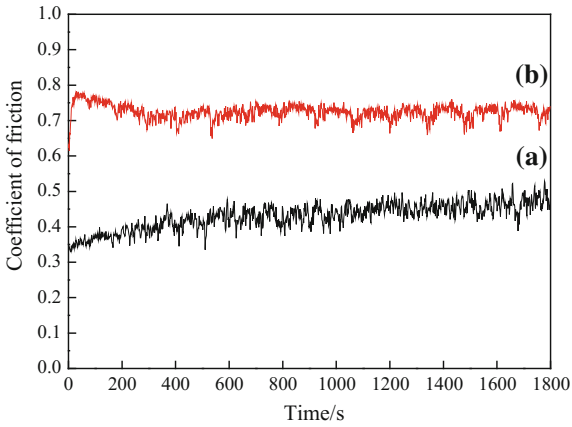

Fig. 3 Relationship between friction coefficient and time **a** substrate; **b** coating

Wear Resistance of the Coating

Figure 4 shows the wear mass loss and wear rate of alloy without (a, a′) and with (b, b′) enamel coating. Under dry friction condition, the wear mass losses of alloy without and with enamel coating are 0.024 and 0.006 g, respectively. The wear mass loss of alloy with enamel coating is only quarter than that of alloy without enamel coating. According to formula $K = V/SF$, the wear rate of alloy without enamel coating calculated from data is 26.6×10^{-4} mm^3 N^{-1} m^{-1}, while the wear rate of alloy with enamel coating is 7.88×10^{-4} mm^3 N^{-1} m^{-1}, the wear rate of alloy with enamel coating is only 29.6% than that of alloy without enamel coating.

From the result, it can be concluded that the alloy with enamel coating can significantly improve the wear resistance of base alloy. When the alloy without enamel coating underwent wear with GCr15 steel ball under dry friction condition, the friction layer has not remarkable antifriction function owing to the contact of metal-metal, the shear resisting force at low ductility and work hardening of alloy lead to higher wear mass loss and wear rate. After application the enamel coating on the surface of Ti–6Al–4V ELI titanium alloy, the hardness of sample improved significantly since there are a large number of hard oxide particles in the enamel coating, hence, the resistance of plastic deformation of alloy with enamel coating was enhanced to make the metal-metal contact changing into the metal- enamel coating contact. The wear decreased effectively, and anti-wear protection effects came into being. Consequently, the wear mass loss and wear rate decreased dramatically to reach a lower value. As a result, the wear property of alloy with enamel coating is better than that of alloy without enamel coating.

Figure 5 shows the wear track morphologies of samples without and with enamel coating.

From Figs. 5a, a′, it can be seen that plastic deformation, tearing trace and plough along with sliding direction occurred on the surface of alloy without enamel coating through the squeeze and plough effect between friction part at room temperature. The worn surface was the predominant fatigue delamination and plastic

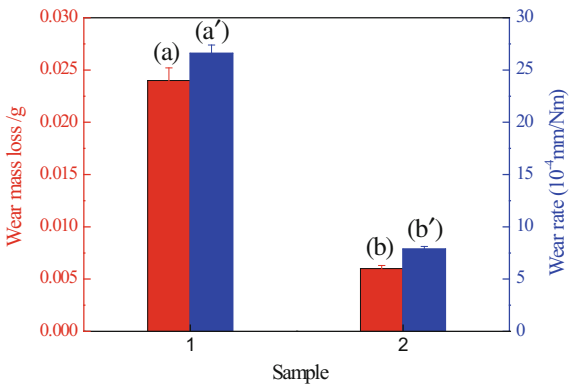

Fig. 4 Wear mass loss and wear rate of alloy without (a, a′) and with enamel coating (b, b′)

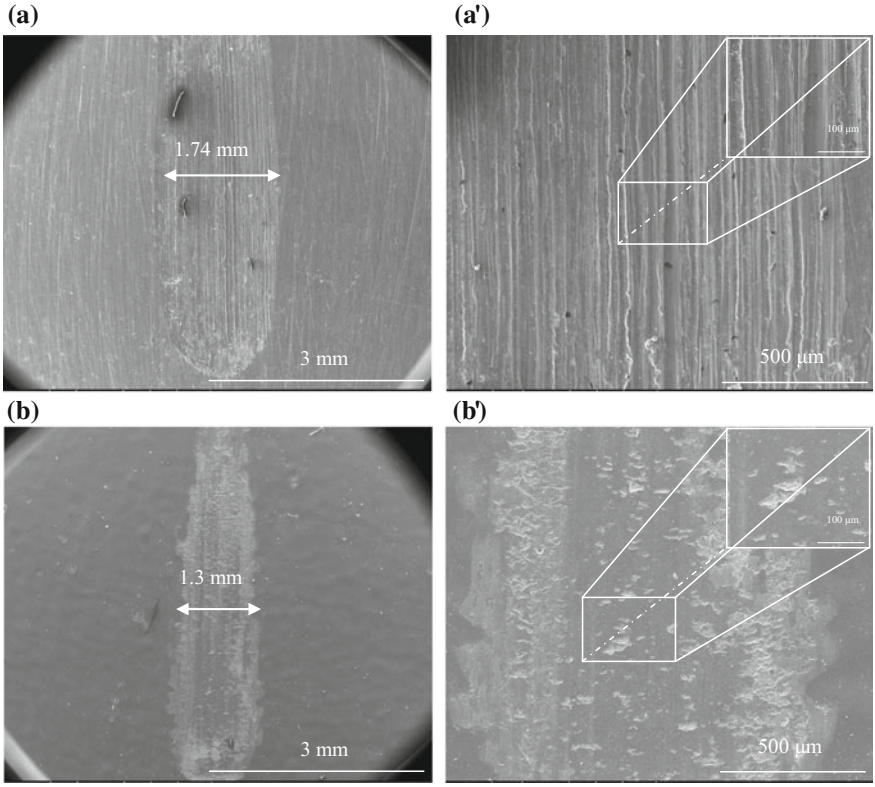

Fig. 5 SEM morphology of worn surfaces of the base metal (a, a′) and enamel coating (b, b′)

deformation. From above analysis, it can be concluded that the wear mechanism of Ti–6Al–4V ELI titanium alloy is adhesion wear and abrasive wear. The worn surface of base alloy presented typical adhesion mark and groove morphology. The main characteristic of worn surface shows that the grooves are deeper, the wear tracks are wider (about 1.74 mm, see Fig. 5a), so, wear mass losses are larger and a lot of abrasive debris produce on the worn surface. Wear tracks consisted of abraded regions with continuous grooves parallel to the sliding direction and regions of accumulated material surrounded by fine wear debris particles. The reason can be attributed to the hardness of friction pair of GCr15 steel ball is higher (the value is about HRC55), but the hardness of base alloy is lower (about HRC32). The bearing capacity of alloy is poor when wear occurred between alloy and steel ball. Therefore, the hardening of alloy took place on wear surface during wear stage, resulting in plasticity decreasing and brittleness increasing. In the procedure of reciprocation wear of counterpart, the surface of alloy was scratched and grooves were ploughed. Plastic deformation in metal occurred on both sides of grooves to produce accumulation. In the following wear procedure, the accumulation metal was crushed. Plastic deformation occurred again and again through this way, give

rise to crack initiation, expansion and spallation from the substrate. Finally, the abrasive debris formed, and this debris will deteriorate wear. Fresh surface of alloy exposed continuously along with friction and wear, the wear went deep into base alloy inward. Abrasive debris produced dissociation plough the surface of alloy to make the wear surface form a wider and deeper groove (see the magnified morphology on top right corner in Fig. 5a′), this is the typical characteristic of adhesion wear and abrasive wear. The researches of Mao et al. [25], Chen et al. [26] and Yang et al. [27] revealed that the wear mechanism of Ti–6Al–4V and TC11 titanium alloy are also adhesion wear and abrasive wear under dry friction condition at room temperature.

The worn surfaces of alloy with enamel coating are slight. The grooves are shallow, and the wear tracks are narrow (about 1.3 mm, see Fig. 5b) compared to that of Ti–6Al–4V ELI titanium alloy without enamel coating. So, only a few of abrasive debris produce on the wear surface, the wear mass loss is very little. The wear mechanism of alloy with enamel coating is mainly abrasive wear, accompany to a small amount of spallation phenomenon, see Figs. 5b, b′. After application enamel coating on Ti–6Al–4V ELI titanium alloy, the reason why the wear resistance of coating remarkable improved can be described as follows:

On the one hand, because the enamel coating is sintered by enamel powders, the surface roughness is higher. When coating contacts with GCr15 steel ball friction counterpart, only local bulge actually contacts with later, the contact area is very small. The tiny abrasive debris produced in wear procedure had been filled in void which formed in sintering procedure (see the magnified morphology on top right corner in Fig. 5b′), and act as solid lubricant to decrease the coefficient of friction and wear loss of coating. Fu et al. [28, 29] thought that increasing surface roughness can reduce the fretting damage.

On the other hand, the hardness of enamel coating is about $660HV_{0.2}$, more two times higher than that of base alloy, it can significantly reduce the friction pair's plough and scratch affect, hence, the probability of abrasive wear decreases, and the wear tracks of coating are slight and ploughs looks shallow. The coupon with enamel coating shows the superior wear resistance compared to that of alloy without enamel coating. From above analysis, it can be concluded that the hardness and plastic resistance to deformation of Ti–6Al–4V ELI titanium alloy with enamel coating increased, therefore, the friction and wear of base alloy decreased obviously.

Conclusions

(1) About 30 μm thickness enamel coating has been successfully prepared on the surface of Ti–6Al–4V ELI titanium alloy. The enamel coating is compact, uniform and smooth, and combines well with substrate. The hardness of enamel coating is approximately 660 $HV_{0.2}$, more two times higher than that of base alloy.

(2) The coefficient of friction of Ti–6Al–4V ELI titanium alloy without and with enamel coating is about 0.4 and 0.7, respectively. The wear mass loss and wear rate of alloy with enamel coating is only quarter and 29.6% of that of alloy without enamel coating. The wear performance of alloy is improved after preparing enamel coating on it.
(3) The wear mechanism of Ti–6Al–4V ELI titanium alloy is adhesion wear and abrasive wear, while the wear mechanism of enamel coating is abrasive wear. Enamel coating is an effective approach for improving the wear resistance of titanium alloy.

Acknowledgements The authors would like to acknowledge Prof. Zhiming Yu and Dr. Qiuping Wei from Zhongnan University for their assistance with experimental work.

References

1. G.B. Kenneth, Tribological properties of titanium alloys. Wear **151**, 203–217 (1991)
2. H.Y. Wu, P.Z. Zhang, J. Xu, Z. Xu, Current situations and applications of titanium alloys wear resistance coatings. Mater. Rev. **20**, 74–77 (2006). (In Chinese)
3. Z.M. Tu, N. Li, Y.M. Zhu, *Application and technology on Surface treatment of titanium and titanium alloys* (National Defense Industry Press, Beijing, 2010). (In Chinese)
4. A. Zhecheva, W. Sha, S. Malinov, A. Long, Enhancing the microstructure and properties of titanium alloys through nitriding and other surface engineering methods. Surf. Coat. Technol. **200**, 2192–2207 (2005)
5. H. Mohseni, P. Nandwana, A. Tsoi, R. Banerjee, T.W. Schsrf, In situ nitrided titanium alloys: microstructural evolution during solidification and wear. Acta Mater. **83**, 61–74 (2015)
6. X.Y. Li, A.L. Fan, B. Tan, J.D. Pan, D.X. Liu, H. Huang, Z. Xu, Tribological behavior of molybdenum alloying layer on Ti6Al4V by double glow discharge technique. Tribology **23**, 108–111 (2003). (In Chinese)
7. L. Qin, B. Tang, J.X. Zhao, Z. Xu, Friction and wear behavior of Ti-Mo diffusion layer on Ti6Al4V alloy substrate in sliding against GCr15. Chin. J. Nonferrous Met. **13**, 570–573 (2006). (In Chinese)
8. S. Aliasghari, P. Skeldon, G.E. Thompson, Plasma electrolytic oxidation of titanium in phosphate/silicate electrolyte and tribological performance of the coatings. Appl. Surf. Sci. **316**, 463–476 (2014)
9. Y. Wang, H.J. Yu, C.Z. Chen, Z.H. Zhao, Review of the biocompatibility of micro-arc oxidation coated titanium alloy. Mater. Des. **85**, 640–652 (2015)
10. L.D. Zhao, E. Lugscheider, Reactive plasma spraying of Ti–6Al–4V alloy. Wear **253**, 1214–1218 (2002)
11. S.P. Zhao, S.K. Lv, W.J. Hao, *Titanium alloy and its surface treatment* (Haerbin University of Technology Press, Haerbin, 2003). (In Chinese)
12. S.X. Hui, Z. Zhang, J.S. Xiao, G.S. Yuan, Influence of Nb implantation on oxidation behavior of a high temperature titanium alloy at 650 °C. Acta Metall. Sin. **35**, S127–S130 (1999)
13. W.L. Wu, X.W. Li, Research progress on laser cladding of titanium alloys. Rare Metal Mat. Eng. **35**, 850–854 (2006). (In Chinese)
14. F. Weng, C.Z. Chen, H.J. Yu, Research status of laser cladding on titanium and its alloys: a review. Mater. Des. **58**, 412–425 (2014)
15. Z.L. Tang, F.H. Wang, W.T. Wu, Effect of Al_2O_3 and enamel coatings on 900 °C oxidation and hot corrosion behaviors of gamma-TiAl. Mater. Sci. Eng., A **276**, 70–75 (2000)

16. X.X. Rao, S.B. Hu, D.S. Qian, Preparation and property of enamel coating on titanium alloy. Electroplat. Finish. **29**, 50–52 (2010). (In Chinese)
17. C.H. Guan, Z.L. Tang, F.H. Wang, W.T. Wu, S.Q. Li, Effect of enamel coating on oxidation and hot corrosion resistance of Ti–24Al–14Nb–3V. Chin. J. Mater. Res. **14**, 75–80 (2000)
18. Y.M. Xiong, S.L. Zhu, F.H. Wang, Effect of ultrafine enamel coating on the oxidation and mechanical property of Ti60 alloy. Acta Metall. Sin. **40**, 768–772 (2004)
19. C.H. Zhang, H.G. Yang, S. Zhang, X.C. Zhang, S.L. Zhu, F.H. Wang, Effect of cerium oxide on the microstructure and friction and wear behavior of enamel coating. Tribology **25**, 198–202 (2005). (In Chinese)
20. W. Liu, W.Z. Li, J.B. Yang, H.Q. Liu, Current research status of enamel coatings on titanium alloys. Mater. Rev. **27**, 45–48 (2013). (In Chinese)
21. J. Li, Y.Y. Wu, D.L. Wang, X.G. Hu, The microstructure and wear resistance characteristics of electroformed nickel and partially stabilized zirconia composite coatings. J. Mater. Sci. **35**, 1751–1758 (2000)
22. F.Y. Mi, S.L. Zhu, Long-term high temperature oxidation and hot corrosion behavior of an enamel coating on γ-TiAl intermetallics at 700 °C. Corros. Sci. Prot. Technol. **27**, 254–258 (2015). (In Chinese)
23. J. Tao, Z.D. Huang, H.B. Liu, T. Wang, Y.Q. Wang, X.Z. Guo, Preparation and characterization of anti-oxidation enamel coating for Ti-based alloys at high temperature. J. Nanjing U. Aeronaut. Astronaut. **42**, 505–509 (2010). (In Chinese)
24. V. Ocelík, D. Matthews, JThM De Hosson, Sliding wear resistance of metal matrix composite layers prepared by high power laser. Surf. Coat. Technol. **197**, 303–315 (2005)
25. Y.S. Mao, X.H. Cui, S.Q. Wang, D.S. Li, Z.R. Yang, Y. Sun, Wear and friction characteristics of Ti6Al4V alloy. J. Aeronaut. Mater. **33**, 41–45 (2013). (In Chinese)
26. K.M. Chen, Q.Y. Zhang, X.X Li, L. Wang, S.Q. Wang, Dry sliding wear behavior of TC11 alloy/GCr15 steel tribo-pair, Rare Metal. Mat. Eng. **44**, 1531–1535 (2000). (In Chinese)
27. K. Yang, J.W. Huang, X.M. Fan, D.S. Xiong, Preparation and properties of Al_2O_3/MoS_2 composite coatings on Ti6Al4V alloy by cathodic plasma electrolytic deposition. Trans. Mater. Heat Treat. **37**, 164–171 (2016). (In Chinese)
28. Y.Q Fu, N.L. Loh, A.W Batchelor, D.X. Liu, X.D. Zhu, J.W. He, K.W. Xu, Improvement in fretting wear and fatigue resistance of Ti–6Al–4V by application of several surface treatments and coatings. Surf. Coat. Technol. 106, 193–197 (1998)
29. Y.Q. Fu, H.J. Du, Effects of the counterface materials on the tribological characteristics of CN_X coating deposited on plasma-nitrided Ti–6Al–4V. Mater. Sci. Eng., A **298**, 16–25 (2001)

Effect of Fiber Content on Surface Performance of Potassium Titanate Whiskers and Carbon Fiber-Reinforced Phenolic Composites

Rui Wang, Meifeng He, Junhao Huo, Baozhong Fan and Fang Liu

Abstract The mechanical and tribological properties of potassium titanate whiskers (PTW) and carbon fiber (CF)-reinforced, tung oil-modified phenolic resin (PR) composites were investigated by utilizing a pad-on-disk type friction tester. It was found that the tung oil-modified phenolic composites showed superior wear resistance and steady variation of friction coefficients. It was revealed that the synergistic effects of sub-micrometer PTW and micrometer CF existed in the tung oil-modified PR composites. Then the friction stability, wear rate and morphology of the worn surfaces were examined to study the synergistic effects. The tung oil-modified PR/PTW/CF composites showed superior wear resistance and steady variation of friction coefficients. The friction coefficient increased with increasing addition of PTW. The wear resistance increased with increasing addition of CF. And the outcropped PTW around the CF to protect CF from easy damage and pulled-out. When the content of PTW was high the degradation of wear resistance and the friction coefficient increased, which was of due to the agglomeration and lapping joint of PTW. CF could improve the wear resistance of the tung oil-modified PR composites at the high temperatures significantly because of its suitable thermal conductivity.

Keywords Potassium titanate whiskers ($K_2O6{\cdot}TiO_2$) · Carbon fiber
Friction

R. Wang · M. He (✉) · J. Huo · B. Fan · F. Liu
School of Materials Science and Engineering, University of Shanghai for Science and Technology, Shanghai 200093, China
e-mail: hmf752@usst.edu.cn

R. Wang
e-mail: 2386230826@qq.com

F. Liu
e-mail: liufang@usst.edu.cn

© Springer Nature Singapore Pte Ltd. 2018

Y. Han (ed.), *Advances in Materials Processing*, Lecture Notes in Mechanical Engineering, https://doi.org/10.1007/978-981-13-0107-0_6

Introduction

Friction materials in braking systems need to met many consumer expectations, such as suitable wear resistance, stable friction performance, minimal noise and vibration at a wide range of complex environments [1]. A monolithic material couldn't effective used in commercial brake lining. In order to make the performance of the multiphase composites for a friction material better, it has been extensively studied [2–4]. Friction materials generally contained dozens of ingredients. These ingredients include matrix, reinforcing fiber, friction modifiers, and fills. Reinforcing fibers could enhance the matrix, and the most commonly used types were potassium titanate whiskers (PTW), carbon fiber (CF), metallic fiber, and glass fiber. These fibers also largely influenced the wear and friction properties of friction materials [5].

PTWs ($K_2O{\cdot}6TiO_2$) had been confirmed as excellent reinforcing fibers with a tunneling structure. Owing to their exceptional wear resistance, mechanical and properties, coefficient of thermal expansion (6.8×10^{-6} K^{-1}) and they were very soft (the Mohs hardness is 4). PTW could largely reinforced the matrix because of its relatively small size and high length-to-diameter ratio [6, 7]. The peculiar structure and high surface energy of PTW led to its easy agglomeration, thereby leading to the degradation of its composite performance [7]. Kim et al. [1] investigated the effects of PTW and aramid pulp on friction and wear characteristics with an emphasis on the friction film formation at the friction interface; PTW had strong synergistic effects that provided friction stability and wear resistance and high cohesive strength of the friction film. Kim et al. [8] also examined the variation in the average friction coefficient, wear rate, and friction-induced noise propensity with different amounts of phenolic resin, potassium titanate, and CNSL of brake friction materials; they pointed out that fade resistance is improved by increasing PTW, but such increase also decreased the friction coefficient. Zhuang et al. [7] studied the tribological behavior of PEEK reinforced with PTW, thereby demonstrating the significant reinforcement effect of PTW. Hence, compounding PTW into friction materials to improve both mechanical and tribological properties was an effective approach.

CFs were widely used to the organic and ceramics friction materials because of their superior properties, i.e. high tensile strength and elastic modulus, excellent self-lubricating ability, and high wear resistance [9–11]. Xie et al. [12] investigated the tribological behavior of the PEEK composites reinforced by CF and PTW under a water-lubricated condition; the said authors pointed out that the CF and PTW worked synergetically to improve the wear resistance of the PEEK composites. The CF carried the main load between the contact surfaces and protected the matrix from further severe abrasion of the counterpart.

The PR bound other ingredients firmly so that they could perform their desired functions. Both modified and unmodified PR were constantly used as binders in different friction materials because of their suitable compatibility with other

ingredients, high hardness, compressive strength, moderate heat-resistance, and excellent wetting capability with most ingredients [13].

This study investigated the density, hardness, shear strength, variation in the average friction coefficient, and wear rate when the PTW and CF contents were changed. The worn surfaces and wear debris were observed and analyzed. We focused on the mechanical and tribological properties of PTW and CF-reinforced tung oil-modified PR composites as well as the synergistic effect of PTW and CF.

Experimental Details

Materials and Sample Preparation

The friction materials utilized in this investigation consisted of 13 ingredients (Table 1) and were based on a non-asbestos organic type formulation. Seven friction material specimens were fabricated for this study. Commercially available tung oil-modified phenolic resin was applied as the matrix materials. PTWs were procured from Jia-Chen New Material Co., Ltd. (Shanghai, China), which had an average diameter of 0.35 ± 0.15 μm and average length of 15 ± 5 μm. CF was supplied by SINOCARB Co. Ltd. (Anshan, China), which had an average diameter of 5–8 μm and length of 100–200 μm. These specimens were labeled C16, P16, P10C6, P13C6, P16C6, P16C2, and P16C4. The numbers used in the items represented their fiber weight contents (e.g., P10C6 referred to a specimen filled with 10 wt% PTW and 6 wt% CF). The presence or absence of PTW and CF was the primary discrepancy in the specimens because the amounts of the other ingredients were fixed. The PTW gradually changed in specimens P10C6, P13C6, and P16C6 to analyze the PTW content effect on the friction and wear properties. The CF weight was also gradually changed in specimens P16C6, P16C2, and P16C4. The steps of fabricating friction material specimens were mixing, hot pressing, and post curing. Each friction material type was generally weighted with a sensitivity of

Table 1 Compositions of the investigated friction materials

Materials and content (wt%)					
Items	Reinforcing fiber		Friction modifiers	Fills	Matrix
	PTW	CF	Graphite + MoS_2 + Sb_2S_3	$CaCO_3$ + Potash feldspar + Alumina	Phenolic resin
P10C6	10	6	24	51	9
P13C6	13	6	24	48	9
P16C6	16	6	24	45	9
P16C2	16	2	24	49	9
P16C4	16	4	24	47	9

0.1 g and then mixed in a high-speed mixing machine for 20 min. The mixture was then molded and pressed under 25 MPa at 155 °C on an YX32-500 type hydraulic machine. Finally, the specimens were placed in a convection oven for post curing.

Measurement of Physical Properties

The hardness of the friction material specimen was measured with a Rockwell hardness tester (XHRD-150 Laizhou). Shear strength was measured utilizing a shear strength tester (XJ-A Xianyang). Density was measured with a density tester (MH-300A Xiamen).

Friction and Wear Test

Figure 1 showed a schematic diagram of the friction and wear tests. The friction and wear properties were obtained by adopting a constant speed friction tester (XD-MSM Xianyang), which consisted of a polished carbon steel 45 disc with constant rotating velocity n (7.54–7.85 m s^{-1}). The wear track radius r was 150 mm. Two pieces of the specimen were cut into 25 (W) × 25 (L) × 6 (D) mm^3 sizes and pressed with a constant normal load F (1225 N). The polished carbon steel 45 disc was 30 mm thick.

The tester was generally applied to rapidly evaluate the friction materials by conducting a standard method based on the Chinese National Standard GB 5763-2008 [14–16]. Before testing, two specimens were run-in until they were mostly in contact with the counter disc surface.

The counter disc temperature could change in principle because of the working of air blower and heating device. The average frictional coefficients during 5000 rotations were obtained by a friction torque transducer and transferred to a personal computer at 100, 150, 200, 250, 300, and 350 °C. The decreasing of the specimen thickness was measured by a micrometer caliper with an accuracy of 0.01 mm

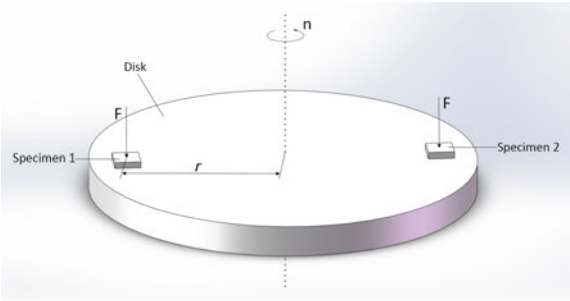

Fig. 1 Schematic diagram of friction and wear tests

before and after a wear test to calculate the wear rate. The final results of friction tests were test datas which had the steadiest friction coefficient at different temperature among three test results. The final results of wear tests were more representative among three test results, so they were chosen.

Before testing, the density of each specimen was measured with the density tester. The surface hardness was determined with the Rockwell hardness tester. Shear strength was measured with the Shear strength tester. Each experimental data value was an average value of five tests. The interface between the fibers and matrix was characterized through the shear fractured specimens. The worn surfaces and wear debris morphology of the specimen were observed using scanning electron microscopy (SEM) to understand the wear mechanisms.

Results

Physical and Mechanical Properties

The physical and mechanical properties of the tung oil-modified PR composites filled with CF and PTW are shown in Table 2. PR can increase hardness. Cho et al. [17] investigated the effect of ingredients on the tribological characteristics of a brake lining; the said authors determined that PTW decreased the specimen hardness because the PTW was in the shape of fine whiskers. The high Mohs hardness of the ingredients tends to produce more brake noise, so the hardness should be controlled.

Specimen P16C4 evidently has higher shear strength compared with specimens P16C2, P10C6, and P13C6. CF can improve the shear strength of the specimens, but the shear strength continue to decrease with high CF content. The SEM images of the fracture surfaces of specimens C16, P16, and P16C6 are shown in Fig. 2. The CF pullout and fiber surfaces adhere to many particles, as observed in Fig. 2a. The said figure shows the occurrence of interface cohesive strength between the CF and matrix. The worn surface of the PTW composites without CF is full of several blocks, nicks, and apparent pores, as clearly shown in Fig. 2b. A naked CF surrounded by PTW is observed in the fracture surface, and several agglomerated PTWs are present in zone A, as shown in Fig. 2c. The agglomeration and lapping joint of PTW can degrade the wear resistance and increase the friction coefficient when the PTW content is high.

Tribological Behavior

Figures 3 and 4 show the variation in the friction coefficient of the investigated specimens with different temperatures. The temperature effects on the friction

Table 2 Physical and mechanical properties of the investigated composites

Properties	C16	P16	P10C6	P13C6	P16C6	P16C2	P16C4
Density (g cm^3)	1.76 ± 0.11	2.11 ± 0.23	1.96 ± 0.07	1.95 ± 0.12	1.93 ± 0.19	2.02 ± 0.21	2.01 ± 0.14
Hardness (HRR)	91 ± 4	102 ± 2	95 ± 3	97 ± 2	99 ± 4	101 ± 3	100 ± 2
Shear strength (MPa)	3.878 ± 2	3.954 ± 3	2.615 ± 2	3.038 ± 2	3.225 ± 2	5.117 ± 2	5.320 ± 2

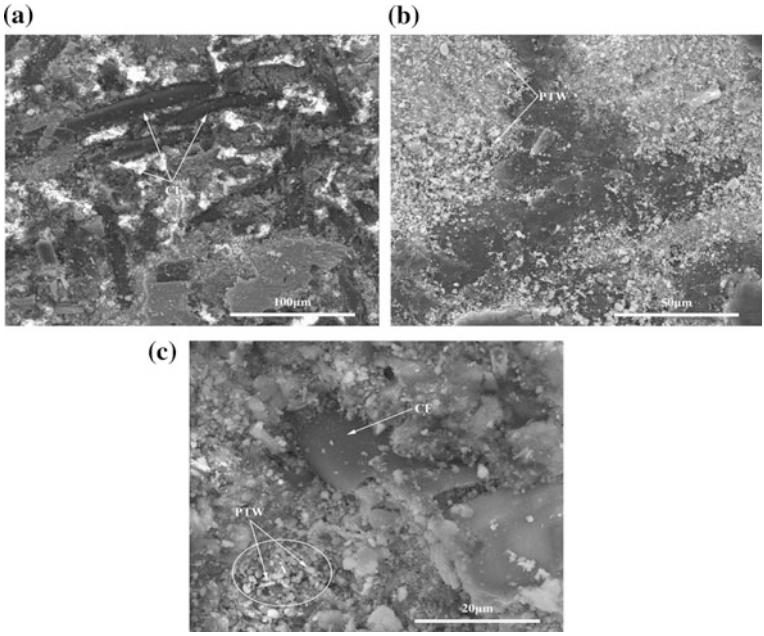

Fig. 2 SEM images of the fracture surfaces of **a** specimen C16, **b** specimen P16, and **c** specimen P16C6

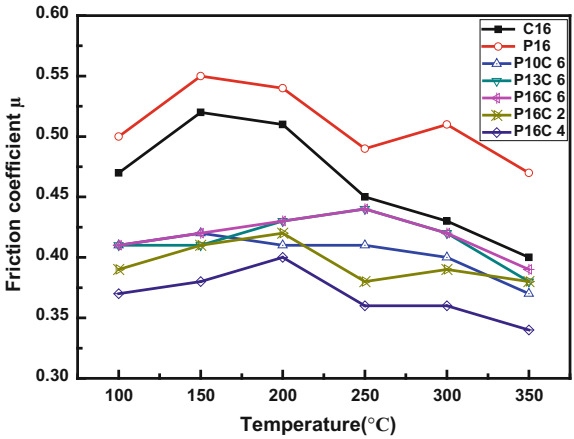

Fig. 3 Effects of temperature increase on the friction coefficients for the specimens

coefficients of these specimens are shown in Figs. 3 and 4. The temperature effects increase from 100 to 350 °C on the friction coefficients of the specimens, as shown in Fig. 3. The temperature effects similarly decrease from 300 to 100 °C on the friction coefficients for the specimens, as shown in Fig. 4. The friction coefficient of a multiphase material is generally determined by two factors, as follows: one is the

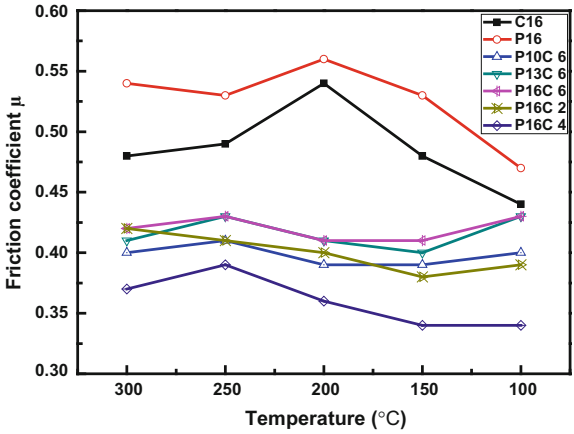

Fig. 4 Effects of temperature decrease on the friction coefficients for the specimens

sum of the tribological properties from the ingredients; the other is the change in the real area of contacts on the sliding interface [18, 19]. Almost all specimens have an analogous variation trend in the friction coefficient, except for specimens C16 and P16, as shown in Figs. 3 and 4. The friction coefficient for specimen P13C6 significantly decreases and reaches the minimum value of 0.38 at 350 °C, which indicates a notable decrease at high temperatures. The friction coefficient for specimen P16C4 gradually decrease with the increasing temperature. The friction coefficient decrease from 0.4 at 200 °C to 0.34 at 350 °C. The average friction coefficient is smaller than those of the other specimens. The variation magnitude of the friction coefficient for specimens P10C6, P16C6, and P16C2 is relatively low, and severe fading is not observed. These observations suggest that the friction coefficients of specimens P10C6, P16C6, and P16C2 are stable. The friction materials with high friction coefficients tend to produce more noise, so the friction coefficients should be controlled.

The friction coefficient for the PTW added friction material at each temperature in specimens P10C6, P13C6, and P16C6 increase with increasing addition of PTW as shown in Figs. 3 and 4. However, wear resistance degradation and friction coefficient increasing occur because of the agglomeration and lapping joint of PTW in phenolic composites when the PTW content is high. Thus, specimens P16C2 and P16C4 have lower friction coefficients even though they have high PTW content. However, Cho et al. [17] directly indicated that PTWs decreased the friction coefficient because of their morphological effects. The size of PTW used in this study is less than 1 μm in diameter. Therefore, a synergetic effect of PTW and CF in the tung oil-modified PR/PTW/CF composites appeared to occur. Severe fading is also observed in specimen P16C4. The friction coefficient for specimens P10C6, P16C6, and P16C2 remain stable. In the elevated temperatures, PTW exhibits suitable fade resistance because of the fine whiskers can strengthen the wear debris.

The temperature effects on the wear rates for the seven specimens are shown in Fig. 5. The wear rates were evidently influenced by the disc temperature. The wear

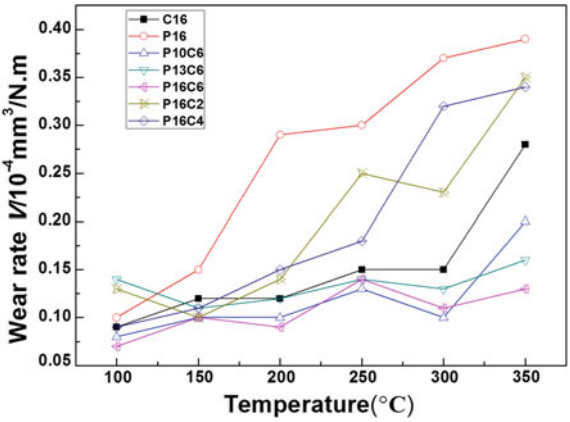

Fig. 5 Temperature effects on the wear rates for the specimens

rates for all specimens increased when the disc temperature increased. For instance, the CF composites compounded with the nano- or sub-micro particles; the CF and particles experience a synergetic effect when the wear resistance of composites are enhanced [20, 21]. The wear resistance for the CF added friction material at each temperature point in specimens P10C6, P13C6, P16C6, P16C2, and P16C4 increase with the increasing addition of CF as shown in Fig. 5. The wear resistance degradation for specimen P16 can be associate with the agglomeration and lapping joint of PTW. Specimens P16C6, P13C6, and P10C6 have lower average wear rates.

Worn Surface and Wear Debris Analysis

The worn surface of specimen P16C6 reinforced with 6 wt% CF is relatively smooth as shown in Figs. 6c, d. Several micro-grooves and micro-cracks can also be observed. By contrast, the worn surface of specimen P16 without CF is full of plowing tracks, grooves, and scratches, as shown in Figs. 6a, b. The wear mechanisms are as follows: (a) matrix wear and fiber thinning; (b) fiber breakage; (c) interfacial debonding, and (d) fiber peeling [20, 22]. The matrix soften when the temperature increase, Steps (c) and (d) were essential in wear resistance. CF is protected by the rolling effect of particles during the friction process, which inhibiter CF removal. After the fiber peel off from the surface, the matrix is easily attacked by steel asperities because of the inadequate reinforced effect of CF. Hence, the matrix surface has more grooves and plowing tracks, and matrix wear could occur [23], as shown in Figs. 6a, b. Given that CF has the microcrystalline structure of graphite, the CF that peel off from the surface spread on the worn surface. Therefore, no severe wear occurs during the friction process and the worn surface was protected by CF. The protruded CF on the worn surface maintains high seizure against the counter disc, and the excellent CF thermal conductivity enhances

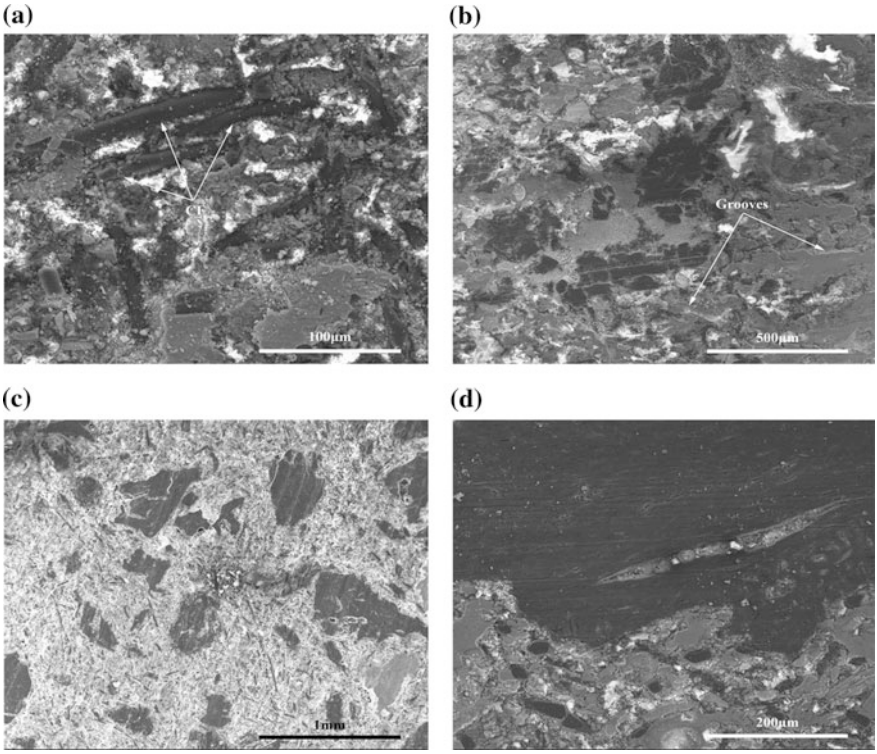

Fig. 6 SEM images of the worn surface of (**a** and **b**) specimen P16C6 and (**c** and **d**) specimen P16

the surface heat that rapidly penetrates the inner section of the specimen. This scenario lower the transient temperature of the friction interface. As previously mentioned, the counterpart could be protected by the CF, which improve the wear resistance.

The SEM images of the worn surfaces of specimens C16 and P10C6 are shown in Figs. 7a, b. The transfer film of composites without PTW is comparatively clumpy and thick (Fig. 7a). Conversely, the transfer film of composites filled with 10 wt% PTW is uniform and smooth (Fig. 7b). Therefore, the worn surface of specimen P10C6 produces a smoother transfer film than that of specimen C16. The high quality transfer film could protect composites from direct contact with the counterface, so the wear rate largely decreases.

Figure 8 clearly shows many agglomerated whiskers on the worn surface of specimen P16. More whiskers are easy to worn out from the surface and become abrasive at the starting run when the PTW content increases, which increase the frictional force on the specimens' surfaces. The higher frictional force lead to higher thermal effect as well as soften the surface of specimens. The transfer film is also formed and the counterface is abraded. Thus, the abrasive effect on the counterface and formation of the transfer film was faster because of the PTW enrichment.

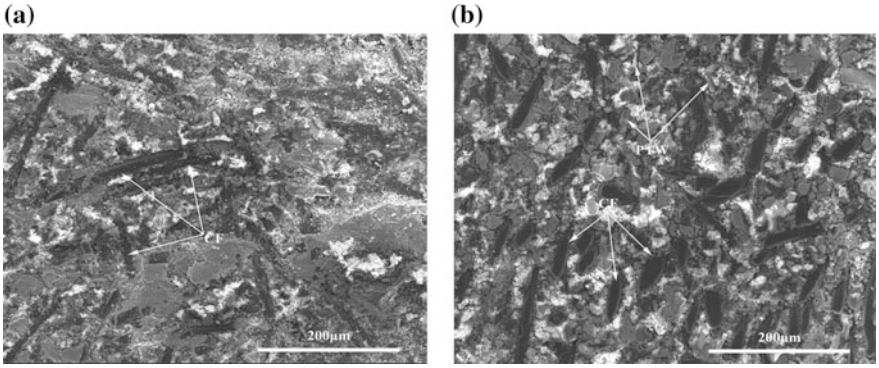

Fig. 7 SEM images of the worn surfaces of **a** specimen C16 and **b** specimen P10C6

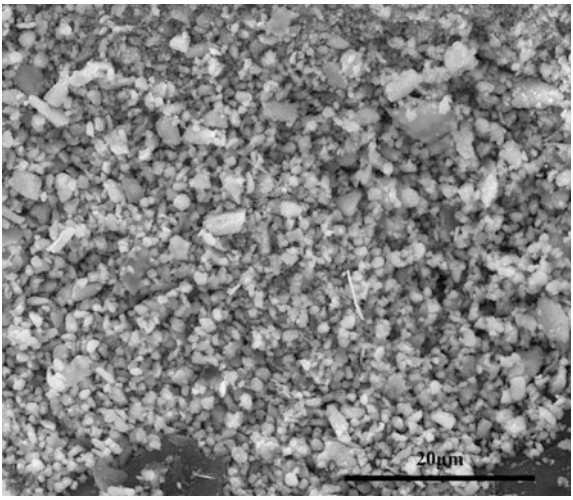

Fig. 8 SEM images of the worn surface of specimen P16

The PTW reinforcement effect is also clearer when the PTW content is high. Then the wear rate decreasing when the PTW content increasing. The matrix is protected by the high content whiskers on the surface of specimens so that the matrix couldn't expose to the steel disk. Moreover, the enriched embedded whiskers could also reinforce and strengthen the surface of specimens. All of the aforementioned factors significantly improve the wear resistance.

The composite surface is soft at the beginning of the test because of the thermal effect caused by high frictional force. Then the soft surface of specimens increase the possibility of the transfer film formation. The uniform transfer film could decrease the wear rate. Friedrich et al. [24] pointed out that mild abrasive could polish the counterfaces and form the transfer film that slides against the counter

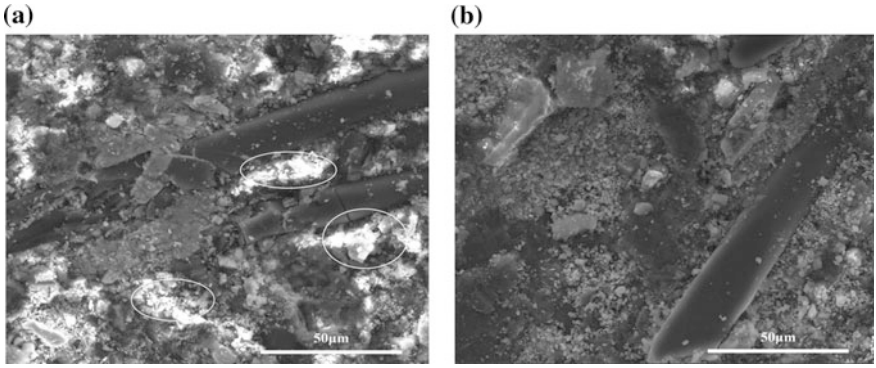

Fig. 9 SEM images of the worn surface of **a** specimen C16 and **b** specimen P10C6

disc. Therefore, a friction film could prevent the composite specimens from severe plowing. A stable friction film could effectively lower the wear rate and noise occurrence.

The friction coefficients and wear rates of the PTW/CF composites 16CF and 16PTW are shown in Figs. 3, 4 and 5. Compared with 16CF and 16PTW, the tung oil-modified PR/PTW/CF composites showed superior wear resistance and steadier variation of its friction coefficients. Therefore, a synergetic effect of PTW and CF appears to have occurred in the wear behavior of the PTW/CF composites. Several bright areas are observed around the fiber on the worn surfaces of specimen C16 as shown in Fig. 9a. The bright areas in the SEM pictures serve as evidence of the transferred iron on the worn surface. However, this type of material transfer is rarely observed on the worn surface of the PTW/CF composites (specimen P10C6), as shown in Fig. 9b. Therefore, a clear change in the wear process is promoted by the conjunction of the PTW and CF. The matrix was then ground off, and the fiber is exposed and thinned [20]; the counterpart steel is also largely scuffed by the CF. Direct scuffing between the CF edge and counterpart tip is inhibited by the outcropped PTW around the CF. In particular, the outcropped PTW could protect CF from easy impairment and pullout [20].

The surface of specimens could also be reinforced and strengthened by embedding the free whiskers into the surface of specimens during the friction process. The matrix wear rate matrix would decrease for the same reason. As reinforcing fibers in friction materials, CF can lower hot spotting possibility and upgrade thermal diffusivity on the friction interface because of its excellent thermal conductivity. The heat dissipation on the friction interface decreases when the CF content is lower. The friction-induced heat is then caused by the increased temperature on the friction interface at high temperatures. The friction surface strength of the specimens would then likely decrease. Thus, the friction surface could easily fracture in the friction process, and the wear rate increases. Thus, the decrease in the CF content increases the wear rates of the tung oil-modified PR composites at high temperatures.

Conclusion

1. The addition of CF can largely decrease the density of the tung oil-modified PR/PTW/CF composites. The hardness of the friction materials increases with increasing the content of PTW. CF and PTW synergetically improve the mechanical properties.
2. The tung oil-modified PR/PTW/CF composites show superior wear resistance and steady variation in friction coefficients. The friction coefficient for the PTW added friction material increases with increasing content of PTW. The wear rate for the CF added friction material increases with the decreasing content of CF. PTW and CF are all effective reinforcements for the tung oil-modified PR composites. The interaction of mixing CF and PTW can significantly enhance the wear resistance of the tung oil-modified PR composite.
3. The outcropped PTW around the CF can avoid direct scuffing of the counterpart tip to the CF. And therefore CF is protected from pullout and grave impairment.
4. The degradation of wear resistance and the increase in friction coefficient occur because of the agglomeration and lapping joint of PTW when its content is high. CF can significantly improve the wear resistance of the tung oil-modified PR composite at high temperature because of its suitable thermal conductivity.

References

1. S.J. Kim, M.H. Cho, D.S. Lim, H. Jang, Synergistic effects of aramid pulp and potassium titanate whiskers in the automotive friction material. Wear **251**, 1484–1491 (2001)
2. M.G. Jacko, S.K. Rhee, *Kirk-Othmer Encyclopedia of Chemical Technology*, 4th edn. (Wiley, New York, 1992)
3. M.G. Jacko, P.H.S. Tsang, S.K. Rhee, Automotive friction materials evolution during the past decade. Wear **100**, 503–515 (1984)
4. A.E. Anderson, ASM handbook, friction, lubrication and wear technology. ASM Int. **18**, 569–577 (1992)
5. S.C. Ho, J.H. Chern Lin, C.P. Ju, Effect of fiber addition on mechanical and tribological properties of a copper/phenolic-matrix friction material. Wear **258**, 861–869 (2005)
6. X. Feng, J.Z. Lü, X.H. Lu, Application of potassium titanate whisker in composite. Acta Materiae Compositae Sin. **16**, 1–7 (1999)
7. G.S. Zhuang, G.X. Sui, H. Meng, Z.S. Sun, R. Yang, Mechanical properties of potassium titanate whiskers reinforced poly(ether ether ketone) composites using different compounding processes. Compos. Sci. Technol. **67**, 1172–1181 (2007)
8. Y.C. Kim, M.H. Cho, S.J. Kim, H. Jang, The effect of phenolic resin, potassium titanate, and CNSL on the tribological properties of brake friction materials. Wear **264**, 204–210 (2008)
9. G.J. Xian, Z. Zhang, Sliding wear of polyetherimide matrix composites: i influence of short carbon fibre reinforcement. Wear **258**, 776–782 (2005)
10. J. Bijwe, R. Rattan, M. Fahim, Abrasive wear performance of carbon fabric reinforced polyetherimide composites: influence of content and orientation of fabric. Tribol. Int. **40**, 844–854 (2007)
11. J.P. Davim, N. Marques, A.M. Baptista, Effect of carbon fibre reinforcement in the frictional behavior of peek in a water lubricated environment. Wear **251**, 1100–1104 (2001)

12. G.Y. Xie, G.X. Sui, R. Yang, Effects of potassium titanate whiskers and carbon fibers on the wear behavior of polyetheretherketone composite under water lubricated condition. Compos. Sci. Technol. **71**, 828–835 (2011)
13. A.I. Olabisi, A.N. Adam, O.M. Okechukwu, Development and assessment of composite brake pad using pulverized cocoa beans shells filler. Int. J. Mater. Sci. Appl. **5**, 66–78 (2016)
14. Q.F. Guan, G.Y. Li, H.Y. Wang, J. An, Friction-wear characteristics of carbon fiber reinforced friction material. J. Mater. Sci. **39**, 641–643 (2004)
15. D.Q. Cheng, X.T. Wang, J. Zhu, D.H. Qiu, X.W. Cheng, Q.F. Guan, Friction and wear behavior of carbon fiber reinforced brake materials. Front. Mater. Sci. Chin. **3**, 56–60 (2009)
16. GB 5763-2008, *Brake Linings for Automobiles* (Standards Press of China, Beijing, 2008)
17. M.H. Cho, S.J. Kim, D. Kim, H. Jang, Effects of ingredients on tribological characteristics of a brake lining: an experimental case study. Wear **258**, 1682–1687 (2005)
18. E. Rabinowicz, *Friction and Wear of Materials*, 2nd edn. (Wiley, New York, 1995)
19. D.H. Buckley, *Surface Effect in Adhesion, Friction, Wear and Lubrication, Tribology Series 5* (Elsevier, Amsterdam, 1981)
20. L. Chang, Z. Zhang, Tribological properties of epoxy nanocomposites-part II-a combinative effect of short carbon fibre with nano-TiO_2. Wear **260**, 869–878 (2006)
21. K. Friedrich, Z. Zhang, A.K. Schlarb, Effects of various fillers on the sliding wear of polymer composites. Compos. Sci. Technol. **65**, 2329–2343 (2005)
22. Z.Y. Jiang, L.A. Gyurova, A.K. Schlarb, K. Friedrich, Z. Zhang, Study on friction and wear behavior of polyphenylene sulfide composites reinforced by short carbon fibers and sub-micro TiO_2 particles. Compos. Sci. Technol. **68**, 734–742 (2008)
23. H. Zhang, Z. Zhang, K. Friedrich, Effect of fiber length on the wear resistance of short carbon fiber reinforced epoxy composites. Compos. Sci. Technol. **67**, 222–230 (2007)
24. K. Friedrich, Z. Lu, A.M. Hager, Overview on polymer composites for friction and wear application. Theoret. Appl. Fract. Mech. **19**, 1–11 (1993)

Influence of Surface Buffer Layer Thickness and Deposition Rate on the Release Rate of Silver Ions in Ag–TiOx Nanocomposites

Jian Xiong and Luying He

Abstract In this paper, different surface buffer layers (barrier layer) were deposited on Ag–TiO_2 2D and 3D structure of nanocomposite films by using magnetron sputtering, and the influence of different deposition conditions of buffer layers on silver ion release rate were investigated. The results showed that the buffer layer obtained at relative higher deposition rate (about 20 nm/min) had better inhibitory effect on the control of silver nano particle agglomeration on the surface of composite thin films and silver ion release rate, compared with the buffer layer produced at lower rate of deposition conditions (5 nm/min). Therefore, high rate deposition is the recommended condition for better composite film morphology and lower release rate of silver ions in the process of sputtering deposition of Ag–TiO_x nanocomposite films.

Keywords Surface buffer layer · Deposition rate · Silver ions Ag–TiO_x nanocomposite

Introduction

Optical and Structural properties of Silver Titanium Oxide thin film was first under consideration in 2004 by RF (Radio Frequency) magnetron co-sputtering. Titanium oxide growth effected by calcinations at 900 °C simultaneously increase in the optical scattering was also revealed due to the agglomeration of particles. Metal doping and calcinations produce, change in physical structure of the films. Anatase

J. Xiong
Hubei Collaborative Innovation Center for High-Efficiency Utilization of Solar Energy, Hubei University of Technology, Wuhan 430068 China
e-mail: 2003xxcj@163.com

L. He (✉)
School of Chemical Engineering and Pharmacy, Wuhan Institute of Technology, Wuhan 430205, China
e-mail: lyhewit@163.com

© Springer Nature Singapore Pte Ltd. 2018

Y. Han (ed.), *Advances in Materials Processing*, Lecture Notes in Mechanical Engineering, https://doi.org/10.1007/978-981-13-0107-0_7

to Rutile transformation affects the transmittance due to change in crystallite size [1]. Silver effect was seemed to be totally opposite to other metallic doped elements, by the increase in silver amount anatase to rutile transformation is suppressed rather brookite phase transformation was promoted, brookite suppress increase in titanium dioxide crystallite size. Transition temperature of anatase to rutile phase is reduced. Increase in the silver concentration modulate transmittance and band gap to the lower level, meanwhile increase in surface plasmon absorption peak was observed [2]. Research showed, titanium dioxide surface roughness increases by increasing thin film layer configuration and also spreading of cell on rougher surface is favorable [3]. Silver is known to be an antibacterial agent and used with the combination of ceramic hydroxyl apatite and titanium dioxide to promote bactericidal affect. Ceramic immobilized antibacterial metals, silver or copper are the versatile antibacterial inorganic materials. Titanium dioxide can exhibit strong photo-catalytic reaction only under UV illumination. Bactericidal effect is of great importance to, sterilize contaminated surfaces and enhance cleaning of tools, used for dental application [4]. Properties of nanoparticles is dependent on many factors such as particle size, shape, distribution and surface charge density etc. can influence surface Plasmon absorption band. Broader and longer wavelength is obtained by increasing size of particle and also broader peak is the reason of increase in particle size distribution. However, the photocatalytic activity, of silver titanium dioxide nanocomposite, decreased due to increase in film thickness and also silver ion concentration because of trapping of silver ion between the layers and coverage of titanium dioxide surface by silver ions. Significant photo-catalytic property is revealed by anatase crystalline phase. Also silver loading onto titanium dioxide film increases its photo-catalytic efficiency [5]. Research made on silver titanium dioxide nanocomposite shows that high release in the amount of silver result in the reduction of effective life of antibacterial activity [6]. Different combinations of layer systems are made like single layer titanium dioxide, two layers system consists of silver/titanium dioxide and three layers system of nanocomposite silver-titanium dioxide/silver/titanium dioxide. Solar light sensitivity is more pronounced in three layers system with nanocomposite and relatively effective to reduce bacteria. Also, life time of three layers system is relatively 11 times higher than two layers system [7].

It was reported that silver ion release rate is dropped off while dispersing with the rutile mesoporous layer of titanium dioxide. The bactericidal activity was also examined, between nanocomposite and titanium dioxide and bacterial rate of reduction was 4.6 times greater for nanocomposite under the illumination of UV light [8]. Another parameter is the amount of silver, which can give maximum efficiency to promote photocatalytic activity. Jin Xian Zhao estimated, up to 15% silver, boost photo-catalytic activity and extending silver amount from 15% reduces its effectiveness [9]. Silver Titania nanocomposite was recently studied in 2011 with the co-deposition of Silver and titanium dioxide different magnetron sources. Silver was deposited by DC planner magnetron source and RF magnetron source was used for sputtering titanium dioxide. Basically, volume filling factor of Silver was chosen from 15 to 47%. This high filling factor resulted in the increase in

particle size and relatively decreased the interparticle distance. Silver grows to the surface due to many reasons, large surface energy of silver clusters and Ostwald ripening. It was also shown that surface segregation can be suppressed by producing capping or barrier layer onto the nanocomposite. It was also suggested in the paper that antibacterial effect is dependent on silver ions release. This release can be controlled by using barrier layer [10].

Experimental

To deposit silver titanium dioxide nano sized antibacterial coating on silica substrate, co-sputtering process in combination with reactive ion sputter was used. Initially deposition chamber was evacuated to low pressures almost 10^{-6} Pa. In co-sputtering process the metallic silver (99.99%, Goodfellow GmbH) and titanium targets (99.99%, Goodfellow GmbH) were deposited consecutively in the presence of oxygen and argon with the flow rate of 2 and 120 sccm respectively. Oxygen in this process worked as reactive specie. While argon was used as process gas for stimulate plasma. Oxygen flow was very sensitive to this process. Initially argon was introduced to clean the oxide present on the surface of titanium target for almost 10 min at 90 W. As cleaning was performed, oxygen was introduced to increase chamber pressure up to 0.0002 mbar. Power was dropped to the required value of 60 W after maintaining the gas pressure and voltage. Meanwhile sputter rate was also checked through quartz calibrator under the sputtering targets. To initiate film deposition, the substrate rotation increased to produce continuous deposition and quartz crystal was turned back to its original position.

Results and Discussion

Different Thickness Barrier Deposition with Moderate Rate (5 nm/min)

Figure 1 is the new set of experiments regarding 2D structure, which describe better understanding to evaluate barrier effect. Black line in the graph demonstrate XPS outcome of 2 nm silver structure without barrier. With the provision of the barrier there is a rapid decrease in the silver content for high rate deposited barrier. And the silver content further decreased gradually, but highest barrier thickness (50 nm) is still unable to protect silver, as shown by green line in the graph.

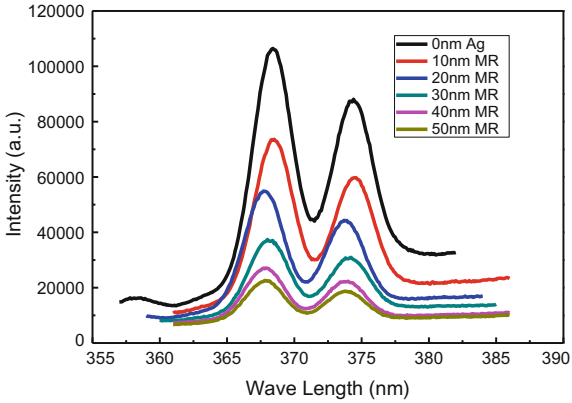

Fig. 1 XPS spectra of 2 nm silver and barriers deposited with moderate rate

Different Thickness Barrier Deposition with High Rate (20 nm/min)

Second set of experiments contain 2D structure with high rate barrier Area under the curve is also provided in Fig. 2. Smooth and gradual decrease in silver amount is described by the graphs for increasing barrier thickness.

To better understand the mechanism of Ag NPs diffusion on the surface, a set of samples with Ag nanoparticle layer of 2 nm nominal thickness coated onto a 10 nm TiO_x was produced. TiO_x barrier layers with varying thickness were deposited on top with the same moderate (5 nm/min) as used for TiO_x buffer layer. As shown in Fig. 3, the SEM images indicate that silver is still segregating to the surface even if the silver nanoparticle layer was covered by a 30 nm TiO_x barrier layer in one step. However, no silver surface segregation happened when high deposition rate was used under same condition.

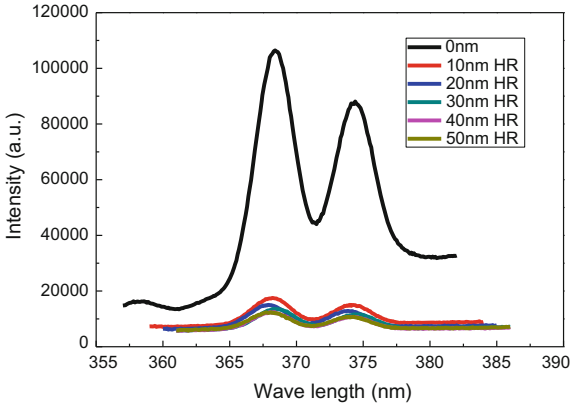

Fig. 2 XPS spectra of 2 nm silver and barrier deposited with high rate

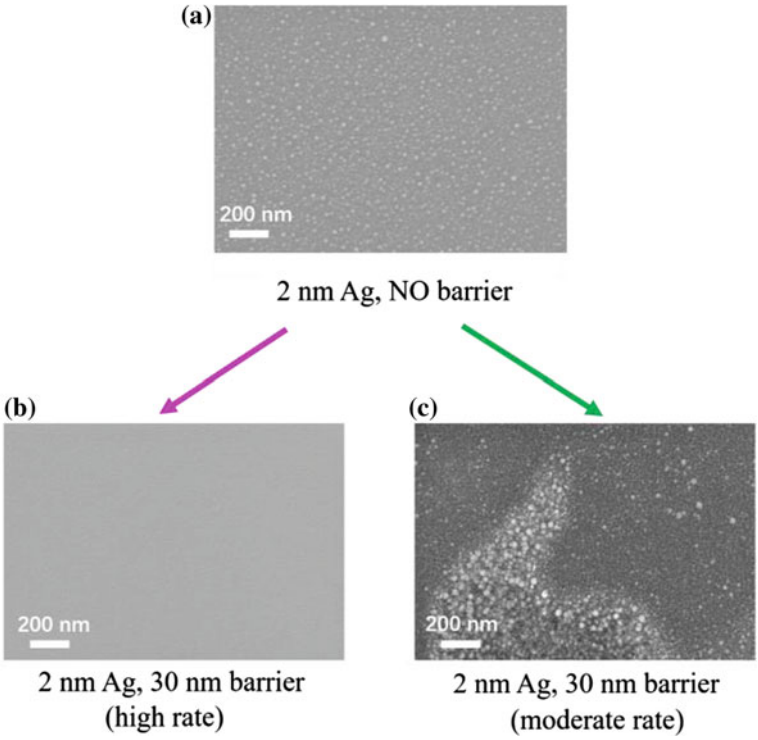

Fig. 3 SEM images of 2 nm silver and barrier with different rate

Figure 4 is the 2D structure AAS measurement profile. High rate barrier for 2D structure has provided frequent protection properties (40 nm) and decreasing trend of silver ion release. Decreasing trend remained continuously for 40 min and 2 h release time for all set of barriers deposited at the high rate. 1, 3 and 7 days has provided synchronized profile up to 20 nm barrier, there is a slight increase in release compared to 10 nm barrier. 30 nm barrier with high rate gives a sharp decrease in the release which remains constant up to 50 nm barrier. Moderate rate deposition showed complex release mechanism for 2D structure. 40 min, 2 h and 1 day release of silver ion showed the similar trend. Up to 20 nm barrier, the silver ion release amount came to its highest level in 1 day, and the silver ion release rate decreased when the barrier layer thickness further increased up to 50 nm, high limits the silver into the structure and does not allow it to come out to the water. So finally barrier works at its optimum protection level. In case of long time samples dipping into the water, for example 3 and 7 days, overall decrease in release is observed. With 10 nm barrier, release profile is decreased and further increase in barrier size up to 20 nm barrier, slight increase in release is depicted 30, 40 and 50 nm barrier provide its maximum ability to protect silver ions into the structure because of agglomeration and surface segregation.

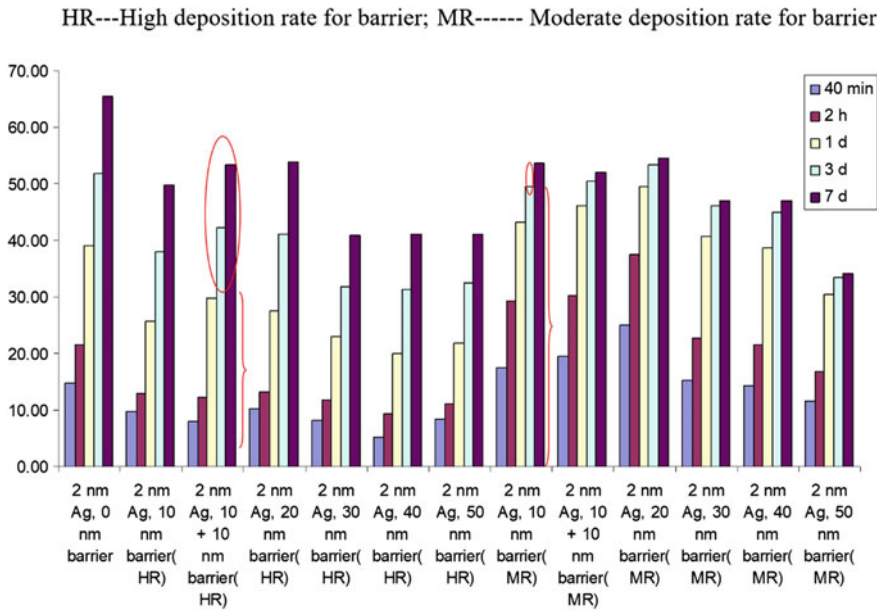

Fig. 4 AAS measurement of 2 nm silver and barrier with HR and MR

Summary

The 2D Ag/TiOx composite thin films have been deposited by reactive magnetron sputtering. The morphology of Ag/TiO_x composite thin films have been studied by using scanning electron microscopy, X-ray photoelectron spectra and atomic absorption spectrometry. The results show that high sputter rate of titanium oxide has better effect on the release of silver ions as agglomeration, and the growth does not take place for silver NPs. However in moderate barrier deposition rate, micrographs clearly show the growth of particles and agglomeration.

Acknowledgements This work is supported by Hubei Provincial Natural Science Foundation of China (2016CFB292). The financial support by Open Research Fund Program of Key Laboratory of Hydraulic Machinery Transients, Ministry of Education of the People's Republic of China (201504) and the Startup Foundation of Hubei University of Technology (BSQD14020) are also appreciated.

References

1. S.W. Ryu, E.J. Kim, S.K. Ko, S.H. Hahn, Effect of calcination on the structural and optical properties of M/TiO_2 thin films by RF magnetronco-sputtering. Mater. Lett. **58**, 582–587 (2004)
2. J.G. Yu, J.F. Xiong, B. Cheng, S.W. Liu, Fabrication and characterization of Ag–TiO_2 multiphase nanocomposite thin films with enhanced photocatalytic activity. Appl. Catal. B-Environ. **60**, 211–221 (2005)
3. D.S. Kommireddy, S.M. Sriram, Y.M. Lvov, Stem cell attachment to layer-by-layer assembled TiO_2 nanoparticle thin films. Biomaterials **27**, 4296–4303 (2006)
4. A.C. Mo, J. Liao, W. Xu, Preparation and antibacterial effect of silver–hydroxyapatite/titania nanocomposite thin film on titanium. Appl. Surf. Sci. **255**, 435–438 (2008)
5. A.R. Malagutti, H. Mourao, J.R. Garbin, Deposition of TiO_2 and Ag:TiO_2 thin films by the polymeric precursor method and their application in the photodegradation of textile dyes. Appl. Catal. B-Environ. **90**, 205–212 (2009)
6. D.H. Song, S.H. Uhm, S.B. Lee, Antimicrobial silver-containing titanium oxide nanocomposite coatings by a reactive magnetron sputtering. Thin Solid Films **509**, 7079–7085 (2011)
7. O. Akhavan, Lasting antibacterial activities of Ag-TiO_2/Ag/a-TiO_2 nanocomposite thin film photocatalysts under solar light irradiation. J. Coll. Inter. Sci. **336**, 117–124 (2009)
8. O. Akhavan, E. Ghaderi, Self-accumulated Ag nanoparticles on mesoporous TiO_2 thin film with high bactericidal activities. Surf. Coat. Technol. **204**(2010), 3676–3683 (2010)
9. J.X. Zhao, B.P. Zhang, Y. Li, Optical and photocatalytic properties of TiO2/Ag-SiO2 nanocomposite thin films. J. Alloy. Comp. **535**, 21–26 (2012)
10. V.S.K. Chakravadhanala, T. Hrkac, V. Zaporojtchenko, F. Faupel, Nanostructural and functional properties of Ag-TiO_2 coatings prepared by co-sputtering deposition technique. J. Nanosci. Nanotechnol. **11**, 4893–4899 (2011)

Analysis on the Major Environmental Factors Affecting the Weather Resistance of Polyester Coating

Xin Xu, Quan Jiang and Yannan Shi

Abstract Three types of polyester coatings were selected and subjected to 2-year natural exposure in Qionghai, Shenyang and Turpan. After natural weathering, the signs of discoloration and losing light were found on all the three polyester coatings. The polyester coatings under atmospheric environment with higher corrosion concentration were more impacted at the initial stage by such factors as pollutant, rain-wash and temperature, i.e. with large color aberration and aging rate, while at the late stage, the color aberration and aging rate either dropped or slowed down. Similar to the environmental factors affecting color aberration, the variation in glossiness indicated that high temperature or high irradiance simply did not keep glossiness degrading greatly in long term; instead, the combined environmental factors such as high temperature and humidity, high irradiance and high salt were mutually promoted and synthetically acted to accelerate the aging of coating. By comparing among the test results from the three sites, Qionghai has stronger ultraviolet radiation, higher salt concentration in the atmosphere, and higher temperature and humidity throughout the year. Therefore the weather in Qionghai is harsh enough to produce good accelerating effect, which enables rapid establishment of the methodology system for evaluating the environment adaptability of polyester coating.

Keywords Polyester coating · Natural exposure · Weather resistance Environmental impact factor

X. Xu (✉) · Q. Jiang · Y. Shi
National Building Material Testing Center, Beijing 100024, China
e-mail: frsxx6@126.com

Q. Jiang
e-mail: jq@ctc.ac.cn

Y. Shi
e-mail: 462738134@qq.com

© Springer Nature Singapore Pte Ltd. 2018

Y. Han (ed.), *Advances in Materials Processing*, Lecture Notes in Mechanical Engineering, https://doi.org/10.1007/978-981-13-0107-0_8

Introduction

With the rapid development of architectural decoration industry in China, the metal and metal-composite decorative materials are largely used, which calls for higher durability of the metal and metal composite for architectural decoration. Polyester coating is applied onto the metal base to isolate and protect the metal base from atmosphere. Compared with fluorocarbon coating, polyester coating costs less and has better weather resistance. It is extensively used as common decorative plate in interior decoration.

Polyester coating is extensively applicable, decorative and protective [1]. In atmospheric environment, particularly polluted atmospheric environment, with repeated actions of such factors as irradiance, rain-wash, condensation and air pollutants, polyester coating ages progressively, affecting the appearance and performance, i.e. losing light, discoloration, powdering, cracking and peeling. As a result, the coating losses its inherent properties, and also its protective and decorative functions for the base gradually [2, 3]. Therefore, it is necessary to study the weather resistance of polyester coating.

Natural exposure is the most common test method for researching atmospheric corrosion as it approximates to the actual use environment and the result obtained also approximates to the actual use condition. However, since climate differs considerably throughout the vast territory of China, the corrosion rates of the same material may differ drastically, by several to dozens of times, in different natural environments. As for polyester coating, the major environmental impact factors in natural exposure test are meteorological factors and corrosive factors [4]. The meteorological factors include temperature, relative humidity, wetting time of coating surface, solar radiation, precipitation, etc. The corrosives mainly consist of the compound gases containing elements such as S, C and N and other tiny solid particles borne in air [5, 6].

The characteristics of atmosphere vary with regional environment conditions. For example, the salinity of marine atmosphere varies with the distance to coastline; industrial atmospheres contain corrosive gases, e.g. SO_2, NO_2, NH_3 and H_2S and various solid suspended particles, while the atmospheres in rural areas are relatively cleaner. As climates differ drastically across the vast territory of China and, considering economic applicability, the weathering properties of coatings vary with climatic regions, it is of considerable practical significance in evaluating the weather resistance and selecting the polyester coating suitable for the region, to respond to the demands of energy conservation, emission reduction and green building today.

Test Procedure

Specimen Preparation

All specimens were prepared based on 75 mm × 150 mm 1 mm-thick aluminum veneers. Three types of polyester coated aluminum veneer were selected from the same manufacturer and were ensured that their base plates, primers, intermediate paints, coating thicknesses and coating processes were the same, their surfaces were defect free and smooth, and their coatings differed in color. Each group consisted of 3 parallel specimens with the coating colors and thicknesses as shown in Table 1.

Test Sites

The test sites selected called for harsh and representative test environments. Considering the major climatic types of China, the natural exposure test stations in Qionghai, Shenyang and Turpan were selected. Qionghai and Turpan test stations are members of the global system for typical natural environment test and are demonstration stations in the national test station system for environmental corrosion of material.

Qionghai station has a tropical humid rural climate and is 1 km distanced from River Wanquan and about 20 km from seacoast. It provides a harsh environment of high humidity, temperature and radiation, in which the tested samples age fast, so it is a perfect site for natural exposure test. Shenyang station, located in the urban area, has a low annual average temperature. Arising from the heavy industry base, Shenyang produces air pollutants mainly including sulfur dioxide and nitrogen oxide and has a typical middle-temperature sub-humid urban atmospheric environment with industrial pollution. Turpan test station, located in the hottest and most arid Turpan Basin with the lowest altitude, is abundant in sunshine and heat, and has a typical continental warm temperate desert climate.

Test Method

Color Aberration

The chromaticity coordinates L, a and b were determined with colorimeter (X-Rite); the color aberrations of the coatings before and after the test were calculated from Eq. 1; and the grade was evaluated according Table 2 (refer to GB/T 1766-2008).

Table 1 Coating types

No.	Average thickness (mm)	Color
Coating 1	28	Blue
Coating 2	31	Gray
Coating 3	29	Silvery

Table 2 Color aberration evaluation grade

Grade	Aberration degree (measured visually)	Color aberration value (measured with meter) (%)
0	No	≤ 1.5
1	Very minor	1.6–3.0
2	Minor	3.1–6.0
3	Significant	6.1–9.0
4	Severe	9.1–12.0
5	Completely	>12.0

Color aberration value

$$\Delta E = \sqrt{\Delta L^2 + \Delta a^2 + \Delta b^2} \tag{1}$$

Glossiness

The glossiness of test specimens was determined with the 60° glossiness index of glossiness tester (micro-TRI-Gloss); the gloss retention was calculated from Eq. 2; and the grade was evaluated according Tables 2, 3 and 4 (refer to GB/T 1766-2008).

$$\text{Glossiness retention } (\%) = \frac{A_1}{A_0} \times 100\% \tag{2}$$

A_1 the glossiness value after test;
A_0 the glossiness value before test.

Experiment Result Analysis

Polyester coatings 1, 2 and 3 were respectively tested in Shenyang, Turpan and Qionghai. The naturally aged specimens, after cleaning, showed minor aberration and gloss loss. The coating tested in Shenyang was more contaminated. No other change was observed.

Table 3 Gloss retention rating

Grade	Gloss loss degree (measured visually)	Gloss retention (measured with tester) (%)
0	No	97–100
1	Very minor	85–96
2	Minor	70–84
3	Significant	50–69
4	Severe	20–49
5	Completely	0–20

Table 4 Polyester coatings color aberration and glossiness data summary

Coating type	Test site	Average aberration					Average glossiness				
		Test duration (year(s))					Test duration (year(s))				
		0	0.5	1	1.5	2	0	0.5	1	1.5	2
Coating 1	Shenyang	0.12	1.18	1.31	1.03	0.92	52.3	51.5	47.0	48.8	41.5
	Turpan	0.13	0.22	0.66	0.62	1.07	55.3	53.4	55.5	56.4	53.0
	Qionghai	0.14	0.59	0.69	0.83	1.46	51.8	45.6	29.7	26.4	11.4
Coating 2	Shenyang	0.08	0.69	1.81	1.34	1.20	48.6	49.7	50.4	45.3	25.6
	Turpan	0.15	0.12	0.37	0.41	0.76	52.1	49.3	50.5	49.6	45.5
	Qionghai	0.12	0.69	0.50	0.46	1.39	53.3	32.2	6.4	3.2	1.8
Coating 3	Shenyang	0.36	0.39	1.00	1.13	1.63	32.9	33.0	32.1	29.3	24.4
	Turpan	0.11	0.55	1.22	1.35	2.16	31.8	27.6	25.9	24.5	16.3
	Qionghai	0.39	0.59	1.23	1.22	1.85	39.7	33.5	21.6	16.8	12.4

The three types of polyester coating were respectively tested in Shenyang, Turpan and Qionghai test stations and samples were intended to be drawn after outdoor exposure for 0.5, 1.5 and 2 years to determine the color aberration and glossiness. There were 3 parallel samples for each type drawn from the same test station at the same sampling time. The tested and calculated color aberrations and glossiness of the polyester coatings are listed in Table 4.

Table 4 lists the color aberrations and glossiness of polyester coatings. However, it is difficult to check out the variation trends of color aberration and glossiness from the data listed. In this case, the color aberration Origin graphs of the three polyester coatings respectively are plotted in Figs. 1, 2 and 3.

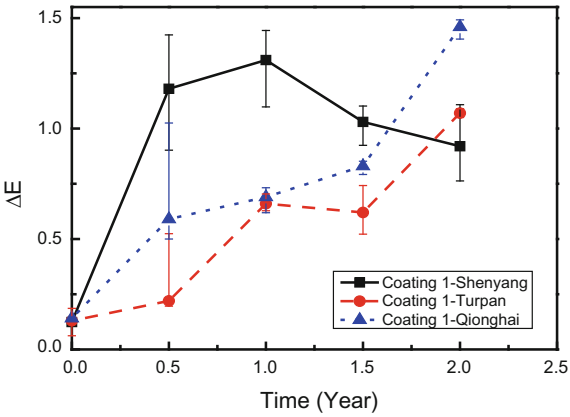

Fig. 1 Coating 1 natural exposure color aberration

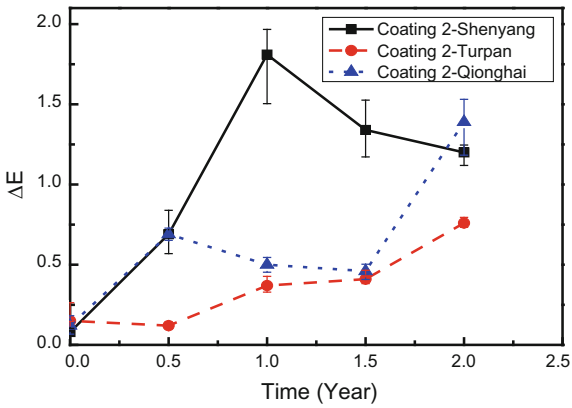

Fig. 2 Coating 2 natural exposure color aberration

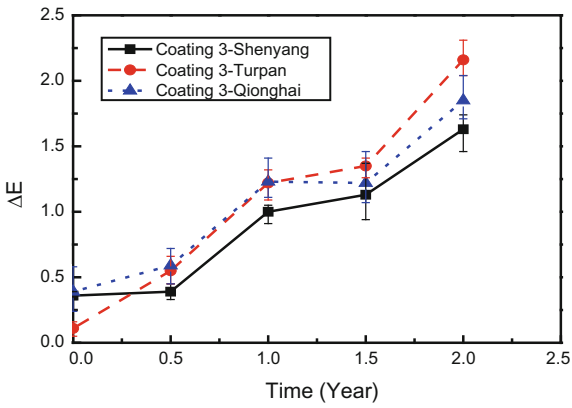

Fig. 3 Coating 3 natural exposure color aberration

Color Aberration Analysis

Comparison of the coatings of the same type tested in different test stations. For coating 1: the coating 1 in Shenyang shows significant color aberration after half-year exposure, which slightly increases until reaches the peak around 1-year exposure and then slightly drops; the coatings 1 tested in Qionghai and Turpan produce a color aberration which basically keeps increasing; after 2-year exposure, the coating 1 in Qionghai shows the largest color aberration, followed by Turpan and Shenyang. For coating 2, the color aberrations tested in the three test stations are similar to those of coating 1. For the coating 2 in Shenyang, the color aberration increased obviously at the beginning, then slightly increases and finally drops; for the coating 2 in Qionghai, the color aberration value is close to that in Shenyang after 0.5-year exposure, slightly drops after 0.5–1.5-year exposure, and then increases; for the coating 2 tested in Turpan, the color aberration keeps stable and

increases slowly; after 2-year exposure, the coating in Qionghai shows the largest color aberration, followed by Shenyang and Turpan. For the coating 3 tested in the three sites, all the color aberrations slowly increase and in terms of the color aberration values, Turpan > Qionghai > Shenyang.

To figure out the color aberration change law of the three polyester coatings tested in the three test stations, the average data on the meteorological factors and corrosion concentration in the atmospheric environments in Qionghai, Shenyang and Turpan in 2015 and 2016 are compared as shown in Tables 5 and 6. Shenyang has heavy-industry polluted atmosphere, large difference of seasonal temperatures, low radiation, and an annual precipitation 2–3 times that of Qionghai, more than 4000 times that of Turpan. Moreover, the concentrations of pollutants, e.g. sulphate ion, sulfur and nitride, in rainwater of Shenyang are higher than those of Qionghai and Turpan. The meteorological conditions of larger precipitation and higher corrosion concentration accelerate the aging corrosion to coating caused by acid rain. From the test data, in terms of the 0.5–1.5-year color aberration values of coatings 1 and 2, Shenyang > Qionghai > Turpan is always the case. At early stage of natural aging, the samples in Shenyang were severely polluted and produced the largest color aberration, from which it can be inferred that at early aging stage, the coatings were affected comprehensively by such factors as pollutants, rain-wash and temperature and aged fast. As for the coatings 1 and 2 tested in Shenyang after 1–2-year exposure, the color aberrations slightly drop, which is inferred being caused by interactions of tiny dust particles on the ageing process of coating. For example, ultraviolet-absorbing dust particles, e.g. aerogel, can filter off ultraviolet components from irradiated light, and some semi-permanent dust particles attaching to the coating can prevent coating from further atmospheric aging corrosion.

In the atmosphere of Qionghai, the sea salt particle concentration is more than 6 times higher than that in Shenyang, the chlorine ion contents are more corrosive, and the relative humidity, temperature and radiation are all at high levels. In Qionghai, the relative humidity is up to 80% and exists in the forms of H^+ and OH^- which participate in chemical actions of coating aging. Irradiance can directly cause breakage of the crosslink between macromolecules. The cycle with water absorbed, on one hand, will cause coating alternation between wetting and drying and thus introduce stresses to result in pulverized and cracked coating. On the other hand, humidity may serve as pH regulator. As the corrosive contents are higher particularly in the atmospheres of Shenyang and Qionghai, humidity will accelerate the photochemical reactions of coating.

The test data shows that as aging goes on, under the combined actions of such meteorological factors as high irradiance, high temperature and humidity, and high salt fog in Qionghai, the aging of coating was accelerated, so the coatings 1 and 2 in Qionghai showed the largest overall aging-related color aberration.

The total solar radiation in Turpan ranks the highest, Qionghai comes the second and Shenyang the last, and it is the same case when it comes to the monthly average maximum temperatures. As for coating 3, irradiance and temperature effects are more highlighted, which corresponds with the color aberrations of coating 3 after 2-year exposure in the three sites.

Table 5 Meteorological data of atmospheric environment in Qionghai, Shenyang and Turpan

Site	Average annual temperature (°C)	Average monthly maximum temperature (°C)	Average monthly minimum temperature (°C)	Relative humidity (%)	45° Total radiation (MJ/m^2)	Annual precipitation (mm)
Shenyang	10.6	30.9	−12.9	60.2	3708.7	4174.2
Qionghai	26.1	30.7	18.7	80.0	5096.9	1569.4
Turpan	17.1	37.1	−7.1	28.8	6605.6	9.0

Table 6 Data of atmospheric corrosion concentration in Qionghai, Shenyang and Turpan

Site	Continuous process (mg/100 cm^2/day)					Rainwater (mg/m^3)	
	NO_2	H_2S	Sulphation rate	Ammonia	Sea salt particle	SO_4^{2-}	Cl^-
Shenyang	0.054	0.091	1.114	0.156	0.005	7825.533	3218.200
Qionghai	0.022	0.020	0.066	0.036	0.032	666	3238
Turpan	0.001	0.007	/	0.015	/	0.028	0.150

Glossiness Analysis

The gloss retentions of coatings 1–3 are calculated according to Table 4 and Origin graphs of gloss retention are plotted, as shown in Figs. 4, 5 and 6. By comparing the 2-year-exposure gloss retentions of the three coating types tested in the same station, in Shenyang, coating 2 > coating 3 > coating 1; in Turpan, coating

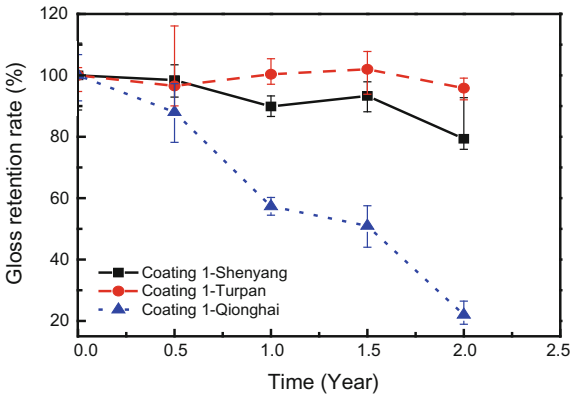

Fig. 4 Coating 1 natural exposure gloss retention rate

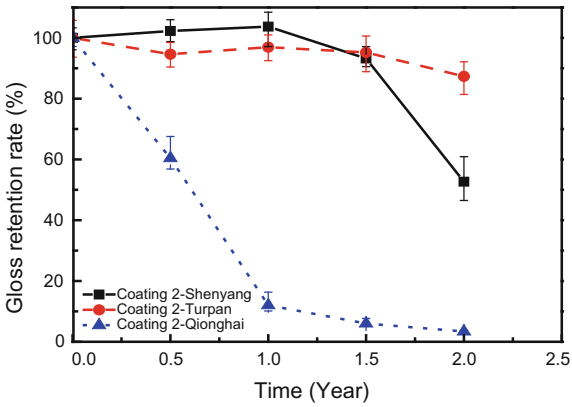

Fig. 5 Coating 2 natural exposure gloss retention rate

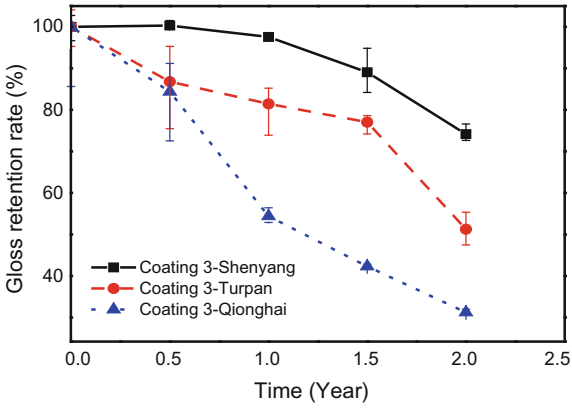

Fig. 6 Coating 3 natural exposure gloss retention rate

3 > coating 2 > coating 1; in Hainan, coating 2 > coating 1 > coating 3. Coating 1 is better than coatings 2 and 3 in terms of glossiness index. The glossiness of coating 2 in Qionghai has dropped to 1.8, i.e. severe gloss loss.

As for the three polyester coatings in Qionghai, all their gloss loss rates are much faster than those in Turpan and Shenyang. In the first year, the gloss retention of coating 3 in Turpan drops significantly, the gloss retentions of the coatings 1 and 2 in Shenyang drop slightly, the gloss retentions of coatings 1 and 2 in Turpan do not change significantly. As for coatings of the same type, the gloss retentions drop as: For coatings 1 and 2: Qionghai > Shenyang > Turpan; for coating 3: Qionghai > Turpan > Shenyang. Similar to the said analysis results on color aberration influencing factors, the combined actions of such factors as high temperature and humidity, high irradiance and high-salt fog in Qionghai accelerate the aging process of coating. In Turpan, the radiation is higher than that in Qionghai and Shenyang, the average monthly maximum temperature is up to 37.1 °C, the relative humidity is low and the corrosion concentration is very low. Such variation trend of gloss retention indicates that high temperature or high irradiance simply cannot make glossiness drop significantly in long term. This is supported by the largest decrement in glossiness of the three coatings in Qionghai.

The natural aging grades of the three polyester coatings are assessed according to the data listed in Table 4, the actual appearance of the polyester coatings and GB/T 1766-2008. The three types of polyester coating are found with slightly aberration but not at high grade, and with severe gloss loss of Grades 4 and 5 (Table 7).

In atmospheric environment of higher corrosion concentration, the color aberration of polyester coatings, at early aging stage, are more affected by such factors as pollutant, rain-wash and temperature and the aging rate is fast; the color aberration of coating at late stage drops or slows down, and the aging degree is decelerated.

Similar to the analysis results of color aberration influencing factors, the variation trend of glossiness change rate indicates that the combined actions of such factors as high temperature and humidity, high irradiance and high-salt fog in

Table 7 Polyester coatings color aberration and glossiness grade after natural exposure

Coating	Test site	Aberration grade				Glossiness grade			
		Test duration (year(s))				Test duration (year(s))			
		0.5	1	1.5	2	0.5	1	1.5	2
Coating 1	Shenyang	0	0	0	0	0	1	0	4
	Turpan	0	0	0	0	1	0	0	0
	Qionghai	0	0	0	0	1	3	3	4
Coating 2	Shenyang	0	1	0	0	0	1	1	4
	Turpan	0	0	0	0	1	1	1	2
	Qionghai	0	0	0	0	3	5	5	5
Coating 3	Shenyang	0	0	0	1	0	1	1	2
	Turpan	0	0	0	1	1	2	2	3
	Qionghai	0	0	0	1	2	3	4	4

Qionghai can accelerate coating aging; in Turpan, the high temperature and high irradiance simply cannot keep glossiness dropping significantly in long term.

Taking color aberration and glossiness into comprehensive consideration, in the natural exposure of the three-type polyester coatings, the performance of coating 1 ranks the best, coating 2 the second, and coating 3 the last.

Summary

The 2-year natural exposure test results from Qionghai, Shenyang and Turpan indicate that environmental factors such as irradiance, temperature and humidity, salt fog are mutually promoted and interacted so that aging of coating is accelerated.

Qionghai has stronger ultraviolet radiation, higher salt concentration in the atmosphere, and higher temperature and humidity throughout the year. Therefore the weather in Qionghai is harsh enough to produce good accelerating effect, which enables rapid acquisition of the coating performance change status and rapid establishment of the methodology system for evaluating the environment adaptability of polyester coating.

The overall metal-base decoration coating system in the future may be subjected to natural exposure test in Qionghai so as to rapidly establish a methodology system for evaluating the natural exposure adaptability of polyester coating.

References

1. L.V. Guiying, Z. Hua, L. An et al., On the aging and anti-aging evaluation system for polymer materials. Chem. Bio. Eng. **23**, 1–4 (2003)
2. M. Omastova, S. Podhradska, J. Prokes et al., Thermal ageing of conducting polymeric composites. Polym. Degrad. Stab., **82**, 251–256 (2003)
3. L. Xiaogang, G. Jin, Z. Sanping et al., *Aging Rules and Mechanism of Polymer Material in Natural Environment* (Science Press, Beijing, 2011)
4. P.K. Sharma, M. Khandelwal, T.N. Singh, Variation on physico-mechanical properties of kota stone under different watery environments. Build. Environ. **42**(12), 4117–4123 (2007)
5. C. Arroyave, F.A. Lopez, M. Morcillo, The early atmospheric corrosion stages of carbon steel in acidic fogs. Corros. Sci. **37**(11), 1751–1761 (1995)
6. M. Yamashita, H. Miyuki, Y. Matsuda et al., The long term growth of the protective rust layer formed on weathering steel by atmospheric corrosion during a quarter of a century. Corros. Sci. **36**(2), 283–299 (1994)

Structural Analysis and Optical Properties of Sol-gel Derived $CuCoMnO_x$ Spinel Composite Oxide Coatings

Jie Min and Weiyang Guo

Abstract Solar selective absorption coatings were prepared on 304L stainless steel using $CuCoMnO_x$ composite oxide by sol-gel. The absorptance and emittance of the coatings were measured over the UV-Vis-NIR wavelength range. The $CuCoMnO_x$ coatings revealed a normal optical properties with the absorptance (α) reached to 0.90 and the emittance (ε) lowed to 0.10, which were much excellent than what can be achieved by $CuMnO_x$ coatings. By measuring the phase composition, microstructure and FT-IR of the coatings, the spinel structure oxide generated with the increasing of annealing temperature. It was found that, the enhancement in absorptance of the coatings was ascribed to the doping of Co. Hence the spinel $CuCoMnO_x$ composite oxide coatings could be used as a new kind of candidate materials for solar selective coatings.

Keywords $CuCoMnO_x$ · Selective absorption · Absorptance · Emittance Spinel structure

Introduction

Solar selective coatings (SSC) for a solar thermal collector, can essentially improve the efficiency of the solar to thermal energy conversion [1]. However, SSC with high solar absorptivity either needed vacuum processes and high cost, such as chemical vapor deposition and sputtering [2]. Any improvement for SSC optical properties would directly resulted in reducing the cost of thermal energy storage.

J. Min (✉)
Hubei Collaborative Innovation Center for High-Efficient Utilization of Solar Energy, Hubei University of Technology, Wuhan, China
e-mail: whutminj@163.com

W. Guo
State Key Laboratory of Advanced Technology for Materials Synthesis and Progressing, Wuhan University of Technology, Wuhan, China
e-mail: 42638478@qq.com

© Springer Nature Singapore Pte Ltd. 2018

Y. Han (ed.), *Advances in Materials Processing*, Lecture Notes in Mechanical Engineering, https://doi.org/10.1007/978-981-13-0107-0_9

Recent developments in SSC were the creation of materials with high durability and selectivity which required a environmentally friendly and cost-effective synthesis process [3]. Vacuum-based magnetron sputtering techniques have been the next candidate route for high selectivity in SSC preparation, though the cost was too high [4, 5]. Sol-gel process was a universal relevance surface engineering technique, which compared to vacuum-based techniques due to their immanent advantages like: (a) being environmentally friendly, (b) suitable to coat large areas, (c) suitable to variety of substrates, especially for stainless steel substrates, (d) coatings with good adhesion, and (f) easy to realize automation [6]. According to the aforementioned advantages of sol-gel derived coatings, these coatings had widely potential use in preparing SSC on stainless steel substrates.

In the past years, hexavalent chrome-based coatings were prepared for SSC; but in recent years, they had been strictly banned across the world due to the toxic of hexavalent chrome. In addition, transition metals oxides were also widely studied in the field of solar energy conversion as SSC. The mixed oxides of copper, cobalt and manganese for individual layers SSC were studied by Kaluza in their research [7, 8]. Their study found that, a solar absorptance of $\alpha = 0.90$ and a thermal emissivity of $\varepsilon = 0.05$ (measured at 100 °C) can be achieved with individual layers deposited by sol-gel dip-coating on aluminum substrates (not stainless-steel substrates). These excellent optical properties were explained by the intrinsic properties of the complex oxide, which had a electronic interband transitions produce a very large absorption in the visible spectral range, whereas a weak absorption in the infrared spectral range as few vibrational bands exist at 1000 cm^{-1}. More recently, further research indicated that the solar absorption of a multilayered copper–manganese oxides coatings was significantly improved by Bayón, which up to 0.95 [9]. The further research by X-ray diffraction (XRD) and X-ray photoelectron spectroscopy (XPS) showed that the completely increasing of solar absorptance would due to the special crystal structure of $Cu_{1.5}Mn_{1.5}O_4$ [10]. Spinel structural $Cu_{1.5}Mn_{1.5}O_4$ coatings have been synthesized on aluminum substrates (not stainless-steel substrates), whereas the same $Cu_{1.5}Mn_{1.5}O_4$ coatings on stainless steel (commonly substrates for SSC) showed low solar absorptance. And the corresponding absorption spectrums and improved coatings were not reported in literature.

The optimal optical properties for such coatings (high absorptance and low emittance, as far as possible) based on transition metals oxides were presented together with durability experiments in previous research [11]. In this paper, the multilayered $CuCoMnO_x$ spinel composite oxide coatings were prepared by sol-gel. The structural analysis and optical properties were investigated by measuring microstructure, morphology, FT-IR and phase composition of the coatings. In addition, a kind of coatings for stainless steel substrates and two meters long stainless-steel tubes were prepared.

Experimental

Coatings Deposition

304L flat plates of dimensions 100 mm × 100 mm × 1 mm, were used as substrates. The Cu/Co/Mn precursor solution was made from $Mn(CH_3COO)_2 \cdot 4H_2O$(98 wt%, AR), $Cu(CH_3COO)_2 \cdot H_2O$(98 wt%, AR), $CoCl_2 \cdot 6H_2O$(98 wt%, AR). According to the mole ratio of Cu:Co:Mn = 3:1:3, the corresponding weigh mixed metal salt and corresponding weigh absolute ethanol (as solvent) were taken for the concentration of 0.4 mol/L. Suitable amount of citric acid and coalescent agent were added to the solution which was placed in 70 °C water bath under constant magnetic stirring. The pH was adjusted by ammonia. In order to improve hydrolysis and condensation reactions in the solution, ammonia was slowly dripped, and then the homogeneous mixed metal salt was formed. After 3–5d, the solution was ready for dip-coating. In order to obtain uniform, homogeneous and uncontaminated coatings, a amenable equipment was independently developed in the research. The samples (stainless steel substrates with $CuCoMnO_x$ coatings) were placed in a rotary furnace after dipping. Then the temperature of furnace was increased at a rate of 1.5 °C per minute up to kinds of temperature. The dip-coatings together with their substrates were thermally treated for 90 min at the maximum temperature before cooling down freely in the furnace.

Structural Analysis and Optical Properties

The phase compositions of $CuCoMnO_x$ coatings were measured by X-ray diffraction (XRD, D8 Advance, Bruker, Karlsruhe, Germany) employing Cu Kα radiation (λ = 1.54056 Å). The microstructure and morphology were characterized by scanning electron microscopy (SEM, JSM-IT300, JEOL Ltd., Tokyo, Japan). The chemical composition was investigated by FT-IR The near-normal spectral reflectance (R) and transmittance (T) of the coatings were measured in the wavelength range of 0.3–2.5 μm by a Shimadzu UV3600 UV/VIS spectrophotometer (Kyoto, Japan). The near-normal spectral reflectance in the wavelength range of 2.5–25 μm was measured by a Bruker Tensor 27 Fourier Transform spectrometer (Bruker, Karlsruhe, Germany). The absorptance (α) and emittance (ε) of the deposited $CuCoMnO_x$ coatings were calculated according to the reflectance [12].

Results

XRD Analysis

The spinel oxides generated with the annealing temperature higher than 450 °C and holding time greater than 60 min [13]. The increase of annealing temperature was in favor of enhancing the crystallinity and particles size. However, the solar absorptance of coatings did not show continuous rising until the annealing temperature rising to 550 °C. In a previous study, the optimal optical properties of such coatings based on the solution pH of 3.5 and the annealing temperature of 550 °C with the introduction of Co in the $CuMnO_x$ process [11].

The diffraction pattern of the coatings with different annealing temperature showed similar peak characteristics without emergence of any new peaks (Fig. 1). XRD analysis showed that the type, granularity and relative content of $CuCoMnO_x$ were affected by annealing temperature and sol pH. The diffraction peaks of both pH = 3.5 and 550 °C were sharp and intense, indicating their highly crystalline nature. No impurity peaks were observed, confirming the high purity of the coatings. It was noted that the diffraction with stronger peaks at 2θ value of 36.02° and 0.855° which correspond to the (2 2 0) and (3 1 1) crystal planes of the spinel structure $CuCoMnO_4$ (ICDD PDF card 74-2422). With the introduction of Co in the $CuMnO_x$ process, the strongest peak in diffraction of the deposits was changed crystal planes from (2 0 0) to (2 2 0). In the case of the annealing temperature for dried sol which deposited on the stainless-steel substrates was higher than 500 °C, the total heat released during the exothermic decomposition process was enough for the completely conversion of transition metals oxides to form spinel structure and removal of all the organic materials.

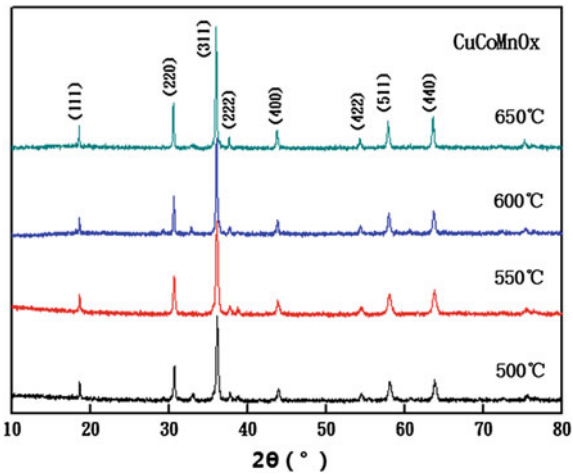

Fig. 1 XRD patterns of $CuCoMnO_X$ coatings with different annealing temperature

SEM Analysis

The surface SEM images and corresponding Cross-sectional SEM images of $CuCoMnO_x$ coatings deposited on stainless steel substrates were shown in Fig. 2. The surface SEM images showed that the as-deposited coatings consist of platelets roughly 400–600 nm in diameters that tend to be vertically oriented and randomly distributed (Fig. 2a). This morphology was consistent with that typically observed for layered oxides, which adopting a spinel-like structure with octahedral coordinated metal cations hexagonally packed in sheet that were separated by hydrolysis and condensation reactions. Corresponding Cross-sectional SEM images showed that the $CuCoMnO_x$ coatings was less than 1 μm and dispersed uniformly, which had porous structure and the aperture of coatings increased with annealing temperature (Fig. 2b).

FT-IR Analysis

FT-IR analysis was further carried out to verify the conversion of $CuCoMnO_x$ in the annealing process. As shown in Fig. 3, several absorbance peaks appeared in the spectrum at 500, 609, 697 and 3437 cm^{-1}, compared with absorption band at 700–400 cm^{-1} that of spinel $CuCoMnO_x$ [14]. Strong absorbance peaks at 500 cm^{-1} could be ascribed to the stretching vibration of Cu–O, and strong absorbance peaks at 609 cm^{-1} could be ascribed to the stretching vibration of Mn–O, while weak absorbance peaks at 697 cm^{-1} could be ascribed to the stretching vibration of Co–O. Another absorbance peaks at 3437 cm^{-1} could be ascribed to the weak stretching vibration of H–O in liquid. Mn–O bonds existed in octahedral spinel structure, while Cu–O bonds exist in the spinel structure of the tetrahedron [15]. The wave number, respectively, had a little deviation to infrared wavelengths. The figure showed that the coatings were $CuCoMnO_x$ oxide with spinel structure under the condition of the preparation.

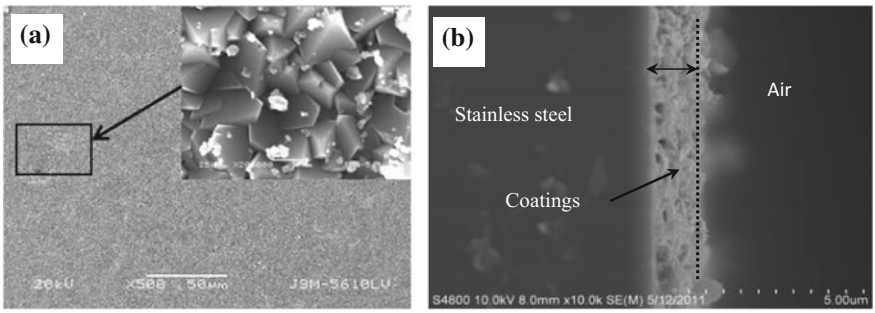

Fig. 2 Surface images and corresponding cross-sectional images of $CuCoMnO_x$ coatings

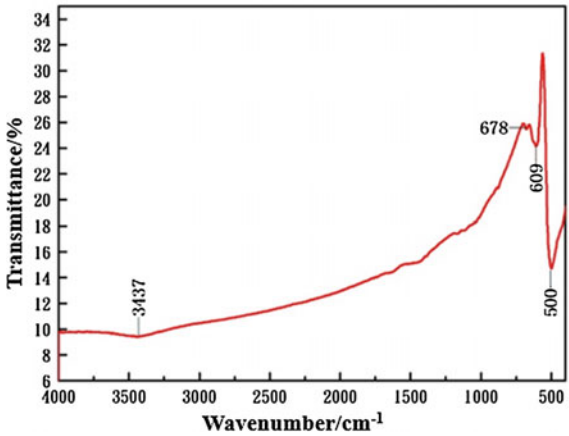

Fig. 3 FT-IR of $CuCoMnO_x$ coatings deposited on stainless steel substrates

Optical Properties

The reflectance spectra of $CuCoMnO_x$ coatings with varies annealing treatment temperatures were shown in Fig. 4. The $CuCoMnO_x$ coatings revealed a normal optical properties with the absorptance (α) reached to 0.90 and the emittance (ε) lowed to 0.10, which were much excellent than what can be achieved by $CuMnO_x$ coatings. It could be explained that the reflectance spectra in the UV–VIS–NIR (0.3–2.5 μm) regions and IR (2.5–5 μm) wavelength regions were obtained by two types of equipment [11]. Obviously, all of the reflectance spectra were similar in shape, but the absorptance and the emittance were different. The test data of

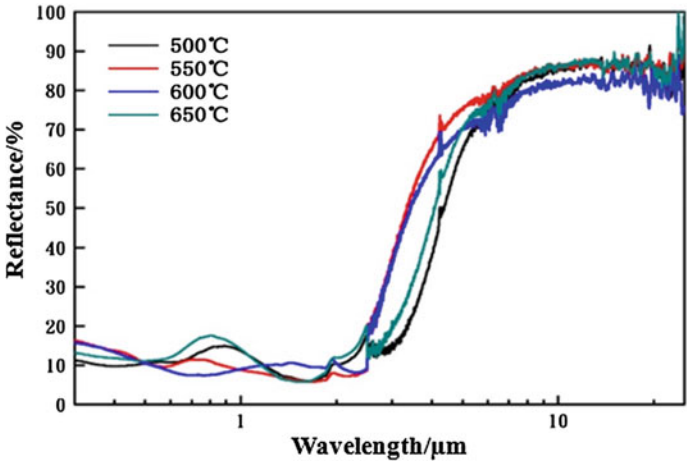

Fig. 4 Reflectance spectra of $CuCoMnO_x$ coatings with different annealing temperature

reflectance spectra showed that the solar absorptance rising while the thermal emittance decreased when the annealing treatment temperature increased.

Thermal Shock Resistance and Corrosion Resistance

The prepared solar selective coatings with excellent property of thermal shock resistance and corrosion resistance can be used in nature environment. Some experiments for thermal shock resistance were carried out according to the following method: the coatings were placed in a muffle furnace which the temperature was raised from room temperature to 600 °C at the rate of 100 °C/h, and then maintained at 600 °C for 15 min before air cooling to room temperature. The result of the experimental tests showed that there were macroscopic structural integrity and not peeling off in coatings after 100 times thermal shock.

The salt-fog tests were employed in NaCl solution, and the results showed that $CuMnO_x$ coatings had good anti-corrosivity against the salt water. After salt-fog corrosion test, the $CuMnO_x$ coatings coated on the brown materials could be ascribed to the formation of Fe_2O_3. The stainless steel substrate were pretreated before the preparation of the coatings. The corrosion resistance of stainless steel was deteriorated by the grain boundary corrosion during the pretreatment of substrates. Although the composition of spinel coatings have good corrosion resistance, the pretreating stainless steel substrates have weak resistance to salt fog corrosion when the stainless steel substrates in contact with the corrosion solution.

Discussion

As shown above, solar absorptance and thermal emittance were greatly influenced by metal composition of the coatings. According to authors' previous studies, optical properties with higher solar absorptance and lower thermal emittance resulting from the perfect crystallinity and the pure composition of the coatings. Transition metal oxides were extensively investigated because of their various applications in electronics, magnetism, catalysis or optics. Cu and Mn have been extensively studied to fine effect such as the comprehension of interaction and distribution of the atoms in a solid. These basic theories can explain the existing experimental phenomena. According to the Jahn-Teller effect, the instruction of Co^{3+} which formed on octahedral sites may be the result of an increasing degree of tetragonal distortion, which can affect crystal symmetry [16]. The lower symmetry of the spinel phase crystals in the solar coatings can cause lower solar absorptance.

In addition, the optical properties of $CuCoMnO_x$ coatings may significantly influenced by their surface morphology. The representative SEM images of the $CuCoMnO_x$ coatings with varies annealing temperatures were showed above. Solar absorptance did not show a continuous increase until the annealing temperature

rising to 550 °C. The low-magnification SEM images in Fig. 2a showed that the surface of $CuCoMnO_x$ coatings were relatively uniform, without obvious microscopic holes. The surface morphology of the $CuCoMnO_x$ coatings have better sintering effect as the annealing temperature rising. The solar absorptance and thermal emittance were also greatly influenced by optical trap in surface morphology, because of the high reflectivity of the long wave band. For another, the solar absorptance and thermal emittance were also greatly influenced by the roughness of the surface morphology, which can not only increase the absorption rate, while would not improve the emissivity. It has been reported that an appropriate surface roughness (RMS 5–100 nm) can effectively increase in solar absorptance and the slightly increase in thermal emittance [17]. Under the present research conditions, the surface roughness of $CuCoMnO_x$ coatings was not studies.

Conclusions

The $CuCoMnO_x$ spinel coatings derived from the cost-effective sol-gel technique enable to coat large areas with a wide variety of substrates especially stainless steel. The normal optical properties with the absorptance (α) reached to 0.90 and the emittance (ε) lowed to 0.10 can be realized. The spinel structure oxide generates with the increasing of annealing temperature. The enhancement in absorptance of the coatings is ascribed to the doping of Co. Furthermore, the $CuCoMnO_x$ coatings show good property of thermal shock resistance and corrosion resistance, which can be used in nature environment. Consequently, these $CuCoMnO_x$ spinel coatings can be used as a new kind of candidate materials for solar selective absorber coatings.

Acknowledgements Open Foundation of Hubei Collaborative Innovation Center for High-efficient Utilization of Solar Energy (HBSKFMS2014024).

References

1. A. Fernández-García, E. Zarza, L. Valenzuela et al., Parabolic-trough solar collectors and their applications. Renew. Sustain. Energy Rev. **14**, 1695–1721 (2010)
2. J. Moon, D. Lu, B. VanSaders et al., High performance multi-scaled nanostructured spectrally selective coating for concentrating solar power. Nano Energy **8**, 238–246 (2014)
3. A. Amri, Z.T. Jiang, T. Pryor et al., Developments in the synthesis of flat plate solar selective absorber materials via sol-gel methods: a review. Renew Renew. Sustain. Energy Rev. **36**, 316–328
4. N. Selvakumar, H.C. Barshilia, Review of physical vapor deposited (PVD) spectrally selective coatings for mid-and high- temperature solar thermal applications. Solar Energy Mater. Solar Cells **98**, 1–23 (2012)

5. H.C. Barshilia, P. Kumar, K.S. Rajam et al., Structure and optical properties of Ag–Al_2O_3 nanocermet solar selective coatings prepared using unbalanced magnetron sputtering. Solar Energy Mater. Solar Cells. **95**, 1707–1715
6. R. Subasri, K.R.C. Soma Raju, D.S. Reddy et al., Sol-gel derived solar selective coatings on SS 321 substrates for solar thermal applications. Thin Solid Films **598**, 46–53 (2015)
7. L. Kaluza, A. Surca-vuk, B. Orel et al., Structural and ir spectroscopic analysis of Sol-Gel processed $CuFeMnO_4$ spinel and $CuFeMnO_4$/silica films for solar absorbers. J. Sol-Gel. Sci. Technol. **20**, 61–83 (2001)
8. L. Kaluza, B. Orel, G. Drazic et al., Sol-gel derived $CuCoMnO_x$ spinel coatings for solar absorbers: structural and optical properties. Sol. Energy Mater. Sol. Cells **70**, 187–201 (2001)
9. R. Bayón, G. San, A. Morales, Durability tests and up-scaling of selective absorbers based on copper-manganese oxide deposited by dip-coating. Solar Energy Mater. Solar Cells **94**, 998–1004 (2010)
10. R. Bayón, G. San Vicente, C. Maffiotte et al., Characterization of copper-manganese-oxide thin films deposited by dip-coating. Sol. Energy Mater. Sol. Cells **92**, 1211–1216 (2008)
11. W. Guo, J. Min, D. Gong et al., Effect of annealing and pH value on structure and optical properties of $CuCoMnO_X$ composite oxide. J. Wuhan Univ. Technol. **38**, 1–7 (2016). (In Chinese)
12. Xiaobo Wang, Taoyuan Ouyang, Xiaohua Duan et al., Improved solar absorptance of WC/Co solar selective absorbing coating with multimodal WC particles. Metals **137**, 1–10 (2017)
13. Y. Gao, J. Xiong, D. Gong et al., Improvement of solar absorbing property of Ni–Mo based thermal spray coatings by laser surface treatment. Vacuum. **121**, 64–69 (2015)
14. W. Mäntele, *Infrared and Fourier-Transform Infrared Spectroscopy*, vol. 3 (Springer Netherlands, 1996), pp. 137–160
15. P. Ma, Q. Geng, X. Gao et al., Aqueous solution-derived $CuMn_2O_4$ ceramic films for spectrally selective solar absorbers. Ceram. Int. **42**, 19047–19057 (2016)
16. P. Wei, M. Bieringer, L.M.D. Cranswick et al., In situ high-temperature X-ray and neutron diffraction of Cu–Mn oxide phases. J. Mater. Sci. **45**, 1056–1064 (2010)
17. M. Farooq, Z.H. Lee, Computations of the optical properties of metal/insulator-composites for solar selective absorbers. Renew. Energy **28**, 1421–1431 (2003)

Effect of Cooling Rate on Solidification Structure of Zinc–Aluminum–Magnesium Alloy

Guanghui Liu, Guangrui Jiang and Haiquan Wang

Abstract Zinc–Aluminum–Magnesium coating are paid more attention recently due to the appearance of the surface and superior corrosion resistance. The research on the solidification structure of Zinc–Aluminum–Magnesium alloy is less. In this paper, the solidification structure of Zinc–Aluminum–Magnesium alloy with different zinc content and aluminum content under water cooling, air cooling and furnace cooling conditions was studied. The industrial pure Zinc (99.99 wt%), industrial pure Aluminum (99.99 wt%), Magnesium and Zinc alloy ($Mg_{11}Zn$) were selected for smelting in resistance furnace. The molten alloy components were Z3A3M (3 wt% Al, 3 wt% Mg), Z5A3M (5 wt% Al, 3 wt% Mg). The solidification structure of the alloy was observed by scanning electron microscopy. The composition of the phase was analyzed by X-ray Diffraction (XRD). The corrosion property of the alloy was analyzed by electrochemical experiment. It was found that four phases existed in these two alloys: Zn phase, Al phase, $AlMg_4Zn_{11}$ phase and Mg_2Zn_{11} phase in different cooling modes. And in air-cooled conditions, the two alloys showed a good corrosion resistance.

Keywords Zn–Al–Mg · Electrochemical test · Corrosion resistance

G. Liu (✉) · G. Jiang · H. Wang
Shougang Research Institute of Technology, No. 69 YangZhuang Street, Beijing 100043, China
e-mail: liuganghui17@sina.com

G. Jiang
e-mail: jiangguangrui@shougang.com.cn

H. Wang
e-mail: whq@shougang.com.cn

G. Liu · G. Jiang · H. Wang
Beijing key Laboratory of Green Recyclable Process for Iron& steel Production Technology, No. 69 YangZhuang Street, Beijing 100043, China

© Springer Nature Singapore Pte Ltd. 2018

Y. Han (ed.), *Advances in Materials Processing*, Lecture Notes in Mechanical Engineering, https://doi.org/10.1007/978-981-13-0107-0_10

Introduction

Hot-dip galvanized zinc–aluminum–magnesium coating is a very promising new coating in the world's industrial manufacturing. It has excellent corrosion resistance, coating performance, ductility and high surface strength, and can be adapt to a lot of serious corrosion environment. In the accelerated corrosion test, corrosion resistance of Zinc–Aluminum–Magnesium alloy coated steel plate is 10–20 times better than pure zinc steel plate, 5–8 times better than Zn-5% Al alloy coated steel plate [1]. Compared with the traditional hot-dip galvanized steel, Zinc–Aluminum–Magnesium alloy coating has better scratch resistance, longer service life of the coating. Zinc–Aluminum–Magnesium alloy is resource-saving and environment-friendly product, and has other good qualities, such as better welding performance. In recent years, domestic and foreign research on Zinc–Aluminum–Magnesium alloy coating are more and more [2]. However, the research on the solidification structure of the coating alloy is very limited at home and abroad. And there are different interpretations of the existing research on the solidification structure of the alloy. Therefore, this paper attempts to find out the connection between them by studying the phase and structure and the corrosion resistance of Zinc–Aluminum–Magnesium alloy with different Magnesium content and Aluminum content under different cooling conditions (water cooling, air cooling, furnace cooling).

Experiments

Zn–Mg alloy ($Mg_{11}Zn$), pure Zn ingot (99.99 wt%) and pure Al ingot (99.99 wt%) were used as raw materials to melt Zn–Al–Mg alloy in order to eliminate the adverse effect of impurity elements on the microstructure and corrosion properties of Zn–Al–Mg alloy. According to the results of several smelting experiments and chemical analysis, the burning rate of Zn, Al and Mg was determined. The composition of qualified Zn–Al–Mg alloy was prepared. The composition of the alloy was shown in Table 1.

Put a graphite crucible into a well resistance furnace and begin to heat, then put Zn ingots and Al ingots into the crucible, continually heat up to 600 °C for melting. After Zn ingots and Al ingots were completely melted, the cover agent was sprayed on the surface of the alloy liquid. Push a Mg block into the bottom of the alloy liquid with a rod, waited until the Mg block to be completely melted, used steel rods on the metal liquid for appropriate mixing, placed at 550 °C for half an hour,

Table 1 Chemical composition of the smelting Zn–Al–Mg specimens

No.	Al (wt%)	Mg (wt%)
Z3A3M	2.96	3.01
Z5A2 M	5.12	2.97

removed impurities and cover agent on the metal surface. Then the alloy liquid was poured into a graphite sampler with a inner size of φ20 mm × 50 mm which was put separately into water tank, bare air and in the furnace for different cooling conditions. Samples were taken at 15 mm height from the bottom of the ingot [3].

Metallographic samples were prepared by grinding and polishing and the samples were etched with 4 vol% HNO3 alcohol solution. The microstructures of the samples were observed by a scanning electron microscopy (SEM). Energy dispersive spectrometer (EDS) attached to the SEM was used to analyze the elemental composition of the alloy.

The alloy phase was analyzed by D8 Advance X-ray diffraction meter (XRD) of Bruker Company. The accelerated electricity current is 40 mA and the voltage is 35 kV. The range of diffraction angle (2θ) is 20°–105°, and the scanning speed is 1°/min.

An electrochemical workstation was used to test the electrochemical polarization curves and impedance spectra. The test solution was 3.5 vol% NaCl and the test temperature was 25 °C. The reference electrode was Ag/AgCl and the Pt mesh was the counter electrode. For polarization curves, the current density values were measured at the set scanning rate (1 mV/s) and potential interval (±0.25 V), and the important corrosion resistance parameters such as the self-corrosion potential (Ecorr) and the self-corrosion current density (Icorr) were measured. The test area of the sample was also 1 cm^2.

Results and Discussion

X-Ray Diffraction Pattern Analysis

Figures 1 and 2 show the X-ray phase analysis result. Z3A3M-W and Z5A3M-W represents in water cooling mode, Z3A3M-A and Z5A3M-A in air cooling mode. Z3A3M-F and Z5A3M-F represents in furnace cooling mode. Table 2 shows the phase component and content of the two alloys in water cooling, air cooling and furnace cooling conditions.

The XRD patterns of Z3A3M alloy shows that the Z3A3M alloy has four phases in water cooling and air cooling conditions: Zn phase, Al phase, $AlMg_4Zn_{11}$ phase and Mg_2Zn_{11} phase. In the furnace cooling state, only three kinds of phase existed: Zn phase, Al phase and $AlMg_4Zn_{11}$ phase, no Mg_2Zn_{11} phase. And the Mg_2Z_{11} phase generated in the air cooled state reached the maximum (36.4%) in Table 2.

The XRD patterns of Z5A3M alloy shows that there are four phases in three cooling conditions: Zn phase, Al phase, $AlMg_4Zn_{11}$ phase and Mg_2Zn_{11} phase. Similarly, the Mg_2Zn_{11} phase is the maximum (13.8%) in the air-cooled condition. At the same time the Aluminum-rich phase also reached the maximum (17.3%) in air cooling condition.

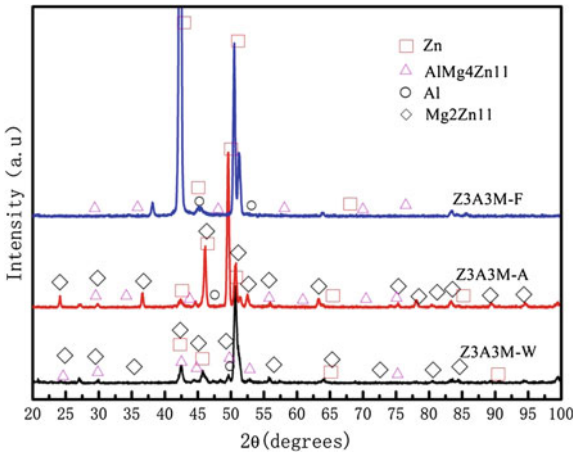

Fig. 1 XRD pattern of Z3A3M in different cooling mode

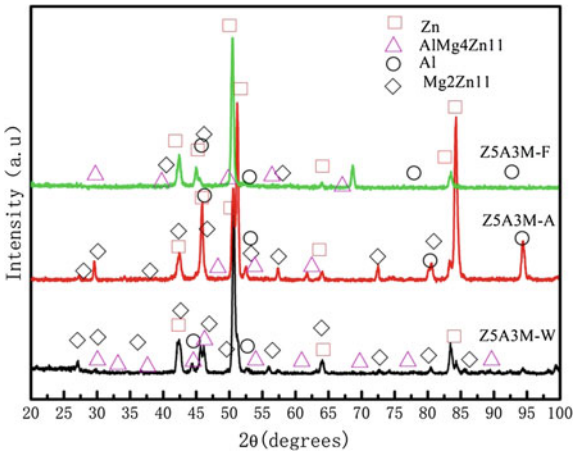

Fig. 2 XRD pattern of Z5A3M alloy in different cooling mode

Table 2 Phase component of Z3A3M and Z5A3M in different cooling mode

No.	Zn (%)	AlMg4Zn11 (%)	Al (%)	Mg2Zn11 (%)
Z3A3M-W	75.8	4.8	1	18.4
Z3A3M-A	57.3	4.8	1.5	36.4
Z3A3M-F	93.1	4.6	2.3	–
Z5A3M-W	86	1.7	1.7	10.5
Z5A3M-A	65.2	3.6	17.3	13.8
Z5A3M-F	84.4	2.9	10.1	2.5

Microstructure and Phase Structure

Figure 3a is the microstructure of Z3A3M alloy in water cooling mode. The binary eutectic phase was not found in water cooling mode. Point 1 is the lamellar zinc-rich area. At point 3 near point 1, it is block-like aluminum rich phase. Point 2 is a dense ternary eutectic region. Since its element content does not meet any of the Mg_2Zn_{11} and $AlMg_4Zn_{11}$, it is likely that the Zn/Al/Mg_2Zn_{11} ternary eutectic structure and Zn/Al/$AlMg_4Zn_{11}$ ternary eutectic tissue coexists in this phase [4].

Figure 3b is the microstructure of Z3A3M alloy in air cooling mode. At point 3, there is the highest zinc content in the chrysanthemum-like structure so it is Zn-rich phase. At point 1, the magnesium content (6.01%) is close to the content of the Mg element in Mg_2Zn_{11}. So it should be Al/Mg_2Zn_{11} binary eutectic phase. At point 2, according to the EDS composition analysis in Table 3, it is possible for Zn/Al/Mg_2Zn_{11} ternary eutectic structure and Zn/Al/$AlMg_4Zn_{11}$ ternary eutectic structure to coexist in this phase.

Figure 3c is the microstructure of Z3A3M alloy in furnace cooling mode. At point 1, it is the Zn-rich phase with higher Zn content. At point 2, Mg content and aluminum content are higher. But according to the XRD results in Table 2, there is no Mg_2Zn_{11} phase. Also the content of components does not meet the $AlMg_4Zn_{11}$ phase, it is likely to be the Zn/Al/$AlMg_4Zn_{11}$ ternary eutectic organization. Point 3 is the massive aluminum-rich phase.

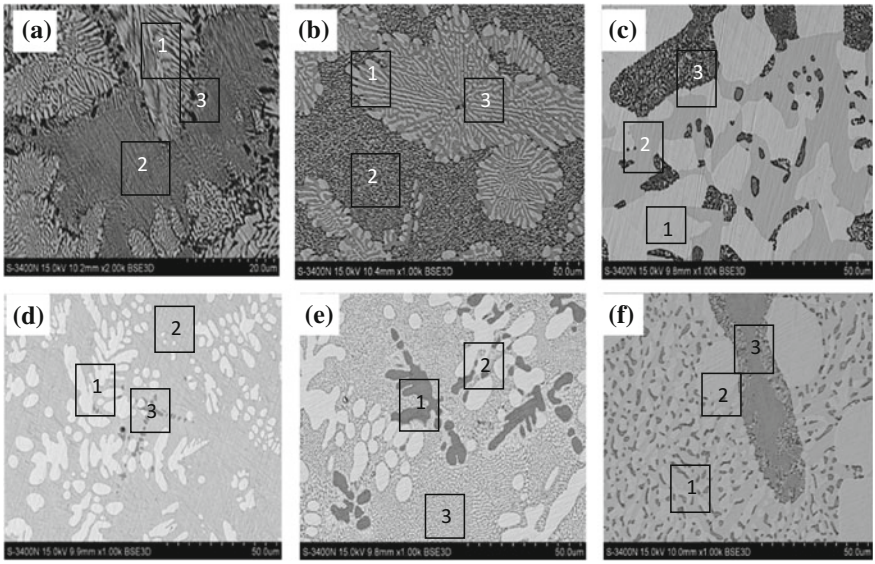

Fig. 3 Microstructures of Z3A3 M and Z5A3 M alloy. **a** Z3A3M-W, **b** Z3A3M-A, **c** Z3A3M-F, **d** Z5A3M-W, **e** Z5A3M-A, **f** Z5A3M-F

Table 3 Elemental compositions of different locations in Fig. 3

Positions	O (wt%)	Mg (wt%)	Al (wt%)	Zn (wt%)	Total
A1	0.75	1.02	0.64	97.59	100.00
A2	0.68	3.04	3.70	92.57	100.00
A3	0.88	0.69	14.93	83.50	100.00
B1	0.76	6.01	1.03	92.20	100.00
B2	1.33	3.56	3.21	91.90	100.00
B3	0.69	–	0.70	98.61	100.00
C1	1.04	–	0.29	98.67	100.00
C2	0.67	3.03	3.59	92.72	100.00
C3	0.94	–	40.89	58.17	100.00
D1	1.20	–	0.94	97.86	100.00
D2	0.86	3.01	5.23	90.90	100.00
D3	1.99	–	15.23	82.78	100.00
E1	1.20	–	16.17	82.63	100.00
E2	1.08	–	0.55	98.37	100.00
E3	1.29	6.35	0.57	91.79	100.00
F1	0.85	4.69	5.61	88.85	100.00
F2	1.12	–	0.48	98.40	100.00
F3	1.19	1.49	42.34	54.98	100.00

Figure 3d is the microstructure of Z5A3M alloy in water cooling mode. The binary eutectic phase was not found in water cooling mode. According to the analysis of EDS in Table 3, point 1 is zinc-rich phase, and the zinc-rich phase is dispersed in the ternary eutectic matrix in a much smaller way. At point 3, the aluminum content is higher, so it is block-like aluminum rich phase. At point 2, the Zn content is higher and the Mg and Al content is also higher than in the Zn-rich area. When the cooling rate is large, the Zn is dispersed in the Zn/Al/Mg_2Zn_{11} ternary eutectic structure or the Zn/Al/$AlMg_4Zn_{11}$ ternary eutectic structure.

Figure 3e is the microstructure of Z5A3M alloy in air cooling mode. At point 1, there shows the highest aluminum content, so it should be the aluminum rich phase. At point 2, the zinc content is higher, so it is zinc rich phase. At point 3, the magnesium content is higher, and the atomic percentage of Mg is 6.35% which is close the Mg content in Mg_2Zn_{11} phase. So it is likely to be the Mg_2Zn_{11}. So the lamellar structure of point 3 is Al/Mg_2Zn_{11} binary eutectic phase.

Figure 3f is the microstructure of Z5A3M alloy in furnace cooling mode. According to the XRD pattern in Table 2, the phases are included: Zn phase, Al phase, $AlMg_4Zn_{11}$ phase and Mg_2Zn_{11} phase. In point 3, the Al content is much higher than the content of Mg and Zn, so this massive structure should be aluminum-rich phase. The aluminum-rich phase is the primary phase. In the process of solidification it will be accompanied by the Zn and Mg enrichment, so there is the presence of Mg and Zn in Al phase area. At point 1, combined with EDS data analysis in Table 3, its element content does not meet any of the Mg_2Zn_{11} and

Table 4 Fitting Results E_{corr} and I_{corr} of Tafel

No.	Icorr (A cm^{-2})	Ecorr (V)
Z3A3M-A	−5.84	−1084E−3
Z3A3M-F	−5.37	−1046E−3
Z5A3M-A	−5.66	−1167E−3
Z5A3M-F	−5.62	−1156E−3

$AlMg_4Zn_{11}$, it is likely the coexistence of both $Zn/Al/Mg_2Zn_{11}$ ternary eutectic structure and $Zn/Al/AlMg_4Zn_{11}$ ternary eutectic organization. At point 2, there shows the high content of Zn, and the aluminum and magnesium content is very small, so here is the zinc-rich phase.

Electrochemical Behaviors

The extrapolation method of TAFEL is one of the electrochemical methods to determine the corrosion rate. After the extrapolation of Tafel polarization, the electrochemical corrosion parameters such as corrosion potential and self-corrosion current are obtained. It can be seen from the Table 4. In Table 4, the corrosion current is lower in air cooling condition than in furnace cooling condition for both two alloys indicating its good corrosion resistance. This is due to the formation of a large number of Al/Mg_2Zn_{11} binary eutectic in air cooling condition. The corrosion resistance of high aluminum alloy Z5A3M is lower than that of Z3A3M, which

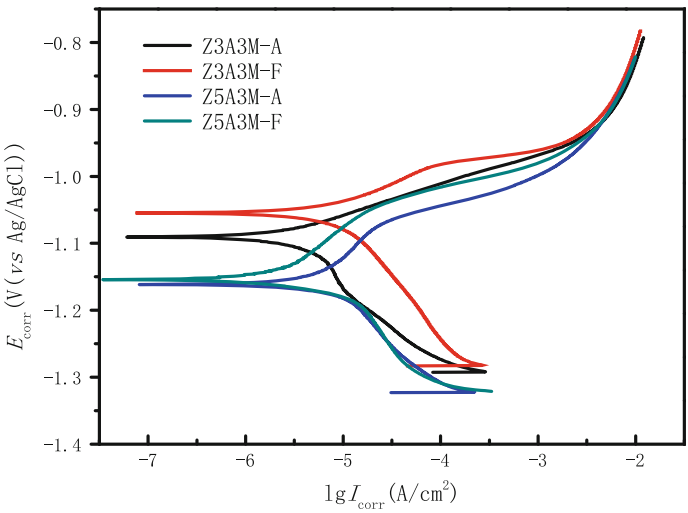

Fig. 4 Polarization curves of prepared specimens

indicates that its corrosion resistance is better, which is mainly due to the existence of aluminum and precipitation in the microstructure. Among them, the corrosion potential of Z5A3M in air-cooled condition reached a minimum value (−1167E −3 V), so as to achieve the best corrosion resistance (Fig. 4).

Conclusions

For both alloys Z5A3M and Z3A3M, four phases mainly exited in three different cooling methods: Zn phase, Al phase, AlMg4Zn11 phase, Mg2Zn11 phase. While it does not have the AlMg4Zn11 phase in the Z3A3M alloy of the furnace cooled state.

For two alloys, the specimens in the air-cooled state show good corrosion resistance since the corrosion current of air cooled state is lower than that of the furnace cooling state. It may be attributed to the existence of Al/Mg2Zn11 eutectic phase. As the Al, Mg and Mg2Zn11 phase are more easily to form a stable compound, the corrosion current density decreases in the electrochemical test [5].

The high aluminum alloy (Z5A3M) in the air cooling state shows the best corrosion resistance since the corrosion potential reaches to minimum. In addition to the eutectic phase Al/Mg2Zn11 generated internally, the aluminum is precipitated due to the increase in aluminum content.

References

1. S. Schuerz, M. Fleischanderl, Corrosion behavior of Zn–Al–Mg coated steel sheet in sodium chloride-containing environment. J. Corros. Sci. **59**, 2355–2363 (2009)
2. E.D. Bruycker, *Zn–AL–Mg Alloy Coatings: Thermodynamic Analysis and Microstructure-Related Properties* (Gent University, Belgium, 2005)
3. S.M.A. Shibli, Process and performance improvement of hot dip zinc coating by dispersed nickel in the under layer. J. Surf. Coat. Technol. **197**, 108–114 (2005)
4. V. Raghavan, Al–Mg–Zn phase diagram evaluations: section II, J. **28**, 208–210 (2007)
5. H. Kwak, Cationic doping of MgO surfaces to build corrosion protection in Mg alloys. J. Alloys Compd. **509**, 818–819 (2011)

Effect of Nanosecond Pulse Laser Shock Peening on the Microstructure and Performance of Welded Joint of 316L Stainless Steel

Yuqin Li, Y. H. Li, X. D. Wang, W. S. Xu, F. D. Qiao and S. J. Wang

Abstract The tensile stress and microstructure of 316L stainless steel welded joints are heterogeneous, and therefore the great risks of stress damage corrosion will be introduced. In the present study the welded joints were treated by laser shock peening (LSP) with different power density. Through residual stress test, microscopic analysis by XRD, SEM and TEM, the residual stress distribution, phase structure and microstructure were characterized, and the mechanism of LSP was discussed. The results showed that by the use of different power density, the residual tensile stress of welded joint decreased in comparison with welded sample. With the increasing of power density, these residual tensile stresses generated were superseded by the compressive residual stresses, and the maximum compressive residual stress reached about −100 MPa. By laser shock processing under different power density, the severe plastic deformation appeared in the surface layer of welded joint, high density nanocrystals and dislocation formed. However, there was difference for the plastic deformation characteristic among the three regions from weld seam, heat-affected zone, matrix zone, this should be accomplished by the interaction of the grain state, size and orientation with the laser shock peening. Moverover, the phase transformation from austenite to martensite was observed in the surface layer of welded joint, when the power density increased to 6.63 GW/cm^2, while this is

Y. Li (✉) · Y. H. Li · X. D. Wang · W. S. Xu · F. D. Qiao · S. J. Wang
Science and Technology on Plasma Dynamics Laboratory, Air Force Engineering University, Xi'an 710038, China
e-mail: yuqin511@163.com

Y. H. Li
e-mail: yinghongli@126.com

X. D. Wang
e-mail: 383789664@qq.com

W. S. Xu
e-mail: 18789430752@163.com

F. D. Qiao
e-mail: qiaofudong@qq.com

S. J. Wang
e-mail: 1518950427@qq.com

© Springer Nature Singapore Pte Ltd. 2018

Y. Han (ed.), *Advances in Materials Processing*, Lecture Notes in Mechanical Engineering, https://doi.org/10.1007/978-981-13-0107-0_11

harmful for the improvement of stress corrosion resistance. Therefore, a specific laser power density is propitious to improve the residual compressive stress and microstructure of the weld joint, thus to gain better stress corrosion resistance.

Keywords Laser shock peening · Different power density · Welded joint Microstructure · Performance

Introduction

316L austenitic stainless steel has widely used in pressure vessels, marine engineering, nuclear capacitors and other fields, because of its excellent mechanical properties, good welding performance and high temperature, strong acid corrosion resistance [1–3]. Compared with ordinary carbon steel, 316L austenitic stainless steel has high resistivity, large coefficient of linear expansion, small thermal conductivity, slow cooling speed of the metal during welding, large welding deformation and residual stress [4], which could determine the uniformity of the structure (including base metal, heat affected zone, weld, etc.) and the performance in welded joints, lead to a decrease in stress corrosion resistance and the failure of stainless steel welded joints in service.

Stress corrosion cracking generally initiates at the surface of the component, which occurs under the combined action of tensile stress and corrosive medium. Surface treatment technology can improve the stress state of the welded joint and the uniformity of the microstructure, which is an effective way to improve the resistance of the stress corrosion of welded component [5, 6].

Laser shock peening (LSP) is a new type of surface hardening technology developed in recent decades. It uses plasma shock wave induced by high-power pulsed laser to affect metal materials, not only form residual compressive stress in several hundreds of MPa in the surface layer of the component, and also can increase the surface hardness and grain refinement, and thereby significantly improving fatigue resistance, wear resistance and stress corrosion resistance of the stainless steel welding component [7–13]. Japan has used laser peening without protective coating for the stress corrosion problems of the nuclear reactor pressure vessel, pipe joints and so on [14, 15]. The universities and other organizations of domestic have studied the influences of stress corrosion by laser impact spot overlap rate in stainless steel welded joint, the microstructures and performances have been also studied [16–18]. The results show that laser shock can improve the stress corrosion resistance of stainless steel welded joints, but the current study on the different zones of the welded joints treated with different laser process parameters is still unsystemic, while this plays an important role to the structure and properties of 316L stainless steel welded joints. In this paper, different laser power density will be used in stainless welded joints, the influences on structure and properties of different welded joints zones and different directions had been studied, and the mechanism of LSP was discussed.

Experiment Materials and Scheme

Experiment Materials

The experiment material is 316L austenitic stainless steel plate, the structure and dimensions are shown in Fig. 1, and the filler material is also 316L. The chemical composition (mass fraction, wt%) of the material is listed in Table 1.

The shaded area in the Fig. 2 means the welding seam, and the width of the welding is about 5 mm, which is formed by NSA-300 DC manual TIG welding machine.

The Laser Shock Parameters of the Specimen

The LSP experiments are carried out with SGR-25A. The path is perpendicular to the weld direction, as shown in Fig. 2. In this paper, the laser has a wavelength of 1064 nm and a pulse width of 20 ns, and the spot diameter is 2.4 mm, the

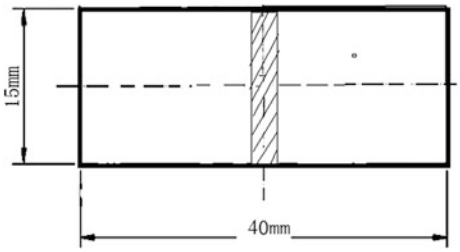

Fig. 1 Shape and size of welded stainless steel specimen (mm)

Table 1 Chemical composition of 316L stainless steel (wt%)

Element	C	Cr	Ni	Mo	Mn	Si	P	S	Fe
wt%	0.02	17.0	10.3	2.41	1.51	0.51	0.03	0.003	bal

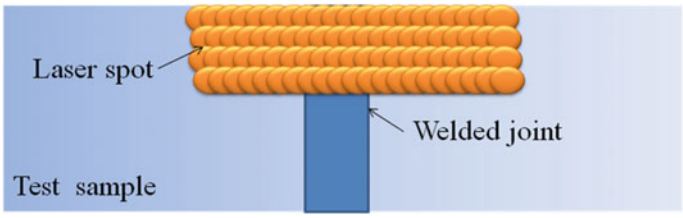

Fig. 2 Schematic of laser shock peening on welded sample

constraining layer is water, the absorbing layer is aluminum foil, the laser power density is 4.42, 5.52 and 6.63 GW/cm^2, respectively, and the number of shocks was 2 times.

Experiment Methods

The microstructures of 316 stainless steel surface without and with LSP were characterized by using TEM-3010 transmission electron microscope. Cross sectional microstructures and texture were observed by Quanta200 scanning electron microscope (SEM) and 4XC optical microscope. The surface phases of the sample were analyzed by the MFS-7000 X-ray diffraction, and the scanning angle range was 30°–90°. The residual stress was measured by X-350A type X-ray stress tester, and the average value was taken at four points, and the cross-correlation peak was adopted. The diffraction plane was {220}, the stress constant is −601 MPa, scanning angle (2θ) is 138° ∼ 121°, scanning increment is 0.10/s, counting time is 0.5 s.

Experimental Results and Analysis

Residual Stress Analysis

Residual stresses were measured in different areas of the weld surface before and after the LSP treatment. The measured points are shown in Fig. 3.

The results of residual stress on 316L stainless steel welded joints with different laser power density impact are shown in Fig. 4. From the measurement results, the residual tensile stresses are up to 330 MPa on the surface of the welding, and local residual tensile stress is even more than the yield strength of the welding. When the

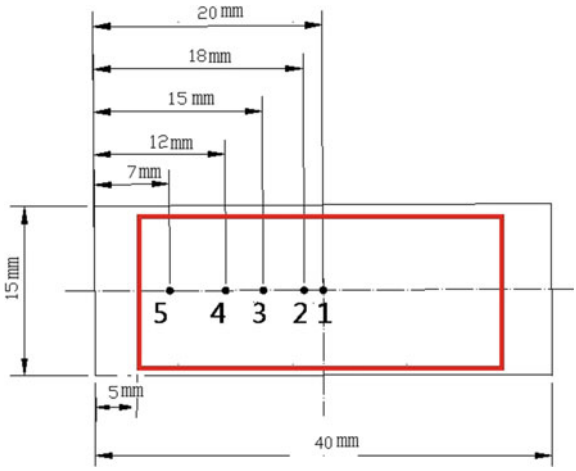

Fig. 3 Distribution of test points about residual stress

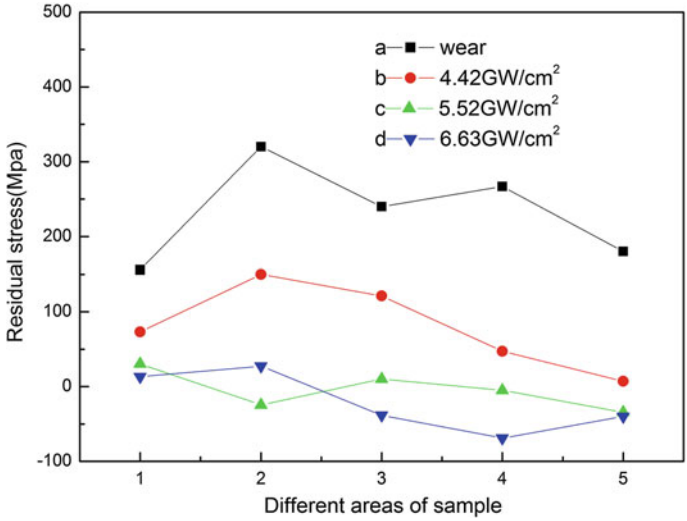

Fig. 4 Contrast of residual stress of 316L stain streel shock

laser power density are 4.42, 5.52 and 6.63 GW/cm^2, the residual stress distribution decreases with the increase of the impact power density, and the stresses of different welding regions tend to be the same. When the power density is 4.42 GW/cm^2, the residual stress in the heat affected zone was reduced to about 150 MPa. When the power density is 5.52 GW/cm^2, the residual tensile stress was almost eliminated and when the power density further reaches to 6.63 GW/cm^2, the residual compressive stress appears, and the stress distribution tends to be uniform, which significantly improves the residual stress state of welded joints.

From the perspective of fracture mechanics, stress corrosion cracking of materials need to meet the following criterion [19]:

$$K_I = F\sigma\sqrt{\pi a} > K_{ISCC} \tag{1}$$

where K_{ISCC} is the critical intensity factor of stress corrosion, σ is the nominal stress, α is the initial crack length, F is the shape factor of cracking.

It can be seen that the magnitude of the nominal stress and the critical stress intensity factor determine the crack propagation after the crack initiation. The residual tensile stress of the 316L stainless steel welding joints in welding surface is effectively reducing, and even residual compressive stress formed. Residual stress on the surface of welded joints can be offset by more than 50% of the tensile load, and effectively reduce the local stress concentration, and the nominal stress level at the tip of the corrosion microcrack is reduced, which reduce the rate of stress corrosion cracking growth and improve the stress corrosion cracking resistance. Moreover, the LSP reduces the driving force of dislocation slip, and thus delays the rupture of the passivation film on the surface of the specimen. The corrosion pits are not easy to form and this can improve the stress corrosion resistance.

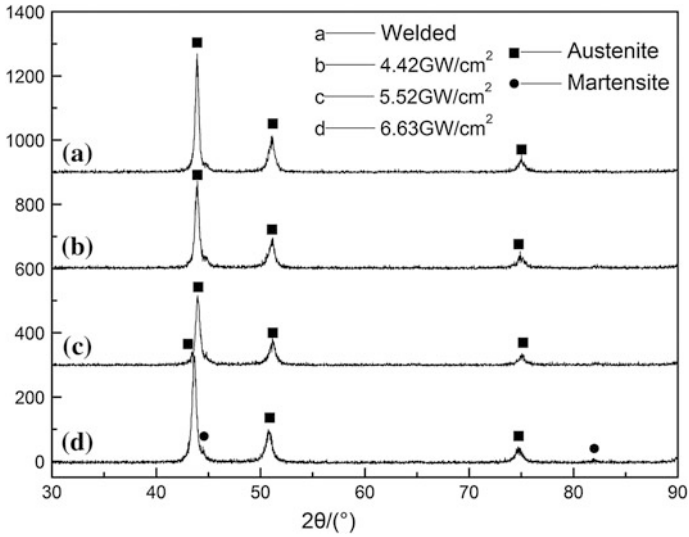

Fig. 5 The XRD patterns of 316L stainless steel weldzone treated by different laser power density

Phase Structure Analysis

Figure 5 is the XRD patterns of 316L stainless steel welded joints with different power densities. As can be seen from the Fig. 5, the phase structure of 316L stainless steel welded joints is austenite. When the laser power density are 4.42 and 5.52 GW/cm^2, there are no new peak in X-ray spectrum of stainless steel welded joint, and the diffraction peak decreases with the increase of power density, which is related to the grain refinement. When the power density increases to 6.63 GW/cm^2, martensite transformation increase, which indicates the formation of new phase, and which could increase the electrochemical corrosion. So the laser impact power density lower than 6.63 GW/cm^2 will be better.

Microstructure Analysis

The microstructure of weld seam, heat affected zone and matrix of the welded joint treated by different laser power density were studied.

Weld Seam

The perpendicular direction cross-section metallographs of stainless steel weld seam under different laser power density are shown in Fig. 6. It can be seen from the Fig. 6a, the 316L stainless steel weld seam is a typical coarse dendritic

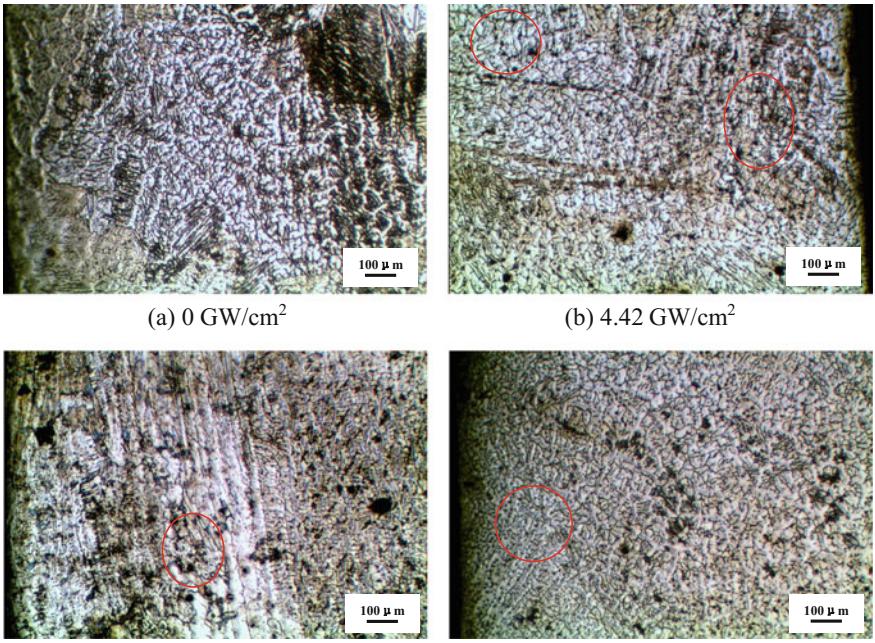

(a) 0 GW/cm^2 (b) 4.42 GW/cm^2

(c) 5.52 GW/cm^2 (d) 6.63 GW/cm^2

Fig. 6 The metallographs of 316L stainless steel weld seam treated by different laser power density

structure. When the laser power density is 4.42 GW/cm^2, the dendritic structure of the weld seam is broken. With the increase of the laser power density, it can been seen from the markings in Fig. 6c, d, there are obvious destruct phenomenon of 316L stainless steel weld seam grain boundary and the grain fragmentation trend is obvious.

The parallel direction cross-section SEM diagrams of stainless steel welded zones under different laser power density are shown in Fig. 7. The results show that the welding microstructure of 316L stainless steel is coarse dendritic structure as shown in Fig. 6a. When the LSP treatment at 4.42 GW/cm^2 (Fig. 7b), there is a plastic deformation zone of about 6 μm in the surface layer, and the grain are elongated; When the power density is 5.52 GW/cm^2 (Fig. 7c), the depth of the severe plastic deformation layer reaches about 9 μm. With the increase of the power density to 6.63 GW/cm^2 (Fig. 7d), the depth of the severe plastic deformation layer increases to about 18 μm. With LSP treatment, the dendritic structure of the weld seam is elongated and refined uniformly, which reduces the driving force of crack, raises the micro-crack initiation condition, and reduces the possibility of anodic dissolution of the base metal, it enhances the stress corrosion resistance.

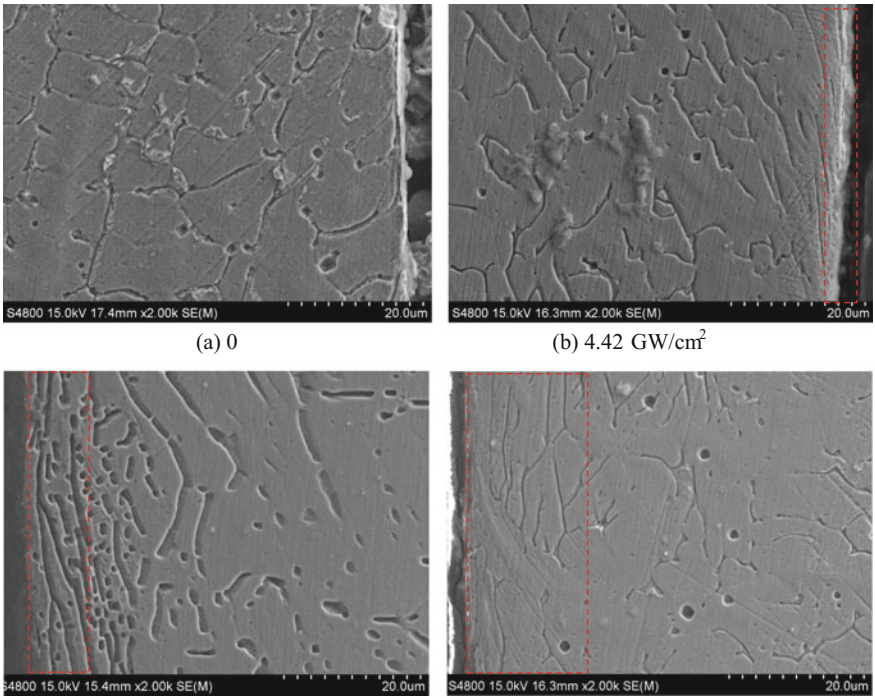

(a) 0 (b) 4.42 GW/cm^2

(b) 5.52 GW/cm^2 (d) 6.6 3GW/cm^2

Fig. 7 SEM photos of 316L stainless steel welded joint treated by different laser power density

Heat Affected Zone

The cross-section metallographs of 316L stainless steel heat affected zone treated by different laser power density are shown in Fig. 8. In Fig. 8a, there are a large amount of coarse equiaxed grains formed in the heat affected zone of 316L welded joint without LSP, and the microstructure of stainless steel welded joints heat affected zone is different greatly. The compatibility of deformation between grains is poor, so it is easy to stress concentration when forming force, forming cracks and becoming weak link. After laser shock peening with 4.42 GW/cm^2 (Fig. 8b) the shock wave spreads out by reflection, refraction and transmission on the surface and inside of grains, severe plastic deformation occurred in the heat affected zonea, for example, a large number of slip lines are formed in the larger grains when the shock wave act on the slip orientation of the grains and some grains have been refined, With the laser power density increasing, the slip lines and grain refinement further increases, coarse grain due to grain refinement is too large, difficult in the propagation process of laser shock wave in different grain orientation force, slip occurs in different direction of austenite grain, the formation of a large number of slip bands in the ease slip firection, when the deformation is blocked, began deformation twinning. When the laser power density

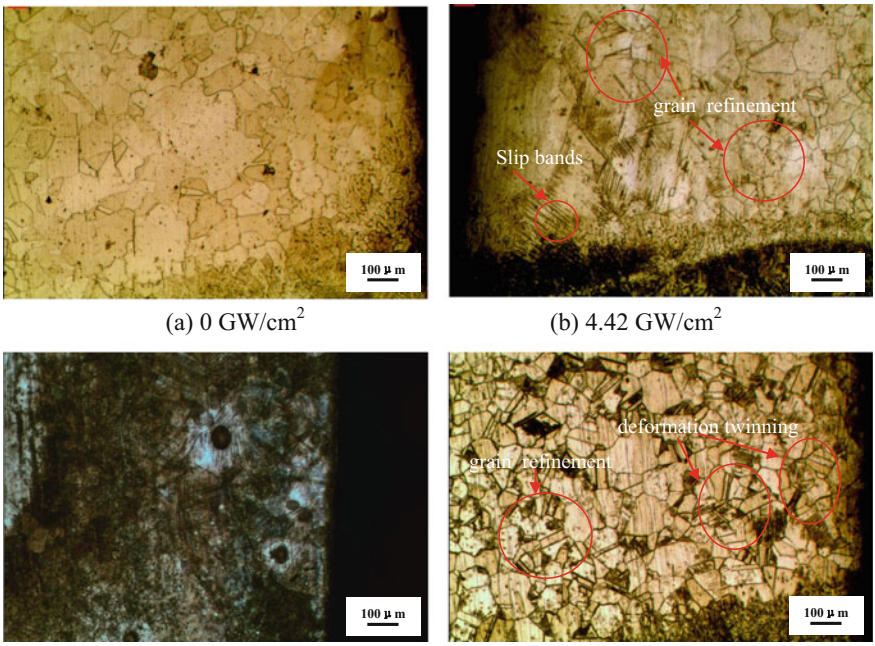

(a) 0 GW/cm^2 (b) 4.42 GW/cm^2

(c) 5.53 GW/cm^2 (d) 6.63 GW/cm^2

Fig. 8 Metallurgical structures of 316L stainless steel welded joint heat-affected zone treated by different laser power density

is 6.63 GW/cm^2 (Fig. 8d), there are deformation twinning and refined grain in the heat affected zone showed in red zone. Accordingly, After laser shock peening, there are slip bands, grain refinement and deformation twinning in the heat affected zone of the stainless steel welded joint.

Matrix Zone

The cross-section metallographs of 316L stainless steel matrix zone treated by different laser power density are shown in Fig. 9. In Fig. 9a, The matrix zone of untreated stainless steel welded joints is typical equiaxed grain, and there is annealing twinstructure. When the stainless steel matrix is treated with laser shock peening in Fig. 9b, multiple-slip is found to develop in the grains near the sample surface, With the increase of the distance from the surface, the plastic deformation of stainless steel is difficult, and it is difficult to slip and deformation twins are formed, and grain refinement is obvious. With the increase of laser power density, the matrix grain refinement trend more obvious, deformation twins and slip bands have been formen in the original grain.

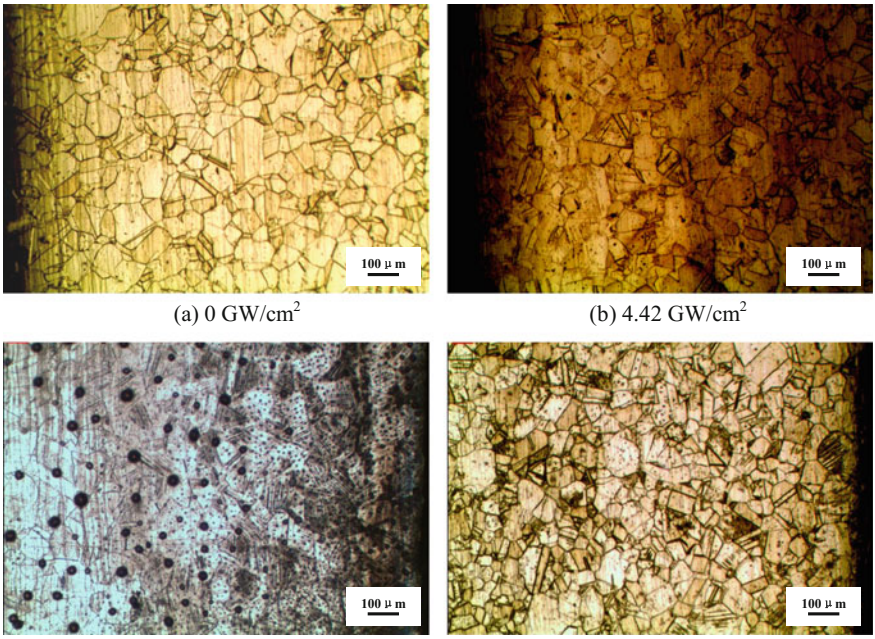

(a) 0 GW/cm^2 (b) 4.42 GW/cm^2

(c) 5.53 GW/cm^2 (d) 6.63 GW/cm^2

Fig. 9 Metallurgical structures of 316L stainless steel welded joint matrix zone treated by different laser power density

TEM Analysis

The TEM images of 316L stainless steel welded joints treated with and without LSP are shown in Fig. 10. The initial textures of the sample without LSP is shown in Fig. 10a, in which there is low density dislocations in austenite grain. Figure 10b shows the TEM image of the 316L stainless steel welded joints treated by 5.53 GW/cm^2. It can been seen that the high density dislocations and grain refinements were induced by shock wave in the material. The size of grains is smaller than 100 nm and reaches nanometer scale. This demonstrates that two impacts processing is able to generate high density dislocation and nanocrystallization on the surface stainless steel welded joint.

In summary, the mechanism of 316L stainless steel welded joint treated by laser shock peening is discussed, by the severe plastic deformation appeared in the surface layer of welded joint, high density nanocrystals and dislocation are formed, or even the martensitic transformation, and the surface residual compressive stress also formed, there is difference for the plastic deformation characteristic among the three regions from weld seam, heat-affected zone, the substrate:

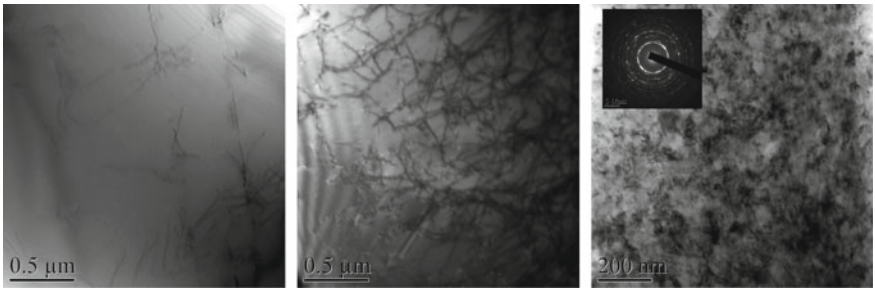

(a) 0 GW/cm^2 (b) 5.53 GW/cm^2 (c) 5.53 GW/cm^2

Fig. 10 TEM images of 316L stainless steel welded joint without LSP and with LSP

(1) weld seam. The welding microstructure of 316L stainless steel is coarse dendritic structure. With the increase of the power density, the depth of the severe plastic deformation layer increases with LSP treatment, the dendritic structure of the weld seam is elongated and refined uniformly, which reduces the driving force of crack, raises the micro-crack initiation condition, and reduces the possibility of anodic dissolution of the base metal, and it enhances the stress corrosion resistance.
(2) heat affected zone. The heat affected zone microstructure for grain sizes due to the thermal effect of the grain size, With the laser power density increasing, the slip lines and grain refinement further increases when the shock wave act on the slip orientation of the grains and some grains, coarse grain due to grain refinement is too large, difficult in the propagation process of laser shock wave in different grain orientation force, slip occurs in different direction of austenite grain, the formation of massive slip bands in the ease slip firection, when the deformation is blocked, began deformation twinning. After laser shock peening, there are slip bands, grain refinement and deformation twinning in the heat affected zone of the stainless steel welded joint.
(3) matrix zone, the grain refinement occurs surface to nanoscale, forming high dislocation density and massive slip bands in the near surface layer, the formation of a certain depth, the depth is greater than the heat affected zone, the grain refinement is obvious and the deformation twins are formed, the slip band decreases when depth increase, deformation twins are dominant. As the laser power density increasing, the depth of the affected layer is also increasing.

Summary

316L stainless steels welded joints treated by different laser power density have been conducted in this work. The results show that by the use of different power density, the residual tensile stress of welded joint decreases in comparison with the

welded sample. With the increasing of power density, these residual tensile stresses generated are superseded by the compressive residual stresses, and the maximum compressive residual stress reaches about −100 MPa, which reduce the rate of stress corrosion cracking growth and improve the stress corrosion cracking resistance. By laser shock processing under different power density, there is difference for the plastic deformation characteristic among the three regions from weld seam, heat-affected zone, matrix zone. The dendritic structure of the weld seam is elongated and refined. After laser shock peening, there are slip bands, grain refinement and deformation twinning in the heat affected zone, compared with heat affect zone, and there are more grain refinement and deformation twinning formed from matrix zone. Moreover, the phase transformation from austenite to martensite can be observed in the surface layer of welded joint, when the power density increases to 6.63 GW/cm^2, while this is harmful for the improvement of stress corrosion resistance. Therefore, a specific laser power density is propitious to improve the residual compressive stress and microstructure of the weld joint, and hence to gain better stress corrosion resistance.

Acknowledgements The research was supported by the National Natural Science Foundation of China (51305456).

References

1. M. Wang, G. Michel, J.F. Jullien, Thermal simulation on the welding heat affected zone of 316L steel. J. Shanghai Jiaotong Univ. **35**, 424–426 (2001)
2. X. Jijin, Effect of material hardening model on welding residual stresses of 316L stainless steel. Trans. China Weld. Inst. **35**, 97–100 (2014)
3. S.Q. Han, W.H. Ma, Y.Q. Zhao et al., The submerged arc welding technology of 316 stainless sheet steel. Weld. Technol. **40**, 51–53 (2011)
4. X. Xiangjiu, S. Wei, H. Chao, Study on welding procedure and joint properties of austenitic stainless steel 316L thick plate. Bloler Manuf. **45–47**, 57 (2015)
5. J.Z. Lu, K.Y. Luo, D.K. Yang et al., Effects of laser peening on stress corrosion cracking (SCC) of ANSI 304 austenitic stainless steel. Corros. Sci. **3**, 223–226 (2012)
6. P. Peyre, X. Scherpereel, L. Berthe et al., Surface modifications induced in 316L steel by laser peening and shot-peening: Influence on pitting corrosion resistance. Mater. Sci. Eng., A **280**, 294–302 (2000)
7. S. Lou, Y. Li, L. Zhou et al., Surface nanocrystallization of metallic alloy with different stacking fault energy induced by laser shock processing. Mater. Des. **104**, 320–326 (2016)
8. C. Wang, Y.Q. Xue, Y. Chai et al., Laser shock processing for improving fatigue property of k403 cast superalloy. High Power Laser Part. Beams **26**, 26109001–26109005 (2014)
9. X. Ding-yuan, H. Wei-feng, J. Yang et al., Study on high cycle fatigue performance of TC17 titanium alloy improved by micry-scale laser shock processing. Laser Infrared **46**, 1189–1194 (2016)
10. N. Xiang-fan, H. Wei-feng, Z. Shun-lai et al., Effects on structure and mechanical properties of TC11 titanium alloy by laser shock peening. J. Aerosp. Power **29**, 321–327 (2014)
11. L. Jing, L. Jun, H. Weifeng et al., Improvement of wear resistance by laser shock processing and carburization composite technology used on 12CrNi3A steel. High Power Laser Part. Beams **26**, 059005-1–059005-6 (2014)

12. S. Kalainathan, S. Sathyajith, S. Swaroop, Effect of laser shot peening without coating on the surface properties and corrosion behavior of 316L steel. Opt. Lasers Eng. **50**, 1740–1745 (2012)
13. M. Bang, Z. Jin, C. Zhimin, Effect of laser shock processing on residual stress of strain steel welded joints. High Power Laser Part. Beams **27**, 089001-1–089001-6 (2015)
14. Y. Sano, M. Obata, T. Kubo et al., Retardation of crack initiation and growth in austenitic stainless steels by laser peening without protective coating. Mater. Sci. Eng., A **417**, 334–340 (2006)
15. Y. Sano, I. Chida, N. Mukai, *Applications of Laser Peening without Protective Coating to Enhance Structural Integrity of Metallic Components*, The Second International Conference on Laser Shock Peening (San Francisco, 2010)
16. X. Zhu, M. Zhou, Q. Dai et al., Deformation modes in stainless steel during laser shock peening. J. Manuf. Sci. Eng. **131**, 054503 (2009)
17. Y.Q. Li, X.D. Wang, F.L. Song et al., The effect of residual stress and microstructures on 316 stainless steel treated by LSP. Mater. Sci. Forum Hot Work. Technol. **42**, 39–42 (2013)
18. J.Z. Lu, K.Y. Luo, D.K. Yang et al., Effects of laser peening on stress corrosion cracking (SCC) of ANSI 304 austenitic stainless steel. Corros. Sci. **60**, 145–152 (2012)
19. S. Li, *The strength of aircraft and engine* (National Defense Industry Press, Beijing, 2007)

The Effect of Mechanical Shot Blasting in Producing the Surface Ultrafined Grain Layer on Large-Size Titanium Plate

Quantong Yao, Guanglan Zhang, Ying Gao and Weiping Tong

Abstract This paper reported that the mechanical shot blasting was a feasible method for producing ultra-fined grain layer on large-size titanium plate. The MSB effects on producing ultra-fined layer were investigated by optical microscopy, X-ray diffraction, transmission electron microscopy, and micro-hardness tester. The experimental results showed that the thickness of the surface severe plastic deformation layer increased with the improvement in processing speed, but presented stabilization with prolonging the processing durations. The maximum thickness of the ultra-fined grain layer was about 320 μm, and the minimum grain size in the topmost surface was about 180 nm. The ultra-fined grain presented equiaxed grain morphology with random crystallographic orientation.

Keywords Titanium plate · Mechanical shot blasting · Ultra-finedgrain layer Hardness

Introduction

Titanium-based metals such as titanium and its alloys have been extensively used for aircraft manufacturing, petrochemical production, and medical implants, because of their high strength-to-weight ratio and corrosion resistance [1–4]. However, titanium and its alloys are susceptible to wear-out failure due to low

Q. Yao · G. Zhang · Y. Gao · W. Tong (✉)
Key Laboratory of Electromagnetic Processing of Materials, Ministry of Education, Northeastern University, Shenyang 110004, China
e-mail: wptong@mail.neu.edu.cn

Q. Yao
e-mail: tongtong282@126.com

G. Zhang
e-mail: zhgulacc@126.com

Y. Gao
e-mail: ggy6255@163.com

© Springer Nature Singapore Pte Ltd. 2018

Y. Han (ed.), *Advances in Materials Processing*, Lecture Notes in Mechanical Engineering, https://doi.org/10.1007/978-981-13-0107-0_12

hardness and poor wear resistance, which have seriously restricted their further application in some industrial fields. A large number of experimental results showed that the hardness and wear resistance could be greatly improved by inducing ultra-fined grain or nanocrystalline layer fabricated by severe plastic deformation (SPD) method on titanium and its alloys surface [5, 6]. Until now, a variety of SPD methods such as equal channel angular pressing (ECAP) [7], high pressure torsion (HPT) [8], ultrasonic shot peening (USSP) [9], high energy shot peening (HESP) [10], surface mechanical attrition treatment (SMAT) [11], and laser shot peening (LSP) [12], etc. have been sequentially developed by material engineers. However, various SNC methods have been developed just stay at experimental stage, but neither one is applied in practical production. As an extension of the SPD methods, we developed a new approach of mechanical shot blasting (MSB) to fabricate ultra-fined grain layeron large size titanium plates. By adjusting MSB parameters, such as processing durations or processing speed, different microstructures can be obtained.

The purpose of this work is to investigate MSB effects on fabricating large-size titanium plate. The microstructural characterization of the ultra-fined grain layer was examined by X-ray diffraction (XRD), scanning electron microscope (SEM), and transmission electron microscope (TEM). The experimental results showed that the hardness of the surface layer have been obviously improved by comparing with coarse-grained specimen.

Experimental Details

The titanium plate used in this work was annealed plate of commercial titanium with a size of 1000 mm × 500 mm × 3 mm. The chemical compositions (wt%) were 0.3 Fe, 0.08 C, 0.03 N, 0.015 H, 0.25 O, and balance Ti. All the titanium plate surfaces were polished by $60^{\#}$–$240^{\#}$ abrasive papers to achieve a fine finish. The MSB technique was described by the schematic illustration in Fig. 1. The mechanism of the grain refinement on MSB device has been detailedly described in previous paper [13]. In brief, the MSB consists of multiple sets of blades driven by a high-speed motor, and the blades continuously eject shot particles onto the titanium plate surface. The various processing durations and speed are achieved by controlling the feed rate of the rollers and motor rotational speed, respectively. In this work, the impact area was 500 mm × 100 mm, and the shot particle diameter was 1.6 mm with the composition of 1Cr18Ni9Ti. In order to prevent the titanium plate from oxidizing in subsequent impacts, a flow of argon gas was used as a protective environment. The cross-sectional morphology of plates treated with MSBwas observed using an optical microscope (OM; Leica DMR). The X-ray diffraction analysis of the surface layer was carried out on an X-ray diffractometer (XRD; X' Pert Pro PW3040/60) with Cu-Kα radiation (λ = 0.154056 nm).The microstructures of the plates were also characterized by transmission electron microscopy (TEM; TECNAI G^{20}). The samples were prepared for TEM

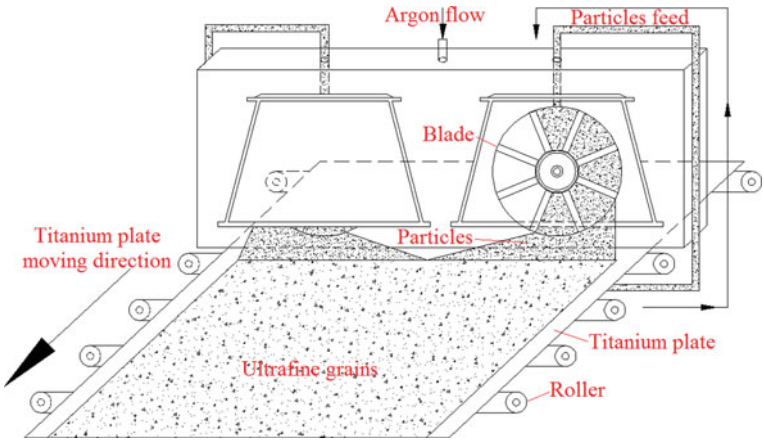

Fig. 1 Schematic illustrations of mechanical shot blasting (MSB) treatment

observations by grinding and mechanical polishing using an ion beam thinner (Gatan Model 691).

Results and Discussion

The Effects of the Various MSB Durations

Figure 2 shows OM images of the titanium plate at various MSB durations. As evident in Fig. 2a, the titanium plate surface was covered by an180 μm thick SPD layer after the MSB treatment. As the MSB processing time increased, the thickness of the SPD layer stabilized. Because the impact between ejected shot particles and the titanium plate is dependent on the elasticity of the materials, the stabilization can be explained by classical Hertz theory. The thickness of the SPD layer (h) can be calculated as follows [14]:

$$h = \frac{3\pi^{1/5}}{(1.145)^{1/4}(2/3)^{1/12}(2.5)^{1/20}} \frac{\rho^{1/5} v^{3/20} R^{2/3}}{E_H^{1/6} E_S^{1/30}} \tag{1}$$

where ρ, v and R are the density, velocity and radius of the shot particle, respectively, E_S is the elastic modulus of the titanium plate and E_H is the equivalent modulus related to the Young's modulus and Poisson's ratios of the ejected shot particle and the titanium plate. The h is the thickness of the SPD layer. From the equation, the ρ, R, E_S, and E_H are constants in this work, and the v is fixed due to the fixed motor rotational speed.

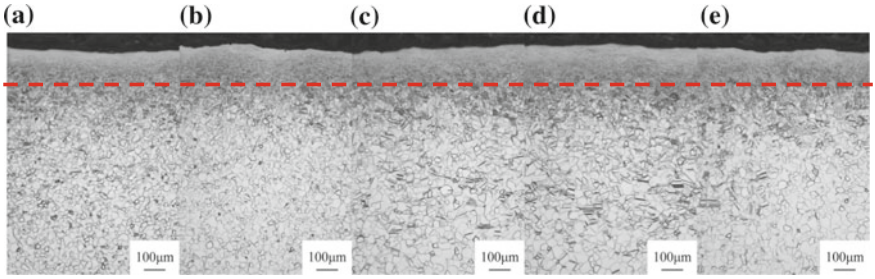

Fig. 2 Cross-sectional OM images of the titanium plate for various MSB durations: **a** 1 h, **b** 2 h, **c** 3 h, **d** 4 h, and **e** 5 h

Figure 3 shows XRD patterns and average grain sizes on the plate surface for various MSB durations. As shown in Fig. 3a, the XRD peaks broadened after initial MSB compared to the untreated plate, but the broadening rate decreased as the MSB duration increased. Because the Bragg reflection broadening is mainly induced by grain refinement, lattice deformation, and micro-strain development [15], the broadening rate can be considered an estimate of grain size variations in the surface layer. As shown in Fig. 3b, the average grain size was refined from the untreated plate at 283–221.3 nm after 1 h of MSB treatment, and further refined to 195.7 nm as the MSB durations increased to 2 h. As the duration of the MSB process increased, the average grains size generally became stable at about 180 nm. Therefore, at 800 rpm rotation motor speed, the minimum grain size is about 180 nm and the thickness of the SPD layer is about 180 μm.

Figure 4a is the hardness curve of the topmost surface layerfor various MSB durations. As shown in Fig. 4a, the average hardness of the titanium substrate is about 180 HV. Besides, the hardness of the topmost surface sharply increased to about 270 HV in MSB processing 1 h. The hardness increase rate is about 50%. With the MSB durations extending to 2 h, the topmost surface hardness further

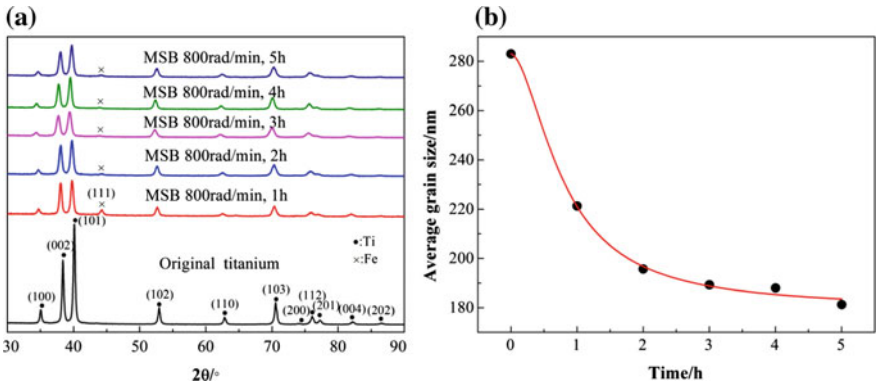

Fig. 3 XRD patterns of the titanium plate for various MSB durations

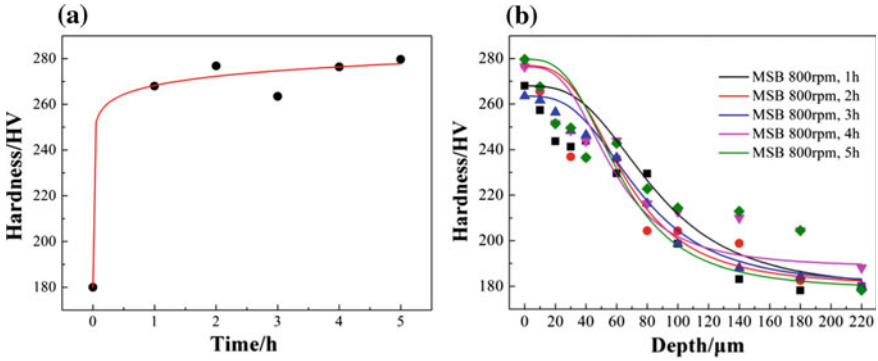

Fig. 4 The hardness curve for various MSB durations: **a** the topmost surface layer, **b** along the depth on cross-sectional direction

increased to about 280 HV, and the increase rate is merely about 4%. Therefore, the hardness increased rate sharply decreased after MSB processing 2 h. Although the topmost surface hardness increased as the MSB durations further extended, the hardness value was generally stable. Therefore, at 800 rpm rotation motor speed, the maximum topmost surface hardness was about 280 HV. Figure 4b is the hardness curve of the surface layer along the depth in cross-sectional directionfor various MSB durations. As shown in Fig. 4b, various hardness curves were generally consistent and gradient to decrease along the depth from the topmost surface layer to the substrate. The hardened layer was about 140 μm in depth defined by the distance from the surface to the point, where the hardness is 50 HV higher than that of the substrate. According to the classical Hall-Petch relation [16]:

$$H_v = H_{V0} - K' \cdot d^{-\frac{1}{2}} \tag{2}$$

where H_V is the Vickers-hardness, H_{V0} is the single crystal Vickers-hardness, K' is a constant, and d is grain size, the hardness H_V is closely related to grain size d. Therefore, the grain size in surface layer sharply increases in the depth of 0–60 μm and achieved the substrate hardness at depth of 160 μm.

The Effects of the Various MSB Speed

Figure 5 shows OM images of the titanium plate at various MSB speed. As shown in Fig. 5, the SPD layer became thicker as the MSB speed increased. This result can attributed to the Eq. 1, where the ρ, R, E_S, and E_H are constants, but the v increased with the improvement in motor rotational speed. Therefore, the h of the SPD layer became thicker with the rotational speed became faster. Besides, in the SPD layer, a large number of twin crystals can be observed. Previous studies have reported that

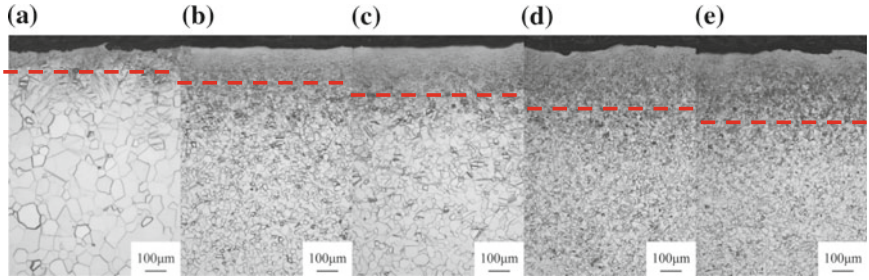

Fig. 5 Cross-sectional OM images of the titanium plate for various MSB speed: **a** 600 rpm, **b** 800 rpm, **c** 1000 rpm, and **d** 1200 rpm, for 2 h

the main deformation mode of the pure titanium is mechanical twin [17, 18]. This result is similar to previous reports. Furthermore, grain boundaries gradually become indistinguishable from the free-deformed substrate to the topmost surface layer, which is considered to be the grain size gradually decreases with a decrease in the depth. According to the observation of Fig. 5, the maximum SPD layer thickness is about 321 μm in MSB device.

Figure 6 shows XRD patterns and average grain sizes on the plate surface for various MSB speed. As shown in Fig. 6a, there is an evident XRD peaks broadening after various MSB processing comparing with the untreated plate, but the broadening rate decreased as the MSB speed increased. As shown in Fig. 6b, the grain size in the surface layer decreased with the MSB speed increased, but the decreasing rate achieved maximum at MSB speed of 600–800 rpm. Although the grain size in surface layer decreased as the MSB speed further increased, the grain size was generally stable after MSB speed of 1000 rpm. Besides, Fe element can be observed in the XRD patterns after the MSB process, and the Fe content increased with increasing MSB duration. The emergence of Fe can be attributed to abrasion of

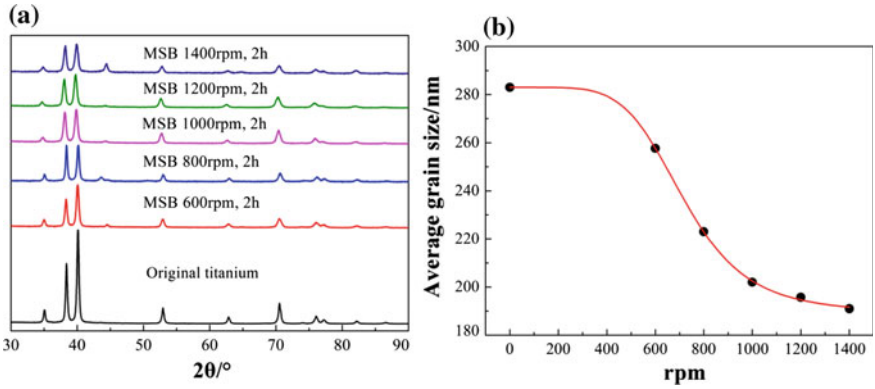

Fig. 6 XRD patterns of the titanium plate for various MSB speed

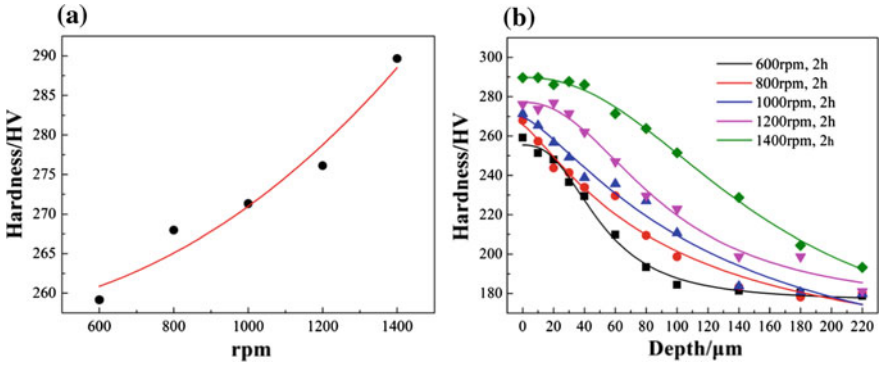

Fig. 7 The hardness variation curve of the topmost surface layer for various MSB speed

Fe-based particles by the severe impact between them and the plate, which causes debris to attach onto the titanium plate surface. Except for the Fe phase, all of the Bragg reflections belong to α-Ti, showing no evidence of new phases and no disappearance of the original phases during the MSB treatment. Oxides are not observed, mainly due to the protection provided by the argon atmosphere.

Figure 7a is the hardness curve of the topmost surface layer for various MSB speed. As shown in Fig. 7a, the hardness of the topmost surface gradually increased as the MSB speed increased. As explained in Eq. 2, this result can be attributed to the grains in the topmost surface layer being constantly refined with as the MSB speed increase. However, the maximum motor rotational speed of the developed MSB device is 1500 rpm, so the maximum hardness of the topmost surface could achieve to about 300 HV. Figure 7b is the hardness curve of the surface layer along the depth in cross-sectional direction for various MSB speed. As shown in Fig. 7b, the hardness in various depths increased as the MSB speed increased. This result can be attributed to the shot particles ejected by MSB inducing the SPD layer thicker with the MSB speed increased, and the grain size became smaller in various depths. Therefore, the hardness became higher in various depths.

Conclusions

A new developed mechanical shot blasting (MSB) device was utilized to fabricated ultra-fined grain layer on large sized titanium plate. The thickness of the ultra-fined grain layer increased as the MSB speed became faster, but presented stabilization with the prolonging of the MSBdurations. The thickness of the ultra-fined grain layer achieved maximum of 321 μm at MSB speed of 1400 rpm. The hardness of the topmost surface layer achieved maximum of 300 HV at MSB speed of 1400 rpm.

References

1. Q.T. Yao, J. Sun, Y.Z. Fu, W.P. Tong, H. Zhang, Materials **9**, 993 (2016)
2. Q.T. Yao, J. Sun, G.L. Zhang, W.P. Tong, H. Zhang, Vacuum **142**, 45 (2017)
3. J. Sun, Q.T. Yao, Y.H. Zhang, X.D. Du, Y.C. Wu, W.P. Tong, Surf. Coat. Tech. **309**, 382 (2017)
4. R. Huang, Y. Han, Mat. Sci. Eng. C-Mater. **33**, 2353 (2013)
5. Q.T. Yao, J. Sun, D.P. Shen, W.P. Tong, L. Zuo, submitted to Adv. Eng. Mater. (2017)
6. Q.T. Yao, J. Sun, G.L. Zhang, W.P. Tong, H. Zhang, submitted to Nano (2017)
7. M.J. Qarni, G. Sivaswamy, A. Rosochowski, S. Bocakal, Mater. Design. **122**, 385 (2017)
8. A.P. Murugesan, V. Rajinikanth, B. Mahato, M. Wegner, M. Witte, G. Wilde, S.G. Chowdhury, Mat. Sci. Eng. A. **700**, 487 (2017)
9. N.R. Tao, M.L. Sui, J. Lu, K. Lu, Nanostruct. Mater. **11**, 433 (1999)
10. G.B. Li, J. Chen, D.L. Guan, Tribol. Int. **43**, 2216 (2010)
11. W.P. Tong, N.R. Tao, Z.B. Wang, J. Lu, K. Lu, Science **299**, 686 (2003)
12. C.T. Wang, H. Zhou, P.Y. Lin, N. Sun, Q.C. Guo, J.X. Yu, M.X. Wang, Y. Zhao, L.Q. Ren, J. Phys. D Appl. Phys. **43**, 1 (2010)
13. Q.T. Yao, J. Sun, G.L. Zhang, W.P. Tong, L. Zuo, submitted to Adv. Eng. Mater. (2017)
14. A.L. Ortiz, J.W. Tian, L.L. Shaw, P.K. Liaw, Scripta Mater. **62**, 129 (2010)
15. J. Sun, W.P. Tong, L. Zuo, Z.B. Wang, Mater. Design. **47**, 408 (2013)
16. X.D. Zhang, N. Hansen, Y.K. Gao, X.X. Huang, Acta Mater. **60**, 5933 (2012)
17. K. Lu, N. Hansen, Scr. Mater. **60**, 1033 (2009)
18. J.Z. Lu, L.J. Wu, G.F. Sun, K.Y. Luo, Y.K. Zhang, J. Cai, C.Y. Cui, X.M. Luo, Acta Mater. **127**, 252 (2017)

Research on Influence of Abrasive Particles on Lubricating Performance of the Emulsion for Cold Rolling Strip

Yan Li, Yiqing Chen, Peng Gao, Bin Zhong, Fangfang Ai, Lin Li and Yu Xiao

Abstract The tribological performance of different emulsions was tested by MRS-10A four-ball friction and wear testing machine. The JC2000C1 contact angle measurement instrument was used to measure the wetting angle of emulsions. The LEXT OLS4000 laser scanning confocal microscope was applied in analyzing worn spot size of different emulsions. Lubricating properties of the various emulsions were examined on a 4-high cold-rolling mill. The results show that 39.4% significantly reduced the wetting angle of emulsion BG-1 than emulsion BG-2. Friction and wear experiments have demonstrated that the BG-1 emulsion ω were 9.194. The abrasive particles in emulsions have special antiwear and antifriction effects during cold rolling strip steels. The process lubrication experiments results show that abrasive particles affected the stability of emulsion lubricating performance, causing rolling friction coefficient fluctuation. Finally, it changes the rolling technological parameters and cold rolled steel strip surface quality.

Y. Li (✉) · Y. Chen · P. Gao · B. Zhong · F. Ai · L. Li · Y. Xiao
State Key Laboratory of Metal Material for Marine Equipment and Application, Anshan 114009, China
e-mail: 2323liyan@sina.com

Y. Chen
e-mail: chenyiqing2003@163.com

P. Gao
e-mail: neugp@126.com

B. Zhong
e-mail: zhong3416@tom.com

F. Ai
e-mail: ansteelaff@163.com

L. Li
e-mail: ansteellilin@163.com

Y. Xiao
e-mail: ansteelxy@163.com

Y. Li · Y. Chen · P. Gao · B. Zhong · F. Ai · L. Li · Y. Xiao
Iron & Steel Research Institutes of Ansteel Group Corporation, Anshan 114009, China

© Springer Nature Singapore Pte Ltd. 2018

Y. Han (ed.), *Advances in Materials Processing*, Lecture Notes in Mechanical Engineering, https://doi.org/10.1007/978-981-13-0107-0_13

Keywords Cold rolled strip · Abrasive particles · Emulsion · Process lubrication

Introduction

In conventional tandem cold rolling mills, the oil-in-water emulsions (O/W) are supplied by a recirculation system for lubricating strips and cooling rolls, further, improve the surface quality of rolled piece [1]. The lubrication effect of the emulsion is mainly reflected in the formation the lubricating oil film between strip surface and roll during the cold rolling production process so that the rolling deformation zone is mixed lubrication state. It can effectively reduce the friction and abrasion between piece and rolls [2, 3]. However, there were many abrasive particles in the emulsion during the long cycles working. Eventually, the existence of abrasive particles can seriously affect the integrity of the lubricating oil film, causing the rolling friction coefficient to fluctuate, result in a decrease the surface quality of the rolled strip products. All this produced the instability lubricating property of the emulsion during the rolling process [4, 5]. In this study, the influence of abrasive particles on the lubricating performance of the emulsion being evaluated on the four-ball tester and Φ170/Φ400 × 600 mm the four-high reversible cold strip mill. The experimental results have essential theoretical sense and using values on improved rolled strip surface quality and optimized rolling process parameters.

Materials and Experimental Methods

The Strips and Emulsion

The annealed Q235 strips are used as the experimental material for cold rolling test. The specimen size is 500 mm × 100 mm × 1 mm. As shown in Fig. 1, the emulsion BG-1 is from the cold rolling mill, the color of emulsion BG-1 becomes black, because of the mixing of abrasive particles and dust particles during the rolling process. The emulsion BG-2 is a newly prepared commercial emulsion. Its concentration is 2%. The two kinds of emulsions physical and chemical indexes in Table 1.

Wetting Ability Test

The wetting ability of different emulsions was examined by the JC2000C1 contact angle measurement instrument. The contact angles of emulsions were measured by

Fig. 1 The two types of emulsion appearance

Table 1 The two types of emulsions physical and chemical indexes

Emulsions	Viscosity ($mm^2 \cdot s^{-1}$)	Saponification value (mgKOH/g)
BG-1	0.7442	119
BG-2	0.8147	145
Standard	GB/T265	GB/T8021

the dropping liquid test method. Device for measuring range from 0° to 180° is available, and measurement error is ±0.5°. The Q235 steel strip was used as the base plate during contact angle measurement. The sessile drop method was applied to measure the wetting angle. Each contact angle was measured for five times, with the average value accepted as the actual data [6] (Fig. 2).

Cold Rolling Experiment

The 4-high reversing cold rolling mill was used to test the lubricating properties of the emulsion. The lubrication capacity of the emulsion was evaluated by the minimum rolling gauge of the steel strips and surface quality. Cleaning the roller

Fig. 2 Schematic diagram of the contact angle

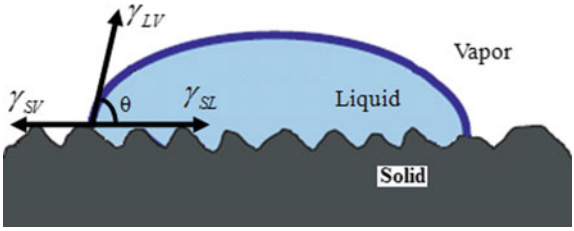

was necessary, petrol for washing, ethanol for wiping, then medical cotton for drying, before rolling. When replacing the rolling liquid, the same method was used in the cleaning process, to avoid the last residual rolling fluid to affect the test results. Before the experiment, the rolling liquid would be evenly sprayed on the rollers and tick over for 1 min to infiltrate the roller surface. At the beginning of the test, the emulsion was continuously sprayed to the surface of both rollers and workpiece during the rolling process. The initial thickness and the rolled thickness were measured for each pass by a micrometer each time.

Results and Discussion

Wetting Ability of Emulsions

The plating-out ability of emulsions on the rolled steel surface can directly affect the emulsion's lubrication ability during the rolling process. The wetting angle measurement can be used to explain the information such as surface roughness, chemical diversity, surface adsorption and other properties [7], and the wetting angle value can be taken as a visual check of emulsion's wetting ability [8]. Therefore, the experiment had investigated the variation in different emulsion's wetting ability was shown in Fig. 3. It can be seen from Fig. 3a that abrasive particles could improve the wetting properties of the emulsion, and the wetting angle of BG-1 39.4% lower than emulsion BG-2. Because the Nano-sized abrasive particles were dispersed in the emulsion, the total free energy of the emulsion BG-1 system was reduced, and the surface tension between the emulsion and the strip surface was decreased, which would eventually improve the wetting properties of the emulsion system.

The Tribological Properties of Emulsions

The oil film strength (P_B) and frictional coefficient (μ) not only reflect the bearing capacity of the emulsions under specific working conditions but also reflect the

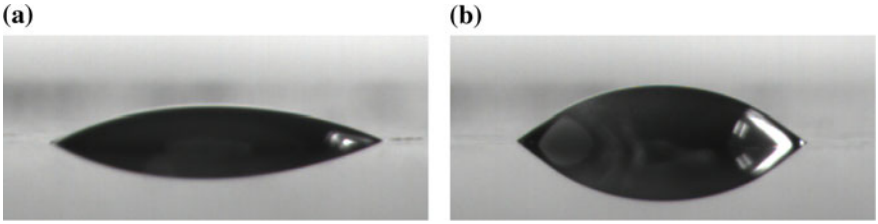

Fig. 3 Wetting performance of different emulsions on the Q235 strip steel

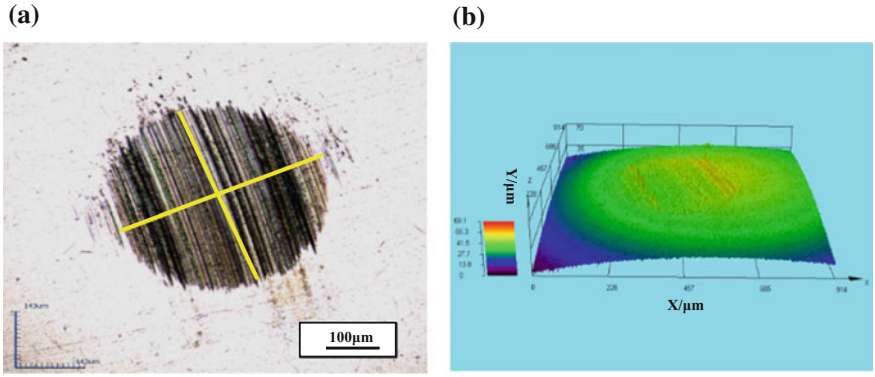

Fig. 4 The 2D and 3D topography of wear scar with emulsion BG-1

characteristics of the adsorption film [9]. According to the GB/T12583-1998 standard, tribological properties of different emulsions were investigated by the MRS-10A four-ball friction wear testing machine. As shown Fig. 4, the wear scars of the steel balls frayed by the four-ball tribological tester under lubricated with different emulsions for 30 min. Figure 4a is a two-dimensional (2D) wear scar with the emulsion BG-1 as lubricating condition,its edges have more burrs and scratches, its WSD is 446 μm. The Fig. 4b present the three-dimensional (3D) surface topography of wear scar that lubricated with emulsion BG-1. There is a significant amount of abrasive wear and adhesion wear defects on the wear scar area. The main reason for the formation of surface defects is the existence of metal particles in the emulsion.

Figure 5 shows wear scar lubricated with emulsion BG-2. The 2D and the 3D topographies of the corresponding wear scars are shown in Fig. 5a, b, respectively. Figure 5a is a 2D topography of wear scar with the emulsion BG-2 as lubricating

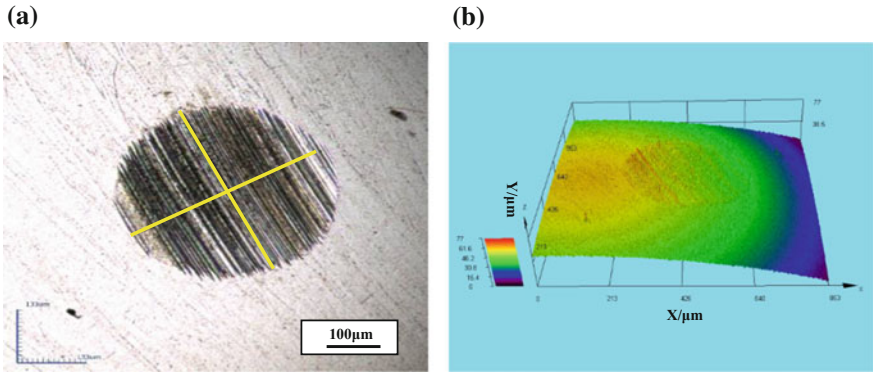

Fig. 5 The 2D and 3D topography of wear scar lubricated with emulsion BG-2

Table 2 The tribological properties of different emulsions

Emulsions	μ	$D_{30\text{min}}^{392N}/\mu\text{m}$	P_B/N	ω
BG-1	0.0628	446	618	9.194
BG-2	0.0712	460	559	8.968

condition, its edge morphology is normal morphology. It can be confirmed from the 3D topography of the corresponding worn surface in Fig. 5b, which showed the most significant WSD about 460 μm. Although the WSD is slightly larger than that of the emulsion BG-1, the overall appearance of the wear scar is better. By comparing the results of data analysis, it can be found that abrasive particles in emulsion BG-1 can play a particular role in antiwear and anti-attrition effect during the experiment. However, due to the uneven distribution of abrasive particles in the emulsion BG-1, resulting in reduced lubrication stability. In this situation of emulsion BG-1 lubrication, it was difficult to form sufficiently thick boundary lubrication film, because of existing the abrasive particles. Convex points on the friction surface were easy to contact and scratch the counter-friction surface, deep grooves, and some abrasives can be produced. This metal-metal contact led to the abrasive wear and more grooves in the subsequent friction process.

The maximum nonseizure load (P_B) and friction coefficient (μ) are two critical indexes of extreme pressure lubricant performance of the rolling fluid [10]. The bigger the P_B value is, the stronger the oil film and the better the lubrication performance of the rolling liquid. Similarly, the less the μ value is, the better the lubricity. However, the two factors are not always coherent. For the convenience of the analysis, the P_B value and the μ value are normalized, as shown in Formula (1) [11]. In Formula (1), ω stands for the extreme pressure and antiwear coefficient. The bigger the value of ω is the better the extreme pressure lubricant performance of the rolling fluid. The tribological properties of emulsion BG-1 and BG-2 were shown in Table 2. The extreme-pressure antiwear property of emulsion BG-1 is better than BG-2 by comparing and analyzing the ω.

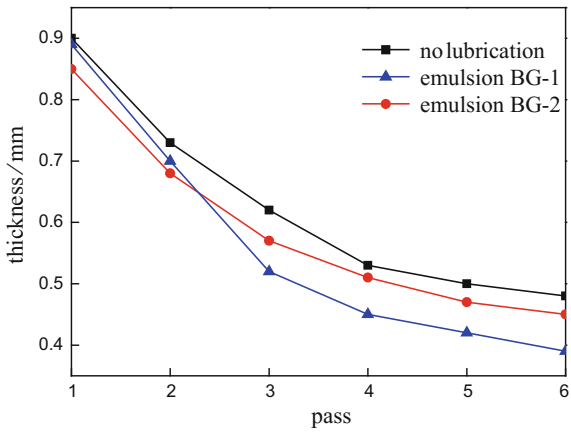

Fig. 6 The experiment results of cold-rolled Q235 with different lubricating conditions

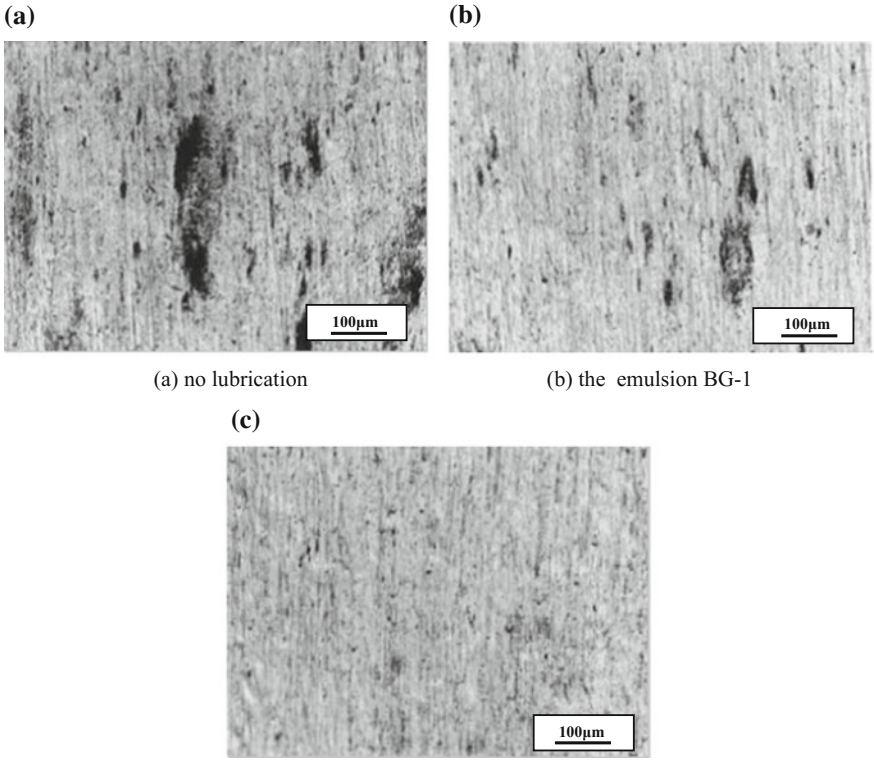

(a) no lubrication (b) the emulsion BG-1

(c) the emulsion BG-2

Fig. 7 The surface topography of cold-rolled Q235 under different lubricating conditions

$$\omega = \log_{10}(P_B/\mu) \tag{1}$$

Lubricating Properties of the Emulsions

The technological lubrication performance of emulsion BG-1 and BG-2 was carried out by using Φ170/Φ400 × 600 mm four-high reversible cold rolling mill.

It is known from the Stone theorem that when other conditions remain unchanged. The minimum rolling gauge is only related to the friction coefficient at the rolling deformation zone. The minimum rolling gauge of rolled pieces under different lubrication conditions is shown in Fig. 6. The minimum rolling gauge of the rolled piece with theBG-1 emulsion as the lubricating condition was reduced by 13.3% with the BG-2 emulsion as the lubrication condition. The minimum rolling gauge of the sample under lubrication with emulsion BG-1 has decreased 13.3%,

compared with that of the emulsion BG-2. The results show that abrasive particles in emulsion BG-1 can reduce friction and wear during the rolling process.

The surface quality changes continuously in rolling process. The surface quality is considerably different for different oil film thicknesses. The optical microscope was applied to examine the strip surface after six passes of rolling process under different lubricating conditions, and the surface topography of cold-rolled Q235 was shown in Fig. 7. In the absence of lubrication during the cold rolling process, the direct contact between the surface of the roller and the steel strip may cause abrasive wear and adhesive wear during the rolling process, leading to poor quality of the strip surface, as shown in Fig. 7a. The black spots on the rolled steel surface were caused by adhesive wear. Compared with the no lubrication, a better quality of rolling strip under lubrication by emulsion BG-1 had been obtained, an apparent rolling texture with a few surface defects was identified as shown in Fig. 7b. Due to the abrasive particles in the emulsion, a whole lubricant oil film cannot be formed in the rolling deformation zone in the rolling process; it will eventually lead to the generation of surface defects on the cold-rolled surface. Figure 7c was the surface topography of cold-rolled Q235 with the emulsion BG-2 as the lubrication condition. The rolling texture was evident, and the surface morphology was regular. The comprehensive analysis shows that the existence of abrasive particles in the emulsion can play a particular antiwear effect, but its impact on the stability of lubrication was also very apparent. The presence of abrasive particles leads to poor lubrication performance of emulsion. Finally, the surface quality of the rolled steel was apparently deteriorated.

Conclusions

(1) It is found that the wetting angle of emulsion BG-1 was significantly reduced by 39.4% than emulsion BG-2. The results showed that emulsion surface tension was decreased considerably when nano-sized abrasive particles in the emulsion were added. Wetting property of emulsion was improved, and the contact angle was diminished.
(2) By comparing and analyzing the ω, the extreme-pressure antiwear properties of the emulsion BG-1 are better than that of the emulsion BG-2. The results show that the abrasive particles in the emulsion have a particular antiwear and antifriction effect.
(3) The comprehensive analysis shows that the existence of abrasive particles in the emulsion can play a specific antiwear effect, but its impact on the stability of lubrication was also very apparent. The presence of abrasive particles leads to poor lubrication performance of emulsion. Finally, the surface quality of the rolled steel was apparently deteriorated.

References

1. Y. Kimura, N. Fujita, Y. Matsubara et al., High-speed rolling by hybrid-lubrication system in tandem cold rolling mills [J]. J. Mater. Process. Technol. **216**(1), 357–368 (2015)
2. Y. Kimura, K. Okada, Lubricating Properties of Oil-In-Water Emulsions [J]. ASLE Trans. **32** (4), 524–532 (1989)
3. Y.Q. Shang, S.Y. Wang, Research progress of lubricating technology in cold-rolling strips [J]. Technol. Innov. Appl. **5**, 115–117 (2016)
4. S. Wang, J. Sun, Y. Zhao et al., An investigation of the stability and lubricity of emulsions for strip cold rollings [J]. Pet. Process. Petrochemical **41**, 58–62 (2010)
5. S. Huart, M. Dubar, R. Deltombe, Asperity deformation lubricant trapping and iron fines formation mechanism in cold rolling processes [J]. Wear **257**, 471–480 (2004)
6. R. Ahmed, M.P.F. Sutcliffe, Identification of surface features on cold-rolled stainless steel strip [J]. Wear **244**, 60–70 (2000)
7. Wei Danping, Lan Xiaoyan, Fan Jingyun, The development and application of a new hot rolling oil for steel plates [J]. Acta Petrol. Sin. **23**, 17–23 (2007)
8. X.D. Wang, X.F. Peng, J.F. Lu et al., Technique for measuring contact angle and contact angle hysteresis on rough solid surfaces: I. Measuring technique of contact angle [J]. Basic Sci. Eng. **11**, 174–184 (2003)
9. H.Y. Zhang, J.W. Deng, Z. Yi, The relationship between particle size and lubrication performance of cold rolling emulsion [J]. Lubr. Eng. **4**, 110–114 (2015)
10. X. Zhang, S.T. Wang, J.L. Sun et al., Tribological properties of emulsions for strip cold rolling [J]. Chin. J. Eng. **32**, 622–627 (2010)
11. M.R. Yi, J. Sun, X. Zhang et al., Effect of environmental lubricating additives on rolling lubrication of cold strip rolling emulsions [J]. Acta Petrol. Sin. **2012**(28), 858–864 (2012)

Properties of Carbon Nanotubes (CNTs) Reinforced Copper Matrix Composites by Ultrasonic Welding

Zhengqiang Zhu, Mingfeng Li, Qiankun Xiao and Yifu Zhang

Abstract In this research, multi-walled CNTs' surface was firstly coated with a good binding copper layer successfully by electroless plating method, to solve the multi-walled CNTs clusters wrapped problem effectively. Then copper matrix composites reinforced with the electroless copper plated multi-walled CNTs were prepared successfully by ultrasonic metal welding process. The Effects of copper surface state and CNTs content on the mechanical properties and microstructure characterization of the prepared composites were analyzed. And multi-walled CNTs reinforced mechanism was discussed.

Keywords Multi-walled CNTs · Ultrasonic metal welding · Electroless copper plating · Copper matrix composites

Introduction

The carbon nanotubes (CNTs) were synthesized by Baconin 1960 [1]. A large number of theories and experiments show that CNTs have been found to be the most unique and multifunctional material so far. It has excellent chemical stability, thermoelectric performance and electromagnetic shielding performance [2–4].

Z. Zhu (✉) · M. Li · Q. Xiao
School of Mechanical and Electrical Engineering, Nanchang University, Nanchang, Jiangxi 330031, China
e-mail: zhuzhq01@126.com

M. Li
e-mail: lmfg007@163.com

Q. Xiao
e-mail: 316702965@qq.com

Y. Zhang
School of Mechanical and Electrical Engineering, Jiujiang University, Jiujiang Jiangxi 332005, China
e-mail: zhangyifulj@163.com

© Springer Nature Singapore Pte Ltd. 2018

Y. Han (ed.), *Advances in Materials Processing*, Lecture Notes in Mechanical Engineering, https://doi.org/10.1007/978-981-13-0107-0_14

Many researchers committed to using CNTs instead of carbon fibers to manufacture advanced nano-electronic devices and composite materials [5, 6]. CNTs are often used in matrix such as polymer, ceramic and metal to improve its electrical properties, thermal properties and mechanical properties. In general, metal matrix composite in some specific performance, comparing with the original metal has a certain improvement. Studies have found that by adding 5 vol.% of CNTs, the yield strength of composite materials can be more than double, as structural materials having a broad application prospect [7].

The most common preparation method of CNTs-reinforced metal matrix composites is powder metallurgy, secondarily electrochemical deposition and thermal spraying. For the low melting point metal and metal glass, also melting and solidification method can be adopted. Now the main challenges to preparation of CNTs-reinforced metal matrix composites are to achieve a single CNT evenly dispersing in the matrix, the good interfacial bonding and high compactness, while still solving some disadvantages poor wettability between CNTs and metal matrix, thermal stability reducing in high temperature processing [8]. So, in the preparation of CNTs-reinforced metal matrix composites, the CNTs are needed to preprocess which covers the surface modification of CNTs.

Tanset al. [9] had shown that CNTs have lower chemical activity than those of carbon fiber and graphite, moreover being insoluble in water and common organic solvents. But also CNTs had the similar properties of graphite, such as low wettability with metal. Therefore the surface performance did not have catalytic effect. Dujardin et al. [10] have studied wettability of CNTs in detail. They deemed that the deciding factor was the surface tension. And to 100 and 200 mN/M as the critical value, they showed that the typical pure metal will be not readily wetted in multi-walled CNTs surface. So as to strengthening phase in the preparation of metal matrix composites, the binding energy between CNTs and the metal base is very small without any surface treatment, resulting in difficult to achieve high-strength interfacial bonding. Between the CNTs and the matrix, the interface slip was produced under the relatively low external stress. Moreover CNTs of large length to diameter ratio (100–1000) have high surface energy. Carbon nanotubes absorbed together by means of van der Waals force, so agglomerating easily, which is difficult to be uniformly distributed in matrix [11]. In order to improve the mechanical properties of CNTs-reinforced metal matrix composites, it is necessary to improve the interface bonding strength between CNTs and metal matrix, and the dispersal uniformity of CNTs.

Cho et al. [12, 13] prepared CNTs/copper matrix composites of uniform dispersion by wet mixing and spark plasma sintering. While the content of CNTs was 1 vol.%, the thermal conductivity of the composite increased significantly. Rajkumar et al. [14] successful sintered CNTs/copper matrix composites by use of microwave, and found that chemical coating of CNTs could effectively improve the interfacial strength. Due to the presence of clustering and twining in CNTs, in this paper, based on the copper plating of multi-wall CNTs, ultrasonic metal welding was used to prepare multi-wall CNTs-reinforced copper matrix composites, in addition mechanical properties and microstructures of welded joints were analyzed.

Experimental Materials

Experimental materials were T2 purple copper foils with a size of 100 × 18 0.3 mm. Chemical compositions of materials were shown in Table 1. Used to enhance the base was multi-walled CNTs. The main technical parameters of the material were shown in Table 2.

Experimental Procedure

Electroless Copper Plating of Multi-wall CNTs

Multi-walled CNTs surface did not have catalytic activity. Sensitization treatment and activation treatment were required during electroless plating. According to L. M. Ang's experiment [15], multi-walled CNTs were weighed 0.1 g for test. Copper sulfate pentahydrate was used in electroless copper plating. Figure 1 shows a scanning electron micrograph of the multi-wall CNTs after electroless copper plating. Agglomeration phenomenon of multi-walled CNTs was improved as can be seen from the figure. The thin layer formed on the surface effectively reduced the van der Waals force between them. For different multi-walled CNTs, the quality of the coating was different. The quality of multi-walled CNTs surface coating at a place was the most ideal. The continuous thickness of coating was about a few nanometers. The multi-walled CNTs at B place were almost completely surrounded by copper powders. Coating was too thick. Effective continuous coating was not formed C Department. These differences were due to the orientation and surface defects of multi-walled CNTs. By electroless plating the purity of multi-walled

Table 1 Chemical composition of T2 copper (wt%)

Cu + Ag	Bi	Sb	As	Fe	Pb	S
99.90	0.001	0.002	0.002	0.005	0.005	0.005

Table 2 Multi-walled CNTs of the main technical parameters

Parameter name	Value
Diameter (nm)	10–30
Length (μm)	0.5–100
Purity (wt%)	≥ 85
Amorphous carbon particle impurities (wt%)	≤ 15
Ashes (wt%)	≤ 0.3

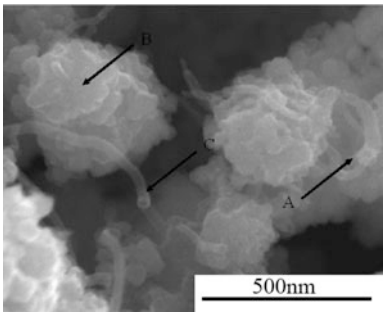

Fig. 1 SEM image of copper plated multi-walled CNTs

CNTs was improved, the rate of agglomeration reduced, the wettability with metal improved, and the interfacial bonding capacity of the composites enhanced.

Copper Foil Surface Pretreatment

Physical polished copper foil using particle size 14–20 μm metallographic sand paper to remove the surface oxide film and impurities, improve the surface roughness. Low density multi-walled CNTs was powder form in the macro. In preloading process with ultrasonic welding, the multi-walled CNTs were sprayed directly on the surface of untreated the copper foil, to make the multi-walled CNTs splash at electrode instantaneous pressure. After surface pretreatment, multi-walled CNTs distributed uniformly on the rough surface after polishing, to solve the problem effectively of splashing during the welding process.

Preparation of Multi-walled CNTs Reinforced Copper Matrix Composites by Ultrasonic Welding

The pretreated multi-walled CNTs were added ethanol solution, and then sprayed onto the copper foil surface using a spray method, dispersed uniformly. After volatilization of ethanol, the copper foil by ultrasonic welding. And the welding process is provided in Fig. 2.

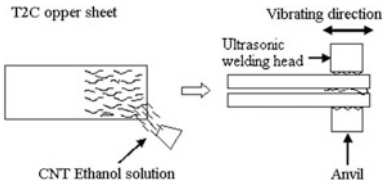

Fig. 2 Preparation process schematic diagram of multi-walled CNTs/copper matrix composites

CNTs content was 0.2–5wt% in metal matrix composites. The copper foil mass of ultrasonic welded joints about 0.25 g, the plastically deformed and a connecting of the copper foil is 0.05–0.13 g. To reinforce effect of multi-walled CNTs, the mass must not exceed 0.0006 g. Such a small mass range is difficult to make ultrasonic welding as powder metallurgy, multi-walled CNTs content in quantitative analysis before preparation.

Ultrasonic metal welding parameters: welding pressure = 0.45–0.75 MPa; welding time = 180 ms; ultrasonic vibration frequency = 20 kHz; ultrasonic amplitude = 35 μm. To analyze the effect of multi-walled CNTs content and pretreatment to weld properties, the specimens were prepared as follows.

(1) Specimens A without adding multi-walled CNTs;
(2) Specimens B with adding untreated multi-walled CNTs;
(3) Specimens C with adding purified multi-walled CNTs, the content of (C1 = 0.1, C2 = 0.4, C3 = 0.7, C4 = 1.0wt%) in alcohol solution;
(4) Specimens D with adding electroless copper multi-walled CNTs.

Results and Discussion

Tensile Test

The maximum tensile strength of the welding joint with the multi-walled CNTs different pretreatments in the condition of the welding pressure was 0.45–0.75 MPa and the welding time was 185 ms as shown in Fig. 3. It can be seen from Fig. 3 that the optimum welding pressure was 0.7 MPa. The joint strength of Specimen B was lowest since the multi-walled CNTs without any treatment were not serious clusters, and also carried a lot of impurities, which hinder the formation of the weld

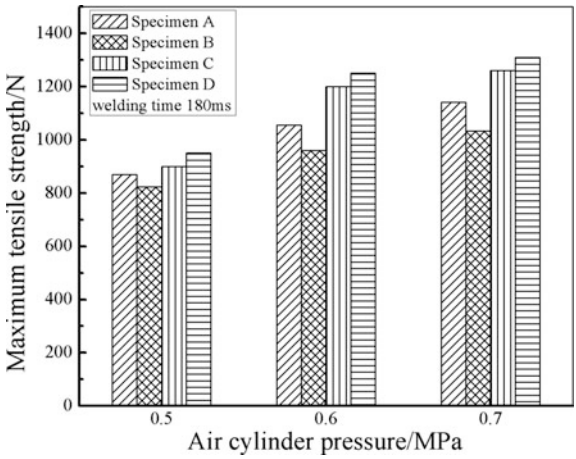

Fig. 3 The effects of multi-walled CNTs with different surface states to specimens joint tensile strength

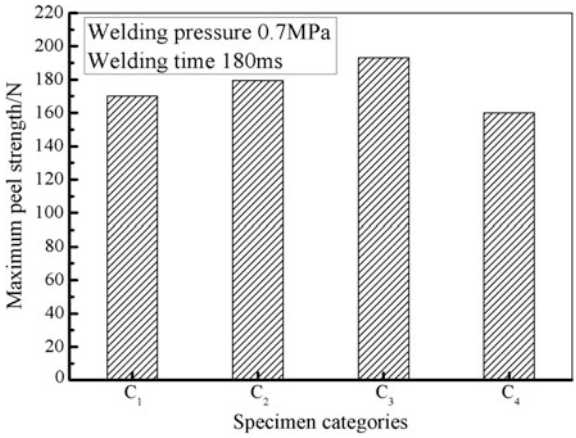

Fig. 4 The specimen joint maximum peel force at different multi-walled CNTs content

interface. The intensities of Specimen C, D were higher than that of Specimen A. The reinforced effect in Specimen D was the best. Although the impurities was removed by purification, poor wettability with the metal interface, low surface activity and weak binding capacity, multi-walled CNTs is embedded physically in the weld of Specimen C. While Specimen D, multi-walled CNTs were effectively improve the surface activity after electroless copper. And more importantly, the forming a copper layer excellent bonding effect on multi-walled CNTs surfaces. Multi-walled CNTs are not in direct contact with matrix metal during the welding process, reducing the multi-walled CNTs reunited and destruction largely, therefore specimen has the highest joint strength.

Specimens C1, C2, C3 and C4 were welded using ultrasonic welding in the welding time 180 ms and welding pressure 0.7 MPa. Peel strength test performed on weld specimens and the results shown in Fig. 4. The results show that multi-walled CNTs content at 0.5–0.8wt% in ethanol solution, specimens has the highest peel strength.

Microstructural Examinations

For a more intuitive observation and analysis morphology and distribution of multi-walled CNTs in the weld, weld-sectional microstructure was observed through the optical microscope and SEM method, multi-walled CNTs content and distribution was analyzed in the matrix metals through EDS method.

Figure 5 shows microstructure of specimens C_2, C_3 and C_4. Specimens C_2 with good weld interface due to multi-walled CNTs low content. Specimens C_4 formed insulating film at interface during the welding process due to excessive multi-walled CNTs content, hinder the contacts and the plastic deformation of the specimen, direct impact on the interfacial bonding. Specimens C_3 though not forming an

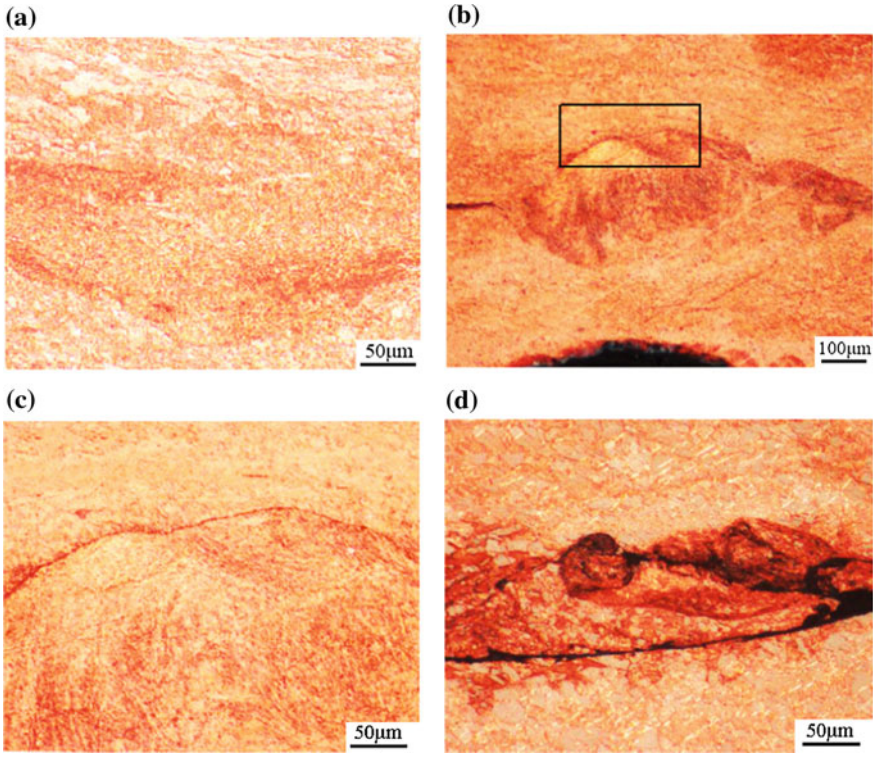

Fig. 5 Microstructure images of welded joint at different multi-walled CNTs content, **a** Specimens C2; **b** Specimens C3; **c** an enlarged view of C3 welds; **d** Specimens C4

isolation film, it will not appear reunion obviously in the weld. However, due to multi-walled CNTs only purified, low surfactant and low wettability with metal of multi-walled CNTs is not improved. It enables multi-walled CNTs affect the weld interface combined, Fig. 5b, c as shown has a significant cracking of the junction at the interface. If it does not improve the surface activity in multi-walled CNTs, multi-walled CNTs content will be greatly restricted in the preparation of metal matrix composites.

Figure 6a, b shows microstructure of specimens B welded joint, as can be seen from the figure clusters serious of multi-walled CNTs, and contains a lot of catalytic impurities. Making multi-walled CNTs did not promote the formation of weld, but large gathered in the weld. When load bearing, these places can cause stress concentration and cracks, reducing the quality of the weld.

Figure 6c, d shows microstructure of specimens C, D welded joint. It shows multi-walled CNTs clusters and wettability with metal is improved by electroless copper. Surface coating protect and transition effects for multi-walled CNTs during the welding process, multi-walled CNTs can be added to the composite material to the greatest extent and well interface bonding.

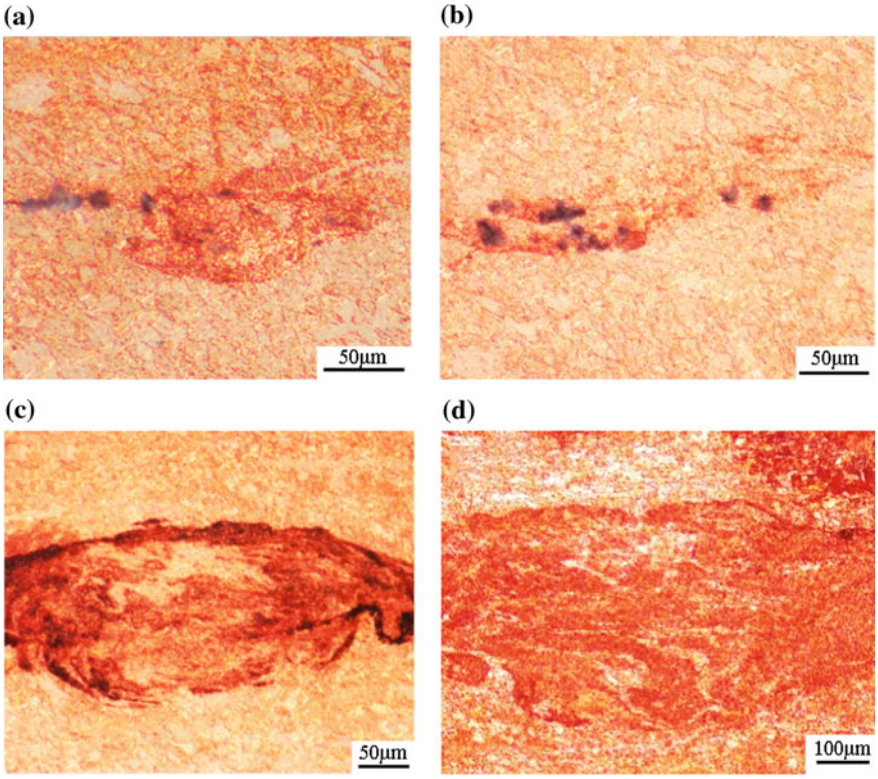

Fig. 6 Microstructure images of (**a**) **b** Specimens B; **c** Specimens C; **d** Specimens D

Figure 7 shows the part of the welding area energy dispersive spectroscopy (EDS) of the Specimens C_4. As can be seen from the figure, multi-wall CNTs gathered serious in the weld affect the weld quality. Elemental analysis shows that the content of multi-walled CNTs about 0.36wt% in the weld (Table 3).

Figure 8 shows the part of the welding area EDS of the Specimens C_3. As can be seen from the Fig. 8a, Specimen welded result is good, there is no visible gap and multi-walled CNTs clusters point. As can be seen from the Fig. 8b, Multi-walled CNTs distributed uniformly around the weld, no have larger reunion point. But compared with the PM, the distribution of multi-walled CNTs to be improved. Because multi-walled CNTs moving with material plastic deformation during ultrasonic welding process. If the plastic deformation zone width is large, multi-walled CNTs distribution is sparse in this position. Elemental analysis shows that the content of multi-walled CNTs about 0.26wt% in the weld (Table 4).

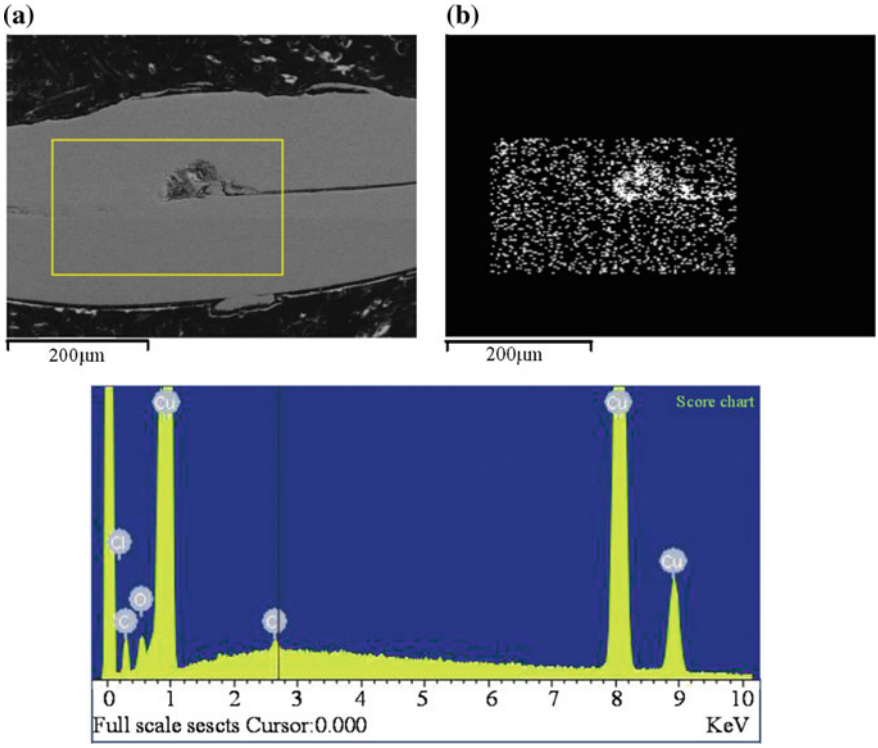

Fig. 7 EDS analysis results from Specimens C_4

Table 3 Chemical composition analysis of Specimens C_4 in weld (wt%)

Element	Weight percentage	Atom percentage
C K	0.36	1.77
O K	2.38	8.69
Cl K	0.32	0.53
Cu K	96.93	89.01
Total	100.00	

Analysis of Reinforced Mechanism

Adding multi-walled CNTs can improve the mechanical properties of base metal by ultrasonic welding. To metal matrix composites, the main strengthening mechanisms include such as dislocation strengthening, precipitation hardening, solid solution strengthening, fine-grain strengthening and work hardening. And for the preparation of multi-walled CNTs-reinforced copper matrix composites with ultrasonic welding, the main mechanisms are dislocation strengthening, fine-grain strengthening and strengthening of the second phase.

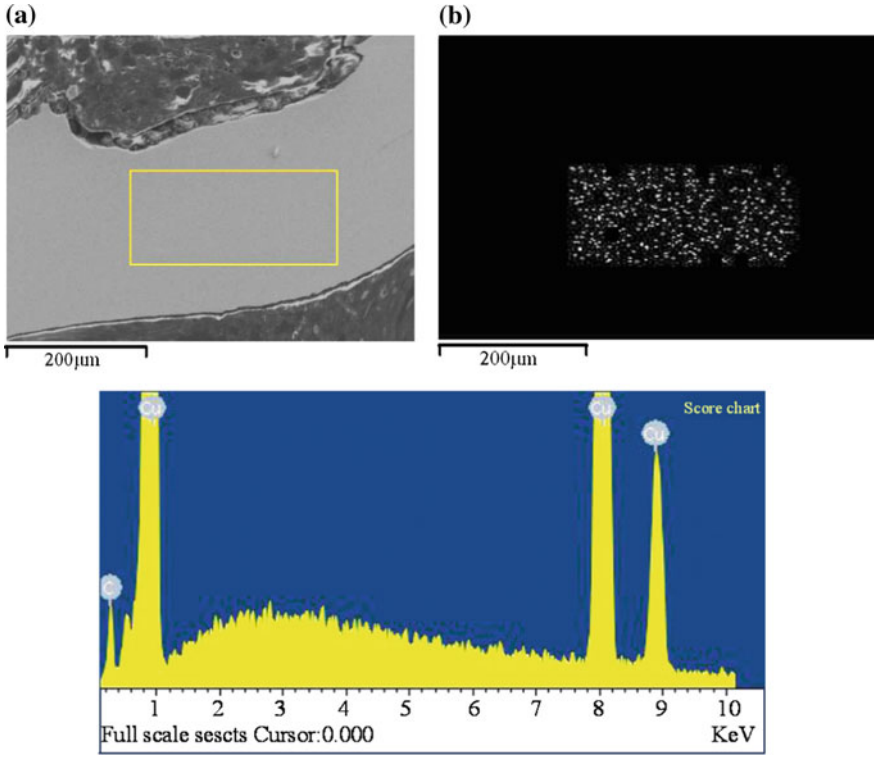

Fig. 8 EDS analysis results from Specimens C3

Table 4 Chemical composition analysis of Specimens C3 in weld (wt%)

Element	Weight percentage	Atom percentage
C K	0.26	1.36
Cu K	99.74	98.64
Total	100.00	

During ultrasonic welding process, severe plastic deformation and dynamic recrystallization of the matrix occurred in the ultrasonic vibration. The welding time was very short, limiting the grain growth. Grains in welds found by scanning electron microscopy were refined to the nanometer level. The greater the grain boundary area with finer grain, the effect of grain boundary hindering dislocation movement was greater. A large number of dislocations were blocked in the vicinity of grain boundaries, so that increased the strength of the material. Grain refinement can not only improve the material's strength and hardness, but also improve its ductility and toughness. After the addition of multi-walled CNTs, multi-wall CNTs restrain grain growth in a certain extent. But obstruction effect is limited because of a short time.

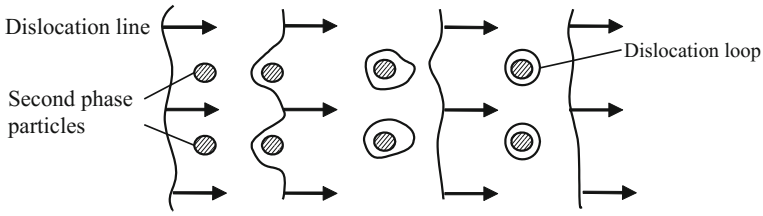

Fig. 9 Schematic diagram of dislocation bypassing the second phase particle

According E. Orowan mechanism, when the dislocation motion are blocked by non-deformable particles, dislocations bend and left dislocation loops bypassing them as shown in Fig. 9. Multi-walled CNTs are not deformable particles. There are a lot of dislocation motions in the ultrasonic welding. Around the multi-wall CNTs forming multiple dislocation loops, which is a major enhancement mechanism of multi-walled CNTs on substrate material. Also to make the dislocation line bypass the particle, the minimum critical shear stress required can be determined by using the following formula:

$$\tau = \frac{Gb}{\lambda} \tag{1}$$

where G is the shear modulus of the material; is b Brinell; λ is the distance between the particles.

Thus, the spacing is inversely proportional to strengthen the role of particles and particles. Thus, strengthening effect of particle is inversely proportional to the distance between the particles. To improve the strength of multi-walled CNTs-reinforced copper matrix composites, the higher volume fraction of multi-wall CNTs is better. Therefore, the realization of multi-walled CNTs content maximized and its uniform distribution ensured fundamental to improve multi-wall CNTs-reinforced metal matrix composites.

Conclusions

The findings from this study are summarized below:

(1) The multi-walled CNTs reinforced copper matrix composites can be prepared successfully by ultrasonic welding.
(2) Multi-walled CNTs can be uniformly dispersed in the specimens interface by spray method. But it enables multi-walled CNTs easily reunion in the weld when multi-walled CNTs content exceeds 0.5wt% in the copper matrix, which will affect the performance of composite materials seriously.

(3) It is capable of producing high-quality welded joints due to electroless copper multi-walled CNTs have high wettability with the matrix metal.
(4) Preparation of multi-walled CNTs Reinforced Copper Matrix Composites by Ultrasonic Welding major enhancement mechanism are dislocation strengthening, fine-grain strengthening and strengthening of the second phase.

Acknowledgements This project is supported by the National Natural Science Foundation of China (Grant No. 51365039).

References

1. R. Bacon, Growth, structure, and properties of graphite whiskers. J. Appl. Phys. **2**, 283–290 (1960)
2. M. Treacy, T.W. Ebbesen, J.M. Gibson, Exceptionally high young's modulus observed for individual carbon nanotubes. Nature **381**, 678–680 (1996)
3. E.W. Wong, P.E. Sheehan, C.M. Lieber, Nanobeam mechanics: elasticity, strength, and toughness of nanorods and nanotubes. Science **277**, 1971–1975 (1997)
4. M.F. Yu, O. Lourie, M.J. Dyer, K. Moloni, T.F. Kelly, R.S. Ruoff, Strength and breaking mechanism of multiwalled carbon nanotubes under tensile load. Science **287**, 637–640 (2000)
5. P.M. Ajayan, J.M. Tour, Materials science—nanotube composites. Nature **447**, 1066–1068 (2007)
6. Y. Matsuda, W. Deng, W.A.I. Goddard, Improving contact resistance at the nanotube-Cu electrode interface using molecular anchors. J. Phys. Chem. C **112**, 11042–11049 (2008)
7. S.R. Bakshi, D. Lahiri, A. Agarwal, Carbon nanotube reinforced metal matrix composites—a review. Int. Mater. Rev. **55**, 41–64 (2010)
8. S.M. Uddin, T. Mahmud, C. Wolf, C. Glanz, I. Kolaric, C. Volkmer, H. Hoeller, U. Wienecke, S. Roth, H. Fecht, Effect of size and shape of metal particles to improve hardness and electrical properties of carbon nanotube reinforced copper and copper alloy composites. Compos. Sci. Technol. **70**, 2253–2257 (2010)
9. S.J. Tans, A. Verschueren, C. Dekker, Room-temperature transistor based on a single carbon nanotube. Nature **393**, 49–52 (1998)
10. E. Dujardin, T.W. Ebbesen, H. Hiura, K. Tanigaki, Capillarity and wetting of carbon nanotubes. Science **265**, 1850–1852 (1994)
11. S. Hippmann, Q. Li, R. Addinal, W. Volk, Carbon nanotubes-reinforced copper matrix composites produced by melt stirring. Proc. Inst. Mech. Eng., Part N: J. Nanoeng. Nanosyst. **227**, 63–66 (2013)
12. S. Cho, K. Kikuchi, T. Miyazaki, K. Takagi, A. Kawasaki, T. Tsukada, Multiwalled carbon nanotubes as a contributing reinforcement phase for the improvement of thermal conductivity in copper matrix composites. Scr. Mater. **63**, 375–378 (2010)
13. S. Cho, K. Takagi, H. Kwon, D. Seo, K. Ogawa, K. Kikuchi, A. Kawasaki, Multi-walled carbon nanotube-reinforced copper nanocomposite coating fabricated by low-pressure cold spray process. Surf. Coat. Technol. **206**, 3488–3494 (2012)
14. K. Rajkumar, S. Aravindan, Tribological studies on microwave sintered copper-carbon nanotube composites. Wear **270**, 613–621 (2011)
15. L.M. Ang, T. Hor, G.Q. Xu, C.H. Tung, S.P. Zhao, J. Wang, Decoration of activated carbon nanotubes with copper and nickel. Carbon **38**, 363–372 (2000)

Effect of Print Method Based on SLM Technology on the Microstructure and Property of 316L Stainless Steel

Zhenghua Huang, Wenjun Qi, Yongxin Zhou, Chunjie Xu, Zhongming Zhang, Jianye Liu and Gaofeng Hu

Abstract Samples of 316L stainless steel were fabricated by focus print and defocus print under the similar other process parameters with the scanning power, interval and speed of 450 W, 0.05 mm and 2000 mm/s, respectively. The microstructures and defects were observed by optical microscope and scanning electron microscope. Meanwhile, the density, hardness and tensile mechanical property were tested. The results show that only few micro-cracks exist in the microstructure of the focus-printed sample with density of 95.54%, however some holes do in the microstructure of the defocus-printed sample with density of 92.21%. The focus-printed sample exhibits the better comprehensive mechanical property, where the hardness, tensile strength, yield strength and elongation reach

Z. Huang (✉) · W. Qi
Guangdong Provincial Key Laboratory for Technology and Application of Metal Toughening, Guangdong Institute of Materials and Processing, Guangzhou 510650, China
e-mail: zhhuang@live.cn

W. Qi
e-mail: 13925162166@qq.com

Y. Zhou · C. Xu · Z. Zhang
School of Materials Science and Engineering, Xi'an University of Technology, Xi'an 710048, China
e-mail: zhouyongxin_88@126.com

C. Xu
e-mail: xuchunjie@xaut.edu.cn

Z. Zhang
e-mail: zmzhang@xaut.edu.cn

J. Liu · G. Hu
Zhongshan Hantong Laser Equipment Co., Ltd., Zhongshan 528400, China
e-mail: 13544596700@163.com

G. Hu
e-mail: hanbang3d@163.com

J. Liu · G. Hu
Guangdong Hanbang Laser Technology Co., Ltd., Zhongshan 528400, China

© Springer Nature Singapore Pte Ltd. 2018

Y. Han (ed.), *Advances in Materials Processing*, Lecture Notes in Mechanical Engineering, https://doi.org/10.1007/978-981-13-0107-0_15

206 HV, 645 MPa, 560 MPa and 45.0%, respectively. While they are 195 HV, 625 MPa, 545 MP and 38.0% for the defocus-printed sample, respectively.

Keywords SLM technology · 316L stainless steel · Print method
Microstructure · Mechanical property

Introduction

The technology of selective laser melting (SLM) has become one of the most development potential technologies in the rapid prototyping and manufacturing field, and the important preparation method for the 3D print of metals [1]. With aided design and manufacture by the computer, the laser beam with high energy can melt metal powder to form the dense three dimensional parts directly based on the "discrete–hierarchical–overlay" principle. The forming process requires no tooling mold and is not limited by the complex shape of parts [2–4]. The metal parts fabricated by SLM technology, which can exhibit the dimension accuracy of 0.1 mm and surface roughness of 20–30 μm, are mainly used in the aerospace, medical instruments and moulds fields [5–7]. In addition to the scanning power, interval and speed, the print method can also affect the defects and comprehensive mechanical property of 3D print casting significantly. When the defocusing distance is in the range from −3 to +3 mm, the center of beam exhibits relatively high energy density owing to small focal spot under certain values of laser power and scanning speed. The thermal effect range is roughly equal to laser facula with homogeneous distribution of energy density, so the defocusing distance plays almost no influence on the width of weld pool with single pass. However, it plays a significant effect on the melting depth. With increasing the defocusing distance, the continuity of molten pool deteriorates gradually [8]. Therefore, the present paper is focused on comparing the microstructure and defects, density, hardness and tensile mechanical property of 316L stainless steel samples fabricated by focus print and defocus print with the similar other process parameters including the scanning power, interval and speed. Then, it can provide the technical support for the industrialization of 3D printing technology of metals.

Experimental

The nominal and measured contents of each element of 316L stainless steel powder produced by the British company LPW are listed in Table 1. Figure 1 shows the micro-morphology of the powder and particle size distribution measured by the laser particle size distribution tester (JL-1166). The average particle size of the powder is 46.9 μm.

Table 1 Nominal and measured contents of each element of 316L stainless steel powder (weight percent, wt%)

Element	Cr	Ni	Mo	Mn	Si	Cu
Nominal content	17.5–18.0	12.5–13.0	2.25–2.50	≤ 2.00	≤ 0.75	≤ 0.5
Measured content	17.6	12.5	2.29	0.77	0.63	0.02

Element	N	O	C	P	S	Fe
Nominal content	≤ 0.10	≤ 0.1	≤ 0.03	≤ 0.025	≤ 0.010	Bal.
Measured content	0.09	0.02	0.024	0.007	0.005	Bal.

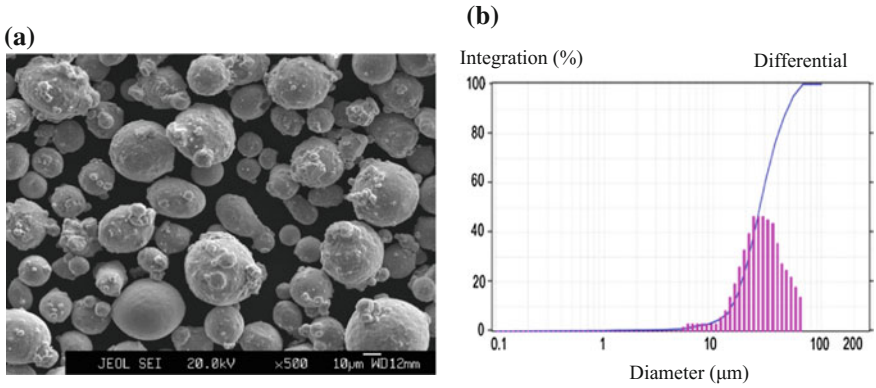

Fig. 1 SEM graph **a** and particle size distribution **b** of 316L stainless steel powder

The 316L stainless steel samples were fabricated by two printing ways i.e. focus print and defocus print in metal printing equipment (SLM-150) produced by Guangdong Hanbang Laser Technology Co., Ltd. Meanwhile, the scanning power, interval and speed were 450 W, 0.05 mm and 2000 mm/s, respectively. Finally, the cylindrical samples with the diameter of 10 mm and the length of 10 mm and plate tensile samples were obtained, respectively. The defocusing distance is usually regulated by adjusting the diameter of spot. There is a relationship between the defocusing distance and the diameter of spot [8]:

$$D_S = D_{\min} \pm 2s \tan\frac{\theta}{2} = D_{\min} \pm s\frac{(nD_0 - D_{\min})}{f} \quad (1)$$

where, D_s is the diameter of laser spot when the defocusing distance is s. θ is the exit angle of beam after enlarging. Symbols "+" and "−" represent positive and negative defocusing distances, respectively.

All specimens were etched with chloroazotic acid. Then, microstructural observation was carried out on optical microscope (OM, Leica DM IRM) and scanning electron microscope (SEM, JEOL JXA-8100). Tensile test at ambient temperature was performed on material test machine (DNS200) at a rate of 2 mm/

min. Hardness HV was measured by Vicker's indentation test machine (MH-5L) with the loading load and time of 9.8 N and 20 s, respectively. Density K was carried out on analytical balance (TG328B). First, the original quality m1 was weight when the sample is cleaned by ultrasonic. Then, the quality m2 was weight when glycerol was evenly coated to the surface of the sample for inhibiting the water, and subsequently the sample was hanged by one hair. Finally, the quality m3 was weight when the sample was immersed in water with hanging by the hair. Density K could be calculated by the following formula.

$$K = \frac{\rho_c}{\rho_{mth}} \tag{2}$$

$$\rho_c = \frac{m_1}{m_2 - m_3} \tag{3}$$

where, ρ_{mth} is the theoretical density of the sample, which is 7.98 g/cm^3 for 316L stainless steel.

Results and Discussion

Figure 2 shows the SEM graphs of 316L stainless steel fabricated by focus print and defocus print, respectively. It is seen that there exists only few micro-crack in the focus-printed sample, while many holes can be observed in the defocus-printed sample. They are two major types of defects during the SLM process. The holes exhibit irregular size, and sometimes unmelted powder particles can be observed within the holes. The crack is discontinuous and irregular. This is mainly because the SLM is a complex process of physical and chemical metallurgy. Metal powder melts and solidifies quickly with short times for few milliseconds under the rapid

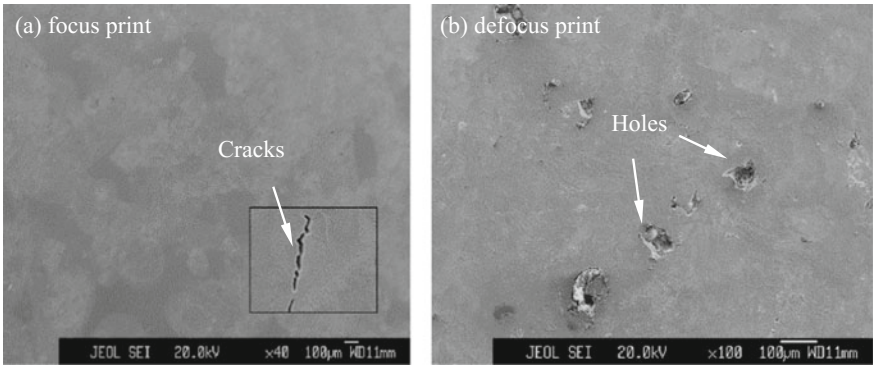

Fig. 2 SEM graphs of 316L stainless steel fabricated by focus print and defocus print

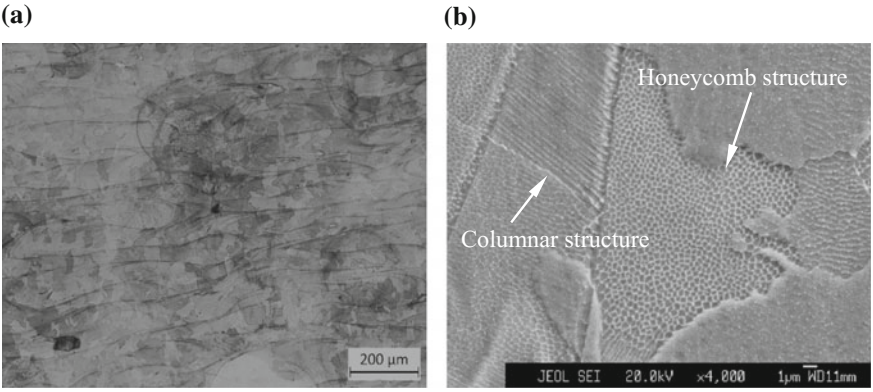

Fig. 3 Microstructure of 316L stainless steel fabricated by focus print

and ordered moving of laser beam. High thermal stress is easy to produce in the process, and then the bend and crack can form. Meanwhile, it is also easy to make spheroidization during the melting and solidification process of metal powder, resulting in the rough and discontinuous surface. The abovementioned two factors eventually lead to the defects such as holes, cracks and pores in the formed metal parts, and then the parts cannot reach the complete densification. Obviously, the laser energy density is greater for the focus print, and then the energy absorbed by powder can melt the powder more quickly and solidify rapidly to form relatively compact parts. On the contrary, when the laser energy density is low, the partial powder can be melted, and then the defects including many holes can occur [9].

Figure 3 shows the microstructure of 316L stainless steel fabricated by focus print. A scaly layered trajectory can be observed clearly (see Fig. 3a). This is the bonding line between the last one pass and the present pass produced by melting the powder, and its formation is related to the Gauss mode of the laser. Because the energy is the strongest for the center of laser spot and is weaker for both sides, therefore the middle zone exhibits the deepest melting depth. Then, the arc fusion line is formed. At the same time, fine grains mainly consisting of columnar and honeycombed structures can be seen in the microstructure (see the arrows in Fig. 3b) [9, 10]. This is because the temperature of 3D printing parts first rises instantaneously, and then declines rapidly during the forming process, leading to high supercooling degree. The greater the heating rate is, and the greater the superheat degree during the austenite transformation is. Then, the austenite forms at higher actual temperature. Thus, higher nucleation rate leads to fine grains.

Table 2 lists the properties of 316L stainless steel fabricated by focus print and defocus print, respectively. The density K is 95.54% for the focus-printed sample, which is larger than the value (92.21%) for the defocus-printed sample. Meanwhile, the focus-printed sample exhibits better comprehensive mechanical properties. The hardness, tensile strength σ_b, yield strength $\sigma_{0.2}$ and elongation δ are 195 HV, 625 MPa, 545 MPa and 38% for the defocus-printed sample, respectively, while

Table 2 Properties of 316L stainless steel fabricated by focus print and defocus print

Method	K (%)	HV	σ_b (MPa)	$\sigma_{0.2}$ (MPa)	δ (%)
Focus print	95.54	206	645	560	45.0
Defocus print	92.21	195	625	545	38.0

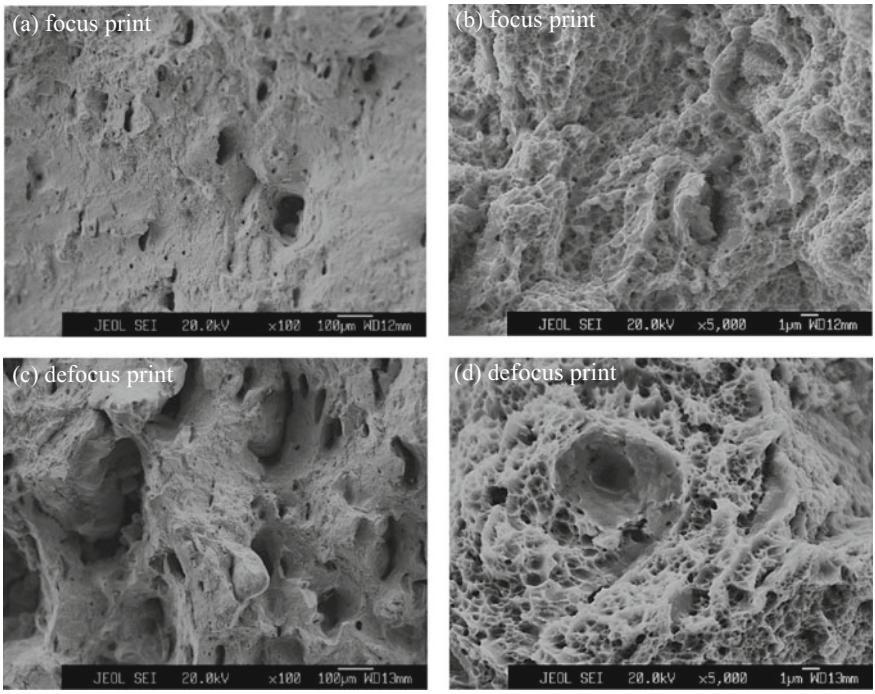

Fig. 4 SEM graphs of tensile fracture morphology of 316L stainless steel fabricated by focus print and defocus print

they increase to 206 HV, 645 MPa, 560 MPa and 45% by the amplitude of 6, 3, 3 and 18%, respectively. The focus-printed sample exhibits few defects i.e. only micro-cracks, resulting in high density, excellent hardness and tensile mechanical properties. While, the defocus-printed sample does more defects i.e. large pores, leading to low density, slightly worse hardness and tensile mechanical properties.

Figure 4 shows the SEM graphs of tensile fracture morphology of 316L stainless steel fabricated by focus print and defocus print, respectively. From low magnification, few and small holes can ben observed in the tensile fracture of the focus-printed sample; while there exist many large pores, some of which can be connected, in the tensile fracture of the focus-printed sample. From high magnification, all two samples exhibit the typical ductile fracture with many dimples.

However, the large tunnels can be observed in the tensile fracture of the defocus-printed sample. It is consistent with the change in the tensile mechanical property for the two samples.

Summary

316L stainless steel sample fabricated by focus print exhibits that only few micro-cracks occurs in the sample, the density is as high as 95.54%, and excellent comprehensive mechanical property is obtained, i.e., the values of HV, σ_b, $\sigma_{0.2}$ and δ reach 206, 645 MPa, 560 MPa and 45.0%, respectively. While, the defocus-printed sample exhibits some holes in the microstructure, relatively low density of 92.21% and comprehensive mechanical property that the values of HV, σ_b, $\sigma_{0.2}$ and δ are 195, 625 MPa, 545 MP and 38.0%, respectively. The focus-printed and defocus-print samples exhibit the typical ductile fracture with many dimples.

Acknowledgements This work is supported by the Guangdong Key Laboratory of Metal Toughening Technology and Application (2014B030301012), Guangzhou Key Laboratory of Advanced Metal Structural Materials (201509010003), Major Science and Technology Projects of Guangdong Province (2014B01013100 and 2016B090914001) and Research Platform Environment and Capacity Construction Project of Guangdong Academy of Sciences (2016GDASPT-0320).

References

1. R. Morgan, C.J. Sutcliffe, W. O'Neill, Density analysis of direct metal laser re-melted 316L stainless steel cubic primitives. J. Mater. Sci. **39**, 1195–1205 (2004)
2. J.P. Kruth, P. Mercelis, J.V. Van Vaerenbergh, Binding mechanisms in selective laser sintering and selective laser melting. Rapid Prototyp. J. **11**, 26–36 (2005)
3. C.C. Ng, M. Savalani, H.C. Man, Fabrication of magnesium using selective laser melting technique. Rapid Prototyp. J. **17**, 479–490 (2011)
4. D.M. Xiao, Y.Q. Yang, X.B. Su, Topology optimization of microstructure and selective laser melting fabrication for metallic biomaterial scaffolds. Trans. Nonferrous Met. Soc. China **22**, 2554–2561 (2012)
5. F. Abe, K. Osakada, M. Shiomi, K. Uematsu, M. Matsumoto, The manufacturing of hard tools from metallic powders by selective laser melting. J. Mater. Process. Technol. **111**, 210–213 (2001)
6. Y.S. Shi, R.D. Li, W.X. Zhang, J.H. Liu, A study on selective laser melting rapid prototyping technology about stainless steel powder. Electromech. Mould **S1**, 67–72 (2010). (in Chinese)

7. E. Santos, K. Osakada, M. Shiomi, M. Morita, F. Abe, Fabrication of titanium dental implants by selective laser melting. Proc. Soc. Photo-Optical Instrum. Eng. **5662**, 268–273 (2004)
8. W.H. Wu, Y.Q. Yang, H.W. Wang, D. Wang, Research on direct rapid manufacturing of 316L fine metal part using fiber laser. Laser Technol. **33**, 486–489 (2009). (in Chinese)
9. L.D. Fu, *Study on metal parts in selective laser melting of stainless steel powder* (Huazhong University of Science and Technology, Wuhan, 2008). (in Chinese)
10. B. Vandenbroucke, Selective laser melting of biocompatible metals for rapid manufacturing of medical parts. Rapid Prototyp. J. **13**, 196–203 (2007)

Precipitation Behavior of 1.3%Si Non-oriented Silicon Steels During Strip Casting Process

Feng Fang, Xiang Lu, Mengfei Lan, Yuanxiang Zhang, Yang Wang, Guangming Cao, Guo Yuan, Yunbo Xu and Guodong Wang

Abstract In this work, the precipitation behaviors of 1.3%Si non-oriented silicon steel during the sub-rapid solidification process under different melt superheat were investigated using scanning electron microscope and transmission electron microscope, based on strip casting process. The results showed that the precipitates of as-cast strips were dominated by coarse AlN, and MnS particles were seldom observed. The mean size of AlN particles rapidly increased from 75 to 1060 nm, and the volume fraction increased from 0.028 to 0.069%, when the melt superheat increased from 20 to 70 °C. Besides, the precipitation quantity in the center layer of as-cast strip was obviously more than the surface layer. According to the different solubility ability in the liquid and ferrite matrix, Al or N elements tend to segregate

F. Fang · X. Lu · M. Lan · Y. Zhang · Y. Wang · G. Cao · G. Yuan (✉)
Y. Xu · G. Wang
State Key Laboratory of Rolling and Automation, Northeastern University, Shenyang, China
e-mail: yuanguo@ral.neu.edu.cn

F. Fang
e-mail: fangfengdbdx@163.com

X. Lu
e-mail: lx_neu@126.com

M. Lan
e-mail: 1875939247@qq.com

Y. Zhang
e-mail: neuzhangyuanxiang@126.com

Y. Wang
e-mail: wy069024019@163.com

G. Cao
e-mail: caogm@ral.neu.edu.cn

Y. Xu
e-mail: yunboxu@126.com

G. Wang
e-mail: wanggd@mail.neu.edu.cn

© Springer Nature Singapore Pte Ltd. 2018

Y. Han (ed.), *Advances in Materials Processing*, Lecture Notes in Mechanical Engineering, https://doi.org/10.1007/978-981-13-0107-0_16

during the sub-rapid solidification process, which is attributed to the nucleation and coarsening of AlN. On the condition of low melt superheat, the solidified layers suffered from hot deformation from the solidification end point to the nip point, which provided additional nucleation sites for precipitates and can be attributed to fine particles size. In addition, different heat conductivity and hot deformation degree in various thickness layer resulted in inhomogeneous distribution of particles through the thickness of as-cast strips.

Keywords Strip casting · Non-oriented silicon steel · Precipitation behavior Melt superheat

Introduction

Non-oriented electrical steel sheets are used for rotated electrical machinery cores and required high magnetic flux density and low core loss [1], which has significant contribution in reducing electrical consumption. The magnetic properties of these steels are governed by microstructural features such as grain size, crystallographic texture, and precipitates of the final products. Among the main metallurgical factors, the precipitates play an important role to obtain low core loss, either directly by interference the domain wall movement, or indirectly by grain growth inhibition [2], which has received much less attention as compared with texture control. To obtain optimized magnetic properties, the precipitation of fine precipitates should be avoided, which has been widely studied in conventional process [3, 4]. Recently, in order to simplify the production processes, the strip casting process was proposed to manufacture silicon steel, which has shown obvious advantages to obtain favorable {001} <0vw> texture and initial coarse grains in as-cast strip, which is different from the conventional process. Many experimental investigations [5–8] on strip-casting silicon steel have been carried out and the focus is the characterization of the texture and solidification structure of the as-cast strips. In addition, Mou et al. [9] investigated the precipitation behavior of second phase particles during the heat treatment of Fe–2.7%Si as-strip, and reported that the size of precipitates in strip can be optimized. However, the precipitation behaviors of non-oriented silicon steel during the sub-rapid solidification process under different melt superheat is as yet unclear, which may have significant influence on the evolution of precipitates and relevant magnetic properties.

In the present work, 1.3%Si non-oriented silicon steels were produced by twin-roll strip casting at different melt superheats. The effect of melt superheats on precipitation behavior was discussed in detail.

Materials and Experimental Procedure

The nominal composition of tested silicon steels in weight% was Fe–0.003C–1.3Si–0.25Mn–0.3Al–0.003S–0.0065 N. And the relevant Fe–Si phase diagram was calculated using Thermo-Calc 5.0 software, as shown in Fig. 1. It can be seen that the liquidus temperature and precipitation temperatures for AlN and MnS are 1506, 1375 and 1240 °C in equilibrium state, respectively.

The strip casting experiments were carried out using a vertical type laboratory twin-roll caster [7]. The melten steel supplied from an induction furnace was poured into a preheated tundish, and then flowed into the water-cooled internally casting rollers through a nozzle under the Ar shield. The superheat of liquid steel was controlled to be 20, 30, 50 and 70 °C, respectively. After strip casting, the as-cast strips of dimensions 2.0 mm thickness and 110 mm width were directly air-cooled to room temperature. The morphologies and size distributions of precipitates in as-cast strips were studied via TEM (FEI Tecnai G2 F20) equipped with an energy dispersive spectroscopy and SEM (Zeiss Ultra-55). The plate sections as defined by the rolling direction and transverse direction in various thickness layer (0, 0.25, 0.5, 0.75, 1 mm from the center of strip) were tested in turn to investigate the precipitate distribution through thickness. The size, and number density of precipitates were determined using 20 SEM micrographs in this work.

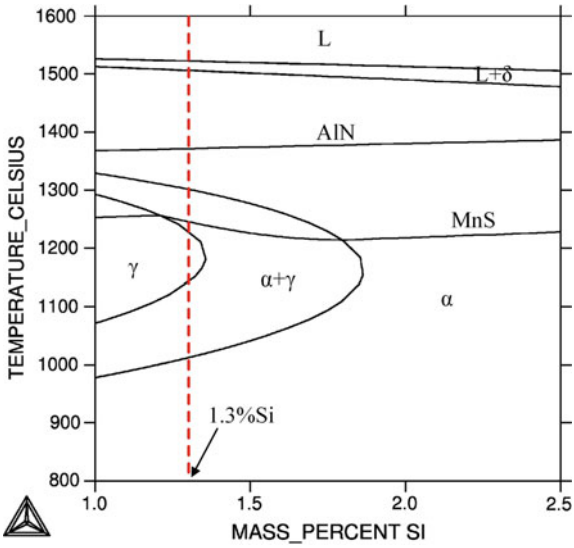

Fig. 1 Equilibrium phase diagram of Fe–Si (L, δ, γ, and α represent liquid, δ-ferrite, austenite and α-ferrite, respectively)

Results

Precipitates during Strip Casting

Figure 2 shows the typical morphology of precipitates of the as-cast strips at different melt superheat. According to the EDS analyses (Fig. 2e), it can be confirmed that the main polygonous precipitates in the as-cast strips are AlN, and MnS particles were seldom observed. The average grain size was rapidly increased when the superheat was increased from 20 to 70 °C. It is of particular interest to note that the AlN of size ~1.9 μm was obtained in the case of 70 °C in Fig. 2d, which is relatively smaller than that in conventional process. The result indicated that the nucleation and growth of precipitates was partly suppressed because of rapid cooling, which is quite distinct from the slab casting process.

The size distributions of precipitates are presented in Fig. 3. It is observed that the precipitates size remarkably increased from 75 to 1060 nm with increase in the superheat from 20 to 70 °C. Additionally, the volume fraction of AlN precipitates in as-cast strips was obtained based on TEM results, and is shown in Fig. 4. Fraction of precipitates at 70 °C is as high as 0.069%, which show obvious advantages over 0.028% at 20 °C. That is to say, much coarse AlN precipitates

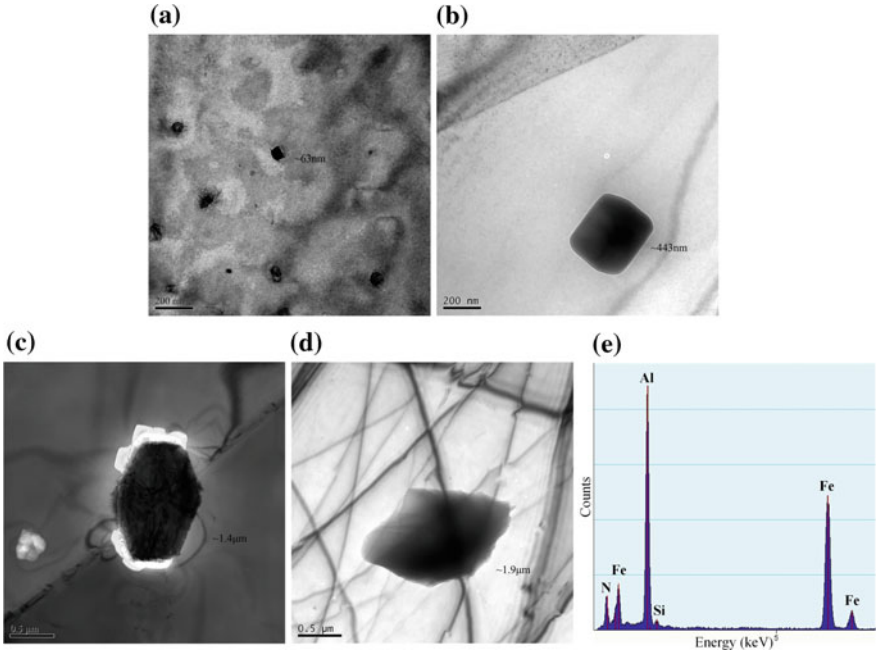

Fig. 2 Morphology of AlN precipitates in as-cast strips produced at different melt superheats: **a** 20 °C, **b** 30 °C, **c** 50 °C, **d** 70 °C, and **e** the EDS result at 20 °C

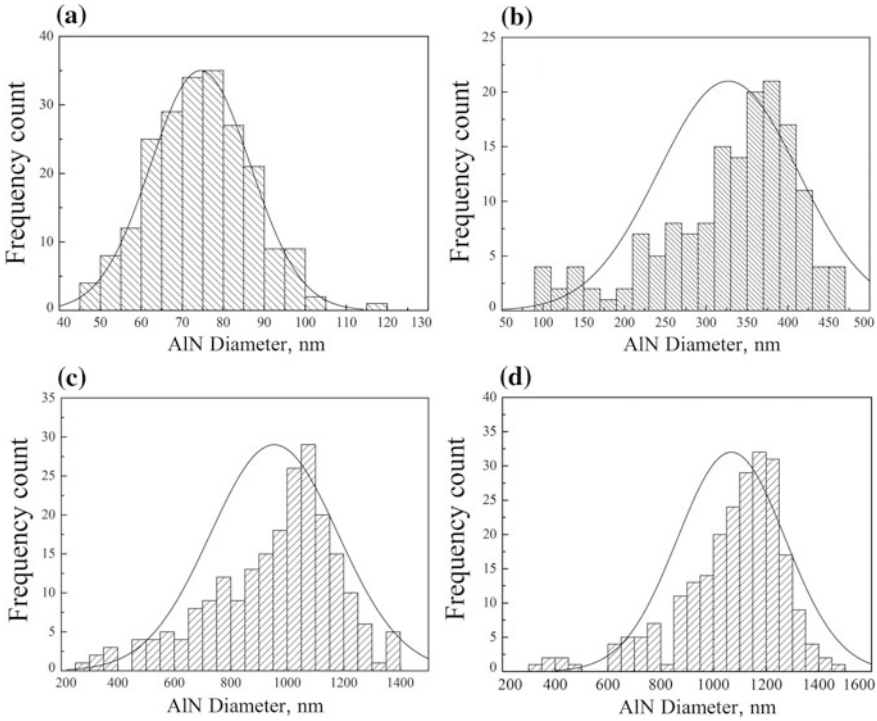

Fig. 3 Size distribution of precipitates in as-cast strips produced at different melt superheats: **a** 20 °C, **b** 30 °C, **c** 50 °C, **d** 70 °C

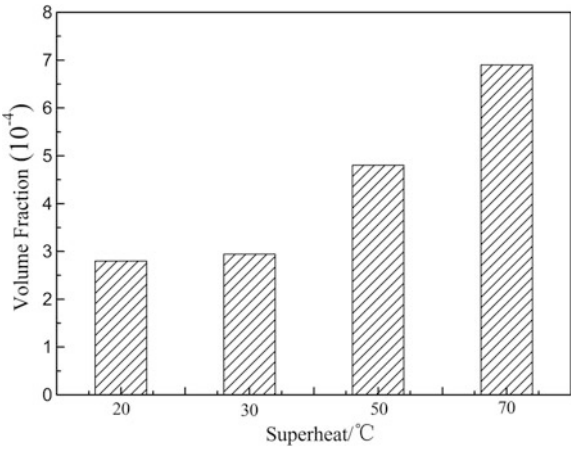

Fig. 4 Volume fraction of precipitates in as-cast strips produced at different melt superheats

formed under the condition of high superheat. It is worth noting that the fraction of precipitates at 20 and 30 °C remained similar level, which indicated that the precipitation behavior is dominated by melt superheat.

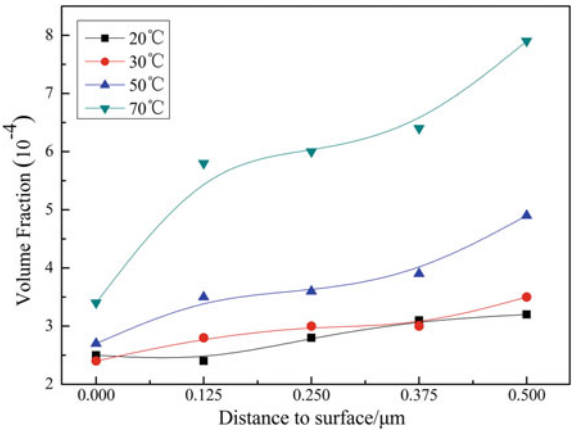

Fig. 5 Volume fraction of precipitates in various thickness layer of as-cast strips produced at different melt superheats

Distributions of Precipitates through Thickness Direction

The inhomogeneity of the texture and microstructure through the thickness direction has been generally realized in early literatures [5, 10]. The fraction of precipitates in various thickness layer of as-cast strips was studied and is shown in Fig. 5. Near surface regions, the fractions of precipitates were relatively low under all superheat conditions, as compared to the average level. However, in the center layer, high fraction of precipitates was obtained, especially at 70 °C. Meanwhile, the fraction of precipitates rapidly increased from the surface layer to center layer, while the strip at low superheat (~20–30 °C) exhibited similar precipitates distribution.

Discussion

It is well accepted that the strip casting process integrates solidification and hot rolling into a single process to produce thin strips, which is significant different from conventional process. Among the process parameters, the melt superheat is the most effective one to control the microstructure and texture by affecting the solidification and hot deformation process. In this study, the precipitation behavior of 1.3%Si non-oriented silicon steels was also indirect effected by the superheat during strip casting process. Due to rapid solidification and fast secondary air-cooling, the precipitation or growth of second phase particles was partly suppressed and some coarse AlN particles were observed in the as-cast strip. The precipitates order is determined by solubility ability. Given that the different solubility ability of liquid and ferrite, the micro-segregation of solute N and Al element in the inter-dendritic regions during solidification process occurred and contributed to the precipitate nucleation. Then, AlN particles with higher precipitation

temperature preferentially nucleated at appropriate sites, and subsequent rapid coursed due to the high diffusion rate of N element during high temperature. However, the precipitation behavior of MnS with low precipitation temperature was suppressed because of limited nucleation sites available for new precipitates. As a result, very few MnS particles were observed in the as-cast strip.

The effect of superheat on the precipitates behaviors can be well explained when taking the solidification and hot deformation into consideration. Figure 6 shows the schematic diagram of twin-roll strip casting process. In the case of high melt superheat, the solidification layers from roller meet at relatively low position, which indicated that the solidification end point was nearly above the roll nip point, as shown in Fig. 6a. And the strip suffered from weak hot deformation, or even remained in unformed state. However, with the decrease of melt superheat, the solidification process finished early and the position of end point was relatively high above the nip point, leading to heavy hot deformation in the as-cast strip before leaving the nip point. As a result, additional nucleation sites were provided for high temperature precipitates of AlN at low superheat. Meanwhile, the heat conductivity between molten steel and as-cast strongly depend on the melt superheat during strip casting process. In the case of low superheat, the heat conductivity is greatly increased under the condition of high roll separating force and thus the particle coarsening process was highly inhibited due to the rapid cooling rate. While, the existing particle tended to coarse rapidly due to the large volume of heat generated in the solidification interface region in the case of high superheat. Therefore, high fraction of precipitates with large particle size was obtained at high superheat and low fraction of precipitates with fine size for low superheat, which can be attributed the combined effect of hot deformation and heat conductivity respectively.

The reason of the inhomogeneity distribution was the different heat conductivity in various thickness layer of as-cast strips, which originated from the temperature

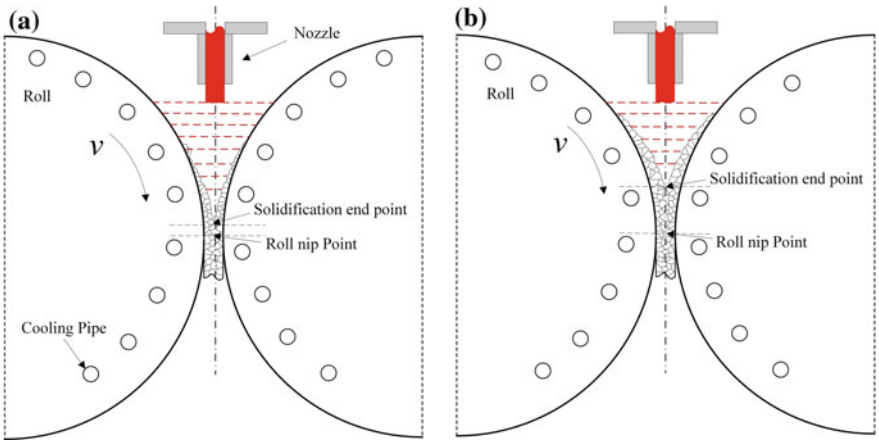

Fig. 6 Schematic diagram of twin-roll strip casting process at **a** high and **b** low melt superheats

gradient through thickness direction. The molten steel solidified immediately when in contact with roll surface and a large undercooling was achieved in the surface layer. As a result, the precipitates behavior was inhibited and low fraction of precipitates was obtained in the surface layer. Then the two solidified strip shells meet at the solidification end point above the roll nip point, and the strip was deformed before leaving the nip point. The center layer of high temperature was relatively soft and suffered from much deformation as compared to the surface layer, which is expected to accelerate the nucleation of precipitates. Besides, with the increase of melt superheat, the heat transfer coefficient is decreased, and a large amount of heat was hard to be released in the center layer which provide appropriate condition for the coarsening of precipitates, leading to high fraction of precipitates in center layer, as shown in Fig. 5. Consequently, it is indicated that the precipitates behaviors can be well controlled by the melt superheat during strip casting process, which may provide a potential and effective way to produce non-oriented silicon steel with desired precipitates and optimized magnetic properties in the further.

Conclusions

In summary, coarse AlN particles dominated the precipitates of as-cast strip and MnS particles were seldom observed, which is highly related to the precipitation temperature and limited nucleation sites. The melt superheat strongly affects the solidification process and hot deformation during the strip casting process, leading to different precipitates behaviors at different superheat. The precipitates size remarkably increase from 75 to 1060 nm and the fraction of precipitates increase from 0.028 to 0.069%, with the increase in the superheat from 20 to 70 °C. On the condition of high melt superheat, the solidified layers suffered from little hot deformation and low heat conductivity was achieved, which provided appropriate condition for the coarsening of precipitates. In addition, the fraction of precipitates rapidly increase from the surface layer to center layer, especially for high melt superheat. This study indicates that melt superheat has strong effect on the precipitation behavior during strip casting process of 1.3%Si non-oriented silicon steel.

Acknowledgements The authors acknowledge support by the National Natural Science Foundation of China (Nos. 51674080 and 51774083), the Program for New Century Excellent Talents in University (NCET-13-0111) and the Program for Liaoning Excellent Talents in University (LR2014007).

References

1. F.J.G. Landgraf, Nonoriented electrical steels. J. Miner. Met. Mater. Soc. **64**, 764–771 (2012)
2. K. Jenkins, M. Lindenmo, Precipitates in electrical steels. J. Magn. Magn. Mater. **320**, 2423–2429 (2008)

3. T. Semuma, Present status of and future prospects for precipitation research in the steel industry. ISIJ Int. **42**, 1–12 (2002)
4. L. Xiang, E.B. Yue, D.D. Fan et al., Calculation of AIN and MnS precipitation in non-oriented electrical steel produced by CSP process. J. Iron. Steel Res. Int. **15**, 88–94 (2008)
5. J.Y. Park, K.H. Oh, H.Y. Ra, Microstructure and crystallographic texture of strip cast 4.3 wt% Si steel sheet. Scr. Mater. **40**, 881–885 (1999)
6. H.T. Liu, Z.Y. Liu, C.G. Li et al., Solidification structure and crystallographic texture of strip casting 3 wt% Si non-oriented silicon steel. Mater. Charact. **62**, 463–468 (2011)
7. Y.X. Zhang, Y.B. Xu, H.T. Liu et al., Microstructure, texture and magnetic properties of strip-cast 1.3%Si non-oriented electrical steels. J. Magn. Magn. Mater. **324**, 3328–3333 (2012)
8. Y.B. Xu, Y.X. Zhang, Y. Wang et al., Evolution of cube texture in strip-cast non-oriented silicon steels. Scr. Mater. **87**, 17–20 (2014)
9. J.S. Mou, H.T. Jiao, Q.Q. Han, et al., Characterization of precipitates in strip-cast 2.7%Si steel under different heat treatment conditions, in *MATEC Web of Conferences*, vol. 21 (2015) 07004
10. J.Y. Park, K.H. Oh, H.Y. Ra, Texture and deformation behavior through thickness direction in strip-cast 4.5 wt%Si steel sheet. ISIJ Int. **40**, 1210–1215 (2000)

Influence of Initial Microstructure on the Hot Working Flow Stress of ZK60 Mg Alloy

Yunteng Liu, Di Zhang, Tao Lin, Jixue Zhou, Yu Liu, Changwen Tian and Yuansheng Yang

Abstract The hot working flow stress of as-cast and two as-extruded magnesium alloys ZK60 was investigated through uniaxial compression tests. It was found that the hot deformation behavior was sensitive to the deformation conditions and initial microstructure. The peak flow stress was affected by the deformation temperature and the strain rate. Its value was decreased with increasing the deformation temperature or decreasing the deformation rate. The peak flow stresses for the as-cast and as-extruded samples showed a different Z dependency. However, the correlations between Z parameters and as-extruded materials with different initial microstructures were almost the same. These key features of deformation behavior can be explained by twinning and dynamic recrystallization.

Keywords Magnesium alloys · Initial microstructure · Uniaxial compression High temperature · Deformation behavior

Y. Liu (✉) · T. Lin (✉) · J. Zhou · Y. Liu · C. Tian
Shandong Key Laboratory for High Strength Lightweight Metallic Materials, Advanced Materials Institute, Shandong Academy of Sciences, Jinan 250014, China
e-mail: liu_yunteng@126.com

T. Lin
e-mail: tlin@alum.imr.ac.cn

D. Zhang
College of Materials Science and Engineering, Shandong Jianzhu University, Jinan 250014, China

T. Lin · Y. Liu
Shandong Engineering Research Center for Lightweight Automobiles Magnesium Alloys, Jinan 250014, China

Y. Yang
Institute of Metal Research Chinese Academy of Sciences, Shenyang 110016, China

© Springer Nature Singapore Pte Ltd. 2018

Y. Han (ed.), *Advances in Materials Processing*, Lecture Notes in Mechanical Engineering, https://doi.org/10.1007/978-981-13-0107-0_17

Introduction

Due to the advantages of low density and high specific strength, the application of wrought magnesium alloys is increasing. However, Mg alloys have only two independent basic slip systems at room temperature, so their workability is poor. The effect of grain size on room temperature deformation is well known and its yield stress follows the Hall-Petch relationship [1]. That is, the yield stress is inversely proportional to the square root of grain size. At high temperatures, Mg alloys have better process ability due to the activation of non-basic slip systems [2]. Under such conditions, the effect of grain size on flow stress becomes complicated because of non-basal slipping, twinning, grain growth [3, 4], dynamic recovery (DRV) [5], dynamic recrystallization (DRX) [6, 7] and so on. Based on the above softening process, in addition to strain rate and deformation temperature, the deformation mechanism is also sensitive to changes in grain size. Further understanding of the constitutive behavior of Mg alloy will help to optimize its hot processing performance. Especially, a proportion of profiles and plates of Mg alloy require secondary deformation at high temperatures. The constitutive equation can be related to the Zener-Hollomon parameter Z, defined as $\dot{\epsilon}\exp\left(Q/RT\right)$, for which $\dot{\epsilon}$ is the strain rate, Q is the activation energy, R is the ideal gas constant and T is deformation temperature. During the uniaxial compression of AZ31, Beer et al. found that the peak stress of as-cast sample is higher at the low Z regime, and that of the wrought AZ31 is higher at the high Z regime [8]. Wu et al. reported that, there is a more pronounced hardening and then softening at the high Z regime, and a dynamic equilibrium is quickly achieved between hardening and softening at the low Z regime [9]. The flow curve shows the typical flow characteristics of dynamic softening associated with DRV and DRX.

So far, the study on deformation behavior of deformed magnesium alloy is limited to the initial microstructure with only a single grain size. There are a few studies [10] on the deformation behavior of high strength magnesium alloy for ZK60, especially, those at the high strain rate with different initial microstructure. As we know, high strain rate can increase productivity and reduce cost.

In this study, the hot compression tests of as-extruded ZK60 Mg alloy with two different grain sizes were performed at the temperature of 523−723 K with a strain rate of 0.01−10 s^{-1}. The results were also compared with that of as-cast state, to determine the correlation of hot working flow stress. Understanding the magnitude of these effects is necessary for a flow stress model applied to extrusion, rolling and forging.

Experimental Procedure

The cast ZK60 (Mg-5.2Zn-0.58Zr-0.02Mn) Mg alloy semi-continuous cast ingot, with 125 mm in diameter, was extruded into rods with two different diameters at a billet preheating temperature of 673 K through an 8000 KN extrusion press. The two

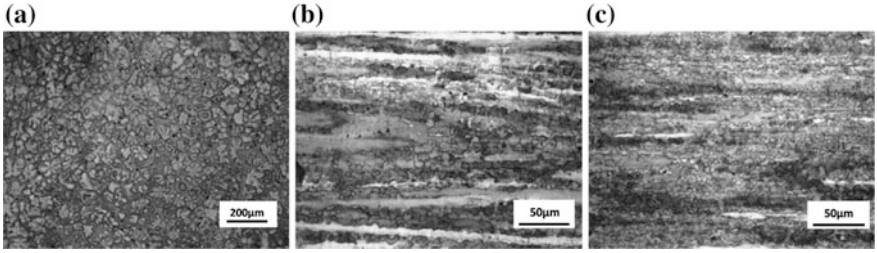

Fig. 1 The initial microstructure of the **a** as-cast, **b** E15 and **c** E60 as-extruded material

extrusion ratios were 15 and 60. These samples were referred to "E15" and "E60" wrought materials respectively. The as-cast and as-extruded microstructures were given in Fig. 1. These microstructures were composed of as-cast dendrites, bimodal size distribution grains and fine equiaxed grains. The corresponding average grain sizes are about 140, 25 and 10 μm, respectively. The average grain size was calculated according to D = 1.74L [11], where L is the average grain size got by the line intercept method. It should be noted that bimodal size distribution grains contained coarse deformed grains and fine recrystallized grains.

Cylindrical specimens with a diameter of 10 mm and a height of 15 mm were machined from the extruded rod by aligning their axes along the casting direction and the extrusion direction. Hot compressed tests were conducted on a Gleeble 3500 thermal simulation machine at temperatures of 523−723 K and at constant strain rates of 0.01−10 s^{-1}. Graphite foil was used as a lubricant between the specimen and the compression dies. Thermocouple was welded on the surface of the compression specimen to measure the temperature. The specimens were heated to the test temperature and held for 120 s to ensure that the specimen temperature was uniform. Then the initial height was reduced to 5.5 mm to obtain a true strain of approximately 1. The specimens after hot compression were immediately quenched in water to retain the high temperature microstructures. The specimens for microscopic examination were prepared using conventional metallographic techniques. The polished specimens were etched for approximately 15−30 s with a solution that was made with 25 ml of saturated solution of picric acid in ethanol, 10 ml acetic acid, 5 ml deionized water and 5 ml methanol. Subsequently, the specimens were washed thoroughly with ethanol and dried. Optical microscopy was performed using a Zeiss Axio-Observer-Aim inverted metallurgical microscope.

Results and Discussions

The selected true stress-strain curves obtained during the hot compression deformation of the as-cast and as-extruded ZK60 alloy at 673 K and/or a strain rate of 10 s^{-1} were shown in Fig. 2a–c. The flow curve consists of a work hardening

region, which is then followed by work softening. The curve exhibits a peak in the stress-strain curve. In some cases, for example at high or low strain rates, it is followed by a steady state region. The peak flow stress is affected by the temperature and the strain rate. As the strain rate decreases or the deformation temperature increases, the peak flow stress gradually decreases and the corresponding strain value decreases too.

The inspection of the shape of the flow curve in Fig. 2 also shows a change in shape as the temperature rises and/or the strain rate decreases. At lower temperatures and/or higher strain rates, the flow curves show the steep linear and sometimes even "concave" work hardening regions of all three test materials. The characteristics of the "concave" and the degree of high work hardening of the flow curve have been extensively reported for the compression deformation of Mg alloy extrusions at low temperatures [12]. As described in the above, this is the result of the $\{10\bar{1}2\}$ twinning, which repositions the lattice as hard crystallographic orientation. During the hot compression of the as-extruded samples, the load is applied parallel to most of the basal planes. This results in an extension of the c-axis that runs the $\{10\bar{1}2\}$ twinning. In this type of twinning, the basal planes in the twins are reorientated through 86°. It makes the c-axis closely aligned with the compression direction, which is "hard" for the basal slip. Due to the effect of twinning, as the strain increases, continuous plastic deformation leads to a rapid increase in stress.

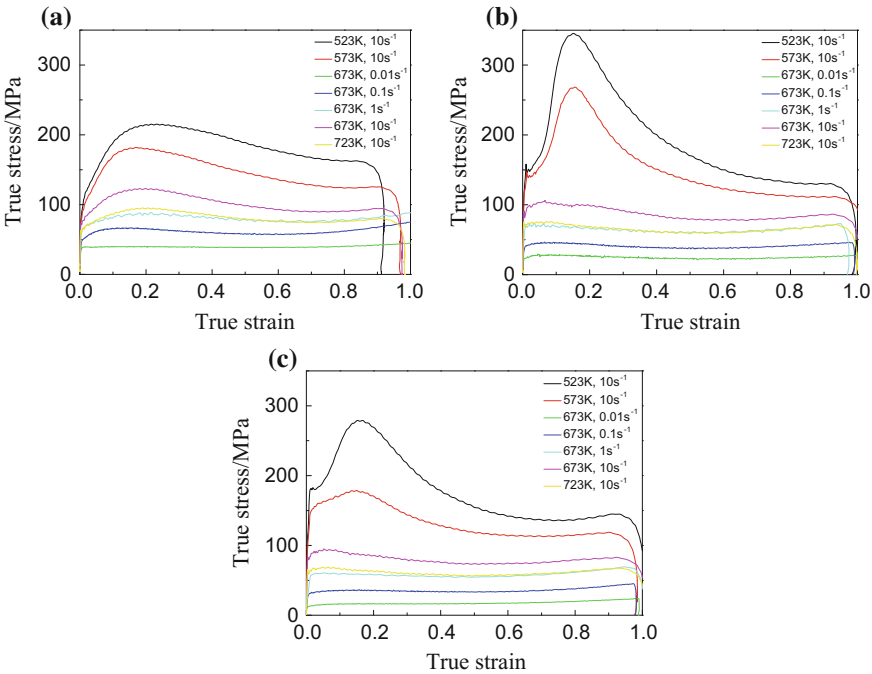

Fig. 2 The flow curves for the compression of **a** as-cast material, **b** E15 and **c** E60

On the other hand, the twining caused more obstacles to the dislocation movement. As the strain rate decreases and the temperature increases (Z decreases), the deformation mechanism changes from twining to slip dominated. It should be noted that DRV and DRX are expected to become more active and therefore are expected to be more softened during the deformation at lower Z values.

The peak flow stress varies between the three starting materials according to the deformation conditions. These differences can be seen in Fig. 4, where the magnitude of the peak flow stress is plotted against the Z parameter.

At lower Z values, the peak flow stress in the deformation of as-cast material is higher than that of as-extruded material. Under the same conditions, the flow curve reaches a steady value at the beginning of the deformation, e.g., at 673 K. As we know, there are many high energy storage regions, i.e., dislocations pile-up and shear bands, around the grain boundary during the deformation, which are prone to stimulate nucleation. Therefore, much more recrystallization nucleation will occur in the materials of finer grain for high temperature deformation. The softening mechanism leads to lower peak flow stresses for as-extruded samples. The development of DRX grains at original grain boundaries can clearly be seen in Fig. 3b, c for as-extruded material deformed at a temperature of 673 K and a strain rate of 1 s^{-1}. Under the same conditions, the microstructure developed in the as-cast material, Fig. 3a, reveals a lower degree of DRX.

At the high values of Z, the peak flow stress in the as-extruded material is larger than that of the as-cast material. This can be explained by the fact that a finer as-extruded sample will exhibit higher strength at lower deformation temperatures and/or higher strain rates. The higher peak flow stress of as-extruded material may be due to the combination of fine grain size and the strong initial texture, which facilitates the operation of $\{10\bar{1}2\}$ twinning. As mentioned above, at the higher Z value, although some twinning is expected to be active in the as-cast material, more twinning will be generated in the as-extruded material, and thus the enhancement effect of the flow stress is more significant.

To describe the present data set, a power law of the form shown below was fitted to the data.

$$\sigma = aZ^m \tag{1}$$

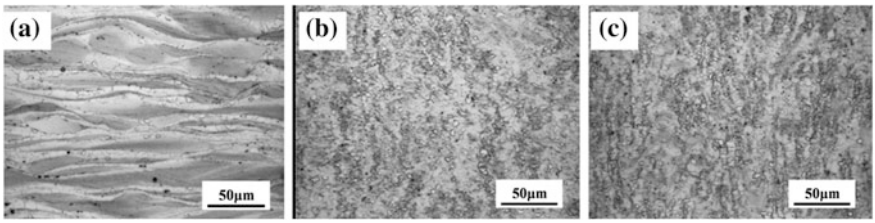

Fig. 3 Microstructures of **a** as-cast material, **b** E15 and **c** E60 deformedat a temperature of 673 K and a strain rate of 1 s^{-1}

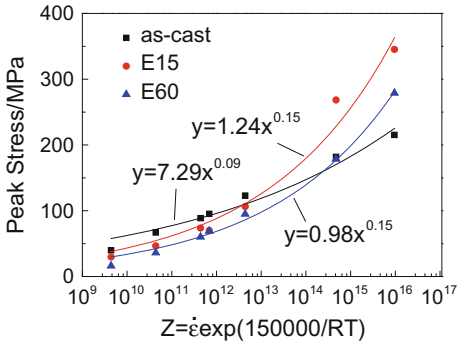

Fig. 4 Influence of the Z parameter on the peak flow stress for the hot deformation of ZK60 Mg alloy

where A the constant, m the average rate sensitivity, Q is the self-diffusion activation energy (150 kJ/mol) [13]. For the as-cast material, the mean value of the rate sensitivity, m, was found to be 0.09. This value was higher for the two as-extruded materials, being 0.15 for both of them, interestingly (Fig. 4). This is because that the as-extruded materials contained fine equiaxed grains, and the equiaxed grains sizes are almost the same. The effect of fine equiaxed grains on recrystallization and twinning may play a major role in the hot compression tests relative to the coarse deformed grains. The deformation mechanism should be further studied by EBSD method.

Summary

The hot working flow stress was examined for as-extruded and as-cast ZK 60 Mg alloy, by uniaxial compression. It has been found that the hot deformation behavior is related to the deformation conditions and initial microstructure.

(1) The shape of the stress-strain curve changes significantly with the decrease of the Z value and the decrease of the grain size of the sample.
(2) The peak flow stresses for the as-cast and as-extruded samples shows different Z dependencies such that the peak stresses decreased in relative magnitude as the temperature is increased. However, the correlations between the as-extruded materials with different initial microstructures and Z parameters are almost the same.

Acknowledgements This work was supported by "The National Key Research and Development Program of China" (No. 2017YFB0103904, 2016YFB0301105), Shandong Provincial Natural Science Foundation, China (No. ZR2015EQ 019).

References

1. R. Armstrong, I. Codd, R.M. Douthwaite, N.J. Petch, The plastic deformation of polycrystalline aggregates. Philos. Mag. A **73**, 45–58 (1962)
2. D.L. Yin, K.F. Zhang, G.F. Wang, W.B. Han, Warm deformation behavior of hot-rolled AZ31 Mg alloy. Mater. Sci. Eng., A **392**, 320–325 (2005)
3. R. Panicker, A.H. Chokshi, R.K. Mishra, R. Verma, P.E. Krajewski, Microstructural evolution and grain boundary sliding in a superplastic magnesium AZ31 alloy. Acta Mater. **57**, 3683–3693 (2009)
4. S. Abdessameud, H. Azzeddine, B. Alili, D. Bradai, Grain growth in AZ31 alloy after uniaxial compression. Trans. Nonferrous Met. Soc. China **20**, 2215–2222 (2010)
5. U.F. Kocks, H. Mecking, Physics and phenomenology of strain hardening: the FCC case. Prog. Mater Sci. **48**, 171–273 (2003)
6. T. Al-Samman, X. Li, S.G. Chowdhury, Orientation dependent slip and twinning during compression and tension of strongly textured magnesium AZ31 alloy. Mater. Sci. Eng., A **527**, 3450–3463 (2010)
7. S.W. Xu, S. Kamado, T. Honma, Effect of homogenization on microstructures and mechanical properties of hot compressed Mg–9Al–1Zn alloy. Mater. Sci. Eng., A **528**, 2385–2393 (2011)
8. A.G. Beer, M.R. Barnett, Influence of initial microstructure on the hot working flow stress of Mg–3Al–1Zn. Mater. Sci. Eng., A **423**, 292–299 (2006)
9. H.Y. Wu, J.C. Yang, J.H. Liao, F.J. Zhu, Dynamic behavior of extruded AZ61 Mg alloy during hot compression. Mater. Sci. Eng., A **535**, 68–75 (2012)
10. J.Q. Li, J. Liu, Z. Cui, Characterization of hot deformation behavior of extruded ZK60 magnesium alloy using 3D processing maps. Mate. Des. **56**, 889–897 (2014)
11. H. Somekawa, H. Hosokawa, H. Watanabe, K. Higashi, Diffusion bonding in superplastic magnesium alloys. Mater. Sci. Eng., A **339**, 328–333 (2003)
12. M.R. Barnett, Z. Keshavarz, A.G. Beer, D. Atwell, Influence of grain size on the compressive deformation of wrought Mg–3Al–1Zn. Acta Mater. **52**, 5093–5103 (2004)
13. Y. Qin, Q. Pan, Y. He, W. Li, X. Liu, X. Fan, Hot compression behavior of ZK60 magnesium alloy. Mater. Sci. Technol. **18**, 712–718 (2010)

Effects of Post-welded Heat Treated on the AZ31B Magnesium Alloy Joint Welded by Automatic TIG Welding

Hongtao Liu, Wenyi Cheng, Ruochao Wang, Jixue Zhou, Yanfei Chen, Jinwei Wang and Yuansheng Yang

Abstract The automatic TIG welding on AZ31B alloys was carried out by the six-axis robot in the present work. After post-welded heat treatment (PWHT), the microstructure, precipitates, and mechanical properties of the AZ31B joints were investigated by using the optical microscope (OM), scanning electron microscopy (SEM), energy-dispersive X-ray spectroscopy (EDS), and X-ray diffraction (XRD). The experimental results reveal that after PWHT, the microstructure and mechanical properties of the AZ31B joints were both significantly improved. After PWHT, the grains of the AZ31B joint were still fine, whereas the number of the precipitates along with the grain boundaries was dramatically decreased. The ultimate tensile

H. Liu (✉) · J. Zhou · J. Wang
Shandong Key Laboratory for High Strength Lightweight Metallic Materials, Advanced Materials Institute, Shandong Academy of Sciences, Jinan 250014, China
e-mail: Hongtaoliu@sdas.org

J. Zhou
e-mail: zhoujx@sdas.org

J. Wang
e-mail: mabch@sdas.org

W. Cheng
Shandong Urban Construction Vocational College, Jinan 250103, China
e-mail: chengwy9886@sina.com

R. Wang
Shandong Institute of Commerce and Technology, Jinan 250103, China
e-mail: 243820144@163.com

Y. Chen
Shandong Engineering Research Center for Lightweight Automobiles Magnesium Alloys, Advanced Materials Institute, Shandong Academy of Sciences, Jinan 250014, China
e-mail: chenyf@sdas.org

Y. Yang
Institute of Metal Research, Chinese Academy of Sciences, Shenyang 110016, China
e-mail: ysyang@sdas.org

© Springer Nature Singapore Pte Ltd. 2018

Y. Han (ed.), *Advances in Materials Processing*, Lecture Notes in Mechanical Engineering, https://doi.org/10.1007/978-981-13-0107-0_18

strength (UTS) and the elongation (EL) of the PWHT AZ31B joints were up to the 100 and 96.9% of the base metal (BM), respectively.

Keywords Automatic TIG welding · AZ31B magnesium alloy
Post-welded heat treated (PWHT) · Microstructure · β-$Mg_{17}Al_{12}$ precipitates
Mechanical properties

Introduction

Owing to the high specific properties, magnesium alloys have the potential to replace steel and aluminum in many areas such as automotive, aerospace, and ship industries [1–3]. The effective welding technology would be inevitable to promote the applications of Mg alloys. To improve the welding quality of Mg alloys, a large number of welding methods have been investigated, such as tungsten-inert gas (TIG) welding [4], laser beam welding (LBW) [5], laser-arc hybrid welding [6], and friction stir welding (FSW) [7].

Among these welding methods, TIG welding is widely used in Mg alloys, because of the good weld appearance, and the advantages of economy and utility [4, 8]. Because the automatic welding technology is more precise and reliable, it is more suitable in large-scale industrial manufacture. Whereas, some welding defects, including oxide film, coarse grains, crack, and porosity are unavoidable during TIG welding. Sun et al. [9] investigated the TIG, CO2, and pulsed Nd:YAG laser welded AZ31 joins and indicated that TIG welding can be adopted to weld AZ31 alloys, but noted that coarser grain sizes in TIG welds would decrease the mechanical properties. In addition to coarse grain, the β-$Mg_{17}Al_{12}$ precipitate particles also greatly influence the strength and fracture behavior of the TIG welded Mg alloy joints [10].

The appropriate post-weld heat treatment (PWHT) process is an effective approach to improve the microstructure and mechanical properties of the Mg joints [11]. However, limited studies have been reported to determine the effects of PWHT on the Mg alloy joints. Therefore, in the present work the automatic TIG welding on AZ31B Mg alloys was conducted by the argon arc welding torch installed on a six-axis robot. And then the post-weld heat treated (PWHT) process of the AZ31 alloy join was performed to improve the welding quality. The effects of the PWHT on the microstructure, precipitates, and mechanical properties of the AZ31B joints were investigated.

Experimental Procedures

The base metal (BM) for automatic TIG welding in the present work was 2.6-mm-thick commercial AZ31B Mg alloy hot-rolled sheets, which chemical composition is shown in Table 1. Before automatic TIG welding, the AZ31B Mg

Table 1 The chemical composition of the AZ31B sheet (wt%)

Al	Zn	Mn	Fe	Si	Mg
3.11	1.03	0.33	<0.003	<0.017	Balance

alloy sheets were mechanically ground by SiC paper to remove the surface oxides, and then cleaned using acetone to eliminate surface contaminations. The butt welding of AZ31B alloys was conducted using an argon arc welding torch installed on the six-axis robot. The robot reproducible tolerance of the programmed position is ±0.2 mm. The automatic TIG welding parameters were as follows: 20 V welding voltage, 150 A welding current, 650 mm/min welding speed. Simultaneously, the argon shielding gas was used to protect the top surface at 15 L/min and the bottom surface at 20 L/min during the welding process.

The AZ31B joint was post-welded heat treated (PWHT) at 350 °C for 1 h. The tensile tests were conducted perpendicular to the welding direction to determine the tensile properties of the welded joints. The microstructure of the untreated and PWHT specimens was characterized by optical microscopy (OM) and scanning electron microscopy (SEM). Energy dispersive spectroscopy (EDS) and X-ray diffraction (XRD) were employed to analyze the precipitates in the welded joint. For SEM and OM observations, the specimens were polished with 200, 600, 1000, and 2000 abrasive SiC papers and etched with a corrosive solution (4.2 g picric acid, 70 mL ethanol, 10 mL glacial acetic, and 10 mL deionized water). The XRD was carried out using CuK radiation at 45 kV and 40 mA. The diffraction angle varied from 20° to 90° with a step size of 0.2°.

Results and Discussion

The microstructure of the untreated and PWHT AZ31B welds are shown in Fig. 1. As shown in Fig. 1a, d, the microstructure of untreated and PWHT AZ31B welds could divide into three zones with different microstructural features including base metal (BM), heat affected zone (HAZ) near the fusion boundary, and the fusion zone (FZ). No obvious welding defects including cracks and pores were observed in the BM, HAZ and FZ. From Fig. 1a–c, it is can be seen that relative fine equiaxed grains were observed in the FZ. And a large number of black particles were distributed both within the grains and along the grain boundaries (GBs) in the HAZ and FZ of the untreated AZ31 alloy specimen. After PWHT, the obvious changes in grain size of BM (from 200 to 500 μm) and FZ (from 25 to 50 μm) were detected (Fig. 1d–f). And also, after heat treated, the volume fraction of the precipitate phase particles in the FZ decreased dramatically from 21.8 to 0.8%. Only very fine particles in the grains were retained, which is shown in Fig. 1f.

As illustrated in Fig. 2, the EDS and XRD were employed to analyze the precipitate phase particles in welded joints. In Fig. 2a, b, the EDS analysis revealed that the particles were divorced eutectic β-$Mg_{17}Al_{12}$ precipitates in Mg alloy joints.

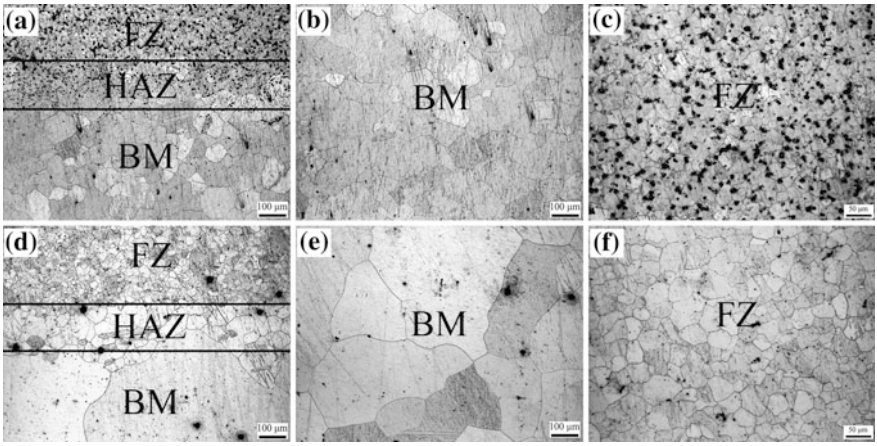

Fig. 1 Typical microstructure of the untreated and PWHT AZ31 joints: **a** transition zone of the untreated AZ31 joint; **b** base metal (BM) of the untreated AZ31 joint; **c** fusion zone (FZ) of the untreated AZ31 joint; **d** transition zone of the PWHT AZ31 joint; **e** BM of the PWHT AZ31 joint; **f** FZ of the PWHT AZ31 joint

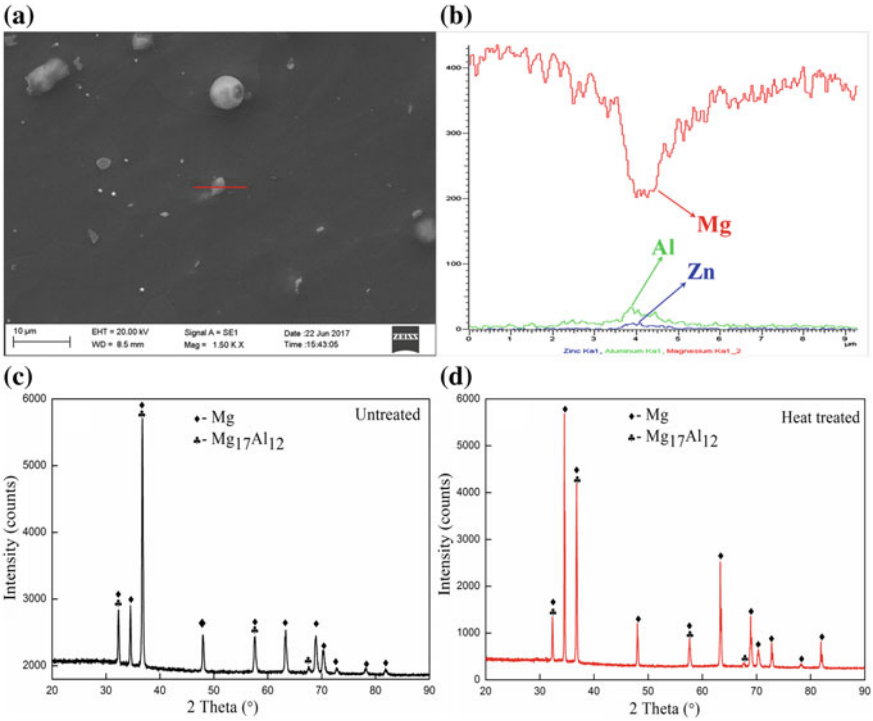

Fig. 2 **a** SEM image of the white particle in the fusion zone (FZ); **b** result of EDS line scan across a particle in **a**; **c** XRD pattern from the FZ of the untreated AZ31 joint; **d** XRD pattern from the FZ of the PWHT AZ31 joint

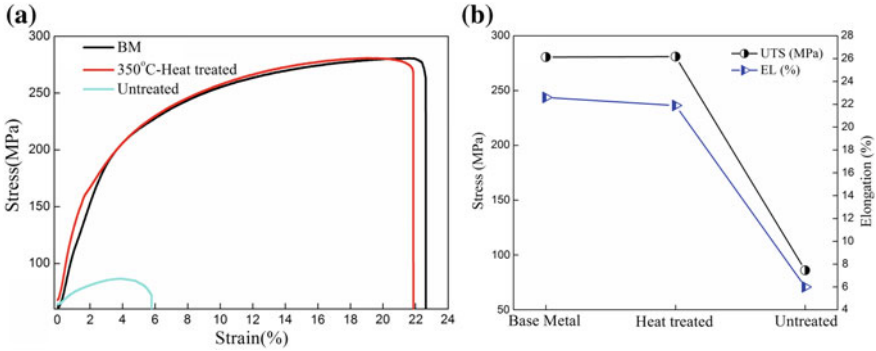

Fig. 3 Mechanical properties of the BM, treated, and PWHT tensile specimens: **a** stress-strain cures; **b** varied curves of the ultimate tensile strength (UTS) and the elongation (EL)

And also, the XRD patterns in Fig. 2c, d further confirmed the appearance of the β-$Mg_{17}Al_{12}$ precipitate phase in the FZ of the untreated and PWHT AZ31 alloys joints. Similarly, β-$Mg_{17}Al_{12}$ precipitates were also observed in other fusion welding processes such as electron beam welding [12], resistance spot-welding [10], and laser-arc hybrid welding [13]. According to the Mg-Al equilibrium phase diagram [14], the eutectic reaction L $\rightarrow$ α-Mg + β-$Mg_{17}Al_{12}$ could occur at the melting temperature ($\sim$450 °C). Because of the high cooling rate of the welding pool, which was caused by the high thermal conductivity of the AZ31 alloys, the non-equilibrium solidification process during automatic TIG welding process occurred and induced the occurrence of the divorced eutectic structure β-$Mg_{17}Al_{12}$ particles.

Figure 3 shows the typical stress-strain curves and varied curves of the ultimate tensile strength (UTS) and the elongation (EL) of the BM, treated, and PWHT tensile specimens. It is revealed that the UTS and the EL of the untreated AZ31 joins were only about 83 MPa and 5.8%, respectively. After PWHT, the UTS and the EL of the AZ31 joins were nearly up to 100 and 96.9% of the BM, respectively. As described in the Fig. 1, after PWHT, the number of the β-$Mg_{17}Al_{12}$ precipitates, especially the coarse β-$Mg_{17}Al_{12}$ precipitates distributed along grain boundaries (GBs), decreased dramatically. Meanwhile, many very fine β-$Mg_{17}Al_{12}$ precipitates in grains appeared. Niknejad et al. [10] have been reported that the coarse β-$Mg_{17}Al_{12}$ intermetallic compound along GBs of the welded joint greatly reduced the ductility and the fracture toughness of the Mg-Al alloys. And the fine intra-granular precipitation on the hexagonal-close packed α-Mg matrix could increase the strength and elongation of the AZ31B alloy joint [15]. Therefore, after PWHT, owing to the variation of the β-$Mg_{17}Al_{12}$ precipitates, the UTS and the EL of the AZ31B alloy joints is significantly increased.

Conclusion

AZ31B Mg alloy has been joined by using automatic TIG welding in the present work, and then the PWHT on the AZ31B alloy joint was performed. Before and after PWHT, the microstructure, the precipitates, and the mechanical properties of the AZ31B joints have been investigated. During automatic TIG welding, owing to the non-equilibrium solidification process, many β-$Mg_{17}Al_{12}$ precipitates are observed in the AZ31B alloy joint. After PWHT, the grains of the AZ31B joints are still fine, whereas the number of the precipitates along with the GBs dramatically decrease. The UTS and the EL of the PWHT AZ31B joint are nearly up to the 100 and 96.9% of the BM, respectively.

Acknowledgements This work is supported by the National Key Research and Development plan of China (Grant No. 2017YFB0103904, 2016YFB0301105), the Shandong Province Key Research and Development Plan, China (Grant No. 2017CXGC0404, 2016ZDJS02A09), and the Youth Foundation of Shandong Academy of Sciences, China (Grant No. 2016QN015).

References

1. T.M. Pollock, Weight loss with magnesium alloys. Science **328**, 986–987 (2010)
2. M.K. Kulekci, Magnesium and its alloys applications in automotive industry. Int. J. Adv. Manuf. Technol. **39**, 851–865 (2008)
3. H. Hu, A. Yu, N. Li, J.E. Allison, Potential magnesium alloys for high temperature die cast automotive applications: a review. Mater. Manuf. Processes **18**, 687–717 (2003)
4. H.T. Liu, J.X. Zhou, D.Q. Zhao, Y.T. Liu, J.H. Wu, Y.S. Yang, B.C. Ma, H.H. Zhuang, Characteristics of AZ31 Mg alloy joint using automatic TIG welding. Int. J. Miner. Metall. Mater. **24**, 102–108 (2017)
5. H.T. Liu, R.C. Wang, Q. Liu, J.X. Zhou, Y.F. Chen, B.C. Ma, Y.S. Yang, Microstructure characterization of AZ31B Mg Alloy Welds Processed by Nd:YAG Laser Welding. Mater. Sci. Forum **898**, 1051–1055 (2017)
6. M. Gao, S. Mei, Z. Wang, X. Li, X. Zeng, Process and joint characterizations of laser-MIG hybrid welding of AZ31 magnesium alloy. J. Mater. Process. Technol. **212**, 1338–1346 (2012)
7. S. Mironov, T. Onuma, Y.S. Sato, H. Kokawa, Microstructure evolution during friction-stir welding of AZ31 magnesium alloy. Acta Mater. **100**, 301–312 (2015)
8. K.N. Braszczyńska-Malik, M. Mróz, Gas-tungsten arc welding of AZ91 magnesium alloy. J. Alloys Compd. **509**, 9951–9958 (2011)
9. Z. Sun, D. Pan, J. Wei, Comparative evaluation of tungsten inert gas and laser welding of AZ31 magnesium alloy. Sci. Technol. Weld. Joining **7**, 343–351 (2002)
10. S. Niknejad, L. Liu, T. Nguyen, M.-Y. Lee, S. Esmaeili, N. Zhou, Effects of Heat Treatment on Grain-Boundary β-Mg17Al12 and Fracture Properties of Resistance Spot-Welded AZ80 Mg Alloy. Metall. Mater. Trans. A **44**, 3747–3756 (2013)
11. G. Wang, Z. Yan, H. Zhang, X. Zhang, F. Liu, X. Wang, Y. Su, Improved properties of friction stir-welded AZ31 magnesium alloy by post-weld heat treatment. Mate. Sci. Technol. **33**, 854–863 (2017)
12. S.H. Wu, J.C. Huang, Y.N. Wang, Evolution of microstructure and texture in Mg-Al-Zn alloys during electron-beam and gas tungsten arc welding. Metall. Mater. Trans. A **35**, 2455–2469 (2004)

13. M. Gao, H.G. Tang, X.F. Chen, X.Y. Zeng, High power fiber laser arc hybrid welding of AZ31B magnesium alloy. Mater. Des. **42**, 46–54 (2012)
14. T. Zhu, Z.W. Chen, W. Gao, Microstructure formation in partially melted zone during gas tungsten arc welding of AZ91 Mg cast alloy. Mater. Charact. **59**, 1550–1558 (2008)
15. S. Celotto, TEM study of continuous precipitation in Mg-9 wt%Al-1 wt%Zn alloy. Acta Mater. **48**, 1775–1787 (2000)

High Temperature Hot Deformation Behavior and Constitutive Model Construction of High Quality 51CrV4 Spring Steel

ZhiGang Wang, FeiMing Xie, ChaoBin Lai, HongWei Li, Qing Zhang and Diqiang Luo

Abstract In order to investigate the hot deformation behavior of alloy 51CrV4, the single pass compression experiments were carried out in deformation temperature range of 800–1120 °C and strain rate range of 0.01–10 s^{-1}. And the deformation amount of all the samples was 50%. The results showed that the steady flow behavior was observed at deformation with low temperature and high strain rate, where the dynamic recovery mechanism was dominated. Meanwhile, the formation of dislocation cell structures and polygonal characteristics further supported the mechanism of dynamic recovery. The dynamic recrystallization (DRX) phenomenon of alloy occurred with the increase of strain. With the increase of deformation temperature and decrease of strain rate, the peak stress gradually decreased due to DRX. Finally, the hot deformation constitutive equation was established and the thermal deformation activation energy was calculated as 367.87 kJ/mol.

Keywords 51CrV4 spring steel · Dynamic recrystallization · Constitutive equation · Activation energy

Z. Wang (✉) · F. Xie · H. Li · Q. Zhang
Fangda Special Steel Technology Stock Co, Ltd., Nanchang 330012, China
e-mail: wzgang2008cn@163.com

F. Xie
e-mail: bxiefeiming@163.com

H. Li
e-mail: hongweili2003@163.com

Q. Zhang
e-mail: zhangqing1964@sina.com

Z. Wang · C. Lai · D. Luo
School of Material Science and Engineering, Jiangxi University of Science and Technology, Ganzhou 341000, China
e-mail: lcb5115@126.com

D. Luo
e-mail: luodiqiang92@126.com

© Springer Nature Singapore Pte Ltd. 2018

Y. Han (ed.), *Advances in Materials Processing*, Lecture Notes in Mechanical Engineering, https://doi.org/10.1007/978-981-13-0107-0_19

Introduction

To multi-microalloying design is the future trend of advance high strength spring steel. 51CrV4 spring steel is widely application and deeply researched due to its excellent comprehensive performance including a higher strength, better anti-surface decarburization, impact resistance and anti-fatigue [1]. Numerous researches of hot deformation behaviors have been reported on TC18 titanium alloy [2], GH4698 superalloy [3] and Cr–Ni–Mo alloyed steels [4]. Based on Arrhenius equation, the relationship between true stress and true strain is described and a reliable mechanical constitutive model is obtained, which is a relatively mature approach to study hot deformation behavior.

Dynamic softening and work hardening occur simultaneously during high temperature hot deformation, which involves the movement of dislocations and the migration of grain boundaries. Wei [5] considers that high-carbon vanadium steel is less prone to dynamic recrystallization at low temperature deformation stage. In this paper, the effect of deformation parameters on the dynamic recovery and recrystallization of alloy 51CrV4 was analyzed by TEM observation and stress-strain curves. Meanwhile, the constitutive equation and activation energy will be established, which provided the theoretical basis for the optimization of controlled rolling process.

Experimental Procedures

The chemical composition (wt%) of alloy is shown in Table 1. The size of compression sample is φ10 mm × 15 mm. In order to reduce the influence of friction on the stress state, two pieces of graphite carbon were coated to the both ends of sample, and then a single compression test was conducted on Gleeble3800 thermo-simulator. First of all, the sample was heated to 1150 °C at the rate of 20 °C/S and preserved 60 s for austenitizing. The compression parameters were as follows: the deformation temperatures were 1000, 950, 900, 850, 800 °C respectively; Deformation rates were 0.01, 0.1, 1–10 s^{-1} respectively; The compression reduction was 50%, with the true strain was 0.69. The specimen after each compression was immediately quenched by the cold water.

The sub-structure of the specimen was observed by FEI Tecnai G2 transmission electron microscope (TEM). The sample was sprayed with electrolytic double spray, and the electrolyte was 50% perchlorate alcohol solution. The electrochemical polishing temperature was −30 to −20 °C, the voltage was 50 V, and the current was 25 mA.

Table 1 Chemical composition of 51CrV4 spring steel (wt%)

C	Si	Mn	P	S	Ni	Cr	V
0.48	0.23	0.88	0.016	0.006	0.03	0.98	0.14

Results and Discussion

Stress-Strain Behaviors

The true stress and true strain curves of 51CrV4 spring steel with true strain of 0.69 under the different deformation temperature and deformation rate are shown in Fig. 1. when the strain rate is 0.01 s^{-1}, with the increase of true strain, true stress all present the trend of firstly increasing then reducing at different temperature. Different degrees of recrystallization will occur in 51CrV4 steels. It can be seen from Fig. 1a that the flow stress increases quickly to a peak with the increase of the strain in the initial stage of compression deformation and gradually decreases to some extent as the deformation exceeds the peak strain (0.2). Finally, it enters the stage of steady state, which is simultaneously caused by work hardening and softening in the process of plastic deformation. As shown in Fig. 1b, the deformation behavior is mainly controlled by steady-state rheological characteristics at higher strain rates, especially in the low temperature stage.

With the decrease of deformation rate, the driving force of recrystallization increases. Thus, the rate of dynamic recrystallization accelerates and softening

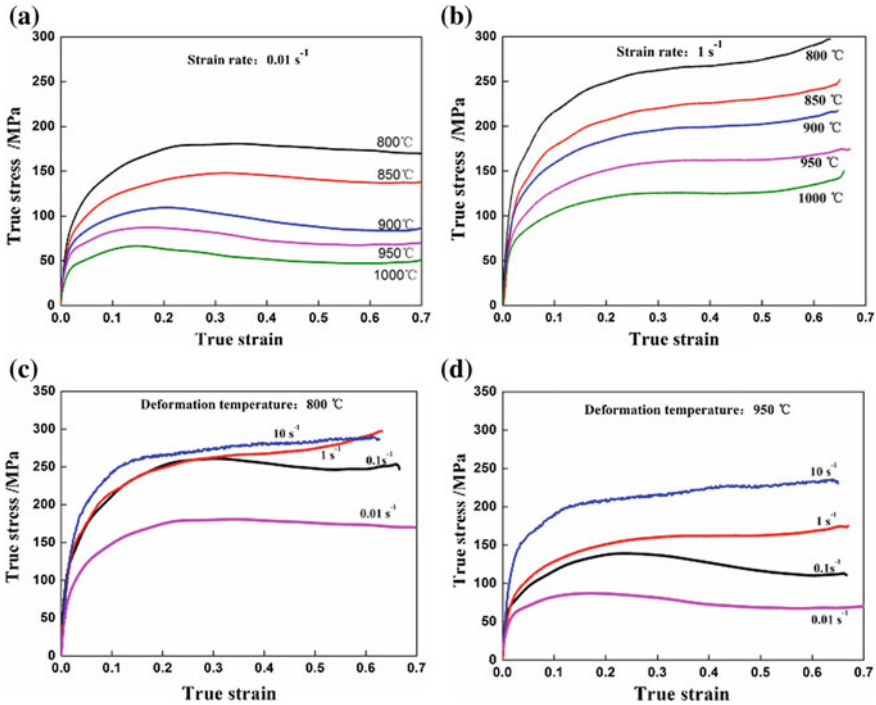

Fig. 1 True stress-true strain curve of 51CrV4 spring steel under different hot deformation conditions. **a** 0.01 s^{-1}; **b** 1 s^{-1}; **c** 800 °C; **d** 950 °C

effect gradually increases shown in Fig. 1c, d. After reaching the peak stress, the softening effect turns to a dominant role, so the flow stress decreases at this moment. Finally, the softening effect of dynamic recrystallization and the work hardening effect tend to dynamic balance.

In order to further study the variation of peak stress or steady stress with deformation temperature, the stress hardening rate ($\theta = d\sigma/d\varepsilon$) was used to indirectly characterized the peak stress (σ_p). As shown in Fig. 2a, the point where the curve intersects the X-axis at the first time characterized as peak stress, and when the work hardening rate achieves to zero, the corresponding stress recognize as the peak stress. Hence, the change rules of σ_p with the increase of deformation temperature under different strain rate presented in Fig. 2b. It can be found that with the increase of temperature, the peak stress gradually decrease from 800 to 1000 °C. At constant deformation temperature, the peak stress continuously increases with the increase of the strain rate. When hot deformation at low temperature and high strain rate, the thermal activation of material is not enough, and the average kinetic energy of atoms reduce and the critical shear stress of crystal slip increase, which increase obstruction of dislocation motion and crystal slip, lead to dynamic recovery and recrystallization are more difficultly to occur. Thus, the work hardening behavior observed and the peak stress increase [6]. When the dislocation accumulates to a certain extent, there has sufficient time and activation energy making dislocation density of dislocations decrease and the effect of work hardening to be offset. Moreover, dynamic recovery and recrystallization are more likely to occur, which lend to the peak stress increase.

Figure 3 shows the substructure of the sample at deformation conditions of 800 °C and 1 s^{-1}. It can be seen from Fig. 3a, the dislocation pile up seriously near the grain boundary, and the dislocation cells formation inside of material as shown in Fig. 3b. It is note that when deformation occurs in this low temperature, the several characteristics of dynamic recovery can be found. Polyganization is a typical feature of dynamic recovery due to movement of dislocation, and the final result of polyganization is the formation of sub-grains [7]. As shown in Fig. 3c, the arrangement of

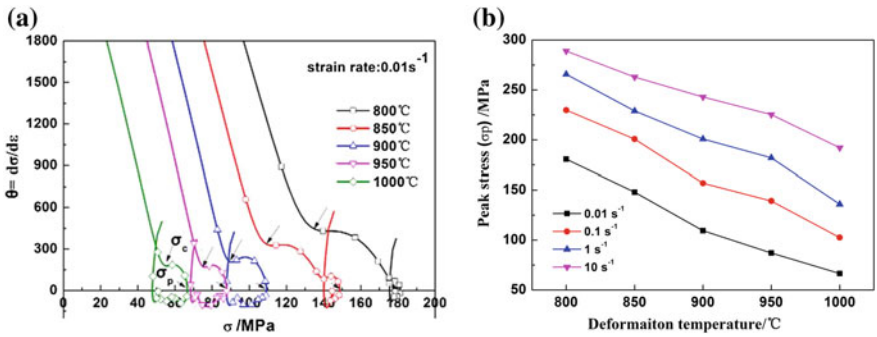

Fig. 2 **a** Change curve of strain hardening rate with true stress; **b** the change curve of peak stress with deformation temperature

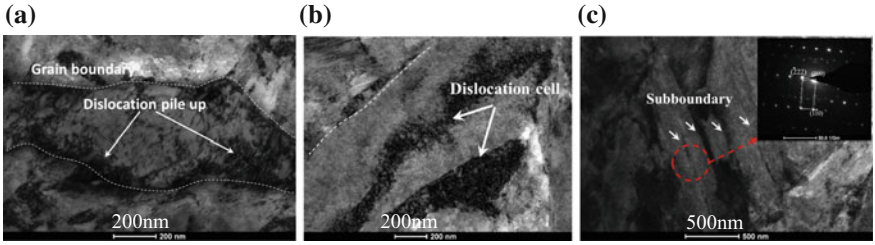

Fig. 3 TEM observation results of 51CrV4 steel at deformation temperature of 800 °C, strain rate of 0.01 s^{-1}. **a** Dislocation pile up; **b** dislocation cell; **c** polyganization and diffraction pattern (red circle position)

dislocation changes from horizontal to vertical through sliding, climbing, and cross-sliding, making the formation of dislocation wall (white arrow). The crystal is separated by dislocation wall to form many sub-grains. The diffraction pattern calibration results of Fig. 3c show the misordinations between sub-grains about 9°. This result indicates that polyganization actually happening in 51CrV4 steel during the low temperature deformation, and further proved that the dynamic recovery is the main deformation mechanism.

Thermal Deformation Activation Energy and Constitutive Equation

In this paper, considering the dynamic recrystallization is the main mechanism when deformation at high temperature and low strain rate, and the steady flow behavior was appeared to at low temperature and high strain rate. Therefore, the flow stress variation can be exactly described by means of peak stress and steady stress. High temperature deformation of steel is a thermally activated process. The impacts of deformation temperature and strain rate on the flow stress at high and low stress levels are complied with Arrhenius equation (Eq. 1) containing the activation energy Q. As shown in Fig. 1c, d, the deformation mechanism make obviously different under the different conditions. Thus, the rules obtained by thermal processing of different metal materials indicate that the relationship between flow stress and strain rate can be described by the following models at high and low stress levels:

$$\dot{\varepsilon} = A_1[\sinh(\alpha\sigma_P)]^{n_1}\exp\left(-\frac{Q}{RT}\right) \tag{1}$$

$$\dot{\varepsilon} = A_2\sigma_p^{n_2}\exp\left(-\frac{Q}{RT}\right) \quad \text{(at low stress level)} \tag{2}$$

$$\dot{\varepsilon} = A_3 \exp(\beta\sigma_p) \exp(-\frac{Q}{RT}) \quad \text{(at high stress level)} \tag{3}$$

where σ_p is the peak stress; $\dot{\varepsilon}$ is the strain rate, s^{-1}; Q is thermal deformation activation energy, KJ/mol; R is the integrated gas constant (8.31441 J/mol•K); T is the absolute temperature, K; A1, A2, A3, α, β, n_1 and n_2 are material constants, where $\alpha = \beta/n_2$. When the temperature is constant, and the Q value is assumed to be constant, the first step is taking the logarithm of Eqs. 2 and 3, respectively.

$$\ln\dot{\varepsilon} = \ln A_2 + n_2 \ln\sigma_p - \frac{Q}{RT} \tag{4}$$

$$\ln\dot{\varepsilon} = \ln A_3 + \beta\sigma_p - \frac{Q}{RT} \tag{5}$$

In order to simplify the calculations, take the partial derivative for $\ln\sigma_p$ and σ_p of both sides of Eqs. 4 and 5, respectively. It can be found out $n_2 = \frac{\partial \ln\dot{\varepsilon}}{\partial \ln\sigma_p}$, $\beta = \frac{\partial \ln\dot{\varepsilon}}{\partial \sigma_p}$, and the value can be obtained from $\ln\dot{\varepsilon} - \ln\sigma_p$, $\ln\dot{\varepsilon} - \sigma_p$ curve as shown in Fig. 4a. Hence, the average value of n_2 is 7.417 by calculation from high temperature and low stress level (900–1000 °C). According to relationship $\ln\dot{\varepsilon} - \sigma_p$ showed in Fig. 4b, the average value of β can be obtained as 0.061 when deformation at low temperature and high stress level (800–850 °C). Therefore, α can be calculated as 0.0083. Substitute a value for Eq. (1), and take natural logarithm to both sides of Eq. 1 for obtaining the following Eq. 6. It can be found that $\ln\dot{\varepsilon}$ and $\ln[\sinh(\alpha\sigma_P)]$ are still coincidence linear relation at constant temperature, as showed in Fig. 4c. Therefore, the average value of n_1 can be obtained as 5.852 from the slope of line. When the deformation rate is constant, take the partial derivative for 1/T of the Eq. 6, and obtains the Eq. 7 as follows.

$$\ln\dot{\varepsilon} = \ln A_1 + n_1 \ln[\sinh(\alpha\sigma_p)] - \frac{Q}{RT} \tag{6}$$

$$Q = Rn_1 \frac{\partial \ln\left[\sinh\left(\alpha\sigma_p\right)\right]}{\partial \frac{1}{T}} \tag{7}$$

The Fig. 4d shows the relationship between $\ln[\sinh(\alpha\sigma_P)]$ and 1/T, and there has a linear changes between the two parameters. Thus, the $\frac{\partial \ln\left[\sinh\left(\alpha\sigma_p\right)\right]}{\partial \frac{1}{T}}$ values can be obtained from the slope. And then R and n_1 value was substitute into the Eq. 7, the average activation energy Q = 367.87 kJ/mol of 51CrV4 spring steel from 800 and 1000 °C at different strain rate.

Controlling the heat activation process is a remarkable characteristic for hot deformation. When the activation energy Q does not depend on stress variations, the Zener-Hollomon factor (Z-factor) can be used to describe thermal deformation process. As shown in Eq. 8. Substituting the Q value into Eq. 8, the expression of

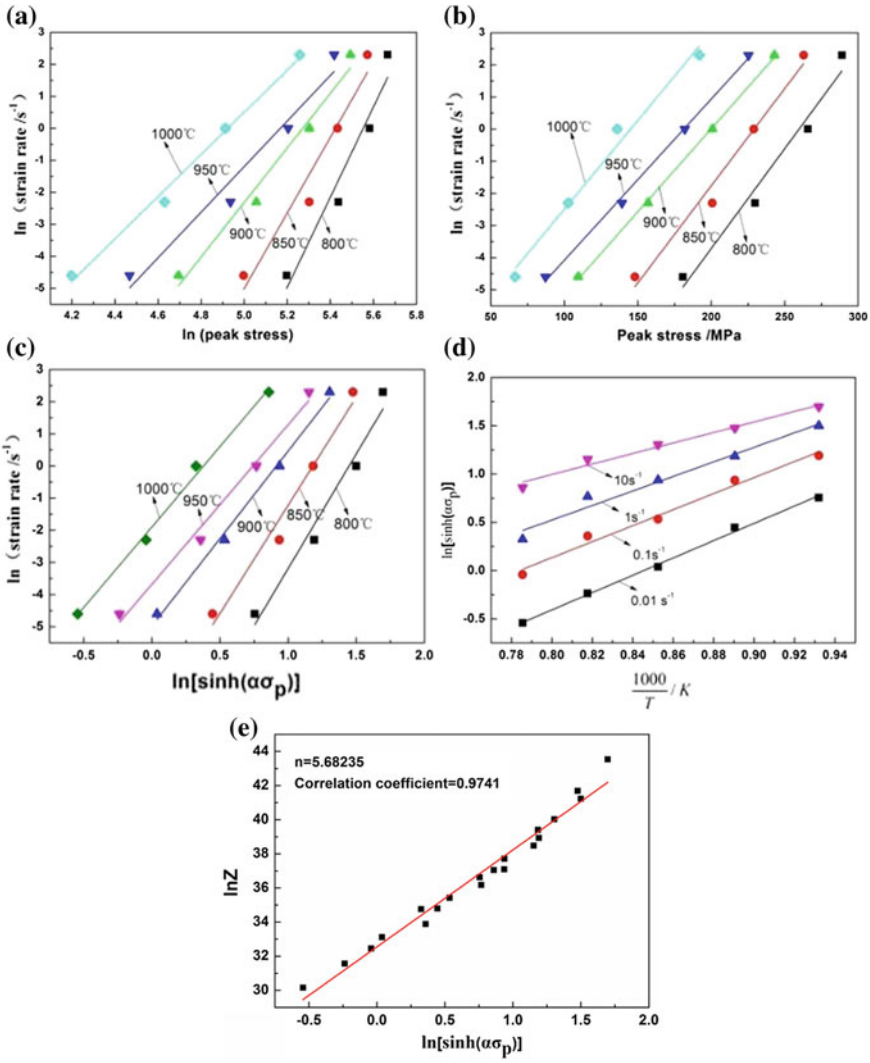

Fig. 4 Parameter fitting **a** $\ln\dot{\varepsilon} - \ln\sigma_p$; **b** $\ln\dot{\varepsilon} - \sigma_p$; **c** $\ln\dot{\varepsilon} - \ln[\sinh(\alpha\sigma_P)]$; **d** $\ln[\sinh(\alpha\sigma_P)] - 1/T$; **e** the lnZ-lnsinh $(\alpha\sigma_p)$ curve

the Z-factor can be obtained in Eq. 9. Combining with Eq. 1 and substituting $\dot{\varepsilon}$ solution into Eq. 8, the relationship between the Z value and σ_p can be obtained as Eq. 10. Take the natural logarithm for both sides of the Eq. 10 getting the Eq. 11. Finally, substituting the $\dot{\varepsilon}$, T and σ_p into Eqs. 10 and 11, and drawing the lnZ-lnsinh $(\alpha\sigma_p)$ curve as shown in Fig. 4e. According to linear regression, it was found that the correlation coefficient is 0.9741, which further proved that the hot deformation

behaviors can be described by this constitutive equation. Meanwhile, the value of n_1 and A_l can be calculated as 5.68235 and 1.366 × 1014, respectively.

$$Z = \dot{\varepsilon}\exp\left(\frac{Q}{RT}\right) \tag{8}$$

$$Z = \dot{\varepsilon}\exp\left(\frac{44245}{T}\right) \tag{9}$$

$$Z = A_1\left[\sinh\left(\alpha\sigma_p\right)\right]^{n_1} \tag{10}$$

$$\ln Z = \ln A_1 + n_1 \ln\sinh\left(\alpha\sigma_p\right) \tag{11}$$

The hot deformation constitutive equation can be determined after substituting A_1, n_1, Q, α into Eq. 1, as shown in Eq. 12. According to the Eq. 10, σ_p can be expressed as a Z-factor function, and then according to the definition of the inverse function of hyperbolic sine function, the constitutive equation can also expressed by Z-factor Z as shown in Eq. 13.

$$\dot{\varepsilon} = 1.366 \times 10^{14} \times \left[\sinh\left(0.0083\sigma_p\right)\right]^{5.682}\exp\left(\frac{-367870}{8.314T}\right) \tag{12}$$

$$\sigma_p = 12.048\ln\left\{\left(\frac{Z}{1.366 \times 10^{14}}\right)^{\frac{1}{5.682}} + \left[\left(\frac{Z}{1.366 \times 10^{14}}\right)^{\frac{2}{5.682}} + 1\right]^{\frac{1}{2}}\right\} \tag{13}$$

Summary

(1) The deformation temperature and deformation rate have a significant influence on the thermal deformation behavior of 51CrV4 spring steel. With the decrease of deformation temperature and increase of deformation rate, the peak stress gradually increases due to dynamic recrystallization.
(2) The dynamic recovery was observed during deformation with low temperature and high strain rate, and the dynamic recrystallization of alloy occurs with the increase of deformation temperature and decrease of strain rate.
(3) The average thermal deformation activation energy of 51CrV4 spring steel is 367.87 kJ/mol, the relationship between the flow stress, the strain rate and the temperature can be described by the constitutive equation of the hyperbolic sine function:

$$\dot{\varepsilon} = 1.366 \times 10^{14} \times \left[\sinh\left(0.0083\sigma_p\right)\right]^{5.682} \exp\left(\frac{-367870}{8.314T}\right)$$

Acknowledgements This work was financially supported by china postdoctoral science foundation (No. 2016M592101).

References

1. C.S. Lee, K.A. Lee, D.M. Li, Mater. Sci. Eng., A **241**, 30–37 (1998)
2. Y.Q. Ning, X. Luo, H.Q. Liang et al., Mater. Sci. Eng., A **635**, 77–85 (2015)
3. P. Zhang, C. Hu, Q. Zhu et al., Mater. Des. **65**, 1153–1160 (2015)
4. C. Zhang, L.W. Zhang, W.F. Shen, Mater. Des. **90**, 804–814 (2016)
5. H. Wei, G. Liu, H.T. Zhao, Mater. Sci. Eng., A **596**, 112–120 (2014)
6. H. Mirzadeh, Mech. Mater. **85**, 66–79 (2015)
7. S. Saadatkia, H. Mirzadeh, J. Cabrera, Mater. Sci. Eng., A **636**, 196–202 (2015)

Effect of Process Parameters on the Interface Microstructure and Thickness of Silver Cladding Copper Wires Prepared by Core-Cladding Continuous Casting

Feng Yi, Xuefeng Liu and Yue Pan

Abstract Liquid silver and solid copper with diameter of 8 mm were used as raw materials, and the silver cladding copper (SCC) wires with a diameter of 10 mm were prepared by the self-developed core-cladding continues casting (CCC) method at the silver casting temperature of 1000–1100 °C, casting speed of 30 –90 mm min^{-1}, cooling water temperature of 20 °C and cooling water flow of 300 L h^{-1}. The microstructure and morphology, distribution of chemical components, and phase composition of the interface between Ag and Cu were characterized by optical microscope (OM), field emission scanning electron microscope (FESEM), and energy dispersive spectrometer (EDS). The effect of the silver casting temperature and casting speed on the interface microstructure and thickness of silver cladding copper wires and formation mechanism of the interface were investigated. The results showed that the interface microstructure which from the surface to the Cu core of the silver cladding copper wire was Ag (Cu) solid solution, hypoeutectic, eutectic and Cu (Ag) solid solution when the silver casting temperature was 1050 °C and casting speed was 30–60 mm min^{-1}. And the interface microstructure which from the surface to the Cu core of the silver cladding copper wire was Ag (Cu) solid solution, eutectic and Cu (Ag) solid solution when the casting speed increase to 90 mm min^{-1} and the silver casting temperature was 1000–1050 °C. The interface microstructure which from the surface to the Cu core of the silver cladding copper wire is all hypereutectic, when the silver casting temperature was

The original version of this chapter was revised: Incorrect temperature ranges have been corrected. The erratum to this chapter is available at https://doi.org/10.1007/978-981-13-0107-0_124

F. Yi · X. Liu (✉) · Y. Pan
School of Materials Science and Engineering, University of Science and Technology Beijing, Beijing 100083, China
e-mail: liuxuefengbj@163.com

X. Liu
Beijing Laboratory of Metallic Materials and Processing for Modern Transportation, University of Science and Technology Beijing, Beijing 100083, China

© Springer Nature Singapore Pte Ltd. 2018

Y. Han (ed.), *Advances in Materials Processing*, Lecture Notes in Mechanical Engineering, https://doi.org/10.1007/978-981-13-0107-0_20

1100 °C, casting speed was 90 mm min^{-1}. With the increase of the casting speed, the thickness of the interface transition layer decreased sharply, the thickness of the hypoeutectic layer and Ag (Cu) solid solution layer decreased, and the eutectic layer thickness increased first and then decreased, but the thickness of Cu (Ag) solid solution remained almost constant. Under the condition of low casting temperature and high casting speed, core-cladding continues casting technology is advantageous to prepare the bimetallic composite material which is prone to eutectic reaction.

Keywords Silver cladding copper wire · Core-cladding continuous casting Process parameters · Interface quality

Introduction

Silver, the metal of the highest electrical conductivity, is used widely in electronic information field, usually in the form of a wire. However, high cost and high density (ρ_{Ag} = 10.49 g/cm^3) restrict its application in price-and/or-weight sensitive fields such as automobile and aerospace industries. Silver cladding copper (SCC) wire provides a promising substitution of silver wire owing to its lowered density and high electrical conductivity comparable with silver for high-frequency current because of skin effect [1, 2].

Nowadays, cyanide plating methods dominate industrial production of SCC wires [3]. However, the solution used for cyanide plating is highly toxic, which severely pollutes environment and endangers workers' health. Moreover, plating methods prepare a low bonded interface, and additives in plating solution easily cause formation of voids and pollute clad layer with impurities. Compared with pure silver, density of plating silver is about 24% lower, while the maximum resistivity can be increased by 700%. In addition, thickness of clad layer is limited due to the stress emerged during electroplating [4, 5].

Liquid-solid composite continuous casting method is a new way for preparing cladding materials which a liquid metal with lower melting temperature cladding another solid metal with higher melting temperature. It is widely used in the development of bimetallic composite materials, for example, Liu et al. [6] invent a core-cladding continuous casting (CCC) method, which is a kind of typical liquid-solid composite casting method. CCC method has an outstanding advantage for preparing bimetallic composite material, and has successfully prepared the copper clad steel wires [7].

However, Ag–Cu has a eutectic reaction at 778.1 °C. Liquid Ag, whose temperature is higher than 960 °C, continuously contacts with solid Cu during a cladding process, and the temperature of their contacting interface will be easily heated over the eutectic temperature. Diffusion of Ag atoms results in rapid saturation of Ag (8 wt%, mass fraction, the same below) in a thin layer under the surface of Cu, which causes dissolving of this layer and thus significantly promotes diffusion of Cu atoms into liquid Ag [8]. Copper dissolves in a very short time, for

example, Li et al. [9] found that solid copper with a thickness of 500 μm could dissolve 80 μm in the liquid of eutectic composition of 800 °C in 2 s. The diffusion coefficient of the dissolved copper atoms in the liquid is several orders of magnitude higher than that of the diffusion coefficient in the solid, and there is a great concentration difference in the liquid. Therefore, cladding a metal with lower melting temperature on another metal with higher melting temperature by continuous casting faces a big challenge when the two metals have a eutectic reaction at high temperature. Therefore, it is necessary to investigate the case that CCC method prepares the bimetallic composites with a eutectic reaction during cladding process at high temperature.

In this paper, liquid silver and solid copper wire with diameter of 8 mm will be used as raw materials, and the SCC wires with a diameter of 10 mm will be prepared by the self-developed core-cladding continues casting (CCC) method. The effect of silver casting temperature and casting speed on the interface microstructure and thickness of SCC wires and the formation mechanism of the interface will be investigated.

Material and Experimental Procedures

Liquid silver and solid copper with diameter of 8 mm were used as raw materials, and the SCC wires with a diameter of 10 mm were prepared by the self-developed CCC method at the silver casting temperature of 1000–1100 °C, casting speed of 30–90 mm min^{-1}, cooling water temperature of 20 °C and cooling water flow of 300 L h^{-1}. The schematic diagram of the preparation method was shown in Fig. 1, through the induction heating of the crucible to melt silver, then starting the pinch rolls to let the copper core move down through the core guide positioning device and the core material protection device, then opening the stopper, the pure liquid silver flow from the flow hole into the cavity, achieving pure liquid silver solidification on the surface of copper wire.

In this paper, process parameters of SCC wires prepared by CCC method as shown in Table 1. Specimens were sectioned normal to the casting direction, which were ground with 800–2000 grit emery papers before mechanically polishing. The silver was etched for 3 s with a reagent consisting of 20 ml aqueous ammonia, 20 ml hydrogen peroxide and 10 ml deionized water. The Cu was etched for 10 s with a reagent consisting of 3.5 g ferric chloride, 25 ml hydrochloric acid and 75 ml deionized water. Interface microstructure was characterized by a Zeiss Axio Scope.A1 optical microscope (OM) and a Zeiss Auriga field emission scanning electron microscopy (FESEM). Distribution of chemical components, and phase composition of the interface between Ag and Cu were characterized by energy dispersive spectrometer (EDS) equipped in the FESEM. Interface thickness was statistically analyzed with the help of Image Tool software. Each specimen was measured 5 times, and taken the average value.

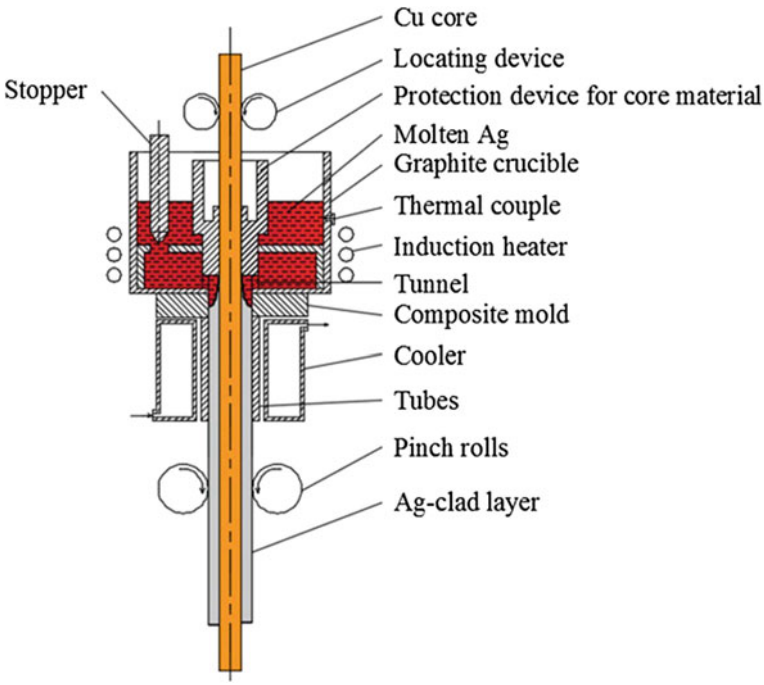

Fig. 1 Schematic diagram of prepared SCC wires using a self-developed CCC method

Table 1 Processing parameters of fabricating SCC wires by CCC method

No.	Ag casting temperature [°C]	Casting speed [mm min^{-1}]	Cooling water temperature [°C]	Cooling water flow [L h^{-1}]
1	1100	90	20	300
2	1050	30	20	300
3	1050	60	20	300
4	1050	90	20	300
5	1000	90	20	300

Results and Discussion

Effect of the Casting Speed on the Interface Microstructure

The OM images of interface microstructure of SCC wires were shown in Fig. 2 when the Ag casting temperature is 1050 °C, casting speed is 30, 60 and 90 mm min^{-1}, respectively. It can be seen from Fig. 2a that the interface microstructure of SCC wire is multi-layer structure when the casting speed is 30 mm min^{-1}. Hypoeutectic structure appears near the side of the silver-cladding

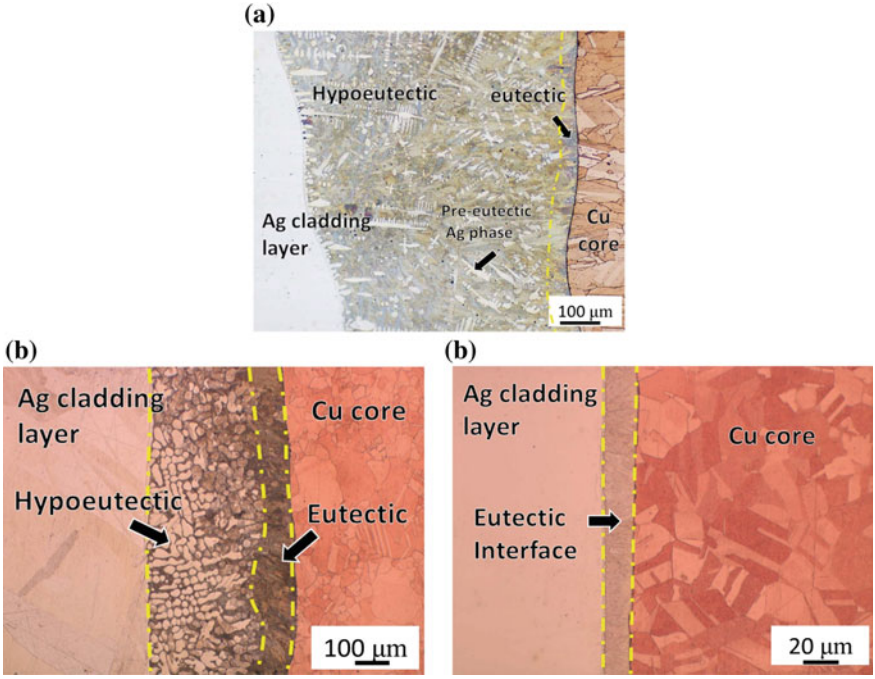

Fig. 2 OM images of SCC wires prepared at different casting speed when other processing parameters are invariable: **a** 1050 °C/30 mm min^{-1}; **b** 1050 °C/60 mm min^{-1}; **c** 1050 °C/90 mm min^{-1}

layer, and the white areas are the pre-eutectic Ag phases. Eutectic structure appears near the side of copper core. The interface between the silver-caldding layer and the hypoeutectic layer and the interface between the copper core and the eutectic layer are both not uniform. It can be seen from Fig. 2b that the interface microstructure of the SCC wire is still multi-layer structure when the casting speed increases to 60 mm min^{-1}. Hypereutectic structure appears near the side of the silver-cladding layer, and white areas are pre-eutectic Ag phases. Eutectic structure appears near the side of copper core. It can be seen from Fig. 2c that the interface microstructure of SCC wire is single eutectic structure when the casting speed is increased to 90 mm min^{-1}.

The SEM images of interface microstructure of SCC wires were shown in Fig. 3 when the Ag casting temperature is 1050 °C, the casting speed is 30 mm min^{-1}. It can be seen from Fig. 3a that lamellar eutectic structure appears near the silver-cladding layer, which white lamellas are Ag phase, black lamellas are Cu phase, and the interface morphology between silver-cladding layer and eutectic structure is tooth-like. Point "A" in the silver-cladding layer contains 2% Cu, indicating that the Cu atoms diffuse to the silver-cladding layer. The pre-eutectic Ag phase is equiaxed in the eutectic structure, and the composition is 96% Ag and 4%

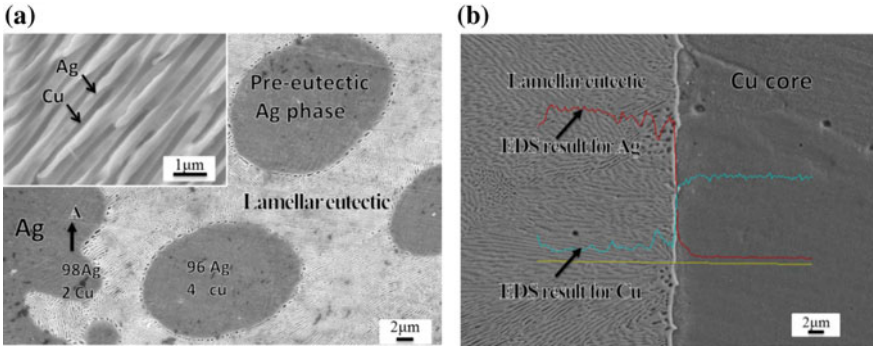

Fig. 3 SEM images of interface microstructure of SCC wire prepared at Ag casting temperature of 1050 °C and casting speed of 30 mm min^{-1}: **a** near silver-cladding layer side; **b** near Cu core side

Cu, which belongs to the supersaturated solid solution. As can be seen from Fig. 3b, the interface morphology between the lamellar eutectic structure and copper core is straight.

The SEM images and EDS of interface microstructure of SCC wires were shown in Fig. 4a when the Ag casting temperature is 1050 °C, the casting speed is 60 mm min^{-1}. It can be seen from Fig. 4a, the interface microstructure between silver-cladding and copper core is mainly hypoeutectic structure and eutectic structure. Region A in Fig. 4a is enlarged in Fig. 4b, Ag (Cu) solid solution appears near the silver-cladding layer and the interface between Ag (Cu) solid solution and hypoeutectic is a cellular shape. The content of Cu in the solid solution layer decreased gradually to the silver-cladding layer and the two black spots showed 7.2% Cu and 6.6% Cu, respectively, which belonged to supersaturated solid solution. Region B in Fig. 4a is enlarged in Fig. 4c, lamellar eutectic structure appears near Cu core.

The SEM images and EDS of interface microstructure of SCC wires were shown in Fig. 5a when the Ag casting temperature is 1050 °C and the casting speed is 90 mm min^{-1}, the interface microstructure between silver-cladding layer and copper core is mainly eutectic structure. Region A in Fig. 5a is enlarged in Fig. 5b, the interface microstructure from silver-cladding layer to copper core is Ag (Cu) solid solution, eutectic structure and Cu (Ag) solid solution, respectively. The interface between silver-cladding layer and Ag (Cu) solid solution is a cellular shape, but the interface between Cu core and Ag (Cu) solid solution is straight. The black spot in Fig. 5b contains 6.89% Cu, which is supersaturated solid solution. The content of Cu in the solid solution layer decrease gradually to the silver-cladding layer. Region B in Fig. 5a is enlarged in Fig. 5c, Cu (Ag) solid solution and small Ag precipitation phases appear in Cu core. Rod-like eutectic associated with the copper core appears.

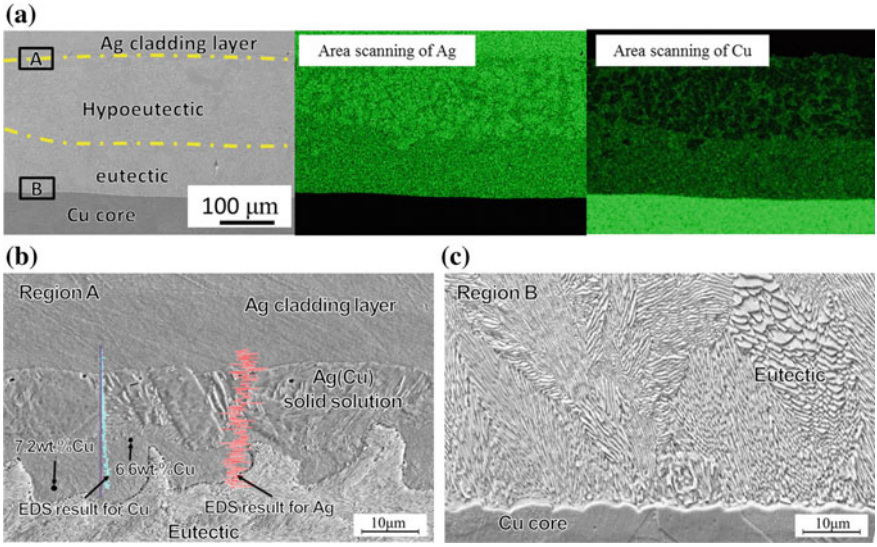

Fig. 4 **a** SEM images of interface microstructure of SCC wire prepared at Ag casting temperature of 1050 °C and casting speed of 60 mm min^{-1}; **b** enlargement of region A in **a**; **c** enlargement of region B in **a**

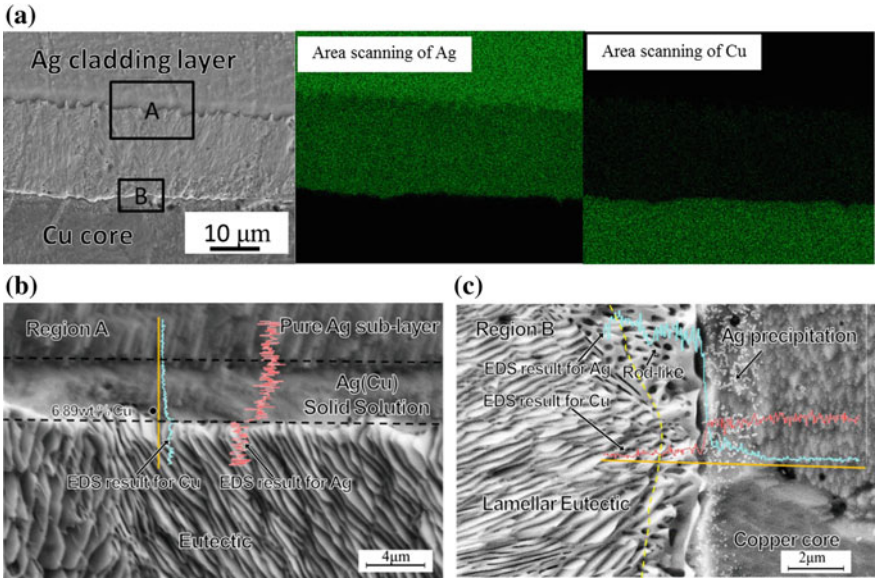

Fig. 5 **a** SEM images of interface microstructure of SCC wire prepared at Ag casting temperature of 1050 °C and casting speed of 90 mm min^{-1}; **b** enlargement of region A in **a**; **c** enlargement of region B in **a**

Effect of the Ag Casting Temperature on the Interface Microstructure

OM images of interface microstructure of SCC wires were shown in Fig. 6 when the casting speed is 90 mm min^{-1}, the Ag casting temperature is 1100, 1050 and 1000 °C, respectively. It can be seen from Fig. 6a that the interface structure of cladding layer is all hypereutectic structure when the Ag casting temperature is 1100 °C. The dark areas dendritic are the pre-eutectic Cu phases, and part of the pre-eutectic Cu phase nucleates on the copper core. As can be seen from Fig. 6b, the interface structure is a single eutectic structure when the Ag casting temperature is 1050 °C. As can be seen from Fig. 6b, the interface structure is also a single eutectic structure when the liquid silver temperature is 1000 °C.

The SEM images and EDS of interface microstructure of SCC wire was shown in Fig. 7a when the Ag casting temperature is 1100 °C, the casting speed is 90 mm min^{-1}. It can be seen from Fig. 7a that outside the copper core is all hypereutectic structure. Region "A" in Fig. 7a is enlarged in Fig. 7b, pre-eutectic Cu phase contains 8.8% Ag, which belongs to supersaturated solid solution. Point "B" in Fig. 7b contains 72.8% Ag and 27.2% Cu, which is the same as the eutectic

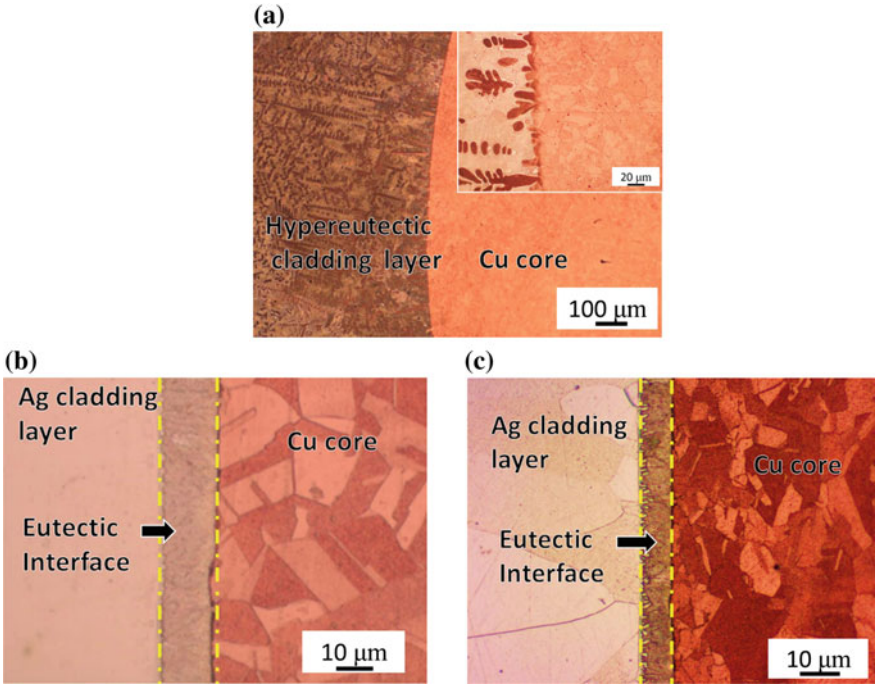

Fig. 6 OM images of interface microstructure of SCC wire prepared at different silver casting temperature: **a** 1100 °C/90 mm min^{-1}; **b** 1050 °C/90 mm min^{-1}; **c** 1000 °C/90 mm min^{-1}

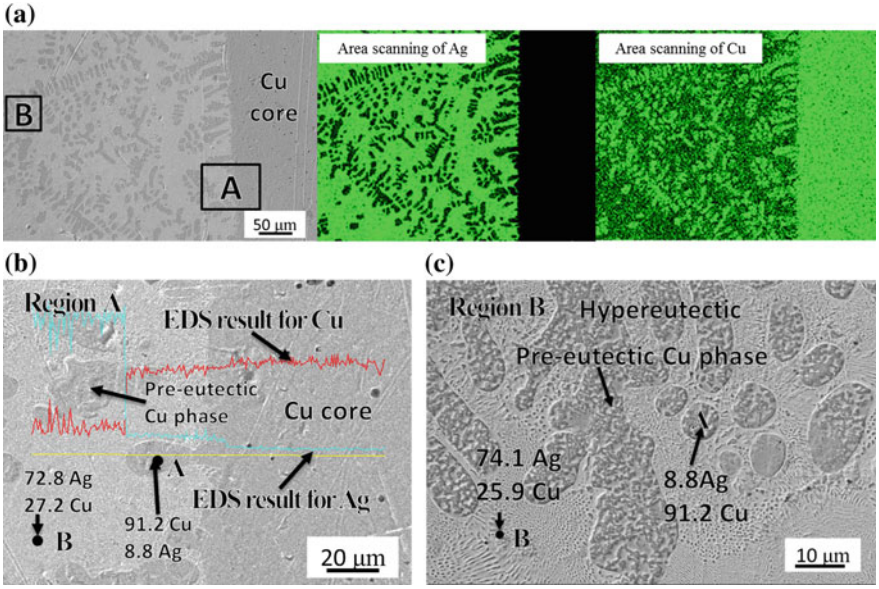

Fig. 7 **a** SEM images of interface microstructure of SCC wire prepared at Ag casting temperature of 1100 °C and casting speed of 90 mm min^{-1}; **b** enlargement of region A in **a**; **c** enlargement of region B in **a**

component in the equilibrium phase diagram. Region B in Fig. 7a enlarged in Fig. 7c, pre-eutectic Cu phase contains 8.8% Ag, which is the same content with the near copper core, indicating that the copper atoms homogenized before the liquid solidifies. The eutectic composition at point "B" is Ag–25.9% Cu that deviation from the equilibrium phase diagram, due to the unbalanced solidification of the liquid.

The SEM images and EDS of interface microstructure of SCC wire were shown in Fig. 8a when the Ag casting temperature is 1000 °C, casting speed is 90 mm min^{-1}. Region A in Fig. 8a enlarged in Fig. 8b, It can be seen that the Ag (Cu) solid solution layer exists between the silver cladding layer and the eutectic layer. The interface morphology between Ag (Cu) solid solution layer and the silver-cladding layer is straight, and with eutectic layer is cell shape. Region B in Fig. 8a enlarged in Fig. 8c, it can be seen that lamellar eutectic structure connected with the copper core, and the interface morphology is straight.

Effect of the Casting Speed on the Interface Thickness

Figure 9 shows the thickness of the interface layers at Ag casting temperature of 1050 °C, and casting speed of 30, 60 and 90 mm min^{-1}, respectively. Figure 9a

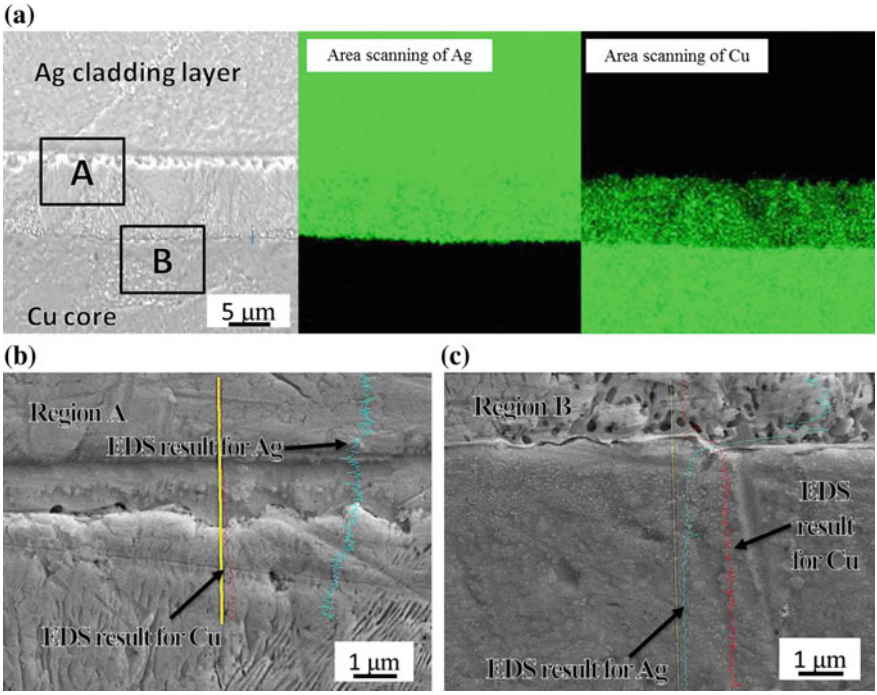

Fig. 8 **a** SEM images of interface microstructure of SCC wire prepared at Ag casting temperature of 1100 °C and casting speed of 90 mm min^{-1}; **b** enlargement of region A in **a**; **c** enlargement of region B in **a**

shows the effect of the casting speed on the thickness of the interface transition layer, indicting that the thickness of the interface transition layer decreases with the increase of the casting speed. When the casting speed is 30 mm min^{-1}, the average thickness of the transition layer is 677 μm. The thickness of the transition layer is not uniform, and the upper and lower deviation is 90 and 83 μm, respectively. When the casting speed is 60 mm min^{-1}, the average thickness of the transition layer decreases to 436 μm, that is decreases by 35.6%, and the upper and lower deviation of the transition layer is 18 and 38 μm. When the casting speed increase to 90 mm min^{-1}, the average thickness of the transition layer decreases to 20 μm, and the upper and lower deviation is 2.2 and 2.7 μm, respectively.

Figure 9b shows the effect of the casting speed on the thickness of the hypoeutectic layer in the interface transition layer. It can be seen that the thickness of the hypoeutectic layer decreases with the increase of the casting speed. When the casting speed is 30 mm min^{-1}, the average thickness of the hypoeutectic layer is 587 μm. The thickness is not uniform, and the upper and lower deviation is 59 and 76 μm respectively. With the increase of the casting speed to 60 mm min^{-1}, the thickness of the hypoeutectic layer decreased to 322 μm, that decreased by 45.1%,

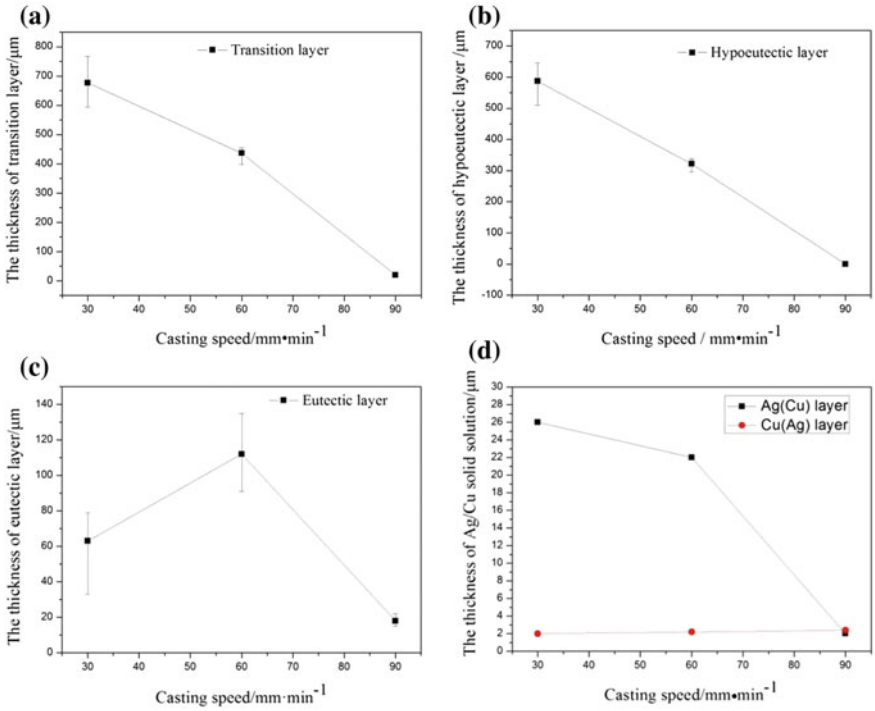

Fig. 9 Effect of casting speed on the interface thickness (T = 1050 °C; V = 30, 60, 90 mm min^{-1}, respectively.): **a** interface transition layer; **b** hypoeutectic layer; **c** eutectic layer; **d** Ag/Cu solid solution layer

and the upper and lower deviation is 16 and 26 μm, respectively. When the casting speed increase to 90 mm min^{-1}, the hypoeutectic layer disappears.

Figure 9c shows the effect of the casting speed on the thickness of the eutectic layer in the interface transition layer. It can be seen that the thickness of the eutectic layer increases first and then decreases with the casting speed increases. When the casting speed is 30 mm min^{-1}, the average thickness of the eutectic layer is 63 μm. When the casting speed is 60 mm min^{-1}, the average thickness of the eutectic layer rises to 112 μm. When the casting speed is 90 mm min^{-1}, the thickness of the eutectic layer decreases to 18 μm.

Figure 9d shows the effect of the casting speed on the thickness of Ag/Cu solid solution, and the black color and red color represents Ag (Cu) solid solution and Cu (Ag) solid solution, respectively. It can be seen that the thickness of Ag (Cu) solid solution in the silver-cladding layer decreases with the increase of the casting speed. The thickness of the Cu (Ag) solid solution almost unchanged with the increase of the casting speed. The thickness of Ag (Cu) decreases from 26 to 2 μm when the casting speed increases from 30 to 90 mm min^{-1}. The thickness of Cu (Ag) solid solution is between 2 and 2.4 μm when the casting speed increases from 30 to 90 mm min^{-1}.

Effect of the Ag Casting Temperature on the Interface Thickness

Figure 10 shows the thickness of interface transition layer and Ag (Cu) solid solution in silver-cladding layer and Cu (Ag) solid solution in copper core at the casting speed is 90 mm min^{-1}, the Ag casting temperature is 1100, 1050 and 1000 °C respectively. Figure 10a shows the effect of the Ag casting temperature on the thickness of the interface transition layer. It can be seen that the thickness of the interface transition layer decreases with the Ag casting temperature increases. When the Ag casting temperature is 1100 °C, the thickness of cladding layer is 1600 μm, owing to copper core dissolved. The reason is that liquid temperature is higher than the melting point of copper (1083 °C), thus the copper core dissolved and melted quickly, resulting in the diffusion of copper atoms to the cladding boundary, resulting in no silver-cladding layer. When the Ag casting temperature reduce to 1050 °C, the interface thickness of the transition layer drastically decreases to 20 μm, and the temperature decrease to 1000 °C, the interface transition layer thickness drops down to 10 μm. Figure 10b shows the effect of the Ag casting temperature on the thickness of Ag (Cu) solid solution in silver-cladding layer and the thickness of Cu (Ag) solid solution in Cu core. Black color is Ag (Cu) solid solution and red color is Cu (Ag) solid solution. It can be seen that Ag (Cu) solid solution is not present in silver-cladding layer at 1100 °C. When the temperature reduces to 1050 °C the thickness of Ag (Cu) solid solution is 2 μm. The temperature reduces to 1000 °C, and the thickness of Ag (Cu) solid solution is 1.4 μm. With the temperature decreases, the thickness of Cu (Ag) solid solution in the copper core decreases from 3 to 0.86 μm.

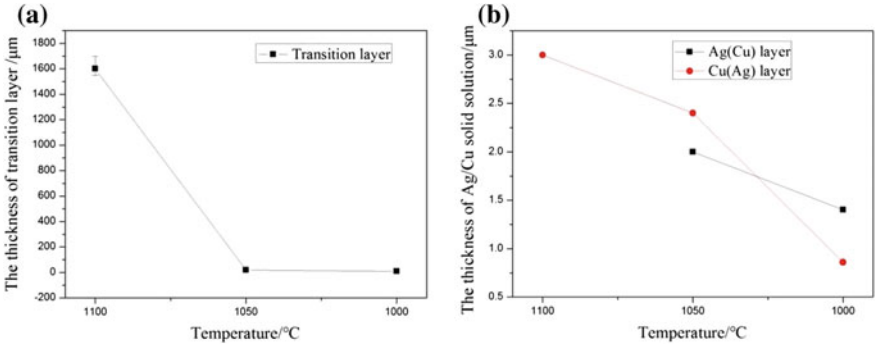

Fig. 10 Effect of the Ag casting temperature on the interface thickness (V = 90 mm min^{-1}; T = 1100, 1050, 1000 °C, respectively.): **a** interface transition layer; **b** Ag/Cu solid solution layer

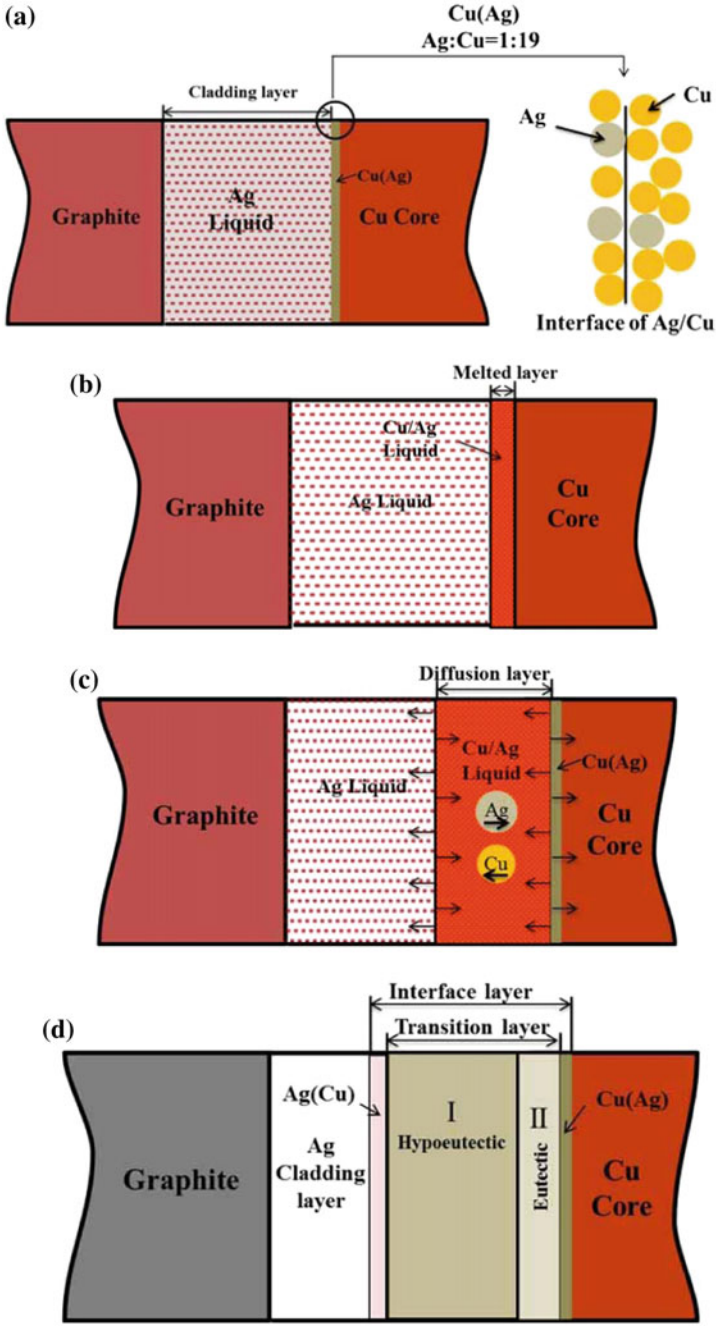

Fig. 11 Schematic diagram of SCC wires prepared by CCC method: **a** wetting and diffusion; **b** solid dissolution and expansion; **c** diffusion in liquid; **d** liquid solidification

Interface Formation Mechanism

As shown in Fig. 11, the process of SCC wires were prepared by SCC method can be summarized in four stages: (a) wetting and diffusion; (b) solid dissolution and expansion; (c) atoms diffusion in liquid; (d) liquid solidification. Figure 11a shows the liquid silver wetting and diffusing on the surface of solid copper. When the liquid silver contact with the solid copper, the liquid silver wets on the surface of the solid copper and silver atoms diffuse into the solid copper. The Cu (Ag) solid solution layer forms on the surface of the solid copper. Figure 11b is the dissolution and expansion of solid Cu. According to the Ag–Cu binary alloy phase diagram, the diffusion of Ag atoms exceed the saturated solubility of Ag in solid Cu, that is, above the eutectic temperature (779.8 °C), the atomic ratio of silver atoms to copper atoms is greater than 1:19, then the solid copper will dissolute. Figure 11c shows the diffusion of the two elements. Since the diffusion coefficient of copper atoms in liquid is higher than that in solid with several orders of magnitude, and there is a great difference in concentration between Ag and Cu, so the copper atoms diffuse rapidly to the liquid Ag, forming Ag–Cu alloy liquid. The silver atoms continue to diffuse toward the solid copper surface, and the solid copper continues to dissolve and expand.

Figure 11d shows the liquid solidification. The different diffusion distance of copper atoms, resulting in the liquid composition is different. Therefore, the liquid will stratify solidification. Pure silver-cladding layer solidified firstly, and the remaining liquid divided into “I” and “II”. The hypoeutectic layer is “I”, when the amount of copper atoms is less than 28.1%, and vice versa. Pure silver-cladding layer is general not obtained when the concentration of copper atom beyond 28.1%. The liquid near the copper core is the “II” and its composition remains at the eutectic point component, resulting in “II” solidified finally. Therefore, the interface transition layer appears multi-layer microstructures.

Conclusions

Silver cladding copper wires have been prepared by a self-developed core-cladding continuous casting method with a diameter of 10 mm at Ag casting temperature of 1000–1100 °C, casting speed of 30–90 mm min^{-1}, cooling water temperature of 20 °C and cooling water flow of 300 L h^{-1}. The effect of silver casting temperature and casting speed on the interface microstructure and thickness of silver cladding copper wires and formation mechanism of the interface have been investigated.

(1) The interface microstructure which from the surface to the Cu core of the silver cladding copper wire is Ag (Cu) Solid solution, hypoeutectic structure, eutectic structure and Cu (Ag) solid solution, when the Ag casting temperature is 1050 °C, casting speed is 30–60 mm min^{-1}. The interface microstructure is Ag (Cu) solid solution, eutectic structure, and Cu (Ag) solid solution, when the

casting speed increase to 90 mm min^{-1}. With the increase of the casting speed, the thickness of the interface transition layer decreases sharply, the thickness of the hypoeutectic layer and Ag (Cu) solid solution layer decreases, and the eutectic layer thickness increases first and then decreases, but the thickness of Cu (Ag) solid solution remains almost constant.

(2) The microstructure which from the surface to the Cu core of the silver cladding copper wire is all hypereutectic, when the Ag casting temperature is 1100 °C, casting speed is 90 mm min^{-1}. The thickness of interface transition layer of t the silver cladding copper wire decreases from 20 to 10 μm when the Ag casting temperature decreases from 1050 to 1000 °C.

(3) The process of silver cladding copper wires prepared by core-cladding continuous casting method can be summarized in four stages: (a) wetting and diffusion; (b) solid dissolution and expansion; (c) diffusion in liquid; (d) liquid solidification.

(4) Under the condition of low casting temperature and high casting speed, core-cladding continues casting method is advantageous to prepare the bimetallic composite material which is prone to eutectic reaction.

Acknowledgements This research was financially supported by the National Natural Science Foundation of China (Grant No. 51674027) and the National Key Research and Development Program of China (Grant No. 2016YFB0301301).

References

1. J. Du, D.X. Zhuang, S.X. Sun, Study on the microstructure and mechanical properties of silver covered copper composite wire. Precious Met. **36**, 20–26 (2015)
2. L. Zhang, L. Meng, S.P. Zhou, F.T. Yang, Behaviors of the interface and matrix for the Ag/Cu bimetallic laminates prepared by roll bonding and diffusion annealing. Mater. Sci. Eng., A **371**, 65–71 (2004)
3. A. Liu, X. Ren, J. Zhang, D. Li, M. An, Complexing agent study for environmentally friendly silver electrodeposition (II): electrochemical behavior of silver complex. Rsc. Adv. **6**, 7348–7355 (2016)
4. B.D. Dunn, D.E. Rooij, D.S. Collins, Corrosion of silver-plated copper conductors. Esa J. **8**, 307–335 (1984)
5. Y. Chen, *Modern Practical Electroplating Technology* (National Defense Industry Press, Beijing, 2003)
6. X.F. Liu, W.Y. Wu, J.X. Xie, C.N., Patent 104148598. (2016)
7. W.Y. Wu, *Fundamental Research on Preparation of Copper Clad Steel Wires by Core-Cladding Continuous Casting* (University of Science and Technology Beijing, Beijing, 2016)
8. I.T. Poku, M. Dollar, T.B. Massalski, A study of the transient liquid phase bonding process applied to a Ag/Cu/Ag sandwich joint. Metall. Trans. A **19**, 675–686 (1988)
9. N.Y. Li, W.C. Wang, L.Z. Peng, J.C. Yan, X.S. Liu, Dissolution behavior of Cu in Cu–Ag and Cu–P brazing alloys using weld brazing. Trans. Nonferrous Met. Soc. China **21**, s394–s399 (2011)

Modelling and Analysis of the Relationship Between Process Parameters and Cross Section Geometry of Tin Single Tracks in Liquid Metal Flow Rapid Cooling Additive Manufacturing

Ang Li, Xuefeng Liu, Bo Yu, Yang Yan and Baoqiang Yin

Abstract The cross section geometry of single tracks has critical effects on the dimensional accuracy of metallic parts in self-developed liquid metal flow rapid cooling metal additive manufacturing. Tin single tracks were formed by a self-developed liquid metal flow rapid cooling metal additive manufacturing equipment with different process parameters. The cross sections of tin single tracks were observed by metallographic microscope, and fitted by Matlab software. The relational model between the process parameters and the cross section geometry of tin single tracks was established using BP neural network, and the influence of process parameters on the cross section geometry was also analyzed. The results demonstrate that tin single tracks have a good size uniformity, with the standard deviation 0.0556 for cross section width and 0.0111 for cross section height. The cross section geometry of tin single tracks is fitted with ellipse function with a fitting degree 0.9956. For the cross section width and height of tin single tracks, the average error between experimental value and predicted value by the BP neural network model is as small as 2.42 and 3.75%, respectively. The most influencing parameter on the cross section geometry of tin single tracks is the nozzle scanning speed, and then, with a sequence of decreasing importance, are the nozzle-to-substrate distance, the molten tin level and the molten tin superheat.

Keywords Liquid metal flow rapid cooling additive manufacturing
Tin single tracks · Process parameters · Cross section geometry
BP neural network model

A. Li · X. Liu (✉) · B. Yu · Y. Yan · B. Yin
School of Materials Science and Engineering, University of Science and Technology Beijing, Beijing 100083, China
e-mail: liuxuefengbj@163.com

X. Liu
Beijing Laboratory of Metallic Materials and Processing for Modern Transportation, University of Science and Technology Beijing, Beijing 100083, China

© Springer Nature Singapore Pte Ltd. 2018

Y. Han (ed.), *Advances in Materials Processing*, Lecture Notes in Mechanical Engineering, https://doi.org/10.1007/978-981-13-0107-0_21

Introduction

Metal additive manufacturing is a new type of material forming technology developed in 1980s. The production process of metal material manufacturing includes creation of geometric model in a solid modeler, slicing of expected thickness, design of the scanning paths with a certain scanning interval, layer-by-layer deposition using the metal additive manufacturing equipment [1]. The layer thickness and scanning interval have important influences on the forming efficiency, surface smoothness and dimensional accuracy of metal additive manufacturing technology [2–4]. It is of great significance to study the single tracks cross section geometry, because it plays a major role in choosing the layer thickness and scanning interval [5].

The process parameters have a significant influence on the single tracks cross section geometry in the process of metal additive manufacturing [6–8]. Yadroitsev et al. [9] analyzed the effect of process parameters on the single tracks cross section geometry in selective laser melting, and found that the most influencing parameter is the laser power and the influence of the particle size is the smallest. Lu et al. [10] adopted BP-AM and LS-SVM networks to establish the model of single tracks cross section height and laser power, scanning speed and powder feeding rate in Laser Engineered Net Shaping. Xiong et al. [11] developed BP neural networks models between width and height of single tracks cross section and different welding parameters in GMAW-based rapid manufacturing. Zhong [12] used parabola model, cosine model and arc model to fit the single droplet cross section geometry in metal micro-droplet deposition manufacture, and found that the arc model has a better fitting. However, the relationship between the single tracks cross section geometry and the process parameters for liquid metal flow rapid cooling additive manufacturing (LMFRC) devised by Liu et al. [13] has not been studied.

In this study, tin single tracks were formed by a self-developed LMFRC equipment with different process parameters. The cross section geometry of tin single tracks was fitted by contour fitting method. The BP neural network was used to establish the model of the relationship of the width and height of tin single tracks cross section geometry with the nozzle scanning speed, the nozzle-to-substrate distance, the molten tin level, and the molten tin superheat. The influence of the process parameters on the cross section geometry of tin single tracks was also analyzed.

Experimental Equipment and Methods

Experimental Equipment

LMFRC equipment mainly includes pressing block, crucible, motion system, stopper rod, nozzle, substrate, cooling groove and control system, as shown in Fig. 1. In the LMFRC process, the metal material in the crucible is firstly heated,

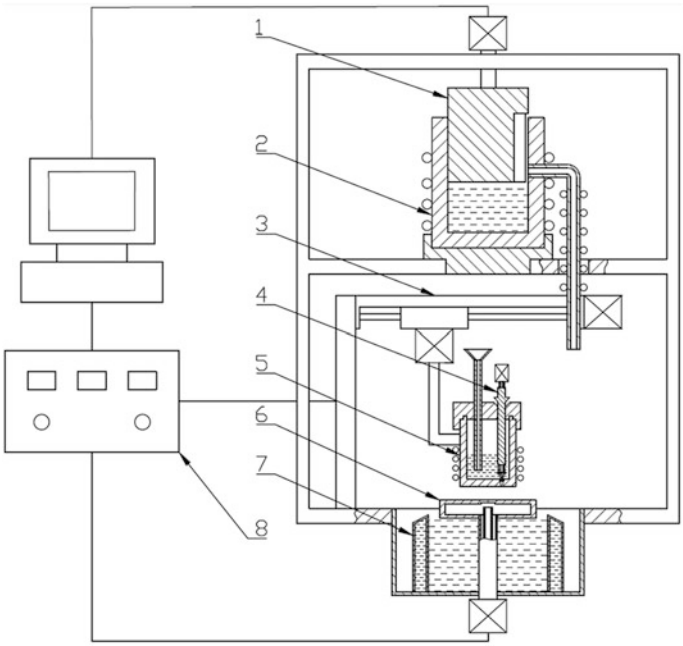

Fig. 1 Schematic diagram of LMFRC equipment. 1—Pressing block; 2—crucible; 3—motion system; 4—stopper rod; 5—nozzle; 6—substrate; 7—cooling groove; 8—control system

melted, and transported to the nozzle under the action of the pressing block. Then, the metal melt flows out of the nozzle in the form of liquid flow, finally the metal melt is deposited on the substrate according to the scanning paths of the components under the rapid cooling condition of the cooling groove and the substrate.

Experimental Methods

The experimental material is 99.99% pure tin. The discharge hole diameter of nozzle is 1.2 mm. Cooling water flows through the channel within pure copper substrate. The tin liquid flow was deposited on the substrate from the nozzle under different conditions of the nozzle scanning speed, the nozzle-to-substrate distance, the molten tin level, and the molten tin superheat to form the tin single tracks. The orthogonal experimental scheme is shown in Table 1.

The tin single tracks were cut transversely from the center, and the cross section of tin single tracks was observed by Zeiss Scope A1 microscope after grinding and polishing. The cross section geometry of tin single tracks was fitted using Matlab software. The relationship model between the process parameters and the width and height of tin single tracks cross section is established by BP neural network, and the

Table 1 Orthogonal test table of liquid metal flow rapid cooling single tracks forming

No.	Nozzle scanning speed [mm s^{-1}]	Nozzle-to-substrate distance [mm]	Molten tin superheat [°C]	Molten tin level [mm]
1	20	20	50	40
2	20	30	75	45
3	20	40	100	50
4	25	20	50	50
5	25	30	75	40
6	25	40	100	45
7	30	20	50	45
8	30	30	75	50
9	30	40	100	40

influence weight of each process parameters on the width and height of tin single tracks cross section geometry is calculated.

Results and Discussion

Part of tin single tracks obtained from the experiment are shown in Fig. 2. The geometry parameters of tin single tracks cross section include width W, height H and bottom width Z, as shown in Fig. 3. The width W, height H and bottom width Z of five different parts of tin single tracks are measured, and the average variance of the width W, height H and bottom width Z are 0.0556, 0.0111 and 0.0489, respectively. So it can be seen that the size uniformity of tin single tracks is better. The average measurement results of the cross section width W, the height H and the bottom width Z of the tin single tracks which is obtained from the nine groups shown in Table 2.

Fig. 2 Part of tin single tracks obtained from the experiment. **a** Sample 3; **b** sample 4; **c** sample 8

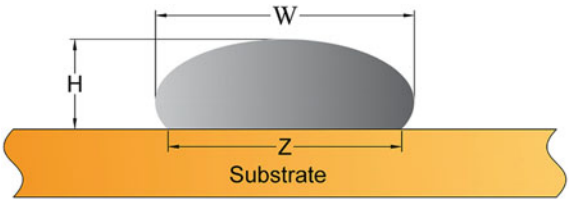

Fig. 3 Schematic diagram of tin single tracks cross section geometry. W—cross section width; H—cross section height; Z—cross section bottom width

Table 2 Orthogonal test results of liquid metal flow rapid cooling single tracks forming

No.	Cross section width [mm]	Cross section height [mm]	Cross section bottom width [mm]
1	8.89	4.35	8.02
2	10.08	4.07	8.87
3	10.61	4.25	9.51
4	8.25	4.37	7.55
5	7.91	3.64	7.19
6	9.34	3.85	8.02
7	6.72	3.81	6.21
8	7.47	3.93	6.51
9	7.64	3.38	6.71

Fit of Tin Single Tracks Cross Section Geometry

Taking sample 5 as an example, its cross section geometry is shown in Fig. 4. The image was processed with binarization and de-noising using the Matlab software. Canny operator was used to extract its contour, and Gaussian operator was used to smoothing the contour, and then coordinated the contour. The ellipse function was used to fit the contour as shown in Fig. 5 with a fitting degree 0.9956.

The cross section geometry of tin single tracks obtained in the other 8 groups were fitted by the same method, and the result is shown in Fig. 6. It can be seen that the ellipse function has a good agreement with the cross section geometry of each sample under different process parameters.

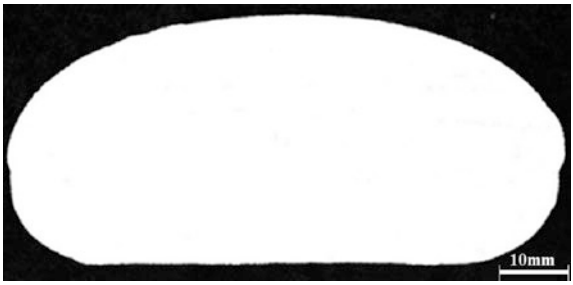

Fig. 4 Cross section geometry of sample 5

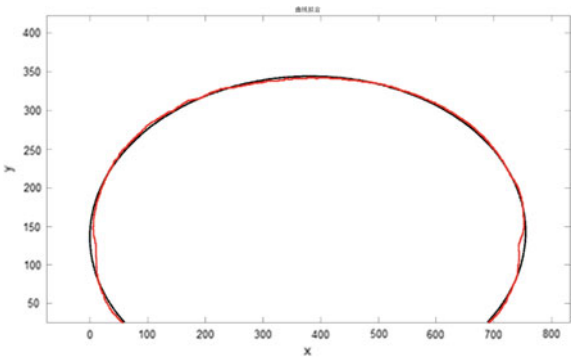

Fig. 5 Fitting results of cross section contours and elliptic functions of sample 5

In order to determine the elliptic function equation, the cross section width W and the cross section bottom width Z of the samples in Table 2 were plotted as a scatter plot and fitted as shown in Fig. 7.

The fitting result can be expressed by Eq. (1):

$$Z = 0.89W \tag{1}$$

The fitted correlation coefficient is 0.9740. The standard elliptic curve equation is shown in Eq. (2):

$$\frac{x^2}{a^2} + \frac{y^2}{b^2} = 1 \tag{2}$$

Among them, the ellipse long axle can be approximated by the cross section width of tin single tracks, the ellipse short axis can be calculated from the cross section height of tin single tracks as shown in Eqs. (3) and (4):

$$a = \frac{W}{2} \tag{3}$$

$$b = \frac{H}{1 + \sqrt{1 - 0.89^2}} \approx 0.69H \tag{4}$$

The elliptic function equation can be derived by Substituting Eqs. (3) and (4) into the Eq. (2):

$$\frac{4x^2}{W^2} + \frac{2.12y^2}{H^2} = 1 \tag{5}$$

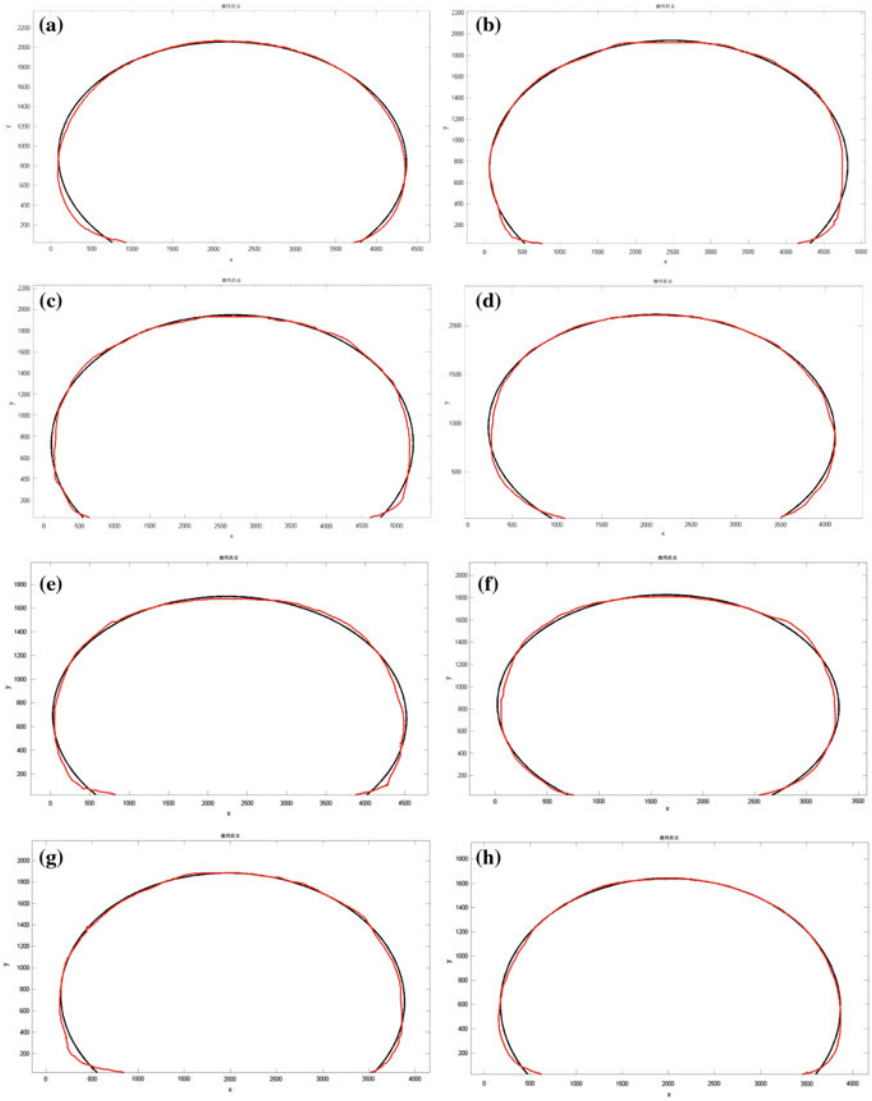

Fig. 6 Fitting results of cross section contours and elliptic functions of other 8 samples. **a** Sample 1; **b** sample 2; **c** sample 3; **d** sample 4; **e** sample 6; **f** sample 7; **g** sample 8; **h** sample 9

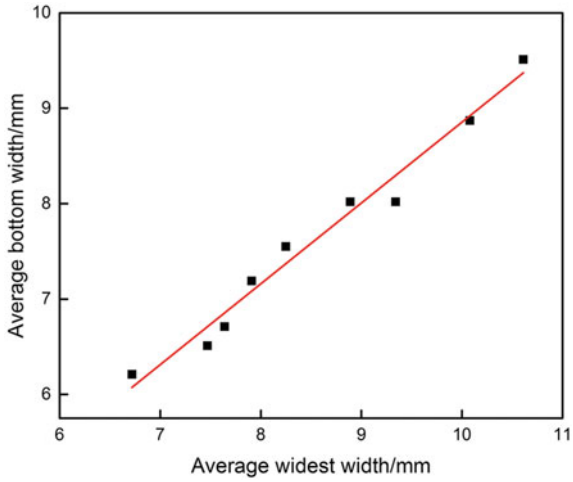

Fig. 7 Fitting results of cross section width and bottom width

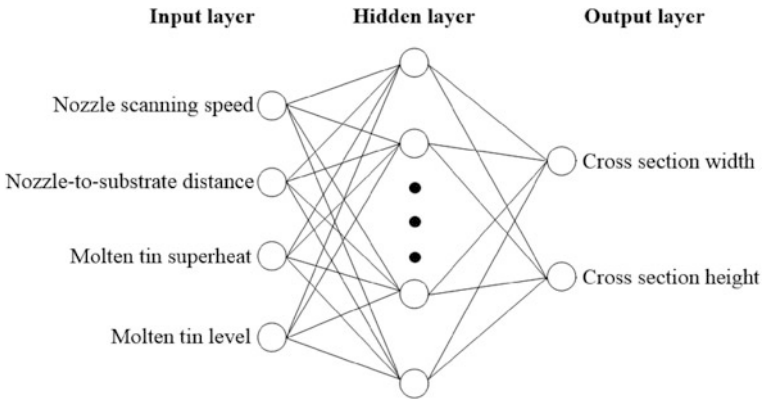

Fig. 8 Architecture of BP neural network

Relationship Model Between Process Parameters and Cross Section Geometry of Tin Single Tracks

The relationship between the nozzle scanning speed, nozzle-to-substrate distance, molten tin superheat, molten tin level and the width and height of tin single tracks cross section is established using the BP neural network model, and the architecture is shown in Fig. 8.

Table 3 BP neural network model test data

No.	Nozzle scanning speed [mm s^{-1}]	Nozzle-to-substrate distance [mm]	Molten tin superheat [°C]	Molten tin level [mm]	Cross section width [mm]	Cross section height [mm]
10	30	40	100	40	7.53	3.68
11	20	40	75	50	11.06	4.09
12	30	20	100	50	7.63	3.85

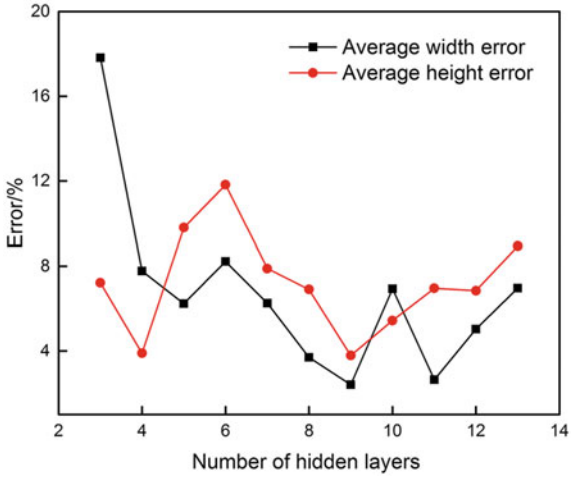

Fig. 9 Effect of hidden layer neuron numbers on the cross section width and height of tin single tracks

The number of hidden neurons is set as l, and l should satisfy the Eq. (6):

$$l = \sqrt{m+n} + a \tag{6}$$

where m represents the number of nodes in the input layer; n represents the number of nodes in the input layer; a represents the regulation constant, with a range of 1–10. In this model, the range of l is 3–13, m is 4, and n is 2. The newff function is called to create BP neural network in Matlab software, "logsig" and "purelin" are selected as transfer function. The data in Tables 1 and 2 are trained as training data, and the maximum number of training is 10,000 with the training error of 10^{-5}. In order to minimize the prediction error, different number of hidden nodes is trained, and the test data in Table 3 is brought into the BP neural network model with different hidden layer neuron nodes. The test error is shown in Fig. 9.

It can be seen from Fig. 9 that the prediction errors of the cross section width and height of tin single tracks are small when the hidden neurons number is 9, and the specific test results are shown in Table 4. It can be seen that the average errors of the cross section width and height of tin single tracks are 2.42 and 3.75%,

Table 4 Prediction error of cross section width and height when the number of hidden neurons is 9

No.	Actual width [mm]	Prediction width [mm]	Error [%]	Actual height [mm]	Prediction height [mm]	Error [%]
10	7.53	7.64	1.46	3.68	3.53	4.07
11	11.06	10.84	1.99	4.09	4.32	5.62
12	7.63	7.34	3.80	3.85	3.91	1.56
Average			2.42			3.75

respectively, which means that the model can predict the cross section width and height of tin single tracks under different process parameters.

In order to realize the prediction of tin single tracks cross section geometry under different forming parameters, the relationship between process parameters and cross section geometry of tin single tracks was obtained by combining the BP neural network model with the geometric fitting equation.

Effect of Process Parameters on the Cross Section Geometry of Tin Single Tracks

The influence of process parameters on the cross section width and height of tin single tracks was calculated and output using the BP neural network model with the number of hidden layer neuron of 9 as shown in Table 5.

As can be seen from Table 5, the effect of nozzle scanning speed, nozzle-to-substrate distance, molten tin level and molten tin superheat on the cross section width is gradually reduced; The effect of nozzle scanning speed, molten tin level, nozzle-to-substrate distance and molten tin superheat on the cross section height is gradually reduced. The nozzle scanning speed has the greatest effect on the cross section width and height, because when the nozzle discharge flow is constant, the product of the cross section area and the nozzle scanning speed is fixed. When the nozzle scanning speed is changed, the cross section width and height would subsequently be changed; The nozzle-to-substrate distance and molten tin level have little effect on the cross section width and height, because the nozzle-to-substrate distance and molten tin level have a certain influence on the impact speed of

Table 5 Effect of each process parameter on the cross section width and height of tin single tracks

Process parameters	Weight of width	Weight of height
Nozzle scanning speed	0.3388	0.3063
Nozzle-to-substrate distance	0.2894	0.2589
Molten tin superheat	0.1034	0.1744
Molten tin level	0.2684	0.2663

the liquid flow, and thus affect the spread of molten tin on the substrate, and finally the cross section geometry of tin single tracks is affected. The molten tin superheat has the least influence on the cross section width and height. The molten tin superheat only affects the solidification process of molten metal. So it shows that the solidification process of molten metal has less effect on the cross section geometry compared to the spread process. This reflects the spread time is shorter than the solidification time after the metal flow impact on the substrate, i.e. when the metal melt is not completely solidified, the spreading process of the metal melt has been completed.

Conclusions

(1) The size uniformity of tin single tracks is good, and the average variance of width W, height H and bottom width Z are 0.0556, 0.0111 and 0.0489, respectively in LMFRC.
(2) The fitting degree of the ellipse function and cross section geometry of tin single tracks is 0.9956, and elliptic function equation for the width and height of the cross section is established.
(3) The prediction errors of the cross section width and height of tin single tracks are small when the hidden neurons number is 9, and the average error of the cross section width and height of tin single tracks are 2.42 and 3.75%, respectively.
(4) The most influencing parameter on the cross section geometry of tin single tracks is the nozzle scanning speed, and then, with a sequence of decreasing importance, are the nozzle-to-substrate distance, the molten tin level and the molten tin superheat.

Acknowledgements This research was financially supported by the State Key Laboratory for Advanced Metals and Materials (2017Z-05) and the National High Technology Research and Development Program of China (2015AA034304).

References

1. P.M. Pandey, N.V. Reddy, S.G. Dhande, Slicing procedures in layered manufacturing: a review. Rapid Prototyping J. **9**, 274–288 (2003)
2. Y. Cao, S. Zhu, X.B. Liang, W.L. Wang, Overlapping model of beads and curve fitting of bead section for rapid manufacturing by robotic MAG welding process. Robot. Cim Int. Manuf. **27**, 641–645 (2011)
3. K. Monroy, J. Delgado, L. Sereno, J. Ciurana, Geometrical feature analysis of Co–Cr–Mo single tracks after selective laser melting processing. Rapid Prototyping J. **21**, 287–300 (2015)
4. S. Jhavar, N.K. Jain, C.P. Paul, Enhancement of deposition quality in micro-plasma transferred arc deposition process. Mater. Manuf. Process. **29**, 1017–1023 (2014)

5. S. Jhavar, C.P. Paul, N.K. Jain, Micro-plasma transferred arc additive manufacturing for die and mold surface remanufacturing. JOM **68**, 1801–1809 (2016)
6. L.H. Qi, Y.P. Chao, J. Luo, J.M. Zhou, X.H. Hou, H.J. Li, A novel selection method of scanning step for fabricating metal components based on micro-droplet deposition manufacture. Int. J. Mach. Tool Manuf. **56**, 50–58 (2012)
7. S. Suryakumar, K.P. Karunakaran, A. Bernard, U. Chandrasekhar, N. Raghavender, Weld bead modeling and process optimization in hybrid layered manufacturing. Comput. Aided Design **43**, 331–344 (2011)
8. D.H. Ding, Z.X. Pan, D. Cuiuri, H.J. Li, A multi-bead overlapping model for robotic wire and arc additive manufacturing (WAAM). Robot. Cim Int. Manuf. **31**, 101–110 (2015)
9. I. Yadroitsev, I. Yadroitsava, P. Bertrand, I. Smurov, Factor analysis of selective laser melting process parameters and geometrical characteristics of synthesized single tracks. Rapid Prototyping J. **18**, 201–208 (2012)
10. Z.L. Lu, D.C. Li, B.H. Lu, A.F. Zhang, G.X. Zhu, G. Pi, The prediction of the building precision in the laser engineered net shaping process using advanced networks. Opt. Laser. Eng. **48**, 519–525 (2010)
11. J. Xiong, G.J. Zhang, J.W. Hu, L. Wu, Bead geometry prediction for robotic GMAW-based rapid manufacturing through a neural network and a second-order regression analysis. J. Intell. Manuf. **25**, 157–163 (2014)
12. S.Y. Zhong, *Research on Uniform Metal Droplet Generation and Surface Topography Control in Metal Micro-droplet Deposition Manufacture* (Xi'An, Northwestern Polytechnical University, 2016)
13. X.F. Liu, A. Li, B. Yu, B.Q. Yin, C.N. Patent 106925783A (2017)

Dependence of Microstructure, Relative Density and Hardness of 18Ni-300 Maraging Steel Fabricated by Selective Laser Melting on the Energy Density

Jie Tian, Zhenghua Huang, Wenjun Qi, Yajiang Li, Jianye Liu and Gaofeng Hu

Abstract 18Ni-300 maraging steel samples were fabricated by Selective Laser Melting technology (SLM). Microstructure and phase transformation before and after aging treatment were investigated by Optical Microscopy (OM), Scanning Electron Microscopy (SEM) and X-Ray Diffraction (XRD). Meanwhile, hardness and relative density of samples were also tested. The results showed that there was a positive correlation relationship between energy density and relative density. Samples fabricated with high energy density of 6.0 J/mm^2 could lead to extremely high relative density of 99.34%; After aging heat treatment (763 K for 4 h), the microhardness increased from 370 to 629 HV because of second phases such as Ni_3Mo and Ni_3Ti precipitated in the martensite matrix. When aging temperature reached to 793 K, the hardness was affected by both precipitation of strengthening

J. Tian · Z. Huang (✉) · W. Qi
Guangdong Provincial Key Laboratory for Technology and Application of Metal Toughening, Guangdong Institute of Materials and Processing, Guangzhou, China
e-mail: zhhuang@live.cn

W. Qi
e-mail: 13925162166@qq.com

J. Tian · Y. Li
MOE Key Lab for Liquid Structure and Heredity of Materials, School of Materials Science and Engineering, Shandong University, Jinan, China
e-mail: ahut1026@163.com

Y. Li
e-mail: yajli@sdu.edu.cn

J. Liu · G. Hu
Guangdong Hantang Quantum Photoelectric Technology Co. Ltd, Zhongshan, China
e-mail: 13544596700@163.com

G. Hu
e-mail: hanbang3d@163.com

J. Liu · G. Hu
Guangdong Hanbang Laser Technology Co. Ltd, Zhongshan, China

© Springer Nature Singapore Pte Ltd. 2018

Y. Han (ed.), *Advances in Materials Processing*, Lecture Notes in Mechanical Engineering, https://doi.org/10.1007/978-981-13-0107-0_22

phase and austenite reversion which had the opposite effect. The XRD results showed the appearance of austenite and the decrease of martensite.

Keywords Selective laser melting · 18Ni-300 maraging steel · Microstructure Mechanical properties

Introduction

As a crucial branch of additive manufacturing (AM) processes, selective laser melting (SLM) has gained widespread attention since the late 1980s [1]. In recent years, this powder-based process has been used to produce functional 3D parts through a laser beam with high intensity energy acting on metallic powder layer by layer. With a great advantage of processing in complex and abnormal shape parts, which can not be fabricated by traditional methods, SLM technology is able to solve the remaining technical problems such as long production cycle, high cost and difficult processing [2, 3]. The schematic diagram of SLM technology is shown in Fig. 1.

During the SLM process, metal powder is set in the build cylinder. After computer-controlled laser beam finished one layer scanning, base plate would descend a thickness of layer and the added powder in feed container would rise the same distance. Under the action of laser, metallic powder is heated to melt and re-solidify during cooling. The whole entity will be formed after total layers have been bonded together. Due to the extremely high rate of heating and cooling during SLM, fine microstructure and non-equilibrium phases always can be observed [2, 4, 5].

The target material in this study is 18Ni-300 maraging steel, which is widely applied in aircraft and aerospace industry, rocket castings and tools manufacturing because of its excellent material properties like high strength, good toughness and

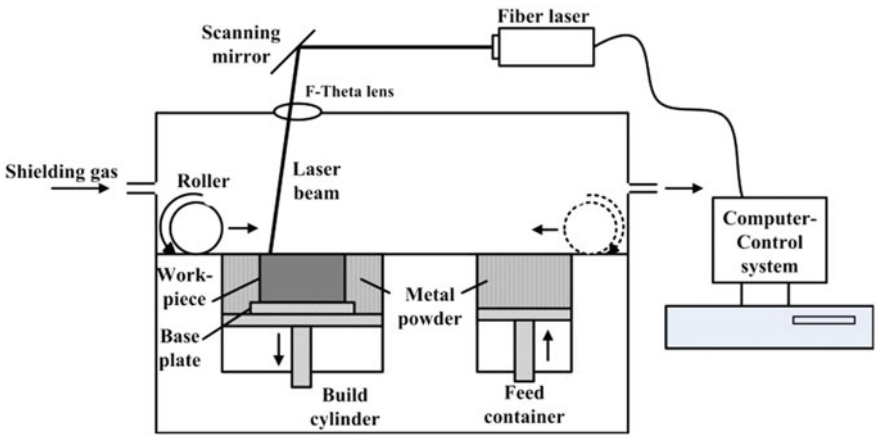

Fig. 1 Schematic diagram of the SLM process

Table 1 Chemical composition of the employed powder (weight percent, wt%)

Elements	Ni	Co	Mo	Ti	C	Fe
Content [wt%]	17.89	8.98	4.79	0.63	<0.01	Bal.

weldability [6]. Maraging steel is an iron-nickel alloy with low carbon content. The steel uses other elements such as molybdenum, cobalt, titanium and aluminum to precipitate second-phase on martensite matrix during aging treatment. Currently, the study of 18Ni-300 maraging steel made by SLM is limited to surface quality, porosity and parameter optimization [4, 7].

To combine both the advantages of SLM technology and maraging steel, the influence of parameters on density and mechanical properties is investigated in this study. 18Ni-300 maraging steel parts fabricated by SLM are treated at different temperatures and duration time for aging heat-treatment to improve the mechanical properties. The microstructure and phase composition of SLMed and heat-treated samples were also investigated. This study is aimed to provide support in subsequent industrialization of 3D printed molds.

Experimental Procedure

Material and Equipment

Commercial gas 18Ni-300 powder as precursor material was supplied by Additive Metal Alloys, Ltd. The main chemical composition of the powder is shown in Table 1. High nickel and low carbon are the characteristics of maraging steel. The particle morphology of powder investigated by SEM is shown in Fig. 2. The near spherical particles ranging from a few to 46 μm are good to achieve uniform distribution on base plate. And the average size of powder is 31 μm.

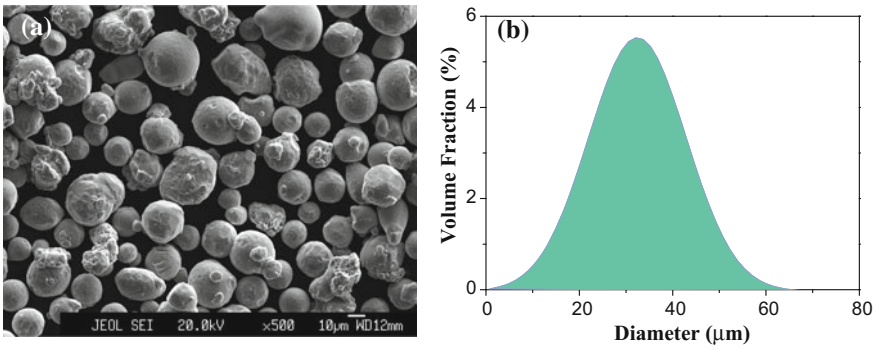

Fig. 2 Morphology and size distribution of precursor powders

All specimens in this study are carried out on SLM-150 machine designed by Hanbang 3D technology CO., LTD, which equips with a fiber laser with maximum power output of 500 W, maximum scanning speed of 7 m/s. Before SLM experiment, the base plate was pre-heated to approx. 373 K to reduce thermal gradient and stress. During the process, the build chamber was filled with argon gas and the oxygen content is below 100 ppm.

The as-cast specimen, which is used to study the difference from SLMed condition, is prepared by vacuum arc furnace. The specimen is cylinder with diameter of 10 mm and height of 50 mm.

Processing Parameters

In this study, orthogonal scanning strategy is chosen as shown in Fig. 3. The overview of specimens is also revealed in Fig. 3. Cylindrical specimens with diameter of 10 mm and height of 15 mm are produced. Scanning vector changed 90° every two layers. The influence of process parameters including velocity v, laser power p and hatching space h on the properties of parts manufactured by SLM are investigated.

The other parameters are constant. The layer thickness t is fixed at 40 μm in order to obtain accurate dimension parts. The energy density(E), which represents a measure for evaluating the average energy transmitted to per area of single-track, is calculated by Eq. (1) [8]:

$$E = p/(h * v) \tag{1}$$

where E is the energy density, p is the laser power, h is the hatching space and v is the scanning velocity. The E is affected by both thermophysical characteristic of material and basic processing parameters during the selective laser melting.

Table 2 shows the specific experimental design and energy density for applied experiment.

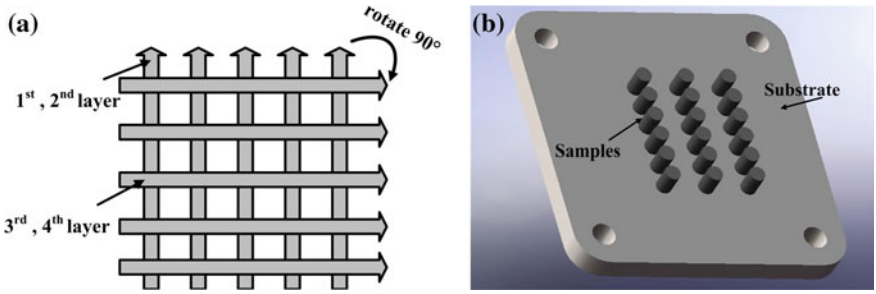

Fig. 3 Schematic diagram of orthogonal scanning strategy and overview of specimens

Table 2 An overview of process parameters

Sample	Velocity, v [mm/s]	Laser power, p [W]	Hatching space, h [μm]	Energy density, E [J/mm^2]	Relative density [%]
1	2500	300	50	2.40	96.90
2	2500	300	70	1.71	95.86
3	2500	300	100	1.20	84.17
4	2500	350	50	2.80	96.27
5	2500	350	70	2.00	97.41
6	2500	350	100	1.40	92.53
7	2500	450	50	3.60	97.47
8	2500	450	70	2.57	99.34
9	2500	450	100	1.80	97.87
10	1500	450	50	6.00	99.19
11	1500	450	70	4.29	98.85
12	1500	450	100	3.00	98.65
13	2000	450	50	4.50	99.19
14	2000	450	70	3.21	98.78
15	2000	450	100	2.25	97.88
16	3000	450	50	3.00	97.79
17	3000	450	70	2.14	98.06
18	3000	450	100	1.50	95.80

Test Methods

Archimedes-method is used to evaluate the relative density of 18Ni-300 specimens made by SLM. The weight of samples in air is test and subsequently in distilled water. Table 2 also shows the results of relative density.

The hardness of specimens before and after heat-treatment with all parameters are determined using both Rockwell C macro-hardness (HR 150-A) and Vickers micro-hardness tests (MH-5L, 500 g load is applied for 10 s).

Aging heat treatment is aimed to achieve improved mechanical properties. All samples are treated in vacuum heat treatment furnace with argon gas protection to avoid oxidation. The factorial design is set with 3 levels of temperature (733, 763, 793 K) and 4 levels of soaking time (1, 2, 4, 6 h).

The morphologies and microstructure of two different condition, the as-built and aged condition, are analyzed using both Optical Microscopy (OM, Leica DM IRM 3000) and Scanning Electron Microscopy (SEM, JEOL JXA-8100 and FEI QUANTA-650). The samples are polished by abrasive paper and diamond paste. To reveal the microstructure, the polished samples are etched in 10% nital for 15 s and a solution containing 2 g picric acid and 100 ml alcohol for 10 s. X-Ray Diffraction (XRD, SmartLab) is used to analyze the phases in samples underwent various heat-treatment.

Results and Discussion

Relative Density

Figure 4 shows the influence of energy density (*E*) on relative density of SLM processed 18Ni-300 samples. Majority of relative density of samples made by SLM are beyond 97% and energy density ranges from 1.2 to 6.0 J/mm^2. The experimental result shows that the density of specimens increases with energy imported to scanning track. The maximum relative density is up to 99.34% with energy density of 6.0 J/mm^2 (hatching space of 50 μm, laser power of 450 W, scanning velocity of 1500 mm/s), which is nearly full density. When hatching space fixes at 100 μm, the minimum relative density is only about 84% because the gap between two tracks is too wide to let molten metal to fill adequately.

Equation (2) is the fitting curve formula shown in Fig. 5.

$$y = A1 * \exp(-x/t1) + A2 * \exp(-x/t2) + y0 \tag{2}$$

where, y0 = 99.10611, A1 = −1.53123E10, t1 = 0.05602, A2 = −25.18149, t2 = 0.97032

The optical and SEM morphologies of cross-section (perpendicular to building direction) of sample 6 and sample 8 are represented in Fig. 5. Sample 6 with relative density of 92.53% shows a very high porosity, which are dark in Fig. 5a. It can be seen in SEM image (Fig. 5c) that irregular holes are filled with incomplete melted powders. That means there is not enough energy transmitted to metal powder to bond adjacent layers. In sample 8 (Fig. 5b) with relative density of 99.34%, no obvious cave is obtained. Metal powder melted entirely and lead to tight coupling between layers. Regular rounded holes in sample 8 (Fig. 5d) are caused by gas inclusion [9].

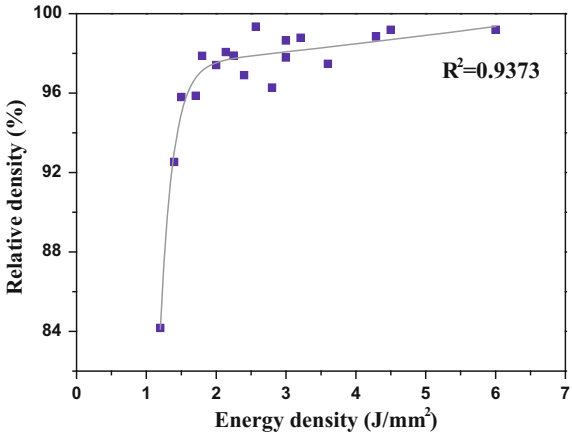

Fig. 4 Relationship between energy and relative density

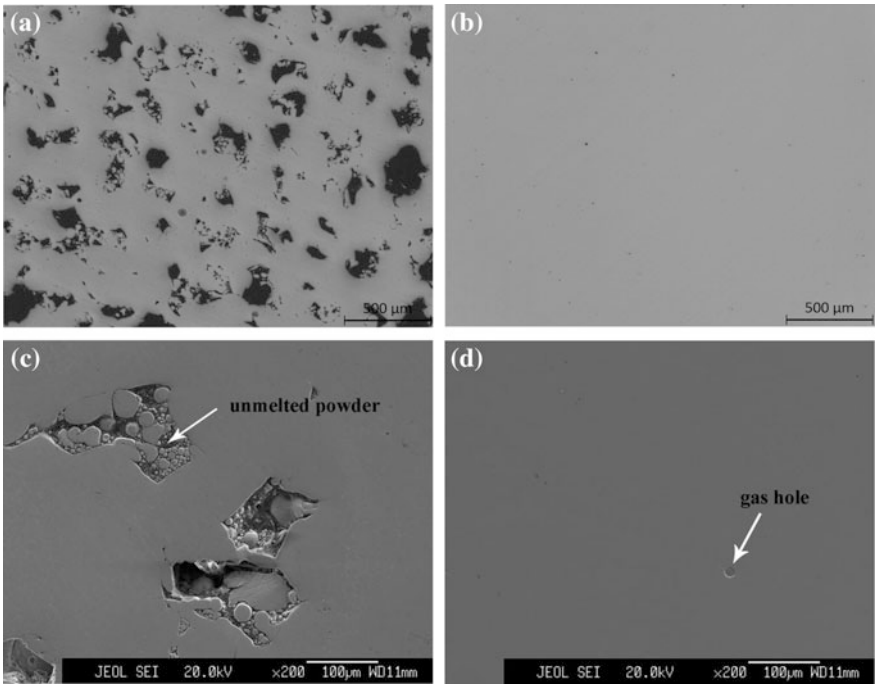

Fig. 5 Microgrphs showing pores: **a**, **c** OM and SEM of sample 6 with relative density of 92.53% and energy density of 1.40 J/mm^2; **b**, **d** OM and SEM of sample 8 with relative density of 99.34% and energy density of 2.57 J/mm^2

Hardness

The influence of hatching space *h* and scanning velocity *v* on macro-hardness of SLM processed 18Ni-300 samples are depicted in Fig. 6. At the constant laser power of 450 W, the increasingly hatching space results in low macro-hardness of samples. Similarly, hardness decreases with increasing scanning velocity while other process parameter held constant. In comparison with relative density, which is also shown in Fig. 6, there is a close connection between density and hardness. The sample with relative density of only 95.8% shows the lowest macro-hardness of 32 HRC while other samples with relative density above 98% possesses 38 HRC or higher macro-hardness. The reason is that the indentations of macro-hardness are so big that pressure spots can not avoid distribution of pores and other defects in samples with low density.

To make it possible to avoid the influence of pores on measurement of hardness, Vickers micro-hardness test is also carried out (shown in Fig. 7). Tiny pressure head can ensure to indent the consolidated area. All 18 groups of samples and as-cast specimen are tested. The micro-hardness of as-cast specimen is about 317 HV and the average hardness of various samples is in standard deviation of

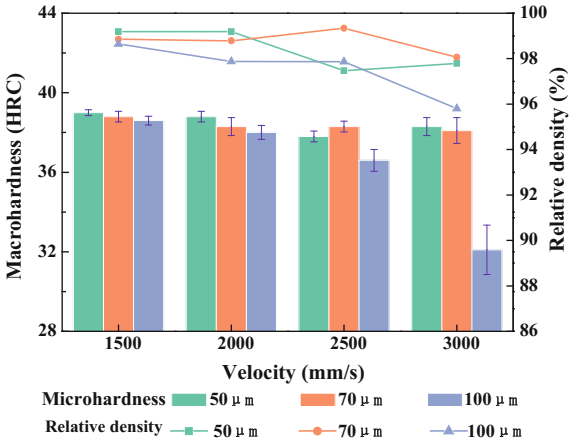

Fig. 6 Macro-hardness and relative density for samples of various process parameters (at constant laser power of 450 W)

368 ± 7 HV, which means an increase of about 50 HV compared with the as-cast value. No significant fluctuation of micro-hardness in samples fabricated by SLM under different parameters is observed.

Microstructure

The optical microscope (OM) photographs of the as-cast and SLMed specimen are as it shows in Fig. 8. The microstructures of these two kinds of processing methods are quite different from each other. Figure 8a, b show the typical as-cast structure with columnar crystal towards the center of sample where represents the most favorable heat dissipating direction. However, as for the SLMed samples, it is

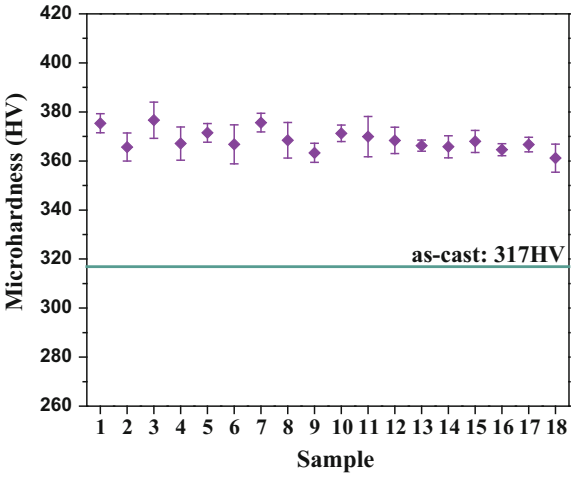

Fig. 7 Micro-hardness of 18Ni-300 samples fabricated by SLM

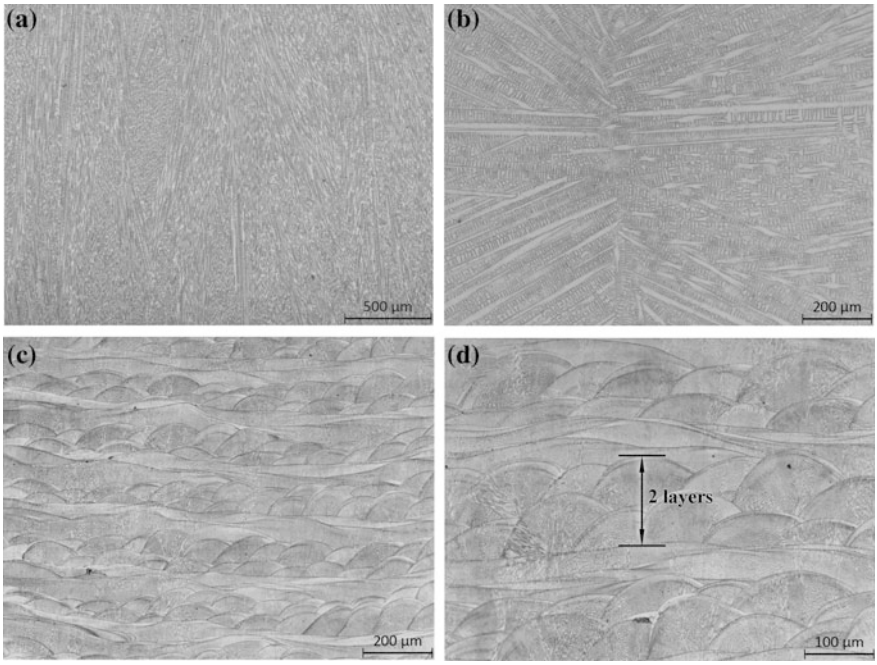

Fig. 8 Optical Microscope pictures of 18Ni-300 samples: **a**, **b** as-cast condition; **c**, **d** longitudinal sections of sample produced by SLM

evident from longitudinal section pictures (Fig. 8c, d) that scanning track overlapped each other to eliminate pores and caves. Sandwich construction formed because laser scanning direction rotated 90° every two layers. Due to ultra-shot cooling time, liquid metals re-solidify rapidly and not enough time is left to gas and inclusion to escape along building direction. Lath martensite is also prevented from generation. Figure 8d depicts the cellular/dendritic microstructure which is also shown clearly in scanning electron microscope (SEM) micrographs at different magnifications (Fig. 9).

Fine microstructure with intercellular space less than 1 μm contributes to superior mechanical properties such as hardness mentioned before [10]. Columnar crystalline grains could grow through several layers because of extraordinary thermal gradient. Grains grow in direction of heat dissipation and traversed boundaries of layers indicate that metallurgical bonding occurred between layers.

Aging Heat-Treatment

18Ni-300 maraging steel is a kind of high strength steel with high content of nickel and low carbon and also with other elements such as cobalt, molybdenum and

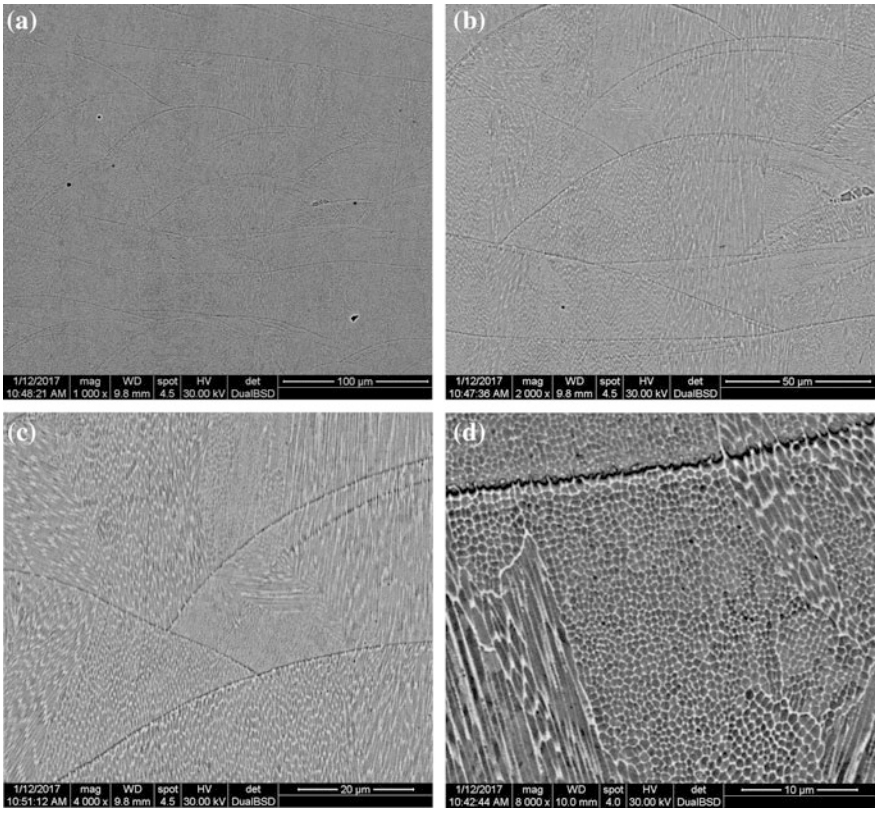

Fig. 9 SEM pictures of the longitudinal sections of a sample produced by SLM at different magnifications

titanium. Aging strengthening, as one of the most important strengthening ways for maraging steels, is indispensable to precipitate intermetallic compound on martensite matrix to improve strength and toughness. In this study, specimens fabricated by SLM with optimized process parameters (hatching spacing of 50 μm, scanning velocity of 1500 mm/s and laser power of 450 W) experiences aging heat treatment under different temperature (733, 763 and 793 K) and duration time (1, 2, 4, 6 h).

The results of micro-hardness of 18Ni-300 specimens undergoing heat-treatment are evaluated and depicted in Fig. 10. The samples fabricated by SLM are about 370 HV, while the hardness of specimen raised to 567–630 HV after aging heat-treatment. When the aging temperature fixes at 733 and 763 K, the hardness increases with extension of aging time and the maximum hardness could reach to 629 HV in terms of optimal heat-treatment selected as 4 h at 763 K.

However, with prolonging aging time to 6 h, the hardness becomes to drop. The reason of this phenomenon is that the precipitation of rich nickel second phase such as Ni_3Mo, Ni_3Ti strengthened the martensite which had a mass of dislocation to

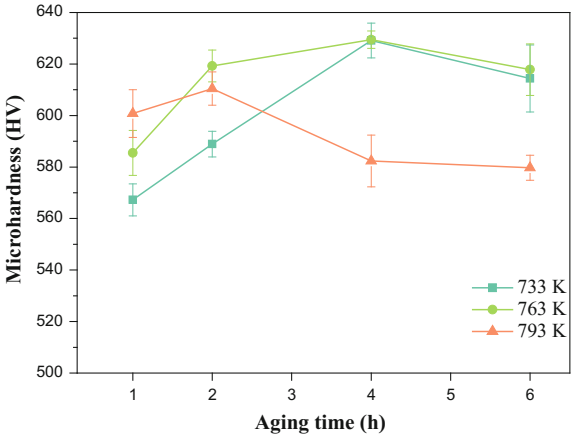

Fig. 10 Micro-hardness of 18Ni-300 samples fabricated by SLM with different aging parameters

provide nucleation sites [11]. The intermetallic compound could continue to precipitate with the prolonged duration. When the soaking time reached to 6 h, the over-aging resulted in the decrease of hardness due to metastable martensite reversing to ferrite and austenite. During that time, the austenite transformation temperature decreases with increasing content of nickel in martensite matrix because the generation of Fe_2Mo replaced Ni_3Mo and Ni_3Ti. When aging temperature reaches to 793 K, the hardness is affected by both the precipitation of strengthening phase and the austenite reversion which has the opposite effect. Under two or more hours of duration, the hardness dropped radically because of reversion and grains growth.

In microstructure pictures of samples underwent 4 h of aging treatment at different temperature shown in Fig. 11, martensite could be observed clearly. The quantity of martensite decreases with the rise of temperature. At 733 K, lath martensite is fine and homogeneous and can't be stopped by grain boundaries. At 763 K, the whole specimen is full of coarse martensite and layer morphology features cloud hardly be viewed. While the specimen was aged at 793 K which is beyond martensite starting temperature the volume of martensite decreased significantly.

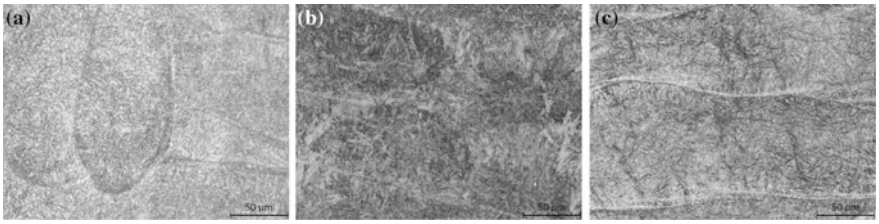

Fig. 11 Microstructure of SLM specimens after aging heat-treatment: **a** 4 h at 733 K; **b** 4 h at 763 K; **c** 4 h at 793 K

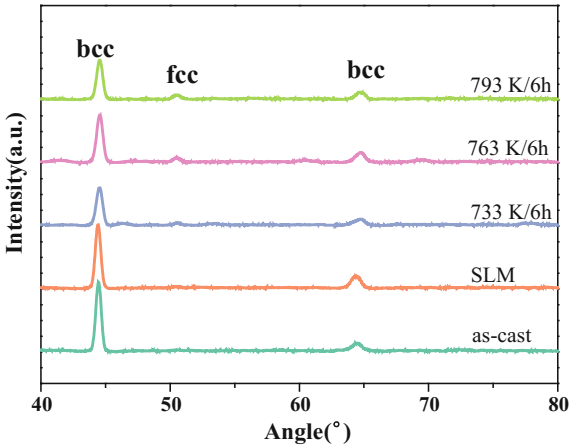

Fig. 12 X-Ray diffractograms of as-cast specimens and SLMed specimens aging at 733, 763 and 793 K for 6 h

Figure 12 shows the X-Ray diffractograms of SLMed and as-cast specimens. The comparison among the XRD results of samples aged at 733, 763 and 793 K for 6 h is also depicted in the same picture. There is few difference of phase composition between SLMed and as-cast conditions. Although martensite is the main phase and there is not any distinct austenite diffraction peaks and other precipitation such as Ni_3Mo and Ni_3Ti in these two conditions, probably because their volume fraction is too little to detect [12].

The applied aging treatment causes the appearance of austenite peaks and the intensity decrease of martensite peaks according to the results. Due to metastable martensite, austenite reversion could easily take place under long time aging. The content of austenite increases with the increase of aging temperature. This is attributed to the dissolution of Ni_3Mo and Ni_3Ti, which leads Ni release into matrix and lowers the austenite reversion beginning temperature.

Conclusions

This paper studies the 18Ni-300 maraging steel parts fabricated by selective laser melting process. The microstructure characteristics and mechanical properties of samples with and without aging treatment are investigated.

(1) The results show that there is a positive correlation relationship between energy density and relative density. Samples fabricated with an energy density as high as 6.0 J/mm^2 can lead to extremely high relative density of 99.34%. Unmelted powders and pores decrease the macrohardness of samples with low relative density because the indenter can not avoid the influence of these defects. Fine cellular/dendritic microstructure with intercellular space less than 1 μm is observed, which shows great difference with as-cast condition.

(2) After aging heat treatment, the microhardness increased from 370 HV to ~600 HV because of second phases such as Ni_3Mo and Ni_3Ti precipitated on the martensite matrix. When aging temperature reached to 793 K, the hardness is affected by both the precipitation of strengthening phase and austenite reversion which has the opposite effect. The XRD results show the appearance of austenite and the decrease of martensite.

Acknowledgements This work is supported by the Guangdong Key Laboratory of Metal Toughening Technology and Application (2014B030301012), Guangzhou Key Laboratory of Advanced Metal Structural Materials (201509010003), Major Science and Technology Projects in Guangdong Province(2014B01013100 and 2016B090914001), Special Environment and Ability Construction on Scientific Research Platform of Guangdong Academy of Science (2016GDASPT-0320), Project on the Integration of Industry, Education and Research of Guangdong Province (2014B090903016).

References

1. M. Simonelli, Y.Y. Tse, C. Tuck, Effect of the build orientation on the mechanical properties and fracture modes of SLM Ti–6Al–4V. Mater. Sci. Eng. A **616**, 1–11 (2014)
2. L. Hao, S. Dadbakhsh, O. Seaman, M. Felstead, Selective laser melting of a stainless steel and hydroxyapatite composite for load-bearing impant development. J. Mater. Process. Technol. **209**, 5793–5801 (2009)
3. X.L. Li, J.X. Ma, P. Li, Q. Chen, W.M. Zhou, 3D printing technology and its application trend. Process Autom. Instrum. **35**(1), 1–5 (2014)
4. K. Kempen, E. Yasa, L. Thijs, J.P. Kruth, J.V. Humbeeck, Microstructure and mechanical properties of Selective Laser Melted 18Ni-300 steel. Phys. Proc. **12**, 225–263 (2011)
5. R. Casati, J. Lemke, M. Vedani, Microstructure and fracture behavior of 316L austenitic stainless steel produced by selective laser melting. J. Mater. Process. Technol. **32**, 738–744 (2016)
6. T.H. Becker, D. Dimitrov, The achievable mechanical properties of SLM produced Maraging Steel 300 components. Rapid Prototyping J. **22**, 487–494 (2016)
7. G. Casalino, S.L. Campanelli, N. Contuzzi, A.D. Ludovico, Experimental investigation and statistical optimisation of the selectivelaser melting process of a maraging steel. Opt. Laser Technol. **65**, 151–158 (2015)
8. L. Thijs, F. Verhaeghe, T. Craeghs, J.V. Humbeeck, J.P. Kruth, A study of the microstructural evolution during selective laser melting of Ti–6Al–4V. Acta Mater. **58**, 3303–3312 (2010)
9. C. Panwisawas, C.L. Qiu, Y. Sovani, J.W. Brooks, M.M. Attallah, H.C. Basoalto, On the role of thermal fluid dynamics into the evolution of porosity during selective laser melting. Scr. Mater. **105**, 14–17 (2015)
10. Q.S. Wei, S. Li, C. Han, W. Li, L.Y. Cheng, Selective laser melting of stainless-steel/nano-hydroxyapatite composites for medical applications: microstructure, element distribution, crack and mechanical properties. J. Mater. Process. Technol. **222**, 444–453 (2015)
11. S.H. Nedjad, S. Meimandi, A. Mahmoudi, T. Abedi, S. Yazdani, H. Shirazi, M.N. Ahmadabadi, Effect of aging on the microstructure and tensile properties of Fe–Ni–Mn–Cr maraging alloys. Mater. Sci. Eng., A **501**, 182–187 (2009)
12. J.M. Pardal, S.S.M. Tavares, M.P.C. Fonseca, Study of the austenite quantification by X-ray diffraction in the 18Ni–Co–Mo–Ti maraging 300 steel. J. Mater. Sci. **41**, 2301–2307 (2006)

Influence Law of Process Parameters on the Continuity and Dimensional Uniformity of 7075 Aluminum Alloy Single Tracks Manufactured by Selective Laser Melting

Xuefeng Liu, Ang Li, Baoqiang Yin, Bo Yu and Yang Yan

Abstract 7075 aluminum alloy powders were used as raw materials. The selective laser melting single tracks forming experiment of 7075 aluminum alloy was carried out at scanning speed of 50–700 mm s^{-1}, laser power of 80–100 W. The continuity and dimensional uniformity of selective laser melting 7075 aluminum alloy single tracks were characterized by OM and SEM. The influence law of laser power and scanning speed on the continuity and dimensional uniformity of selective laser melting 7075 aluminum alloy single tracks were revealed. The results show that: when the laser power was increased from 80 to 100 W and the scanning speed of 50–700 mm s^{-1}, the continuity and dimensional uniformity of selective laser melting 7075 aluminum alloy single tracks were improved, the morphology was changed from discrete irregular particles to continuous single line. When the laser power was 80 W, the continuity of selective laser melting 7075 aluminum alloy 3D printing single tracks was deteriorated, but the dimensional uniformity was improved, with the increases of scanning speed from 100 to 700 mm s^{-1}. When the laser power was 100 W, the continuity and dimensional uniformity of the 7075 aluminum alloy selective laser melting 3D printing single tracks were improved with the increases of scanning speed from 50 to 300 mm s^{-1}; the continuity and dimensional uniformity of the 7075 aluminum alloy selective laser melting 3D printing single tracks reduced with the increase of scanning speed from 500 to 700 mm s^{-1}. Laser power has a great impact on the continuity and dimensional uniformity of 7075 aluminum alloy selective laser melting 3D printing single tracks, high laser power and low scanning speed are beneficial to obtaining continuous and dimensional homogeneous of the 7075 aluminum alloy single tracks.

X. Liu (✉) · A. Li · B. Yin · B. Yu · Y. Yan
School of Materials Science and Engineering, University of Science and Technology Beijing, Beijing 100083, China
e-mail: liuxuefengbj@163.com

X. Liu
Beijing Laboratory of Metallic Materials and Processing for Modern Transportation, University of Science and Technology Beijing, Beijing 100083, China

© Springer Nature Singapore Pte Ltd. 2018

Y. Han (ed.), *Advances in Materials Processing*, Lecture Notes in Mechanical Engineering, https://doi.org/10.1007/978-981-13-0107-0_23

Keywords 7075 aluminum alloy · Selective laser melting · Process parameters Single line shape · Influence law

Introduction

7075 aluminum alloy is the high strong commercial aluminum alloys which are widely used in the aerospace, transportation and automobile manufacturing and other fields [1]. However, most parts of 7075 aluminum alloys are manufactured by conventional techniques such as plastic processing and precision machining. When the traditional plastic processing method is used to form 7075 aluminum alloy, there are several issues in terms of complex forming equipment, simple geometry structural as well as materials waste [2]. Selective laser melting 3D printing technology has the advantages of easily forming complex structure parts, efficient use of raw material and so on.

At present, the Ti_6Al_4V, IN718 have been used to fabricate metal components by selective laser melting technology [3, 4]. However, selective laser melting of aluminum alloy is difficult, because the low density, low laser absorption rate, high thermal conductivity and poor flowability [5]. There are some problems that the continuity of the forming part is difficult to be ensured, the dimensional accuracy is poor and the density is not high, when selective laser melting 3D printing technology was used to manufacture aluminum alloy parts. Aboulkhair et al. [6] studied the effect of the scanning speed and the layer thickness on the single tracks of $AlSi_{10}Mg$ by using the single variable method. They found that increasing the scanning speed will lead to the decrease of the width of the single pass forming part and the increase of the height; with the increases of layer thickness, the single pass forming part produced balling defects, which reduced the continuity of single pass forming part. Yadroitsev et al. [7] investigated the effect of linear energy input on the morphology of single pass forming part and found that the line width of single pass forming part was similar, when the energy density was the same. The scanning strategy in lengthwise direction was conducive to dimensional precision control. Shi et al. [8] investigated the main factors influencing the dimensional characteristics of single pass forming part of selective laser melting 3D printing by using the method of linear regression analysis. They found an unstable melt tracks reduces the density of the samples. Yadroitsev et al. [9] further analyzed the effect of different contact widths on the stability of single pass forming parts of selective laser melting 3D printing. They considered that the larger the contact width, the more stable the single pass forming parts, and the more continuous the single pass forming parts. Researches have shown that the size characteristics and morphology of selective laser melting single tracks have a significant effect on the dimensional accuracy and density of the selective laser melting 3D printing aluminum alloy parts.

So far, very few works have been focused on selective laser melting of 7075 aluminum alloys. Kaufmann et al. [10] investigated the effect of the scanning speed and the laser power on the density of 7075 aluminum alloy. They found that there

were many porosity in the selective laser melting 7075 aluminum alloys specimens, when the laser power is less than 150 W. However the continuity and dimensional uniformity of 7075 aluminum alloy single pass forming parts manufactured by selective laser melting haven't been clear yet.

The properties of a part produced by selective laser melting technology depend strongly on the properties of each single track. Therefore, this paper mainly carried out selective laser melting 3D printing single pass forming experiment of 7075 aluminum alloy. The influence law of laser power and scanning speed on the continuity and dimensional uniformity of selective laser melting single pass forming parts of 7075 aluminum alloy were studied, which lays the foundation for the continuity and dimensional uniformity selective laser melting 3D printing single pass forming part of 7075 aluminum alloy.

Material and Experimental Procedures

The material used in the experiment was gas-atomised 7075 aluminum alloy powder **produced b*y ShenZhen Minatech Co., Ltd. The average particle size of the 7075 aluminum alloy powder is 27.7 μm. The morphology is shown in Fig. 1. The morphology is spherical shape. The chemical compositions of the 7075 aluminum alloy powder as shown in Table 1.

Selective laser melting equipment was utilized in this study, which was manufactured by Guangdong Hanbang Laser Technology Co., Ltd. The forming volume is $100 \times 100 \times 150$ mm^3. The equipment used a fiber laser with a maximum power of 100 W, a wavelength of 1060 nm and a minimum spot diameter of 20 μm. The substrate used in the experiment was 7075 aluminum alloy. It was cleaned with alcohol before used, and the substrate was not preheated.

In the conditions of laser power of 80–100 W, scanning speed of 50–700 mm s^{-1}, powder layer thickness of 50 μm, 10 sets of 7075 aluminum alloy selective laser

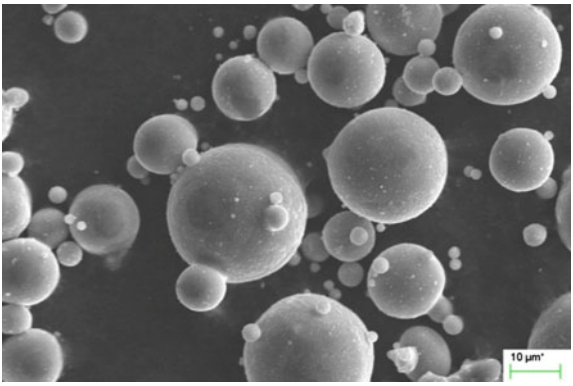

Fig. 1 Morphology of 7075 aluminum alloy powder

Table 1 Chemical compositions of the 7075 aluminum alloy powder

Element	Zn	Mg	Cu	Cr	Si	Mn	Fe	Ti	Al
Content [wt%]	5.45	2.46	1.62	0.22	<0.1	<0.1	<0.1	<0.05	Bal.

Table 2 Processing parameters used in this study

No.	Laser power [W]	Scan speed [mm s^{-1}]
1	80	100
2	80	300
3	80	500
4	80	700
5	90	50
6	100	50
7	100	100
8	100	300
9	100	500
10	100	700

melting 3D printing single pass forming experiment were carried out, the specific process parameters as shown in Table 2.

The morphology of the 7075 aluminum alloy powder and the surface morphology of the single pass forming part were observed by ZEISS EVO 18 scanning electron microscopy. The longitudinal section morphology of the single pass forming part was observed by an Olympus BX53 optical microscope. When observing the longitudinal section morphology of the single pass forming part, the metallographic sample was first etched with Keller's reagent, and then the morphology was observed by optical microscope. The dimensional uniformity of the single pass forming part was represented by a normal distribution probability graph. The smaller the mean square deviation is, the more concentrated of the data distribution, the better the dimensional uniformity of the single pass forming part.

Results and Discussion

Continuity of Single Pass Forming Part

The surface morphology of 7075 aluminum alloy selective laser melting 3D printing single pass forming part at the laser power of 80 W and different scanning speed ranging from 100 to 700 mm s^{-1} as shown in Fig. 2. It can see from Fig. 2, the low laser absorption rate and the high thermal conductivity of 7075 aluminum alloy power, leading to most of the energy was dissipation; at the same time, due to laser power is low, the droplet can not maintain the molten state in the process of laser movement [11]. The melt shrinks under the action of the surface tension, forming a

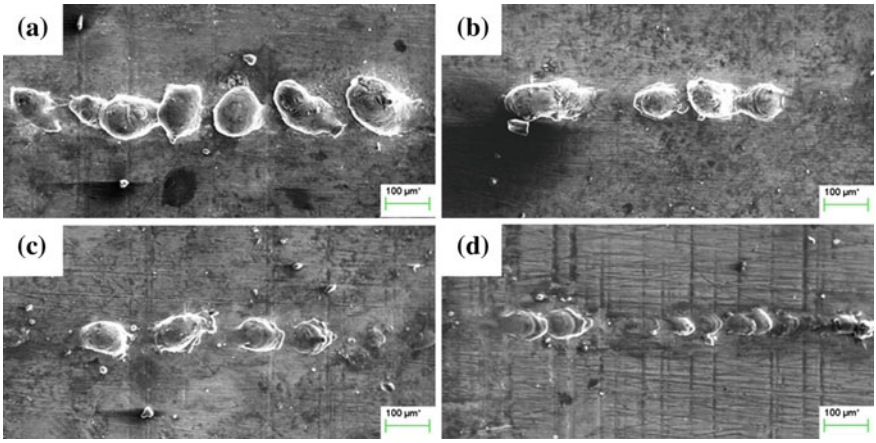

Fig. 2 Surface morphology of single pass forming part at the laser power of 80 W and different scanning speed: **a** v = 100 mm s^{-1}; **b** v = 300 mm s^{-1}; **c** v = 500 mm s^{-1}; **d** v = 700 mm s^{-1}

number of irregular particles along the single pass forming path, breaking the continuity of the single line. In the range of 4 mm, the number of irregular particles of 7075 aluminum alloy selected laser melting 3D printing single pass forming part at the laser power of 80 W and different scanning speed as shown in Fig. 3. The average spacing of irregular particles in single pass forming part at different scanning speed is shown in Fig. 4. It can see from Figs. 3 and 4 that with the increase of the scanning speed, the number of irregular particles in the 7075 aluminum alloy selective laser melting 3D single pass forming part is gradually decreasing, and the average spacing between the irregular particles is gradually increasing. At the scanning speed of 100 mm s^{-1}, the number of irregular particles is 23, the average spacing between the irregular particles is 80.5 μm. When the scanning speed is increased to 300 mm s^{-1},

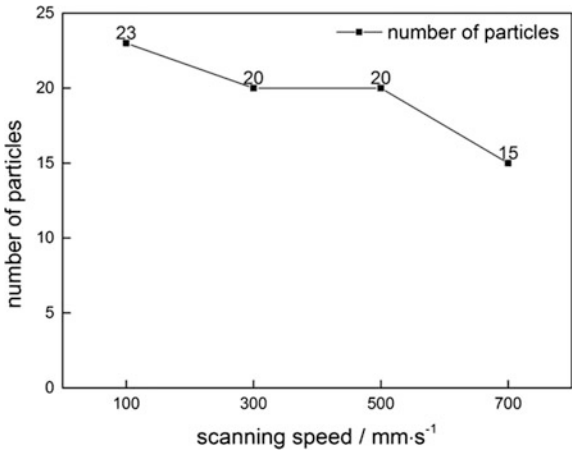

Fig. 3 Effect of scanning speed on the number of particles

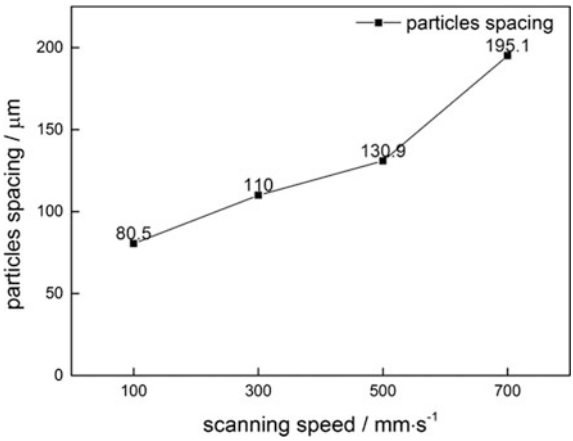

Fig. 4 Effect of scanning speed on particles spacing

the number of irregular particles is reduced to 20, and the average spacing between the irregular particles is increased to 110.0 μm. When the scanning speed is increased to 500 mm s^{-1}, the number of irregular particles is not reduced, but the average spacing between the irregular particles increases to 130.9 μm, due to the decrease of the energy density. When the scanning speed is increased to 700 mm s^{-1}, the energy density further decreased, the number of irregular particles is further reduced to 15, the average spacing between the irregular particles is increased to 195.1 μm. When the laser power is low, 7075 aluminum alloy powder can not be completely melted, so that the selected laser melting 3D single pass forming part is broken into a number of irregular particles, which seriously reducing the continuity of single pass forming part. The greater the spacing between the particles, the more severe the cleavage of the single pass forming part, the worse the continuity of the single pass forming part.

The surface morphology of 7075 aluminum alloy selective laser melting 3D printing single pass forming part at the scanning speed of 50 mm s^{-1} and different laser power as shown in Fig. 5. It can see from the comparison of Figs. 2 and 5 with the increases of laser power, the morphology of selective laser melting 3D printing single pass forming part is changed from irregular particles to single line with break points. In the range of 6 mm, the number of break points of 7075 aluminum alloy

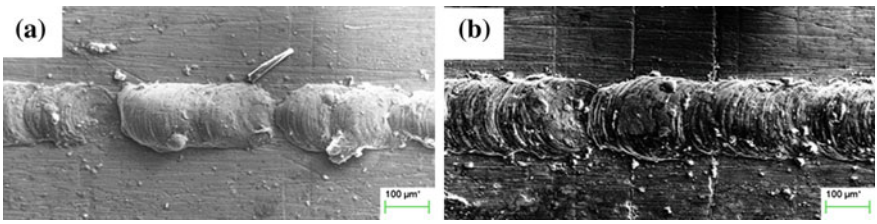

Fig. 5 Surface morphology of single pass forming part at the scanning speed of 50 mm s^{-1} and different laser power: **a** P = 90 W; **b** P = 100 W

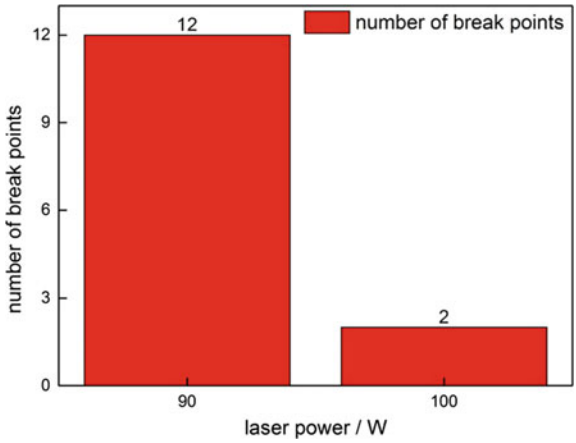

Fig. 6 Effect of laser power on the number of break points

selective laser melting 3D print single pass forming part at different laser power as shown in Fig. 6. When the laser power is 90 W, the number of break points of single pass forming part is 12; when the laser power is increased to 100 W, the number of break points of single pass forming part is reduced to 2. It can be seen that increasing of laser power in the process of 7075 aluminum alloy laser melting 3D printing single pass forming part is beneficial to improve the continuity of single pass forming part.

The surface morphology of 7075 aluminum alloy selective laser melting 3D printing single pass forming part at the laser power of 100 W and different scanning speed ranging from 100 to 700 mm s^{-1} as shown in Fig. 7. It can see from Fig. 7 that the 7075 aluminum alloy powder was fully melted at the laser power of 100 W.

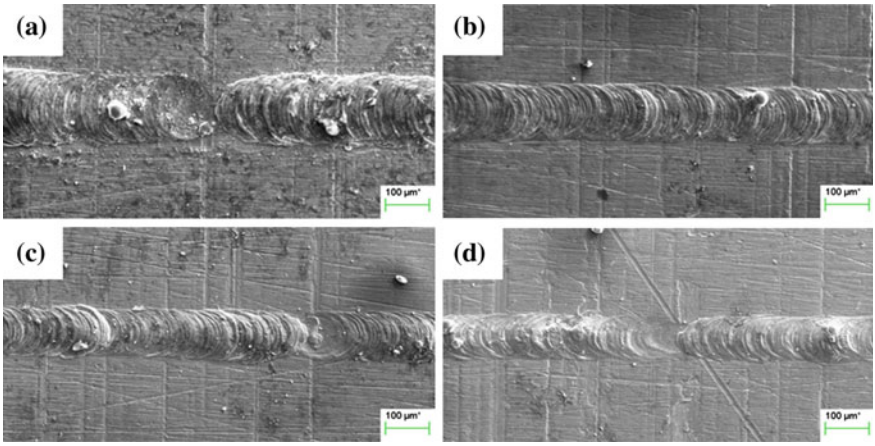

Fig. 7 Surface morphology of single pass forming part at the laser power of 100 W and different scanning speed: **a** v = 100 mm s^{-1}; **b** v = 300 mm s^{-1}; **c** v = 500 mm s^{-1}; **d** v = 700 mm s^{-1}

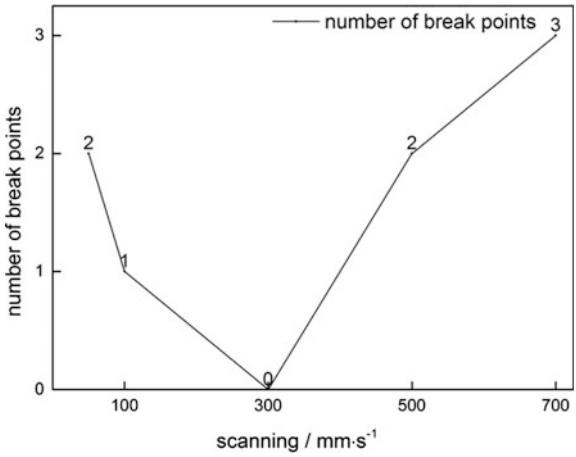

Fig. 8 Effect of scanning speed on the number of break points

The temperature of the liquid phase in the molten pool is higher and melt flowability becomes better, due to the increase of the laser energy density. The continuity of the single pass forming part is better. In the range of 6 mm, the number of break points in 7075 aluminum alloy selective laser melting 3D printing single pass forming parts at different scanning speed as shown in Fig. 8. It can see from Fig. 8, with the increase of scanning speed, the number of break points of 7075 aluminum alloy selective laser melting 3D printing single pass forming part first decrease and then increase. At the scanning speed of 50 mm s^{-1}, the number of break points in single line is 2. When the scanning speed is increased to 100 mm s^{-1}, the number of break points in single line is reduced to 1. When the scanning speed is increased to 300 mm s^{-1}, the number of break points in single line is reduced to zero. when the scanning speed further is increased to 500 mm s^{-1}, the number of break points in single line is increased to 2. When the scanning speed is increased to 700 mm s^{-1}, the number of break points in single line is increased by 3. When the laser power is 100 W, a single line with better continuity can be formed in the scanning speed range of 50–700 mm s^{-1}, which facilitates the formation of high density parts. In the low speed scanning, the time of the reaction of the laser with the metal powder is long. There is more liquid phase in the molten pool. Break points occur in the single pass forming part for the reason that the metal melt fluctuate within the molten pool driven by the surface tension gradient, gravity, and evaporation. When the scanning speed is increased, the time of the reaction of the laser with the metal powder was decreased. The content of liquid phase in the molten pool decreases. At the same time, due to the thermal conductivity of aluminum alloy is high [12], the liquid phase in the molten pool is rapidly solidified, so the break points in the single pass forming part is reduced to 0 at 300 mm s^{-1}. When the scanning speed is further increased, the energy density of laser beam decreases and the liquid phase can not spread sufficiently. Break points occur in the local unstable region of the single pass forming part, and therefore the number of break points in the single pass forming part is increased.

Dimensional Uniformity of Single Pass Forming Part

The particles dimensional uniformity of 7075 aluminum alloy selective laser melting 3D printing single pass forming part at the laser power 80 W, and the different scanning speed ranging from 100 to 700 mm s^{-1} as shown in Fig. 9. In order to compare the particles dimensional uniformity, the normal distribution probability graph was translated. In the range of 4 mm, the size of the irregular particles in 7075 aluminum alloy selective laser melting single pass forming part was measured, and the distribution of the size of irregular particles was analyzed by normal distribution, and the mean square deviation of irregular particles size was calculated. It can see from Fig. 9, with the increases of scanning speed, the mean square deviation of the irregular particles size gradually is decreased and the dimensional uniformity is gradually increased. At the scanning speed of 100 mm s^{-1}, the mean square deviation of the irregular particles size is 39.38 μm, when the scanning speed is low, the molten pool adsorbs the surrounding aluminum alloy powder, which leading to instability fluctuation of the liquid phase. During the solidification process, the metal melt is split into irregular particles so that the dimensional uniformity of the irregular particles deteriorates. When the scanning speed is increased to 300 mm s^{-1}, due to the laser energy density decreases, the amount of powder melting is reduced, and the fluctuation degree of liquid phase is weakened, so the mean square deviation of the irregular particles size is reduced to 28.89 μm. When the scanning speed is increased to 500 mm s^{-1}, the liquid phase is rapidly solidified into the solid phase, because of good thermal conductivity of aluminum alloy. The fluctuation degree of liquid phase is small so the mean square deviation of irregular particles size is reduced to 20.63 μm. When the scanning speed is further increased to 700 mm s^{-1}, because the energy input of the laser beam becomes low, the solidification speed is accelerated, leading to the mean square deviation of irregular particles size is reduced to 18.85 μm. In the process of 7075 aluminum alloy selective laser melting 3D printing single pass forming part, if the 7075 aluminum alloy powder is not completely melted, the amount of irregular particles is gradually reduced, and the dimensional uniformity of the irregular particles in the single pass forming part is increased, with the increases of scanning speed.

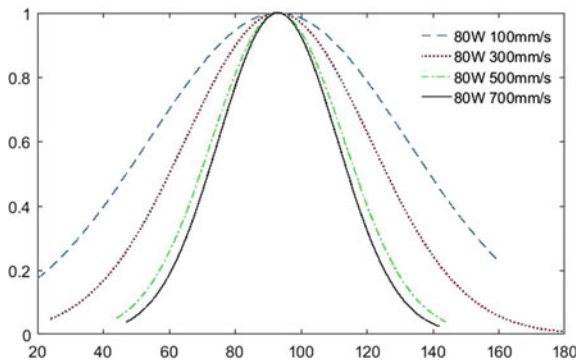

Fig. 9 Normal distribution probability graph of the particles size at the laser power of 80 W and different scanning speed

The line width uniformity of 7075 aluminum alloy selective laser melting 3D print at scan speed 50 mm s^{-1}, and different laser power as shown in Fig. 10. During the experiment, 16 sets of data were measured. The result of normal distribution analysis showed that: When the laser power is 90 W, the average width of the single line of the 7075 aluminum alloy is about 158 μm, and the mean square deviation of line width is 12.33 μm. When the laser power is increased to 100 W, the average line width of single line of the 7075 aluminum alloy is about 182 μm, the mean square deviation of line width is 10.76 μm. It can see from Fig. 10 that with increases of laser power, the line width uniformity of 7075 aluminum alloy selective laser melting 3D print single pass forming part is improved, but the size of single pass forming part still have a large fluctuation, which is not conducive to the control of dimensional accuracy of components.

The line width uniformity of 7075 aluminum alloy selective laser melting 3D printing single line at laser power 100 W and different scanning speed as shown in Fig. 11. When laser power is 100 W, with the increases of scanning speed, the mean square deviation of 7075 aluminum alloy selective laser melting 3D printing single line is decreased first and then increased. At the scanning speed of 50 mm s^{-1}, the mean square deviation of single line width is 10.76 μm, because the scanning speed is low, there is a small hole in the bottom of the molten pool, as shown in Fig. 12a. The escape of metal vapor in the pores causes the fluctuation of the liquid phase in the melt pool [13], resulting in a decrease in the uniformity of the single line width. When the scanning speed is increased to 100 mm s^{-1}, the average line width of the single line is 156 μm, the mean square deviation of the line width is reduced to 5.21 μm. We noticed that the average line width is close to the fifth set of experiments namely laser power 90 W, scanning speed 50 mm s^{-1}, but the size uniformity of the fifth set of experiments is bad. Therefore, when the size characteristic is same, in order to improve the dimensional accuracy, we should choose the process with good dimensional uniformity. When the scanning speed is increased to 300 mm s^{-1}, the average line width of single line is 135 μm, the mean square deviation of single line width is 4.46 μm. At the scanning speed of 100–300 mm s^{-1}, it can see from Fig. 12b, c that as the scanning speed increased, the shape of the molten pool becomes slender and no holes are formed at the bottom of the molten pool. The line

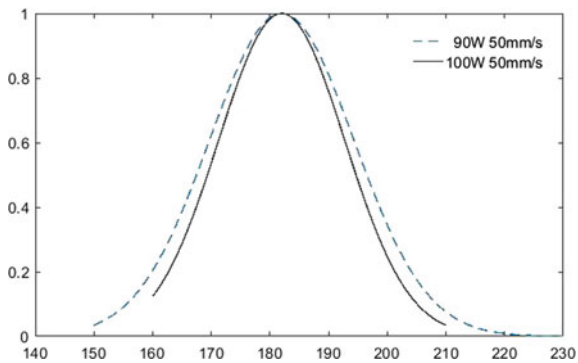

Fig. 10 Normal distribution probability graph of single line width at scanning speed 50 mm s^{-1} and different laser power

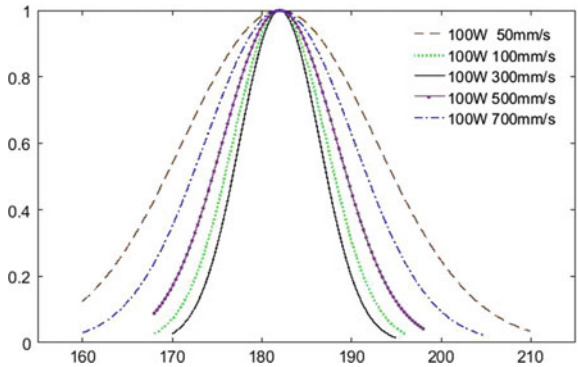

Fig. 11 The normal distribution probability graph of single line width at laser power 100 W and different scanning speed

width uniformity is increased. When the scanning speed is increased to 500 mm s^{-1}, the average line width of single line is reduced to 114 μm, the mean square deviation of line width is 6.35 μm; When the scanning speed is increased to 700 mm s^{-1}, the average line width of the single line is reduced to 102 μm, and the mean square deviation of the line width is 8.29 μm. At the scanning speed of 500–700 mm s^{-1}, as the scanning speed is increased, it can be seen from Fig. 12d, e that the penetration depth of the molten pool is lowered and the stability of the molten pool is decreased, leading to a large fluctuations. of single line width in solidification. With the increases of scanning speed, the single line width of the 7075 aluminum alloy

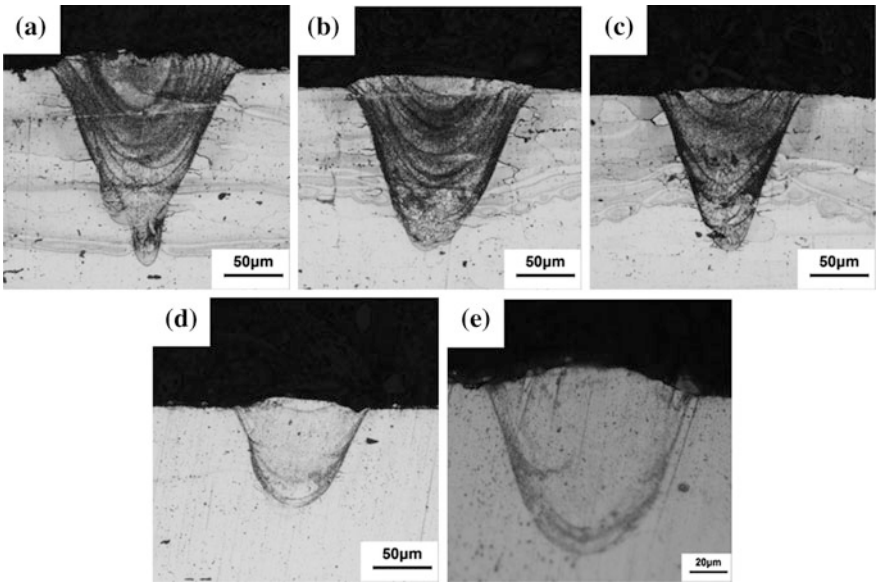

Fig. 12 Molten pool morphology of laser power 100 W and different scanning speed: **a** v = 50 mm s^{-1}; **b** v = 100 mm s^{-1}; **c** v = 300 mm s^{-1}; **d** v = 500 mm s^{-1}; **e** v = 700 mm s^{-1}

selective laser melting 3D printing single pass forming part is gradually decreased. This is because as the scanning speed increased, the melting temperature field becomes slender, so the width of the single line is gradually reduced [14].

Conclusions

(1) In the 7075 aluminum alloy selective laser melting 3D printing process, the laser power has a great impact on the continuity and dimensional uniformity of the single pass forming part. When the laser power is 100 W, the continuity and dimensional uniformity of the 7075 aluminum alloy selective laser melting 3D printing single pass forming part is superior to that of the single pass forming part when the laser power is 80 W.
(2) In the 7075 aluminum alloy selective laser melting 3D printing process, the high laser power and slow scanning speed are beneficial to obtaining continuous and dimensional uniformity of 7075 aluminum alloy single line. Under the condition of laser power of 100 W and scanning speed of 300 mm s^{-1}, the continuity and dimensional uniformity of 7075 aluminum alloy selective laser melting 3D printing single pass forming part are better, the single pass forming part without break points, the mean square deviation of the line width is 4.46 μm.
(3) In the 7075 aluminum alloy selective laser melting 3D printing process, when the laser power is small, the size characteristics and dimensional uniformity of single pass forming part need to take into account. The small mean square deviation is conducive to access to high precision parts.

Acknowledgements This research was financially supported by the National High Technology Research and Development Program of China (2015AA034304).

References

1. G. Chen, Y.M. Zhang, Z.M. Du, Mechanical behavior of Al–Zn–Mg–Cu alloy under tension in semi-solid state. Trans. Nonferrous Met. Soc. China **26**, 643–648 (2016)
2. V. Kilicli, N. Akar, M. Erdogan, K. Kadir, Tensile fracture behavior of AA7075 alloy produced by thixocasting. Trans. Nonferrous Met. Soc. China **26**, 1222–1231 (2016)
3. L. Thijs, F. Verhaeghe, T. Craeghs, J.V. Humbeeck, J.P. Kruth, A study of the microstructural evolution during selective laser melting of Ti–6Al–4V. Acta Mater. **58**, 3303–3312 (2010)
4. K.N. Amato, S.M. Gaytan, L.E. Murr, E. Martinez, P.W. Shindo, J. Hernandez, S. Collins, F. Medina, Microstructures and mechanical behavior of Inconel 718 fabricated by selective laser melting. Acta Mater. **60**, 2229–2239 (2012)
5. M.L.M. Sistiaga, R. Mertens, B. Vrancken, X.B. Wang, B.V. Hooreweder, J.P. Kruth, J.V. Humbeeck, Changing the alloy composition of Al7075 for better processability by selective laser melting. J. Mater. Process. Tech. **238**, 437–445 (2016)

6. N.T. Aboulkhair, I. Maskery, C. Tuck, I. Ashcroft, N.M. Everitt, On the formation of $AlSi_{10}Mg$ single tracks and layers in selective laser melting: microstructure and nano-mechanical properties. J. Mater. Process. Tech. **230**, 88–98 (2016)
7. I. Yadroitsev, P. Bertrand, I. Smurov, Parametric analysis of the selective laser melting process. Appl. Surf. Sci. **253**, 8064–8069 (2007)
8. X.Z. Shi, S.Y. Ma, C.M. Liu, Q.R. Wu, Parameter optimization for Ti–47Al–2Cr–2Nb in selective laser melting based on geometric characteristics of single scan tracks. Opt. Laser Technol. **90**, 71–79 (2017)
9. I. Yadroitsev, A. Gusarov, I. Yadroitsava, I. Smurov, Single track formation in selective laser melting of metal powders. J. Mater. Process. Tech. **210**, 1624–1631 (2010)
10. N. Kaufmann, M. Imran, T.M. Wischeropp, C. Emmelmann, S. Siddique, F. Walther, Influence of process parameters on the quality of aluminium alloy EN AW 7075 using selective laser melting (SLM). Phys. Proc. **83**, 918–926 (2016)
11. R.C. Cao, *Study on the Fabrication Process of 18Ni 300 Maraging Steel by Selective Laser Melting and the Experimental Analysis on Laser Melting of Metal Powders* (Shanghai Jiao Tong University, Shanghai, 2014)
12. N.T. Aboulkhair, N.M. Everitt, I. Ashcroft, C. Tuck, Reducing porosity in $AlSi_{10}Mg$ parts processed by selective laser melting. Additi. Manuf. **4**, 77–86 (2014)
13. S.C. Wu, Z.T. Zhu, X.W. Li, *Laser Welding and Evaluation of Aluminum Alloy* (National Defense Industry Press, Beijing, 2014)
14. Z.Y. Du, *Fundamentals of Welding Science: Fundamentals of Material Welding* (China Machine Press, Beijing, 2012)

Void Evolution Law and Its Control in Steel Ingot Forging

Xin-li Wen, Qing-quang Zhang and Chao-lei Zhang

Abstract In order to figure out the void evolution law and its control technology during forging, systematic study was carried out by both numerical simulation method and industrial test. Firstly, void evolution during forging along the height direction and the width direction of the ingot was simulated by deform-3D which is a widely used numerical simulation software. Subsequently, the void closure law by single direction forging and double direction forging was analysed comparatively, the results showed that the single direction forging was more beneficial to close the void. Based on the above study, the new forging technology to control void defect was proposed and industrial experiment was carried out. The results showed that the void defect in the forging produced by the new technology was lighter than that by the original.

Keywords Void evolution · Common defect · Steel ingot · Forging
Void closure

Introduction

In important civilian and military equipment, large size forging have been widely used for significant parts, for example, bearings, gears, shafts. Because of bad working environment for the parts, no flaw is allowed in large size forging [1]. In general, the quality of large section forging in developed countries is better than that

X. Wen (✉) · Q. Zhang
Beijing Beiye Functional Materials Corporation, Beijing 100192, China
e-mail: 810439486@qq.com

Q. Zhang
e-mail: 1320050765@qq.com

C. Zhang
School of Materials Science and Engineering, University of Science and Technology Beijing, Beijing 100083, China
e-mail: 258052706@qq.com

© Springer Nature Singapore Pte Ltd. 2018

Y. Han (ed.), *Advances in Materials Processing*, Lecture Notes in Mechanical Engineering, https://doi.org/10.1007/978-981-13-0107-0_24

of our state [2]. Loose (void) is one of the most common and dangerous types of defects. In an important domestic special steel factory, the loose flaw endanger the quality of large section forging accounted for 20% of all kinds of defects. Many previous studies on loose focused on void evolution behavior during forging, but studies on the control technology of voids were rare [3–6]. It has important practical meaning to study both the void evolution law and its control in ingot forging.

In this paper, in order to explore the control technology for voids, the numerical simulation software deform-3D was used. First of all, void evolution during forging along the height direction and the width direction of the ingot was simulated respectively. Subsequently, the void closure law by single direction forging and double direction forging was analysed comparatively, the results showed that the single direction forging was more beneficial to close the void. Based on the above study, the new forging technology to control void defect was proposed and industrial experiment was carried out. The void defect in the two forgings produced respectively by the original and newly proposed forging technology were inspected, the results showed that the void defect in the forging produced by the new technology was lighter than that by the original. The new forging technology has been successfully applied in industry.

Experimental Materials and Method

Experimental Materials

The tested steel is 20Cr13 which is a kind of martensite stainless steel. Forging diameter is 300 mm. The compositions of the 20Cr13 are shown in Table 1.

Experimental Method

The numerical simulation software deform-3D was used to simulate the evolution law of the voids in steel ingot. The geometric model of the steel ingot was shown in Fig. 1a. In oder to save simulation time, the 1/8 model of the steel ingot was used and nine cavities were drawn in the cross section as shown in Fig. 1b. The 'X' represents the width direction and the 'Z' represents the height direction of the

Table 1 The chemical compositions of 20Cr13 (mass fraction, %)

C	Mn	S	P	Si	Balance
0.19–0.21	0.55–0.65	≤ 0.02	≤ 0.02	0.25–0.40	Iron

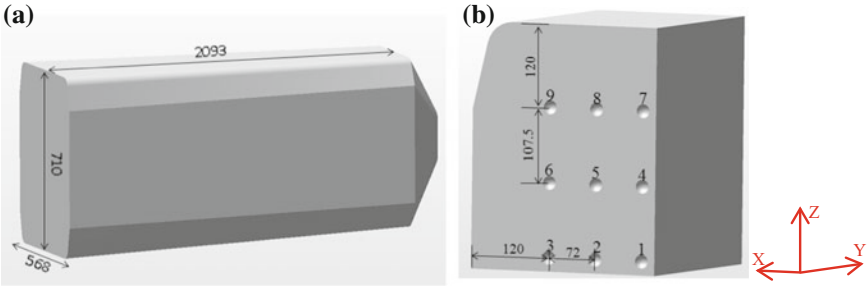

Fig. 1 **a** Geometric model of the steel ingot; **b** 1/8 model of the steel ingot

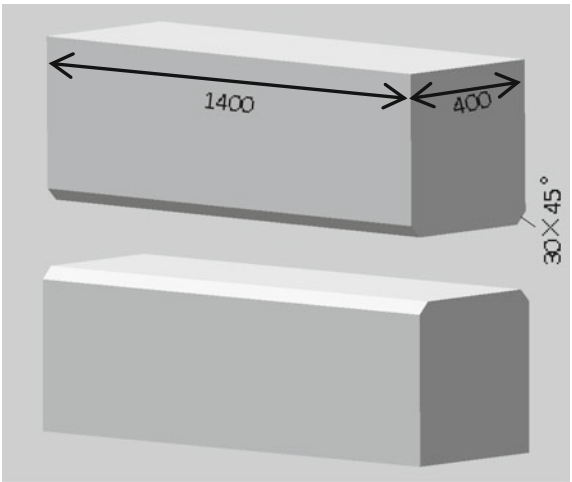

Fig. 2 3D profile of the flat anvils (unit: mm)

ingot. Both the upper and lower flat anvils can be seen in Fig. 2, the length of the anvils was 1400 mm and the width was 400 mm, the feed value during forging was 300 mm.

The initial condition: when t = 0, the ingot temperature was 1200 °C. The anvils temperature was 300 °C as constant. The boundary conditions: (1) radiative and convection heat transfer between ingot and air accord with the third kind boundary condition, the general heat transformation coefficient was set as 20 W/(m^2 K), air temperature was 20 °C. (2) the heat transfer between ingot and anvils was contact heat conduction, the heat transformation coefficient was set as 5000 W/(m^2 K). (3)The shear friction coefficient was 0.3.

The simulation process: the forging direction in the first pass was along the height direction (z direction in Fig. 1b) of the ingot, the total deformation was 55%, the forging direction in the second pass was along the height direction (x direction in Fig. 1b) of the ingot, the total deformation was 60%. The void evolution behavior under any deformation can be seen by the post process function of the soft ware.

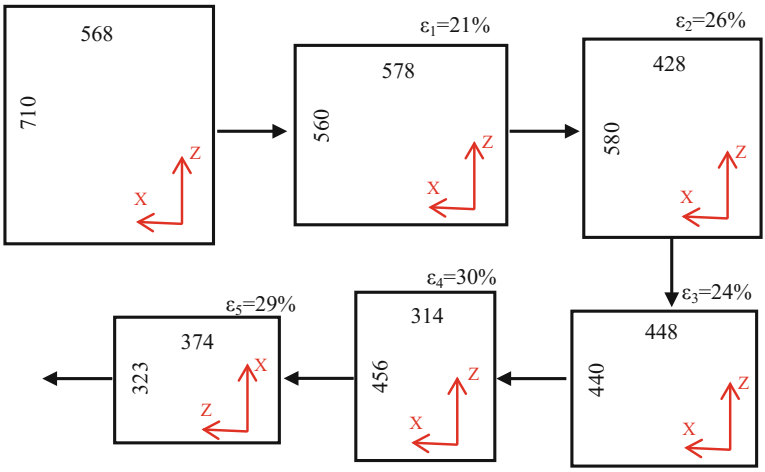

Fig. 3 Original forging method (unit: mm)

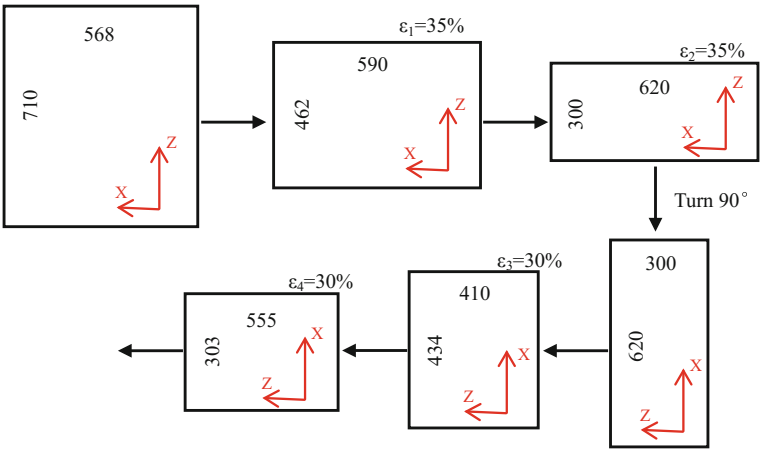

Fig. 4 New forging method (unit: mm)

Based on the numerical simulation, a new forging method was put forward and the industrial experiment was carried out on a 20MN hydraulic forging press. The tested steel was 20Cr13, the ingot size was shown in Fig. 1a. There were two forging methods: the original and the new, they were respectively shown in Figs. 3 and 4. The heating temperature of the ingot was 1200 °C.

Table 2 Void evolution during Z direction forging (XZ section)

No.	ε: 0	ε: 10%	ε: 20%	ε: 30%	ε: 35%	ε: 55%
1						
2						
3						
4						
5						
6						
7						
8						
9						

Results and Discussion

Void Evolution During Z Direction Forging

Morphology of the nine voids on XZ section during Z direction forging was shown in Table 2. With the increasing of deformation, the void shape transformed from round to oval and the size in Z direction decreased gradually. The void evolution law was 'round → oval → line or point chain → completely closed'. When the deformation up to 55%, No. 1, No. 2, No. 3, No. 5 and No. 6 voids completely closed, voids in other position didn't close totally. It was thus clear that the evolution law of voids in different position was different. The deformation in industrial forging was about 20%, No. 1–No. 9 voids cann't be closed according to Table 2, it means that the industrial deformation was small. The relationship between deformation and the size in Z direction of the voids were shown in Fig. 5. With the increasing of deformation, the size in Z direction of the voids first decreased rapidly and then decreased slowly. When the deformation was the same, the size in Z direction of No. 7–No. 9 voids was larger than that of No. 1–No. 6 voids. The critical deformation to close No. 1–No. 9 voids respectively were 35.5, 36.5, 37, 65, 35, 53, 68, 65 and 80%.

Previous studies have shown that void closure is closely related to effective strain. Lin thought that effective strain in the centre of the large section forging was one of the most important factor relevant to void closure, enough effective strain was the key to eliminate the defect in forging centre. Jiang and Zhao also showed that void closure degree was relevant to effective strain, for the void in the same position, the larger the effective strain was, the smaller the void size was [7–11].

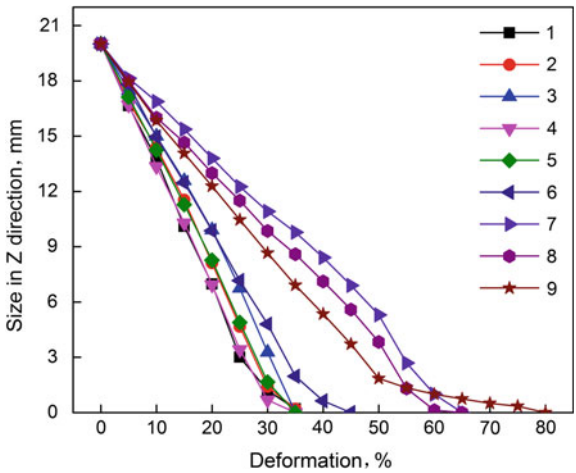

Fig. 5 Relation between void size and deformation

Void Evolution During X Direction Forging

Morphology of the nine voids on YZ section during X direction forging was shown in Table 3. With the increasing of deformation, the void shape transformed from oval to round and the size in X direction decreased gradually. The void evolution law was 'oval → round → line or point chain → completely closed'. When the deformation up to 60%, No. 1–No. 9 voids completely closed totally. It was thus clear that the evolution law of voids in different position was different. The deformation in industrial forging was about 20%, No. 1–No. 9 voids can't be closed according to Table 2, it means that the industrial deformation was small. The relationship between

Table 3 Void evolution during X direction forging (YZ section)

No.	ε: 0	ε: 10%	ε: 20%	ε: 30%	ε: 40%	ε: 50%	ε: 60%
1							
2			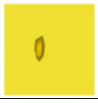				
3							
4							
5							
6							
7	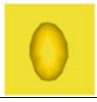						
8		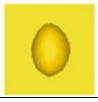		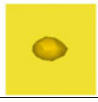			
9		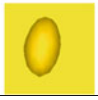	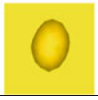	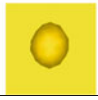	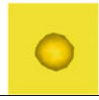		

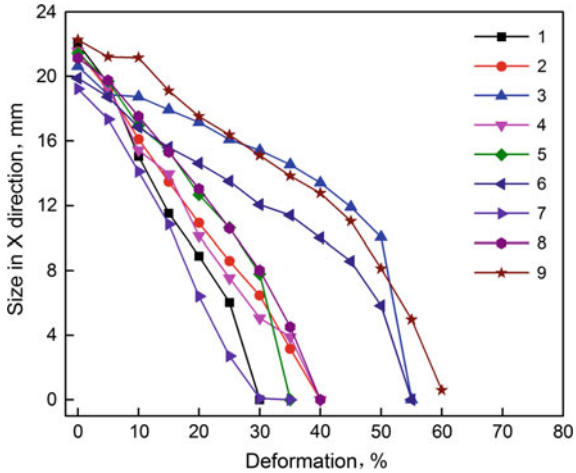

Fig. 6 Relation between void size and deformation

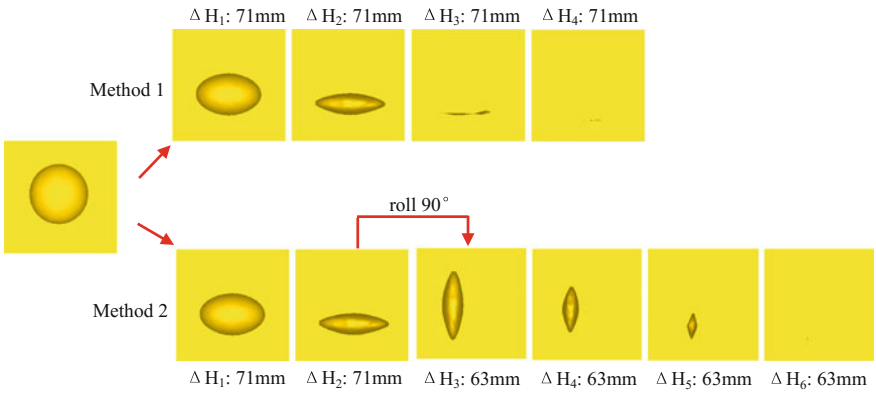

Fig. 7 Void 1 evolution law by two forging method

deformation and the size in Z direction of the voids were shown in Fig. 6. With the increasing of deformation, the size in X direction of the voids decreased rapidly. The critical deformation to close No. 1–No. 9 voids respectively were 30.0, 40.0, 55.0, 39.7, 35.0, 55.0, 35.0, 40.5 and 60.0%. In industrial forging, deformation in X direction in the second pass forging was about 25%, Table 3 showed that neither of No. 1–No. 9 voids can be closed.

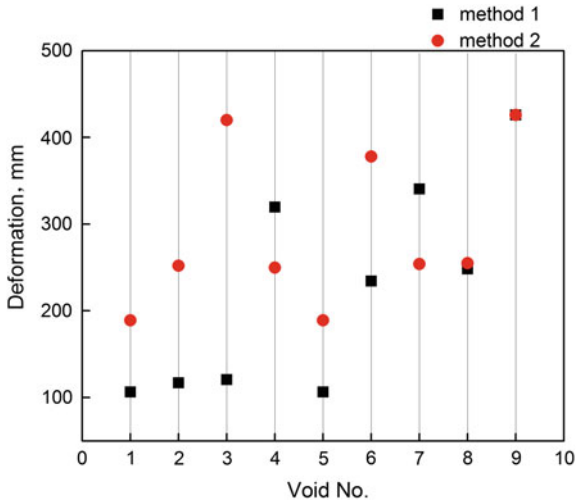

Fig. 8 Minimum deformation for voids closure from No. 3 pass

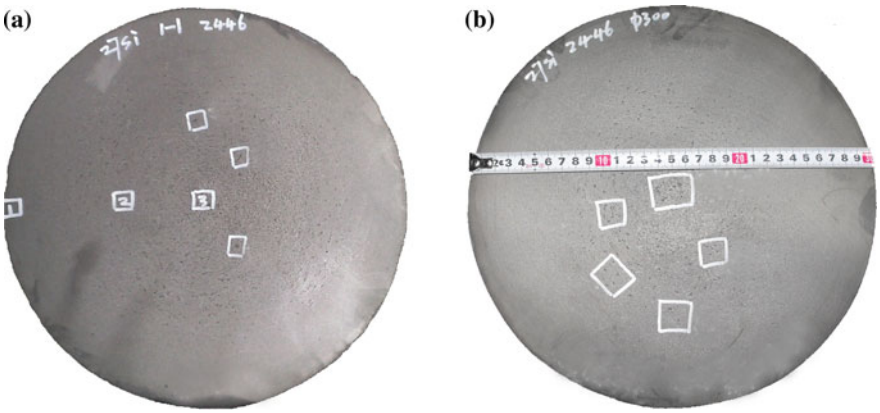

Fig. 9 Macro morphology of the loosen area. **a** original method: 50%; **b** new method: 33%

Comparison of Cavity Evolution

Two forging technology were designed for numerical simulation. The feed rate during simulation was 300 mm. As can be seen in Fig. 3, method 1 always forged along Z direction in the whole process, unlike it, method 2 forged along Z direction first and then X direction. For method 1, with the raise of deformation, the No. 1 void first turn to a ellipse and then a line, ultimately closed absolutely. For method 2, when the forging was rolled 90° and forged along X direction, not only the major but also the minor axises of the ellipse decreased, and the major axis of

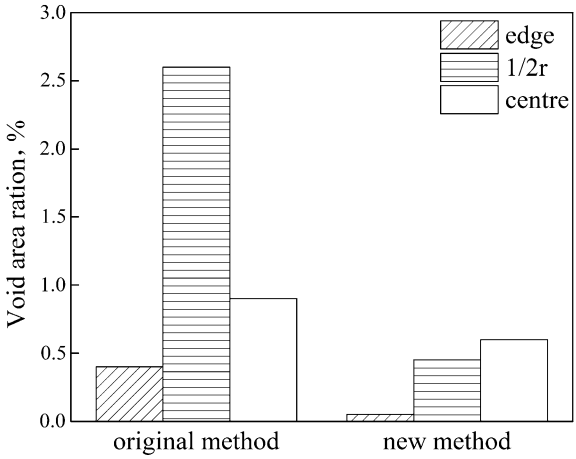

Fig. 10 Comparison of void area ratio of the two forging method

the void decreased more rapidly. It was definitely showed that the minimum deformation for No. 1 void closure by forging method 2 and forging method 2, respectively: it was 110 mm for method 1 and 190 mm for method 2 from No. 3 pass (Fig. 7).

The minimum deformation needed for the nine voids closure calculated from pass 3 was shown in Fig. 8, except for No. 4 and No. 7 voids, the minimum deformation for most voids by method 1 was smaller than by method 2. In a word, compared with method 2, method 1 was more effective for void closure. This conclusions tell us the deformation in directions that paralleled to the minor axis of the void should be larger.

Results of Industrial Forging Test

Ultrasonic flaw detection was used for inspecting the two forgings produced by two methods respectively, the result showed that there was no defect in both of the two forgings. The macro morphology o of the riser end of the two forging were shown in Fig. 9, the loosen area ratio of the forging by original method was 50% and the forging by new method was 33%. Comparison of void area ratio of the two forging method was shown in Fig. 10, the void area ratio of the forging made by the new method was lower than that by the original method.

Conclusions

During Z direction forging, with the increasing of deformation, the void shape transformed from round to oval, and the size in Z direction decreased gradually. The void evolution law was 'round → oval → line or point chain → completely closed'. The critical deformation to close No. 1–No. 9 voids respectively were 35.5, 36.5, 37, 65, 35, 53, 68, 65 and 80%.

In X direction forging, with the increasing of deformation, the void shape transformed from oval to round and the size in X direction decreased gradually. The void evolution law was 'oval → round → line or point chain → completely closed'. The critical deformation to close No. 1–No. 9 voids respectively were 30.0, 40.0, 55.0, 39.7, 35.0, 55.0, 35.0, 40.5 and 60.0%.

The single direction forging was more beneficial to close the void, the new forging technology to control void defect was proposed and industrial experiment was carried out. The void defect in the forging produced by the new technology was lighter than that by the original.

References

1. A. Milenin, W. Walczyk, M. Pietrzyk, Numerical modeling of microstructure evolution during forging of crank shafts. Steel Res. Int. **83**(8), 808–816 (2012)
2. F. Chen, Z. Cui, Mesoscale simulation of microstructure evolution during multi-stage hot forging processes. Modell. Simul. Mater. Sci. Eng. **20**(4), 359–371 (2012)
3. R. Ebara, Fatigue crack initiation and propagation behavior of forging die steels. Int. J. Fatigue **32**(5), 830–840 (2010)
4. Y.S. Na, J.T. Yeom, N.K. Park et al., Prediction of microstructure evolution during high temperature blade forging of a Ni−Fe based superalloy, Alloy 718. Met. Mater. Int. **9**(1), 15–19 (2003)
5. H.W. Lee, S.H. Kang, Y. Lee, Prediction of microstructure evolution during hot forging using grain aggregate model for dynamic recrystallization. Int. J. Precis. Eng. Manuf. **15**(6), 1055–1062 (2014)
6. J. Xu, W. Zeng, X. Sun et al., Microstructure evolution during isothermal forging and subsequent heat treatment of Ti-17 alloy with a lamellar colony structure. J. Alloy. Compd. **637**, 449–455 (2015)
7. M. Mukherjee, U. Prahl, W. Bleck, Modelling of microstructure and flow stress evolution during hot forging. Steel Res. Int. **81**(12), 1102–1116 (2010)
8. Zhu Q, Li L, Zhang Z, Microstructure evolution of AZ80 magnesium alloy during multi-directional forging process. Mater. Trans., 270–274 (2014)
9. G.X. Qi, R.B. Mei, F. Wang et al., A numerical simulation of microstructure evolution of GH4169 alloy blade during finish forging. Adv. Mater. Res. **704–705**, 113–118 (2011)
10. W.W. He, J.S. Liu, H.Q. Chen et al., Simulation and analysis on microstructure evolution of large generator retaining ring during multi-fire forging. Adv. Mater. Res. **97–101**, 176–181 (2010)
11. Kipelova A, Odnobokova M, Belyakov A et al. Microstructure evolution in a 304-type austenitic stainless steel during multidirectional forging at ambient temperature. Mater. Sci. Forum., 831–836 (2014)

Comparison of the High Cycle Fatigue Behavior of Ti–6Al–4V Produced Respectively by EBM and Hot-Rolling

Yunxi Liu, Wei Chen, Zhiqiang Li, Zheyuan Chen and Gang Yao

Abstract In this study, the microstructure, texture, and mechanical properties of Ti–6Al–4V(Ti-64) alloy produced by electron beam melting (EBM) and rolling were comparatively researched. The results showed that the microstructure of EBM Ti-64 consisted of columnar β grains growing epitaxially along the build direction. The c axis of α grains was oriented along the build direction, and the intensity was about 27 times random. The plate Ti-64 consisted of about 60 vol% of α_p and 40 vol% of β_T. The c-axis of α grains were parallel to the transverse direction of the plate and the texture strength was 5 times random. The tensile strength of EBM Ti–6Al–4V material was lower than that of the plate, but the ductility was higher. The EBM material exhibited a much larger variation of strength and ductility. This is because of the finer microstructure in the EBM material and also the microtextured regions in the plate material. The cracks in the plate material all initiated from the surface area but cracks in the EBM material occurred both on sample surface and in interior. The smaller lamellar thickness in the EBM material reduces the dislocation slip length, thus improves the life during the crack initiation stage.

Y. Liu (✉) · W. Chen · Z. Li · Z. Chen · G. Yao
AVIC Manufacturing Technology Institute, Beijing 100024, China
e-mail: liuyunxi9906@163.com

W. Chen
e-mail: werner_nju@163.com

Z. Li
e-mail: zqlee98@126.com

Z. Chen
e-mail: xgd610@126.com

G. Yao
e-mail: miuke0083@139.com

Y. Liu · Z. Li
Aviation Key Laboratory of Science and Technology on Plastic Forming, Beijing 100024, China

W. Chen · Z. Chen
Power Beam Processing Laboratory, Beijing 100024, China

© Springer Nature Singapore Pte Ltd. 2018

Y. Han (ed.), *Advances in Materials Processing*, Lecture Notes in Mechanical Engineering, https://doi.org/10.1007/978-981-13-0107-0_25

Keywords Ti–6Al–4V · Additive manufacturing · High cycle fatigue (HCF) Texture

Introduction

Ti alloys are widely used in many fields such as aerospace and chemical industry due to their high specific strength, excellent corrosion resistance and good fatigue properties [1–6]. Using as main aircraft and engine structures, Ti components have high processing cost and long lead time, which greatly limits their application. Electron Beam Melting (EBM) is one of the new additive manufacturing (AM) techniques that emerged during the last two decades [7–11]. It can form parts of high complexity with decent mechanical properties. The energy efficiency of AM comes from the near-net-shape fabrication capability and nearly full utilization of feedstock materials. Another advantage is that no tooling is required, which can save months of cycle time for the production of a part. Even though the contribution of the cost of capital to each part made in an expensive AM machine is significant, the overall cost per part can be considerably lower for small lot sizes.

The fatigue performance has always been a concern for Ti alloys used in aerospace components [12]. The fatigue behavior of Ti–6Al–4V(Ti-64) plates has been studied extensively [12–18], and results show that crystallographic texture is one of the major factors that affect its performance. However, the study about the fatigue behavior of EBM Ti-64 is very limited. In this paper, the microstructure and texture of EBM Ti-64 is characterized. In addition, the high cycle fatigue properties, life distribution and crack initiation mechanism of this material are also investigated and compared with Ti-64 plate.

Materials and Methods

Two kinds of Ti-64 materials were selected, one was produced by electron beam melting (EBM), and the other was 25 mm thick rolled plate. The chemistry is shown in Table 1. The EBM Ti-64 rods was produced by Arcam^{TM} A2X machine and then HIPed at 910 °C/100 MPa for 2 h to remove possible porosity inside.

Microstructure samples were prepared by conventional metallographic method, and then they were observed by Zeiss Supra-55 field emission electron microscope (SEM). The volume fraction of each phase and primary α grains size were measured

Table 1 Chemical composition of Ti-64 (wt%)

Elements	Al	V	O	C	N	Fe	H	Ti
EBM rod	6.06	4.08	0.17	0.01	0.20	/	0.002	Bal.
Plate	6.38	4.09	0.20	0.025	0.0031	0.17	0.001	Bal.

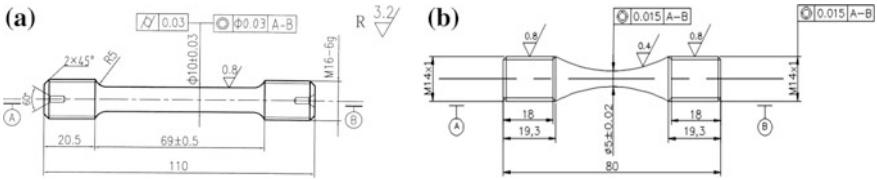

Fig. 1 Sample dimensions for **a** tensile tests, **b** fatigue tests

using ImageJ software and line interception method, respectively. EBSD samples were prepared by metallographic grinding and electrolytic polishing. Afterwards, texture analysis was carried out on field emission SEMs with an EDAX-TSL system or an Oxford system. The scanning regions were no less than 500 × 500 μm, and the step length was 0.5–1 μm.

The room temperature tensile specimens were prepared according to GB/T 228.1-2010, as shown in Fig. 1a, and the strain rate was set to be 0.001 s^{-1}. Hourglass shaped samples were prepared according to GB/T 3075-2008 for fatigue test (Fig. 1b). Stress controlled high cycle fatigue tests were performed with R = 0.1 and f = 100 Hz. Post-mortem analysis was perform on representative fractured samples using SEM.

Results and Analysis

The microstructures of EBM Ti-64 material and rolling plate are shown in Figs. 2 and 3, respectively. Due to the line scanning and layer-wise building sequence, the microstructure of the EBM samples was different along and perpendicular to the build direction. However, there were no distinctive layers of deposited materials observed in the EBM build. The microstructure of EBM Ti-64 contains columnar grains of prior β phase growing epitaxially along the build (z) direction (Fig. 2a). The columnar β grains can be up to several millimeters high and 100–200 μm wide. They are separated by grain boundary (GB) α phase. Within each column βgrain, basketweaved microstructure was dominant due to fast cooling, and small colonies of α/β lamellae (about 2.5 μm thick) are also present (Fig. 2b). The texture of the EBM Ti-64 is shown in Fig. 2c. It can be seen from the pole figures that the c axis of α grains were oriented along the build direction, and the intensity is about 27 times random. The grain orientation in each β columnar grain is similar.

The microstructure of Ti-64 plate (Fig. 3) is quite different. It consists about 60 vol% of globular primary-α(α_p) particles and 40 vol% transformed-β (β_T). The α_p grains and β_T colonies are 15 ± 5.8 μm and 18 ± 6.5 μm in diameter, respectively. The α-lath within β_T colonies is about 1.2 μm in thickness. The EBSD map of the Ti-64 plate is shown in Fig. 3c. There are a great number of microtextured regions (MTRs) distributed along the thickness direction (S direction) of the plate, which are composed of grains with similar crystal orientation. Pole figures (Fig. 3d)

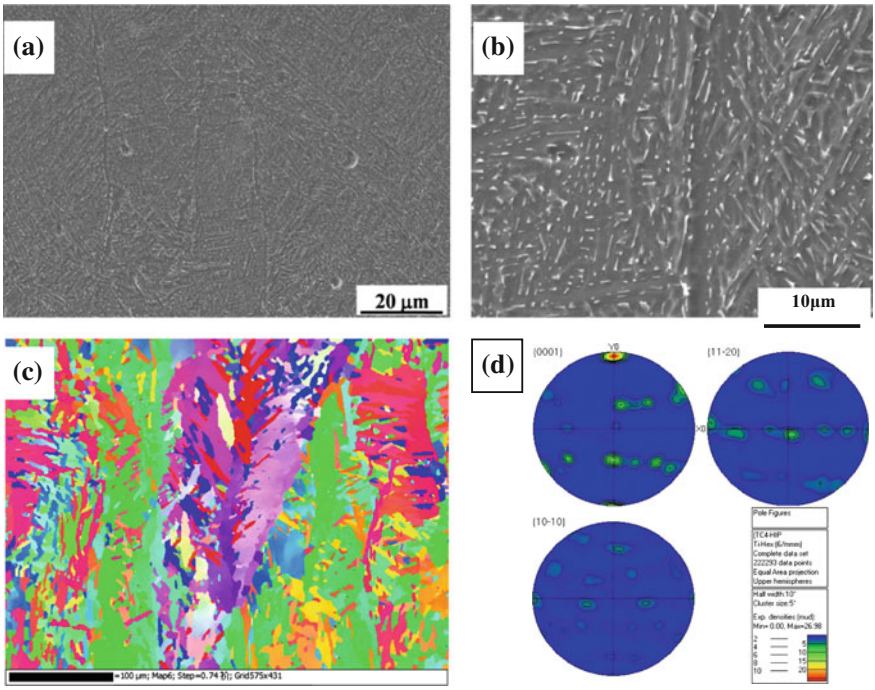

Fig. 2 EBSM Ti-64. **a** Microstructure, **b** high magnification, **c** grain orientation distribution, **d** pole figures

show that there is a strong transverse texture (TD), in which the c-axis of α grain is parallel to the TD of the plate. The texture strength is 5 times random. Since the Ti-64 plate was obtained by cross rolling, there is also texture along the rolling direction(RD), but it is a little weaker than the transverse texture.

The tensile properties of EBM and plate Ti-64 are shown in Table 2. The tensile strength of EBM Ti-64 material is lower than that of the plate, but the ductility is higher. Specifically, average UTS/YS of the two materials are 918/861 MPa and 1002/920 MPa, respectively. The elongation of EBM Ti-64 is 28.7% higher than that of the plate material. However, the EBM material exhibits a much larger variation of strength and ductility. The EBM material experienced rapid heating and cooling process during the "micro-casting" process. Due to the layer-wise process, the solidified layer also experienced remelt and subsequent heating-cooling when the next few layers on top were melted. The heat history is so complicated and this caused inhomogeneous microstructure (Fig. 2) and hence the variation of tensile properties. While the Ti-64 plate material exhibited uniform microstructure (Fig. 3) and tensile properties.

The fatigue S-N plots of EBM and rolling plate Ti-64 are shown in Fig. 4a, b. For the EBM Ti-64, 5 samples were tested at each stress level. Fatigue life of all the samples tested at 600 MPa exceeded 1×10^7 cycles. At all stress levels, the life

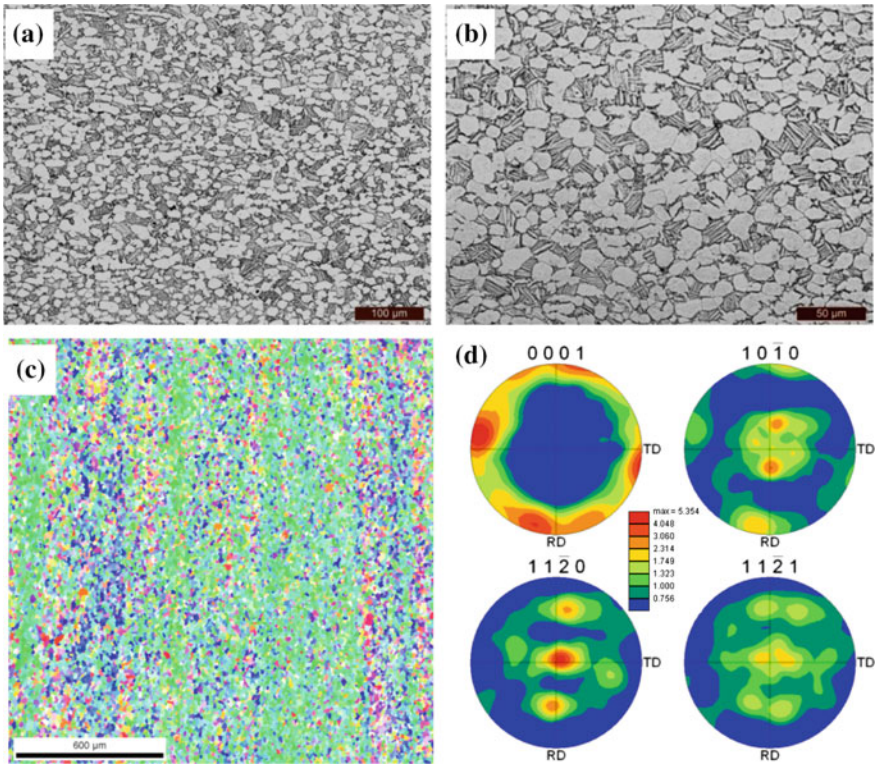

Fig. 3 Ti-64 rolling plate. **a** Microstructure, **b** high magnification, **c** Grain boundary misorientation distribution, **d** pole figures

Table 2 The average tensile properties of Ti-64

Sample	UTS[MPa]	$YS_{0.2\ \%}$[MPa]	Elong.[%]
EBM	918 + 52	861 + 35	18.4 + 1.7
Plate	1002 ± 2	920 ± 3	14.3 ± 0.29

scatter of the EBM Ti-64 material is relatively large. Usually, the fatigue life scatter becomes smaller when the testing stress is increased, but this material does not follow this trend. For example, at 750 MPa, the minimum and maximum fatigue lives is still two orders of magnitude different; at 650 MPa, two samples ran out of 1×10^7 cycles, but one sample lasted only 1.1×10^5 cycles. For the Ti-64plate, at least 5 specimens were tested at each stress level. The fatigue limit is 425 MPa. The fatigue life scatter is much smaller comparing with the EBM material. The scatter also becomes smaller as the testing stress level was increased. At 450 MPa, there are samples lasted over 1×10^7 cycles, but one sample only lasted 429,915 cycles.

The fracture surface of both materials exhibits typical fatigue fracture features. The surface can be divided into three zones: crack initiation, propagation

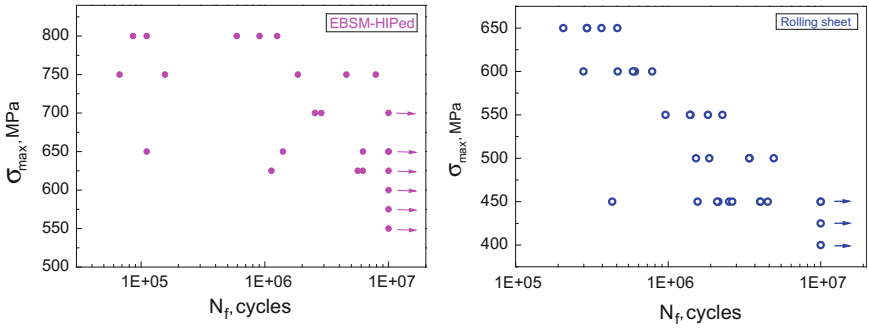

Fig. 4 Fatigue S-N curves of Ti-64 alloy. **a** EBM HIPed, **b** rolled plate

and overloaded zones (Fig. 5a, b). The crack initiation sites of EBM samples can be inside or on surface, but the ones with lower fatigue life are close to the surface. However, the fatigue crack of all plate samples initiated from the surface.

In titanium alloys, fatigue crack initiation sites were usually accompanied by facets, and these facets mostly formed in equiaxed α grains [14–17]. The EBM Ti-64 material consists of Widmanstätten microstructure and the facets started from the colony region with parallel α/β lamellae. Because the lamellae orientation within the colony is similar, so their slip systems are almost parallel. Figure 5c shows the fracture surface of an EBM sample tested at σ_{max} = 750 MPa and failed at N_f = 1,850,000 cycles. The fatigue crack initiation site is located deep inside, and the diameter of crack initiation and propagation area is about 2 mm. Facets were formed on parallel α/β lamellae as the crack initiation site (Fig. 5c). A higher magnification image shows striations on the facet (Fig. 5e), which indicates that the facet did not form in one cycle. The fatigue facets of the plate Ti-64 formed in equiaxed grains, and these facets are smooth (Fig. 5d). The propagation facets exhibit rougher surface and the river lines indicate the direction of fatigue crack propagation. Fatigue striations can be observed in crack propagation regions, the direction of which is perpendicular to the main crack (Fig. 5f) [18]. Each striation implies a fatigue loading cycle, where the striation spacing varies with the stress intensity factor range (ΔK), and the fatigue striations in the same area are continuous and parallel.

During the HCF process, the crack initiation stage occupies most of the fatigue life, and this stage mainly consists of dislocation slip and micro-crack formation. Many results show that the influence of microstructure on fatigue crack initiation of titanium alloy is mainly determined by lattice strength and dislocation slip length [19]. In general, higher lattice strength and shorter dislocation slip length lead to better HCF performance [19]. The yield strength (YS) of a material can be used as a reference of its lattice strength. In this paper, the YS of EBM material is about

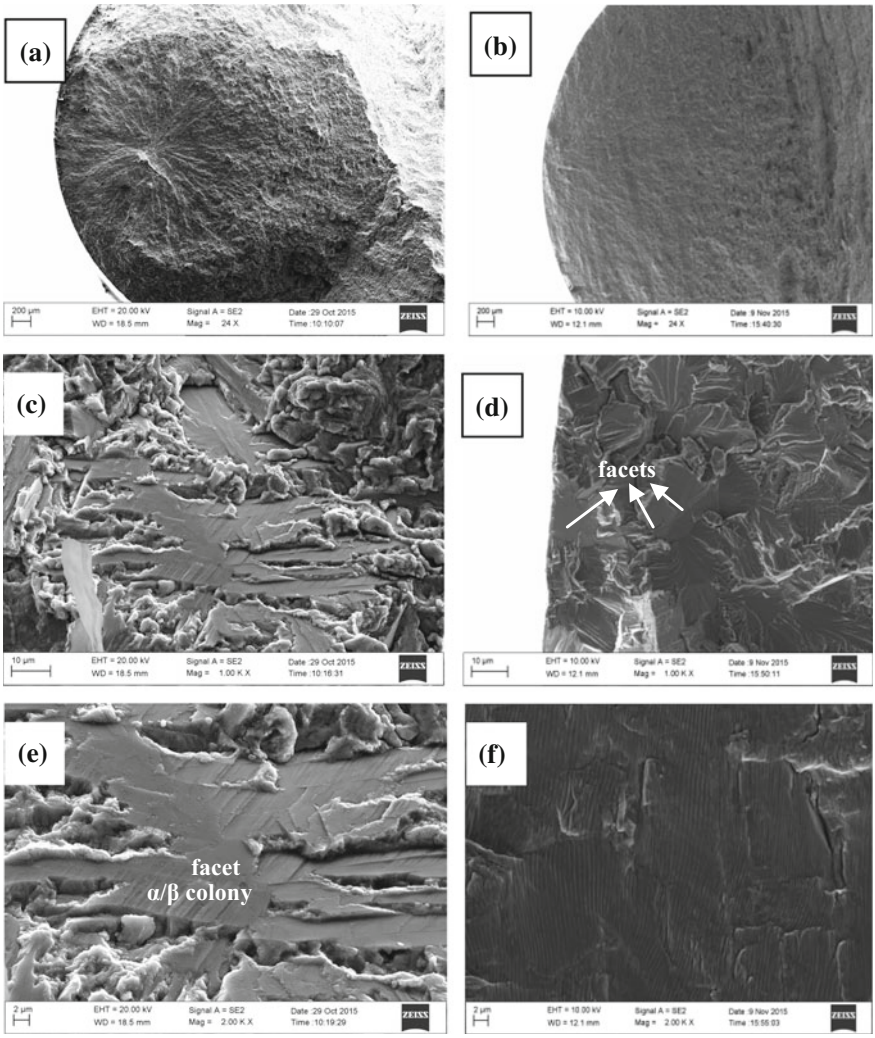

Fig. 5 Fatigue fracture surface of Ti-64 (**a/c/e** EBM HIPed; **b/d/f** Rolling plate). **a**, **b** Overview, **c**, **d** crack initiation area, **e**, **f** crack propagation area

60 MPa lower than that of the plate material (Table 2), but the fatigue performance is better. The main reason is that the α/β lath is fine in the EBM material so the dislocation slip length is small. The presence of microtextured zones in plate material is another important reason for its lower fatigue strength than EBM material. Within the same MTR, most of the grain orientation is similar so the low angle boundaries do not act as strong barrier to dislocation slip [20].

Summary and Conclusions

(1) The microstructure of EBM Ti-64 consists of columnar β grains growing epitaxially along the build direction. The columnar grains grow up to several millimeters high and are separated by grain boundary α phase, which is caused by the epitaxial growth of columnar dendrites during solidification. The c axis of α grains is oriented along the build direction, and the intensity is about 27 times random. The plate Ti-64 consists of about 60 vol% of α_p grains and 40 vol% of β_T. Many microtextured regions (MTRs) composed of grains with similar orientation are found. The c-axis of α grains is parallel to the transverse direction of the plate and the texture strength is 5 times random.

(2) The tensile strength of EBM Ti-64 material is lower than that of the plate, but the ductility is higher. The EBM material exhibits a much larger variation of strength and ductility. Even with 60 MPa lower YS, the fatigue limit of the EBM material is 600 MPa, while the plate material is only 425 MPa. This is because of the finer microstructure in the EBM material and also the microtextured regions in the plate material.

(3) The cracks in the plate material all initiated from the surface area. The initiation zone is accompanied by multiple facets, which formed in the α_p grains, and the crack initiation facets are smooth. The crack initiation in the EBM material occurred both on sample surface and in interior. The smaller lamellar thickness reduces the dislocation slip length, thus increasing the life of the HCF crack initiation stage.

References

1. C. Leyens, M. Peters, *Titanium and Titanium Alloys* (WILEY-VCH Verlag GmbH and Co. KGaA, Weinheim, 2003)
2. G. Lütjering, J.C. Williams, *Titanium* (Springer, Berlin, 2007)
3. Z. Lian, Review of titanium industry progress in America, Japan and China. Rare Metal Mat. Eng. **32**, 577–584 (2003)
4. R.R. Boyer, An overview on the use of titanium in the aerospace industry. Mater. Sci. Eng., A **213**, 103–114 (1996)
5. Y. Yang, Y. Luo, H. Zhao et al., Current status of research and application of titanium alloys for ships in China. Rare Metal Mat. Eng. S **2**, 538–544 (2011)
6. Y. Li, Y.Y. Li, T.T. Dong, Influence of stress ratio and residual stress on fracture modes of Ti-64 under high cycle fatigue. Chin. J. Mech. Eng. **51**, 45–50 (2015)
7. I. Gibson, D.W. Rosen, B. Stucker, *Additive Manufacturing Technology: Rapid Prototyping to Direct Digital Manufacturing* (Springer Science and Business Media LLC, New York, 2010)
8. C.K. Chuna, K.F. Leong, C.S. Lim, *Rapid Prototyping: Principles and Applications*, 2nd edn. (World Scientific, Singapore, 2003)
9. H. Tang, J. Wang, S. Lu et al., Progress in melt-forming technology of electron beam selection. Mat. Chin. **34**, 225–235 (2015)

10. L.E. Murr, E. Martinez, K.N. Amato et al., Fabrication of metal and alloy components by additive manufacturing: examples of 3D materials science. J. Mater. Res. Technol. **1**, 42–54 (2012)
11. W.E. Frazier, Metal additive manufacturing: a review. J. Mater. Eng. Perform. **23**, 1917–1928 (2014)
12. W. Zhou, Z. Zhao, W. Chen, Analysis of influencing factors of high cycle fatigue properties of titanium alloy. Mod. Mach. **3,** 90–93 (2009)
13. J. Schijve, *Fatigue of Structures and Materials* (Kluwer Academic, Dordrecht, 2001)
14. M.R. Bache, W.J. Evans, H.M. Davies, Electron back scattered diffraction (EBSD) analysis of quasi-cleavage and hydrogen induced fractures under cyclic and dwell loading in titanium alloys. J. Mater. Sci. **32**, 3435–3442 (1997)
15. F. Bridier, P. Villechaise, J. Mendez, Slip and fatigue crack formation processes in an α/β titanium alloy in relation to crystallographic texture on different scales. Acta Mater. **56**, 3951–3962 (2008)
16. S.K. Jha, C.J. Szczepanski, R. John et al., Deformation heterogeneities and their role in life-limiting fatigue failures in a two-phase titanium alloy. Acta Mater. **82**, 378–395 (2015)
17. S.K. Jha, C.J. Szczepanski, P.J. Golden et al., Characterization of fatigue crack-initiation facets in relation to lifetime variability in Ti–6Al–4V. Int. J. Fatigue **42**, 48–257 (2012)
18. A.L. Pilchak, J.C. Williams, Observations of facet formation in near-α, titanium and comments on the role of hydrogen. Metall. Mater. Trans. A **42**, 1000–1027 (2011)
19. Li Xingwu, Xia Shaoyu, Sha Aiyue, Fatigue properties of Ti-64 alloy. Acta Metall. Sin. **38**, 277–279 (2002)
20. A.C. Collop, Deformation and fracture mechanics of engineering materials (4th edition). Eng. Struct. **19**, 283–283 (1997)

Microstructure and Texture of Hot Rolled Plate and Finished Product in Fe–3%Si Common Grain-Oriented Silicon Steel

Rong Zhu, Lifeng Fan, Feng Guo and Jianzhong He

Abstract The microstructure and texture of hot rolled plate and finished product of Fe-3%Si common grain-oriented silicon steel were studied by means of optical microscope (OM) and X-ray diffraction (XRD). The results showed that the surface of the hot rolled plate was recrystallization structure, the center was non-recrystallized fiber structure, and the subsurface was mixture structure of the recrystallization and fiber structure. The surface of the hot rolled plate was mainly Goss texture {110}<001>, and the content of Goss texture reached 5.66%, and the strength of Goss texture was 3 times random. The complementary textures were {112}<111> and {100}<011>; the finished product was complete secondary recrystallization structure in the condition of grain size of 6.4–8.5 mm, and the texture was single Goss texture of {110}<001>.

Keywords Common grain-oriented silicon steel · Structure · Texture

Introduction

The grain-oriented silicon steel is an essential soft magnetic material for the electricity, electronic and military industry, consisting of {110}<001> large-size oriented grains in the finished product, which is used for the production of transformer

R. Zhu · L. Fan (✉) · F. Guo
School of Materials Science and Engineering, Inner Mongolia University of Technology, Hohhot 010051, Inner Mongolia, China
e-mail: fanlifeng829@163.com

R. Zhu
e-mail: 384054187@qq.com

F. Guo
e-mail: guofengnmg@sina.com

L. Fan · J. He
Baotou Iron And Steel Group Co.,Ltd., Baotou 014010, Inner Mongolia, China
e-mail: 349964568@qq.com

© Springer Nature Singapore Pte Ltd. 2018

Y. Han (ed.), *Advances in Materials Processing*, Lecture Notes in Mechanical Engineering, https://doi.org/10.1007/978-981-13-0107-0_26

core and large generator stator core [1–3]. The grain-oriented silicon steel is the only production that is being manufactured by applying the secondary recrystallization phenomenon of steel industry that with a sharp {110}<001> preferred crystallographic orientation called Goss texture [4, 5]. It is significant for grain-oriented silicon steel to get the mechanism of crystal nucleus and growth of Goss secondary grains, for that the perfection of Goss texture in the finished product has a major effect on the efficiency of power transformers [6]. The two most important performance parameters of the grain-oriented silicon steel are magnetic induction and iron loss that can be measured by B_{800} and $P_{1.7/50}$. The factors to affect the magnetic properties are mainly inhibitors, grain orientation and grain size, while the magnetic properties largely depend on the texture of the finished product [3, 7]. The excellent magnetic properties of the grain-oriented silicon steel are related to the occupancy of the Goss orientation grains in the material, the higher the aggregation degree of the {110}<001> is, the better the magnetic properties [8].

In this study, the microstructure and texture of hot rolled plate and finished product of Fe-3%Si common grain-oriented silicon steel were studied by means of optical microscope (OM) and X-ray diffraction (XRD), the purpose of this investigation is to acquire grain-oriented silicon steel with better performance.

Materials and Experimental Procedure

The test material was Fe-3%Si common grain-oriented silicon steel (CGO) with the grain orientation of 85–90%. Figure 1 shows the production process. The hot rolled plate and finished product at different locations were prepared, and the uniformity of the samples was analyzed.

The metallographic samples with the size of 20 mm × 15 mm (RD × TD; RD: rolling direction, TD: transverse direction) was prepared from the hot rolled plate, and the samples were etched with alcohol solution containing 4% of nitric acid (volume fraction), and the microstructure was observed by the optical microscope (OM) OLYMPUS GX51F.

The samples of the finished product was rough grinded, fine grinded and polished, then placed into 50% concentration of hydrochloric acid solution heated to 60–70 °C. Finally the slab macrostructure of the finished product was observed.

X-ray diffraction (XRD) X' Pert PRO MPD was used to measure the surface macrotexture of hot rolled plate and finished product. The three incomplete pole

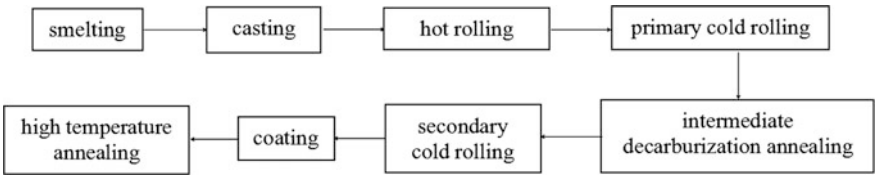

Fig. 1 Production process of CGO

figures {110}, {200} and {112} were measured, the orientation distribution function (ODF) was calculated from the measured data by the TexViewer. And then the content of a certain texture was calculated. The ODF section at constant $\varphi_2 = 45°$ were used as the standard of texture.

Results and Discussion

Microstructure and Texture of the Hot Rolled Plate

Figure 2 shows the microstructure of the hot rolled plate. From Fig. 2 it can be observed that the microstructure was inhomogeneous along the thickness direction, which was divided into decarburized layer, transition layer and center layer. Dynamic recrystallization occurred in the surface layer during the hot rolling process, and the equiaxed grains with uniform sizes were obtained. It can be seen that the non-recrystallized fiber structure was in the center of the hot rolled plate.

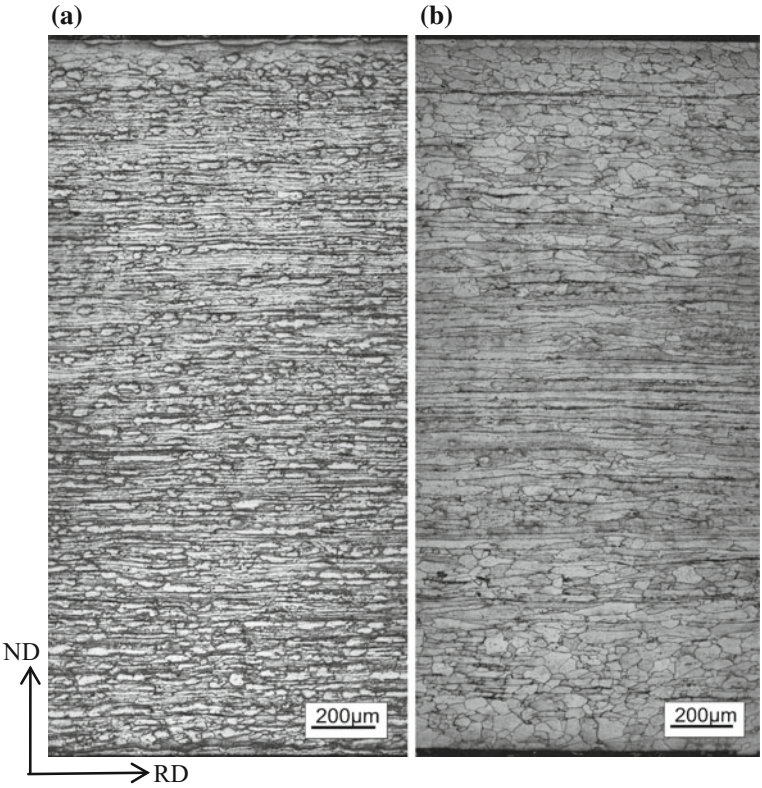

Fig. 2 Microstructure of hot rolled plate. **a** 1 plate; **b** 2 plate; ND normal direction

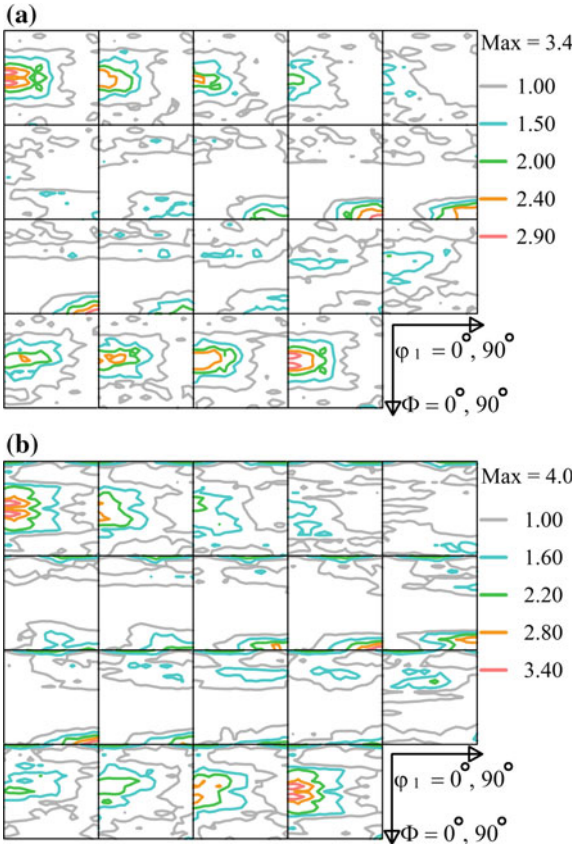

Fig. 3 ODF of the hot rolled steel. **a** Plate 1; **b** plate 2

Since the temperature in center was lower than the surface, it was difficult to recovery and recrystallization. The mixture structure of the recrystallization and fiber structure existed in the transition layer.

The inhomogeneity of the hot rolled microstructure along the thickness direction was very important for the secondary recrystallization of grain-oriented silicon steel [9]. The inhomogeneity of the hot rolled plate microstructure was mainly due to the dynamic recrystallization and partial phase transition during the hot rolled process, compared with other low-carbon steels, and the microstructure of the grain-oriented silicon steel were inhomogeneity obviously [10]. The generation of a lot of heat between plate surface and roller during the hot rolling process leads to the recrystallization of the steel. The more the content of Si was, the lower the thermal conductivity. When the content of Si in grain-oriented silicon steel reached to 3%, the thermal conductivity reduced clearly, so the temperature in center was lower than the surface, and hence the recovery and recrystallization was difficult.

Figure 3 shows the surface texture of hot rolled plate 1 and plate 2. The textures were mainly concentrated on the (100) face, (112) face and (110) face, which concentrated on Goss texture {110}<001>, copper texture {112}<111> and

Table 1 Main texture and content of hot rolled plate

Texture (%)	Plate 1	Plate 2
{110}<001>	5.26	5.66
{100}<011>	1.76	1.64
{112}<111>	4.39	4.54

rotating cubic texture {100}<011> exactly. The (100) face was the line of $\Phi = 0°$ and $\varphi_2 = 45°$, the (110) face was the line of $\Phi = 90°$ and $\varphi_2 = 45°$, the main textures of (112) face were {112}<110> and {112}<111>, {112}<110> was the texture of $\Phi = 35°$, $\varphi_1 = 0°$ and $\varphi_2 = 45°$, {112}<111> was the texture of $\Phi = 30°$, $\varphi_1 = 90°$ and $\varphi_2 = 45°$. But the Goss texture {110}<001>was the main , and other two textures were subordinate. From Fig. 3 we also can see that the texture strength of plate 1 was slightly lower than that of plate 2, which reached to 2.9 and 3.4 respectively.

Table 1 shows the contents of texture. The main content of Goss texture {110}<001> reached 5.26 and 5.66% respectively, which means the favorable texture component increased 0.4%; the unfavorable texture component of {100}<011> decreased 0.12%, which from 1.76 to 1.64%. the favorable texture content of hot rolled plate 2 was slightly above that of plate 1.

The Goss oriented grains in the hot rolled plate were originated of {110}<001> grains [11], which abnormal growth during the secondary recrystallization. According to the texture genetic effect, the number of secondary recrystallization crystal nucleus were increased with the content of {110}<001> in hot rolled plate. Also the recrystallization degree of plate 2 was better than plate 1, it would produce the more secondary recrystallization crystal nucleus in the deformation band during the cold rolling process.

Macrostructure and Texture of Finished Product

As shown in Fig. 4 the finished product macrostructure of plate 1 and plate 2, the average grain size were 8.5 mm and 6.4 mm, respectively. From Fig. 4 we can see that the uniformity of grain size in plate 1 was higher than the one of plate 2. In fact, the size of the biggest grain in plate 2 was bigger than plate 1, but it had the higher number of small grains, which lead to the average grain size smaller.

Figure 5 shows the finished product ODF of plate 1 and plate 2. From Fig. 5 we can see that the textures in the two samples were mainly focused on Goss texture {110}<001>, the texture strength of plate 1 and plate 2 were 115.40 and 244.80, the strength of plate 2 was higher than the plate 1.

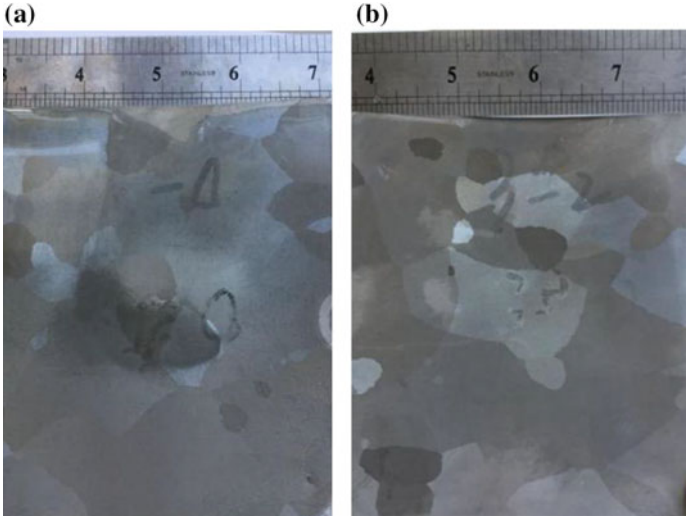

Fig. 4 Macrostructure of the finished product. **a** Plate 1; **b** plate 2

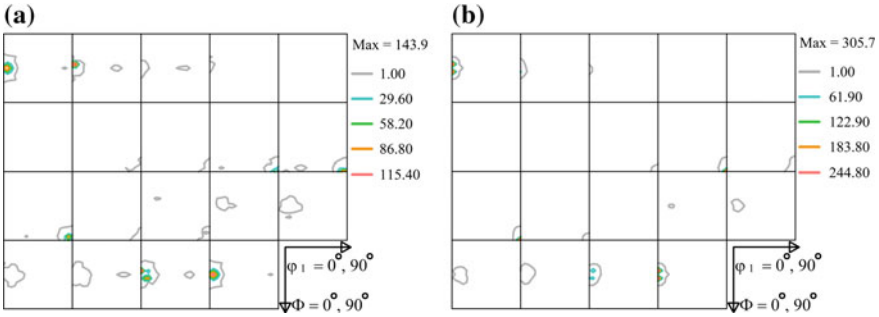

Fig. 5 ODF of the finished product. **a** plate 1; **b** plate 2

Conclusions

In this study, the microstructure and texture of hot rolled plate and finished product of Fe-3%Si ordinary grain-oriented silicon steel have been studied. The conclusions are as follows:

The surface of the hot rolled plate is recrystallization structure, the center is non-recrystallized fiber structure, and the subsurface is mixture structure of the recrystallization and fiber structure.

The surface of the hot rolled plate is focused on Goss texture {110}<001>, where the content reaches to 5.66%, and the strength is 3 times random. The complementary textures are {112}<111> and {100}<011>.

The finished product is complete secondary recrystallization structure with the grain size of 6.4–8.5 mm, and the texture is single Goss texture {110}<001>.

Acknowledgements This research was funded by National Natural Science Foundation of China (51661026), China Postdoctoral Science Foundation (2016M602914XE), Inner Mongolia Natural Science Foundation (2015BS0508), Key project of Inner Mongolia University of Technology (ZD201509) and Innovative experiment of college students at Inner Mongolia University of Technology (2016037).

References

1. N. Wang, *Dynamic Study of Microstructural Evolution During Secondary Recrystallization of Grain Oriented Silicon Steel* (Northeastern University, Shenyang, 2011)
2. C. Zhang, L. Xiang, T. Dong, E. Yue, S. Qiu, Decarburizing annealing of grain oriented silicon steel. J. Iron Steel Res. **21**, 55–58 (2009)
3. Z. He, *Electrical Steel*, vol. 1 (Metallurgical Industry Press, Beijing, 2012)
4. T. Kumano, T. Haratani, Y. Ushigami, The relationship between primary and secondary recrystallization texture of grain oriented silicon steel. ISIJ Int. **42**, 440–448 (2002)
5. H.Y. Song, H.T. Liu, H.H. Lu, H.Z. Li, W.Q. Liu, X.M. Zhang, G.D. Wang, Effect of hot rolling reduction on microstructure, texture and ductility of strip-cast grain-oriented silicon steel with different solidification structures. Mater. Sci. Eng., A **605**, 260–269 (2014)
6. I. Yukio, M. Chizuko, I. Yo, S. Hiroshi, Transmission kossel study of origin of goss texture in grain oriented silicon steel. Trans. Iron Steel Inst. Jpn. **23**, 440–449 (1983)
7. J. Li, *Lowering the Core Loss of Grain-Oriented Silicon Steel Sheets by Means of Laser Processing* (Tsinghua University, Beijing, 1992)
8. X. Yu, *The Study on Normalization Process and the Primary Recrystallization Mechanism of Fe-3%Si Oriented-Silicon Steel* (Shandong Agricultural University, Shandong, 2016)
9. X. Yifan, Hot rolled texture of 3% Si oriented silicon steel for the production. Phys. Test **1**, 20–22 (1990)
10. L. Seidel, M. Hölscher, K. Lücke, Rolling and recrystallization textures in iron–3% silicon. Texture, Stress, and Microstructure. **11**, 171–185 (1989)
11. S. Mishra, C. Därmann, K. Lücke, On the development of the Goss texture in iron-3% silicon. Acta Metall. **32**, 2185–2201 (1984)

Effect and Mechanism of Cold-Hot Roll Bonding Process on Interfacial Bonding Properties of Aluminum/Steel Laminated Composite Plate

Xuefeng Liu, Xing Ming, Dandan Zhang and Zhangzhi Shi

Abstract Low carbon steel plate and pure aluminum plate were used as raw materials, the self-developed cold-hot roll bonding technology was used to prepare aluminum/steel laminated composite plate, the flexural properties, interface diffusion layer thickness and intermetallic compounds of aluminum/steel laminated composite plates were characterized by 90° repeated bending test, OM (optical microscope), SEM (scanning electron microscope) and EDS (energy spectrum analysis), the effects of cold rolling reduction, hot rolling reduction and hot rolling temperature on the interfacial bonding properties of aluminum/steel laminated composite plates were analyzed, the influence mechanism of cold-hot roll bonding process on the interfacial bonding properties of aluminum/steel laminated composite plates was discussed. The results show that the bending resistance of aluminum/steel laminated composite plates increased with increasing the cold rolling reduction or the hot rolling reduction, and increased first and then decreased with increasing the hot rolling temperature. The effect of cold rolling reduction, hot rolling reduction and hot rolling temperature on the bending resistance increased in turn. Under the condition of cold rolling reduction of 45% and hot rolling reduction of 35–50%, when the hot rolling temperature was 400 °C, the interface diffusion layer thickness of aluminum/steel laminated composite plates was 1.5–2.5 μm, no intermetallic compounds within the interface, and the interfacial bonding properties increased with increasing the interfacial diffusion layer thickness; when the hot rolling temperature was 500 °C, the interface diffusion layer thickness was 3–5 μm, and the spherulite $FeAl_3$ phase intermetallic compound with diameter less than 5 μm distributed in the interface, the interfacial bonding properties increased with increasing the interface diffusion layer thickness; when the hot rolling temperature

X. Liu (✉) · X. Ming · D. Zhang · Z. Shi
School of Materials Science and Engineering, University of Science and Technology Beijing, Beijing 100083, China
e-mail: liuxuefengbj@163.com

X. Liu
Beijing Laboratory of Metallic Materials and Processing for Modern Transportation, University of Science and Technology Beijing, Beijing 100083, China

© Springer Nature Singapore Pte Ltd. 2018

Y. Han (ed.), *Advances in Materials Processing*, Lecture Notes in Mechanical Engineering, https://doi.org/10.1007/978-981-13-0107-0_27

was 600 °C, the interface diffusion layer thickness was 8–14 μm, the intermetallic compound was Fe_2Al_5 phase with 6–12 μm thickness, and the interfacial bonding properties decreased sharply.

Keywords Cold-hot roll bonding · Aluminum/steel laminated composite plate Preparation process · Interfacial bonding properties · Influence mechanism

Introduction

Metal layered composite material is the use of composite technology to two or more layers of physical, chemical, mechanical properties of different metals in the interface to achieve a new combination of metallurgical materials. Through the rational selection of components and processing technology, the same or different metals can be compounded to form a layered composite material with more than a single component metal. As a kind of laminated composite material, aluminum/steel laminated composite plate combines the high strength of steel and the advantages of aluminum: light weight, good corrosion resistance, excellent conductivity, thermal conductivity, permeability, have been widely used in the aerospace, petroleum, Machinery, chemical, automotive, shipbuilding, construction, electricity, electronics, nuclear energy, household appliances and daily necessities, and many other areas [1].

Interfacial bonding performance is an important performance index for evaluating the merits and demerits of aluminum/steel laminated composite plate. Aluminum/steel laminated composite plate are easy to form intermetallic compounds at a certain temperature, which can lead to aluminum/steel layering by destroying the metallurgical bonding between the substrate and the clad material through the interdiffusion of elements, thus seriously affect the mechanical properties of materials. Domestic and foreign scholars have done a lot of research on the influencing factors of the interfacial bonding properties of aluminum/steel laminated composite plate [2–5]. Chen et al. [2] used 4A60 aluminum as clad material and 08Al steel as substrate for cold rolling, and carried out diffusion annealing at 605–625 °C, 3–60 min to study the effect of the intermetallic compound layer on interfacial bonding properties, found that interfacial metal when the thickness of the intermetallic compound layer was less than 12 μm, the composite strip still maintained a good interfacial bonding strength (greater than 45 MPa). Composite strip had a good interfacial bonding strength (greater than 45 MPa) when the thickness of the intermetallic compound layer was below 12 μm. As the thickness of the intermetallic compound layer continued to increase, the interfacial bonding strength decreased significantly, when the thickness of the intermetallic compound layer was 25–43 μm, the bonding strength was reduced to 10–20 MPa; when the thickness of the intermetallic compound layer was 54–68 μm, the interfacial bonding strength was only 5–10 MPa. Wang et al. [3] studied the effect of hot-dip aluminized steel on interfacial bonding properties at 620–630 °C, and found that the $FeAl_3 + Fe_2Al_5$ intermetallic compound layer of 16–35 μm significantly

reduced the interfacial bonding strength of aluminum/steel laminated composite plate, the bonding strength value from 70 MPa down to 20 MPa. Zu et al. [4] studied the effect of intermetallic compound layer on the interfacial bonding properties of L3M industrial pure aluminum and Q235A low carbon steel after cold rolling composite + diffusion annealing, found that the $FeAl_3$ layer was continuously distributed along the interface and had a thickness of 10 μm would seriously damage the aluminum/steel laminated composite plate interfacial bonding properties, resulted in aluminum/steel laminated composite plate layered phenomenon. Tatham et al. [5] studied the interface of Al (0.5% Mg)/low carbon steel bonded by rolling composite, found that the interfacial tearing strength decreased as the thickness of the interface phase increased, when the interface phase thickness was 1–2 μm, the interfacial tearing strength is 8–18 N/mm; when the interface phase thickness exceeded 4 μm, the interfacial tearing strength was zero. Wu et al. [6] study found that the effect of the interface diffusion layer thickness on the interfacial bonding properties showed the stage: in the initial stage, the interfacial bonding strength increased rapidly with increasing the interface diffusion layer thickness; in the middle stage, the interfacial bonding strength increased slowly with increasing the interface diffusion layer thickness; in the later stage, the interfacial bonding strength was almost unchanged, and did not change with the change of the interface diffusion layer thickness. However, the effects of interface diffusion layer thickness and intermetallic compound on the interfacial bonding properties of cold-hot roll bonding aluminum/steel laminated composite plates are not clear.

In this paper, aluminum/steel laminated composite plates were prepared by the self-developed cold-hot roll bonding technology, the effects of cold rolling reduction, hot rolling reduction and hot rolling temperature on the interfacial bonding properties of aluminum/steel laminated composite plates were analyzed, the influence mechanism of cold-hot roll bonding process on the interfacial bonding properties of aluminum/steel laminated composite plates was discussed, which is great significant for the further development of high performance aluminum/steel laminated composite plates.

Material and Experimental Procedures

In this experiment, the 1.85 mm thick plate of low carbon steel Q235A was used as substrate and the 0.85 mm thick plate of pure aluminum 1060 used as clad material, with chemical compositions of Q235A and 1060 as shown in Table 1.

Table 1 Chemical composition of Q235A and 1060

Q235A	Element name	C	Mn	Si	Fe
	Content [wt%]	0.05	0.2	0.28	Balance
1060	Element name	Si	Fe	Mn	Al
	Content [wt%]	≤ 0.1	0.39	0.02	Balance

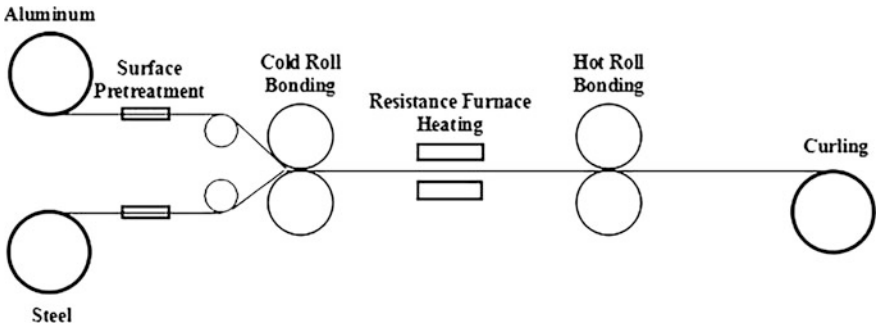

Fig. 1 Schematic diagram of prepared aluminum/steel laminated composite plate using a self-developed cold-hot roll bonding method

Cold-hot roll bonding technology is a kind of new laminated composite material preparation technology with the advantages of high production efficiency, short process flow and good product quality. It is composed of four steps of surface treatment, cold rolling pre-bonding, intermediate heating and hot roll bonding. First, the two contacting surface of the laminated composite plates was degreased and wire brushed at room temperature; then carried out single-pass room temperature rolling in a certain amount of reduction, so that the contacting surface of the pre-composite plates achieved close mechanical bite, and obtain pre-bonding slab, replaced the welding, vacuum and other processes in the traditional hot roll bonding, and could reduce the subsequently middle heating temperature, shorten the heating time; followed by the use of resistance heating furnace on the pre-bonding slab for a short time insulation to ensure that the pre-bonding slab in the process of heating recovery, while its composite interface did not occur oxidation; finally, single-pass hot roll bonding is carried out to promote the diffusion of atoms in the metal elements between the composite interfaces to achieve effective metallurgical bonding, and high-performance metal laminated composite plates are prepared.

The principle of the preparation method of aluminum/steel laminated composite plates shown in Fig. 1. Specific experimental steps were as follows: First, used alcohol clean the surface of the aluminum and low carbon steel plate to remove the surface impurities, get a clean surface; then used a diameter of 0.9 mm stainless steel wire brush on the contacting surface of aluminum and low carbon steel plate polishing treatment to obtain a rough surface and a certain thickness of the surface hardened layer, stainless steel wire brush wire diameter of 0.30 mm, steel brush speed of 1100 r/min; kept clean the contacting surface of the aluminum and the low carbon steel plate after the surface treatment, cold rolled under the use of guide, the cold rolling pre-bonding of aluminum and low carbon steel plates was carried out on a four-high rolling mill with a rolling force of 80 t and a work roll diameter of 170 mm at a rolling speed of 0.04 m s^{-1}; then the aluminum/steel pre-bonding slab

Table 2 Cold-hot roll bonding process parameters

No.	Cold rolling reduction [%]	Hot rolling temperature [°C]	Hot rolling reduction [%]
1	45	400	35
2	45	400	45
3	45	400	50
4	35	500	45
5	40	500	45
6	45	500	35
7	45	500	45
8	45	500	50
9	45	600	35
10	45	600	45
11	45	600	50

was placed into the resistance heating furnace constant temperature heating 20 min, and then used the same rolling mill for hot roll bonding. Cold-hot roll bonding process parameters in Table 2.

The interface diffusion layer thickness, the morphology and distribution of the interfacial compounds and the peeling surface of the aluminum/steel laminated composite plate after cold-hot roll bonding were tested by using S250MK3 scanning electron microscope, EDS energy spectrum analysis, Axio Scope A1 metallographic microscope and TTR Ш multifunction X-ray diffractometer respectively. According to GB/T4461-2007, the interfacial bonding properties of the aluminum/steel laminated composite plate were tested by repeated bending method. The specimens were bent 90° to one side, and then the specimens were restored (called the first bending). The specimens were then bent 90° in the reverse direction, and then the specimens were restored (called the second bend) until the break, and the interface cracking of the aluminum/steel laminated composite plate was observed macroscopically.

Results and Discussion

Effect of Cold Rolling Reduction on Interfacial Bonding Properties at Hot Rolling Temperature of 500 °C

The repeated bending results are shown in Fig. 2 when the hot rolling reduction is 45% and the hot rolling temperature is 500 °C, the cold rolling are carried out under the cold rolling reduction of 35, 40 and 45%, respectively. It can be seen from Fig. 2 that when the hot rolling reduction is 45% and the hot rolling temperature is 500 °C, the repeated bending times of cold rolling reduction of 35, 40 and 45% is 49, 52, 54, respectively. And the layered phenomenon does not occur between the

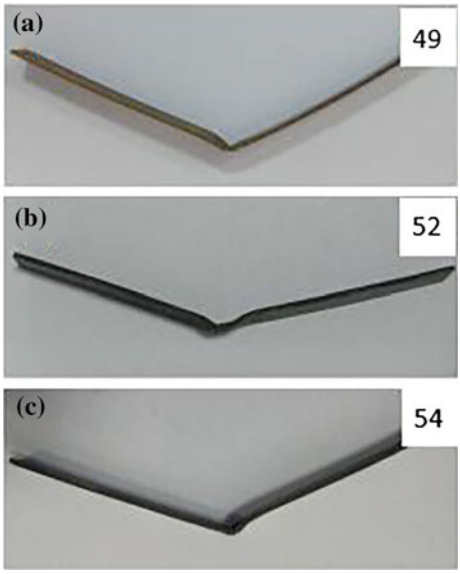

Fig. 2 Repeated bending test specimens of laminated composite plates prepared at different hot rolling reduction when the hot rolling reduction is 45%, the hot rolling temperature is 500 °C. **a** Cold rolling reduction of 35%; **b** cold rolling reduction of 45%; **c** cold rolling reduction of 50%

base layer and cladding layer of the aluminum/steel laminated composite plates. At the same time, the times of repeated bending increase with increasing cold rolling reduction. It is shown that the increase of cold rolling reduction can improve the interfacial bonding properties of aluminum/steel laminated composite plates while maintaining the hot rolling reduction of 45% and the hot rolling temperature of 500 °C.

The SEM and EDS images of aluminum/steel laminated composite plates interface are shown in Fig. 3 when the hot rolling reduction is 45% and the hot rolling temperature is 500 °C. It can be seen from Fig. 3 that the interface diffusion layer thickness is about 2.7, 3, and 3.4 μm prepared at cold rolling reduction of 35, 40, 45%, respectively when the hot rolling reduction is 45% and the hot rolling temperature is 500 °C. The interface diffusion layer thickness increases with increasing the hot rolling reduction.

The comparison of repeated bending test results and interface diffusion layer thickness are shown in Fig. 4 when the hot rolling reduction is 45% and the hot rolling temperature is 500 °C. Compared with the results of the repeated bending test, it can be seen from Fig. 4 that the interface diffusion layer thickness has a close relationship with the interfacial bonding properties. With the increase of the interface diffusion layer thickness, the interfacial bonding properties is also improved accordingly. It is also found that the discontinuous $FeAl_3$ intermetallic

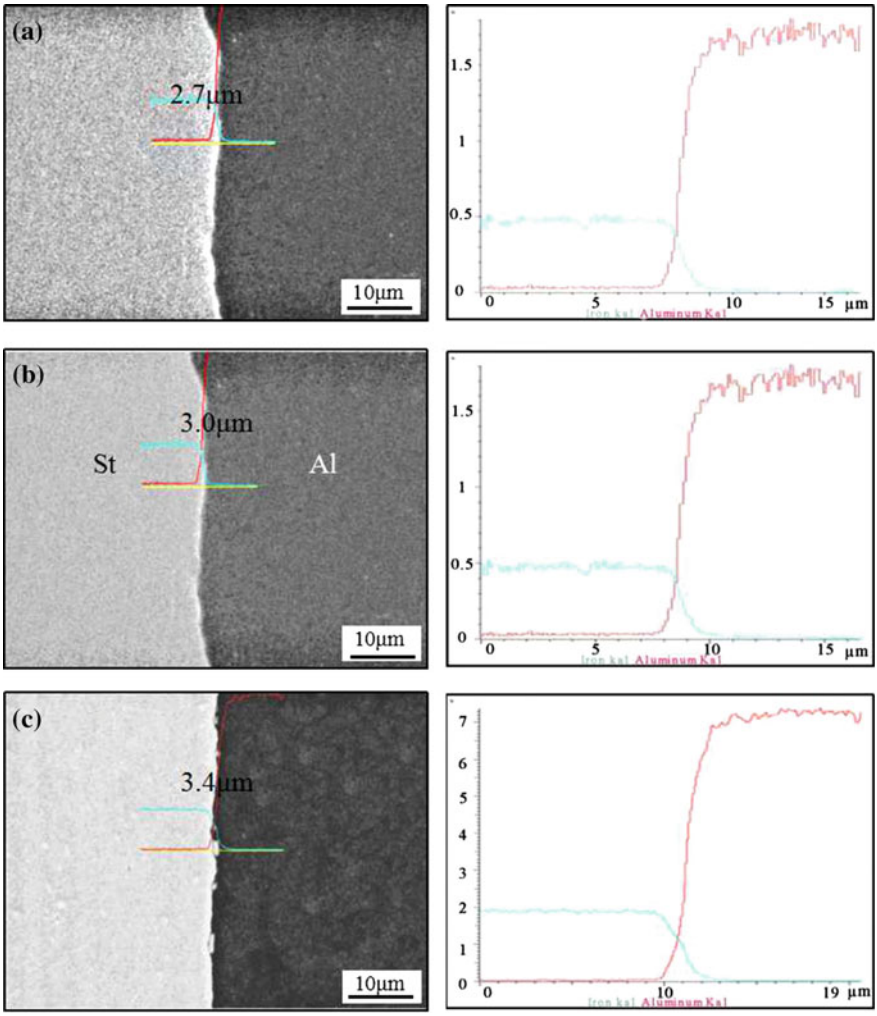

Fig. 3 Distribution of components of laminated composite plates prepared at different hot rolling reduction when the hot rolling reduction is 45%, the hot rolling temperature is 500 °C. **a** Cold rolling reduction of 35%; **b** cold rolling reduction of 45%; **c** cold rolling reduction of 50%

compound with a width of about 0.5 μm appeared at the interface of the aluminum/steel laminated composite plates when the cold rolling reduction was 45%. Even with smaller granular intermetallic compounds, the interfacial bonding strength is not significantly affected.

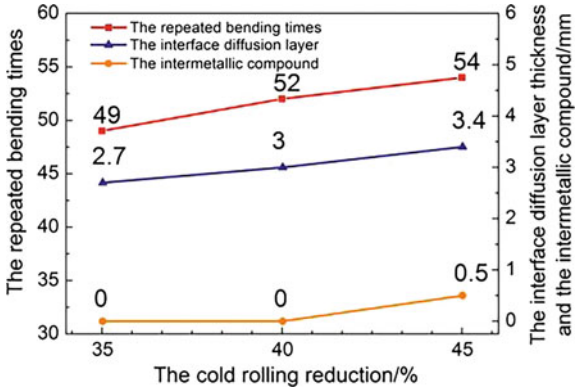

Fig. 4 Comparison of repeated bending test results and interface diffusion layer thickness prepared at different cold rolling reduction when the hot rolling reduction is 45%, the hot rolling temperature is 500 °C

Effect of Hot Rolling Reduction on Interfacial Bonding Properties at Hot Rolling Temperature of 400 °C

The repeated bending results are shown in Fig. 5 when the cold rolling reduction is 45% and the hot rolling temperature is 400 °C, the hot rolling are carried out under the hot rolling reduction of 35, 45 and 50%, respectively. It can be seen from Fig. 5 that when the cold rolling reduction is 45% and the hot rolling temperature is 400 °C, the repeated bending times of hot rolling reduction of 35, 45 and 50% is 25, 30, 34, respectively. And the layered phenomenon occurs between the base layer and cladding layer of the aluminum/steel laminated composite plates. At the

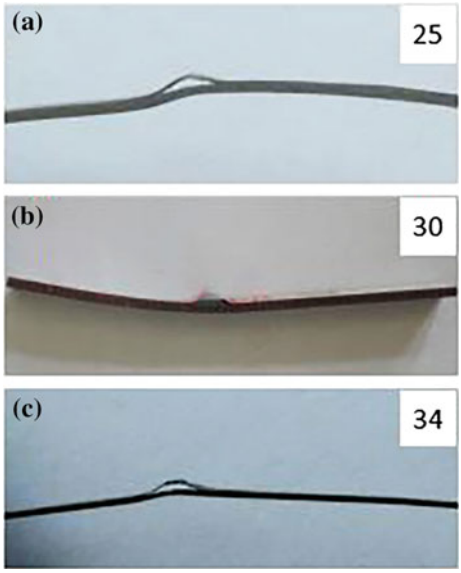

Fig. 5 Repeated bending test specimens of laminated composite plates prepared at different hot rolling reduction when the cold rolling reduction is 45%, the hot rolling temperature is 400 °C. **a** Hot rolling reduction of 35%; **b** hot rolling reduction of 45%; **c** hot rolling reduction of 50%

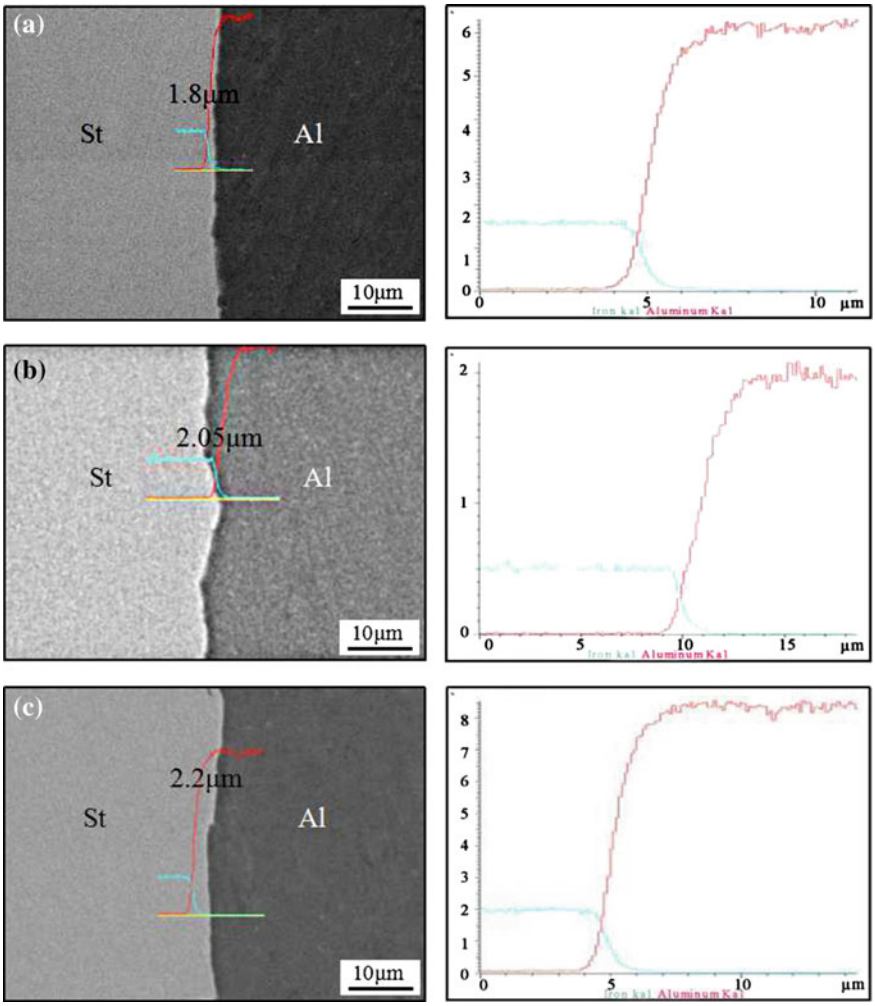

Fig. 6 Distribution of components of laminated composite plates prepared at different hot rolling reduction when the cold rolling reduction is 45%, the hot rolling temperature is 400 °C. **a** Hot rolling reduction of 35%; **b** hot rolling reduction of 45%; **c** hot rolling reduction of 50%

same time, the times of repeated bending increase with increasing hot rolling reduction. It is shown that the increase of hot rolling reduction can improve the interfacial bonding properties of aluminum/steel laminated composite plates while maintaining the cold rolling reduction of 45% and the hot rolling temperature of 400 °C.

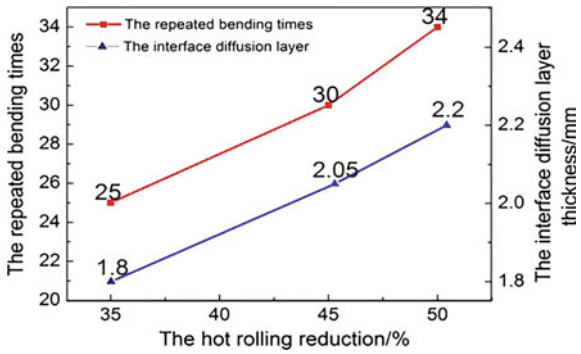

Fig. 7 Comparison of repeated bending test results and interface diffusion layer thickness prepared at different hot rolling reduction when the cold rolling reduction is 45%, the hot rolling temperature is 400 °C

The SEM and EDS images of aluminum/steel laminated composite plates interface are shown in Fig. 6 when the cold rolling reduction is 45% and the hot rolling temperature is 400 °C. It can be seen from Fig. 6 that the interface diffusion layer thickness is about 1.8, 2.05, and 2.2 μm prepared at hot rolling reduction of 35, 45, 50%, respectively when the cold rolling reduction is 45% and the hot rolling temperature is 400 °C. The interface diffusion layer thickness increases with increasing the hot rolling reduction.

The comparison of repeated bending test results and interface diffusion layer thickness are shown in Fig. 7 when the cold rolling reduction is 45% and the hot rolling temperature is 400 °C. Compared with the results of the repeated bending test, it can be seen from Fig. 7 that the interface diffusion layer thickness has a close relationship with the interfacial bonding properties. With the increase of the interface diffusion layer thickness, the interfacial bonding properties is also improved accordingly.

Effect of Hot Rolling Reduction on Interfacial Bonding Properties at Hot Rolling Temperature of 500 °C

The repeated bending results are shown in Fig. 8 when the cold rolling reduction is 45% and the hot rolling temperature is 500 °C, the hot rolling are carried out under the hot rolling reduction of 35, 45 and 50%, respectively. It can be seen from Fig. 8 that when the cold rolling reduction is 45% and the hot rolling temperature is 500 °C, the repeated bending times of hot rolling reduction of 35, 45 and 50% is 50, 54, 57, respectively. And the layered phenomenon does not occur between the base layer and cladding layer of the aluminum/steel laminated composite plates. At the same time, the times of repeated bending increase with increasing hot rolling

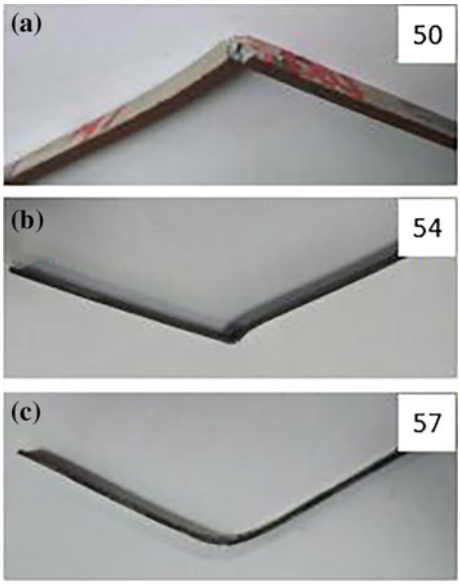

Fig. 8 Repeated bending test specimens of laminated composite plates prepared at different hot rolling reduction when the cold rolling reduction is 45%, the hot rolling temperature is 500 °C. **a** Hot rolling reduction of 35%; **b** hot rolling reduction of 45%; **c** hot rolling reduction of 50%

reduction. Compared to the hot rolling temperature of 400 °C bending test, when the hot rolling temperature increases to 500 °C, the interfacial bonding properties improved significantly.

The SEM and EDS images of aluminum/steel laminated composite plates interface are shown in Fig. 9 when the cold rolling reduction is 45% and the hot rolling temperature is 500 °C. It can be seen from Fig. 9 that the interface diffusion layer thickness is about 2.8, 3.4, and 4 μm prepared at hot rolling reduction of 35, 45, 50%, respectively when the cold rolling reduction is 45% and the hot rolling temperature is 500 °C. The interface diffusion layer thickness increases with increasing the hot rolling reduction. The effect of hot rolling reduction on the interface diffusion layer thickness when the hot rolling temperature is 500 °C is enhanced compared to the hot rolling temperature of 400 °C. When the hot rolling reduction is increased to 50%, the width of the intermetallic compound became larger, the width is about 2 μm.

The comparison of repeated bending test results and interface diffusion layer thickness are shown in Fig. 10 when the cold rolling reduction is 45% and the hot rolling temperature is 500 °C. Compared with the results of the repeated bending test, it can be seen from Fig. 10 that the effect of hot rolling reduction on the intermetallic compounds is more pronounced than that of 500 °C cold rolling.

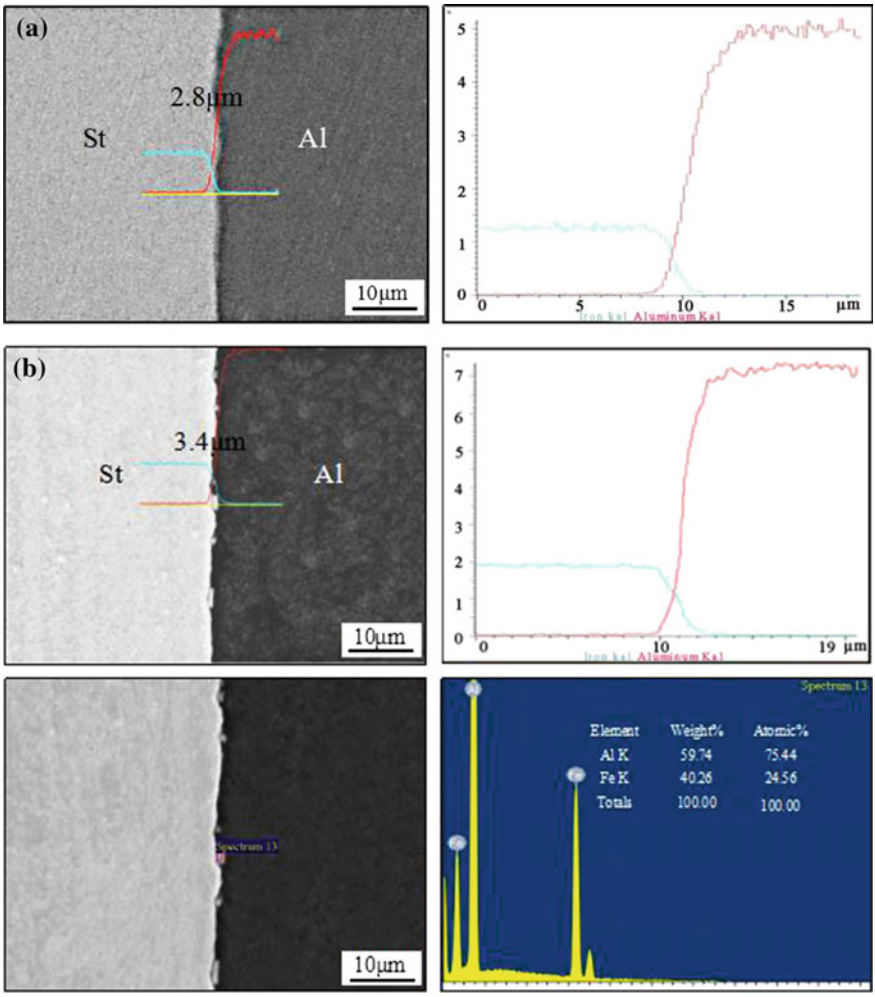

Fig. 9 Distribution of components of laminated composite plates prepared at different hot rolling reduction when the cold rolling reduction was 45%, the hot rolling temperature was 500 °C. **a** Hot rolling reduction of 35%; **b** hot rolling reduction of 45%; **c** hot rolling reduction of 50%

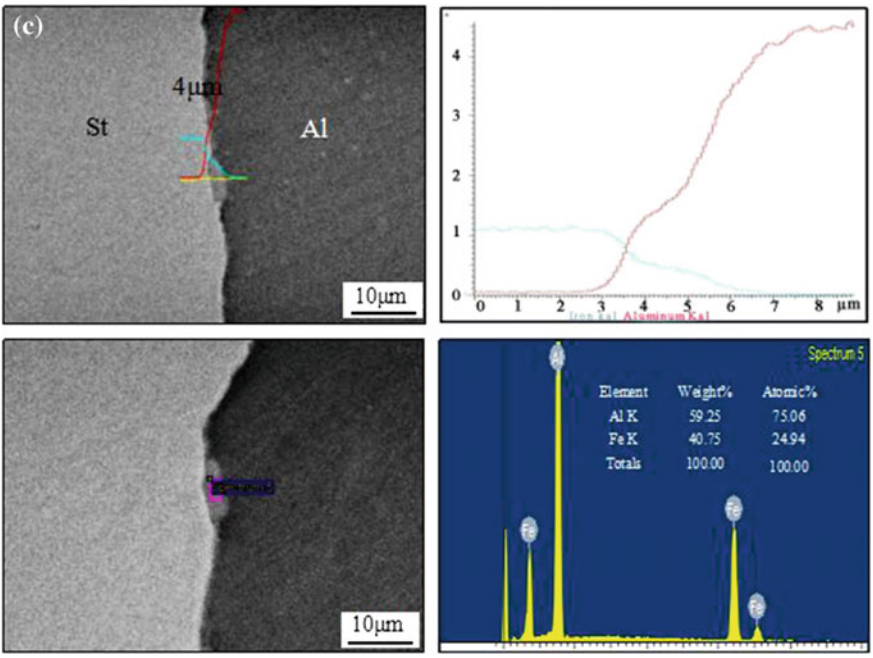

Fig. 9 (continued)

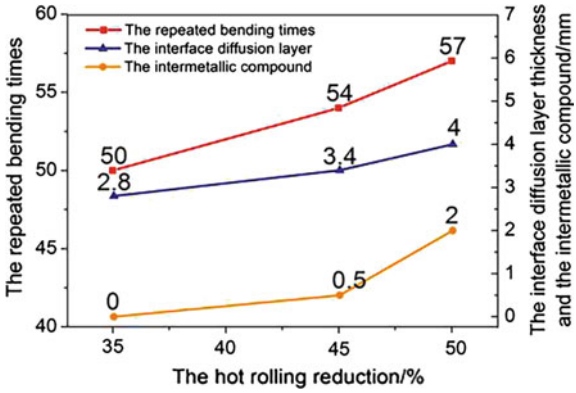

Fig. 10 Comparison of repeated bending test results and interface diffusion layer thickness prepared at different hot rolling reduction when the cold rolling reduction is 45%, the hot rolling temperature is 500 °C

Effect of Hot Rolling Reduction on Interfacial Bonding Properties at Hot Rolling Temperature of 600 °C

The repeated bending results are shown in Fig. 11 when the cold rolling reduction is 45% and the hot rolling temperature is 600 °C, the hot rolling are carried out under the hot rolling reduction of 35, 45 and 50%, respectively. It can be seen from

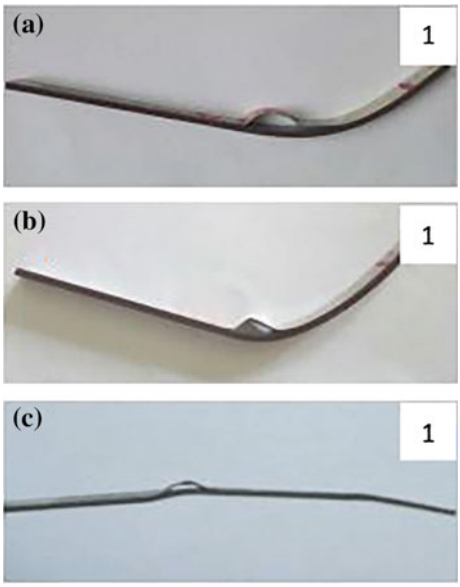

Fig. 11 Repeated bending test specimens of laminated composite plates prepared at different hot rolling reduction when the cold rolling reduction is 45%, the hot rolling temperature is 600 °C. **a** Hot rolling reduction of 35%; **b** hot rolling reduction of 45%; **c** hot rolling reduction of 50%

Fig. 11 that when the cold rolling reduction is 45% and the hot rolling temperature is 600 °C, the repeated bending times of hot rolling reduction of 35, 45 and 50% is 1, 1, 1, respectively. And the layered phenomenon occurs between the base layer and cladding layer of the aluminum/steel laminated composite plates. It is shown that when the hot rolling temperature is increased to 600 °C, the interfacial bonding properties of the aluminum/steel laminated composite plates are seriously deteriorated compared with the hot rolling temperature of 400 and 500 °C. In the repeated bending test, the first bending of the aluminum/steel laminated composite plates and cladding layer will be obviously layered.

The SEM and EDS images of aluminum/steel laminated composite plates interface are shown in Fig. 12 when the cold rolling reduction is 45% and the hot rolling temperature is 600 °C. It can be seen from Fig. 12 that the interfacial diffusion layer thickness is about 7.5, 9.3, and 11 μm prepared at hot rolling reduction of 35, 45, 50%, respectively when the cold rolling reduction is 45% and the hot rolling temperature is 600 °C. And the aluminum/steel laminated composite plates interface generated ≥ 8 μm rod-like intermetallic compounds, it can be found that the intermetallic compound atomic ratio Fe:Al = 2:5 by EDS analysis, the Fe_2Al_5 phase was determined by XRD test. It is shown that the intermetallic compound Fe_2Al_5 phase increases at the interface when the hot rolling temperature is increased to 600 °C, which seriously damages the interfacial bonding properties of the aluminum/steel laminated composite plates. Due to the increase in intermetallic compounds and lateral growth, even if the interface diffusion layer is still increasing, the interface binding performance is also seriously decreased.

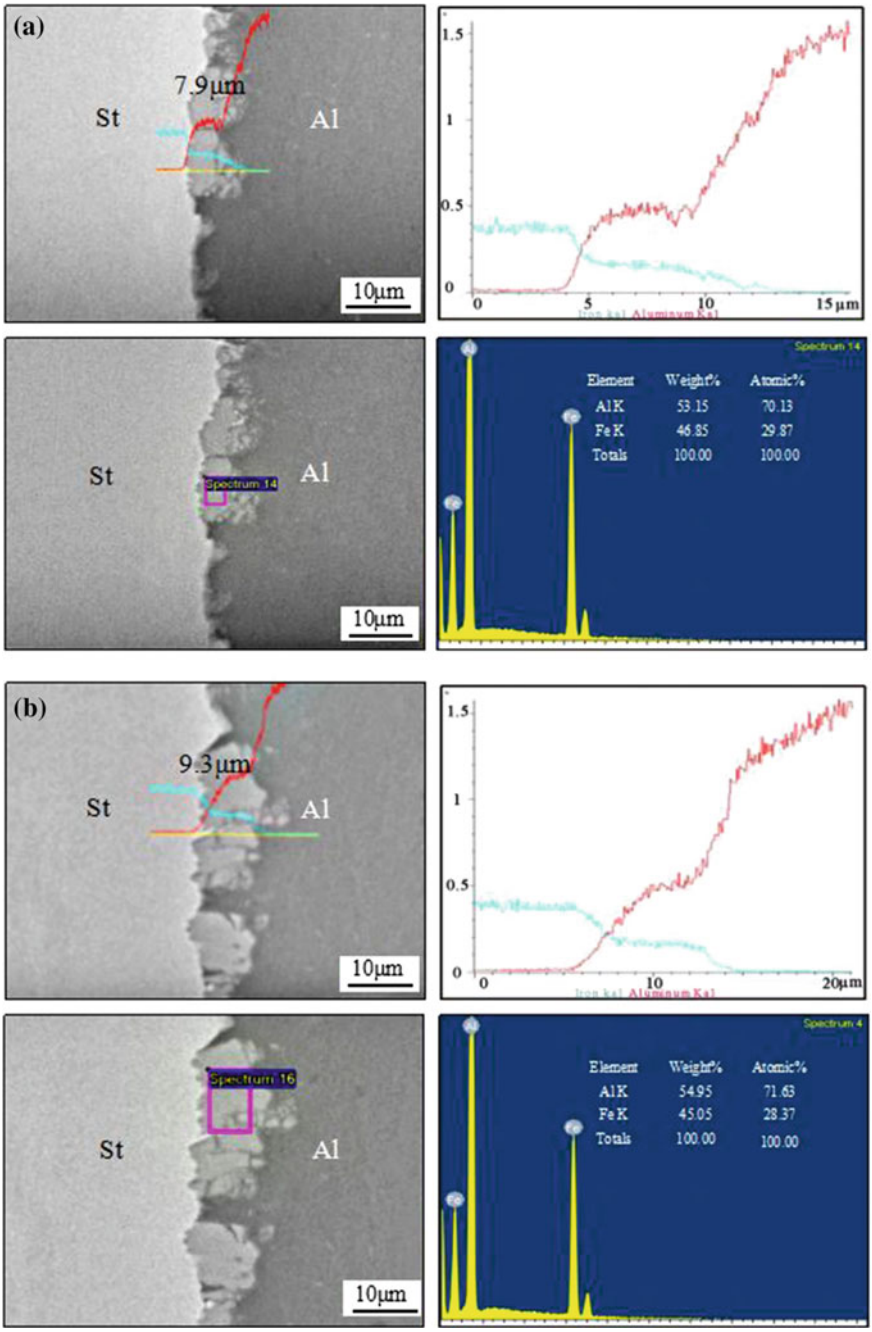

Fig. 12 Distribution of components of laminated composite plates prepared at different hot rolling reduction when the cold rolling reduction is 45%, the hot rolling temperature is 600 °C. **a** Hot rolling reduction of 35%; **b** hot rolling reduction of 45%; **c** hot rolling reduction of 50%; **d** the X-ray diffractometer respectively results of the peeling surface

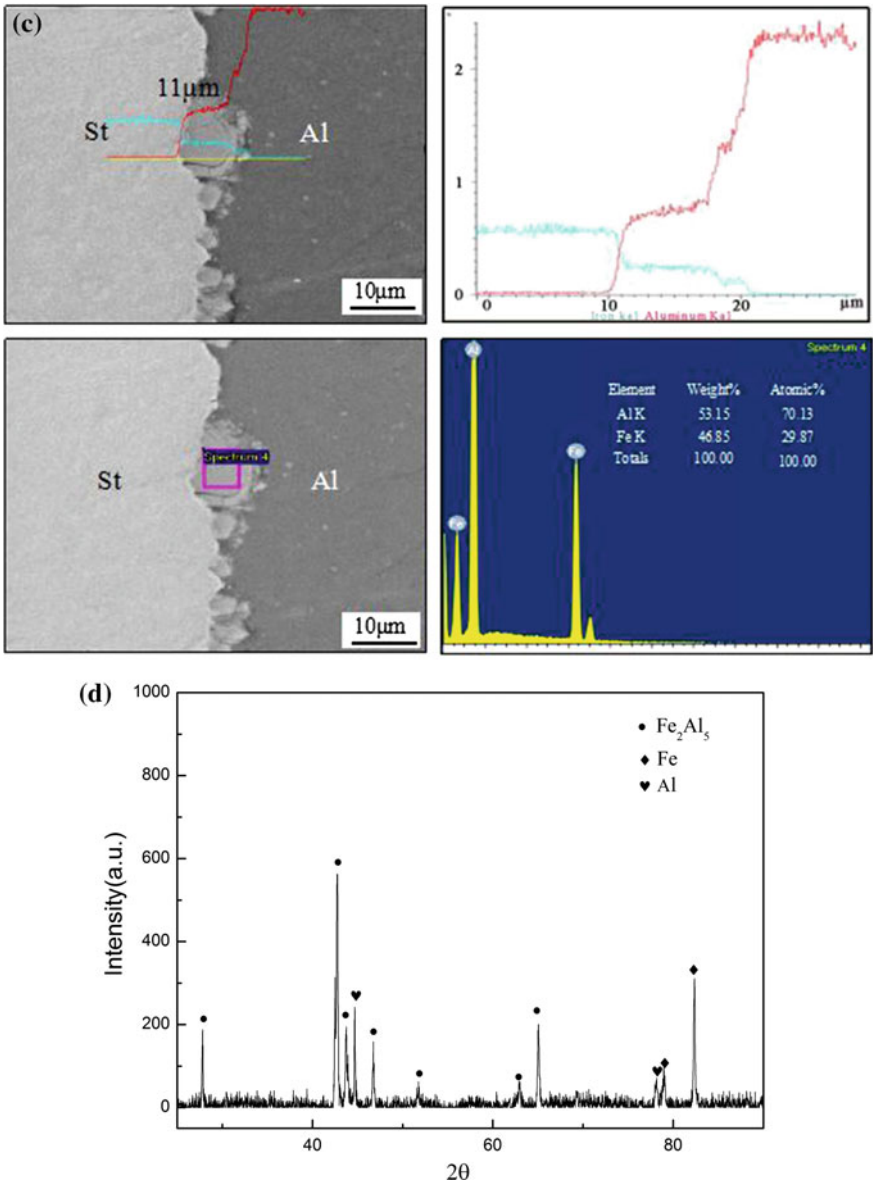

Fig. 12 (continued)

The comparison of repeated bending test results and interface diffusion layer thickness are shown in Fig. 13 when the cold rolling reduction is 45% and the hot rolling temperature is 600 °C. Compared with the results of the repeated bending test, it can be seen from Fig. 13 that the effect of hot rolling temperature on the intermetallic compounds is more pronounced than that of hot rolling reduction and

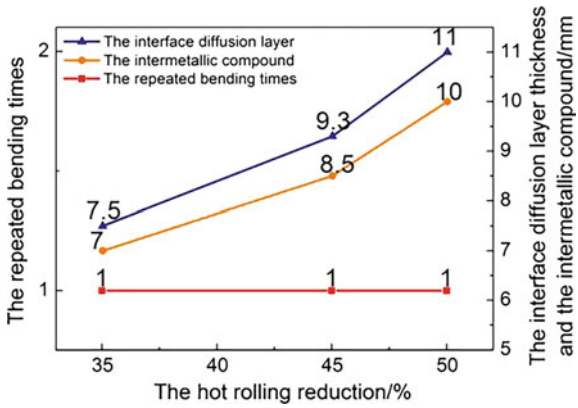

Fig. 13 Comparison of repeated bending test results and interface diffusion layer thickness prepared at different hot rolling reduction when the cold rolling reduction is 45%, the hot rolling temperature is 600 °C

cold rolling reduction. When the hot rolling temperature increases to 600 °C, the interfacial bonding properties decrease sharply even if the interface diffusion layer thickness increases.

Effect of Hot Rolling Temperature on Interfacial Bonding Properties

The repeated bending results are shown in Fig. 14 when the cold rolling reduction is 45% and the hot rolling reduction is 45%, the hot rolling are carried out under the

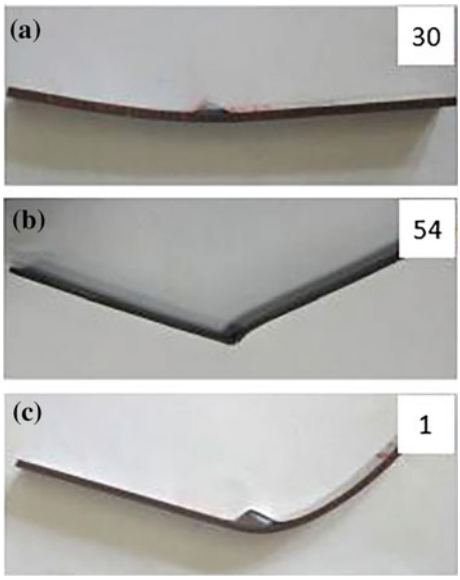

Fig. 14 Repeated bending test specimens of laminated composite plates prepared at different hot rolling reduction when the cold rolling reduction is 45%, the hot rolling reduction is 45%. **a** Hot rolling temperature of 400 °C; **b** hot rolling temperature of 500 °C; **c** hot rolling reduction of 600 °C

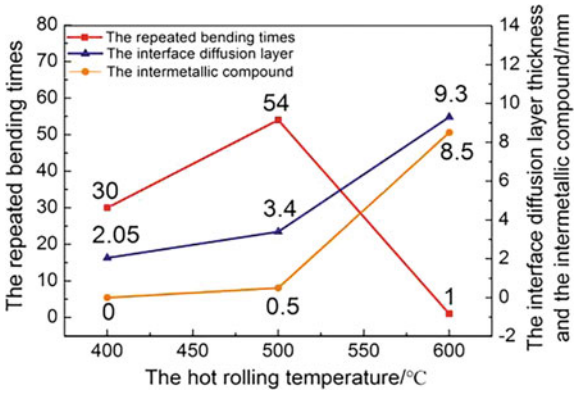

Fig. 15 Comparison of repeated bending test results and interface diffusion layer thickness prepared at different hot rolling temperature when the cold rolling reduction is 45%, the hot rolling reduction is 45%

hot rolling temperature of 400, 500 and 600 °C, respectively. It can be seen from Fig. 14 that when the cold rolling reduction is 45% and the hot rolling reduction is 45%, the repeated bending times of hot rolling temperature of 400, 500 and 600 °C is 30, 54, 1, respectively. And the layered phenomenon occur between the base layer and cladding layer of the aluminum/steel laminated composite plates when the hot rolling temperature is 400 and 600 °C. It is shown that when the hot rolling temperature is increased from 400 to 600 °C, the interfacial bonding properties of the aluminum/steel laminated composite plates increase first and then decrease. In the repeated bending test, the first bending of the aluminum/steel laminated composite plates and cladding layer will be obviously layered.

The comparison of repeated bending test results and interface diffusion layer thickness are shown in Fig. 15 when the cold rolling reduction is 45% and the hot rolling reduction is 45%. Compared with the results of the repeated bending test, it can be seen from Fig. 15 that the effect of hot rolling temperature on the intermetallic compounds is more pronounced than that of hot rolling reduction and cold rolling reduction.

Conclusions

Aluminum/steel laminated composite plate have been prepared by a self-developed cold-hot roll bonding technology at a cold rolling reduction of 45%, a hot rolling reduction of 35%, a hot rolling temperature of 500 °C. Effects of cold rolling reduction, hot rolling reduction and hot rolling temperature on the interfacial bonding properties of aluminum/steel laminated composite plates have been analyzed, the influence mechanism of cold-hot roll bonding process on the interfacial bonding properties of aluminum/steel laminated composite plates have been discussed.

(1) When the hot rolling temperature is kept constant, the increase of cold rolling reduction hot rolling reduction will increase the interface diffusion layer thickness, thus affecting the interfacial bonding properties of the aluminum/steel laminated composite plates, and the impact of the hot rolling reduction is greater than that of cold rolling reduction.
(2) The effect of the interfacial bonding properties from strong to weak is the hot rolling temperature, hot rolling reduction, cold rolling reduction, respectively.
(3) When the hot rolling temperature is 400 °C, the intermetallic compound is not formed at the interface of the aluminum/steel laminated composite plates. The interfacial bonding properties increase with increasing the interface diffusion layer thickness.
(4) When the hot rolling temperature is 500 °C, the interface of the aluminum/steel laminated composite plates prepared at a cold rolling reduction of 45% and a hot rolling reduction of 45% start to generate a discontinuous particulate intermetallic compound $FeAl_3$ phase, the interfacial bonding properties increase with increasing the interface diffusion layer thickness.
(5) When the hot rolling temperature is 600 °C, the interface of the aluminum/steel laminated composite plates begin to form a continuous rod-like intermetallic compound Fe_2Al_5 phase, which has serious damage to the interface bonding performance.

Acknowledgements This research was financially supported by the State Key Laboratory for Advanced Metals and Materials (Grant No. 2014Z-05).

References

1. L. Li, D.J. Zhou, Investigation and application of aluminum clad steel materials. Metal World. **1**, 15–20 (2016)
2. X. Chen, L. Li, D.J. Zhou, Formation and bonding properties of Al(4A60)–steel(08Al) clad strip intermetallic compound. Trans. Nonferrous Metal. Soc. China. **5**, 1176–1184 (2015)
3. Q. Wang, X.S. Leng, T.H. Yang, J.C. Yan, Effects of Fe–Al intermetallic compounds on interfacial bonding of clad materials. Trans. Nonferrous Metal. Soc. China **24**, 279–284 (2014)
4. G.Y. Zu, L. Wang, W. Wang, J.M. Yu, Effect of annealing process on microstructure and properties of Al–Carbon Steel–Al sandwich strip by roll cladding. J. Northeast. Univ. **8**, 1127–1130 (2009)
5. K. Muneharu, R. Manoj, K. Yoritada, K. Yukihiko, Bonding mechanism in roll bonding of low carbon steel and aluminium alloys. Quart. J. Jpn. Weld. Soc. **21**, 101–108 (2003)
6. Q.M. Wu, D.Q. Wang, Y. Gao, Effects of annealing treatment of CCS on interface diffusion and bonding strength. J. Funct. Mater. **23**, 3245–3248 (2012)

Analysis of Large Inclusions in the Working Layer of Centrifugally Cast High-Chromium Steel Composite Roll

Hongliang Fan, Aimin Zhao, Wei Pei, Shaoheng Sun, Wei Liu and Bing Zhang

Abstract The source and formation of large inclusions in the working layer of a centrifugally cast high chromium steel composite roll was investigated using scanning electron microscopy (SEM) and energy dispersive spectrometer (EDS). The results showed that the large inclusions were mainly composed of Si, O and Na, being compounds of SiO_2–Na_2O–Al_2O_3–MnS. The inquiry of the source of Na, as well as the investigation into centrifugal casting process indicated that the large inclusions might be attributed to the refractory coating sprayed on the pouring system and the inner surface of iron mold. The refractory coating was eroded by molten steel during centrifugal casting process and then underwent complicated chemical reactions with molten steel. In the present work, the measures are put forward to prevent large inclusions in the working layer, including reducing the involvement of refractory materials and promoting inclusions floating.

Keywords High chromium steel · Centrifugal casting · Working layer Inclusion · Floating · Coating

H. Fan · A. Zhao (✉) · W. Pei · S. Sun · W. Liu · B. Zhang
Collaborative Innovation Center of Steel Technology, University of Science and Technology Beijing, Beijing 100083, China
e-mail: aimin.zhao@ustb.edu.cn

H. Fan
e-mail: fhl@bit.edu.cn

S. Sun
e-mail: sunshaoheng@139.com

H. Fan
Beijing Institute of Technology Press, Beijing Institute of Technology, Beijing 100081, China

© Springer Nature Singapore Pte Ltd. 2018

Y. Han (ed.), *Advances in Materials Processing*, Lecture Notes in Mechanical Engineering, https://doi.org/10.1007/978-981-13-0107-0_28

Introduction

Hot rolling is one of the most important industrial processes to manufacture finished or semi-finished bulk products, where metal is plastically deformed between mill rolls [1]. Particularly, high chromium steel composite rolls (referred as HCS composite roll hereafter) have been widely used as work rolls for roughing stands in modern hot strip mills by virtue of its excellent performance to endure extreme service conditions [2]. HCS composite rolls are double layered with a high chromium steel shell and a nodular graphite iron core, typically manufactured by centrifugal casting process. The working layer is firstly poured into the spinning mold, creating a centrifugal force to push the molten metal to fill the mold till solidification, and then the core layer is filled under static condition to attain metallurgical combination [3]. Compared to conventional casting method, the working layer of roll produced by centrifugal casting tends to gain finer and more compact microstructure, which can be beneficial to the service life of roll [4].

During hot rolling, both cyclic mechanical and thermal loads are imposed on the work roll surface. The control of non-metallic inclusions is crucial to roll performance. Guan et al. [5] have reported that non-metallic inclusions can act as stress raiser and the maximum von Mises stress appears near inclusions. As a result, fatigue cracks can be induced near inclusions, deteriorating the surface condition as well as the service life of work rolls [6–8]. Fatigue cracks often originate from large inclusions, which tend to be exogenous and emerge here or there casually. The larger and the closer from the surface the inclusion is, the shorter the fatigue life [9]. The present study aims at identifying the ultimate source of large inclusions in an industrial HCS composite roll provided by a roll company. Moreover, preventive measures are figured out.

Experimental Material and Method

In the present work, an HCS composite roll (ø1200 × 1780 mm, Fig. 1) was provided by a roll company. A ring (15 mm in thickness) of working layer was cut from the end of the roll body and then a sample with size of 15 × 20 mm^2 in cross section were machined from the ring. The sample was were ground with abrasive paper of different mesh sizes (180, 320, 400, 600, 1000 and 1500), followed by polishing on nylon cloth with 6 μm diamond paste as the abrasive and then 1 μm paste. Finally, alcohol was used to clean the sample surface for observation.

The sample was observed under an scanning electron microscope (Zeiss Ultra 55) equipped with an energy dispersive spectrometer (EDS) to determine the morphology, and chemical composition of large inclusions.

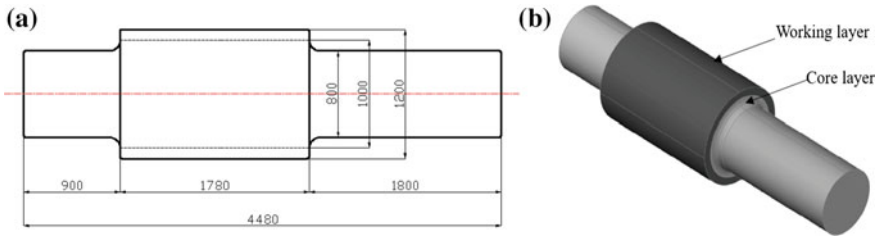

Fig. 1 Dimension (**a**) and Schematic diagram (**b**) of the centrifugally cast HCS composite roll

Results and Discussions

The Morphology, Chemical Composition of Large Inclusions

It should be noted that, the size distribution of large inclusions had to be ignored considering the large size of roll body (ø1200 mm × 1780 mm), though it is an important factor for roll performance. In terms of the sample, four large inclusions visible to naked eyes have been counted in the cross section (15 mm × 20 mm), as shown in Fig. 2. The large inclusion in the middle circle was selected to conduct EDS analysis.

Figure 3a shows the SE micrograph of the selected large inclusion. It appeared spherical with size about 500 μm, embedded in the high chromium steel matrix. Energy dispersive analysis revealed that the inclusion mainly contained O, Si, Na, Al, Mg, Mn, S and Ca (Table 1). Among them, O, Si and Na accounted for the major 95% of weight in total.

Figure 3b–f shows the element distribution maps of the large inclusion. The distinct brightness between the inclusion and the high chromium steel matrix presented in Fig. 3c–f indicates far higher contents of O, Si, Na, and Al inside the inclusion. In addition. Mn content was higher in the edge of the inclusion than that

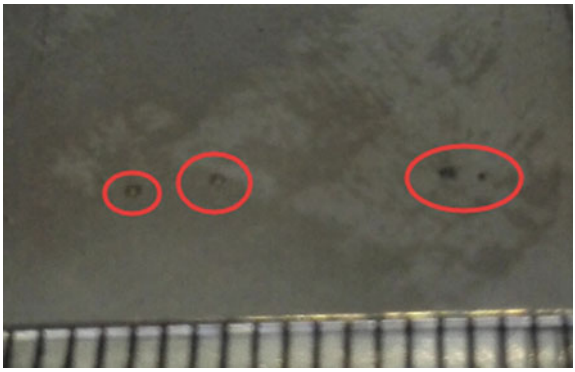

Fig. 2 Macrograph of the large inclusions visible to naked eyes (1 mm per unit)

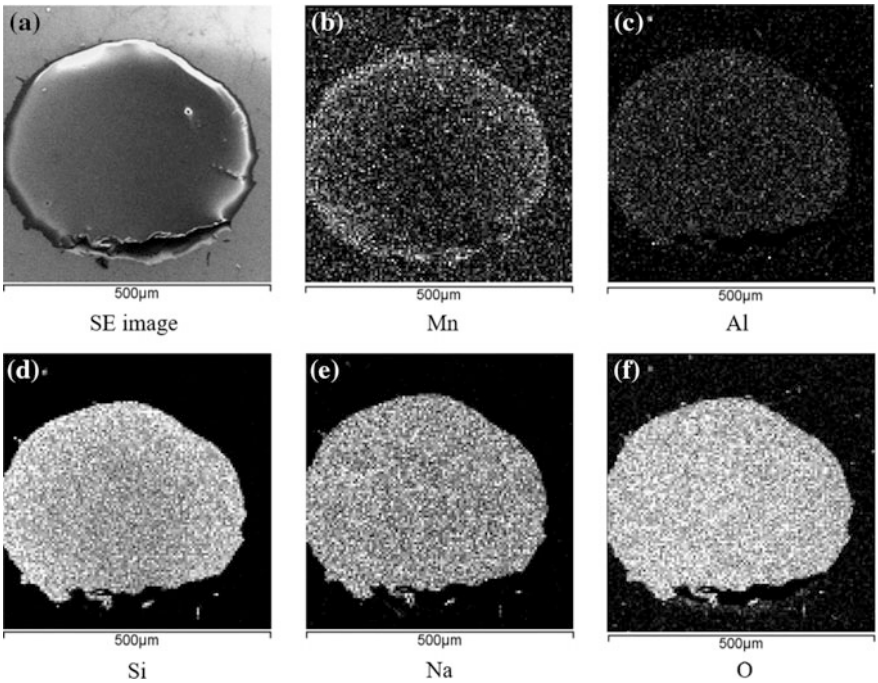

Fig. 3 Micrograph and element distribution maps of a large inclusion

Table 1 Chemical composition of the selected inclusion

Element	O	Na	Mg	Al	Si	S	Ca	Mn
Wt [%]	58.80	15.60	0.28	1.39	21.33	0.23	0.30	2.06

inside the inclusion (Fig. 3b), which implies that the inclusion is wrapped by MnS. Thus, the inclusion is a compound of SiO_2–Na_2O–Al_2O_3–MnS.

According to the morphology and size of the inclusion, it can be inferred that the large inclusion is exogenous. It should be noted that Na accounted for 15% in weight. Based on inquiry of the source of Na, further investigation into centrifugal casting process was made. It was understood that, prior to centrifugal casting, foundry coating was sprayed on the pouring system as well as the inner surface of iron mold, acting as refractories. The foundry coating was a multi-phase material mixed by ingredients including refractory aggregate, binder, suspension concentrate as well as assistant agent [10]. The binder was Na-Bentonite, which was very likely to be the source of Na mentioned above. Therefore, The Na-Bentonite was further studied.

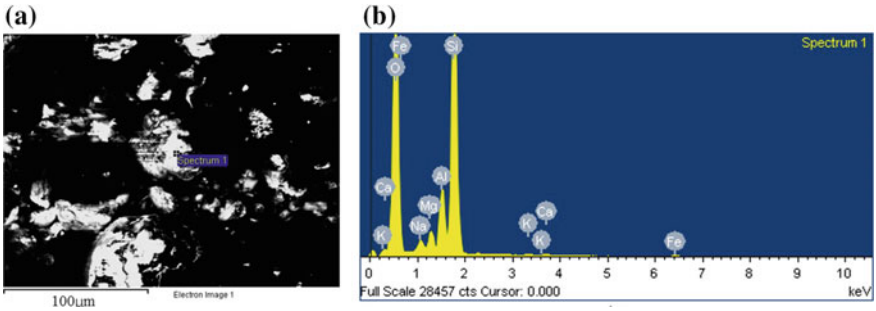

Fig. 4 **a** Micrograph and **b** energy spectrum of Na-Bentonite particles

The Morphology and Chemical Composition of Na-Bentonite

Na-Bentonite powders from the roll company were collected, absorbed onto conductive adhesive, and examined by scanning electron microscope as well as energy dispersive spectroscope. Figure 4a shows the micrograph of Na-Bentonite particles, which were irregularly shaped. Energy dispersive analysis revealed that it contained O, Si, Na, Al, Mg, Fe, and K (Fig. 4b).

Table 2 lists the composition of Na-Bentonite particles. It should be noted that Na content was lower in Na-Bentonite than that in the inclusion, while Mg, Al and Si contents were higher. The differences in size and chemical composition imply that complex chemical reactions have occurred between Na-Bentonite particles and the molten steel.

Brief Summary

Based on results above, definite conclusion can be drawn that the large inclusions originated from the Na-Bentonite, component of the foundry coating. During centrifugal casting, the foundry coating, especially that sprayed on the pouring system, contacted directly with the molten steel. As a result of the insufficient refractoriness, it was eroded and involved into the molten steel. Subsequently, complicated chemical reactions took place between foundry coating particles and molten steel, changing both size and chemical composition to reach thermodynamic stability [11]. Meanwhile, the molten steel solidified rapidly because of the chill effect of the iron mold. As a result, inclusions failed to float up to the free surface of molten steel and remained in the working layer.

Table 2 Chemical composition of Na-Bentonite particles

Element	O	Na	Mg	Al	Si	K	Ca	Fe
Wt [%]	59.53	1.64	2.31	6.67	28.53	0.11	0.24	0.98

Preventive Measures

Improving the Fireproof System

Considering the insufficient refractoriness of the foundry coating, attempts were made to improve the fireproof system. In actual practice, firebricks are stacked to form the fireproof system, which proves to be effective to prevent the fireproof materials from being involved into the molten steel. As a result, the large inclusions are eliminated effectively.

Promoting Floatation of Inclusions

When floatation is accelerated, inclusions will be able to move towards the free surface of the molten steel before solidification [11]. Therefore, the motion law of inclusions during centrifugal casting of the working layer should be analyzed. The floating or sinking speed of inclusions in liquid steel under gravitational field can be depicted by Stokes formula [12], namely:

$$v_g = 2r^2(\rho_1 - \rho_2)g/9\eta. \quad (1)$$

where r is the radius of inclusion, m; ρ_1 is the density of liquid steel, kg/m^3; ρ_2 is the density of inclusion, kg/m^3; g is the gravitational acceleration, m/s^2; η is the viscosity of liquid steel, Pa s.

Figure 5a illustrates the centrifugal casting system. Inclusions in liquid steel are subjected to both centrifugal field and gravitational field during centrifugal casting,

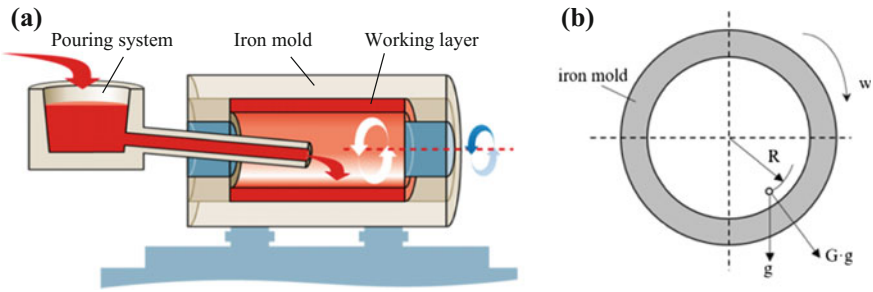

Fig. 5 Schematic diagram of **a** centrifugal casting system and **b** force field

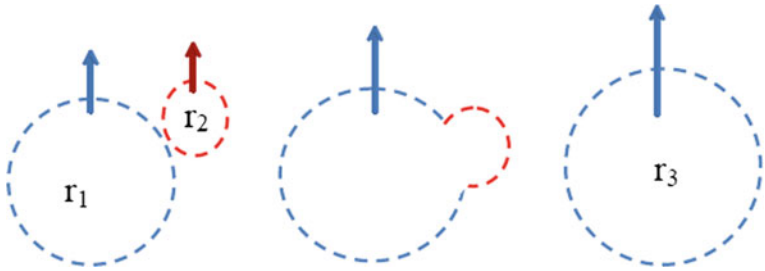

Fig. 6 Schematic diagram of mutual collision and amalgamation of inclusions

as presented is Fig. 5b. Therefore, the inclusions obtain an extra floating or sinking speed v_c in centrifugal field, the formula of which is similar to that of v_g, except the acceleration.

The acceleration ratio of the centrifugal field to gravitational field can be depicted as:

$$G = \omega^2 R/g = n^2 \cdot R/895. \tag{2}$$

where ω is the angular velocity, rad/s; R is the rotary radius, m; n is the rotary radius, r/min; g is the gravitational acceleration, 9.8 m/s^2. Thereby, the motion speed in centrifugal field is given by:

$$v_c = G \cdot v_g. \tag{3}$$

During the practical production, the value of G is designated to dozens or over 100 to obtain compact microstructure. Accordingly, v_g is negligible compared to v_c. The centrifugal casting process itself is favorable for inclusions floatation.

Equation (1) reveals that the floating speed is positively correlated to the size of inclusions. During inclusions floating, the bigger one will catch up with the smaller one, resulting in mutual collision. Subsequently, inclusions grow up gradually by mutual collision and amalgamation, as illustrated in Fig. 6 [13, 14]. As a result, the floating speed of the inclusion increases.

Based on the idea mentioned above, an alternative measure is taken by adding glass slags into iron mold prior to centrifugal casting of molten steel. Glass slags are expected to collide with inclusions when molten steel is poured into the spinning iron mold. Therefore, inclusions are able to reach the free surface before the solidification of molten steel. The practice has shown that the measure is effective in the prevention of large inclusions in the present work.

Conclusions

(1) The large inclusions in the working layer of high chromium steel composite roll are mainly composed of Si, O, Na, Al, Mn and S, being compounds of SiO_2–Na_2O–Al_2O_3–MnS.
(2) The large inclusions originate from the Na-Bentonite in fireproof coating, which are eroded and react with molten steel during centrifugal casing process.
(3) On the one hand, the foundry coating sprayed on the pouring system is replaced by firebricks. On the other hand, considering that the floating speed is positively correlated with the size of inclusions, glass slags are added into iron mold prior to centrifugal casting to promote mutual collision and amalgamation of inclusions. Both measures prove effective to prevent the large inclusions in the present work.

References

1. G. Deng, Q. Zhu, K. Tieu, H.t. Zhu, M. Reid, A.A. Saleh, L.H. Su, T.D. Ta, J. Zhang, C. Lu, Q. Wu, D.L. Sun, Evolution of microstructure, temperature and stress in a high speed steel work roll during hot rolling: experiment and modelling. J. Mater. Process. Tech. **240**, 200–208 (2017)
2. M. Drobne, P. Goncz, S. Glodež, Fatigue behavior of high chromium steel for rolls. Proc. Eng. **10**, 1202–1207 (2011)
3. N. Song, Y. Luan, Y. Bai, Z.A. Xu, X. Kang, D. Li, Numerical simulation of solidification of work roll in centrifugal casting process. J. Mater. Sci. Tech. **28**, 147–154 (2012)
4. D.M. Fu, H.G. Fu, Research process for the manufacturing technique of the composite roll. Heavy Cast. Forgings **2**, 48–52 (2006)
5. J. Guan, L. Wang, C. Zhang, X. Ma, Effects of non-metallic inclusions on the crack propagation in bearing steel. Tribol. Int. **106**, 123–131 (2017)
6. R.D. Mercadosolis, J. Talamantessilva, J.H. Beynon, M.A. Hernandezrodriguez, Modelling surface thermal damage to hot mill rolls. Wear **263**, 1560–1567 (2007)
7. N.F. Garza-Montes-de-Oca, R. Colás, W.M. Rainforth, On the damage of a work roll grade high speed steel by thermal cycling. Eng. Fail. Anal. **18**, 1576–1583 (2011)
8. F.J. Belzunce, A. Ziadi, C. Rodriguez, Structural integrity of hot strip mill rolling rolls. Eng. Fail. Anal. **11**, 789–797 (2004)
9. S.Q, Y. Liang, F. Zhao, Influences of inclusion size and position on fatigue life of 51CrV4 spring steel. Mater. Mech. Eng. **35**, 85–87 (2011)
10. T.Z. Wen, Y.Z. Guo, Overview of roll new technology and future development, 1st edn (Shijiazhuang 2014)
11. W.X. Song, Metallography, 2nd edn (Beijing, 2008)
12. H. Fu, Q. Xiao, J. Xing, A study of segregation mechanism in centrifugal cast high speed steel rolls. Mater. Sci. Eng. A **479**, 253–260 (2008)
13. L. W, M. Deng, D. Zhang, Y. Shu, Polymerization and removal control of non-metallic inclusion, in *18th Symposium of Steel Making* (The Chinese Society for Metals, 2014)
14. S.Z. Hao, S.S. Cheng, Z.J. Jing, Z.J. Cheng, Inclusion coagulation and removal rate in molten steel. J. Univ. Sci. Technol. Beijing **30**, 118–120 (2009)

Optimization of 6005 Aluminum Alloy Components

Gang Sun, Pengwei Li, Qingmei Ma, Pilin Cui, Xiangjie Wang, Bo Huang and Jianzhong Cui

Abstract By comparing nine groups of experiments, the influences of Mg, Si, Cu and Mn on the strength, plasticity and conductivity of 6005 alloy were researched. The results show that α-Al, Mg_2Si, Si and β-AlFeSi are mainly present in the as-cast microstructure of 6005 aluminum alloy. The strength, plasticity and electrical conductivity of the 6005 aluminum alloy of 9 groups were compared and then select a good overall performance of an alloy composition, which is Al–0.53Mg–0.72Si–0.2Cu–0.28Mn–0.18Cr–0.05Ti (wt%). The tensile strength, yield strength, elongation, hardness and electrical conductivity of the extruded alloy are 310.9, 280.1 MPa, 11.95%, 102.3 HV and 47.2% IACS, respectively, after solid solution, air-cooling and 175 °C × 8 h aging.

Keywords 6005 aluminum alloy · Composition optimization · Heat treatment Microstructure

G. Sun · P. Li · Q. Ma · P. Cui · X. Wang (✉) · B. Huang · J. Cui
Key Lab of Electromagnetic Processing of Materials, Ministry of Education, Northeastern University, Shenyang 110004, People's Republic of China
e-mail: wangxj@epm.neu.edu.cn

G. Sun
e-mail: 508359545@qq.com

P. Li
e-mail: 29189340@qq.com

Q. Ma
e-mail: 347181027@qq.com

P. Cui
e-mail: 821255801@qq.com

B. Huang
e-mail: 791953243@qq.com

J. Cui
e-mail: jzcui@epm.neu.edu.cn

© Springer Nature Singapore Pte Ltd. 2018

Y. Han (ed.), *Advances in Materials Processing*, Lecture Notes in Mechanical Engineering, https://doi.org/10.1007/978-981-13-0107-0_29

Introduction

At present, with the development of the rail transit construction in China, materials performance of high-speed train body also put forward higher requirements [1–3]. Due to the high corrosion resistance and high specific strength, aluminum alloys are currently being used in rail vehicles [3–5]. 6005A is a medium-strength Al–Mg–Si aluminum alloy with excellent resistance to extrusion and good weldability [6]. It was a good material which high-speed train body requires for manufacturing the thin wall hollow large wall profile profiles.

6005 aluminum alloy is an excess of silicon containing Al–Mg–Si alloy, magnesium and silicon as the main strengthening elements, and Mg_2Si is the main strengthening phase [5]. After heat treatment, it has the characteristics of moderate strength, high impact toughness, no sensitivity to the gap, wide quenching temperature range and low quenching sensitivity [7–11]. In this paper, the influence of the main alloying agent Mg, Si, Cu and trace elements Mn on the microstructure and properties of the aluminum alloy was investigated.

The strength, plasticity and electrical conductivity of the 6005 aluminum alloy of 9 groups were compared and a good overall performance of an alloy composition was selected.

Experimental Procedure

The raw materials used in the experiment were industrial pure aluminum, industrial pure magnesium, pure copper, 80 wt% Chromium agent, and 75 wt% Manganese agent. The grain refinement agent used in the experiment was A1–5% Ti–1% B, the smelting device adopted the SCR intermediate frequency resistance furnace, the melting temperature was 750–800 °C and the degassing agent was hexachloroethane. The order of addition of the smelting process was Al, Si, Cu, Mn, Cr, Mg, and the Al–Ti–B was finally added. After the melt transfer was completed, it is transferred to the holding furnace, the alloy was maintained at a temperature of 750–760 °C, and the slag was removed. Finally, the melt was poured into a water-cooled copper mold. And then took it out in water and cooled to room temperature. The experiment obtained an ingot, which length was 300 mm and the diameter was adjusted to 85 mm. The homogenization temperature of the experiment was 540 °C, the heat preservation time was 8 h, and cooling method was furnace cooling. Then the ingot was homogenized by a well furnace, and the composition and organization of the ingot were homogeneous and the internal stress was eliminated. The ingot was subjected to positive extrusion, and the homogenized annealed ingot was peeled to remove the ingot surface oxide to obtain a rod of φ80 mm. And then squeezed into a section size of 40 mm × 4 mm plate. Finally, the extruded sheet was subjected to on-line air-cooled solid solution and placed in an electric blast oven for aging.

Table 1 Composition of the alloys designation (wt%)

Alloy	Mg	Si	Cu	Mn	Cr	Ti	Bal.
1	0.53	0.62	0.1	0.23	0.18	0.05	Al
2	0.58	0.62	0.15	0.28	0.18	0.05	Al
3	0.63	0.62	0.2	0.33	0.18	0.05	Al
4	0.63	0.67	0.1	0.28	0.18	0.05	Al
5	0.53	0.67	0.15	0.33	0.18	0.05	Al
6	0.58	0.67	0.2	0.23	0.18	0.05	Al
7	0.58	0.72	0.1	0.33	0.18	0.05	Al
8	0.63	0.72	0.15	0.23	0.18	0.05	Al
9	0.53	0.72	0.2	0.28	0.18	0.05	Al

The prepared ingot and extruded sheet were subjected to metallographic observation, XRD analysis, scanning analysis, hardness and conductivity tensile test. At the same time, the experimental data were recorded.

In this experiment, the effects of different Mg, Si, Cu and Mn contents on the microstructure and properties of the aluminum alloy were researched. The purpose is to find a group of the best Mg, Si, Cu, Mn ratio, so that the alloy has a good overall performance. Table 1 is the design of the experiment 9 alloys composition.

Results and Discussion

Analysis of As-Casting Microstructure and Properties

Figure 1 for the as-cast alloy 1–9 anode coating picture, the average grain size of 9 alloys was measured by a straight line cut method which was adopted the Image-Pro Plus6.0 software. The results show that the grain size of alloy 1 is 119.8 μm, the grain size of alloy 8 is 88.3 μm, the other seven grains are about 80 μm. And the grain size of the alloy 9 was the smallest, which was 71.3 μm. It is thus judged that the composition of alloy 9 is best for finely grained grains. It is judged that the composition of the alloy 9 has the best effect on the grain refinement.

Figure 2 shows the hardness and conductivity of cast alloys. With the change of composition, the hardness of casting alloy is 59.1–69.3 HV. Alloy 1 has a minimum hardness of 59.1. Among them, the hardness of alloy 7 and 9 is higher, and the hardness of alloy 9 up to 69.3 HV. At the same time, the change of composition had no obvious effect on the trend of conductivity change, and most of them fluctuated around 34% IACS. The hardness and conductivity were compared, and the alloy 9 had the highest hardness (69.3 HV) and excellent conductivity (34.9% IACS).

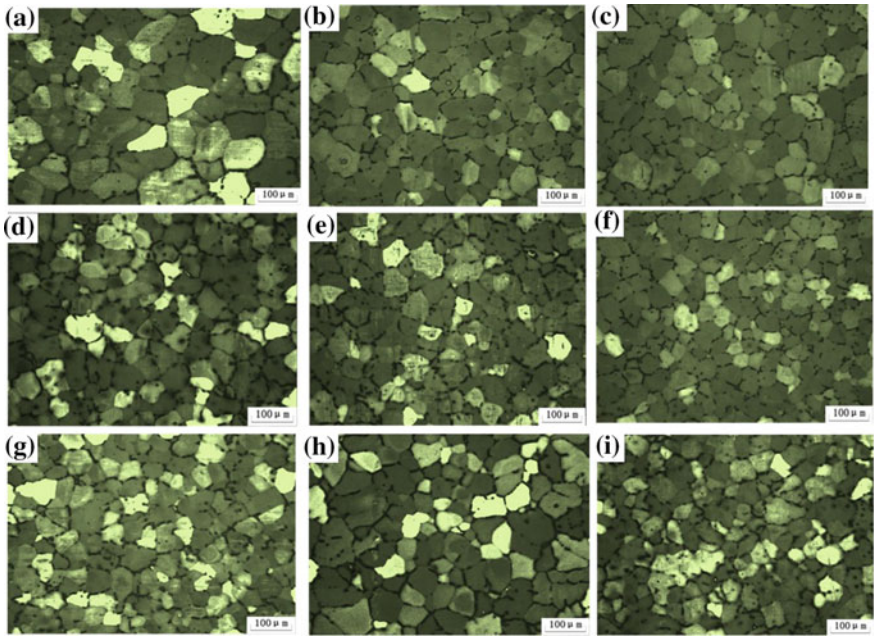

Fig. 1 Microstructure of orthogonal alloys by polarized light. **a** alloy1; **b** alloy2; **c** alloy3; **d** alloy4; **e** alloy5; **f** alloy6; **g** alloy7; **h** alloy8; **i** alloy9

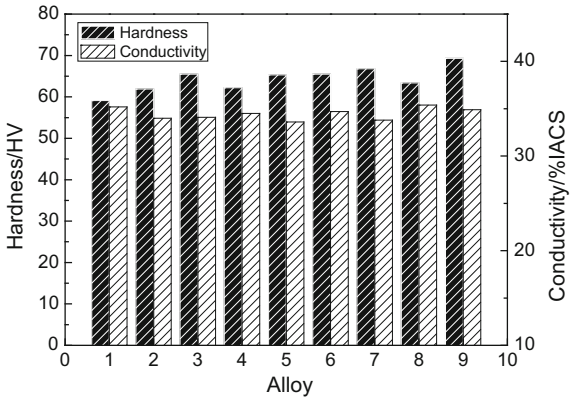

Fig. 2 Hardness and conductivity of as-cast alloys 1–9

Performance Analysis of Extruded Alloy After Heat Treatment

The performance of the extruded plate was tested after heat treatment, which solid solution system is on-line solution, cooling methods is air-cooled and aging system is 175 °C × 8 h [12].

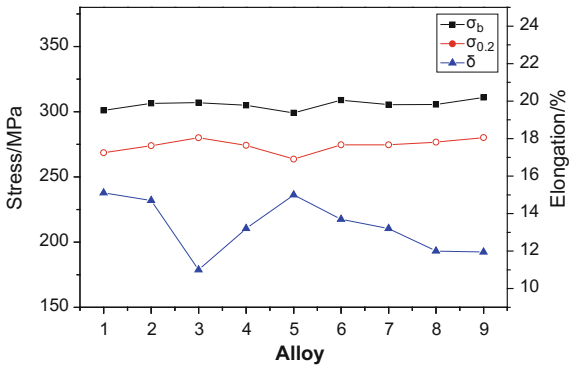

Fig. 3 Mechanical properties of alloy 1–9 after heat treatment of extruded sheet

Figure 3 shows the mechanical properties of alloy after heat treatment of extruded sheet. In the alloy 1–9, with the composition of the change, there are same trend on the tensile strength and yield strength. The tensile strength of alloy 6 and alloy 9 is the highest while the yield strength of alloy 9 is also the highest of 280.1 MPa. It can be seen from the line graph that the plasticity of 9 alloys is inversely proportional to the strength. The tensile strength (299.1 MPa) and the yield strength (263.7 MPa) of alloy 5 are the lowest, and the elongation is the highest (15%).

According to Fig. 4, the hardness and conductivity of the extruded alloy are similar to those of the as-cast, and the hardness and conductivity of the extruded alloy are greatly improved after heat treatment. Hardness range of 9 alloys is 95.1–102.3 HV and alloy 9 has the highest hardness value of 102.3 HV. The conductivity varies smaller with the alloy composition. The conductivity of alloy 3 is lowest of 45.6% IACS, the highest 47.7% IACS of alloy 7, where alloy 9 has excellent electrical conductivity (47.2% IACS).

By comparing the mechanical properties and electrical conductivity of 9 alloys cast and extruded heat treatment, considering the most important strength index of

Fig. 4 Hardness and conductivity of extrusion sheet after heat treatment alloy 1–9

alloy, it is concluded that the comprehensive performance of alloy 9 is the best after the same extrusion process and aging system. Therefore, the optimum alloy composition was determined in this research as: Al–0.53Mg–0.72Si–0.2Cu–0.28 Mn–0.18Cr–0.05Ti (wt%).

Phase Analysis

The as-cast samples of alloy 9 were subjected to XRD analysis, and the phases existed in the as-cast alloys were qualitatively analyzed. Figure 5 shows the XRD results of Alloy 9.

The Mg_2Si strengthened phase in the alloy was detected by XRD analysis of alloy 9. Since the 6005 alloy composition is designed according to the excess Si principle, the excess Si can refine the Mg_2Si of the main strengthening phase, Simultaneous growth of Si after precipitation, and Al with $Al_{3.21}Si_{0.47}$ phase [13]. While the impurity element Fe forms an impurity phase AlFeSi with Al and Si elements.

Figure 6 shows the alloy 9 as-cast microstructure analysis. From the metallographic analysis of the as-cast microstructure of the alloy of Fig. 1, it is found that many black spots and a large amount of block material exist in the crystal and grain boundaries. In order to further determine the phase contained in the as-cast structure, the alloy phase composition and the distribution of the main alloying elements were analyzed by SEM.

As shown in Fig. 6a, a large number of long strip phase can be found. It mainly containing Al, Mg, Si elements, and the phase of Mg, Si atomic ratio close to 2:1, and the predicted phase is Mg_2Si. It can be seen from Fig. 6c that there are also large white stripes in the alloy which are not dissolved in the matrix. The phase

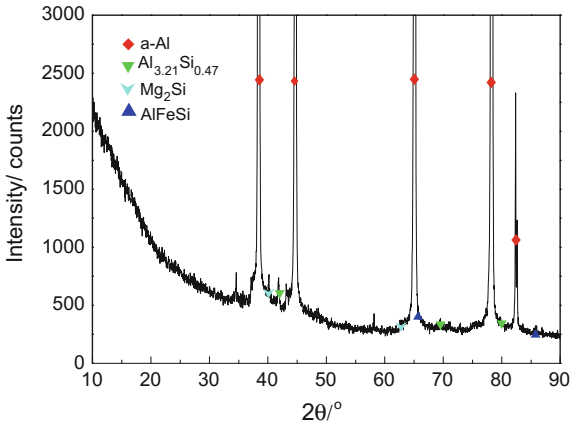

Fig. 5 XRD graph of alloy 9

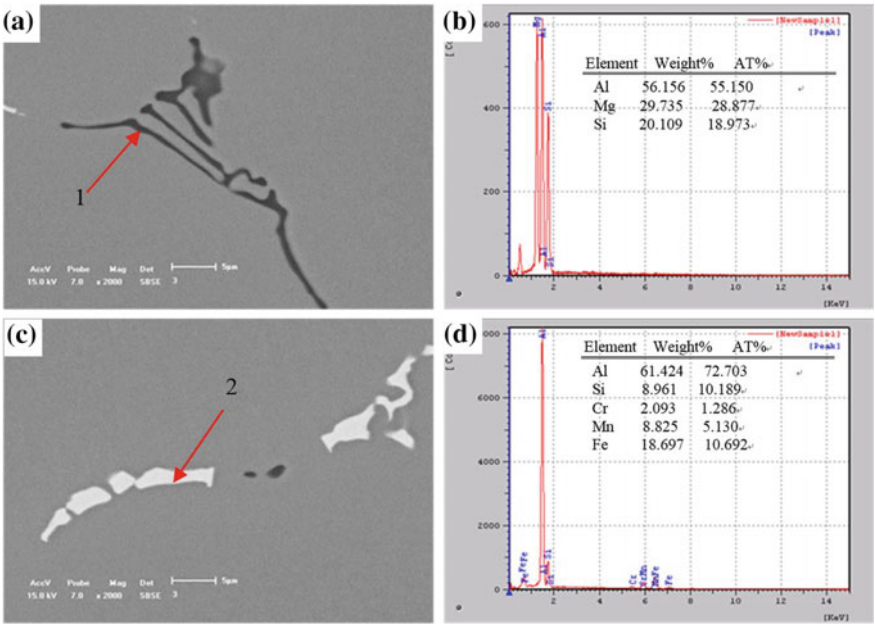

Fig. 6 SEM images of alloy 9. **a, c** SEM images; **b** EDS analysis result of phase 1 in image (**a**); **d** EDS analysis result of phase 2 in image (**c**)

mainly contains Al, Si and Fe, and the content of Si and Fe is high, and it is presumed to be β-AlFeSi phase [14].

Figure 7 shows the surface scan profile of the main alloying elements in the cast alloy 9, It can be seen a white plate-like phase that is not dissolved in the matrix. And the main element of the phase containing Al, Si, Fe, while Si, Fe content is very high, initially presumed to β-AlFeSi phase [15]. The presence of this phase increases fragility of grain boundary, which adversely affects the properties of the

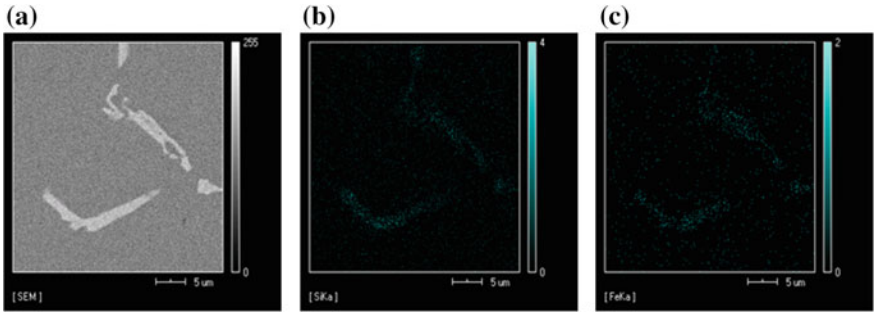

Fig. 7 SEM images showing the element distribution in alloy 9. **a** SEM observation of alloy 9; **b** Si; **c** Fe

alloy. Therefore, it is necessary to strictly control the incorporation of impurities in the smelting process.

The strengthening phase after extrusion is small, dispersed and relatively dense distribution in the matrix, which play a pinning sub-grain boundary and inhibit the role of its rearrangement. In addition, the fine dispersion phase can strongly inhibit the nucleation and growth of recrystallized grains. At the same time, 6005 aluminum alloy in the process of aging will also precipitate a large number of small dispersion strengthening phases, thus achieved a higher strength.

As fine grain in the as-cast can reduce the size of the recrystallized grains. Because the increase of large-angle grain boundaries in the ingot increases the nucleation rate of the recrystallization, which is beneficial to improve the microstructure and properties of the alloy. It is for these reasons that alloy 9 has the best overall performance.

Summary

The effects of Mg, Si, Cu and Mn on the properties of 6005 alloy were analyzed by comparison experiment and the mechanical properties and electrical conductivity of the 9 groups of alloys after cast and extrusion were researched. The results show that the comprehensive performance of alloy 9 is the best. The preferred alloying composition is: Al–0.53Mg–0.72Si–0.2Cu–0.28Mn–0.18Cr–0.05Ti (wt%).

The tensile strength, yield strength, elongation, hardness and electrical conductivity of the extruded alloy were 310.9, 280.1 MPa, 11.95%, 102.3 HV and 47.2%. After solid solution, on-line air-cooled and 175 °C × 8 h aging treatment.

The α-Al, Mg2Si, Si and β-AlFeSi phases are mainly existed in as-cast microstructure of 6005 aluminum alloy.

Acknowledgements This work was supported by the Liaoning Provincial Natural Science Foundation of China (2015021002), Hi-Tech Research and Development Program of China (2013AA032402), the Fundamental Research Funds for the Central Universities (N150904001 and N160913001), the National Natural Science Foundation of China (51574075 and U1608252), the National Key Research and Development Program of China (2016YFB0300901) and the China Postdoctoral Science Foundation (2015M570250).

References

1. Y.J. Wang, H.G. Ding, Development status and prospect of aluminum alloy body manufacturing technology in China. J. Weld. **10**, 5–7 (2004)
2. S.G. Yao, P. Xu, New materials in the application of high-speed bus railway locomotive vehicles. J. Railway Rolling Stock. **2**, 24–26 (2010)
3. B.H. Li, S.C. Yan, 6005 selection of chemical composition of aluminum alloy. J. Light Alloy Process. Technol. **29**, 29–30 (2001)
4. F.S. Pan, *Aluminum Alloys and Applications* (Chemical Industry Press, Beijing, 2006), pp. 90–93

5. M. Liu, J. Banhart, Effect of Cu and Ge on solute clustering in Al–Mg–Si alloys. Mater. Sci. Eng., A **194**, 238–245 (2016)
6. B.S. Murty, S.A. Kori, M. Chakraborty, Grain refinement of aluminum and its alloys by heterogeneous nucleation and alloying. Int. Mater. Rev. **47**, 3–29 (2012)
7. M.C. Zhu, Y. Dong, D.D. Ji, Heat treatment technology of aluminum alloy. J. Silicon Valley **21**, 7–13 (2011)
8. Z.T. Wang, R.Z. Tian, *Aluminum Alloys and Their Machining Handbook* (Central South University of Technology Press, Changsha, 1988), pp. 9–17
9. S.R. Claves, D.L. Elias, W.Z. Misiolek, Analysis of the intermetallic phase transformation occurring during homogenization of 6000 aluminum alloys. J. Mater. Sci. Forum **20**, 396–402 (2002)
10. Y.L. Liu, S.B. Kang, H.W. Kim, The complex microstructures in an as-cast Al–Mg–Si alloy. J Mater. Lett. **12**, 267–272 (2014)
11. C.W. Ravi, First-principles study of crystal structure and stability of Al–Mg–Si–(Cu) precipitates. J. Acta Mater. **52**, 4213–4227 (2004)
12. M.C. Zhu, Y. Dong, Performance studies and organizations of 6005 aluminum alloy aging treatment. J. Hot Working Technol. **9**, 7–13 (2012)
13. A.R. Anderson, Study on organizational performance of 6005A aluminum alloy. J. AFS Trans. **83**, 53–56 (1997)
14. S.M. Hirth, G.J. Marshall, S.A. Court et al., Effects of Si on the aging behavior and formability of aluminum alloys based on 6005. J. Mater. Sci. Eng. A **12**, 452–456 (2001)
15. A.K. Gupta, D.J. Lloyd, S.A. Court, Precipitation hardening in Al–Mg–Si alloys with and without excess Si. J. Mater. Sci. Eng. A **31**, 11–17 (2011)

Role of Annealing Time in Thin-Gauge Non-oriented Silicon Steels Processed by Strip Casting

Haitao Jiao, Wei Xiong, Jiapeng Yang, Yuangxiang Zhang, Feng Fang, Chenggang Li, Guangming Cao, Yunbo Xu and Yongmei Yu

Abstract Cold-rolled Fe–2.6%Si sheets of 0.20 thickness prepared by strip casting and two-stage cold rolling were annealed for different time. The microstructure and texture of all samples were investigated by optical microscopy, electron backscattered diffraction and X-ray diffraction to illustrate the effect of annealing time on the development of texture and magnetic properties. The sample in the initial stage of complete recrystallization was characterized by strong η, γ and α component. Goss grains possessed size advantage, and γ grains showed the highest number density. Subsequently, γ-fiber and α-fiber was gradually weakened, whereas η-fiber always predominated the texture. However, with further increase in annealing time, γ-fiber was significantly enhanced and being a dominant component as a result of growth

H. Jiao · W. Xiong · J. Yang · Y. Zhang · F. Fang · C. Li · G. Cao · Y. Xu (✉)
State Key Laboratory of Rolling and Automation, Northeastern University, Shenyang 110819, China
e-mail: yunbo_xu@126.com

H. Jiao
e-mail: andrewjiao@163.com

W. Xiong
e-mail: 411179432@qq.com

J. Yang
e-mail: 287796930@qq.com

Y. Zhang
e-mail: redyuanxiang@126.com

F. Fang
e-mail: fangfengdbdx@163.com

C. Li
e-mail: licg@ral.neu.edu.cn

G. Cao
e-mail: caogm@ral.neu.edu.cn

Y. Yu
School of Mechanical Engineering, Shenyang University of Chemical Technology, Shenyang 110142, China
e-mail: yongmei_yu@126.com

© Springer Nature Singapore Pte Ltd. 2018

Y. Han (ed.), *Advances in Materials Processing*, Lecture Notes in Mechanical Engineering, https://doi.org/10.1007/978-981-13-0107-0_30

selection of γ grains. Ultimately, the magnetic induction gradually decreased after an increase over time, whereas the core loss displayed a continuous decrease. Texture development with annealing time in the present study could be explained by orientated nucleation mechanism and orientation pinning effect.

Keywords Thin-gauge non-oriented silicon steels · Annealing time
Texture · Magnetic properties

Introduction

Thin-gauge non-oriented silicon steel is an important functional material to fabricate iron cores in medium and high frequency motor [1, 2]. The magnetic properties directly influence the traction performance and fuel consumption. For instance, high magnetic permeability can raise the motor torque and low core loss will increase the motor efficiency. It is well known that conventional processing route of non-oriented silicon steel is rather complicated, generally consisting of casting, reheating, hot rolling, normalizing or not, cold rolling and annealing. Moreover, detrimental γ-fiber ($\langle 111\rangle//\mathrm{ND}$) and α*-fiber ($\{11h\}\langle 1\,2\,1/h\rangle$) recrystallization texture are readily developed because of multi-pass hot rolling with heavy reduction and small grain size prior to cold rolling [3]. For the sake of simplifying the process and improving magnetic properties, various technological means, such as thin slab continuous casting and rolling, are explored and carried out [4]. In recent years, low-cost strip casting has widely been paid attention and employed to fabricate silicon steels [5–8]. It can obtain strips of 1–5 mm thickness directly from molten steel without reheating and heavy-reduction hot rolling. Previous studies indicated that non-oriented silicon steel with thickness of 0.35–0.50 mm (the commonly used grade) exhibited stronger Cube ($\{100\}\langle 001\rangle$) and higher magnetic induction compared to the conventional products [8, 9]. However, the research on the relationship between the processing route and the evolution of structure and texture in thin-gauge silicon steel, such as 0.20 and 0.10 mm, was rather little.

In general, annealing is the final process in preparing non-oriented silicon steel besides coating. Microstructure and texture of the annealed sheets directly determine the magnetic properties. During annealing of cold-rolled sheets with single-phase ferrite, recovery, recrystallization and grain growth occur, which are considerably influenced by annealing parameters. The previous works mainly focused on the relationship between recrystallization texture and annealing atmosphere [10], or heating rate [11] or heat transport [12] during final annealing processes. The role of annealing time on the development of recrystallization texture has not been studied to better understanding.

In the presented work, non-oriented silicon steel with thickness of 0.20 mm was prepared by strip casting and two-stage cold rolling, and heat-treated at 950 °C for different holding time (25 s–25 min). The aim of this paper is to illustrate the role

of annealing time in the development of recrystallized microstructure, texture and magnetic properties during a continuous annealing process.

Materials and Experimental Procedure

A Fe–2.6%Si–0.005%C as-cast strip with thickness of 1.8 mm was produced using a laboratory twin roll strip caster with copper rollers of 110 mm in width [8]. The air-cooled strip was cold rolled to 0.20 mm by a two-stage schedule of first rolling reduction of 68%. Intermediate annealing was performed at 950 °C for 4 min. Subsequently, samples in size of 100 mm (rolling direction) × 30 mm (transverse direction) was cut from cold-rolled sheets and annealed at 950 °C for 25 s, 1, 2, 4, 8, 25 min, respectively. Nitrogen was used as a protective atmosphere in this experiment.

Microstructure of cold-rolled sheet was observed by an optical microscope (OM). Grain orientation maps at different annealing time were determined by the electron backscatter diffraction (EBSD) technique. Macro-textures of cold rolled and annealed sheets were characterized by ODFs (orientation distribution functions) that were calculated from three incomplete pole figures {110}, {200} and {211} measured by Bruker D8 Discover X-ray diffractometer. In addition, the specific core loss $P_{10/400}$ and magnetic induction B_{50} were measured using a single sheet tester.

Results and Discussion

Microstructure

Figure 1 shows the microstructure and texture of cold-rolled sheets with thickness of 0.2 mm. An inhomogeneous microstructure composed of lightly etched structure and darkly etched deformation structure with a number of shear bands (as shown in Fig. 1a). Generally, grain boundaries can be easily etched and display black in the metallography. However, the greater the degree of deformation, the more seriously the grain is fragmented. It suggests that darkly etched areas contained more boundaries and stored energy as a result of severe deformation. In analogy to the results observed in cold-rolled sheets of 0.35–0.5 mm thickness [8, 9], the inhomogeneity of microstructure here is related to the different deformation behavior of grains with different Taylor factors [13]. Furthermore, the cold-rolled sample exhibited strong γ-fiber and α-fiber (⟨110⟩//RD) texture with a maximum at {223}⟨110⟩ besides weak {100} texture (as shown in Fig. 1b), which are typical components in cold-rolled bcc metals.

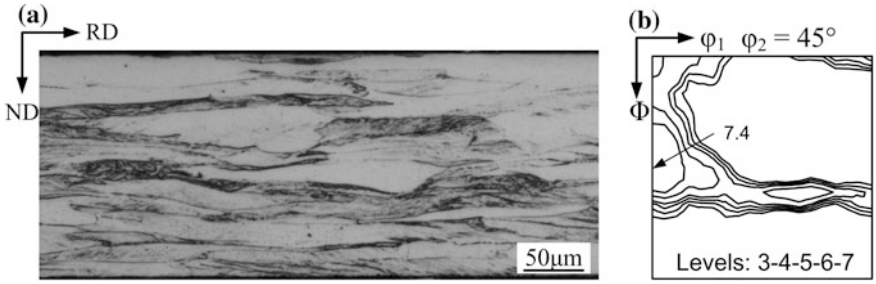

Fig. 1 Optical microstructure (**a**) and ODF (**b**) of the cold-rolled sheets

According to the phase diagram, microstructure under this chemical composition is in whole ferrite region. It suggests that only recrystallization and grain growth without phase transformation occur during annealing process. The microstructure of samples annealed at 950 °C for different time is presented in Fig. 2. It was found that complete recrystallization had been seemingly achieved at 25 s, and the microstructure was inhomogeneous. With increase in annealing time, the average grain size increased from 26 μm at 25 s to 88 μm at 25 min, as shown in Fig. 3. Meanwhile, the homogeneity of microstructure was gradually deteriorated over time, which is related to the inheritance of cold-rolled microstructure and the progress of grain growth. As discussed by Park [14], the stored energy in deformed grains was different and increased in the order of $\{001\}\langle 110\rangle$, $\{112\}\langle 110\rangle$, $\{111\}\langle 110\rangle$ and $\{111\}\langle 112\rangle$ orientations. That suggests that the nucleation in (111) deformed grains will be earlier, resulting different sizes of grains (as shown in Fig. 2a). In addition, some recovered grains could present size advantage compared with the recrystallized grains, such as the large grains in the middle region of Fig. 2d. However, during the subsequent grain growth, the diversity of grain size further increased as a result of the different migration rates of grain boundaries. This inhomogeneity of microstructure is expected to generate detrimental effect on the property of silicon steel sheets.

Texture

Figures 4 and 5 respectively display $\varphi_2 = 0°$ section and $\varphi_2 = 45°$ section of ODFs in all annealed sheets. Samples annealed for 25 s and 1 min consisted of strong α-fiber concentrating on $\{223\}\langle 110\rangle$ and γ-fiber including $\{111\}\langle 110\rangle$–$\{111\}\langle 112\rangle$. In addition, pronounced η-fiber ($\langle 001\rangle//\mathrm{RD}$) with peaks at $\{110\}\langle 001\rangle$ and $\{310\}\langle 001\rangle$ was developed. With regard to the samples annealed for 2 min, α-fiber and γ-fiber texture was significantly weakened, while the Cube component was enhanced. However, the density of γ-fiber in samples annealed for 4–25 min was gradually increased together with the weakening of η-fiber except for 25 min.

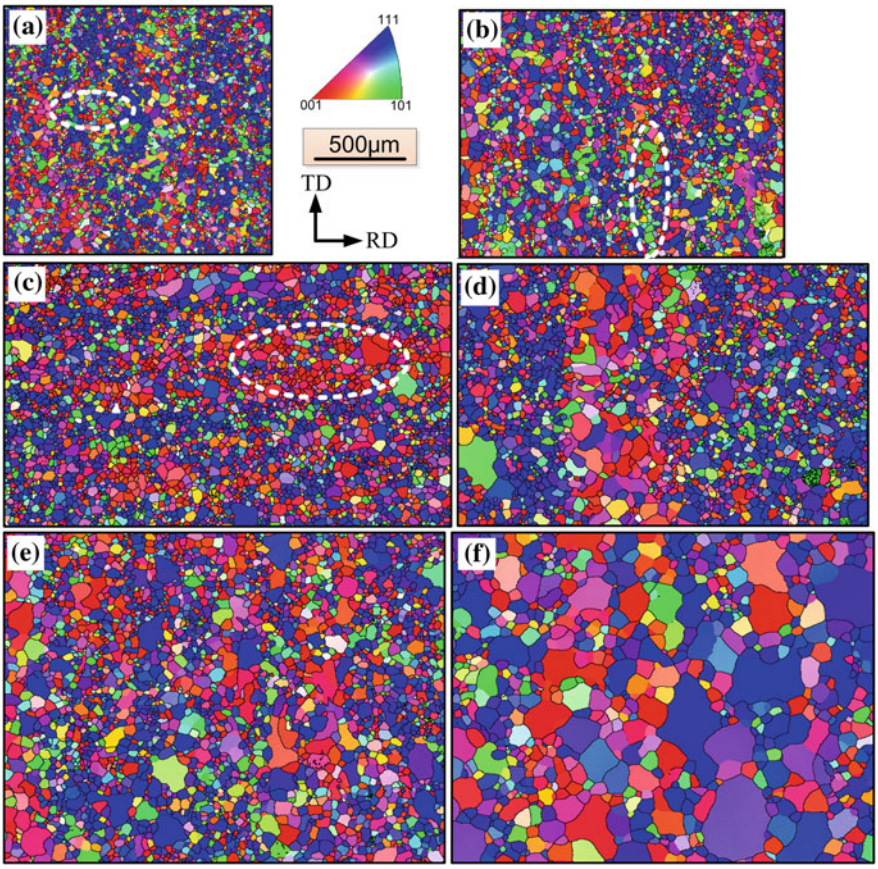

Fig. 2 IPF map of samples annealed at 1000 °C for different time: **a** 25 s; **b** 1 min; **c** 2 min; **d** 4 min; **e** 8 min; **f** 25 min

According to the recrystallized microstructure shown in Fig. 2, the texture evolution during this annealing process consists of two stages: the first stage is the development of recrystallization texture, and the second stage is the change of texture during grain growth.

In order to further investigate the texture evolution during annealing, the proportion and average size of main nuclei components in various annealed sheets, derived from the EBSD micrographs, were presented in Fig. 6. It was found that γ grains had a significant advantage in number density at any time. Prior to 1 min, which was the early stage of complete recrystallization, the average size of Goss grains was the largest while the Cube grains were smallest. It is well known that shear bands within γ deformed matrix with high stored energy provide nucleation sites for η grains [15]. In addition, new $\{111\}\langle 110\rangle$ grains can nucleate at $\{111\}\langle 112\rangle$ deformed matrix, or in reverse [16]. Therefore, γ grains in cold-rolled

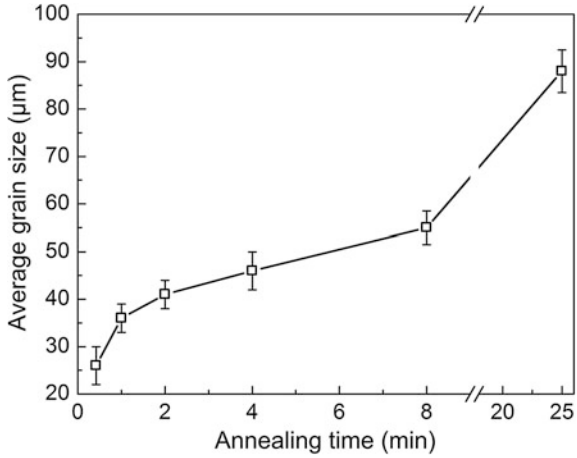

Fig. 3 Average grain size of final sheets annealed for different time

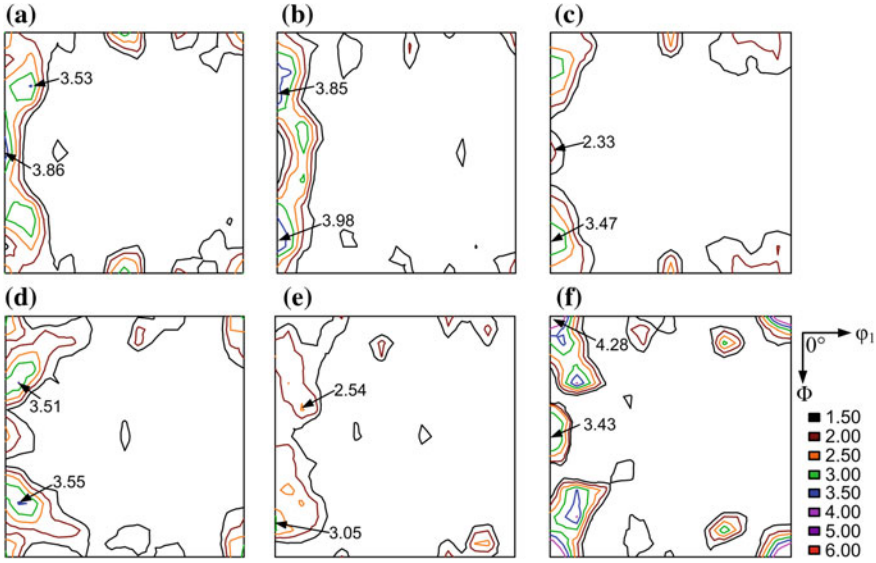

Fig. 4 $\varphi_2 = 0°$ section ODF of the samples annealed for different time: **a** 25 s, **b** 1 min, **c** 2 min, **d** 4 min, **e** 8 min, **f** 25 min

sheets can be gradually replaced by new η and γ grains, and earlier nucleation of Goss grains compared with other grains ensures its size advantage. In addition, α deformed microstructure is easy to recover but hard to recrystallization, thus resulting in strong α-fiber after complete recrystallization (as observed in Fig. 5a, b). The mechanism of oriented nucleation plays a major role in the development of recrystallization texture in this case. Furthermore, many colonies of grains with

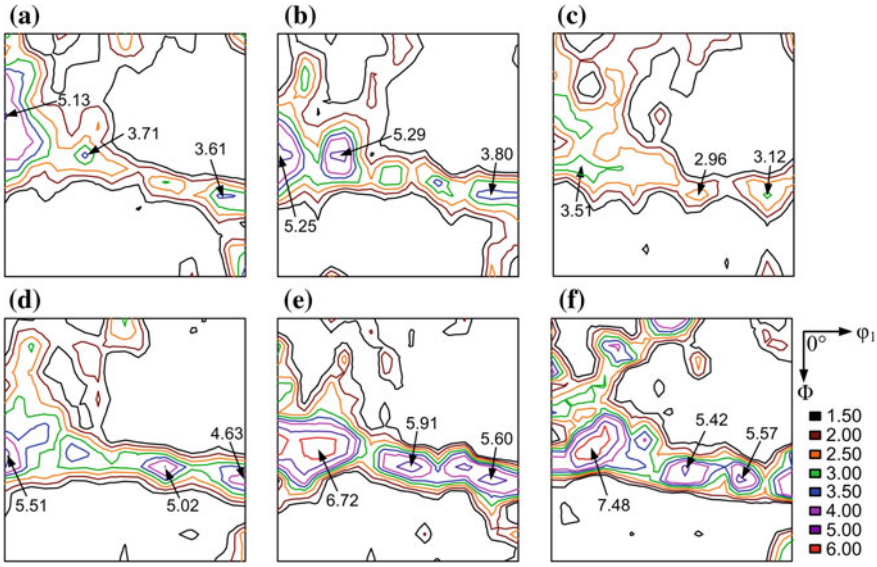

Fig. 5 $\varphi_2 = 45°$ section ODF of the samples annealed for different time: **a** 25 s, **b** 1 min, **c** 2 min, **d** 4 min, **e** 8 min, **f** 25 min

similar orientation indicated by dotted white line in Fig. 2 are observed, which verifies this mechanism.

As the time increased to 4–25 min, γ grains displayed a distinct increase in size and showed the maximal value, whereas the number of Goss grains was reduced together with a slow increase in size, which are related to the process of grain growth. The colonies in samples annealed for 2 min or less suggest a large amount of low-angle grain boundaries with low mobility, which can act as obstacles to the moving grain boundary and inhibit grain growth by orientation pinning [17].

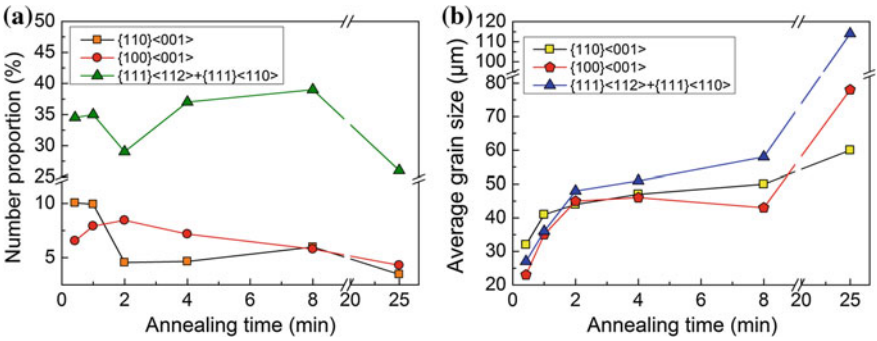

Fig. 6 Number proportion (**a**) and average size (**b**) of main nuclei components in sheets annealed for different time

In these samples, γ grains with largest number have a relatively low probability of being pinned and could gradually predominate in the recrystallization textures in virtue of growth selection (as shown in Fig. 2c, d). On the contrary, colony distributed Goss grains with low number proportion are easily pinned or may even been consumed in this case, thereby gradually losing the advantage of size and orientation density. It is certainly that the colony of grains with similar orientation will be decreased as a result (shown in Fig. 2d–f). Therefore, orientation pinning gives rise to the subsequent growth selection of γ grains and the change of recrystallization texture. Samples annealed for 2 min displayed the optimal situation of recrystallization and growth pinning of favorable η grains. The strong η-fiber in sample annealed for 25 min may be related to the growth behavior of large-sized Cube or Goss grains.

Magnetic Properties

Magnetic properties in all specimens as a function of annealing time are presented in Fig. 7. Magnetic induction and core loss showed significant dependence on annealing time, but the variation trend was not the same. As for the magnetic induction, it gradually increased at first two minutes, and then decreased as the time progressively increased. All the samples in present study exhibited improved magnetic inductions than the commercial products [18], and the maximal value B_{50} reached 1.745 T that was higher by about 0.105 T than the commercial value. Compared with ups and downs of magnetic induction, the core loss presented monotonously decreasing over annealing time. However, the rate of reduction was not constant but decreasing. The minimum value $P_{10/400}$ = 15.92 W/kg existed in the sample annealed for 25 min, which was reduced by 7.06 W/kg in comparison to the sample annealed for 25 s.

Magnetic properties of silicon steel are mainly related to the crystallographic texture and grain size [19]. It is well known that ⟨001⟩ is the easy direction of

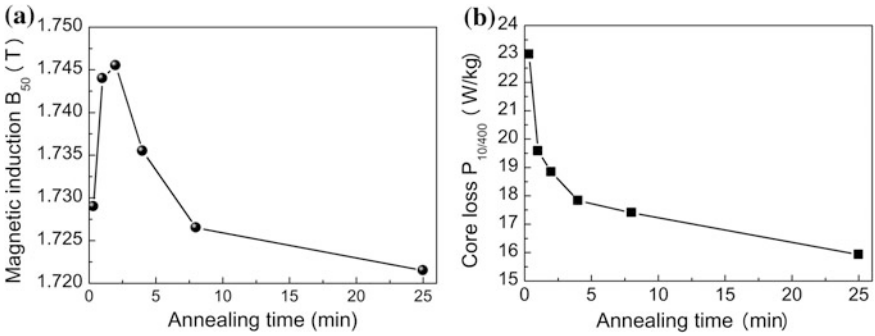

Fig. 7 Magnetic induction B_{50} (**a**) and core loss $P_{10/400}$ (**b**) in all annealed sheets

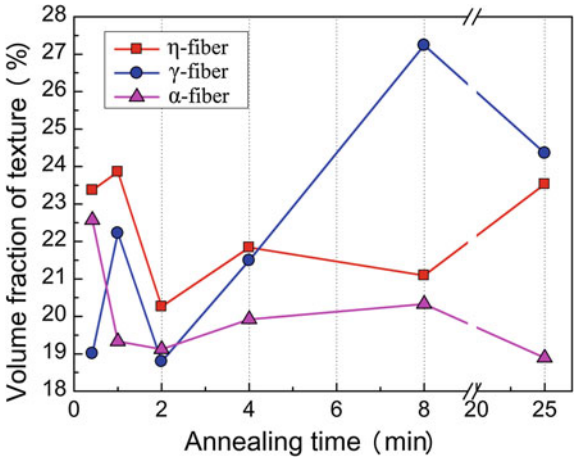

Fig. 8 Volume fraction of γ-, η- and α-fiber texture in final sheets annealed for different time

magnetization while ⟨111⟩ is the hardest direction, i.e. λ and η fiber having ⟨001⟩ axis is desire for good magnetic property. Figure 8 shows the volume fraction of three typical fibers in final sheets with different annealing time. It was noted that the volume fraction of η-fiber was higher than γ-fiber or α-fiber during the first 4 min, while γ-fiber predominated the samples after that. Furthermore, volume fraction of detrimental γ-fiber and α-fiber continued to decline before 2 min, but showed an increase trend during 4–25 min, especially for γ-fiber. However, volume fraction of η-fiber decreased before 2 min and then stabilized with a slight fluctuation. This change gave rise to increase first and then decrease in magnetic induction, as shown in Fig. 7a. In terms of the core loss, an optimal grain size exists to balance eddy current lose (increasing with grain size) and hysteresis lose (decreasing with grain size) [20]. Moreover, the enhancement of texture with ⟨001⟩ direction can diminish the hysteresis lose. According to the results in Figs. 3 and 8, here the gradual decrease in grain size is primary responsible for the reduction of core loss.

Conclusions

The studies carried out on strip cast non-oriented silicon steel with thickness of 0.20 mm show the importance of annealing time on the control of recrystallization texture and magnetic properties. With increase in annealing time, the main mechanism determining recrystallization texture transforms from orientation nucleation to orientation pinning. η-fiber predominates the sample during first two minutes annealed. However, γ grains gradually become the dominant texture during subsequent grain growth because of the advantage in growth rate induced by low probability of orientation pinning. Magnetic induction increases first and then decreases over annealing time.

Acknowledgements The authors acknowledge support by the National Natural Science Foundation of China (Nos. 51674080, 51404155 and U1260204), the Program for New Century Excellent Talents in University (NCET-13-0111) and the Program for Liaoning Excellent Talents in University (LR2014007).

References

1. M. Ishida, N. Shiga, K. Sadahiro, Improvement of motor performance by use of high-efficiency electrical steels. Kawasaki Steel Tech. Rep. **48**, 39–46 (2003)
2. M. Komatsubara, K. Sadahiro, O. Kondo, T. Takamiya, A. Honda, Newly developed electrical steel for high-frequency use. J. Magn. Magn. Mater. **242**, 212–215 (2002)
3. K. Verbeken, J. Schneider, J. Verstraete, H. Hermann, Y. Houbaert, Effect of hot and cold rolling on grain size and texture in Fe–2.4 wt.%Si strips. IEEE Trans. Magn. **44**, 3820–3823 (2008)
4. L. Wang, C. Deng, M. Dong, L. Shi, J. Zhang, Development of continuous casting technology of electrical steel and new products. J. Iron. Steel Res. Int. **19**, 1–6 (2012)
5. K. Shibuya, M. Ozawa, Strip casting techniques for steel. ISIJ Int. **31**, 661–668 (1991)
6. S. Ge, M. Isac, R.I.L. Guthrie, Progress of strip casting technology for steel; historical developments. ISIJ Int. **52**, 2109–2122 (2012)
7. N. Zapuskalov, Comparison of continuous strip casting with conventional technology. ISIJ Int. **43**, 1115–1127 (2003)
8. Y. Zhang, Y. Xu, H. Liu, C. Li, G. Cao, Z. Liu, G. Wang, Microstructure, texture and magnetic properties of strip-cast 1.3% Si non-oriented electrical steels. J. Magn. Magn. Mater. **324**, 3328–3333 (2012)
9. Y.B. Xu, Y.X. Zhang, Y. Wang, C.G. Li, G.M. Cao, Z.Y. Liu, G.D. Wang, Evolution of cube texture in strip-cast non-oriented silicon steels. Scripta Mater. **87**, 17–20 (2014)
10. D. Kohler, Promotion of cubic grain growth in 3% silicon iron by control of annealing atmosphere composition. J. Appl. Phys. **31**, S408–S409 (1960)
11. F. Fang, Y.B. Xu, Y.X. Zhang, Y. Wang, X. Lu, R.D.K. Misra, Evolution of recrystallization microstructure and texture during rapid annealing in strip-cast non-oriented electrical steels. J. Magn. Magn. Mater. **381**, 433–439 (2015)
12. Y. Sidor, F. Kovac, T. Kvackaj, Grain growth phenomena and heat transport in non-oriented electrical steels. Acta Mater. **55**, 1711–1722 (2007)
13. I.L. Dillamore, J.G. Roberts, A.C. Bush, Occurrence of shear bands in heavily rolled cubic metals. Met. Sci. **13**, 73–77 (1979)
14. J.T. Park, J.A. Szpunar, Evolution of recrystallization texture in nonoriented electrical steels. Acta Mater. **51**, 3037–3051 (2003)
15. S.D.C. Paolinelli, M.A.D. Cunha, A.B. Cota, The influence of shear bands on final structure and magnetic properties of 3% Si non-oriented silicon steel. J. Magn. Magn. Mater. **320**, e641–e644 (2008)
16. Y. Nagataki, Y. Hosoya, Origin of the recrystallization texture formation in an interstitial free steel. ISIJ Int. **36**, 451–460 (1996)
17. O. Engler, On the influence of orientation pinning on growth selection of recrystallisation. Acta Mater. **46**, 1555–1568 (1998)
18. N. Zhang, P. Yang, W.M. Mao, Through process texture evolution of new thin-gauge non-oriented electrical steels with high permeability. J. Magn. Magn. Mater. **397**, 125–131 (2016)
19. K.M. Lee, S.Y. Park, M.Y. Huh, J.S. Kim, O. Engler, Effect of texture and grain size on magnetic flux density and core loss in non-oriented electrical steel containing 3.15% Si. J. Magn. Magn. Mater. **354**, 324–332 (2014)
20. M.F. de Campos, J.C. Teixeira, F.J.G. Landgraf, The optimum grain size for minimizing energy losses in iron. J. Magn. Magn. Mater. **301**, 94–99 (2006)

Temperature Distribution Laws During Selective Laser Melting Process of Nickel Base Alloy GH4169

Bin Liu, Le Tan, Zhanyong Zhao, Hao Zhang, Jing Li, Peikang Bai, Jianhong Wang and Yahui Cheng

Abstract In this paper, the temperature distribution laws during selective laser melting process of GH4169 alloy were studied. When the laser power was certain, with the scanning speed reduced the temperature of the melt pool increased, which caused the accumulation of lot of heat, and making the maximum temperature over the boiling point of metal, and thus resulted in the melt pool splash and hence affected the quality of forming. When the scanning speed was a constant, with the increase of laser power, the maximum temperature in melt pool increased. And when the laser power was more than 300 W, it was prone to give rise to the vaporization of powder, and reduced the forming quality. During the forming process, the spot center temperature of each scan line decreased firstly and then increased. The temperature increased in the head and the tail of the scan line, and was stable in the middle of the scan line. The change of midpoint temperature of the

B. Liu · L. Tan · Z. Zhao (✉) · H. Zhang · J. Li · P. Bai · J. Wang · Y. Cheng
School of Materials Science and Engineering, North University of China, Taiyuan 030051, China
e-mail: syuzzy@126.com

B. Liu
e-mail: liubin3y@qq.com

L. Tan
e-mail: 473058100@qq.com

H. Zhang
e-mail: 695315502@qq.com

J. Li
e-mail: 515914907@qq.com

P. Bai
e-mail: baipeikang@nuc.edu.cn

J. Wang
e-mail: 442566856@qq.com

Y. Cheng
e-mail: 1903174665@qq.com

© Springer Nature Singapore Pte Ltd. 2018

Y. Han (ed.), *Advances in Materials Processing*, Lecture Notes in Mechanical Engineering, https://doi.org/10.1007/978-981-13-0107-0_31

scan line was stable, which ensured the performance of each layer was consistent during multi-layer scan process.

Keywords Temperature distribution laws · GH4169 alloy · Selecting laser melting · Laser power · Scanning speed

Introduction

In recent years, the nickel base superalloy GH4169 parts formed by selective laser melting (SLM) which can form complex shape metal parts were used extensively in aviation engine [1]. During the forming process of SLM, GH4169 alloy powders whose melting point is more than 1200 °C are melted by laser beam in a very short period of time, which cause the dynamic temperature change greatly, and thus lead to cracks, warping, delamination problems that gain a failed product or reduce mechanical performance after forming [2, 3]. Because SLM has high heating and cooling rates which make it is difficult to measure the temperature distribution and variation law directly, studying the temperature distribution and variation law by means of finite element method has been widely adopted [4]. Li and Gu [5] investigated the effects of laser power and scan speed on the SLM thermal behavior of AlSi10Mg powder during SLM process by using the finite element method. Huang et al. [6] analyzed the effects of the linear energy density, volume shrinkage, scanning track length, hatch spacing and time interval between two neighboring tracks on the temperature distribution and molten pool dimensions by means of the finite element methods. Shi et al. [7] proposed a three-dimensional finite element model to study the effects of laser power and scan speed on the thermal behavior and melting/solidification mechanism during selective laser melting (SLM) of TiC/Inconel 718 powder system. Previous research on simulation of temperature field during SLM process has focussed on studying Al alloys and Ti alloys, but the temperature distribution during SLM process of GH4169 has generally been uncommon. In this paper, a three-dimensional finite element model was established in order to investigate the effects of scan speed, laser power on the maximum temperature in the melt pool. And analyzed the temperature distributions of single layer scanning and multi layer scanning.

Computational Models

Figure 1 shows the finite element model of SLM. The dimensional finite element model was divided into two components: powder bed and substrate. The powder layer with the dimension of 0.6 mm × 0.6 mm × 0.45 mm was placed on the Q235 steel substrate with the dimension of 4 mm × 4 mm × 0.9 mm. In order to minimize effect of substrate temperature on the powder bed, the Eight node

hexahedron SOLID70 3D solid element was adopted as the powder bed mesh type, the three dimensional twenty node thermal solid element SOLID90 was adopted as the substrate mesh type. Scanning strategy is shown in Fig. 2, there were six scanning tracks during single layer scan process and three layers during multi layer scan process.

The three dimensional nonlinear transient heat conduction equation takes the following form:

$$\rho c\frac{\partial T}{\partial t} - \rho Q - \frac{\partial}{\partial x}k_x\frac{\partial T}{\partial x} + \frac{\partial}{\partial y}k_y\frac{\partial T}{\partial y} + \frac{\partial}{\partial z}k_z\frac{\partial T}{\partial z} = 0. \quad (1)$$

where ρ is material density, c is specific heat capacity, k_x, k_y, k_z are the thermal conductivity along the x, y, z axis, T is the temperature, t is the time, $Q = Q(x, y, z, t)$ is the internal heat source intensity.

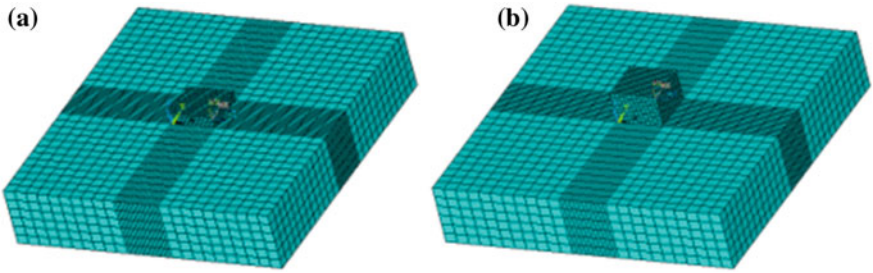

Fig. 1 The finite element model. **a** Single layer finite element model; **b** multi layer finite element model

Fig. 2 Scanning strategy

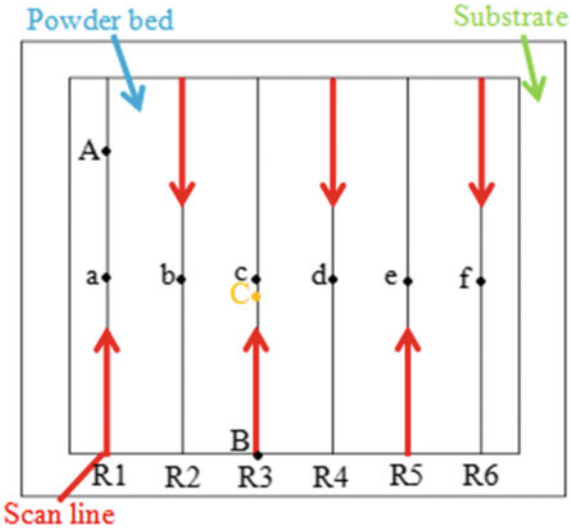

The effective thermal conductivity of the powder layer which has ideal spheres powder particles k_ε is defined as follows:

$$\frac{k_\varepsilon}{k_g} = (1-\sqrt{1-\varphi})\left[1+\frac{\varphi k_r}{k_g}\right] + \sqrt{1-\varphi}\left\{\frac{2}{1-\frac{k_g}{k_s}}\left[\frac{1}{1-\frac{k_g}{k_s}}\ln\left(\frac{k_s}{k_g}\right)-1\right]+\frac{k_r}{k_g}\right\}. \tag{2}$$

where k_g is the thermal conductivity of air, k_s is the thermal conductivity of solid materials, φ is the initial void fraction of the powder bed. In the paper, the porosity of powder bed is 0.447, k_r is the thermal conductivity due to the radiation among particles in powder bed, which is defined by:

$$k_r = 4F\sigma T_h^2 D_h. \tag{3}$$

where σ is Stefan Boltzmann constant, D_h is the average diameter of powder particle, T_h is the temperature of particle, F is a view factor, which is estimated as 1/3.

The relationship between latent heat and enthalpy can be described as:

$$H = \int \rho c(T) dT. \tag{4}$$

where H is enthalpy, ρ is the density, $c(T)$ is the Specific heat capacity function which vary with temperature, T is the temperature.

The laser heat source is loaded onto the powder bed in the form of heat flux, which obey the Gaussian distribution:

$$q = \frac{2AP}{\pi\omega^2}\exp\left(-\frac{2r^2}{\omega^2}\right). \tag{5}$$

where q is laser power density, P is laser power, A is thermal absorptivity of material to wavelength, in the paper, A = 0.38, the wavelength of laser beam is 1.06 μm, ω is radius os laser spot, r is the distance from a point on the surface of powder bed to the laser spot center.

Results and Discussion

The Temperature Distribution of Single Line Scan

Figure 3 shows the temperature change curves of the point A under the different processing parameters during single line scan process according to the simulation results by means of the finite element software postprocessing module. As shown in Fig. 3a, when the laser power was 150 W and other process parameters were

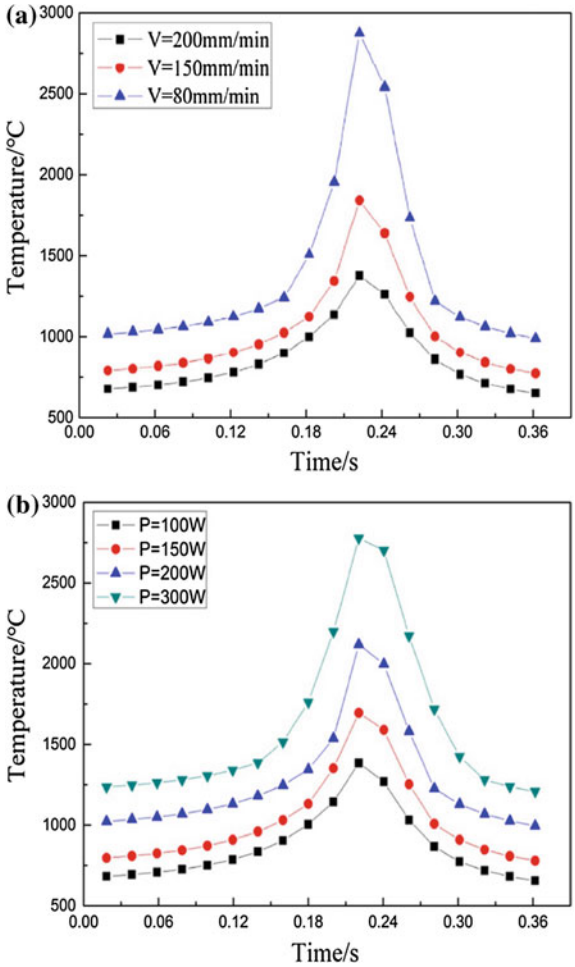

Fig. 3 Temperature change curves of single scanning. **a** Under different scanning speed; **b** under different laser power

certain, the maximum temperature decreased with the scanning speed increased, there was an inverse relationship between the two. The heating rate was very fast when scanning speed was 80 mm/min during single line scan process, the maximum temperature could reach approximately 3000 °C, which over the boiling point of the GH4169 alloy. It could attributed to that the slower scanning speed allows the alloy powder to melt sufficiently, which made the maximum temperature inside the melt pool reach the melting point. But the excessive heat source energy caused by the too slow scanning speed was easy to result in heat affecting between powder and substrate, and thus produced temperature gradients. The accumulation of heat made the maximum temperature inside the melt pool over the boiling point, which caused the phenomenons of splashing or carbonization of materials. The average temperature was lower when the scanning speed was 200 mm/min, but the powders could not be melted and formed due to the maximum temperature was lower than

the melting point of powder. When the scan speed was 150 mm/min, the scanning temperature reached the boiling point and powders were melted, then the temperature began decrease. They were in line with the characteristics of selective laser melting forming.

As shown in Fig. 3b, when the scanning speed was 150 mm/min and other process parameters were certain, the maximum temperature increased with the laser power increased, there was an proportional relationship between the two. When the laser power was 100 W, the average temperature was lower and the scanning temperature was lower than the melting point of powder, which resulted in powder could not be completely melted and thus caused easily the phenomenon of disconnection. When the laser power at 200–300 W, as the laser power was too large make the initial temperature be higher, the powder has started to be melted before it had been scanned, which caused the size of melt pool to become larger and the maximum temperature inside melt pool closed to the boiling point of material, and thus caused powder vaporization and reduced the surface quality of forming tracks.

Figure 4 describes the temperature distribution at the points B and C during single line scanning process. The temperature distribution nephogram at the beginning of powder melted when the laser beam irradiated the point B was shown in Fig. 4a. The maximum temperature of the spot center was 1687 °C, which reached the melting point of powder and powder could be melted. Figure 4b is the temperature distribution nephogram at the point C, the maximum temperature of the spot center decreased to 1403 °C, which attributed to powder absorbed the heat emitted by a laser beam. As shown in Fig. 4, the heat affecting on substrate was very small, the powder bed was not affected by excessive substrate temperature. The isotherms at the front of the melt pool were denser, however, they were sparse at the back of the melt pool. The size and temperature of melt pool gradually increased with the increase of absorbed heat. The elliptical temperature distribution nephogram formed by laser heat source was different from the theoretical model of circular, which was consistent with the temperature field distribution characteristics of SLM.

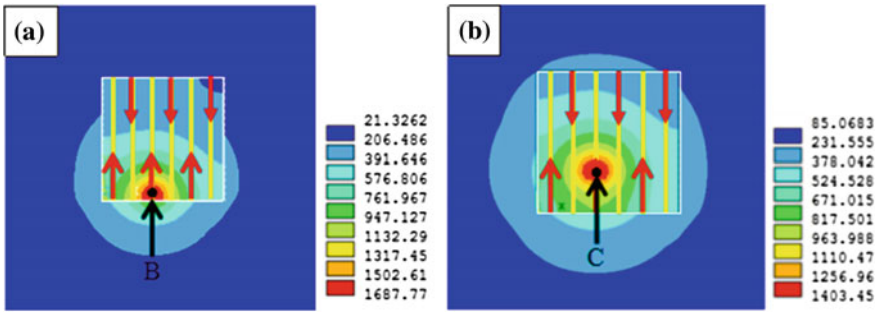

Fig. 4 Temperature distribution of different position during single line scanning

The Temperature Variation of Laser Beam Center During Single Layer Scanning Process

Each scan line had 18 sub steps in simulation of temperature field of single layer scanning. According to the scan strategy, R1 and R2 can be refer to as one complete scanning step during single layer scanning process, thus they were adopted as example to study the temperature variation of laser beam center in the paper. Figure 5 describes the change curve graphs of the maximum temperature at the center point of laser beam along R1 and R2 scan lines during single layer scanning process. As shown in Fig. 5, the maximum temperature at center point of each scan line change trend with time were similar, which decreased firstly and then increased. The temperature would rise at the head and tail of the scan line and be stable in the middle region. The reasons of temperature rose at the head and tail of the scan line were that the absorbed energy was in an unbalanced state with the input energy at the beginning of scanning and the large temperature gradients were easily generated near the turning of scan direction. When the energy dissipation and input reached balance at the forth sub step of each scan line, the temperature distribution trend to be stable.

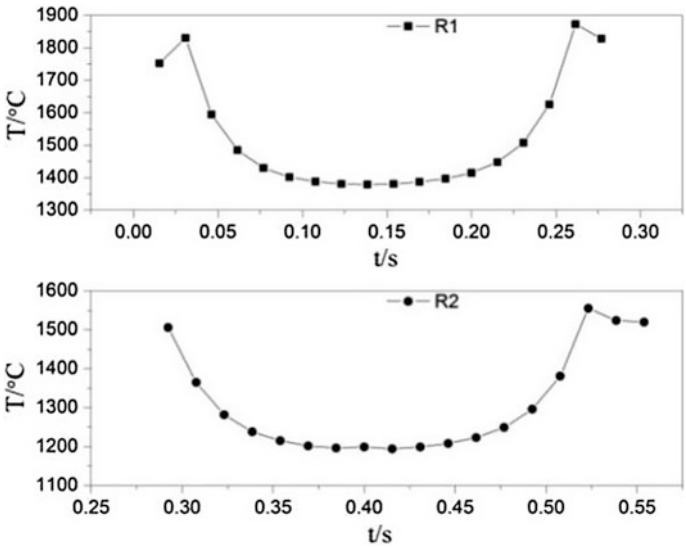

Fig. 5 Change curve graphs of the maximum temperature at the center point of laser beam

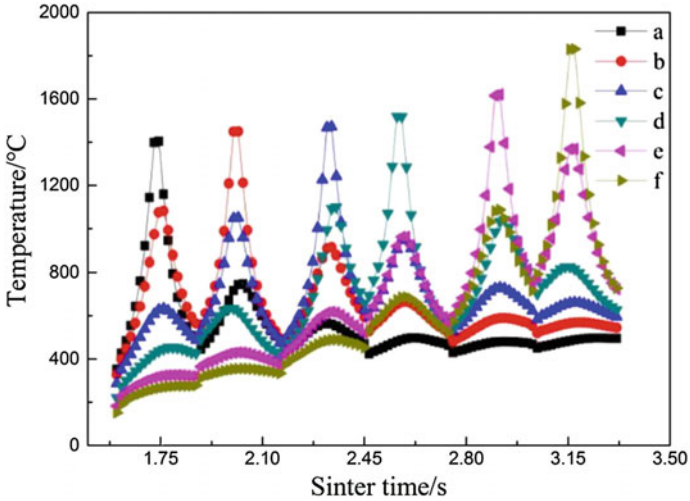

Fig. 6 Temperature change curve of scanning line midpoint in the second layer

The Temperature Distribution Laws in Multi Layer Scanning Process

Taking the midpoint of each scanning line on each layer as the characteristic point to analyze the change laws of the center position temperature with time in the whole multi-layer scanning. As shown in Fig. 6, taking the second layer as the example to describe the change laws. The temperature change laws of six scanning line midpoints in each layer were similar to that of cyclical change and there were the same number of peaks. The maximum temperature of characteristic points increased gradually, this was due to the effect of heat accumulation in the forming process. However, the temperature change of the whole block forming process was stable, and the performance of each layer in the multilayer scanning was basically the same. The pre formed region had a preheating effect on the post forming region, and the post forming region would remelting the formed zone to achieve metallurgical bonding, thus ensuring the quality of the formed parts.

Conclusions

(1) Under the certain laser power the temperature of the melt pool increases with the decease of scanning speed, which will cause the accumulation of the heat, and make the maximum temperature over the boiling point of the metal, and thus result in the melt pool splashing, and hence affecting the quality of forming. When the scanning speed is a constant the maximum temperature in

melt pool increases with the increase of the laser power. And when the laser power is more than 300 W, it is prone to give rise to the vaporization of powder, and reduce the forming quality.

(2) During the forming process, the spot center temperature of each scan line decreases first and then increases. The temperature increases in the head and the tail of the scan line, and is stable in the middle of the scan line. The change of midpoint temperature of the scan line is stable, which ensures the performance of each layer be consistent during the multi layer scan process.

Acknowledgements The authors thank for The National Natural Science Foundation of China under grant Nos. 51604246, and 51775521, the Primary Research and Development Plan of Shanxi Province under grant No. 201603D121020-1, the supports of the North University of China for Young Academic Leaders.

References

1. M. Cloots, K. Kunze, P.J. Uggowizer, K. Wegener, Microstructural characteristics of the nickel-based alloy IN738LC and the cobalt-based alloy Mar-M509 produced by selective laser melting. Mat. Sci. Eng. A-Struct. **658**, 68–76 (2016)
2. N.J. Harrison, I. Todd, K. Mumtaz, Reduction of micro-cracking in nickel superalloys processed by selective laser melting: a fundamental alloy design approach. Acta Mater. **94**, 59–68 (2015)
3. A. Basak, S. Das, Microstructure of nickel-base superalloy MAR-M247 additively manufactured through scanning laser epitaxy (SLE). J. Alloy. Compd. **705**, 806–816 (2017)
4. K. Dai, L. Shaw, Thermal and mechanical finite element modeling of laser forming from metal and ceramic powders. Acta Mater. **52**, 69–80 (2004)
5. L.Y. Li, D.D. Gu, Parametric analysis of thermal behavior during selective laser melting additive manufacturing of aluminum alloy powder. Mater. Design. **63**, 856–867 (2014)
6. Y. Huang, L.J. Yang, X.Z. Du, Y.P. Yang, Finite element analysis of thermal behavior of metal powder during selective laser melting. Int. J. Therm. Sci. **104**, 146–157 (2016)
7. Q.M. Shi, D.D. Gu, M.J. Xia, S.N. Cao, T. Rong, Effects of laser processing parameters on thermal behavior and melting/solidification mechanism during selective laser melting of TiC/Inconel 718 composites. Opt. Laser Technol. **84**, 9–22 (2016)

Microstructure, Residual Stress and Corrosion Resistance in Electrodeposited Copper Foils

Yanhong Hua, Zhihua Nie, Guojie Huang, Yanfeng Li, Haofeng Xie and Dongmei Liu

Abstract The current collector is a key component in rechargeable lithium ion batteries, which helps to carry electrode materials and collect the current. Copper foil, a thin sheet of Cu, is usually used as the current collector. To meet the requirement of lighter weight and higher energy density of lithium ion batteries, thinner copper foil with lower cost is demanded. In this paper, two commercial electrodeposited copper foils with thickness of 9 μm were studied by X-ray diffraction, scanning electron microscope and electron backscatter diffraction techniques. The corrosion resistance for the copper foils was also estimated by polarization curves. The crystal structure, microstructure, grain preferred orientation, residual stress, and corrosion resistance property were compared for the two foils.

Keywords Copper foils · Corrosion resistance · Electrodeposition

Introduction

Rechargeable lithium ion batteries (LIBs) have been widely used in electric vehicles and modern portable electronics because of their good performance such like high energy density, high working voltage, and long cycle life [1, 2]. A LIB is an electrochemical system containing anode, cathode, separator, current collector, and electrolyte. The working mechanism of a standard LIB includes lithium ions deintercalating from the cathode material, migrating through the electrolyte and intercalating into the anode material during charging process. And the discharging

Y. Hua · Z. Nie (✉)
School of Materials Science and Engineering, Beijing Institute of Technology, Beijing 100081, China
e-mail: znie@bit.edu.cn

G. Huang · Y. Li · H. Xie · D. Liu
State Key Laboratory for Fabrication and Processing of Nonferrous Metals, General Research Institute for Nonferrous Metals, Beijing 100088, China

© Springer Nature Singapore Pte Ltd. 2018

Y. Han (ed.), *Advances in Materials Processing*, Lecture Notes in Mechanical Engineering, https://doi.org/10.1007/978-981-13-0107-0_32

reverses the above process. The current collector is considered to be a key component in LIBs, which helps to carry electrode materials and collect the current [3]. Due to the particular working conditions in charging-discharging process, the current collector has to satisfy many requirements including (i) good mechanical properties, (ii) chemical stabilities in the electrolyte solution, (iii) adhesiveness to the electrode materials, and (iv) low cost [4].

Copper foil, a thin sheet of Cu, is normally used as the current collector in standard LIBs. To meet the requirement of lighter weight and higher energy density of LIBs, thinner copper foil with lower cost is demanded. Copper foil for electronics is one important high-end product, which is list in the Made in China 2025 blueprint. The conventional methods to fabricate copper foils include rolling-annealing method and electrodeposition method [5]. The electrodeposited copper foils are fabricated by electroplating the Cu onto a rotating drum from electrolytic solution, which can be used to produce copper foil with thickness less than 10 μm [6]. In addition, the cost of the electrodeposited copper foil is relatively low cost [2]. Much work so far has focused on the electrochemical characteristics and mechanical properties of copper foils [7, 8]. In this paper, two commercial electrodeposited copper foils are compared. One is made in China and another one is made overseas. The microstructure, crystal preferred orientation, and residual stress is studied in both copper foils. The corrosion resistance for copper foils is also estimated by polarization curves.

Experimental

Commercial electrodeposited copper foils were bought from Qinghai Electronic Materials Industry Development Co Ltd. (foil-A) and Furukawa Electric Co Ltd (foil-B). The thickness of the copper foils was 9 μm. The copper foils were electrodeposited by industrial means. Copper sulfate was first gained from sulfuric acid (H_2SO_4) and copper in the heating condition, and was pumped into electrolyte pool after filtration. Electrolysis process occurred in the electrolysis machine, including the cathode roller, anode silver alloy plate and electrolyte pool. Under the action of direct current, the divalent copper ions in copper sulfate electrolyte moved towards the interface of the cathode roller. After reduction reaction, pure copper crystallized on the rotating roller and raw foils were formed. The X-ray diffraction (XRD) patterns were collected by a Rigaku Smartlab Diffractometer equipped with X-ray tube with rotating Cu anode operating at 9 kW. The 2-theta angle was scanned from 20° to 100° with a speed of 3°/min. The (311) reflection was used for residual stress analysis. The microstructure of the foils was studied by the scanning electron microscope (SEM). Electron backscatter diffraction (EBSD) was employed to study the crystal preferred orientation via calculated inverse pole figures (IPFs) and the grain size distribution. Electrochemical workstation (PARSTAT 2273 Potentiostat Galvanostat) was used to acquire polarization curves to evaluate the corrosion resistance property.

Results and Discussion

Figure 1 shows the XRD patterns for foil-A and foil-B. The diffraction patterns can be indexed by a face-centered-cubic structure (FCC, space group 225). The indexes and a sketch of FCC structure are also shown in Fig. 1. No extra reflections are detected, which suggests that both foils are Cu monophase. The lattice parameters are 3.619 and 3.613 Å for foil-A and foil-B, respectively. The reflections for foil-A are narrower than those for foil-B, suggesting a good crystallization for foil-A. The reflection intensity ratio $I_{(200)}/I_{(111)}$ for foil-B is larger than that for foil-A. The crystal preferred orientation for both foils is different, which has been quantitatively studied by EBSD technique and shown later.

Figure 2 shows the SEM images for foil-A and foil-B. Foil-A has a flat surface. And the surface for foil-B is rough with stripes. The influence of surface roughness on the interface adhesion between the electrode materials and the current collector has been reported [9]. The interface adhesion is enhanced by means of increasing the roughness of the Cu foil [10]. Hence, prior to usage, the surface of copper foils normally needs further treatments to obtain chemically passivated rough surfaces for enhanced slurry adhesion and oxidation prevention [11].

EBSD orientation maps for the copper foils are shown in Fig. 3. Grains marked blue are oriented with the (111) plane parallel to the surface, grains in red are (100) oriented and grains labelled green possess a (101) orientation. The calculated IPFs, shown in Fig. 4, clearly show the grain orientation along the normal direction (ND). Foil-A has (111) and (100) oriented grains along ND. And foil-B has (101) oriented grains along ND. While the mere reduction of grain boundary energy, as in normal grain growth, the anisotropy of surface and interface energy can supply an orientation dependent driving force. This often results in a (111) orientation of FCC metal films, because the (111) plane has the lowest surface energy [12–14]. In contrast, the strain energy of an FCC metal film under thermal strain favors (100) oriented grains, which possess the smallest strain energy density [12, 15, 16].

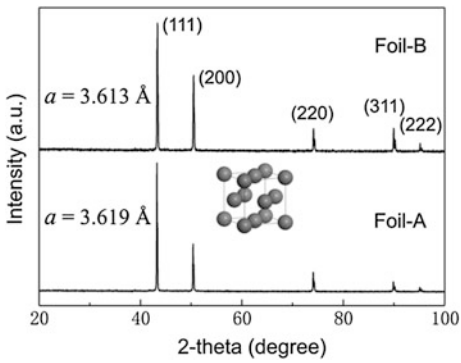

Fig. 1 XRD patterns for foil-A and foil-B

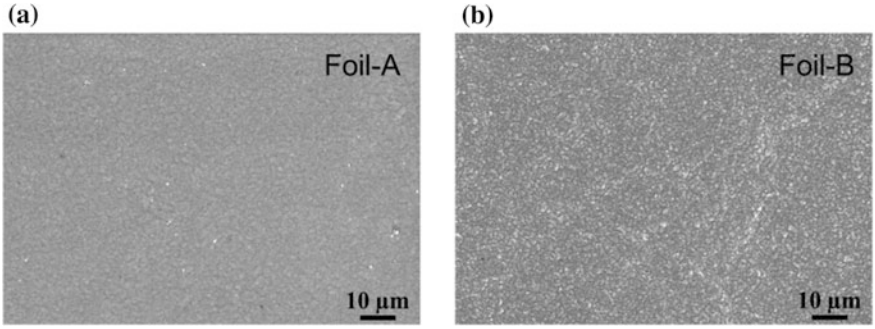

Fig. 2 SEM images for foil-A (**a**) and foil-B (**b**)

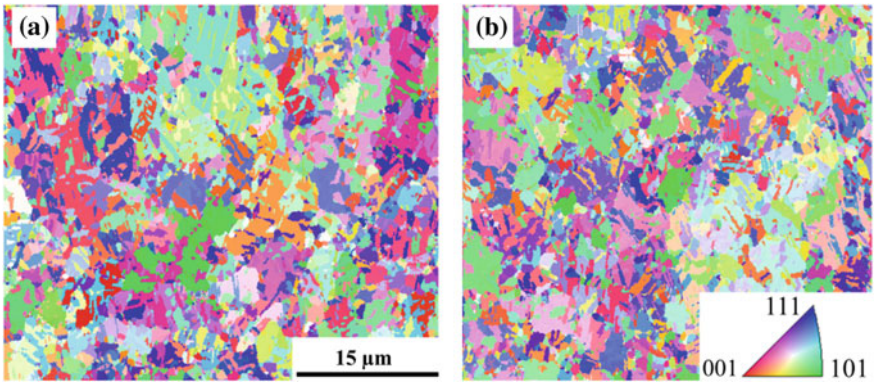

Fig. 3 EBSD orientation maps for foil-A (**a**) and foil-B (**b**)

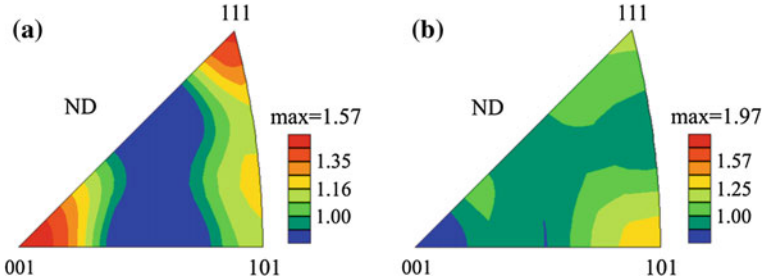

Fig. 4 Inverse pole figures for foil-A (**a**) and foil-B (**b**)

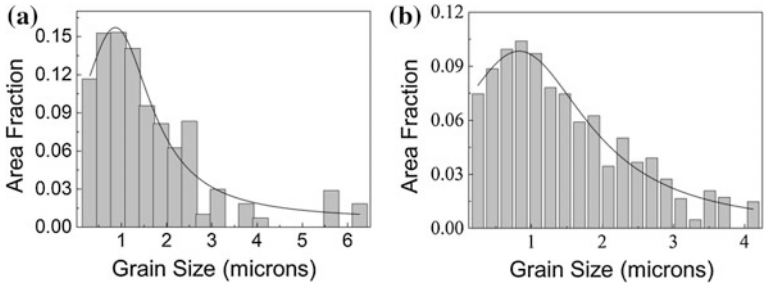

Fig. 5 Distribution of grain size for foil-A (**a**) and foil-B (**b**)

The distribution of grain size for copper foils has been quantitatively studied base on the EBSD data. Figure 5 shows the distribution of grain size for foil-A and foil-B. Both foils have sub-micro mean grain size. The distribution of grain size for foil-A is narrower than that for foil-B. But foil-A has some grains with size beyond 5 μm.

Residual stress generated during the electro-deposition process has big influence on the properties of copper foils, such as chemical, electrical and mechanical behaviors [17–19]. The residual stress is strictly controlled during fabrication process. The Cu (311) reflection is measured at a broader range of tilt angles ψ (0°, 15°, 30°, 45° and 60°) to evaluate the in-plane residual stress. Figure 6 shows the 2-theta versus $\sin^2\psi$ plot for foil-A and foil-B. The in-plane residual stress (σ) can be calculated using the following equation

$$\sigma = K \cdot \frac{\Delta 2\theta}{\Delta \sin^2 \psi}. \tag{1}$$

K is a function of the elastic constants E and Poisson ratio ν [20]. We use −258.9 MPa (pure Cu) here for K.

The 2-theta versus $\sin^2\psi$ plot is fitted by a linear function using least-squares method. The fitting lines are shown in Fig. 6. The measured residual stress for

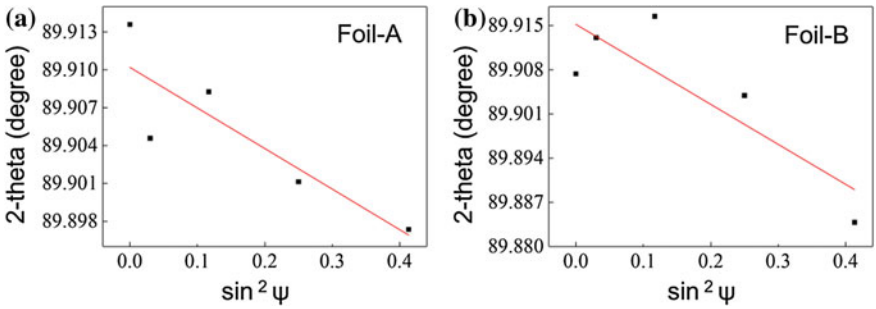

Fig. 6 2-theta versus $\sin^2\psi$ plot for foil-A (**a**) and foil-B (**b**)

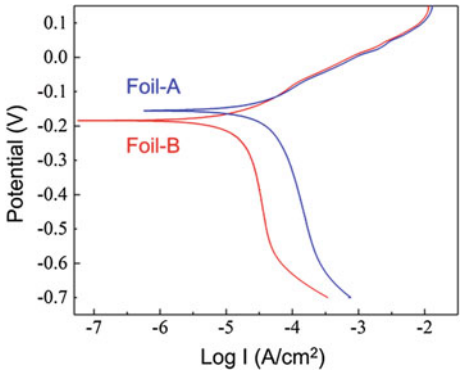

Fig. 7 Polarization curves in 10 wt% HCl solution for foil-A and foil-B

foil-A and foil-B is 8.3 and 16.4 MPa, respectively. The positive value indicates an in-plane compression stress.

Figure 7 shows the polarization curves (Tafel plot) for foil-A and foil-B. 10 wt% HCl solution is used here as electrolytic solution. The polarization curve has similar shape for both foils. The corrosion potential (E_{corr}) for foil-A and foil-B is calculated from the Tafel plot. The E_{corr} for foil-A and foil-B is −155.5 and −184.5 mV, respectively. In comparison with foil-B, foil-A had a high corrosion potential and a low corrosion current density, revealing a superior corrosion resistance [21].

Conclusions

Copper foil for electronics is one important high-end product, which is listed in the Made in China 2025 Blueprint. Here, two commercial electrodeposited copper foils have been studied. One is made in China and another one is made overseas. We find that both foils have similar mean grain size. The grain size distribution for the domestic one is narrower than the one from overseas. The domestic foil has a lower residual stress and a better corrosion resistance. The domestic foil may need further treatments to obtain chemically passivated rough surfaces for enhanced slurry adhesion and oxidation prevention.

Acknowledgements This work is supported by the National Key R&D Program of China under Contract No. 2016YFB0301300 and the National Natural Science Foundation of China (Grant No. 51401026).

References

1. W. Yuan, J. Luo, Z.G. Yan, Z.H. Tan, Y. Tang, Electrochim. Acta **226**, 89–97 (2017)
2. H.C. Chu, H.Y. Tuan, J. Power Sources **346**, 40–48 (2017)

3. K. Abe, H. Yoshitake, T. Kitakura, T. Hattori, H. Wang, M. Yoshio, Electrochim. Acta **49**, 4613 (2004)
4. C. Iwakura, Y. Fukumoto, H. Inoue, S. Ohashi, S. Kobayashi, H. Tada, M. Abe, J. Power Source **68**, 301–303 (1997)
5. H.C. Shin, J. Dong, M. Liu, Adv. Mater. **15**, 1610–1614 (2003)
6. B. Bozzini, C. Mele, L. D'Urzo, J. Appl. Electrochem. **36**, 789–800 (2006)
7. M.A. Getrouw, A.J.B. Dutra, Appl. Electrochem. **31**, 1359–1366 (2001)
8. Y.E. Lee, T.J. O'Keefe, J. Miner. Met. Mater. Soc. **54**, 37–41 (2002)
9. Z.J. Han, N. Yabuuchi, K. Shimomura, M. Murase, H. Yui, S. Komaba, Energy Environ. Sci. **5**, 9014 (2012)
10. J.B. Wu, Z.W. Zhu, H.W. Zhang, H.M. Fu, H. Li, A.M. Wang, Electrochim. Acta **146**, 322–327 (2014)
11. L. Chen, X. Xie, J. Xie, K. Wang, J. Yang, J. Appl. Electrochem. **36**, 1099–1104 (2006)
12. P. Sonnweber-Ribic, P. Gruber, G. Dehm, E. Arzt, Acta Mater. **54**, 3863–3870 (2006)
13. C.F. Gu, M. Hoffman, L.S. Toth, Y.D. Zhang, Mater. Charact. **101**, 180–188 (2015)
14. B.Z. Cui, K. Han, Y. Xin, D.R. Waryoba, A.L. Mbaruku, Acta Mater. **55**, 4429–4438 (2007)
15. H.D. Merchant, W.C. Liu, L.A. Giannuzzi, J.G. Morris, Mater. Charact. **53**, 335–360 (2004)
16. T. Sharma, P. Shaver, D.A. Brown, R. Brüning, V. Peldzinski, Electrochim. Acta **196**, 479–486 (2016)
17. U. Welzel, J. Ligot, P. Lamparter, A.C. Vermuelen, E.J. Mittemeijer, J. Appl. Crystallogr. **38**, 1 (2004)
18. D. Rafaja, V. Valvoda, A.J. Perry, J.R. Treglio, Surf. Coat. Technol. **92**, 135 (1997)
19. P. Colombi, P. Zanola, E. Bontempi, R. Roberti, M. Gelfi, L.E. Depero, J. Appl. Crystallogr. **39**, 176 (2006)
20. I.C. Noyan, J.B. Cohen, *Residual Stress Measurement by Diffraction and Interpretation* (Springer-Verlag New York Inc, New York, 1987), p. 123
21. L. Hou, S.Y. Bi, H. Zhao, Y.M. Xu, Y.H. Mu, Y.X. Lu, Appl. Surf. Sci. **403**, 248–259 (2017)

Effect of Co Addition on Microstructure and Properties of Cu–Ni–Si Alloy

Jiang Li, Guojie Huang, XuJun Mi, LiJun Peng, HaoFeng Xie and Yonglin Kang

Abstract Cu–Ni–Si system alloys have been the research hotspots because of high strength and high electrical conductivity in recent years. In this study, the influence of Co addition on microstructure and properties of Cu–Ni–Si alloys were investigated by transmission electron microscopy (TEM) and high resolution transmission electron microscopy (HRTEM). The result shows that the hardness of alloys increase firstly, gradually decline and leveled off while reaching a certain peak with the prolongation of aging time, which the electrical conductivity gradually increased. The best integrated performance is obtained at 500 °C aging for 4 h, which reaches the peak value of 233 HV and the conductivity was 37.3% IACS, the ultimate and yield strength reached 583 and 496 MPa, At the same time, the ductility of Cu–Ni–Si–Co alloy reached 12.9%. The phases of $(Ni, Co)_2Si$ precipitated with the addition of Co, which strengthens the alloy and enhances the mechanical properties. However, the formation of Co_2Si phase leads to Ni element dissolved in the matrix, which gives rise to the reduction of conductivity.

Keywords Cu–Ni–Si alloy · Microstructure · Solution heat treatment Diffusion

J. Li · G. Huang (✉) · X. Mi · L. Peng · H. Xie
General Research Institute for Nonferrous Metals, Beijing, China
e-mail: huangguojie@grinm.com

J. Li
e-mail: lijiangjyo@163.com

X. Mi
e-mail: mxj@grinm.com

L. Peng
e-mail: penglijun198677@163.com

H. Xie
e-mail: xiehaofeng@grinm.com

J. Li · Y. Kang
University of Science and Technology, Beijing, China
e-mail: kangylin@ustb.edu.cn

© Springer Nature Singapore Pte Ltd. 2018

Y. Han (ed.), *Advances in Materials Processing*, Lecture Notes in Mechanical Engineering, https://doi.org/10.1007/978-981-13-0107-0_33

Introduction

The development of the next generation of elastic materials should ensure its high strength while satisfying its high conductivity. At present, copper alloys are widely used in many fields owing to their excellent conductive thermal conductivity, thus, it will be a good alternative. Most of the alloys are usually of the precipitation-strengthened types and are alloyed with elements of very low solubility to preserve high levels of properties. Recently, among precipitation hardened copper alloys being developed, Cu–Ni–Si alloys have created considerable interest due to their ultrahigh strength and high electrical conductivity [1]. The strengthened is achieved by the well-proportioned distribution of Ni–Si precipitates in copper matrix, increase the electrical conductivity while maximizing the hardness and strength of these alloys.

In recent years, a great deal of researches use method of adding alloying elements and optimizing aging process to further improve the strengthen of Cu–Ni–Si alloys. For example, addition of Co element can form stable precipitate phases directly—$(Ni, Co)_2Si$ phases and decrease the dislocation density [2]. Adding Cr can decrease the grain size and improve the strength of alloy effectively. Mg addition affect the precipitation kinetics and greatly increases elongation. Moreover, the precipitate phase of δ-Ni_2Si is reduced and the driving force of precipitation from solid solution is accelerated by trace Ti [3]. Different aging parameters have significant effects on the performance of Cu–Ni–Si alloys.

In the present study, the influence on microstructure and properties of Cu–Ni–Si alloys by adding Co element were discussed. Different heat treatment systems were designed to affirm the optimum aging system for Cu–Ni–Si–(Co) alloys, moreover, the influence of solution treatment and aging on microstructural evolution and mechanical behavior of alloys were investigated.

Experimental

Ingots of Cu–3.2 wt%Ni–0.6 wt%Si alloys with Co addition were melted in a high frequency induction melting furnace under the protection of the gas environment. The chemical compositions of alloys are listed in Table 1. The ingots were hot forged with 85% reduction in thickness at 1203 K and cut into the metal plates of

Table 1 Designed and tested compositions of Cu–Ni–Si and Cu–Ni–Si–Co alloys

Alloys	Designed				Tested			
	Ni	Si	Co	Cu	Ni	Si	Co	Cu
Cu–Ni–Si	3	0.67	–	Bal.	3.2	0.6	–	Bal.
Cu–Ni–Si–Co	3	0.7	0.6	Bal.	3.3	0.6	0.64	Bal.

25 × 20 × 2 mm. And then the hot rolling plates were solution treated at 1248 K for 1 h and quenched in water before isothermally aged at 773 K for various time.

For microstructural observations, the samples were gradually ground with waterproof emery papers from 200# to 5000# and subsequently mechanical polishing, then etching with a solution of 10 g $FeCl_3$ and 30 ml HCl in 120 ml of ethanol. Metallographic observation was carried out with Axiovert-200MAT light microscope.

Transmission electron microscope (TEM) samples were prepared by double jet electrolytic-polishing at −50 °C within a bath containing 20% nitric acid and 80% methanol [2]. The resulting foil specimens were observed under JEOL JEM-2010 microscope with an acceleration voltage of 200 kV.

A type of 7501 eddy current conductivity meter was applied for the electrical conductivity. The Vickers hardness was measured at room temperature on the polished specimens using a 430SVD Vickers hardness tester with a 500 g indentation load and a 15 s dwell time. The hardness tests were carried out 5 times for each specimen and the average of hardness were obtained.

Results and Discussion

Microstructure

Figure 1 presents the TEM images treated from the sample aged at 500 °C for 4 h. Figure 1a shows that a large number of small precipitates with a lobe-shaped appear in the copper matrix. It illustrates that these tiny precipitates are orbicular and fully intercoupled with the matrix. The average size of particles are approximately 12–15 nm and the grains appear as disc-like and rod-like shapes. In the SAED pattern from the zone axis of $[001]_{Cu}$ are shown in Fig. 1b, three series of weak spots appear between matrix spots, two grains (marked with A and B) as the location of mutually perpendicular lying on $\{101\}_{Cu}$ align in the two $\langle 101 \rangle_{Cu}$ directions, the other in the place of $1/2(\bar{2}02)_{Cu}$ position testifies the presence of ordering phase (marked with C) [4]. The HRTEM images is shown in Fig. 1c, it can be confirmed that the existence of the phase is also δ-Ni_2Si phase by Fourier transforms, not the ordered fcc β-Ni_3Si in previous studies. At the same time, it can be seen the disk-shaped and rod-shaped precipitates clearly, both of δ-Ni_2Si precipitates have mutual perpendicular directions, as shown in HRTEM images (Fig. 1c). And the δ-Ni_2Si have the same crystal lattice and orientation relationship with matrix, which agrees well with the selected area diffraction pattern shown in Fig. 1b. The δ-Ni_2Si phases with orthorhombic structure are identified and indexed in Fig. 1b according to the lattice parameters (a = 0.708 nm, b = 0.502 nm, c = 0.371 nm) reported in the literature [5]. Based on the above analysis, the crystallographic orientation relationships between the matrix and precipitates has been determined as following: $(\bar{2}02)_{Cu}//(010)_{\delta 1}//(100)_{\delta 2}//(300)_{\delta 3}$, $[001]_{Cu}//[100]_{\delta 1}//[100]_{\delta 2}//[100]_{\delta 3}$.

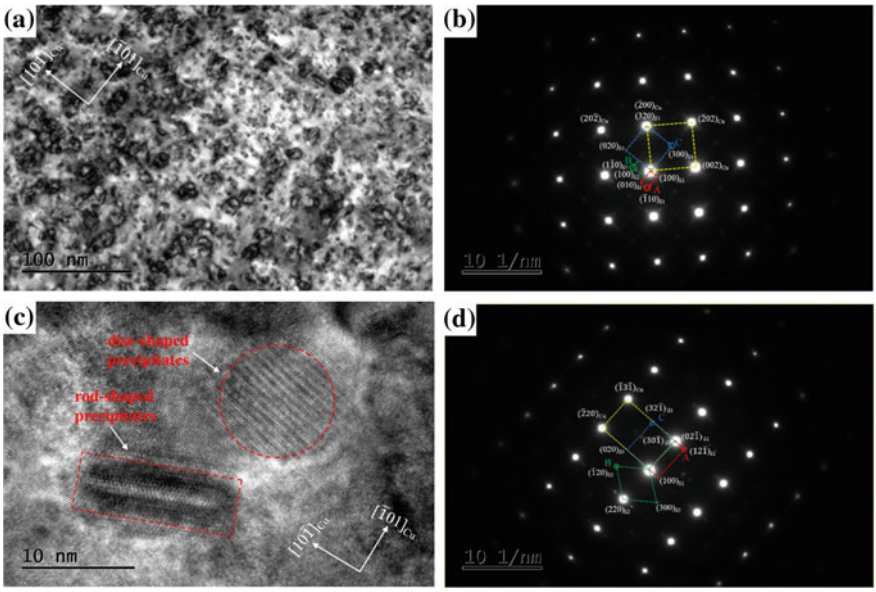

Fig. 1 TEM and HRTEM images of the Cu–Ni–Si aged at 500 °C for 4 h. **a** Bright-field TEM image along $[001]_{Cu}$; **b** SAED image of a; **c** HRTEM image along $[001]_{Cu}$; **d** SAED image along $[112]_{Cu}$

In order to further confirm the type of precipitates and determine the crystal orientation relationship, the SAED pattern from the zone axis of $[112]_{Cu}$ are shown in Fig. 1d, the results of calibration further demonstrates the presence of three ordering phases (marked with A, B and C), which is consistent with the observation from the zone axis of $[001]_{Cu}$. The corresponding crystal orientation relationship between matrix and precipitates has been determined as following: $(11\bar{1})_{Cu}//(02\bar{1})_{\delta1}//(220)_{\delta2}//(30\bar{1})_{\delta3}$, $[112]_{Cu}//[0\bar{1}\bar{2}]_{\delta1}//[001]_{\delta2}//[103]_{\delta3}$.

Microstructures and selected-area electron diffraction patterns (SAEDs) of Cu–Ni–Si–Co alloy after ageing treatment at 500 °C for 4 h are shown in Fig. 2. Some nano-scale precipitating particles can be seen from the Bright-field TEM image, the average size is only about 8–10 nm, as measured in Fig. 2a. The results showed that the particles become finer, more homogeneous and rounder with the addition of Co. And both of precipitates also have two sets of mutual perpendicular directions from the central dark field images in Fig. 2b. According to the SAED pattern from the zone axis of $[001]_{Cu}$ in Fig. 2c, illustrates the presence of three phases: Cu matrix, Ni_2Si and Co_2Si precipitates. It is worthwhile mentioning that three series weak spots (marked with A, B and C) also identified and indexed between matrix spots, which have the same orientation relationships with Cu–Ni–Si alloys.

In the SAED pattern from the zone axis of $[112]_{Cu}$, the consequence of calibration further testifies the existence of three ordering phases, which is consistent with the observation from the zone axis of $[001]_{Cu}$ [6]. The corresponding crystal

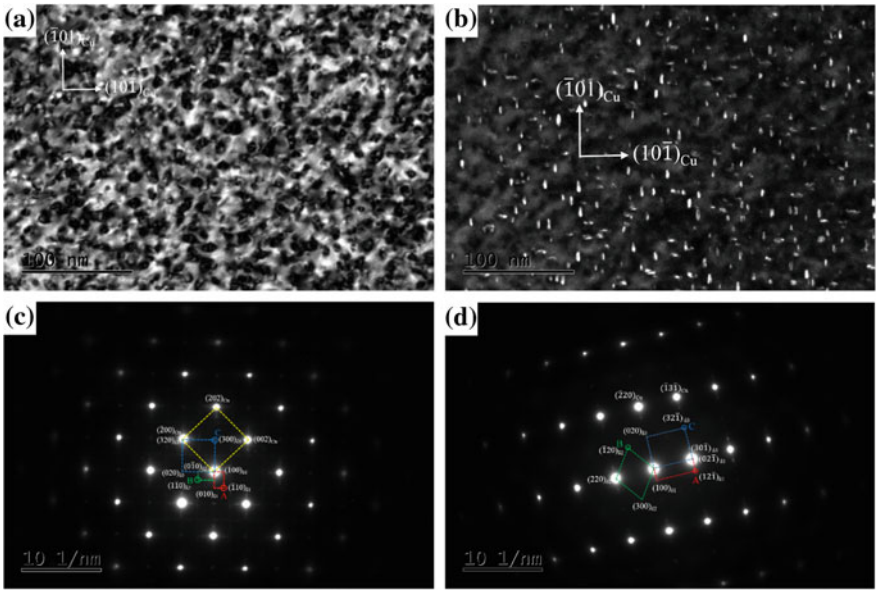

Fig. 2 TEM and HRTEM images of the Cu–Ni–Si–Co aged at 500 °C for 4 h. **a** Bright-field TEM image along $[001]_{Cu}$; **b** Dark-field TEM image along $[001]_{Cu}$; **c** SAED image of a; **d** SAED image along $[112]_{Cu}$

orientation relationship between copper matrix and precipitates has been determined as following: $(\bar{2}02)_{Cu}//(010)_{p1}//(100)_{p2}//(300)_{p3}$, $[001]_{Cu}//[100]_{p1}//[100]_{p2}//[100]_{p3}$, $(11\bar{1})_{Cu}//(02\bar{1})_{p1}//(220)_{p2}//(30\bar{1})_{p3}$, $[112]_{Cu}//[0\bar{1}\bar{2}]_{p1}//[001]_{p2}//[103]_{p3}$.

Mechanical and Electronic Properties

Figure 3a illustrates the variation of hardness with the different aging time at 500 °C. It is clearly that the hardness of specimens increased rapidly and approached a peak value until 4 h, which results from the faster precipitation and therefore faster solute depletion of the matrix in the initial ageing process. Subsequently, the hardness decreases continuously with aging time. In the early aging time, the precipitates keep coherent relationship with matrix and appear a large number of lattice distortion zones [7]. With the increasing of the aging time, the growing up of precipitated phase destroys the coherent relationship, which cause lattice distortion and hardness declining slightly.

The relation of the electrical conductivity and the aging time aged at 500 °C is shown in Fig. 3b. It is obvious that the electrical conductivity increased rapidly in the initial ageing states. When the specimens aged for 4 h, the electrical conductivity keeps increasing slightly. This is because the solute atoms precipitate out from the supersaturated solid solution [8]. The solute atomic scattering effect on

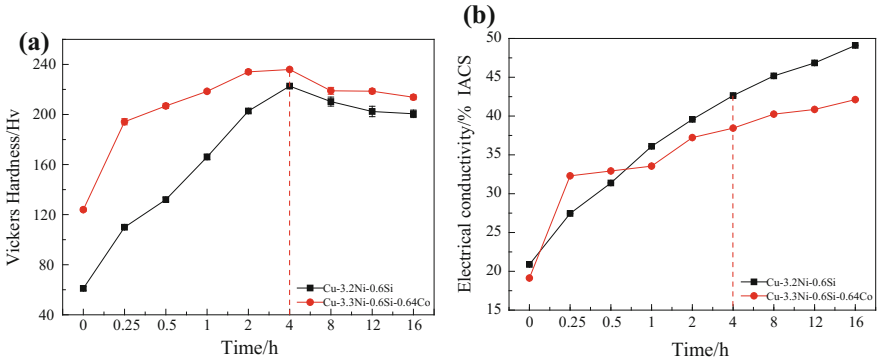

Fig. 3 The hardness and electrical conductivity of Cu–Ni–Si–Co alloys with different ageing times at 500 °C

Table 2 Comprehensive properties of peak-aged Cu–Ni–Si–(Co) alloys

Alloys	UTS (MPa)	YTS (MPa)	δ (%)	HV	Electrical conductivity (%IACS)
Cu–Ni–Si	532	477	8.2	223	42.7
Cu–Ni–Si–Co	583	496	12.9	233	37.3

electric reduces and leads to the conductivity increases greatly at the initial stage of aging. The precipitation of (Ni, Co)$_2$Si phase leads to the number of solute atoms reduces, which results in the electrical conductivity continuous increasing with the extension of aging time. Finally, the electric conductivity trends to be stability result from the decrement in the kinetics of the precipitation [9]. It is worth noting that the conductivity without Co is much better than the alloys of Co addition. When the matrix of Ni and Si not in proper proportion of chemical form Ni_2Si (relative surplus Ni), Co will react with Si and forming Co_2Si phase by priorities, the rest of the Ni in the matrix produce scattering on the electron, which affect the electrical conductivity of the alloy.

The comprehensive properties are shown in Table 2. The ultimate tensile strength and yield strength of Cu–Ni–Si alloy are 532, 477 MPa, respectively. Addition of Co improve the mechanical strength at the same time, the ultimate and yield strength reaches 583, 496 MPa, respectively. However, the electrical conductivity decrease to 37.3% IACS. There is a remarkable fact that the elongation of Cu–Ni–Si–Co alloy reaches 12.9%, while Cu–Ni–Si alloy only 8.2%.

Effects of Co Addition on Mechanical Properties

Precipitation hardening is the main strengthening mechanism responsible for the high strength of the Cu–Ni–Si alloys. The microstructural change in the alloys

during aging is similar to the structural transition sequence in the Cu–Ni–Si alloy. The size of precipitates become finer and rounder in the samples with Co than that without Co (Figs. 1a, 2a). Consequently the microhardness and strength of the alloy can be improved by nano-scale (Ni, Co)$_2$Si precipitates. This is consistent with the ultimate tensile strength tests-the maximum values of the Cu–Ni–Si–Co samples (583 MPa) being generally 50 MPa higher than those of the Cu–Ni–Si samples (532 MPa) in Table 2. Addition of Co affected the precipitation kinetics and increased the formation rate of precipitates. The precipitation particles were difficult to shear by dislocation, and the dislocation only bypassed them [10]. As a result, Cu–Ni–Si–Co alloy was strengthened effectively by the Orowan strengthening mechanism. Moreover, Co elements reduce the grain size of recrystallized grains during solution treatment and subsequently refine the microstructure. According to the Hall-Patch theory, strengthening and hardening is improved by grain refinement [11]. In conclusion, the addition of Co improve mechanical property.

Effects of Co Addition on Electrical Conductivity

According to Matthiessen's theory, electrical conductivity affected by resistivity sourcing from solute atoms, dislocations, interfaces and vacancy, respectively. And solution scattering is dependent on the amount of solution atoms, which is the dominating factor for aging strengthening alloys [12]. When adding Co into the Cu–Ni–Si alloys, Co has hcp structure rather than fcc structure, so Co is difficult to dissolve into the fcc matrix. In addition, δ-Ni$_2$Si phase has the prototype of δ-Co$_2$Si phase, and these two phases can form continuous solid solution [13]. Therefore replacing part of Ni atoms by adding Co atoms will result in less Ni or Co solute atoms in the copper matrix, and at the same time formation of more (Ni, Co)$_2$Si phase will reduce Si composition in Cu matrix. However, the addition of Co will react with Si and forming Co$_2$Si phase by priorities, because the binding energy of Co with Si is greater than that of Ni with Si. And the rest of the Ni in the matrix produce scattering on the electron [14], which reduces the electrical conductivity of the alloy. Hence, the electrical conductivity will go down.

Conclusions

(1) The best integrated performance of Cu–Ni–Si–Co alloys is obtained at 500 °C aging for 4 h, which reaches a peak value of 233 HV and the electrical conductivity is 37.3 IACS%, the ultimate and yield strength reaches 583 and 496 MPa, the elongation reaches 12.9%.
(2) Cu–Ni–Si–Co alloy have the same orientation relationships with Cu–Ni–Si alloys, microstructure analysis confirms the existence of Cu–Ni–Si–Co alloys are all (Ni, Co)$_2$Si phases, both of (Ni, Co)$_2$Si precipitates have mutual

perpendicular directions, the phases true morphology should be disk-shaped and the crystal orientation relationship between matrix and precipitates is: $(\bar{2}02)_{Cu}//(010)_{p1}//(100)_{p2}//(300)_{p3}$, $[001]_{Cu}//[100]_{p1}//[100]_{p2}//[100]_{p3}$, $(11\bar{1})_{Cu}//(02\bar{1})_{p1}//(220)_{p2}//(30\bar{1})_{p3}$, $[112]_{Cu}//[0\bar{1}\bar{2}]_{p1}//[001]_{p2}//[103]_{p3}$.

(3) The mechanical properties of Co addition is much better than the alloys without Co, Owing to the addition of Co introduces additional Co particles into copper matrix, thus enhancing Orowan strengthening. The addition of Co will react with Si and forming Co_2Si phase by priorities, Ni element dissolves into copper matrix, which gives rise to the reduction of conductivity.

Acknowledgements Our study is supported by the National Key R&D Program of China (No. 2016YFB0301300).

References

1. X.P. Xiao, B.Q. Xiong, Q.S. Wang et al., Age-hardening characteristics of Cu–Ni–Si alloy after cold deformation. Appl. Mech. Mater. **217–219**, 294–298 (2012)
2. W. Wang, H. Kang, Z. Chen et al., Effects of Cr and Zr additions on microstructure and properties of Cu–Ni–Si alloys. Mater. Sci. Eng.: A **673**, 378–390 (2016)
3. E. Lee, S. Han, K. Euh et al., Effect of Ti addition on tensile properties of Cu–Ni–Si alloys. Met. Mater. Int. **17**(4), 569–576 (2011)
4. J.Y. Cheng, B.B. Tang, F.X. Yu et al., Evaluation of nanoscaled precipitates in a Cu–Ni–Si–Cr alloy during aging. J. Alloy. Compd. **614**, 189–195 (2014)
5. T. Hu, J.H. Chen, J.Z. Liu, Z.R. Liu, C.L. Wu, Acta Mater. **61**, 1210–1219 (2013)
6. D.M. Zhao, Q.M. Dong, P. Liu et al., Structure and strength of the age hardened Cu–Ni–Si alloy. Mater. Chem. Phys. **79**(1), 81–86 (2003)
7. S.Z. Han, L.S. Hwan, K. Sangshik et al., Increasing strength and conductivity of Cu alloy through abnormal plastic deformation of an intermetallic compound. Sci. Rep. **6**, 30907 (2016)
8. L.J. Peng, B.Q. Xiong, G.L. Xie et al., Precipitation process and its effects on properties of aging Cu–Ni–Be alloy. Rare Met. **32**(4), 332–337 (2013)
9. K. Wang, K.F. Liu, J.B. Zhang, Microstructure and properties of aging Cu–Cr–Zr alloy. Rare Met. **33**(2), 134 (2014)
10. X.P. Xiao, Z.Y. Yi, T.T. Chen et al., Suppressing spinodal decomposition by adding Co into Cu–Ni–Si alloy. J. Alloy. Compd. **660**, 178–183 (2016)
11. Q. Lei, Z. Li, C. Dai et al., Effect of aluminum on microstructure and property of Cu–Ni–Si alloys. Mater. Sci. Eng.: A Struct. Mater. Prop. Microstruct. Process. **572**(6), 65–74 (2013)
12. C. Watanabe, F. Nishijima, R. Monzen et al., Mechanical properties of Cu–4.0 wt%Ni–0.95 wt%Si alloys with and without P and Cr Addition. Mater. Sci. Forum **561–565**, 2321–2324 (2007)
13. Q.S. Wang, G.L. Xie, X.J. Mi et al., The precipitation and strengthening mechanism of Cu–Ni–Si–Co alloy, in *Materials Science Forum*, vol. 749 (Trans Tech Publications, 2013), pp. 294–298
14. S.Z. Han, L.S. Hwan, K. Sangshik et al., Increasing strength and conductivity of Cu alloy through abnormal plastic deformation of an intermetallic compound. Sci. Rep. **6**, 30907 (2016)

Effect of Controlled Rolling and Cooling on Microstructure and Properties of Cold Heading Steel Containing Boron and Titanium

Shipeng Ruan, Aimin Zhao, Lijun Wang, Guangjie Han and Peng Zhang

Abstract The effect of controlled rolling and cooling on microstructure and mechanical properties of micro-alloyed cold heading steel 6AB-Ti and 35KB-Ti with diameter 6.5 mm was studied. The results showed that the controlled rolling and cooling process had a great effect on the microstructure and properties of 6AB-Ti than 35KB-Ti. For 6AB-Ti steel, the tensile strength value decreased from 460 to 360 MPa and the microstructure evolved from quasi-polygonal ferrite and pearlite to polygonal ferrite and pearlite when the finish rolling decreased from 920 to 850 °C (and the laying head temperature decreased from 900 to 800 °C). For 35KB-Ti steel, the tensile strength decreased from 630 to 610 MPa and the microstructure with ferrite net disappeared for controlled rolling and cooling process. The above phenomena are explained by the CCT curve of steel and the influence of boron and titanium on the phase transformation of steel.

Keywords Controlled rolling and cooling · Boron and titanium Microstructure · Mechanical properties · CCT

S. Ruan (✉) · A. Zhao
Metallurgy Engineering Research Institute, University of Science and Technology Beijing, Beijing 100083, China
e-mail: shipengruan@163.com

A. Zhao
e-mail: aimin.zhao@ustb.edu.cn

S. Ruan · L. Wang · G. Han · P. Zhang
Xingtai Iron and Steel Corp., Ltd., Xingtai 054027, China
e-mail: wljun0604@126.com

G. Han
e-mail: jszx2014@xtsteel.com

P. Zhang
e-mail: xcyyyj@xtsteel.com

S. Ruan · L. Wang · G. Han · P. Zhang
Hebei Engineering Research Center for Wire Rod, Xingtai 054027, China

© Springer Nature Singapore Pte Ltd. 2018

Y. Han (ed.), *Advances in Materials Processing*, Lecture Notes in Mechanical Engineering, https://doi.org/10.1007/978-981-13-0107-0_34

Introduction

Cold heading steel is mainly used for the production of all kinds of standard parts which require good cold upsetting performance and hardenability [1]. SWRCH6A and SWRCH35K are two commonly used cold heading steel grades in JIS G3507 standard. Boron or titanium alloy elements are often added to these steel grades for improving performance or export rebates. 6AB-Ti steel added 0.0050% boron and 0.07% titanium relative to SWRCH6A, and 35KB-Ti steel added 0.0020% boron and 0.03% titanium relative to SWRCH35K. The addition of boron and titanium can improve the hardenability of steel [2, 3], but it is harmful to other properties when added more [4]. For example, it may cause the rise of tensile strength, which is detrimental to cold upsetting.

Besides chemical composition, the process of controlled rolling and cooling has great influence on the microstructure and properties of wire rod by controlling the recrystallization or grain growth of austenite and subsequent transformations [5–7]. So it is very important to study and optimize the process of rolling and cooling for different grades, especially for the steel which contain more boron and titanium.

In this paper, the influence of controlled rolling and cooling process on the microstructure and properties of 6AB-Ti and 35KB-Ti hot rolled wire rod with diameter 6.5 mm was studied.

Experimental Material and Procedure

Table 1 shows the main chemical composition of experimental steels, which were supplied by Xingtai Iron & Steel Corp., Ltd. The experimental steels were first cast into billet with the section size of 160 × 160 mm^2, and then rolled into wire rod with diameter of 6.5 mm by heating, rough rolling, medium rolling and final rolling process.

Table 2 shows the tested rolling and cooling process of experimental steels. There are two processes, the process 1# is the traditional process, the finish rolling temperature is 920 °C, the laying head temperature is 900 °C, and the cooling mode is slow cooling with first cooling roller speed 0.25 m s^{-1}. The process 2# is the controlled rolling and cooling process, the finish rolling temperature is reduced to 850 °C, the laying head temperature is 800 °C, and the cooling mode is also slow cooling with first cooling roller speed 0.18 m s^{-1}.

Table 1 Chemical composition of experimental steels (wt%)

Steel grade	C	Si	Mn	P	S	Al	B	Ti
6AB-Ti	0.06	0.04	0.40	0.008	0.005	0.05	0.0050	0.07
35KB-Ti	0.34	0.15	0.80	0.009	0.004	0.04	0.0020	0.03

Table 2 Rolling and cooling process of experimental steels

Process number	Finish rolling temperature (°C)	Laying head temperature (°C)	Cooling mode	First cooling roller speed (m s^{-1})
1#	920	900	Slow cooling	0.25
2#	850	800	Slow cooling	0.18

The mechanical properties of the wire rod were tested by WDW50 universal testing machine, and the microstructure was observed by Leica DM2700M optical microscope (OM).

Results and Discussion

Mechanical Properties

Table 3 shows the mechanical properties of experimental steels wire rod of 6.5 mm diameter with two different processes.

For 6AB-Ti steel wire rod, the controlled rolling and cooling process has a great influence on its mechanical properties. When traditional process 1# is taken, the tensile strength is 460 MPa and the elongation is 31%, but when controlled rolling and cooling process 2# is taken, the tensile strength decreased to 360 MPa, reduced by 100 MPa, but the elongation increased to 42%, increased by 11%. There is no significant change in the reduction of area.

For 35KB-Ti steel wire rod, the controlled rolling and cooling process has an effect on tensile strength, but no influence on reduction of area and elongation. When process 1# is taken, the tensile strength is about 630 MPa, but when process 2# is taken, the tensile strength decreased to 610 MPa, reduced by 20 MPa.

Compared to 35KB-Ti steel, 6AB-Ti steel contains more boron and titanium, so it can be conclude that the more content of B and Ti micro-alloy elements, the greater influence of mechanical properties by controlled rolling and cooling process.

Table 3 Mechanical properties of the experimental steels wire rod with diameter 6.5 mm

Steel grade	Process	Tensile strength (MPa)	Reduction of area (%)	Elongation (%)
6AB-Ti	1#	460	74	31
	2#	360	75	42
35KB-Ti	1#	630	53	29
	2#	610	54	30

Microstructure

Figure 1 shows the microstructure of experimental 6AB-Ti steel wire rod with two different processes. We can see that the microstructure is quite different. Under the traditional process 1#, the microstructure is composed of irregular quasi-polygonal ferrite and pearlite. There is a bending phenomenon in the grain boundary and the grain size is coarse (about 50 μm). Under the controlled rolling and cooling process 2#, the microstructure of the steel is composed of equiaxed uniform polygonal ferrite and pearlite, the grain size is fine (about 20 μm), the grain boundary is straight and smooth.

Figure 2 shows the microstructure of experimental 35KB-Ti steel wire rod with two different processes. We can see that the microstructure is composed of ferrite

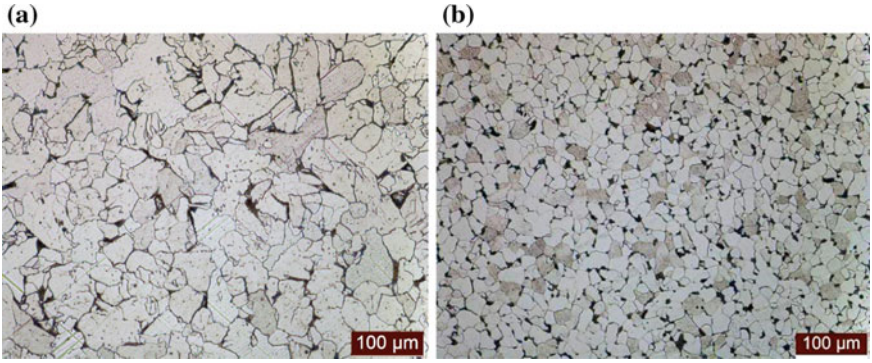

Fig. 1 Microstructure of 6AB-Ti with different processes. **a** Traditional process 1#, **b** controlled rolling and cooling process 2#

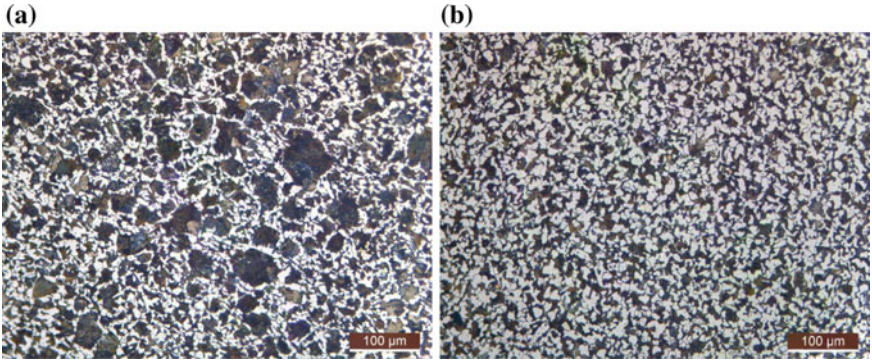

Fig. 2 Microstructure of 35KB-Ti wire rod with different processes. **a** Traditional process 1#, **b** controlled rolling and cooling process 2#

and pearlite both, but there are some differences. Under the traditional process 1#, the ferrite is reticulated and the pearlite is bulky. But under the process 2#, the ferrite of the steel is uniform polygonal ferrite and the percentage of pearlite is reduced from 57 to 48% which will reduce the tensile strength.

Discussion

In the case of the same chemical composition, the microstructure of the steel is affected by the controlled rolling and cooling process [5, 6]. During the traditional process rolling, the recrystallization and grain growth of deformed austenite at high temperature, large grain size is obtained due to the high driving force. During controlled rolling and cooling process, with the decrease of deformation temperature, the driving force of grain growth is reduced, and it's easy to obtain the fine grain.

A study reported that boron can make the grain coarsening of low carbon steel [7]. The experiment 6AB-Ti steel obtains coarse grain in the traditional process 1#. According to Hall–Petch formula $\sigma_s = \sigma_i + K_1 D^{-1/2}$, the coarse grain reduces the strength, but the strength of 6AB-Ti with process 1# is higher than the strength of 6AB-Ti with process 2# which grain is finer. It shows that there are some other factors caused the strength increasing.

We can see that there is also adding titanium element in 6AB-Ti steel except boron. Boron can make CCT curve moves to the right of low carbon Ti micro-alloyed steel [4], which delays the austenite to ferrite transformation. In other words, boron promotes the formation of quasi-polygonal ferrite of 6AB-Ti steel. Quasi-polygonal ferrite is a transition product of lower temperature, which has a higher dislocation density and the substructure [4], which would significantly increase the strength of the 6AB-Ti steel. In order to avoid the formation of quasi-polygonal ferrite, on the one hand, the cooling rate should be reduced; and on the other hand the method of low temperature rolling can be adopted. Low temperature deformation can make CCT curve moves left [5], which results in the formation of polygonal ferrite and the decrease of the tensile strength.

For 35KB-Ti steel, the content of boron and titanium is lower than that of 6AB-Ti steel, and the effect of the controlled rolling and cooling process on its microstructure and properties is smaller than 6AB-Ti steel. But the influence law of controlled rolling and cooling process on microstructure and grain size is the same. When the traditional process 1# with high rolling temperature is taken, the microstructure are reticular ferrite and bulky pearlite; however, when controlled rolling and cooling process 2# with low-temperature rolling is adopted, the uniform fine ferrite and pearlite are obtained.

Conclusions

By studying the influence of controlled rolling and cooling process on the microstructure and properties of 6AB-Ti and 35KB-Ti steel, the following conclusions can be obtained.

(1) The tensile strength of 6AB-Ti steel wire rod with diameter 6.5 mm is reduced from 460 to 360 MPa when the traditional process 1# is changed to control rolling and cooling process 2#, and the elongation increases from 31 to 42%. There is no significant change in the reduction of area. The microstructure changes from irregular quasi-polygonal ferrite and pearlite to uniform polygonal ferrite and pearlite.
(2) The tensile strength of 35KB-Ti steel wire rod with diameter 6.5 mm is reduced from 630 to 610 MPa when the traditional process 1# is changed to controlled rolling and cooling process 2#, and there is no significant change in the elongation and the reduction of area. The microstructure changes from reticulated ferrite and bulky pearlite to uniform ferrite and pearlite.
(3) Low temperature rolling makes the CCT curve move to the left, which can easily get the uniform ferrite and pearlite organization, so as to reduce the tensile strength of the steel. The higher the content of boron and titanium micro-alloy element in the steel, the bigger the influence of controlled rolling and cooling process.

References

1. S.P. Ruan, A.M. Zhao, J.L. Chen et al., Study on energy saving cold heading steel wire rod containing boron. Steel Rolling **32**(Supplement 1), 30–34 (2015)
2. S.P. Ruan, A.M. Zhao, M.Y. Guo et al., Effect of boron and titanium on microstructure and properties of low carbon Al-killed steel. Iron Steel **51**(7), 71–75 (2016)
3. S.P. Ruan, A.M. Zhao, J. Cui et al., Continuous cooling transformation behavior of 10B33 boron micro alloyed medium carbon steel for cold heading. Heat Treat. Met. **41**(9), 18–21 (2016)
4. N. Tsuji, Y. Matsubara, T. Sakai et al., Effect of boron addition on the microstructure of hot-deformed Ti-added interstitial free steel. ISIJ Int. **37**(8), 797–806 (1997)
5. H. Hata, H. Yaguchi, M. Shimotsusa et al. Development of high quality wire rod through thermo mechanical control process. Kobe Steel Eng. Rep. 1, 29–32 (2000)
6. S.P. Ruan, L.J. Wang, J.L. Chen et al., Effect of control-rolling-cooling process on structure and properties of steel SCM435 rod coil. Spec. Steel **5**, 45–47 (2016)
7. C. Camurri, C. Carrasco, I. Bello et al., Development of low carbon boron steel for wire drawing. Mater. Sci. Forum **539–543**, 4238–4242 (2007)

Preparation of TiAl Based Metallic Fibers

Yongchuan Yu, Shuling Zhang and Weiye Chen

Abstract The microstructure and outward of Ti-44Al-8Nb fibers prepared by melt spinning method were investigated by X-ray diffraction, scanning electron microscopy, transmission electron microscopy, and analyzed by line scan energy spectrum and energy dispersive X-ray detector. The fibers were manufactured at two rotation speeds. The outward of the fibers with Rayleigh-wave was defaulted when the rotation speed was 2000 r/min. But when the rotational speed up to 2600 r/min, the fibers became a ribbon shape. The fiber quality of the fibers prepared with these two rotation speeds were unsatisfactory. The microstructure was mainly composed of fine α_2 phase, γ phase dendritic crystal and a second phase which was confirmed to be Ti_5Si_3. The above analysis results showed that the reaction among Ti-44Al-8Nb alloy, quartz tube, and BN crucible occurred. The feasibility of zirconia crucible and zirconia tube were speculated. In all respects, the above work laid the foundation for the latter part of the preparation process which also needs to be optimized.

Keywords Microstructure · Rapid-solidification · Melt extracted

Y. Yu · S. Zhang (✉)
School of Mechanical Engineering, Ningxia University,
Ningxia Yinchuan 750021, China
e-mail: slzhang1229@163.com

Y. Yu
e-mail: 2546765670@qq.com

W. Chen
School of Materials Science and Engineering,
Beifang University of Nationalities, Ningxia Yinchuan 750021, China
e-mail: 43260027@qq.com

© Springer Nature Singapore Pte Ltd. 2018

Y. Han (ed.), *Advances in Materials Processing*, Lecture Notes in Mechanical Engineering, https://doi.org/10.1007/978-981-13-0107-0_35

Introduction

TiAl-based intermetallics, a kind of high-temperature lightweight structural material, have the advantages of excellent temperature strength and oxidation resistance, low density [1]. However, the use of TiAl-based intermetallics were limited due to their relatively low ductility [2]. Fortunately, metallic glass (MG) as a newcomer in the world of glass possesses many excellent properties, such as high yield strength, lower shear modulus, soft magnetic properties, outstanding wear resistance, and superior corrosion resistance. It is hoped that the formation of MG will solve these defects in applications of TiAl alloy [3]. Heat treatment [4], adding alloying elements [5], and thermo mechanical treatment [6] are also used to enhance the mechanical properties. However, these methods can only refine the grain size and it is invariably hard to eliminate α_2/γ lamellar structures [7]. For example, the solidification segregation of high Nb-containing TiAl alloy is hard to eliminate by heat treatment [1].

The rapid solidification can produce fine microstructures and other strong points like the decreased segregation and the formation of metastable or amorphous phase. So rapid solidification alloys have been great concerned due to high mechanical properties at room and elevated temperature [8]. Getting the ideal structure by controlling the cooling rate. In melt spinning method, there are many parameters influencing cooling rate like melt temperature, wheel speed, molten metal–wheel gap among which the wheel speed is easiest to control [9]. The wheel speed has a linear relationship with the cooling rate. Accordingly, the effect of cooling rate was analyzed by different wheel speed [10]. Melt extraction, a kind of melt spinning technique, could prepare metallic fiber or ceramic fiber and the diameter of fibers less than 30 μm. However, the study of TiAl alloy fiber fabricated by melt extraction technique has not been widely carried out.

The rare earth element, especially Y, is an effective element for refining the microstructure, purifying the TiAl alloys and improving the mechanical properties [11]. Y element promotes γ phase nucleation, leading to more γ phase with more Y addition, γ phase was found mainly located at the grain boundaries Besides the main two phases [9]. Melt extraction's cooling rate higher than other rapid solidification technique, greater undercooling which strongly influences the primary phase and solidification path can be obtained [12]. When the preparation technology is perfect, considering the effect of adding Y on the fiber properties is very important.

In this paper, Ti-44Al-8Nb fibers were fabricated by melt extraction. The microstructure outward and characterization of fibers were investigated. The fibers' outward are difference at two rotation speeds. The formation of second phase, especially Ti_5Si_3 was studied. What's more, we found that When the copper wheel's speed was 1600 r/min, the reaction of Ti-44Al-8Nb alloy and quartz tube, BN crucible were occurred. The feasibility of zirconia crucible and zirconia tube were speculated.

Experimental

A Vacuum Arc Remelting furnace was used to prepare Ti-44Al-8Nb alloy sponge Ti (99.9 wt%) and pure Al (99.99 wt%) crystals were the crude materials. Nb was added in the form of Al-Nb master alloy. The dimensions of Ti-44Al-8Nb were φ 100 mm × 120 mm. Subsequently, the Ti-44Al-8Nb alloy ingots were cut into a cylinder which has a diameter of 10 mm and a length of 10 mm by electrical discharge machine. Ti-44Al-8Nb fibers were prepared through a rotating copper wheel which the diameter of 160 mm thrown crude materials, and it was electromagnetic melting into the fiber. The copper wheel's speeds were 2000 and 2600 r/min. And the feed speed of molten metal was about 70 μm/s.

The morphology of the fibers were characterized by scanning electron microscopy (Japan Electronics Corporation, JSM-7500F, Japan). The phases of the fibers were investigated by XRD (Dandong Hao Yuan Instrument Co. Ltd, DX, China). The ingredients of the fibers were proved by energy dispersive X-Ray spectroscopy (EDX) Display and line scan energy spectrum, transmission electron microscopy (TEM), high resolution transmission electron microscopy (HRTEM) (ZEISS, Gemini, Germany).

Results

Figure 1 shows the different geometrical morphology of the fibers. Different geometric forms of fibers were obtained at different rotational speeds of the copper wheel. The fiber (Fig. 1a, c) was fabricated at a rotation speed of 2000 r/min. The unevenness of the surface due to the unstability of the extracted molten metal and the heterogeneous appearance was rayleigh-wave. In Fig. 1b, d, we can see that when the rotation speed up to 2600 r/min, The characteristic of fiber surface has some drawbacks. Compared with the high speed, when the speed reduced, the surface tension and self weight were in unstable state, forming the liquid metal column under the default action of rayleigh-wave. In Fig. 1f, the sample prepared by densely arranging the fibers on the carrier substrate were analyzed by XRD. Figure 1e shows the XRD result of fibers prepared at the rotation speed of 2600 r/min. It was proved that the fibers' main phase were α_2 phase and γ phase.

Compared with the master alloy the content of α_2 in the fibers increased, which may be due to that the cooling rate was very fast, leading to $\alpha/\alpha_{2+\gamma}$ transformation uncompleted, and a large number of α phase rapidly solidified to form α_2 phase. But Chai [13] adopted rapid solidification technique of malt spinning to prepare Ti-46Al-2Cr-2Nb based alloys with different contents of Y. The XRD results showed that a large amount of B phase appears in the rapidly solidified TiAl-based alloy containing 1.5 at.% or more. This indicating that the addition of high concentrations of Y increased the β-phase region while.

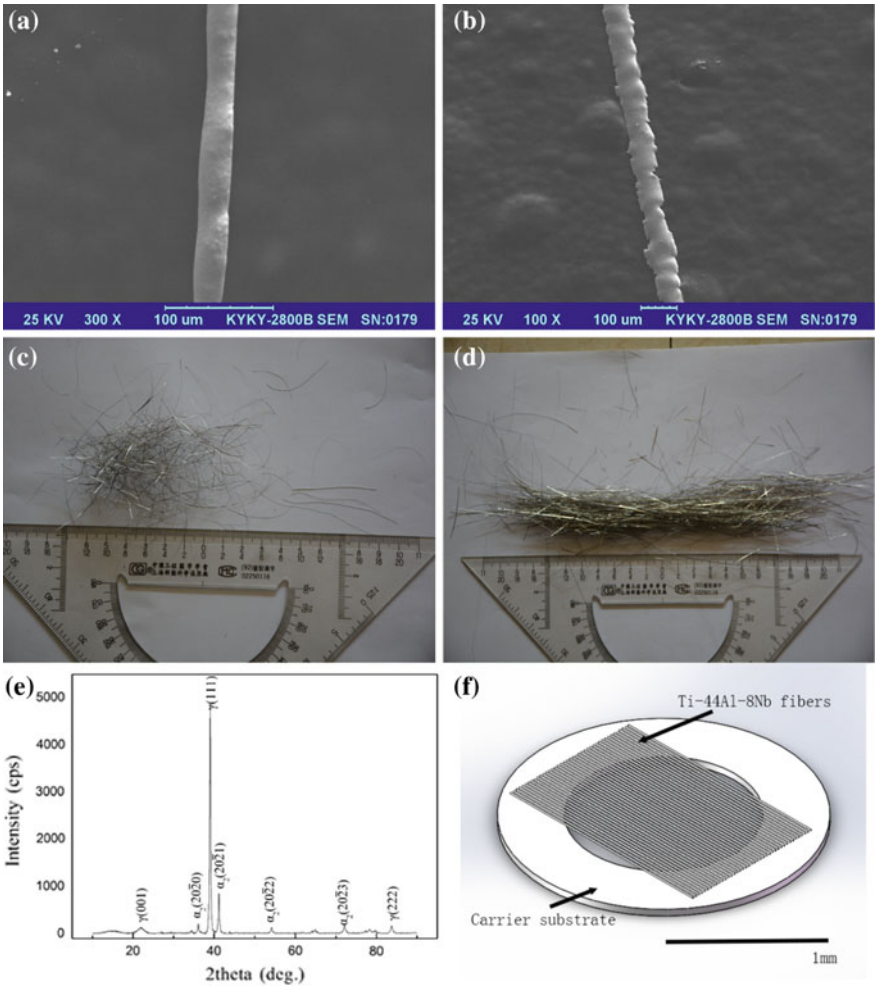

Fig. 1 SEM micrograms and morphology of the fibers at different speed of rotation: **a**, **c** 2000 r/min; **b**, **d** 2600 r/min; **e** XRD results of fibers; **f** Ti-44Al-8Nb fibers sample for XRD

β phase was maintained at high cooling rates, and it was ordered into B phase during the cooling process. Kong et al. [14] researched the influences of rare earth metal (Y) on the microstructure and mechanical properties of Ti-43A1-9V by OM, XRD, SEM and TEM measurements. The results showed that Ti-43Al-9V-0.3Y alloy were composed of γ phase, α_2 phase, B_2 phase and YAl_2 phase. The above studies showed that The Ti-44Al-8Nb alloy was not simply melting, and it may react with something else.

Discussion

The microstructure of fibers were researched by TEM, and the result is shown in Fig. 2. Figure 2a, d show two different microstructure of the fibers. The structure which was marked by numbers 1 in Fig. 2a was matrix which is mainly composed of fine dendrite crystal, and its high resolution image is shown in Fig. 2b. The structure which was marked by numbers 2 in Fig. 2d was partial crystal, and its high resolution image in Fig. 2f, which was mainly composed of second phase completely different from RS technique [15]. The dendrites were α_2 (Fig. 2) which were revealed by the selected area diffraction (SAD), and the composition of second phase was not very clear. The microstructure on the lower half of the Fig. 2a far away from the side of the wheel was main composed of α_2 and γ, and it can be found that the phase marked by numbers 2 in Fig. 2 has no dendritic morphology. There is no complete transformation of α phase into α_2 phase through the results of SAD study, as shown in Fig. 2. The aperture part was clearly different from the spot array, which was suspected to be metastable, but the specific composition remained to be studied.

The TEM results from the fiber's microstructure are shown in Fig. 3, on line 1. The EDX display and line scan energy spectrum of the RS Ti-44Al-8Nb alloy were performed (Figs. 4 and 5). The EDX display results revealed that the prepared Ti-44Al-8Nb fibers contain silicon. The line scan energy spectrum results showed that the line 1 distribution of Ti, Nb, B, N, O, and V were homogeneous. The β phase was the stabilizing element, where Ti, Nb, and B were segregated in the β phase during the routine solidification. The solubility of Ti, Nb, B elements in α_2 phase were improved by the RS technique more so than the conventional solidification. The Al and the Si fluctuated up and down significantly. The Al decreased significantly in the middle of line 1, while the Si increased significantly in the middle of line 1. The location of Al was replaced by other elements that reacted with the Si in order to produce a compound. These results suggest that the reaction between the Ti-44Al-8Nb alloy and the quartz tube, as well as the BN crucible occurred.

As shown in Fig. 6, the study of the second phase was performed with TEM. Figure 6a illustrates the distribution and the morphology of the second phase. The HRTEM in Fig. 6d was performed in order to investigate the region signed by the cyan arrow in Fig. 6a. FFT graph of this area is depicted in Fig. 6c. Figure 6b illustrates the amplification of the corresponding region. This phase consisted of stacking faults. This was observed by the HRTEM in Fig. 6d and the diffraction spot in Fig. 6c, where the elongated mans lines were observed by the corresponding FFT result. The crystal structure which is depicted in Fig. 6c could be analyzed by the diffraction spot which in the FFT image. The precipitated second phase was confirmed by the presence of Ti_5Si_3 via the HRTEM and the corresponding FFT result.

The experiment showed that the γ phase and the fine α_2 phase were the main phases of the RS Ti-44Al-8Nb fiber, which was markedly different from the main

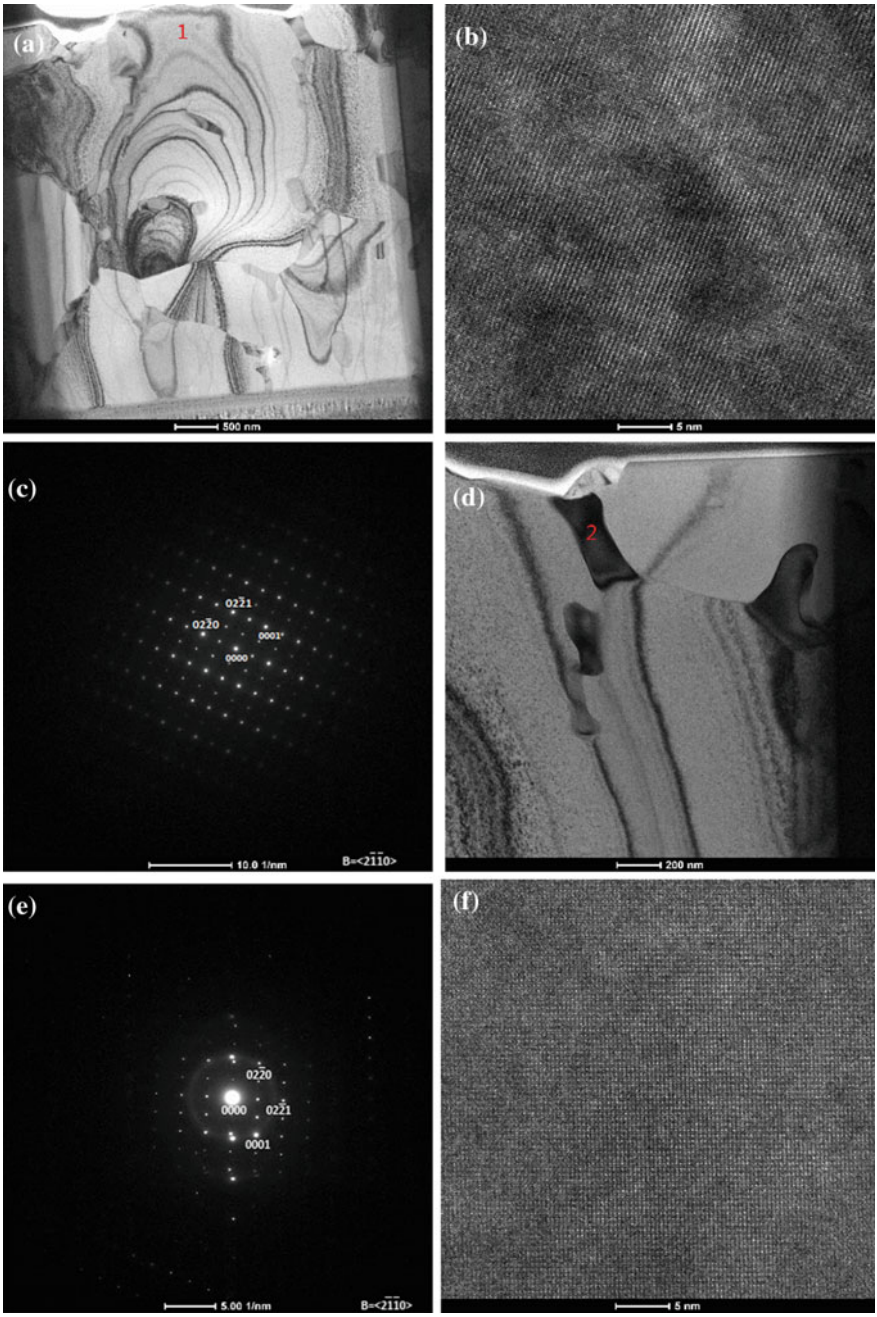

Fig. 2 TEM micrograph of fiber section. **a**, **d**, **f** TEM image of the bright field, **c**, **e** constituency diffraction pattern in **a**, **d** signed by numbers 1, 2. **b**, **f** high resolution image of corresponding position

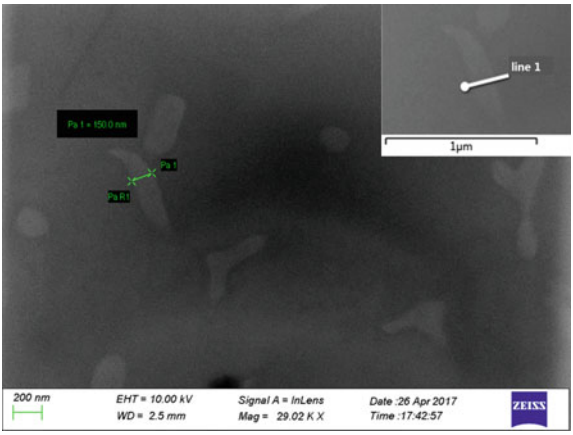

Fig. 3 Cross-sectional TEM micrographs of the fiber

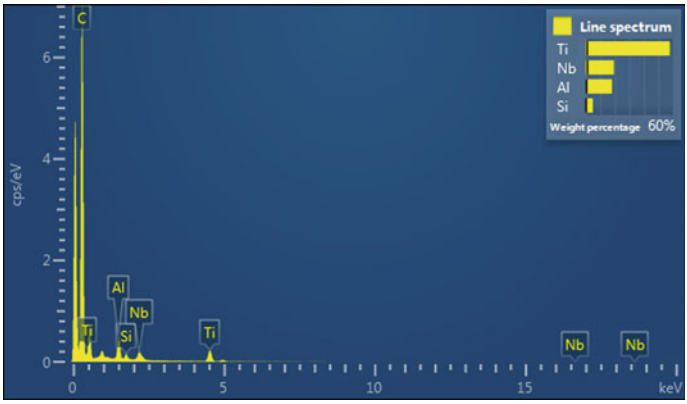

Fig. 4 Acquire EDX display

phase of the β solidification alloy obtained with conventional casting [16]. When the wheel speed was increased to 30 m/s, the matrix changed from the γ phase to the α_2 phase [15]. The cooling rate of the melt extraction technique was faster than the single roll melt spinning technology, suggesting that the β phase was absent in the microstructure of the Ti-44Al-8Nb wires. It is possible that α phase could nucleate as the primary phase, once the rotation speed reached 2600 r/min.

The preparation process of the melt drawn fibers was not sustainable. The above analysis showed that the Ti-44Al-8Nb alloy was obtained during the induction heating process. As shown in Fig. 7, the copper wheel's speed reached 1600 r/min, causing the alloy to react with the BN crucible and the quartz tube wall. The reaction led to the collapse of the molten liquid surface and could not result in the

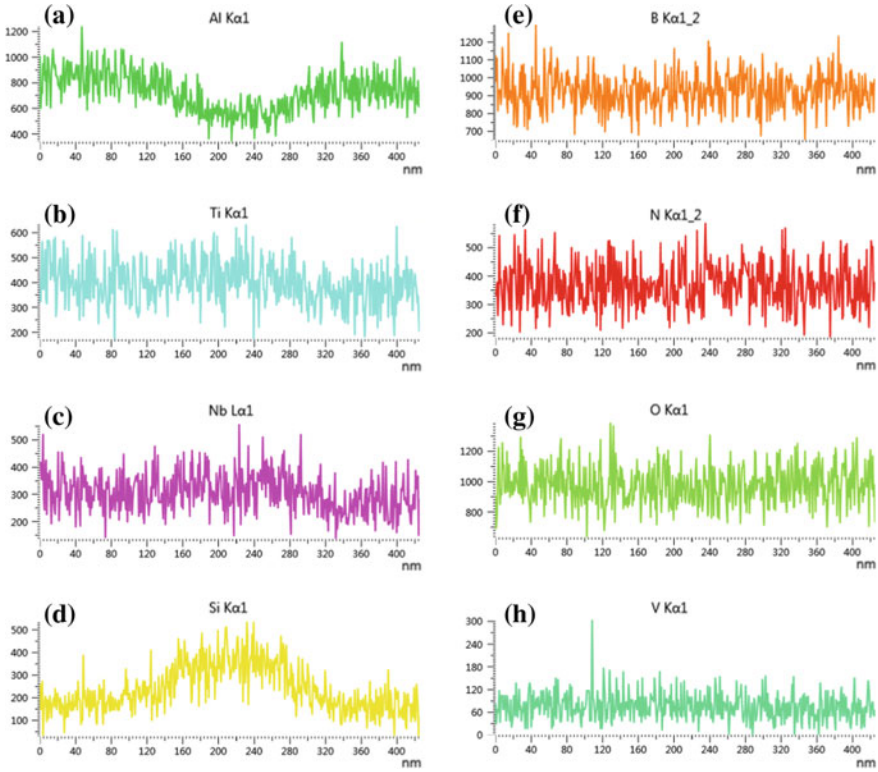

Fig. 5 Line scan energy spectrum of RS Ti-44Al-8Nb alloy: **a** Al-Kα; **b** Ti-Kα; **c** Nb-Kα; **d** Si-Kα; **e** B-Kα; **f** N-Kα; **g** O-Kα; **h** V-Kα

continuously prepared fiber. Chen et al. [17] investigated the joining of the SiO_{2f}/SiO_2 composite with TC_4, Ti_3Al, TiAl, Titanium, and silica via the following reaction:

$$Ti + SiO_2 \rightarrow Ti_2O + Si \tag{1}$$

$$Ti + Si \rightarrow TiSi \tag{2}$$

Yang et al. [18] studied the interfacial microstructure of the BN doped metal brazed Ti/SiO_2-BN joints. The following chemical reactions could happen at the brazing temperature.

$$3Ti + 2BN = TiB_2 + 2TiN \tag{3}$$

$$2Ti + BN = TiB + TiN \tag{4}$$

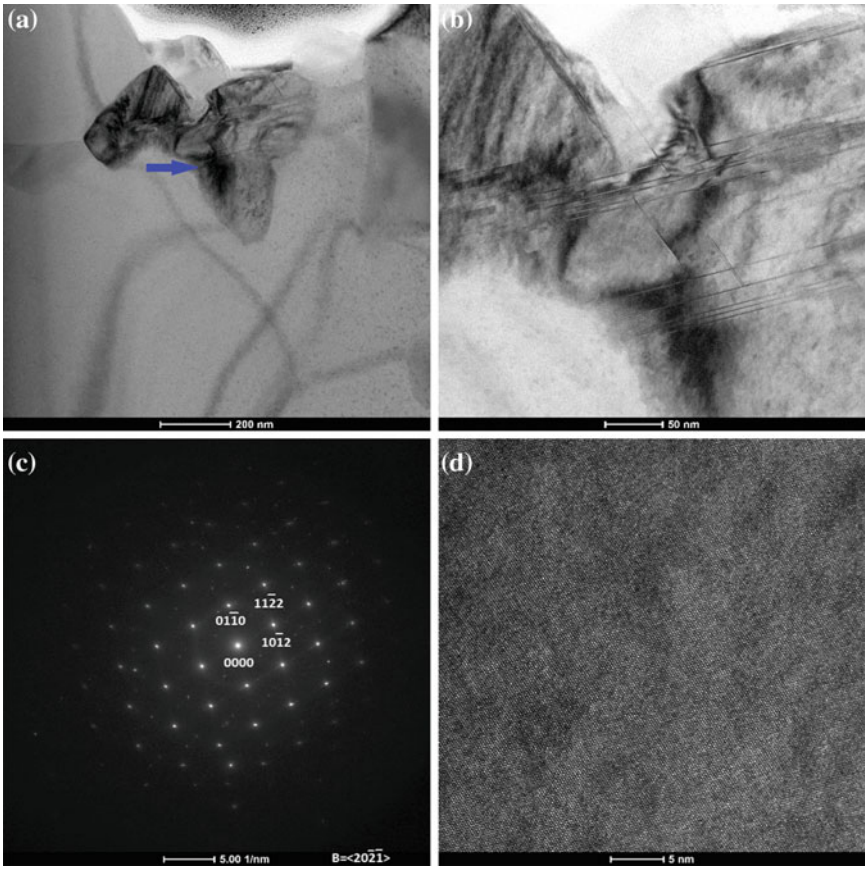

Fig. 6 TEM micrograms of second phases: **a**, **b** TEM image of the bright field; **c**, **d** FFT and the HRTEM of the region signed by the cyan arrow in **a**

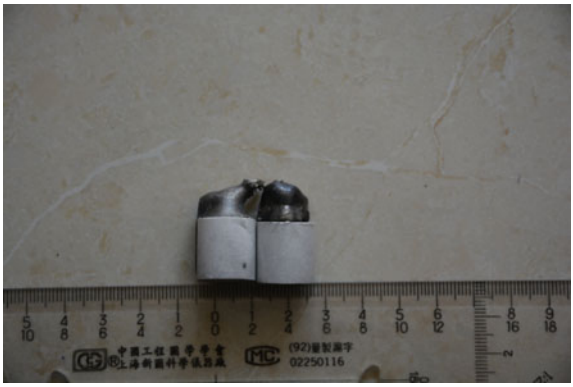

Fig. 7 Reaction of the crucible and Ti-44Al-8Nb alloy

$$Ti + TiB_2 = 2TiB \tag{5}$$

Li et al. [19] investigated the influence of the SiO_2 coating on the high temperature oxidation resistance of a TiAl based alloy. The following reactions occur at 1000 °C heat treatment process:

$$O_2 + TiAl + SiO_2 \rightarrow Al_2O_3 + Ti_5Si_3 + TiSi_2 \tag{6}$$

The crucible reacted with raw material during the Ti-44Al-8Nb fibers preparation. The black part was the reaction of the BN crucible and the TiAlNb after the induction heating lead to the preparation of the melt drawn fiber that was not sustainable. The reaction that released the heat also limited the fiber preparation process of the solidification cooling rate. The energy spectrum analysis found a certain amount of Si in the tissue that bound to the Ti to form the Ti_5Si_3 phase. The experimental alloy and crucible formed a quartz tube reaction that led to the short formed fiber. This is the main reason that mass production can not be achieved.

Conclusions

The RS Ti-44Al-8Nb fibers were prepared by the melt extraction technique. The characteristic of fiber surface were inhomogeneous when the rotation speed was 2000 r/min. As the rotation speed up to 2600 r/min, the fibers became a ribbon shape. The XRD and the TEM analysis revealed that the structure was principally composed of the γ phase, the fine α_2 phase, the fine dendritic crystal, the second phase. And the second phase was confirmed as Ti_5Si_3. The results showed that the Ti-44Al-8Nb alloy underwent a chemical reaction during the induction heating and the melting process. The alloy reacted with the BN crucible and the quartz tube wall, which resulted in the collapse of the molten liquid surface, where it could not be continuously prepared. This limited the rate of solidification cooling during the fiber preparation. The energy spectrum analysis revealed that a certain amount of the Si was present in the tissue, where it bound to the Ti to form the Ti_5Si_3 phase. The reaction of the alloy with the crucible and the quartz tube was the key to the preparation of the TiAl-based fibers. The results from this study provided the experimental basis for subsequent process improvement.

References

1. H. Peng, C.K. Hong, R.Y. Jie, Solidification microstructure characteristics of Ti–44Al–4Nb–2Cr–0.1B alloy under various cooling rates during mushy zone. J Rare Metals **35**, 35–41 (2016)
2. Q. Li, Z.W. Chen, Q. Luo, Experimental investigation and thermodynamic calculation of the Al-rich corner in the ternary Al-Ti-V system. J. Mat. Design **115**, 339–347 (2017)
3. Z.C. Xie, T.H. Gao, X.T. Guo et al., Evolution of icosahedral clusters during the rapid solidification of liquid TiAl alloy. J. Physica B: Condens. Matter. **440**, 130–137 (2014)
4. S. Bolz, M. Oehring, J. Lindemann et al., Microstructure and mechanical properties of a forged β-solidifying γ TiAl alloy in different heat treatment conditions. J. Intermetallics **58**, 71–83 (2015)
5. R.M. Imayev, V.M. Imayev, M. Oehring et al., Alloy design concepts for refined gamma titanium aluminide based alloys. J. Intermetallics. **15**, 451–460 (2007)
6. F.C. Ma, S.Y. Lu, P. Liu et al., Microstructure and mechanical properties variation of TiB/Ti matrix composite by thermo-mechanical processing in beta phase field. J. J. Alloys Compd. **695**, 1515–1522 (2017)
7. H.Z. Niu, Y.F. Chen, Y.S. Zhang et al., Phase transformation and dynamic recrystallization behavior of a β-solidifying γ-TiAl alloy and its wrought microstructure control. J. Mat. Design **90**, 196–203 (2016)
8. J. Zhu, J.B. Chen, T. Liu et al., High strength Mg94Zn2.4Y3.6 alloy with long period stacking ordered structure prepared by near-rapid solidification technology. J Mat. Sci. Eng. A. **679**, 476–483 (2017)
9. Z.G. Liu, L.H. Chai, Y.Y. Chen, Effect of cooling rate and Y element on the microstructure of rapidly solidified TiAl alloys. J. J. Alloys Compd. **504**, 491–495 (2010)
10. H.W. Wang, D.D. Zhu, C.M. Zou et al., Microstructure and nanohardness of Ti-48%Al alloy prepared by rapid solidification under different cooling rates. J. Trans. Nonferrous Met. Soc. China. **21**, 328–332 (2011)
11. Y.Y. Chen, B.H. Li, F.T. Kong, Microstructural refinement and mechanical properties of Y-bearing TiAl alloys. J. J. Alloys Compd. **457**, 265–269 (2008)
12. S.Z. Zhang, S.L. Zhang, Y.F. Chen et al., Microstructural characterization of melt extracted high-Nb-containing TiAl-based fiber. J. Materials. **10**, 195–203 (2017)
13. L.H. Chai., Effect of rare earth yttrium on microstructure of rapidly solidified titanium aluminum based alloys, in D. Harbin. School of materials science and engineering (Harbin institute of technology, 2006)
14. F.T. Kong, Y.Y. Chen, J. Tian et al., Effect of yttrium on microstructure and mechanical properties of Ti-43Al-9V alloy. J. Chin. J. Rare Met. **28**, 75–77 (2004)
15. D.D. Zhu, D. Duo, C.Y. Ni et al., Effect of wheel speed on the microstructure and nanohardness of rapidly solidified Ti–48Al–2Cr alloy. J. Mat. Charact. **99**, 243–247 (2015)
16. J.C. Han, S.L. Xiao, J. Tian et al., Grain refinement by trace TiB2 addition in conventional cast TiAl-based alloy. J. Mat. Charact. **106**, 112–122 (2015)
17. B. Chen, H.P. Xiong, W. Mao et al., Joining of SiO_{2f}/SiO_2 composite to TC4, Ti_3Al and TiAl. J. Mat. Eng. **2**, 41–44 (2012)
18. Z.W. Yang, L.X. Zhang, W. Ren et al., Interfacial microstructure and strengthening mechanism of BN-doped metal brazed Ti/SiO2-BN joints. J. J. Eur. Ceram. Soc. **33**, 759–768 (2013)
19. Z.L. Li, W. Liang, S.J. Teng et al., Effect of SiO_2 coating on high temperature oxidation resistance of TiAl-based alloy. J. Trans. Mat. Heat Treat. **29**, 124–128 (2008)

Microstructure and Microhardness of a Laser Additive Forming Repaired Steam Turbine Blade

Xiangdong Zhang, Tianwei Liu, Shugang Wang and Chi Jiang

Abstract The laser additive forming repair (LAFR) of a damaged turbine blade with pre-fabricated defects was carried out. The parameters were as follows: the laser power 800 W, the laser beam diameter 3 mm, the laser beam moving speed 6 mm/s, the 17-4PH powder feeding speed 0.4 L/min. The microstructure and the microhardness were examined along the positions from the 2Cr13 matrix to the 17-4PH LAFRed zone top. The results showed that the pre-fabricated defects were repaired successfully. Three distinguished zones can be recognized, i.e., the column grain zone, the heat affected zone (HAZ), and the 2Cr13 martensite matrix. Optical microscopy and scanning electron microscopy analysis indicated that the LAFRed zone was free of pores and contained very fine martensite variants. The microhardness test results showed that the 2Cr13 matrix possessed the minimum microhardness of about 320 HV. The microhardness profile showed an oscillation feature with the peak value of 440 HV, which is believed to be the result of microstructure modification induced by the cyclic heat input during the LAFR processing. This study confirmed that 17-4PH is a promising material for the laser additive forming repairing of the damaged 2Cr13 steam turbine blade.

Keywords Laser additive forming repairing · 2Cr13 turbine blade 17-4PH · Microstructure · Microhardness

X. Zhang (✉) · T. Liu · S. Wang · C. Jiang
Institute of Materials, China Academy of Engineering Physics,
P. O. BOX No. 9-4 huafengxincun, Jiangyou 621908, Sichuan, China
e-mail: zhangxiangdong@caep.cn

T. Liu
e-mail: liutianwei@caep.cn

S. Wang
e-mail: wsh7470@163.com

C. Jiang
e-mail: jiangchi@caep.cn

© Springer Nature Singapore Pte Ltd. 2018

Y. Han (ed.), *Advances in Materials Processing*, Lecture Notes in Mechanical Engineering, https://doi.org/10.1007/978-981-13-0107-0_36

Introduction

2Cr13 steam turbine blades, as the key components of power generators, are often facing severe steam and sand erosion, which can result in their final failure. Normally, the power plant has to stop the problematic turbines and replace the damaged blades with good ones, which is recognized time and cost consuming. Laser additive forming repair (LAFR) can efficiently repair the specific damage zones of the damaged turbine blades. For example, Lin et al. investigated the microstructure and mechanical properties of laser forming repaired 17-4PH stainless steel. They found that the comprehensive mechanical properties of the repaired17-4PH stainless steel were equivalent with those of the wrought [1]. Yao et al. performed laser surface alloying and laser solution strengthening on the local region of inset edge for 2Cr13 and 17-4PH stream turbine blades [2, 3]. They confirmed that the laser surface modification techniques are safe and reliable in significantly improving the life of the blades. Wilson et al. succeeded in repairing the defect in two blades with high geometry accuracy on a semi-automated geometric reconstruction algorithm and a laser direct deposition process [4].

Through choosing the proper material, renovation of the damaged blades and improvement of their performance can be achieved. In our study, we chose the 17-4PH martensite stainless steel, which is believed of better erosion resistance, to carry out the repair work. We investigated the microstructure and microhardness of the 2Cr13 matrix and the 17-4PH LAFRed zone.

Materials and Methods

The chemical compositions of 17-4PH and 2Cr13 are listed in Table 1.

The equipment used to perform the laser additive forming repairing is a RRW60-1 type machine. This machine is equipped with a Laserline 3 kW diode laser source, an inferred pyrometer, a coaxial powder nozzle, a six-axis Fanuc robot and an integrated working interface controlling all above parts. The parameters of LAFR processing were as follows: the laser output power 800 W, the laser beam diameter 3 mm, the scanning speed 6 mm/s, the powder feeding speed 0.4 L/min. The LAFR process was carried out in argon protection. Figure 1 gives the illustration of the LAFR of the turbine blade.

The samples of the LAFRed zone and the matrix were sectioned from the blade to study their microstructure and properties. The etch solution used to reveal the

Table 1 Chemical compositions (wt%) of 2Cr13 and 17-4PH stainless steel powder

	C	Cr	Mn	Si	Ni	Cu	Nb	Fe
2Cr13	0.16–0.21	12–14	<0.8	<0.6	/	/	/	Balance
17-4PH	0.04	16.5	0.7	/	4.5	3.3	0.3	Balance

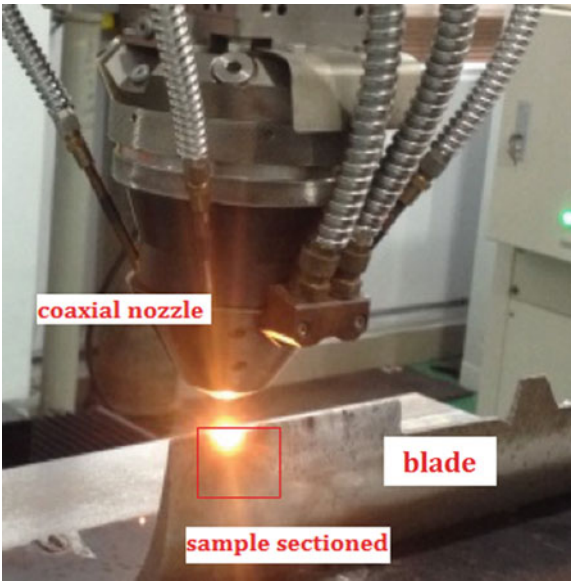

Fig. 1 Illustration of the LAFR process

microstructure consists of 1 g picric acid, 5 ml HCl and ethanol 100 ml. An OLYMBUS GX71 optical microscopy (OM) and an FEI SIRION 200 scanning microscopy (SEM) equipped with a field emission electron gun and an EDAX-TSL electron back scattering diffraction (EBSD) system were used to examine the microstructure in the LAFRed zone and the matrix. The phases were achieved by using a TD-3500 X-ray diffractometer (XRD) equipped with a Cu target. Microhardness profile along the matrix to the LAFRed zone top was obtained by using an HXD-1000TMC type Vicker's hardness tester with the load of 200 g and the dwell time of 15 s.

Results and Discussion

Figure 2 gives the XRD patterns recorded from the matrix and the repaired zone. The results indicated that the 2Cr13 matrix contains only three peaks attributed to the BCC iron solid solution phase, or specifically the martensite phase. Different from that of the matrix, the XRD trace of the LAFRed zone showed two sets of peaks belonging to the FCC iron solid solution and the BCC iron solid solution, respectively. The BCC phase is recognized as the martensite phase and the FCC phase is corresponding to the retain γ phase [5–7]. In fact, there lie arguments in identification of this FCC phase. Most researchers identify this FCC phase as γ iron solid solution retained from cooling. However, some researchers index this peak as the copper phase [8]. In our research, we find it reasonable to index this FCC phase as the retained γ iron phase, even though we cannot identify this FCC phase in

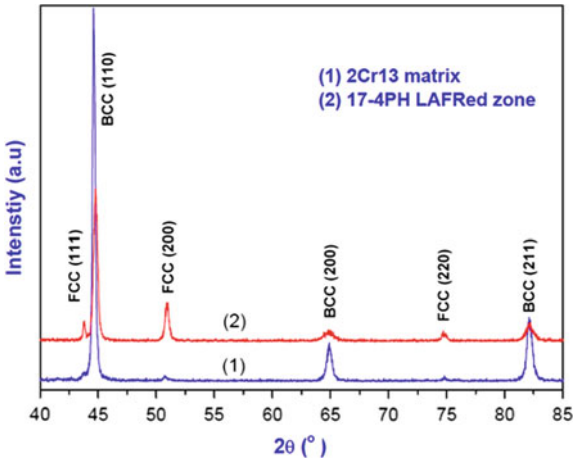

Fig. 2 XRD patterns of the 2Cr13 matrix and the LAFRed 17-4PH zone

Fig. 3 Panorama view of the microstructure along the matrix to the LAFRed zone top

EBSD mapping (see Fig. 4d). Because if it is the precipitated nano copper phase, a broadening of the XRD peaks must be clearly seen, which is not the case in the present study.

Figure 3 gives an OM image showing the panorama of the microstructure along the matrix to the LAFRed zone top. On the right end is the 2Cr13 matrix, one the left end is the LAFRed zone top. These two zones are separated by a curved line (arrowed). We can see that the LAFRed zone is free of pores and contains long column grains with fine martensite laths inside. The column arms become coarser when they are close to the LAFRed top. This is because the accumulative layer deposition of 17-4PH leading to the decreasing of the temperature gradient and the repeat tempering of the already deposited layers.

Figure 4a–c gives SEM pictures of the microstructure of the matrix, the HAZ and the LAFRed zone. Figure 4d is the EBSD inverse pole figure (IPF) map (the inset gives the color-orientation legend) showing the fine martensite laths in the LAFRed column grains. The dark lines in Fig. 4d represent the 60° grain boundaries. The microstructure of the 2Cr13 matrix (Fig. 4a) showed a typical lath martensite feature that contained in the relatively large prior-γ phase grains.

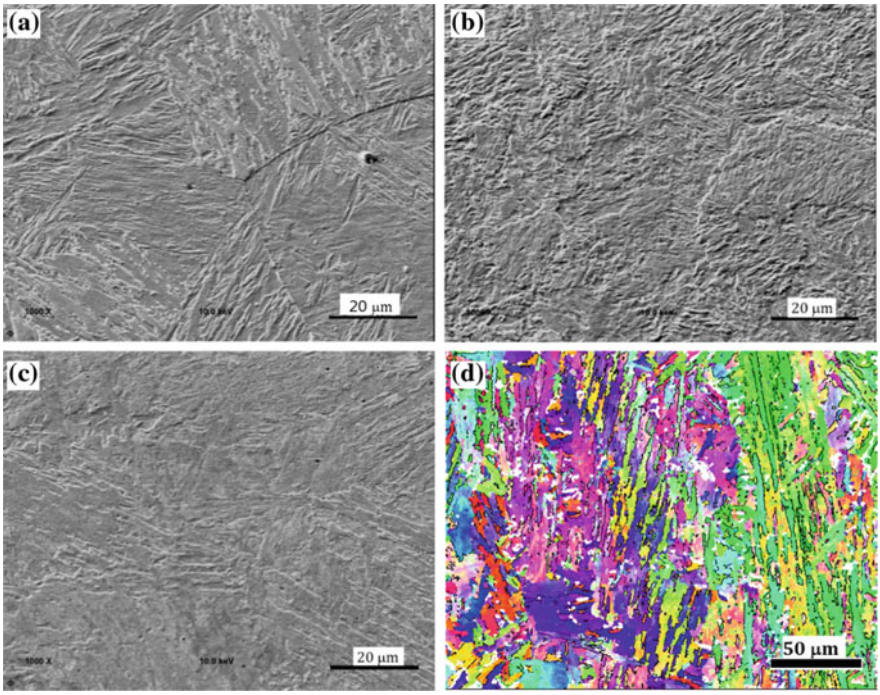

Fig. 4 SEM images showing detailed microstructure of the different zones, **a** matrix; **b** HAZ; **c** LAFRed zone; **d** EBSD inverse pole figure (IPF) map of the LAFRed zone

Figure 4b possessed a similar feature with that of Fig. 4a, however, the lath width and the size of the prior-γ phase grains were relatively smaller. This may be because the HAZ was heated to the γ phase zone and then rapidly cooled down to room temperature when the first several layers were deposited. During the process, the turbine blade is acting as a heat reservoir that conducted the heat quickly. The fast heating and cooling process led to the rapid γ to martensite phase transformation and inhibited the martensite laths from growing larger and wider. In Fig. 4c, d, the martensite laths in column grains can be witnessed. These martensite laths are wider than that of the matrix and the HAZ. This can be attributed to the tempering generated by the repeat layer deposition, which resulted in the growth of martensite laths in the LAFRed zone.

Figure 5 presents the microhardness results taken along 2Cr13 matrix to the repaired zone top. The microhardness of the 2Cr13 matrix is about 320 HV. The microhardness peaks at the HAZ with the microhardness value of about 440 HV. The microhardness of the LAFRed zone is generally higher than that of the 2Cr13 matrix. However, the microhardness profile of the LAFRed zone showed an oscillation feature. From the HAZ to the LAFRed zone top, the microhardness variation reached about 90 HV. As can be seen in Fig. 3, the column grains become larger when reaching the LAFRed zone top, which is due to the decreasing of the

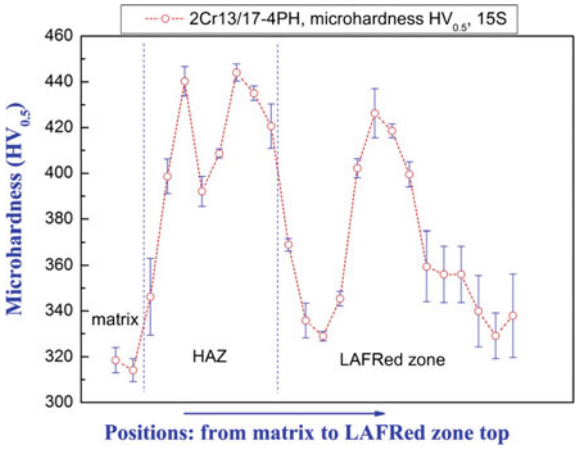

Fig. 5 Microhardness of different positions along the matrix to LAFRed zone top

temperature gradient with the progressive increment of the deposited layers. However, the repeat tempering induced by the accumulative layer deposition can favor the precipitation of nano copper particles and/or carbides. This is why the microhardness of the repaired zone is generally higher than that of the matrix. The peculiarly low microhardness in the LAFRed zone may be corresponding to the ferrite phase or without strengthening particle precipitation [1]. The highest hardness value achieved at the HAZ means that a better metallurgical combination of two materials obtained by laser additive forming repairing. Due to the higher erosion resistance of the 17-4PH stainless steel, better performance of the LAFRed steam turbine blade is expected.

Conclusions

A laser additive forming repairing of a 2Cr13 turbine blade with prefabricated defects by using the 17-4PH martensite stainless steel powders has carried out in this study. It demonstrates that LAFR technique is quite promising in repairing the defects of the 2Cr13 turbine blades. The conclusions are as follows:

(1) Along the matrix to the LAFRed top, three different zones can be seen: the matrix, HAZ and the 17-4PH column grain zone.
(2) The microstructure in the matrix is lath martensite confined in the equiaxed prior-γ grains. The microstructure in the HAZ is similar with that of the matrix; only the lath martensite variants are much smaller than that of the matrix. The LAFRed zone consists of column grains with very fine lath/needle martensite.
(3) The microhardness results show an oscillation feature with the highest hardness achieved in the HAZ zone. The LAFRed zone obtains a little bit lower hardness than that of the HAZ, which is still higher than that of the matrix. Due to the

higher erosion resistance of the 17-4PH steel, better performance of the LAFRed steam turbine blade can be expected. Further property study such as the tensile tests and the erosion resistance tests will be carried out later.

Acknowledgements This work was financially supported by the National Natural Science Foundation of China (No. 51401188).

References

1. X. Lin, Y. Cao, X. Wu, H. Yang, J. Chen, W. Huang, Microstructure and mechanical properties of laser forming repaired 17-4PH stainless steel. Mater. Sci. Eng. A **553**, 80–88 (2012)
2. J. Yao, L. Wang, Q. Zhang, F. Kong, C. Lou, Z. Chen, Surface laser alloying of 17-4PH stainless steel steam turbine blades. Opt. Laser Technol. **40**(6), 838–843 (2008)
3. J. Yao, Q. Zhang, F. Kong, Q. Ding, Laser hardening techniques on steam turbine blade and application. Phys. Procedia **5**, 399–406 (2010)
4. J.M. Wilson, C. Piya, Y.C. Shin, F. Zhao, K. Ramani, Remanufacturing of turbine blades by laser direct deposition with its energy and environmental impact analysis. J. Clean. Prod. **80**, 170–178 (2014)
5. Z. Hu, H. Zhu, H. Zhang, X. Zeng, Experimental investigation on selective laser melting of 17-4PH stainless steel. Opt. Laser Technol. **87**, 17–25 (2017)
6. H. Dong, M. Esfandiari, X.Y. Li, On the microstructure and phase identification of plasma nitrided 17-4PH precipitation hardening stainless steel. Surf. Coat. Technol. **202**(13), 2969–2975 (2008)
7. Z. Wang, W. Luan, J. Huang, C. Jiang, XRD investigation of microstructure strengthening mechanism of shot peening on laser hardened 17-4PH. Mater. Sci. Eng. A **528**(21), 6417–6425 (2011)
8. J. Wang, H. Zou, C. Li, R. Zuo, S. Qiu, B. Shen, Relationship of microstructure transformation and hardening behavior of type 17-4 PH stainless steel. J. Univ. Sci. Technol. Beijing Miner. Metall. Mater. **13**(3), 235–239 (2006)

Regeneration Technology of Coated Sand for Selective Laser Sintering

Rui Pan, Bingrong Zhang and Jianxiang Liu

Abstract With the rapid development of 3D printing technology, the requirement of coated sand for Selective Laser Sintering (SLS) is becoming higher in terms of performance and volume. As a molding material with higher performance requirement and much more expensive than common shell molding sand, the emissions of one-time used SLS coated sand could lead to not only environmental pollution but also waste of resources. In this paper, the regeneration processes of coated sand for SLS was studied to discover the best parameters for the regeneration technology. Subsequently, the regenerated sand was coated. The samples for tensile strength and bending strength testing were sintered using HRPS-VI SLS equipment. Afterwards, the original sand for SLS and the regenerated sand was analyzed and compared in terms of sand microstructure, tensile strength, bending strength and cauterant decrease are analyzed and compared between original SLS sand and generated sand. The primary results show that: The morphology of regenerated sand is approximately close to spherical; the tensile strength and bending strength of the samples sintered using SLS coated regenerated sand are almost the same of the original SLS coated sand.

Keywords Selective laser sintering · Old sand regeneration · Tensile strength

R. Pan · B. Zhang (✉)
School of Mechanical & Automotive Engineering, Qilu University of Technology, Jinan 250353, China
e-mail: brzit@aliyun.com

R. Pan
e-mail: 314649114@qq.com

B. Zhang · J. Liu
Shandong Tailai Aluminum Foundry Tech. Co. Ltd., Laiwu 271100, China
e-mail: 287791205@qq.com

© Springer Nature Singapore Pte Ltd. 2018

Y. Han (ed.), *Advances in Materials Processing*, Lecture Notes in Mechanical Engineering, https://doi.org/10.1007/978-981-13-0107-0_37

Introduction

SLS (Selective Laser Sintering) is a new technology in which the designed products are formed layer by layer throughout the selective laser beam. It is sufficient to position the 3D model of the designed product into the rapid prototyping system (SLS equipment), without the use of any traditional tooling. After the slicing processing of the 3D model, powder material is sintered together by the laser beam and the products are shaped layer by layer. SLS technology is used more and more widely in automotive, aerospace and other advanced manufacturing fields, because of the outstanding advantages such as high accuracy, short cycle and no product shape limitation [1–3]. There is also a good potential for industrial application in the production of iron and steel and non-ferrous alloy castings [4].

The pearl sand, which is the raw material for SLS process, is expensive. The release of lots of molding material after pouring and cleaning of castings, not only leads to waste of resources, but also environment pollution [5, 6]. Therefore, the study on the regeneration of SLS coated sand will help to, on one hand, avoid the environment pollution, on the other hand, bring greater economic benefits, such as reduced cost and resource optimization.

The United States began to study the regeneration technology of coated sand in 1912. The study conducted by Chongqing Changjiang Molding Material Company is mainly on old sand roasting regeneration processes. Although a lot of researches about old sand recycling have been conducted both domestically and abroad, these works were only on the regeneration of resin sand, water glass sand and clay sand [7–11]. Few studies were found on the research on the regeneration of SLS coated sand because it has been applied for 3D printing only in recent years. Therefore, the study on the SLS coated sand regeneration process could bring new insights in the field.

Experimental Materials

Five types of materials were used in this study: pearl sand (70/140), phenolic resin, urotropin, coupling agent and calcium stearate. The screening results of pearl sand were given in Table 1.

Experimental Produces

Raw Material

Firstly, the raw sand was added to the heater through an elevator. After having been heated to a certain temperature, the hot sand was put into a sand mixer. The pre-designed ratio phenolic resin was mixed with the hot sand for 20 s. Reached to the resin softening point, phenolic resin began to soften gradually and clad the pearl

Table 1 Granularity distribution of pearl sand

Screen size	Weight on the screen (g)	(%)
40	0.0080	0.02
50	1.7905	3.60
70	9.2020	18.46
100	14.3555	28.80
140	18.5120	37.14
200	5.5530	11.14
270	0.3265	0.66
Chassis	0.0918	0.18
Total	49.8393	100
Granularity	70/140	

Table 2 Preparation process of SLS coated sand

Preparation process	Parameter	Note
Resin content	3.2 (%)	Weight percent of raw sand
The temperature of adding resin	150 (°C)	
Mixing time after adding resin	20 (s)	
Coupling agent content	6.0 (%)	Weight percent of resin
Mixing time after adding coupling agent	50 (s)	
Urotropin content	13 (%)	Weight percent of resin
The temperature of adding urotropin	110 (°C)	
Mixing time after adding urotropin	38 (s)	
Calcium stearate content	3 (%)	Weight percent of resin

sand. Afterwards, the urotropin and coupling agent were added in turn. Hot sand cooled rapidly with the addition of the urotropin, and became bulk mixture. It was broken up under the stirring mixer and had a good fluidity with the calcium stearate being added. After crushing and screening in a vibration cooling screening, the SLS coated sand was obtained. The amount of raw materials and process parameters are shown in Table 2.

Old Sand Regeneration

The coated sand was prepared according to the process described in 2.1 and sintered to sand core with SLS technology. Then the mold prepared with printed core was poured in the foundry. The used sand (mold and cores) were collected and crushed mechanically.

High temperature roasting was carried out after screening and magnetic separation. Roasting temperature and roasting time are two main factors that affect the

Table 3 Experiment scheme

Order number	Roasting temperature (°C)	Roasting time (h)
1	550	0.5
2	550	1.0
3	550	1.5
4	600	0.5
5	600	1.0
6	600	1.5
7	650	0.5
8	650	1.0
9	650	1.5

performance of reclaimed sand. If the roasting temperature is too high, the energy consumption will be larger. In contrast, if the roasting temperature is too low, the residual phenolic resin and other impurities will still be mixed within the sand grains. Hence, the experiment has been conducted with the combination of three different temperatures: 550, 600 and 650 °C and three roasting times: 0.5, 1.0 and 1.5 h. Experiments were designed as shown in Table 3.

Under the different roasting processes, the SLS coated sand of the same weight were roasted. The microscopic morphology of reclaimed sand was observed, and it was found that when roasted at 650 °C for 1.0 h, the resin on the sand has been burned cleanly.

Reclaimed Sand Coated

Reclaimed sand was coated. The preparation process parameters were the same as those of the raw sand preparation, as shown in Table 2.

Samples Preparation

The SLS reclaimed coated sand and SLS coated sand were sintered in the rapid prototyping system respectively. The laser power was set to 75 W, the scanning speed was 2500 mm/s, the scanning distance was 0.1 mm, and the powder coating thickness was 0.4 mm. Under these circumstances, the tensile strength sample ("8-shaped" block as shown in Fig. 1a) and the bending strength sample ("1-shaped" block as shown in Fig. 1b) were separately sintered. The dimensions and shapes of these samples were shown in Fig. 1.

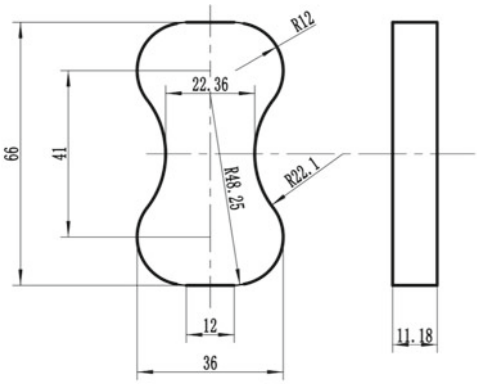

(a) Tensile strength sample ("8" block).

(b) Bending strength sample ("1" block).

Fig. 1 Strength samples. **a** Tensile strength sample ("8" block), **b** bending strength sample ("1" block)

Performance Testing

Strength testing was carried out on SWY-2 digital display hydraulic universal strength tester. Several important steps are summarized as below. The tensile clamp/bending clamp were placed on the instrument. Then the tensile/bending button on the sensor was pressed. The zero button was rotated to make the digital meter showing "000". After that, the tensile sample/bending samples were put into the strength clamp, and the shafts of the strength tester were shaken under a constant speed at room temperature until the sample was broken. Then the numerical value of the digital meter should indicate the tensile/bending strength.

The procedures for cauterant decrease test are described in detail as following. First of all, the magnetic boats were roasted at the temperature of 1000 °C for 30 min. Then they were cooled to room temperature inside a dryer. The fracture surfaces of the strength samples were milled with each other. With a high-accuracy scale, 2 ± 0.001 g powder were weighed into the heated magnetic boat and were heated at 1000–1050 °C in the muffle furnace. Then the magnetic boats were put

into a dryer, let cool to room temperature and then weighed after being heated for 30 min. The cauterant decrease was calculated as follows:

$$D = (W_1 - W_2)/(W_1 - W_0) \times 100\% \quad (1)$$

where D is the cauterant decrease, W_0 is the weight of the empty magnetic boat, W_1 is the weight of the samples before roasted, and W_2 is the weight of the samples after roasted.

Result Analysis

Microstructure

Figure 2a, b show that the typical micro-structure images of raw sand and reclaimed sand respectively. Figure 2c, d show the typical micro-structure images of SLS coated sand and SLS reclaimed coated sand respectively. It can be observed from Fig. 2 that the particles of the reclaimed coated sand were closer to the sphere and their surface was flatter. However, some impurity particles were distributed in the reclaimed sand after multiple treatments. This can be explained from two perspectives. On one hand, when sand was roasted at high-temperature, the crystal water, organic pollutants, oxides of sand particles were burnt clean, so the reclaimed sand had a flatter surface and a smaller angular coefficient. On the other hand, the burnt impurities which emerged in the high temperature roasting process inevitably were dispersed into sand particles, as shown in Fig. 2b.

Performance of the SLS Reclaimed Coated Sand and SLS Coated Sand

Figure 3 shows that the performance of the SLS reclaimed coated sand and SLS coated sand, including room temperature tensile strength, room temperature bending strength and cauterant decrease. Compared with the SLS coated sand, SLS reclaimed coated sand has a slight lower tensile strength and bending strength. However, there is no change in cauterant decrease, which may be resulted from the diffusing effect caused by residual impurity particles after high-temperature roasted. Although the reclaimed sand had a smaller angular coefficient, the presence of impurities made it difficult to bond each together. At the same time, the resin content of SLS coated sand and SLS reclaimed coated sand was the same when they were prepared.

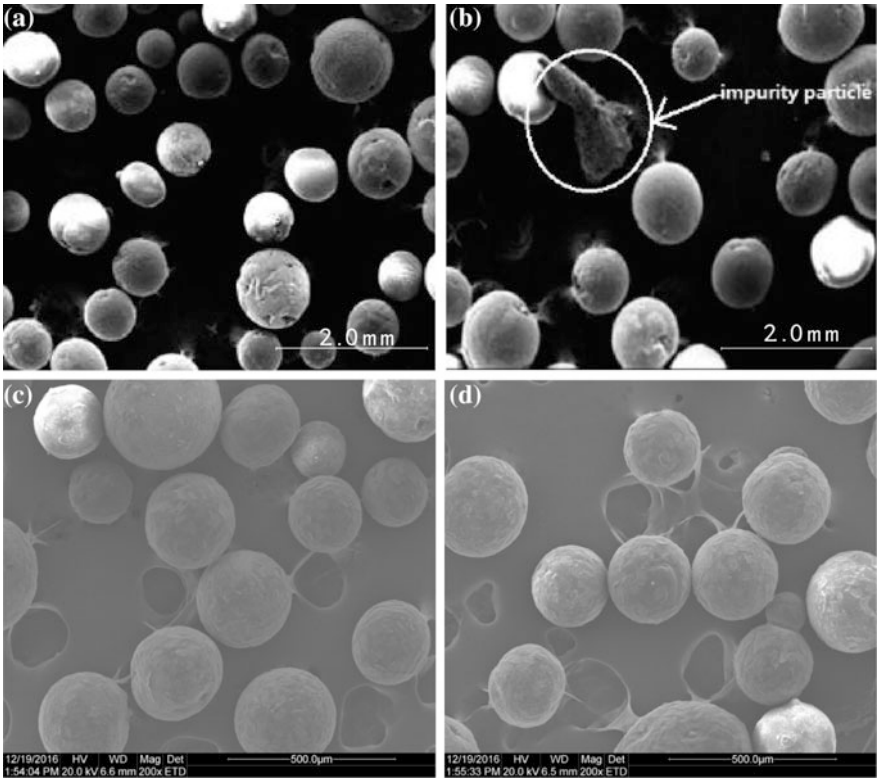

Fig. 2 Microstructure of sand. **a** Pearl sand, **b** reclaimed sand, **c** SLS coated sand, **d** SLS reclaimed coated sand

The Morphology of Fracture Surface

Figure 4a, b show the images of typical fracture surface of SLS coated sand strength specimens and SLS reclaimed coated sand respectively. It can be observed that all fracture surfaces contained fractured resin film, bonding bridge and sand. Many bonding bridges were noticed between adjacent sand. A few impurity particles were also observed from Fig. 4b. In addition, the fractured surface of the resin film depressed obviously. That's because micro-cracks formed on the resin film and sand grain surface, propagated along the sand surface, and eventually leading to the resin film to peel off from the sand surface.

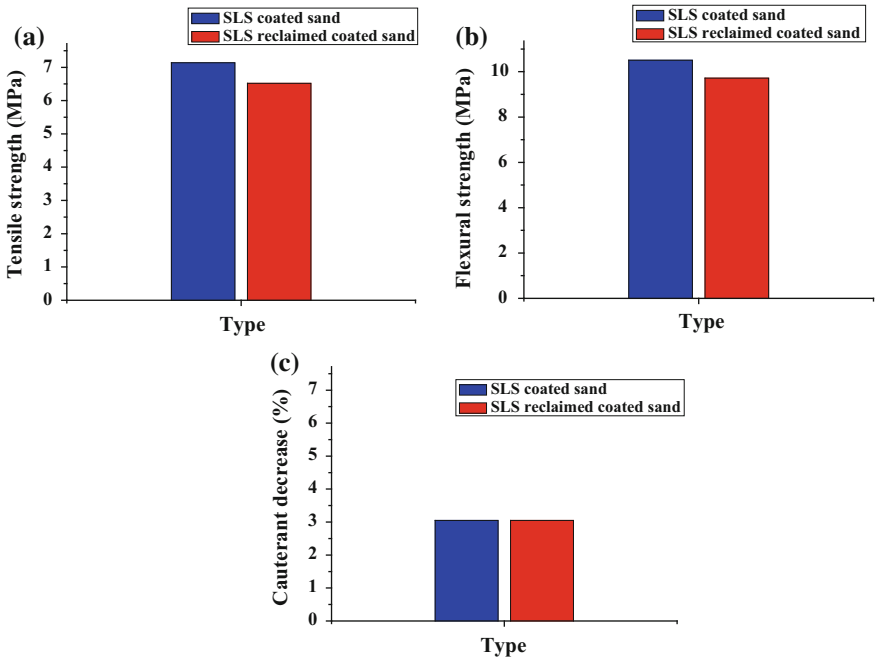

Fig. 3 Performance of coated sand. **a** Tensile strength, **b** bending strength, **c** cauterant decrease

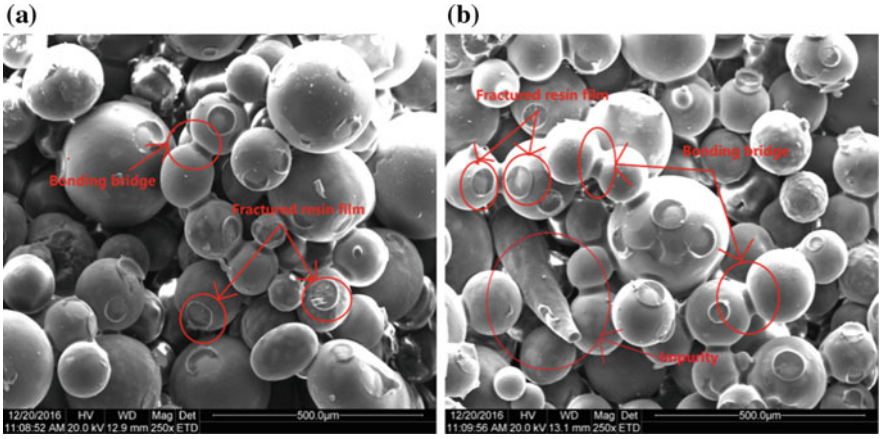

Fig. 4 The morphology of fracture surface. **a** SLS coated sand, **b** SLS reclaimed coated sand

Conclusions

The microstructure, tensile strength, bending strength, cauterant decrease, the morphology of fracture surface and sintering accuracy of the SLS reclaimed sand have been investigated systematically. The main conclusions are as follows:

(1) Through the study of the regeneration process of used coated sand, a suitable regeneration process has been built.
(2) By comparing the properties of the original coated sand for SLS and the reclaimed coated sand, it is observed that the morphology of regenerated sand is more approach to ball shape. The tensile strength and bending strength of two types of coated sand are almost the same.
(3) It is worth to continue the study in order to obtain more precision parameters of the regeneration technology, up to the mass production of regeneration sand.

Acknowledgements This work was financially supported by the major project of Shandong Science and Technology (No. 2015ZDZX03004) and the project of Natural Science Foundation of Shandong Province (No. ZR2016EEM48). The collaboration of the Shandong Tailai Aluminum Foundry Tech. Co. Ltd. is also acknowledged.

References

1. U. Behrendt, M. Shellabear, The EOS rapid prototyping concept. Comput. Ind. **5**, 57–61 (1995)
2. C.M. Cheah, C.W. Lee, C. Feng et al., Rapid prototyping and tooling techniques: a review of applications for rapid investment casting. Int. J. Adv. Manuf. Technol. **25**, 308–320 (2005)
3. Z.F. Xu, P. Liang, W. Yang et al., Effects of laser energy density on forming accuracy and tensile strength of selective laser sintering resin coated sands. China Foundry **11**, 151–156 (2014)
4. G.L. Ding, Q.X. Zhang, Y.H. Zhou, Strengthening of cold-setting resin sand by the additive method. J. Mater. Process. Technol. **72**, 239–242 (1997)
5. J.T. Fox, F.S. Cannon, N.R. Brown et al., Comparison of a new, green foundry binder with conventional foundry binders. Int. J. Adhes. Adhes. **34**, 38–45 (2012)
6. R.M. Lazzarrin, M. Noro, Energy efficiency opportunities in the production process of cast iron foundries: an experience in Italy. Appl. Therm. Eng. **90**, 509–520 (2015)
7. Y. Kurokawa, H. Kambayashi, H. Ota et al., Reclamation mechanism of waste green sand adhered with oolitics. J. Jpn. Foundry Eng. Soc. **71**, 468–474 (1999)
8. M. Stachowicz, K. Granat, Influence of melt temperature on strength parameters of cyclically activated used-up sandmixes containing water-glass, hardened with microwaves. Arch. Civ. Mech. Eng. **15**, 831–835 (2015)
9. N. Guigo, A. Mija, L. Vincent et al., The influence of reclaim on properties of moulding sand with furan resin. Arch. Foundry Eng. **10**, 61–64 (2010)
10. Q.Z. Sun, R.F. Xu, Z.K. Zhao et al., Reclamation of green sand containing hot-box resin sand and its application. Adv. Mater. Res. **21**, 435–438 (2008)
11. N. Cruz, C. Briens, F. Berruti, Green sand reclamation using a fluidized bed with an attrition nozzle. Resour. Conserv. Recycl. **54**, 45–52 (2009)

Technic Study on Polycrystalline Cubic Boron Nitride Tools Dry Cutting Harden GCr15 Based on the Finite Element Analysis and the Orthogonal Experiment

Yunhai Jia, Shaoning Lv and Lixin Zhu

Abstract Polycrystalline cubic boron nitride cutting tools in hard dry precision cutting bearing steel has got more and more widely used, on account of their higher hardness, high wear resistance and high temperature red hardness. It is set as an example that the GCr15 rod is dry hard turned with welded PcBN cutting tools. In the present study, the temperature distribution cloud and equivalent stress distribution nephogram of PcBN tool rake surface were obtained by using the finite element simulation analysis method under different processing parameters. Then reasonable processing parameters of dry hard-turning were obtained by comparison and analysis. Based on orthogonal experiment design, the appropriate parameters such as cutting speed, cutting depth and feed rate were given in taking surface roughness of the workpiece and the tool flank wear as the evaluation indexes. The result of the turning test was as same as that of the finite element analysis, which confirms the validity of the finite element analysis. The experiments and finite element analysis results showed that the equivalent low stress, workpiece ideal surface roughness and the smaller flank wear of cutting tool could be obtained in which the cutting speed was at 200 m/min, the cut depth was 0.20 mm and the feed rate was 0.15 mm/rev. This research provides an important experimental basis for a reasonable formulation of the process of dry turning ball bearing steel.

Keywords Polycrystalline cubic Boron Nitride (PcBN) cutting tools
Dry cutting · Finite element analysis (FEA) · Orthogonal experiment design
Technic study

Y. Jia (✉) · L. Zhu
Beijing Institute of Electro-Machining, Beijing 100191, China
e-mail: jyh308401@sina.com.cn

Y. Jia
Beijing Key Laboratory of Electrical Discharge Machining Technology,
Beijing 100191, China

S. Lv
China University of Mining and Technology (Beijing), Beijing 100083, China

© Springer Nature Singapore Pte Ltd. 2018

Y. Han (ed.), *Advances in Materials Processing*, Lecture Notes in Mechanical Engineering, https://doi.org/10.1007/978-981-13-0107-0_38

Introduction

Polycrystalline cubic boron nitride tool that is one of substitution products of traditional cutting tool has been widely applied on manufacturing industry in developed countries for the past 20 years [1]. Compared to tungsten carbide, the use of PcBN tool has enabled machining speed to be completed, the burr to be virtually eliminated and thread quality to be improved [2]. To utilize PcBN cutting tool makes precision hard dry turning in automotive, bearing industries and super alloys to become a viable process, in which the hardness of the workpiece up to 60–65 HRC [3]. Dry hard cutting has many advantages than grinding or polishing, such as process flexibility, shorter cycle time, higher material removal rate, better surface finish and less environmental problems without the use of turning fluid [4]. Finite element analysis (FEA) and turning experiments have been widely used in order to research the effects of cutting tools angle on the cutting tool stresses and the cutting forces.

There have been many valuable research results about PcBN cutting tool hard-turning. Yen et al. [5], studied the effects of edge preparation of the cutting tool on cutting forces, chip formation, and process variables (temperature, strain and stress) in orthogonal cutting as determined with a finite element method simulation. In Kurt study [6], cutting experiments and have been used in order to investigate the effects of chamfer angle on the cutting tool stress and cutting forces. The tests and finite element analysis results showed that the chamfer angle has a great impact on the tool stress and cutting forces. In literature [7], using PcBN inserts for machining AISI H13 steel, 3-D finite element modeling of precision hard-turning has been used to investigate the effects of cutting edge micro-geometry on tool forces, stresses and temperatures. PcBN inserts with honed micro-geometry cutting edge resulted in lower tool flank wear in all turning conditions. In Uhlmann's research [8], They believe that the deposition of cBN coatings is twice as hard as traditional coatings, such as TiALN, and higher chemical and oxidative stability; Due to its high hardness and high temperature stability, the coating has high processing performance. In literature [3], Numerical simulation of high speed in orthogonal machining was carried out to study the change of feeding, cutting speed, tool geometry and workpiece hardness in the machining process. The feed has the most significant effect on cutting and feed forces among process parameters, workpiece hardness and cutter geometry. In literature [9], the author presents oxidation wear and felt wear was mainly invalidation factors using PcBN tools dry cutting cold-die steel and bearing steel samples. In cutting process, the heated-stability, the granularity of cBN and chemical characteristic of felt material have key function to the tools wear.

In this paper, the orthogonal experiment and the finite element analysis are used to analyze the change of the equivalent stress, the temperature distribution and the deformation of the PcBN tool when it is dry turning GCr15 round rods. The relationship among the cutting parameters, surface quality of the workpiece and the wear of the tool flank are studied, which provides an important experimental basis for the rational formulation of hard cutting bearing steel process.

Experimental Equipments and Method

The GCr15 round rods with dimension 60 mm diameter and 300 mm long has been selected as the workpiece. It's material composition is shown in Table 1. The mechanical and physical properties of the GCr15 are listed in Table 2. BZN 8200 produced by DI Corporation, that's physical properties are presented in Table 3 has been selected as PcBN cutting tools. The cutting tool geometry parameters are given in Table 4. Cutting tests have been done on the CK6140 lathe. During the cutting process, the tool flank wear rate at one time is measured using a universal tool microscope 19JPC-V at intervals. The surface roughness of the workpiece and the surface roughness of the flank are measured by the surface roughness tester TR240. After ten minute continuous turning, the wear morphology and local chemical composition of the front and back of the tool are analyzed by S-4800 scanning electron microscope (SEM) and energy spectrum analyzer.

Surface roughness is the fundamental quality index of machining surface. The formation of a rough surface is a complex mechanism involving many parameters. The quality (roughness or size) of the workpiece is greatly influenced by cutting conditions, such as tool material, workpiece material, tool geometry, tool wear and machining process.

The relationships between the cutting parameters and workpiece surface quality have been analyzed by orthogonal experimental design. The corresponding measured values of the surface roughness generated after the machining operations and the combinations of the factors at their different levels are shown in Table 5.

Table 1 Workpiece material composition (Φ60 × 300 mm) (%)

Workpiece material	C	Cr	Mn	Si	P	Mo	S
GCr15	0.95–1.05	1.40–1.65	0.25–0.45	0.15–0.35	≤ 0.025	≤ 0.10	≤ 0.025

Table 2 Mechanical and physical properties of the GCr15

Density (g/cm^3)	Melting point (°C)	Specific heat capacity (J/kg °C)	Thermal conductivity (W/mK)	Poisson's ratio	Fracture toughness (MPa $m^{1/2}$)	Elastic modulus (GPa)	Hardness (HRC)
7.85	1395–1460	550	39	0.36	17–35	217	63.5

Table 3 Physical properties of the BZN 8200

Density (g/cm^3)	Melting point (°C)	Thermal conductivity (W/mK)	Fracture toughness (MPa $m^{1/2}$)	Elastic modulus (GPa)	Preface hardness (HV)
4.5	1649	42	4.2	580	4500

Table 4 Cutting tool geometry

Rake angle γ_0 (°)	Flank angle α_0 (°)	Blade angle λs (°)	Edge angle kr (°)	Nose radial r_ε (mm)	Vice chamfering width b_{r1} (mm)	Vice chamfering angle γ_{01} (°)
0	8	0	80	0.5	0.2	−15

Table 5 Orthogonal experiment results (continue turning 20 min)

S/N	Cutting speed v (m/min)	Feed rate f (mm/rev)	Depth of cut a_p (mm)	Workpiece surface roughness R_{aw} (μm)	Flank face wear VB (mm)
1	150	0.10	0.15	0.812	0.086
2	150	0.15	0.20	0.605	0.057
3	150	0.25	0.25	1.088	0.122
4	200	0.10	0.20	0.831	0.105
5	200	0.15	0.25	0.537	0.075
6	200	0.25	0.15	0.941	0.080
7	250	0.10	0.25	1.124	0.134
8	250	0.15	0.15	0.60	0.0605
9	250	0.25	0.20	1.182	0.084

Finite Element Analysis of Cutting Tools

The design of simulation structure model selection parameters listed in Table 3, processing parameters listed in Table 4. The finite element analysis software DEFORM-3D is adopted. The cutting tool and workpiece are meshed by Lagrange's tetrahedral element, the number of workpiece units is 50,000, and the number of cutting tool units is 35,000. The analytical model and meshing information are shown in Fig. 1. The Johoson-Cook model is used to describe the performance of GCr15 material. The model can accurately express the deformation

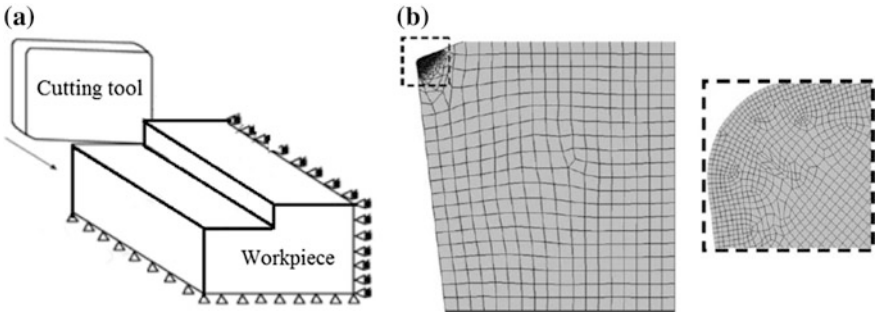

Fig. 1 PcBN cutting tools model for FEA

process of high speed hard cutting with high strain and high temperature. The boundary condition of the cutting process is to fix the workpiece and the cutting tool moves in the determined cutting speed, feed rate and depth of cut. The cutting tool is an active part and the workpiece is a driven part.

A set of PcBN tools cutting temperature distribution, as showed in Fig. 2, and equivalent stress distribution of PcBN tool, as showed in Fig. 3, are gotten by turning simulation in DEFORM software. It is known that heat-resistance temperature of cBN can reach above 1400 °C, but the cutting tools turning temperature is under 1400 °C. The highest point of cutting temperature distribution is not on the cutting edge, but the centralized distribution near the blade. This may be in the cutting process, the friction heat along the cutting tool surface increasing, the high temperature of the chip failed to discharge the edge.

From the simulation data shown in Fig. 2 and Table 6, it can be seen that the cutting temperature of the tool increases with an increase in cutting speed. No matter how the cutting condition changes, the maximum value of the cutting temperature is always distributed at a distance from the main cutting edge to the rake face. In this region, the pressure between the blade and the chip is high, and the friction is large, which indicates that a major factor causing the temperature rise is the friction between the tool and the chip. From the simulation data shown in Fig. 3, in the cutting process, the maximum equivalent stress of the tool is distributed on the main cutting edge of the rake face. The simulation results are in good agreement with the actual cutting process. When the turning speed is at

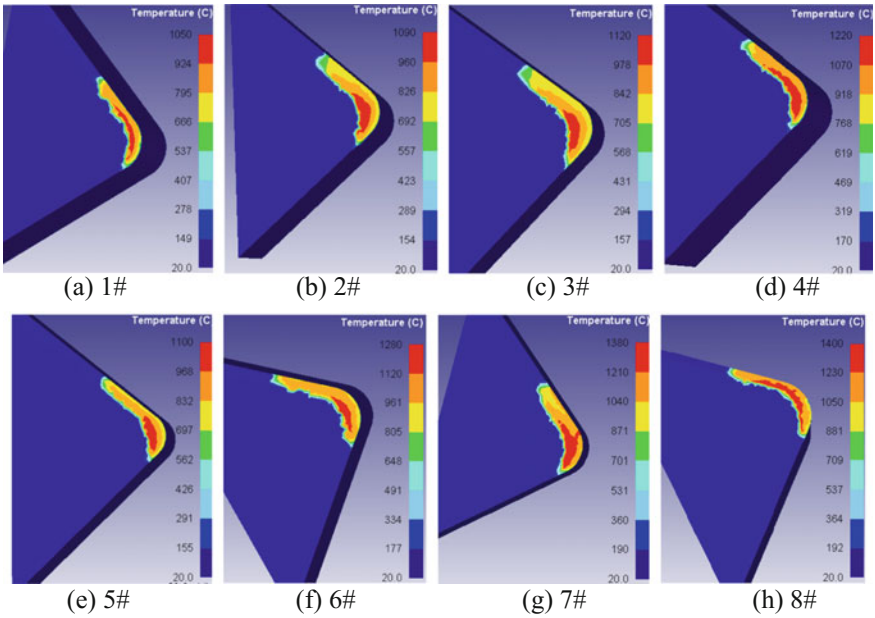

Fig. 2 PcBN cutting tool temperature distribution cloud under different processing parameters

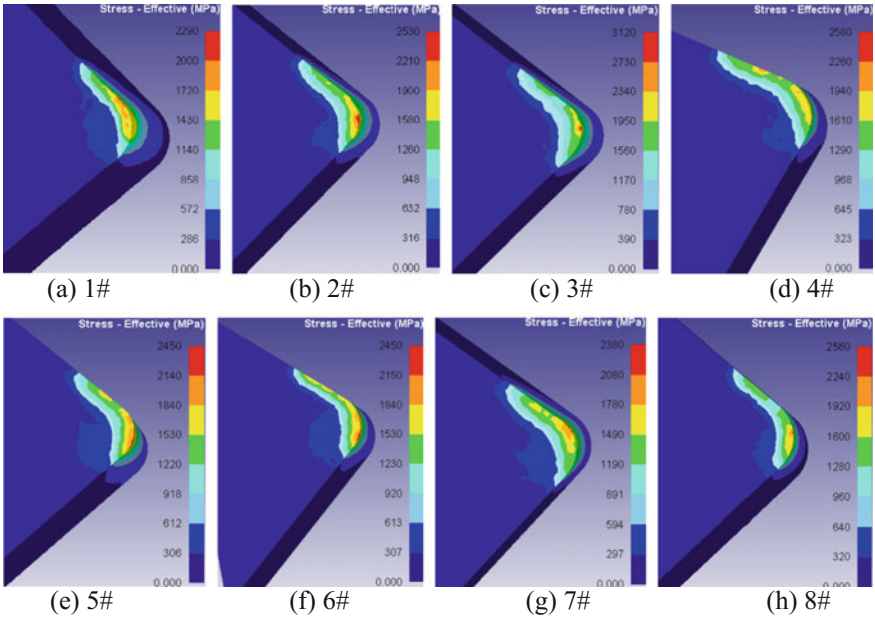

Fig. 3 PcBN cutting tool equivalent stresses distribution under different processing parameters

Table 6 Simulation results of cutting tools temperature, equivalent stress and deformation

S/N	1	2	3	4	5	6	7	8	9
Temperature (°C)	1050	1090	1120	1220	1080	1280	1380	1400	1390
Equivalent stress (MPa)	2290	2530	3120	2580	2450	2450	2380	2560	2500
Deformation (μm)	3.3	5.3	6.0	4.6	2.6	4.9	4.9	4.2	5.0

200 m/min, feed rate is 0.15 mm/r and cutting depth is 0.2 mm, the temperature of the PcBN cutting tool is lower than 1100 °C, the equivalent stress and deformation are both smaller.

Relationship Between Cutting Parameters and Workpiece Roughness

The values of workpiece surface roughness are compared in Fig. 4a on the condition of cutting speed from 80 to 250 m/min, the feed rate of 0.15 mm/rev, depths of cut is 0.15, 0.20 and 0.25 mm respectively. As can be seen from this figure, with the increase of cutting speed, the surface roughness of the workpiece is reduced

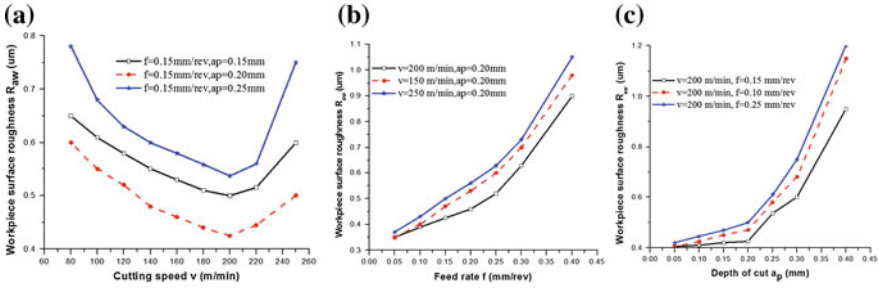

Fig. 4 Relation curves between turning parameters and work piece surface roughness

until the minimum value is reached, then the surface roughness value increases. When cutting speed is at 200 m/min, the lowest workpiece surface roughness value has been occurred.

The values of workpiece surface roughness are contrasted in Fig. 4b on the condition of depth of cut 0.20 mm, feed rate from 0.05 to 0.40 mm/rev, cutting speed is 150, 200 and 250 m/min respectively. From this figure, it can be obtained that workpiece surface roughness values increase with increasing of the feed rate. This is because of the increase in feed rate, the increase of lathe vibration that is caused by the increase of residual area height and radial force. Figure 4c shows the relationship between depth of cut and workpiece surface roughness. As can be seen in this figure that with depth of cut increasing, the values of workpiece surface roughness increase.

Discuss on Cutting Tool's Flank Wear

In Fig. 5a, b, the influence of cutting speed and feed speed value on the cutting tools flank wear is given. From Fig. 5a, it can be known that with the cutting speed increase, flank face wear decreased when cutting speed is below 200 m/min, after

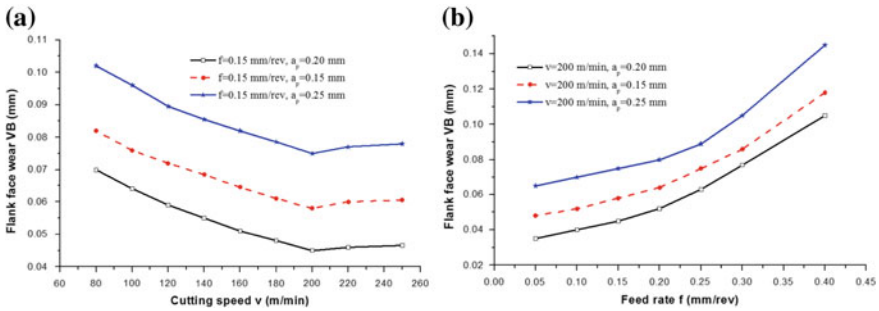

Fig. 5 Relation curves between turning parameters and turning tools flank wear

that flank face wear slow increase. This may be the result of softening of the material metal. From Fig. 5b, when the feed rate is below 0.20 mm/rev, flank face wear slow increase, after that flank face wear rapid increase.

Conclusions

(1) With the increase of cutting speed, the turning temperature of cutting tools also increases. The maximum value of turning temperature is always distributed at a distance from the main cutting edge to the rake face.
(2) When the turning speed is lower than 220 m/min, the cutting speed has less influence on the flank wear than the feed rate and the depth of cut. The influence of turning speed on the surface roughness of the work piece is weaker than that of the depth of cut and the feed rate.
(3) The ideal surface roughness of the workpiece and smaller flank wear of cutting tool can be achieved as the depth of cut is 0.20 mm, the feed rate is 0.15 mm/rev and the cutting speed is on 200 m/min.

Acknowledgements This research is supported by Beijing Natural Science Foundation the Grant No. 3162013. The authors also would like to thank the anonymous reviewers whose comments helped to improve the structure and readability of the paper.

References

1. A. Jose, A.E. Diniz, D.J. Ursolino, J. Mater. Process. Technol. **209**, 5262–5270 (2009)
2. G. Poulachon, B.P. Bandyopadhyay, I.S. Jawahir, Int. J. Mach. Tools Manuf. **43**, 139–144 (2003)
3. L. Qian, M.R. Hossan, Effect on cutting force in turning hardened tool steels with cubic boron nitride inserts. J. Mater. Process. Technol. **191**, 274–278 (2007)
4. H. Aouici, M.A. Yallese, K. Chaoui, Analysis of surface roughness and cutting force components in hard turning with CBN tool: prediction model and cutting conditions optimization. Measurement **3**, 344–353 (2012)
5. Y.C. Yen, A. Jain, T. Altan, A finite element analysis of orthogonal machining using different tool edge geometries. J. Mater. Process. Technol. **146**, 72–81 (2004)
6. A. Kurt, U. Şeker, Mater. Des. **26**, 351–356 (2005)
7. Y. Karpat, T. Ozel, 3-D FEA of hard turning: investigation of PCBN cutting tool micro-geometry effects. Trans. NAMRI/SME **35**, 1–8 (2007)
8. E. Uhlmann, J.A. Oyanedel Fuentes, M. Keunecke, Thin Solid Films **518**, 1451–1454 (2009)
9. Y. Jia, J. Li, Mechanism study on the wear of polycrystalline cubic boron nitride cutting tools. Proc. SPIE **7997**, 79970E 1–8 (2010)

Microstructures and Tensile Behaviors of Stainless Steel Clad Plate

CuiXin Chen, MingYang Liu, BaoXi Liu, FuXing Yin, YanChun Dong, Wei Fang and Xin Zhang

Abstract A novel bi-layers clad plate comprising of stainless steel and carbon steel has been successfully fabricated by vacuum hot rolling at a high temperature of 1100 °C. The microstructure observation showed an interfacial transition zone about 80–100 μm in width, which is attributed to the diffusion of carbon element at the interface. The stainless steel clad plate exhibited a high ultimate tensile strength (578 MPa) and high uniform elongation (52%), and the elastic modulus and stress mismatch at the interface resulted into severe warping resilience phenomenon. Fracture characterizations highlight that the delamination and intergranular cracks presented at the interfacial transition zone.

Keywords Metallic composites · Laminates · Microstructure · Interfaces Deformation and fracture · Elastic properties

C. Chen · M. Liu · B. Liu (✉) · F. Yin · Y. Dong · W. Fang · X. Zhang
TianJin Key Laboratory of Materials Laminating Fabrication and Interfacial Controlling Technology, School of Materials Science and Engineering, Research Institute for Energy Equipment Materials, Hebei University of Technology, Tianjin 300130, China
e-mail: liubaoxiliubo@126.com

C. Chen
e-mail: karenccx@126.com

M. Liu
e-mail: twzzyyx@126.com

F. Yin
e-mail: yinfuxing@hebut.edu.cn

Y. Dong
e-mail: hbgddych@163.com

W. Fang
e-mail: cl.mrfw@163.com

X. Zhang
e-mail: gzhang_xin@hebut.edu.cn

© Springer Nature Singapore Pte Ltd. 2018

Y. Han (ed.), *Advances in Materials Processing*, Lecture Notes in Mechanical Engineering, https://doi.org/10.1007/978-981-13-0107-0_39

Introduction

Metallic clad plates, especially stainless steel clad plates, have a widespread application in nuclear power plant for safety injection tank, which realize the possibility of combining the weldability, formability of carbon steel substrates with the corrosion resistance of stainless steel layer [1]. Meanwhile, multi-or bi-layered composites have been initially designed to enhance the damage tolerance, toughness, ductility, weldability and bending formability due to the presence of interfaces [1–5]. Ohashi et al. [6] proposed that superior bending ductility can be obtained in the laminated steel-brass composites without interfacial debonding. Yanagimoto et al. [3, 7] reported that multilayered steel possess remarkable tensile ductility and bending formability by delaying necking of brittle layer.

In order to develop stainless steel clad plates with high toughness and corrosion resistant, Jing et al. have reported the interfacial characteristics and shear behavior of stainless steel clad plates in detail [8, 9]. However, the topics on the tensile deformation process and fracture modes of stainless steel clad plates have yet to be studied systematically. In this paper, it is really interesting to further investigate the tensile behavior and fracture characteristics of stainless steel clad plates, which is useful to further comprehend the relationship between structure and performance, and guide the microstructure design for property improvement of bi-layered metal composites.

Experimental Procedures

The chemical composition of raw stainless steel and carbon steel is listed in Table 1. A stainless steel sheet with a thickness of 12 mm and carbon steel with a thickness of 60 mm were stacked together and subjected to vacuum hot rolling for eight passes at the temperature of 1100 °C followed by air cooling. The total thickness of stainless steel clad assemble is 145 mm with a 1 mm thick insulating cloth. Finally, it was rolled to 14.5 mm, and the total rolling reduction ratio is 90%. Herein, the layer thicknesses of stainless steel cladding and carbon steel substrate are about 1.2 and 6.0 mm, respectively. The fabrication parameters during the hot roll bonding process are listed in Table 2.

Samples were cut from the stainless steel clad plates and prepared using metallographic corrosion and electrical polishing technologies. The microstructures and fracture characteristics are investigated by optical microscope (OM) and scanning

Table 1 The chemical composition of the stainless steel and carbon steel (wt%)

Elements	Fe	Cr	Ni	C	Mn	Si	P	S
SUS304	68.95	18.5	8.5	0.025	2	2	0.025	0.001
Q235	98.91	–	–	0.2	0.5	0.3	0.045	0.05

Table 2 Fabrication parameters during the hot roll bonding process

Passes	Roll gap (mm)	Reduction (%)	Rolling force (kN)	Rotating speed (m/s)
1	116	20	1802	288
2	93	20	1841	288
3	74	20	1785	288
4	57	23	2119	288
5	44	23	2227	288
6	32	28	2639	360
7	22	31	3066	360
8	14	36	4097	360

electron microscopic (SEM), respectively. The longitudinal tensile tests were carried out using an Instron-5569 universal testing machine at a constant crosshead speed of 2 mm/min, and a total of five samples were tested for each material. Tensile dog bone samples have dimensions of 110 mm × 20 mm × 2.4 mm.

Results and Discussions

As shown in Fig. 1, five different microstructural layers are located in the stainless steel clad plate: carbon steel layer, decarburized layer, interface, carburized layer and stainless steel layer. The carbon steel layer contains ferrite phase and dark pearite phase. During the hot rolling process, the decarburized layer and carburized layer are caused by the diffusion of carbon element from carbon steel substrate into the stainless steel layer. It can be found that the thickness of purity ferrite decarburized layer and carburized layer are about 50–60 μm and 20–30 μm, respectively. Herein, many equiaxed polygon grains with size of 10–15 μm were well-distributed in the carburized layer, and the clear grain boundary may be pinned by $Cr_{23}C_6$ carbides precipitates [10, 11]. Many rolling twinning were decorated in the stainless steel layer caused by severe rolling deformation rate. In addition, complete interface with slight undulation realizes the metallurgical bonding as shown in Fig. 1a. However, from the high magnified view shown in Fig. 1b, a small amount of very fine pores (diameter < 1.5 μm) were distributed at the interface.

Figure 2 shows the macro fracture characteristics of the stainless steel clad plate. The clad plate has displayed a high uniform plastic deformation capacity and slight localized necking until failure as shown in Fig. 2a. It is interesting to note that severe warping resilience and interfacial delamination phenomena are shown in Fig. 2b. There is serious localized necking and interfacial delamination phenomena existed at the fracture zone, and the depth of interfacial delamination crack is about 800 μm as shown in Fig. 2c.

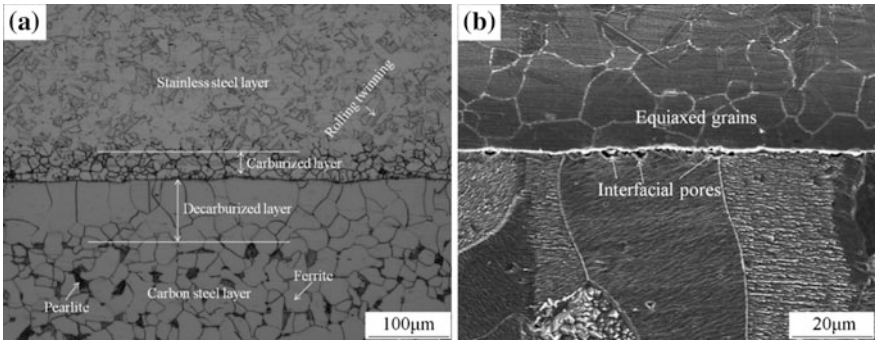

Fig. 1 Microstructures of stainless steel clad plate fabricated by vacuum hot rolling at 1100 °C, **a** a low magnificent; **b** a high magnificent

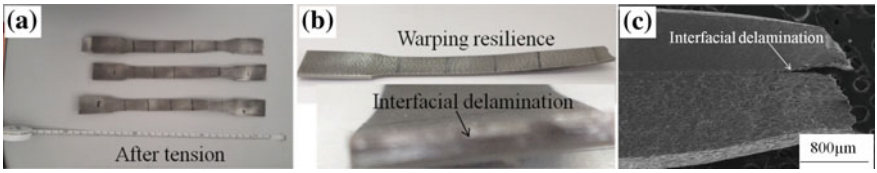

Fig. 2 The macro fracture characteristics of stainless steel clad plate, **a** after tension; **b** warping resilience and delamination phenomena; **c** localized necking and interfacial delamination crack

Figure 3 shows the micro fracture morphologies of the stainless steel clad plate. The moderate interfacial bonding strength results into a deep interfacial delamination crack as shown in Fig. 3a, which may be related to the fine interfacial pores. Figure 3b shows many intergranular cracks in the carburized layer. The Cr23C6 carbides often precipitate at the grain boundary of stainless steel due to the diffusion carbon element, leading to the high brittleness of grain boundary. Therefore, many cracks propagate along the grain boundary and form intergranular tunnel cracks [11]. According to elastic plastic deformation model [12]:

$$t \leq \frac{2\sqrt{3}\,K_{IC}^{2}\,\sigma_s}{\sigma^3} = t_{critical} \tag{1}$$

where t and K_{IC} are the thickness and fracture toughness of carburized layer, respectively. $t_{critical}$ is the critical tunnel crack size, σ_s is the yielding strength of stainless steel layer, and σ is the stress imposed on the carburized layer. It is revealed that when the size of tunnel crack is lower than the critical crack size, the tunnel crack will be blunted by the adjacent stainless steel layer. Therefore, the thinner carburized layer can result into more intergranular cracks and higher fracture toughness.

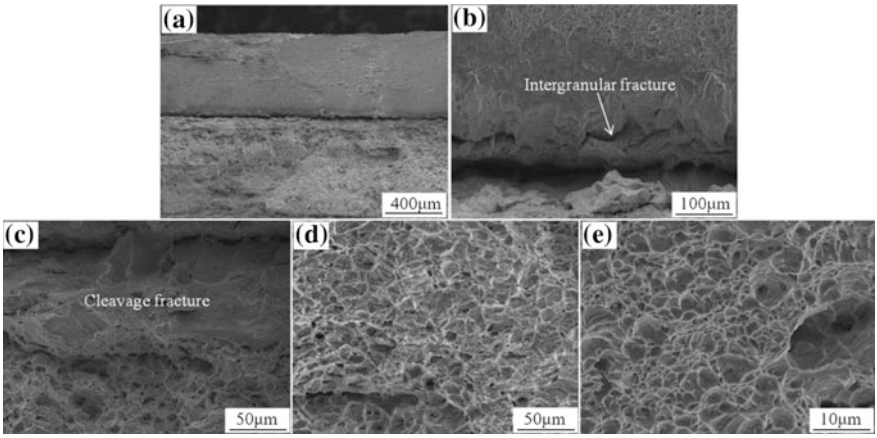

Fig. 3 Micro fracture characteristics of stainless steel clad plate; **a** interfacial delamination; **b** carburized layer; **c** decarburized layer; **d** carbon steel layer; **e** stainless steel layer

Figure 3c shows the fracture characteristics of decarburized layer. There are many transgranular fracture characteristics accompanying with river-like patterns and cleavage fracture. It is because that the plastic deformation of decarburized layers was constrained by carbon steel substrate and moderate interface, forming super-high triaxial tensile stress and resulting into ductile brittle transition of decarburized layer, which is similar with that of the laminated Al-2024Al composites [13]. As shown in Figs. 3d, e, it is observed that both carbon steel layer and stainless steel layer show ductile fracture surface. However, the size of dimples in carbon steel layer and stainless steel layer are about 20–30 and 2–5 μm, respectively.

The tensile stress-displacement curves of raw materials and stainless steel clad plate are shown in Fig. 4, and the corresponding tensile properties are listed in Table 3. The stainless steel clad plate demonstrates a "rule of mixture effect" i.e., an intermediate yield strength (298 MPa), ultimate strength (578 MPa) and fracture elongation (46%) between carbon steel and stainless steel. The prediction of the true tensile stress-strain relationship on the clad plate requires the tensile behavior of individual layers. During the longitudinal tensile deformation stage, the deformation behavior of stainless steel layer and carbon steel layer is fitting to the iso-strain condition. One class of metals considered is a pure power-law hardening (Hollomon) materials, finite strain J2 deformation theory solid with hardening exponent (N). In plane strain tension, the true stress-strain relation is expressed as follows [14]:

$$\sigma = K\,\varepsilon^{N} \tag{2}$$

where K is the strength coefficient. Therefore, the stress-strain curve of stainless steel clad plates can be computed by the following expression:

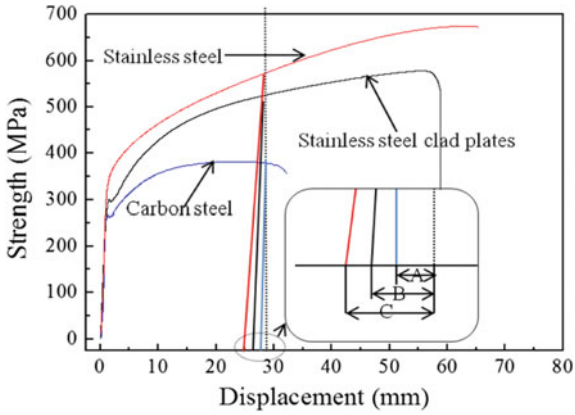

Fig. 4 Tensile behavior of stainless steel clad plate. A, B, C values show the elastic recovery displacement of carbon steel, stainless steel clad plates and stainless steel, respectively

Table 3 Tensile properties of stainless steel clad plates and raw materials

Materials	Elastic modulus (GPa)	Yield strength (MPa)	Ultimate strength (MPa)	Elongation (%)
Q235	203	254	380	28
SUS309	190	350	675	57
Clad plates	197	298	578	46

$$\sigma = (1 - f_{ss})\,\sigma_{cs} + f_{ss}\,\sigma_{ss} = (1 - f_{ss})\,K_{cs}\,\varepsilon^{N_{cs}} + f_{ss}\,K_{ss}\,\varepsilon^{N_{ss}} \tag{3}$$

where f_{ss} is the volume fraction of stainless steel layer, and the "cs" and "ss" represent the carbon steel and stainless steel. Therefore, the tensile stress-displacement curve of stainless steel clad plates is located in between carbon steel and stainless steel.

Based on the Consider criterion, the condition of diffuse necking, which leads to non-uniform plastic deformation even fracture failure defined by the following equations:

$$\frac{d\sigma}{d\varepsilon} = \sigma \tag{4}$$

$$\frac{d\sigma}{d\varepsilon} = KN\,\varepsilon^{N-1} = K\,\varepsilon^{N} \tag{5}$$

$$\varepsilon_{necking} = N \tag{6}$$

Actually, the uniform plastic deformation up to necking strain is mainly depended on the strain hardening coefficient N. Since the stainless steel experiences

a longer deformation stage and higher fracture elongation than the carbon steel. Substituting Eq. (4) into (3), the diffuse necking strain of clad plates can be expressed as follows:

$$N_{ss} > N_{cs} \tag{7}$$

$$\frac{K_{ss} f_{ss}}{K_{cs}(1 - f_{ss})} = \frac{N_{cs}\, \varepsilon_{necking(L)}^{N_{cs}-1} - \varepsilon_{necking(L)}^{N_{cs}}}{\varepsilon_{necking(L)}^{N_{ss}} - N_{ss}\, \varepsilon_{necking(L)}^{N_{ss}-1}} \tag{8}$$

where $\varepsilon_{necking(L)}$ is the clad plates limit strain at the onset of necking. Serror et al. [15] reported that the necking strain of laminates is bounded by the necking strain of carbon steel as a lower bound and that of stainless steel as an upper bound, respectively. Therefore, the stainless steel clad plate reveals a intermediate fracture elongation.

In addition, severe warping resilience phenomenon is attributed to the different deformation behavior of carbon steel and stainless steel. The stainless steel clad plates will experience an elastic recovery stage after fracture. Because that the elastic modulus is lower, whereas the stress of stainless steel is higher than that of carbon steel as shown in Table 3, the elastic recovery displacement of stainless steel layer is longer than that the carbon steel layer as shown in Fig. 4. Therefore, residual compression stresses are distributed in the stainless steel layer, whereas residual tensile stresses in the carbon steel layer, resulting into apparent warping resilience phenomenon.

Summaries

(1) The tensile behavior of stainless steel clad plates reveals “rule of mixture effect” i.e., an intermediate tensile strength, ultimate strength and fracture elongation locate in between carbon steel and stainless steel.
(2) The fracture characteristic of clad plate reveals an obvious interfacial delamination crack and many intergranular tunnel cracks, which are attributed to the moderate interfacial bonding and brittleness of carburized layer, respectively.
(3) The stainless steel clad plates displays severe warping resilience phenomenon, which is attributed to the elastic modulus and stress mismatch between carbon steel layer and stainless steel layer.

Acknowledgements This work is financially supported by the National Natural Science Foundation of China (NSFC) under Grant No. 51304059, the Hebei Science and Technology program under Grant Nos. 130000048, the National Natural Science Foundation of Hebei Province under Grant Nos. E201620218, E2015202190, ZD20131018 and QN2016029.

References

1. T. Koseki, J. Inoue, S. Nambu, Development of multilayer steels for improved combinations of high strength and high ductility. Mater. Trans. **55**, 227–237 (2014)
2. O. Bouaziz, J.P. Masse, G. Petitgand, M.X. Huang, A novel strong and ductile TWIP/Martensite steel. Adv. Eng. Mater. **18**, 56–59 (2015)
3. T. Oya, N. Tiesler, S. Kawanishi, J. Yanaimoto, T. Koseki, Experimental and numerical analysis of multilayered steel sheets upon bending. J. Mater. Process. Technol. **210**, 1926–1933 (2010)
4. A. Atrian, F. Fereshteh-Saniee, Deep drawing process of steel/brass laminated sheets. Compos. B **47**, 75–81 (2013)
5. E. Afshin, M. Kadkhodayan, A experimental investigation into the warm deep-drawing process on laminated sheet under various grain sizes. Mater. Des. **87**, 25–35 (2015)
6. Y. Ohashi, J. Wolfenstine, R. Koch, O.D. Sherby, Fracture behavior of a laminated steel-brass composite in bend tests. Mater. Sci. Eng. A **151**, 37–42 (1992)
7. J. Yanagimoto, T. Oya, S. Kawanishi, N. Tiesler, T. Koseki, Enhancement of bending formability of brittle sheet metal in multilayer metallic sheets. CIRP Ann. Manuf. Technol. **59**, 287–290 (2010)
8. Y. Jing, Y. Qin, X.M. Zang, Y.H. Li, The bonding properties and interfacial morphologies of clad plate prepared by multiple passes hot rolling in a protective atmosphere. J. Mater. Process. Technol. **214**, 1686–1695 (2014)
9. Y. Jing, Y. Qin, X.M. Zang, Q.Y. Shang, H. Song, A novel reduction-bonding process to fabricate stainless steel clad plate. J. Alloy. Compd. **617**, 688–698 (2014)
10. H. Pommier, E.P. Busso, T.F. Morgeneyer, A. Pineau, Intergranular damage during stress relaxation in AISI 316L-type austenitic stainless steels: effect of carbon, nitrogen and phosphorus. Acta Mater. **103**, 893–908 (2016)
11. R. Jones, V. Randle, G. Owen, Carbide precipitation and grain boundary plane selection in overaged type 316 austenitic stainless steel. Mater. Sci. Eng. A **496**, 256–261 (2008)
12. B.X. Liu, L.J. Huang, X.D. Rong, L. Geng, F.X. Yin, Bending behaviors and fracture characteristics of laminated ductile-tough composites under different modes. Compos. Sci. Technol. **126**, 94–105 (2016)
13. L.H. Han, L. Li, J. Sun, Ductile to brittle transition of pure Al sheet constrained by strength mismatched parallel bi-interface. Scripta Mater. **52**, 1157–1162 (2005)
14. J.W. Hutchinson, Necking modes in multilayers and their influence on tearing toughness. Math. Mech. Solids **19**, 39–55 (2014)
15. M.H. Serror, Analytical study for deformability of laminated sheet metal. J. Adv. Res. **4**, 83–92 (2013)

Transformation Behavior During Isothermal Partitioning Process in Micro-alloyed Q&P Steel

Fei Peng, Yunbo Xu, Xingli Gu, Yuan Wang, Xunda Liu and Yongmei Yu

Abstract A low-carbon steel micro-alloyed with Nb, V and Ti was subjected to partial austenitized followed by two-step quenching and partitioning (Q&P) process. Combined use of static dilatometer, SEM and EPMA techniques revealed the microstructure evolution and elements variation during partitioning process. The result shows that the retained austenite normally located inside or around M/A the island with blocky morphology as well as obvious carbon enrichment. With increasing partitioning time, the carbon enrichment region expanded and the carbides precipitated inside the tempered martensite. The rate of Bainite transformation dilatation during partitioning process accelerated with increasing partitioning time, whereas carbide precipitation during martensite temper lead to a compression at the same time.

Keywords Quenching and partitioning · Isothermal partitioning Bainite · Temper martensite

F. Peng · Y. Xu (✉) · X. Gu · Y. Wang · X. Liu
State Key Laboratory of Rolling and Automation, Northeastern University, Shenyang 110819, China
e-mail: yunbo_xu@126.com

F. Peng
e-mail: pengfeiral@126.com

X. Gu
e-mail: 597662026@qq.com

Y. Wang
e-mail: 2240480646@qq.com

X. Liu
e-mail: 821632952@qq.com

Y. Yu
School of Mechanical Engineering, Shenyang University of Chemical Technology, Shenyang 110142, China
e-mail: yongmei_yu@126.com

© Springer Nature Singapore Pte Ltd. 2018

Y. Han (ed.), *Advances in Materials Processing*, Lecture Notes in Mechanical Engineering, https://doi.org/10.1007/978-981-13-0107-0_40

Introduction

The quenching and partitioning (Q&P) heat treatment was a novel method to deliver great mechanical properties with high strength and long elongation [1–3]. It involves a full or partial austenitization followed by a fast quenching to martensite transformation region to form a controlled fraction of initial martensite (M1), then holding or raising the temperature to stabilize austenite by carbon partitioning from supersaturated martensite to austenite [1]. Finally, the microstructure was quenched to ambient temperature and some of the austenite with insufficient stability was transformed into secondary martensite (M2). During the whole heat treatment, other austenite decomposition reactions, such as bainite transformation, carbide precipitation and so on, were all suppressed [4].

However, due to the relatively high partitioning temperature of two-step process, which is normally ~400 °C, the carbide-free bainite transformation of unstable austenite was usually observed in experimental results [5, 6]. In the other hand, the formation of carbide precipitation, such as cementite or transition carbide, could not be entirely suppressed to achieve the ideal partitioning situation, even though a high silicon addition [5, 7, 8]. Hence, it is easily to conclude that bainite transformation and carbide precipitation make a key role during the partitioning process [9–11].

In this work, the transformation behaviour during partitioning process of a 0.2C-2.11Mn-1.49Si-0.81Al-0.035Ti-0.045Nb-0.22V (wt%) steel was investigated. The microstructure evolution and elements distribution variation were also taken into account.

Materials and Experimental Procedure

Cylindrical specimens of 0.2C-2.11Mn-1.49Si-0.81Al-0.035Ti-0.045Nb-0.22V (wt%) steel sheets were machined with length of 10 mm and diameter of 3 mm and the length axis was parallel to the hot-rolling direction. The annealing temperature was selected as 850 °C, which corresponds to the status of 50 vol% ferrite as the thermal-calc software predicted. The critical temperatures were measured by dilatometer as Fig. 1 shows and the corresponding Ms (martensite start temperature) and Mf (martensite finish temperature) were 172 and 292 °C, respectively. Then the quenching temperature was determined to be 225 °C and the corresponding martensite volume fraction was obtained by lever rule method as 37 vol%. The schematic diagram of heat treatment is presented as Fig. 2. The specimens were heat treated by Formaster F-II dilatometer, where samples were annealed at 850 °C for 300 s, then quenched to 225 °C for 5 s, followed by raising temperature to 250, 300, 350, 400 and 450 °C for 1200 s. Finally, the samples were all fast quenched to ambient temperature.

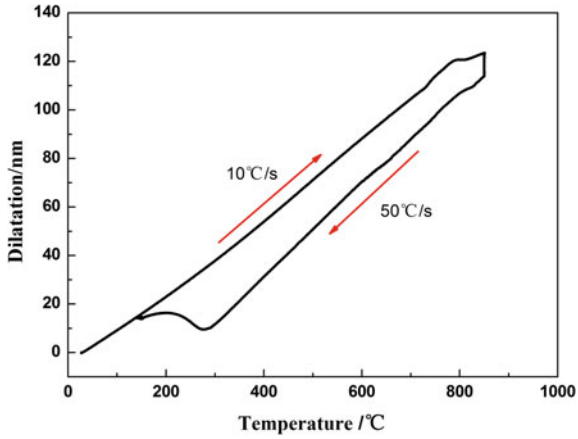

Fig. 1 Schematic diagram for measurement of critical temperature

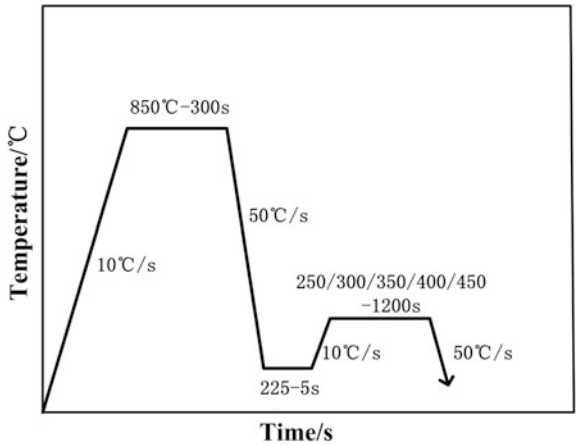

Fig. 2 Schematic diagram of heat treatment

After traditional metallographic preparation, the specimens were etched by 2% Nital for subsequent observation by optical microscopy (OM) and scan electron microscopy (SEM) using a FEI Quanta600 field emission gun scanning electron microscopy (FEG-SEM) operated at 15 kV. The elements distribution of different heat treating conditions was measured by a JEOL JXA-8530F electron probe microprobe (EPMA). The map scanning of C, Mn and Al was conduct under such conditions: working distance 11 mm, accelerating voltage 20 kV, absorbed current 2.0×10^{-8} A, step size of 60 nm, dwell time 10 ms.

Results and Discussion

Microstructure Observation and Elements Distribution Measurement

SEM micrographs of typical partitioning temperature are presented in Fig. 3. The tempered martensite (i.e. initial martensite) was internally etched, and some carbides were observed precipitated inside martensite, which means that the addition of Si and Al could not suppress carbide formation for a time as long as 1200 s.

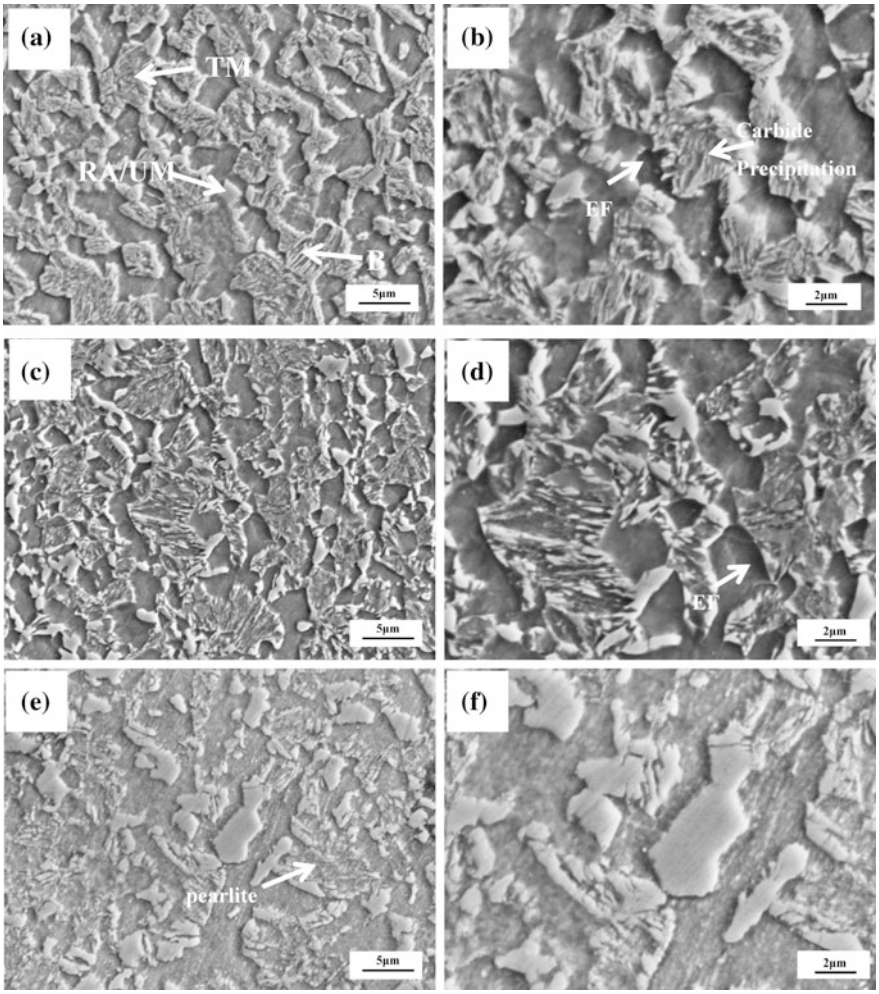

Fig. 3 SEM observation of microstructures in typical partitioning temperatures, **a**, **b** 250 °C; **c**, **d** 350 °C; **e**, **f** 450 °C. *TM* tempered martensite; *EF* epitaxial ferrite

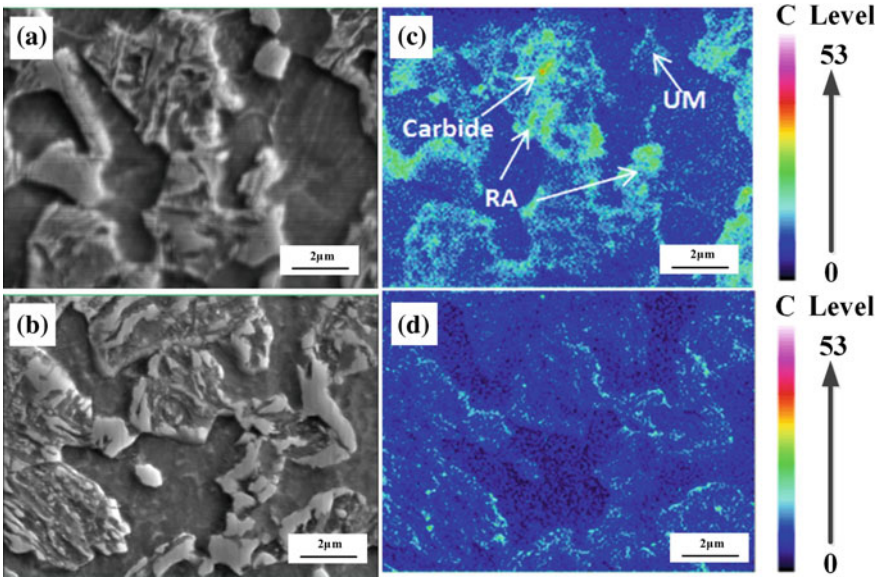

Fig. 4 Microstructure and C distribution of specimens partitioned at 250 and 400 °C, 400 °C: **a** microstructure; **c** C distribution; 250 °C: **b** microstructure; **d** C distribution

Retained austenite and un-tempered martensite (i.e. secondary martensite) were both with featureless and smooth surface. With partitioning temperature increased, the featureless region was expanded gradually. Furthermore, a specific ferrite existed adjacent to intercritical ferrite was observed (as Fig. 3b shown), which was defined as epitaxial ferrite (EF) in some other article. Figure 3a has also shown the existence of bainite with lath morphology. When partitioning temperature raised to 450 °C, some particle carbide, probably cementite, was appeared in a wide range, which corresponds to a pearlite reaction.

The element distribution of C for specimens partitioned at 250 and 400 °C are shown in Fig. 4. It can be easily obtained from Fig. 5c, d that carbon enrichment was only existed outside of the M/A island at 250 °C, while an obvious enrichment inside and outside the M/A island at 400 °C. It is well known that carbon partitioning kinetic has a close relationship to partitioning temperature. A higher partitioning temperature means a faster and more sufficient carbon partitioning process, which means that carbon-enriched austenite after partitioning process would have a more sufficient stability that could be retained after final quenching. The variation of retained austenite morphology could show the carbon partitioning result effectively. With partitioning temperature increased, retained austenite presented a particle or small blocky morphology near in the outside of M/A island firstly, then expanded to be blocky outside and lath inside the M/A island and the volume fraction of retained austenite increased obviously at the same time. However, the temper behavior of martensite and decomposition of austenite would also make a

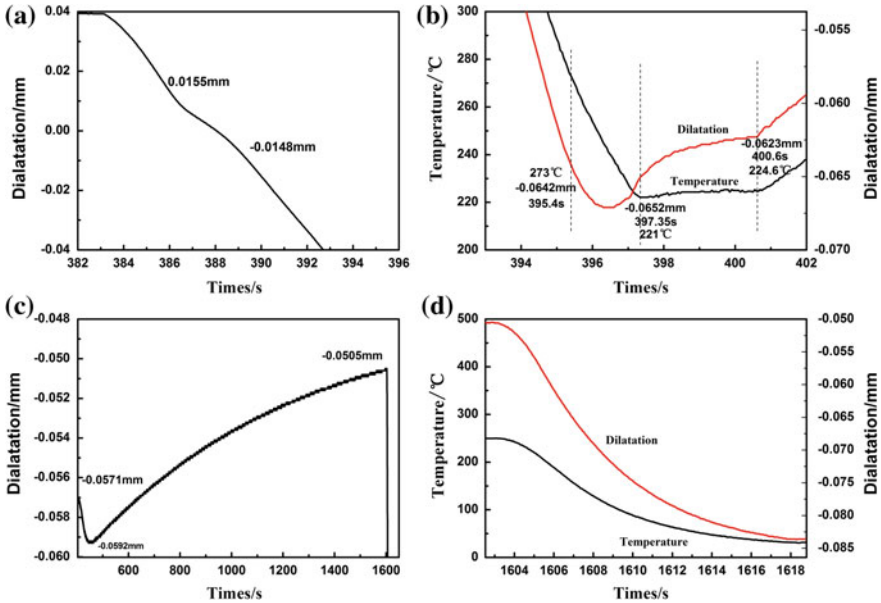

Fig. 5 Typical dilatation variation of specimen partitioned at 250 °C, **a** first quenching stage; **b** quenching isothermal stage; **c** partitioning stage; **d** final quenching stage

key role in carbon partitioning. Carbide precipitation would decrease the carbon content that can partitioned from martensite to austenite. Hence, an appropriate partitioning temperature should be chosen to achieve the best carbon partitioning result.

Dilatation Measurement and Transformation Analysis

Due to different dilatation coefficients of phases, the transformation behavior can be observed by the dilatation variation. The typical dilatation curves of specimen partitioned at 250 °C were presented in Fig. 5. An obvious transformation was observed among the first quenching stage, which corresponds to 519–737 °C. This transformation was identified to be epitaxial ferrite formation, which has a relatively higher Mn concentration compared with that in intercritical ferrite and it had also been observed in SEM micrograph as Fig. 3b shows. As this new ferrite is also with lean C and Mn compared to martensite, the formation of epitaxial ferrite resulted in a carbon enrichment and stabilized the austenite further. Figure 5b shows the martensite transformation during the first quenching process and the volume fraction can be determined to be 37% by lever rule method. The partitioning procedure presented an obvious dilatation, which is defined as bainite formation (see Fig. 5c). In traditional Q&P process, the formation of bainite formation is suppressed

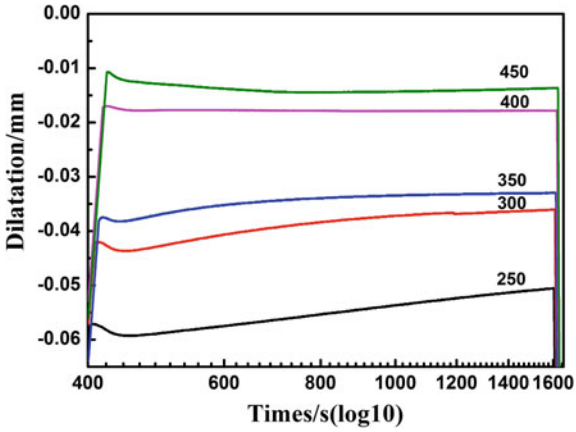

Fig. 6 Dilatation variation of specimens partitioned at different temperatures

entirely. However, the realistic partitioning process is always related to bainite formation, which could partition from bainite ferrite to austenite to enhance the austenite stability further as well as enhance the stability of austenite by decreasing austenite size. It seems that the bainite formation could decrease the volume fraction of unstable austenite. Figure 6d shows the secondary martensite formation during final quenching. It means that some austenite is still unstable after partitioning process, hence transfers to secondary martensite finally. The formation of secondary martensite is determined to be deteriorate to the ductility of steel.

Figure 6 shows the dilatation variation during partitioning procedure of different partitioning temperature. When the partitioning temperature was 250 °C, the dilatation decreased first followed by a continuous increment. When raising partitioning temperature, the decrement of dilation decreased and the dilatation increment in the second stage decreased and reached a maximum value before the end of partition, when the temperature reached to 400 °C, the dilatation keep a constant value basically, while only decreasing at 450 °C. It could be explained that the dilatation decrement was introduced by dislocation recovery, martensite temper, while dilatation increment was related to bainite formation. The bainite formation kinetic depends on temperature. A higher partitioning temperature means a faster bainite formation, which would offset the decrement and reach the maximum value in an earlier time. When the temperature reached 450 °C, pearlite formation happened and a larger decrement made a major influence. It should be mentioned that the volume fraction of bainite was decreased with raising partitioning temperature, which means a higher stability of austenite and a more effective carbon partitioning.

Conclusions

A 0.2C-2.11Mn-1.49Si-0.81Al-0.035Ti-0.045Nb-0.22V (wt%) steel was subject to two-step Q&P process. The transformation and element variation during partitioning procedure as a function of partitioning temperature has been investigated. It may be concluded that: The final microstructure is composed of intercritical ferrite, epitaxial ferrite, retained austenite, secondary martensite and tempered martensite precipitated with carbide. The existence of retained austenite is mainly in the outside of M/A island. The formation of epitaxial ferrite during first quenching step could make the austenite stable further by increasing the grain size and carbon-enrichment. With partitioning temperature increasing, the bainite formation is accelerated and the decrement resulting from martensite temper will counteract and the whole status reaches to be stable in an earlier time. When partitioned at 450 °C, the pearlite formation happens and dilatation of bainite formation is suppressed entirely.

Acknowledgements The authors acknowledge support by the National Natural Science Foundation of China (Nos. 51674080, 51404155 and U1260204), the Program for New Century Excellent Talents in University (NCET-13-0111) and the Program for Liaoning Excellent Talents in University (LR2014007).

References

1. J.G. Speer, D.K. Matlock, B.C.D. Cooman, J.G. Schroth, Carbon partitioning into austenite after martensite transformation. Acta Mater. **51**, 2611–2622 (2003)
2. D.V. Edmonds, K. He, F.C. Rizzo, B.C. De Cooman, D.K. Matlock, J.G. Speer, Quenching and partitioning martensite—a novel steel heat treatment. Mater. Sci. Eng. A **438–440**, 25–34 (2006)
3. A.J. Clarke, J.G. Speer, M.K. Miller, R.E. Hackenberg, D.V. Edmonds, D.K. Matlock, F.C. Rizzo, K.D. Clarke, E. De Moor, Carbon partitioning to austenite from martensite or bainite during the quench and partition (Q&P) process: a critical assessment. Acta Mater. **56**, 16–22 (2008)
4. A.J. Clarke, J.G. Speer, D.K. Matlock, F.C. Rizzo, D.V. Edmonds, M.J. Santofimia, Influence of carbon partitioning kinetics on final austenite fraction during quenching and partitioning. Scripta Mater. **61**, 149–152 (2009)
5. Y. Toji, G. Miyamoto, D. Raabe, Carbon partitioning during quenching and partitioning heat treatment accompanied by carbide precipitation. Acta Mater. **86**, 137–147 (2015)
6. F. Hajyakbary, J. Sietsma, G. Miyamoto, T. Furuhara, M.J. Santofimia, Interaction of carbon partitioning, carbide precipitation and bainite formation during the Q&P process in a low C steel. Acta Mater. **104**, 72–83 (2016)
7. H.K.D.H. Bhadeshia, D.V. Edmonds, The bainite transformation in a silicon steel. Metall. Mater. Trans. A. **10**, 895–907 (1979)
8. X. Tan, Y. Xu, X. Yang, D. Wu, Microstructure—properties relationship in a one-step quenched and partitioned steel. Mater. Sci. Eng. A **589**, 101–111 (2014)
9. K.O. Findley, J. Hidalgo, R.M. Huizenga, M.J. Santofimia, Controlling the work hardening of martensite to increase the strength/ductility balance in quenched and partitioned steels. Mater. Des. **117**, 248–256 (2017)

10. H.Y. Li, X.W. Lu, W.J. Li, X.J. Jin, Microstructure and mechanical properties of an ultrahigh-strength 40SiMnNiCr steel during the one-step quenching and partitioning process. Metall. Mater. Trans. A **41**, 1284–1300 (2014)
11. J.G. Speer, D.V. Edmonds, F.C. Rizzo, D.K. Matlock, Partitioning of carbon from supersaturated plates of ferrite, with application to steel processing and fundamentals of the bainite transformation. Curr. Opin. Solid State Mater. Sci. **8**, 219–237 (2004)

Effects of Heat Treatment on Microstructures and Mechanical Properties of Stainless Steel Tubes for Rivet Parts

Sirui Cheng, Qingyun Zhao, Hong Huang and Fenglei Liu

Abstract The heat treatments of 0Cr18Ni9Ti (0Cr) and 1Cr18Ni9Ti (1Cr) stainless steel tubes, which are commonly used to produce the rivet parts, were performed under different experimental conditions. The mechanical properties of the two stainless steel tubes after solution processes were also tested to study the influences of experimental temperature, holding time and cooling rate. In addition, the microstructures of these two stainless steel tubes were observed by using optical microscope (OM) and scanning electronic microscope (SEM). The results showed that these two stainless steel tubes possessed similar microstructures after solution process, which composed of austenite grains. However, compared with 1Cr stainless steel tubes used in the manufacturing of rivet sleeve, 0Cr stainless steel tubes exhibited more significant holding time and solution temperature dependence of microstructures and mechanical properties. These performance variation sections are in favor in adjusting the structural parameters and installation process of rivets.

Keywords Stainless steel tube · Microstructure evolution · Mechanical property Heat treatment

S. Cheng (✉) · Q. Zhao · H. Huang · F. Liu
Department of Mechanical Joining, Beijing Aeronautical Manufacturing Technology Research Institute, Beijing 100024, China
e-mail: csr4500888@163.com

Q. Zhao
e-mail: zhaoqy_1997@163.com

H. Huang
e-mail: hhong625@163.com

F. Liu
e-mail: lfl625105@sina.com

© Springer Nature Singapore Pte Ltd. 2018

Y. Han (ed.), *Advances in Materials Processing*, Lecture Notes in Mechanical Engineering, https://doi.org/10.1007/978-981-13-0107-0_41

Introduction

The mechanical connection technology as an important method, which is represented by rivet connection and screwing connection, has been widely applied in aviation manufacturing field because of its higher reliability, simple and convenient process [1–3]. At present, the quantity of fasteners used in mechanical connection process is so huge that their number is over 70% of the total components and the weight takes up also about 5–6% in the total weight of an aircraft. Thus, the comprehensive property of fastener plays a key role in determining the structural performance of an aircraft [4, 5]. Stainless steels are important materials in the design and manufacturing processes of aviation fasteners as a result of excellent mechanical properties and lower costs [6, 7]. Thus, the stainless steel, as a type of preferred material, has been extensively used to produce the sleeve of thread rivet.

The circular footing will be formed by plastic deformation of the sleeve during installation stage and provide clamping force by cooperating with other parts of thread rivet. Hence, the mechanical properties of sleeve not only influence service performances, but also determine the installation quality. Higher strength of rivet sleeve means that the joint will possess better connection performance during service stage, but it also improves equipment requirement and installation difficulty. Besides, it is well known that the rivet sleeve with lower plastic, which follows the higher strength, will be easy to damage in installation and application process. For solving the conflict between mechanical properties and installation, it is necessary to research the microstructure evolution of rivet sleeve in manufacturing process. At present, the main material used to product rivet sleeve is 1Cr18Ni9Ti (1Cr) stainless steel tube. However, with the development of aviation industry, high-performance aircraft set the higher requests to mechanical connection technology, especially in long-life connection [8, 9]. It is difficult for traditional 1Cr stainless steel tube to satisfy these requirements of modern aircraft for physical and mechanical properties. In order to find a suitable material, which can replace the 1Cr stainless steel tube and be applied in aviation manufacturing field, some researches related to 0Cr18Ni9Ti (0Cr) stainless steel tube with better corrosion resistance to produce the rivet sleeve have been performed for solving those problems of 1Cr stainless steel tubes exposed in service process [10, 11].

In this paper, the microstructure evolutions of 0Cr and 1Cr stainless steel tubes have been controlled by different heat treatment processes so as to adjust their mechanical properties. The relationship between solution parameters and the microstructure as well as the mechanical properties of the two stainless steel tubes have been investigated based on microstructure observations and tensile tests. Meanwhile, the test results can provide useful data for the development of mechanical connection technology and new aviation fasteners.

Experimental Method

The nominal components of the two stainless steel tubes we used in the experiments were listed in Table 1. Their original microstructures have been exhibited in Fig. 1a, b, respectively. The equiaxed austenitic grains with the size about 20 μm can be obtained in those 1Cr stainless steel tubes. The microstructure of 0Cr stainless steel tubes retains the deformed austenitic grains, which is elongated along the axial direction of tubes, because further heat treatment has not been performed after cold extrusion process.

The heat treatments have been performed in the temperature range of 920–1150 °C, meanwhile, time factor has also been considered in our experiments by setting different holding time, as listed in Table 2. The whole process of vacuum heat treatments consists of three stages: First, the furnace has been heated to set

Table 1 Nominal components of the 0Cr and 1Cr stainless steel tubes [wt%]

Element	C	Cr	Ni	Si	Mn	P	S	Cu	Fe
0Cr	0.04	18.22	8.08	0.44	1.21	0.19	0.002	0.01	Bal.
1Cr	0.10	18.53	8.65	0.32	1.70	0.20	0.002	0.01	Bal.

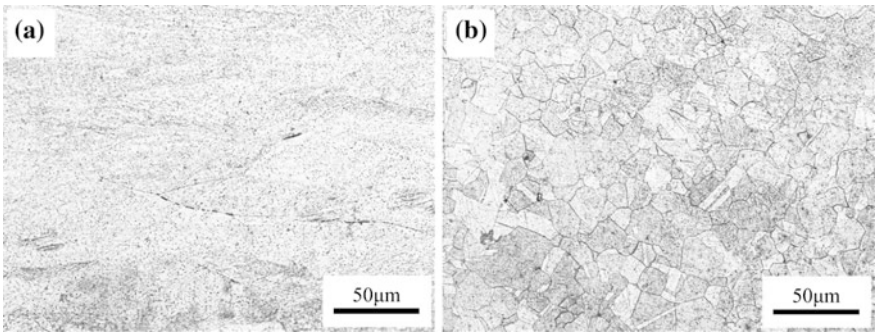

Fig. 1 Original microstructures of 0Cr and 1Cr stainless steel tubes: **a** 0Cr stainless steel tube; **b** 1Cr stainless steel tube

Table 2 Test parameters of heat treatment for 0Cr and 1Cr stainless steel tubes

Time [s]	Temperature [°C]			
	920	1050	1100	1150
10	W/F	W/F	W/F	W/F
20	–	F	–	F
30	–	F	–	F
40	–	F	–	F

"W"—means water quenching; "F"—notes furnace cooling

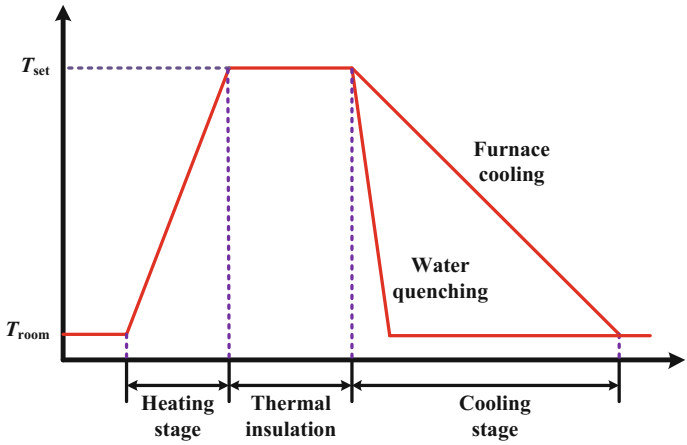

Fig. 2 Heat treatment processes of 0Cr and 1Cr stainless steel tubes

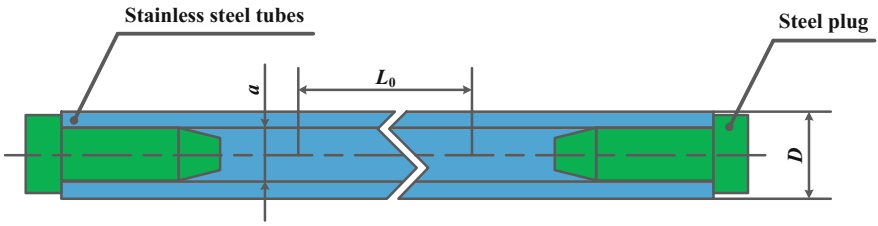

Fig. 3 Uniaxial tension test specimens of 1Cr and 0Cr stainless steel tubes

temperature with a constant rate, and the heating stage lasts for about 1 h; Second, when the furnace temperature reaches the set value, the insulation stage begins and will last for different time; Finally, for investigating the effects of cooling method on microstructure and mechanical properties, the stainless steel tubes have been cooled to room temperature by water quenching and furnace cooling, as shown in Fig. 2.

The gauge length of uniaxial tension test specimen is 80 mm. In order to obtain relatively accurate experimental data, the steel plugs have been inserted the tips of stainless steel tubes to prevent the plastic deformation at the ends of specimens, as shown in Fig. 3. The mechanical property tests were achieved by using the Instron 5982 electronic universal material testing machine.

The metallographic specimens were cut from the original and annealed stainless tube with 5 mm length, respectively. Their cross sections were pretreated to make them smooth by SiC sandpaper, then polished to mirror surface by using the colloidal SiO_2 with particle size of 0.04 μm. The etchant consists of 75 vol% HCl and 25 vol% HNO_3. The microstructures of stainless steel tubes were examined using

optical microscope (OM, DM6000M) and scanning electron microscope (SEM, Quanta250FEG).

Results and Discussion

Figure 4 shows the microstructures of 0Cr and 1Cr stainless steel tubes after solution at different temperatures and furnace cooling. It can be seen that both of 0Cr and 1Cr stainless steel tubes consist of equiaxed austenite grains and these are no obvious precipitated phases on austenite matrix. Heat treatment process eliminates the effect of plastic deformation on microstructures for 0Cr stainless steel tubes. The grain sizes of the 0Cr stainless steel tubes significantly increase from about 20 μm to over 100 μm as solution temperatures increase from 920 to 1150 °C. However, it is not obvious to the microstructural evolutions for 1Cr stainless steel tubes at the temperature range of 920–1050 °C. The grain sizes of 1Cr stainless steel tubes are about 20 μm without significant growing at the temperature of 920 °C, which are similar to the 0Cr stainless steel tubes after solution. When the solution temperature reaches 1100 °C, the equiaxed austenite grains of 1Cr stainless steel tubes grow rapidly. In addition to the solution temperature, many researchers have pointed that the cooling rate can also influences the microstructure evolution so as to determine the mechanical properties of stainless steels. Figure 5 exhibits the microstructures of the two stainless steel tubes after solution and cooling to room temperature by water quenching. It is worth noting that by comparing the Figs. 4 and 5, there are no significant differences between the microstructures of two stainless steel tubes after furnace cooling and water quenching, respectively. The 0Cr and 1Cr stainless steel tubes undergoing various

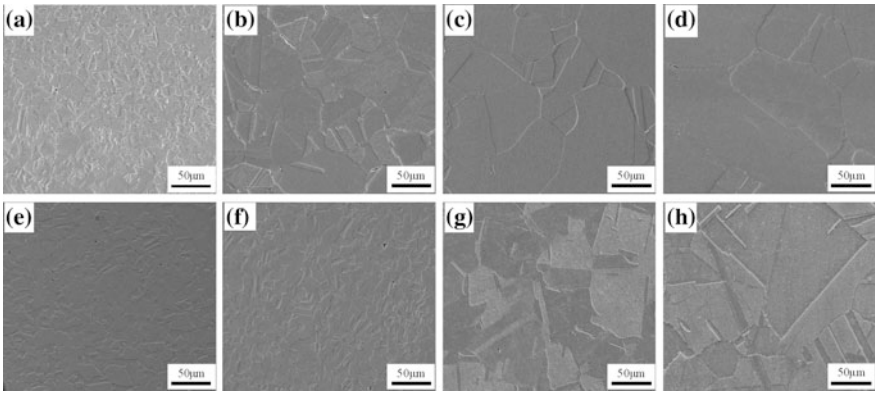

Fig. 4 Microstructures of the two stainless steel tubes after solution at the temperature range of 920–1150 °C for 10 min and cooling to room temperature by furnace cooling: **a**, **c**, **e**, **g** for 0Cr stainless steel tubes; **b**, **d**, **f**, **h** for 1Cr stainless steel tubes

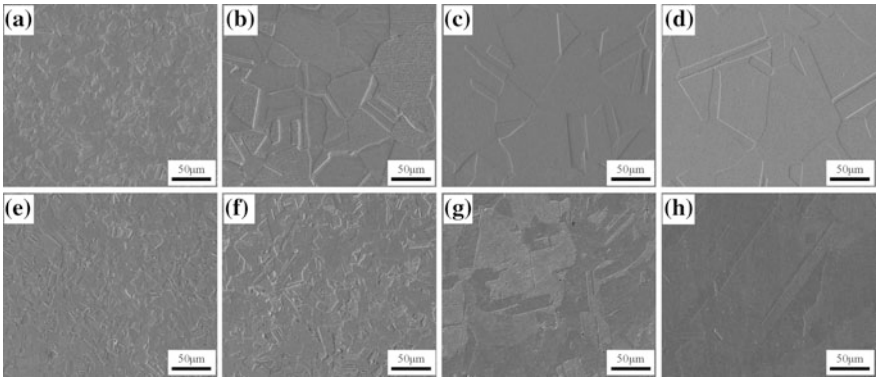

Fig. 5 Microstructures of the two stainless steel tubes after solution at the temperature range of 920–1150 °C for 10 min and frozen to room temperature by water quenching: **a**, **b**, **c**, **d** for 0Cr stainless steel tubes; **e**, **f**, **g**, **h** for 1Cr stainless steel tubes

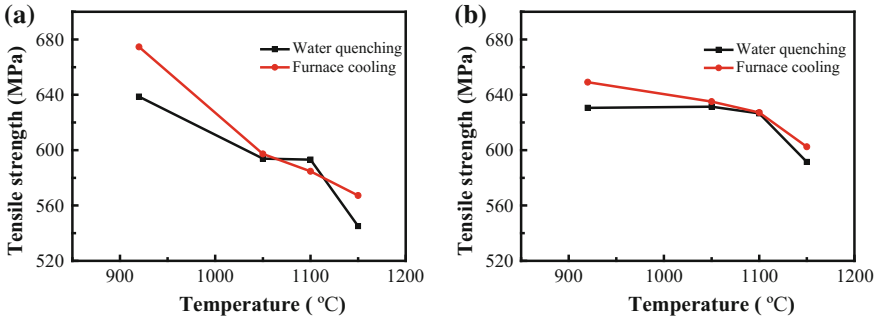

Fig. 6 Relationship between experimental temperature and tensile strength of 0Cr and 1Cr stainless steel tubes after solution for 10 min: **a** 0Cr stainless steel tubes; **b** 1Cr stainless steel tubes

cooling methods possess similar grain size. This results means that the whole microstructure evolutions of the two stainless steel tubes may have completed during the heating and holding stages so that the subsequent cooling stages have less effects on microstructure evolutions of these two stainless steel tubes.

The mechanical test results reveal that the tensile strengths of the two stainless steel tubes present decline trend as solution temperature increases from 920 to 1150 °C, as shown in Fig. 6. Based on the Hall-Petch relationship, it is clear that the strength of crystal material decreases with increasing grain size in a certain scale range. So the tensile strengths of two stainless steel tubes decrease with the increasing solution temperature. Similar to the microstructure features of the two stainless steel tubes, the tensile strengths also have not exhibited obvious dependence on cooling rate, when the solution temperature is between 1050 and 1100 °C. By contrast, when solution temperatures are 920 and 1150 °C, the tensile strengths

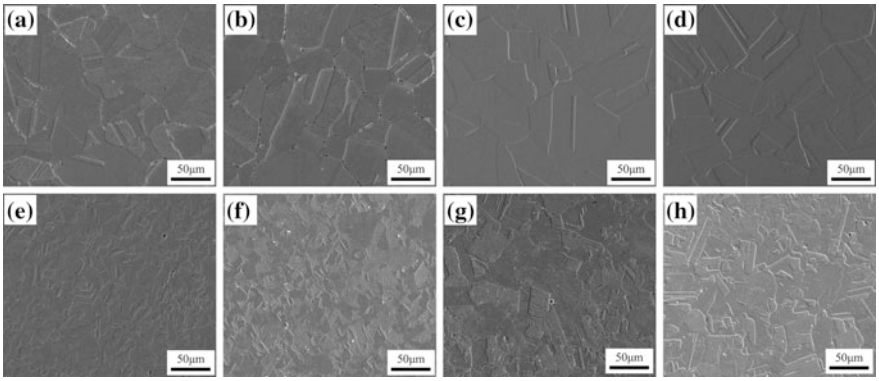

Fig. 7 Time dependences of the microstructures for 0Cr and 1Cr stainless steel tubes at the solution temperature of 1150 °C: **a–d** for 0Cr stainless steel tubes, t = 10, 20, 30, 40 min, respectively; **e–h** for 1Cr stainless steel tubes, t = 10, 20, 30, 40 min, respectively

of two stainless steel tubes under various cooling condition show distinct differences that the stainless steel tubes undergoing furnace cooling have higher tensile strengths. On the other hand, it is found that the tensile strengths decrease by about 100 MPa for 0Cr stainless steel tubes as the temperature increases by 230 °C, but less than 50 MPa for 1Cr stainless steel tubes, indicating that the tensile strength of 0Cr stainless steel tube has more significant temperature dependence. The reason for these differences in microstructure and mechanical properties probably is higher carbon content in 1Cr stainless steel tube impedes the microstructure evolution, leading to a higher thermal stability of microstructure, and then reduces the impact of solution temperature on tensile strength.

Figure 7 shows the microstructures of two stainless steel tubes after solution at the temperature of 1150 °C for various holding time. It is found that the grain sizes of 0Cr stainless steel tubes, which are over 50 μm, have not been obviously changed by the increasing holding time and are larger than those of 1Cr stainless steel tubes, as shown in Fig. 7a–d. On the other hand, Fig. 7e–h exhibit that the grain sizes of 1Cr stainless steel tubes increase slightly with the holding time increasing from 10 min to 40 min. This result can also accords with the inference mentioned above-the 1Cr stainless steel exhibits higher microstructure stability during solution process. It is deduced that the microstructure evolutions of these two stainless steels are mainly controlled by solution temperature instead of holding time. So the solution temperature should be considered as a key parameter to adjust the performances during the design process of manufacturing method for the rivet sleeve.

Figure 8 presents the time dependences of the mechanical properties for two stainless steel tubes after solution at different temperatures. Under various solution condition, the tensile strengths of 1Cr stainless steel tube are scarcely influenced by holding time (only decrease about 5 MPa), leading to the relatively better thermal stability of mechanical properties for 1Cr stainless steel tubes. This result also

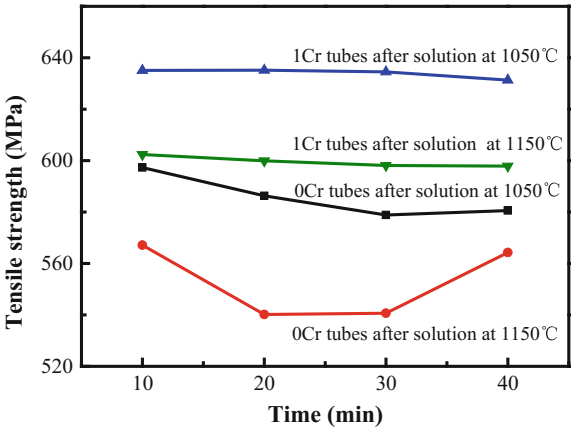

Fig. 8 Comparison of tensile strength for 0Cr and 1Cr stainless steel tubes after solution and furnace cooling

agrees with the microstructure evolution observed above. For 0Cr stainless steel tubes, their tensile strengths gradually decrease as the holding time increases, but when the holding time exceeds 30 min, their tensile strengths begin to increase. Especially, this phenomenon become more obvious at higher solution temperature (T = 1150 °C). The tensile strength of stainless steel is not only controlled by the grain size, but also determined by dislocation configuration in the grains. The dislocations produced by dislocation sources slip to the specimen surface and generate plastic deformation during loading process. A great part of these dislocation sources consist of microstructural defects. For a long heating process, the activated atoms have enough time for long distance transitions and rearrangements, causing that the microstructural defects are annihilated at the solution stage, which reduces the number of mobile dislocations in the grains and increases the plastic deformation resistance. The reason why the 0Cr stainless steel tubes after solution for a long time (t = 40 min) have higher tensile strengths probably because that the residual dislocations after solution cannot support the need of plastic deformation, resulting in an increasing strengths.

The yield strength is also an important parameter for rivet to ensure the lower installation difficulty and better installation quality. Similar to tensile strengths, the yield strengths of these two stainless steel tubes both decrease with increasing solution temperature, meanwhile, the yield strengths of 0Cr stainless steel tubes are obviously lower than those of 1Cr stainless steel tubes, as shown in Fig. 9a. Moreover, Fig. 9b exhibits the relationships between yield strengths and holding time for 0Cr and 1Cr stainless steel tubes. It can be seen that the yield strengths of the two tubes slightly decrease as the holding time increased, when the solution temperature is 1050 °C. However, the effects of holding time on yield strengths for two stainless steel tubes can be ignored at the solution temperature of 1150 °C. Besides, the yield strengths of 0Cr stainless tubes are always lower than those of 1Cr stainless steel tubes. Lower yield strength of 0Cr stainless steel tube reduces the installation force, which means that the foot can be formed at the bottom of rivet

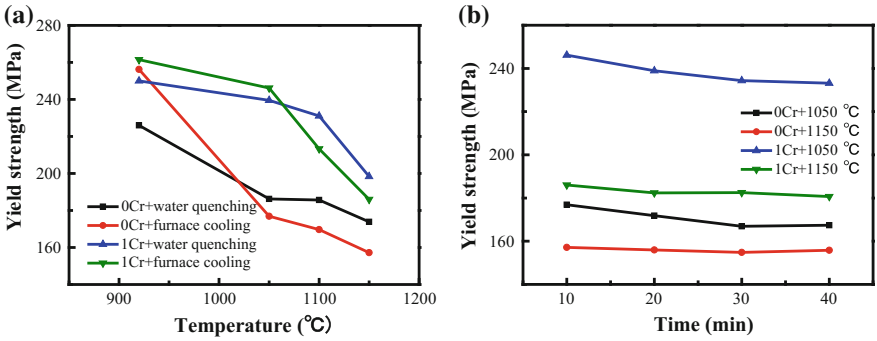

Fig. 9 Yield strengths of 0Cr and 1Cr stainless steel tubes: **a** two tubes after solution for 10 min, then cooled by different methods; **b** two tubes after solution for different time at 1050 and 1150 °C

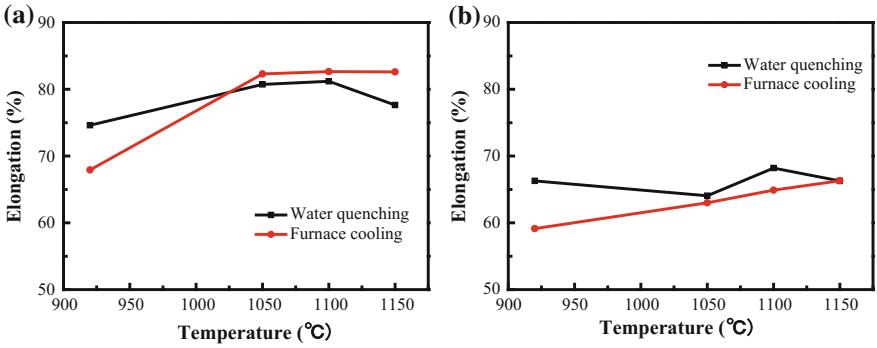

Fig. 10 Elongation of two stainless steel tubes under different experimental temperatures: **a** 0Cr stainless steel tubes; **b** 1Cr stainless steel tubes

sleeve more easily and avoids the fracture of rivet pin prematurely. For these 0Cr stainless steel tubes, the holding time has only minor influence on yield strength compared with the tensile strength, particularly at higher solution temperature (T = 1150 °C). Although a large number of microstructural defects and dislocations disappear due to the atom rearrangement induced by high temperature during long heating stage, the residual dislocations can support the initial plastic deformation. Thus, different from the tensile strengths, the yield strengths of 0Cr stainless steel tubes have not distinct holding time dependences.

The stainless steel tube used to produce the rivet sleeve should have better plasticity, which is beneficial to improve the installation quality and service life. Figure 10 shows the relationships between elongations of the two stainless steel tubes after solution. It can be seen that the elongation changes ΔA (where $\Delta A = A_{max} - A_{min}$) of these two stainless steel tubes after water quenching are relatively smaller at the temperature range of 920–1150 °C (ΔA ≈ 6% for 0Cr, and

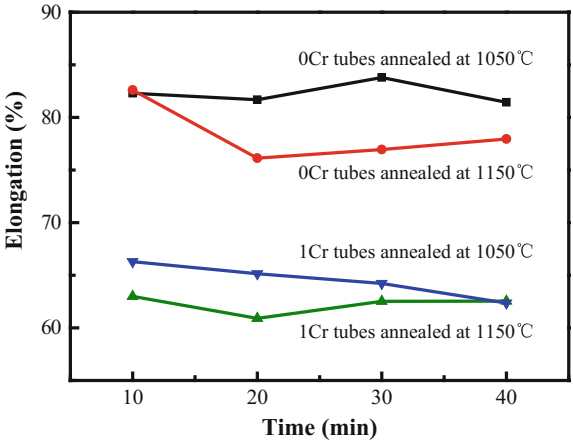

Fig. 11 Elongation versus holding time for two stainless steel tubes after solution at different experimental temperatures

4% for 1Cr). However, the elongations of the two stainless steel tubes undergoing furnace cooling not only increase with increasing solution temperature, but also have wider range ($\Delta A \approx 15\%$ for 0Cr, and 7% for 1Cr). That means the process parameters of rivet sleeve can obtain relatively larger adjustment range by furnace cooling. Besides, the comparison results also indicate that the 0Cr stainless steel tubes after solution possess higher elongation than 1Cr stainless steel tubes. The influences of holding time on elongations for the two stainless steel tubes have been plotted in Fig. 11. The test results reveal that the elongations of these two stainless steel tubes have no obvious time dependences. Although the elongations of 0Cr stainless steel tubes commonly higher than those of 1Cr stainless steel tubes undergoing solution, the elongations of the two stainless steel tubes exhibit no distinct variations with increasing holding time ($\Delta A \approx 6\%$ for 0Cr stainless tube, and 4% for 1Cr stainless tube).

Conclusion

The effects of heat treatment process on the microstructure evolutions and mechanical properties for 0Cr and 1Cr stainless steel tubes have been investigated in order to support the need of rivet sleeve manufacturing. The results are summarized as follows:

(1) For 0Cr stainless steel tubes, there is obvious grain coarsening when the solution temperature reaches 1050 °C. The grain sizes of 1Cr stainless steel tubes do not increase significantly, until the solution temperature exceeds 1100 °C. The two stainless steel tubes have no evident cooling rate dependences of microstructure evolutions.

(2) The microstructures of 0Cr stainless steel tubes, whose grain sizes are approximately 50–100 μm, have not been changed by the increasing holding time. But the grain sizes of 1Cr stainless steel tubes slightly increase with the holding time increases from 10 min to 40 min. It is clear that the microstructure evolutions of these two stainless steels are mainly controlled by solution temperature instead of holding time.
(3) The tensile strengths elongations of 0Cr stainless steel tubes exhibit stronger temperature and time sensitivity than those of 1Cr stainless steel tubes. Meanwhile, their yield strengths both decrease with increasing solution temperature. Compared with 1Cr stainless steel tubes, 0Cr stainless steel tubes possess better plasticity, which is beneficial to improve the installation quality and service life.

References

1. C.A. Cheatham, C.F. Acosta, D.P. Hess, Tests and analysis of secondary locking features in threaded inserts. Eng. Fail. Anal. **16**, 39–57 (2009)
2. D.P. Hess, O.P. Keifer, C.B. Moody, Tests on loosening of aviation threaded fasteners with different washer configurations. J. Fail. Anal. Preven. **14**, 683–689 (2014)
3. G.Q. Yang, J. Hong, L.B. Zhu, B.T. Li, M.H. Xiong, F. Wang, Three-dimensional finite element analysis of the mechanical properties of helical thread connection. Chin. J. Mech. Eng. **26**, 564–572 (2013)
4. M. Mansoor, N. Ejaza, Fatigue failure of an aircraft wings due to fitting error in hi-locks. Eng. Fail. Anal. **16**, 2195–2201 (2009)
5. W.C. Wilson, M.D. Rogge, B.H. Fisher, Fastener failure detection using a surface acoustic wave strain sensor. IEEE Sens. J. **12**, 1993–2000 (2012)
6. J. Yan, M. Gao, X.Y. Zeng, Study on microstructure and mechanical properties of 304 stainless steel joints by TIG, laser and laser-TIG hybrid welding. Opt. Lasers Eng. **48**, 512–517 (2010)
7. A.N. Isfahany, H. Saghafian, G. Borhani, The effect of heat treatment on mechanical properties and corrosion behavior of AISI420 martensitic stainless steel. J. Alloys Compd. **509**, 3931–3936 (2011)
8. N.H. Hoang, M. Langseth, R. Porcaro, A.G. Hanssen, The effect of the riveting process and aging on the mechanical behavior of an aluminum self-piercing riveted connection. Eur. J. Mech. A Solids **30**, 619–630 (2011)
9. R. Porcaro, A.G. Hanssen, M. Langseth, A. Aalberg, The behavior of a self-piercing riveted connection under quasi-static loading conditions. Inter. J. Solids Struct. **43**, 5110–5131 (2006)
10. J.L. Lv, H.Y. Lu, Comparison of corrosion properties of passive films formed on phase reversion induced nano/ultrafine-grained 321 stainless steel. App. Surf. Sci. **280**, 124–131 (2013)
11. M.B. Leban, R. Tisu, The effect of TiN inclusions and deformation-induced martensite on the corrosion properties of AISI 321 stainless steel. Eng. Fail. Anal. **33**, 430–438 (2013)

Effect of Post-weld Heat Treatment on Microstructure and Mechanical Properties of 309L/E5015 Fusion Zone of Bimetal Lined Pipe Weld

Dongming Liu, Yuheng Ning, Tao Jiang and Xu Sun

Abstract The effect of different post-weld heat treatment (PWHT) on microstructure, low temperature impact toughness fracture morphology and hardness, of 309L/E5015 fusion zone of bimetal lined pipe weld was investigated by using optical microscopy (OM), electron probe microscope analysis (EPMA), scanning electron microscopy (SEM) and hardness test. The results showed that the microstructure of the fusion zone of the 309L/E5015 under non thermal treatment was martensite, and the lath was fine acicular. At 550 °C, the lath of martensite was bulky, and the feature was obvious; at 650 °C, the microstructure was tempered martensite, and the microstructure was obviously refined; at 750 °C, the microstructure was further refined and became multilateral; at 850 °C, the martensite microstructure was gradually analyzed, and the carbides were dispersed. With the increase of heat treatment temperature after welding, the element distribution gradient of fusion zone slowed down and the hardness first decreased and then increased. At 750 °C, the weld had the best toughness, because the lath of martensite was multilateral, and the hardness reached the qualified range, and the low temperature impact energy was maximum than other temperatures.

Keywords Welded joint · 309L/E5015 fusion zone · Post-weld heat treatment

D. Liu (✉) · Y. Ning · T. Jiang · X. Sun
Datang Northeast Electric Power Test & Research Institute,
Changchun 130012, China
e-mail: dongming_liu@163.com

Y. Ning
e-mail: 191299526@qq.com

T. Jiang
e-mail: 380541075@qq.com

X. Sun
e-mail: 1195985540@qq.com

© Springer Nature Singapore Pte Ltd. 2018

Y. Han (ed.), *Advances in Materials Processing*, Lecture Notes in Mechanical Engineering, https://doi.org/10.1007/978-981-13-0107-0_42

Introduction

With the growth of global energy demand, oil and natural gas exploitation trend toward the development of high corrosion, resulting in the production environment is worse which makes the service life of ordinary production equipment shorter [1, 2]. If the inhibitor is not stable, the effect of preventing corrosion is not obvious; if using the lining coating, the action of preventing corrosion is closely related to its performance, and the defects of the lining coating can promote corrosion [3, 4]. So the high corrosion resistant alloy material is the most commonly used during the process of exploitation of oil and natural gas. Because the cost of high alloy material is very high, it is greatly limited [5]. And the corrosion resistance of non-metal pipeline is very good, but its mechanical properties are usually not up to the requirements of the use of oil or gas exploration. Research shows that the double metal composite pipe is one of the most effective way to solve the corrosion of metal [6–9]. The lining is generally 1.5–3 mm high alloy and can be selected according to the corresponding material corrosion condition, and basic pipeline generally use carbon steel or low alloy tube. The corrosion resistance of double metal composite pipe is not lower than the high alloy pipe, and its strength is not lower than carbon steel pipe, but its price is only about half of the high alloy pipe, and its application market is very broad [10, 11].

At present, the ground pipeline and water injection pipeline in the Daqing oilfield, Changqing Oilfield and Tarim Oilfield pipe began to use the double metal composite pipe, but it is still in the initial stage and its use is a limited range. The reason is that the physical properties between the double metal composite pipe base tube and a liner is large to lead to welding difficulties. In the production of composite pipe technology, the United States announced the APl5LD at the end of twentieth Century and don't mention for the double metal composite pipe butt welding. The relevant domestic lined composite pipe welding refers to NB/T 47014-2011 and GB/T 13149-2008, and do not conform to the actual situation of bimetal composite pipe with lining only one side welding. Study on the preparation at home and abroad have focused almost exclusively on the composite pipe system, for its less welding process research.

Welding of the double metal pipe adopts corrosion resistant alloy welding material which composition close to lining layer and can be divided into three layers including root layer, transition layer and capping layer. The welding process is low in cost and high in efficiency. This paper analyzes the influence of post-weld heat treatment on the fusion zone of 309L/E5015, and provides a theoretical basis for the diffusion layer of bimetal composite pipe, which is of great practical value [12].

Experimental Material and Procedures

The20#/316L bimetal lined pipe in the experiments is Φ355 mm × (11 + 2)mm, and the measured chemical composition is given in Table 1. In order to reduce residence time at high temperature TIG welding is used to weld surface layer because of its small heat input. The welding method of the transition layer adopts TIG to reduce the dilution rate. SMAW is used to fill the cap layer to improve the production efficiency. The weld cross section is given in Fig. 1 and the welding process is given in Table 2. And the chemical compositions of the welding material are shown in Table 3 Post weld heat treatment process is given in Table 4.

Table 1 Chemical composition of L415/316L bimetal lined pipe steel (mass fraction, %)

	C	Cr	Ni	Mo	Si	Mn	P	S	Fe
20#	0.14	0.06	0.03	0.01	0.34	1.40	0.01	0.001	Bal.
316L	0.04	16.32	10.03	2.04	0.64	1.13	0.045	0.001	Bal.

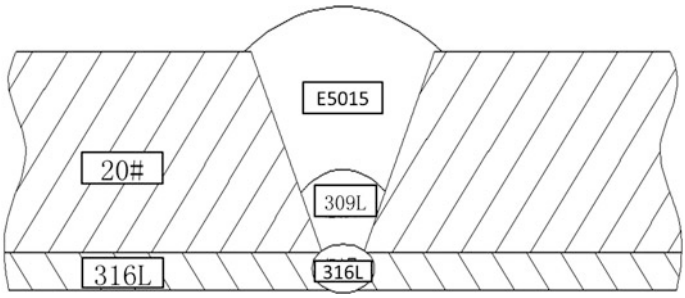

Fig. 1 Weld cross section

Table 2 Welding process

Welding materials				Welding process	Back protection way
Sealing layer	Root layer	Transition layer	Filling/ capping layer		
ER309	ER316L	ER309L	E5015	GMAW + FCAW	100% Ar

Table 3 Chemical composition of L415/316L bimetal lined pipe steel (mass fraction, %)

	C	Cr	Ni	Mo	Si	Mn	P	S	Fe
ER309L	0.12	23.83	13.26	0.75	0.34	2.05	0.03	0.03	Bal.
E5015	0.10	9.25	0.4	1.03	1.2	1.0	0.04	0.03	Bal.

Table 4 Post weld heat treatment process 309L/E5015 fusion zone

Sample number	Heat treatment temperature (°C)	Holding time (h)	Rise and fall temperature speed (°C/h)
1	0	0	0
2	550	2	120
3	650		
4	750		
5	850		

The corrosive is $FeCl_3$ (10 g)/HCl (24 ml) and distilled water (96 ml). And the analysis of microstructure and chemical composition of the fusion zone were investigated by optical microscope and electron probe. Low temperature impact test measured Weld impact absorbing energy, and specimen size is 10 mm * 10 mm * 55 mm. The hardness was investigated by Vickers, which test load is 98 N.

Results and Discussion

Microstructure

Figure 2 shows the microstructure of the fusion zone of 309L/J507 under non thermal treatment, 550, 650, 750 and 850 °C heat treatment temperatures. The microstructure of the fusion zone of the 309L/E5015 under non thermal treatment is martensite shown in Fig. 2a, and the lath is fine and acicular, and the feature is obvious. At 550 °C, the lath of martensite is bulky, and this is due to the high Mo content of welding material shown in Fig. 2b. Figure 2c shows the microstructure is tempered martensite, and the microstructure is obviously reduced to acicular at 650 °C. At 750 °C, the microstructure is further refined and becomes multilateral, and the morphology of martensite is difficult to be observed under the optical microscope shown in Fig. 2d. At 850 °C, the martensite microstructure gradually decomposed, and it's hard to see the martensitic morphology. There is a large number of small carbide depositing to separate out and diffuse distribution shown in Fig. 2e.

Analysis of Chemical Components

Figure 3 shows the path of line scanning analysis. Figure 4 shows results of line scanning analysis. The distribution of elements presents ladder shaped. The main reason is that the content of Ni and Cr in 309L is significantly higher than those in E5015. The graded distribution depends on the size and thickness of weld bead and

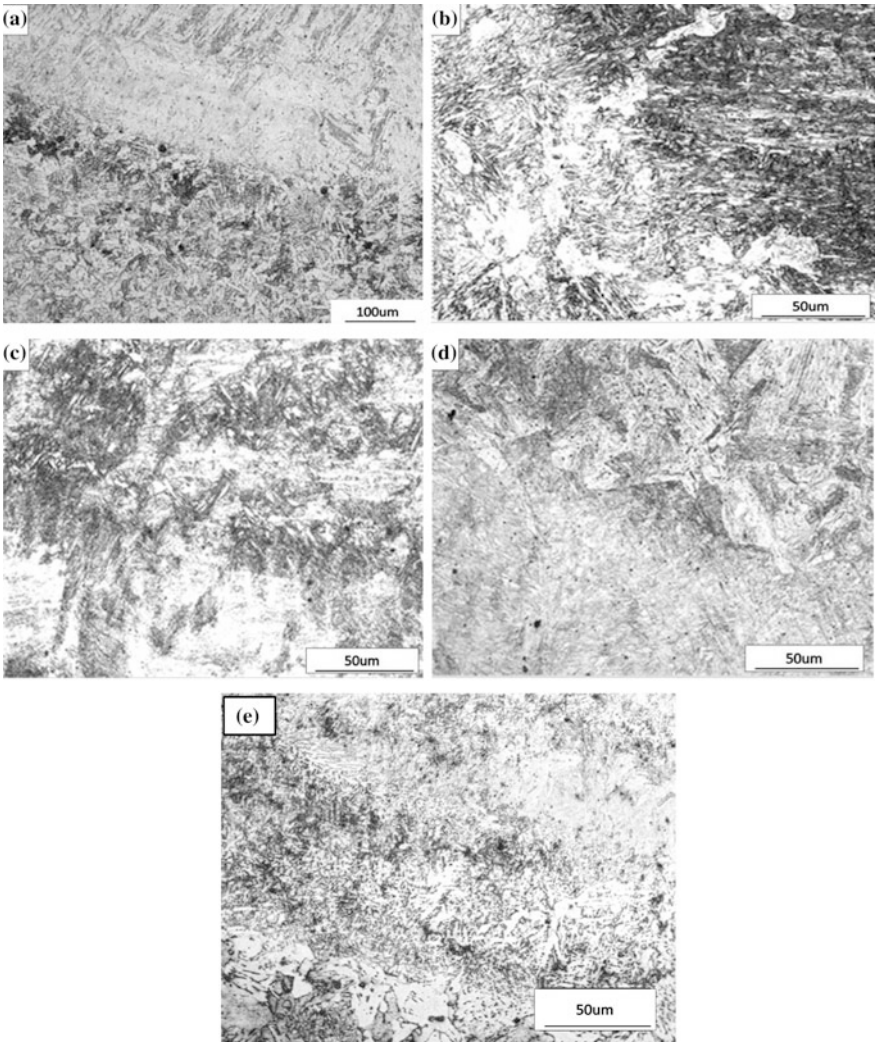

Fig. 2 Microstructure of the fusion zone of 309L/J507 under different heat treatment temperature. **a** Non thermal treatment; **b** 550 °C; **c** 650 °C; **d** 750 °C; **e** 850 °C

the welding heat input. With the increase of heat treatment temperature the distribution of alloy element in the fusion zone of 309L/E5015 becomes flat and the element diffusion region becomes wider because the temperatures over 500 °C is in the sensitization temperature range of welding. Under the action of welding thermal cycle, carbon is dissolved in austenite in supersaturated state. The supersaturated carbon is soluble in austenite under the effect of welding thermal cycle resulting in that the organization becomes unstable. When heated to 850 °C the gradient of distribution of elements decreases. It is mainly that the carbon element diffuses

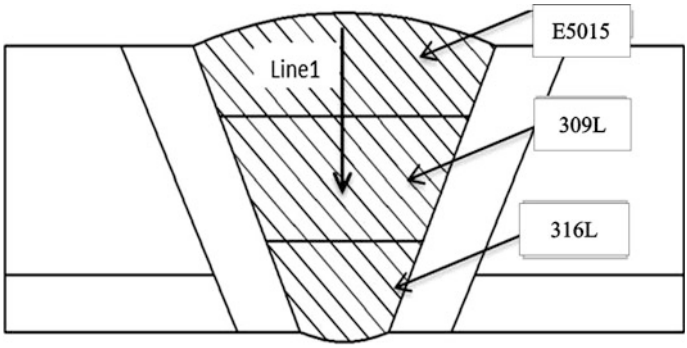

Fig. 3 Path of line scanning analysis

toward the grain boundary, then C and chromium form chromium–carbon compounds depositing in the grain boundary.

Impact Test

The results of Impact test are shown in Table 5. With the increase of heat treatment temperature impact absorbing energy value increases first and then decreases. When the heat treatment temperature is 750 °C the impact absorbing energy value is the largest and 91 J. It is proved that the weld has the best toughness at 750 °C of the heat treatment temperature.

Impact Fracture Appearance

The fracture appearance of the fusion zone of 309L/J507 is shown in Fig. 5. The fracture appearance of unheated fusion zone is dissociation fracture. With the increase of heat treatment temperature, the fracture characteristics gradually change from dissociation to dimple. At 750 °C, the fracture of the fusion zone is all changed into dimple fracture. The reason is that the Heat treatment temperature at 750 °C leads to martensite become more fine and higher toughness. Continuing to improve heat treatment temperature the fracture presents a quasi-cleavage feature again. Because the martensite structure decomposes gradually and there are more fine carbides precipitated.

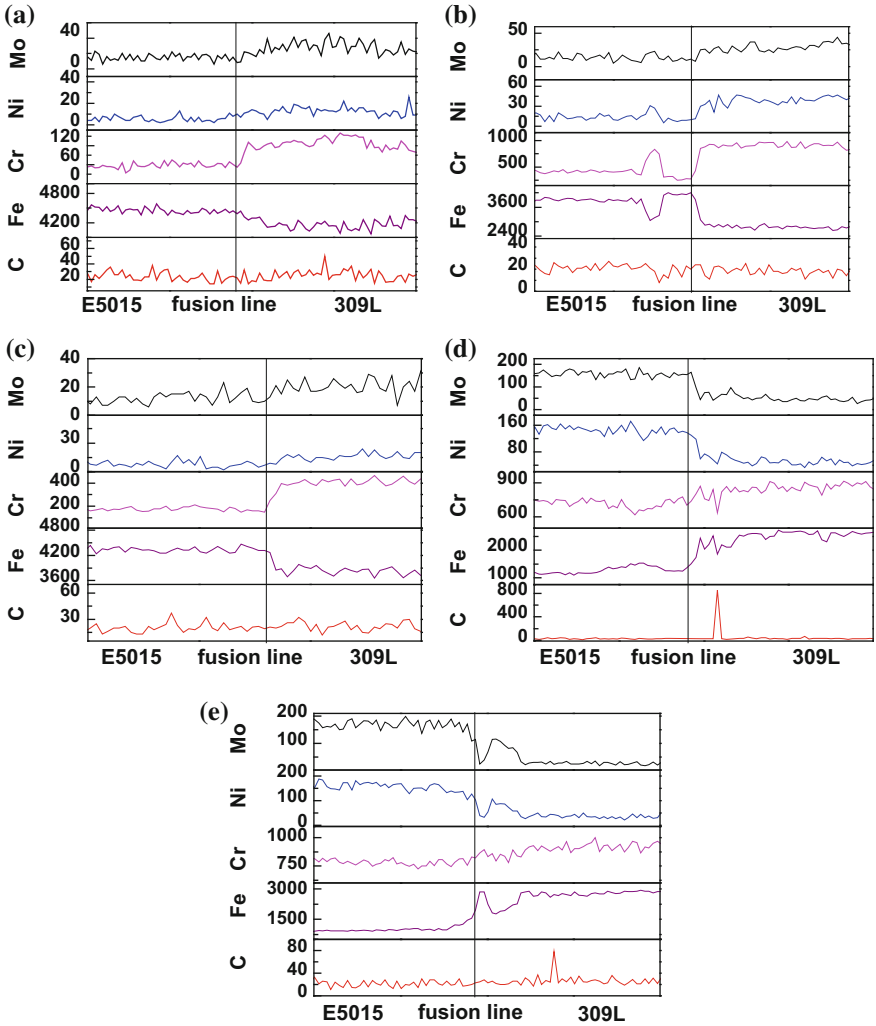

Fig. 4 Results of line scanning analysis under different heat treatment temperature. **a** Non thermal treatment; **b** 550 °C; **c** 650 °C; **d** 750 °C; **e** 850 °C

Table 5 Results of Impact test

Heat treatment temperature (°C)	Impact absorbing energy value AKV, −20 °C/J
Non thermal treatment	56
550	71
650	83
750	91
850	67

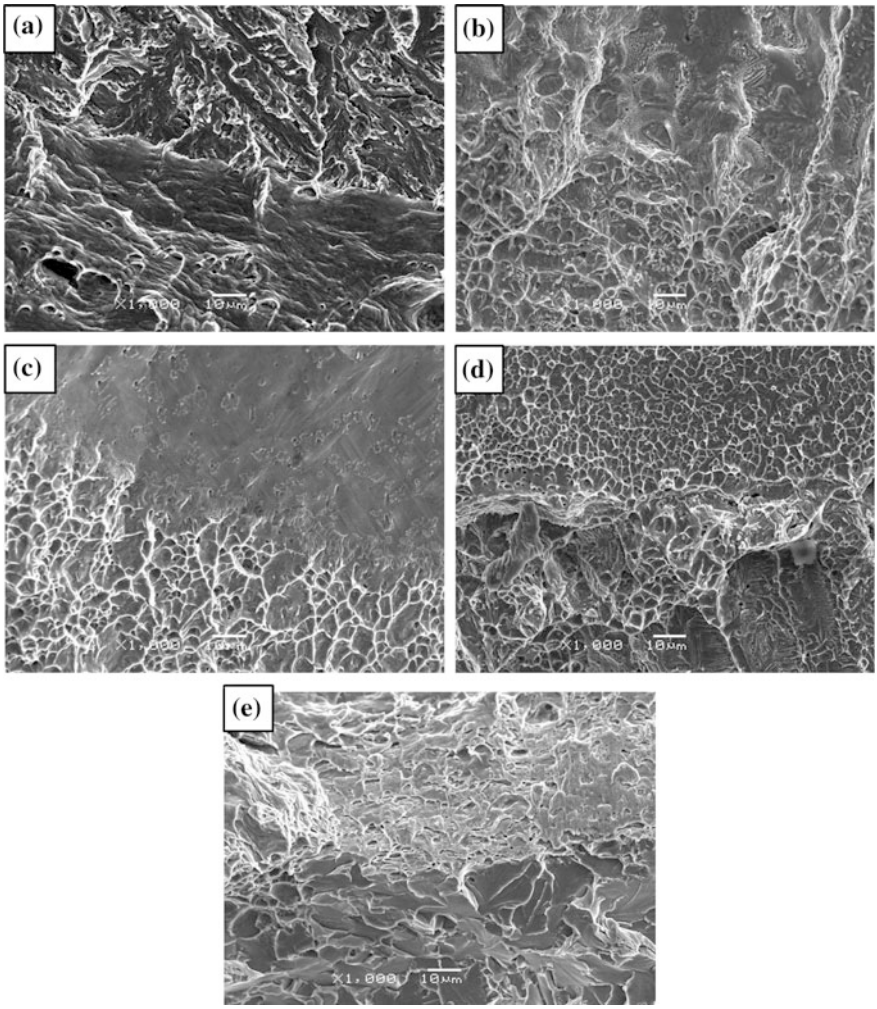

Fig. 5 Fracture appearance of the fusion zone of 309L/J507 under different heat treatment temperature. **a** Non thermal treatment; **b** 550 °C; **c** 650 °C; **d** 750 °C; **e** 850 °C

Analysis of Hardness

The results of the hardness of the fusion zone of 309L/E5015 under non thermal treatment, 550, 650, 750 and 850 °C heat treatment temperature is shown in Table 6.

The curve of hardness is shown in Fig. 6. From the curve change of Fig. 6, the hardness of the 309L side firstly increases and then decreases with the increase of the heat treatment, which is related to the change of the microstructure. And the

Table 6 Results of the hardness of the fusion zone of 309L/E5015 under different heat treatment temperature

Distance from the fusion line/mm	Hardness/HV0.2				
	Non thermal treatment	550 °C	650 °C	750 °C	850 °C
−2.0	175.3	151.2	336.5		414.8
−1.6	193.8	149.5	317.1	298	398.7
−1.2	196.0	150.7	301.0	291	413.5
−0.8	196.0	160.9	308.0	289	370.2
−0.4	207.8	164.4	296.8	285	398.7
0	215.3	204.5	257.5	245	309.4
0.4	282.2	252.1	263.7	261.7	392.2
0.8	300.6	301.2	362.3	342.2	355.5
1.2	398.7	358.5	365.1	354.0	367.9
1.6	335.5	322.9	394.3	362.7	396.1
2.0	392.2	385.1	386.2	356.0	396.1

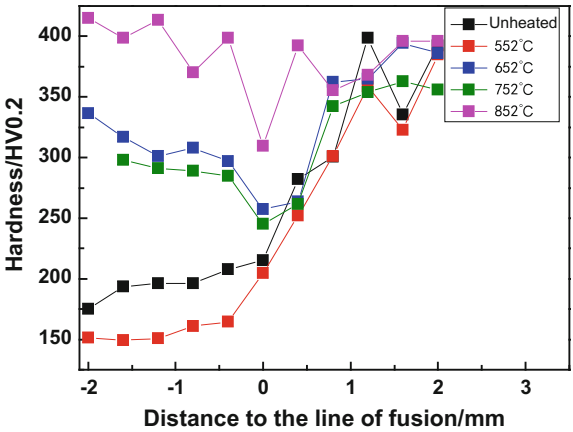

Fig. 6 Curve of hardness

change of hardness of the 309L side is no regularity. At550 °C, the hardness decreases, because the high density dislocation of martensite decreases and the internal stress decreases. At 650 °C, the microstructure is tempered martensite, and the grain size becomes fine to result in hardness increasing. When the heat treatment temperature reaches 750 °C, the lath of martensite became multilateral and fine, and the hardness decreased to the qualified range. At this heat treatment temperature, the complete dislocation network is formed in the lath, which retains the strengthening effect of martensite forming the metastable structure and the excellent toughness. At 850 °C, the hardness of fusion zone is very high, because the martensite structure decomposes gradually and there are more fine carbides precipitated to increase hardness.

Conclusions

(1) The microstructure of the fusion zone of the 309L/E5015 under non thermal treatment is martensite, and the lath is bulky. With the increase of heat treatment temperature the martensite microstructure is fine and distribution of alloy element becomes flat. At 750 °C, the microstructure is finer and the morphology of martensite is difficult to be observed under the optical microscope. At 850 °C, the martensite microstructure gradually decomposed, and it's hard to see the martensitic morphology. There is a large number of small carbide depositing to separate out and diffuse distribution.
(2) With the increase of heat treatment temperature impact absorbing energy value increases first and then decreases. When the heat treatment temperature is 750 ° C the weld has the best toughness.
(3) The hardness of the 309L/E5015 fusion zone presents irregular changes. When the heat treatment temperature reaches 750 °C, the lath of martensite became multilateral and fine, and the hardness decreased to the qualified range.

References

1. M.X. Lu, Z.Q. Bai, X.W. Zhao et al., Actuality and typical cases for corrosion in the process of extraction, gathering, storage and transmission for oil and gas. J. Corros. Protect. **23**(3), 105–113 (2002)
2. M.B. Kermani, A. Morshed, Carbon dioxide corrosion in oil and gas production-a compendium. J. Corros. **59**(8), 659–683 (2003)
3. M.H. Jin, The research method of corrosion inhibitor of pipeline. J. Mater. Protect. **06**, 26–29 (1993)
4. F.M. Song, A comprehensive model for predicting CO_2 corrosion rate in oil and gas production and transportation systems. J. Electrochim. Acta **55**(3), 689–700 (2010)
5. B.S. Huang, Z.K. Wang, State of art and trends of Internal coating technology of oil and gas pipeline. J. Corros. Sci. Protect. Technol. **04**, 345–348 (2012)
6. J.C. Qi, M.P. Wang, Characteristic and application of the pipe that carbon steel inside lining stainless steel compounds. J. China Build. Mater. Sci. Technol. **3**, 23–25 (2005)
7. F. Yu, J.P. Qin, Application of dual metal pipe in pipe line service. J. Steel Pipe **29**(1), 34–36 (2000)
8. M.A. Spence, C.V. Roscoe, Bi-metal CRA-lined pipe employed for north sea field development. J. Oil Gas J. **97**(18), 80–88 (1999)
9. W.C. Chen, C.W. Petersen, Corrosion performance of welded CRA-lined pipes for flow lines. J. SPE Prod. Eng. **7**(4), 375–378 (1992)
10. J.B. Liu, J.T. Jing, S.Q. Bao et al., Effect of heat treatment on microstructure and mechanical properties of bimetal clad pipe X60/2205. J. Mater. Heat Treat. **04**, 125–127 (2009)
11. A.M. Torbati, R.M. Miranda, L. Quintino et al., Optimization procedures for GMAW of bimetal pipes. J. Mater. Process. Technol. **211**(6), 1112–1116 (2011)
12. N.L. Wang, X.D. Pan, J. Xue, Welding procedure and resistant to corrosion properties for welded joint of 20/0Cr18Ni9 clad pipe. J. Weld. Joining **5**, 23–26 (2003)

Efficient Water-Based Rust Inhibitor for Surface Treatment of Iron and Steel

Kunkui Wu, Jinfeng Bai, Yang Liu and Yan Zhang

Abstract In order to improve anti-rust effect on hot-rolled pickling plate for cars, a new nontoxic and efficient water-based rust inhibitor was developed. The optimal compositions of the rust inhibitor were determined through orthogonal test. In main rust inhibitor, the mass ratio of potassium zirconium fluoride, sebacic acid, boric acid, monoethanolamine, and triethanolamine was 5:5:1:16:8. 100 g concentrated solution contained 0.1 g sodium phosphate, 10 g urotropine, 10 g polyethylene glycol and polyvinyl alcohol as auxiliaries. The water-based rust inhibitor was nitrite-free, non-toxic, environmentally friendly and well-stable. The promoters and polymer film forming agents effectively enhanced corrosion resistance of anti-rust film. The 8% working solution of the water-based rust inhibitor had good rust resistance for hot-rolled steel plate under wet and hot conditions of RH > 0.95 and 50 °C.

Keywords Water-based rust inhibitor · Zirconium compound · Hot-rolled steel plate · Orthogonal design · Environmental friendliness

Introduction

The metal is prone to rust by chemical or electrochemical action of oxygen, water and other materials under certain conditions in the atmosphere. Surface rust of hot-rolled steel plate is the most concerned issue for the quality of products. The corrosion seriously affects phosphating and coating processing of automobile plate,

K. Wu (✉) · J. Bai · Y. Liu
University of Science and Technology LiaoNing, Anshan Liaoning 114001, China
e-mail: wu_kunkui@sina.com

J. Bai
e-mail: baijf863@163.com

Y. Liu
e-mail: ly780122@163.com

Y. Zhang
Beijing of Angang Steel, Beijing 100001, China

© Springer Nature Singapore Pte Ltd. 2018

Y. Han (ed.), *Advances in Materials Processing*, Lecture Notes in Mechanical Engineering, https://doi.org/10.1007/978-981-13-0107-0_43

so the development of high-efficiency, environmentally friendly water-based rust inhibitor is urgently needed. At present anti-rust oil is often used for corrosion protection of hot-rolled plate. Anti-rust oil can keep longer protection of the products when they are placed in the factory. It not only increases great costs but also makes oil removal processing difficult. The water-based rust inhibitors for steel plate mostly contain sodium nitrite which are easy to flow away from metal surface, form frost on the metal surface after water volatilizing, and nitrite is highly toxic and pollute environment [1].

Research on high-efficiency and environmentally friendly water-based rust inhibitor has attracted extensive attention at home and abroad. Some study achievements were reported such as drawing effective compositions of rust inhibitor from abundant natural resources or agricultural by-products [2]. Based on potassium zirconium fluoride and amine compounding with other corrosion inhibitors and surfactant, a high-efficiency, environmentally friendly water-based rust inhibitor for hot-rolled steel plate had been developed. By means of actual car phosphating and production test, it was verified that rust resistance period was not only longer but also easy to be treated for automotive plate products.

Experimental

Apparatus

Electrothermal constant-temperature oven (202), dryer (φ250 mm), salt-fog cabinet.

Materials

Hot-rolled steel plate (size 100 mm × 100 mm × 2 mm), 20% hydrochloric acid, absolute ethyl alcohol.

Reagents

Potassium zirconium fluoride (PZF), ricinoleic acid, orthoboric acid, monoethanolamine, triethanolamine, hexamethylenetetramine, trisodium phosphate, polyethylene glycol, polyvinyl alcohol, alkylphenol ethoxylates.

Sample Retreatment Process

The hot-rolled samples were immersed into dilute 20% hydrochloric acid for 20 min, then water washed and hot air blowing dried. The anhydrous ethanol-absorbent cotton was used to wipe clean. The samples were cooled to

25 °C, and immersed in 8% antirust solution for 30 s. The samples were hung in electrothermal constant temperature oven at 50 °C for 15 min to form a coat of protective film.

Preparation of Anti-rust Agent

Water-soluble PZF is suitable for preparation of water-based rust inhibitor. It can form deposited film on surface of steel plate to prevent the steel from rusting. Based on the film formation mechanism, long carbon chain dicarboxylic organic, orthoboric acid, monoethanolamine, triethanolamine were mixed to make up rust inhibitors. They were compounded under heating at 100 °C and magnetic stirring reflux for 2 h. Then the diluted solution of 3% with deionized water was used as basic fluid. Orthogonal experimental design with five factors and four levels for preparing the main corrosion inhibitor are shown in Table 1.

Hexamethylenetetramine, trisodium phosphate, polyethylene glycol, polyvinyl alcohol were added into deionized water at 50 °C, then stirring them to be dissolved completely. 100 g diluted assistant rust inhibitor were compounded to 8% working liquid. According to optimizing the proportion of L_{16} (4^5) orthogonal experiment, the main assistant agent and surfactant were mixed successively into 40 °C deionized water and kept for 30 min. The assistant rust inhibitor orthogonal experimental factors and levels are shown in Table 2.

Table 1 Factors and levels of orthogonal test for main rust inhibitor

Levels	Factor A	Factor B	Factor C	Factor D	Factor E
	PZF [g]	Ricinoleic acid [g]	Orthoboric acid [g]	Monoethanolamine [g]	Triethanolamine [g]
1	1	1	0	1	1
2	2	2	1	8	8
3	5	5	3	16	16
4	8	8	5	24	24

Table 2 Factors and levels of orthogonal test for assistant rust inhibitor

Levels	Factor F	Factor G	Factor H	Factor I
	Trisodium-phosphate [g]	Hexamethyle-netetramine [g]	Polyethylene glycol [g]	Polyvinyl alcohol [g]
1	0.1	10	0	0
2	0.5	6.5	2	1.5
3	0.9	3.5	3	3.5
4	1.25	0	5	5

Antirust Performance Evaluation

(1) Resistance to heat and humidity: A clean cloth was placed on the plate in a dryer,until the steam rose evenly. The air-dried sample was put into electrothermal constant-temperature dry oven at 65 °C, and covered a lid. Then the resistance effect of the heat and humidity was observed after 40 h [3].
(2) Tafel polarization performance: The polarization curve was tested by potentiostatic anodic polarization method. Saturated calomel electrode was used as a reference electrode, platinum electrode was used as an auxiliary electrode, and the sample was used as a working electrode. 3% NaCl solution with distilled water was configured as electrolyte, and high purity nitrogen gas was piped for 10 min. At last electrode was put into solution with linear scanning speed of 0.005 mV/s.
(3) Anti-rust film morphology: The surface morphology was observed with SEM-JEd-6380 scanning electron microscope, and the film formation mechanism of rust inhibitor was analyzed on surface of steel plate [4].

Results and Discussions

Distribution of Water-Based Rust Inhibitor

The orthogonal test results of main rust inhibitor are listed in Table 3. The optimal component of main reagent is $A_3B_3C_1D_3E_2$ which means A(PZF):B(ricinoleic acid):C(orthoboric acid):D (monoethanolamine):E (triethanolamine) = 5:5:1:16:8. The optimal proportion test showed that the red rust was built for average 145 h. Range order is D > A > B > C > E And the solution pH value was adjusted to 9.5 (that is steel rust effective pH range). Both composition of onoethanolamine and PFZ played a very important role. Nitrogen atoms of monoethanolamine and triethanolamine have lone pair electrons that can make up coordinate bond formation with empty orbital of metal atoms or ions to be adsorbed chemically on the metal surface [5]. The amide generated with ricinoleic acid and orthoboric acid is a kind of effective rust inhibitor. In order to make up film defects of the main agent, trisodium phosphate was used directly or indirectly to oxidize metal, so that metal oxide film was formed on surface to prevent corrosion reaction.

The orthogonal experiment results of assistant rust inhibitor are shown in Table 4. The optimized quality ratio of assistant reagent is $F_1G_1H_4I_4$, which means quality of F(trisodium phosphate), G(hexamethylenetetramine), H(polyethylene glycol), I(polyvinyl alcohol) in 100 g concentrate were 0.1, 10 g and 5, 5 g, respectively. Experiment was carried out in accordance with 8% working liquid for rust protection, so optimum mass fraction was trisodium phosphate 0.008%, hexamethylenetetramine 0.8%, polyethylene glycol 0.4%, polyvinyl alcohol 0.4%. The optimal ratio test showed that average non-rust size of steel plate was 90%. Range sequence is G > F > H and I, so it suggests that hexamethylenetetramine play main role for rust resistance.

Table 3 Result of orthogonal test for main rust inhibitor

Factor	A	B	C	D	E	t (corrosion) [h]
1	1	1	1	1	1	2
2	1	2	2	2	2	72
3	1	3	3	3	3	145
4	1	4	4	4	4	80
5	2	1	2	3	4	90
6	2	2	1	4	3	114
7	2	3	4	1	2	3
8	2	4	3	2	1	5
9	3	1	3	4	2	110
10	3	2	4	3	1	120
11	3	3	1	2	4	130
12	3	4	2	1	3	2
13	4	1	4	2	3	20
14	4	2	3	1	4	6
15	4	3	2	4	1	122
16	4	4	1	3	2	124
K1	74.75	55.45	92.45	3.25	62.25	
K2	53.00	78.00	71.45	56.25	75.25	
K3	94.75	105.25	67.35	116.65	70.45	
K4	64.05	53.65	52.45	109.25	76.25	
R	36.45	46.75	35.85	114.75	16.65	

Table 4 Result of orthogonal test for assistant rust inhibitor

Factor	F	G	H	I	(Rust-prevention) [%]
1	1	1	1	1	48
2	1	2	2	2	55
3	1	3	3	3	67
4	1	4	4	4	63
5	2	1	2	2	70
6	2	2	1	1	38
7	2	3	4	4	80
8	2	4	3	3	45
9	3	1	3	3	82
10	3	2	4	4	85
11	3	3	1	1	26
12	3	4	2	2	32
13	4	1	4	4	90
14	4	2	3	3	76
15	4	3	2	2	38
16	4	4	1	1	18
K1	58.25	72.45	17.45	15.55	
K2	38.00	63.25	25.45	23.75	
K3	56.75	52.25	34.35	32.65	
K4	54.05	39.65	39.45	38.55	
R	3.00	33.75	24.85	22.15	

Tafel Polarization Performance

Tafel polarization curves of coating rust inhibitor or not are shown in Fig. 1. The anti-rust trend of the samples with rust inhibitor was significantly better than naked plate. Corrosion rate of the naked was 2.4×10^4 times samples with rust inhibitor, and corrosion performance is shown in Table 5. The polarization curves with anti-rust processing moved towards lower corrosion current density (*I*corr reduce from 0.042 to 0.0084 mA cm^{-2}), corrosion potential moved forward (*E*corr increased from 0.737 to 0.596 V), and polarization resistance increased by 5.5 times. Lower corrosion current, corrosion electric potential moving forward, widen passivation zone and high polarization resistance show deposition of anti-rust film on the surface of electrode make electron transfer on the electrode surface more difficult which means anodic process is blocked. The anti-rust film has effect of isolation and corrosion protection.

Anti-rust Film Microstructure Observation

The anti-rust films are thin transparent film with configuration of different concentrations (5, 10% working liquid) on surface of hot-rolled plate. SEM morphology analysis results are shown in Fig. 2. Grain of 10% concentration have

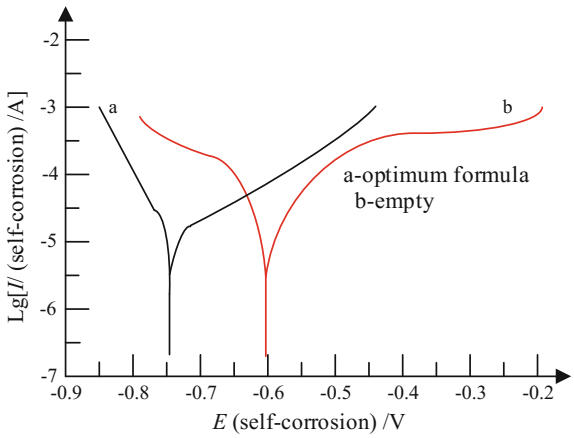

Fig. 1 Electrochemical polarization curve of 5%NaCl solution

Table 5 electrochemical polarization curve parameters

Specimens	*E*corr [V]	*I*corr [A]	*J*corr [A m^{-2}]	*V* [$gm^{-2}h^{-1}$]
Coating	−0.44	7.45×10^{-1}	6.22×10^4	43.39
No coating	−0.01	3.04×10^{-6}	0.25	1.79×10^{-3}

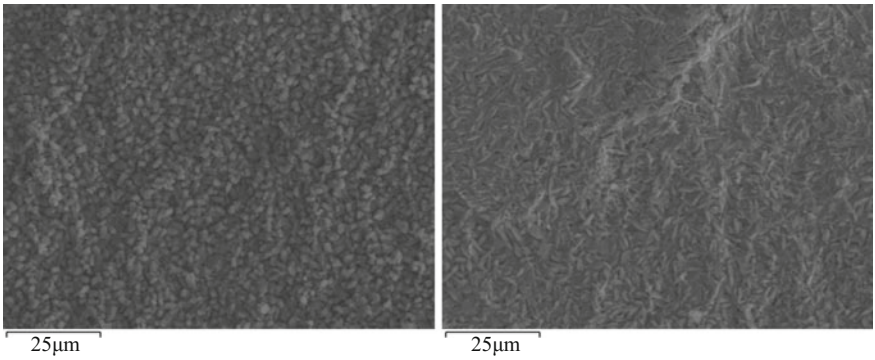

Fig. 2 5% (left) and 10% (right) SEM morphology of surface antirust film

uniform size, density, porosity and the thickness are 3–4 μm. Grain of 5% concentration has uneven size, porosity, and the thickness are 3–7 μm. The quality of 5% phosphating film was better than 10% from process phosphating effect. From energy spectrum analysis results, anti-rust film of hot-rolled plate contain C, O, Fe, Cu, Zr elements and O, Fe, Zr element content are higher which shows that coating film is mainly composed of Fe, Zr oxide and small amount of other elements. Anti-rust film was very thin, and covered relatively uniform on surface of steel plate. The coating film had small number of micro cracks which were caused by uneven specimen surface that was suitable for spray processing.

Anti-rust Test Results and Mechanism

Shown as in Fig. 3, hot-rolled plate processed with 10% anti-rust solution was contrasted with the naked plate in pickling production field for 120 h static test. The water-based rust inhibitor showed good rust resistance to hot rolled plate under the condition of high temperature, high humidity and SO_2, HCl gas. Anti-rust effect was better than rust inhibitor with sodium nitrite, but there were still small amount of rust at the edge of samples. Due to limited effusion of dissolved oxygen, oxygen concentration of effusion intersect was different so that oxygen concentration difference corrosion was caused. Although corrosion phenomenon appeared at the edge of samples, test result was still within the qualified criteria of anti-rust.

Conclusion

(1) The zirconate, long carbon chain carboxylic acid and mixed amine as main agent compounding with other antirust additive were used A new water-based metal

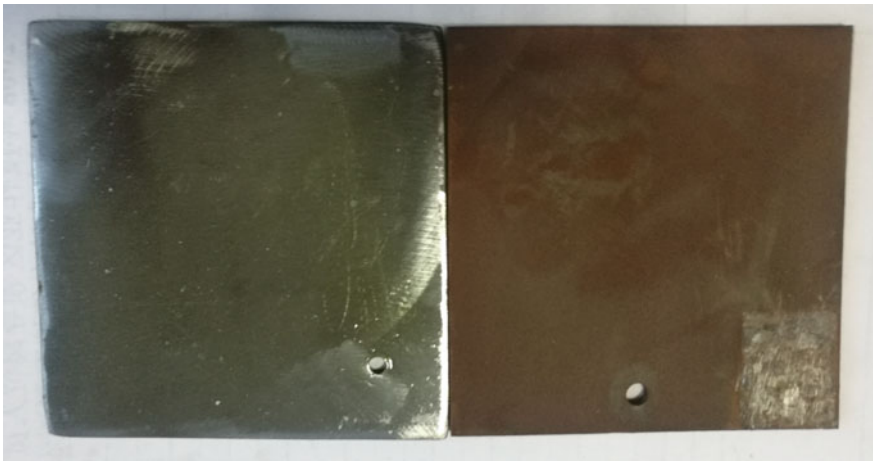

Fig. 3 Static antirust test contrast between hot rolled plate of 10% antirust treatment (left) and the untreated plate (right) in pickling plant for 120 h

rust inhibitor was developed which is high-efficiency and environmentally friendly. The optimized component is potassium zirconium fluoride: ricinoleic acid: orthoboric acid: monoethanolamine: triethanolamine =5:5:1:16:8.

(2) The rust inhibitor can form into uniform film on surface of hot-rolled plate. Corrosion rate of unpainted anti-rust film plate is 2.4×10^4 times by the coated. The film to build was unbroken and transparent.

(3) Because zirconium oxide has excellent corrosion resistance, hot-rolled steel plate coating zirconium oxide on surface can keep long time anti-rust. As long carbon chain carboxylic acid ester and boric acid ester generate, the strong force coordination bond forms. The sodium phosphate is good promoter in corrosion inhibitor because it can increase the rate of film to be built.

References

1. Z.-M. Chen, P. Lu, Y.-L. Su, Preparation and performance evaluation of water-based rust inhibitor for iron and steel. J. Mater. Protect. **6**, 58–59 (2011)
2. Y. Li, S.-Z. Yi, J.-Q. Wu, Preparation of environmentally acceptable water-based rust inhibitor. J. Mater. Protect. **5**, 31–33 (2011)
3. Z.-L. Li0, Study on aqueous antirusting agent of type of environmental protection. J. Hebei Chem. Eng. Ind. **7**, 13–15 (2006)
4. X.-L. Zhong, Z.–X. Yang, P.-K. Guo, Preparation and antirust performance of a nontoxic water-based rust inhibitor. J. Surface Technol. **3**, 115–119 (2014)
5. H.-Z. Jiang, D.-H. Tao, B. Wang, Study of relation between the molecular structures and the rust inhibiting properties on aqueous soluble organic acid salts. J. Lubricat. Eng. **2**, 72–74 (2005)

Effects of Fiber Laser Welding Speeds on Microstructures and Properties of E36 Steel Butt Joints

Yan Gao, Li Cui, Changshi Gu and Dingyong He

Abstract A 6 kW fiber laser YSL-6000 was chosen to weld the E36 steel with a thickness of 6 mm. The effects of laser welding speeds on the welded joint appearance were examined, and the microstructures and properties on the typical butt joints were investigated. Results showed that narrow and fully penetrated welded joints without obvious defects could be obtained at different welding speeds. With the welding speed increasing, the welding seam width decreased, and the welding seam (WS) and heat affected zone (HAZ) hardness increased. The microstructures of weld metal and HAZ were consisted of martensite, but the contents of it were significantly different. Welding speeds had no remarkable effect on the tensile strength and yield strength, except elongation. But the increase of welding speeds resulted in improvement of micro-hardness, which reached the maximum value of 426.38 HV at 45 mm/s. Weld metals of different welded joints were active in corrosion solution, and corrosion potential became more negative with the welding speeds increased from 35 mm/s to 50 mm/s, except at 45 mm/s.

Keywords Laser welding · E36 steel · Microstructures · Mechanical properties Corrosion properties

Y. Gao · L. Cui (✉) · D. He
College of Materials Science and Engineering, Beijing University of Technology, Beijing 100124, China
e-mail: cuili@bjut.edu.cn

Y. Gao
e-mail: zisefengling8026@emails.bjut.edu.cn

C. Gu
Shipbuilding Technology Research Institute, Shanghai 200032, China
e-mail: zisefengling8026@emails.bjut.edu.cn

© Springer Nature Singapore Pte Ltd. 2018

Y. Han (ed.), *Advances in Materials Processing*, Lecture Notes in Mechanical Engineering, https://doi.org/10.1007/978-981-13-0107-0_44

Introduction

E36 steel has received high attention in shipbuilding industrial technologies because of its excellent mechanical properties and welding performance. In recent years, researchers have adopted many methods to further develop its practical value, especially its corrosion resistance. Coating is one of the well-known corrosion prevention methods, which isolates the steel surface from corrosion environment [1]. If we can used the developed E36 steel to replace coating and gained good results, which can meet the relevant requirements of the International Maritime Organization (IMO), it will broaden its range of applications.

In the shipbuilding industry, the welding efficiency not only has a great effect on the construction cost of the ship, but also affects the construction speed and determines the delivery cycle [2]. In comparison to the conventional arc welding methods, laser welding process is widely used in industrial area due to its numerous advantages: deeper penetration, narrow heat affected zone, high welding speed and small distortion after welding [3–5]. Moreover, comparing to other laser welding methods, fiber laser welding is being steadily increased due to its unique advantages, such as high power, high beam quality and high efficiency to produce deep penetration [6, 7].

In this study, 6-mm-thick E36 steels were welded by a continuous-wave fiber laser (IPG YLS-6000) with a maximum power of 6 kW. The cross sectional morphologies and microstructures at different welding speeds were observed, besides, the mechanical properties and corrosion properties were researched.

Experimental Procedures

Material

In the present welding test, E36 steel with a thickness of 6 mm was chosen as the welding material. The chemical composition (wt%) and mechanical properties of the experimental steel are shown in Tables 1 and 2.

Table 1 Chemical compositions of base metal (wt%)

Chemical position	Fe	Mn	Al	Si	S
	99.2921	0.4092	0.1330	0.1231	0.0425

Table 2 Mechanical properties of the experimental steel

Material	Tensile strength (MPa)	Yield strength (MPa)	Elongation (A%)
E36 steel	465	300	33.2

Laser Welding Process

The tests were carried out by a continuous-wave fiber laser (IPG YLS-6000) with a maximum power of 6 kW, and the laser welding head was mounted on a robotic arm (IRB4600). The laser wavelength was about 1070 nm and focus beam diameter was around 0.2 mm used in the fiber laser. During laser welding, high purity argon at a flow rate of 22 L/min was used to shield the top and bottom surfaces of the work-pieces. In order to obtain the better laser welding quality quickly and use less material, keep the defocusing desistance and laser power constant, meanwhile change the welding speeds. The laser beam was focused at 0 mm. Table 3 lists the main processing parameters used in this study. No joint gap or filler wire were used.

Morphologic Observation

After the fiber laser welding, typical cross-section of the samples were cut by electro-discharge machining. Then the samples were polished and etched with 4% nital for 10 s before being examined by the optical microscope (OLYMPUSSZ61 and OLYMPUSBX51M) and the scanning electron microscope (FEI QUANTA FEG 650).

Measurement of Mechanical Properties

The micro-hardness of the fiber laser welding butt joints were performed by micro-hardness tester (HXD-1000 TMC/LCD) using a diamond indenter at room temperature of 25 °C. The micro-hardness gauge was HV, the multiplying power of the objective lens was 40×, the force was 0.4903 N, and the holding time of the force was 10 s. The transverse tests were conducted using a universal tensile testing machine operated with a crosshead speed of 1 mm/min.

Table 3 Parameters used in the laser welding tests

Number	Laser power	Welding speeds (mm/s)	Focusing distance
1	5 kW	35	0 mm
2		40	
3		45	
4		50	

Measurement of Corrosion Properties

In order to observe the corrosion properties of laser welded butt joints at various welding speeds, potentiodynamic polarization tests were conducted in PH = 0.85, 10 wt% NaCl solution at 30 °C. Corrosion tests simulating inner bottom environment of cargo oil tank (COT) were carried out according to the corrosion resistant steel standard approved by IMO. Potentiodynamic polarization tests were conducted for weld metal. Electrochemical experiments were carried out in a three-electrode cell. The counter and reference electrode were Pt sheet and saturated calomel electrode (SCE), respectively. The working electrode was made of E36 steel. The potentiodynamic polarization measurements were performed using an electrochemical workstation (PARSTAT 2273) with a potential scan rate of 0.5 mv/s.

Results and Discussion

Macrographs of Weld Joints

A good welding quality can be reflected directly from external features, such as the width of the welded butt joints, the penetration depth, the smoothness of the surface appearances, and so on [8]. Transverse metallographic samples were achieved from each pair of the welded joints and plotted in Fig. 1. It is obvious that fully penetrated butt joints can be achieved under different welding speeds and there are no cracks and porosities in the welded joints. In each macrograph, the Fusion Zone (FZ), Heat Affected Zone (HAZ) and Base Metal (BM) can be easily discriminated, and the weld widths decreased along with the welding speeds increased.

It is clear that the underfill defects mainly appeared on the top surface of the butt welded joints. The top underfill area increased with decreasing welding speeds which resulted in heat input decreased [9]. As shown in Fig. 1, with the welding speeds increased, the direction of columnar crystal was changed and no solidification cracking was found in the weld structures. For weld metal, a dendritic microstructure was developed at fusion boundary due to fast cooling conditions. However, with welding speeds increased, line energy per unit length decreased, which resulted in the increase of undercooling.

Microstructure of Weld Butt Joints at Different Welding Speeds

As shown in Fig. 2, microstructure of base metal consists of ferrite and pearlite, which can be seen from the white regions (ferrite) and dark regions (pearlite).

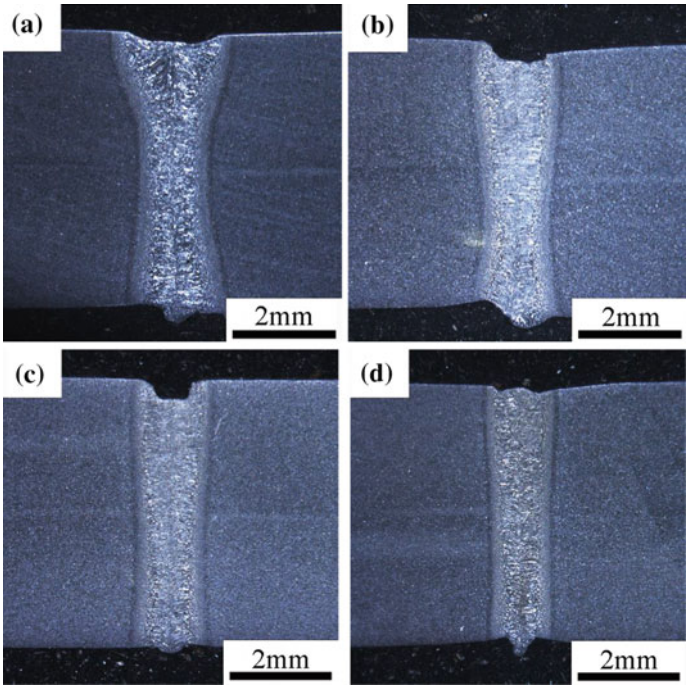

Fig. 1 Macrostructures of butt welded joints at different welding speeds: **a** 35 mm/s; **b** 40 mm/s; **c** 45 mm/s; **d** 50 mm/s

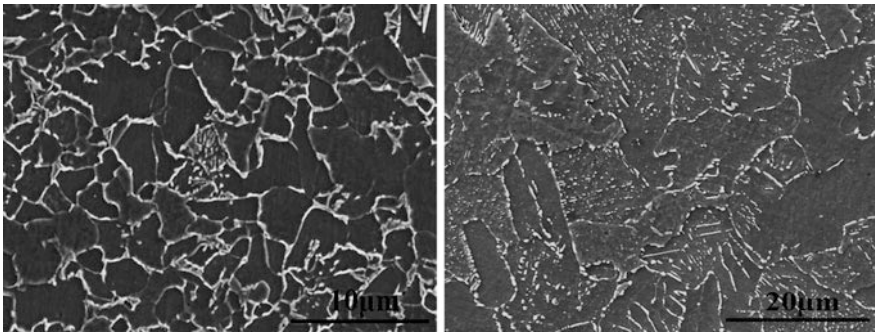

Fig. 2 Microstructure of base metal

Figure 3 shows the microstructures of weld metal at different welding speeds. As shown in Fig. 3, microstructures of weld metal mainly consist of lath martensite, which produced by extremely fast heating and cooling rates of fiber laser welding. Laser welding is a process of rapid heating and cooling and the hold time at high temperature is less, such that the formation of martensite [10, 11]. When the

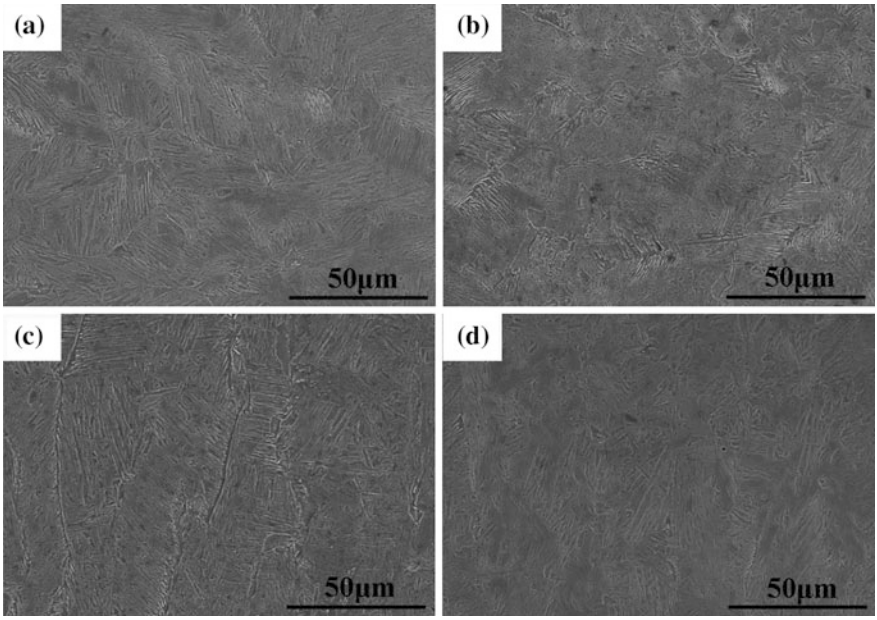

Fig. 3 Microstructures of weld metal at different welding speeds

welding speeds increased from 35 to 50 mm/s, the martensite content increased gradually and its size was finer.

The base metal was affected by welding thermal cycles such that form HAZ after cooling. Because of different distances from welding center, the local peak temperature, hold time at high temperature and cooling rate were different [12]. Figure 4 shows the microstructures of HAZ at different welding speeds. With the welding speeds increase, the microstructures of HAZ mainly consist of martensite and ferrite [13], and its size were finer.

Mechanical Properties of Butt Joints at Different Welding Speeds

Excellent mechanical properties including suitable tensile strength, yield strength and elongation were obtained for fiber laser welded joints [14]. Figure 5 reveals the strength and elongation of butt welded joints at different welding speeds. Results indicated that welding speeds have no remarkable effect on tensile strength and yield strength, except elongation. The elongation of butt welded joints reached a maximum value of 23.5% at 45 mm/s, but the tensile strength reached the minimum value of 470 MPa. The increase of elongation owing to the alloying elements dissolved at 45 mm/s decreased comparing to that of other welding speeds.

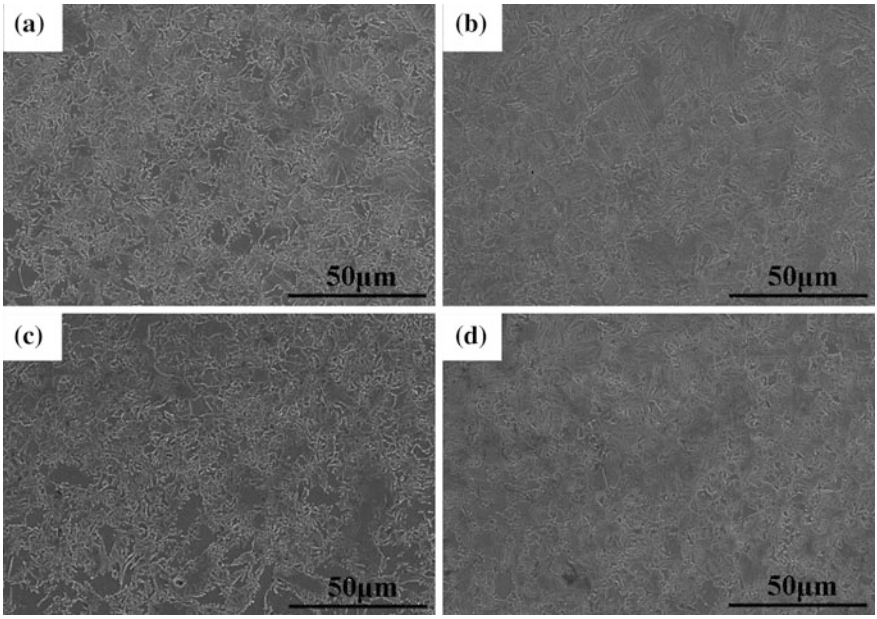

Fig. 4 Microstructures of heat affected zone at different welding speeds

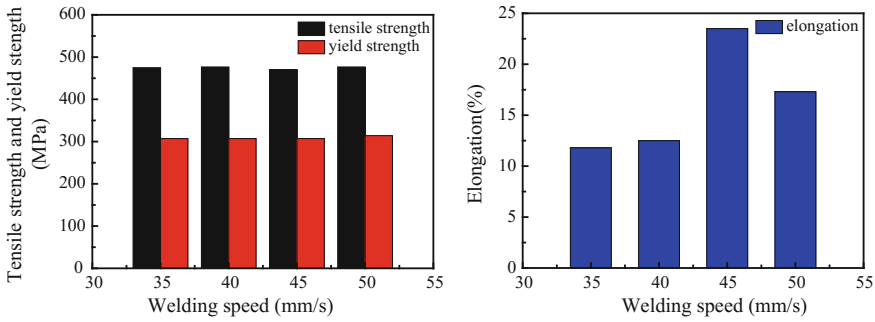

Fig. 5 Strength and ductility of butt joints at different welding speeds

Figure 6 shows the micro-hardness law of E36 steel welded joints at different welding speeds at a laser welding power (P) 5.0 kW and defocusing distances(Δf) 0 mm. It is seen that the hardness profile exhibited a similar characteristics with a higher hardness on the weld metal and a lower hardness on the base metal. As seen in Fig. 6, the micro-hardness of weld metal and heat affected zone is higher than that of base metal, because the alloy elements have no time to form the second phase to precipitate due to the extremely high cooling rate, and these elements dissolve to a great degree, which makes solid solution strengthening to occur after the laser welding process [15].

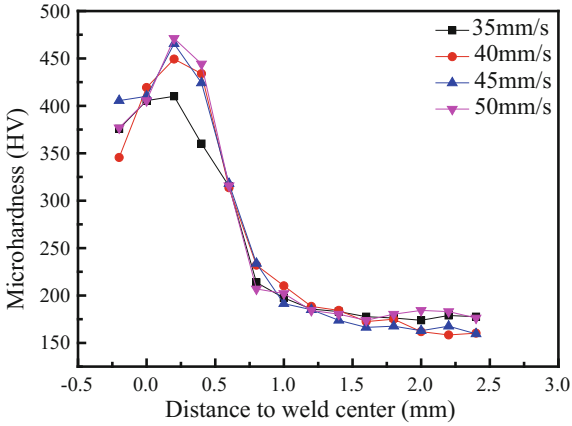

Fig. 6 Micro-hardness of butt joints at different welding speeds

Increasing the welding speeds from 35 to 50 mm/s at constant laser power level and defocusing distance cause an increase in the weld metal and HAZ hardness as a whole. This is because, with increasing the welding speeds, the cooling rate was increased [8], more alloy elements were dissolved, and solid solution strengthening was improved, so the hardness increased. When the welding speed increased to 45 mm/s, the average micro-hardness of weld metal reached to the maximum value of 426.38 HV.

Corrosion Properties of Weld Butt Joints

Figure 7 shows the potentiodynamic polarization curves of welded joints at different welding speeds in 10 wt% NaCl solution at (30 ± 2) °C. Typical active dissolution behavior could be seen on all curves. The anodic and cathodic branches

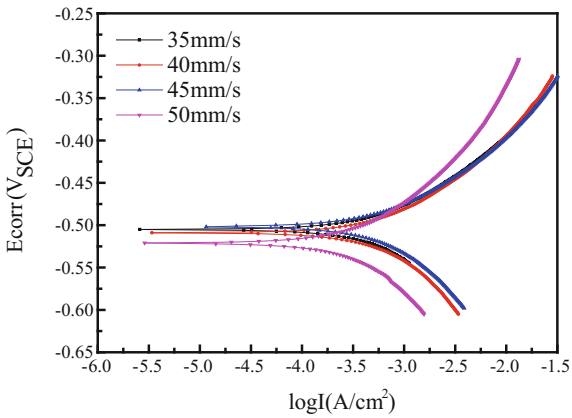

Fig. 7 Potentiodynamic polarization curves of welded joints at different welding speeds in 10 wt% NaCl solution at (30 ± 2) °C

of the polarization curves of welded joints at different welding speeds display Tafel behavior. Weld metals of different welded joints are active in corrosion solution, and corrosion potential becomes more negative with the welding speeds increase from 35 to 50 mm/s, except at welding speed of 45 mm/s.

Conclusion

1. Fully penetrated butt joints can be achieved under different welding speeds and there are no cracks and porosities in the welded joints.
2. With the welding speeds increase, the microstructures of weld metal and heat affected zone change.
3. Welding speeds have no remarkable effect on tensile strength and yield strength, except elongation. Increasing the welding speeds causes an increase in the weld metal and HAZ hardness as a whole.
4. Weld metals of different joints are active in corrosion solution, and corrosion potential becomes more negative with the welding speeds increase, except at welding speed of 45 mm/s.

References

1. F.L. Sun, X.G. Li, F. Zhang et al., Corrosion mechanism of corrosion-resistant steel developed for bottom plate of cargo oil tanks. Acta Metall. Sin. (Eng. Lett) **26**, 257–264 (2013)
2. P. Zhang, L. Xie, M. Wei et al., The development and microstructure analysis of high strength steel plate NVE36 for large heat input welding. HSLA Steels 2015, Microalloying 2015 & Offshore Engineering Steels (2015)
3. M. Mazar Atabaki, N. Yazdian, J. Ma, R. Kovacevic, High power laser welding of thick steel plates in a horizontal butt joint configuration. Opt. Laser Technol. **83**, 1–12 (2016)
4. C.Y. Cui, X.G. Cui, X.D. Ren et al., Microstructure and microhardness of fiber laser butt welded joint of stainless steel plates. Mater. Des. **49**, 761–765 (2013)
5. Long Chen, Longzao Zhou, Chao Tang et al., Study of laser butt welding of SUS301L stainless steel and welding joint analysis. Int. J. Adv. Manuf. Technol. **73**, 1695–1704 (2014)
6. J. Pekkarinena, V. Kujanpää, The effects of laser welding parameters on the microstructure of ferritic and duplex stainless steels welds. Phys. Proc. **5**, 517–523 (2010)
7. W. Xu a, D. Westerbaan b, S.S. Nayak,et al. Tensile and fatigue properties of fiber laser welded high strength low alloy and DP980 dual-phase steel joints[J]. Materials and Design, 43 (2013) 373–383
8. L. Zhang, J.Z. Lu, K.Y. Luo, A.X. Feng, F.Z. Dai, J.S. Zhong, M. Luo, Y.K. Zhang, Mater. Sci. Eng. A **561**, 136 (2013)
9. C. Bayley, N. Aucoin, X. Cao, Fiber laser welding of HY-80 steel: procedure development and testing. DRDC Atlantic TM 2009–187, Canada
10. D.C. Saha, D. Westerbaan, S.S. Nayak, E. Biro, A.P. Gerlich, Y. Zhou, Microstructure-properties correlation in fiber laser welding of dual-phase and HSLA steels. Mater. Sci. Eng. A **607**, 445–453 (2014)

11. N. Farabia, D.L. Chen, Y. Zhou, Microstructure and mechanical properties of laser welded dissimilar DP600/DP980 dual-phase steel joints. J. Alloy. Compd. **509**, 982–989 (2011)
12. X.-N. Wang, Q. S, Zhi Zheng et al., Microstructure and fracture behavior of laser welded joints of DP steels with different heat inputs. Mater. Sci. Eng. A **699**, 18–25 (2017)
13. D. Parkes, D. Westerbaan, S.S. Nayak et al., Tensile properties of fiber laser welded joints of high strength low alloy and dual-phase steels at warm and low temperatures. Mater. Des. **56**, 193–199 (2014)
14. X. Cao, M. Jahazi, Effect of welding speed on butt joint quality of Ti–6Al–4V alloy welded using a high-power Nd: YAG laser. Opt. Lasers Eng. **47**, 1231–1241 (2009)
15. M. Zhang, X.N. Wang, G.J. Zhu et al., Effect of laser welding process parameters on microstructure and mechanical properties on butt joint of new hot-rolled nano-scale precipitation-strengthened steel. Acta Metall. Sin. (Engl. Lett.) **27**(3), 521–529 (2014)

Preparation and Mechanical Properties of 42CrMo/40CrNiMo Dissimilar Steel Joints Prepared by Diffusion Bonding

Jie Wang, Fuqi Zhang, Guanzhong Yang, Bin Wang and Minmin Xia

Abstract In this paper, using CuZn alloy as interlayer, 42CrMo/40CrNiMo dissimilar steel joints were prepared by vacuum diffusion bonding, and the effects of holding time on microstructure and properties of 42CrMo/40CrNiMo joints were studied. The microstructure and mechanical properties of 42CrMo/40CrNiMo joints were analyzed and characterized by optical microscope (OM), scanning electron microscope (SEM), energy disperse spectroscopy (EDS), universal mechanical testing machine and vickers hardness tester. The results showed that when the bonding temperature was 780 °C, the bonding pressure was 0.02 MPa and the holding time were 5–30 min, obvious interface transition zones formed through diffusion reaction of CuZn interlayer to 42CrMo and 40CrNiMo base materials. The bonding region was dense and continuous with a good combination. In the joints prepared at different conditions, the microhardness of interlayer was lower than base materials. With the increase of holding time, the shear strength of 42CrMo/40CrNiMo joints increased at first and then decreased. The maximum joint shear strength, with the value of 135.86 MPa, was obtained when the holding time was 15 min. Meanwhile, the load-displacement curves and fracture surfaces indicated that the fractural mode of 42CrMo/40CrNiMo joints was ductile-brittle mixed fracture, in which brittle fracture was dominating.

J. Wang (✉) · F. Zhang · G. Yang · B. Wang
School of Materials Science and Engineering,
Southwest Petroleum University, Chengdu 610500, China
e-mail: wangjie_4212@163.com

F. Zhang
e-mail: fqzhang90@163.com

G. Yang
e-mail: 1163572522@qq.com

B. Wang
e-mail: wangbincn89@163.com

M. Xia
The Oil Production Technology Institute, CNPC Da Gang Oilfield Company,
Tianjin 300280, China
e-mail: 271283476@qq.com

© Springer Nature Singapore Pte Ltd. 2018

Y. Han (ed.), *Advances in Materials Processing*, Lecture Notes in Mechanical Engineering, https://doi.org/10.1007/978-981-13-0107-0_45

Keywords Diffusion bonding · Dissimilar materials · Holding time
Microstructure · Mechanical properties

Introduction

42CrMo is a kind of chromium-molybdenum steel, which can be used as tool joints and downhole salvage tools, such as the oil drill pipe joints below two kilometers. It can also be used in a variety of demanding molds, large gears for locomotives, some special drive gears, pressure vessel gears [1]. 40CrNiMo is commonly used as high strength quenched and tempered steel, which has high hardenability and is mainly applied as high strength parts such as aero-engine shaft, wheel gear, fastener [2, 3]. High temperature preheating is required before welding, and relieving the internal stresses treatment is required after welding due to the weldability of 40CrNiMo is poor. As 42CrMo has similar weldability with 40CrNiMo, it needs to be preheated and retarded cooling after welding as well [4, 5]. Compared with other joining methods, diffusion bonding technology has free from contamination, easy welding process, low heating temperature, small stress-strain and some other advantages [6–8]. Hence, it can effectively avoid some problems caused by conventional welding methods through diffusion bonding technology to join 42CrMo/40CrNiMo dissimilar steel.

Researchers have studied vacuum brazing YG8/42CrMo using CuMnNi as brazing filler metal, the flexure strength reached 436 MPa at 950 °C [9]. Luo [10] studied the joining of nickel-based superalloy K418-alloy steel and 42CrMo dissimilar metals using a new current hybrid inertia friction welding technology, and the results indicated that tensile strength of the joints were obviously improved by the new technology. There are various methods for joining different kinds of steels and other materials, such as brazing, friction welding, diffusion bonding and conventional fusion welding technology [11–15]. It can be found that new phases formed easily at welding joints, internal stress caused by the diverse coefficient of thermal expansion of dissimilar materials, and some other factors were the main problems during bonding process. Therefore, relieving the internal stresses, inhibiting the formation of harmful phases et al can be the key factors for bonding dissimilar materials.

To sum up, CuZn interlayer is adopted to join 42CrMo and 40CrNiMo dissimilar steel by diffusion bonding method in the present experiment. The effects of holding time on the microstructure and mechanical properties of 42CrMo/40CrNiMo joints made at a certain bonding temperature and pressure on vacuum conditions are mainly studied.

Experimental Procedures

The chemical compositions of 40CrNiMo and 42CrMo are shown in Table 1, and the interlayer is CuZn foil with a thickness of 200 μm.

Before preparation of the samples, the parent metals were sliced to 10 mm × 10 mm × 5 mm by wire cut. Those specimens were polished with SiC sandpaper, and cleaned in alcohol. The sliced CuZn interlayer was larger than the size of those 40CrNiMo and 42CrMo specimens, and then those rectangular CuZn foils were cleaned in 5% hydrochloric solution. The interlayer was put onto the faying surface of a 42CrMo specimen. The other 40CrNiMo specimen was put onto the interlayer to form a 'sandwich-like' structure as shown in Fig. 1. This prepared specimen was fastened by the graphite clamps, and then they were put into a vacuum furnace. This assembly was heated to 650 °C with a heating rate of 10 °C/min and dwelled at this temperature for 10 min with a pressure of 0.02 MPa. Next, joining temperature was elevated to 780 °C with a heating rate of 7 °C/min and dwelled at this temperature for various holding times (5, 15 and 30 min) with a pressure of 0.02 MPa. The whole bonding process was carried out in a vacuum environment ($\leq 2 \times 10^{-1}$ Pa). When the diffusion bonding stage was finished, furnace power was turned off and joints were cooled down to room temperature in the furnace.

In order to study the microstructure and mechanical properties of the joints, OM, SEM, EDS, universal mechanical testing machine and vickers hardness tester (HVS-1000 type) were used. The microhardness was tested every 100 μm across the profile of the joints with a load of 100 gf and loading time was 10 s. Room temperature shear tests were conducted on the universal testing machine with 0.5 mm/min loading rate. The joint shear strength can be calculated by the following equation [16]:

$$\tau = \frac{F}{S} \tag{1}$$

where F is the maximum load and S is the joining area. The illustration of the shear test setup was cited in the reference [17] shown in Fig. 2.

Results and Discussion

Microstructure Characterization of 42CrMo/40CrNiMo Joints

Figure 3 shows the cross-section OM images of 42CrMo/40CrNiMo joints prepared by diffusion bonding at different holding time. It can be seen that all the joints achieved reliable joining with holding time varying from 5 min to 30 min, in which the joints were dense and there were no obvious gaps. From metallurgical structure,

Table 1 Chemical compositions of 40CrNiMo and 42CrMo (wt%)

Materials	Chemical compositions								
	C	Si	Mn	Cr	Mo	S	P	Ni	Cu
40CrNiMo	0.37–0.44	0.17–0.37	0.50–0.80	0.60–0.90	0.15–0.25	≤ 0.025	≤ 0.025	1.25–1.65	≤ 0.25
42CrMo	0.38–0.45	0.17–0.37	0.50–0.80	0.90–1.20	0.15–0.25	≤ 0.04	≤ 0.035	–	–

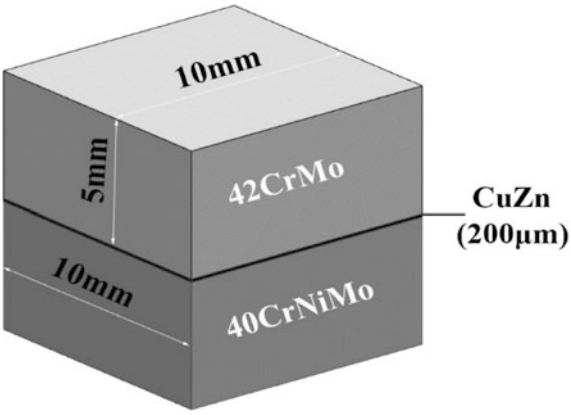

Fig. 1 Schematic drawing of the sample assembly

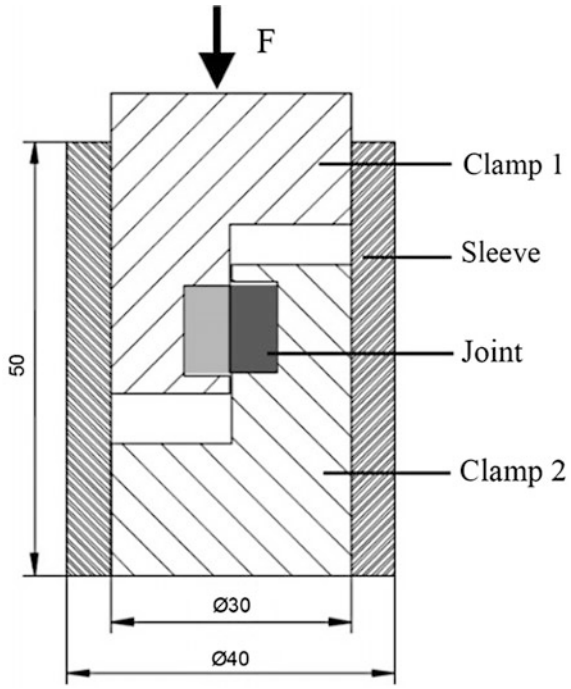

Fig. 2 Illustration of the shear test setup

the CuZn interlayer and the two sides of the based metal have diffusion reaction to a certain extent. On account of lower magnification, the reaction zones of the joints were unapparent. The bonding joints mainly consist of 42CrMo and 40CrNiMo parent metal, CuZn interlayer, reaction zone between the interlayer and parent metal, in which the left side of the joints were 42CrMo and the right side were 40CrNiMo. Compared Fig. 3a–c, the interlayer thickness of the prepared joints decreased gradually with the increasing of holding time, and it was apparently

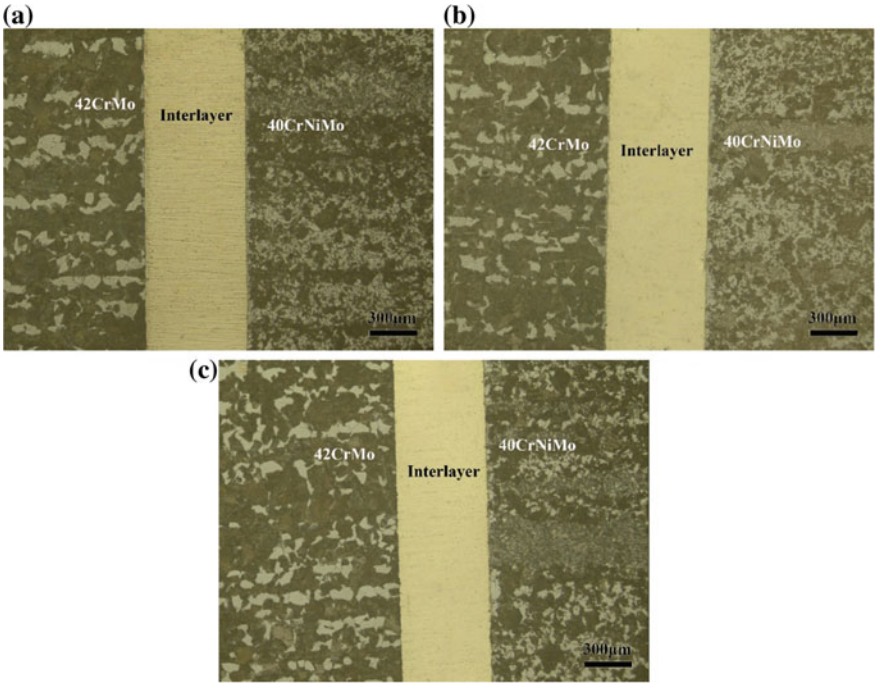

Fig. 3 Metallurgical structure of diffusion bonding joints at different holding time at 780 °C: **a** 5 min; **b** 15 min; **c** 30 min

decreased while the holding time was 30 min. This was due to the more sufficient diffusion between the based metals and interlayer with longer holding time, the thickness of reaction zone increased correspondingly.

In order to observe the microstructure of the bonding joints thoroughly, SEM and EDS analysis were used, Fig. 4 and Table 2 shows the cross-section SEM images and EDS analysis of 42CrMo/40CrNiMo joints prepared by diffusion bonding at different holding time.

From Fig. 4a, it can be observed that a discontinuity interface formed between 42CrMo, 40CrNiMo based metals and core interlayer, holes and cracks were in a large quantity. This indicated that the reaction of the interface area of the joints fabricated at 780 °C, 5 min were insufficient. At longer holding times (15 and 30 min), with more sufficient diffusion of the atomics, holes and cracks at the interface were decreased gradually and the reaction layer has been increasingly continuous. It is observed from Fig. 4b, c that the joints were in good metallurgical bonding. However, there were also some holes and cracks at the interface, this was possibly because of the insufficient bonding pressure (0.02 MPa). The interface of the bonding joints apparently changed with the holding time increased. The reaction layer formed on the interface was gray with short holding time. With the extension

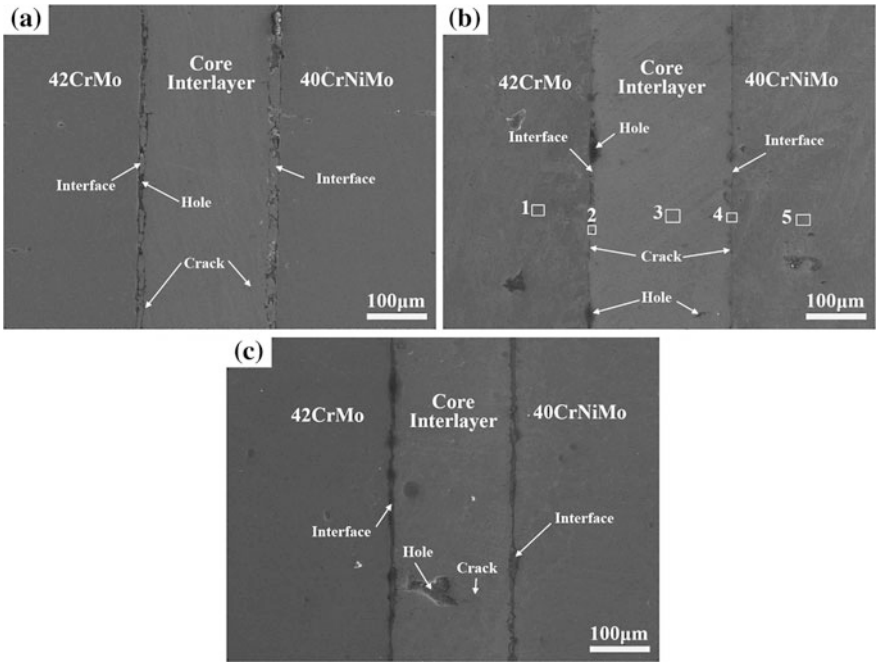

Fig. 4 SEM structure of diffusion bonding joints at different bonding time on 780 °C: **a** 5 min; **b** 15 min; **c** 30 min

Table 2 EDS analysis results for the microzones in Fig. 4b (wt%)

Microzones	Cr	Fe	Ni	Cu	Zn	Mo	Total
1	1.50	97.57	0.20	0.48	0	0.25	100
2	0.67	50.87	0.04	43.63	4.57	0.22	100
3	0.05	0.30	0.02	84.20	15.35	0.08	100
4	0.50	38.05	0.52	54.90	5.90	0.13	100
5	0.90	97.56	1.25	0.11	0.01	0.17	100

of holding time, reaction layer turned to black microstructures, which was dense and continuous as shown in Fig. 4.

To further confirm the reaction phase in the bonded joints, the chemical composition of each phase formed in 42CrMo/40CrNiMo joints were measured by EDS, and Table 2 shows the EDS analysis results for the microzones in Fig. 4b. According to EDS result, the sequence of the bonding joints from left side to right side can be described as follows: 42CrMo/reaction zone/unreacted CuZn interlayer/reaction zone/40CrNiMo. The microzone 2 and 4 were diffusion reaction layer, microzone 1 and 5 were the based metals and microzone 3 was unreacted interlayer. It can be seen that the content of Cu, Zn at the interface of CuZn interlayer and

40CrNiMo (microzone 4) were higher than microzone 2 apparently. This indicated the dispersal ability of interlayer elements diffused to 40CrNiMo was better than to 42CrMo. There were also a spot of based metal elements on microzone 2, 3 and 4, indicated the elements diffusion also happened from based metal to interlayer.

Mechanical Properties of 42CrMo/40CrNiMo Joints

Microhardness analysis has been performed on the cross-section of the bonding joints, and Fig. 5 shows the relationship between the microhardness value of the joints fabricated at 780 °C, 15 min and distance from the joint center. Figure 6 and Table 3 shows the microhardness value results of the joints fabricated at different holding times.

As shown in Fig. 5, the microhardness of the interlayer was lower than the two side of based metals, and 40CrNiMo had higher microhardness than 42CrMo. The microhardness near 40CrNiMo side was higher than the microhardness in core interlayer, this could attribute to the formation of some hard phase during the diffusion reaction of the joints, and those hard phase lead to the increase of the microhardness.

It can be seen from Fig. 6 and Table 3, the variation tendency of microhardness for the joints made at different holding times were basically consistent, the interlayer microhardness were all lower than the two side of based metals. Compared

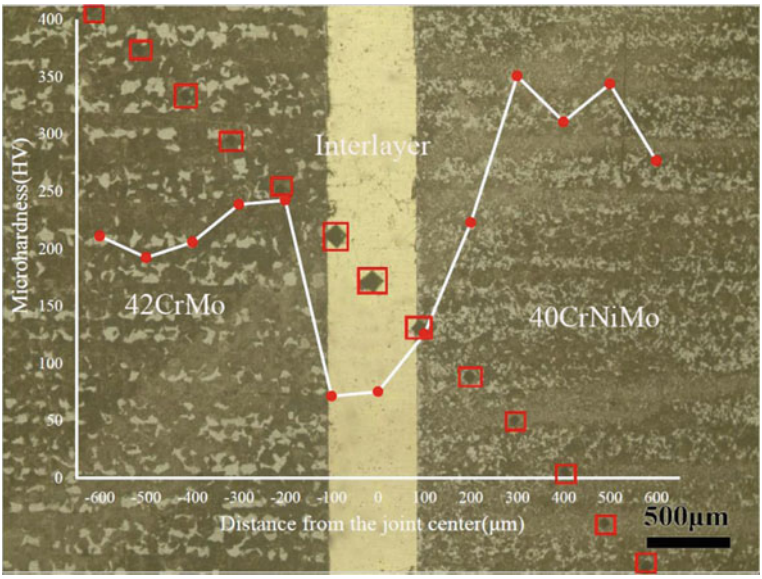

Fig. 5 Microhardness profile for the joints fabricated at 780 °C, 15 min

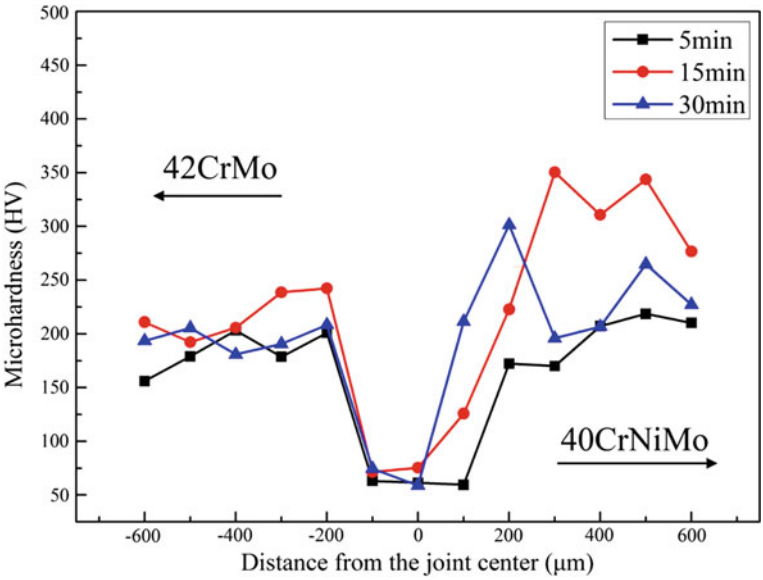

Fig. 6 Microhardness profile for the joints fabricated at different holding times

with shorter holding times, just two points of the microhardness were detected on the interlayer when the holding time was 30 min, this was due to the sufficient elements diffusion made the interlayer thinner and reaction layer thicken with the extended holding time.

It can be seen from Fig. 6 and Table 3, the variation tendency of microhardness for the joints made at different holding times were basically consistent, the interlayer microhardness were all lower than the two side of based metals. Compared with shorter holding times, just two points of the microhardness were detected on the interlayer when the holding time was 30 min, this was due to the sufficient elements diffusion made the interlayer thinner and reaction layer thicken with the extended holding time.

In order to better test the joints mechanical properties, shear strength test was used in the current study. Table 4 and Fig. 7 shows the variation of joint shear strength conducted at room temperature with the increase of holding times. It can be seen from Table 4 that maximum shear strength was obtained when the holding time was 15 min at 780 °C, and the shear strength was 135.86 MPa. The shear strength was just 39.28 MPa when the joint fabricated at 780 °C, 5 min. This was due to the insufficient interdiffusion between elements for the short holding time, and it leads to the reaction layer thinner and incontinuous. As the holding time increased to 30 min, the excessive diffusion of the elements made the thickness of reaction layer increase, and there was more stress produced during the bonding process, which could affect the shear strength of the joints. It can be seen from Fig. 7a–c that all the load-displacement curves have an obvious peak, but it showed

Table 3 Microhardness profile for the joints fabricated at different holding times (HV)

Holding time (min)	Distance from the joint center (μm)												
	−600	−500	−400	−300	−200	−100	0	100	200	300	400	500	600
5	156	179	203.3	178.7	200.9	63.2	61.4	59.5	172.3	170	207.2	218.6	210.2
15	210.9	192.3	205.7	238.6	242.3	71.4	75.3	125.8	222.8	350.5	310.8	343.7	276.7
30	193.5	205.5	180.8	190.6	208.4	74.5	58.9	211.6	301.4	195.9	206.7	264.8	227.3

Table 4 Shear strength for the joints at different holding times

Holding time (min)	5	15	30
Shear strength (MPa)	39.28	135.86	87.93

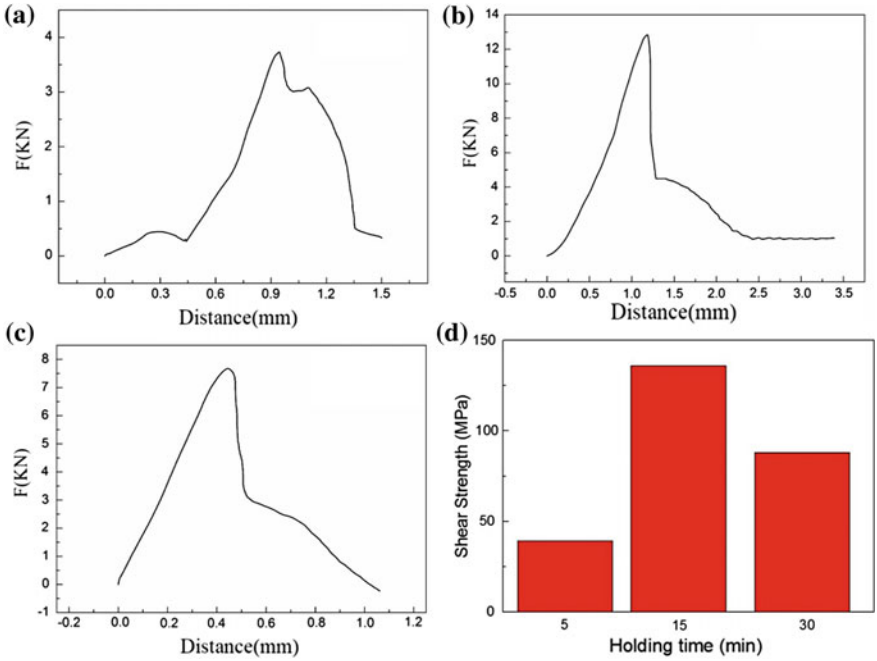

Fig. 7 Load-displacement curves and shear strength for the joints fabricated at different holding times: **a** 5 min; **b** 15 min; **c** 30 min; **d** shear strength at different holding times

the tendency of gradual decline during the beginning of the fracture process. This indicated a ductile-brittle fracture to some extent. From Fig. 7d, the shear strength of the joints increased at first and then decreased, and the maximum shear strength was obtained when the holding time was 15 min.

Fracture Analysis of 42CrMo/40CrNiMo Joints

Fracture analysis was carried out to reveal the correlation between interfacial microstructure and bonding properties of the joints. The SEM micrographs and XRD results were as shown in Figs. 8 and 9, which obtained from the fractured surfaces of 42CrMo/40CrNiMo joints prepared at 780 °C with holding 15 min. Table 5 is the EDS results of chemical compositions at each location in Fig. 8.

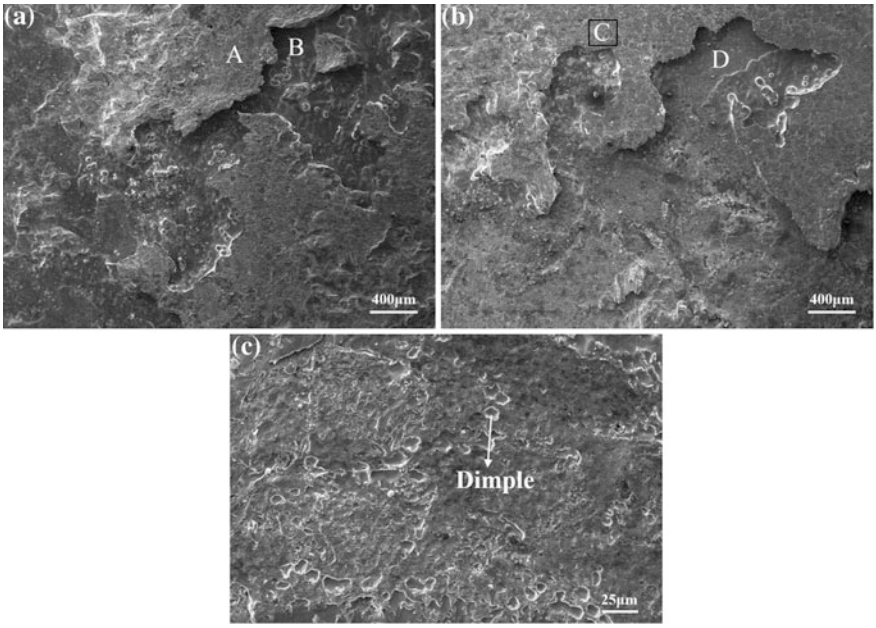

Fig. 8 Fracture surfaces of 42CrMo/40CrNiMo joints fabricated at 780 °C, 15 min after room temperature shear test: **a** 40CrNiMo side; **b** 42CrMo side; **c** locally magnified of (**b**)

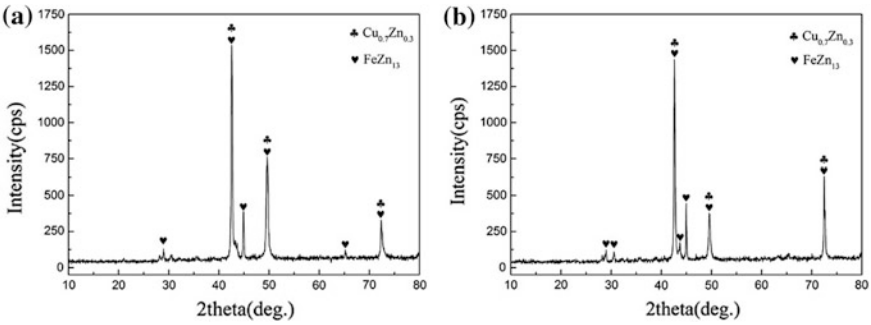

Fig. 9 XRD analysis of the fracture surface of 42CrMo/40CrNiMo joints fabricated at 780 °C, 15 min after room temperature shear test: **a** 40CrNiMo side; **b** 42CrMo side

From Fig. 8a, b, it can be seen that the shear fracture surfaces at room temperature were not flat and presented a step-like fracture characteristics. The main fracture mechanism was brittle fracture. According to Fig. 8c which was locally magnified of Fig. 8b, there were certain amount of dimples on the fracture surface, which indicated a ductile fracture characteristic to some extent. In consequence, the fracture mechanism of the room temperature shear specimen was ductile-brittle mixed fracture, in which brittle fracture was dominating. The fracture mainly occurs

Table 5 EDS results of chemical compositions at each location in Fig. 8 (at.%)

Locations	Cu	Zn	Fe	Cr	Mo	Ni
A	57.94	36.40	2.43	3.04	0.03	0.16
B	18.78	13.98	66.11	0.48	0.26	0.39
C	60.12	36.88	2.76	0.05	0.01	0.18
D	5.71	5.14	87.71	1.16	0.25	0.04

at the interlayer and the interface between the substrate and interlayer, which indicated that the weak position of the bonding joints was the middle zone of the interlayer.

The main chemical compositions of the feature region were similar from Table 5. Region A and C was mainly Cu and Zn, while region B and D was mainly Fe, Cu and Zn, which indicated that region A and C was interlayer, region B and D could be the reaction zone between the base metal and interlayer. From the XRD results, main phases of the fracture surface were $Cu_{0.7}Zn_{0.3}$ and $FeZn_{13}$, which indicated the reaction of interlayer elements and Fe from the base metals. It can further confirm that the main fracture position of the joints occurred in the interlayer and the interface between substrate and interlayer from the EDS and XRD analysis.

Summary

A Cu–Zn interlayer was used for the diffusion bonding of 42CrMo to 40CrNiMo in the present study. The main conclusions can be summarized as the follows.

Reliable bonding joints of 42CrMo/40CrNiMo dissimilar steel can be fabricated using CuZn alloy as interlayer by diffusion bonding. With the increase of holding time, the thickness of the interlayer decreases gradually, as well as the reaction layer increases and the structure of the reaction layer changes apparently under the bonding temperature 780 °C, bonding pressure 0.02 MPa, and holding time varying from 5 to 30 min. The microhardness of the interlayer is lower than base materials. The shear strength of the 42CrMo/40CrNiMo joints increases at first and then decreases with the increasing of holding time from 5 min to 30 min. The maximum joint shear strength reaches 135.86 MPa with the holding time of 15 min. The load-displacement curves and fracture surfaces indicate that the ductile fracture exists in 42CrMo/40CrNiMo joints to some extent.

Acknowledgements This research work was sponsored by the National Natural Science Foundation of China (No. 51602269), and Young Scholars Development Fund of SWPU (No. 20149901006).

References

1. N. Nan, Fatigue reliability analysis and crack initiation micromechanism for 42CrMo steel, Ph.D., Shandong University, Jinan, China, (2006)
2. G.H. Chen, X.C. Zhang, R.J. Yu, Effect of zonal segregation on microstructure and mechanical properties of 40CrNiMo steel. Hot Work. Technol. **8**, 16–18 (2012)
3. J.J. Zhao, 40CrNiMo steel hard cutting process and surface morphology research, MS., Zhengzhou University, Zhengzhou, China, (2014)
4. X.S. Liu, J.Y. Wu, T. Cheng, Welding process research on 42CrMo and Q345D forge welding gear. Welded Pipe Tube **11**, 45–48 (2016)
5. X.M. Yan, The welding of 42CrMo gear ring. Mech. Electr. Technol. **01**, 66–68 (2009)
6. T. Gang, Y. Takahashi, Review of quality evaluation of diffusion bonded joints. NDT **8**, 410–414 (2003)
7. C.F. Wei, B. Zhang, J. Tang et al., Development and application of material diffusion bonding technology. Mater. Rev. **s2**, 103–106 (2015)
8. X.Y. Guo, J.P. Lin, B. Sun, Research progress of diffusion bonding technology. Hot Work. Technol. **17**, 15–20 (2014)
9. J. Zhou, H.L. Wang, Research on Vacuum Brazing of 42CrMo Steel and Hard Alloy YG8. Hot Work. Technol. **7**, 109–111 (2009)
10. J. Luo, L. Li, Y. Dong et al., A new current hybrid inertia friction welding for nickel-based superalloy K418-alloy steel 42CrMo dissimilar metals. Int. J. Adv. Manuf. Technol. **9**, 1673–1681 (2014)
11. T. Wang, T. Ivas, C. Leinenbach et al., Microstructural characterization of Si3N4/42CrMo joint brazed with Ag–Cu–Ti + TiNp composite filler. J. Alloys Compd. **651**, 623–630 (2015)
12. L.Y. Xu, Z.J. Xia, Research on welding process of dissimilar steel welding between 42CrMo and Q345B. Hot Work. Technol. **11**, 208–211 (2013)
13. S.G. Du, L. Fu, J.W. Wang et al., Forming mechanism of carbide band in friction welding joint of superalloy K418 and steel 42CrMo. Chin. J. Nonferrous Metals **2**, 323–327 (2003)
14. Y. Li, H. Wu, F.J. Shang et al., Vacuum diffusion bonding of TiAl intermetallics and 42CrMo alloy steel. Ord. Mater. Sci. Eng. **3**, 45–47 (2001)
15. Y.L. Li, M.Y. Lv, J.C. Feng et al., The properties of the phase and the effects on mechanical properties of the TiAl alloy/42CrMo steel brazing joints. Trans. China Weld. Inst. **1**, 41–44 (2014)
16. J. Wang, K.Z. Li, H.J. Li et al., Partial transient liquid phase bonding of carbon/carbon composites using Ti–Ni–Al_2O_3–Si compound as interlayer. J. Alloys Compd. **6**, 57–62 (2013)
17. K.Z. Li, J. Wang, X.B. Ren et al., The preparation and mechanical properties of carbon–carbon/lithium–aluminum–silicate composite joints. Mater. Des. **44**, 346–353 (2013)

Effect of Cold Drawing on Microstructure and Mechanical Properties of 410 Martensite Stainless Steel Wire

Haonan Yu, Renbo Song, Yao Tan, Tianyi Wang and Lun Li

Abstract The microstructure and mechanical properties of 410 martensite stainless steel wire during the cold drawing process have been investigated by means of universal testing machine, optical microscope (OM) and transmission electron microscope (TEM) techniques. The results showed that the microstructure of 410 stainless steel was consisted of martensite and ferrite. During the cold drawing, when the wire was drawn from a diameter of 7.5 mm to a diameter of 5.0 mm, the average grain size decreased from 22.7 to 13.8 μm, the tensile strength increased from 504 to 741 MPa, elongation decreased from 38.2 to 13.1%. The strain hardening of the steel wire could be divided into two stages. In the first stage, the n value increased gradually and peaked at 0.85 which was associated with the plastic deformation of ferrite. In the second stage, the n value decreased to 0.25 which was associated with plastic deformation of martensite and the declined compatibility of the duplex phase. Moreover, the workhardening mechanism was discussed. The main work-hardening mechanism of 410 steel wire during the cold drawing process is fine grain strengthening and dislocation strengthening. When the steel wire was drawn from a diameter of 7.5 mm to a diameter of 5.0 mm, the strengthening benefit increased by 46.8 MPa and the dislocation strengthening increased by 173 MPa.

H. Yu · R. Song (✉) · Y. Tan · T. Wang
School of Materials Science and Engineering, University of Science and Technology Beijing, Beijing, China
e-mail: songrb@mater.ustb.edu.cn

H. Yu
e-mail: mejoryu@163.com

Y. Tan
e-mail: caitentan1103@163.com

T. Wang
e-mail: 1716012176@qq.com

L. Li
Anshan Steel Group Corporation Limited,
East Anshan Sintering Plant, Anshan, Liaoning, China
e-mail: 1760369030@qq.com

© Springer Nature Singapore Pte Ltd. 2018

Y. Han (ed.), *Advances in Materials Processing*, Lecture Notes in Mechanical Engineering, https://doi.org/10.1007/978-981-13-0107-0_46

Keywords 410 martensite stainless steel wire · Cold drawing · Work-hardening

Introduction

The corresponding domestic brand of 410 martensite stainless steel is 1Cr13, which belongs to the semi-martensitic stainless steel containing martensite and a small amount of ferrite [1]. Due to the toughness, good corrosion resistance low temperature strength and excellent mechanical properties, the 410 stainless is mainly used for the production of equipment and components requiring high toughness, such as turbine blade [2, 3]. The forming of 410 stainless steel wire is the cold drawing progress where there are many changes of microstructure and mechanical properties. The research on working-hardening mechanism and the evolution of microstructure during the cold drawing is very important, as the performance parameters of the cold-drawn wire are closely related to the microstructure [4, 5]. At present, the application of austenite stainless wire on the market becomes more extensive and the many reports focus on the mechanical properties and work-hardening of 304 stainless steel during the cold drawing [6, 7]. However, the reports about mechanical properties and work-hardening of 410 martensite stainless steel during cold drawing are less common.

In this paper, the relationship among material, cold drawing and properties was investigated in order to find the appropriate process and to obtain the best mechanical properties, by controlling work-hardening behavior and microstructure evolution. The results can provide theoretical basis for the enterprise production significantly.

Experimental

Experimental Materials

The raw material used in the experiment was 410 stainless steel wire with initial size of Φ7.5 mm. Table 1 lists the chemical composition of the as-received material used in this study. The production process of 410 stainless steel is: steel

Table 1 Chemical composition of 410 martensite stainless steel wire (wt%)

C	Mn	Si	P	S	Cr	Mo
0.075	0.35	0.41	0.025	0.001	12.5	0.6

wire → pickling → film processing → straight wire-drawing machine → washing → drying → coiling. The 410 stainless steel coil was made of three passes cold drawing, and the diameter of the steel wire was changed as follows: Φ7.5 mm → Φ6.5 mm → Φ5.5 mm → Φ5.0 mm.

Experimental Methods

Mechanical property test: The tensile test was carried out on wire coil and cold-drawn 410 stainless steel wire, by CMT4105 microcomputer electronic universal testing machine.

Sample preparation and metallographic observation: The metallographic samples of materials were taken from the coil and 410 stainless wire after each pass cold-drawn. The samples were smoothed down by sandpaper and then mechanically polished. Due to the good corrosion resistance of the samples, samples were eroded by a mixture of HCl and HNO_3 in 3:1 ratio, further swabbing by few drops C_2H_5OH to improve precision of analysis. OM and TEM techniques were applied in order to investigate the microstructure evolution during the deformation process.

Results and Discussions

OM Observation

It can be seen from the microstructure of four kinds of stainless steel wires in Figs. 1 and 2 that the metallographic microstructure of coil (Φ7.5 mm) contains 80% martensite and 20% ferrite. The horizontal average grain size is 19.6 μm and the longitudinal average grain size is 25.9 μm by using Image tool. The second phase can clearly be observed at the black points, which are evenly distributed in the core of the cross section. In the corresponding case, a portion of the banded structure along the longitudinal section was distributed along the deformation direction. The presence of duplex phase in fiber structure caused the inhomogeneity of structure and the decline of mechanical properties. When the wire was drawn to Φ6.5 mm, the longitudinal average grain size was 18.9 μm and the grain was extended and presented an inhomogeneity. When the wire was drawn from Φ5.5 to Φ5.0 mm, the original grain was completely broken and the grain boundary was blurred. The original grain was elongated and a fibrous tissue was formed, which decreased the plasticity and increased the cold work-hardening rate [8]. Meanwhile, the grain size of the horizontal section became smaller due to the obvious elongated grain, and the elongated second phase structure formed the fibrous tissue which could increase the strength and decrease the plasticity [9].

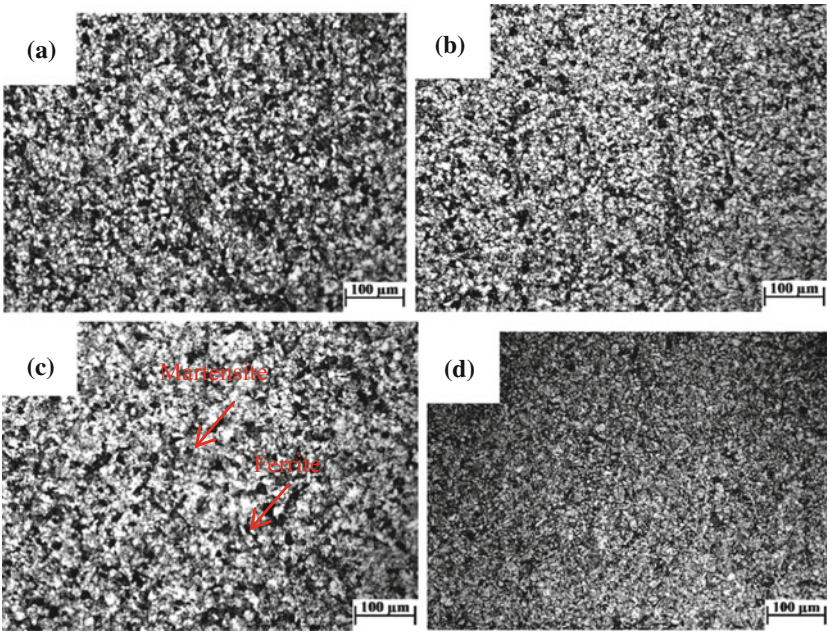

Fig. 1 Microstructure of cross section of 410 stainless steel wires with different diameter **a** Φ7.5 mm, **b** Φ6.5 mm, **c** Φ5.5 mm, **d** Φ5.0 mm

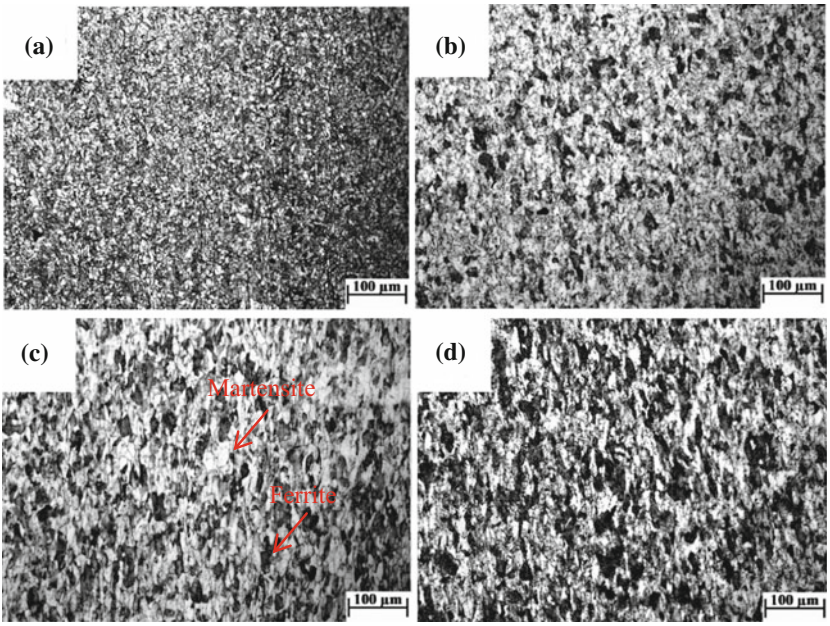

Fig. 2 Microstructure of longitudinal section of 410 stainless steel wires with different diameter **a** Φ7.5 mm, **b** Φ6.5 mm, **c** Φ5.5 mm, **d** Φ5.0 mm

Table 2 Mechanical properties of 410 steel wires after different drawing deformation

Diameter (mm)	R_m (MPa)	Elongation (%)
7.5	504	38.2
6.5	665	16.7
5.5	737	15.3
5.0	741	13.1

Mechanical Properties

Table 2 shows the mechanical properties of 410 stainless steel wire after different cold drawing deformation. The tensile strength of 410 stainless steel was increasing and elongation was decreasing during the cold drawing. The tensile strength of wire coil (Φ7.5 mm) was 504 MPa and the elongation was 38.2%. The diameter of 410 stainless steel was reduced from 7.5 to 6.5 mm after the cold drawing, the tensile strength of the hard line was 665 MPa and the elongation was 16.7%. When the diameter was 5.5 mm, tensile strength rose to 737 MPa while the elongation slightly decreased. When the wire was drawn from Φ5.5 to Φ5.0 mm, the tensile strength increased to 741 MPa and the elongation decreased to 13.1%.

Figure 3 presents the drawing hardening and stress-strain curves of 410 stainless steel wire before and after drawing. It can be seen that the tensile strength and work-hardening decreased with the increase of the reduction of area (shown in Fig. 3a). The strength of martensite and ferrite is different (shown in Fig. 3b). The strain hardening of the steel wire could be divided into two stages. In the first stage, the n valued increased gradually and peaked at 0.85 which associated with the ferrite deformation. In the second stage, the n decreased to 0.25 which associated with martensite deformation and the declined compatibility of the duplex phase.

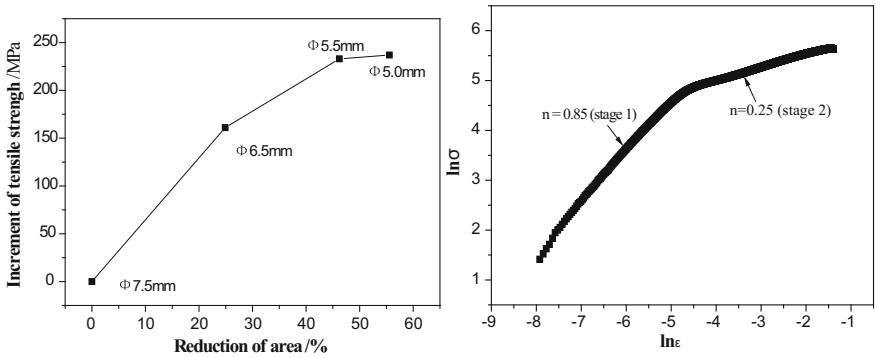

Fig. 3 Drawing hardening and stress-strain curves of 410 stainless steel wire before and after drawing **a** drawing hardening curve, **b** double logarithmic true stress-strain curve

Work Hardening Mechanism

The main work-hardening mechanism of 410 steel wires during the cold drawing process is fine grain strengthening and dislocation strengthening. The cross-section area was gradually reduced with the cold drawing process, and the grain size decreased with the presence of partial deformation twinning. The lattice of the inner grain was distorted and the dislocation density was increasing with the plastic deformation. Due to the interaction between dislocations, dislocation pile-up and dislocation wall were formed inside the wire, which could hinder the following movement of dislocation and the deformation resistance increased sharply [10].

The grain size and grain size number are shown in Table 3. It shows that the average grain size was decreasing and the grain size number was increasing. The fine grain strengthening has a great influence on the performance of stainless steel wire which can be calculated by Hall-Petch formula.

$$\sigma_s = \sigma_i + KD^{-1/2} \tag{1}$$

Where σ_s, σ_i, D, and K show yield stress, constant related to crystal type, average grain diameter and K = 600 MPa × $\mu m^{1/2}$, respectively. When the steel wire was drawn from Φ7.5 to Φ5.0 mm, the increment of strength was 46.8 MPa.

The microstructure of TEM with different cold drawing deformation is shown in Fig. 4. The dislocation density increased with the increase of deformation and dislocation piled up and tangled at the grain boundary. When the cold drawing deformation was small, dislocation lines were linear or curved. In the high density region, stacking fault was formed, which was the resistance for the plastic deformation. Finally, a large number of dislocations gathered together and became dislocation wall and dislocation cell, which can be seen in Fig. 4d. When dislocation cell was found around grain boundaries, martensite deformation could be serious [11]. Thus, additional stress could promote the generation of dislocation defect. Because the crystal plastic deformation produced dislocation multiplication in the slip process, the dislocation density was rapidly increased, which hinderes the slip and produced work-hardening [12].

Table 3 Average grain size of the organization of rod-wire and wire

Diameter (mm)	Horizontal grain size number	Horizontal grain size (μm)	Longitudinal grain size number	Longitudinal grain size (μm)
7.5	8–8.5	19.6	7–7.5	25.9
6.5	8–8.5	16.3	7.5–8	21.6
5.5	9–9.5	13.8	8–8.5	19.1
5.0	9.5–10	10.8	8.5	16.8

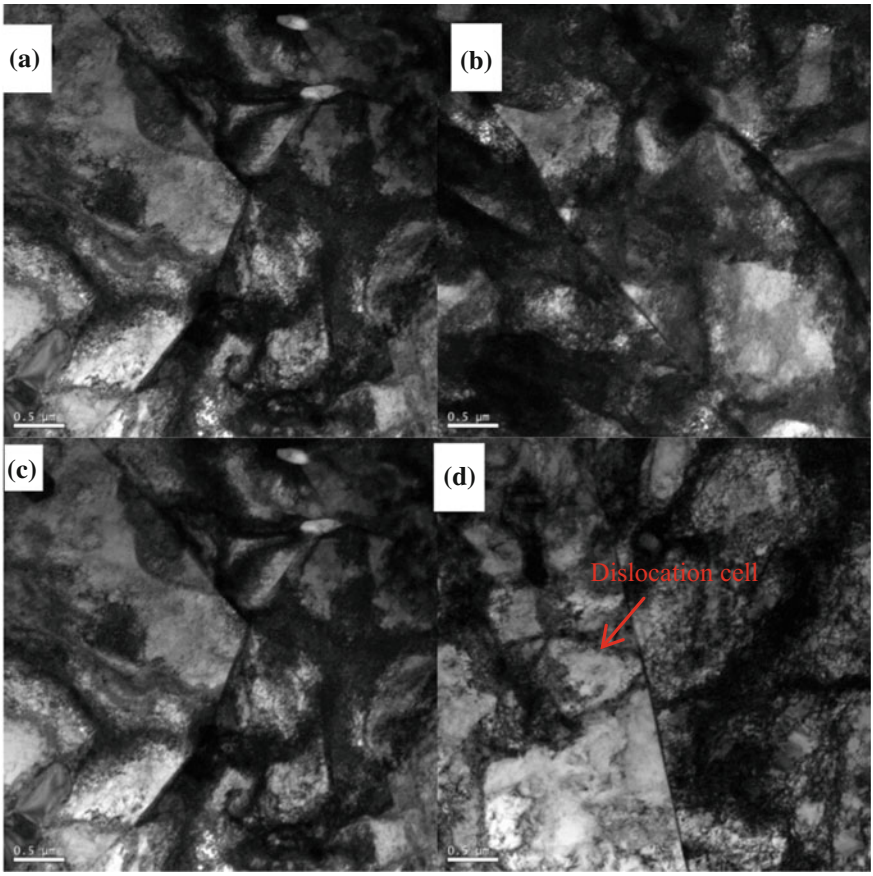

Fig. 4 High density dislocation of different diameter steel wires **a** Φ7.5 mm, **b** Φ6.5 mm, **c** Φ5.5 mm, **d** Φ5.0 mm

The formula of dislocation strengthening is as following:

$$\Delta\sigma_d = \alpha G b \rho^{1/2} \tag{2}$$

where G, b, ρ, n, and α show shear modulus = 0.79×10^5, Burgers vector = 0.248 nm, dislocation density, $\rho = n^2/(4.35 \bullet b^2)$, half-peak value measured by XRD diffractometer, and α = 0.5. The dislocation density of experimental steel was measured by XRD was $3.14 \times 10^{10}/cm^2$. When the wire was drawn from Φ7.5 to Φ5.0 mm, dislocation strengthening was calculated to be ~173 MPa by the Eq. 2.

Conclusions

(1) The metallographic microstructure of 410 martensite stainless steel is consisted of martensite and ferrite and a few duplex phases. The grain size is elongated along the deformation direction, which decreases from 22.7 to 13.8 μm. Besides, the deformation of each grain is inhomogeneous during the cold drawing.
(2) The tensile strength increases from 504 to 741 MPa and the elongation decreases from 38.2 to 13.1% during the cold drawing. The strain hardening of the steel wire can be divided into two stages. In the first stage the n value increases gradually and reaches the peak at 0.85 which associated with the ferrite deformation. In the second stage, the n decreases to 0.25 which associated with martensite deformation and the declined compatibility of the duplex phase.
(3) The main work-hardening mechanism of 410 steel wire during the cold drawing process is fine grain strengthening and dislocation strengthening. When the steel wire is drawn from Φ7.5 to Φ5.0 mm, the fine strengthening increases by 46.8 MPa and the dislocation strengthening increases by 173 MPa.

References

1. J. Yao, J. Liu, Y. Jia et al., Forming mechanism and control for longitudinal cracks on continuous casting billet of 1Cr13 semi-martensite stainless steel. Hebei Metall. **04**, 18–22 (2014)
2. B. Xintao, Development trend of stainless steel. Heat Treat. (04), 5–9 (2007)
3. X. Jimei, The metal problem of stainless steel. Metallurgical Industry Press (2006), pp. 155–286
4. S. Vafaeian, A. Fattah-Alhosseini, Y. Mazaheri et al., On the study of tensile and strain hardening behavior of a thermomechanically treated ferritic stainless steel. Mater. Sci. Eng., A **669**, 480–489 (2016)
5. X. Kangping, Z. Meng, Study on microstructure and mechanical properties of ultrafine stainless steel microfilament during drawing. J. Nanchang Univ. (02), 173–177 (2008)
6. L. Jiang, K. Feng, Z. Guo et al., Research on performance contrast between 321 stainless steel and 410 stainless steel. Hot Working Technol. **41**(6), 124–126 (2012)
7. S.A. JenabaliJahromi, A. Khajeh, B. Mahmoudi, Effect of different pre-heat treatment processes on the hardness of AISI 410 martensitic stainless steels surface-treated using pulsed neodymium-doped yttrium aluminum garnet laser. Mater. Des. **34**, 857–862 (2012)
8. Sokol. Duplex stainless steel. Atomic Energy Publishing House, Beijing (1979) p. 108
9. G. Liu, B. Wang, X. Shi et al., Research present situation of work-hardening and evolution of microstructure and mechanical properties of cold drawing pearlitic steel wires. Mater. Rev. **S2**, 204–207 (2008)

10. M.C. Tsai, C.S. Chou, J.S. Du et al., Phase transformation in AISI 410 stainless steel. Mater. Sci. Eng., A **332**(1–2), 1–10 (2002)
11. L. Chen, R.B. Song, F.Q. Yang et al., Working hardening mechanism and aging treatment behaviors of D631 precipitation hardening stainless steel wire. Mater. Sci. Forum **788**, 362–366 (2014)
12. H. Yu, Study on strain strengthening technology and properties of austenitic stainless steel. J. Mech. Eng. **2**, 87–92 (2012)

Microstructural Properties and Hardening Mechanism of Explosion Hardening of Mn13Cr2 Steel Surface

Qinan Ba, Renbo Song, Yifan Feng and Lun Li

Abstract This article is aimed at the surface explosion hardening of Mn13Cr2 steel. The mechanical properties of Mn13Cr2 steel after explosion hardening were tested. The microstructure of Mn13Cr2 steel after explosion hardening was studied using optical microscopy (OM), scanning electron microscopy (SEM), X-ray diffraction (XRD). The experimental results showed that after an explosion hardening the surface hardness of Mn13Cr2 increased from 220 to 400 HB, and the impact toughness decreased from 60 to 15 J cm^{-2}, the depth of the hardened layer was about 35 mm. The tensile strength increased from 500 to 690 MPa, yield strength increased from 400 to 430 MPa, the elongation was 15%. After the second aryexplosion, the surface hardness of Mn13Cr2 increased from 400 to 420 HB, and the impact toughness decreased from 15 to 12 J cm^{-2}, the depth of the hardened layer was about 38 mm. Tensile strength increased from 690 to 750 MPa, yield strength increased from 430 to 460 MPa. A large number of slip bands appeared in Mn13Cr2 steel specimens after an explosion, and the deformation twins were not observed, and the martensite phase did not appear on Mn13Cr2 steel according to XRD analysis. But martensite phase appeared after the secondary explosion. Therefore, an explosion hardening mechanism of high manganese steel is mainly dislocation hardening, the secondary explosion hardening mechanism of high manganese steel is mainly martensite hardening and dislocation hardening.

Q. Ba · R. Song (✉) · Y. Feng
School of Materials Science and Engineering, University of Science and Technology Beijing, Beijing, China
e-mail: songrb@mater.ustb.edu.cn

Q. Ba
e-mail: baqinan930913@163.com

Y. Feng
e-mail: ustbfyf@126.com

L. Li
Anshan Steel Group Corporation Limited, East Anshan Sintering Plant, Anshan, Liaoning, China
e-mail: 1760369030@qq.com

© Springer Nature Singapore Pte Ltd. 2018

Y. Han (ed.), *Advances in Materials Processing*, Lecture Notes in Mechanical Engineering, https://doi.org/10.1007/978-981-13-0107-0_47

Keywords Mn13Cr2 steel · Mechanical properties · Explosion hardening Hardening mechanism

Introduction

Since the R. A. Hadfield invented high manganese steel in 1882, the high manganese steel has been playing a very important role in the wear-resistant materials because of its excellent strength, better toughness, excellent work hardening performance and excellent wear resistance under the impact of wear conditions. But in the early service wear resistance and resistance to deformation is not ideal, so people put forward some surface pretreatment process. In 1955, NA Macleod applied for the first patent on the high manganese steel explosion hardening technique. Subsequently, a lot of researches on the mechanism of explosion hardening were carried [1–6].

In the 21th century, the researchers selected different explosives for high manganese steel explosion hardening technology research [7, 8]. Di Jianhua [9, 10] et al. used the TNT, PBXN-5, RDX and No. 2 rock explosives to experiment with high-manganese steel. They believed that the explosive hardening effect of high-explosive RDX and PBXN-5 was better, and in the same dose of the case, the secondary explosion effect was better than the effect of an explosion. This also showed that the high manganese steel explosives should have a high burst speed and stiffness, detonation critical diameter and so on.

In this paper, the surface of Mn13Cr2 steel was subjected to an explosion hardening and secondary explosion hardening. The explosives were laid in the same position. The hardening effect was compared, and analyzed the best number of explosions for such explosive. Hardening mechanism was studied by the microstructure and mechanical properties of Mn13Cr2 steel.

Experiment

The chemical composition of the experimental steel is shown in Table 1. Explosion was C–4, the density is 1.59 g/cm^3, explosive speed is 8000 m/s, explosive thickness was 3 mm. After homogenized at 1050 °C for 1 h, the experimental steels were subjected to an explosion and secondary explosion treatment, respectively. The room temperature tensile tests were operated with a beginning velocity of 10^{-3} s^{-1} by CMT4105 electronic universal experiment machine. Its toughness was tested by ZBC2452-B pendulum impact testing machine with 10 mm × 10 mm × 55 mm V-notch standard sample and its hardness was tested by XHB-3000 brinell hardness machine. After etching the mechanically polished

Table 1 Chemical composition of the experimental steel (wt%)

C	Mn	Si	Cr	Fe
1.18	13.3	0.55	1.81	Bal.

specimens with 4% (volume fraction) Nital, the microstructure was examined by Axio Imager M2 m microscope (OM) and Zeiss Ultra 55 scanning electron microscopy (SEM), and then the volume fraction of martensite was determined by X-ray diffraction (XRD).

Results and Discussions

Mechanical Properties

Table 2 shows the mechanical properties of Mn13Cr2 steel after an explosion hardening and secondary explosion hardening. We can see that after an explosion hardening the surface hardness of Mn13Cr2 steel increased by 82%, the impact toughness decreased by 75%, tensile strength increased by 38%, yield strength increased by 7.5%. Mechanical properties have been greatly improved. After an explosion hardening, the surface hardness of Mn13Cr2 steel increased by 91%, and the impact toughness decreased by 80%, tensile strength increased by 50%, yield strength increased by 15%. Although compared to unexploded high manganese steel the mechanical properties had a much improvement, compared to the mechanical properties of an explosion enhanced not very obviously. Due to the cracks of Mn13Cr2 surface after secondary explosion, the surface hardness increased not obviously, so that mechanical properties were not improved significantly.

It can be seen from Table 2 that the impact toughness increased with the depth, and the impact toughness of manganese steel specimens outside hardened layer and the unexploded specimens was basically the same. The main reason for this phenomenon is that under the impact of the larger pressure, the plastic deformation of the surface of the high manganese steel specimen occurred, and a large number of stacking faults and dislocations were generated inside the material. Resulted in

Table 2 Mechanical properties of the experiment steel after an explosion hardening

	Hardness (HB)	a_k (J cm^{-2})	R_m (MPa)	$Rp_{0.2}$ (MPa)	A (%)
An exploded surface	404	15	690	430	15
Secondary exploded surface	420	12	750	460	6
Outside hardened layer	220	60	500	400	40

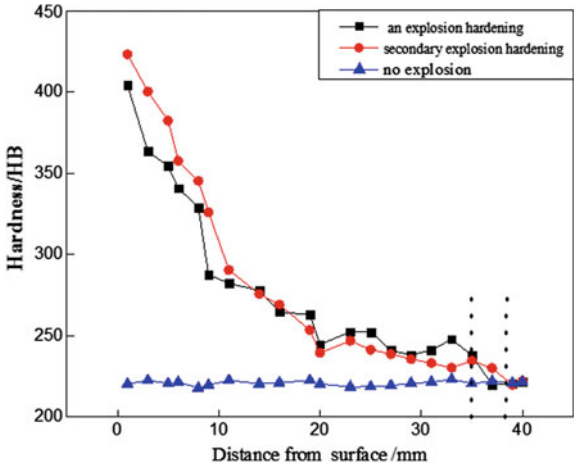

Fig. 1 Hardness gradient curve after an explosion, secondary explosion and no explosion

strain concentration and reduced impact toughness. As the impact of the surface of the material by the largest impact at the interface of the largest concentration of strain generated, impact toughness of high manganese steel specimen surface after explosive hardening was less than the impact toughness within the material. The martensite produced by the secondary explosion also reduced the toughness, and with the increase of hardening depth, and the toughness increased.

Figure 1 shows the comparison of hardness gradient curve after an explosion and secondary explosion. Their hardening gradients were basically the same. The depth of the hardened layer was about 35 mm after an explosion hardening. The depth of the hardened layer was about 38 mm after secondary explosion hardening.

The hardening effect of an explosion is obvious, and the hardening effect of the secondary explosion is not much better than that of an explosion.

Microstructural Characteristics

Figure 2 illustrates the microstructure of Mn13Cr2 steel after an explosion, secondary explosion and no explosion. We can see that the matrix of the experimental steel was austenite, no martensite was observed. It can be seen that a large number of slip bands occurred on the surface of the high manganese steel after explosion hardening from Fig. 2a, b, and no significant twins were observed. Although the performance of high manganese steel after secondary explosion has improved, the surface of the material has been damaged. As shown in Fig. 2c, cracks were observed on the surface of the specimens after the secondary explosion. So the secondary explosion with C–4 explosives was not suitable for Mn13Cr2 steel.

Followed by XRD analysis, Fig. 3 shows XRD analysis of experimental steel with an explosion, secondary explosion and no explosion. There was only austenite

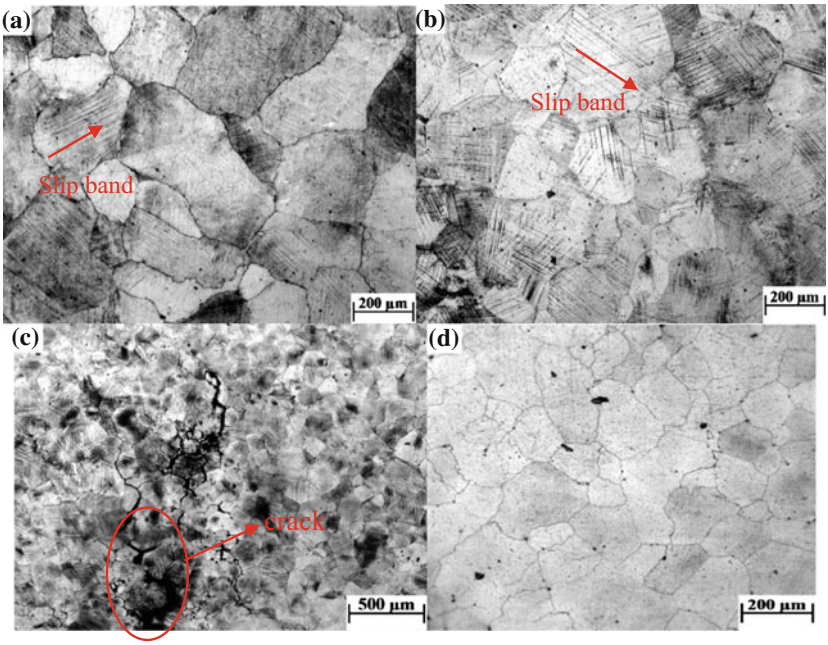

Fig. 2 Optical micrographs of experimental steel **a** an explosion specimens, **b** secondary explosion specimens, **c** the crack of the secondary explosion, **d** no explosion specimens

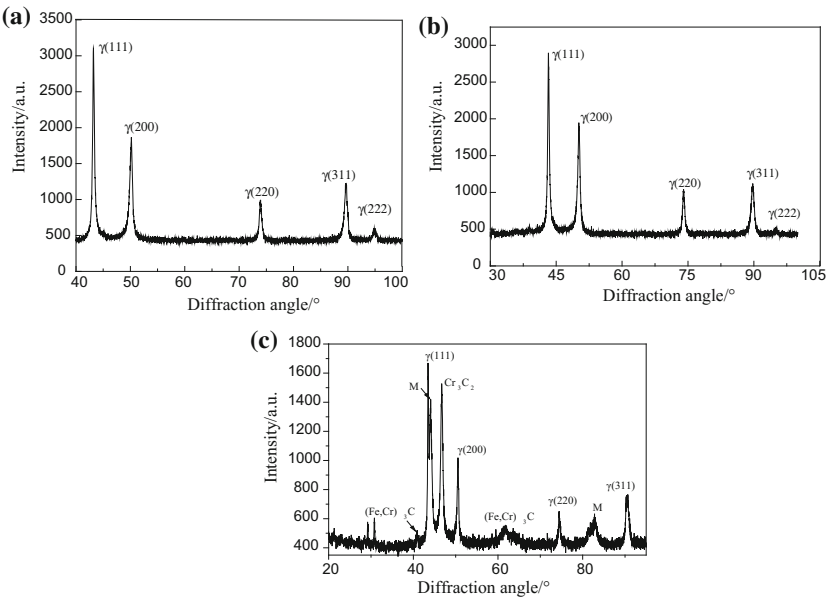

Fig. 3 XRD analysis of experimental steel with an explosion, secondary explosion and no explosion **a** no explosive specimens, **b** an explosive specimens, **c** secondary explosion specimens

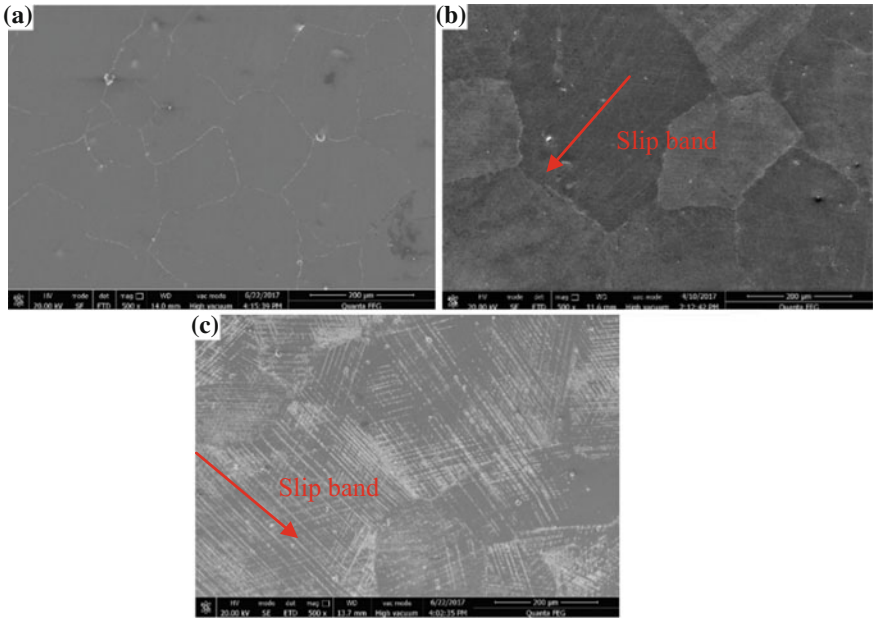

Fig. 4 SEM micrographs of experimental steel with an explosion, secondary explosion and no explosion **a** no explosive specimens, **b** an explosive specimens, **c** secondary explosion specimens

matrix in the microstructure and there was no martensite in the microstructure after an explosion hardening. But martensite appeared in the microstructure of the secondary explosion, so one reason for hardening was martensitic transformation [11]. The volume fraction of available martensite was calculated to be ~20.1% after secondary explosion according to the formula (1) expressed as follows:

$$W_\varepsilon = \frac{I_\varepsilon}{I_\varepsilon + I_r K_\varepsilon} \tag{1}$$

where I_ε, I_r and K_ε show ε-martensite strength integral, austenite strength integral and RIR. The value of I_ε, I_r and K_ε were 579.7, 308.3 and 7.47, respectively, which could be obtained by Jade 6.0 software. It can be concluded that after the secondary explosion, the surface of the high manganese steel produced martensitic transformation to increase the hardness and reduce the toughness.

Figure 4a shows the high manganese steel SEM image without exploding hardening, and only austenite matrix was shown. It can be thought the dislocation hinders the slip motion, resulting in hardening [12, 13]. Figure 4b shows the SEM image of Mn13Cr2 steel surface after an explosion hardening. A large number of slip bands and the slip bands delivery appeared in austenite matrix as shown in Fig. 4b. So an explosion hardening mechanism of high manganese steel is mainly dislocation hardening. Figure 4c shows the SEM of Mn13Cr2 steel after secondary

explosion. After the secondary explosion, the surface of the high manganese steel had more slip bands. Compared to an explosion, the dislocation density of the secondary explosion was greater, and the higher dislocation density lead to more dislocations entangled, and thus the greater force hindered the slip motion, the hardening effect of the secondary explosion was better than an explosion. In a word, in addition to martensitic hardening, the hardening mechanism of the high manganese steel after secondary explosion hardening also was dislocation hardening.

Conclusions

(1) After an explosion, the surface hardness of Mn13Cr2 steel reaches 400 HB, increased by 82%. The tensile strength reaches 690 MPa, increased by 38%. The yield strength reaches 430 MPa, increased by 7.5%. The hardened layer was 35 mm. Compared to an explosion, the performance after the secondary explosion is still improved, but the increase was very small, and the surface cracks generate. So the effect of an explosion is better than the secondary explosion.
(2) The surface microstructure of Mn13Cr2 steel after an explosion hardening is matrix austenite, without martensite and twinning. The surface microstructure of Mn13Cr2 after secondary explosion hardening is austenite matrix and martensite (20.1%).
(3) The hardening mechanism of Mn13Cr2 steel after an explosion is dislocation hardening. The hardening mechanism of Mn13Cr2 steel after secondary explosion is mainly composite hardening of martensitic transformation and dislocation.

References

1. R.A. Hadfield, Hadfield's manganese steel. Science **12**, 284–286 (1888)
2. A. Handbook, Properties and selection: irons, steels, and high performance aIloys. ASM Int. **1**, 140–194 (1990)
3. B.F. Cheng, P.R. Liu, Effect of explosive hardening on service life of high manganese steel frog. Metall. Equip. **81**, 131–132 (2013)
4. M. Zhang, B. Lv, F. Zhang et al., ISIJ Int. **52**(11), 2093–2095 (2012)
5. F.C. Liu, B. Lv, F.C. Zhang et al., Mater. Lett. **65**(15–16), 2333–2336 (2011)
6. R.A. Hadfield, *Manganese Steel* (Oliver & Boyd, Edinburgh, 1956)
7. F. Zhang, B. Lv, T. Wang, et al., ISIJ Int. **48**(12), 1766–1770 (2008)
8. G. Zhang, *Explosion Hardening Performance and Hardening Mechanism of High Manganese Steel* (Henan University of Science and Technology, Luoyang, 2007)
9. J.H. Di, C.L. Lv, X.S. Song, Study on explosive hardening of high manganese steel. (01), 17–19 (2001)

10. J.H. Di, *Study on Explosive Burning and Hardening Technology of Metal Materials* (North China Institute of Technology, Taiyuan, 2001)
11. X.X. Li, G. Zhao, G.J. Zhang, Hot Working Technol. **6**, 94–96 (2013)
12. I. Karaman, H. Sehitoglu, A.J. Beaudoin et al., Acta Mater. **48**(9), 2031–2047 (2000)
13. S. Allain, J. Chateau, D. Dahmoun et al., Mater. Sci. Eng., A **387–389**, 272–276 (2004)

Effects of Solution Temperature on Microstructure and Properties of Fe–Mn–Al–C Ferrite-Based Steel

Xuan Li, Renbo Song, Naipeng Zhou, Jiajia Li and Lun Li

Abstract The effects of solution temperature of 700–950 °C on microstructure and properties of Fe–8Mn–6Al–0.2C ferrite-based steel were investigated. Optical microscopy (OM), scanning electron microscopy (SEM), energy dispersive spectrometer (EDS) and X-ray diffraction (XRD) were used to study the morphology and composition of microstructure. The tensile test at room temperature was used to detect mechanical properties. The results showed that the as-hot-rolled steel exhibited a complex microstructure, consisting of banded ferrite, martensite and small amount of retained austenite. With the increase of solution temperature, δ-ferrite solidified from the liquid phase and existed during subsequent heat treatment at all the temperatures, while the other phases varied from M_5C_2, α-ferrite, austenite and martensite. At 900 °C, dual phase microstructure with ferrite and island of austenite was obtained. With increasing solution temperature, the ultimate tensile strength (UTS) decreased at first and then increased after reaching the minimum at 850 °C, while the total elongation (TE) increased firstly and declined after the peak value of 44.5% at 850 °C. Therefore, the as-hot-rolled experimental steel heat treated at 900 °C had an excellent combination of tensile strength and elongation, with UTS of 846.4 MPa, TE of 32%, and UTS × TE of 27.1 GPa%. The remarkable mechanical properties, both strength and elongation, were attrib-

X. Li · R. Song (✉) · N. Zhou · J. Li
School of Materials Science and Engineering,
University of Science and Technology Beijing, Beijing, China
e-mail: songrb@mater.ustb.edu.cn

X. Li
e-mail: runfastxuan@163.com

N. Zhou
e-mail: znp628@163.com

J. Li
e-mail: 1379591093@qq.com

L. Li
Anshan Steel Group Corporation Limited, East Anshan Sintering Plant,
Anshan, Liaoning, China
e-mail: 1760369030@qq.com

© Springer Nature Singapore Pte Ltd. 2018

Y. Han (ed.), *Advances in Materials Processing*, Lecture Notes in Mechanical Engineering, https://doi.org/10.1007/978-981-13-0107-0_48

uted to the relative fraction and stability of austenite. And the partition of elements, especially for Mn, had great effect on the austenite stability.

Keywords Fe–Mn–Al–C steel · Solution temperature · Microstructure evolution Mechanical properties

Introduction

Fe–Mn–Al–C steels have been widely used for automobile industry not only because of their optimized combination of high strength and ductility, but their contribution on enhancing fuel efficiency and reducing carbon dioxide emission [1–3].

Recently, Fe– (2–7) Mn– (0–9) Al– (0–0.4) C ferrite based low density steels were reported, which yield excellent mechanical properties due to the transformation-induced plasticity (TRIP) effect [4–7]. For example, Park et al. investigated an alloy under a specific heat treatment condition showed deformation-induced martensitic transformation, tensile strength of >900 MPa and a high total elongation of >50% were obtained [8]. Seo et al. claimed that the austenite phase was retained at room temperature and transformed to martensite during deformation, resulting in a tensile strength of 990 MPa and elongation of 28% [9].

Actually, retained austenite stability would be essential for superior mechanical properties of TRIP steels, which associated with austenite-stabilizing elements, grain size, grain morphology, crystallographic orientation relationship and so on [10–12].

This study focuses on the microstructure and mechanical properties of Fe–Mn–Al–C ferrite-based steel under different heat treatment conditions, in the endeavor to figure out the effect of heat treatment temperature on microstructural evolution and mechanical properties.

Experimental

The steel used in this study has a nominal composition of Fe–7.35 Mn–6 Al–0.15 C (wt%). The ingot were casted using a vacuum furnace and heated at 1200 °C for 2 h and hot forged to rods of section size 35 mm × 70 mm × 100 mm, followed by air cooling to room temperature. The rolling and heat treatment conditions are illustrated in Fig. 1. Subsequently, the ingot was homogenized at 1200 °C for 2 h, and hot rolled to 3 mm thickness between 1150 and 850 °C, and finally water quenched to 550 °C then air cooled to room temperature. The hot-rolled sheets were solution treated at 700–950 °C for 1 h and then quenched in water. Tensile tests were conducted using specimens with a gage length of 12.5 mm and a gage

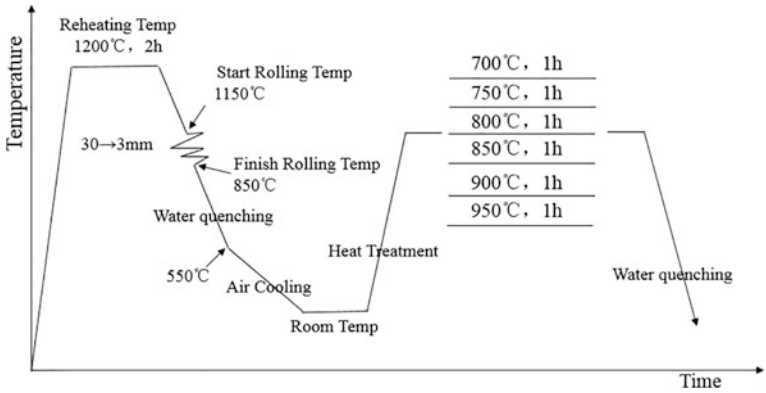

Fig. 1 Schematic illustration of the rolling conditions for the experimental steel

length of 50 mm that were machined from the heat-treated sheets in the longitudinal direction. The microstructure was analyzed by optical microscopy (OM), scanning electron microscopy (SEM). Energy dispersive spectrometer (EDS) was used to investigate the partition of Al and Mn elements in ferrite. The volume fraction of austenite was determined by X-ray diffraction (XRD) with CuK_{α} radiation using the direct comparison method according to the integrated intensities of the $(200)_{\alpha}$ and $(211)_{\alpha}$ peaks and the $(220)_{\gamma}$ and $(311)_{\gamma}$ peaks [13].

Results and Discussions

Microstructure Evolution

Figure 2a, b shows the microstructure of the alloy after hot rolling. The hot rolled microstructure exhibited δ-ferrite band and martensite band parallel to the rolling

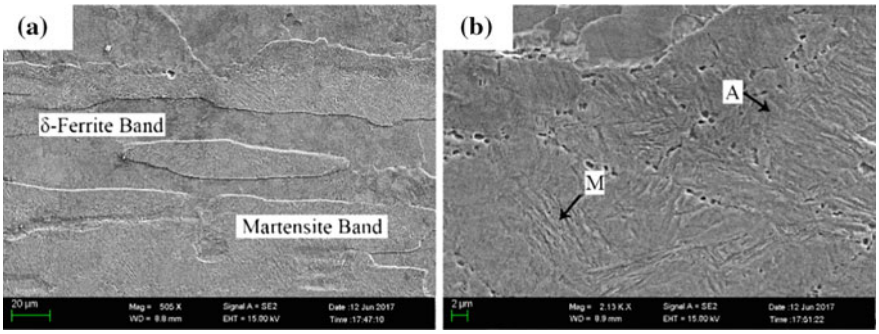

Fig. 2 SEM microstructure of hot-rolled specimen (M-martenite, A-austenite)

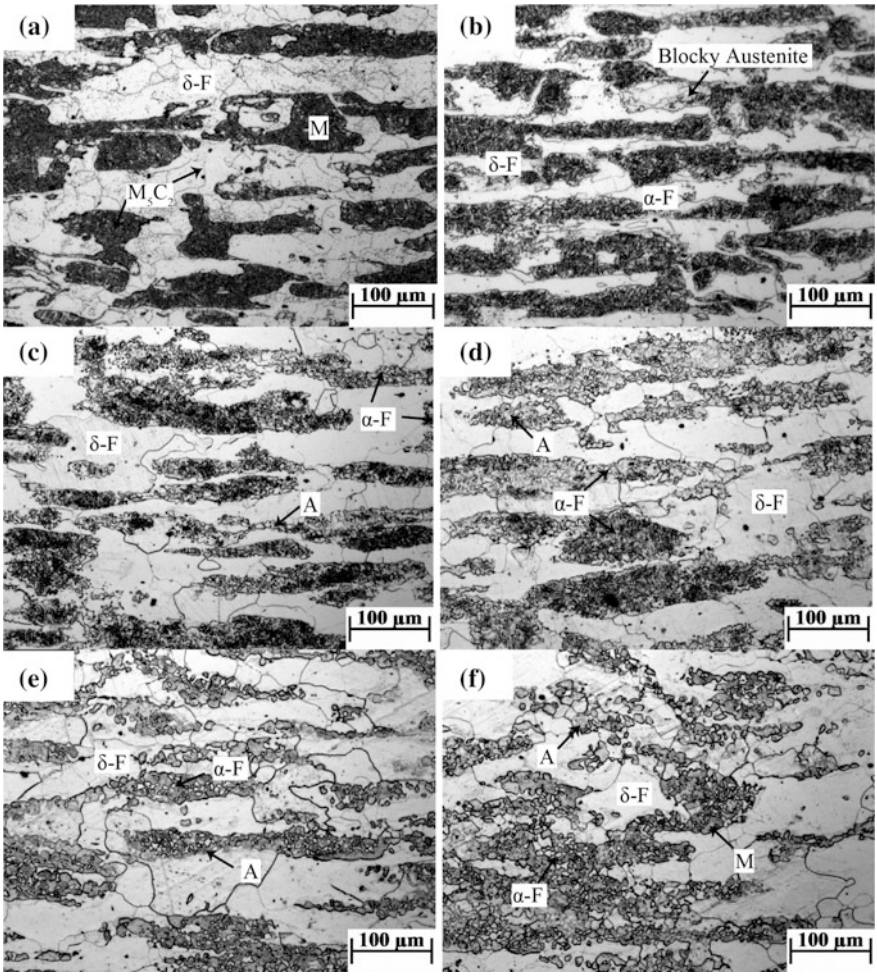

Fig. 3 SEM micrographs of experimental steels after solution treatment for 1 h at **a** 700 °C, **b** 750 °C, **c** 800 °C, **d** 850 °C, **e** 900 °C, **f** 950 °C

direction, and martensite band contained a number of martensite and a few retained austenite.

Figure 3a–f show the SEM micrographs of experimental steels after treated at 700–950 °C for 1 h. It can be seen that δ-ferrite solidified from the liquid phase and existed during subsequent solution treatment at all the temperatures, so the morphology and transformation of other phases were mainly discussed talked about here. When treated at 700 °C, austenite has almost decomposed to martensite and spheroidal M_5C_2, which widely distributed in both δ-ferrite grain boundaries and martensite lathes. In the specimen treated at 750 °C, M_5C_2 disappeared, marteniste transformed into austenite including blocky austenite and island austenite. At the

Table 1 Vickers microhardness of constituent phase

Phase	Vickers microhardness, HV
Austenite	275 ± 10
δ-ferrite α-ferrite	314 ± 15 374 ± 10
Martensite	438 ± 15

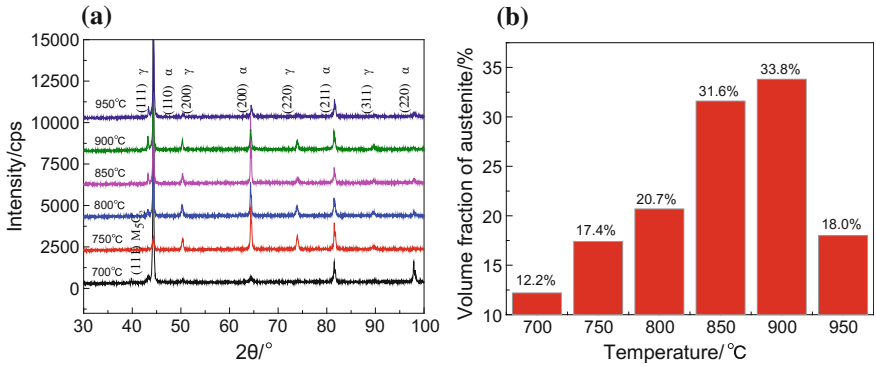

Fig. 4 XRD patterns and measured austenite fractions of heat treated specimens at different temperature. **a** XRD patterns, **b** measured austenite fractions

same time, small amount of fine α-ferrite were presented in island austenite, which is different from δ-ferrite both in morphology and microhardness (Table 1). When the solution temperature was among 800–900 °C, the microstructure of specimen consisted of α-ferrite, δ-ferrite and austenite. However, the morphology of fine α-ferrite has changed into strip and decreased at 900 °C, the fraction of austenite increased apparently with increasing heat treatment temperature. At 950 °C, austenite was obviously coarser and a small amount of martensite was formed again. The different phase can be distinguished according to the Vickers microhardness as is presented in Table 1. It can be seen that the microhardness of martensite was higher than austenite and ferrite.

The XRD patterns and measured austenite fractions of heat treated specimens are presented in Fig. 4. It's clear that the volume austenite fraction varied with different temperatures, and there was a small amount of austenite (12.2%) at 700 °C. As shown in Fig. 4b, the fraction of retained austenite had a higher value with the increasing temperature, reaching to 33.8% when heat treated at 900 °C and then decreased significantly at 950 °C to 18.0%. Actually, the stability of austenite was of great importance and governed the mechanical property of steel, the details of which will be further discussed.

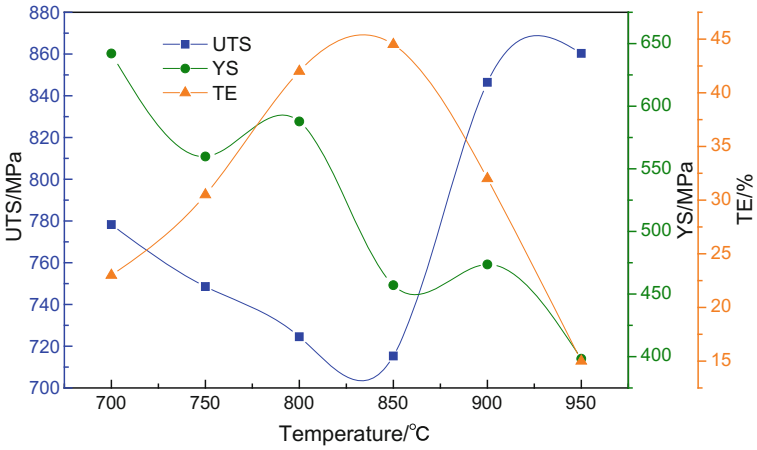

Fig. 5 Mechanical properties of experimental steel heat-treated at different temperatures

Mechanical Properties

The mechanical properties of experimental steel heat-treated at different temperatures are summarized in Fig. 5. The ultimate tensile strength (UTS) decreased at first with the temperature rises from 700 to 850 °C and began to increase at 900 °C. The yield strength (YS) decreased as a whole with increasing temperature but rose slightly at 800 and 900 °C, respectively. As for the tendency of total elongation (TE), it was completely opposite with UTS, it increased firstly and declined after the peak value of 44.5% at 850 °C. Compared with Fig. 4b, it's clear that TE had a similar trend with volume fraction of austenite. Therefore, it can be inferred that the amount of austenite play a significant role in influencing ductility. To sum up, the as-hot-rolled experimental steel heat-treated at 900 °C had an excellent combination of tensile strength and elongation, with UTS of 846.4 MPa, TE of 32%, and UTS × TE of 27.1 GPa%.

Element Partition and Austenite Formation

The element compositions of different phase in experimental steel were measured by EDS as shown in Fig. 6. The formation of austenite with different value fractions and stabilities was induced by element partition, including the first partition of elements in the dual-phase region at high temperature and the second partition of elements at relatively low temperature by short-range diffusion, especially for Mn element [14].

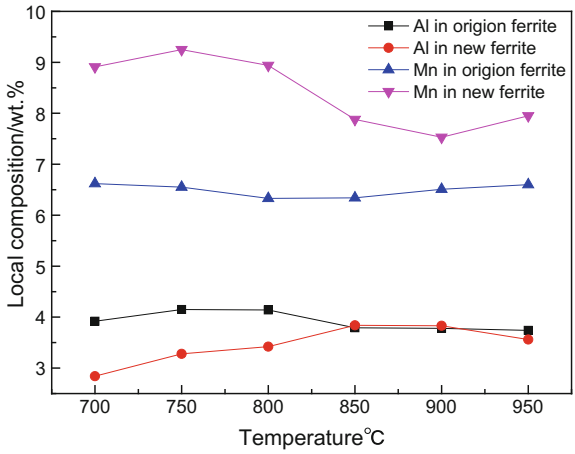

Fig. 6 Element compositions of different phase in experimental steel

As is shown in Fig. 6, it's clear that, the Mn, Al contents of original δ-ferrite and α-ferrite barely changed with increasing heat treatment temperature, and the content of Al element in the original δ-ferrite and α-ferrite tended to be the same eventually. What's more, the Mn content of α-ferrite decreased sharply at 800 °C and kept constant at higher temperature. Although it's difficult to study the element partition in austenite due to the multiple phases, we can infer it according to the partition of Mn, Al elements in ferrite, which means the Mn elements enriched in austenite with increasing temperature and largely prompted the formation and stability of austenite. This is the reason why the volume fraction of austenite at 800–900 °C were so much higher than that at the other temperature. Simultaneously, the enrichment of Al elements promoted the formation of α-ferrite.

EDS line scanning was done during SEM observation of the specimens heat-treated at 900 °C to examine the elements concentration in different phases, as shown in Fig. 7. It can be seen that Mn elements were enriched in austenite while Al elements were enriched in ferrite. The result was well in accord with the previous research in this paper.

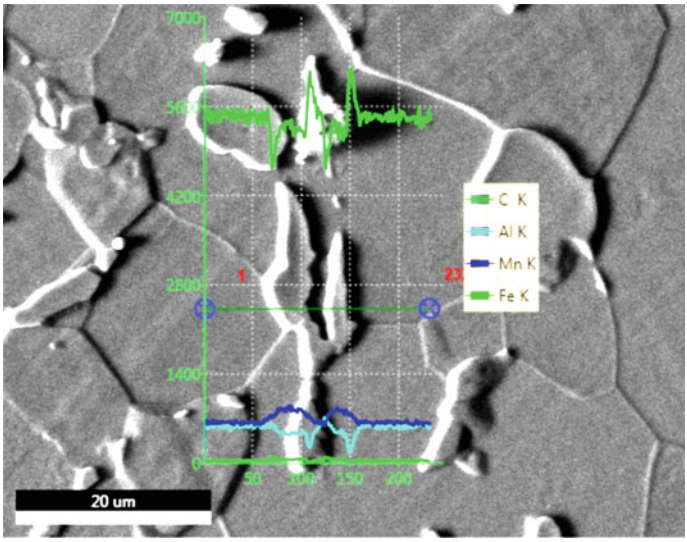

Fig. 7 EDS line scanning result of specimen heat-treated at 900 °C

Conclusions

The microstructural evolution, mechanical properties, element partition and the stability of austenite of the Fe–8Mn–6Al–0.2C steel have been studied in detail. The main conclusions are as follows:

(1) The excellent combination with tensile strength and elongation is achieved at the heat treatment temperature of 900 °C, with UTS of 846.4 MPa, TE of 32%, and UTS × TE of 27.1 GPa%, respectively.
(2) δ-ferrite solidifies from the liquid phase and exists during subsequent heat treatment at all the temperatures. When the alloy is heat-treated at 700 °C, the austenite almost decomposes to martensite and spheroidal M_5C_2, which widely distributes in both δ-ferrite grain boundaries and martensite lathes. When heat-treated at 750–900 °C, the microstructure consists of austenite, α-ferrite and δ-ferrite, and the fraction of austenite increases apparently with increasing heat treatment temperature. At 950 °C, the austenite is obviously coarser and a small amount of martensite forms again.
(3) UTS decreases at first with the temperature increase from 700 to 850 °C and begin to increase at 900 °C. YS decreases as a whole with increasing temperature but fluctuated slightly at 800 and 900 °C, respectively. As for the tendency of TE, it is completely opposite with UTS that increases firstly and declines after the peak value of 44.5% at 850 °C.

(4) The remarkable mechanical properties, both strength and elongation, are attributed to the relative fraction and stability of austenite. And the partition of elements, especially for Mn, has a great effect on the austenite stability, while the enrichment of Al elements induces the formation of new ferrite.

References

1. R. Sun, W. Xu, C. Wang et al., Work hardening behavior of ultrafine grained duplex medium-Mn steels processed by ART-annealing. Steel Res. Int. **83**(4), 316–321 (2012)
2. L. Zhang, R. Song, C. Zhao, F. Yang, S. Qin, Y. Xu, Mater. Rev. **28**(19), 111–118 (2014)
3. P.J. Jacques, Transformation-induced plasticity for high strength formable steels. Curr. Opin. Solid State Mater. Sci. **8**(3–4), 259–265 (2004)
4. Z.H. Cai, H. Ding, R.D.K. Misra et al., Unique serrated flow dependence of critical stress in a hot-rolled Fe–Mn–Al–C steel. Scripta Mater. **71**(2), 5–8 (2014)
5. S. Zaefferer, J. Ohlert, W. Bleck, Acta Mater. **52**(9), 2765–2778 (2004)
6. Z. Cai, H. Ding, Z. Ying et al., J. Mater. Eng. Perform. **23**(4), 1131–1137 (2014)
7. Z.C. Li, R.D.K. Misra, Z.H. Cai et al., Mechanical properties and deformation behavior in hot-rolled 0.2C–1.5/3Al–8.5Mn–Fe TRIP steel: the discontinuous TRIP effect. Mater. Sci. Eng., A **673**, 63–72 (2016)
8. R. Rana, C. Liu, R.K. Ray, Evolution of microstructure and mechanical properties during thermomechanical processing of a low-density multiphase steel for automotive application. Acta Mater. **75**(16), 227–245 (2014)
9. C.H. Seo, K.H. Kwon, K. Choi et al., Deformation behavior of ferrite–austenite duplex lightweight Fe–Mn–Al–C steel. Scripta Mater. **66**(8), 519–522 (2012)
10. S.S. Sohn, B.J. Lee, S. Lee et al., Effect of annealing temperature on microstructural modification and tensile properties in 0.35 C–3.5 Mn–5.8 Al lightweight steel. Acta Mater. **61** (13), 5050–5066 (2013)
11. Z.C. Li, H. Ding, R.D.K. Misra et al., Microstructure-mechanical property relationship and austenite stability in medium-Mn TRIP steels: the effect of austenite-reverted transformation and quenching-tempering treatments. Mater. Sci. Eng., A **682**, 211–219 (2017)
12. P.J. Gibbs, E.D. Moor, M.J. Merwin et al., Austenite stability effects on tensile behavior of manganese-enriched-austenite transformation-induced plasticity steel. Metall. Mater. Trans. A **42**(12), 3691–3702 (2011)
13. A. Dosho, K. Kakefuda, X-ray diffraction measurement method and X-ray diffraction apparatus. US, US7443952 (2008)
14. M. Zhang, W. Cao, H. Dong et al., Mater. Sci. Eng., A **654**, 193–202 (2016)

Interfacial Peel Strength and Microstructure of Titanium/ Aluminium Foil Manufactured by Ultrasonic Consolidation Process

Yujie Han, Yaoqi Wang, Hongliang Hou and Yanling Zhang

Abstract An experimental investigation was performed on the ultrasonic consolidation of bi-metallic foil materials, 1100 aluminium and TA1 titanium. The layer-metal composite laminate specimens were prepared using the ultrasonic consolidated Ti/Al foilto investigate effects of amplitude and static force on the interface bonding strength of Ti/Al foil by peel test. In addition, the microstructure morphology observation and energy spectrum analysis of the peeled interfaces were performed using SEM and EDS respectively. The results showed that a good bonding interface of Ti/Al foil was obtained using the ultrasonic consolidation technique. The interface bonding strength increased first then decreased with increasing the static force, while increasing monotonically with increasing the amplitude. The optimum ultrasonic consolidated interface with a peeling strength 11.325 N/mm could be obtained using an amplitude 35 μm and static force 2.0 kN. A uniform distribution of Al element was found in the peeled interface of Ti foil accompanying with the obvious nest microstructure, which further certificated the good interface quality using ultrasonic consolidation process.

Y. Han (✉) · Y. Wang · H. Hou · Y. Zhang
Beijing Aeronautical Manufacturing Technology Research Institute,
Beijing 100024, China
e-mail: hanyujiehao@126.com

Y. Wang
e-mail: xiaoqigh@sina.com

H. Hou
e-mail: hou_hl@163.com

Y. Zhang
e-mail: zhangyanling205@163.com

Y. Wang · H. Hou · Y. Zhang
Aeronautical Key Laboratory for Plastic Forming Technology,
Beijing 100024, China

Y. Wang · H. Hou · Y. Zhang
Beijing Key Laboratory of Digital Forming Technology and Equipment,
Beijing 100024, China

© Springer Nature Singapore Pte Ltd. 2018

Y. Han (ed.), *Advances in Materials Processing*, Lecture Notes in Mechanical Engineering, https://doi.org/10.1007/978-981-13-0107-0_49

Keywords Ultrasonic consolidation · Peel strength · Mechanical property

Introduction

Ultrasonic consolidation technique is a novel method to manufacture low cost, environmental friendly advanced material structures, which directly bonds metal materials in a stacking layer pattern to achieve forming using low amplitude, high frequency and mechanical stir welding. Ultrasonic consolidation process combines properties of both ultrasonic welding [1, 2] and laminate enhancing material manufacturing [3, 4], which can achieve the consolidation between two surfaces of metal material. Currently, the fundamental theories of ultrasonic consolidation have been improved, and the processing techniques are relatively mature. As a new manufacturing technology to produce high performance composite material, ultrasonic consolidation process has a huge potential in producing metallic laminate composite, functional tailored, fiber enhancing metallic matrix composite and intelligent metal composite structures [5–10]. Material structures produced by such a technique exhibit significant influences on manufacturing advanced materials with advantages of high efficiency, good property and low cost. These structures have wide applications in aerospace, automotive, electronic industries and manufacturing of novel materials. The over-layer stacking manufacturing process of laminate metal material is an important application of metal ultrasonic consolidation technology, which has been extensively investigated for the ultrasonic consolidation of same and hybrid foil materials. Foreign researchers established the physical model of multi-layer metal foils and transfer model of ultrasonic consolidation using theoretical calculation and finite element simulation [11]. The bonding of stainless foil, copper foil, aluminium alloy foil and nickel alloy foil materials have been performed. A metallurgy bonding, with good interfacial bonding quality, can be obtained for aluminium alloy pair and aluminium alloy/steel pair using proper ultrasonic consolidation process parameters [12, 13]. In addition, researchers utilized ultrasonic consolidation integrated with hot compression method to produce $Ti/TiAl_3$ laminate composite material [14] and analyzed corresponding material properties. The results have shown that, increased amplitude, static pressure, welding temperature and decreased welding velocity are beneficial for increasing soldering density.

This paper investigated mechanical properties and microstructures of the ultrasonic consolidated interfaces of 1100 aluminium foil and TA1 titanium fol. The interfacial bonding strength of ultrasonic consolidated Ti/Al laminate composite material and the microstructure morphology were obtained. The element distribution of the interface was analyzed also.

Materials and Experimental Methods

The materials used in this paper were 1100 aluminium foil and TA1 titanium foil, with a thickness of 200 μm. The foils are in annealed condition. Figure 1 shows the microstructures of raw materials.

Ti/Al laminate composite material was produced using ultrasonic consolidation equipment. The friction and temperature increasing can be generated at interfaces between two layers resulting from static pressure and elastic vibration energy, which promotes the diffusion of metal atomics at the interfaces. Figure 2 illustrates the schematic mechanism of experiments. The width of ultrasonic machining tool was 25 mm, the consolidation speed was 30 mm/min. The experimental temperature selected was 200 °C and the static normal force was 1.0, 1.5, 2.0 and 3.5 kN. The amplitudes of ultrasonic wave were 20, 25, 30 and 35 μm. The preparation procedure was that: the foil material with a clean surface was consolidated an aluminium foil on the foundation plate first, then consolidated a titanium layer again. The above procedure was repeated three times in total. The specimen dimension was 200 mm × 1.8 mm. Figure 3 shows the microstructure of laminate metallic material obtained from experiments.

The peering experiments were performed using Z100 electronic material testing machine, as shown in Fig. 4. The experimental standard followed GJB446-88 "Determination methods of 90° peering strength for the adhesive". The peering length was 30 mm and peering velocity was 100 mm/min. The interfacial peering strength can be calculated according to equations to investigate effects of ultrasonic wave amplitude and static force on the bonding strength of Ti/Al interfaces. The microstructure of peered interface and element were analyzed using SEM and EDS respectively.

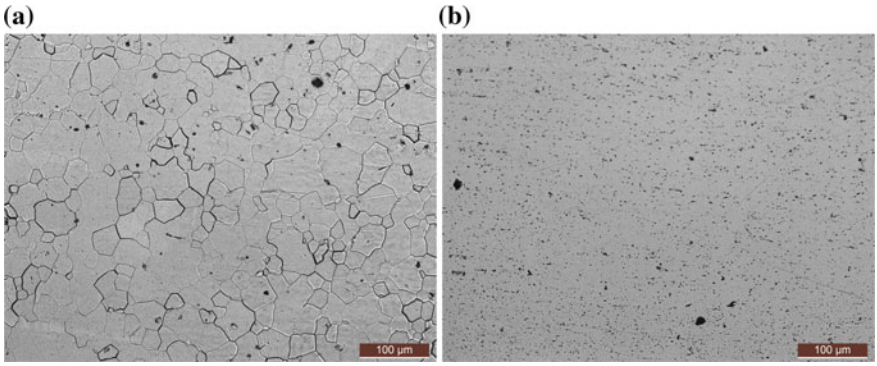

Fig. 1 Microstructure observation of raw material **a** TA1 Titanium, **b** 1100 aluminium

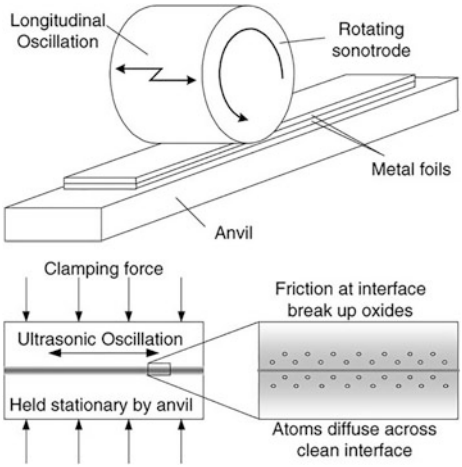

Fig. 2 Schematic of ultrasonic consolidation process

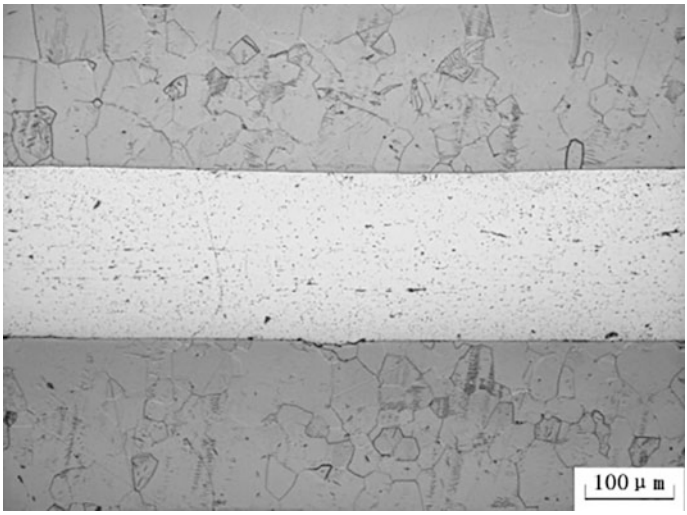

Fig. 3 Microstructure observation of ultrasonic consolidated specimen

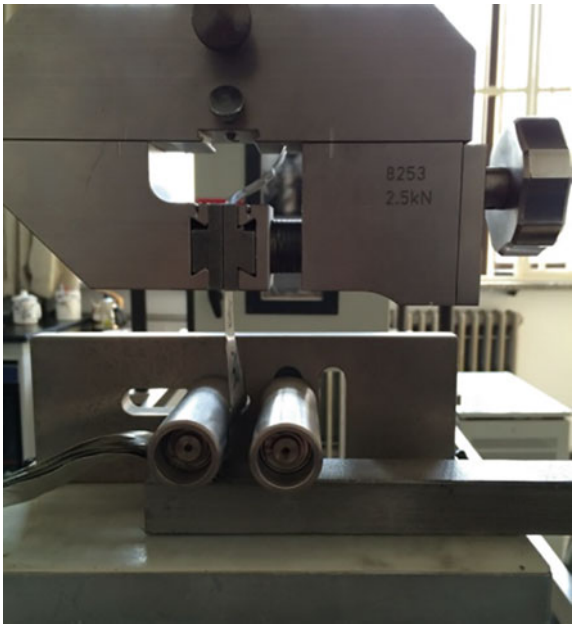

Fig. 4 Experimental set-up of peering tests

Results and Discussion

Figure 5 shows the peering test results in the condition of an amplitude 35 μm and different pressure conditions. As can be seen from this figure, the magnitude of peering force became stable when the peering length reached 8 mm. Then, the peering strength magnitude under a certain condition can be calculated, as shown in

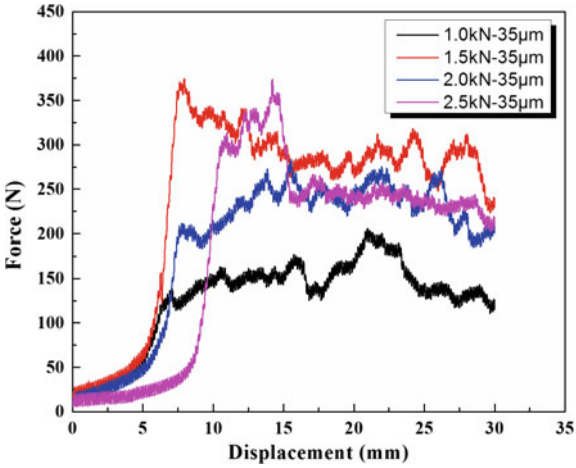

Fig. 5 Experimental results of specimen peering tests

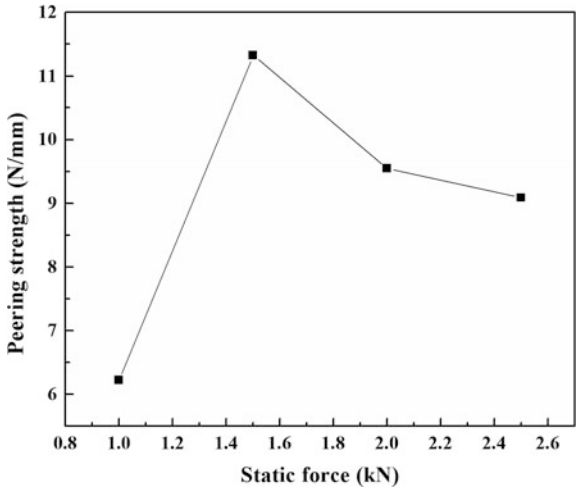

Fig. 6 Relationships between static force and peering strength

Fig. 6. With increasing static force, the peering strength increased first then decreased, and peaked at 1.5 kN. The reason is believed to be caused by that, the static force made the effective functioning zone of ultrasonic vibration occurred at the metal foil interfaces. When the static force was enough low, vibration energy of ultrasonic wave cannot be effectively transferred to foil interfaces. The interface sliding between machining tool and foil resulted in the energy loss of ultrasonic wave, which results in a reduced friction effect and an unsuccessful bonding. When the static force was too large, the friction constraint became too large which made relative friction movement between foils weaken and effective amplitude decreased to reduce peering strength.

Figure 7 shows peering test results in the condition of a static force 2.0 kN with different ultrasonic wave amplitudes. As can be seen in this figure, magnitude of

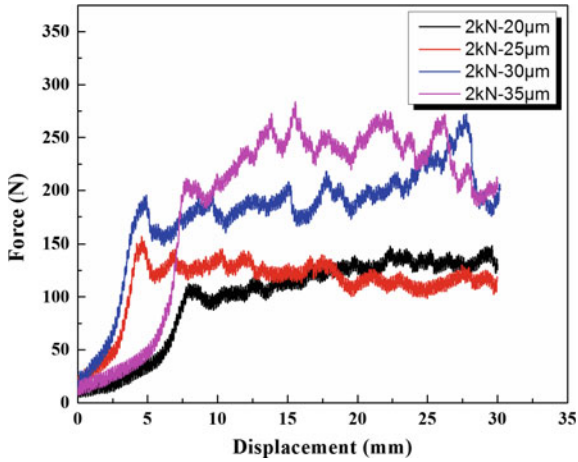

Fig. 7 Experimental results of peering tests

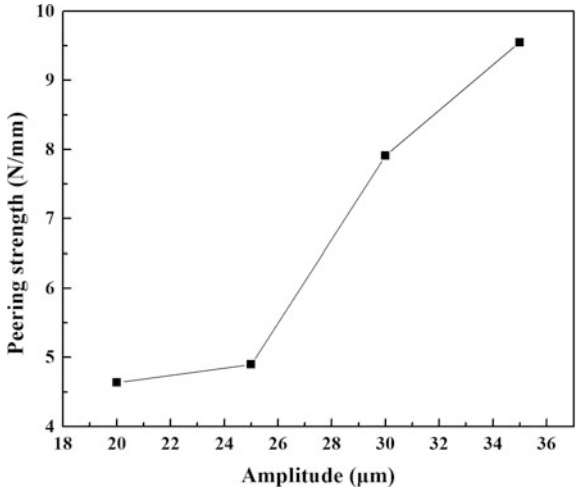

Fig. 8 Relationship between amplitude and peering strength

peering strength became stable when the peering length reached 8 mm. The peering strength under corresponding condition was obtained, as shown in Fig. 8. The peering strength increases with increasing amplitude of ultrasonic wave. In the condition of a fixed static force, the vibration amplitude between foil interfaces increases with increasing ultrasonic amplitude, the friction effect becomes more obvious which is beneficial for the bonding of foil interfaces and improving bonding quality of interface.

The microstructures of peered interfaces were investigated using scanning electron microscope. Figure 9 shows low resolution microstructures of peered interfaces under different amplitude. As can be seen in this figure, the peered interface of Ti/Al foil was composed by white and grey zones. With increasing amplitude, interface bonding quality was increased, white zones of interfaces increased and distributed more uniformly. High resolution microstructure observation of white zones was shown in Fig. 10. As can be seen in this figure, this zone was composed by stretched and equal-axial dimple microstructure. The specimen exhibited ductile fracture features. The microstructure distributed more uniform with increasing peer strength.

Chemical composition analysis of dimple locations was performed using EDS for typical titanium/aluminium peered interfaces. Figure 11 shows the microstructure morphology of peered interface, and EDS analysis was shown in Fig. 12. In this location selection, Al atomic proportion was 94.9% and that of Ti atomic is 5.1%. Aluminium cannot be observed at the grey zones. Pure titanium TA1 foil was

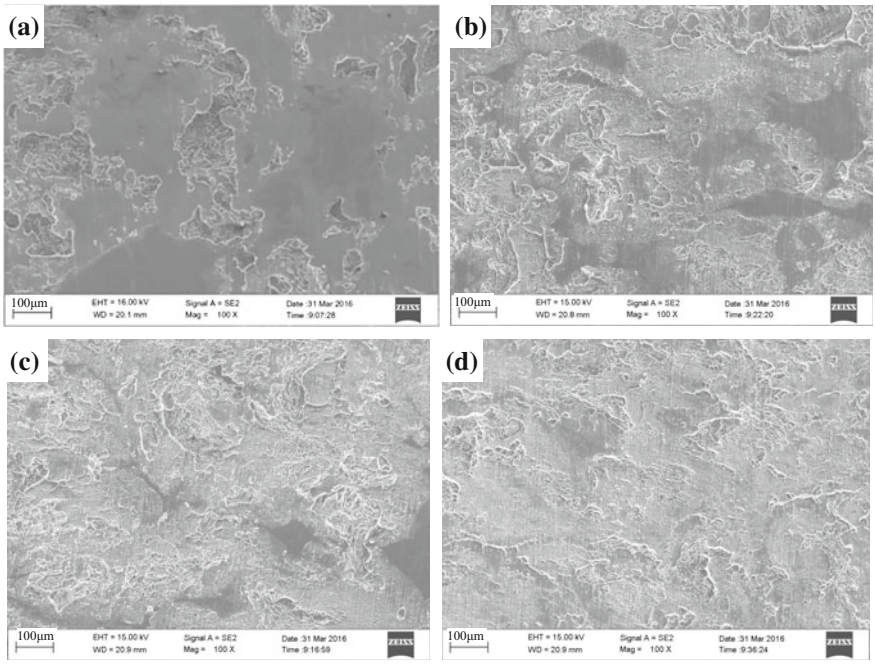

Fig. 9 Low resolution crack interface microstructures under different amplitudes **a** 2 kN–20 μm **b** 2 kN–25 μm **c** 2 kN–30 μm **d** 2 kN–35 μm

used for experiments, the absence of aluminium element indicated a strong bonding of titanium aluminium interfaces. During the peering process of titanium foil, the aluminium foil in contact with titanium foil was peered off and attached on the titanium foil, which further indicated a good quality of interface. Based on above discussions, the selecting low resolution titanium foil crack shown in Fig. 13 to perform surface scanning analysis, as shown in Fig. 14. Titanium and aluminium elements existed within this region, which further indicated a good interface bonding between titanium and aluminium foils during ultrasonic consolidation. During the peering test, surface metal of aluminium foil was peered with titanium foil and distributed uniformly.

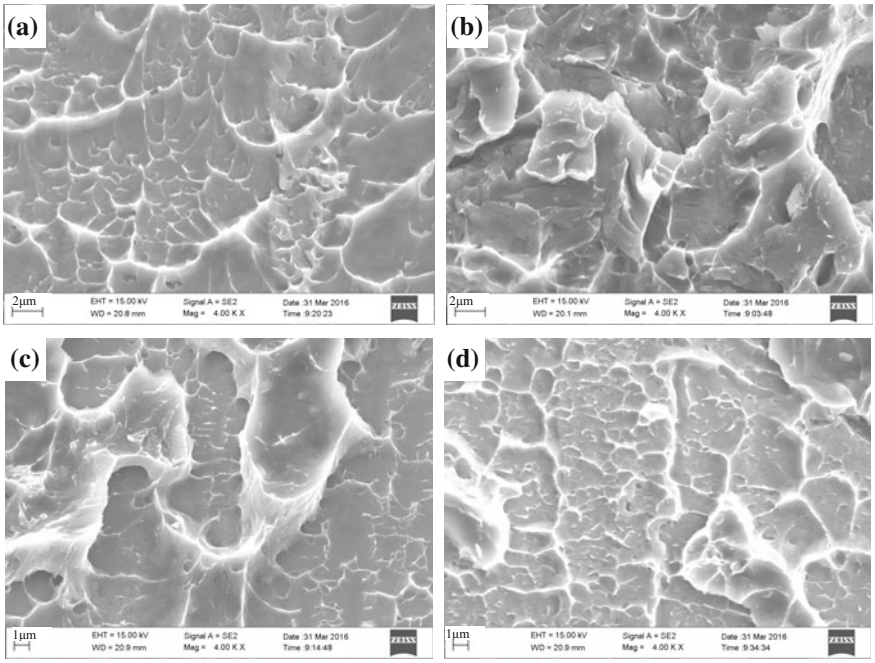

Fig. 10 High resolution crack interface microstructures under different amplitudes **a** 2 kN–20 μm **b** 2 kN–25 μm **c** 2 kN–30 μm **d** 2 kN–35 μm

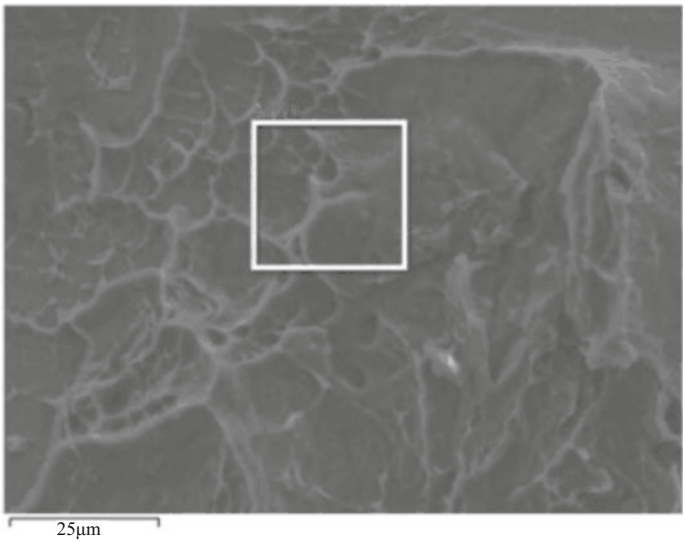

Fig. 11 EDS analysis of interface

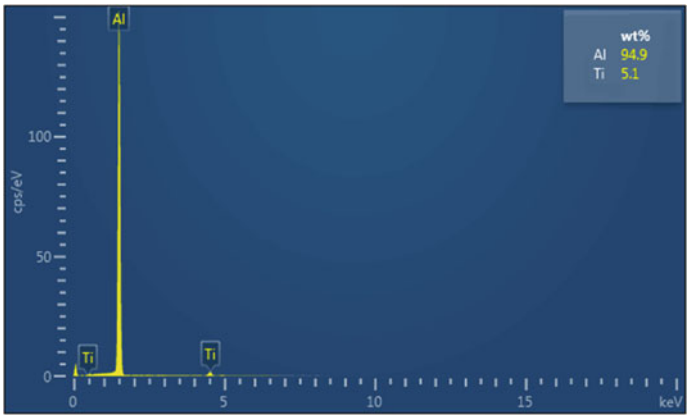

Fig. 12 EDS analysis of Ti and Al subscrate

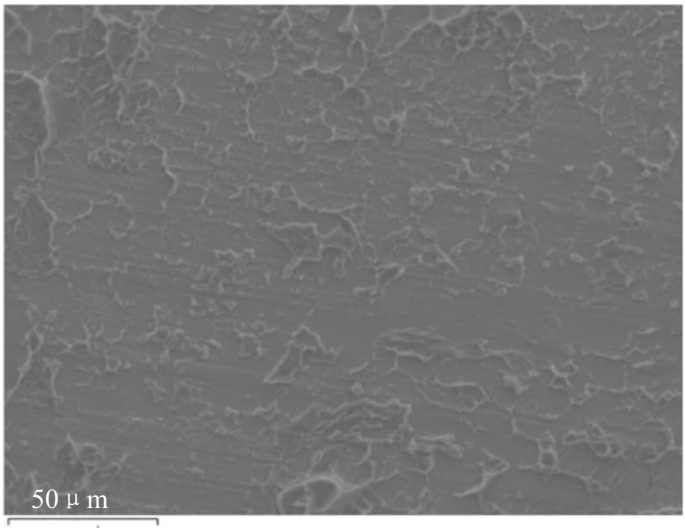

Fig. 13 Surface scanning region

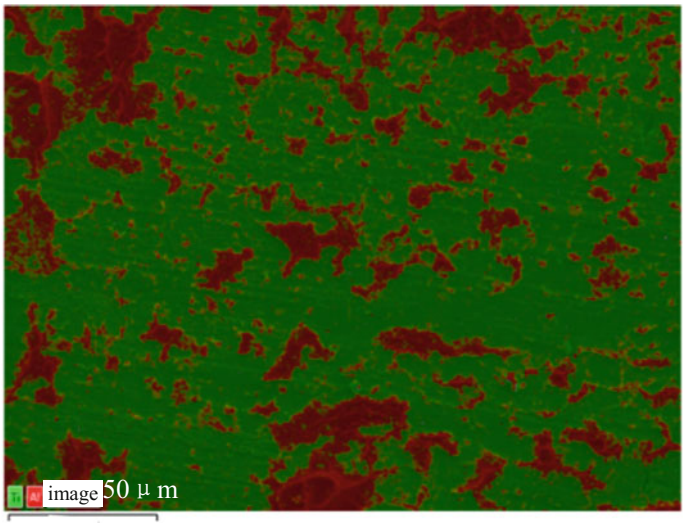

Fig. 14 Distributions of Ti and Al elements

Conclusions

(1) Interfaces of Ti/Al laminate metallic composite specimen were flat and uniform, and bonding quality of interface was better. Interface bonding strength increased first then decreased with increasing static force, while increased monotonic with increasing amplitude. The optimum ultrasonic consolidated interface was obtained in the condition of a 35 μm amplitude and a 2.0 kN static force with a peering strength 11.325 N/mm.

(2) White and grey regions existed at the titanium foil peered interface. A portion of aluminium foil in contact with titanium foil was peered off during the peering, and became the white region attached on the titanium foil surface, and the grey region was titanium substrate. The area of white region increased with increasing peer strength, and a more uniform distribution was observed.

(3) The white region was composed by stretched and equal-axial dimples. The crack was ductile crack. The distribution was more uniform with increasing peer strength.

References

1. J. Tsujino, T. Ueoka, Studies on Ultrasonic Welding. Proceeding of the China-Japan Joint Conference on Ultrasonics, (Nanjing, China, 1987), pp. 471–474
2. X.-H. He, H.-J. Shi, Y.-D. Zhang, W.-X. Fu, Z.-G. Yang, C.E. Wilkinson, In-situ scanning electron microscopy studies of small fatigue crack growth in ultrasonic consolidation bonded aluminum 2024 laminated structure. Mater. Lett. **112**, 47–50 (2013)
3. G.S. Kelly, S.G. Advani, J.W. Gillespie Jr., A model to describe stick–slip transition time during ultrasonic consolidation. Int. J. Adv. Manuf. Technol. **79**, 1931–1937 (2015)
4. S. Zhang, D. Yi et al., Towards understanding of ultrasonic consolidation process with "process map". Rapid Prototyping J. **21**(4), 461–468 (2015)
5. R.J. Friel, R.A. Harris, Ultrasonic additive manufacturing—a hybrid production process for novel functional products. The Seventeenth CIRP Conference on Electro Physical and Chemical Machining (ISEM), Procedia CIRP 6, (2013), pp. 35–40
6. D. Christopher, B.S. Hopkins, *Development and Characterization of Optimum Process Parameters for Metallic Composites Made by Ultrasonic Consolidation*. (Dissertation of Utah State University, Logan, Utah, 2010), pp. 4–100
7. M.R. Sriraman, M. Gonser, H.T. Fujii, S.S. Babu, M. Bloss, Thermal transients during processing of materials by very high power ultrasonic additive manufacturing. J. Mater. Process. Technol. **211**, 1650–1657 (2011)
8. D.R. Foster, M.J. Dapino, S.S. Babu, Elastic constants of ultrasonic additive manufactured Al 3003-H18. Ultrasonics **53**, 211–218 (2013)
9. E. Mariani, E. Ghassemieh, Microstructure evolution of 6061 O Al alloy during ultrasonic consolidation: an insight from electron backscatter diffraction. Acta Mater. **28**, 2492–2503 (2010)
10. R. Hahnlen, M.J. Dapino, NiTi–Al interface strength in ultrasonic additive manufacturing composites. Compos. B **59**, 101–108 (2014)
11. G.S. Kelly, M.S. Just, S.G. Advani, J.W. Gillespie Jr., Energy and bond strength development during ultrasonic consolidation. J. Mater. Process. Technol. **214**, 1665–1672 (2014)
12. J.O. Obielodana, B.E. Stucker et al., Optimization of the shear strengths of ultrasonically consolidated Ti/Al 3003 dual-material structures. J. Mater. Process. Technol. **211**, 988–995 (2011)
13. K. Sojiphan, Effects of very high power ultrasonic additive manufacturing process parameters on hardness, microstructure, and texture of aluminum 3003-H18 alloy. Ph. D. Dissertation of The Ohio State University, Ohio, United States, 2015, pp. 23–80
14. J. Obielodan, B. Stucker, A fabrication methodology for dual-material engineering structures using ultrasonic additive manufacturing. Int. J. Adv. Manuf. Technol. **70**, 277–284 (2014)

Deep Densification of ZrB_2 by Hot Pressing

Tao Gui, Lei Yang, Yuyang Liu, Xue Bai, Xingming Wang and Bo Song

Abstract ZrB_2 powder was prepared by ZrO_2, H_3BO_3 and C as raw materials and boron (B) as additive. The powder was subjected to deep densification study by hot pressing sintering. The powder and the crystal structure were determined by X-ray diffraction (XRD), scanning electron microscopy (SEM) with energy dispersive spectrometer (EDS), and transmission electron microscopy (TEM) with selective area electron diffraction (SAED). The results show that the product was a ZrB_2 single phase powder by carbothermal reduction method with regular morphology. The average particle size was 3–4 μm. The crystal structure of the powder was complete and no obvious lattice defect was obtained. The hot-pressing sintered product is a ZrB_2 single phase ceramic target. By introducing a certain amount of M-type ZrB_2 powder, the deep densification ZrB_2 ceramic target can be obtained with a relative density of 99.9%.

Keywords Zirconium boride · Carbothermal reduction · Additive
Hot pressing sintering · Densification

Introduction

Burnable Absorber is used to control excessive reactivity and reduce the power peak factor in pressurized water reactors [1]. In recent years, Integral Fuel Burnable Absorber (IFBA) which does not produce any residual absorbent isotopes after

T. Gui (✉) · L. Yang · Y. Liu · X. Bai · X. Wang
Division of Metallurgy and Materials for Rare Metals, General Research Institute for Non-Ferrous Metals, Beijing 100088, China
e-mail: gt2013@foxmail.com

X. Wang
e-mail: mansionwang010@163.com

T. Gui · B. Song
School of Metallurgical and Ecological Engineering, University of Science and Technology Beijing, Beijing 100083, China

© Springer Nature Singapore Pte Ltd. 2018

Y. Han (ed.), *Advances in Materials Processing*, Lecture Notes in Mechanical Engineering, https://doi.org/10.1007/978-981-13-0107-0_50

depletion of the neutron absorber isotope (^{10}B), and has good economic fuel cycle and power distribution control than other absorbers [2, 3], is widely used in the pressurized water reactor of the third generation nuclear power plant (such as AP1000, NPP, etc.) [1, 4, 5]. IFBA is composed of UO_2 pellets with its surface coated with ZrB_2 coating using ZrB_2 target by magnetron sputtering process [4] which is rich in ^{10}B isotope. The quality of the coating primarily depends on the composition and density of the sputtering target. For the ZrB_2 target, it is difficult to densification without second phase or any sintering aid due to the strong covalent bonding and low self-diffusion coefficient of ZrB_2 [6]. There are many micropores in the low-density target which result in poor coating uniformity and product quality. The preparation of high-density ZrB_2 targets (relative density > 95%) is critical to achieving the desired ZrB_2 coating for IFBA.

The methods of preparation of high density ZrB_2 target mainly contain hot pressing sintering, pressureless sintering and spark plasma sintering. The studies of ZrB_2 sintering indicate that the oxide impurities on the surface of the grains form a fast diffusion channel between the grain boundaries to accelerate grain coarsening below the densification temperature. What's more, the presence of oxides is another important factor to block the densification of ZrB_2 [7]. The results of the study on densification of single phase ZrB_2 sintering are shown in Table 1. It can be seen from the table that the densification of single phase ZrB_2 has high requirements on the particle size of the raw material and sintering temperature. At high temperature (>2000 °C), the rate of grain coarsening tends to exceed the rate of densification which become the dominant process in sintering [8], so that increasing the difficulty of deep densification.

The results of the current study of deep densification of ZrB_2 exist the prevalence of high cost, complex process, safety risk of the process, uniformity of the product and easily to introduce impurities. In order to prepare homogeneous and high density of single phase ZrB_2 with simple, safe and low cost process, ZrB_2 powder was prepared by carbothermal reduction and hot pressing sintered in this paper.

Experimental Procedure

ZrO_2 (>99.5 wt%), H_3BO_3 (>99.5 wt%) and graphite (>99.0 wt%) powders were used as raw materials. B powder were used as additive with different contents (0, 2.5, and 5 wt%) mixed with raw materials at a certain molar ratio. The mixtures underwent heat treatment and then were placed in a carbon tube furnace with Ar gas protection heating up to 1900 °C to prepare ZrB_2 powder. The whole reaction is shown in Eq. 1.

$$ZrO_2 + 2H_3BO_3 + 5C = ZrB_2 + 3H_2O + 5CO \quad (1)$$

The prepared powder was molded into a blank in steel mould by cold pressing and then the blank was put into a graphite mould for hot pressing. The process of

Table 1 Sintering conditions, advantages and disadvantages of single phase ZrB_2 densification

Particle size [μm]	Process characteristics	Sintering conditions			Density [%]	Advantages and disadvantages	References
		Temperature [°C]	Time [min]	Pressure [MPa]			
0.5–1	Heat treatment at 1650 °C and vacuum pressureless sintering commercial ZrB_2 at 2100 °C	2100	120		93	High cost	[9]
2	Vacuum hot pressing commercial ZrB_2 20 min at 1000 °C	1850	90	12	90	High cost, complex process	[6, 10]
1	Spark plasma sintering 90% commercial ZrB_2 + 10% homemade ZrB_2 mixture	1900	10	50	93	High cost, complex process, safety risk of the process, uniformity of the product	[11]
	Spark plasma sintering Zr + B mixture	2000	20	50	96	High density, safety risk of the process, uniformity of the product	[12]
1.5–2.5	Spark plasma sintering commercial ZrB_2	1900	3	50	97	High density, safety risk of the process, uniformity of the product	[13]
	Pressureless sintering homemade ZrB_2 and polyvinyl alcohol blank in argon atmosphere	1950			97.5	High density, complex process	[14]
	Spark plasma sintering ZrH_2 + B mixture	1800	10	50	97.2	High density, high cost, safety risk of the process, uniformity of the product	[15]
<2 μm	Pressureless sintering commercial ZrB_2 in helium atmosphere	2150	540	30	98	High density, long time, introduce impurities	[16]
<2 μm	Hot pressing commercial ZrB_2 in argon atmosphere	1900	45	32	99.8	High density, introduce impurities	[17]
	Reactive hot pressing Zr + B mixture in argon atmosphere	2100	45	40	99	High density, high cost, complex process, safety risk of the process, uniformity of the product	[18]

(continued)

Table 1 (continued)

Particle size [μm]	Process characteristics	Sintering conditions			Density [%]	Advantages and disadvantages	References
		Temperature [°C]	Time [min]	Pressure [MPa]			
>2 μm 60–80 nm	Vacuum hot pressing micron and nano scale ZrB_2 mixture	1900	30	30	99.2	High density, high cost	[19]
2.3	Vacuum hot pressing sol-gel precursor prepared by commercial ZrB_2	2000	60	40	99.5	High density, complex process	[20]

Table 2 Experimental scheme of ZrB_2 sintering densification

Number	Densification materials	Sintering process
ZB0	The product without B additive	Hot pressing with 90 MPa for 3 h at 1980 °C
ZB25	The product with 2.5 wt% B additive	
ZB0-M	M–ZrB_2 + the product without B additive	
ZB25-M	M–ZrB_2 + the product with 2.5 wt% B additive	

the hot pressing is shown in Table 2. In order to obtain the deep densification, a kind of ZrB_2 powder named M–ZrB_2 was added which was also prepared ourselves. After washing and drying the product (powder and target), the samples of that were tested for phase, morphology, composition and crystal structure analysis.

The phase of the product was examined by X-ray diffraction (XRD, D/max 2500, Rigaku, Japan). Morphology and composition of the product (powder and target) were analyzed by scanning electron microscope (SEM, JSM-6510, JEOL, Japan) with its energy dispersive spectrometer (EDS). The high resolution images and the crystal structure were analyzed by transmission electron microscope (TEM, Tecnai G2 F20 S-TWIN, FEI, USA) with its selected area electron diffraction (SAED). The theoretical density of ZrB_2 is 6.085 g/cm^3. The ratio of the actual density of the target which was measured by Archimedes method to the theoretical density is the relative density of the target.

Results and Discussion

Composition and Morphology of the Prepared ZrB_2 Powder

The XRD patterns of the powders obtained by adding different contents of B powder are shown in Fig. 1. Comparing with the curve, we can see that there is a

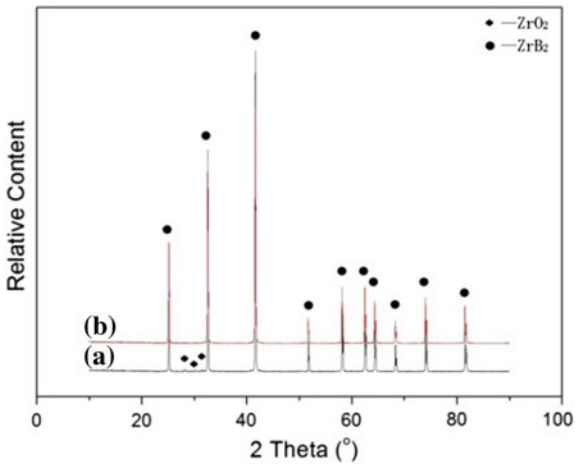

Fig. 1 XRD patterns of the products with different content of B additives **a** 0 wt %, **b** 2.5 wt%

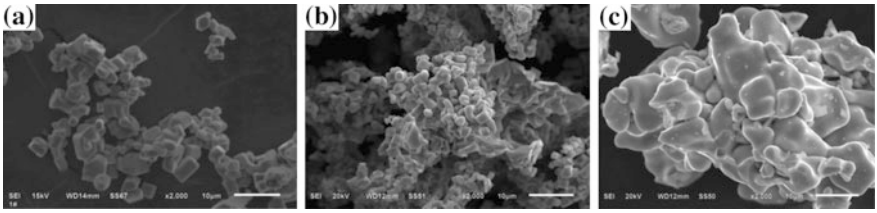

Fig. 2 SEM pictures of synthesized ZrB_2 powders with different content of B additives **a** 0 wt%, **b** 2.5 wt%, **c** M–ZrB_2

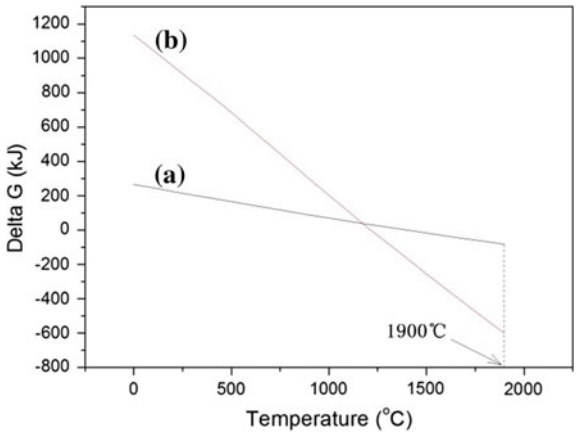

Fig. 3 Relationship of $\Delta G - T$ calculated by HSC **a** $B + ZrO_2$, **b** $B_4C + ZrO_2$

weak ZrO_2 diffraction peak without B powder which indicates that there is ZrO_2 impurity in the product. No obvious ZrO_2 diffraction peak in the XRD pattern of the product with B powder addition which indicates that the addition of B powder may react with ZrO_2 to a certain extent to produce more ZrB_2 and then increasing the ZrB_2 content in the product.

The SEM pictures of synthesized ZrB_2 powders with different content of B additives are shown in Fig. 2. The results show that B powder has a significant effect on the particle size and morphology of the ZrB_2 powder. The particle size of the product without B powder is about 7–8 μm, showing a hexagonal structure and obvious holes in the particles. While the particle size of the product with 2.5 wt% B powder addition is about 3–4 μm which shows a spherical structure and the holes in the particles are reduced obviously. The main reason for this change may be that the addition of B powder causes a side reaction shown in formula (2) which forms the B_4C intermediate product. From the calculation of $\Delta G - T$ of $B + ZrO_2$ and $B_4C + ZrO_2$ by HSC showing in Fig. 3, B_4C will earlier react with ZrO_2 than B. So the B_4C intermediate enhances the mass transfer between the components of the system and promotes the formation of carbothermal reduction and inhibits the growth of ZrB_2 grains to a certain extent and thereby changes the particle

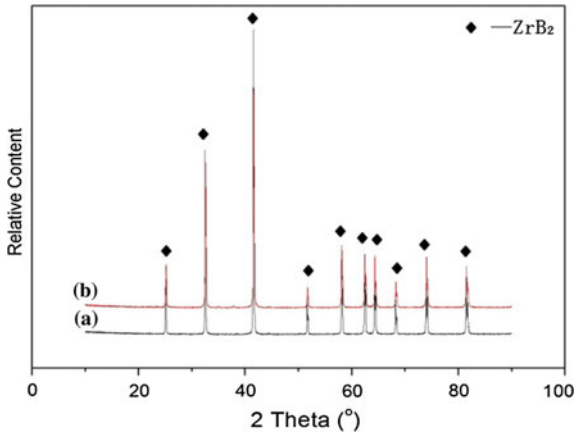

Fig. 4 XRD patterns of the products prepared by hot pressing using synthesized ZrB_2 powders **a** 0 wt%, **b** 2.5 wt%

morphology and particle size [21]. On the other side, the product prepared with B powder has a certain agglomeration phenomenon with some holes which are mainly openings in it.

$$4B + C = B_4C \tag{2}$$

Composition and Section Morphology of the Hot Pressing Products

The XRD patterns of the hot pressing products are shown in Fig. 4. The diffraction peaks of the two products are the same indicating that the ZrB_2 powder had no phase change during hot pressing and no impurity phase was introduced.

Figure 5 shows the SEM pictures of the hot pressing products. The product sintered by the ZrB_2 powder prepared without B powder has some sintering neck

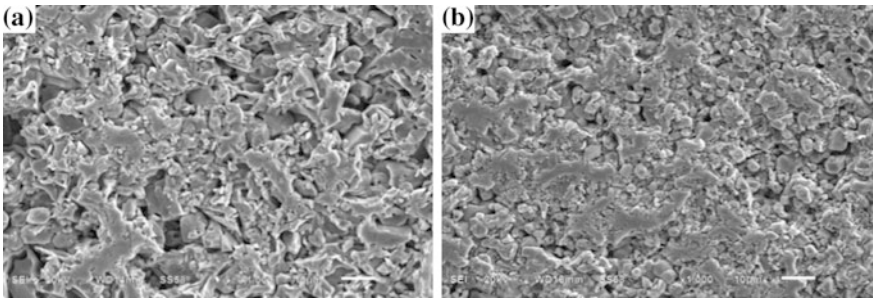

Fig. 5 SEM pictures of the products prepared by hot pressing using synthesized ZrB_2 powders **a** 0 wt%, **b** 2.5 wt%

which means the sintering was incomplete and a lot of holes among the particles. The densification of that is low with 74% relative density. While the product sintered by the ZrB_2 powder prepared with 2.5 wt% B powder addition has less sintering neck and holes than that without B powder. The sintered product shows better densification with 89% relative density.

Composition and Section Morphology of the Hot Pressing Products with M–ZrB_2 Powder Addition

The XRD patterns of the sintered products with M–ZrB_2 addition are shown in Fig. 6. The diffraction peaks of the two products are the same indicating that there was no phase change during hot pressing and no impurity phase was introduced.

Figure 7 shows the SEM pictures of the sintered products with M–ZrB_2 addition. There was no obvious sintering neck in the two sintered product meaning the particles were closely packed and the sintering was completed. However, due to the large shrinkage cavity the ZB0-M sintered product could not get deep densification with 94.7% relative density finally. While with very few shrinkage cavity the ZB25-M sintered product obtained deep densification with up to 99.9% relative density finally.

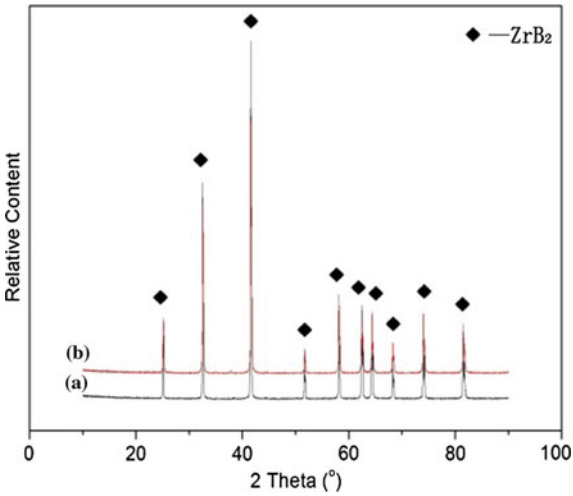

Fig. 6 XRD patterns of the products prepared by hot pressing with M–ZrB_2 addition **a** ZB0-M, **b** ZB25-M

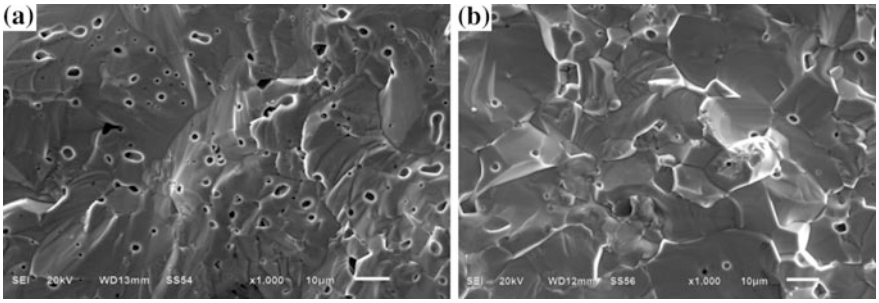

Fig. 7 SEM of the products prepared by hot pressing with M–ZrB_2 addition **a** ZB0-M, **b** ZB25-M

TEM Analysis of Different Density of the Sintered Products

The TEM analysis was performed on three sintered products with density from low to high (74, 94.7 and 99.9%). The results are shown in Fig. 8. It can be clearly seen that with the increase of the density, the impurity at the grain boundary of the target is obviously reduced.

There is no obvious grain boundary in the sample which has 74% relative density shown in Fig. 8a. The space between the grains is so large that

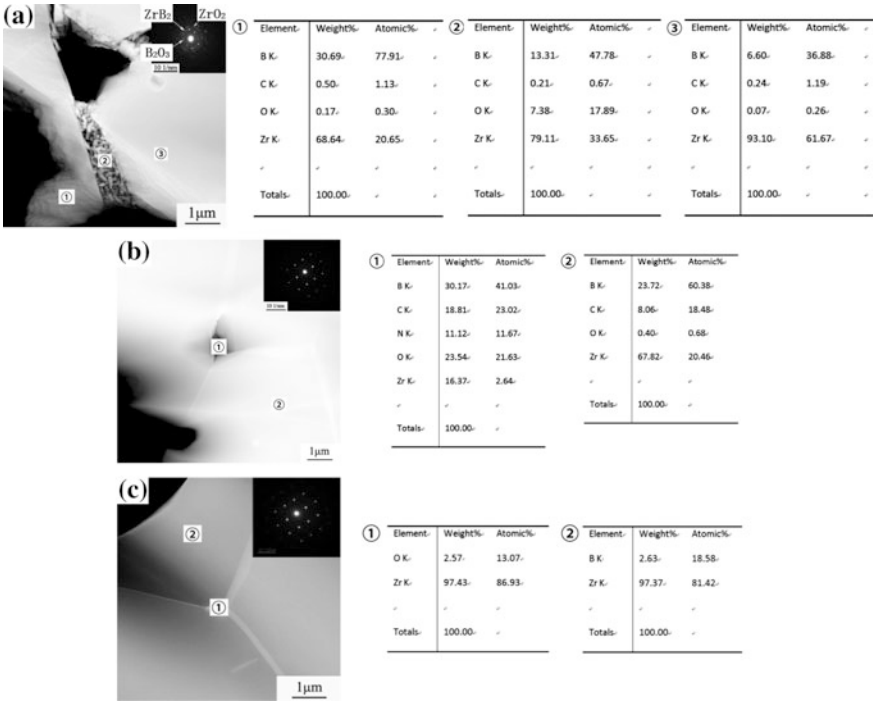

(a) ①

Element	Weight%	Atomic%
B K	30.69	77.91
C K	0.50	1.13
O K	0.17	0.30
Zr K	68.64	20.65
Totals	100.00	

(a) ②

Element	Weight%	Atomic%
B K	13.31	47.78
C K	0.21	0.67
O K	7.38	17.89
Zr K	79.11	33.65
Totals	100.00	

(a) ③

Element	Weight%	Atomic%
B K	6.60	36.88
C K	0.24	1.19
O K	0.07	0.26
Zr K	93.10	61.67
Totals	100.00	

(b) ①

Element	Weight%	Atomic%
B K	30.17	41.03
C K	18.81	23.02
N K	11.12	11.67
O K	23.54	21.63
Zr K	16.37	2.64
Totals	100.00	

(b) ②

Element	Weight%	Atomic%
B K	23.72	60.38
C K	8.06	18.48
O K	0.40	0.68
Zr K	67.82	20.46
Totals	100.00	

(c) ①

Element	Weight%	Atomic%
O K	2.57	13.07
Zr K	97.43	86.93
Totals	100.00	

(c) ②

Element	Weight%	Atomic%
B K	2.63	18.58
Zr K	97.37	81.42
Totals	100.00	

Fig. 8 TEM of different densities of the sintered products **a** 74%, **b** 94.7%, **c** 99.9%

accumulating a lot of irregular particles ranging from tens to hundreds of nanometer in it. The components analysis of (1), (2) and (3) shown in Fig. 8a indicate that the composition inside the grains (1) and (3) are relatively uniform with the main components of Zr and B. while the main components of the irregular particles in the space between the grains are Zr, B and O. The EDS result shows that there are polycrystalline structures which were calculated as B_2O_3, ZrB_2 and ZrO_2 in the sample. The irregular particles may be mainly for ZrO_2 and B_2O_3 impurities.

There is a large hole with the size of about 1 μm on the grain boundary shown in Fig. 8b. The components analysis of (1) shown in Fig. 8b indicates that the composition on the hole edge (1) is complex with the main components of B, C, O, N and Zr which means there may be ZrO_2, C, B_2O_3, B_4C or BN impurities. The components inside the grain (2) are relatively uniform with the main components of B and Zr. The EDS result shows an obvious single crystal structure of the sample.

In Fig. 8c, the grain boundary structure is clear and no obvious impurities or holes are found on it. The main components of the grain boundary (1) are Zr and O which means there may be ZrO_2. The components inside the grain (2) are uniform with the main components of B and Zr. The EDS result shows an obvious single crystal structure of the sample.

In summary, the existence of oxide impurities on the grain boundary is one of the reasons that affect the deep densification of single phase ZrB_2 target. The synthesized ZrB_2 powder with M–ZrB_2 addition can effectively reduce oxygen element content and obtain the deep densification of ZrB_2 target which can reach up to 99.9% relative density.

Conclusion

A single phase ZrB_2 powder can be prepared by carbothermal reduction. The average particle size of that with regular morphology is about 3–4 μm. The crystal structure of the powder is complete and no obvious lattice defects has been obtained. A single phase ZrB_2 ceramic target can be prepared by hot pressing. The presence of the oxide impurities on the grain boundary is one of the reasons preventing deep densification. The synthesized ZrB_2 powder with M–ZrB_2 addition can effectively reduce oxygen element content and obtain the deep densification of ZrB_2 target which can reach up to 99.9% relative density.

References

1. H. Jinhua, X. Hui, C. Pingdong, Characteristics of some new type burnable poison and its application prospect in China. At. Energy Sci. Technol. **32**(1), 90–96 (1998)
2. T. Wang, L. Zhou, Y. Zhang, Research progress of zirconium boride coating material. China Ceram. **49**(6), 5–8 (2013)

3. F. Franceschini, B. Petrović, Fuel with advanced burnable absorbers design for the IRIS reactor core: combined Erbia and IFBA. Ann. Nucl. Energy **36**(8), 1201–1207 (2009)
4. Z. Wang, H. Zhang, S. Gong, J. Yao, Study on the IFBA Pellets Coating Process. Nucl. Sci. Eng. **35**(4), 633–638 (2015)
5. M. Kromar, B. Kurinčič, Optimization of the IFBA pattern in the NPP Krško Fuel. Proceedings of the International Conference Nuclear Energy for New Europe. Nuclear Society of Slovenia, 114 (2007), pp. 1–114
6. M.S. Asl, M.G. Kakroudi, B. Nayebi, H. Nasiri, Taguchi analysis on the effect of hot pressing parameters on density and hardness of zirconium diboride. Int. J. Refract Metal Hard Mater. **50**, 313–320 (2015)
7. G.-J. Zhang, J. Zou, D.-W. Ni, H.-T. Liu, Y.-M. Kan, Boride ceramics: densification, microstructure tailoring and properties improvement. J. Inorg. Mater. **27**(3), 225–233 (2012)
8. G.W. Fahrenholtz, E.J. Wuchina, W.E. Lee, Y. Zhou, Ultra-high temperature ceramics: materials for extreme environment applications. (National Defense Industry Press, Beijing, 2016), pp. 99
9. G.-J. Zhang, W.-M. Guo, D.-W. Ni, Y.-M. Kan, Ultrahigh temperature ceramics (UHTCs) based on ZrB_2 and HfB_2 systems: Powder synthesis, densification and mechanical properties. 16th International Symposium on Boron, Borides and Related Materials. J. Phys: Conf. Ser. **012041**(1–012041), 12 (2009)
10. M.S. Asl, M.G. Kakroudi, M. Rezvani, F. Golestani-Fard, Significance of hot pressing parameters on the microstructure and densification behavior of zirconium diboride. Int. J. Refract Metal Hard Mater. **50**, 140–145 (2015)
11. N. Patra, NAl Nasiri, D.D. Jayaseelan, W.E. Lee, Synthesis, characterization and use of synthesized fine zirconium diboride as an additive for densification of commercial zirconium diboride powder. Ceram. Int. **42**, 9565–9570 (2016)
12. R. Licheri, C. Musa, R. Orrù, G. Cao, Influence of the heating rate on the in situ synthesis and consolidation of ZrB_2 by reactive Spark Plasma Sintering. J. Eur. Ceram. Soc. **35**, 1129–1137 (2015)
13. S.-Q. Guo, T. Nishimura, Y. Kagawa, J.-M. Yang, Spark plasma sintering of zirconium diborides. J. Am. Ceram. Soc. **91**(9), 2848–2855 (2008)
14. A.K. Khanra, L.C. Pathak, S.K. Mishra, M.M. Godkhindi, Sintering of ultrafine zirconium diboride powder prepared by modified SHS technique. Adv. Appl. Ceram. **104**(6), 282–284 (2005)
15. S. Guo, T. Nishimura, Y. Kagawa, Preparation of zirconium diboride ceramics by reactive spark plasma sintering of zirconium hydride–boron powders. Scripta Mater. **65**, 1018–1021 (2011)
16. A. Chamberlain, W.G. Fahrenholtz, G.E. Hilmas, Pressureless sintering of zirconium diboride. J. Am. Ceram. Soc. **89**(2), 450–456 (2006)
17. A.L. Chamberlain, W.G. Fahrenholtz, G.E. Hilmas, High-strength zirconium diboride-based ceramics. J. Am. Ceram. Soc. **87**(6), 1170–1172 (2004)
18. A.L. Chamberlain, W.G. Fahrenholtz, G.E. Hilmas, Reactive hot pressing of zirconium diboride. J. Eur. Ceram. Soc. **29**, 3401–3408 (2009)
19. R. He, R. Zhang, Y. Pei, D. Fang, Two-step hot pressing of bimodal micron/nano-ZrB_2 ceramic with improved mechanical properties and thermal shock resistance. Int. J. Refract Metal Hard Mater. **46**, 65–70 (2014)
20. C. Tallon, D. Chavara, A. Gillen, D. Riley, L. Edwards, S. Moricca, G.V. Franks, Colloidal processing of zirconium diboride ultra-high temperature ceramics. J. Am. Ceram. Soc. **96**(8), 2374–2381 (2013)
21. Y. Lei, S. Jing, G. Tao, L. Yuyang, B. Xue, W. Xingming, Particle size and morphology of ZrB_2 powder prepared by carbon thermal reduction reaction with additives. Chin. J. Rare Met. (2016)

Effect of Welding Thermal Cycle on Mechanical Properties and Corrosion Resistance of A7N01-T5 Aluminum Alloy

Cui Huang, Shufang Zhang, Jie Hu and Xiaomin Wang

Abstract In this paper, the thermal cycle treatment of A7N01-T5 aluminum alloy was carried out with the peak temperatures of 480, 420, 320 and 260 °C, and the thermal simulation specimens with four kinds of peak temperatures were obtained. Electrochemical methods such as open circuit potential, polarization curve and impedance were used to investigate the corrosion behavior about the four kinds of thermal simulated specimens. The results showed that the mechanical properties and corrosion properties of the specimens after thermal cycle changed significantly, and the specimens which experienced high temperature (480, 420 °C) thermal cycle was more significant than that experienced low temperature (320, 260 °C) thermal cycle. The mechanical properties results showed that the tensile strength of the specimens under high temperature thermal cycle was higher than that of base metal, while the strength of the low temperature cycle was lower than that of base metal, and the specimens were softened after low temperature thermal cycle. Electrochemical experimental results showed that the corrosion resistance of the specimens under high temperature thermal cycle was weaker than the low temperature thermal simulation. However, the corrosion resistance about four kinds of thermal simulation parts was worse than that of the parent material base metal. The grain size and the distribution of precipitation phase changed by the rapid of heating and cooling process in welding heat cycle, thereby affecting the mechanical properties and corrosion resistance performance of the thermal simulation parts, and

C. Huang · X. Wang (✉)
School of Life Science and Engineering, Southwest Jiaotong University, Chengdu 610031, China
e-mail: xmwang991011@163.com

C. Huang
e-mail: 18215562364@163.com

S. Zhang · J. Hu
School of Material Science and Engineering, Southwest Jiaotong University, Chengdu 610031, China
e-mail: 1126178081@qq.com

J. Hu
e-mail: hujie1992011@163.com

© Springer Nature Singapore Pte Ltd. 2018

Y. Han (ed.), *Advances in Materials Processing*, Lecture Notes in Mechanical Engineering, https://doi.org/10.1007/978-981-13-0107-0_51

the specimens that experienced different peak temperature would have been experienced different evolution process, so the distribution of grain boundary continuity was different. Thus, the welding thermal simulation parts with different thermal cycles also exhibit different corrosion resistance.

Keywords A7N01-T5 aluminum alloy · Welding thermal cycle
Grain size · Precipitated phase · Mechanical property · Corrosion resistance

Introduction

A7N01-T5 is Al–Zn–Mg aluminum alloy, which can be heat treated. The heat treatable Al–Zn–Mg alloy (7xxx series) have been widely used in the aerospace, high-speed train automobile, ship building etc., industries for their attractive properties after the appropriate heat treatment especially their high specific strength [1–4]. The joints is very important to alloys, so it is necessary to study the performance of joints, but the problem has been appeared, it is very difficult to study the weld, heated-affected zone and overwork zone in detail, because they are too small to investigate carefully. The softening mechanism and property of heat-affected zone about weld joints have gained much interesting. However, it is hard to research the property of heat-affected zone, because it too narrow. Hence magnifying the heat-affected zone with the help of weld thermal simulation technique is a worth considering way to reach the microstructure and property of heat-affected zone. So the welding thermal simulation technology was appeared. In the past decades, the thermal simulation technology has been applied in many fields. It has been found that it was possible to use a weld thermal simulation sample instead of the actual mechanical properties of the welded joint material due to the large uniformity of the structure of the thermal test specimen [5]. Ping simulated the cooling process at a different cooling, and the result showed that the strength and plasticity of the alloy increased [6]. The HAZs were simulated using Gleeble simulator with high heat input weld condition of 300 kJ/cm and the peak temperature of the HAZs was changed from 1200 to 1350 °C to examine the effect of δ-ferrite, the results show that both pitting corrosion resistance and interphase corrosion resistance were seriously deteriorated by δ-ferrite formation in the HAZ and their aspects were different with increasing δ-ferrite fraction [7]. SCCT curve of 7A04 aluminum alloy showed that the phase changed start temperature and end temperature reduced with the increase of the cooling rate [8]. Phase transformation took place mainly in the intermediate temperature range (170–430 °C) from the CCT curve, and different cooling rates corresponded to different precipitates [9]. Li pointed out that the larger the weld heat input, the larger of grain size was, the heating peak temperature was higher and the coarsen of the grain would become more obvious [10]. Farhad Gharavia found that the welding process has a major effect on the corrosion resistance, by decreasing the grain size in the weld regions, the susceptibility to corrosion is enhanced, pitting corrosion and intergranular attack

are the dominant corrosion types in the weld regions and the parent alloy [11]. With the increased of heat input, the sizes of grain became larger [12]. The study showed that precipitation of intermetallic phases and the formation of galvanic corrosion couplings contribute to the corrosion of the hybrid laser–GMA welding of AA6061 alloy [13]. Emilie Bousquet investigated the relationship between microstructure, micro-hardness and corrosion sensitivity of an AA 2024-T3 friction stir welded joint, the result showed that micro-hardness variations are essentially related to the fraction volume of GBP zones and to the size and the density of S′(S) intra-granular precipitates, and the size of grains and density of intermetallics and on intergranular precipitation influence the severity of corrosion [14]. Stefano Maggiolino and other scholars found that the potential decreasing gradually form weld to overwork area, the potential became the most negative in the overwork area, and then along the direction of the base metal the potential gradually became positive [15–17]. Kelsey, R. A. studied the effect of welding heat input on the heat affected zone strength about the Al–Zn–Mg alloy, which could be significantly reduced the loss of strength by increasing the number of weld passes and keeping the low intercostal temperature [18].

This paper was mainly study the A7N01-T5 aluminum alloy that went through different thermal cycle with different peak temperature. The mechanical properties and corrosion resistance have been studied.

Materials and Experimental Procedures

The A7N01-T5 aluminum alloy with the thickness of 15 mm was selected as the base meatal (BM). And for laser-MIG welding, the chemical composition of BM, and the welding parameters are exhibited in Tables 1 and 2. After welding, the thermal simulation parameters have been gotten, and the parameters are exhibited in Table 3.

Table 1 Chemical composition of A7N01s-T5 aluminum alloy (mass fraction, %)

Materials	Si	Fe	Cu	Mn	Mg	Cr	Ni	Zn	Ti	V	Zr
A7N01-T5	<0.001	0.069	0.086	0.307	1.038	0.224	0.003	4.23	0.057	0.019	0.157

Table 2 Process parameters of laser-MIG hybrid welding

Laser method	Power (kW)	Wirefeed peed (m/min)	Welding speed (m/min)	Welding voltage (V)	Welding current (A)
Laser-MIG welding	2	9	0.72	22.4	240

Table 3 Thermal simulation parameters

Parameter group number	Heating rate V_h (°C/s)	Maximum temperature T_m (°C)	High temperature residence time t_m (s)	Cooling rate ωc (°C/s)
1#	168	480	1.0	200 < T < 480, v = 78 °C/s; 100 < T < 200, v = 6 °C/s; 60 < T < 100, v = 0.2 °C/s
2#	150	420	1.0	200 < T < 420, v = 72 °C/s; 100 < T < 200, v = 5.5/s; 60 < T < 100, v = 0.2 °C/s
3#	130	320	1.0	200 < T < 300, v = 50 °C/s; 100 < T < 200, v = 4 °C/s; 60 < T < 100, v = 0.2°C/s
4#	110	260	1.0	200 < T < 250, v = 30°C/s; 100 < T < 200, v = 3.5 °C/s; 60 < T < 100, v = 0.2 °C/s

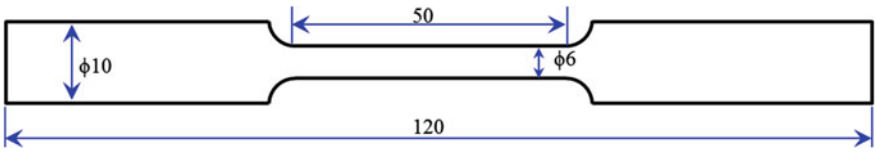

Fig. 1 Thermal cycle specimen

The A7N01-T5 aluminum alloy was used as the base mental for thermomechanical controlled processing. The microstructure of the A7N01-T5 aluminum alloy was observed by AX10 Optical Microscopy and JSM-6490LV Scanning Electron Microscopy after polishing by 400#, 600#, 800#, 1000# and 2000# grit abrasive papers respectively. And then etching with mixed acid corrosion etching solution the ratio of which is HF:HCl:HN03:H2O = 2:3:5:90. A Φ6 mm × 120 mm, which was shown in Fig. 1, rectangular sample of the A7N01-T5 aluminum alloy was subjected to thermal cycle in the Gleeble-3500 thermomechanical simulator. Heating and cooling parameters provided in Table 3 were selected to simulate possible HAZ microstructures occurred in real welding production. After the thermal cycle got four different samples were maned 1#, 2#, 3#, 4#, which are corresponding to the four parameters, the grain morphology of the four were observed using electron back-scattered diffraction(EBSD), the alloying element distribution about the four were analyzed using the black of scanning electron microscope(SEM).

The tensile tests at room temperature of BM and the thermal sample were carried out according to the GB/T 228.1-2010 Tensile test for metallic materials—Part 1: Test methods for room temperature [19]. The dimensions of a tensile test sample are shown in Fig. 2 the tensile speed is 1 mm/min, and the tensile test was the average

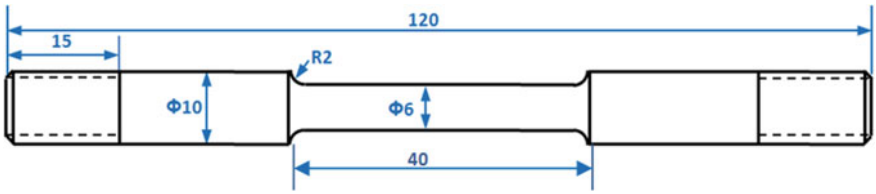

Fig. 2 Tensile specimen

of three sample to ensure accuracy and reproducibility of the result. Electrochemical impedance spectrum test selected amplitude of 10 mV AC sine wave as the excitation signal, it was applied to the electrode in a frequency range of 0.1–100,000 Hz. OPC was recorded for 0.5 h to reach a steady-state freely corroding condition before potentiodynamic test.

Results and Discussion

Microstructure Morphology

Figure 3 shows the microstructure morphology of A7N01-T5 base metal and thermal simulated specimens. It can be seen that the base metal has flattened grains which are deformed along the rolling direction, the alloy has happened incomplete recrystallization. Grain growing happens after thermal cycle under peak temperatures of 480, 420, 320 and 260 °C. Grains of 1# are bigger than those of base metal, which means that grains will grow obviously under the thermal cycle treatment with peak temperature of 480 °C. Some grains of 2# are bigger but some small, the distribution of it is uneven. Grains of 3# are smaller than those of 1# due to its lower peak temperature during thermal cycle, but the distribution of grain is even. The grains of 4# are mainly the small grains which are deformed along the extrusion direction. The size of the sample is highly different, which went through the different peak temperatures thermal cycle, the problem may be the unevenness of the original matrix.

Figure 4 shows the second phase distribution of base metal and thermal simulation specimens. Along the extrusion direction list the second phase which has different size and shapes. The second phase size of thermal simulation specimens are bigger then base metal, however the 4# is smaller than other thermal simulation specimens and the second phase is mainly distributed along the grain boundary.

The EDS test result about A7N01-T5 have been shown in Fig. 5 and Table 4. From the picture and the table, we can see the Fe and Si elements are the main element in the second phase of specimen thermal simulation, which will be harmful to the mechanical properties of alloy, thus, the mechanical properties about the thermal simulation specimen will be lower than the base metal (Figs. 6 and 7).

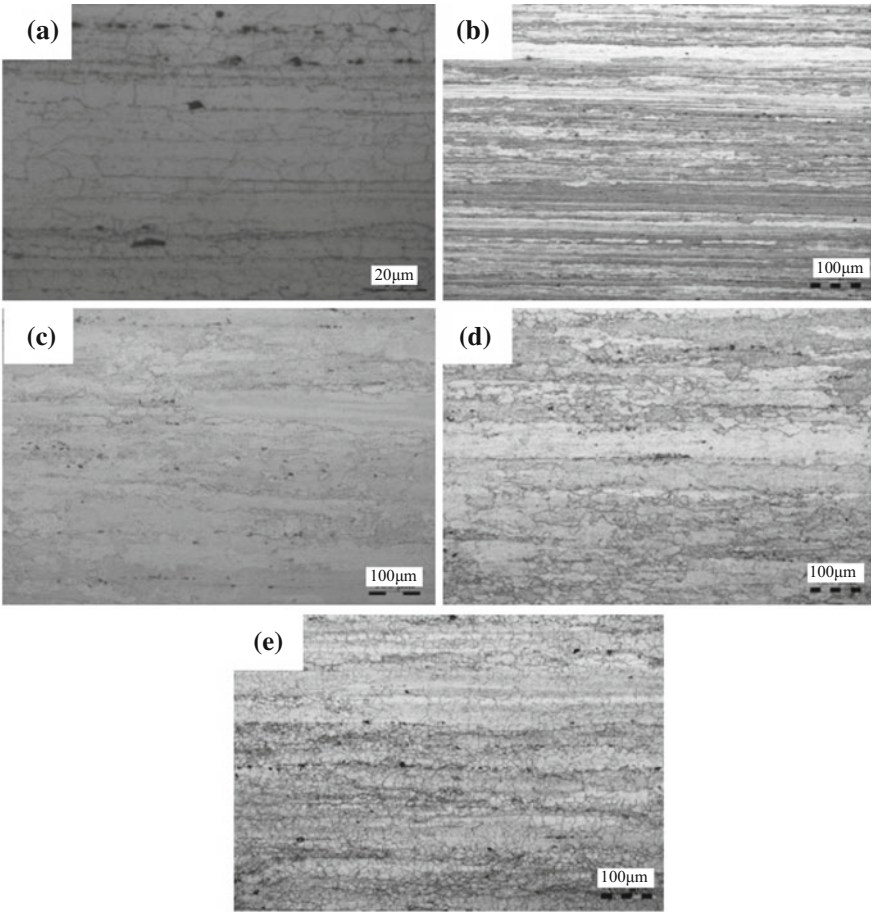

Fig. 3 Metallurgical structure of A7N01-T5 base metal and thermal simulation specimens **a** M, **b** 1#, **c** 2#, **d** 3#, **e** 4#

The EBSD technology has been employed more and more to study the grain morphology rather than traditional optical metallograph inspection in recent years due to its high clarity and accuracy. In the present work, the grain morphology in base metal and thermal simulated specimens were observed, it should be noted that the size and distribution about base metal, 4# are similar, the 1# is bigger than others. The grain become bigger at high temperature thermal cycle, the distribution of it is uneven, and this is cooperated with the microstructure morphology. The recrystallized grains with broad band shape are the secondary grains growing at superior direction during high temperature deformed procedure. The deformed grains are composed of fine grains which are directionally stretched and broken accompany with recrystallization to some extent. Grains of 4# and 3# are fine and evenly distribute uneven, and it can be seen from the magnified images that the fine

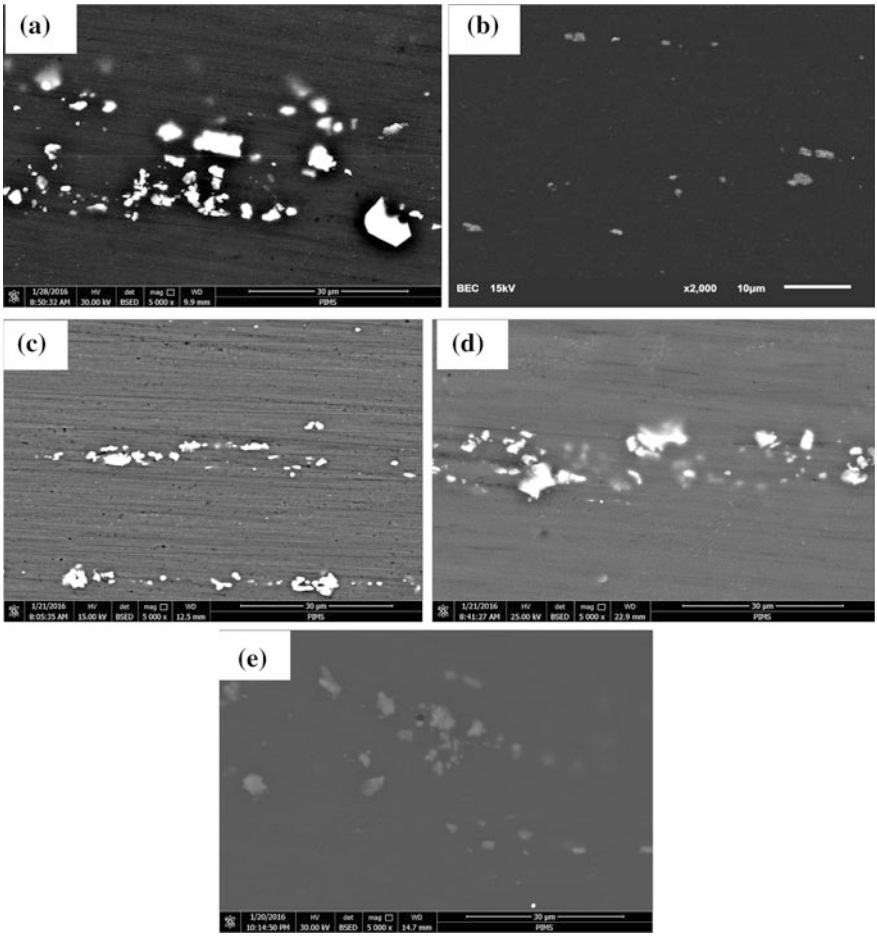

Fig. 4 Second phase distribution of base metal and thermal simulation specimens **a** M, **b** 1#, **c** 2#, **d** 3#, **e** 4#

grains with band shape are consist of tiny grains with different directions. Compared with those of 4# and 3#, the band shape grains of 1# are larger, and many sub-grains distribute in the band shape grains. Compared to the base metal, the grains of 2# are bigger but its smaller than 3#, that possible due to the unevenness of the original matrix.

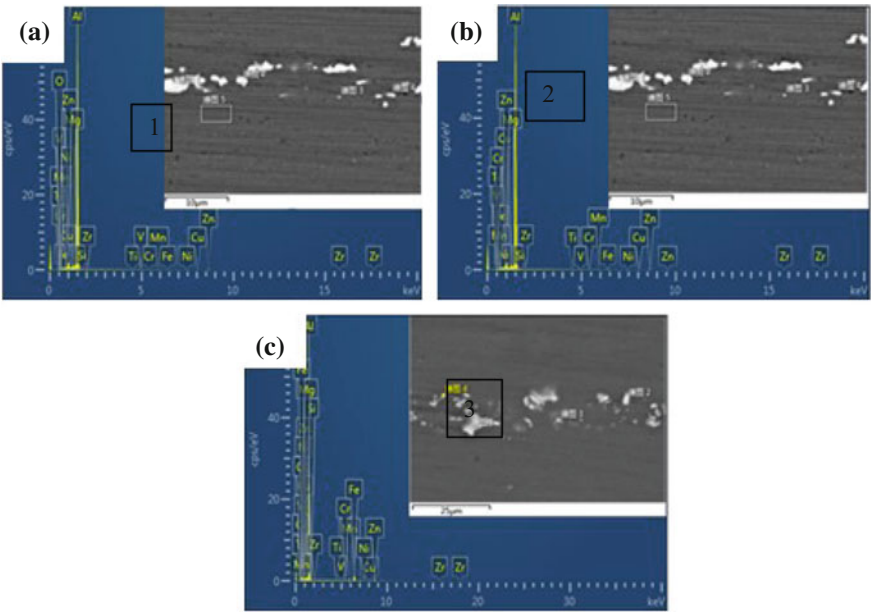

Fig. 5 EDS analysis of aluminum alloy thermal simulated specimens

Table 4 EDS results of the second phase of thermal specimens

Location	Si	Fe	Mn	Mg	Cr	Zn	Ti	Cu	Zr	Al
Point 1	0	0	0.28	1.22	0.23	5.54	0.02	0.31	0.09	91.50
Point 2	0.25	1.44	0.52	1.26	0.06	5.40	0.01	0.45	0	90.44
Point 3	1.24	7.65	1.42	0.94	0.24	0.15	0.01	0.200.18	0.18	83.22

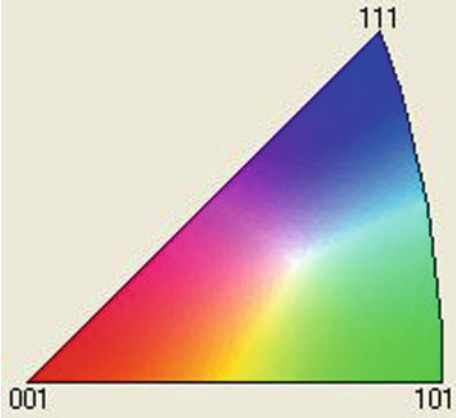

Fig. 6 The inverse polo figure

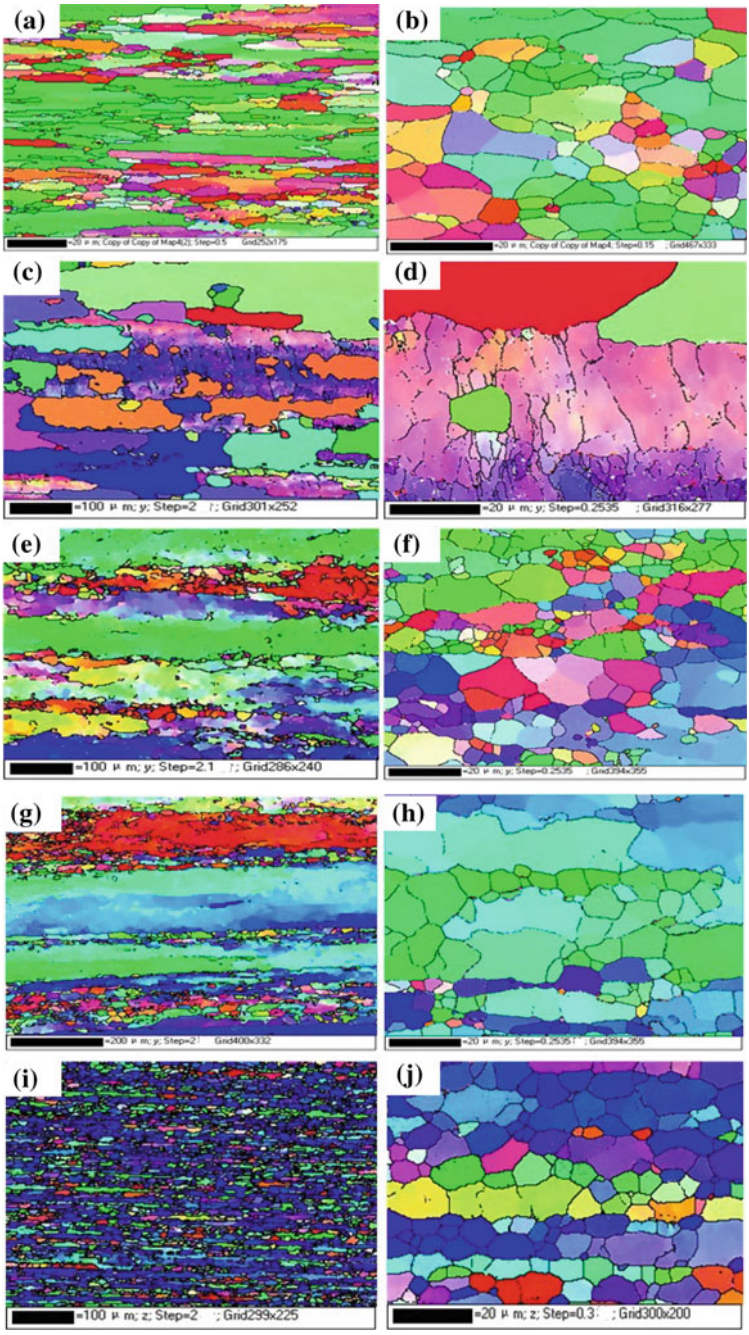

Fig. 7 Microstructure of A7N01-T5 base metal and thermal simulated specimens under EBSD **a**, **b** M, **c**, **d** 1#, **e**, **f** 2#, **g**, **h** 3#, **i**, **j** 4#

Mechanical Properties of Base Metal and Thermal Simulated Specimens

The tensile test results of A7N01-T5 base metal and thermal simulated specimens are shown in Fig. 8 and Table 5. The tensile strength of 4# and 3# thermal simulated specimens are lower than that of base metal, but the 1# and 2# of the tensile strength are higher than base metal. The elongation is show the same trend to the tensile strength except the 2#.

Electrochemical Characterization

Potentiodynamic Polarization Curves

Figure 9 shows the potentiodynamic polarization curves of base metal and thermal simulation specimens about A7N01-T5 alloy. It is suggests that both the anodic and cathodic processes of base metal and thermal simulation specimens are controlled by activation processes. The corrosion potential (Ecorr) and corrosion current density (icorr) of base metal and thermal simulation specimens are simulated from the potentiodynamic polarization curves by suing Tafel Curve Fitting method [20], and the present in Table 6. It is apparent that the most positive corrosion potential appears in the base metal, 4# has more positive corrosion potential than other temperatures. 480 has the most negative corrosion potential. The 1# and 2# have the higher corrosion current density and corrosion rate, so they have poor corrosion resistance.

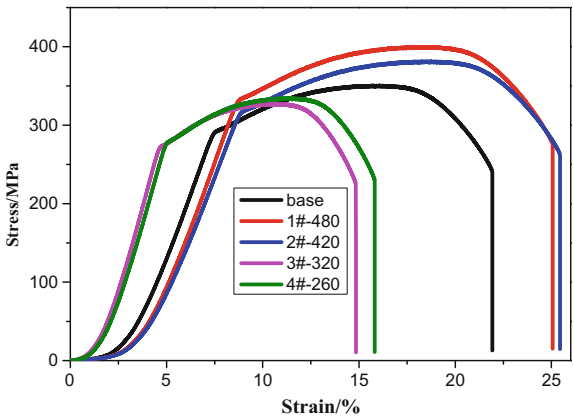

Fig. 8 Tensile stress-strain curves of A7N01-T5 base metal and thermal simulation specimens

Table 5 Tensile properties of A7N01-T5 base material and thermal simulation specimen

Number	Thermal simulation parameters	Tensile strength (MPa)	Average tensile strength/MPa	Elongation (%)	Average elongation (%)
1#	480 °C	394.79	391.56	18	18.06
1#	480 °C	388.52		17.83	
1#	480 °C	391.37		18.34	
2#	420 °C	386.31	374.33	14.37	14.13
2#	420 °C	379.94		15.43	
2#	420 °C	379.42		14.03	
3#	320 °C	329.82	329.88	10.64	11.28
3#	320 °C	324.59		11.71	
3#	320 °C	335.23		11.49	
4#	260 °C	343.01	336.72	12.00	11.97
4#	260 °C	331.12		11.51	
4#	260 °C	337.01		11.83	
Base	Base	354.13	351.38	15.66	15.97
Base	Base	345.31		15.97	
Base	Base	354.70		16.27	

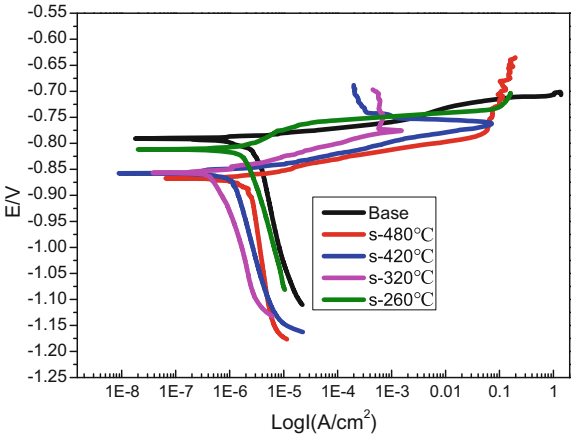

Fig. 9 Potentiodynamic polarization curves of base metal and thermal simulation specimens corrosion rate/v ($mm.a^{-1}$)

EIS Characterization

Figure 10 shows the EIS Nyquist diagrams of base metal and thermal simulation specimens. The amplitude of the resistance arc (radius of curvature) can determine the corrosion of aluminum alloy, the radius of curvature the sample is greater, the smaller the ion exchange degree the sample is, than the greater the polarization resistance is, the better the corrosion resistance is [21]. From Fig. 8 it is found that

Table 6 The corrosion potential (Ecorr) and corrosion current density (icorr) of base metal and thermal simulation specimens

No	Corrosion potential (V)	Corrosion current density (mA cm^2)	Corrosion rate/v (mm a^{-1})
Base	−0.79077	3.8741×10^{-4}	0.02106
480 °C	−0.81157	8.7933×10^{-4}	0.05288
420 °C	−0.85729	8.0865×10^{-4}	0.04521
320 °C	−0.85746	6.9184×10^{-4}	0.03614
260 °C	−0.86779	4.5325×10^{-4}	0.02795

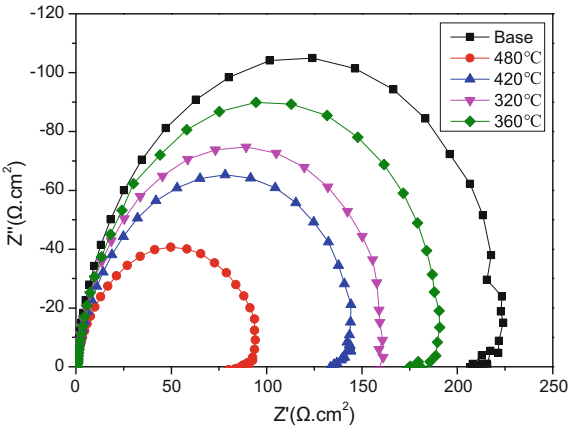

Fig. 10 EIS Nyquist diagrams of base metal and thermal simulation specimens

the radius of curvature about base metal is the biggest, thermal simulation specimens of that are smaller than the base metal, the higher the peak temperature is the lower the curvature is. That is say the specimens that experience higher temperature the corrosion of it become bad. The result is similar with the potentiodynamic polarization.

OPC

Open circuit potential of base metal and thermal simulation specimens is shown in Fig. 11. It is see that the base metal has the most positive OPC values in the 3.5% sodium chloride solution, indicating that thermal simulation specimens experience 480 peak temperature is lower in comparison with the other thermal simulation specimens and base metal.

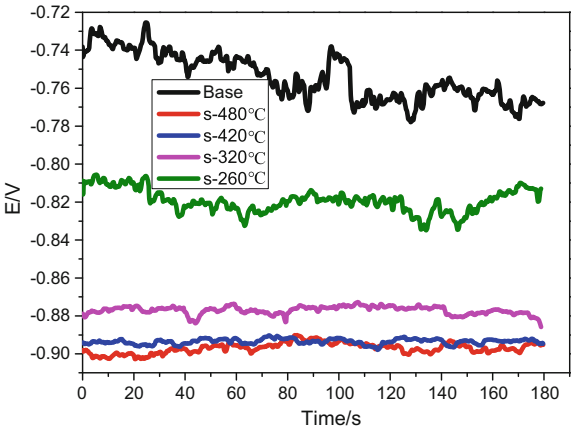

Fig. 11 Open circuit potential of base metal and thermal simulation specimens

Conclusions

In this paper, the welding thermal cycle curves of A7N01 aluminum alloy have been measured during laser-MIG hybrid welding. The microstructure of welding heat affected zone is simulated by Gleeble-3500 thermal simulation test machine. The microstructure of base metal and thermal simulated specimen undergoing thermal cycle treatment with peak temperature of 480, 420, 320 and 260 °C has been observed, and the mechanical properties tested.

(1) The strength of specimen treated at higher peak temperature (480, 420 °C) is higher than that of base metal, the specimen treated at lower peak temperature (320, 260 °C) is lower than that of base metal. After thermal cycle treated at higher peak temperature, the grains grow coarsening, the solid solution and natural aging of precipitate happen strengthen the alloy. The Grains growing in the specimen treated at lower peak temperature are not as obvious as the specimen treated at higher peak temperature, and the precipitates aggregate for the lower cooling rate, which lead to the strength decreasing. Compared with grain changes, the precipitates change has greater influence on the strength change of A7N01 alloy.

(2) Electrochemical test results show that base metal has the best corrosion resistance. The specimen treated at peak temperature 480 °C has the worst corrosion resistance. The grain and precipitates change has greater influence on the potential change of A7N01 alloy, and then influence the corrosion resistance of A7N01 alloy.

References

1. T. Dursun, C. Soutis, Recent development in advanced aircraft aluminium alloys. Mater. Des. **56**, 862–871 (2014)
2. J.C. Williams, E.A. Strake, Progress in structural materials for aerospace systems. Acta Mater. **51**, 5775–5799 (2003)
3. R.O. Vakhromov, V.V. Antipov, E.A. Tkachenko, Research and development of high-strength of Al–Zn–Mg–Cu alloys. TCAA13: 13th international conference on aluminum alloys wiled online library, pp. 1514–1520 (2012)
4. L. Zhang, X.Y. Li, Z.R. Nie et al., Microstruture and mechanical properties of a new Al–Zn–Mg–Cu alloy joints welded by laser beam. Mater. Des., pp. 451–458 (2015)
5. Q. Duan, X.G. Zhang, Z.J. Li et al., Nonlinear temperature field analysis and thermal simulation of welding thermal cycle. J. Xi'an Jiaotong Univ. **4**,**35**(4), 412–417 (2001)
6. J.P. Wu, Y.L. Yang, B. Zhao et al., Effect of welding thermal cycle on microstructure and properties of Ti35 titanium alloy. **10** (2010)
7. J. Moon, H.Y. Ha, T.H. Lee, Corrosion behavior in high heat input welded heat-affected zone of Ni-free high-nitrogen Fe-18Cr-10Mn-N austenitic stainless steel. Mater. Charact. **82**(5), 113–119 (2013)
8. H.Y. Li, X.F. Wang, Y. Tang et al., Determination of continuous cooling transition curve of 7A04 aluminum alloy. Chin. J. Nonferrous Metals **20**(4), 640–646 (2010)
9. H.Y. Li, J. Bin, Y.K. Zhao et al., Establishment of continuous cooling transformation diagrams of aluminum alloys using in situ voltage measurement. Sci Direct **21**, 1944–1949 (2011)
10. G. Li, *Diffusion Interface Field Variations of Grain Growth in Heat Affected Zone*. Zhengzhou University (2006)
11. F. Gharavi, K.A. Matori, R. Yunus et al., Corrosion behavior of Al6061 alloy weldment produced by friction stir welding process. J. Mater. Res. Technol. **4**(3), 314–322 (2015)
12. B.S. Wang, W. Wu, T.J. Ma, Effect of heat input on the microstructure about heat affected zone in Inconel 625 alloy. Weld. Technol. **11**, 12–14 (2014)
13. D.Q. Zhang, X. Jin, L.X. Gao et al., Effect of laser–arc hybrid welding on fracture and corrosion behaviour of AA6061-T6 alloy. Mater. Sci. Eng., A **528**(6), 2748–2754 (2011)
14. E. Bousquet, A. Poulon-Quintin, M. Puiggali et al., Relationship between microstructure, microhardness and corrosion sensitivity of an AA 2024-T3 friction stir welded joint. Corros. Sci. **53**(9), 3026–3034 (2011)
15. Stefano Maggiolino, Chiara Schmid, Corrosion resistance in FSW and in MIG welding techniques of AA6XXX. J. Mater. Process. Technol. **197**, 237–240 (2008)
16. L.Z. Yan, Y.A. Zhang, X.W. Li et al., Microstructural evolution of Al-0.66Mg-0.85Si alloy during homogenization. Trans. Nonferrous Met. Soc. China, pp. 939–945 (2014)
17. M. Zain-ul-abdein, Thermo-mechanical characterization of AA 6056-T4 and estimation of its material properties using genetic algorithm. Mater. Des. **31**, 4302–4311 (2010)
18. M.P. Liu, T.H. Jiang, J. Wang et al., Aging behavior and mechanical properties of 6013 aluminum alloy processed by severe plastic deformation. Trans. Nonferrous Met. Soc. China **24**, 3858–3865 (2014)
19. Y. Wang, H.J. Liu, J.C. Feng et al., 7075 aluminum alloy FSW welding thermal cycle and its influence on the heat affected zone. Hot Forg. Weld. **37**(17), 22–25 (2008)
20. E. McCatterty, Validation of corrosion rates measured by the Tafel extrapolation method. Corros. Sci. **47**, 3202–3215 (2005)
21. M.Y. Wu, J.Q. Tian, L.X. Cao et al., Electrochemical corrosion behavior of tungsten aluminum alloy in different Nacl solutions. Corros. Sci. Protect. Technol. **27**(1), 47–52 (2015)

Experimental Investigation of Selective Laser Melting AlSi10Mg Alloy

Wei Pan, Yangjie Tang, Yantao Liu, Yongzhong Zhang and Pengyue Wu

Abstract The material used in this study was AlSi10Mg alloy powder. And the particle morphology, particle size distribution and chemical properties of the aluminum alloy powder were characterized. The AlSi10Mg alloy powder was used for selective laser melting (SLM) forming. The SLM processes were conducted under the same process parameters, for example, material powder layer depth, scanning interval, and different volume energy density. The interaction between volume power density and organizational performance of the forming parts was analyzed through the density test, hardness test, and microstructure observation. It was found that the properties of forming parts by SLM was fine when the volume energy density was 50–80 J/mm^3. Finally, suitable parameter of volume energy density for SLM manufactured AlSi10Mg alloy was confirmed, and the high density and hardness aluminium alloy forming parts were confirmed by SLM.

Keywords AlSi10Mg alloy · Selective laser melting · Process parameters Microstructure and properties

W. Pan · Y. Tang · Y. Liu · Y. Zhang (✉)
Center for Composites, General Research Institute for Non-Ferrous Metals, Beijing 100088, China
e-mail: yyzhang@grinm.com

W. Pan
e-mail: panweiyzzzl@163.com

Y. Tang
e-mail: beiketyj@126.com

Y. Liu
e-mail: liuyantaobj@163.com

P. Wu
Beijing e-Plus 3D Tech. Co., Ltd., Beijing 100088, China
e-mail: wupengyue@eplus3d.com

© Springer Nature Singapore Pte Ltd. 2018

Y. Han (ed.), *Advances in Materials Processing*, Lecture Notes in Mechanical Engineering, https://doi.org/10.1007/978-981-13-0107-0_52

Introduction

The goal of the modern industry is to reduce the weight and improve the strength of structural materials [1]. As light metal, aluminum alloy, with its excellent physical, chemical and mechanical properties, have been widely used in high-speed trains, light vehicles and other fields. At the same time, advanced transportation means also need us to reduce the weight of structural materials with high specific strength and stiffness to improve the speed and carrying capacity. AlSi10Mg aluminum alloy, with low density, low cost, good corrosion and heat resistance and easy processing, has become one of the preferred material of all kinds of advanced manufacturing [2–4].

The selective laser melting forming technology is a kind of advanced rapid prototyping technology developed in recent years, which using high energy laser beam selectively to melt metal powder to form the part layer by layer, directly forming high performance and complex metal parts. SLM is one of the most promising technologies in the field of additive manufacturing. Compared with the traditional manufacturing of cutting materials, SLM can form a complex structure which can not be processed by traditional processing methods and break through the limitations of traditional processing methods. And the SLM has a significant advantage on manufacturing a single piece and small batch of aerospace aluminum alloy parts, improving the utilization of materials, shorting the manufacturing cycle, reducing manufacturing costs and other aspects. Therefore, SLM has a broad application prospect in aerospace, personalized biological manufacturing and complex mold inserts [5–8].

Buchbinder et al. prepared AlSi10Mg alloy with high power laser (1 kW) [9]. Brandl et al. used the SLM method to form AlSi10Mg alloy. It was found that the fatigue properties of the SLM prepared samples were better than those of the room temperature forming parts after the application of the substrate preheating means [10].

Olakanmi et al. researched the influence of SLM forming parameters on the density and microstructure of AlSi12 alloy. The results showed that the processing technique had an enormous influence on the porosity of the formed parts [11].

Zhang et al. [12] suggested that different aluminum alloy powders had different processing thresholds, which provided the possibility of obtaining completely dense aluminum alloy parts. At the same time, the reasons of poor performance and poor surface performance in SLM aluminum alloy were analyzed. Zhao et al. [13] argued that the spheroidizing of the aluminum alloy produced by the SLM was due to the strong reflexivity of the aluminum alloy. Sun et al. [14] suggested that the application temperature of selective laser melting Al–Fe–V–Si alloy parts was expected to reach 400 °C by optimizing the process parameters.

As the aluminum alloy is easily oxidized, high thermal conductivity and high reflectivity to laser, SLM puts forward higher requirements on laser power and oxygen content. Due to that the low density of aluminum alloy lead to poor liquidity, for increasing the liquidity of AlSi10Mg alloy material, the requirements of

aluminum alloy powder micro-morphology is higher. In this study, the performance of AlSi10Mg alloy powder was characterized, and suitable AlSi10Mg alloy powder was choosed to SLM experiment. The study provide the reference and guidance for the preparation of AlSi10Mg alloy by SLM process with optimized SLM technology parameters.

Experimental Procedure

The AlSi10Mg alloy powder was prepared by gas atomization. Two different particle sizes powder were obtained by screening with different sizes of sieves. The particle size of the powder were +500 to −270 mesh and +800 to −270 mesh respectively. Before the experiment, aluminum alloy powder was put in the vacuum oven for drying at temperature of 80 °C for 6 h, to observe the shape of aluminum alloy powder. SLM experiments were carried out on the SLM system of Beijing e-plus 3D Tech. Co., Ltd, and the system was equipped with 500 W fiber laser and rubber scraper. The protective atmosphere was Argon. The aluminum substrate was grinded and wipe clean with alcohol before the experiment. This needs to define the laser volume energy density. The volume power densities E is the consumption of laser energy on the unit volume of alloy powder, it can be defined as follows:

$$E = P/(v \cdot h \cdot t) \tag{1}$$

In the above formula Eq. 1, P, v, h, t respectively represent the laser power, scanning speed, scanning spacing and powder layer depth. It can be seen from the formula that the laser energy density reflects the laser energy consumed by unit volume of alloy powder, it's determined by multiple SLM process parameters.

The powder thickness of process parameters selected in this experiment was 30 μm, scanning spacing of 100 μm. Volume energy density of 30–80 J/mm^3 was divided into six groups. The difference of each adjacent group is 10 J/mm^3. The content of Oxygen in the atmosphere was not higher than 0.1%.

In this experiment, the morphology, particle size and composition of the aluminum alloy powder were characterized before SLM forming, and the mainly performance of the SLM aluminum alloy was detected by relative density test, hardness test and structure morphology. The relative density is the ratio of the actual density of the alloy to the theoretical density. For a particular material, higher relative density means less pores, cracks, spheres and other defects inside the material. In this paper, the actual density was gauged through the archimedes principle, the surface of the specimen was polished before the density measured to make sure that the accuracy of the measurement. The surface of the sample was grinded with different specifications of sandpaper and then polished to the surface without scratches before microscopic observation.

Results and Discussion

Analysis of AlSi10 Mg Alloy Powders

Table 1 shows the grain size distribution of the two kinds of aluminum alloy powder, and Table 2 is the element of the alloy material. It can be seen that the size of most particle +500 to −270 mesh AlSi10Mg alloy powder is between 21 and 53 μm, particle distribution is more concentrated. The liquidity of powder with less fine powder is good, which is beneficial for SLM, as size of the most particle +800 to −270 mesh AlSi10Mg alloy powder is between 11 and 47 μm.

Figure 1 shows two kinds of aluminum alloy powders with different particle size distributions under canning electron microscopy. Figure 1a shows the micro-morphology of +800 to −270 mesh AlSi10Mg alloy powder. Many fine powder can be seen in the aluminum powder from the picture. And many fine powder adhesion in the coarse powder surface resulting in more agglomeration of the powder, which is detrimental to SLM as the SLM has high requirements of powder flow ability. Figure 1b shows the micro-morphology of +500 to −270 mesh

Table 1 Particle size distribution of +800 to −270 mesh and +500 to −270 mesh AlSi10Mg aluminum alloy powder

Unit (μm)	D(10)	D(25)	D(50)	D(75)	D(90)
+800 to −270 mesh	11.44	18.99	28.83	38.82	47.25
+ 500 to −270 mesh	21.44	28.39	36.92	45.40	53.80

Table 2 Composition of AlSi10Mg aluminum alloy powder

Element	O	Mg	Si	Al
Content (wt/%)	0.049	0.28	9.97	Bal.

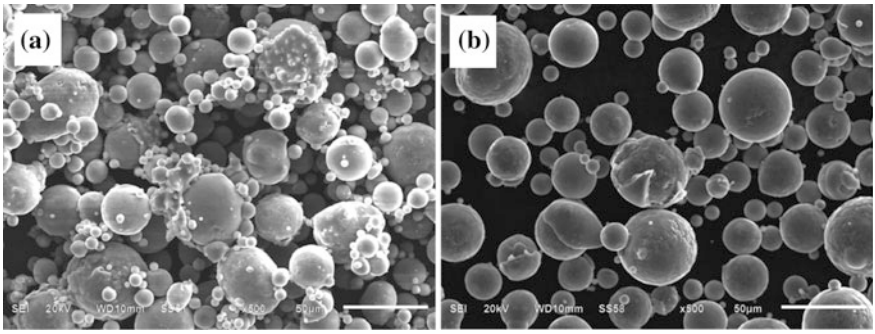

Fig. 1 Morphology of aluminum alloy powder with different particle size distribution: **a** +800 to −270 mesh aluminum alloy powder, **b** +500 to −270 mesh aluminum alloy powder

AlSi10Mg alloy powder. It can be seen that the particle size of the aluminum alloy powder spherical shape is larger, lesser fine powder can be observed from the photo. There is no similar phenomenon of agglomeration in the figure to Fig. 1a, which is beneficial to improve the flow ability of the powder. Therefore, in order to ensure a better effect of laying powder, this experiment selected +500 to −270 mesh AlSi10Mg alloy powder.

As shown in Table 2, the oxygen content of the aluminum alloy powder is low. Due to the content of the oxygen affects the wettability of the aluminum alloy solution and the surface quality of each layer as processing. Therefore, this is very important to strictly control the oxygen content of the raw material powder and atmosphere to ensure the quality of the forming parts.

Morphology and Performance Analysis of SLM forming AlSi10Mg

Fig. 2 shows the metallograph of aluminum alloy formed by SLM at different bulk energy densities. As shown in Fig. 2a, when the bulk density density of the SLM is 30 J/mm^3, there are many pores in the forming part. However, as the volume energy density increases, the number of stomata of the forming part decreases rapidly. The quantity of the pores is relatively less when the volume energy density increase to 60 J/mm^3. It can be seen from the above that the amount of pores of the forming part decreases with the increase of the volume energy density in certain range. Because the energy input is insufficient when the volume energy density is only 30 J/mm^3. And the aluminum alloy powder can not be melted sufficiently, leading to the formation of stomata.

Figure 3 presents the relative density and the rockwell hardness corresponding to the parts processed at different volume energy density. From the Fig. 3, it can be seen that the relative density of the parts is low when the volume energy density of the selective laser melting is 30 J/mm^3. With the increase of the volume energy density, relative density also has a corresponding increase. The reason is that the energy input is serious insufficient with the low volume energy density. And aluminum alloy powder can not be melted fully leading to produce more pores. With the unit volume of powder energy input increased when the volume energy density increases, powder melting is relatively more fully, thus leading to less pores and higher density. The changing rule of the hardness and relative density is similar, which reflect the relationship between porosity and the volume energy density formed before.

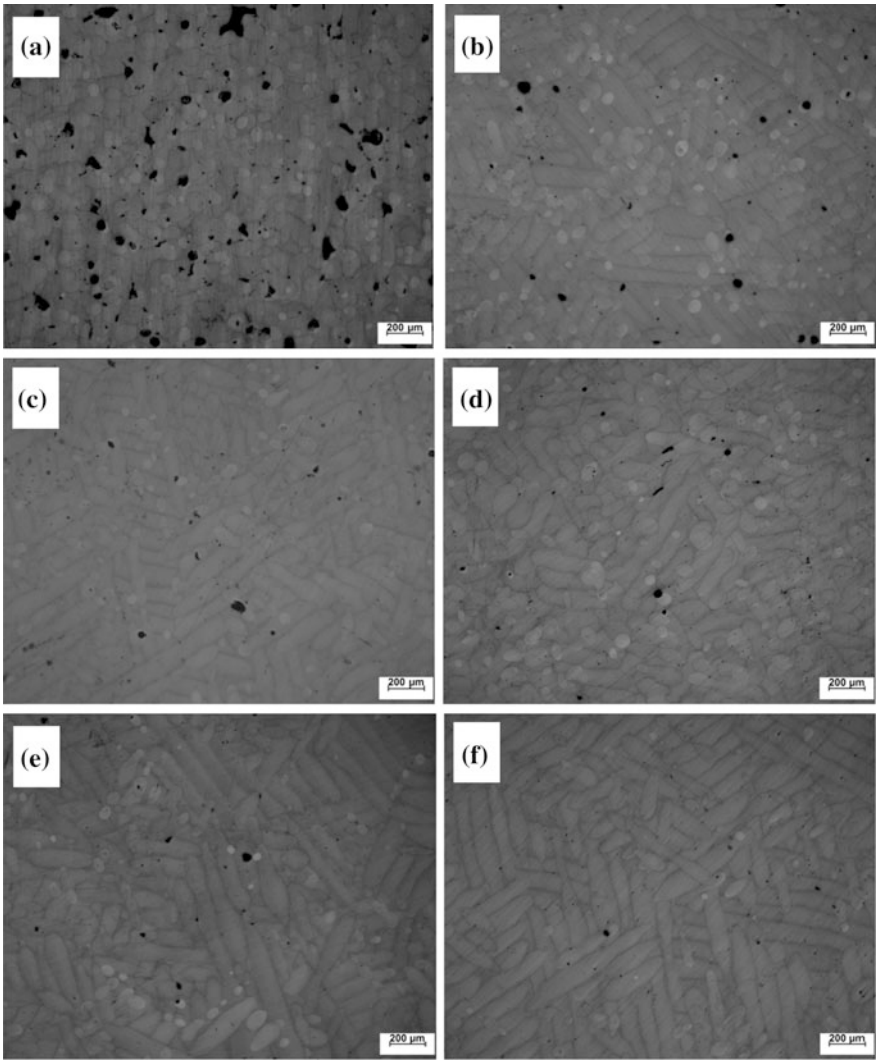

Fig. 2 Metallograph of SLM forming aluminum alloys at disparate volume power densities: **a** 30 J/mm^3, **b** 40 J/mm^3, **c** 50 J/mm^3, **d** 60 J/mm^3, **e** 70 J/mm^3, **f** 80 J/mm^3

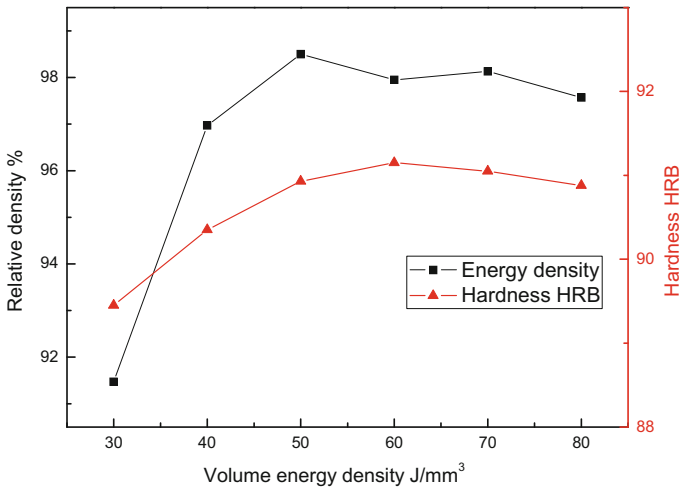

Fig. 3 Density and hardness of the forming parts at different volume energy densities

Conclusion

(1) For AlSi10Mg alloy powder, more serious agglomeration occurs when the fine powder is more, which will affect the flow ability and the effect of laying powder. When the fine powder is less, the agglomeration is less, which is conducive for improving the flow ability of powder and the effect of laying powder.
(2) In certain range of volume energy density, the amount of pores of the forming parts decreases as the volume energy density increases.
(3) In certain extent of volume energy density input, the relative density and hardness of the forming parts have similar laws of variation, and they will increase as the volume energy density increasing.

References

1. E.A. Starke, J.T. Staley, Application of modern aluminum alloys to aircraft. Prog. Aerosp. Sci. **32**(2), 131–172 (1996)
2. X.M. Zhang, Y.L. Zheng, Y. Zhang, The development and preparation technology of high strength aluminum alloy. Acta Metall. Sin. **51**(3), 257–271 (2015)
3. M. Peters, C. Leyens, Aerospace and space materials. Mater. Sci. Eng. **3**, 12–18 (2009)
4. K.M. Liu, D.P. Lu, B. Yang et al., The present situation and development of rapidly solidified heat—resistant aluminum alloys. Mater. Rev. **22**(2), 57–60 (2008)
5. G. Rolink, S. Vogt, L. Senčekova et al., Laser metal deposition and selective laser melting of Fe–28 at.% Al. J. Mater. Res. **29**(17), 2036–2043 (2014)

6. T.B. Sercombe, G.B. Schaffer, Rapid manufacturing of aluminum components. Science **301** (5637), 1225–1227 (2003)
7. L.E. Murr, S.M. Gaytan, D.A. Ramirez et al., Metal fabrication by additive manufacturing using laser and electron beam melting technologies. J. Mater. Sci. Technol. **28**(1), 1–14 (2012)
8. Q. Jia, D. Gu, Selective laser melting additive manufacturing of TiC/Inconel 718 bulk-form nanocomposites: densification, microstructure, and performance. J. of Mater. Res. **29**(17), 1960–1969 (2014)
9. D. Buchbinder, H. Schleifenbaum, S. Heidrich et al., High power selective laser melting(HP SLM) of aluminum parts. Phys. Proc. **12**, 271–278 (2011)
10. E. Brandl, U. Heckenberger, V. Holzinger et al., Additive manufactured AlSi10Mg samples using selective laser melting (SLM): microstructure, high cycle fatigue, and fracture behavior. Mater. Des. **34**, 159–169 (2012)
11. E.O. Olakanmi, R.F. Cochrane, K.W. Dalgarno, Densification mechanism and microstructural evolution in selective laser sintering of Al-12Si powders. J. Mater. Process. Technol. **211**(1), 113–121 (2011)
12. D.Y. Zhang, Manufacturing aluminum alloy model by selecting laser melting method. Chin. J. Lasers **34**(12), 1700–1704 (2007)
13. G.Y. Zhang, D.D. Wang, P.K. Bai et al., Research progress of laser rapid prototyping technology for aluminum alloy. Hot Working Technol. **9**, 170–173 (2010)
14. S.B. Sun, Study on the Process, Microstructure and Properties of Al–Fe–V–Si Heat-Resistant Aluminum Alloy by Laser Selective Melts (Beijing University of Aeronautics and Astronautics, Beijing, 2016)

Corrosion Behavior Evolution of A7N01 Aluminum Alloys with Different Heat Treatments in the IGC Solution

Jie Hu, Cui Huang and Xiaomin Wang

Abstract Three different heat treatments, peak aging (T6), over-aging (T74) and retrogression and re-aging (RRA), were conducted for the A7N01 aluminum alloy respectively. The evolution of the corrosion behavior in the intergranular corrosion (IGC) solution of the three alloys was studied by electrochemical impedance spectroscopy (EIS) and morphology analysis. The results showed that corrosion pits were formed on the three alloys surfaces after 6 h immersion in IGC solution. The T6 alloy had obvious intergranular corrosion and the depths of corrosion pits decreased in the order T6 > RRA > T74. The EIS results showed that in the initial stage of the reaction, the Nyquist plot were composed by a high frequency capacitance loop and a low frequency inductive loop. After 6 h immersion the inductive loop still existed in T74 alloy, while it disappeared in the other two alloys and was replaced by a low frequency capacitance loop. In the initial stage of reaction, pitting corrosion sensitivity of T74 alloy was the smallest, RRA alloy was the second one, and T6 alloy was the highest one. The equivalent circuit results showed that when the immersion time was between 6 and 144 h, the polarization resistance (R_{pit}) increased gradually with the immersion time prolonging. The R_{pit} decreased in the order T6 > RRA > T74 alloy, which attribute to the formation of corrosion products on the new interface. In the later stage of the immersion (after 144 h), the R_{pit} of the three alloys decreased as a result of the abscission of the corrosion products on the alloy surface. After soaking for 168 h, the R_{pit} of T74 alloy reached the maximum value, RRA alloy was slightly higher than T6 alloy. In

J. Hu
School of Materials Science and Engineering, Southwest Jiaotong University, Chengdu 610031, Sichuan, China
e-mail: hujie1992011@163.com

C. Huang · X. Wang (✉)
School of Life Science and Engineering, Southwest Jiaotong University, Chengdu 610031, Sichuan, China
e-mail: xmwang991011@163.com

C. Huang
e-mail: 18215562364@163.com

© Springer Nature Singapore Pte Ltd. 2018

Y. Han (ed.), *Advances in Materials Processing*, Lecture Notes in Mechanical Engineering, https://doi.org/10.1007/978-981-13-0107-0_53

the late stage, the corrosion susceptibility to intergranular corrosion sensitivity decreased in the order T6 > RRA > T74.

Keywords A7N01 aluminum alloys · Heat treatment · Intergranular corrosion Electrochemical impedance spectroscopy · Corrosion behavior evolution

Introduction

7xxx series aluminum alloys are widely used in railway transportation and aerospace industries for their low density and high strength [1, 2]. However, A7N01 aluminum alloys suffered from stress corrosion cracking (SCC) and pitting corrosion frequently as the main material of the key components in the high-speed trains. There is a need to increase corrosion resistance of the aluminum alloy without sacrificing its strength. Previous researches have indicated that the combination of high strength and corrosion resistance was contradictory, while composition and heat treatment can affect it significantly [3].

Many efforts have been carried out to obtain a good combination of strength and SCC resistance property. It has been reported that the effect of heat treatment of 7N01 aluminum alloys on strength and fracture toughness was significant [4]. Some researches show that RRA increases exfoliation corrosion resistance without sacrificing the strength compared to T6 temper for 7085 aluminum alloy [5]. However, few studies show that temper condition has little influence on corrosion resistance of aluminum alloy [6]. The study shows that the microstructure and properties can be improved by performing ageing/precipitation treatments at elevated temperatures to increase the Cu content of grain boundary precipitates to render them less anodic with respect to the matrix [7]. Cao et al. study the exfoliation corrosion of AA7075 aluminum alloy using electrochemical impedance spectroscopy and find the EIS is a potential convenient technique to study the exfoliation corrosion processes [8].

In this work, the corrosion behavior of A7N01 aluminum alloys in three different tempers in the intergranular corrosion solution was investigated by immersion tests and electrochemical impedance spectroscopy (EIS) methods, and their corrosion morphologies were observed by scanning electron microscopy (SEM) and energy dispersive spectrometer (EDS).

Experimental

Material and Heat Treatments

The present study was carried out on the 10 mm thick A7N01 aluminum alloy extrusions with chemical composition of Al–4.37Zn–1.57 Mg–0.1Cu–0.22Mn–

Table 1 Aging treatment applied to the A7N01 aluminum alloy

Aging treatment	1st step	2nd step	3rd step
T6	120 °C/24 h	–	–
T74	120 °C/24 h	168 °C/16 h	–
RRA	120 °C/24 h	230 °C/8 min	120 °C/24 h

0.17Zr–0.15Cr–0.03Ti–0.12Fe–0.08Si (wt%). The simples were firstly subjected to solution treatment at 480 °C for 1 h and followed by a room temperature water quenched, then aged at different temperatures and times, the specific heat treatments and procedures are presented in Table 1. Water quench was subjected to the plates after each aging step.

Immersion Test

The intergranular corrosion test was performed according to the standard IGC test as described in GBT 7998-2005. The dimensions of the IGC specimens are 15 × 25 × 10 mm. All of the specimens were abraded with a sequence of emery papers from 240 to 1000, and rinsed in de-ionized water, degreased in ethyl alcohol and dried in cold air. In order to remove the aluminum coating on the surface, the specimens were put into the 10% NaOH solution for 5 min, put them into the 30% HNO_3 solution until their surface become sheeny, rinsed in de-ionized water and dried. The specimens were immersed in an aqueous solution of NaCl 5.7% and H_2O_2 0.3% for 6 h, and the solution temperature was maintained at 35 ± 2 °C during the test. The morphology of the corroded surface was observed by the laser scanning confocal microscope (LSCM) and the depths of the corrosion pits were measured by the VK analyze on the LSCM pictures simultaneously. The metallography of cross-side was observed by Zeiss metallurgical microscope.

The Electrochemical Impedance Spectroscopy Test

The EIS test of the alloys in IGC solution at different immersion time was carried out by Corrtest electrochemical workstation. Three-electrode system was adopted to the test, the working electrode were the three alloys with a exposed area of 1 cm^2, the reference electrode was a saturated calomel electrode (SCE) and the counter electrode was a platinum plat. The working surfaces were abraded with a sequence of emery papers from 240 to 1500 and polished. The measurements were carried out with a 5 mV sine perturbation at open circuit potential. The measuring frequency range was 10^5 to 10^{-2} Hz. The EIS data were analyzed by ZSimpWin

program, and the simulation consequence was determined by the option of the equivalent circuit. And the corrosion morphologies were observed by FEI Quanta FEG 250 SEM and EDS.

Results and Discussion

Microstructure Morphology

The microstructures of the T6, T74 and RRA alloys are shown in Fig. 1. It can be observed that the precipitation particles distributed as a chain along the rolling direction. The precipitation particles were rich in Fe, Mg, Zn, Si, Mn and Cu elements according to the EDS consequence shown in Table 2. The existing literature indicates that η($MgZn_2$), T ($Al_2Mg_3Zn_3$), S ($CuMgAl_2$), Mg_2Si, Al_7Cu_2Fe, Al–Fe–Mn–Si, (FeMn)Al_6 and θ($CuAl_2$) can form in Al–Zn–Mg–Cu alloys [9]. According to the content of these elements in the precipitate phase (shown in Table 2), it can be speculated that the particles of the A7N01 alloys were η($MgZn_2$), Al_7Cu_2Fe, Al–Fe–Mn and Al–Fe–Si phase.

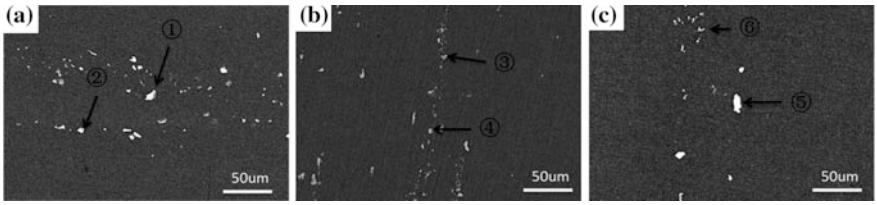

Fig. 1 Microstructures of the T6 (**a**), T74 (**b**) and RRA (**c**) alloys

Table 2 Element content of the phases (wt%)

Element	T6		T74		RRA	
	①	②	③	④	⑤	⑥
Al K	66.35	77.71	90.47	90.45	72.50	88.47
Mg K	0.27	1.03	1.73	1.65	0.60	1.56
Si K	5.04	2.78	0.84	0.22	3.96	0.40
Cr K	1.17	–	–	–	1.35	–
Mn K	4.03	1.62	0.09	0.58	3.42	0.68
Fe K	21.25	13.16	2.37	2.37	15.71	4.16
Zn K	1.82	3.17	4.32	4.48	1.96	4.27
Cu K	0.06	0.53	0.18	0.25	0.50	0.46
Totals	100.00	100.00	100.00	100.00	100.00	100.00

Analysis of the Immersion Test in IGC Solution

The metallography of three alloys in cross-side is shown in Fig. 2. It can be seen that during the 6 h immersion, the specimens of T6 and RRA temper suffered from the intergranular corrosion obviously, which the corrosion extends along the grain boundaries. However, the characteristic of pitting was obvious for T74 temper.

The depth of the corrosion pits was counted for the three alloys, shown in Table 3. The result shows that depth of pits decreased in the order: T6 > RRA > T74. During the 6 h immersion, the intergranular corrosion susceptibility of the T6 and RRA temper were higher than the T74 temper.

Analysis of the EIS Test

The corrosion process was divided into three stages according to the characteristics of the simulation results: the pitting corrosion stage, the intergranular corrosion stage and the corrosion product abscission stage.

The EIS plots of the three alloys for initial pitting corrosion stage were shown in Fig. 3. In Fig. 3a, it can be seen that the Nyquist plot were composed by a high frequency capacitance loop and a low frequency inductive loop for the T6 temper and RRA temper, while there are only a high frequency capacitance loop for the T74 temper. The inductive loop is often explained by the relaxation phenomenon of reaction intermediate, however, KEDDAM et al. [10] indicate that the inductive loop observed is associated with the weakening of the protective effectiveness of the aluminum oxide layer due to the anodic dissolution of aluminum alloy. In some degree, the inductive loop can be regarded as the symbol of the occurrence of the

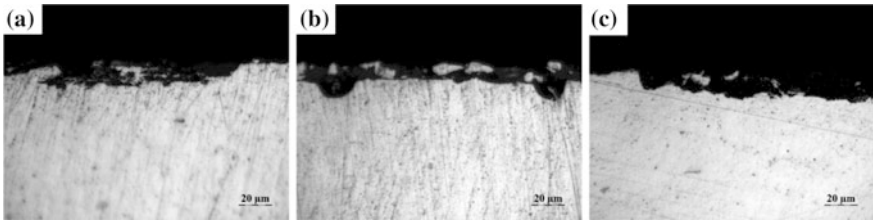

Fig. 2 Metallography of three alloys in cross-side. **a** T6; **b** T74; **c** RRA

Table 3 Depths of the corroded specimens in cross-side

Number	T6	T74	RRA
Depth (μm)	6.882	4.098	5.335

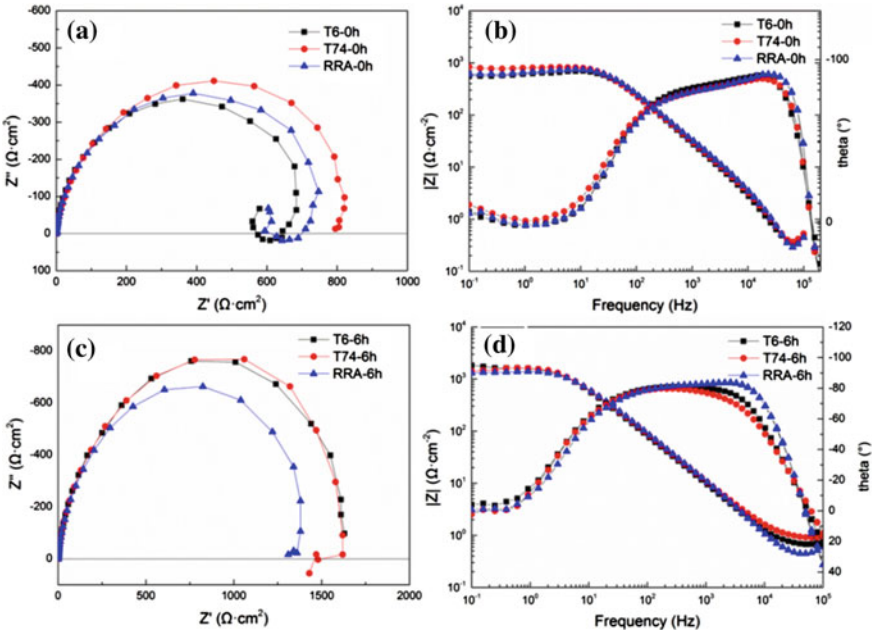

Fig. 3 EIS plots of initial pitting corrosion stage. **a**, **b** 0 h; **c**, **d** 6 h

pitting corrosion. The result shows that the pitting corrosion was occurred to the specimens in T6 temper and RRA temper, their pitting corrosion susceptibility were higher than the specimens in T74 temper. The radius of the high frequency capacitance loop is a characterization of the corrosion resistance performance, the greater of the value of the radius, the better the corrosion resistance. The value of radius for T74 temper is larger than that for T6 temper and RRA temper, the result is consistent with the previous result.

The plots in Fig. 3c show that the inductive loop vanished and the Nyquist plot was composed by a high frequency capacitance loop and a low frequency capacitance loop for T6 and RRA temper with the extension of immersion time. However, the pitting corrosion still dominated the corrosion process for T74 alloy on account of the inductive loop still existed. Cao et al. put forward that the inductive loop occurred during the induction period of passivation film pitting corrosion, the inductive loop vanished after the rupture of the passive film, then the pitting corrosion enter the stage of development [11]. The high frequency loop corresponded to the original surface, while the low frequency capacitance loop was associated with the new formed surface in pits. The radius of the capacitance loop for immersion 6 h stage became larger than the initial immersion stage.

Figure 3b, d show the phase angle plots of the three temper alloys for different immersion time respectively. Only one capacitive time constant can be observed

during the initial immersion stage (Fig. 3b). There were two capacitive time constants when the immersion time came to 6 h (Fig. 3d).

In order to analyze the EIS spectrum, an appropriate equivalent circuit can be used to simulate the reaction process. The capacitance was mathematically modeled using a constant phase element (CPE) in order to obtain a better simulation between the model and the experimental data [12]. Previous works indicated that the CPE behavior was led by the dispersion effect of time constant, and related to the surface toughness of the specimens [13, 14]. Then the impedance was defined by [15, 16]:

$$Z(jw) = (Y_0)^{-1} jw^{-n} \tag{1}$$

where Y_0 is the Q-constant; j is the imaginary unit; w is the angular frequency ($w = 2\pi f$, f is the frequency); n is the diffusion coefficient, the value ranging from −1 to 1. When the n = 1, the CPE element can be replaced by a pure capacitance element; when the n = 0, the element is a pure resistance element.

The corresponding equivalent circuits are shown in Fig. 4. The EIS plots of T6 temper and RRA temper in the initial immersion stage and the T74 temper after 6 h immersion were simulated with the equivalent circuit shown in Fig. 4a, while, the T74 temper was simulated with the equivalent circuit shown in Fig. 4b. The EIS plots of T6 temper and the RRA temper after 6 h immersion were simulated with the equivalent circuit shown in Fig. 4c. The R_s was the resistance of the solution; $Q_p/C_p$and R_t were the oxide-layer capacitance and the charge transfer resistance of the original metal surface, respectively; Q_{dl} and R_{pit} were the the double-layer capacitance and charge transfer resistance of the new formed surface, respectively; R_1 and L_1 were the parameters of the inductance element.

The fitting parameters of the three alloys after 0 h and 6 h immersion are listed in Tables 4 and 5. It can been see from the Table 4, the R_t of the three temper alloys was decreased in the order: T74 > RRA > T6, and the R_1 of the RRA temper was

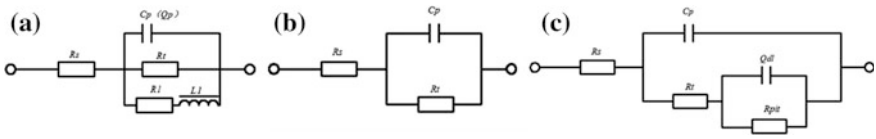

Fig. 4 Equivalent circuits

Table 4 Fitting parameters of the specimens in the initial immersion stage (0 h)

Electrolyte no.	R_s (Ω cm^2)	C_p (S s^p cm^{-2})	R_t (Ω cm^2)	R_1 (Ω cm^2)	L_1 (H cm^2)
T6	0.4706	5.87×10^{-6}	699	3525	343
T74	0.5476	5.36×10^{-6}	805.9	–	–
RRA	0.4599	4.95×10^{-6}	718	4808	1153

Table 5 Fitting parameters of the specimens after 6 h immersion

Electrolyte no.	R_s (Ω cm^2)	Q_p/C_p (S s^p cm^{-2})	n_p	R_t (Ω cm^2)	Q_{dl} (S s^p cm^{-2})	n_{dl}	R_{pit} (Ω cm^2)	R_1 (Ω cm^2)	L_1 (H cm^2)
T6	0.7306	1.59×10^{-5}	–	110.7	2.22×10^{-5}	0.7924	1617	–	–
T74	0.917	2.92×10^{-5}	0.925	1704	–	–	–	8823	4887
RRA	0.5356	1.54×10^{-5}	–	322.7	1.48×10^{-5}	0.9116	1067	–	–

larger than T6 temper. The results show that in the initial stage of immersion (0 h), the pitting corrosion resistance of T74 temper alloy was the best, and the pitting corrosion resistance of T6 temper alloy was the worst, and the RRA temper alloy was in the middle.

The surface morphology of the three alloys is shown in Fig. 5. During the initial 6 h immersion, the pitting corrosion taken place on the surface of both specimens, and the pits distribute along the extrusion direction. As the same time, the passivation membrane dissolves in local area, shown in Fig. 5b, d, f. The corrosion degree of the T6 temper is more serious than other temper obviously, which is the ultimate no matter on size and amount. The size and amount of the pits for T74 temper is much less than RRA temper.

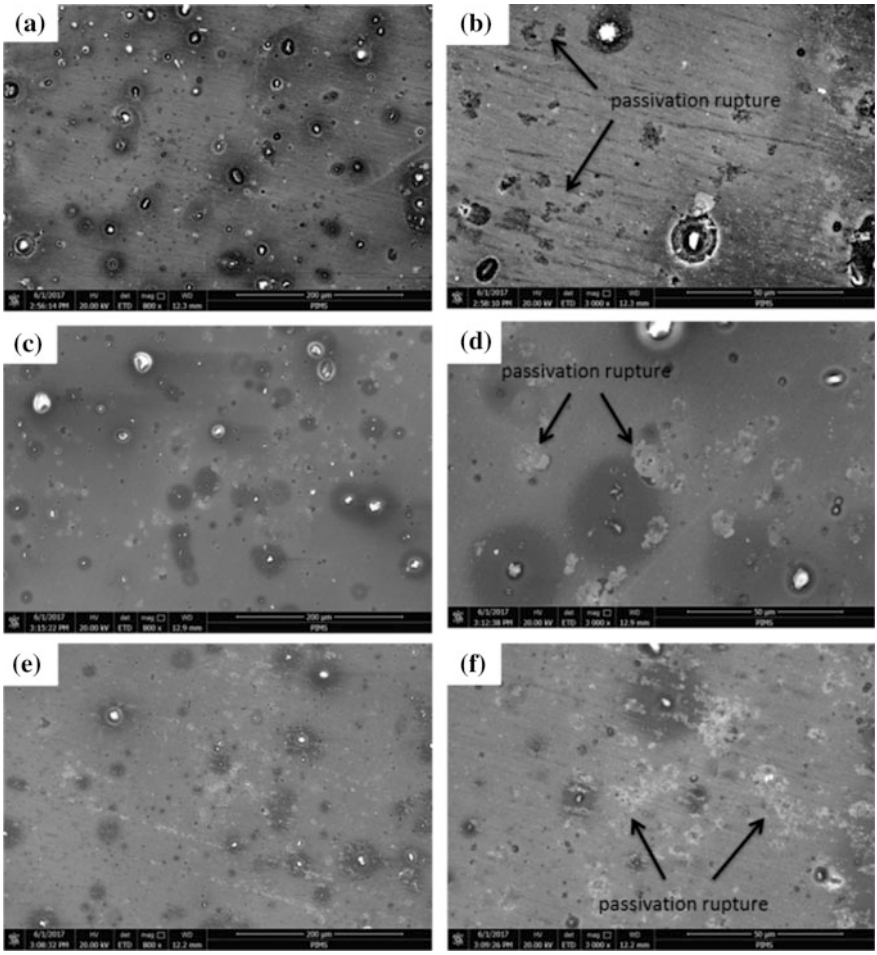

Fig. 5 Corrosion morphology after 6 h immersion. **a**, **b** for T6; **c**, **d** for T74; **e**, **f** for RRA

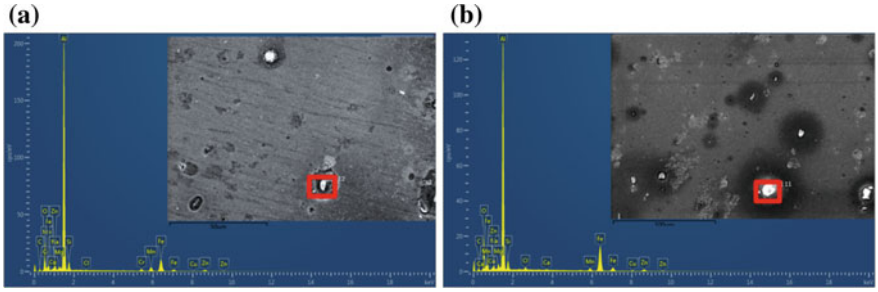

Fig. 6 EDSspectra of the 6 h immersion specimens. **a** T6; **b** RRA

Table 6 Element content of the pits

Element	T6 (wt%)	RRA (wt%)
Al K	67.58	64.60
Mg K	0.84	0.60
Si K	4.12	4.48
Cr K	1.93	1.54
Mn K	4.47	4.44
Fe K	16.91	20.62
Zn K	4.15	3.48
Cu K	–	0.24
Totals	100.00	100.00

The EDS results of pits on the surface of the T6 and RRA were shown in Fig. 6. And the element content of the pits was listed in Table 6. The particles in the pits contains Al, Mg, Fe, Mn, Si, Zn, Cr and Cu elements, the result indicated that the corrosion was originated from the particles in the Al matrix and grain boundaries. It can be inferred that the particles were Al–Fe–Si, Al–Fe–Mn, $\eta(MgZn_2)$ and Al_7Cu_2Fe phases. The electrochemical behavior of these particles is significantly different from the Al matrix, therefore, these particles formed galvanic corrosion micro-cells [17]. The corrosion potential of these Al–Fe–Si, Al–Fe–Mn, $\eta(MgZn_2)$ phase are lower than the Al matrix in the IGC solution, therefore, these particles were dissolved as the anodic electrode relative to the Al matrix. While, the corrosion potential of Al_7Cu_2Fe phase is higher than the Al matrix, the Al matrix surrounding the Al_7Cu_2Fe particle was dissolved as the anodic electrode.

The second period of the corrosion is the intergranular corrosion stage, which ranging from 12 to 144 h. The EIS plots for this period are shown in Fig. 7. With the prolonging of immersion time, the radius of capacitance loop and the impedance modulus in low frequency increased, and the phase angle peak decreased in the high frequency simultaneously. In this period, the Nyquist plots were simulated with the equivalent circuit shown in Fig. 7c. The R_s was the resistance of the solution; C_p

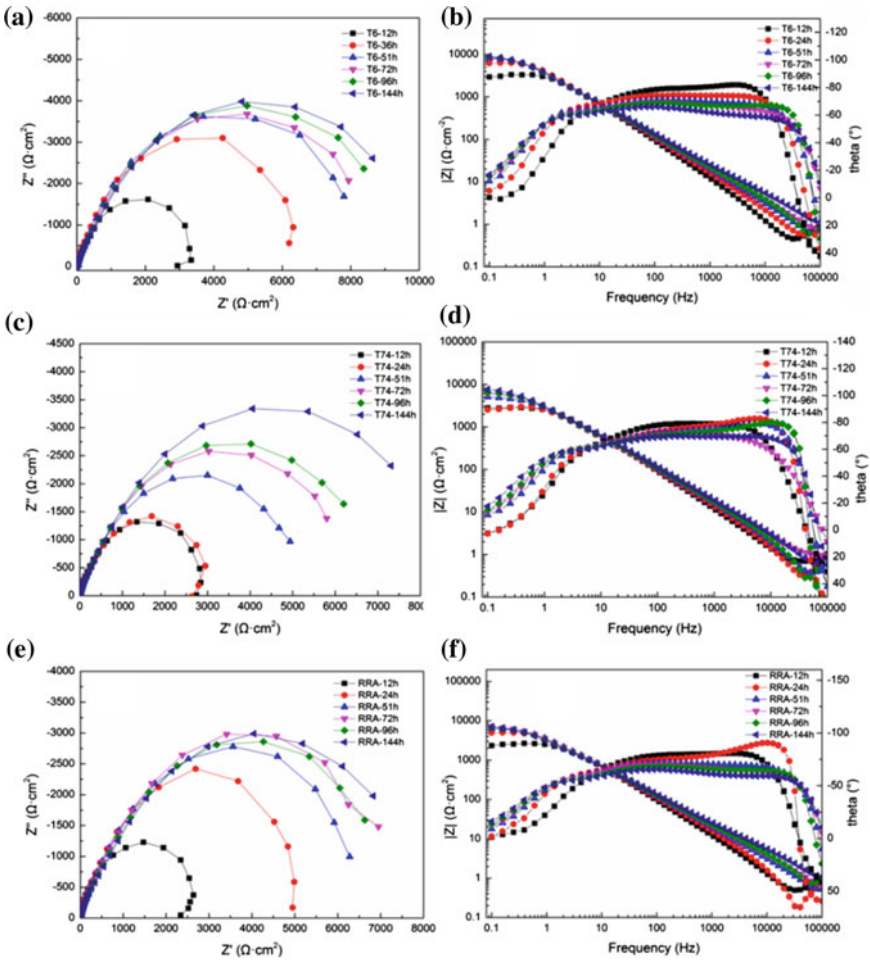

Fig. 7 EIS plots of the intergranular corrosion stage. **a**, **b** T6; **c**, **d** T74; **e**, **f** RRA

and R_t were the oxide-layer capacitance and the charge transfer resistance of the original metal surface, respectively; Q_{dl} and R_{pit} were the double-layer capacitance and charge transfer resistance of the new formed surface, respectively.

The fitting parameters are listed in Tables 7, 8, 9. With the prolonging of immersion time, the C_p and n_{dl} decreased, at the same time, the Q_{dl} and the R_{pit} increased. The R_t decreased rapidly in the early stage of reaction indicated that the reaction occurred quickly and the repair capability of passive film was poor in this period. And then alternating with corrosion and passivation, the trend was gradually easing. The R_{pit} is the charge transfer resistance of the new formed surfaces, the accumulation of the corrosion products in the new surface blocked the transfer of the charges, leading to the increase of the R_{pit} [18, 19].

Table 7 Fitting parameters of the specimens for T6 temper in the second stage

Electrolyte no.	R_s (Ω cm^2)	C_p (F cm^{-2})	R_t (Ω cm^2)	Q_{dl} (S s^p cm^{-2})	n_{dl}	R_{pit} (Ω cm^2)
T6-12 h	0.7612	1.32×10^{-5}	153.8	2.32×10^{-5}	0.8139	3457
T6-24 h	0.7777	8.49×10^{-6}	48.80	3.32×10^{-5}	0.7823	7237
T6-51 h	0.8353	5.51×10^{-6}	21.10	4.85×10^{-5}	0.7430	8252
T6-72 h	0.8441	3.84×10^{-6}	10.50	5.47×10^{-5}	0.7331	10,170
T6-96 h	0.8115	4.44×10^{-6}	20.69	5.34×10^{-5}	0.7277	11,240
T6-144 h	1.174	2.61×10^{-6}	11.59	5.98×10^{-5}	0.7139	12,390

Table 8 Fitting parameters of the specimens for T74 temper in the second stage

Electrolyte no.	R_s (Ω cm^2)	C_p (F cm^{-2})	R_t (Ω cm^2)	Q_{dl} (S s^p cm^{-2})	n_{dl}	R_{pit} (Ω cm^2)
T74-12 h	0.8450	1.35×10^{-5}	129.40	2.94×10^{-5}	0.7789	2917
T74-24 h	0.7040	1.13×10^{-6}	110.50	4.30×10^{-5}	0.7677	3255
T74–51 h	0.5574	9.19×10^{-6}	59.30	5.69×10^{-5}	0.7158	5828
T74-72 h	1.033	6.81×10^{-6}	15.83	6.28×10^{-5}	0.7051	7546
T74-96 h	0.7865	7.71×10^{-6}	49.29	6.28×10^{-5}	0.7040	7987
T74-144 h	0.7944	5.78×10^{-6}	23.76	6.69×10^{-5}	0.6957	10,320

Table 9 Fitting parameters of the specimens for RRA temper in the second stage

Electrolyte no.	R_s (Ω cm^2)	C_p (F cm^{-2})	R_t (Ω cm^2)	Q_{dl} (S s^p cm^{-2})	n_{dl}	R_{pit} (Ω cm^2)
RRA-12 h	0.7780	1.32×10^{-5}	174.10	2.20×10^{-5}	0.8131	2520
RRA-24 h	0.7666	9.45×10^{-6}	105.40	3.79×10^{-5}	0.7531	5620
RRA-51 h	0.6184	5.39×10^{-6}	16.16	4.89×10^{-5}	0.7337	7481
RRA-72 h	0.7484	3.92×10^{-6}	10.36	5.33×10^{-5}	0.7338	8298
RRA-96 h	0.9285	4.18×10^{-6}	17.70	5.86×10^{-5}	0.7147	8309
RRA-144 h	1.117	2.57×10^{-6}	63.58	6.86×10^{-5}	0.6978	9195

The surface morphology of the three alloys after 72 h immersion is shown in Fig. 8. The corrosion pits were distributed on the metal surface unevenly, heterogeneous corrosion occurred to the three aged alloys. Corrosion pits were interconnected and developed into intergranular corrosion. Many corrosion products were accumulated on the corroded surface, shown in Fig. 8b–d.

In the intergranular corrosion stage, the corrosion resistance of the T6 temper is the best, and the RRA temper is higher than T74 temper ranging from 24 to 96 h, and the corrosion resistance of T74 temper exceeded RRA temper after 144 h immersion.

The third period of the reaction is the corrosion abscission stage, the EIS plots are shown in Fig. 9. The radius of the capacitance loop was decreased with the

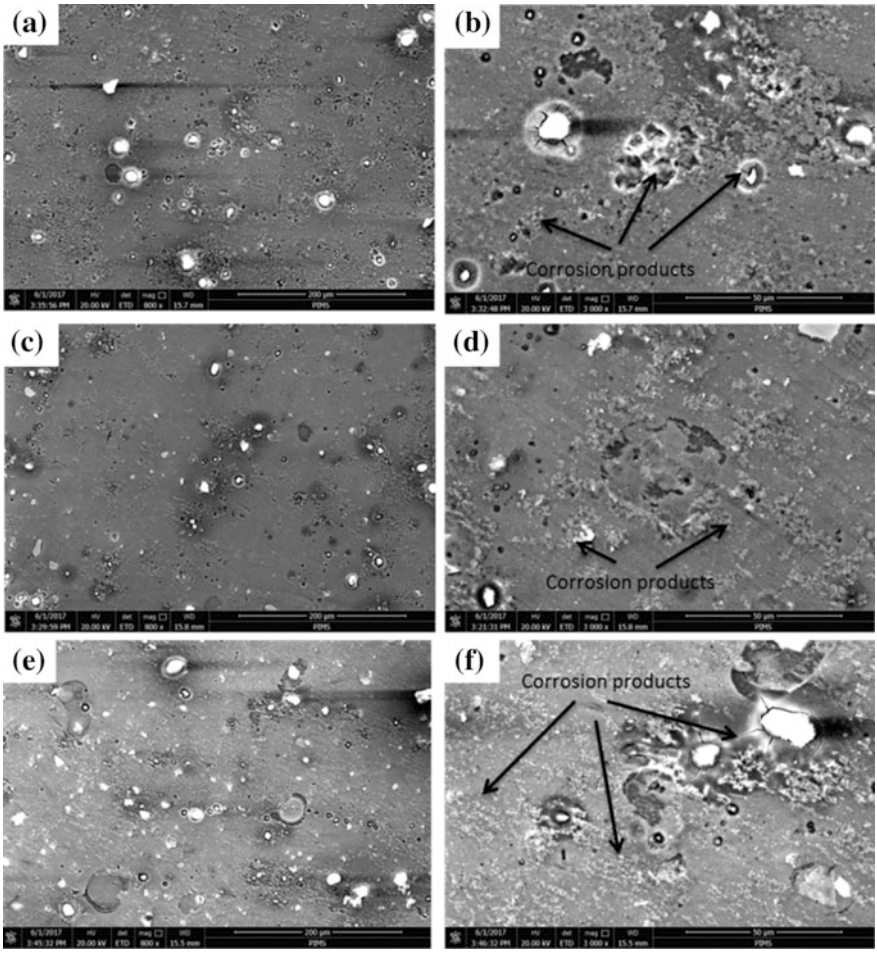

Fig. 8 Corrosion morphology after 72 h immersion. **a**, **b** for T6; **c**, **d** for T74; **e**, **f** for RRA

prolonging of the immersion time, and two capacitive time constants can be observed in the phase angle plots in Fig. 7b, d, f. The EIS plots were simulated with the equivalent circuit shown in Fig. 9c. The fitting parameters are listed in Tables 10, 11, 12. The increase of the R_t shows that the repair capability of the passive film increased gradually. The abscission of the corrosion product on the new formed surface result in an increase in the ion diffusion rate, which made the R_{pit} showed a decrease trend. The morphology of the specimens after 168 h immersion is shown in Fig. 10. Local corrosion was deepened to the three alloys, the corrosion pits were unevenly distributed on the surface. Corrosion products were not observed on the surface of the samples. The size and amount of corrosion pits of the T74 temper specimen was the largest in the three alloys. The corrosion

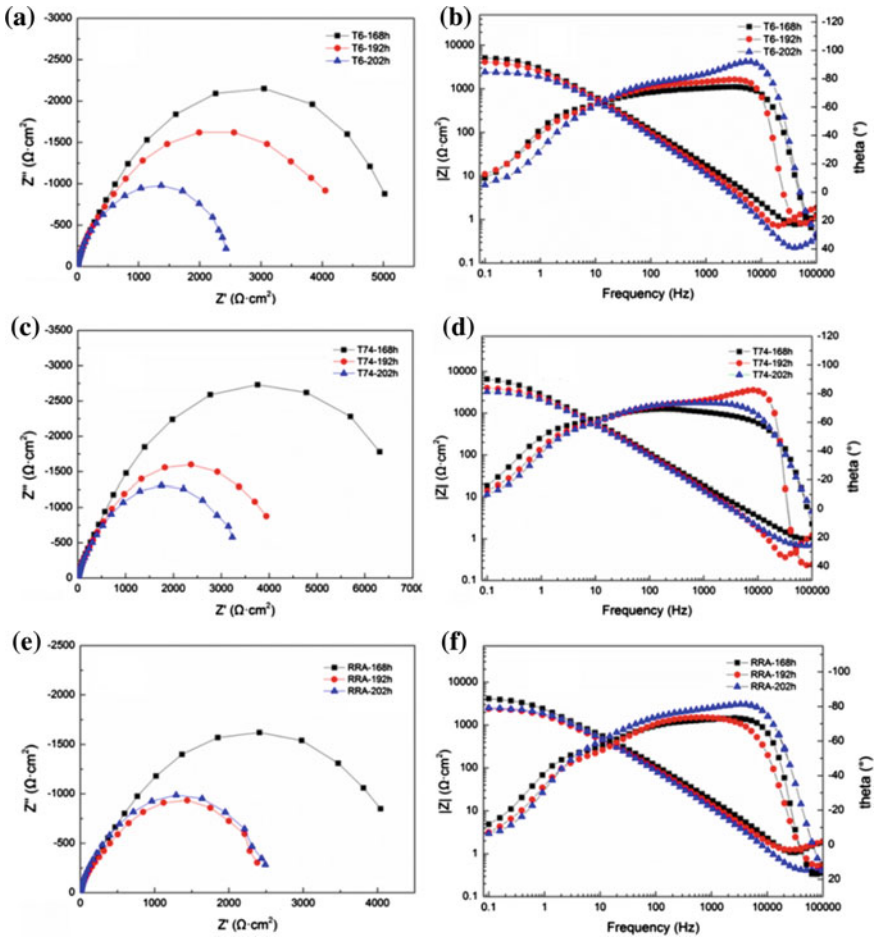

Fig. 9 EIS plots of the corrosion product abscission stage. **a**, **b** T6; **c**, **d** T74; **e**, **f** RRA

Table 10 Fitting parameters of the specimens for T6 temper in the third stage

Electrolyte no.	R_s (Ω cm^2)	C_p (F cm^{-2})	R_t (Ω cm^2)	Q_{dl} (S s^p cm^{-2})	n_{dl}	R_{pit} (Ω cm^2)
T6-168 h	1.04	7.85×10^{-6}	64.10	5.45×10^{-5}	0.7143	5898
T6-192 h	1.347	1.16×10^{-5}	129.3	6.62×10^{-5}	0.6767	4662
T6-202 h	0.3345	1.6×10^{-5}	304.20	5.20×10^{-5}	0.7705	2236

Table 11 Fitting parameters of the specimens for T74 temper in the third stage

Electrolyte no.	R_s (Ω cm^2)	C_p (F cm^{-2})	R_t (Ω cm^2)	Q_{dl} (S s^p cm^{-2})	n_{dl}	R_{pit} (Ω cm^2)
T74-168 h	1.084	5.23×10^{-6}	14.02	6.95×10^{-5}	0.7048	2665
T74-192 h	0.9488	9.58×10^{-6}	72.05	7.52×10^{-5}	0.6866	4650
T74-202 h	0.6920	9.00×10^{-6}	17.05	8.14×10^{-5}	0.6725	3850

Table 12 Fitting parameters of the specimens for RRA temper in the third stage

Electrolyte no.	R_s (Ω cm^2)	C_p (F cm^{-2})	R_t (Ω cm^2)	Q_{dl} (S s^p cm^{-2})	n_{dl}	R_{pit} (Ω cm^2)
RRA-168 h	1.457	8.01×10^{-6}	63.58	8.35×10^{-5}	0.6526	5014
RRA-192 h	1.472	1.09×10^{-5}	64.64	1.05×10^{-5}	0.6364	2770
RRA-202 h	0.4177	1.39×10^{-6}	96.53	6.93×10^{-5}	0.6925	2484

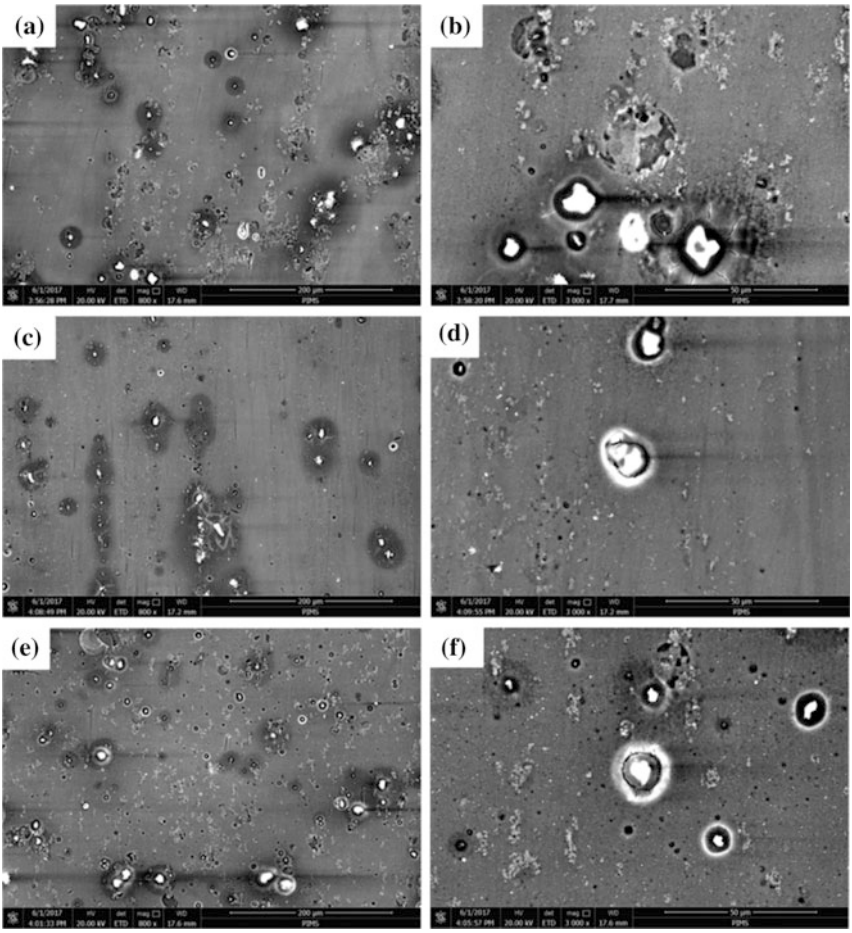

Fig. 10 Corrosion morphology after 168 h immersion. **a**, **b** for T6; **c**, **d** for T74; **e**, **f** for RRA

area of RRA temper specimen was larger than T74 temper specimen obviously. In this stage, the specimen in T74 temper has the better corrosion resistance than the specimens in the other tempers.

Conclusion

The evolution of the corrosion behavior in the intergranular corrosion (IGC) solution of the A7N01 aluminum alloy in T6, T74 and RRA temper is studied, and the following conclusions can be drawn:

(1) The pitting corrosion originates from particles that containing Fe, Si, Mn, Mg, Zn and Cu elements. The particles are presumed to be Al–Fe–Si, Al–Fe–Mn, η(MgZn2) and Al7Cu2Fe phases.
(2) The corrosion process can be divided into three stages for the three alloys in the IGC solution, which are the pitting corrosion stage, the intergranular corrosion stage and the corrosion products abscission stage.
(3) In the first stage, the pitting corrosion dominates the reaction process and the alloy in T74 temper has the best pitting corrosion resistance, the pitting corrosion resistance of T6 temper is the worst and the RRA temper is in the middle. In the second stage, the intergranular corrosion happenson the basis of the pitting corrosion, the corrosion resistance of the alloys is the best due to the accumulation of the corrosion products on the new formed surface. The corrosion resistance of the three alloys decreasesin the order of T6 > RRA > T74. In the third stage, the abscission of the corrosion products results in the decrease of the corrosion resistance. The corrosion resistance of the three alloys decrease in the order of T74 > RRA > T6.

References

1. R. Ranganatha, V.A. Kumar, V.S. Nandi et al., Multi-stage heat treatment of aluminum alloy AA7049. Trans. Nonferrous Metals Soc. Chin. **23**(6), 1570–1575 (2013)
2. T. Marlaud, B. Malki, C. Henon et al., Relationship between alloy composition, microstructure and exfoliation corrosion in Al–Zn–Mg–Cu alloys. Corros. Sci. **53**(10), 3139–3149 (2011)
3. B. Sarkar, M. Marek, E.A. Starke, The effect of copper content and heat treatment on the stress corrosion characteristics of Ai-6Zn-2 Mg-X Cu alloys. Metall. Mater. Trans. A **12**(11), 1939–1943 (1981)
4. B. Li, X. Wang, H. Chen et al., Influence of heat treatment on the strength and fracture toughness of 7N01 aluminum alloy. J. Alloy. Compd. **678**, 160–166 (2016)
5. S. Chen, K. Chen, G. Peng et al., Effect of heat treatment on strength, exfoliation corrosion and electrochemical behavior of 7085 aluminum alloy. Mater. Des. **35**, 93–98 (2012)
6. J. Wloka, T. Hack, S. Virtanen, Influence of temper and surface condition on the exfoliation behavior of high strength Al–Zn–Mg–Cu alloys. Corros. Sci. **49**(3), 1437–1449 (2007)

7. P.A. Rometsch, Y. Zhang, S. Knight, Heat treatment of 7xxx series aluminium alloys—some recent developments. Trans. Nonferrous Metals Soc. Chin. **24**(7), 2003–2017 (2014)
8. F. Cao, Z. Zhang, J. Li et al., Exfoliation corrosion of aluminum alloy AA7075 examined by electrochemical impedance spectroscopy. Mater. Corros. **55**(1), 18–23 (2015)
9. Z. Cvijović, M. Rakin, M. Vratnica et al., Microstructural dependence of fracture toughness in high-strength 7000 forging alloys. Eng. Fract. Mech. **75**(8), 2115–2129 (2008)
10. M. Keddam, C. Kuntz, H. Takenouti et al., Exfoliation corrosion of aluminium alloys examined by electrode impedance. Electrochim. Acta **42**(1), 87–97 (1997)
11. C.N. Cao, J. Wang, H.C. Lin, Effect of Cl-ion on the impedance of passive-film-covered electrodes. J. Chin. Soc. Corros. Prot. **9**(4), 261–270 (1989)
12. X.H. Wang, J.H. Wang, F.U. Cong-Wei, Characterization of pitting corrosion of 7A60 aluminum alloy by EN and EIS techniques. Trans. Nonferrous Metals Soc. Chin. **24**(12), 3907–3916 (2014)
13. R. Jurczakowski, C. Hitz, A. Lasia, Impedance of porous Au based electrodes. J. Electroanal. Chem. **572**(2), 355–366 (2004)
14. T. Pajkossy, Impedance spectroscopy at interfaces of metals and aqueous solutions—surface roughness, CPE and related issues. Solid State Ionics **176**(25–28), 1997–2003 (2005)
15. M.A. Jingling, J.B. Wen, G.X. Li, X.V. ChunHua, The corrosion behaviour of Al−Zn−In −Mg−Ti alloy in NaCl solution. Corros. Sci. **52**(2), 534–539 (2010)
16. Y. Deng, Z.M. Yin, K. Zhao, J.Q. Duan, J. Hu, Z.B. He, Effects of Sc and Zr microalloying additions and aging time at 120 °C on the corrosion behaviour of an Al–Zn–Mg alloy. Corros. Sci. **65**, 288–298 (2012)
17. N. Birbilis, M.K. Cavanaugh, R.G. Buchheit, Corros. Sci. **48**(12), 4202–4215 (2006)
18. C.Q. Ye, R.G. Hu, S.G. Dong et al., J. Electroanal. Chem. **688**(4), 275–281 (2013)
19. X. Lou, P.M. Singh, Phase angle analysis for stress corrosion cracking of carbon steel in fuel-grade ethanol: experiments and simulation. Electrochim. Acta **56**(4), 1835–1847 (2011)

Microstructures of Conventionally As-Cast Mg–Zn–Y Alloys

Qian Li, Zhenghua Huang, Yongxin Zhou, Chunjie Xu, Yangde Li and Weirong Li

Abstract Two series ingots of $Mg_{69+x}Zn_{30-x}Y_1$ and $Mg_{68+x}Zn_{30-x}Y_2$ (x = 0, 3 and 6, atomic percent) alloys with the diameter of 100 mm were obtained by ordinary gravity casting, respectively. The phase compositions and microstructures were investigated by means of optical microscope (OM), scanning electron microscopy (SEM) and X-ray diffraction (XRD). The law that the number, morphology, size and distribution of the quasicrystal phase varied with the content of Zn and Y was discussed. The results showed that the microstructures of the two series alloys were composed of MgZn matrix, $Mg_{30}Zn_{60}Y_{10}$ quasicrystal phase (I) and α-Mg phase. The I-phase directly nucleated and grew during the cooling process of Mg–Zn–Y melt. The morphology of the two series alloys was different obviously. The I-phase exhibited small pentagonal or five-petal shape and six-petal shape in the microstructure of the $Mg_{69+x}Zn_{30-x}Y_1$ alloy, while it was not regular polygon shape in the microstructure of the $Mg_{68+x}Zn_{30-x}Y_2$ alloy. At the same time,

Q. Li · Z. Huang (✉)
Guangdong Provincial Key Laboratory for Technology and Application of Metal Toughening, Guangdong Institute of Materials and Processing, Guangzhou 510650, China
e-mail: zhhuang@live.cn

Q. Li
e-mail: 240008439@qq.com

Q. Li · Y. Zhou · C. Xu
School of Materials Science and Engineering, Xi'an University of Technology, Xi'an 710048, China
e-mail: zhouyongxin_88@126.com

C. Xu
e-mail: xuchunjie@gmail.com

Y. Li · W. Li
DongGuan EONTEC Co., Ltd, DongGuan 523662, China
e-mail: patent@e-ande.com

W. Li
e-mail: patent@e-ande.com

© Springer Nature Singapore Pte Ltd. 2018

Y. Han (ed.), *Advances in Materials Processing*, Lecture Notes in Mechanical Engineering, https://doi.org/10.1007/978-981-13-0107-0_54

with decreasing Zn content, the granularity and homogenization degree of the quasicrystals enhanced gradually. The quasicrystals increased and distributed more evenly.

Keywords Mg–Zn–Y alloy · Quasicrystal · Icosahedral · Alloy composition

Introduction

As the lightest structural metal material, the prospect of magnesium alloys is promising. However, it seems rather difficult to design Mg-based alloy due to lack of effective reinforcement. Mg–Zn series alloys can enhance alloy strength sharply by aging strengthening. The further addition of rare earth RE, being the most effective way to produce the reinforcement effect by second phase, can form large numbers of compounds with high thermal stability [1]. So far, there has been a considerable amount of Mg alloys that have been developed for the enhancement of icosahedral quasicrystal phase (I-phase). They found that the second phase of as-cast Mg–Zn–Y alloy was mainly I-phase when atomic ratio of Zn: RE was about 6. I-phase with the non-periodic arrangement of atoms exhibits high hardness, low interface and strong I-phase/Mg interface, so it can be used as an efficient reinforcing phase for Mg alloy [2–6]. The discovery of quasicrystalline phase in Mg–Zn–Y alloy becomes a new research direction for developing Mg alloys with high performance [7]. The influence of different composition proportion on the solidification phase and microstructure of Mg–Zn–Y alloy had been studied [8]. However, the effect of the Zn and Y contents on quasicrystalline phase in Mg–Zn–Y alloy was rarely reported. Therefore, the present paper is focused on studying the microstructures of as-cast $Mg_{69+x}Zn_{30-x}Y_1$ alloys and $Mg_{68+x}Zn_{30-x}Y_2$ alloys and discussing the relation between the number, morphology, size and distribution of the quasicrystal phase and the Zn and Y contents. Then, it can provide the basis for controlling the microstructure and designing the composition of Mg alloys.

Experimental

The alloy ingots were prepared with industrial pure Mg, pure Zn and Mg–31.7%Y (mass fraction) master alloy in a melting furnace under a mixed CO_2 and SF_6 protective atmosphere. The nominal components are listed in Table 1. Pure Zn and master alloy were added in turn when pure Mg was melted and heated up to 973 K. The melt was stirred twice within 1 h and refined. Then the melt was heated up to 1003 K and stewed for 30 min. When the temperature of the melt cooled down to 973 K, the melt was poured into the round metal mould with the preheating temperature of 473 K, and then the as-cast samples were obtained.

Table 1 Mass ratio of each element of experimental alloys

Alloy	Mg [wt%]	Zn [wt%]	Y [wt%]
$Mg_{69}Zn_{30}Y_1$	44.99	52.63	2.38
$Mg_{72}Zn_{27}Y_1$	48.55	48.98	2.47
$Mg_{75}Zn_{24}Y_1$	52.36	45.08	2.56
$Mg_{68}Zn_{30}Y_2$	43.58	51.73	4.69
$Mg_{71}Zn_{27}Y_2$	47.03	48.12	4.85
$Mg_{74}Zn_{24}Y_2$	50.72	44.26	5.02

As-cast specimens were made as metallographic specimen after being corroded with 4% HNO_3 (volume fraction) in ethanol. Then the microstructure were observed on optical microscope (OM, Leica DM IRM) and scanning electron microscope (SEM, JEOL JXA-8100). The phase composition analysis was performed on X-ray diffractometer (XRD, SmartLab) with Cu K_α radiation.

Results and Discussion

Figures 1 and 2 show the OM and SEM graphs of as-cast $Mg_{69+x}Zn_{30-x}Y_1$ alloys, respectively. Combined with the XRD pattern (Fig. 3a), the microstructure of as-cast $Mg_{69}Zn_{30}Y_1$ alloy includes gray MgZn matrix, and incompletely grown pentagonal, five and six petals-like $Mg_{30}Zn_{60}Y_{10}$ (I-phase). It can be seen from Fig. 1f that I-phase usually exhibits a pentagonal "flower core" and "petal type" dendritic like crystal, which grows outward and is known as "primary petal" of quasicrystal. A "burr" protruding from the edge of primary petal, which is similar to secondary axis of dendrite, is known as "secondary petal" of quasicrystal. With decreasing the Zn content to 27%, the block or tree-like α-Mg solid solution precipiates. At the same time, the incompletely grown pentagonal phase decreases and the petals-like I-phase increases. When the Zn content further decreases to 24%, I-phase grows, and the five and six petals-like I-phase increases significantly. Meanwhile, few laminar eutectic (I-phase + α-Mg) appears.

As a result, the size, quantity and distribution of quasicrystal particles in $Mg_{69+x}Zn_{30-x}Y_1$ alloys change significantly with the alloy composition. With decreasing the Zn content, the granularity and homogenization degree of quasicrystal increase. At the same time, the I-phase increases and distributes more uniformly.

Figures 4 and 5 show the OM and SEM graphs of as-cast $Mg_{68+x}Zn_{30-x}Y_2$ alloys, respectively. Combined with its XRD pattern (see Fig. 3b), the microstructure of as-cast $Mg_{68}Zn_{30}Y_2$ alloy includes gray MgZn matrix, ruleless and polygonal I-phase, α-Mg solid solution with black particles and few laminar eutectic (I-phase + α-Mg).

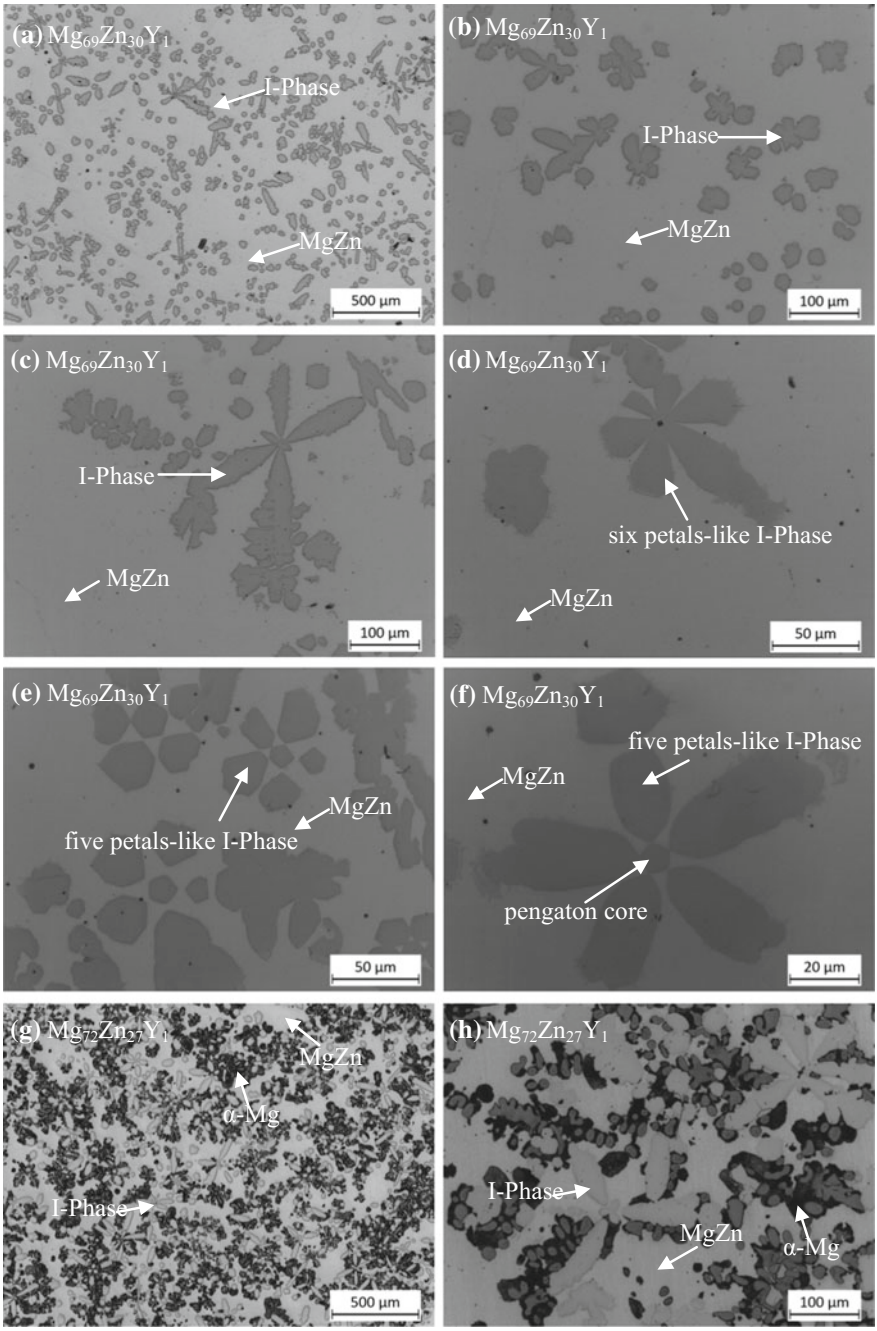

Fig. 1 OM graphs of as-cast $Mg_{69+x}Zn_{30-x}Y_1$ alloys

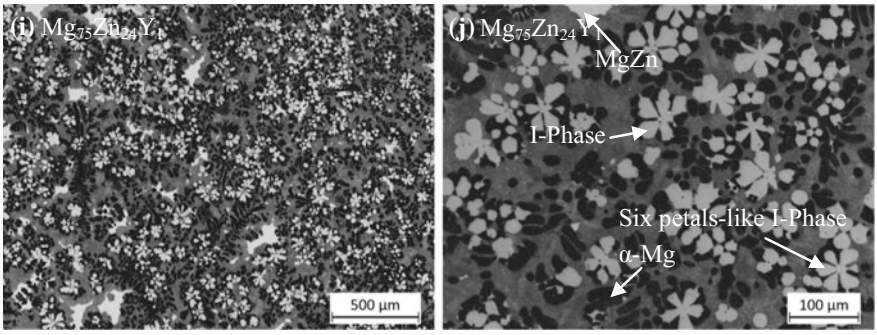

Fig. 1 (continued)

With decreasing the Zn content to 27%, the ruleless and polygonal I-phase decreases and the laminar eutectic (I-phase + α-Mg) increases. When the Zn content further decrease to 24%, the ruleless and polygonal I-phase decreases significantly and the size of I-phase particles also decreases. Meanwhile, the laminar eutectic (I-phase + α-Mg) continuously increases.

Compared with $Mg_{69+x}Zn_{30-x}Y_1$ alloys, the microstructures of $Mg_{68+x}Zn_{30-x}Y_2$ alloys change significantly due to the increase in the Y content. The quasicrystalline phase mainly exists as incompletely grown pentagon, five and six petals for $Mg_{69+x}Zn_{30-x}Y_1$ alloys, while it does in the form of ruleless and polygonal I-phase and laminar eutectic (I-phase + α-Mg) for $Mg_{68+x}Zn_{30-x}Y_2$ alloys.

Despite the fact that the quasicrystalline phase exists in microstructure alloy by specific morphology and exhibits different orientation, its formation process also follows nucleation and growth law. According to reference [9], the eutectic reaction occurs at 823 K when high temperature melt solidifies:

$$L \rightarrow \alpha\text{-Mg} + Mg_3Zn_3Y_2 \tag{1}$$

$Mg_3Zn_3Y_2$ is W phase. With decreasing the temperature, peritectic reaction occurs at 721 K:

$$L + W \rightarrow \alpha\text{-Mg} + \text{I - phase} \tag{2}$$

With further decreasing the melt temperature, the eutectic reaction generates Mg_7Zn_3 phase at 613 K:

$$L \rightarrow \alpha\text{-Mg} + Mg_7Zn_3 \tag{3}$$

Finally, eutectoid reaction, which occurs at 598 K, produces MgZn phase:

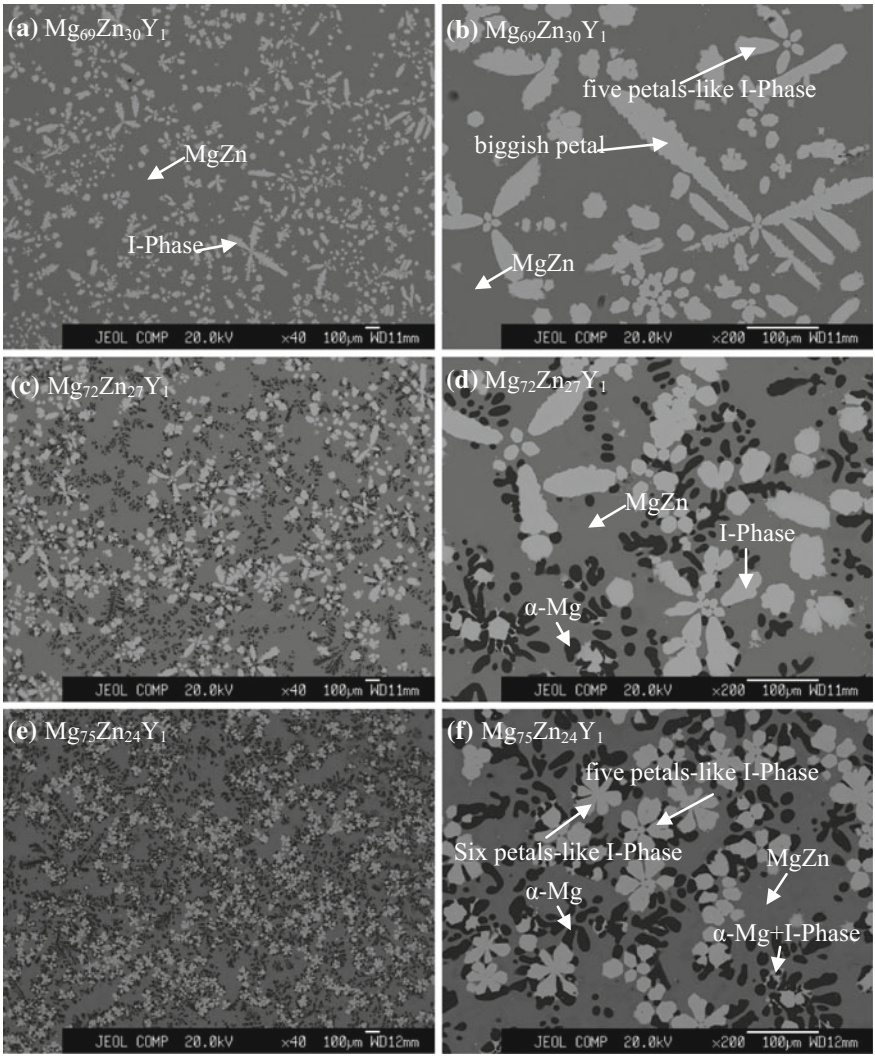

Fig. 2 SEM graphs of as-cast $Mg_{69+x}Zn_{30-x}Y_1$ alloys

$$Mg_7Zn_3 \rightarrow \alpha\text{-Mg} + MgZn \tag{4}$$

In the end, α-Mg solid solution, MgZn matrix and I-phase form, which is consistent with the present results.

The characteristic that crystal nucleus produces stable or metastable phase is to overcome activation energy ΔG^* [10]. According to the classical nucleation theory, each phase ΔG^* expressions can be written as:

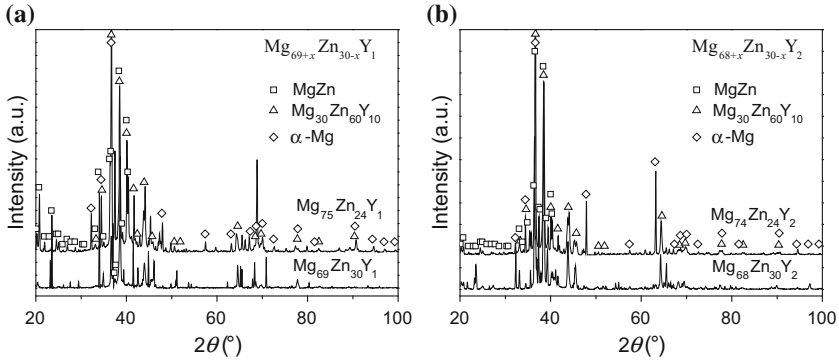

Fig. 3 XRD patterns of as-cast $Mg_{69+x}Zn_{30-x}Y_1$ and $Mg_{68+x}Zn_{30-x}Y_2$ alloys

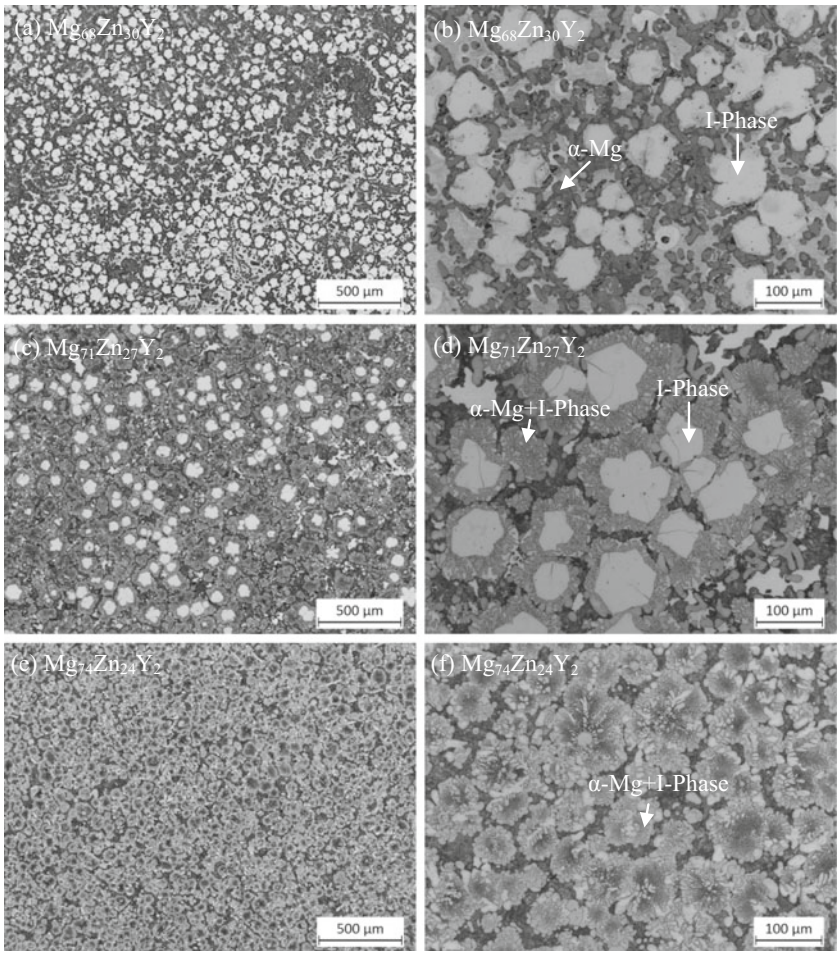

Fig. 4 OM graphs of as-cast $Mg_{68+x}Zn_{30-x}Y_2$ alloys

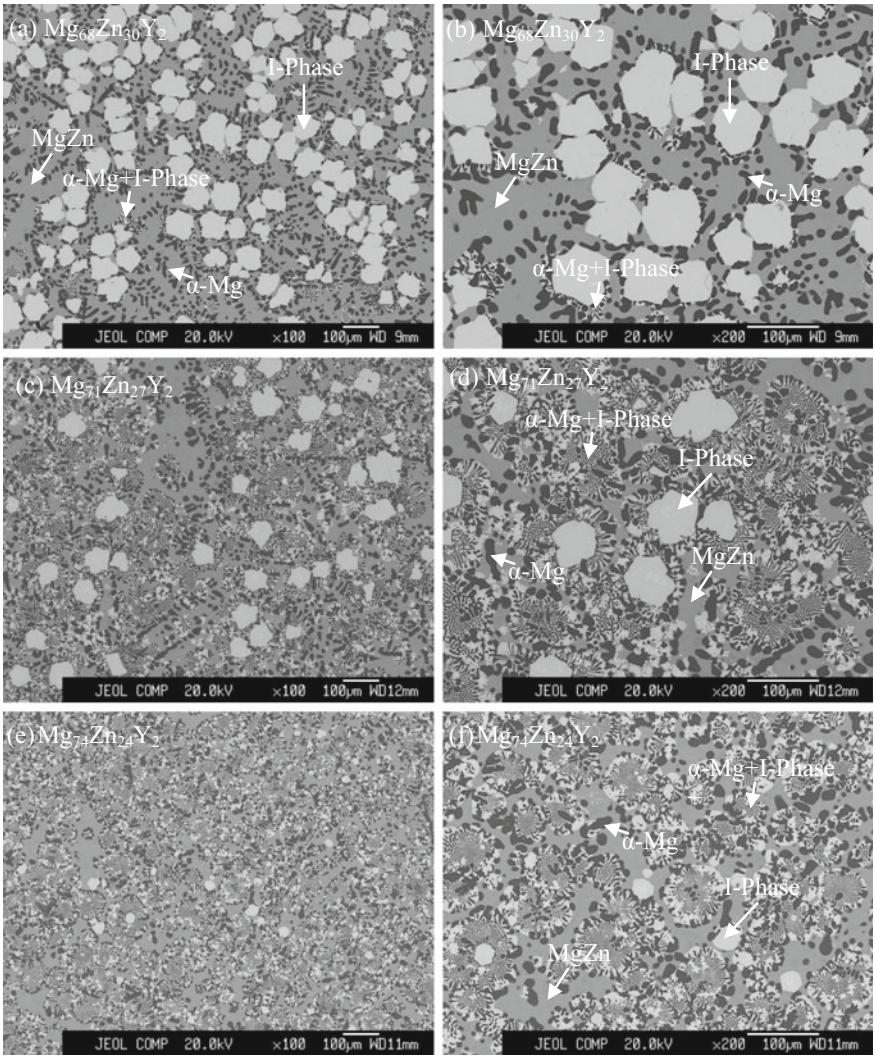

Fig. 5 SEM graphs of as-cast $Mg_{68+x}Zn_{30-x}Y_2$ alloys

$$\Delta G^* = \frac{16\,\sigma_{sl}^3}{3\Delta G^2} f(\theta) \tag{5}$$

where, ΔG is free energy difference between solid and liquid, σ_{sl} is solid-liquid interfacial energy, and $f(\theta)$ is contact angle factor. For homogeneous nuclear systems, $f(\theta) = 1$. ΔG^* consists of two parts: one is ΔG, which is phase-change driving forces, and the other is σ_{sl}, which is phase-change resistance. According to the Spaepen model [11]:

$$\sigma_{sl} = \alpha_s \frac{\Delta S_f}{\left(N_A V_m^2\right)^{1/3}} T \tag{6}$$

where, ΔS_f is melting entropy, N_A is Avogadro constant, V_m is molar volume, T is temperature, and α_s is the parameter associated with the nucleation structure. And for the icosahedral structure and the fcc structure, the value of α_s is 0.36 and 0.86, respectively. It can be seen from Eq. 5 that activation energy ΔG^* is directly proportional to nucleation barrier and directly affects the difficulty of melt nucleation through the size of the nucleation barrier. Therefore, nucleation barrier plays an important role in nucleation process. It can be seen from Eq. 6 that for a certain undercooling temperature, the nucleation barrier depends on the type of crystal structure. As a result, if the crystal structure is similar to the short range order in the melt, the nucleation barrier is lower, which is more favorable for the nucleation of quasicrystalline phase.

According to the morphology, distribution and composition segregation of quasicrystals, it is concluded that quasicrystal formation is quite different from the continuous phase-change of amorphous formation. Similar to the solidification process of crystalline alloys, it follows the nucleation and growth law. In the discussion of the formation mechanism of quasicrystalline phase, it is mentioned that peritectic reaction occurs at 721 K in W phase formed by the eutectic reaction during the solidification process of the melt. At this point, the quasicrystalline phase begins to nucleate and then grows.

The quasicrystal structure has fivefold, threefold and twofold rotational symmetry, whose point group symbol is $m\overline{35}$, and does not belong to any of the 32 crystal point groups. The regular icosahedron contains 12 vertices, each of which is a fivefold axis of rotational symmetry and is 63.43° from the next 5 vertices. If the fastest growth is along 12 vertices, the star shaped grains are obtained. The fivefold symmetrical growth morphologies of the quasicrystal which is made under general solidification reflects and depends on the peculiarity of quasicrystal structure.

The nucleation and growth process of five and six petals-like quasicrystals are explained as follows.

Quasicrystalline phase overcomes the nucleation barrier and grows slowly into a pentagon by peritectic reaction in the permission of nucleation and growth conditions in the liquid alloy (see Fig. 6a). An approximately regular pentagon with five apex angles rapidly grows outward and eventually forms a five-sided petal shape. From the view of morphology of quasicrystal, it may have different growth patterns. First, pentagonal quasicrystal grows into a five petals-like quasicrystal without a flower core, that is, the path from a to b in Fig. 6. Second, pentagonal quasicrystal grows into a five petals-like quasicrystal with a flower core, that is, the path from a to c in Fig. 6. Third, Fig. 6b may also be a transition phase of Fig. 6c. The five vertices of the pentagonal quasicrystal of Fig. 6a extend rapidly toward the alloy liquid, which is shown in Fig. 6b, and then grows into a five petals-like quasicrystalline phase with a flower core, as shown in Fig. 6c.

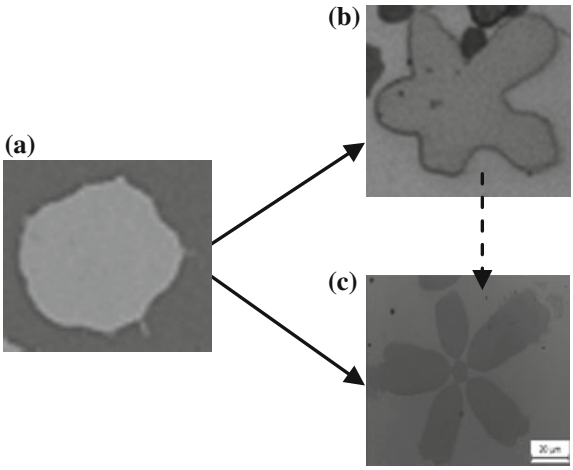

Fig. 6 Schematic diagram of nucleation and growth process of five petals-like quasicrystalline phase

From the formation process, the formation of six petals-like quasicrystal by specific morphology follows the nucleation and growth law. It can be seen from Fig. 7a, b that the embryos grow outwards along six vertices of each other at 60° after the nucleation of quasicrystal. The origin of these six vertices is likely to be the deformation of two-dimensional nucleus or the morphology of I-phase along different sections. However, it can be seen from Fig. 7c that when the six vertices grow to some extent, the three of them which are 120° each other grow rapidly. Then, three other dendrites, each of which are 120°, grow into the melt, as shown in Fig. 7d. The final morphology of the solidification presents six petals-like quasicrystalline phase with different sizes. Compared with five angles, five petals-like and six petals-like quasicrystals, the secondary petal of six petals-like quasicrystals is more developed, as shown in Fig. 7f1, f2. The developed "secondary petal" grows with no direction at the edge of "primary petal".

Figures 1, 2, 4 and 5 show that the morphology of quasicrystalline phase is diverse, which can be divided into the following two categories. (1) Polygon and

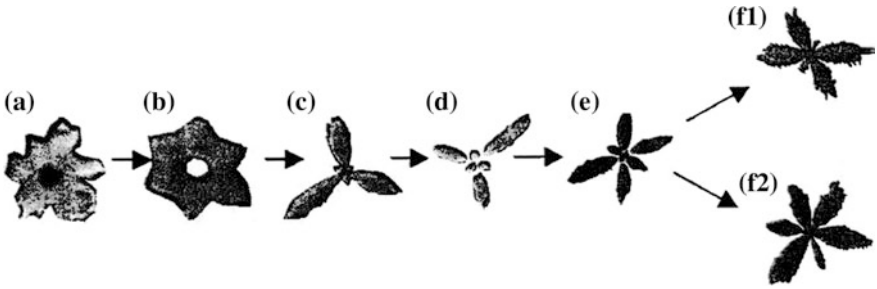

Fig. 7 Schematic diagram of nucleation and growth process of six petals-like quasicrystalline phase [12]

petal-like particles. Some of the quasicrystalline phases have flat and regular geometric shapes, showing the characteristic of faceted growth. And the surface of some quasicrystalline phases is more smooth, showing the characteristic of non faceted growth. (2) Laminar eutectic. Figures 4 and 5 show that the quasicrystalline phase in some alloys exists in the form of laminar eutectic, showing the characteristic of coupled growth.

Under certain conditions, crystals may form polyhedron shapes corresponding to their symmetry. The surfaces of these polyhedra tend to be the lowest in surface energy, or their direction of normal line grows at the slowest rate.

Figure 1e shows a five petals-like quasicrystalline phase with a pentagonal core, and each petal exhibits an obvious pentagonal shape. It can be seen that the petals of the pentagon correspond to the five vertices of the pentagon. And it shows the characteristic of faceted growth. The best growth direction of I-phase is fivefold axis, followed by threefold axis. And the growth speed of twofold axis direction is the slowest [13]. The direction of the center of icosahedral toward vertice is the fivefold axis. Therefore, the optimum growth direction of I-phase is continued to grow at the vertice of I-phase. It can be concluded that the core of petal-like quasicrystalline phase is icosahedral. As the projection of the two-dimensional surface, the direction of the five vertices of the core is fivefold axis direction of I-phase, which is the optimum growth direction of the quasicrystalline phase. In this direction, five petals-like I-phase are grown in faceted growth. And the two-dimensional projection represents five petals-like with a pentagonal core.

As shown in Fig. 1f, the quasicrystalline phase also represents five petals-like with a pentagonal core. It can be seen that the end of the flower petal is round, showing the characteristic of non faceted growth. But the tip of the petals is still flat, indicating that the petals are still growing in faceted growth at the initial stage of growth. With the decrease in the melt temperature, the petals grow further and develop gradually toward non faceted growth patterns. This can be explained by the fact that the driving force of crystal growth has a great influence on the mode of interface growth in accordance with the kinetic theory of crystal growth.

The driving force of crystal growth can be expressed as [14]:

$$\Delta G_{\mathrm{m}} = \frac{\Delta H_0}{T_{\mathrm{m}}} \Delta T_{\mathrm{k}} \tag{7}$$

where, ΔH_0 is latent heat of crystallization and ΔT_{k} is kinetic undercooling of crystals growing up.

Figure 8 shows that the variation of the driving force of crystal growth leads to the transition of crystal growth from discontinuous faceted growth to continuous non faceted growth. The figure is divided into two regions. Area A is a discontinuous faceted growth area, where the smooth faceted interface remains smooth in the range of driving force shown in this region. With the decrease in the melt temperature, the undercooling increases gradually. Equation 7 shows that the driving force of crystal growth increases and reaches Area B. In Area B, the original interface structure becomes unstable. So the smooth faceted interface changes into

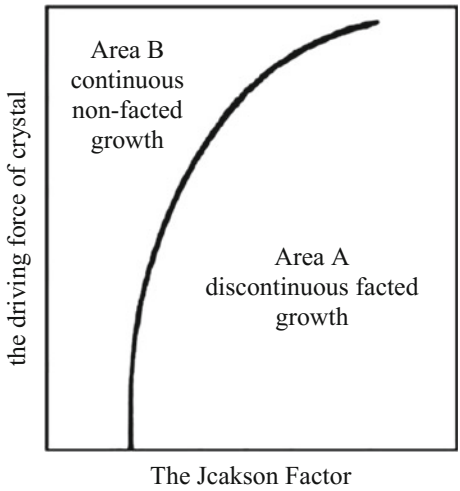

Fig. 8 Variation with driving force of the transition from faceted to continuous growth [15]

rough non-faceted interface. The growth mechanism also translates from discontinuous growth to continuous growth.

In the early stage of solidification, the grain size of the quasicrystal is smaller, which appears to be blocky or globular. With the decrease in the melt temperature, the primary phase in the melt will further grow up. When the primary phase grows and exceeds a critical size, growth will become unstable. The surface inevitably produces some tiny protuberances. These protuberances will continue to grow preferentially and form stable branching, and finally form six petals-like quasicrystalline phase (see Fig. 7). Six petals consist of petals opposing to each other in three opposite directions. In I-phase, only fivefold and threefold axises are opposite axes. The projection of the vertices of icosahedral on the two-dimensional surface in the direction of the threefold axis is exactly six points. And the corresponding directions of the six points are in the direction of the fivefold axis, which is the optimum growth direction of icosahedral.

In a word, quasicrystalline phase has many growth modes, such as faceted growth, non-faceted growth, faceted growth mixing up with non-faceted growth, and coupled growth. From Figs. 1, 2, 4 and 5, it is found that the content of alloying element plays a certain influence on the growth of quasicrystalline phase. With decreasing the Zn content in $Mg_{69+x}Zn_{30-x}Y_1$ alloys, the growth of quasicrystalline phase gradually translates from faceted growth to non faceted growth, and the morphology does from incompletely grown pentagon to five petals and six petals. With decreasing the Zn content in $Mg_{68+x}Zn_{30-x}Y_2$ alloys, the growth of quasicrystalline phase gradually translates from faceted growth to coupled growth.

Summary

The microstructure of as-cast $Mg_{69+x}Zn_{30-x}Y_1$ alloys includes gray MgZn matrix, incompletely grown pentagonal, five and six petals-like $Mg_{30}Zn_{60}Y_{10}$ (I-phase), and few laminar eutectic (I-phase + α-Mg). The microstructure of as-cast $Mg_{68+x}Zn_{30-x}Y_2$ alloys includes gray MgZn matrix, ruleless and polygonal I-phase, α-Mg solid solution with black particles and laminar eutectic. With decreasing the Zn content in $Mg_{69+x}Zn_{30-x}Y_1$ alloys, the growth of quasicrystalline phase gradually translates from faceted growth to non-faceted growth, and the incompletely grown pentagonal phase decreases and the petals-like I-phase increases. With decreasing Zn content in $Mg_{68+x}Zn_{30-x}Y_2$ alloys, the growth of quasicrystalline phase gradually translates from faceted growth to coupled growth, and the ruleless and polygonal I-phase decreases while the laminar eutectic increases.

Acknowledgements This work was supported by Natural Science Foundation of Guangdong Province (2016A030313802), Project on Scientific Research of Guangzhou City (201707010393) and Technology Innovation Project of Science and Technology Small and Medium Enterprise of Guangdong Province (2016A010120024).

References

1. I.J. Polmear, Magnesium alloys and applications. Mater. Sci. Technol. **10**, 1–16 (1994)
2. J.F. Nie, B.C. Muddle, Precipitation in magnesium alloy WE54 during isothermal ageing at 250 °C. Scripta Mater. **40**, 1089–1094 (1999)
3. C. Antion, P. Donnadieu, F. Perrard, A. Deschamps, C. Tassin, A. Pisch, Hardening precipitation in a Mg–4Y–3RE alloy. Acta Mater. **51**, 5335–5348 (2003)
4. D.H. Bae, M.H. Lee, K.T. Kim, W.T. Kim, D.H. Kim, Application of quasicrystalline particles as a strengthening phase in Mg–Zn–Y alloys. J. Alloys Compd. **342**, 445–450 (2002)
5. P.W. Stephens, A.I. Goldman, Metallic phase with long-range orientational order and no translational symmetry. Phys. Rev. Lett. **53**, 1951–1954 (1984)
6. J.S. Zhang, Y.Q. Zhang, Y. Zhang, C.X. Xu, X.M. Wang, J. Yan, Effect of Mg-based spherical quasicrystal on microstructures and mechanical properties of ZA54 alloy. Trans. Nonferrous Met. Soc. Chin. **20**, 1199–1204 (2010)
7. A.I. Goldman, Magnetism in icosahedral quasicrystals: current status and open questions. Sci. Technol. Adv. Mater. **15**, 044801-1–044801-15 (2014)
8. Y.L. Ju, D.H. Kim, H.K. Lim, D.H. Kim, Effects of Zn/Y ratio on microstructure and mechanical properties of Mg-Zn-Y alloys. Mater. Lett. **59**, 3801–3805 (2005)
9. A. Singh, M. Watanabe, A. Kato, A.P. Tsai, Crystallographic orientations and interfaces of icosahedral quasicrystalline phase growing on cubic W phase in Mg–Zn–Y alloys. Mater. Sci. Eng., A **397**, 22–34 (2005)
10. S. Sen, T. Mukerji, A generalized classical nucleation theory for rough interfaces: application in the analysis of homogeneous nucleation in silicate liquids. J. Non-Cryst. Solids **246**, 229–239 (1999)
11. F. Spaepen, A structural model for the solid-liquid interface in monatomic systems. Acta Metall. **23**, 729–743 (1975)

12. F. Shi, *Quasicrystal Phase and Its Formation Mechanism in Ordinary Solidified Mg–Zn–Y Alloy* (Xi'an University of Technology, 2003, in Chinese)
13. Z.P. Luo, S.Q. Zhang, Y.L. Tang, D.S. Zhao, On the stable quasicrystals in slowly coiled Mg-Zn-Y alloys. Scripta Metall. Mater. **32**, 1411–1416 (1995)
14. Y.B. Zhang, S. Yu, Y. Song, X. Zhu, Microstructures and mechanical properties of quasicrystal reinforced Mg matrix composites. J. Alloys Compd. **464**, 575–579 (2008)
15. H.Q. Hu, *Metal Solidification Principle* (China Machine Press, Beijing, 2000, in Chinese)

Influence of Process Parameters by Enclosed Cooling Slope Channel on Microstructures of Semi-solid ZCuSn10P1 Alloy

Yongkun Li, Rongfeng Zhou, Lu Li, Fan Xiao, Yehua Jiang and Dehong Lu

Abstract Semi-solid ZCuSn10P1 alloy slurry was fabricated by a novel enclosed cooling slope channel (ECSC for short). The influence of process parameters on the microstructure and Tin segregation phenomenon of ZCuSn10P1 alloy semi-solid slurry was studied with optical microscope (OM), scanning electron microscope (SEM) and energy dispersive x-ray spectrum (EDS). The results showed that the primary α-Cu phase gradually evolved from the dendrite into worm-like or fine spherical crystal under chilling of ECSC and shearing of the gravitation. The finest microstructure, the equivalent diameter was 46 ± 3 μm, and its shape factor was 0.73, could be obtained under the conditions of the pouring temperature 1080 °C, 300 mm of cooling plate inclined at 45 degrees and 5 mm flow gap. The average concentration of Tin increased from 5.85% in the conventional casting to 6.46% in semi-solid slurry in primary α-Cu phase, and the average concentration of Tin decreased from 27.94% in the conventional casting to 20.59% in semi-solid slurry in liquid. The distribution of Tin element in microstructure was refined obviously and the dendrite segregation reduced.

Y. Li · R. Zhou (✉) · L. Li · F. Xiao · Y. Jiang · D. Lu
Faculty of Material Science and Engineering, Kunming University of Science and Technology, Kunming 650093, China
e-mail: zhourfchina@hotmail.com

Y. Li
e-mail: 717309098@qq.com

L. Li
e-mail: 82225150@qq.com

F. Xiao
e-mail: 935836680@qq.com

Y. Jiang
e-mail: 1742944769@qq.com

D. Lu
e-mail: ldhongkust@126.com

R. Zhou · L. Li
Research Center for Analysis and Measurement, Kunming University of Science and Technology, Kunming 650093, China

© Springer Nature Singapore Pte Ltd. 2018

Y. Han (ed.), *Advances in Materials Processing*, Lecture Notes in Mechanical Engineering, https://doi.org/10.1007/978-981-13-0107-0_55

Keywords Enclosed cooling slope channel (ECSC) · ZCuSn10P1 Semi-solid · Microstructure refinement · Segregation

Introduction

Tin bronze has excellent flexibility, wear resistance, corrosion resistance and high strength, which is widely used in the shipbuilding industry and important gears, valves and worm gear et al. [1]. However, the primary α-Cu phase is a coarse dendrite structure and the segregation of tin in the traditional tin-bronze ZCuSn10P1 is serious [2], which leading to microstructure heterogeneity and poor property, limiting the use in industry. So, it is important to study the forming of tin bronze for get the organization and performance of uniform tin bronze products.

Semi-solid processing, including rheocasting and thixocasting, is widely studied all over the world due to many technical and economical advantages [3]. In recent years, the rheocasting has been greatly developed, and there are several ways to prepare non-dendrite structure [4–6]. The cooling plate method is a simple way to preparing semi-solid slurry. Amir. A. Abdelsalam et al. fabricate A356/Al_2O_3 metal matrix nano composites. The results showed that the average grain size of samples fabricated is obviously refine, finer α-Al grain obtained at the bottom than the top of the ingots. But the addition of the Al_2O_3 nanoparticles did not significantly influenced the shape factor of the primary α-Al grains [7]. Prosenjit Das et al. was studied the microstructure evolution during semi-solid slurry generation of Al–Si–Cu–Fe alloy and the effect of microstructural morphology of the slurry on its rheological behavior [8]. Rycichi Yoshida et al. studied the forming factors of hollow AZ31B magnesium alloy pipe was made by vertical continuous casting using semisolid slurry prepared on an inclined cooling plate. The results showed that we could obtain the hollow material, but holding at 650 °C of molten alloy and no tapering of the mold and the cord rod, 1 mm crack appears both surface of outside and inside of the hollow material [9]. We can find through the above description, the semi-solid research focused on the low melting point alloys, such as aluminum and magnesium alloy. The literature on high melting point alloys is relatively few.

In this investigation, based on the self-made research equipment, the influence of process parameters on the microstructure and Tin segregation phenomenon of ZCuSn10P1 alloy semi-solid slurry was studied.

Experimental

Materials

In this study, the chemical composition of the ZCuSn10P1 alloy is listed in Table 1. The liquidus and solidus temperatures of the alloy are 1020.7 and 830.4 °C, respectively. Measurements by differential scanning calorimetry (STA 449F3) were carried out on about 10 mg samples obtained from the as-cast alloys under an argon atmosphere at a heating rate of 10 K min^{-1}, as shown in Fig. 1.

Fabrication of the Semi-solid ZCuSn10P1 Alloy Slurry

Three-dimensional and schematic illustration of the ECSC apparatus is shown in Fig. 2. The slurry-making apparatus mainly consists of two parts: an enclosed cooling slope channel and an angle adjuster. The enclosed cooling slope channel was made from stainless steel and was fix at 45° with respect to the horizontal plane and was cooled with water circulation around the gap. The length was set to different value for research.

Fabrication of the ZCuSn10P1 semi-solid slurry was carried out according to the following procedures: About 6 kg of ZCuSn10P1 alloy was melted at 1200 ± 5 °C in a graphite crucible in an electrical resistance furnace. After complete melting, the temperature dropped to a certain value poured immediately on the cooling inclined

Table 1 Chemical composition of ZCuSn10P1 alloy (mass%)

Cu	Sn	P	Other
88.95	9.6	0.6	0.85

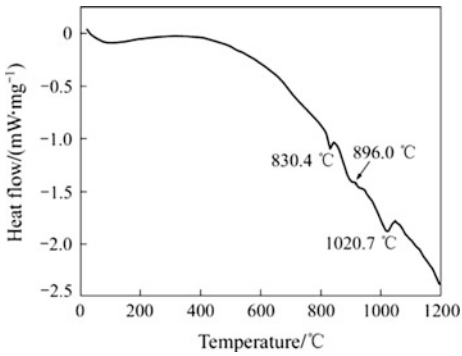

Fig. 1 DSC curve of as-cast ZCuSn10P1 alloy

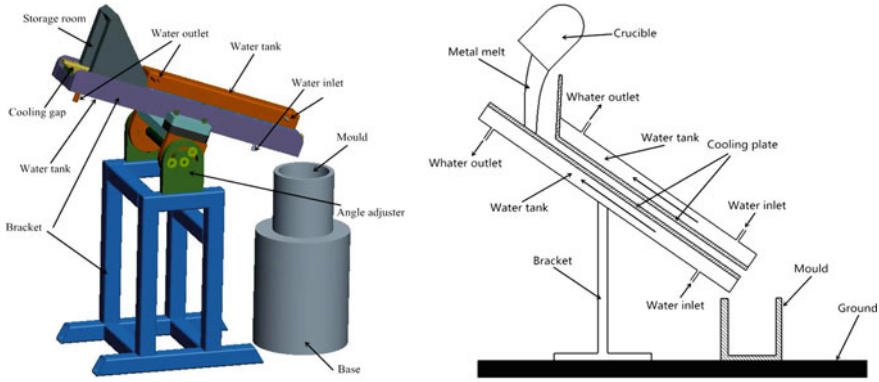

Fig. 2 Three-dimensional and schematic illustration of the ECSC apparatus

steel gap. The ECSC casting of the ZCuSn10P1 involved pouring the molten over an inclined cooling tank of 100 mm wide and 5 mm gap. Samples were extracted out and water quenched immediately. The mold size is $\varphi 100 \times 150$ mm.

By change of pouring temperature and pouring length, the semi-solid ZCuSn10P1 slurry under different rheo-casting conditions has been obtained. A $20 \times 20 \times 20$ mm square was taken out from the center of the metal rod after water quenched immediately as the specimens. Microstructure of the specimens was observed using an optical microscope and measurements of the equivalent diameter (D) and shape factor (F) of the primary α-Cu phase were carried out using image-analyzing techniques. The equivalent diameter and shape factor was determined from the following equation:

$$D = 2(A/\pi)^{1/2} \tag{1}$$

$$F = 4\pi A/p^2 \tag{2}$$

where: A is the area of primary α-Cu phase and p is the perimeter, we can obtain them by the Image-pro plus. The shape factor would be one when it is a perfect circle.

Results and Discussion

The microstructure formation mechanism of preparation of semisolid slurry by inclined plate has been discussed by many researchers. It was considered that a large number of crystal nuclei are formed on the surface of the inclined plate causes the non-dendrite structures formation [10]. The main reason for the formation of non-dendrite structure is the burst nucleation and the dendrite fracture [11, 12]. The

factors influencing the semisolid alloy microstructure mainly include pouring temperature and pouring length.

Influence of Pouring Temperature on Microstructure of the ZCuSn10P1 Semi-solid Slurry

Figure 3 shows the microstructures of ZCuSn10P1 alloy at different pouring temperature with the pouring length of 300 mm, slope angle at 45° and 5 mm flow gap.

The pouring temperature is an important factor affecting the ZCuSn10P1 alloy structure. As shown in Fig. 3a, with the pouring temperature of 1060 °C, the dendrite structure disappeared and the microstructure mainly was worm-like or nearly spherical crystal. However, the solution in the inclined plate surface crusted to affect the chilling effect of the follow-up solution due to the low pouring temperature. The ability to form nuclei reduced and there was more worm-like crystal structure after treatment of the solution, and coarse grains. When the pouring temperature was raised to 1080 °C, the solution did not crusted on the surface of the cooling plate, the heat transfer of the solution and the chilling effect was uniform. The primary α-Cu phase was nearly spherical crystal, and the grain size and distribution was Uniform, as shown in Fig. 3b. When the temperature was further increased to 1100 °C, the primary α-Cu phase was also dominated by nearly spherical, but a small amount of coarse dendrite structure existed. When the solution pouring temperature was higher, the treated solution had a higher liquid fraction and some coarse dendrite structure formed in the cooling process.

Figure 4 shows the relationship between equivalent diameter and shape factor of primary α-Cu phase with pouring temperature (a), and primary α-Cu phase equivalent diameter distribution (b) at different pouring temperature in semi-solid ZCuSn10P1 alloy. Figure 5 shows the relationship between number of primary α-Cu phase per unit area and pouring temperature in semi-solid ZCuSn10P1 alloy. It can be found when the pouring temperature was 1060 °C, the equivalent diameter of primary α-Cu phase was 58.3 μm and the shape factor was 0.72. The equivalent

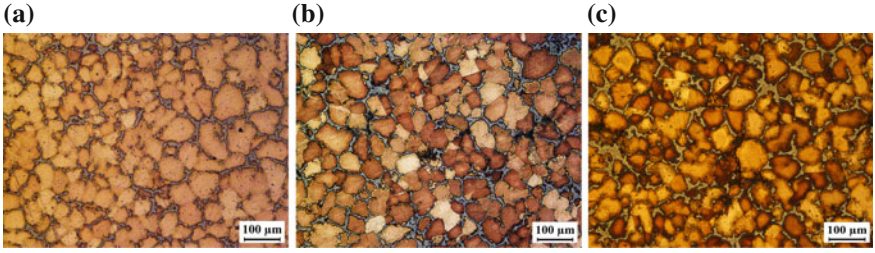

Fig. 3 Microstructures of ZCuSn10P1 alloy at different pouring temperature with pouring length 300 mm. **a** 1060 °C, **b** 1080 °C, **c** 1100 °C

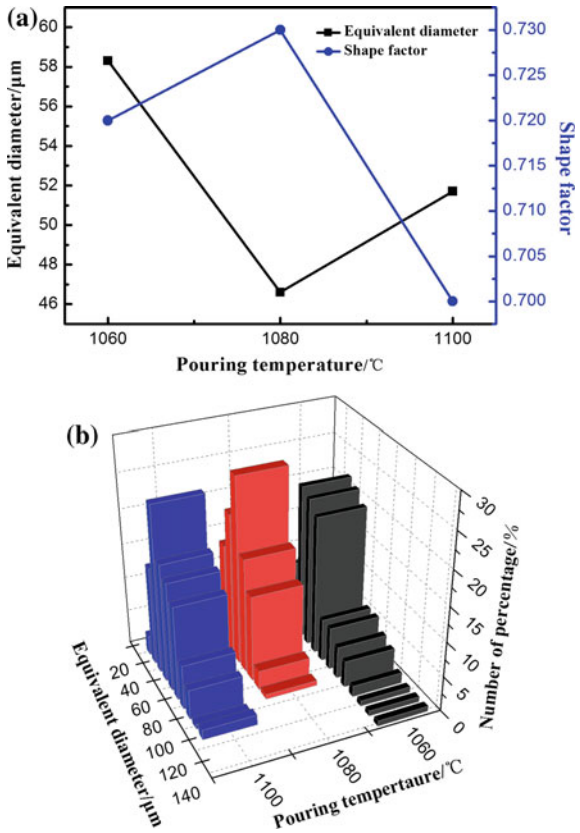

Fig. 4 Relationship between equivalent diameter and shape factor of primary α-Cu phase with pouring temperature (**a**), and primary α-Cu phase equivalent diameter distribution (**b**) at different pouring temperature in semi-solid ZCuSn10P1 alloy

diameter was mainly in the range of 40–60 μm, but the equivalent diameter of more than 100 μm was also more, accounting for 7.69% of the total number. As can be seen from Fig. 5, at this time, the number per square centimeter of primary α-Cu phase was about 31,515. Although the number of grains is not the largest, the larger equivalent diameter resulted in the highest solid fraction after the water quenching, about 81.79%. When the pouring temperature was 1080 °C, the equivalent diameter of primary α-Cu was 46.6 μm and the shape factor was 0.73. The number of grains with equivalent diameter of 20–60 μm was accounts for 83% of the total number. At this point, the number per square centimeter of primary α-Cu phase grains was the largest, about 34,909, and after quenching the solid fraction was 66.34%. When the pouring temperature was 1100 °C, the equivalent diameter of primary α-Cu increased to 51.7 μm and the shape factor decreased to 0.70. The size of primary α-Cu phase mainly distributed between 30 and 70 μm, accounting for 84% of the total number grains. The number per square centimeter of primary α-Cu phase was about 30,303 and the solid fraction was 64.62% after water quenching.

In general, the closer liquidus of the pouring temperature (1060 °C), the higher of undercooling, and the nucleation is the easier. However, when the pouring

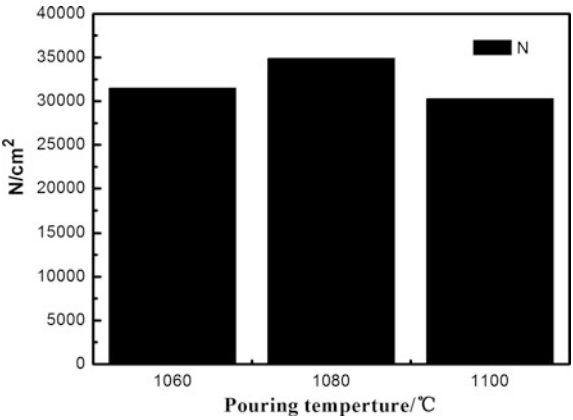

Fig. 5 Relationship between number of primary α-Cu phase per unit area and pouring temperature in semi-solid ZCuSn10P1 alloy

temperature is lower, the cooling rate of the solution is relatively fast, and it is easy to crust on the surface of the sloping plate, so that the chilling effect of the subsequent solution is reduced and the nucleation ability is decreased. We will unable to prepare the semi-solid slurry when the thickness of the crust reaches a certain extent. When the temperature is too high (1100 °C), the solution will nucleate a large number of nuclei instantaneously in contact with the cooling plate. However, the higher solution temperature will dissolve some small nuclei. The solution temperature is higher, the solid fraction is lower and the liquid phase will form some kind of dendrite structure in the cooling process. The proper pouring temperature (1080 °C) can ensure the nucleation of the solution and no crusting. The treated temperature is proper and no coarse grain or dendrite structure will appear during the cooling process. Therefore, when the pouring temperature is 1080 °C, the excellent ZCuSn10P1 semi-solid slurry can be obtained.

Influence of Pouring Length on Microstructure of the ZCuSn10P1 Semi-solid Slurry

The pouring length directly affects the length of the cooling and shearing time of the alloy, so it is an important factor on the microstructure. When the pouring temperature is constant at 1080 °C, the pouring length is 200 mm, the alloy solution flows through the cooling channel rapidly, the cooling time of the solution is shorter, the number of nucleation is less and the solution temperature is higher. The microstructure was mainly worm-like and dendrite-like, as shown in Fig. 6a. With the increase of pouring length to 300 mm, the flows time of the solution in the cooling channel increases. That is, the cooling time of the solution is correspondingly increased, and the number of nucleation of explosion increases and the temperature field is uniform. Due to suppressing the formation of dendrite structures, the resulting microstructure is basically composed of nearly spherical crystal,

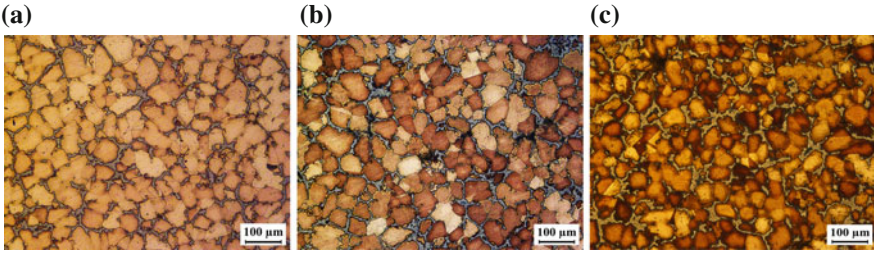

Fig. 6 Microstructures of ZCuSn10P1 alloy at different pouring length with pouring temperature 1080 °C. **a** 200 mm, **b** 300 mm, **c** 400 mm

as shown in Fig. 6b. However, with the increase of the pouring length to 400 mm, the time of flowing in the cooling channel is further increased. Although it is favorable for the nucleation of the eruption and the uniformity of the temperature field and the near spherical shape is obtained, the temperature of the solution decreases. It is easy to crust in the inner channel and it is not conducive to the preparation of semi-solid slurry, as shown in Fig. 6c.

Figure 7 shows the relationship between equivalent diameter and shape factor of primary α-Cu phase with pouring length (a), and primary α-Cu phase equivalent diameter distribution (b) at different pouring length in semi-solid ZCuSn10P1 alloy. Figure 8 shows the relationship between number of primary α-Cu phase per unit area and pouring length in semi-solid ZCuSn10P1 alloy. From Figs. 7 and 8, we can be found when the casting temperature was constant at 1080 °C and the casting length was 200 mm, the equivalent diameter of primary α-Cu was 50 μm and the shape factor was 0.72. The equivalent diameter is mainly in the range of 30–60 μm, but there are also some large particle diameters in excess of 100 μm. At this point, the number per square centimeter of primary α-Cu phase grains are about 33,939 and the solid fraction about 63.58% after quenching. When the pouring length is 300 mm, the equivalent diameter of primary α-Cu is 46.6 μm and the shape factor is 0.73. The number of grains with equivalent diameter in 20–60 μm accounts for 83% of the total number. At this point, the number of per square centimeter of primary α-Cu phase grains is the largest, about 34,909 and the solid fraction about 66.34% after water quenching. When the pouring length is 400 mm, the equivalent diameter of primary α-Cu phase is increases to 53.2 μm and the shape factor decreases to 0.68. The size of primary α-Cu phase mainly distributes between 40 and 70 μm and accounts for 78.8% of the total grains. At this time, the number of per square centimeter of primary α-Cu phase grains is 31,757 and the solid fraction is 75.3% after water quenching.

In summary, the pouring length determines the flow time in the cooling tank of alloy melt, too short or too long can not get the high quality semi-solid slurry. When the pouring length is too short (200 mm), there is not enough time for chilling. When the casting length is too long (400 mm), the semi-solid interval is too long

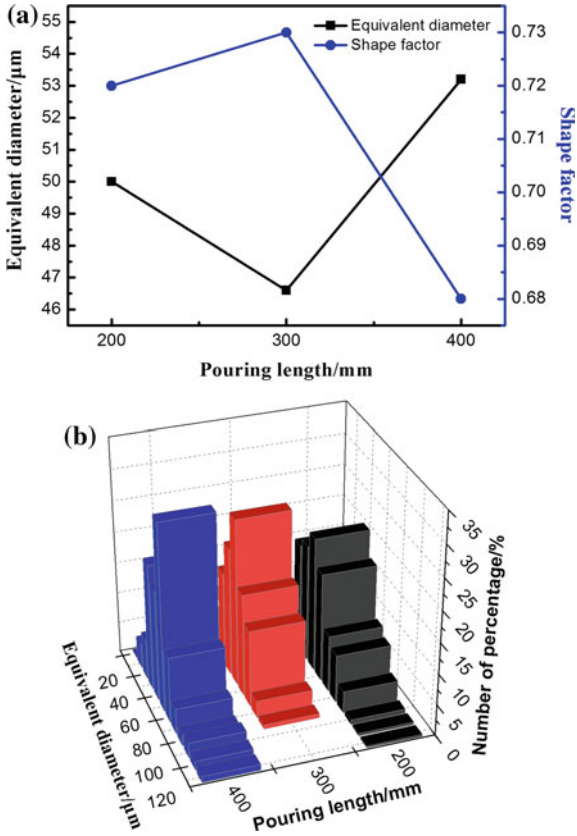

Fig. 7 Relationship between equivalent diameter and shape factor of primary α-Cu phase with pouring length (**a**), and primary α-Cu phase equivalent diameter distribution (**b**) at different pouring length in semi-solid ZCuSn10P1 alloy

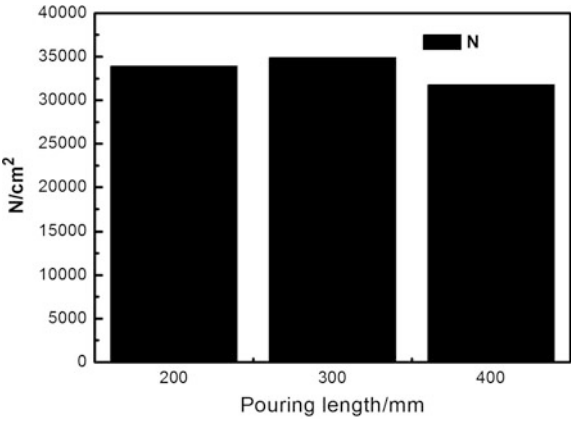

Fig. 8 Relationship between number of primary α-Cu phase per unit area and pouring length in semi-solid ZCuSn10P1 alloy

and it is harmful to prepare semisolid slurry. To ensure the solution has a certain chilling time and can be continuous preparation of fine semi-solid slurry only the pouring length is appropriate. Therefore, the pouring length of 300 mm is the optimal parameter.

Influence of Tin Segregation in Primary α-Cu Phase by ECSC

Figure 9 shows the SEM and element mapping images. The microstructure of the alloy is coarse dendrites in the conventional casting. The shrinkage rate is large in the solidification and a lot of shrinkage and porosity are easy to form due to the liquid phase in the dendritic interstitial is difficult to filled. The microstructure of the alloy after ECSC treatment is equiaxed or spherical crystal. Due to the semi-solid slurry contains a proportion of the solid phase, the shrinkage in the solidification was significantly reduced, and the shrinkage porosity has been significantly improved, as shown in Fig. 9b.

Contrast the Fig. 9c, d, we can see that the tin element is mainly distributed in the liquid phase. The average concentration of tin in the solid phase is relatively lower, but in the semi-solid slurry prepared by ECSC treatment, the average concentration of tin in primary α-Cu phase is higher than the conventional casting. Table 2 shows the EDS results for the microstructure of the as-cast and semisolid

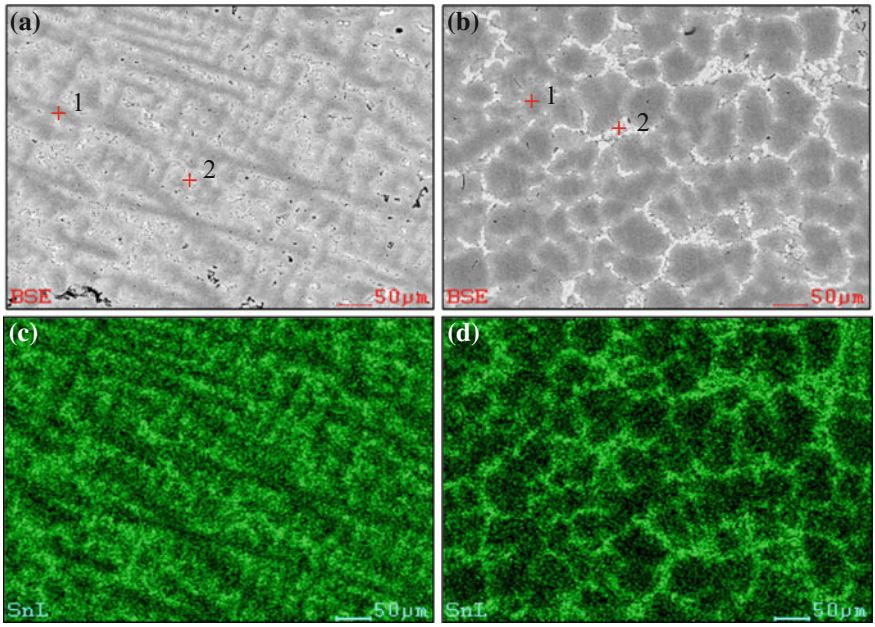

Fig. 9 SEM and element mapping images. **a**, **c** CS and **b**, **d** semi-solid slurry

Table 2 EDS results for the microstructure of the as-cast and semisolid ZCuSn10P1 alloy

Element	as-cast				Semisolid			
	1		2		1		2	
	wt%	at.%	wt%	at.%	wt%	at.%	wt%	at.%
Cu	93.79	96.04	71.53	81.68	93.22	95.78	70.69	70.47
Sn	5.85	3.21	27.94	17.08	6.46	3.56	20.59	11.83
P	0.36	0.75	0.53	1.24	0.32	0.66	8.71	17.7

ZCuSn10P1 alloy. From the EDS can found that the average concentration of Tin increased from 5.85% in the conventional casting to 6.46% in semi-solid slurry in primary α-Cu phase, and the average concentration of Tin decreased from 27.94% in the conventional casting to 20.59% in semi-solid slurry in liquid. The solid solubility of Tin increases in α-Cu phase for rapid cooling, because of Tin in α-Cu phase too late to precipitate. And the solid solubility of Tin decreases in liquid phase. Refine obviously the distribution of Tin element in microstructure and reduced the phenomenon of dendrite segregation.

Conclusions

1. By employing the ECSC in making the semi-solid of ZCuSn10P1, the slurry with fine solid granules is 46 ± 3 μm in mean size and the shape factor is 0.73 can easily be produced.
2. The pouring temperature and pouring length is the significant factors in ECSC, the optimum parameters is 1080 °C and 300 mm, the microstructure of the semi-solid slurry is equiaxed or spherical crystal.
3. The ECSC can refine obviously the distribution of tin element in microstructure and reduce the phenomenon of dendrite segregation. The average concentration of Tin increases from 5.85% in the conventional casting to 6.46% in semi-solid slurry in primaryα-Cu phase, and the average concentration of Tin decreases from 27.94% in the conventional casting to 20.59% in semi-solid slurry in liquid.

Acknowledgements The authors acknowledge funding for the research from National Science Foundation of China (51765026) and (51505205), Science and Technology Project Foundation of Yunnan Province of China (2015Y058). This work is supported by the Advanced Solidification forming and Equipment Technology National Joint Local Engineering Laboratory, Kunming University of Science and Technology, Kunming, China.

References

1. W.A. Baker, T.F. Pearson, Causes of porosity in tin-bronze castings. J. Inst. Met. **67**, 231–235 (1941)
2. H. Kodama, K. Nagase, T. Umeda et al., Microsegregation during dendritic growth in Cu-8% Sn alloys. Imono. **49**, 287–293 (1976)
3. J.L. Jorstad, Semi-solid metal processing from an industrial perspective; the best is yet to come! Solid State Phenom. **256**, 9–14 (2016)
4. S.B. Hassas-Irani, A. Zarei-Hanzaki, B. Bazaz et al., Microstructure evolution and semi-solid deformation behavior of an A356 aluminum alloy processed by strain induced melt activated method. Mater. Des. **46**, 579–587 (2013)
5. J.A. Yurko, R.A. Martinez, M.C. Flemings, Commercial development of the semi-solid rheocasting (SSRTM) process. Met. Sci. Tec. **21**, 10–15 (2013)
6. P. Das, S.K. Samanta, H. Chattopadhyay et al., Effect of pouring temperature on cooling slope casting of semi-solid Al-Si-Mg alloy. Acta Metall. Sin. **25**, 329–339 (2012)
7. A.A. Abdelsalam, T.S. Mahmoud, A.A. El-Betar et al., A study of microstructures characteristics of A356-Al_2O_3 composites produced by cooling slope and conventional stir cast. IJCET **15**, 3560–3571 (2015)
8. P. Das, S.K. Samanta, S. Bera et al., Microstructure evolution and rheological behavior of cooling slope processed Al–Si–Cu–Fe alloy slurry. Metall. Mater. Trans. A **47**, 2243–2256 (2016)
9. R. Yoshida, G. Motoyasu, T. Motegi, Production of continuous casting pipe using semisolid slurry of magnesium alloy. Trans. Mater. Res. Soc. Jpn. **40**, 169–174 (2015)
10. S.J. Luo, W.T. Tian, S.S. Xie et al., Technology and applications of semi-solid forming. Chin. J. Nonferrous. Met. **10**, 765–773 (2000)
11. R. Guan, L. Kang, H. Du et al., Preparing semisolid billet of Al–3% Mg alloy by sloping cooling/shearing process. Chin. J. Nonferrous. Met. **16**, 811–816 (2006)
12. R. Guan, L. Shi, Z. Xing et al., Preparing semisolid $AlSi_6Mg_2$ alloy by novel sloping Plate process and thixoforming. Foundry **56**, 694–697 (2007)

Metal Flow Law of Variable Diameter Metal Wire During Die Drawing

Kaisong Li and Xuefeng Liu

Abstract The dieless drawn variable diameter metal wire often causes blockage or leakage during subsequent die drawing. It is still not clear that the metal flow law of variable diameter metal wire in the die drawing process. In order to prepare high precision metal wire, it is necessary to study the metal wire flow law in the die drawing process. Variable diameter TC4 titanium alloy wire with reference diameter of 6 mm and variation degree of 10–30% was selected as the workpiece. Deform finite element software was used to simulate the die drawing process of variable diameter TC4 wire. The simulation experiments were carried out under the condition of drawing speed of 0.5 mm/s and die drawing deformation amounts of 10–30%. The metal flow law of the variable diameter metal wire in the die drawing process was analyzed. The results showed that the metal flow directions of the die exit and die entry were consistent with the drawing direction when the TC4 titanium alloy wire entered the drawing die, initiating plastic deformation. There was an inclined angle between the metal flow direction in the deformation zone and the drawing direction. This inclined angle decreased gradually to 0° from the edge to the core of the wire. With the wire diameter variation increasing from 10 to 20%, the variation range of the metal flow velocity at the die entry increased from 0.04 to 0.19 mm/s, that is the greater the wire diameter fluctuation, the larger of the variation range of the metal flow velocity at the die entry. When the wire diameter variation degree increased to 30%, the wire fractured at the die exit and the metal flow velocity be 0 at the die entry.

Keywords Variable diameter metal wire · Die drawing · Metal flow law

K. Li · X. Liu (✉)
School of Materials Science and Engineering,
University of Science and Technology Beijing, Beijing 100083, China
e-mail: liuxuefengbj@163.com

K. Li
e-mail: ksonglee@163.com

X. Liu
Beijing Laboratory of Metallic Materials and Processing
for Modern Transportation, University of Science
and Technology Beijing, Beijing 100083, China

© Springer Nature Singapore Pte Ltd. 2018

Y. Han (ed.), *Advances in Materials Processing*, Lecture Notes in Mechanical Engineering, https://doi.org/10.1007/978-981-13-0107-0_56

Introduction

Dieless drawing is a flexible and near net-shape forming technology without using the conventional drawing die to achieve drawing deformation of metal wire [1]. It has many advantages such as large area reduction, low drawing force, without lubricant and drawing die. However, because of no constraint of drawing die during the dieless drawing process, the metal wire is in free deformation state and the process parameters fluctuate greatly, which leads to problems such as poor uniformity of the finished products. Thus, further development and applications of dieless drawing are inhibited [2–4].

In order to eliminate size fluctuations of finished products caused by dieless drawing, researchers combine the die drawing technology with dieless drawing technology and develop a new drawing forming technology that is dieless drawing and traditional die drawing conducted alternatively [5]. Uniform finished wire is prepared by this drawing technology. This technology is characterized by first large deformation of the dieless drawing and then through the die drawing to eliminate the size fluctuations, so it has advantages of large deformation in a single pass and high dimensional accuracy.

The dieless drawn variable diameter metal wire enters the drawing die to initiate plastic deformation. However, when the deformation amount of the die drawing and the variable diameter metal wire does not match, it will lead this drawing technology failure. The peak of the wire at the die entry will block, which result in fracture of the wire at the die exit. The trough of the wire diameter is less than the sizing zone diameter, so the wire doesn't contact with the drawing die and leakage occurs.

At present, the researchers have conducted a lot of research on the die drawing deformation of constant cross section wire [6–9]. However, the die drawing deformation of variable diameter metal wire has not been studied. The metal flow law of variable diameter metal wire in the die drawing process is not clear. In this paper, the Deform finite element software is used to simulate the die drawing process of the variable diameter TC4 titanium alloy wire. The drawing force, the metal flow velocity at the die entry and variation of the wire diameter during the drawing process are analyzed. The metal flow law of variable diameter metal wire in the die drawing process is studied. The influence law of size fluctuation degree and deformation amounts of die drawing on the variable diameter metal wire conducting die drawing deformation is analyzed.

Finite Element Simulation Experiments

Basic Assumption

Assume that the metal material satisfies the following conditions:

The elastic deformation of the metal wire can be ignored since it is much smaller than the plastic deformation;
Regardless of body force and inertia force;
The metal wires are assumed to be uniform and isotropic;
The volume of the wire remains constant during the deformation process;
The material follows the Mises yield criterion and the flow deformation follows the stress-strain rate relationship.

Experimental Material

In the simulation experiment, the variable diameter TC4 titanium alloy wire is selected as the workpiece, and the YG6 cemented carbide (WC94%, Co6%, wt%) is selected as the drawing die. The chemical composition of the TC4 titanium alloy is presented in Table 1. The physical properties of TC4 and YG6 are shown in Table 2.

Geometric Model

The geometric model of the TC4 titanium alloy wire is shown in Fig. 1. The variable diameter wire is divided into homogeneous section and variable section.

Table 1 Chemical composition of TC4, wt%

Al	V	Fe	C	N	O	H	Ti
6.45	4.12	0.219	0.006	0.005	0.040	0.003	Balance

Table 2 Physical properties of TC4 metal wire and YG6 drawing die

Physical properties	TC4	YG6
Heat capacity [J kg^{-1} K^{-1}]	611	210
Thermal conductivity [W m^{-1} K^{-1}]	6.8	70
Heat transfer coefficient between TC4 and air [W m^2 s^{-1}]	0.02	0.02
Heat transfer coefficient between TC4 and drawing die [W m^2 s^{-1}]	11	11
Emissivity	0.5	0.2

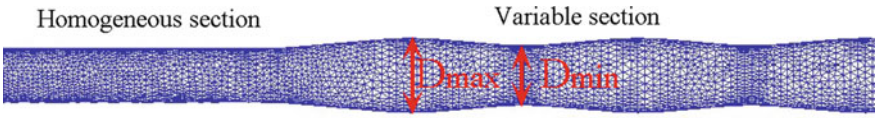

Fig. 1 Geometric model of variable diameter TC4 wire. D_{max}—the peak diameter of the variable wire; D_{min}—the trough diameter of the variable wire

The diameter of the homogeneous section is smaller than the diameter of the sizing zone, which is easy for the wire to pass through the drawing die. The reference diameter of the variable diameter wire is 6 mm. The total length of the wire is 150 mm. The wire model is meshed by tetrahedral element, and the wire is divided into 100,000 elements.

The variation degree of the variable wire is defined as

$$\Delta = \frac{D_{\max} - D_{\min}}{D} \tag{1}$$

where D_{max} is the peak diameter of the variable wire, D_{min} is the trough diameter of the variable wire and D is the reference diameter of the variable wire. The D_{max} and the D_{min} appear alternately on the variable wire.

The geometrical model of the drawing die is shown in Fig. 2. The width b is 13 mm, the outer diameter d is 26 mm, the sizing zone diameter l is 2 mm and the semi-die angle α is 12°. The drawing die model is meshed by tetrahedral element, and the wire is divided into 20,000 elements. The sizing zone diameter corresponding to different die drawing deformation can be calculated by the equation of the die drawing deformation

$$\phi = \frac{D^2 - D_0^2}{D^2} \tag{2}$$

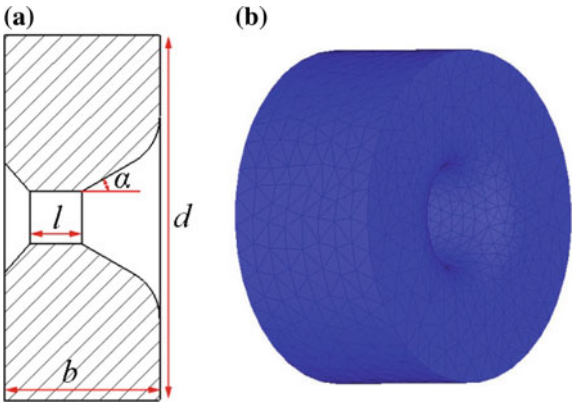

Fig. 2 Geometric model of drawing die **a** structure of drawing die; **b** mesh division of drawing die

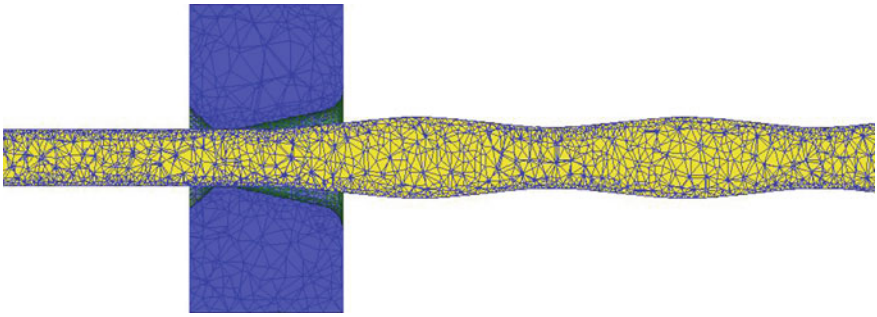

Fig. 3 Geometric model of the variable diameter TC4 titanium alloy wire conducting die drawing

where D is the variable wire reference diameter and D_O is the sizing zone diameter of the drawing die.

The geometrical model of the variable diameter TC4 titanium alloy wire conducting die drawing is shown in Fig. 3. The friction model between the wire and the drawing die is selected as the shear friction model. Due to the characteristics of the titanium alloy easy to stick the drawing die, the friction coefficient is large and is set as 0.25. The heat transfer coefficient between wire and air, drawing die and air, wire and drawing die is shown in Table 1.

Simulation Parameters

The process parameters for the simulation experiment are selected as 10–30% fluctuation degree of the variable diameter wire, 10–30% deformation amounts of the die drawing and 0.5 mm/s drawing speed.

Results and Discussion

Metal Flow Law

The metal flow direction of the variable diameter wire can be obtained by the velocity vector diagram. The metal flow direction changing with the die drawing process is shown in Fig. 4. Figure 4a is the metal flow condition for the 20th step. The wire passes through the drawing die without contacting with it, and the metal flow direction of the wire is the same with the drawing direction. With the drawing process went on, the wire contacts with the drawing die and initiates plastic deformation. There is an inclined angle between the metal flow direction in the deformation zone (within the dashed box in Fig. 4) and the drawing direction. This

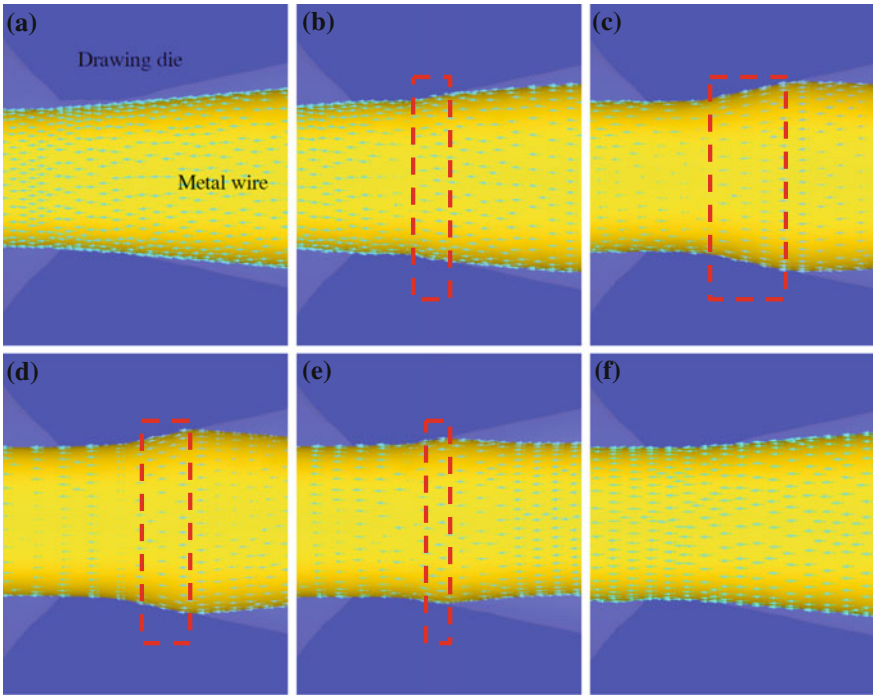

Fig. 4 Metal flow direction changing with drawing steps **a** 20th step; **b** 30th step; **c** 50th step; **d** 70th step; **e** 100th step; **f** 130th step

inclined angle decreases gradually to 0° from the edge to the core of the wire. The metal flow direction outside the deformation zone is the same with the drawing direction, as shown in Fig. 4b. When the peak of the wave begins to deform, the deformation zone is the largest, and the metal flow direction is the same as the 30th step, as shown in Fig. 4c. Figure 4d, e are the metal flow conditions of the 70th and 100th steps. The metal flow conditions are the same as the 30th step, while the deformation zone reduces gradually. Figure 4f is the metal flow condition of the 130th step, while the trough of the wave enters the drawing die. Because the trough diameter is slightly smaller than the diameter of the sizing zone, there is no deformation takes place, and the metal flow direction of the wire is the same as the drawing direction.

Figure 5 shows the relationship between the velocity at the die entry and the drawing force under the condition of 20% fluctuation degree of the TC4 wire. At the initial stage, the homogenous section of the wire enters the drawing die, and it doesn't contact with the drawing die, so the drawing force at this moment is 0. With the drawing process went on, when the variable diameter wire enters the drawing die, the drawing force increases sharply. When the peak of the wire initiates plastic

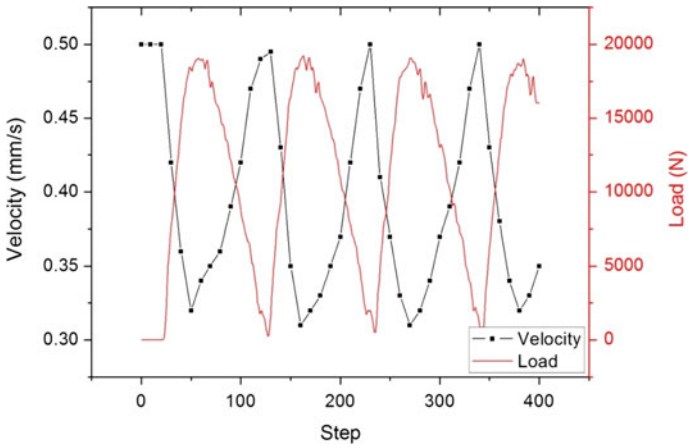

Fig. 5 Velocity at the die entry and the drawing force changing with drawing steps

deformation, the drawing force increases to the maximum of 19 KN. Then the drawing force reduces gradually until the trough of the wave enters the drawing die and the drawing force of the wire reduces to the minimum. It can be seen from the figure that the minimum drawing force corresponding to the trough is 0, since the diameter at the trough is slightly smaller than the sizing zone diameter of the die. There is a large difference in the actual deformation amount between the peak and the trough. The deformation amount at the peak is large, so the work hardening is serious. While the trough doesn't deform, so the deformation of the wire after die drawing is not uniform.

In the conventional drawing or extrusion process, we concern about the metal flow velocity at the die exit. Large variation of the flow velocity will result in inhomogeneous deformation of the workpiece [10]. While the die drawing process of the variable diameter TC4 titanium alloy wire, we concern the metal flow velocity at the die entry. Large variation of the flow velocity at the die entry will result in inhomogeneous deformation of the workpiece. Figure 5 shows the metal flow velocity at the die entry changing with drawing steps. The distance from measuring position of the wire to the sizing zone is 10 mm. It can be seen from the figure that the velocity at the die entry is opposite to that of the drawing force. When the peak of the wave conducts die drawing deformation, the velocity at the die entry v_c can be calculated by volume constancy law as expressed in equation $v_o \cdot D_o^2 = v_c \cdot D_c^2$, which is 0.31 mm/s at this moment. The diameter at the trough is slightly smaller than the sizing zone diameter of the die and it doesn't deform. The corresponding velocity at the die entry is the same as the drawing speed 0.5 mm/s and the fluctuation degree of the velocity at the die entry is 0.19 mm/s.

Effect of Dimensional Fluctuation Degree and Deformation Amount on the Flow Velocity at the Die Entry

Figure 6 shows the effect of the dimensional fluctuation degree on the metal flow velocity at the die entry. It can be seen from the figure that the flow velocity at the die entry reduced first and then increased and then reduced again. The initial values of the metal flow velocity of the wire at different fluctuation degree are all 0.5 mm/s, and the wire doesn't contact with the drawing die. As the wire diameter at the die entry increasing, the metal flow velocity at the die entry reduces gradually. When the wire diameter increases to the maximum value, that is the peak of the wave, the metal velocity at the die entry reduces to the minimum value. When the wire diameter at the die entry reduced gradually from the peak, the metal flow velocity increased gradually. The wire diameter reduced to the minimum value, that is the trough of the wave, the metal flow velocity at the die entry increased gradually to the maximum value. As the fluctuation degree of the wire increases from 10 to 20%, the fluctuation degree of the metal flow velocity increased from 0.09 to 0.19 mm/s. When the fluctuation degree of the wire is 30%, the wire is fractured at the die exit, and the metal flow velocity at the die entry changes to zero.

Figure 7 shows the influence of the deformation amount of die drawing on the metal flow velocity at the die entry. It can be seen from the figure that the flow velocity at the die entry reduced first and then increased and then reduced again, which is similar to the influence of the dimensional fluctuation degree on the metal flow velocity at the die entry. With the deformation amount of die drawing increasing from 10 to 20%, the fluctuation degree of the metal flow velocity at the die entry increased from 0.14 to 0.19 mm/s. When the deformation amount of die drawing is 30%, the wire is fractured at the die exit, and the metal flow velocity at the die entry became zero.

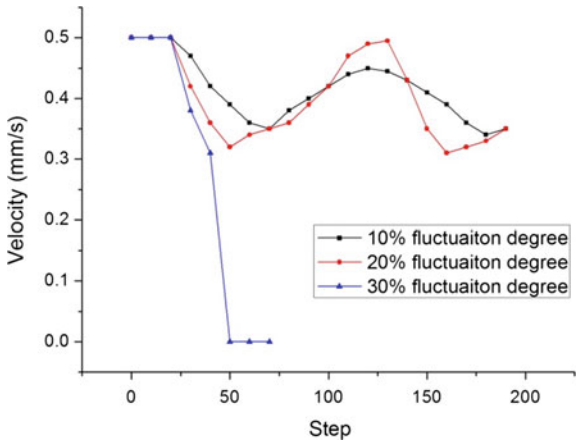

Fig. 6 The influence of fluctuation degree on metal flow velocity at die entry

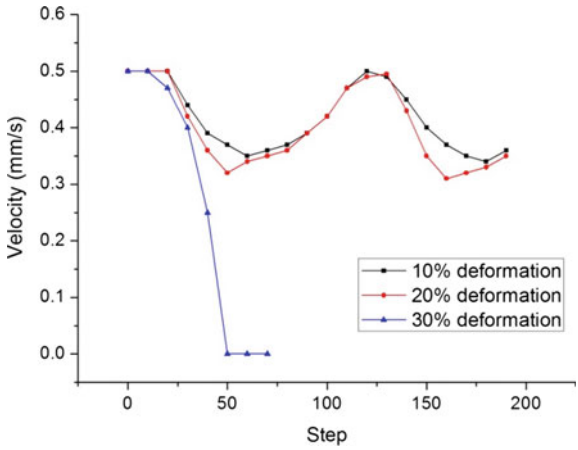

Fig. 7 The influence of deformation amount on metal flow velocity at die entry

Variation of the Wire Diameter

The variation of the wire diameter after die drawing deformation under different fluctuation degree and deformation amount is shown in Table 3. It can be seen from the table, when the fluctuation degree is 30% or deformation amount is 30%, the wire at the die exit will appear necks, and ultimately lead to wire break. When the 20% fluctuation degree of the diameter conducted 10% deformation amount of die drawing, the peak wire can pass through the drawing die successfully. But the

Table 3 The variation of the wire diameter after die drawing deformation under different fluctuation degree and deformation amount

Deformation amount	Fluctuation degree		
	10%	20%	30%
10%	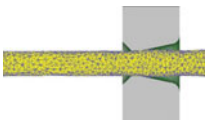	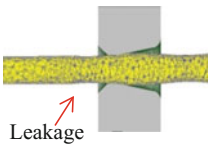	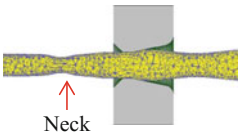
20%	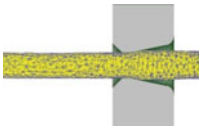	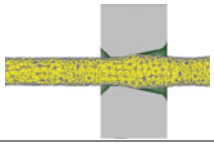	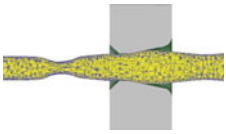
30%	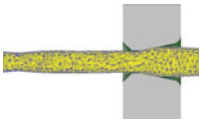	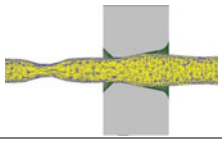	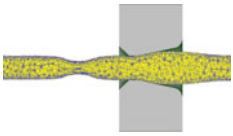

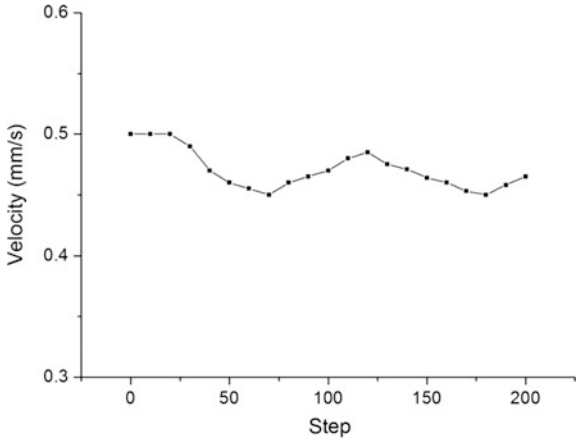

Fig. 8 Metal flow velocity at die entry under the condition of 10% fluctuation degree–10% deformation amount

diameter of the trough wire is smaller than the diameter of the sizing zone, which results in leakage. When the 10 or 20% fluctuation degree of the diameter conducted 20% deformation amount of die drawing or 10% fluctuation degree of the diameter conducted 10% deformation amount of die drawing, the drawing process is successful and it doesn't occur fracture or leakage. However, it can be seen from the previous analysis that the metal flow velocity at the die entry will fluctuate during the variable diameter metal wire conducting die drawing deformation. When the 10 or 20% fluctuations degree metal wire conducted die drawing at 20% deformation amount, the fluctuation of the metal flow velocity is 0.09 and 0.19 mm/s, respectively. When the 10% fluctuation degree metal wire conducted die drawing at 10% deformation amount, the fluctuation of the metal flow velocity is shown in Fig. 8. It can be seen from the figure that the fluctuation of the metal flow velocity at the die entry is 0.04 mm/s, which means the fluctuation degree is small and the wire deformation is uniform.

The variable diameter of the dieless drawn wire conducted die drawing in the subsequent process. When the 10 or 20% fluctuation degree of the diameter conducted 20% deformation amount of die drawing or 10% fluctuation degree of the diameter conducted 10% deformation amount of die drawing, the drawing process is successful and it doesn't occur fracture or leakage. However, when the deformation amount of die drawing is 20%, the drawing force of the wire and the metal flow velocity at the die entry is large and the deformation inhomogeneity is severe, as shown in Fig. 9a, b. Therefore, it is necessary to control the fluctuation degree of the dieless drawn wire diameter within 10%. By doing this, the drawing force of the wire is low and the fluctuation range of the metal flow velocity at the die entry is low so that the wire can pass through the drawing die successfully and the deformation is relatively uniform, as shown in Fig. 9c.

The 20 or 10% fluctuation degree of the dieless drawn diameter conducted 10% deformation amount of die drawing, and the finished product morphology was shown in Fig. 10. When the fluctuation degree is 20%, the size of the peak wire is

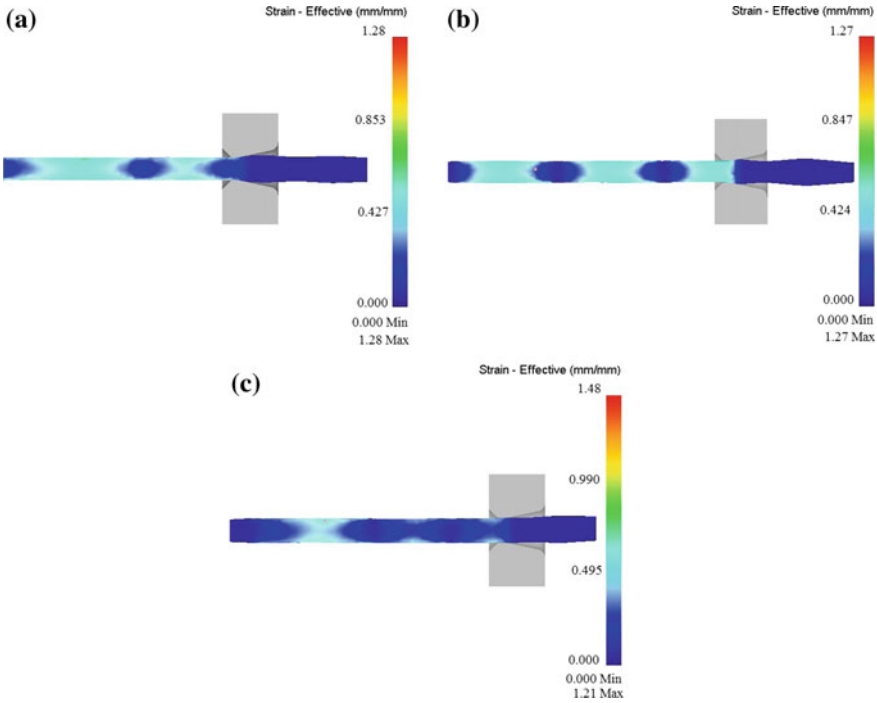

Fig. 9 Die drawing effective strain of variable diameter metal wire **a** 10% fluctuation degree–20% deformation amount; **b** 20% fluctuation degree–20% deformation amount; **c** 10% fluctuation degree–10% deformation amount

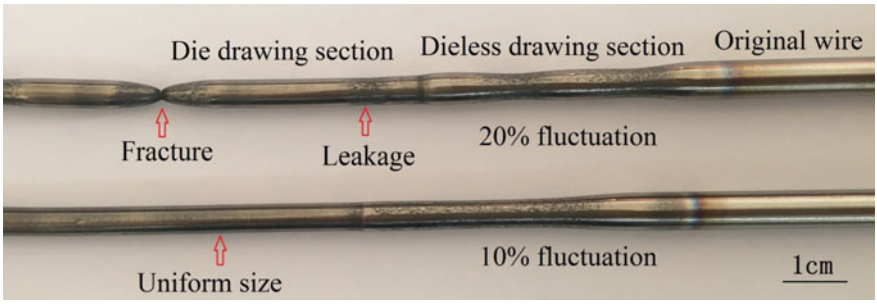

Fig. 10 Morphology of the finished product

uniform after die drawing, while the diameter of the trough wire is smaller than the diameter of the sizing zone, which results in leakage. When the fluctuation degree is 10%, the peak and the trough wire both conducted die drawing. The size of the finished wire is uniform, and the drawing process is successful.

Conclusions

In this paper, Deform finite element software is used to simulate the die drawing process of variable diameter TC4 titanium alloy wire. The metal flow law during the die drawing process of variable diameter wire is revealed. The following conclusions are obtained:

(1) The metal flow directions of the die exit and die entry are consistent with the drawing direction when the TC4 titanium alloy wire enters the drawing die initiating plastic deformation. There is an inclined angle between the metal flow direction in the deformation zone and the drawing direction. This inclined angle decreases gradually to 0° from the edge to the core of the wire.
(2) With the wire diameter variation increasing from 10 to 20%, the variation range of the metal flow velocity at the die entry increases from 0.11 to 0.19 mm/s, that is the greater the wire diameter fluctuation the larger of the variation range of the metal flow velocity at the die entry. When the wire diameter variation degree increases to 30%, the wire will fracture at the die exit and the metal flow velocity becomes 0 at the die entry.
(3) When the 10% fluctuation degree of the wire takes place and the plastic deformation is at 10% deformation amounts of die drawing, the variation range of the metal flow velocity at the die entry is 0.04 mm/s. It is necessary to control the fluctuation degree of the dieless drawn wire diameter within 10%.

Acknowledgements This work was supported by the National Natural Science Foundation of China under Grant 51174027.

References

1. J.M. Allwood, H. Utsunomiya, A survey of flexible forming processes in Japan. Int. J. Mach. Tool. Manu. **46**, 1939–1960 (2006)
2. R. Carolan, P. Tiernan, Computer controlled system for dieless drawing of tool steel bar. J. Mater. Process. Tech. **209**, 3335–3342 (2009)
3. P. Tiernan, R. Carolan, E. Twohig, S.A.M. Tofail, Design and development of a novel load-control dieless rod drawing system. CIRP J. Manu. Sci. Tech. **4**, 110–117 (2011)
4. T. Furushima, K. Manabe, Experimental and numerical study on deformation behavior in dieless drawing process of superplastic microtubes. J. Mater. Process. Tech. **191**, 59–63 (2007)
5. Y. Kawaguchi, K. Katsube, M. Murahashi, Y. Yamada, Applications of dieless drawing to Ti–Ni wire drawing and tapered steel wire manufacturing. Wire J. Int. **24**, 53–58 (1991)
6. G. Vega, A. Haddi, A. Imad, Investigation of process parameters effect on the copper-wire drawing. Mater. Design. **30**, 3308–3312 (2009)
7. K.L. Wang, V. Argyropoulos, Design and analysis of direct cold drawing of section rods through a single die. J. Mater. Process. Tech. **166**, 345–358 (2005)
8. E. Felder, C. Levrau, M. Mantel, N.G.T. Dinh, Identification of the work of plastic deformation and the friction shear stress in wire drawing. Wear **286–287**, 27–34 (2012)

9. K.K. Tang, Z.X. Li, J. Wang, Numerical simulation of damage evolution in multi-pass wire drawing process and its applications. Mater. Design. **32**, 3299–3311 (2011)
10. C.S. Zhang, G.Q. Zhao, H. Chen, Y.J. Guan, F.J. Kou, Numerical simulation and metal flow analysis of hot extrusion process for a complex hollow aluminum profile. Int. J. Adv. Manuf. Tech. **60**, 101–110 (2012)

Dielectric and Impedance Studies on $(K_{0.5}Na_{0.5})NbO_3$-Based Ceramics

Yafei Yan, Minhong Jiang, Jiageng Song, Chongyan Hao, Qi Jin, Shengnan Han, Lin Li, Jinwei Zhang and Xiaoyu Yao

Abstract Polycrystalline, lead-free $(K_{0.5}Na_{0.5})NbO_3$-based ceramics were synthesized using solid-state reaction method. The microstructure, dielectric and impedance characteristics of the ceramics were studied. The results showed that the obtained doped ceramic had a pure perovskite structure with pseudo-cubic phase. Some dielectric anomalies were observed at about 200 °C, and 500 °C for the ceramics, respectively. With the increase of $BaBiO_3$ doping content, the dielectric constant-temperature transition peak value became weaker. The activation energy of conductivity is found to be closely related to the frequency. The activation energy obtained from the dielectric relaxation data was attributed to oxygen vacancies. The calculated activation energies at 10 kHz for the temperature range (200–500 °C) and (200–350 °C) and (350–500 °C) are 0.657, 0.542 and 0.350 eV, respectively.

Keywords $K_{0.5}Na_{0.5}NbO_3$ · Ceramic · Impedance · Dielectric

Introduction

In the modern society, functional materials play a vital role in many application fields. As a kind of functional material, potassium sodium niobate ($K_{0.5}Na_{0.5}NbO_3$, KNN)-based system has been also paid attention in the world due to its particular piezoelectric, ferroelectric and transparent optical-electrical performance [1–5]. KNN has a ferroelectric perovskite structure with a relatively high Curie point (T_c) of ~420 °C [2]. In the KNN ceramic there are two phase changes with temperature from room temperature through its melting point temperature, corresponding to the transformation from cubic (C) to ferroelectric tetragonal (T) at about 420 °C, and from T to ferroelectric orthorhombic (O)/monoclinic at 220 °C, respectively [6].

Y. Yan · M. Jiang (✉) · J. Song · C. Hao · Q. Jin · S. Han · L. Li · J. Zhang · X. Yao
School of Materials Science and Engineering, Guilin University of Electronic Technology, Guilin 541004, China
e-mail: jmhsir@tom.com

© Springer Nature Singapore Pte Ltd. 2018

Y. Han (ed.), *Advances in Materials Processing*, Lecture Notes in Mechanical Engineering, https://doi.org/10.1007/978-981-13-0107-0_57

For polycrystalline ceramics, the existence of different defects, such as oxygen vacancies, space charges, holes and grain boundaries etc., and inhomogeneity of composition are inevitable. The main defects associated with KNN are oxygen vacancies and space charges. These ceramics may strongly affect the electrical properties because these defects may be related to the domain wall [7–9]. In fact, if you know the nature of the defects of the ceramic and charge transfer is to control the basis of its electrical properties. In general, complex impedance spectroscopy (CIS) this method, which widely used in the electronic needle [10, 11]. In addition, it can be used to identify transmission mechanisms, even the characteristics of ferroelectric phase transitions [12, 13].

To the best of our knowledge, the impedance spectroscopy study on the lead-free KNN-based ceramics has been still rarely reported to this day. In this present, we fabricated $BaBiO_3$(BB)-doped KNN ceramics. In order to understand the nature of defects and charge transferring, the electrical property and conductive mechanism in the ceramic were studied by using the CIS method. The investigation results would be able to provide a new way for designing new KNN-based materials and optimizing its performance for the factual applications.

Experimental Procedure

According to the formula $(1 - x)K_{0.5}Na_{0.5}NbO_3$-$xBaBiO_3$($x$ = 0.008, 0.016), KNN-BB ceramics were prepared by a solid-state sintering method using K_2CO_3 (99%), Na_2CO_3 (99.8%), Nb_2O_5 (99.5%), $BaCO_3$ (99%) and Bi_2O_3 (99%) powder as raw materials and then the mixture drying and calcination under 750 °C for 6 h. After calcining, the mixture is used in ethanol for 24 h and dry. The dried powder was pressed into a disk with a diameter of 14 mm and thickness of 2–3 mm under the pressure of 100 MPa. The disk samples were sintered in air at 1130 °C for 15 h over. The sintered samples were finally polished to a disk with the thickness of 0.5 mm. Silver electrodes were coated on both sides of each sample and fired for half an hour at 600 °C.

The phase structure was detected by X-ray diffraction (XRD, D8-2-Advance) and Cu, Kα radiation. Surface and cross-section microstructures were analyzed by scanning electron microscopy (SEM, JSM-5610LV). Dielectric properties are measured with an impedance analyzer (Agilent 4294A).

Results and Discussion

Figure 1 shows the fractured surface SEM images of 99.2KNN–0.8BB ceramic sample. The average grain size of the sample is calculated to be 82, and 69 nm, for x = 0.008, and 0.016, respectively. The XRD patterns of the KNN-BB ceramics are shown in Fig. 2. All the ceramic samples show atypical ABO_3 perovskite structure,

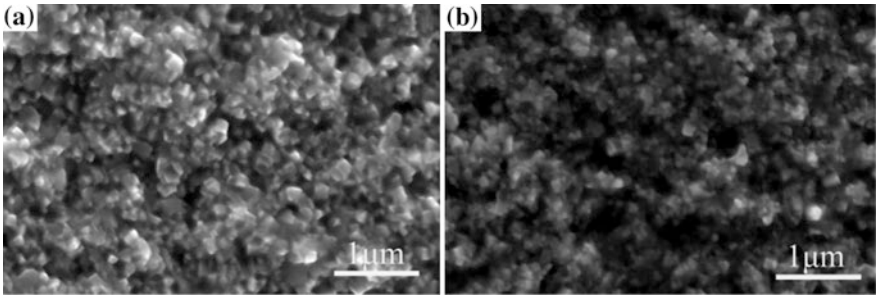

Fig. 1 SEM images of the fracture surface of **a** 99.2KNN-0.8BB, **b** 98.4KNN-1.6BB ceramics

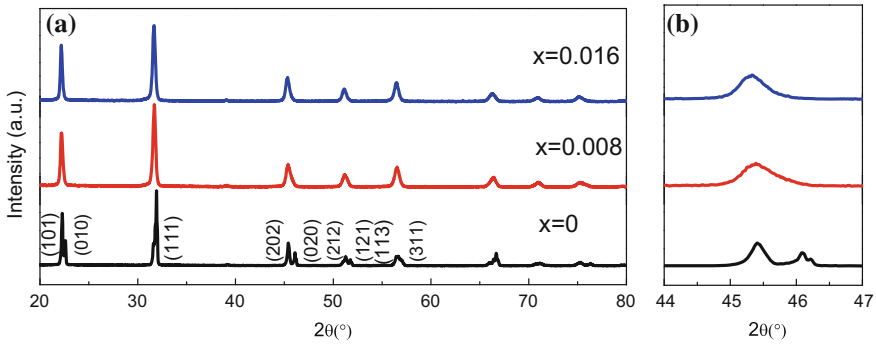

Fig. 2 XRD patterns of the $(1 - x)$KNN-xBB (x = 0, 0.008 and 0.016)

which indicates that BB completely diffuses into the KNN crystal lattice. This suggests that Ba^{2+} and Bi^{5+} have diffused into the KNN lattice, with Ba^{2+} entering the $(K_{0.5}Na_{0.5})$ sites and Bi^{5+} occupying the Nb^{5+} sites. The radius of Bi^{5+} (0.74 Å) is close to that of Nb^{5+} (0.69 Å) while the radius ofBa^{2+} (1.35 Å) is close to that of $(K_{0.5}Na_{0.5})$ (it is 1.38 Å for K^+ and 1.02 Å for Na^+). The ceramic sample without BB addition shows a single orthorhombic phase structure. After doping, the two diffraction peaks (202) and (020) of the ceramic are bonded together (Fig. 2b). The crystalline crystal of the KNN-BB ceramic has transformed into a cubic structure, which leads to a merge of the two diffraction peaks [4–6].

The dielectric-temperature spectrum at 10 kHz of $(1 - x)$KNN-xBB (x = 0.008 and 0.016) system samples is shown in Fig. 3. It can be seen from the Fig. 3 that there are two dielectric transition peaks in the spectrum for all the samples. The two peaks corresponding to the orthogonal → tetragonal transition temperature ($T_{O\text{-}T}$) and tetragonal → cubic phase transition temperature (T_c) were measured. It can also be seen that the spectrums show a dispersion phase transformation characteristics for all KNN-BB ceramics. The increasing of the BB addition in the KNN ceramic resulted in a lower dielectric permittivity and stronger dispersion. The

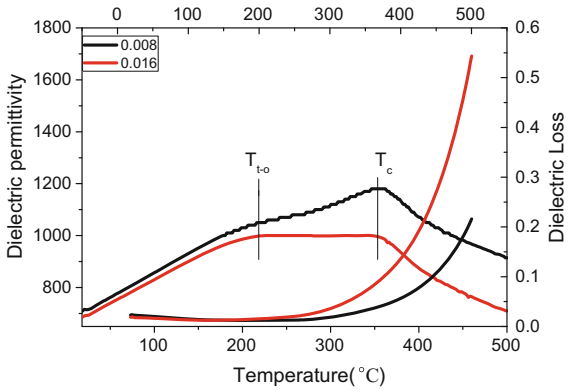

Fig. 3 Dielectric permittivity as a function of temperatures for the $(1 - x)$KNN-xBB ceramics

maximum dielectric permittivity at T_c is strongly suppressed with increasing the BB content. This could be related to the small grain size of the ceramic and the phase transition.

For the first/second phase transitions of ferroelectric materials described by Landau's theory, Curie-Weiss's law ($\varepsilon' = C/(T - T_0)$) can be used to describe the behavior of the reciprocal permittivity above T_c, where T_0 is the Curie–Weiss temperature measured by extrapolation of the curve in the X-axis and C is the Curie–Weiss constant [14, 15]. Also, in the ferroelectrics having the chromatic dispersion or relaxation phase transition, the deviation of Curie-Weiss's law can be observed. Uchino and Nakamura [16] have A theoretical approach is proposed for the quantitative description of discrete behavior. They believe that the bias caused by the relaxation or ferroelectrics is derived from the following equation:

$$\frac{1}{\varepsilon'} - \frac{1}{\varepsilon_m} = \frac{(T - T_m)^y}{C'} \tag{1}$$

where ε_m is the maximum value of the dielectric constant; T_m is the temperature at ε_m; y is the critical exponent for diffuse phase transformation; and C′ is the Curie-Weiss-like constant. When $y = 1$, We have observed the ideal of the curey-weiss law, which is the case of normal ferroelectric, whereas y = 2 corresponds to the ideal relaxation or ferroelectric. Figure 4 shows the curves of log $(1/\varepsilon' - 1/\varepsilon_m)$ versus log $(T - T_m)$ of the sintered samples and the y values as a function of the BB concentration. When x = 0.008 and 0.016, the good linearity of the reciprocal dielectric constant is in agreement with the Eq. (1), indicating a normal ferroelectric with sharp transition. At x = 0.008 and 0.016, the y value was 1.1208 and 1.3614, respectively, which are close to 1. These values are consistent with our previous discussion.

The variation of real part of impedance (Z′) with frequency at various temperatures (from 200 to 500 °C) for KNN-BB ceramics is shown in (Fig. 5a–f). It can

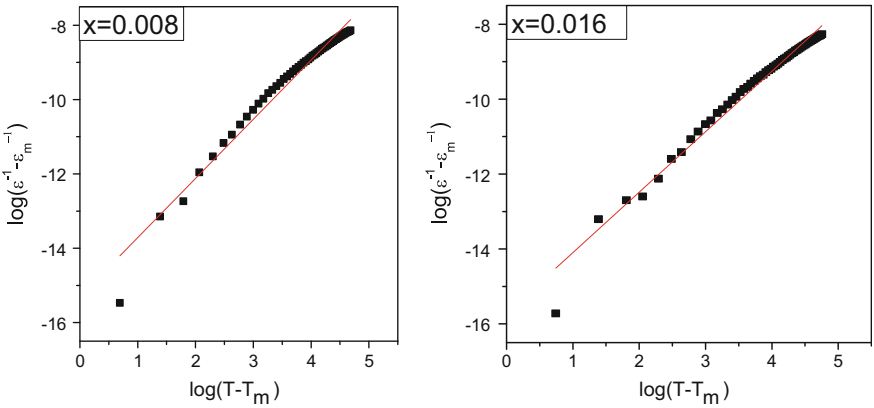

Fig. 4 Plots of $\log(1/\varepsilon' - 1/\varepsilon_m)$ versus $\log(T - T_m)$ for the $(1 - x)$KNN-xBB ceramics (The symbols denote the experimental data, while the solid lines denote the fitting line.)

be seen that the Z′ decreases with the increasing of temperature from (Fig. 5a–b). Increasing of ac conduction (σ_{ac}) in the sample can be observed due to the decrease in the magnitude of Z' with increasing the temperature. This may be due to defects such as hypoxia. In general, the contribution of oxygen vacancy in high temperature perovskite structure is more significant. All samples have higher value of Z′ in low frequency and merge Z′ in higher frequency (>10 kHz) temperature, This is the sign of space charge polarization [17]. The impedance at a higher temperature appears to be independent of frequency and indicates a combination of temperature at a higher frequency.

The imaginary part of the impedance changes with frequency (Z″) KNN-BB at different temperatures (Fig. 5c–d). Initial Z″ value increase, the peak (Z Max), then on frequency measuring temperature. And then, as the temperature goes up, the observed higher frequency is Z maximum peak shift and broadening. The characteristic frequency $(\omega\max = 2\pi f\max)$ under the temperature dependence of the presence of the peak (Z″max) relaxation process, this is dependent on temperature. These relaxation processes may be due to the presence of non-moving species at low temperatures and the defect of moving at high temperatures. Z″ merger with frequency curve is found in a particular area of the frequency of the higher frequency, it is because of the space charge polarization.

Figure 5e–f shows the complex impedance spectrum (Nyquist plot, a picture of the real (Z′) and virtual (Z) of the composite impedance of KNN-BB ceramics. Figure 5g–h is a partial enlarged view. From room temperature to 200 °C impedance data shows, because they only show the large slope of the straight line, show high insulation. However, as the temperature increases the slope decreases and be found to form clear semicircular arcs. The radius of the curvature decreases with increasing the temperature, which indicates the increase in conductivity of the sample with increasing the temperature. At a given temperature, the resistance of the grain (R_g) is equal to the intercept of the semicircle corresponding to the X-axis.

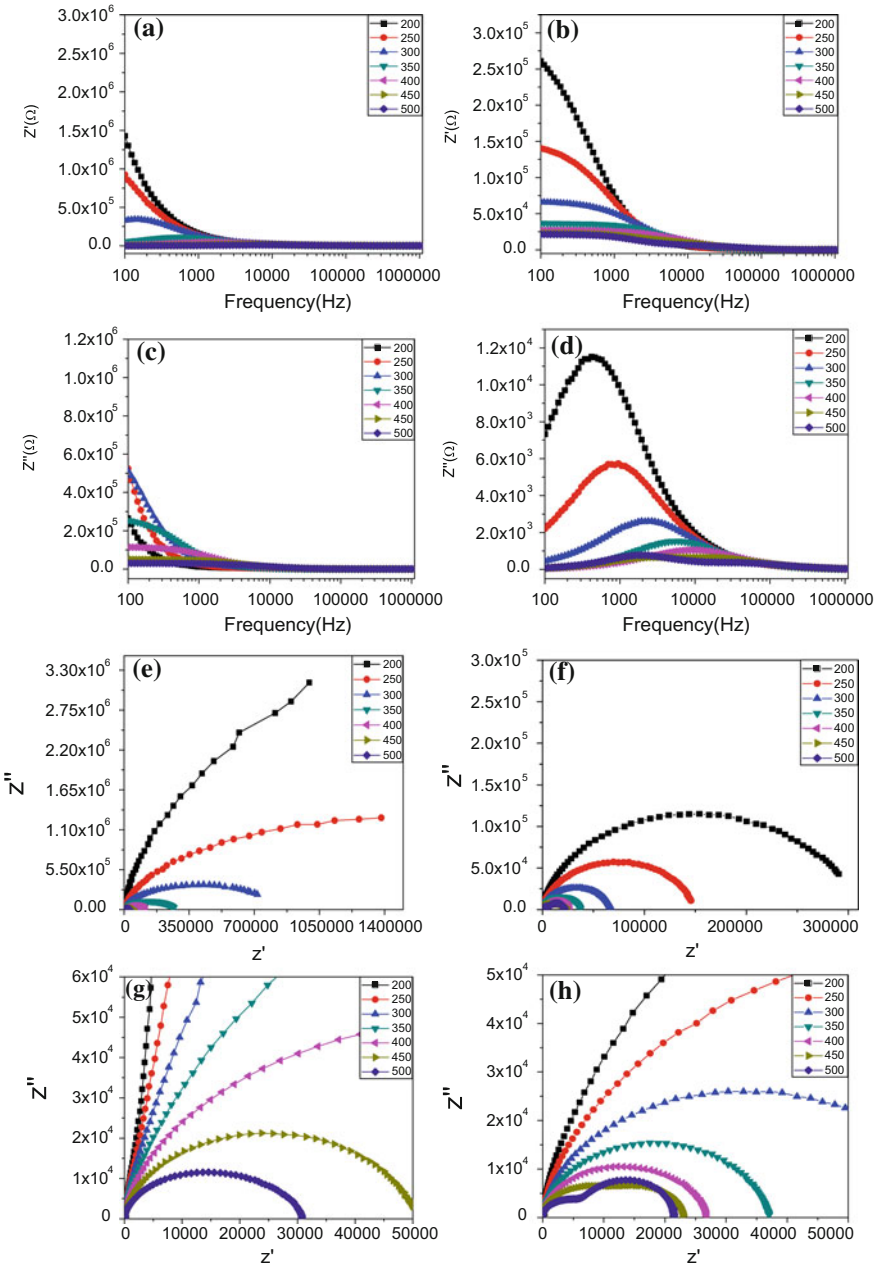

Fig. 5 **a**, **d** Real and imaginary part of impedance variation with frequency and **g**–**h** Nyquist plots between imaginary and real part of impedance at different temperatures for KNN-BB sample

The method of analyzing the electrical response of materials can be formalized by complex modalities. Formalism is sometimes better than complex impedance diagrams to distinguish grain/grain boundary effect. Electric modulus (M) is expressed as:

$$M^* = M' + jM'' = j \times 2\pi f C_o Z^* = j \times 2\pi f C_o (Z' + jZ'') \quad (2)$$

where $C_o = \varepsilon_o A/d$ is the geometrical capacitance, A is the area of the electrode, and d is the distance between the electrodes. Therefore, impedance data has been redrawn in the form of modulus, as shown in Fig. 6a–f. Figure 6a–b show KNN-BB ceramics from 200 to 500 °C real modulus changes with frequency. It is characterized by low value M′ low-frequency region is followed by a continuous dispersion increases with the frequency. Find M′ saturated the highest temperature value of high frequency region, as shown in Fig. 6a–b. This may be the reason for the study of the short-range movement of charge carriers within the temperature range.

Figure 6c–d The imaginary part of KNN-BB ceramics at different temperature is given. In the case of higher temperature, the peak is found to move in a higher frequency direction. At the same time, the peak in the M″ imaginary part said solid dielectric relaxation process, the biggest shows average relaxation time and frequency in this process. It can be seen that the imaginary part of the electric modulus shows a very definite peak.

Figure 6e–f in the complex modulus diagram, two semicircular arcs are shown. At the high frequency, there is a small semicircle. At low frequency, there is a large semi-circular arc at all temperatures. The pattern shows the shape of the change in temperature, which indicates that the capacitance value may change.

Figure 7a–d Display complex impedance spectra (Nyquist diagram, real (Z′) and virtual (Z) of complex impedance Z) and locally amplified KNN-BB ceramic images. Impedance data from 0 to 200 °C is shown in figure display only a straight line of slope, marked the high insulation of behavior. However, as the temperature lower main ′(Z) and found that the slope of the curve axial form clear semicircle arc. The radius of curvature decreases with increasing temperature, which indicates the increasing of the conductivity of the sample. Generally speaking, the existence of a single semi-circular arc represents only one contribution, such as the internal (bulk) nature of the material. Figure 7c–d shows the complex impedance spectrum (Nyquist plot) of samples at 450 and 500 °C, respectively. We have fitted the experimental data for all the compositions by using the equivalent circuit. The residual grain boundary resistance (R_{gb}) is therefore the difference between the total resistance ($R_b + R_{gb}$) and R_b. The R_b, R_{gb} and ($R_b + R_{gb}$) were used to calculate the corresponding values of σ_b (bulk ionic conductivity), σ_{gb} (remaining grain boundary ionic conductivity) and σ_{total} (total ionic conductivity), respectively. The fitted results could support that the total conductivity in the KNN-BB transparent ceramic comes from two contributions: the grain interior (bulk) and grain boundary.

Figure 8 shows the variation of AC conductivity (s_{ac}) with temperature at 10 kHz frequencies for all samples. The nano appreciable variation of s_{ac} with

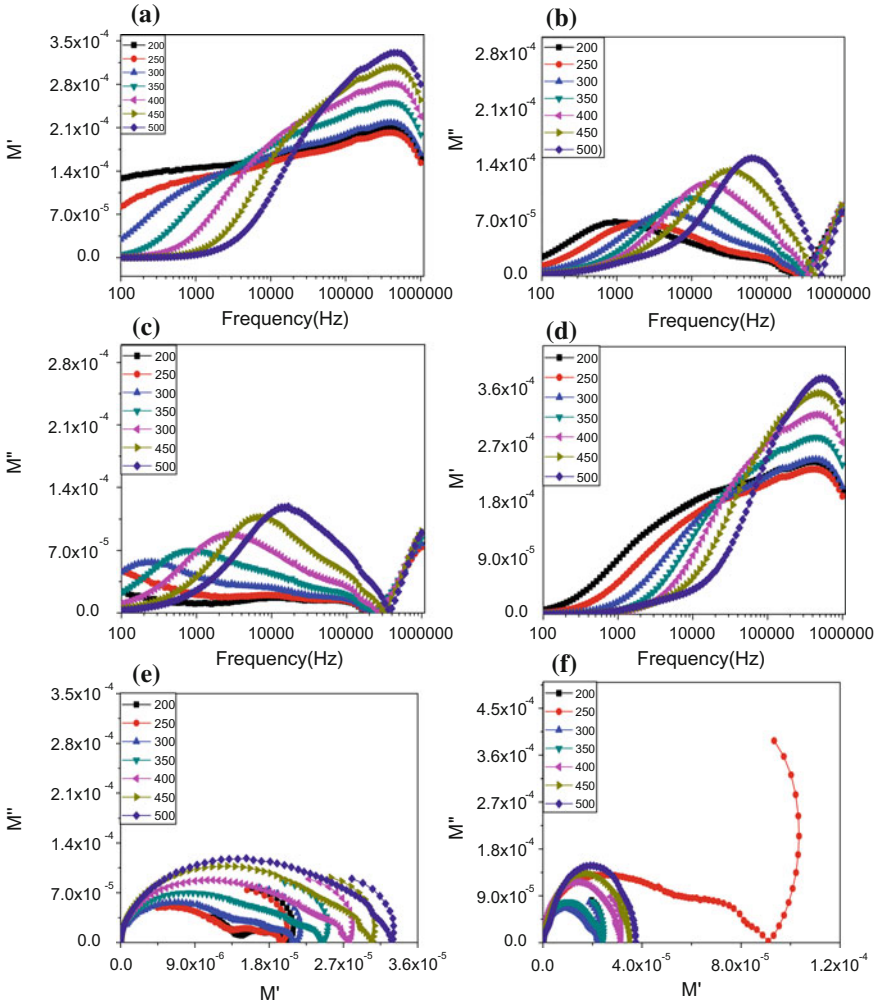

Fig. 6 Graphs, **a**–**b** between real and imaginary part of modulus, **c**–**d** variation of the real and **e**–**f** imaginary parts of modulus as afunction of frequency at different temperatures for KNN-BB sample, respectively

temperature indicates the multiple relaxations. The ac conductivity increases with the increase of temperature, showing the behavior of the negative temperature coefficient (NTCR). The activation energy calculated at 10 kHz in the temperature range (200–500 °C) and (200–350 °C) and (350–500 °C) is between 0.657, 0.542, and 0.350 eV respectively. Due to the loss of oxygen in the sintering process, the conductivity increases with the increase of temperature and leaves the free electron

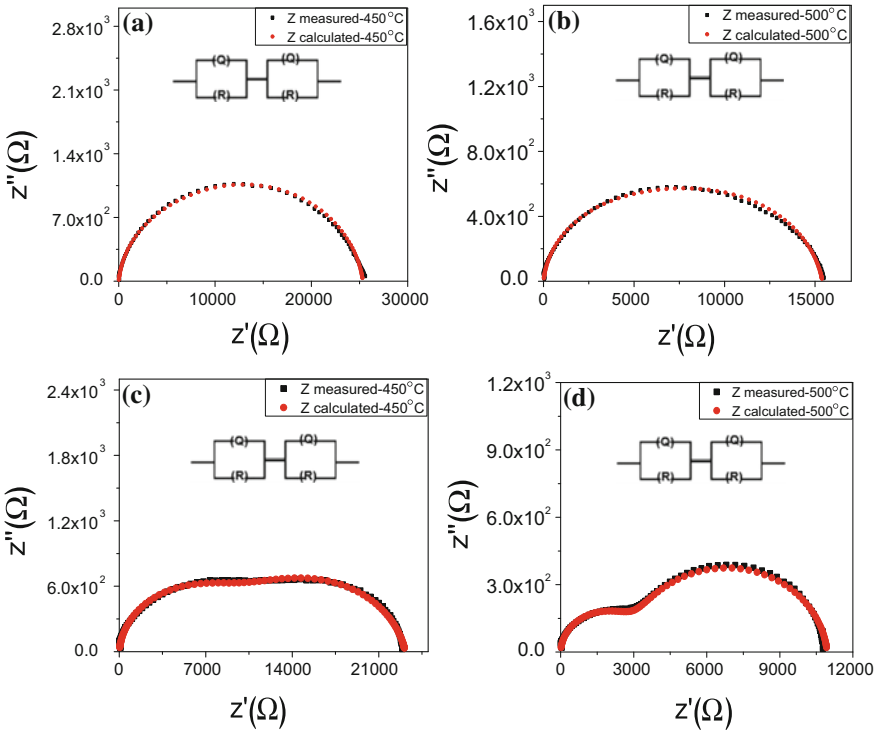

Fig. 7 **a**, **c** Z'' versus Z' Nyquist plots at 450 °C, and **b**, **d** Z'' versus Z' Nyquist plots at 500 °C

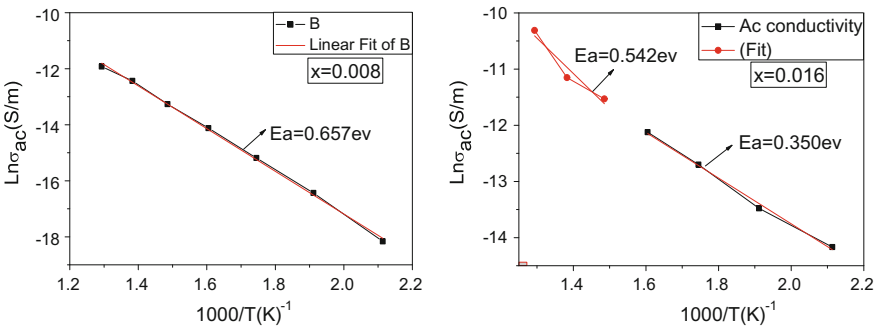

Fig. 8 Temperature dependence of the s_{ac} of $(1 - x)$KNN-xBB ceramics at 10 kHz

to make it an n-type semiconductor [18, 19]. The volatilization of A bit element (Na and K) results in the lack of A cation and the generation of oxygen vacancy caused by price equilibrium, thus changing lattice distortion and affecting the dielectric behavior of ceramics.

Conclusions

$(1 - x)K_{0.5}Na_{0.5}NbO_3$-$xBaBiO_3$ (x = 0.008, 0.016) lead free ceramic has been synthesized by conventional solid state reaction technique. XRD study shows that each component of the ceramic has a typical ABO_3 perovskite structure without obvious second phase. The doped ceramics have a pseudo-cubic structure. There is a dispersion phase transformation characteristics for all ceramics. The increasing of BB addition results in a lower dielectric permittivity and stronger dispersion. The total conductivity in the ceramics comes from two contributions: the grain interior (bulk) and grain boundary. The activation energies for the conductivity of the samples are found to be strongly frequency dependent. The activation energy calculated at 10 kHz in the temperature range (200–500 °C) and (200–350 °C) and (350–500 °C) is between 0.657, 0.542, and 0.350 eV respectively.

References

1. G. Shirane, R. Newnham, R. Pepinsky, Dielectric properties and phase transitions of NaNbO3, and (Na, K)NbO3. Phys. Rev. **96**, 581–588 (1954)
2. D.E. Harrison, G. Shirane, Crystal growth and structural study of the barium-titanium-phosphate phosphor. J. Electrochem. Soc. **108**, 788–790 (1961)
3. R.E. Jaeger, L. Egerton, Hot pressing of potassium-sodium niobates. J. Am. Ceram. Soc. **45**, 209 (1962)
4. M. Jiang, X. Liu, G. Chen, Phase structures and electrical properties of new lead-free $Na_{0.53}$-BiFeO ceramics. Scripta. Mater. **60**, 909–912 (2009)
5. M.H. Jiang, G.Q. Zhao, Z.F. Gu et al., In-depth structure characterization and properties of $(1 - x)(Li_{0.05}Na_{0.475}K_{0.475})(Nb_{0.95}Sb_{0.05})O_3$-$xBiFeO_3$, lead-free piezoceramics. J. Mater. Sci Mater. Electron. **26**, 9366–9372 (2015)
6. J. Tellier, B. Malic, B. Dkhil et al., Crystal structure and phase transitions of sodium potassium niobateperovskites. Solid State Sci. **11**, 320–324 (2009)
7. W. Ge, Y. Ren, J. Zhang et al., A monoclinic-tetragonal ferroelectric phase transition in lead-free $(K_{0.5}Na_{0.5})NbO_3$-x%$LiNbO_3$ solid solution. J. Appl. Phys. **111**, S84–S13 (2012)
8. D. Kobor, B. Guiffard, L. Lebrun et al., Oxygen vacancies effect on ionic conductivity and relaxation phenomenon in undoped and Mn doped PZN-4.5PT single crystals. J. Phy. D: Appl. Phys. **40**, 2920–2926 (2007)
9. M. Jiang, C.A. Randall, H. Guo et al., Seed-free solid-state growth of large lead-free piezoelectric single crystals: $(Na_{1/2}K_{1/2})NbO_3$. J. Am. Ceram. Soc. **98**, 2988–2996 (2015)
10. J.R. Macdonald, W.B. Johnson, *Fundamentals of Impedance Spectroscopy. Impedance Spectroscopy* (2005), pp. 1–26
11. D.C. Sinclair, A.R. West, Impedance and modulus spectroscopy of semiconducting $BaTiO_3$ showing positive temperature coefficient of resistance. J. Appl. Phys. **66**, 3850–3856 (1989)
12. J. Suchanicz, The low-frequency dielectric relaxation $Na_{0.5}Bi_{0.5}TiO_3$ ceramics. Mater. Sci. **55**, 114–118 (1998)
13. D.C. Sinclair, A.R. West, Electrical properties of a $LiTaO_3$ single crystal. Phys. Rev. B Condens. Matter **39**, 13486–13492 (1989)
14. V.V. Kirillov, V.A. Isupov, Relaxation polarization of $PbMg_{1/3}Nb_{2/3}O_3$(PMN)-A ferroelectric with a diffused phase transition. Ferroelectrics **5**, 3–9 (1973)

15. A. Niemer, R. Pankrath, K. Betzler, Dielectric properties and the phase transition of pure and cerium doped calcium-barium-niobate. J. Phys.-Condens. Mat. **2**, 80–84 (2012)
16. K. Uchino, S. Nomura, Dielectric properties and the phase transition of pure and cerium doped calcium-barium-niobate. Ferroelectrics **50**, 191–196 (1983)
17. P. Han, Q. Li, Y.X. Zhu, Mutation of causes meristem defects by failing to confine expression to the organizing center. Spectrochim. Acta Part A J. Mol. Spectrosc. **44**, 853–853 (2008)
18. S. Poykko, D.J. Chadi, First principles study of Pb vacancies in $PbTiO_3$. Appl. Phys. Lett. **76**, 499–501 (2000)
19. S. Steinsvik, R. Bugge, J.G. Jonnes, The defect structure of $SrT_{1-x}FexO_{3-y}$ (x = 0–0.8) investigated by electrical conductivity measurements and electron energy loss spectroscopy (EELS). J. Phys. Chem. Solids **58**, 969–976 (1997)

Solidification Structure of Metastable Immiscible Cu–Fe Alloy Under Different Cooling Rates

Shichao Liu, Hang Li, Jinchuan Jie, Guomao Yin and TingJu Li

Abstract The experimental Cu–10 wt% Fe alloy was prepared by high frequency induction melting and arc melting, respectively. The corresponding microstructure and phase structure of alloy were investigated. The results show that the microstructure of the alloy prepared by high frequency induction melting exhibited Fe-rich droplets and Fe-rich dendrites developed in the copper matrix, suggesting the occurrence of the normal liquid-solid transformation as well as the liquid-liquid phase separation during solidification. Meanwhile the Oswald ripening and coagulation of Fe-rich droplets were also observed in the sample. Moreover, the Fe-rich droplets mainly segregated at the center of sample due to the combined effect of Stokes motion and Marangoni migration. However, the solidification microstructure of the alloy obtained by arc melting presented cellular Fe-rich dendrites in the copper matrix. There was no evidence of the liquid-liquid phase separation. Instead, the alloy experienced liquid-solid transformation during solidification. In general, all the experimental alloy are found to display a crystalline structure of BCC ε-Cu and FCC α-Fe.

Keywords Cu–Fe alloy · Solidification · Phase separation · Coagulation

Introduction

Cu–Fe alloys possess high strength and high thermal conductivity, as well as relative high electrical-conductivity, and also exhibits giant magnetoresistance and other outstanding physical properties [1–4]. Moreover, Fe is a common and cheap metal, widely used in daily life and industry, and also is abundant on Earth.

S. Liu · H. Li · J. Jie (✉) · G. Yin · T. Li
School of Materials Science and Engineering, Dalian University of Technology, Dalian 116024, China
e-mail: jiejc@dlut.edu.cn

S. Liu
e-mail: liushichao0719@163.com

© Springer Nature Singapore Pte Ltd. 2018

Y. Han (ed.), *Advances in Materials Processing*, Lecture Notes in Mechanical Engineering, https://doi.org/10.1007/978-981-13-0107-0_58

Therefore it has great potentials to be used as materials for magnetic recording, optical devices and sensors. Increasing interests have been paid to the Cu–Fe alloys in recent years. However, due to the existence of the metastable immiscible gap in the liquid state, Cu–Fe alloy is prone to take place the liquid-liquid separation, even under microgravity or zero gravity condition. Thus the preparation of the Cu–Fe alloy especially with high Fe content is still a challenge during the conventional solidification process, which certainly limits the application of the alloy. Therefore, more and more attention has been paid to the solidification behavior of the Cu–Fe alloy. Y. Nakagawa [5] studied the solidification behavior of Cu–Fe alloy under the undercooled condition, where he firstly found the liquid-liquid phase separation phenomenon. Since then, researchers calculated the thermodynamic properties and found that the Cu–Fe alloy shows a large and positive enthalpy of mixing [6, 7]. Chuang and Chen et al. [8, 9] calculated binary Cu–Fe phase diagram from the view of thermodynamics and confirmed the existence liquid immiscibility gap of alloy. He and Zhao et al. [10–12] manufactured different size of Powders of Cu–Fe alloy by using the high-pressure gas atomization technique to study microstructure evolution in the atomized droplets during solidification and also presented a model to quantitatively analyze the microstructural evolution during the metastable liquid–liquid phase seperation. Wang and Shi et al. [13–15] prepared self-organized the core-shell or core-shell-core egg-typed microstructure by high-pressure gas atomization, meanwhile the corresponding formation mechanism of the microstructure was clarified and analyzed. Wang et al. [16] studied phase separation process of Cu–Fe melt from the view of molecular dynamics, and found the existence of inhomogeneity and segregation on atomic scale. In this present paper, the Cu–10 wt% Fe alloy is prepared by different methods. The obtained microstructure of the alloy was analyzed to study the solidification structure of metastable immiscible Cu–Fe alloy under different cooling conditions. Meanwhile the corresponding formation mechanism is also clarified in this article.

Experimental

The experimental Cu–Fe alloys were prepared by melting electrolytic copper (99.9% purity) and iron (99.97% purity). The alloy prepared by high frequency induction melting was carried out under the protection of argon gas, then the alloy was casted into a graphite mould with 20 mm in diameter and 50 mm in height. The alloy prepared by arc melting was also melt under the protection of argon gas. The alloys were repeatedly melted about several times to ensure sufficient mixing of all components for homogeneity. Then the alloy was directly solidified in a water-cooled copper hearth. In case of the different density of the Cu and Fe resulting in the buoyancy-driven floatation in experimental alloy, the specimens were sectioned in half, following the direction of gravity to get a representative view of the microstructures. The samples were then polished and etched by a solution consisting of 95 ml CH_2COOH, 5 ml HCl, and 5 g $FeCl_3$. Microstructures

were observed by using an OLYMPUS GX51 optical microscope and a scanning electron microscope (SEM, Zeiss supra 55), equipped with an Energy Dispersive Spectrometer (EDS) operated at secondary electron mode and with an accelerating voltage of 15 kV. The chemical compositions of Fe-riches phases and the copper matrix were analyzed by SEM energy dispersive spectrometry (EDS), and the crystal structure of as-cast samples was characterized by an X-ray diffractometer (XRD, EMPYREAN with Cu radiation target) with the 2Θ scan ranging from 20 to 100° at a speed of 4°/min.

Results and Discussion

Figure 1 shows the complete binary Cu–Fe alloy phase diagram including metastable miscibility gap [8, 9]. Cu–Fe is a typical kind of peritectic system, possessing a relatively flat liquidus and positive deviation from Raoul's law. Thus the binary Cu–Fe alloy system exhibits a metastable immiscible gap which has already been proven both from thermodynamic calculation and experiment, as shown by dotted line in Fig. 1. If the alloy undercools into the metastable immiscible gap, the liquid-liquid phase separation would take place and would inevitably decompose into two liquids. Generally, the two liquids are immiscible with each other. As for a given composition alloy, whether metastable liquid-liquid phase separation occurs or not mainly depends on the degree of undercooling. In this paper, the interval between liquidus and the metastable liquid gap is defined as ΔT_{cu}. If the undercooling of the liquid alloy is less than ΔT_{cu}, the solidification of the alloy occurs above the miscibility gap boundary, and then the liquid–solid transformation occurs. The γ-Fe first solidifies as primary phase. Subsequently, the further cooling leads to the peritectic transformation at 1361 K, i.e. γ-Fe + L → ε-Cu and then the transformation of γ-Fe → α-Fe + ε-Cu takes place at $T_{\alpha \leftrightarrow \gamma}$ = 1123 K. If the undercooling of the liquid alloy exceeds ΔT_{cu}, the solidification occurs below

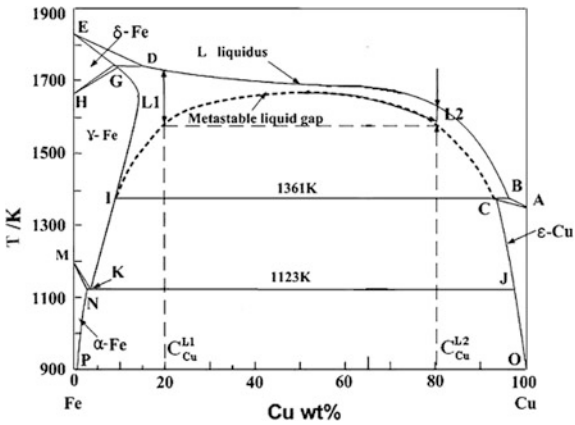

Fig. 1 The binary Cu–Fe alloy phase diagram

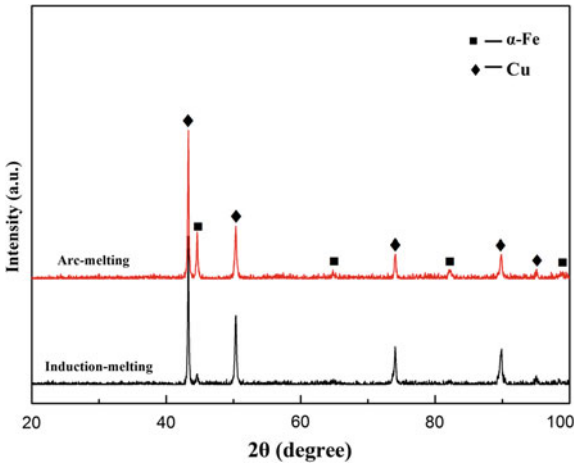

Fig. 2 XRD patterns of experimental prepared Cu–10 wt% Fe alloys

the miscibility gap boundary, the liquid–liquid transformation, so-called metastable phase separation, takes place. i.e. L → L_1(Fe-rich) + L_2(Cu-rich). After liquid–liquid separation, the Fe-rich L_1 phase and the Cu-rich L_2 phase would follow different solidification paths due to the fact that each liquid experiences its own undercooling. Meanwhile, the Fe-rich phase L_1 phase would firstly solidify due to the large undercooling during the solidifation.

Figure 2 presents XRD patterns of experimental prepared Cu–10 wt% Fe alloys by high frequency melting. All alloys display a crystalline structure of BCC ε-Cu and FCC α-Fe regardless of preparation method, which indicates that Cu has not reacted with Fe to form any intermetallic compounds.

Figure 3 shows the microstructure of the Cu–10 wt% Fe alloy obtained by high frequency melting. It can be clearly seen that the Fe-rich dendrites (Fig. 3b) uniformly and arbitrary distributed in the copper matrix. The random distribution of Fe-rich dendrites is mainly due to the uncertainty of the concentration fluctuation in alloy melt. In addition, a certain crystallographic relationship also exists between the primary dendrite arms in one nucleated dendrites. However, the dendrites formed by different nucleation doesn't exist a specific crystallographic orientation. Meanwhile, it can be also found that the spherical Fe-rich droplets (as magnified in Fig. 3c) exists in the Cu–10 wt% Fe alloy, with size ranging from 40 to 200 μm. As confirmed by the EDS analysis (shown in Fig. 3d), the Cu concentration in the spherical Fe-rich droplets is about 29.08 wt%, which results from of the liquid–liquid transformation.

According to the above analysis, if the actual undercooling of the alloy melt is not high enough to enter into the metastable immiscible gap, the alloy would solidify in normal liquid-solid transformation way. Thus the Fe-rich dendrites would precipitate. Therefore, most of the Cu–10 wt% Fe alloy melt solidified in graphite crucible has experienced the liquid-solid transformation and further solidified in the form the Fe-rich dendrites. However, if the actual undercooling of

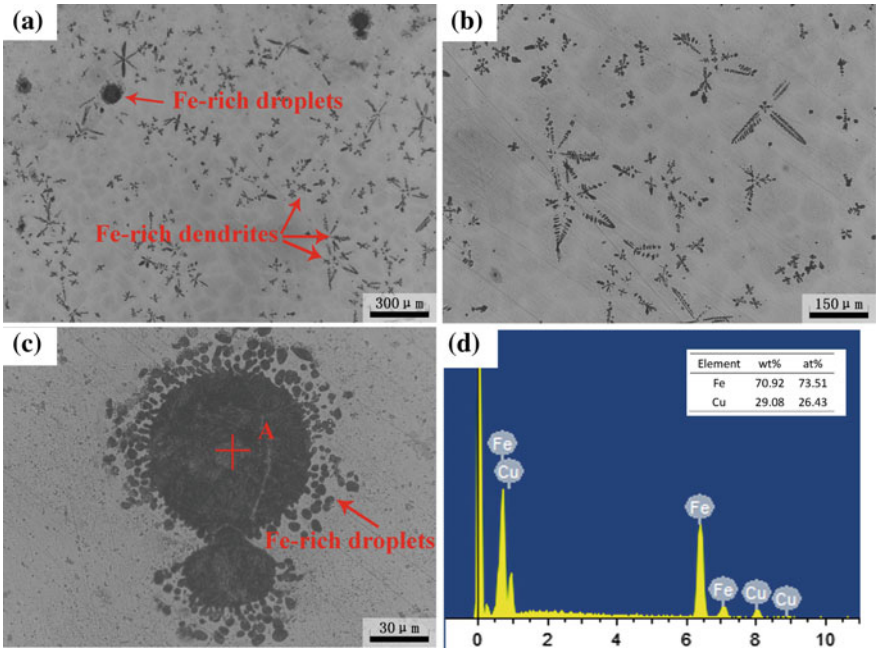

Fig. 3 Microstructure of Cu–10 wt% Fe alloy by high frequency induction melting, **b** and **c** are the enlarged image of **a**, **d** the EDS result of point A

the alloy melt can enter into the metastable immiscible gap, the liquid-liquid phase separation occurs, the alloy melt would sperate into the Fe-rich and Cu-rich phase. The Fe-rich phase tends to form the spherical droplets in order to reduce the interfacial energy. Thus, the spherical Fe-rich droplets are the result of the liquid-liquid phase speration. In general, the Cu–10 wt% Fe alloy prepared by high frequency melting not only occurs the liquid-solid transformation but also undergoes the liquid-liquid phase separation.

Particular notable, an interesting phenomenon can be observed in Fig. 3c, the spherical Fe-rich droplets after the liquid-liquid phase separation are collided and coagulated with each other. Besides, many small spherical Fe-rich droplets surrounds and moves towards the nearest larger Fe-rich droplet, further suggesting the coagulation of the small Fe-rich droplets with the larger one after the liquid-liquid phase separation. According to the previous studies [10–15], the motion of the minor phase droplets is mainly controlled by Brown motion, Oswald ripening, Stokes movement and Marangoni migration. After the liquid-liquid phase separation, the minor phase droplets nucleated and formed the spherical droplets. At the beginning, due to the small radius of the minor phase droplets, the motion mainly depends on the Brown motion, and then undergoes Oswald ripening. However, when the radius of droplet increases to a certain extent, the Brown motion and Oswald ripening effect is not obvious. Instead, the motion of the droplets are

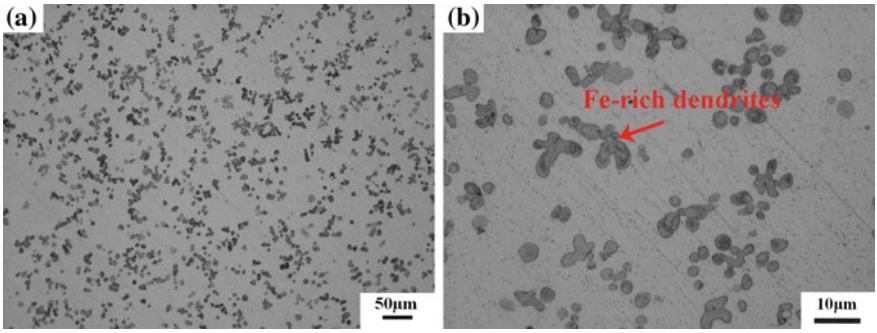

Fig. 4 Microstructure of Cu–10 wt%Fe alloy by arc-melting

dominated by the concurrent actions of the Marangoni migration and the stokes motion. Meanwhile, both the velocity of Marangoni migration and the stokes motion are proportional to the radius of Fe-rich droplets. Therefore, a large droplet may overtake a small one, thus the collision and coagulation would take place. As a result, during the moving process, each droplet is in collision with another and becomes larger in size. Consequently a new larger droplet would generate.

Figure 4 shows the microstructure of Cu–10 wt% Fe alloy prepared by arc melting. As can be seen, the Fe-rich dendrites uniformly and randomly distributed in the copper matrix, with size about 2–4 μm. Compared with the alloy prepared by high frequency melting, no developed dendrites can be found. Meanwhile there is no sign of spherical Fe-rich droplets, suggesting no occurrence of liquid-liquid phase separation in sample obtained by arc melting. Due to the high cooling rate, the Fe-rich dendrites show cellular morphology.

Summary

1. The Cu–10 wt% Fe prepared by high frequency melting not only undergoes the liquid-liquid phase but also undergoes the liquid-solid transformation. However, the liquid-liquid phase separation can't be found in the sample by arc melting. Moreover, both the experimental alloy display a crystalline structure of BCC ε-Cu and FCC α-Fe, regardless of preparation method.
2. The Cu–10 wt% Fe alloy obtained by high frequency melting shows well-developed Fe-rich dendrites after solidification. While the Cu–10%Fe alloy obtained by arc melting experienced the normal solidification phase and exhibits the finely cellular Fe-rich phases.
3. The liquid-liquid phase separation take place in the Cu–10 wt% Fe alloy prepared by high frequency melting. Meanwhile the Oswald ripening and coagulation process has been found due to Stokes motion and Marangoni migration.

Acknowledgements The authors gratefully acknowledge the supports of National Natural Science Foundation of China (Nos. 51501028, 51690163, 51471042, 51525401).

References

1. J.D. Verhoeven, S.C. Chueh, E.D. Gibson, Strength and conductivity of in situ Cu–Fe alloys. J. Mater. Sci. **24**(5), 1748–1752 (1989)
2. C. Biselli, D.G. Morris, Microstructure and strength of Cu–Fe in Situ, composites after very high drawing strains. Acta Mater. **44**(2), 493–504 (1996)
3. K. Liu, Z. Huang, X. Zhang et al., Influence of Ag micro-alloying on the thermal stability and ageing characteristics of a Cu–14Fe in-situ composite. Mater. Sci. Eng. A **673**, 1–7 (2016)
4. H. Gao, J. Wang, D. Shu et al., Effect of Ag on the microstructure and properties of Cu–Fe in situ composites. Scr. Mater. **53**(10), 1105–1109 (2005)
5. Y. Nakagawa, Liquid immiscibility in copper–iron and copper–cobalt systems in the supercooled state. Acta Metall. **6**(11), 704–711 (1958)
6. M.A. Turchanin, P.G. Agraval, I.V. Nikolaenko, Thermodynamics of alloys and phase equilibria in the copper–iron system. J. Phase Equilib. **24**, 307–319 (2003)
7. I.V. Nikolaenko, M.A. Turchanin, Enthalpies of formation of liquid binary (copper + iron, cobalt, and nickel) alloy. Metall. Mater. Trans. B **28**(6), 1119–1130 (1997)
8. Y.Y. Chuang, R. Schmid, Y.A. Chang, Thermodynamic analysis of the iron–copper system I: the stable and metastable phase Equilibria. Metall. Trans. **15A**(10), 1921–1930 (1984)
9. Q. Chen, Z. Jin, The Fe–Cu system: a thermodynamic evaluation. Metall. Mater. Trans. A **26** (2), 417–426 (1995)
10. J. He, J. Zhao, Behavior of Fe-rich phase during rapid solidification of Cu–Fe hypoperitectic alloy. Mater. Sci. Eng. A **404**, 85–90 (2005)
11. J. He, J.Z. Zhao, X.F. Wang et al., Microstructure development in finely atomized droplets of copper–iron alloys. Metall. Mater. Trans. A **36**(9), 2449–2454 (2005)
12. J. He, J.Z. Zhao, Solidification microstructure and dynamics of metastable phase transformation in undercooled liquid Cu–Fe alloys. Acta Mater. **54**, 1749–1757 (2006)
13. P.W. Cui, J.L. Xing, P.S. Rong et al., Design and formation mechanism of self-organized core/shell structure composite powder in immiscible liquid system. Appl. Phys. Lett. **91**(14), 141904–141904-3 (2007)
14. R.P. Shi, Y. Wang, C.P. Wang et al., Self-organization of core-shell and core-shell-corona structures in small liquid droplets. Appl. Phys. Lett. **98**(20), 204106–204106-3 (2011)
15. C.P. Wang, X.J. Liu, I. Ohnuma et al., Formation of immiscible alloy powders with egg-type microstructure. Sci. **297**(5583), 990–993 (2002)
16. H.P. Wang, B.B. Wei, Chin. Sci. Bull. **56**, 3416 (2011)

Microstructure and Properties of Nickel-Based Superalloy Prepared by Two-Phase Zone Directional Solidification

Xue-Feng Liu, Zhang-Ke Wang, Ang Li and Bao-Qiang Yin

Abstract The principle of two-phase zone directional solidification technique is presented in this paper, taking the GH4738 nickel-based superalloy as the object, under the conditions of the mold temperature at 1350 °C and withdrawing speed from 3 to 6 mm/min. GH4738 nickel-based superalloy billets were prepared by two-phase zone directional solidification equipment developed all by the authors. The microstructure and mechanical properties of two-phase zone directionally solidified GH4738 nickel-based superalloy were investigated by metallographic microscope and mechanical testing machine. The effect of withdrawing speed on the microstructure and mechanical properties of the alloy were studied. The results show that, the microstructure of two-phase zone directionally solidified GH4738 nickel-based superalloy was composed of irregular columnar crystals with the branches. As the withdrawing speed increased from 3 to 6 mm/min, the grain size of the columnar crystal decreased, the branches' number of the columnar crystals increased, the tensile strength of the alloy increased from 823 to 844 MPa, the elongation decreased from 43.3 to 36%. When the mold temperature was 1350 °C, the withdrawing speed was 6 mm/min, the tensile strength was 844 MPa and the elongation was 36%. Compared with the traditional vacuum induction melting of cast, the tensile strength of nickel-based superalloy GH4738 increased 20 MPa and the elongation increased by 9.2%. The nickel-based superalloy billets prepared by two-phase zone directional solidification had higher comprehensive mechanical properties.

Keywords Two-phase zone directional solidification · Nickel-based superalloy Microstructure and properties · Evolution law

X.-F. Liu (✉) · Z.-K. Wang · A. Li · B.-Q. Yin
School of Materials Science and Engineering, University of Science and Technology Beijing, Beijing 100083, China
e-mail: liuxuefengbj@163.com

X.-F. Liu
Beijing Laboratory of Metallic Materials and Processing for Modern Transportation, University of Science and Technology Beijing, Beijing 100083, China

© Springer Nature Singapore Pte Ltd. 2018

Y. Han (ed.), *Advances in Materials Processing*, Lecture Notes in Mechanical Engineering, https://doi.org/10.1007/978-981-13-0107-0_59

Introduction

With the development of aviation engines and industrial gas turbines, higher imported gas turbine inlet temperature is required, so as to increase the thrust, improve efficiency and reduce fuel consumption, which put forward higher requirements for superalloy and process [1]. The development of aviation and industrial gas turbines has always depended on the improvement of the properties of superalloys, and also promoted the development of superalloys [2]. With the continuous improvement of the turbine inlet temperature, the environment engine components work becomes worse, the superalloy components must withstand greater thermal and mechanical stress, the increasement of this stress leads to reducing the life of the total components' life. Especially those with complex working conditions, in addition to ensuring sufficient strength, it is also necessary to ensure good plasticity and toughness. For example, the use temperature of the wheel parts of the turbine rotor is approximately 700 °C, but the centrifugal force is very high, so the requirements for superalloy wheel has high tensile strength, yield strength and good plasticity [3].

Liu et al. [4] have studied that the continuous directional solidification in the two-phase zone can greatly improve the strength and plasticity of the alloy, and obtained a good comprehensive mechanical property. Besides alloy under the temperature of the two-phase zone has the advantages of high viscosity, easy to control, weak oxidation of alloy elements, small solidification shrinkage and improved service life of dies, therefore, the development of a new two-phase zone directional solidification technology is of great significance for the improvement of the properties of superalloy. Based on all this, the GH4738 nickel-based superalloy is taken as the research object to make billets, and then the microstructure and mechanical properties of GH4738 nickel-based superalloy prepared by two-phase zone directional solidification under different processing conditions were analyzed to investigate the changing law of the microstructure and mechanical properties, aiming to control the microstructure of the alloy so as to improve the using or processing performance of the superalloy.

Material and Experimental Procedures

Two-phase zone directional solidification technology (TZDS), referred to the mold temperature controlled in the temperature that ranged from solidus temperature to liquidus temperature, then dropped the molten metal and the mold together into liquid metal, the advantage of this method was that a stable temperature gradient can be obtained in the process of directional solidification with temperature controlled mold, and the billets with good mechanical properties could be prepared. The schematic diagram of two-phase zone directional solidification technique was shown in Fig. 1.

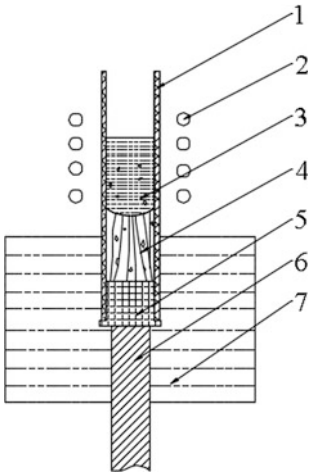

Fig. 1 Schematic diagram of two-phase zone directional solidification. 1—Mold; 2—temperature control coil; 3—alloy under two-phase zone temperature; 4—solidified alloy; 5—molybdenum bottom; 6—pull rod; 7—liquid metal

Table 1 Nominal composition of GH4738 alloy (wt%)

C	Si	Mn	Co	Cr	Mo	Ti	Al	Zr
0.038	0.116	0.003	12.98	19.12	4.44	3.10	1.37	0.027
B	Fe	Cu	P	S	Pb	Bi	Ag	Ni
0.005	0.172	0.029	0.0055	0.001	≤ 0.001	≤ 0.0001	≤ 0.0005	Rest

The experimental material was GH4738 nickel-based superalloy. The temperature range of the solid-liquid two-phase zone was 1325–1375 °C, and the composition of the alloy was shown in Table 1.

Two-phase zone directional solidification GH4738 superalloy billets were prepared by self-developed two-phase zone directional solidification equipment, the schematic diagram of the device was shown in Fig. 2. The device was mainly composed of ceramic mold, temperature control coil, graphite heater, withdrawal mechanism, liquid metal cooling pond, cooling water tank. Through temperature control coil with the graphite heater, the mold was heated until the alloy was melted at the temperature higher than two-phase zone that of the alloy, and then maintained the mold temperature in two-phase zone that of the alloy, the last opened withdrawing mechanism to drop molten metal and mold into the liquid metal cooling pool together [5]. During the dropping process, the mold remaining in the temperature control coil was always maintained in the temperature range of the alloy two-phase zone, the heat was absorbed by the liquid metal cooling circulating water in the water tank to ensure the cooling capacity, thus forming a temperature gradient

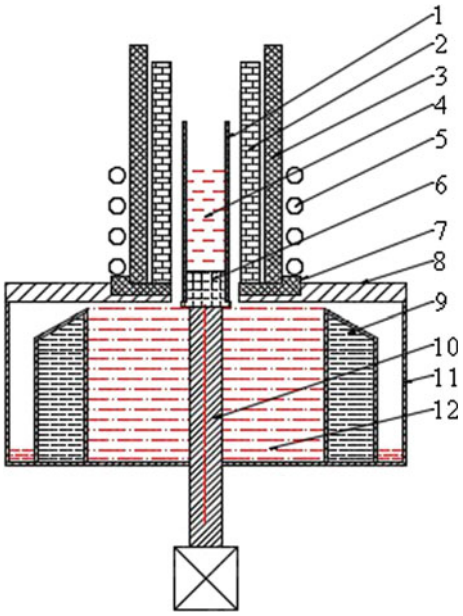

Fig. 2 Schematic diagram of the two-phase zone directional solidification equipment. 1—Ceramic mold; 2—graphite heater; 3—ceramic insulation; 4—molten metal; 5—molten metal; 6—molybdenum bottom; 7—ceramic insulation; 8—stainless steel protective plate; 9—cooling tank; 10—stainless steel pull rod; 11—liquid metal recovery tank; 12—liquid metal

of withdrawing direction, two-phase zone directional solidification alloy billets were prepared.

According to the requirements of learning that how withdrawing speed influences the microstructure and properties of superalloy prepared by TZDS, 2 sets of experiments were designed and carried out under the condition of 4×10^{-3} Pa vacuum and an atmosphere filled with a certain amount of argon.

(1) The GH4738 superalloy weight 178 g was taken into a mold with an inner diameter of 25 mm, heated the mold to 1475 °C and kept it for 15 min, cooled down to 1350 °C and kept it for 5 min, then turned on the pull down mechanism, the mold was pulled down to the liquid metal at a rate of 3 mm/min until the end of the experiment.
(2) The GH4738 superalloy weight 184 g was taken into a mold with an inner diameter of 25 mm, heated the mold to 1475 °C and kept it for 15 min, cooled down to 1350 °C and kept it for 5 min, then turned on the pull down mechanism, the mold was pulled down to the liquid metal at a rate of 6 mm/min until the end of the experiment.

Specimens of transverse and longitudinal cross sections were intercepted from a two-phase zone directionally solidified GH4738 nickel-based superalloy, the morphology of the tissue was observed after erosion, the etchant was treated with sulfuric acid (1 ml) + hydrochloric acid (30 ml) + five water copper sulfate (4 g) + water (16 ml), the microstructure of the sample was observed under OLYMPUS BX53M optical microscope.

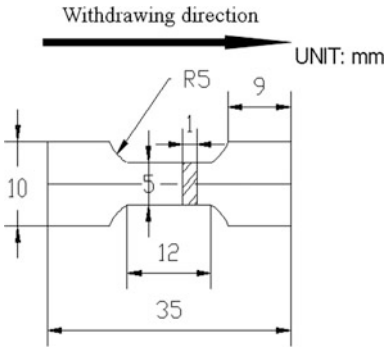

Fig. 3 Sketch of dimension of drawing sample

The axial tensile specimen of the slab was cut on the longitudinal section of the billet prepared by TZDS, the tensile dimensions of the plate are shown in Fig. 3 with the WDW-10E type universal testing machine for tensile tests.

Results and Discussion

Effect of the Withdrawing Speed on the Microstructure of GH4738 Prepared by TZDS

The cross section and longitudinal section of the billet were polished and corroded, the microstructure of GH4738 nickel-based superalloy prepared by TZDS was observed by metallurgical microscope, and the microstructure characteristics were analyzed. For the further study of different variation of withdrawing speed on the microstructure, cross slitting of cylindrical billet, continuous polishing of the cross section was carried out, and then the microstructure of billets was observed and analyzed.

Microstructure Characteristics of GH4738 Nickel-Based Superalloy Prepared by TZDS

The results of metallographic characterization of the longitudinal and cross sections of sample 1 GH4738 nickel-based superalloy were shown as irregular columnar crystal structure.

It could be seen from the Fig. 4 that the columnar crystal was irregular bifurcated in the longitudinal section of the billet, and the vertical structure was composed of vertical columnar crystal, slope columnar crystal and vertical columnar crystal. This was due to the fact that the temperature of controlled mold was always kept in the two-phase zone during the directional solidification process, the direct

Fig. 4 Longitudinal metallograph of sample 1

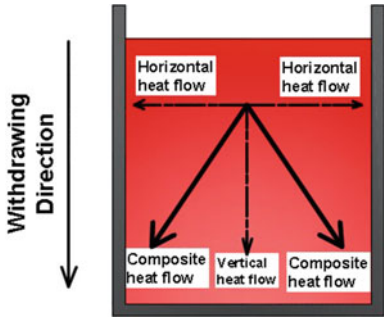

Fig. 5 Vector synthesis of heat flow

contact with the inner wall of the mold was less affected by horizontal heat dissipation, and therefore, the edge of the billet was vertical columnar crystal. The core alloy was away from the inner wall of the mold during the directional solidification, the horizontal heat dissipation was also small, and the vertical columnar crystals were also maintained, but between the two parts, the horizontal and vertical heat flow vectors were synthesized, as shown in Fig. 5, generating a sloping temperature gradient, so the microstructure of this part was sloping columnar crystal.

In the process of microstructural characterization of the cross section of the billet, it was found that the dendrite structure from edge to the core of the billet also had a corresponding law. In Fig. 6, it could be seen that the microstructure of the cross section of the billet was dendritic cross section, and the cross section's microstructure of the edge part was dendrite cross section, we could see the more

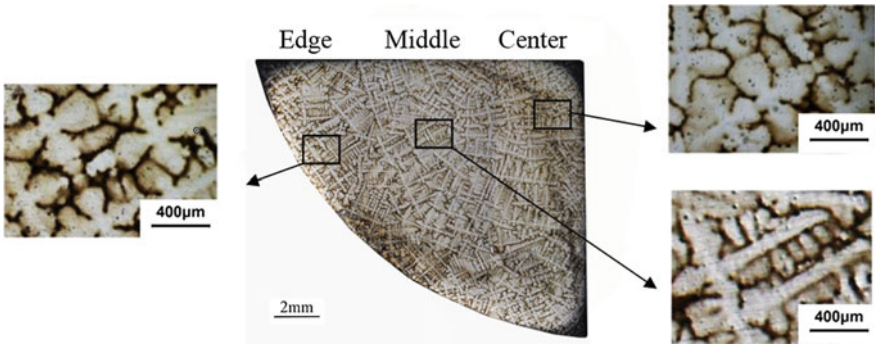

Fig. 6 Microstructure of cross section in GH4738 nickel-based superalloy

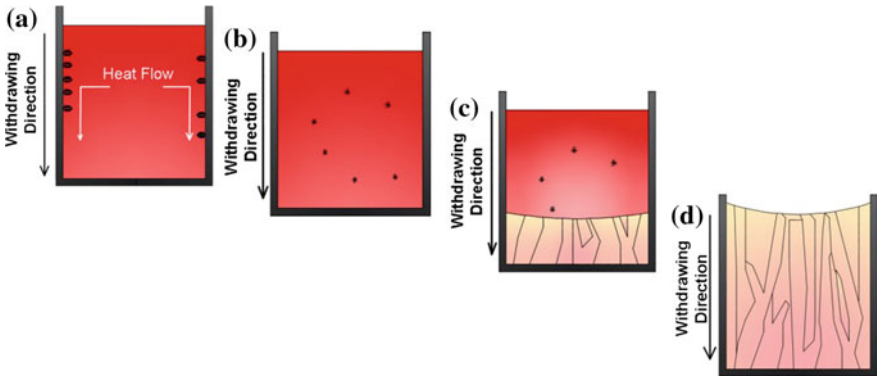

Fig. 7 Schematic diagram of microstructure of GH4738 prepared by TZDS

developed secondary dendrite between the edge and the core part, while the cross section's microstructure of the edge part was also dendrite cross section. The underdeveloped secondary dendrite of the edge and core region also showed that the horizontal heat flow at these sites was not obvious; no larger transverse temperature gradient was formed. However, the secondary dendrite was more developed between the part of the edge and the core. It was clear that there is obvious horizontal heat flow in this section. The growth direction of the secondary dendrite was opposite to that of the horizontal temperature gradient, so the temperature gradient at the part between the edge and the core was directed from the core to the edge [6].

The microstructure of solidified nickel-based superalloy billets prepared by TZDS was irregular columnar with branches, the schematic diagram of its formation was shown in Fig. 7.

During the two-phase zone directional solidification process, the temperature of the mold was kept in the temperature range of the solid-liquid two-phase zone by a

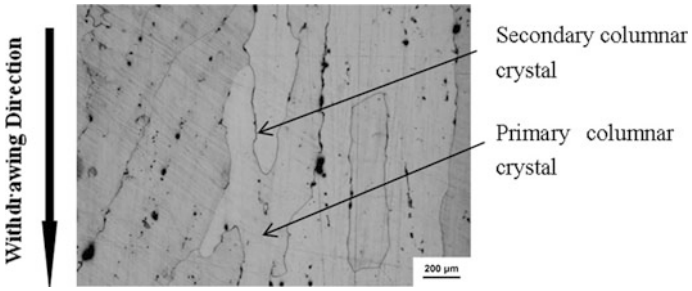

Fig. 8 Microstructure of longitudinal section in sample 1

temperature controlled coil, on the inner wall of the mold, heterogeneous nucleation forms some dendrites, because of the heat flow in the superalloy under the temperature of two-phase zone, some of the dendrite arms on the casting wall fused and fell, and then distributed as the nucleation core in the two-phase zone alloy [7]. When the mold and alloy were integrally dropped into liquid metal, columnar crystals grew in the opposite direction of the temperature gradient, when the solid-liquid interface was pushed forward, the nucleation core fell into the supercooled region, the crystal nucleus grew rapidly and occupied the space of grain growth at the temperature gradient, the initial columnar growth was hindered, dendritic growth between the new columnar crystals led to the growth of primary columnar crystals that bypass these grains [8]. However, as the columnar crystals continued to grow in the directional solidification process, it was difficult to be completely encapsulated, thus forming a primary columnar crystalline semi-wrapped columnar microstructure. The microstructure of the longitudinal section of the billet was observed and analyzed at first (Fig. 8), and then the cross section of the billet was further characterized, the branches of the columnar crystals found in the longitudinal section of the billet, shown to be a structure of that columnar crystals were branched into adjacent columnar crystals on the cross section, the self-enclosed grain was shown to be close to the main columnar crystal on the two-dimensional section of the cross section shown in Fig. 9, the special microstructure featured that the self-enclosed grain in the two-dimensional microstructure could be used as the criterion for the branches of the columnar crystals, and this provided a condition for further quantitative analysis of billet microstructure.

Microstructure Quantification and Change Law of GH4738 Nickel-Based Superalloy Prepared by TZDS

In order to further quantify the microstructure characteristics of GH4738 nickel-based superalloy prepared by TZDS, quantitative statistics should be taken

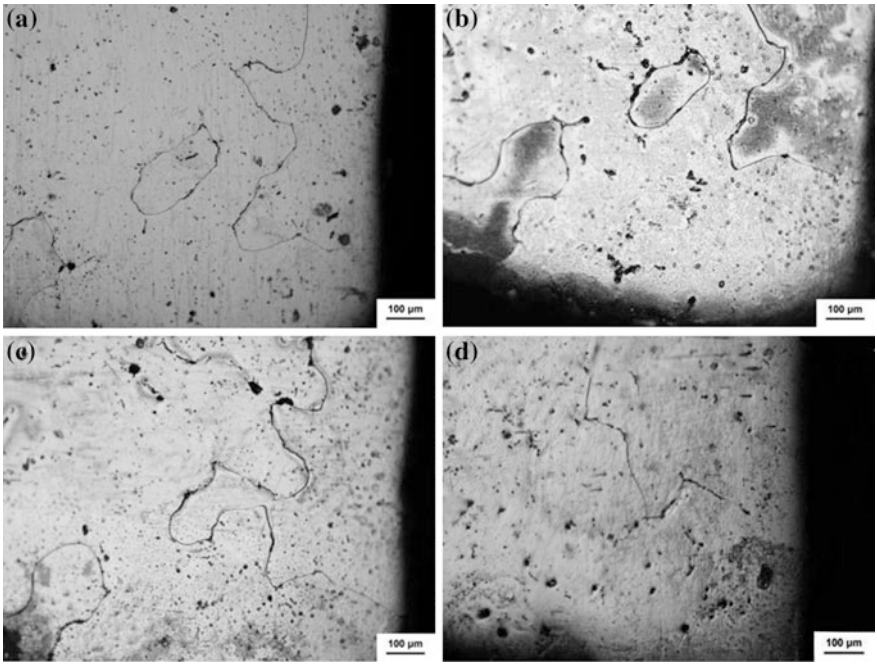

Fig. 9 Microstructure of columnar crystals branched into adjacent columnar crystals on cross section of sample 1. **a** Surface of plate; **b** about 50 μm from surface; **c** about 100 μm from surface; **d** about 150 μm from surface

from the number and size of the columnar crystals. 1/4 was taken as the sample on billet 1 and 2 respectively, the cross section of the sample was continuously polished and its morphology was obtained, the number and size of columnar crystals and the number of branches of columnar crystals were calculated respectively.

For sample 1 and 2, 20 layers of continuous grinding were carried out from the final setting, the grinding depth of each layer was about 50 μm, the overall grinding thickness was around 1 mm, and then the microstructure of each layer was combined to quantify the microstructure. Samples 1 and 2 begun to be ground in the same position and the thickness of the two were same, so the result of quantifying the tissue within this length was taken as a sample, so as to compare the microstructure of billets under the condition of different withdrawing speed.

Number of Columnar Crystals

The number of columnar crystals in the 20 layers metallographic structure of cross section was statistically analyzed, and average values were taken as the number of columnar crystals on the fan-shaped cross section of 1/4 cylindrical billets, we

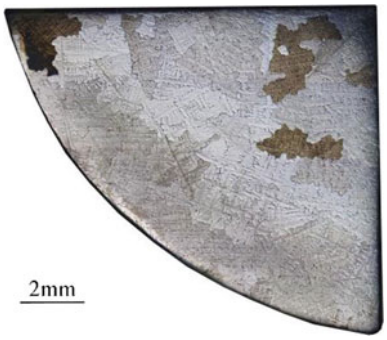

Fig. 10 Metallographic structure of 10th layers on cross section of sample 1

could get that the number of columnar crystals was 41. Metallographic structure of 10th layers on cross section of sample 1 was set as an example shown in Fig. 10.

Columnar Grain Size

The grain size intercept function was evaluated using the OLYMPUS BX53M microscope, the columnar crystal size was calculated, and the average size of the columnar crystals was obtained. The size of the columnar crystal was 953 μm.

Branch Number of Columnar Crystal

The branches of columnar crystal on a two-dimensional metallograph of a cross section behaved like self-enclosed grain close to the main columnar crystals, so the location and number of such two-dimensional self-enclosed small grains were recorded statistically in the continuous grinding observation process, quantified the number of branches on columnar crystals. The number of the branched was 10 for sample 1.

In the same way, the quantitative statistics of the microstructure of sample 2 were given. Table 2 was the statistical result. N represented the number of columnar crystals; D represented the columnar grain size; n represented the number of branches present in the columnar crystals.

Table 2 Quantitative parameters of microstructure of nickel-based superalloy prepared by TZDS

Sample No.	N	D (μm)	n
1	41	953	10
2	53	740	16

Effect of the Withdrawing Speed on the Mechanical Property of GH4738 Prepared by TZDS

The test results of mechanical properties of different withdrawing speed of the GH4738 nickel-based superalloy billets prepared by TZDS were as follows (Tables 3 and 4), when the mold temperature was 1350 °C and the withdrawing speed was 3 mm/min, the tensile strength was 823.4 MPa, the elongation was 44.3%; when the mold temperature was 1350 °C and the withdrawing speed was 6 mm/min, the tensile strength was 844.1 MPa, the elongation was 36%. The mechanical properties of cast nickel-based superalloy GH4738 for vacuum induction melting model was tested for comparison.

Comparing the results of the two sets of experiments, we could get that as the withdrawing speed increased from 3 to 6 mm/min, the tensile strength increased from 823.4 to 844.1 MPa, the elongation decreased from 44.3 to 36%. This was because the number of columnar crystals increased and the number of branches on columnar crystals increased as the withdrawing speed increased. On the one hand, the number of columnar crystals increased, according to Holzer-Page formula, the strength of polycrystalline materials was related to grain size. The finer the grain was, the higher the strength was, therefore, the number of columnar crystals increased, which was equivalent to grain refinement, and then led to the increasement of tensile strength. The branches of columnar crystals were equivalent to the introduction of transverse grain boundaries, when a dislocation slips in a columnar crystal, it would have piled up in this part of transverse grain boundaries, greater external stress was needed, and therefore, tensile strength was improved. On the other hand, pile up of dislocation equivalent to hinder dislocation motion, resulting in the elongation decreased [9].

The mechanical properties of GH4738 nickel-based superalloy prepared by vacuum induction casting were tested and compared with those prepared by TZDS. The mechanical properties of GH4738 nickel-based superalloy in the direction of casting prepared by vacuum induction casting was shown in Table 5.

Table 3 Mechanical properties of sample 1 GH4738 nickel-based superalloy prepared by TZDS

Sample No.	Tensile strength (MPa)	Average (MPa)	Elongation (%)	Average (%)
1	823.5	823.4	43.9	44.3
2	823.2		44.7	

Table 4 Mechanical properties of sample 2 GH4738 nickel-based superalloy prepared by TZDS

Sample No.	Tensile strength (MPa)	Average (MPa)	Elongation (%)	Average (%)
1	828.1	844.1	33.8	36.0
2	860.0		38.1	

Table 5 Mechanical properties of GH4738 alloy prepared by vacuum induction casting

Sample No.	Tensile strength (MPa)	Average (MPa)	Elongation (%)	Average (%)
1	826.6	824.5	26.9	26.8
2	822.4		26.7	

In axial tension, there was coordinated deformation between axial columnar crystals, the maximum force acted on the transverse grain boundary perpendicular to the tensile direction, grain boundary sliding was easy to occur, which led to intergranular fracture. Thus, the columnar crystalline structure parallel to the tensile direction eliminated the transverse grain boundary, the grain boundary fracture could be suppressed and the plasticity could be improved remarkably. Secondly, there were many branches on the columnar grains, the dislocation would pile up in the branches on columnar crystal in the process of tensile deformation, and this effectively prevented the dislocation slipping and caused the deformation difficult, strength was also improved to some extent [10].

Conclusions

(1) The microstructure of nickel-based superalloy GH4738 prepared by two-phase zone directional solidification is composed of irregular columnar with branches.
(2) The microstructure of nickel-based superalloy GH4738 prepared by two-phase zone directional solidification is affected by withdrawing speed. When the mold temperature is 1350 °C, with the withdrawing speed increasing from 3 to 6 mm/min, the number of columnar crystals increases, while the number of branches on columnar crystal also increases.
(3) The withdrawing speed affects the mechanical properties of nickel-based superalloy GH4738 prepared by the two-phase zone directional solidification. When the mold temperature is 1350 °C, with the withdrawing speed increasing from 3 to 6 mm/min, the tensile strength of the alloy increases from 823 to 844 MPa with the elongation decreasing from 43.3 to 36.0%.
(4) The nickel-based superalloy GH4738 prepared by two-phase zone directional solidification has better comprehensive mechanical properties. Compared with the nickel-based superalloy GH4738 prepared by vacuum induction melting, the tensile strength increases by 20 MPa and the elongation increases by 9.2%.

Acknowledgements This research was financially supported by the National Natural Science Foundation of China (Grant No. 51374025) and the State Key Laboratory for Advanced Metals and Materials (2017Z-05).

References

1. C.X. Shi, Z.Y. Zhong, Development and innovation of superalloy in China. Acta Mater. **46**, 1281–1288 (2010)
2. W.G. Zhang, L. Liu, X.B. Zhao, M. Qu, Z.H. Yu, H.Z. Fu, Progress in directionally solidified superalloys. Foundry **58**, 1–6 (2009)
3. A.M. Yang, *Study of Structure Refinement and Optimization of Mechanical Properties for Superalloy K4169* (Northwestern Polytechnical University, Xi´An, 2002)
4. X.F. Liu, J.H. Luo, X.C. Wang, L. Wang, J.X. Xie, Columnar grains-covered small grains Cu-Sn alloy prepared by two-phase zone continuous casting. Prog. Nat. Sci. **23**, 94–101 (2013)
5. A.J. Elliott, T.M. Pollock, S. Tin, W.T. King, S.C. Huang, M.F.X. Gigliotti, T.M. Pollock, Directional solidification of large superalloy castings with radiation and liquid-metal cooling: a comparative assessment. Metall. Mater. Trans. A **35**, 3221–3231 (2004)
6. X. Li, A. Gagnoud, Z. Ren, Y. Fautrelle, R. Moreau, Investigation of thermoelectric magnetic convection and its effect on solidification structure during directional solidification under a low axial magnetic field. Acta Mater. **57**, 2180–2197 (2009)
7. W. Kurz, D.J. Fisher, J.G. Li, Q.D. Hu, *Fundamentals of Solidification* (Higher Education Press, Beijing, 2009)
8. Y.Z. Zhou, X.F. Sun, Effect of solidification rate on competitive grain growth in directional solidification of a nickel-base superalloy. Sci. China Technol. Sc. **55**, 1327–1334 (2012)
9. G.X. Hu, *Fundamentals of Materials Science* (Shanghai Jiao Tong University Press, Shanghai, 2010)
10. X.F. Liu, J.H. Luo, X.C. Wang, Surface quality, microstructure and mechanical properties of Cu–Sn alloy plate prepared by two-phase zone continuous casting. Trans. Nonferrous Met. Soc. China **25**, 1901–1910 (2015)

Rheological Stress Behavior of B10 Copper-Nickel Alloy During Hot Deformation Process

Jianing Zhang, Dongmei Liu, Qiangsong Wang, Fang Liu and Shuyu Yang

Abstract The variation law of internal stress-strain curves of b10 alloy at 800–1050 °C and strain rate 0.01–10 s^{-1} was studied by thermal compression test. The rheological behavior of the alloy showed the characteristic of steady state, as the rheological stress increased rapidly to the peak stress at the beginning of the strain, and then remained unchanging or slowly increase or decrease. The rheological stress of the alloy increased when the strain rate or decreasing strain temperature increased, and the discontinuous dynamic occurred in the process of thermal compression. Moreover the constitutive equation of thermal deformation was established. The stress exponent (n) of the alloy at different temperatures was calculated and the Q-equivalent of strain activation energy was calculated.

Keywords B10 alloy · Flow stress · Constitutive equations

Introduction

Copper and copper alloys are widely used in shipbuilding, petrochemical industry, national defense and military industry for their good electrical and thermal conductivity, high corrosion resistance and ductility, and easy to be processed [1]. The

J. Zhang · D. Liu · Q. Wang (✉) · F. Liu · S. Yang
General Research Institute for Nonferrous Metals, No. 2, XinJieKouWai St., Beijing, XiCheng 100088, China
e-mail: wangqiangsongbj@163.com

J. Zhang
e-mail: zjnly1199197@126.com

D. Liu
e-mail: mandyneu@163.com

F. Liu
e-mail: liufang19912015@163.com

S. Yang
e-mail: yangshuyu331@163.com

© Springer Nature Singapore Pte Ltd. 2018

Y. Han (ed.), *Advances in Materials Processing*, Lecture Notes in Mechanical Engineering, https://doi.org/10.1007/978-981-13-0107-0_60

copper alloys can be divided into high strength and high conductivity copper alloy, corrosion resistant copper alloy, easy cutting copper alloy, wear resistant copper alloy and art copper alloy.

Cupronickel is a copper alloy with nickel as the main alloy element, which was used in ancient China. Copper-nickel alloy has excellent corrosion resistance and excellent mechanical and physical properties [2, 3]. B10 copper-nickel alloy is widely used in condenser tubes of various types of ships [4], heat exchangers in coastal power plants and equipment piping system for seawater desalination due to its good corrosion resistance to flowing seawater. Although the alloy has been applied to the actual application for several decades, the alloy has experienced serious corrosion and leakage accidents in the service process [5]. Therefore, the corrosion of Cu-Ni alloy in sea water has been studied extensively [3, 6–8]. Because of the complexity of the factors involved, the corrosion mechanism of Cu-Ni alloy and how to control effectively is not fully understood. With the development of ocean and the application of Cu-Ni alloy, more and more attention is paid to the corrosion resistance of the alloy in seawater and its potential to be explored, so as to prolong service life, prevent early failure and fully service marine engineering.

Experimental

The experimental material is made of domestic b10 alloy, the composition is 10.5% Ni, 1.5% Fe, 0.5% Mn, and the allowance is Cu. The cut parts and sample size of the hot compression specimen are shown in Fig. 1, and the size of the compression specimen is $\varphi 8 \times 12$ mm cylindrical shape. In order to ensure the thermal compression stress state of the specimen is close to that of the hot extrusion of the ingot, the central axis of the hot compressed specimen is parallel to the central axis of the ingot.

Having considered the influence of the binary phase diagram of Cu-Ni alloy, DSC test results, deformation rate and deformation amount [9–12], the heat compression process parameters of b10 Cu-Ni alloy are determined as follows:

(1) Deformation temperature (T/°C): 800, 850, 900, 950, 1000, 1050, 1100.
(2) Strain rate: 0.01, 0.1, 1, 10.
(3) Total should be (ε): 60%.
(4) Before deformation, holding time: 3.
(5) Cooling mode after deformation: water cooling.

In order to reduce the friction between the two sides of the specimen and the indenter of the thermal simulation tester, a thin layer of graphite sheet was added to the contact between the two ends of the sample and the indenter. The compressed sample is quenched immediately to retain the deformed tissue. The experimental data of true stress, true strain, pressure, displacement, temperature and time are

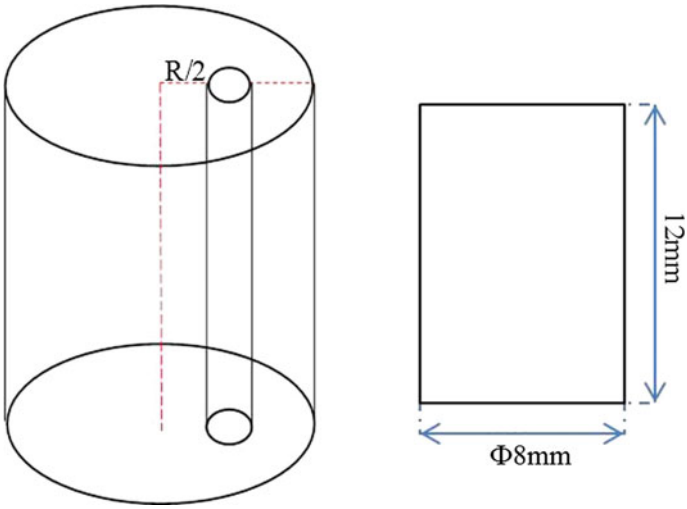

Fig. 1 Diagram of cut parts of hot compression specimen and sample size

collected by the computer of Gleeble-1500 thermal simulator, and the true stress-strain curve is drawn by origin software.

Results and Discussion

True Stress-Strain Curve of B10 Alloy

The flow stress curves of b10 alloy at different deformation rates are shown in Fig. 2. The high temperature flow stress curve of b10 alloy has the following characteristics:

(1) The rheological stress of the alloy increases rapidly to the peak value at the beginning of the strain, and then remains unchanged or slow down, and the rheological curve shows the characteristics of steady flow.
(2) Under certain strain rate, the rheological stress of the alloy decreases with the increase of temperature, and the true stress-strain curves at different temperatures show similar characteristics.
(3) At low strain rate, when the flow stress of the alloy reaches the peak value, the rheological stress of the alloy would remain unchanged or gradually decrease to the end of deformation with the increase of strain, that is, the recrystallization softening of the alloy counteracts the hardening of the alloy; Under high strain rate, the alloy has no obvious peak value with the increase of strain, the rheological stress of the alloy would remain unchanged, gradually decrease or rise to the end of deformation.

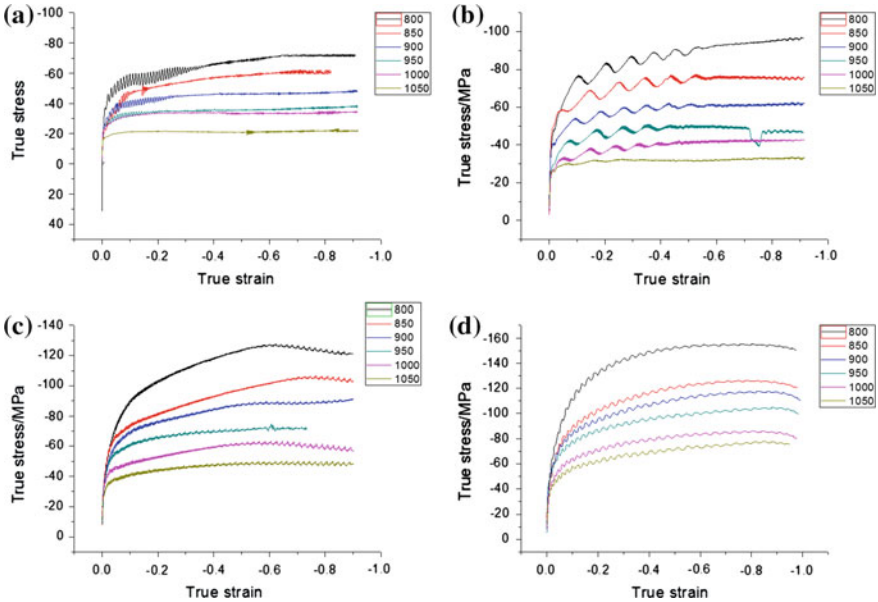

Fig. 2 Flow stress curve of b10 alloy at different strain rates **a** 0.01 s^{-1} **b** 0.1 s^{-1} **c** 1 s^{-1} **d** 10 s^{-1}

(4) At a certain deformation temperature, the strain at peak flow stress decreases when decreasing strain rate. Under certain deformation rate, the change of the alloy to peak flow stress decreases when increasing the deformation temperature.
(5) It is worth noting that under the strain rate of 0.1 s^{-1}, the deformation temperature range of 800–1000 °C, the rheological stress curve of the alloy presents a significant duo shape, which indicates that discontinuous dynamic recrystallization of the alloy occurs, that is, in the process of thermal compression deformation, the strain hardening and recrystallization softening of the alloy alternately occur.

During thermal processing, the joint action synergistic effect of hardening, dynamic recovery and dynamic recrystallization was shown in the stress strain curve. In the initial deformation stage, with the increase of strain, the dislocation density is increasing, and the flow stress increases, this stage belongs to the elastic deformation stage, with the processing hardening mainly, the dislocations would produce and tangle, the linear slope of the initial stage of deformation is basically the same at different temperatures, indicating that the elastic modulus of the alloy is independent of temperature. With the continuous increase of true strain, the rheological stress keeps constant or slow growth, and the steady state rheological characteristics occur, which is due to the dynamic equilibrium of material occurrence dynamic recovery or dynamic recrystallization and processing hardening.

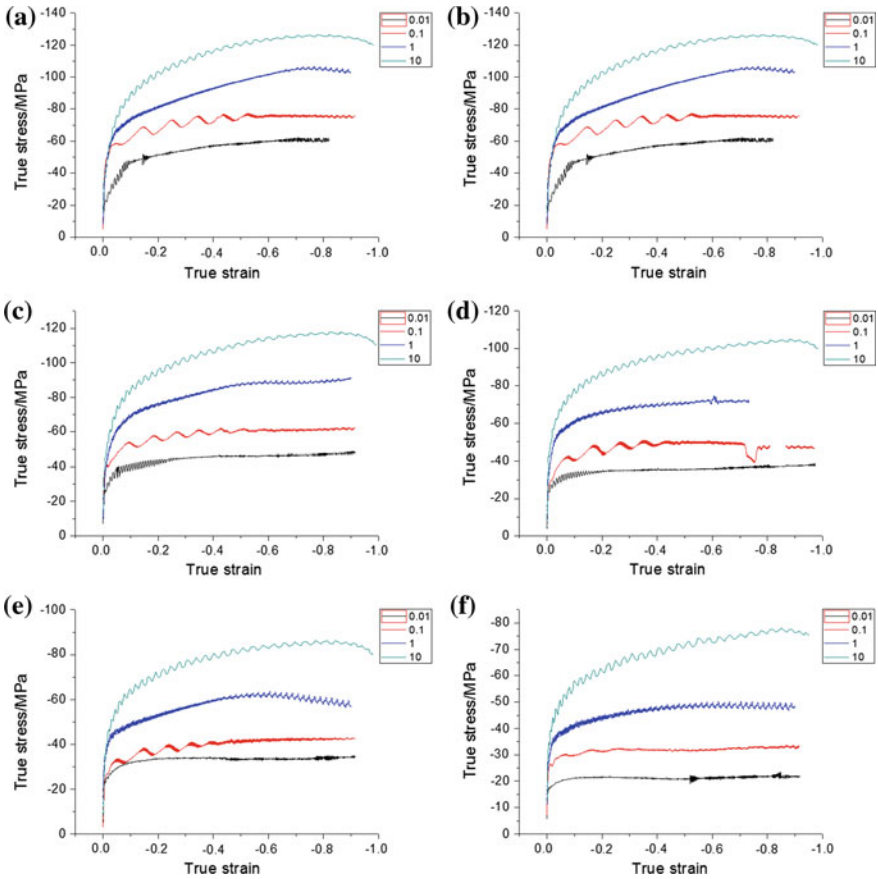

Fig. 3 Flow stress curve of b10 alloy at different temperature **a** 800 °C **b** 850 °C **c** 900 °C **d** 950 °C **e** 1000 °C **f** 1050 °C

Under the same strain rate, the rheological stress decreases with the increase of temperature. The increase of temperature leads to the enhancement of the activation process, the rise of the atomic internal energy, the decrease of various defect potential barriers, also makes it easy for the dislocations generation, then the dislocation slip and climb occurring. While the critical shear stress is reduced, the slip system is increased, and the grain boundary sliding is easy to be carried out, so that the deformation resistance is reduced, and the processing hardening produced in the plastic deformation stage is offset. The higher the temperature, the more easily the dynamic recovery or dynamic recrystallization occurs. The softening and processing hardening of the material is more easily dynamic balance, the true stress basically remains constant, that is, the deformation enters the steady-state rheological stage. In Fig. 3b, the curve of 800–950 °C shows a zigzag change, showing multiple peaks, which is a manifestation of incomplete recrystallization. During the

experiment, the process of material deformation-dynamic recrystallization-deformation is the process of alternating hardening-softening-hardening, and each trough means the appearance of dynamic recrystallization, which can easily lead to abnormal grain growth. At the same temperature, the faster the strain rate, the greater the flow stress is. The peak stress of Cu-Ni alloy at low strain rate is easy to occur. Under this condition, sufficient time can be obtained for energy accumulation, grain nucleation, grain growth and dislocation annihilation, and recrystallization can be fully performed. With the increase of strain rate, the effect of dynamic recovery or dynamic recrystallization becomes weak, and it is difficult to appear steady state, even no peak.

Establishment of Constitutive Equation

The dynamic response of material in plastic processing is the result of the comprehensive action of hardening and softening process caused by the internal microstructure evolution of materials, so the constitutive relation is highly nonlinear, and there is no universally applicable construction method [13, 14]. The high temperature deformation of metal is a thermal activation process, the effect of deformation temperature and strain rate on the convective variable stress can be based on the Arrhenius equation to establish the constitutive relationship by mathematical statistics [15], as shown in Eq. (1):

$$\dot{\varepsilon} = \mathrm{A}[\sinh(\alpha\sigma)]^n \exp(-\frac{Q}{RT}). \tag{1}$$

By simplifying reasonably, the hyperbolic sine function in the Arrhenius equation can be simplified to a power exponential function, as shown in Eq. (2). In high stress state, the hyperbolic sine function in the Arrhenius equation can be simplified as an exponential function, as shown in Eq. (3):

$$\dot{\varepsilon} = \mathrm{A}_1\sigma^{\mathrm{n1}} \exp(-\frac{Q}{RT})\ \alpha\sigma < 0.8 \tag{2}$$

$$\dot{\varepsilon} = \mathrm{A}_2 \exp(\beta\sigma) \exp(-\frac{Q}{RT})\ \alpha\sigma > 1.2 \tag{3}$$

where:

$\dot{\varepsilon}$: strain rate, s^{-1}; Q: the activation energy of material deformation, J/mol; σ: rheological stress, MPa; n: stress index; T: absolute temperature, K; R: molar gas constant, 8.314 J/(mol K); A, a1, a2, n, n1, α, β are related to the material constants, and β = α * n1.

When the temperature is constant, the Q, R, T, a1 and a2 are constants, and the logarithms of the Eqs. (2) and (3) can be obtained by Eqs. (4) and (5):

$$n_1 = \frac{\delta \ln \varepsilon}{\delta \ln \sigma}. \tag{4}$$

$$\beta = \frac{\delta \ln \varepsilon}{\delta \sigma}. \tag{5}$$

According to the Eqs. (4) and (5), the rheological stress of the alloy under different temperature conditions is obtained, the relationship curves of "$\ln\dot{\varepsilon} - \ln\sigma$" and "$\ln\dot{\varepsilon} - \sigma$" are plotted, and the values of n1 and α are determined by linear regression respectively, and then β value is obtained.

When the temperature changes, suppose Q is not related to temperature T, R, α, n and A are constants, and logarithm of logarithm on both sides of Eq. (1) to be obtained Eq. (6):

$$\ln\dot{\varepsilon} = n\ln[\sinh(\alpha\sigma)] + \ln A - Q/RT. \tag{6}$$

The formula of the Eq. 6 can be obtained by solving the partial differential equation, namely

$$Q = Rns. \tag{7}$$

The value of stress index n can be obtained by plotting the relationship curve of $\ln\dot{\varepsilon} - \ln[\sinh(\alpha\sigma)]$ and linear regression under different temperature conditions. Under different strain rate conditions, "$\ln[\sinh(\alpha\sigma)] - 1/T$" relationship curve and linear regression, the slope is the s value, and the deformation activation energy Q of the material can be calculated by Eq. (7).

Zener and hollo propose "temperature compensation strain rate" [16], zener-hollo parameter (Z parameter). The Z values are defined as:

$$Z = \dot{\varepsilon}\exp\left(\frac{Q}{RT}\right) = A[\sinh(\alpha\sigma)]^n. \tag{8}$$

The constitutive equation of alloy thermal deformation based on the Arrhenius equation and applicable to all stress States is obtained by the equivalent of the values A, n, α and Q calculated in the above process.

According to the experimental data, the peak stress (σ_p/MPa) of b10 alloy under different thermal deformation conditions is obtained to calculate the constitutive equation of thermal deformation. Under high strain rate, the rheological curve is still upward trend, without peak stress, which is not suitable to employ peak or steady flow stress, therefore, the experiment adopts the rheological stress when the true strain is 0.7. The peak stress of b10 alloy under different thermal deformation conditions is shown in Table 1.

Draw the relationship curves of "$\ln(\dot{\varepsilon}) - \sigma$" and "$\ln(\dot{\varepsilon}) - \ln\sigma$" of b10 alloy at different temperature, and use the least square method to make linear regression, as shown in Fig. 4. The β can be obtained by the average value of the slope of the three fitting lines in the high stress state in Fig. 4a, β = 0.0936. The average value

Table 1 Peak stress (σ_p/MPa) of alloy under different thermal deformation conditions at 800–1050 °C

$\dot{\varepsilon}/s^{-1}$	T/°C					
	800	850	900	950	1000	1050
0.01	72.462	62.438	48.9	38.667	34.946	23.537
0.1	97.173	77.415	62.703	50.953	42.885	33.616
1	127.92	106.64	91.311	74.674	63.493	50.256
10	155.4	126.43	117.91	104.97	86.257	78.072

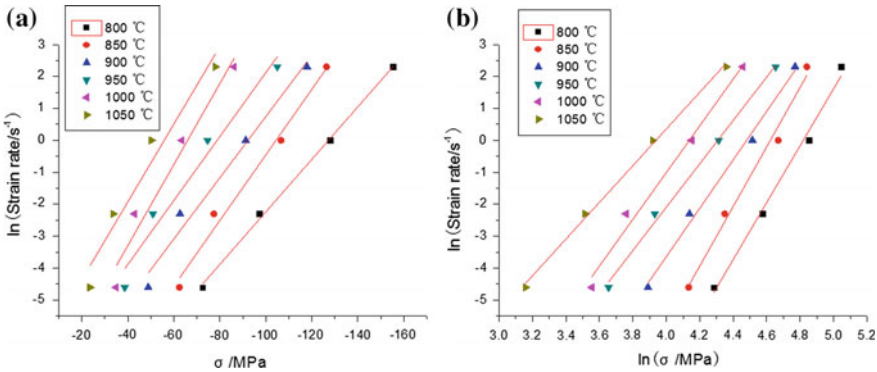

Fig. 4 Relationship between "ln$\dot{\varepsilon}$ − σ" and "ln$\dot{\varepsilon}$ − lnσ" of b10 alloy at different temperatures

of the slope of the three fitted straight lines in the low stress state of (b) is n1, n1 = 6.6198. According to Eq. (6), α value can be obtained

$$\alpha = \beta / n1 = 0.0141. \tag{9}$$

Draw the curve of "ln$\dot{\varepsilon}$ − ln[sinh(ασ)]" and linear regression under different temperature conditions. Draw the different strain rate conditions, "ln[sinh(ασ)] − 1/T" relationship curve and linear regression, as shown in Fig. 5.

Take the average of the slope of the straight line in Fig. 5a and get the n value:

$$n = 5.5302. \tag{10}$$

Take the average of the line slope of the "ln[sinh(ασ)] − 1000/T" relationship in Fig. 5b, and get the s value:

$$s = 7.0935. \tag{11}$$

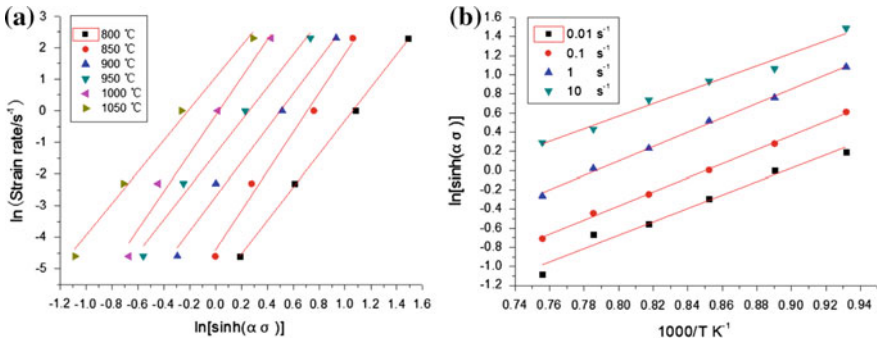

Fig. 5 Relationship between "ln$\dot{\varepsilon}$ − ln[sinh(ασ)]" and "ln[sinh(ασ)] − 1/T" of b10 alloy at different temperatures

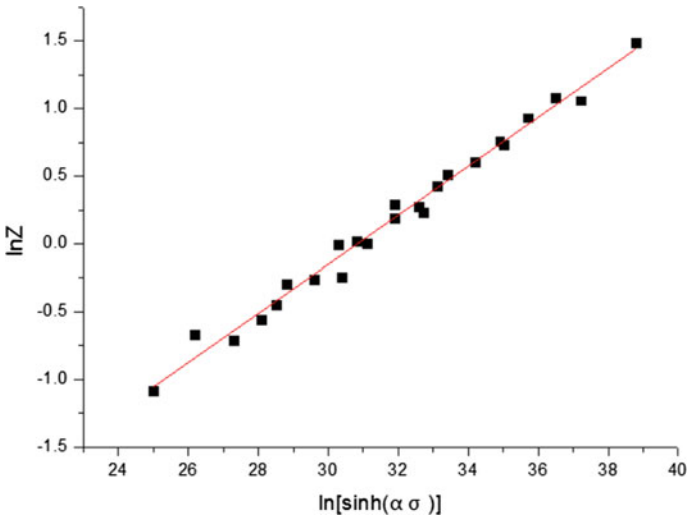

Fig. 6 Relationship between lnZ and ln[sinh(ασ)] under different conditions

The deformation activation energy Q:

$$Q = Rns = 326.146\ \mathrm{kJ/mol}. \tag{12}$$

Draw the lnZ − ln[sinh(ασ)] diagram, as shown in Fig. 6.
The intercept is taken in Fig. 6 and the lnA value is obtained:

$$\ln A = 30.84 \tag{13}$$

$$A = 2.4754 \times 1013. \tag{14}$$

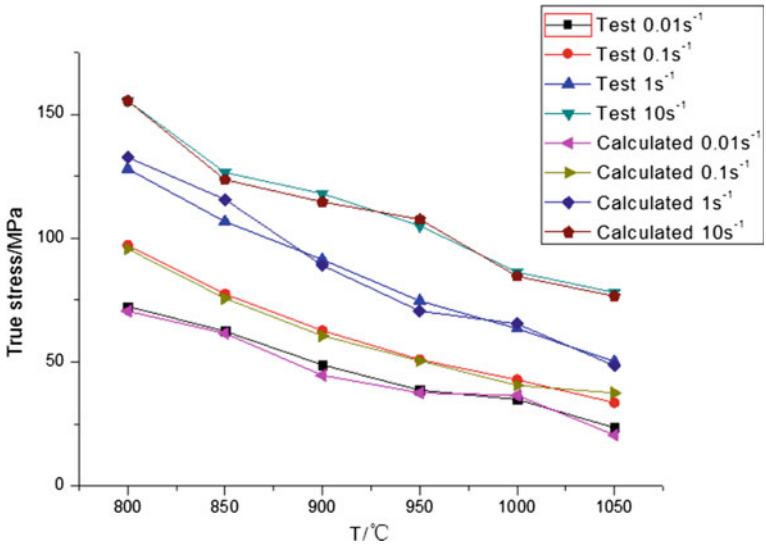

Fig. 7 Comparison of measured value and calculated value of peak stress (σ_p/MPa) under different thermal deformation conditions of alloy

The material constants α, n, Q, and A values obtained above are substituted into the Arrhenius equation of the Eq. (1), and the peak flow stress (σ_p/MPa) of the b10 alloy within the thermal deformation conditions applicable to all stress states is obtained, and the constitutive equations are as follows:

$$\dot{\varepsilon} = 2.4754 \times 10^{13}[\sinh(0.0141\sigma)]^{5.5302}\exp(-\frac{326146}{RT}) \tag{15}$$

The measured values of b10 value stress (σ_p/MPa) under different thermal deformation conditions are compared with the calculated values of constitutive equations, as shown in Fig. 7. The error analysis shows that the relative error between the peak stress calculated by the constitutive equation and the measured value is not more than 8%. The relative error of only 1 thermal deformation condition is more than 8%, for (T = 850 °C, $\dot{\varepsilon}$ = 1 s^{-1}).

In conclusion, the constitutive model is basically applicable in the range of T = 800–1050 °C and $\dot{\varepsilon}$ = 0.01–10 s^{-1} in the b10 alloy. Using this constitutive model to calculate the peak stress of b10 alloy under different thermal deformation conditions is credible and acceptable.

Conclusion

The true stress-strain curve of the alloy in the deformation condition of 800–1050 °C and 0.01–10 s^{-1} has been obtained by isothermal compression test on Gleeble 1500 thermal simulation test machine. The relationship between the deformation stress and strain rate, strain temperature and true strain in high temperature plastic deformation process has been studied. The deformation activation energy of the alloy and the constitutive relation of high temperature plastic deformation has been obtained by regression analysis. The main conclusions are as follows:

(1) The rheological curve of the alloy shows the characteristics of steady state, and the rheological stress increases rapidly to the peak stress at the beginning of the strain, and then remains unchanging or slowly increasing or decreasing. The rheological stress of the alloy increases when increasing strain rate and the decrease of strain temperature. When the true strain exceeds a certain value, the true stress no longer changes when increasing true strain; Some of the stress-strain curves show multiple peaks, indicating that discontinuous dynamic recrystallization of the alloy occurs, that is, during the process of hot compression deformation, the strain hardening and recrystallization softening of the alloy alternately occurs.
(2) The thermal deformation activation energy Q value of b10 alloy is 326.146 kJ/mol. The high temperature rheological constitutive equation is:

$$\dot{\varepsilon} = 2.4754 \times 10^{13}[\sinh(0.0141\sigma)]^{5.5302}\exp(-\frac{326146}{RT})$$

Through the error analysis, the constitutive equation model and experimental data match well, using this constitutive model to calculate the peak stress of b10 alloy under different thermal deformation conditions is credible and acceptable.

Acknowledgements This study was financially supported by the National Natural Science Foundation of China (Grant No.51401026) and National Key Research and Development Program of China (Grant No.2016YFB0301404).

References

1. F.J. Ansuini, F.A. Badia, High strength microduplex Cu-Ni-Zn alloys. Metall. Mater. Trans. B **4**(1), 15–20 (1972)
2. L.J. Drolenga, F.P. Ijsseling, B.H. Kolster et al., The Influence of Alloy Composition and microstructure on the corrosion behaviour of Cu-Ni alloys in seawater. Mater. Corrosion-werkstoffe Und Korrosion **34**(4), 167–178 (1983)
3. Q. Zhou, J. Jiang, Q. Zhong et al., Preparation of Cu–Ni–Fe alloy coating and its evaluation on corrosion behavior in 3.5% NaCl solution. J. Alloy. Compd. 171–175 (2013)
4. K. Abouswa, F. Elshawesh, O. Elragei et al., Corrosion investigation of Cu–Ni tube desalination plant. Desalination 140–146 (2007)

5. B. Sun, T. Ye, Q. Feng et al., Accelerated degradation test and predictive failure analysis of B10 Copper-Nickel alloy under marine environmental conditions. Materials **8**(9), 6029–6042 (2015)
6. P. Cristiani, G. Perboni, A. Debenedetti et al., Effect of chlorination on the corrosion of Cu/Ni 70/30 condenser tubing. Electrochim. Acta **54**(1), 100–107 (2008)
7. K.C. Kumar, B.V. Rao, Mitigation of microbially influenced corrosion of Cu–Ni (90/10) alloy in a seawater environment. Res. Chem. Intermed. **42**(6), 5807–5823 (2016)
8. S.J. Yuan, S.O. Pehkonen, Surface characterization and corrosion behavior of 70/30 Cu–Ni alloy in pristine and sulfide-containing simulated seawater. Corros. Sci. **49**(3), 1276–1304 (2007)
9. N. Liu, L.I. Zhou, L.I. Ling et al., Processing map and hot deformation mechanism of novel nickel-free white copper alloy. Trans. Nonferrous Met. Soc. China **24**(11), 3492–3499 (2014)
10. C.L. Gan, K.H. Zheng, W.J. Qi, M.J. Wang, Constitutive equations for high temperature flow stress prediction of 6063 Al alloy considering compensation of strain. Trans. Nonferrous Met. Soc. China **11**, 3486–3491 (2014)
11. K.L. Wang, S.Q. Lu, M.W. Fu, X. Li, X.J. Dong, Optimization of β/near-β forging process parameters of Ti-6.5Al-3.5Mo-1.5Zr-0.3Si by using processing maps. Mater. Charact. **60**, 492 (2009)
12. J. Zhang, Q. Wang, Y. Wang et al., Revelation of solid solubility limit Fe/Ni = 1/12 in corrosion resistant Cu-Ni alloys and relevant cluster model. J. Mater. Res. **25**(2), 328–336 (2010)
13. A. Momeni, K. Dehghani, Hot working behavior of 2205 austenite–ferrite duplex stainless steel characterized by constitutive equations and processing maps. Mater. Sci. Eng., A **528**(3), 1448 (2011)
14. G. Caille, S.P. Du, P. Gervais, J.G. Besner, M. Vezina, Constitutive analysis to predict high-temperature flow behavior of BFe10-1-2 cupronickel alloy in consideration of strain. Mater. Des. **65**(2), 272 (2015)
15. P. Dadras, J.F. Thomas Jr., Compressive plastic instability and flow localization in Ti-6242. Res. Mech. Lett. **1**(3), 97–103 (1981)
16. H. Shi, A.J. Mclaren, C.M. Sellars, R. Shahani, R. Bolingbbroke, Constitutive equations for high temperature flow stress of aluminium alloys. Mater. Sci. Technol. **13**(3), 210 (2013)

Microstructure and Mechanical Properties of Aluminum Clad Steel Plates by Cold Rolling and Annealing Heat Treatment

Fuxing Yin, Jiule Ma, Baoxi Liu, Jining He, Fanyong Zhang, Mingyang Liu and Yanchun Dong

Abstract Aluminum clad steel plate has been successfully fabricated by cold rolling and annealing heat treatment. The thicknesses of total clad plate and aluminum cladding layer were about 1.5 mm and 50–70 μm, respectively. The grain morphology, mechanical properties revealed a slight anisotropy. Herein, the grains were severe elongated along the cold rolling direction. The clad plates exhibited a superior tensile elongation and slight interfacial delamination, and highest value of multiple bending fracture times was located at the clad plate along the angle of 45°. Moreover, the perfect interfacial brazing bonding presented at the base clad plate and fins, which can be used in the power station.

Keywords Aluminum clad steel plate · Cold rolling and annealing
Elongated grain · Mechanical anisotropy · Interfacial delamination

F. Yin · B. Liu (✉) · J. He · F. Zhang · M. Liu · Y. Dong
School of Materials Science and Engineering, Research Institute for Energy Equipment Materials, TianJin Key Laboratory of Materials Laminating Fabrication and Interfacial Controlling Technology, Hebei University of Technology, Tianjin 300132, China
e-mail: liubaoxiliubo@126.com

F. Yin
e-mail: yinfuxing@hebut.edu.cn

J. He
e-mail: hbgdhjn@126.com

F. Zhang
e-mail: fany_zhang@163.com

M. Liu
e-mail: twzzyyx@126.com

Y. Dong
e-mail: hbgddych@163.com

J. Ma
School of Materials Science and Engineering, Hebei University of Science and Technology, Shijiazhuang 050080, China
e-mail: jdsrsjz@163.com

© Springer Nature Singapore Pte Ltd. 2018

Y. Han (ed.), *Advances in Materials Processing*, Lecture Notes in Mechanical Engineering, https://doi.org/10.1007/978-981-13-0107-0_61

Introduction

Aluminum clad steel sheet has the advantages of high corrosion resistance, thermal conductivity of aluminum alloy and high mechanical properties of steel, which is the main base materials of the cooling tube bundle in the power station. The single row tube of air cooling system is composed of aluminum clad steel sheet, and the Al cladding can be easily brazed with Al aluminum fins to form a tube bundle element. A strong interfacial bonding strength can also obtained between clad sheet and Al fins, and the whole area of the heat exchange tube can be also involve in heat transfer [1–3].

However, there are big difference between aluminum and iron on the atom radius, melting point, density, linear thermal expansion coefficient, and lattice parameters etc. Meanwhile, Al taken as one of the most typical electronegative element can easily react with many positive electrical metallic elements and form brittle intermetallics. For example, many solid solutions, intermetallics ($FeAl_3$, $FeAl_2$, Fe_2Al_5, Fe_4Al_{13}) and eutectics are generated based on the reaction between Fe and Al elements, which seriously limit the fabrication and practical application of aluminum clad steel sheet [4–10].

There are many methods to fabricate aluminum clad steel sheet, such as solid-state bonding [11], accumulative roll bonding [12], warm rolling [13], friction stir welding [14, 15], Defocused Laser Beam [16], butt TIG welding [2], spot welding [17], explosive welding [18], hot rolling [19, 20], and cold rolling [21–24] etc. Herein, many interfacial reaction particles and oxides are easily formed during hot and warm rolling or welding processes, which seriously deteriorate interfacial bonding strength of aluminum clad steel sheet [2, 25].

Recently, the cold roll bonding is the most economic and effective fabrication process among these various technologies [3, 26]. However, there are many difficulties in cold roll bonding process on aluminum clad steel sheet. Firstly, asymmetric deformation in the roll-gap will result in different thickness reduction and wraping phenomena between the two individual sheets due to different flow stresses [27–29]. Secondly, the interfacial bonding strength and stable interface can be effectively affected by many process parameters, such as surface roughness, rolling load, rolling speed, first pass reduction in thickness, thickness ratio, and heat treatment parameters [3, 26, 30–34]. Thirdly, the mechanical properties of cold rolled aluminum clad steel sheet present a low formability due to anisotropy [35]. The aim of this study was to investigate anisotropy and welding behavior of aluminum clad steel sheet, and make a guide to understand the relationship between microstructure and performance.

Experimental Procedures

The compositions of commercial pure aluminum and commercial pure steel plates are shown in Table 1, were used as raw materials. Firstly, in order to obtain perfect bonding, it is necessary to remove contaminant layers present on the surface of the contacting plates, these layers are composed of oxides, adsorbed ions (ions of sulfur, phosphor and oxygen), grease, and humidity and dust particles. Therefore, negative pressure degreasing and wire brushing of two contacting surface of the Al/Fe sheets were carried out using a stainless steel circumferential brush operating at a rotation speed of 2500 rpm/min. Moreover, scratch brushing is not only for cleaning but also for providing rough surfaces, which provide a greater amount of surface asperities and promote a localized shear deformation that breaks unavoidable surface oxide films during cold roll bonding, contributing to the firm bonding of aluminum clad steel sheets. The initial thicknesses of Al and Fe were 0.25 mm and 4.0 mm, respectively. The cold roll bonding process was performed under lubricated condition by 50 and 75% in the first and final rolling pass. Li et al. [3] proposed that the interfacial bonding strength did not develop until reduction greatly exceeded the reduction (50%). The cold rolling mills with roll diameter of 550 mm possess 8 rollers and the rolling speed was 360 rpm/min. Finally, the cold-rolled aluminum clad steel sheets were annealed at 450 °C for 120 min as shown in Fig. 1a.

Figure 1b shows the three directions in the rolling plane (I plane): rolling direction, transverse direction and normal direction. The three perpendicularly planes are named as I, II and III plane, respectively. The uniaxial tensile tests on flat specimens were carried out in order to determine the mechanical properties. The samples were cut from aluminum clad steel sheet in five directions at mentioned angles: $\alpha = 0°, 30°, 45°, 60°, 90°$ in relation to direction of cold rolling. The geometry of the bimetallic specimen is presented in Fig. 2. All tests of uniaxial tensile of specimens were performed on an universal testing machine Instron-5569 plus with traverse speed of 2 mm/min. Measurement of longitudinal deformation took place by using an extensometer of gauge length 10 mm. Starting load of specimen was 0.1 kN.

Table 1 Chemical compositions of the raw materials used in Al/Fe clad plates

Commercial pure Al								
Elements	Al	Si	Fe	Cu	Mn	Ni	Cr	C
wt%	98.71	0.85	0.41	0.01	0.01	0.01	–	–
Commercial pure Fe								
Elements	Fe	C	Si	Mn	P	S	Al	N
wt%	99.71	0.005	0.01	0.24	0.016	0.01	0.001	0.006

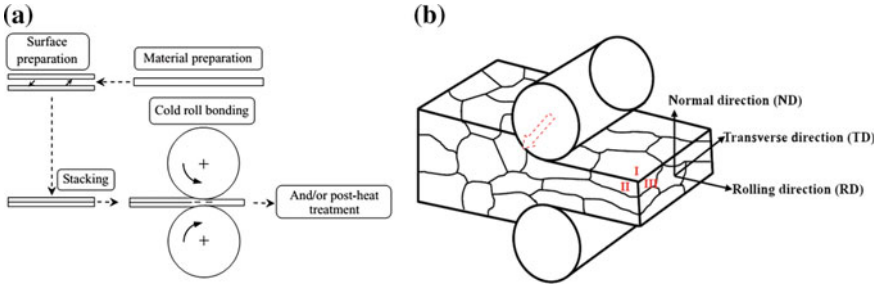

Fig. 1 Schematic illustration showing principle of cold roll bonding (CRB), **a** fabrication process; **b** microstructure evolution during the cold rolling

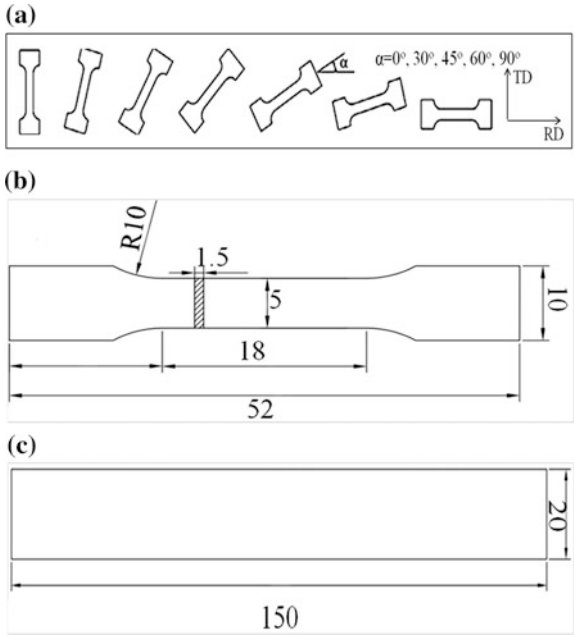

Fig. 2 Geometry of the bimetallic specimen, **a** scheme of cutting of tensile samples from I section; **b** tensile sample; **c** multiple bending sample

Microstructural examinations and fracture characterizations were performed using optical microscopy (OM) and scanning electron microscopy (SEM, Hitachi S-4700) on the aluminum clad steel sheet after etching using a 4% HNO_3 alcohol solution. In order to attain a clear surface, the specimens were glued to a metallic plate and polished using a polishing machine.

Results and Discussions

Figure 3 shows the optical microstructure of aluminum clad steel plate by cold rolling and annealing heat treatment. The total thickness of aluminum clad steel plate is about 1.5 mm, and the aluminum cladding layer is straight, uniform and continuous as shown in Fig. 3a. Herein, the thickness of aluminum cladding layer is about 50–70 μm, as shown in Fig. 3b, and many grains of steel substrate are elongated along the rolling direction [36]. The average size of transverse linear interception for the elongated grains was 10 μm. However, the grains of II cross section are uniform and equiaxed as shown in Fig. 3c, and average size is about 30 μm. Figure 3d shows the microstructure of III cross section, and the average size of equiaxed grain is about 60 μm, the unique grain characteristics of I, II and III cross sections are attributed to the high rolling reduction ratio [37]. The original 3D equiaxed grains are changed to one pancake-like microstructure due to its special deformation characteristics. The grain size is enlarged along the rolling surface, while the transverse linear interception for the elongated grains decreases with the increase of rolling reduction ratio [38].

Figure 4 shows the engineering and true stress-strain curves of aluminum clad steel plates along different angle, and Tables 2 and 3 list the corresponding values of tensile properties. The stress-strain curves reveal a similar elastic deformation and prolong uniform plastic deformation stages. Elastic properties of the tested

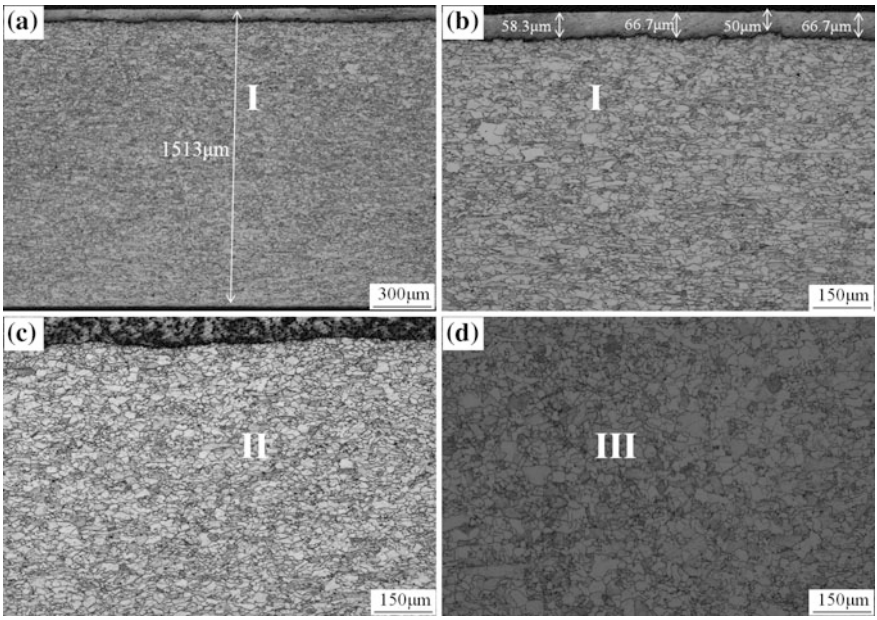

Fig. 3 Microstructure of aluminum clad steel plate. **a** Macroscopic picture; **b** the I cross section; **c** the II cross section; **d** the III cross section

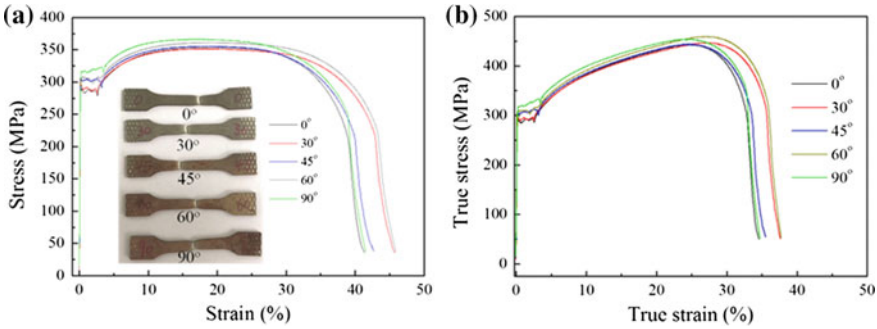

Fig. 4 Sstress-strain curves of aluminum clad steel plates with different angle. **a** Engineering stress-strain curves; **b** true stress-strain curves

Table 2 Mechanical properties of aluminum clad steel plates with different angles

Angle (°)	Elastic modulus (GPa)	Yielding strength (MPa)	Ultimate strength (MPa)	Elongation (%)
0	180	289	354	41.3
30	171	294	352	45.7
45	177	302	356	42.6
60	181	307	361	45.8
90	185	316	367	41.5

Table 3 Calculated mechanical parameters of aluminum clad steel plates with different angles

Angle (°)	K (MPa)	n	$\sigma_{necking}$ (MPa)
0	253	0.178	422
30	256	0.171	417
45	261	0.169	421
60	262	0.172	429
90	278	0.157	428

aluminum clad steel plates were represented by Young's modules E. The values of Young's modules (171 GPa) of clad plate were lowest in the direction β = 30°, and largest value (185 GPa) in the direction β = 90°. Relative differences between the extreme values of Young's modules were 8.18% for aluminum clad steel plate. It is observed that the values of yield strength ($\sigma_{0.2}$) and ultimate strength (σ_b) are gradually increased with the increasing tensile angle. The slight anisotropy of mechanical properties of the tested aluminum clad steel plates was undoubtedly the result of technological processes during the rolling process and subsequent annealing heat treatment. The cold rolling process and interfacial bonding of aluminum and steel layers in the clad plates need to use high rolling force, which generated the clad plate anisotropy. Meanwhile, the annealing heat treatment

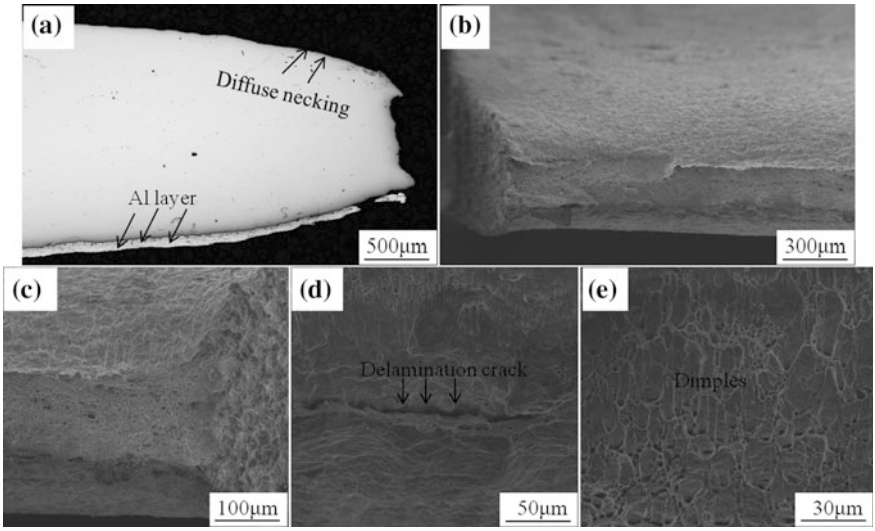

Fig. 5 Tensile fracture characteristics of aluminum clad steel plate. **a** Macroscopic picture; **b**, **c** microscopic pictures; **d** interfacial delamination; **e** steel substrate

eliminates the partial residual stress and severe mechanical anisotropy. Moreover, based on the power low equation as shown:

$$\sigma = K\,\varepsilon^n \tag{1}$$

where K and n are taken as strength coefficient and strain hardening exponent, respectively. The power low equation has been successfully used to predict the true stress-strain relation. The relation is obtained by fitting the true stress-strain relation calculated by Eq. (1) according to empirical data until the maximum load point. The values of K, n, critical strain ($\varepsilon_{necking}$) and critical stress ($\sigma_{necking}$) at the necking point are listed in Table 3. Herein, high value of n shows the prolonged uniform deformation capacity and high formability [39]. The lowest value of n is 0.157 along the cold rolling direction β = 90°, and the highest value of n is 0.178 along the cold rolling direction β = 0°. Relative differences between the extreme values of n were 13.36% for aluminum clad steel plate. Overall, the aluminum clad steel plates reveal a slight mechanical and formability anisotropy.

Figure 5 shows the tensile fracture characteristics of aluminum clad steel plate. The enlarged edge view of the fractured tensile sample reveals an uncontinuous aluminum cladding layer and thickness-wise necking morphologies as shown in Fig. 5a.

Meanwhile, a slight interfacial delamination crack is formed at the fracture position. The delamination along the interface was observed in the aluminum clad steel plate as shown in Fig. 5d. The interfacial crack developed slight open with strain and the debonded Al and Fe plate deformed separately. The weak interface is

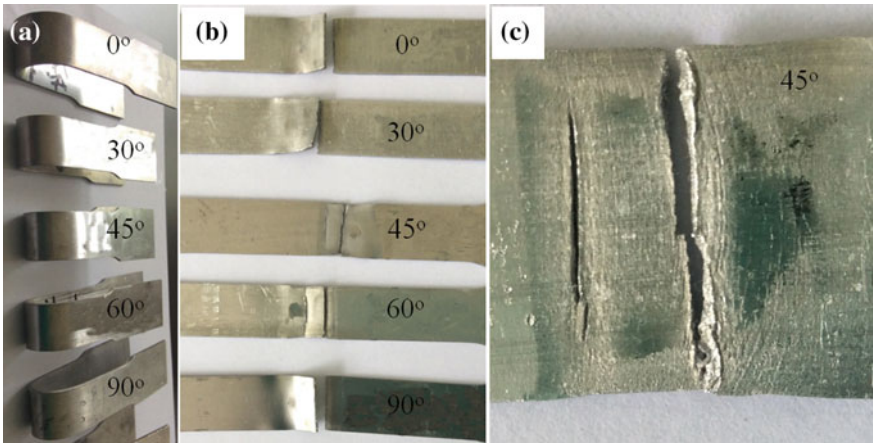

Fig. 6 Cold bending and multiple bending morphologies of aluminum clad steel plates. **a** Cold bending samples; **b** multiple bending fracture morphologies; **c** The microscopic fracture characteristics of multiple bending sample along the angle of 45°

attributed to the interfacial intermetallic layer. In addition, many refined dimples are presented in the steel substrate as shown in Fig. 5e, revealing a typical ductile fracture characteristic.

Figure 6 shows the cold bending and multiple bending morphologies of aluminum clad steel plates. There are no interfacial delamination and fracture characteristics found in the bending samples with different angles along cold rolling direction, exhibiting the perfect interfacial bonding between aluminum cladding and steel substrate as shown in Fig. 6a. Figure 6b shows the multiple bending fracture characteristics of aluminum clad steel plates, and the fold times are listed in the Table 4. It is revealed that the highest value (75 times) of fold times is located at the aluminum clad steel plate along the angle of 45°, and the lowest value (60 times) is present at the clad plate along the angle of 0°. Therefore, the aluminum clad steel plate along the angle of 45° exhibits a high formability. Figure 6c shows the microscopic fracture characteristics of aluminum clad steel plates. Beside the main crack, there is the second crack present at the clad plate, and there are no interfacial delamination phenomena, exhibiting a superior interfacial bonding quality.

Table 4 Fold times of multiple bending aluminum clad steel plates with different angles

Angle (°)	Fold times
0	55
30	66
45	75
60	64
90	60

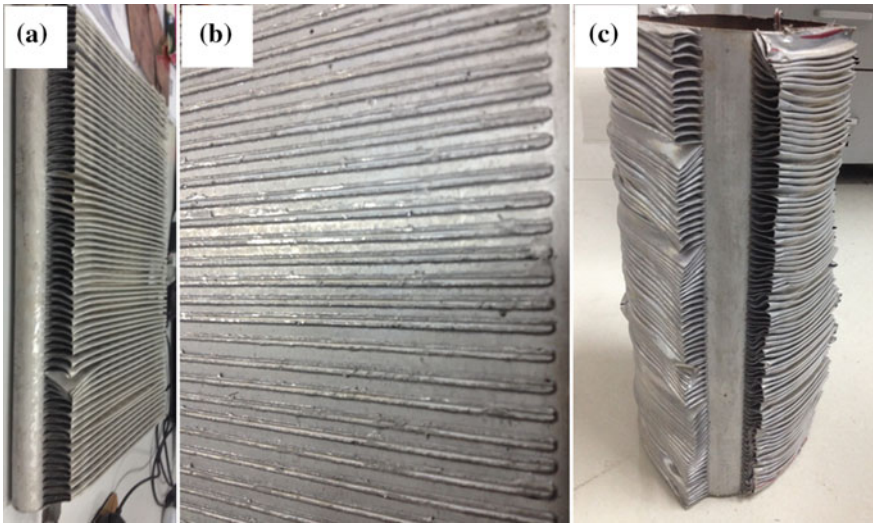

Fig. 7 Samples of air cooled island brazed by aluminum clad steel plate with the Al alloy fins. **a** the profile picture; **b** the interface between clad steel plate with the Al alloy fins; **c** the blasting samples of air cooled island

Figure 7 shows the air cooled island brazed by aluminum clad steel plate with the Al alloy fins. Obviously, the perfect interfacial bonding is presented at the base clad plate and fins as shown in Fig. 7a, b. Meanwhile, there is no interfacial delamination phenomenon between the clad plate and Al alloy fines of the blasted air cooled island as shown in Fig. 7c. Therefore, the aluminum clad steel plates can be used in the power station.

Summaries

(1) Through cold rolling and annealing heat treatment process, the aluminum clad steel plates with the 50–70 μm aluminum cladding layer have been successfully fabricated to used as heat sink substrate in the air cooling island;
(2) The tensile properties of aluminum clad steel plates reveal a slight anisotropy, which is attributed to the unique elongated grains of steel substrate, the clad plates exhibit a superior tensile elongation and slight interfacial delamination, and highest value of multiple bending fracture times is located at the clad plate along the angle of 45°;
(3) The brazing interfacial quality of aluminum clad steel plate and Al alloy fins is perfect, there is no interfacial delamination phenomenon.

Acknowledgements This work is financially supported by the National Natural Science Foundation of China (NSFC) under Grant No. 51601055, 51304059, the Hebei Science and Technology program under Grant No. 130000048, the National Natural Science Foundation of Hebei Province under Grant Nos. E201620218 and QN2016029.

References

1. H. Kawase, M. Makimoto, K. Takagi, Y. Ishida, T. Tanaka, Development of aluminum clad steel by roll bonding. Trans. ISIJ **23**, 628–632 (1983)
2. M.M. Atabaki, M. Nikodinovski, P. Chenier, J. Ma, M. Harooni, R. Kovacevic, Welding of aluminum alloys to steels: an overview. J. Manuf. Sci. Prod. **14**, 59–78 (2014)
3. L. Li, K. Nagai, F.X. Yin, Progress in cold roll bonding of metals. Sci. Technol. Adv. Mater. **9**, 1–11 (2008)
4. Y. Wang, S.G. Zhou, K.S. Vecchio, Annealing effects on the microstructure and properties of an Fe-based metallic-intermetallic laminate (MIL) composite. Mater. Sci. Eng., A **665**, 47–58 (2016)
5. Y. Wang, K.S. Vecchio, Microstructure evolution in a martensitic 430 stainless steel-Al metallic-intermetallic laminate (MIL) composite. Mater. Sci. Eng., A **643**, 72–85 (2015)
6. Y. Wang, K.S. Vecchio, Microstrcutre evolution in Fe-based-aluminide metallic-intermetallic laminate (MIL) composites. Mater. Sci. Eng., A **649**, 325–337 (2016)
7. P.C. Tortorici, M.A. Dayananda, Phase formation and interdiffusion in Al-clad 430 stainless steels. Mater. Sci. Eng., A **244**, 207–215 (1998)
8. H.D. Manesh, A.K. Taheri, The effect of annealing treatment on mechanical properties of aluminum clad steel sheet. Mater. Des. **24**, 617–622 (2003)
9. W.S. Hwang, T.I. Wu, W.C. Sung, Effect of heat treatment on mechanical property and microstructure of aluminum/stainless steel bimetal plate. J. Eng. Mater. Technol. **134**, 014501-1-6 (2012)
10. A. Nishimoto, K. Akamatsu, Preparation of homogeneous Fe-Al intermetallic compound sheet by multi-layered rolling and subsequent heat treatment. Mater. Sci. Forum **561–565**, 857–860 (2007)
11. H.Y Wu, S. Lee, J. Wang, Solid-state bonding of iron-based alloys, steel–brass, and aluminum alloys. J. Mater. Process. Technol. **75**, 173–179 (1998)
12. M. Talebian, M. Alizadeh, Manufacturing Al/steel multilayered composite by accumulative roll bonding and the effects of subsequent annealing on the microstructural and mechanical characteristics. Mater. Sci. Eng., A **590**, 186–193 (2014)
13. M. Soltan, A. Nezhad, A. Haerian Ardakani, A study of joint quality of aluminum and low carbon steel strips by warm rolling. Mater. Des. **30**, 1103–1109 (2009)
14. X. Liu, S. Lan, J. Ni, Analysis of process parameters effects on friction stir welding of dissimilar aluminum alloy to advanced high strength steel. Mater. Des. **59**, 50–62 (2014)
15. K. Kimapong, T. Watanabe, Lap joint of A5083 aluminum alloy and SS400 steel by friction stir welding. Mater. Trans. **46**, 835–841 (2005)
16. K. Lee, S. Kumai, T. Arai, Interfacial microstructure and strength of steel to aluminum alloy lap joints welded by a defocused laser beam. Mater. Trans. **46**, 1847–1856 (2005)
17. R.F. Qiu, H.X. Shi, K. Zhang, Y. Tu, C. Iwamoto, S. Satonaka, Interfacial characterization of joint between mild steel and aluminum alloy welded by resistance spot welding. Mater. Charact. **61**, 684–688 (2010)
18. M. Acarer, B. Demir, An investigation of mechanical and metallurgical properties of explosive welded aluminum-dual phase steel. Mater. Lett. **62**, 4158–4160 (2008)
19. S.H. Choi, J.W. Kwon, K.H. Oh, Prediction of inhomogeneous texture in clad sheet metals by hot roll bond method. Met. Mater. **2**, 133–140 (1996)

20. S.C. Pan, M.N. Huang, G.-Y. Tzou, S.W. Syu, Analysis of asymmetrical cold and hot bond rolling of unbounded clad sheet under constant shear friction. J. Mater. Process. Technol. **177**, 114–120 (2006)
21. Y. Jiang, D.S. Peng, D. Lu, L.X. Li, Analysis of clad sheet bonding by cold rolling. J. Mater. Process. Technol. **105**, 32–37 (2000)
22. H.R. Akramifard, H. Mirzadeh, M.H. Parsa, Cladding of aluminum on AISI 30 4L stainless steel by cold roll bonding: mechanism, microstructure, and mechanical properties. Mater. Sci. Eng., A **613**, 232–239 (2014)
23. H.D. Manesh, A.K. Taheri, Study of mechanisms of cold roll welding of aluminum alloy to steel strip. Mater. Sci. Technol. **20**, 1064–1068 (2004)
24. G. Tzou, M. Huang, Analytical modified model of the cold bond rolling of unbounded double-layers sheet considering hybrid friction. J. Mater. Process. Technol. **140**, 622–627 (2003)
25. M. Voncina, H.S. Hrenko, J. Medved, Interaction between Al99.5 and stainless steel at elevated temperature and pressure. RMZ—M&G **62**, 213–224 (2015)
26. R. Jamaati, M.R. Toroghinejad, Cold roll bonding bond strengths: review. Mater. Sci. Technol. **27**, 1101–1108 (2011)
27. S.H. Choi, K.H. Kim, K.H. Oh, D.N. Lee, Tensile deformation behavior of stainless steel clad aluminum bilayer sheet. Mater. Sci. Eng., A **222**, 158–165 (1997)
28. Q. Qin, Z.H. Wu, Y. Zang, B. Guan, F.X. Zhang, Warping deformation of 316l/q345r stainless composite plate after removal strake. World J. Eng. **13**, 206–209 (2016)
29. Q. Qin, Z.H. Wu, Y. Zang, B. Guan, A simulation study on the multi-pass rolling bond of 316L/Q345R stainless clad plate. Adv. Mech. Eng. **7**, 1–13 (2015)
30. D.N. Lee, Y.K. Kim, Tensile properties of stainless steel-clad aluminum sandwich sheet metals. J. Mater. Sci. **23**, 1436–1442 (1988)
31. H.Y. Wang, X. Li, Z.H. Wang, D.W. Zhao, D.H. Zhang, Analysis of sandwich rolling with two different thicknesses outer layers based on slab method. Int. J. Mech. Sci. **106**, 194–208 (2016)
32. P.S. Stieif, Interfacial instabilities in an unbonded layered solid. Int. J. Solids Struct. **26**, 915–935 (1990)
33. S.L. Semiatin, H.R. Piehler, Forming limits of sandwich sheet materials. Metall. Trans. A **10**, 1107–1118 (1979)
34. F. Afrouz, A. Parvizi, An analytical model of asymmetric rolling of unbounded clad sheets with shear effects. J. Manuf. Process. **20**, 162–171 (2015)
35. R. Uscinowicz, Experimental identification of yield surface of Al-Cu bimetallic sheet. Compos. B **55**, 96–108 (2013)
36. Y. Kimura, T. Inoue, F.X. Yin, K. Tsuzaki, Inverse temperature dependence of toughness in an ultrafine grain-structure steel. Science **320**, 1057–1059 (2008)
37. S.M. Allen, E.L. Thomas, *The Structure of Material* (Wiley, 1999), pp. 359–363
38. L.J. Huang, L. Geng, *Discontinuously Reinforced Titanium Matrix Composites* (Springer, 2007), pp. 1–180
39. A. Cetin, C. Bernardi, A. Mortensen, An analysis of the tensile elongation to failure of laminated metal composites in the presence of strain-rate hardening. Acta Mater. **60**, 2265–2276 (2012)

Analysis of Stripe Defects on the Cold Rolled Aluminum Strip Surface

Yan Li, Lei Xia, Yiqing Chen, Peng Gao, Bin Zhong, Fangfang Ai and Lin Li

Abstract In the cold rolling production process, there are always bright, and dark stripe defects on aluminum strips surface when lubricated with rolling oil. The micromorphology and structure of defects were investigated by the surface profiler, OLYMPUS LEXT OLS4000 microscope, and SEM. The constituent elements of the aluminum surface were detected by EDS. The formation mechanism of surface defects was investigated. The analyses of the data suggested that the dark stripe was tougher than the bright stripe surface and the average surface roughness between them varies to 17.8%. The chemical composition of the residue was the significant difference in oxygen content. The oxygen content of dark stripe was much higher than the bright stripe defects. The reason for the difference may be that in rolling speed process, the oil film failed to spread uniformly in the vast areas of deformation zone infinite time which led to the rolling oil film thickness distributes unevenly.

Y. Li (✉) · Y. Chen · P. Gao · B. Zhong · F. Ai · L. Li
State Key Laboratory of Metal Material for Marine Equipment and Application, Anshan 114009, China
e-mail: 2323liyan@sina.com

Y. Chen
e-mail: chenyiqing2003@163.com

P. Gao
e-mail: neugp@126.com

B. Zhong
e-mail: zhong3416@tom.com

F. Ai
e-mail: ansteelaff@163.com

L. Li
e-mail: ansteellilin@163.com

Y. Li · Y. Chen · P. Gao · B. Zhong · F. Ai · L. Li
Iron & Steel Research Institutes of Ansteel Group Corporation, Anshan 114009, China

L. Xia
Research Institute of Petroleum Processing, Sinopec, Beijing 100083, China
e-mail: charles2248@126.com

© Springer Nature Singapore Pte Ltd. 2018

Y. Han (ed.), *Advances in Materials Processing*, Lecture Notes in Mechanical Engineering, https://doi.org/10.1007/978-981-13-0107-0_62

The areas of the surface with little rolling oil would suffer insufficient lubrication and cause rougher surface. Moreover, the fresh surface without rolling oil is more likely to be oxidized. The different roughness and composition lead to the difference in macro morphology which is the stripe defects on the surface of aluminum strips.

Keywords Cold rolling · Process lubrication · Surface defects

Introduction

Aluminum alloys are usually used in the production of car interior decoration, kitchen furniture, home appliances and electronic products owing to its advantages of high strength, easy to shape, nice surface color et al. [1]. However, the surface quality requirement of it is also quite strict [2, 3]. Aluminum strips are usually produced by rolling. The lubrication technology must be adopted to improving the surface quality of rolled products [4–6]. Cold rolling technology develops towards high exactness, wide in width and high rate [7], which makes the lubrication conditions rigorous. When the lubrication condition of the rolling deformation zone is severe, a large number of stripe defects will appear on the rolled aluminum plate surface.

This paper selected 8011 aluminum alloy strips produced by 6-high reversing mills and lubricated by rolling oil. Using a surface profiler, OLYMPUS LEXT OLS4000 microscope, scanning electron microscope (SEM) and energy dispersive spectrometer (EDS) to analyze microstructure and composition of aluminum surface and then discussed the causes of stripe defects.

Experiments

Experiment Materials

The 8011 aluminum alloy strips were selected whose chemical constituents were as follows: Mg 0.05wt%, Cu 0.10wt%, Cr 0.05wt%, Fe 0.50–0.90wt%, Zn 0.10wt%, Mn 0.20wt%, Ti 0.08wt%, Si 0.60–1.0wt%, impurities 0.15wt% and the rest is Al. The 6-pass rolling process was conducted using 6-high reversing mills, and the total reduction reached 96.1%. The rolled aluminum was cleaned by an ultrasonic cleaner in acetone for 15 min, and then the following experiments were performed using the cleaned samples. The density of rolling oil in the cold rolling experiment is 0.85 g/cm^3, whose kinematic viscosity (40 °C) is about 2.28 mm^2/s^{-1}.

Surface Topographic Analysis

The FTS-S3c surface profiler was used to analyze the surface profile of the aluminum strip. It acquired the surface profile of aluminum strip. The 3D surface morphology of the stripe defects was observed by the OLYMPUS LEXT OLS4000 microscope. An experimental investigation and mechanical analysis were carried out to study the stripe defects formation by using SEM and EDS.

Results and Discussion

Macroscopic Analysis

The feature macro-profile of rolled aluminum strip surface was shown in Fig. 1. There were some stripes on the aluminum strip surface. The characteristics of them were as follows: firstly, the stripes were perpendicular to the rolling direction; secondly, the stripes distributed periodically and regularly; lastly, the width of the bright and dark stripes was similar, about 10 mm.

Surface Roughness

To further study the formation reasons of stripe defects, 3D surface morphology was measured by OLYMPUS LEXT OLS4000 microscope. The 3D morphology of aluminum was shown in the Fig. 2. It showed that the surface of the aluminum had minor fluctuations and natural textures parallel to the direction of rolling. However,

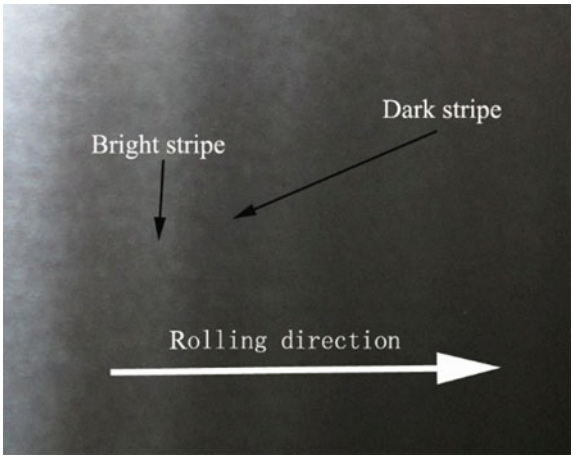

Fig. 1 Macro morphology of the aluminum surface

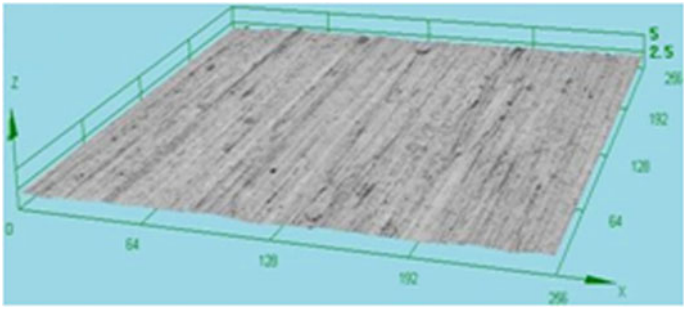

Fig. 2 Three-dimensional morphology of aluminum surface

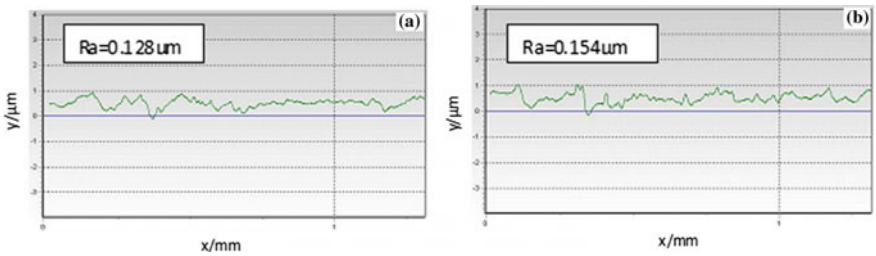

Fig. 3 Aluminum surface profiles: **a** bright stripes **b** dark stripes

some areas had some spots and sticky marks. The roughness of different regions on the strip surface is described, the surface roughness of bright and dark stripes was tested and shown in Fig. 3. The Fig. 3 showed that the fluctuations of the aluminum surface were relatively flat. The midline average of dark stripes was different from bright stripes by 16.9%. Many stripes were tested, it showed that R_a ranged from 0.119 to 0.161 μm, and the average R_a of bright stripes and dark stripes had a difference of 17.8%. To further explain the formation mechanism of stripe defect, it is necessary to observe the microscopic morphology and composition of bright and dark stripes.

SEM Topography and Elemental Analysis

The microtopography of the rolled aluminum surface was illustrated in Fig. 4. The surface of dark stripes was much tougher than that of bright stripes. There were many microspots on the dark stripes surface. These microspots have different shapes, which is narrow in rolling direction. The chemical component s of various regions stripe defects were analyzed by using the EDS, and the results were shown in Fig. 5.

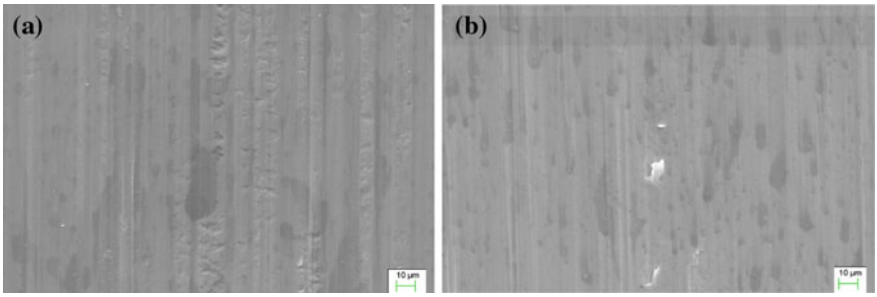

Fig. 4 Micrographs of stripes: **a** dark stripes **b** bright stripes

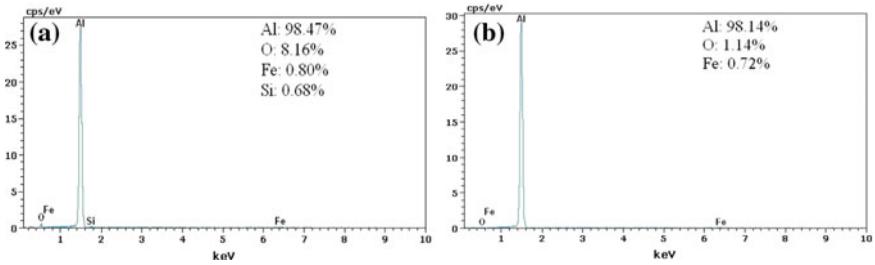

Fig. 5 Elemental component of aluminum surface: **a** dark stripes **b** bright stripes

Figure 5 demonstrated that the strip surface mainly contained elements Al, O, Fe and Si. Fe and Si were from the aluminum alloy elements. The oxygen element primarily came from the oxide layer of the aluminum surface. Element O content of dark stripes was 8.16% while that of bright stripes was only 1.14%. It demonstrated that more oxygen remains occurred in the dark stripes.

In conclusion, the formation of stripes on rolled aluminum strips is related to the difference in surface roughness and chemical component. The diameter and width of work rollers of modern cold rolling mill are large which lead to more extensive deformation zone areas. The lubrication conditions become rigorous in the high-speed rolling process, and the rolling oil cannot spread out in a short time in the deformation zone. The different oil film thickness in the deformation zone causes the shaking of rollers and different lubrication conditions. The areas without enough rolling oil cannot be lubricated sufficiently and would be tougher. Moreover, it is easy to be oxidized after rolled and then the stripes on the surface appear [8].

Conclusions

The formation of stripes on rolled aluminum strips is related to the difference in surface roughness and chemical component. The reason for the difference may be that in the high speed rolling process, the oil film failed to spread uniformly in the broad areas of deformation zone infinite time. It leads to uneven lubrication on the aluminum surface. The surface without enough rolling oil could not be lubricated sufficiently, and the surface will be tougher. Moreover, the fresh surface without rolling oil can be oxidized. The different roughness and composition lead to the difference in macro morphology which are the stripe defects on the surface of aluminum strips.

References

1. Y.F. Li, Q.S. Dai, J.Y. Li, Deng Yun-lai, Study on formation mechanism of black stripe on the surface of aluminum alloy sheet and its prevention measure. Mater. Sci. **05**(3), 144–150 (2015)
2. M. Conserva, G. Donzelli, R. Trippodo, Aluminium and its applications. Edimet (1992)
3. H.X. Yu, C.X. Ji, B. Chen, C. Wang, Y.H. Zhang, Characteristics and evolution of inclusion induced surface defects of cold rolled IF sheet. J. Iron. Steel Res. Int. **22**(Supplement 1), 17–23 (2015)
4. J. Sun, L. Wang, Y. Ma, Q. Shi, A. Zhang, J. Li, Surface quality of cold rolling aluminum strips under lubrication condition. J. Univ. Sci. Technol. Beijing, **15**(3), 335–338 (2008)
5. J. Sun, Y. Kang, T. Xiao, Lubrication in strip cold rolling process. J. Univ. Sci. Technol. Beijing **11**(4), 368–372 (2004)
6. S. Junichi, W. Toshiaki, M. Shigeyuki, Adsorption characteristics and lubrication performance of coolant components in cold rolling of aluminum. Tribol. Int. **40**(5), 748–753 (2007)
7. S. Kojima, A. Yokoyama, M. Komatsu, High-speed deformation of aluminum by cold rolling. Mater. Sci. Eng., A **350**, 81–85 (2003)
8. G. John, Lenard. The effect of roll roughness on the rolling parameters during cold rolling of an aluminum alloy. J. Mater. Process. Technol. **152**, 144–153 (2004)

Effect of Multi-pass Submerged Friction Stir Processing on Microstructure Evolution and Mechanical Properties of AZ61 Magnesium Plate

Xicai Luo, Datong Zhang, Wen Zhang and Cheng Qiu

Abstract In this work, the effect of multi-pass submerged friction stir processing (MSFSP) on a casting AZ61 Mg plate was investigated. AZ61 plate was successfully prepared by repeating the processing with the subsequent pass FSP overlapped the retreating side with an overlapping ratio of 50%. The microstructure and resulting mechanical properties at room temperature were studied. The results revealed that the fine and equiaxed grains with an average grain size of 10.7 μm obtained in stirring zone (SZ) through MSFSP, and the second-phase $Mg_{17}Al_{12}$ was broken into small particles. Compared to BM, MSFSP specimens achieved an improvement in microhardness, tensile strength and elongation but exhibited obvious mechanical anisotropy, especially the ductility. It is considered that the enhancement in mechanical properties is benefit from grain refinement and the texture evolution may be responsible for the mechanical anisotropy.

Keywords AZ61 magnesium alloys · Multi-pass friction stir processing Microstructure · Mechanical properties

X. Luo · D. Zhang (✉) · W. Zhang · C. Qiu
National Engineering Research Center of Near-Net-Shape Forming for Metallic Materials, Guangdong Key Laboratory for Advanced Metallic Materials Processing, School of Mechanical and Automotive Engineering, South China University of Technology, Guangzhou 510640, China
e-mail: dtzhang@scut.edu.cn

X. Luo
e-mail: meluoxicai@mail.scut.edu.cn

W. Zhang
e-mail: jack_eei@scut.edu.cn

C. Qiu
e-mail: cqiu@scut.edu.cn

© Springer Nature Singapore Pte Ltd. 2018

Y. Han (ed.), *Advances in Materials Processing*, Lecture Notes in Mechanical Engineering, https://doi.org/10.1007/978-981-13-0107-0_63

Introduction

Magnesium alloys have many advantages, such as high specific stiffness and strength, therefore, they are expected to be used as lightweight structural materials [1]. However, their poor ductility and formability at ambient temperature restrain their applications. It is well accepted that grain refinement is an effective method for improving the mechanical properties of magnesium alloys, especially ductility [2, 3]. It is well known that conventional severe plastic deformation (SPD) techniques, like high pressure torsion (HPT) and equal channel angular pressing (ECAP), have a remarkable effect on grain refinement. However, they are still difficult to produce bulk plates using these techniques limited by the complexity of processing parameters and shape of the mold [4]. Mishra et al. firstly proposed the new SPD technique of friction stir processing (FSP), which could be used as a promising technique for grain refinement. FSP considered as an effective method to produce fine-grained magnesium alloys was demonstrated by many researchers [5–7]. However, these studies just focused on single-pass FSP or multi-pass FSP (MFSP) with an overlapping ratio of 100%, which generally produced the size of FSP sample limited with a width of several millimeters. In order to produce bulk plates, MFSP with an overlapping rate is employed on magnesium alloys. Su et al. [8] used MFSP to prepare the bulk aluminum alloy plates with fine grains and obtain good mechanical properties. To date, there is no report on AZ61 magnesium alloy plates prepared by MFSP with overlapping ratio of 50% at active cooling condition. Aiming at the industrial application, it is attractive to produce fine-grained magnesium alloy plates through MFSP with good mechanical performance.

It should be noted that the grain growth may take place during MFSP due to the accumulative heat input. Therefore, how to retain the newly formed fine grain structure is a key issue to produce bulk plates through MFSP. In this work, and MFSP is conducted under water for further refining the grains with the rapid cooling rate, and restraining the grain coarsening caused by accumulative heat input. Moreover, some studies reported non-homogeneous microstructure were obtained in aluminum alloys prepared by MFSP, which may result in mechanical anisotropy [8, 9], while the mechanical behaviors of MFSP Mg alloy plates have not been comprehensively studied. In this work, the microstructure evolution and mechanical behavior of the MSFSP AZ61 plate were investigated.

Experimental Procedures

Casting AZ61 Mg plate (6.3Al–0.9Zn–0.3Mn–Mg Bal. wt%) with the thickness of 8 mm was used in present work. FSP was performed on FSW-3LM-003 welding machine equipped with a cooling tank. The workpiece was submerged in ambient temperature water, the flow speed of which was 40 ± 5 ml/s during processing. MFSP was conducted using a FSP tool with a shoulder of 18 mm in diameter, a

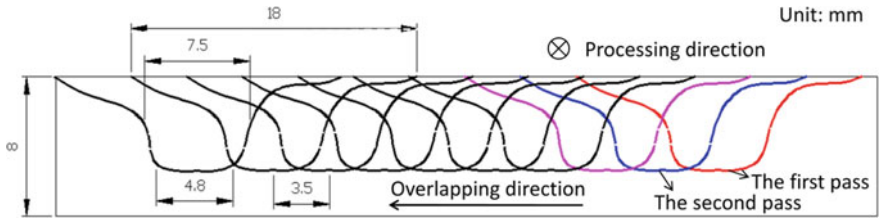

Fig. 1 Schematic illustration perpendicular to the processing direction of the multi-pass submerged FSP plate

threaded conical pin of 7 mm in root diameter and 5 mm in length. A tool rotation speed of 1400 rpm and a linear speed of 60 mm/min were applied throughout FSP. The FSP tool was tilted by 2.5° to the normal of plate. The subsequent pass overlapped the retreating side of last pass with an overlapping ratio of 50% through repeating this process for 28 times. A plate with a width of 220 mm and a length of 150 mm were prepared. The schematic illustration of MSFSP is shown in Fig. 1.

Microstructure characterizations in transverse cross section were performed by optical microscopy (OM) and scanning electron microscopy (SEM). The metallographic specimens were prepared with standard methods, and then etched with a mixed solution of 80 mL ethanol and 10 mL distilled water, 10 mL acetic acid and 5 g picric acid. The average grain size of MSFSP sample was measured using the mean liner intercept method.

Tensile testing was carried out on a Shimadzu AGS-X machine with a strain rate of 1.67×10^{-3} s^{-1} at ambient temperature. Tensile specimens with a gauge section 5 mm × 3.5 mm (length × width) were machined from the MSFSP plate in processing direction (PD), 45° direction (titled by 45° from TD to PD) and transverse direction (TD). In order to avoid premature fracture the surfaces of the tensile specimens were polished before testing with abrasive paper of #2000 until to a final thickness of 1.5 mm. The hardness profiles were measured along the central line of SZ on the cross-section of sample as shown in Fig. 4a. A load of 0.98 N, loading cycle of 10 s and indention interval of 0.5 mm were applied in the microhardness measurement.

Results and Discussion

Macrostructure

Cross section macrograph of the MSFSP sample perpendicular to the processing direction is shown in Fig. 2. No defect is found in the cross section of sample, where the right side of processing profiles of respective pass can be seen clearly. Three distinct zones can be identified: SZ, thermo-mechanically affected zone (TMAZ) and the top region (TR). No distinct heat-affected zone is found due to

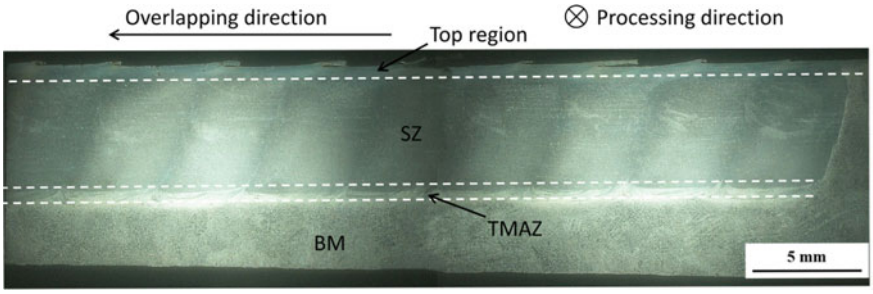

Fig. 2 Cross section of the MSFSP AZ61 Mg plate

rapid cooling provided by flowing water. It is found that the thickness of TR is narrow with a depth of about 0.72 mm. It can be explained that the effect of the cooling medium counteracts the heat input from shoulder and rotating pin on microstructure of plate. TMAZ is unique to the FSW/FSP process, which is a transition zone between BM and SZ. In this work, the TMAZ is also very narrow, resulting in a sharp transition from SZ to BM.

Microstructure

Figure 3 presents SEM images of microstructural characterization of MSFSP samples in TR, SZ and TMAZ. Figure 2a shows that the BM composed of large α-Mg grain and coarse eutectic β-$Mg_{17}Al_{12}$ phases which separately distribute around the boundaries of grains. After multi-pass FSP, fine and equiaxed grains with an average grain size of 10.6 and 10.7 μm were obtained in TR and SZ, respectively (Fig. 3b, c). Grain refinement results from the dynamic recrystallization caused by intense plastic deformation. The network-like second phases $Mg_{17}Al_{12}$ were broken into small particles homogeneously distributed throughout the SZ and TR. Figure 3d displays the structure of TMAZ with partial grains with dynamic recrystallization and deformed grains with elongated shapes.

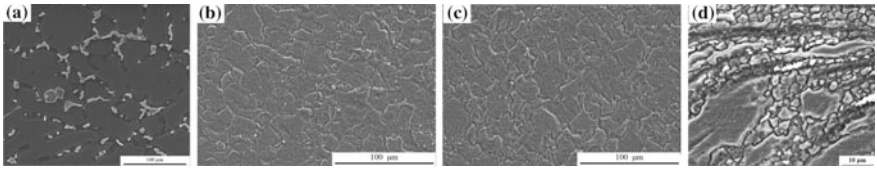

Fig. 3 SEM images of microstructural characterization for multi-pass SFSP samples in **a** BM, **b** TR, **c** SZ and **d** TMAZ

Room-Temperature Mechanical Properties

Figure 4 shows the Vickers microhardness profiles measured along the central line on cross section of MSFSP sample. The average HV value of BM is 55.5, while the hardness of SZ in the MSFSP sample increases to 64 HV. Compared to BM, the hardness of MSFSP specimen are higher, which is mainly attributed to the grain refinement according to the Hall-Petch equation.

Figure 5 shows the room temperature tensile properties of BM and MSFSP AZ61 Mg alloy plate. The corresponding mechanical properties are listed in table attaching in Fig. 5. MSFSP plate shows anisotropic behaviors according to their stress-strain curves. The figure shows that the MSFSP plate achieved an improvement in mechanical properties than BM, which mainly attributed to grain refinement. Comparison among TD, PD and 45° specimens, the tensile specimens in PD presented the best tensile strength of 238 MPa UTS and 73 MPa YS, with elongation of 31.7%. In contrast, the strain to failure in 45° specimen showed the relatively poor ductility, just with elongation of 13.2%. The results reveals that the MSFSP AZ61 Mg alloy plate presents obvious mechanical anisotropy, especially in

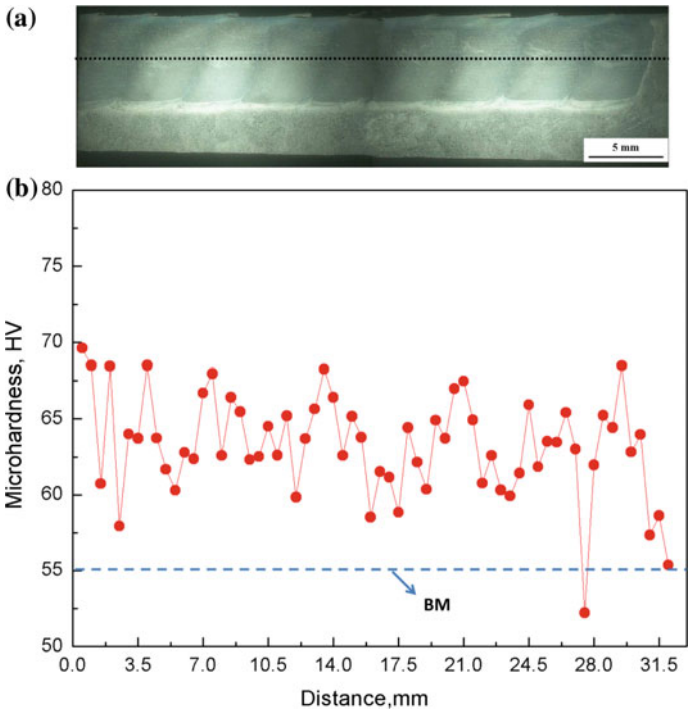

Fig. 4 **a** Cross-section of plate with multiple-passes showing central line of measurement for microhardness. **b** Hardness profiles of a MSFSP AZ61 magnesium alloy plate

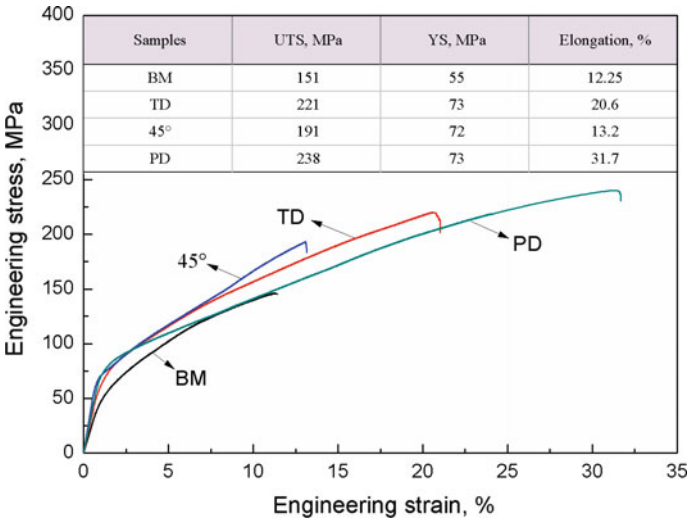

Fig. 5 Engineering stress-strain curves of BM and MSFSP samples in different directions

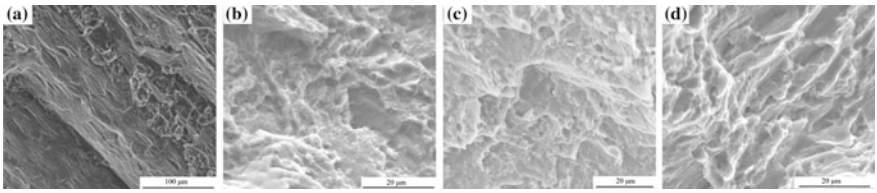

Fig. 6 SEM images of the fracture surface of **a** BM and the tensile specimens in **b** TD, **c** 45° and **d** PD

ductility. The mechanical anisotropy is possibly associated with texture in the MSFSP plate, which need to be further investigated.

Figure 6 shows the tensile fracture morphologies of test specimens. Cleavage facets can be seen on the fractured surface of BM (Fig. 6a). This result indicates the BM fails through brittle fracture mode judged from these typical characteristics. This can be explained why the BM presents low ductility. Figure 6b–d exhibits the fracture morphology of TD, 45° and PD tensile specimens, respectively. Note that the dimples and tearing ridges distribute dispersedly on the fracture surface of these tensile specimens. However, there are deeper dimples and more tearing ridges on the fracture surface of PD tensile specimen, as shown in Fig. 6d. In contrast, less dimples and tearing ridges exhibit on the fracture surface of 45° tensile specimen (Fig. 6c). These fracture surfaces observation is in consistent with the results of the tensile test at room temperature.

Conclusions

(1) MSFSP with an overlapping ratio 50% can produce bulk fine-grained AZ61 Mg alloy plate with average gain size of about 10.7 μm in SZ. The second-phase $Mg_{17}Al_{12}$ is broken into small particles and dissolved into Mg matrix durring MSFSP.
(2) Compared to BM, the microhardness of MSFSP AZ61 Mg alloy plate improves to 64 HV due to grain refinement in SZ.
(3) The mechanical properties of obvious MSFSP AZ61 Mg plate exists in the plate, especially its ductility. The best properties are abtain in PD specimen with an elongation of 31.7%, while the elongation of 45° specimen is 13.2%.

Acknowledgements This work was sponsored by the Research Fund for the Doctoral Program of Higher Education of China (No. 20130172110044), by the Natural Science Foundation of Guangdong for Research Team (No. 2015A030312003).

References

1. R.S. Mishra, Z.Y. Ma, Friction stir welding and processing. Mater. Sci. Eng., R **50**, 1–78 (2005)
2. M.R. Barnett, N. Stanford, Influence of microstructure on strain distribution in Mg–3Al–1Zn. Scr. Mater. **57**, 1125–1128 (2007)
3. X.C. Luo, G.H. Cao, W. Zhang et al., Ductility improvement of an AZ61 magnesium alloy through two-pass submerged friction stir processing. Materials **10**, 253 (2017)
4. Y.S. Sato, S. Park, A. Matsunaga et al., Novel production for highly formable Mg alloy plate. J. Mater. Sci. **40**, 637–642 (2005)
5. G.H. Cao, D.T. Zhang, W. Zhang et al., Microstructure evolution and mechanical properties of Mg–Nd–Y alloy in different friction stir processing conditions. J. Alloy. Compd. **636**, 12–19 (2015)
6. F. Chai, D. Zhang, W. Zhang et al., Microstructure and mechanical properties of submerged friction stir processed AZ91 magnesium alloy. J. Aeronaut. Mater. **32**, 32–37 (2012)
7. C.I. Chang, X.H. Du, J.C. Huang, Producing nanograined microstructure in Mg–Al–Zn alloy by two-step friction stir processing. Scr. Mater. **59**, 356–359 (2008)
8. J.Q. Su, T.W. Nelson, C.J. Sterling, Friction stir processing of large-area bulk UFG aluminum alloys. Scr. Mater. **52**, 135–140 (2005)
9. S. Pradeep, V. Pancholi, Effect of microstructural inhomogeneity on superplastic behaviour of multi-pass friction stir processed aluminium alloy. Mater. Sci. Eng., A **561**, 78–87 (2013)

Effect of Rolling Process on Microstructure and Magnetic Properties of 50W800 Electrical Steel

Ruifeng Dong, Rui Zhang, Lifeng Fan and Rong Zhu

Abstract The effects of microstructure and texture on the magnetic properties of 50W800 non-oriented electrical steel produced by secondary and single cold rolling and annealing process were studied by Zeiss metallographic microscope and X-ray diffraction (XRD). The results showed that under the same composition and the same process parameters, the performance of using secondary cold rolling 50W800 was better than that by single cold rolling method. The iron loss of the final finished steel after annealing by secondary cold rolling was 4.550 W/kg ($P_{15/50}$), the magnetic induction reached 1.749T (50 Hz, 5000 A/m) and the average grain size was 33 μm. The iron loss of the final finished steel after annealing by single cold rolling was 4.924 W/kg ($P_{15/50}$), the magnetic induction reached 1.742T (50 Hz, 5000 A/m) and the average grain size was 24.8 μm. The iron loss of the secondary cold rolling iron loss decreased by 0.374w ($P_{15/50}$), the magnetic induction increased by 0.007T (50 Hz, 5000 A/m), the average grain size increased by 8.2 μm.

Keywords Non-oriented electrical steel · Rolling process · Microstructure Texture · Magnetic properties

R. Dong (✉) · R. Zhang · L. Fan · R. Zhu
School of Materials Science and Engineering, Inner Mongolia University of Technology, Hohhot 010051, Inner Mongolia, China
e-mail: drfcsp@163.com

R. Zhang
e-mail: 496644837@qq.com

L. Fan
e-mail: fanlifeng829@163.com

R. Zhu
e-mail: 625895466@qq.com

L. Fan
Bao tou Steel (Union) Co. Ltd., Baotou 014010, Inner Mongolia, China

© Springer Nature Singapore Pte Ltd. 2018

Y. Han (ed.), *Advances in Materials Processing*, Lecture Notes in Mechanical Engineering, https://doi.org/10.1007/978-981-13-0107-0_64

Introduction

Silicon steels are fundamental for the economy of electrical appliances, and offer the best combination for transmitting and distributing electrical energy. The properties require these steels with a high permeability and induction, low magnetic losses, and low magnetostriction [1].

Each year, most of the power generation in the country is consumed by various motors. Among them, low-grade non-oriented silicon steel manufacturing of small motors, household motors and micro-motor accounted for most of the motor production [2]. The magnetic properties improvement of low-grade non-oriented silicon steel is conducive to energy conservation.

The performance of non-oriented silicon steel is mainly determined by factors such as grain size of steel plate, texture component, inclusions and chemical composition. In previous studies, the emphasis of processing technology was to control the grain size, and the control of texture was not paid enough attention. The performance was optimized by optimizing the production process and taking into account the two. The use of secondary cold rolling method can reduce the hot rolling reduction and reduction of the rolling capacity of hot rolling mills and meet the requirements of different factories. The 50W800 non-oriented silicon steel produced by a steel mill is studied as research object. The changes of microstructure and magnetic properties of primary and secondary cold rolling are studied to provide the basis for improving the performance of the product.

Test Materials and Methods

The experimental material is a 50W800 non-oriented electrical steel plate produced by a steel mill. The chemical composition is shown in Table 1.

The parameters of the process are shown in Table 2. Firstly, the secondary cold rolling method was using cold rolling, letting the thickness of 4.5 mm hot rolled steel strip into to the middle thickness of 2.0 mm and then annealed. After that the steel strip was cold rolled from 2 to 0.5 mm then annealed again, the reduction rate was 75%. Single cold rolling method was used to cold-roll the hot-rolled steel strip with a thickness of 2.48 mm and then cold rolled to 0.5 mm and the total reduction rate was 79.8%. The hot rolling process parameters and the finished steel strip annealing process of the two schemes are totally same. Metallographic samples were treated with 4% nitric acid. The microstructures were observed at 100 times of

Table 1 Chemical composition of experimental steel (wt%)

C	Si	Mn	P	S	Alt
0.002	0.5	0.3	0.1	0.004	0.4

Table 2 50W800 non-oriented electrical steel process parameters

Process	Sample number	Process status	Reduction rate %
Secondary cold rolling	a	Hot rolling	
	b	Once cold rolled	56.50
	c	Hooded annealing	
	d	Secondary cold rolling	75
	e	Continuous annealing	
Single cold rolling	f	Continuous annealing	79.8

Note Under the same conditions of Rolling temperature:1080 °C; Finish rolling temperature: 900 °C; Coiling temperature:730 °C; Intermediate annealing temperature: 660 °C; Final annealing temperature: 890 °C

Zeiss metallographic microscope. The final product texture was analyzed by X-ray diffractometer and the magnetic properties of the finished product were measured by Epstein frame method.

Test Results and Analysis

Microstructure

The microstructure of hot rolled sheet with thickness of 4.5 mm is shown in Fig. 1a. Equiaxed ferrite is relatively coarse with a slight mixed crystal phenomenon, the average grain size of 38.8 μm. The grain size of hot-rolled plates has an important effect on the magnetic property of non-oriented electrical steel. Because of the initial grain boundaries are few the nucleation position is less during annealing, so the recrystallized grains are easy to grow, thus increasing the content of cubic texture and Gauss texture of the finished products [3].

Figure 1b shows the thickness of 4.5 mm hot rolled plate by cold rolling to 2.0 mm of the microstructure, and reduction rate is 55.6%. It can be seen from the figure the grain is obviously stretched and flattened.

Figure 1c is the microstructure of the 2.0 mm thick Cold rolled plate after batch annealing. The elongated flattened grains are re-converted to equiaxed ferrite after recovery, recrystallization and grain growth. The average grain size is 26 μm, compared with the hot rolled plate the grains become fine and uniform.

Figure 1d shows the microstructure of a secondary cold-rolled sheet having a thickness of 0.5 mm and the reduction rate is 75%. Tissue is a typical cold-rolled fibrous tissue.

Figure 1e is microstructure of the 0.5 mm thick secondary cold-rolled plate after the final annealing. The organization re-transformed into equiaxed ferrite but the grain becomes coarse the average grain size of 33 μm.

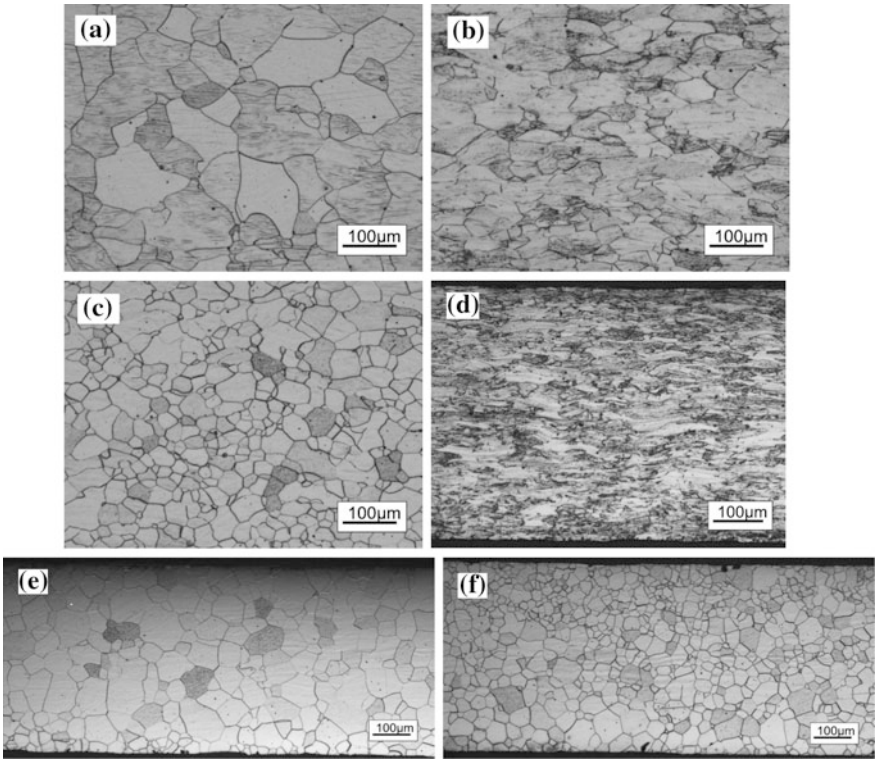

Fig. 1 Experimental steel microstructure photos (100×) **a** 4.5 mm hot-rolled sample **b** 2.0 mm cold rolled sample **c** 2.0 mm annealed sample **d** 0.5 mm cold rolled sample **e** secondary cold rolled 0.5 mm annealed sample **f** single cold rolled 0.5 mm annealed sample

The microstructures of single cold rolling steel strip after final annealing are also equiaxed ferrite, but the average grain size is 24.8 μm which is much smaller than that of the secondary cold rolling method, as shown in Fig. 1f.

When heavy rolling reduction, cold rolled sheet energy storage can have more nuclear location. After the heavy rolling reduction the recrystallization nucleation is mainly formed in the original grain boundary and it begins to crystallize through the migration of high angle grain boundaries before the energy storage is completely released. The energy released by the recovery process accounts for a small portion of the energy storage and most of the energy is used to drive the recrystallization [4, 5]. This may be the main reason for the grain size of single cold rolling is less than the secondary cold rolling.

From the point of view of grain size, the more the grain boundary, the greater the hysteresis loss, and the hysteresis loss decreases with the growth of grain. The results show that for 1% silicon steel, the grain size increases by one grade, and the average iron loss decreases by about 5% [2]. In this experiment, secondary cold

rolling method grain size is larger than single cold about 8.2 μm, the iron loss of the secondary cold rolling method should be lower than that of the single cold rolling method.

Finished Board Texture

Magnetic properties depend on not only the grain size but also the magnetic properties of the texture [6]. The process of recrystallization and grain growth are the main reason for the texture of the final finished sheet. The recrystallization texture of electrical steel is composed of multiple texture components. Some of the components through the annealing process will be strengthened and the other components will be weakened depending on which grains are more conducive to swallowing other bits to grow. {100} surface grain is the most easy to slip, low dislocation density, low energy storage difficult to recrystallize. {111} grain deformation energy storage. {111} oriented grain has high grain boundary mobility and grain growth ability. {111} plane texture grains are easy to swallow other grains and growth [7, 8].

The orientation distribution function $\varphi_2 = 45°$ is the most representative cross-sectional view of the non-oriented silicon steel texture. A series of important orientation positions can be observed in this screenshot [10]. Figure 2 shows the ODF plot for the orientation distribution function $\varphi_2 = 45°$ of the finished annealed plate. It can be seen from Fig. 2 that the texture of the two kinds of experimental steel products is mainly {111} plane texture, but as shown in Fig. 2a the strength of the secondary cold rolling method is about 5.3, and in Fig. 2b, the strength of single cold rolling is 8.5. This is indicating that the secondary cold rolling method of

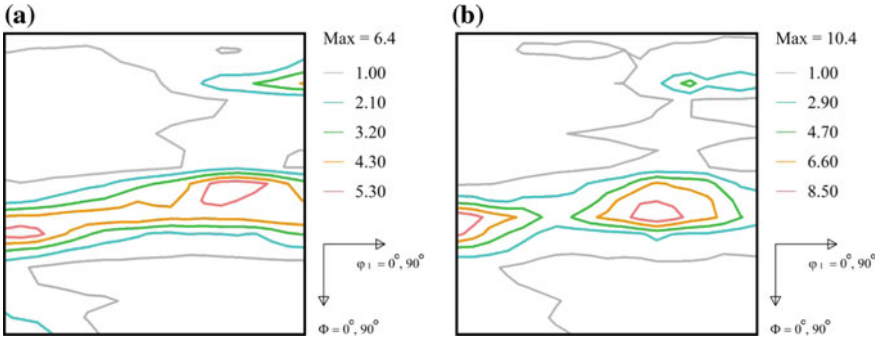

Fig. 2 ODF of $\varphi_2 = 45°$ sections of the tested sheets. **a** Secondary cold rolling finished sheet texture **b** single cold rolling finished sheet texture

magnetic induction should be higher than the single cold rolling method. In Fig. 2a there is still some anti-Gauss texture and the intensity is about 2.1. The anti-Gauss texture is favorable texture so the secondary cold rolling method is better than the single cold rolling method.

Magnetic Properties

As shown in Table 3, the magnetic properties were measured by the Epstein frame measuring system. The iron loss of the Secondary rolled steel strip is 4.550 W/kg ($P_{15/50}$), the magnetic induction is 1.749T (50 Hz, 5000 A/m). The iron loss of the single cold rolling is 4.924 W/kg ($P_{15/50}$) and the magnetic induction is 1.742T (50 Hz, 5000 A/m). Compare with the single cold rolling, the iron loss of the secondary rolling is reduced by 0.374 W/kg ($P_{15/50}$) and the magnetic induction intensity is improved. Indicating the use of secondary cold rolling method, changing the appropriate rolling parameters can improve the performance of 50W800 non-oriented electrical steel. The results of grain size and texture test of two samples also prove this conclusion.

The main factors that affect the steel loss of non-oriented electrical steel are mainly hysteresis loss. The iron core made of electrical steel is subjected to repeated magnetization in the alternating magnetic field and a large number of magnetic domain walls within the polycrystal need to be repeatedly swept through the ferrite matrix to realize the magnetization process. Therefore any factors that impede the migration of magnetic domain walls will cause the iron loss to rise and even lead to a decrease in magnetic susceptibility. Magnetic domain walls usually only migrate within the crystal and can not cross the grain boundary. But the grain boundary and the nearby atoms deviate from the regular structure of the arrangement will interfere with the domain wall migration atomic magnetic moment of the steering so grain boundary will hinder the magnetization process. That is the reason why coarse grain structure is usually conducive to obtain good soft magnetic properties mainly for the iron loss with the increase in grain size decreased [9].

Table 3 Magnetic properties

	Secondary cold rolling finished plate	Single cold rolling finished plate
$P_{15/50}$/(W/kg)	4.550	4.924
B_{50}/T	1.749	1.742

Conclusions

(1) Compare with the single cold rolling, the iron loss of the secondary cold rolling method is reduced by 0.374 W/kg ($P_{15/50}$), and the magnetic induction is improved by 0.007T (50 Hz, 5000 A/m). The magnetic properties of the 50W800 electrical steel produced by the secondary cold rolling process are better than that of the single cold rolling method but the magnetic properties of the two processes meet the standard requirements.
(2) In the case of the same composition and process parameters, the microstructure of the finished steel strip produced by the two processes is equiaxed ferrite. The particle size of the finished steel strip produced by the secondary cold rolling method is larger than that of the single cold rolling method. That is one of the main reasons that the iron core of the secondary cold rolling steel strips is lower than that of the single cold rolling.
(3) The strength of the {111} plane texture of the secondary cold-rolled finished plate is weaker than that of the single cold rolling method. And there is a part of the anti-Gauss texture which is one of the main reasons that the magnetic induction intensity of the secondary cold rolling method is higher than that of the single cold rolling method.
(4) Microstructure observation shows that there are non-uniform phenomena in the microstructure of the two rolling processes and it is necessary to further optimize the hot rolling process, cold rolling process and recrystallization annealing process.

Acknowledgements This research was funded by National Natural Science Foundation of China (51661026), China Postdoctoral Science Foundation (2016M602914XE), Inner Mongolia Natural Science Foundation (2015BS0508), Key project of Inner Mongolia University of Technology (ZD201509) and Innovative experiment of college students at Inner Mongolia University of Technology (2016037).

References

1. D.S. Petrovič, Non-oriented electrical steel sheets. Mater. Tehnol. **44**, 317–325 (2010)
2. Z.Z. He, Y. Zhao, H.W. Luo, *Electrical Steel* (Metallurgical Industry Press, Beijing, 2012)
3. L. Ma, L. Xiao, S.T. Qiu, P. Zhao, Effect of double cold rolling on magnetic property and microstructure of non-oriented high silicon steel sheets cast by strip casting process. J. Iron Steel Res. **25**, 42–46 (2013)
4. W.M. Mao, X.B. Zhao, *Recrystallization and Grain Growth of Metals* (Metallurgical Industry Press, Beijing, 1994)
5. N. Rajmohan, J.A. Szpunar, Monte-Carlo simulation of Goss texture development in silicon steel in the presence of MnS particles. Mat. Sci. Eng. A. **289**, 99–108 (2000)
6. J.W. Zhao, W.K. Zhang, X. Miao, Effect of percentage reduction in two-stage cold rolling on microstructure, texture and magnetic properties of high grade non-oriented silicon steel sheets. Iron and Steel **47**, 69–72 (2012)

7. G.Q. Hu, Y.P. Zeng, H. Luo, L.J. Wang, Annealing microstructure evolution of a new cold-rolled non-oriented electrical steel with high cold rolling reduction. Heat Treat. Met. **36**, 87–90 (2011)
8. C.X. Jia, L. Xiang, G.B. Tang, S.T. Qiu, H.J. Zhao, Evolution of microstructure and texture of 50W1300 non-oriented silicon steels. Iron Steel Vanadium Titan. **33**, 82–87 (2012)
9. W.M. Mao, P. Yang, *Material Science Principles on Electrical Steel* (Higher Education Press, Beijing, 2013)
10. W.M. Mao, X.J. Zhang, *Quantitative Texture Analysis of Crystalline Materials* (Metallurgical Industry Press, Beijing, 1993)

Evaluation on the Dimensional Stability of Filled and Un-Filled Models of Investment Casting Pattern Materials

Liqiang Zeng, Yi Li, Zengjun Wang, Jiaqi Lu and Hua Li

Abstract The dimensional stability of casting is a vital index in the process of the quality control of investment casting and the stability is directly affected by the dimensional stability of models of investment casting pattern materials. By using the Batch Stabilization Process Capability Index (C_{pk}) to give an evaluation on filled pattern materials of investment casting (Brand SP9515 and F28-44B) and unfilled ones (Brand T162 and HH162), it was found that the Index of the former was higher that of the latter. Hence, it is suggested that for manufacturers, utilizing filled pattern materials can improve the dimensional stability of casting when producing high-quality precision parts. Meanwhile, filled pattern materials have better surface properties.

Keywords Investment casting · Filled pattern materials · Unfilled pattern materials · Process capability index

L. Zeng · Y. Li (✉) · Z. Wang · J. Lu · H. Li
SND, No. 1 Xuqing Road, Xuguan Industrial Park, Suzhou, Jiangsu, China
e-mail: wwwlee@chinawaxes.com

L. Zeng
e-mail: liqiang.zeng@chinawaxes.com

Z. Wang
e-mail: zengjun.wang@chinawax.com

J. Lu
e-mail: jiaqi.lu@chinawaxes.com

H. Li
e-mail: hua.li@chinawaxes.com

© Springer Nature Singapore Pte Ltd. 2018

Y. Han (ed.), *Advances in Materials Processing*, Lecture Notes in Mechanical Engineering, https://doi.org/10.1007/978-981-13-0107-0_65

Introduction

In our country, investment casting technology was firstly applied in the field of aviation industry in the 1950s, after which the technology has been used more widely. During the period from the 1980s to the 1990s, according to the development demands of aviation industry, our country began developing a kind of technology of precision investment casting called "no less allowance", which means that casting has a high dimension accuracy and surface smoothness so that it will no longer need a secondary operation. After the 1990s, with the rapid development of national economy and the advancement of investment casting technology, investment casting industry has acquired a giant leap, which, to some extent, benefited from the diversion of investment casting factories from Taiwan to the mainland [1]. Meanwhile, massive private enterprises emerged, the majority of these enterprises produced golf head of stainless steel, tube valve joint, hardware fitting and general machinery part. Most of pattern materials of investment casting are middle temperature mold casting pattern materials [2]. After the development of more than 20 years, there have been about 550 enterprises having reached the standards of precision investment casting in China. Whereas, this period witnessed a very slow development in the field of pattern materials, quite a few casting factories utilized imported recycled pattern materials. Also, a part of casting merchants took advantage of pattern materials investigated all by themselves. However, in high-end fields, like casting of aeroengine, the filled pattern materials have to totally depend on importation. The common features of high-end pattern materials are low shrinkage and expansion rates, stable model dimensions and smooth surface.

Pattern material is a key factor affecting investment casting dimension. The dimensional accuracy of casting is greatly influenced by the dimensional stability of wax pattern. The question on how to acquire a model of stable dimension from every wax injection has bothered every precision casting enterprises. It includes two aspects of evaluation requirements for wax pattern, one is surface quality, the other is dimension accuracy. The impact factors of wax dimension accuracy and surface quality in the process of wax injection include injection temperature, injection pressure, wax flow rate, mold temperature, dwell time and so forth. In addition, factors like proficiency of different operators, physicochemical index fluctuations about different batches of wax and room temperature and humidity of wax injection should also be taken into account. Therefore, casting enterprises ought to conduct an application evaluation test before using wax pattern materials. You can refer to our previous research report [3] to acquire how to conduct the test. This paper attempts to use the Batch Stabilization Process Capability Index (C_{pk}) to evaluate the batch stability of wax pattern materials. Batch stability is conducive for manufacturers to evaluate the stability of wax pattern materials, at the same time, it guides the users to more accurately select wax pattern materials in terms of their own process capabilities and reduces the costs of production and management for precision casting manufacturers.

Experimental

Instruments and Materials

The instruments and materials used in the present study were as follows: the C type wax injection machine (mold clamping pressure 16T) of Taiwan Yiying, filled pattern material SP9515 (Jiangsu Taier Novel Material Co. Ltd.), F28-44B (Paramelt Specialty Materials (American) Co. Ltd.); unfilled pattern material T162 (Jiangsu Taier Novel Material Co. Ltd.), HH162 (Dalian Global-link International Inc.), and Precision digital vernier caliper (Guilin Measuring & Cutting Tools Co. Ltd., precision: 0.01 mm).

Experimental Conditions

For filled wax pattern materials, the injection pressure was 24 bar, the wax injection temperature was 60 °C and the holding time was 15 s. For un-filled wax, the injection pressure was 24 bar, the injection temperature was 55 °C and the holding time was 15 s. The temperature in the wax injection chamber was 23 ± 2 °C and the relative humidity was 60–75%.

Test Conditions

Pattern material models were put under the temperature of 23 ± 2 °C for the test after 24 h.

Results and Discussion

Pattern Material Model

The pattern material model used in the test is shown in Fig. 1. The model had four points for testing shrinkage rate. Please refer to the ref. [4] for more information about the model. The region O1 not only had the maximum shrinkage rate, but also had the maximum shrinkage fluctuation. So the stability of shrinkage rate at O1 can reflect the dimensional stability and the process capability index of the pattern material model best. Therefore, the following results refer to the shrinkage rate of O1.

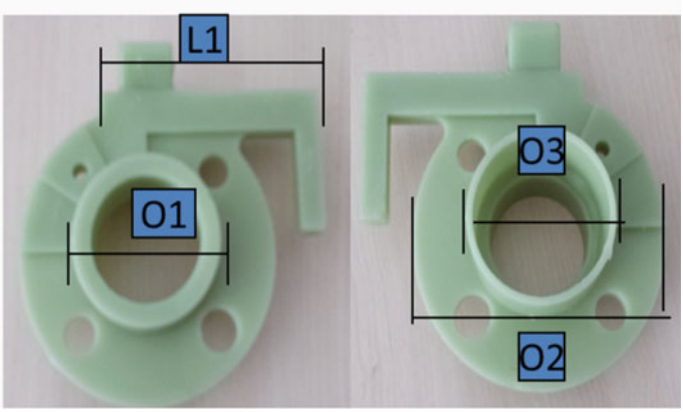

Fig. 1 The testing position of pattern material model. O1: Outside diameter ¢ = 54 mm, inner diameter ¢ = 40 mm, annulus; O2: Outside diameter ¢ = 100 mm, thickness 5 mm, pie; L1: length = 90 mm, width = 15 mm, thickness = 10 mm, rectangle; O3: Outside diameter ¢ = 55 mm, v = 50 mm, annulus

Filled Pattern Materials

Figures 2 and 3 show the process capability indexes of SP9515 and F28-44B in O1 respectively. The control charts show that the general operation of the filled wax

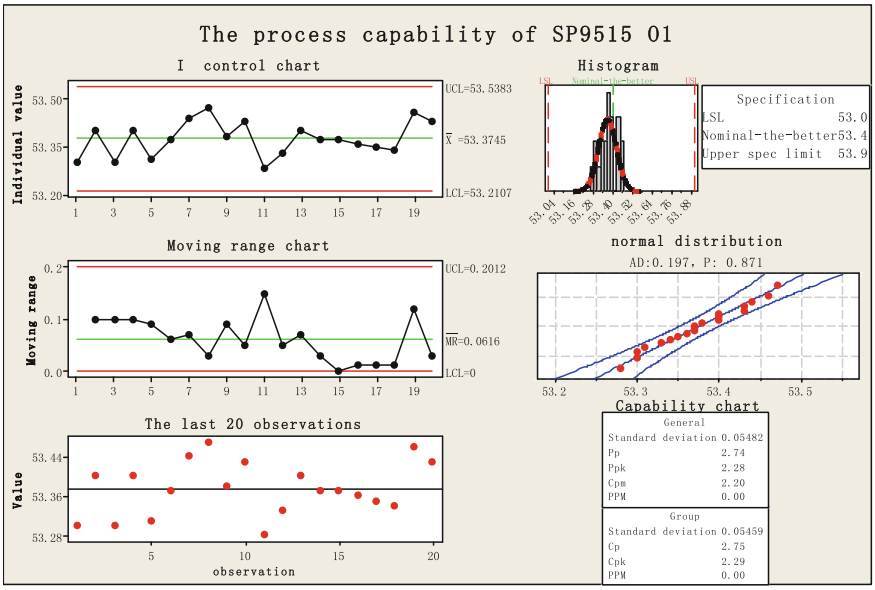

Fig. 2 Process capability of SP9515 at the position of O1

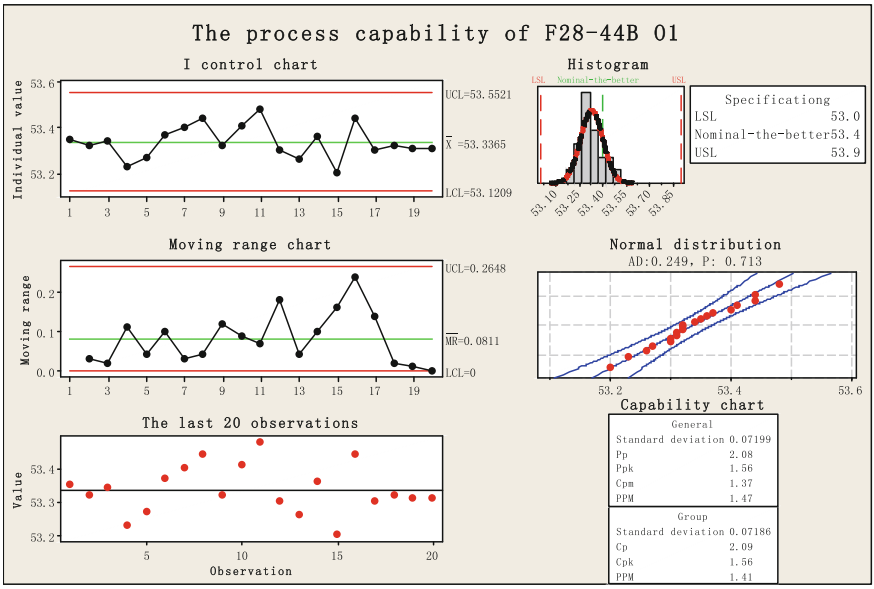

Fig. 3 Process capability of F28-44B at the position of O1

pattern materials is under control. From the moving range control charts, we can draw a conclusion that the process of moving variation is acceptable. The capability histograms and the normal probability graphs of Figs. 2 and 3 conclude that the overall normality assumption is reasonable. The overall variation is stable when both C_{pk} indexes are greater than 1.33. Compare the moving range of SP9515 with that of F28-44B, the former is 0.0616, while the latter is 0.0811. This result shows that the general dispersion of SP9515 is less than F28-44B, which is helpful to the stability of product quality. The C_{PK} of the two filled pattern materials are both greater than 1.67, which indicates that the two brands fully meet the process capability requirements. Reducing operating costs should be considered in actual use.

Un-Filled Pattern Materials

Figures 4 and 5 show the process capability index of T162 and HH162 at the position of O1 respectively. According to the control chart, it is concluded that the operation of T162 is under control. The moving range control chart shows that the process of moving variation is acceptable. It is illustrated from the capability histogram and the normal probability that the overall normality assumption is reasonable. The C_{PK}(1.45) is greater than 1.33, which indicates that the overall variation is stable. Good results by maintaining the running status. According to the control chart of Fig. 5, the operation of HH162 is under control. The moving range

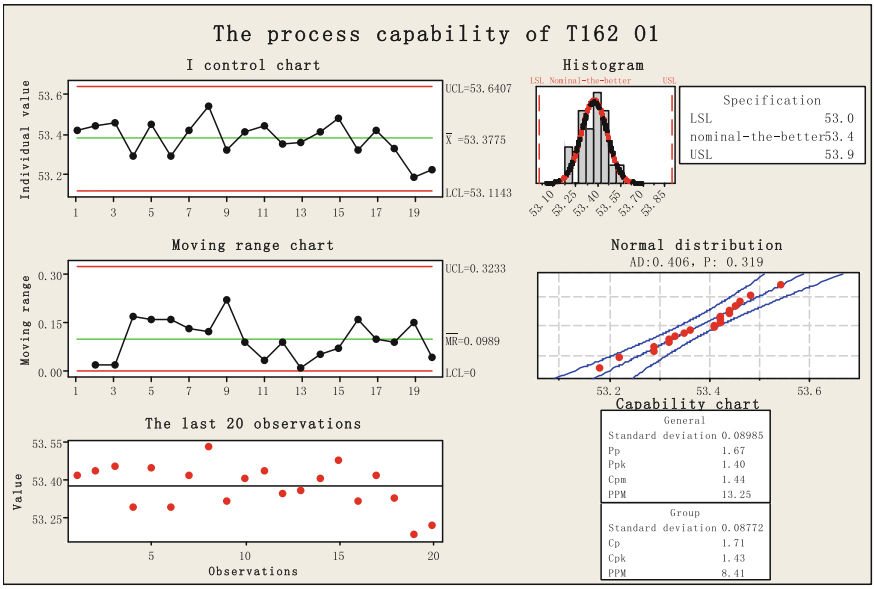

Fig. 4 Process capability of T162 at the position of O1

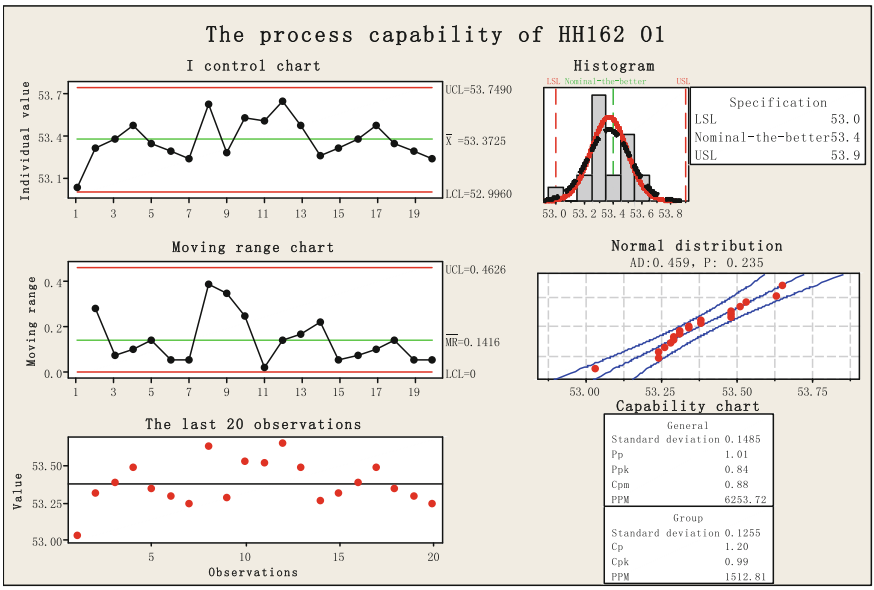

Fig. 5 Process capability of HH162 at the position of O1

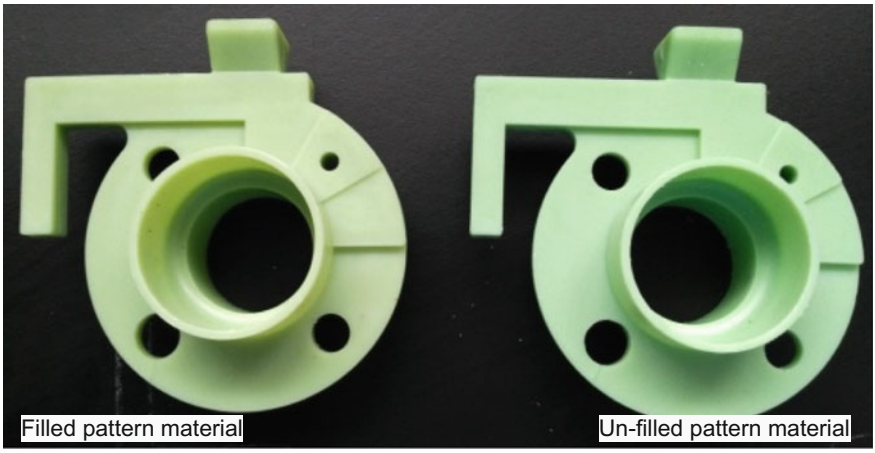

Fig. 6 Filled pattern material

of HH162 (0.1416) is bigger than that of T162 (0.0989), which illustrates that the dispersion of HH162 is greater than that of T162. From the capability histogram and the normal probability graph of HH162, we can draw the conclusion that the overall normality assumption of HH162 is reasonable. The $C_{PK}(0.99)$ of HH162 is less than 1.33 but greater than 0.67, which shows that there are many defective products during the process, so it is necessary to improve the process capability.

Pictures of Filled Pattern Material Models

It can be seen from Figs. 6 and 7 that filled pattern material, which is compared with unfilled one, has better surface quality and smoothness. In addition, filled category has no flaws such as surface flow liner and surface hollow.

Conclusion

By analyzing the process capability index of the same batch of investment casting pattern materials, it is found that:

(1) in contrast to unfilled pattern material, the process capability index of filled pattern material is better.
(2) the comparison graph of moving ranges of filled pattern materials shows that the dispersion of SP9515 is less than that of F28-44B.

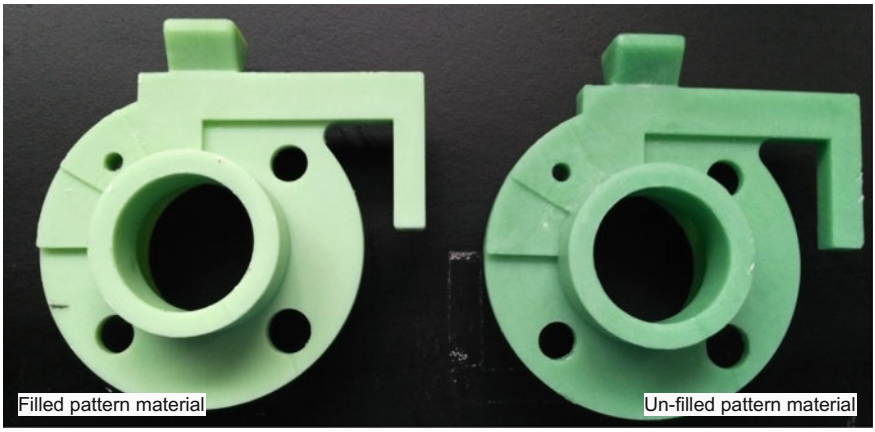

Fig. 7 Models of filled and un-filled pattern materials

(3) in contrast to HH162, the unfilled pattern material T162 has a better process capability, it is a necessity that the index of HH162 should be improved during its practical use.
(4) filled pattern material has better surface quality than its unfilled counterpart.

References

1. X. Pan, B. Qu, M. Sun, P. Liu, A superficial discussion on the development, current situation and gaps of China's "no less allowance" precision investment casting technology. J. Guangxi Univ. (Nat. Sci.) **33**, 178–181 (2008)
2. L.V. Zhi-gang, Historical retrospect and development prospect of China's precision investment casting. Casting **4**, 347–356 (2014)
3. L. Zeng, Y. Li, Study on evaluation method of wax in medium temperature precision casting. The Fourteenth Annual Meeting of Zhejiang Foundry Association Precision Casting Professional Committee, (2016), pp. 41–45
4. L. Zeng, Y. Li, S. Song et al., NB/SH/T 0941-2016, Special Waxes for Precision Casting. (National Energy Board, Beijing, 2016)

Relationship of Oil Composition and Lubricating Characteristics in Cold Rolling Aluminum Strips

Yongtao Zhao, Jianlin Sun, Guangzhao Yuan and Chenglong Wang

Abstract To explore the relationship of oil composition and lubricating characteristics, new base oils with different carbon chain length and aromatics contents for lubrication in cold rolling aluminum process were investigated by means of Gas Chromatography-Mass Spectrometry. Tribological tests were carried out on a four-ball friction and wear testing machine. Results showed that the film strength gradually increased with an increasing of aromatics content in oils and friction coefficients decreases simultaneously. Cold rolling experiments were conducted to be further to analyze the lubrication effects of new rolling oils by a 4-high mill. The curves of lubricating characteristics in rolling were obtained, and the minimum rolling thickness after rolling under different lubricating conditions was found to decrease obviously.

Keywords Rolling oil · Composition · Lubrication characteristics

Y. Zhao (✉) · J. Sun · G. Yuan · C. Wang
School of Materials Science and Engineering, University of Science and Technology Beijing, Beijing, China
e-mail: zhao_yongtao@126.com

J. Sun
e-mail: sjl@ustb.edu.cn

G. Yuan
e-mail: ygz_ygz93@163.com

C. Wang
e-mail: wclfight@163.com

Y. Zhao
School of Mechanical Engineering, Henan University of Engineering, Zhengzhou, China

© Springer Nature Singapore Pte Ltd. 2018

Y. Han (ed.), *Advances in Materials Processing*, Lecture Notes in Mechanical Engineering, https://doi.org/10.1007/978-981-13-0107-0_66

Introduction

High-speed rolling of aluminum strips has made great progress. Rolling speed of aluminum strips is assorting from 30–100 m/min to more than 600–1000 m/min. Rolling velocity of high-speed rolling is assorting from 600–1100 m/min to 1500 m/min or more. Ultra-high speed rolling mills with rolling velocity of more than 2500 m/min have been used currently [1–3]. In the high-speed rolling, it only takes even dozens of milliseconds for the rolled pieces go through the rolling area. In such a short time, it's kept up high speed and produced great deformation heat and friction heat in rolling deformation zone. Friction heat and deformation heat of base oils is obvious in non-Newtonian laminar flow, which can't be ignored. The lubrication state in aluminum strips rolling will have a great influence on rolling process. Moreover, oil composition and lubricating characteristics determines the lubrication state in aluminum strips rolling.

Traditional oiliness additives, including some organic acids, alcohols, lipids, etc. [4, 5], can't satisfy the practical condition of high speed, wide rolling and big pressure rate because of comparative low film strength. Traditional aluminum rolling oils by adding additives can't meet the demands of increasingly stringent lubricating conditions [6–8]. Thus, in order to meet the modern rolling production requirement of higher the extreme-pressure properties, the effects of rolling oils with different carbon chain length and aromatics content on the lubricating characteristics, for example, friction coefficients and the minimum rolling thickness, are deeply studied.

Experimental

New base oil N100 and N80 for aluminum rolling strips and foils with different aromatic contents were explored. Aromatic contents of base oils are shown in Table 1. A gas chromatography-mass spectroscopy experiment was performed to explore the length of carbon chain of the oils, according to the standard of ASTM D2425-04.

MR-S10A four-ball friction and wear testing machine was used to test maximum non-seized load P_B of two type base oils with different contents of aromatics. According to the standard of ASTM D2783-03, four bearing steel balls with a diameter 12.7 mm are made by GCr15 and their hardness is 64–66 HRC. In this technique, one steel ball under load is rotated against three stationary steel balls,

Table 1 Aromatic contents of two type base oils (mass percent)

Base oils	Aromatic contents (mass percent)									
N100	0.1	0.2	0.3	0.4	0.5	0.6	0.7	0.8	0.9	1.0
N80	0.1	0.2	0.3	0.4	0.5	0.6	0.7	0.8	0.9	1.0

Table 2 Technical parameters of four roller reversible rolling mill

Items	Working roll diameter (mm)	Roller width (mm)	Support roll diameter (mm)	Main motor power (kw)	Roller rotary (m s^{-1})	Motor speed (n min^{-1})
Parameters	95	200	200	35	60	30–300

these three stationary balls held in the form of a cradle. All balls are immersed in the lubricant. The P_B value tests are conducted at a rotary speed of 1760 rpm and ambient temperature of about 25 °C. And the wear tests are conducted at a rotary speed of 1200 rpm for 30 min while the load is 392 N. When test is finished, the wear scar diameter of the steel balls was observed by means of the optical microscope.

Cold rolling experiments of aluminum foils were carried out on a Φ95/Φ200 × 200 mm four high mills. The technical parameters of the mill are given in Table 2. The minimum rolling thickness of the aluminum strips were measured by means of 4-high mill.

Results and Discussion

The compositions of base oils N100 and N80 are analyzed by gas chromatography-mass spectrometry, meanwhile that are compared with the similar commercial products named D100 and D80, shown in Table 3. The figures in Table 3 indicate carbon chain of N100 base oil distributed in the range of C13–C18, whereas N80 base oil distributed in the range between C12 and C16.

The distributions of carbon chain in base oils have a fundamental influence on the lubricating behavior of lubricant, as it plays a crucial role in determining the viscosity of lubricated oil. A long carbon chain length always represents high viscosity of oil while short carbon chain length means that a low viscosity of oil is present.

It is shown in Table 3 that the carbon chain of N100 is mainly concentrated in C14–C15 components, which are more than 85% of the total in mass, while carbon chains of the general oil samples are mainly concentrated on C11–C13. Although commercial oil's Carbon chain distribution is concentrated, but the carbon chains

Table 3 Distribution of carbon chain in N100 and N80 base oils with D100 and D80

Base oils	C10	C11	C12	C13	C14	C15	C16	C17	C18
N100	–	–	–	10.46	43.79	43.03	2.340	0.1	0.28
D100	3.2	28.6	41.1	26.1	0.8	–	–	–	–
N80	–	–	12.73	53.33	33.56	0.38	0.38	–	–
D80	–	0.1	8.8	35.7	47.0	8.4	–	–	–

are shorter than those of N100 in general, resulting in the base oils of low viscosity, low film strength, and not beneficial to improve the quality of rolled surface during production. The carbon chain of N80 is mainly concentrated in C12–C14, which is more than 85% of the total in mass, especially the mass of C15–C16 components which is only less than 1% of the total. The rest of C12 component is the light component. Comparing with D80, N80 base oil contains a better carbon chain distribution structure, resulting in the characteristics of wide distillation range, high viscosity, more suitable for modern aluminum foil production. These new type base oils with narrow carbon chain distribution and narrow distillation range are closer to practical production process requirements.

The tribological experiments were carried out to measure film strength, the wear scar diameter and friction coefficients of base oils with different aromatics contents. In the base oil, film strength is changing with the aromatics content. The results are shown in Fig. 1.

When the aromatics content of N100 base oil is 0.1–0.5%, film strength attain to 98 N. When the aromatics content is more than 0.5%, film strength is increasing rapidly. When the aromatics content is more than 0.7%, film strength almost remained constant, Value is 108 N.

However, as for N80 base oil, the aromatics content is 0.1%, film strength is 98 N. The aromatics content is continually increased to 0.3–0.7%, film strength is 108 N. The aromatics content further reaches 0.8–1.0%, film strength increases with the increase of aromatics contents, when the aromatics content increased to 1.0%, film strength reach up to 118 N.

The results indicate that film strength of two type base oil increases simultaneously with the increasing of aromatics content. With lower viscosity, film strength is sensitive to aromatics content. The N80 base oil increases simultaneously with the increasing of aromatics content, which is more obvious than N100 base oil.

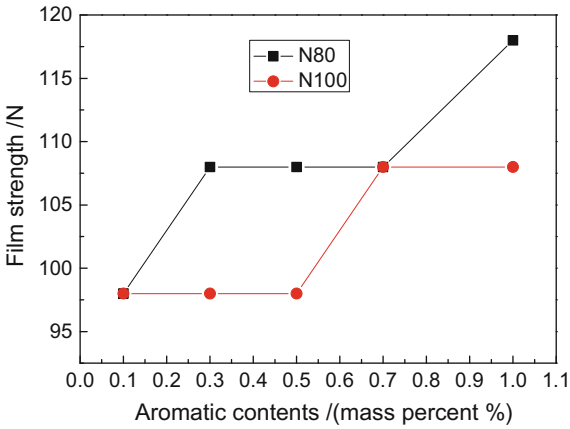

Fig. 1 Film strength of base oils of N80 and N100 base oil

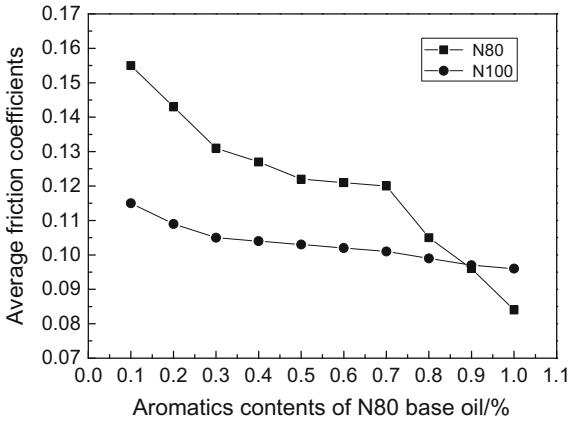

Fig. 2 Average friction coefficient of the N80 base oil

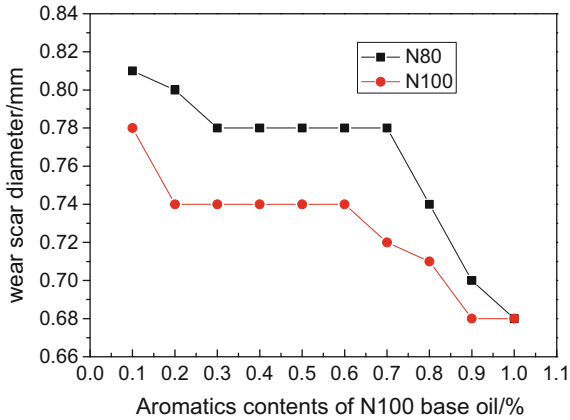

Fig. 3 Average friction coefficient of the N80 base oil

Average friction coefficients and the wear scar diameter of N100 and N80 base oils depend on the content of aromatics in them. Figures 2 and 3 represent the Average friction coefficients and the wear scar diameter of different concentration of aromatics in N100 and N80, respectively. It is seen that average friction coefficients and the wear scar diameter of the base oil decreases with the increase of aromatics, indicating that the addition of aromatics would help to improving the lubrication performance in a large extent. An interesting phenomenon is also found in these two figures. It seems that aromatics in the N80 would cause more outstanding influence on the lubrication performance compared to aromatics in the N100. Possibly due to lubrication characteristics of lubricant is more sensitive to the content of aromatics when the lubricant is in a low viscosity.

Cold rolling experiments were performed on a 4-high mill under different lubricating conditions, and the minimum rolling thickness of the aluminum strips were recorded and shown in Figs. 4 and 5.

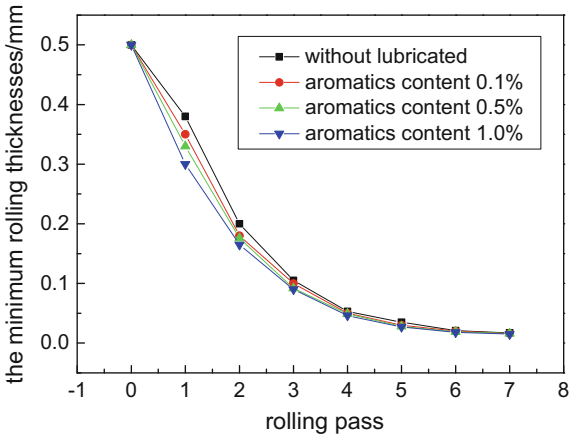

Fig. 4 Minimum rolling thickness of N80 base oil

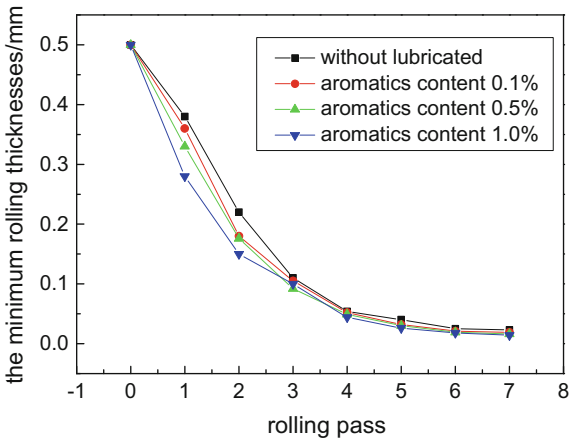

Fig. 5 Minimum rolling thickness of N100 base oil

Under the lubricating condition, smaller minimum rolling thicknesses of the aluminum strips are obtained compared to that without lubricant. For the base oil containing aromatics, boundary lubricating film, which is composed by chemisorbed film and tribochemical film between the aluminum strips and the roller surface, can be formed in the rolling process. Data of cold rolling experiments indicate aromatics in oils have a significant influence on lubricating characteristics. As the friction coefficients and the minimum rolling thicknesses are evidently reduced by adding aromatics to base oil.

Another phenomenon is also found in these two figures. The minimum rolling thickness of aluminum strips decrease with the increasing of aromatic content in oils. The minimum rolling thickness of N100 base oil is 0.021 mm in the non-lubrication condition. Under lubrication of N100 base oil with 1% aromatic content, the minimum rolling thickness is 0.014 mm, which reduced 33.3%

compared with the sample rolled under non-lubricated condition. Under lubrication of N80 base oil with 1% aromatic content, the minimum rolling thickness is 0.015 mm, which reduced 28.6% compared with the sample rolled under without lubricated condition.

With the increase of aromatics content, film strength can be increase, friction coefficient can be decreased and the minimum rolling thickness can be reduced. Not only it meets the requirements of environmental protection, but also ensures the lubricating performance.

Summary

(1) With increasing content of aromatics, the film strength increases. When the viscosity is lower, the sensitivity of the aromatics content on the film strength is higher, which demonstrates that with the increasing of aromatics content, the complement ability of rolling base oil to the extreme-pressure properties is gradually improved, the anti-friction property of the oil is also improved.
(2) Average friction coefficients and the wear scar diameter of the base oil decreases with the increasing of the content of aromatics, indicating that the addition of aromatics helps to improve the lubrication performance in a large extent.
(3) Rolling experiment results show that with the enhancement of aromatic content in rolling oils, the minimum rolling thicknesses of the aluminum strips obviously reduces, which can satisfy the demand of modern aluminum strips rolling with high speed.

References

1. X. Fu, W. Yao, L. Zhang, The current status and development trend of additives in lubricating oils. Automobile Technol. Mater. **5**, 1–6 (2005)
2. W. Du, G. Li, Oil residual on foil surface with wider width high speed aluminum foil mill and improving methods. Light Alloy Process. Technol. **35**(6), 34–35 (2007)
3. C.N. Panagopoulos, E.P. Georgiou, Cold rolling and lubricated wear of 5083 aluminum alloy. Mater. Des. **31**, 1050–1055 (2010)
4. J. Sun, Y. Sun, M.A. Yanli et al., Effect of rolling oil on the surface quality of annealed aluminum foils. J. Univ. Sci. Technol. B **30**(2), 137–140 (2008)
5. J. Shibata, T. Wakabayashi, S. Mori, Adsorption characteristics and lubricating performance of coolant components in cold rolling of aluminum. Tribol. Int. **40**(5), 748–753 (2007)
6. J. Sun, Y. Kang, T. Xiao, J. Wang, Lubrication in strip cold rolling process. J. Univ. Sci. Technol. B **11**(4), 368–372 (2004)
7. J. Sun, Y. Huang, M. Lu, Optimize aluminum's surface roughness in rolling lubrication process. Ind. Lubr. Tribol. **65**(3), 175–180 (2013)
8. Z. Liao, S. Yang, Analysis and discussion on effect factors of aluminum foil rolling process. Nonferrous Met. Process. **43**(1), 21–24 (2014)

Finite Element Simulation for Hot Continuous-Rolled TC4 Alloy Seamless Pipe

Jiaxin Shi, Wei Yu, Entao Dong and Jun Wang

Abstract The rolling difficulty and surface quality of TC4 alloy seamless pipe is related to the rapid decrease of temperature, high deformation resistance in low temperature and the rapid change of friction coefficient with temperature in the hot rolling process. In the present paper the rolling process φ204 mm × 16 mm tubular billet to φ185 mm × 7 mm semi-finished pipe of TC4 alloy by MPM were investigated by thermal-mechanical coupling of finite element method with software ABAQUS. The effect of start rolling temperature and velocity on temperature and the rolling force and power of continuous rolled TC4 pipe were calculated and analyzed, and also the temperature fields, stress fields, strain fields of 900 °C and 2.93 m/s delivered velocity analyzed. The results indicated that rolling groove of steel pipe was suitable for the rolling of TC4 seamless pipe. Under the condition that the initial thickness and the temperature were uniform, the thickness of semi-finished pipe was 7 ± 0.41 mm, the deviation of circular degree was 1.5 mm. The simulation results of TC4 seamless pipe rolling process is verified by practical hot rolling parameters. And the shape of pipe coincides well with the result of simulation.

Keywords Ti alloy · Seamless pipe · MPM · Finite element Thermal-mechanical coupling

J. Shi · W. Yu (✉) · J. Wang
Engineering Research Institute, University of Science and Technology Beijing, 100083 Beijing, China
e-mail: yuwei9451@126.com

J. Shi
e-mail: 15010163415@163.com

J. Wang
e-mail: 1013367947@qq.com

E. Dong
2011 Collaborative Innovation Center, University of Science and Technology Beijing, 100083 Beijing, China
e-mail: etdd@163.com

© Springer Nature Singapore Pte Ltd. 2018

Y. Han (ed.), *Advances in Materials Processing*, Lecture Notes in Mechanical Engineering, https://doi.org/10.1007/978-981-13-0107-0_67

Introduction

Titanium and its alloys are being widely applied in the aerospace industry and oil industry because they have excellent combination of the high mechanical properties and physical characteristics, including high strength-to-weight ratio, hot working ability, outstanding heat treatment capability, excellent biocompatibility, and resistance to corrosion [1, 2].

TC4 alloy pipe is mostly formed by hot extrusion, then further cold rolling and heat treatment. It is difficult to deform TC4 alloy at room temperature because of its high strength, low ductility. To solve this challenge, annealing or heating treatment is necessary during the cold rolling process, leading to the low yield and increased cost [3, 4]. The difficulty of rolling and surface quality control of TC4 alloy seamless pipe is related to the rapid temperature decrease than that of steel, the high deformation resistance at low temperature and remarkable friction coefficient change with temperature in hot rolling process.

The variation of strain, stress and temperature during hot deformation can be analyzed exactly by finite element simulation. And the simulation provides basic data of deformation process parameters and for the cause analysis of surface quality defects of seamless pipe [5, 6]. The results of simulation can be also applied to the technical parameter design for the forming process.

Modeling

Finite Element Model Parameter of Equipment

This paper presented a simulation of the hot continuous rolling process of TC4 alloy tubular after piercing by thermal-mechanical coupling of finite element method with software ABAQU. The rolling equipment was PQF (Premium Quality Finishing) tandem mills. PQF tandem mills adopted three-roller structure which could increase rigidity of roll box, and reduced the stress of single roller. Furthermore, three rollers formed a closed grove, and the roller body was designed short to decrease the bending moment. The three rollers were arranged at 120° in a roll box of the mill. The centerline clearance of stands was 750 mm. The geometry model was shown in Fig. 1.

The groove of roller was formed with five curves. The shapes and dimensions of roller and the gap between the center line and the groove top point were shown in Fig. 2 and the Table 1. And the diameter of roller was 700 mm. The geometry model is generated and simulated with ABAQUS.

Fig. 1 Finite element model

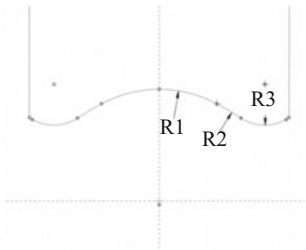

Fig. 2 The groove shape

Table 1 Parameters of groove shape and the gap (unit: mm)

	Roller no. 1	Roller no. 2	Roller no. 3	Roller no. 4	Roller no. 5	Roller no. 6
R1	100.05	96.05	93.5	92.75	91.5	91.5
R2	300.15	336.2	327.25	324.65	251.65	251.65
R3	35.9	25.6	25.9	25.6	9.4	9.4
gap	97	94	92.3	91.6	91.5	91.5

Thermal-Mechanical Coupling Method

The energy conservation equation for continuous body was

$$\int_{\Omega} \rho v_i \frac{\partial v_i}{\partial t} d\Omega + \int_{\Omega} \rho \frac{\partial U}{\partial t} d\Omega = \int_{\Omega} (Q + b_i v_i) d\Omega + \int_{S} (P_i v_i - H) dS \qquad (1)$$

where, Ω stood for volume, S stood for boundary, v_i stood for the field of velocity, U stood for intrinsic energy of unit mass, Q was heat flow of unit volume,

b_i was stress of unit volume, ρ was density, P_i was boundary force of unit area, H was density of heat flow of boundary.

The force-balance equation for continuous body was:

$$\int_{\Omega} \left(b_i - \rho \frac{\partial v_i}{\partial t} \right) d\Omega = \int_{S} P_i dS \tag{2}$$

$$P_i = n_i \sigma_{ij} \tag{3}$$

where n_i was the boundary normal direction, σ_{ij} was the Cauchy stress component (j = 1, 2, 3, and could respect x, y, z direction in rectangular coordinate system.)

So the equation of energy conservation of thermal-mechanical coupling can be obtained as follow:

$$\int_{\Omega} \left[\left(Q - \rho \frac{\partial U}{\partial t} \right) + \sigma_{ij} \frac{\partial v_i}{\partial x_j} \right] d\Omega = \int_{S} H dS \tag{4}$$

Deformation Condition

In the ABAQUS, the heat transfer between pipe and roller or mandrel was determined as 20 MW/mm^2k. The equivalent heat exchange coefficient including radiation, convective and contact with air was 0.17 MW/mm^2k. The friction of roller and pipe was 0.3, and that of pipe and mandrel was 0.1 because of graphite lubrication layer upon the mandrel [7, 8]. The heat conversion coefficient caused by friction and plastic deformation was respectively 0.7 and 0.9.

The outer diameter and wall thickness of tubular billet were 204 and 16 mm respectively, and length was 2 m. As shown in Fig. 3, considering the deformation degree, the meshed elements of head and tail in the tubular billet was smaller than that of middle. 72,000 elements were generated on the tubular billet.

Fig. 3 Elements establishment of tubular billet body and end

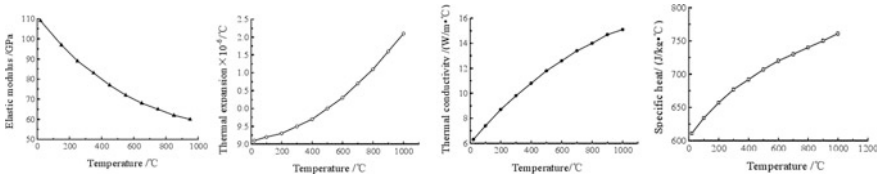

Fig. 4 Some properties of TC4

Table 2 Values of b_0–b_{11}

T/°C	b_0	b_1	b_2	b_3	b_4	b_5	b_6	b_7	b_8	b_9	b_{10}	b_{11}
$<T_\beta$	−1.647	−0.035	0.22	0.22	0.03	0.619	0.808	0.155	4.347	−0.686	−0.872	−0.055
$>T_\beta$	−1.335	1.559	−2.221	−1.357	−0.28	8.363	−0.046	−8.145	10	−10	10	−10

T_β the temperature of phase transformation

The distance between the first roller and the tubular billet was very small. So when rolling, the inner temperature of the work-piece only change a little, so we regard the temperature load of the work as a static load.

The mandrel of PQF is regard as fixed one in milling stage, and the diameter is 170 mm. The deformation of work-piece was mostly considered as elastic-plastic in the FEM, ignore the deformation of rollers and mandrels, regard them as rigid bodies and define them as rigid material model.

The material properties of TC4 were as the Fig. 4. And density was 4.43×10^{-9} t/m^3, Poisson's ratio was 0.34;

The constitutive modeling of TC4 was as following equation and Table 2.

$$\sigma = 10^{B_1 + B_2 + B_3} \tag{5}$$

$$B_1 = b_0 + b_1 \log(\varepsilon) + b_2 \log(\varepsilon)^2 + b_3 \log(\varepsilon)^3 + b_4 \log(\varepsilon)^4 \tag{6}$$

$$B_2 = b_5 \log(\dot{\varepsilon}) + b_6 \log(\dot{\varepsilon})^2 + b_7 \log(\dot{\varepsilon})^3 \tag{7}$$

$$B_3 = \frac{b_8}{T} + \frac{b_9 \log(\dot{\varepsilon})}{T} + \frac{b_{10} \log(\dot{\varepsilon})^2}{T} + \frac{b_{11} \log(\dot{\varepsilon})^3}{T} \tag{8}$$

where:

σ was resistance to deformation; b_0–b_{11} were constant, the values were shown in Table 2; T = (t + 273)/1000, t was deformation temperature; ε was true strain; $\dot{\varepsilon}$ was strain rate, unit: s^{-1}.

Result and Discussion

Influence of Start Rolling Temperature and Rolling Speed on Rolling Pressure

The calculated rolling force is shown in Fig. 5 when the start rolling temperature is 900 °C and the delivered velocity is 2.97 m/s. The max rolling force is under 2500 KN from the results. The minimum rolling force is in the sixth pass, and the second minimum one is the fifth pass. It is considered to improve the accuracy of outer diameter and wall thickness of semi-finished pipe. Large rolling force is setup to enhance the reduction efficiency from the first pass to fourth pass. It is reasonable to hot rolling specification.

The rolling force of every pass is shown in Table 3, while the start rolling temperature is assumed between 800–1000 °C, and the delivery velocity to be 2.03, 2.93, 3.53 m/s. The rolling forces change remarkably when the start rolling temperature changed from 900 to 1000 °C, the reason is that the resistance to deformation changed more quickly. The phase transformation point of TC4 is about 998 °C. When the temperature is over 998 °C, the microstructure changed from $\alpha + \beta$ to α. α phase is more easily deformation than phase [9]. But the grains of phase grow very fast at the temperature of phase region. So the start rolling temperature during 900–950 °C is a proper temperature for deformation [10, 11].

Figure 6 shows the location of the typical elements of the temperature. The temperature of typical elements of 900 °C is shown in Fig. 7, the temperature changed when the contact occur because of the heat flow. There is a temperature increase in b and e during pass deformation because of low thermal conductive and the heat generation by plastic deformation. And the temperature will increase after mill.

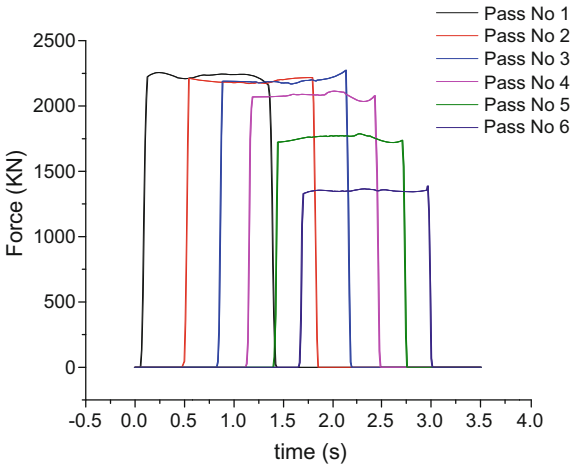

Fig. 5 Rolling force in 900 °C

Table 3 Average rolling force of different process (unit: KN)

T (°C)	v (m/s)	Pass No. 1	Pass No. 2	Pass No. 3	Pass No. 4	Pass No. 5	Pass No. 6
800	2.93	2552	2390	2450	2456	1944	1315
900	2.93	2225	2139	2109	2017	1705	1328
950	2.93	2020	2036	2103	1973	1623	1249
1000	2.93	1371	1832	1830	1772	1288	842
900	2.03	2316	2319	2372	2305	2087	1688
900	3.53	2140	2019	1968	1818	1595	1225

T starting rolling temperature, v delivery velocity

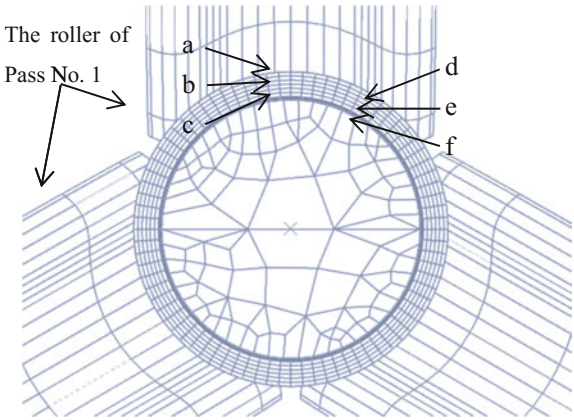

Fig. 6 Diagram of typical elements

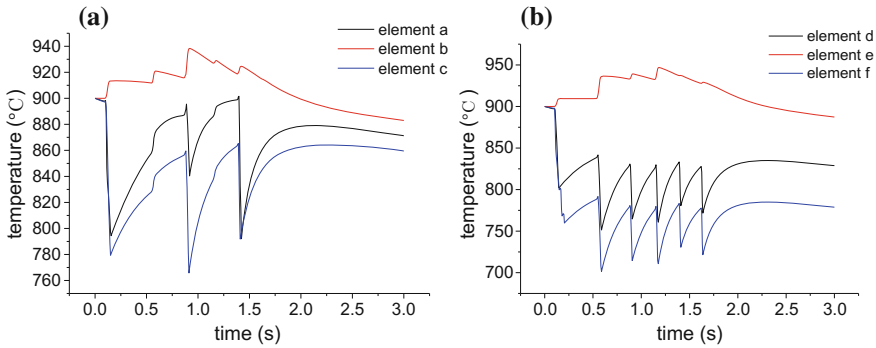

Fig. 7 Temperature of typical elements

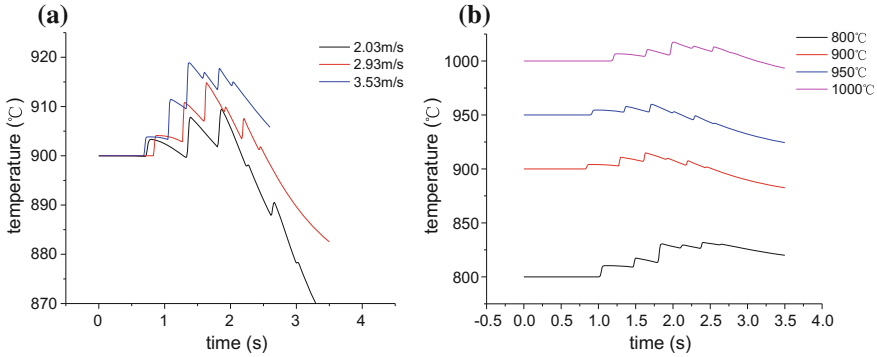

Fig. 8 Temperature change of different start rolling temperature and delivered velocity

Figure 8a is the temperature of different delivered velocity in 900. Figure 8b is the temperature of middle in different start rolling temperature. As it shown in Fig. 8a, the higher delivered velocity is, the higher the temperature of middle is. As it shown in Fig. 8b, the higher start rolling temperature is, the higher the temperature of middle is.

Temperature, Stress and Strain Fields

As shown in Fig. 9, the max stress of surface element will happen when the pipe is transiting the Pass No. 4. So the field of stress, strain and temperature of Pass No. 4 is analyzed.

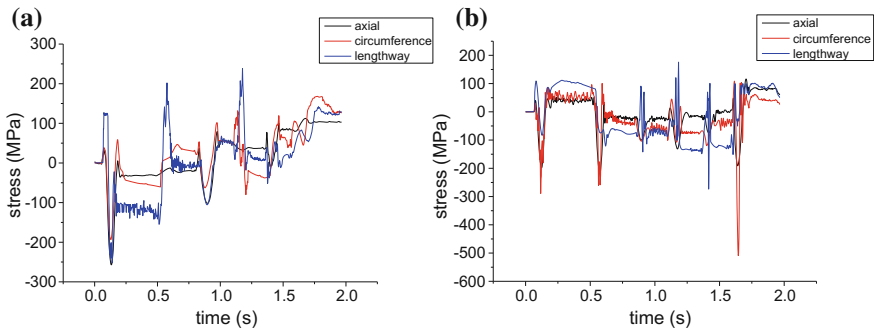

Fig. 9 The stress of surface element when rolling **a** the typical element a; **b** the typical element d

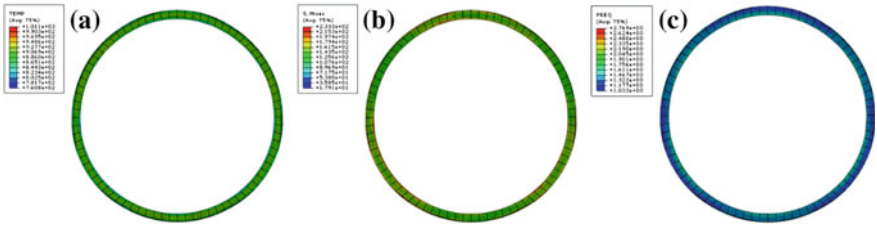

Fig. 10 Temperature fields **a** stress fields **b** strain fields **c** of Pass No. 4

The temperature fields, stress fields, strain fields of Pass No. 4 of semi-finished pipe at 900 °C and 2.93 m/s delivered velocity are shown in Fig. 10.

According to Fig. 10a, the temperature of the wall middle is higher than that of both side, because there is deformation heat. And Fig. 10b, there is a seriously focus of stress in the both side of wall, so surface quantity is more likely occurred in Pass No. 4. And inner surface is a little more seriously than outer surface. According to Fig. 10c, the distribution of strain indicates that the deformation of inside are easier than outside, this is relation to the temperature fields.

Sizes and Shapes of Semi-finished Pipe

The roundness of every pass and thickness of semi-finished pipe were shown in Figs. 11 and 12 respectively. As shown in Fig. 11, the section of fifth and sixth pass is more round than that of the first four pass because the deformation in first four pass is greater, especially in first two pass.

From the Fig. 12, the thickness of semi-finished pipe is 7 ± 0.41 mm, the roundness of pipe can reach 1.5 mm. The diameter and wall thickness ratio of the pipe is above 25.

The rolling experiment has been verified by using parameters of this paper, and the semi-finished tube is shown in Fig. 13.

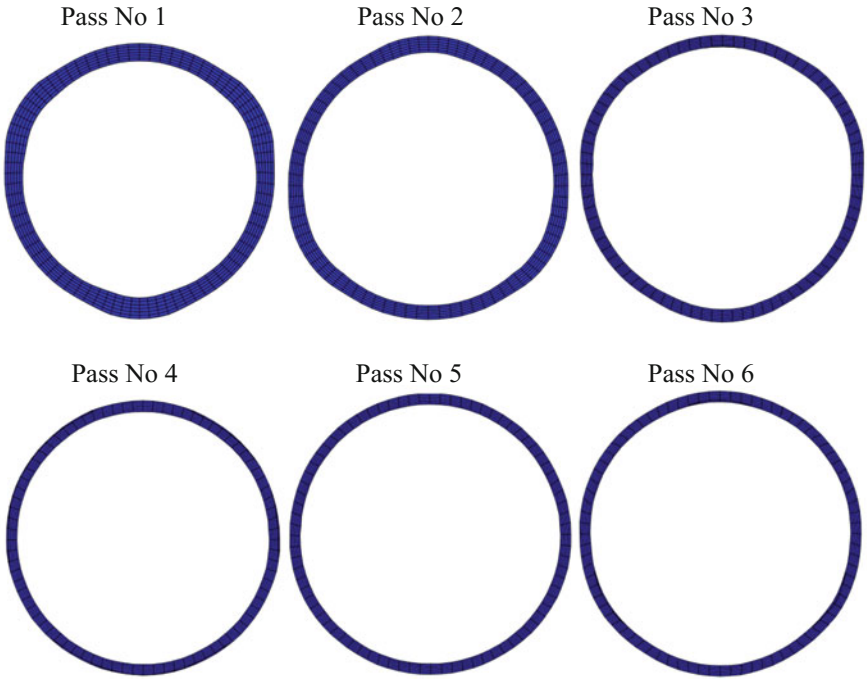

Fig. 11 Roundness of pipes in different passes

Fig. 12 Wall thickness of semi-finished pipe

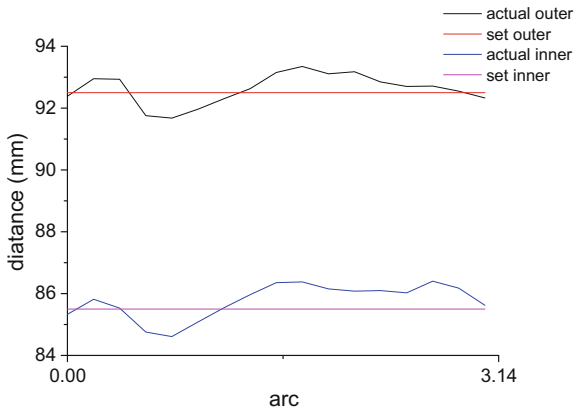

Fig. 13 Semi-finished pipe

Conclusion

1. The simulation result indicates that rolling grooves of steel pipe is suitable for the rolling of TC4 seamless pipe. For semi-finished pipe of 185 mm × 7 mm, the wall thickness deviation is ±0.41 mm, the roundness can reach 1.5 mm. The diameter and wall thickness ratio of the pipe is above 25.
2. The higher the start rolling temperature and delivery velocity are, the less rolling force is. The proper temperature of starting rolling maybe is 900–950 °C for TC4 titanium alloy, which can control the grain growth of phase.
3. The temperature fields, stress fields, strain fields of semi-finished pipe in No. 4 Pass are not uniform. From the view of stress filed, surface quality is more likely occurred in No. 4 Pass.

Acknowledgements The authors would like to thank the support provided by the National Key Research and Development Plan of China (No. 2016YFB0301200).

References

1. H. Yang, H. Li, Z. Zhang, Advances and trends on tube bending forming technologies. Chin. J. Aeronaut. **25**, 1–12 (2012)
2. P. Bella, P. Bucek, M. Ridzon, Influence of die geometry on drawing force in cold drawing of steel tubes using numerical simulation. Key Eng. Mater. **716**, 708–712 (2016)
3. Z.Y. Zhang, H. Yang, H. Li, Quasi-static tensile behavior and constitutive modeling of large diameter thin-walled commercial pure titanium tube. Mater. Sci. Eng. A-Struct. Mater. Prop. Microstruct, Process. **569**, 96–105 (2013)
4. Z. Zhang, H. Yang, H. Li, Thermo-mechanical coupled 3D-FE modeling of heat rotary draw bending for large-diameter thin-walled CP-Ti tube. Int. J. Adv. Manuf. Technol. **72**, 1187–1203 (2014)

5. X. Wang, J. Ye, X. Ma, Finite element simulation analysis of multi-stands three-roller cold rolling process for double metal composite seamless steel tube, in *Applied Mechanics and Materials*, ed. by I. Ihara (2014), pp. 197–199
6. M. Yoshida, 3D FEM simulation of rolling load working on piercer plug in mannesmann piercing process, in *AIP Conference Proceedings*, ed. by F. Barlat, Y.H. Moon, M.G. Lee (2010), pp. 1333–1338
7. K. Takahashi, T. Inoue, S. Uchida, Characteristics of hot friction in commercially pure titanium. Nippon Steel Tech. Rep. **85**, 41–46 (2002)
8. H. Wang, B. Xu, J. Liu, Micro and Nano Sulfide Solid Lubrication (2012)
9. J. Liu, W. Zeng, Y. Zhu, Hot deformation behavior and flow stress prediction of TC4-DT alloy in single-phase region and dual-phase regions. J. Mater. Eng. Perform. **24**, 2140–2150 (2015)
10. T. Wang, H. Guo, L. Tan, Beta grain growth behaviour of TG6 and Ti17 titanium alloys. Mater. Sci. Eng., A **528**, 6375–6380 (2011)
11. S.L. Semiatin, P.N. Fagin, M.G. Glavicic, Influence on texture on beta grain growth during continuous annealing of Ti–6Al–4V. Mater. Sci. Eng., A **299**, 225–234 (2001)

Vibration Effects on Weld Bead Characteristic of FV520B Stainless Steel Remanufactured with Surfacing Deposition Technology

Jian Liu, Sheng Zhu, Zhihai Cai and Ping Zhang

Abstract The surfacing deposition forming method was adopted for the remanufacturing experiment execution of the FV520B precipitation-hardening stainless steel. The "pull-push" model of the weld pool solidification was simultaneously built to research the effects of vibration on the characteristics of the weld bead formation. The results demonstrated that the form factor of the weld was decreased to a certain degree, due to the addition of vibration. Along with the vibration frequency increase, the weld reinforcement coefficient increased firstly and subsequently decreased. When the vibration frequency was $f = 1500$ r/min, the weld bead with the maximum reinforcement coefficient and relatively low form factor was acquired, which was suitable for the surfacing deposition execution for the steel remanufacturing.

Keywords FV520B precipitation hardening stainless steel · Remanufacturing MAG surfacing · Weld bead

J. Liu · Z. Cai · P. Zhang
National Engineering Research Center for Mechanical Product Remanufacturing, Academy of Armored Forces Engineering, Beijing 100072, China
e-mail: baiduxiao@hotmail.com

Z. Cai
e-mail: caizhihai2052@163.com

P. Zhang
e-mail: zhangp5801@sina.com

S. Zhu (✉)
National Key Laboratory for Remanufacturing, Academy of Armored Forces Engineering, Beijing 100072, China
e-mail: 419730824@qq.com

© Springer Nature Singapore Pte Ltd. 2018

Y. Han (ed.), *Advances in Materials Processing*, Lecture Notes in Mechanical Engineering, https://doi.org/10.1007/978-981-13-0107-0_68

Introduction

As a martensitic precipitation-hardening stainless steel, the FV520B stainless steel has been extensively utilized in the product-manufacturing of accessories such as compressors, wheel discs, rotors, axles and gears. This was due to the corresponding advantages such as high strength, flexible processing, good impact toughness, ideal lateral performance on high-sized cross-sections along with similar corrosion resistance and weldability compared to the 18–8 type steel properties. In particular, the FV520B stainless steel attracts high amount of attention in the fan manufacturing industry, where it is mainly utilized in the medium- and high-speed fan blades manufacturing that operate in environments containing corrosive media and wear particles [1–3].

The FV520B stainless steel is proven excellent in performance, however it is expensive. Also, the blade longevity under severe working conditions is quite short, resulting in failure. Such a failure will even lead to global failure and bring about a high loss to the entire machine. Therefore, the investigations and researches on the remanufacturing of failure accessories produced from FV520B stainless steels are of significant academic value and economic benefits. Currently, domestic fundamental researches on the FV520B stainless steel components and accessories remanufacturing are rarely reported, except certain investigations on FV520B stainless steel remanufacturing by the laser cladding forming technology [4, 5]. A deeper study on remanufacturing of the FV520B stainless steel through surfacing deposition technology is not discovered. Moreover, certain literature reports [6–8] indicated that process factors affected the properties of precipitation-hardened stainless steels significantly. The weld beads, formed during remanufacturing with the surfacing deposition technology, are a fundamental element of remanufacture forming, consequently in this paper, the remanufacturing of the FV520B stainless steel was experimentally investigated by the MAG surfacing deposition technology. The effects of mechanical vibration on the weld bead characteristics during remanufacturing was discussed to clarify the remanufacturing characteristics of the FV520B stainless steel with the surfacing deposition technology, which could lay the foundation for FV520B stainless steel components remanufacturing with high quality and high efficiency.

Experimental Design and Method

Experimental Conditions

The equipment employed in this study was provided by the National Key Laboratory of Remanufacturing and it is a system of an “arc-cladding rapid forming/remanufacturing support system based on a robot”, whereas the schematic diagram could be found in the literature [9]. The precision casting FV520B stainless

steel produced by the Beiman Special Steel Co., Ltd. was utilized as the substrate material with a size of 120 mm × 65 mm × 6 mm, whereas the heating treatments were the solid-solution treatment at 1050 °C and the aging treatment at 630 °C, respectively. A specific solid wire for the FV520B stainless steel with a diameter of Φ1.2 mm was utilized as the remanufacturing material. Table 1 lists the chemical compositions of the remanufacturing wire and the substrate materials. A mixture of 98% Ar + 2% O_2 was utilized as the protection gas and the ambient temperature was 20 °C. A microcomputer-controlled vibration aging device provided by the Huawin Electrical and Mechanical Technology Co., Ltd. was utilized as the vibration system. The corresponding vibration platform was produced from a 45 steel with a size of 2000 mm × 500 mm × 20 mm.

Experimental Scheme

The MAG surfacing deposition technology was utilized in the remanufacturing forming experiments, with the optimal technology parameters, such as the wire feed speed, the welding speed, the distance between the torch and the workpiece surface, whereas the arc length correction and gas flow were determined and selected as 8.8 m/min, 21 mm/s, 13 mm, 30% and 21 L/h, respectively. Prior to the experiment initiation, the vibration machine and the remanufacturing substrate were fixed near the middle of the platform, as presented in Fig. 1, since the vibration machine at this position was easy to induce vibrations and generate sympathetic vibrations. Subsequently to the specimen and instrument being fixed, the welding machine was started to carry out the remanufacturing experiment. The length of the formed weld bead was 120 mm. The form factor $\varphi(\varphi = W/H)$ and the reinforcement coefficient $\psi(\psi = W/R)$ were determined with respect to the measurements of the weld width (W), the reinforcement (R) and the penetration (H), subsequently to the experiment.

Regarding the experiment under the applied vibration, the vibration control device was first started and the corresponding vibration frequency was set. Following the vibration stabilization, the remanufacturing experiment by the overlaying cladding technology was immediately executed. The vibration frequency values were selected as f = 1500 r/min, f = 3000 r/min, f = 5000 r/min and f = 8000 r/min, respectively. It was noted that the f = 5000 r/min was the sympathetic vibration frequency, between the vibration machine and the vibration platform, which was obtained in a previous experiment. Following the experiments,

Table 1 Chemical composition of remanufacturing wire and FV520B stainless steel (mass fraction %)

Element	C	Mn	Si	S	P	Cr	Ni	Cu	Mo	Nb	Fe
Base metal	0.062	0.67	0.44	0.005	0.026	13.37	5.33	1.46	1.44	0.29	Bal.
Wire	0.033	0.55	0.35	0.011	0.017	14.2	6.42	–	1.17	0.33	Bal.

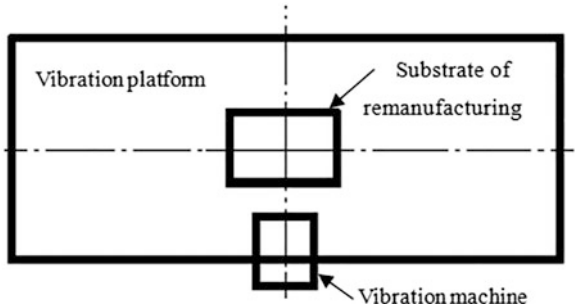

Fig. 1 Schematic diagram of vibration machine and substrate positions on vibration platform

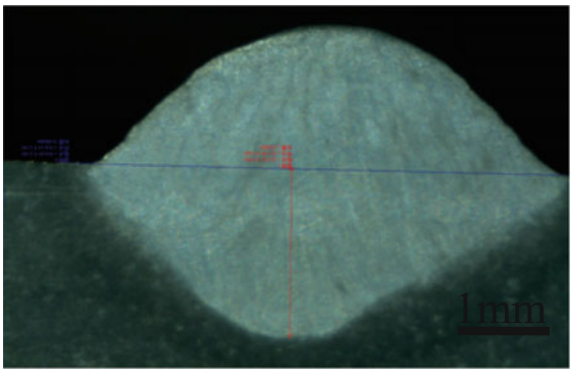

Fig. 2 Schematic diagram of weld penetration measurement

the form factor φ and the reinforcement coefficient ψ of the weld bead were also determined. Also, the effects of vibration on the weld bead characteristics during the remanufacturing of the FV520B stainless steel were further discussed.

Moreover, the weld width (W) and the reinforcement (R) were determined by the average of five measurements at various positions of the weld bead by a vernier caliper. To measure the penetration, the standard specimen was firstly prepared according to the metallographic specimen and subsequently analyzed by the system software and the GE-5 electron microscope following the corrosion treatment, as presented in Fig. 2.

The corrosive liquid for the metallographic specimen was a mixed solution of 5 ml of hydrochloric acid, 1 g of picric acid and 100 ml of alcohol. The corrosion lasted 20–30 s at room temperature, following which the specimen was washed by anhydrous ethanol (purity: 95%) and dried by an air blower.

Results and Discussion

Experimental Results

Figure 3 presents the relationship between the mechanical vibration frequency and the weld bead characteristics of the FV520B stainless steel remanufacturing by the MAG surfacing deposition, where f = 0 denoted the remanufacturing without the applied vibration. It could be observed from Fig. 3a that the reinforcement coefficient ψ of the weld seam increased as the vibration frequency increased first and subsequently decreased. Also, the reinforcement coefficient ψ reached the maximum value, when the vibration frequency increased to $f = 1500$ r/min, beyond which the reinforcement coefficient ψ decreased rapidly and became lower than the reinforcement coefficient ψ without the vibration effect. Generally, the weld bead was flatter as the ψ was higher. The flatter weld bead was significantly favorable to the lap joints and the surface quality of the forming layer was improved under the same conditions. It was indicated that during the cladding shaping of the remanufacturing, the application of vibration with a certain frequency contributed to the overlap rate improvement of the welded bead, subsequently improving the forming layer quality.

Figure 3b indicates that the form coefficient φ had a decreasing trend along with the vibration frequency gradual increase from a global point of view. In contrast, the form factors under the $f \leq 3000$ r/min vibration frequencies were similar to the form factors without vibration. In the literature [10] it was indicated that a lower form factor would reduce the invalid heating zone along the weld width direction, therefore the heat efficiency could be enhanced and the heat affected zone could be reduced. In contrast, the gas emission from the weld pool during forming would become difficult if the form factor was too low and pores would be formed as a result. The results also indicated that the application of vibration with a certain

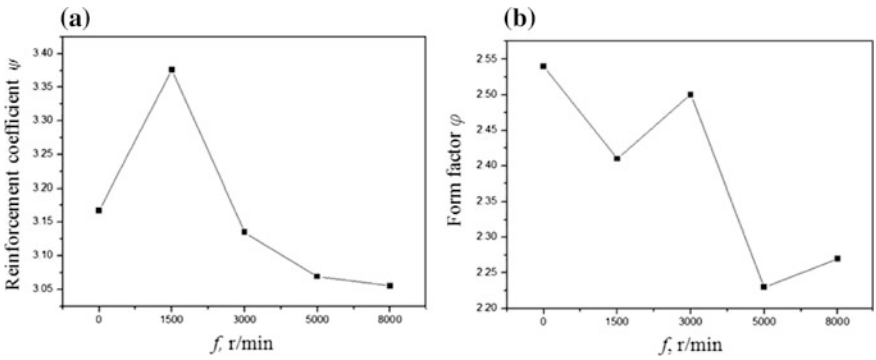

Fig. 3 Weld bead characteristics of remanufacturing versus vibration frequency, where **a** reinforcement coefficient versus vibration frequency and **b** form factor versus vibration frequency

frequency during remanufacturing by the surfacing deposition contributed in the forming layer quality enhancement. With the reinforcement coefficient and form factor comprehensive consideration, the vibration at the frequency of $f = 1500$ r/min was suitable to obtain the weld seam with high reinforcement coefficient and relatively low form coefficient during remanufacturing by the surfacing deposition process.

Discussion

During the remanufacturing through the surfacing deposition technology, the molten droplets move into the weld pool and subsequently solidify, forming weld beads and remanufacturing forming layers under the electromagnetic blow force, the gravity and the surface tension. In other words, the weld pool of the weld bead is the fundamental forming element of the forming layer during the surfacing claddings. The effects of mechanical vibration on the weld bead and the forming layer occur through the corresponding effect on the weld pool.

With the consideration of the weld pool size as relatively low-sized and the duration for solidification as shorter, the weld pool could be assumed as a homogeneous viscoelastic object, where the solidification is instantaneously achieved. The weld pool shape can be considered as an equilibrium result of the gravity F_G, the surface tension σ and the arc force F_A, as presented in Fig. 4a. When mechanical vibration is exerted during remanufacturing by the surfacing cladding technology, the substrate for remanufacturing will exhibit a forced vibration with the vibration platform at a certain frequency. Guan et al. [11] indicated the macroscopic effects of mechanical vibration, exerted on the weld pool by two methods, such as firstly, when the weldment is forced to vibrate, the liquid metal is forced to vibrate as the sidewalls of the weld pool interact with the elements within the weld pool. Secondly, the welding arc length varied with time due to the weldment vibration, leading to an arc pressure variation, which amounted to a periodic exciting force applied to the liquid metal surface in the weld pool. When the arc force became lower, the downward vibration of the substrate exerted a downward pulling force on the lower surface of the weld pool. Also, an upward pulling force on the upper surface of weld pool was also exerted. The upward vibration of the substrate would exhibit the opposite force. In other words, the weld pool during solidification was subjected to a countercurrent and periodic pulling-pushing alternating force. If the weld pool was formed and the solidification was accomplished when the substrate vibrated downwards, in other words, the positioning at the wave trough of the vibration, the weld pool would be correspondingly pulled. Moreover, the droplet and weld pool shapes during solidification are presented in Fig. 4b, where the dashed lines denoted the theoretical profile of the weld pool without vibration. In contrast, if the weld pool was formed and the solidification was accomplished within the wave crest of the vibration, the droplet and weld pool shapes during solidification are presented in Fig. 4c. Under the

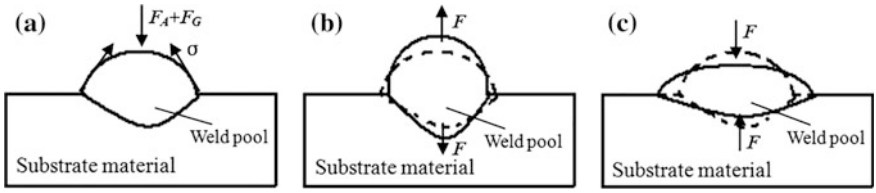

Fig. 4 'Pull-push' model for droplet and weld pool solidification, where **a** shapes of droplet and weld pool during solidification without vibration, **b** shapes of droplet and weld pool during solidification under pulling force and **c** shapes of droplet and weld pool during solidification under pushing force

aforementioned effects, the reinforcement coefficient ψ and the form factor φ of the weld bead would either decrease or increase generally as the generating period was consistent with the vibration period of the weld pool. Consequently, the shape and size of the weld bead would be affected, eventually impacting on the forming layer of remanufacturing. With the remanufacturing consideration at the vibration frequency of f = 1500 r/min, the reinforcement coefficient reached the maximum value as the period of the weld pool generation corresponded to the wave crest of vibration. This was interpreted, that the pushing force on the surface of the weld pool reached the maximum value. Zhao [12] indicated that the vibration frequency should be selected around the frontier of the formant, such as the sub-resonance region as 1/3–2/3 fraction of the resonance frequency. The vibration frequency f = 1500 r/min was approximately 1/3 of the resonance frequency of f = 5000 r/min, which was consistent with the corresponding literature investigation [12].

Conclusions

The mechanical vibration effect on the weld bead characteristics during the FV520B stainless steel remanufacturing by the MAG surfacing cladding technology was investigated. The conclusions were drawn as follows:

(1) The weld reinforcement coefficient increases first and subsequently decreased as the vibration frequency continuously increased, whereas the form factor generally decreased.
(2) During the remanufacturing and forming procedure with the surfacing cladding technology, when the vibration frequency of f = 1500 r/min was applied, the weld pool surface was subjected to the maximum pushing force, which could form weld beads with higher reinforcement coefficient and relatively low form factor, contributing to the quality improvement of the forming layer in remanufacturing.

Acknowledgements This research is supported by the National Science Foundation (Grant Nos. 51405510, 51375492 and 51575527). These supports are greatly appreciated.

References

1. R.P. Li, *The investigation of casting martensite precipitation hardening stainless steel impeller materials and technics* (Shenyang University of Technology, Shenyang, 2006)
2. J.L. Fan, X.L. Guo, C.W. Wu, Heat treatment on fatigue property of FV520B steel. J. Mater. Res. **1**, 61–67 (2012)
3. J.L. Wang, Y.L. Zhang, S.J. Liu, Competitive giga-fatigue life analysis owing to surface defect and internal inclusion for FV520B-I. Inter. J. Fatigue **87**, 203–209 (2016)
4. W.B. Ren, S.Y. Dong, B.S. Xu, Process optimization and forming repair of laser remanufacture of FV520(B) steel blade simulator. J. Mater. Eng. **1**, 6–12 (2015)
5. F.S. Li, F.Y. Li, X.J. Jia, Performance analysis of FeCr repaired coating on FV520B steel by laser cladding. J. Tool Tec. **10**, 55–58 (2015)
6. F.X. Jia, R.M. Hou, X.B. Jia, *Property and selection of stainless steel* (Chemical Industry Press, Beijing, 2013)
7. J. Niu, J.M. Dong, J. Xue, Precipitation-hardening and toughness of precipitation-hardening stainless steel FV520 (B). Chin. J. Mech. Eng. **12**, 78–83 (2007)
8. Q.Q. Zhou, Y.C. Zhai, Aging process optimization for a high strength and toughness of FV520B martensitic steel. Acta Metall. Sin. **10**, 1249–1254 (2009)
9. J. Liu, *Study of GMAW surface forming with non-support structure based on arc weld robot* (Academy of Armored Forces Engineering, Beijing, 2011)
10. Z.J. Wang, *Melting welding technique and equipment* (China Machine Press, Beijing, 2006)
11. J.J. Guan, T.M. Song, G.F. Zhang, The effect of mechanical vibration on solidification of weld pool metal. J. Fushun Petrol. Inst. **4**, 51–54 (2001)
12. X.H. Zhao, *Principle and application of vibration aging* (Shandong Huawin Electrical Technology CO. LTD, Jinan, 2012)

Evolution of Oxide Structures of Low-Alloy Steel Surface During Short-Time Oxidation at High Temperature

Jun Wang, Wei Yu, Entao Dong and Jiaxin Shi

Abstract During hot rolling, high-temperature oxidation has a direct effect on the thickness and structures of oxide scales of hot-rolled steel, even influences the descaling and the final surface quality of product. The GLEEBLE thermal simulator was used to investigate the short-time (30–900 s) oxidation of low-alloy steel Q345B in the temperature ranging from 850 to 1050 °C. The structures, thickness and proportion of each layer were characterized by SEM and EDS. The research showed that the initial surface of the scale was in mesh pattern. The scale blistered with increasing time and the grown crystals surrounded by mesh-like gullies could be observed. The scale thickness increased with the elevating temperature, ranged from 5.19 to 207.59 μm depending on the experiments process. It was less than 10 μm within 60 s at 850 °C, increased slowly with the oxidation time below 950 °C, but increased sharply above 950 °C before 120 s. The oxide scales had triple layers after oxidized at 850 °C, and at 950 °C for 30 s. The scale was a double-layer structure at high temperature, consisted of FeO and Fe_3O_4. With increasing temperature and time of oxidation, the proportion of loose layer (FeO) increased, but compact layer (Fe_3O_4) decreased from 70.13 to 7.30% in the two layers. The bottom oxide layer with main component of Fe_2SiO_4 was found between the scale and substrate. It can improve the scale adhesion and is bad for scale separation from substrate.

Keywords Low-alloy steel · Hot rolling · Oxide · Structure characterization

J. Wang · W. Yu (✉) · J. Shi
Institute of Engineering Technology, University of Science and Technology Beijing, Beijing, China
e-mail: yuwei9451@126.com

J. Wang
e-mail: 1013367947@qq.com

J. Shi
e-mail: 15010163415@163.com

E. Dong
Collaborative Innovation Center of Steel Technology, Beijing, China
e-mail: etdd@163.com

© Springer Nature Singapore Pte Ltd. 2018

Y. Han (ed.), *Advances in Materials Processing*, Lecture Notes in Mechanical Engineering, https://doi.org/10.1007/978-981-13-0107-0_69

Introduction

The oxide scale formed between 800 and 900 °C on the surface of steel plate in hot rolling is the main factor influencing the surface quality, which can lead to rolled-in scale, difficult descaling and red rust [1]. Oxide scale formed on the surface of the hot-rolled steel can be divided into primary, secondary and tertiary scale. The secondary and tertiary scale are formed when the high-temperature surface of steel plate rapidly contacts with air and oxidized in a short-term during hot rolling process after rough descaling [2, 3]. Cracks and blister will generate on the surface of oxide scale due to thermal stress, which will make partial scale peel from substrate, and the attached scale will be removed by descaling later [4]. The typical structure of oxide scale is layered, usually divided into double or triple layers, which are generally composed of Fe_2O_3, Fe_3O_4, FeO [5]. Their crystal structures are different, FeO layer is loose, and Fe_3O_4 layer is compact [6]. The isothermal transformation of FeO occurs below the temperature of 570 °C, producing the pre-eutectoid Fe_3O_4 and eutectoid Fe_3O_4 + α-Fe. Therefore, the proportion of each layer in the oxide scale is affected not only by the oxidation temperature and time, but also by the cooling process [7–9]. In hot rolling process, FeO layer and SiO_2 will react and generate Fe_2SiO_4 (Fayalite) at scale/matrix interface under an appropriate ratio [10]. Studies have shown that the eutectic FeO/Fe_2SiO_4 that exists at the interface of oxide scale and matrix, or in the FeO layer is the main reason for the formation of red oxide defect [11, 12].

Many works focus on steel oxidation in heating process. But the scale is sometimes hard to remove because of its structure and thickness after short-time oxidation in air. The present study attends to elaborate the evolution of oxide structures on the surface of low-alloy steel Q345B and find out the law for scales thickness development during short-time oxidation at high temperatures.

Materials and Methods

The work was performed on the low-alloy steel Q345B casting slab with composition of Fe–0.17C–0.27Si–1.19Mn–0.06Cr (wt%). Samples (10 × 10 × 5 mm) were cut by a wire-electrode cutting device and their surfaces were ground using 200–2000 grit silicon carbide paper, cleaned by ultrasonic wave to remove the oil with alcohol and dried in oven.

The oxidation was carried out by the GLEEBLE thermal simulator. Three heating temperatures (850, 950, 1050 °C) were selected. The isothermal oxidation period was 30, 60, 120, 300 and 900 s respectively. During heating and the first 60 s of isothermal process, argon atmosphere was adopted to prevent oxidation, and isothermal oxidation with different period and subsequent cooling procedure were

performed in air. The maximum cooling rate was 10 °C/s, which was selected according to the sample size, as far as possible to retain the structure of high temperature.

The macro surface patterns of the samples were observed by a micro-spur camera, and the microstructure of the surface were observed by SEM. The images of specimens for cross-sectional observation were obtained by SEM and analyzed by EDS after being epoxy mounted, grounded, roughed and fine polished and carbon film coated in vacuum. The total thickness of the oxide layer and relevant proportion of wustite and magnetite layers of each sample were measured by image processing software Image Pro.

Results and Discussions

Surface Morphology and Blistering of Scale

The surface morphology of short-time oxide scale at high temperature is shown in Fig. 1. The scale blistering appears on the surface except oxidized at 850 °C for 30–900 s and at 950 °C for 30 s, where the outer oxide scale separated from substrate. Some of the scales are peeled off, others remained and can be easily descaled by external force. Therefore, blistering mainly appears above 950 °C, and the blistering area will expand with the temperature augment. It also becomes more severe as time goes on. This is caused by oxide scale volume enlarging and exceeding the steel matrix volume consumed by oxidation. It generates internal stress in the scale, which composed of a compressive stress in the direction parallel to the surface and a tensile stress that is perpendicular to the steel matrix. They work

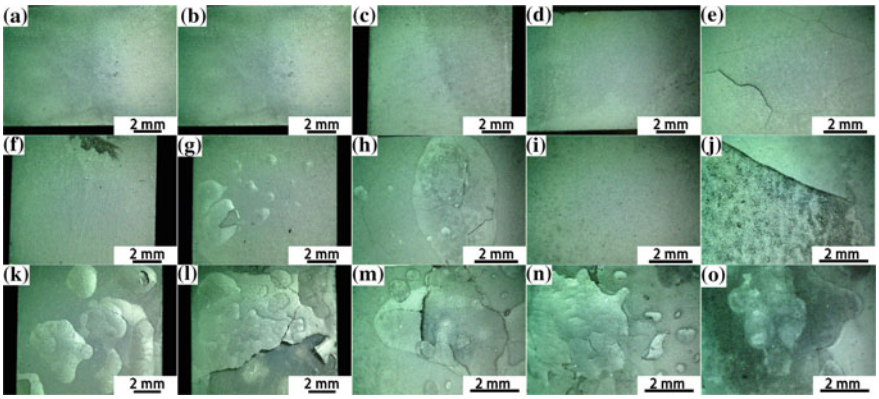

Fig. 1 Surface morphology of short-time oxide scale at high temperature. **a** 850 °C for 30 s; **b** 850 °C for 60 s; **c** 850 °C for 120 s; **d** 850 °C for 300 s; **e** 850 °C for 900 s; **f** 950 °C for 30 s; **g** 950 °C for 60 s; **h** 950 °C for 120 s; **i** 950 °C for 300 s; **j** 950 °C for 900 s; **k** 1050 °C for 30 s; **l** 1050 °C for 60 s; **m** 1050 °C for 120 s; **n** 1050 °C for 300 s; **o** 1050 °C for 900 s

together to separate the scale from the substrate. The internal stress rises with the growth of the oxide scale. The separated scale finally deforms to bubble on the scale surface. As a result, the bulge area continues to increase, and gradually connects into a large area of peeling. Therefore, the elevating temperature or prolonged time of oxidation is conducive to descale during the short-term oxidation.

At high magnification, the surface morphology of the oxide scale is observed and shown in Fig. 2, which was formed in short-time oxidation at high temperature. In order to observe the surface clearly, non-uniform magnifications are selected. For oxidized samples in lower temperature, the higher magnification is used. The blistering area is observed for the samples with scale bubble. In the figure, the scale surface of oxidation at low temperature or shorter oxidation time is flat, but shows a mesh-like microstructure in larger magnification. The microstructure of grown crystals surrounded by gullies with initial mesh-liked structures in it can be found in blistering area at higher temperature or for longer oxidation time. Oxide scales were obtained respectively by 850 °C for 900 s, 950 °C for 60 s and 1050 °C for 30 s have a similar microstructure of folded structures surrounded by mesh-like folds. The folds originate from oxide crystals nucleation and growth, the crystals observed could be magnetite. In addition, this microstructure also appears at the junction of non-peeled blister and the mesh-liked area. The mesh-like structure is distributed on the edge of the crystals, and the height difference between the crystals and the mesh-like boundary increases with the crystal growth, which may lead to oxide scale fracture on positions of a high drop, or even being stripped naturally.

The chemical compositions of the mesh-liked structure at 850 °C for 300 s and the crystal at 850 °C for 900 s are analyzed by EDS spot scanning, shown in Fig. 3. The mass ratio of Fe/O in the network is close to 2.33, while the mass ratio of Fe/O

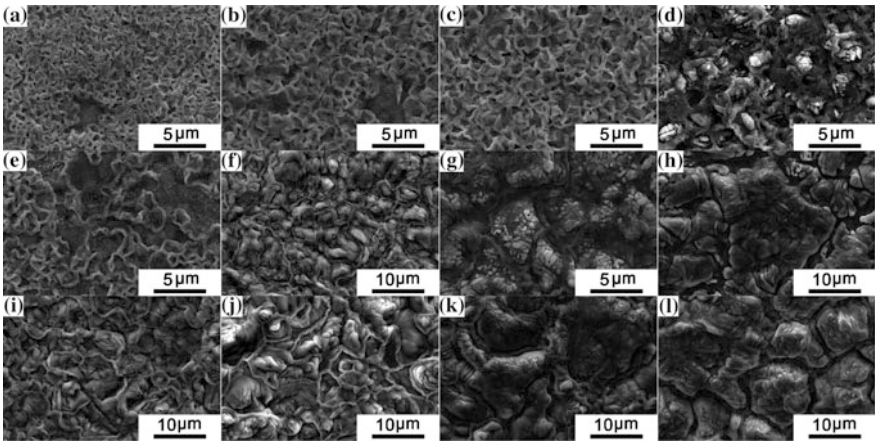

Fig. 2 Surface morphology of the oxide scale at high magnification. **a** 850 °C for 30 s; **b** 850 °C for 60 s; **c** 850 °C for 120 s; **d** 850 °C for 300 s; **e** 850 °C for 900 s; **f** 950 °C for 30 s; **g** 950 °C for 60 s; **h** 950 °C for 120 s; **i** 950 °C for 300 s; **j** 950 °C for 900 s; **k** 1050 °C for 30 s; **l** 1050 °C for 60 s; **m** 1050 °C for 120 s; **n** 1050 °C for 300 s; **o** 1050 °C for 900 s

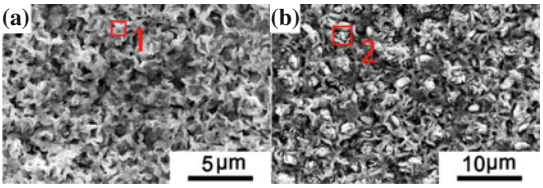

(c)

c	1	2
Element	Weight/%	
O	50.07	38.88
Fe	40.83	9.32

Fig. 3 Chemical compositions of the mesh-liked structure and the crystal. **a** 850 °C for 300 s; **b** 850 °C for 900 s; **c** EDS analysis at the positions marked

in the crystal is about 2.54, which means that the mesh-liked structure might be composed of Fe_2O_3 and the crystal might Fe_3O_4.

Cross Section of Scale Structure

As mentioned above, the typical structure of oxide scale is generally composed of Fe_2O_3, Fe_3O_4, FeO [5]. The cross-sectional morphology of oxide scale is shown in Fig. 4, which formed at high temperature in a short time. To clearly observe scale structure, different magnifications were selected. For oxide scales formed at the temperature of 850 °C or at 950 °C for 30 s, a triple-layer structure can be detected, except for the dark gray secondary oxide layer at the bottom of scales. But oxidation at the temperature above 950 °C for a longer time will generate an oxide

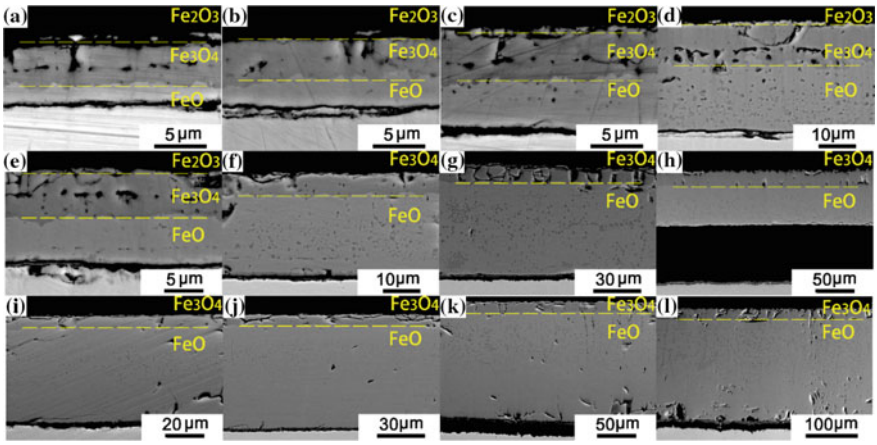

Fig. 4 Cross-sectional morphology of oxide scale. **a** 850 °C for 30 s; **b** 850 °C for 60 s; **c** 850 °C for 120 s; **d** 850 °C for 900 s; **e** 950 °C for 30 s; **f** 950 °C for 60 s; **g** 950 °C for 120 s; **h** 950 °C for 900 s; **i** 1050 °C for 30 s; **j** 1050 °C for 60 s; **k** 1050 °C for 120 s; **l** 1050 °C for 900 s

scale with a double-layer structure, mainly composed of thick loose FeO layer with Fe_3O_4 grains distributed in it and thin compact Fe_3O_4 layer, except for the secondary oxide layer.

It is known that the relative stability of the compounds can be determined by the standard Gibbs free energy change of chemical reactions ($\Delta_r G^{\Theta}$). In other words, the oxidizing procedure will be easier along with the larger Gibbs free energy change in an element oxidation. According to the Ellingham diagram, the stability of each layer of the oxide scale from large to small is FeO > Fe_3O_4 > Fe_2O_3. The higher the oxidation temperature, the less the hematite. The cooling rate in this experiment is so fast that the structure at high temperature is mostly retained. Therefore, the Fe_2O_3 layer can hardly be found in the oxide scale that oxidized at high temperature. In addition, there is magnetite observed in the space of the mesh-liked hematite in short-time oxidation at high temperature, which might nucleate and grow based on thermodynamically unstable hematite. The magnetite grains become larger with the prolonged oxidation time, and so is the height difference between the grains and the mesh-liked hematite that distributed in the crystal boundary. As a result, before the growth of the magnetite grains, that is, when the surface is mainly attached by mesh-liked hematite, the Fe_2O_3 layer can be seen in the cross-sectional scale. When the magnetite grains grow up, it may cover most of the hematite in the sight of cross section. Otherwise, only a small part of the oxide scale can be seen in a high magnification, and it will become more difficult to find the Fe_2O_3 layer in the cross-sectional scale as the oxidation time extends. Above all, oxidation temperature and time may be the reason why the Fe_2O_3 layer cannot be found except at 850 and 950 °C for 30 s.

According to Fig. 5, it can be seen distinctly that the secondary scale layer has main alloy element silicon, by EDS analysis of the cross-sectional scale formed at 950 °C for 120 s. It is verified to be Fayalite (Fe_2SiO_4) by EDS analysis. The secondary oxide layer exists between the matrix and the FeO layer. The greater the

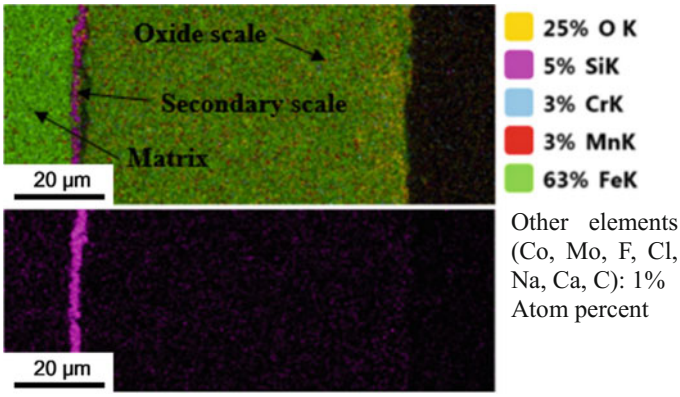

Fig. 5 EDS results of the scale section at 950 °C—120 s

thickness of the oxide scale, the thicker the secondary oxide layer. The formation mechanism of Fayalite will be explained in subsequent paragraph.

In oxidation process, silicon is enriched at the interface of the matrix/scale. There are the following reactions according to the Ellingham diagram [13, 14]:

$$2Fe + O_2 = 2FeO \quad \left(\Delta_r G_1^{\Theta} = -251.4\ \mathrm{kJ\,mol^{-1}}\right) \tag{1}$$

$$Si + O_2 = SiO_2 \quad \left(\Delta_r G_2^{\Theta} = -856.4\ \mathrm{kJ\,mol^{-1}}\right) \tag{2}$$

Combine the two equations, (2)–(1), to get following reaction:

$$Si + 2FeO = SiO_2 + Fe \quad \left(\Delta_r G^{\Theta} = \Delta_r G_2^{\Theta} - \Delta_r G_1^{\Theta} = -605\ \mathrm{kJ\,mol^{-1}}\right) \tag{3}$$

Therefore, $\Delta_r G_3^{\Theta} < 0$, which suggests that reaction (3) is a spontaneous process, the silicon is easier to be oxidized than iron. At the interface, the silicon takes precedence over iron to react with the dissolved oxygen to produce SiO_2, which reacts with FeO to form Fayalite under certain proportions. The Fayalite is enriched only at the interface of matrix/scale because it does not dissolve in FeO [15]. The Fayalite attached to the matrix makes interface rough, and the FeO layer is more difficult to remove from the substrate when the roughness gets greater. A small amount of residual FeO oxidizes to Fe_2O_3 later, which leads to the red rust of steel surface [12].

Thickness and Proportion of Oxides

The scale thickness after oxidized in different process was statistically measured using the image processing software. The thickness of oxide scales varies with time and temperature is illustrated in Fig. 6, which increases along with the elevating temperature and oxidation time, and can be less than 10 μm when temperature is 850 °C, and the holding time is less than 60 s. The scale thickness variation basically follows the linear law before 120 s, and the oxidation rate increases sharply at and above 950 °C. After 120 s, the oxidation rate decreases rapidly. The scales thickness variation at 850 and 950 °C becomes stable, whereas the oxidation rate at 1050 °C remains high. At the initial stage of oxidation, the surface of samples is in full contact with the air through convective mass transfer, so the oxidation rate is large. The surface of samples is covered with scales as time goes on, so that the mass transfer of oxygen is in a diffusion way through the scale. The oxidation rate is affected by the diffusion rate at the time and rapidly reduces. The diffusion rate of oxygen in the steel, depending on oxidation temperature and material compositions, is higher at the temperature of 1050 °C than that of 850 and 950 °C. It results in the high oxidation rate for high-temperature process, even the scale is formed.

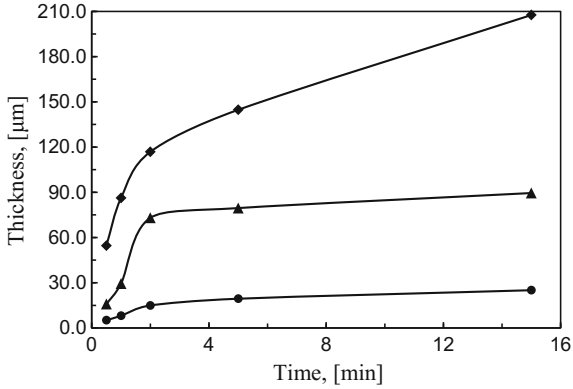

Fig. 6 Thickness of scales varies with time

The isothermal transformation of FeO takes place at the temperature lower than 570 °C in the cooling process that results in the pro-eutectoid Fe_3O_4 and eutectoid Fe_3O_4/α-Fe in the wustite layer. Only a small amount of FeO transforms on account of the fast cooling rate, and most of the high-temperature microstructure is retained. So the isothermal transformation of FeO has little effect on the final scale structure, and the proportion of different layers within the scales is mainly affected by the temperature and the isothermal oxidation time.

With exception of the substrate Fayalite and the outer hematite layer, the proportion of different layers of the oxide scales at 60 s is shown in Fig. 7. The proportion and thickness of Fe_3O_4 layer are exhibited in Table 1, the former decreases with the increasing temperature and oxidation time, changing from 70.13

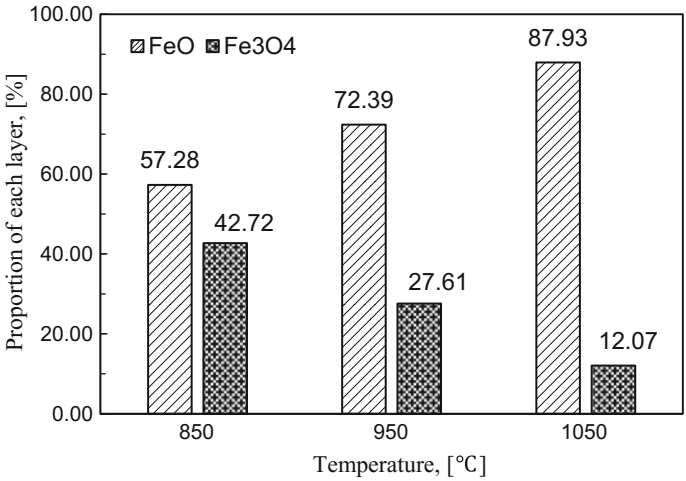

Fig. 7 Proportion of different layers at 60 s

Table 1 Proportion of Fe_3O_4 layer of the oxide scale in different processing

Temperature (°C)		Oxidation time (s)				
		30	60	120	300	900
850	Proportion (%)	70.13	42.72	41.94	36.79	34.29
	Thickness (μm)	3.14	3.46	6.27	7.14	8.59
950	Proportion (%)	50.00	20.23	14.43	14.23	14.01
	Thickness (μm)	7.92	8.95	10.54	11.32	12.54
1050	Proportion (%)	10.29	10.03	9.97	9.71	7.30
	Thickness (μm)	8.62	10.65	11.65	14.05	15.16

to 7.30%, while the latter increases. Following reaction occurs on the FeO/Fe_3O_4 interface when temperature is above 600 °C:

$$Fe^{2+} + 2e + Fe_3O_4 = 4FeO \tag{4}$$

The higher the reaction temperature, the faster diffusion of Fe^{2+} in the scale. It produces more FeO and Fe_3O_4, and increases layer thickness of FeO on the FeO/Fe_3O_4 interface. On the one hand, the consumption of Fe_3O_4 boosts as the oxidation time extends, but since this procedure is slower than generation, the thickness of the Fe_3O_4 layer still slightly expands. On the other hand, the FeO layer generates constantly but not consumed in oxidation process, resulting in increasing proportion of FeO layer and the decreasing proportion of the Fe_3O_4 layer.

Summary

During the short-term oxidation at high temperature, the blistering on surface of the steel gets more serious, which results scale separation from the matrix or even peeling off as the oxidation temperature and time increasing. Elevating temperature and extending time of oxidation can accelerate the peeling, thereby enhance the descaling effect.

The scale of low-alloy steel Q345B has a four-layer structure in air oxidation, mainly composed of secondary oxide layer, FeO layer and Fe_3O_4 layer, and maybe Fe_2O_3 at lower temperature. The main component of the secondary oxide layer is Fayalite that could deteriorate roughness of the matrix/FeO interface and make a small amount of FeO layer firmly attach to the matrix. The thickness of the secondary oxide layer increases with the thickness of the oxide scale. Therefore, in high-temperature short-term oxidation process, the thickness of the scale should be controlled to reduce the formation of Fayalite, which could reduce the adhesion of the scale and improve the efficiency of descaling.

The oxide scale thickness is influenced by oxidation temperature and time. High temperature and oxidation period will extend thickness of the scale. The scale

thickness curve within 120 s basically follows the linear law, and the oxidation rate soars acutely after 950 °C, and then becomes smaller after 120 s.

The oxide scales thickness of low-alloy steel Q345B ranges from 5.19 to 207.59 μm. The proportion of Fe_3O_4 layer decreases with temperature and oxidation time, changing from 70.13 to 7.30%, while its thickness increases.

References

1. R.Y. Chen, W.Y.D. Yuen, Oxide-scale structures formed on commercial hot-rolled steel strip and their formation mechanisms. Oxid. Met. **56**, 89–118 (2001)
2. R.Y. Chen, W.Y.D. Yuen, Review of the high-temperature oxidation of iron and carbon steels in air or oxygen. Oxid. Met. **59**, 433–468 (2003)
3. Y. Yu, J.G. Lenard, Estimating the resistance to deformation of the layer of scale during hot rolling of carbon steel strips. J. Mater. Process. Tech. **121**, 60–68 (2002)
4. R. Endo, T. Yagi, M. Ueda, M. Susa, Thermal diffusivity measurement of oxide scale formed on steel during hot-rolling process. ISIJ Int. **54**, 2084–2088 (2014)
5. B. Gleeson, S.M.M. Hadavi, D.J. Young, Isothermal transformation behavior of thermally-grown wustite. Mater. High Temp. **17**, 311–318 (2000)
6. R.Y. Chen, D.W.Y. Yuen, A study of the scale structure of hot-rolled steel strip by simulated coiling and cooling. Oxid. Met. **53**, 539–560 (2000)
7. N. Otsuka, T. Doi, Y. Hidaka, Y. Higashida, Y. Masaki, N. Mizui, M. Sato, In-situ measurements of isothermal wustite transformation of thermally grown FeO scale formed on 0.048 mass% Fe by synchrotron radiation in air. ISIJ. Int. **53**, 286–293 (2013)
8. C.H. Zhou, H.T. Ma, Y. Li, Eutectoid magnetite in wustite under conditions of compressive stress and cooling. Oxid. Met. **78**, 145–152 (2012)
9. R.Y. Chen, W.Y.D. Yuen, Oxidation of low-carbon, low-silicon mild steel at 450–900 °C under conditions relevant to hot-strip processing. Oxid. Met. **53**, 53–79 (2012)
10. Q. Yuan, G. Xu, M.X. Zhou, B. He, The effect of the Si content on the morphology and amount of Fe_2SiO_4 in low carbon steels. Metals-Basel **6**, 94–103 (2016)
11. E.J. Song, D.W. Suh, H.K.D.H. Bhadeshia, Oxidation of silicon containing steel. Ironmak. Steelmak. **39**, 599–604 (2012)
12. B. He, G. Xu, M.X. Zhou, Q. Yuan, Effect of oxidation temperature on the oxidation process of silicon-containing steel. Metals-Basel **6**, 137–146 (2016)
13. J.G. Speight, *Lange's Handbook of Chemistry*, 16th edn. (The McGraw-Hill Companies, America, 2005), pp. 254–255
14. P. Atkins, J.D. Paula, *Atkins' Physical Chemistry*, 8th edn. (Oxford University Press, Oxford, 2006), pp. 1000–1001
15. D. Genève, D. Rouxel, P. Pigeat, B. Weber, M. Confente, Surface composition modification of high-carbon low-alloy steels oxidized at high temperature in air. Appl. Surf. Sci. **254**, 5348–5358 (2008)

Joining 304 Stainless Steel and TC4 Alloy Using Ag Foil Interlayer by Plasma Activated Sintering

Mei Rao, Jian Zhang, Jiayu He, Guoqiang Luo, Shulong Liu, Qiang Shen and Lianmeng Zhang

Abstract Dissimilar metals 304 stainless steel (SS) and TC4 alloy were bonded using Ag foil interlayer by plasma activated sintering. The microstructure, mechanical properties and fracture failure of bonded joints were investigated. When bonding temperature was below 600 °C, the voids appeared at 304 SS/Ag foil interface. As bonding temperature was above 600 °C, the 304 SS/Ag foil/TC4 joints were free of the voids or cracks, and TiAg intermetallic compounds (IMC) nucleated above 600 °C, and grew into TiAg IMC layer at Ag foil/TC4 interface with the increasing of bonding temperature. The joint free of the voids or cracks was successfully obtained at 600 °C, of which the average shear strength was 125 MPa and the fracture failure was the mixture of ductile rupture in Ag and brittle rupture in TiAg IMC. The formation of TiAg IMC layer decreased the bonding strength of joints. Fracture failure mainly occurred at TiAg IMC layer which is typical brittle fracture when bonding temperature was above 650 °C.

Keywords Diffusion · Ag interlayer · Plasma activated sintering
Microstructure · TiAg IMC

Introduction

Titanium and its alloys have a varied application in areas of aerospace, vessels and metallurgy owing to their excellent performances of high specific strengths, low densities, high melting points and corrosion resistances [1–3]. TC4 (Ti–6Al–4V) possesses an admirable comprehensive mechanical properties such as good

M. Rao · J. Zhang · J. He · G. Luo (✉) · Q. Shen · L. Zhang
State Key Lab of Advanced Technology for Materials Synthesis and Processing, Wuhan University of Technology, Wuhan 430070, China
e-mail: luoguoqiang1980@sina.com

S. Liu
School of Physics and Electronic Information/Information College, Huaibei Normal University, Huaibei 235000, Anhui, China

© Springer Nature Singapore Pte Ltd. 2018

Y. Han (ed.), *Advances in Materials Processing*, Lecture Notes in Mechanical Engineering, https://doi.org/10.1007/978-981-13-0107-0_70

formability and welding property and has gradually become the prominent alloy in titanium industry [4, 5]. Therefore it is unavoidable that joining TC4 alloy with stainless steels for a wider range of use in various fields [6]. However, the solubility of Ti and Fe in the solid state is limited and brittle Ti-base intermetallic phases, such as TixFey, TixNiy, and TixCry are easily generated during the welding process resulting in low quality joints [7, 8]. By employing interlayers, for example Cu, Ni, as the diffusion barrier, Ti-based IMCs are prevented from formation, while the bonding temperature are above 850 °C [9, 10]. It is reported that Ag and Ag-based metals have the advantage of relatively low diffusion bonding temperature [11, 12].

Plasma activated sintering (PAS), consisting of conjoint application of high temperature, axial pressure and pulsed DC current field-assisted sintering, has become widespread in use and attracted considerable attention recently [13]. Recently, PAS has been selected as a joining method to braze dissimilar metals. PAS has been successfully used in bonding Mg and Al, shortened the bonding time and the formation of brittle Mg–Al intermetallics is prevented [14]. Li has found that the Fe–Al interdiffusion coefficient under pulse current was about 46 times higher than that without current at 500 °C [15].

In the present 304 stainless steel (304 SS) and TC4 alloy were bonded with a 25 μm Ag interlayer by using plasma activated sintering process. The aim was to obtain superior quality 304 SS/TC4 joints at relatively low bonding temperature. Microstructure and mechanical properties of bonded joints were investigated.

Experimental Procedures

By wire-electrode cutting, 304 stainless steel and TC4 alloy were sliced into wafers of which the dimension was ⌀25 mm × 5 mm. Ag foil (Ag $\geq$ 99.99 wt%) was cut into 25 mm in diameter. Chemical compositions of the materials are listed in Table 1. Before bonding process, base metals were first polished in proper sequence with various grades of SiC paper, and then cleaned ultrasonically in acetone. PAS apparatus (Ed-Pas) was applied to join 304 stainless steel and TC4 alloy with Ag interlayer assembled into a sandwich structure. The compressive stress of 4.9 kN, converting to a pressure of 10 MPa, was applied during the whole process. The vacuum pressure was less than 10 Pa. The cylindrical samples were heated to the bonding temperature, holding for 1200 s and then free cooling.

MTS-810 universal machine was applied to test shear strength of bonded joints at a loading speed of 0.5 mm/s at room temperature. The microstructure of joints

Table 1 Chemical compositions of welding materials (wt%)

Material	Al	V	Fe	C	Ni	Cr	Ti
304 SS	–	–	Bal.	$\leq$0.08	11.0	19	–
TC4	5.5	4.5	<0.3	<0.1	–	–	Bal.

was observed via a field emission scanning electron microscope (FESEM, FEI Quanta 250FEG). And elements distribution at the interface was analyzed with an electron probe micro-analyzer (EPMA, JXA-8100), while the phase compositions of fracture surfaces were tested through an X-ray diffraction system (XRD, Rigaku Ultima III).

Results and Discussion

Microstructure Characterization

Figure 1 illustrates microstructure of the 304 SS/Ag foil/TC4 joints fabricated at 550–700 °C. It is obvious that micro-voids appear at the 304 SS/Ag foil boundary, indicating that atomic diffusion at the interface is insufficient at 550 °C. And micro-voids at the 304 SS/Ag foil interfaces disappear with the increasing of bonding temperature, indicating that the atomic diffusion between 304 SS and Ag foil is sufficient. While there is a narrow diffusion layer generated at Ag foil/TC4 at 550 °C. TiAg IMC nucleated above 600 °C, and grew into TiAg IMC layer at Ag foil/TC4 interface with the increasing of bonding temperature. And the thickness of diffusing layer at Ag foil/TC4 is about 5 μm at 700 °C.

Figure 1f is elemental distributions across the entire joint bonded at 600 °C. A thin diffusion zone of Ag, Fe, Ni elements were observed with smooth and continuous variations of the concentration profiles at 304 SS/Ag foil interface.

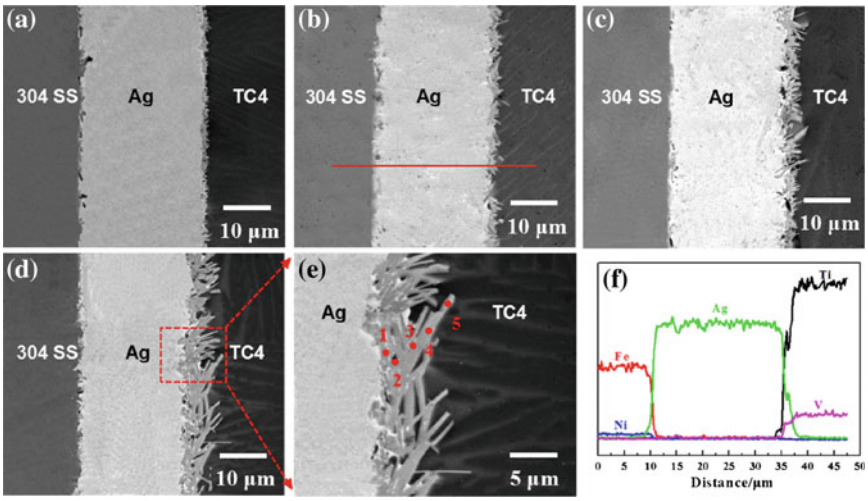

Fig. 1 Microstructure and elemental distribution of 304 SS/Ag foil/TC4 bonded joint: **a** 550 °C; **b** 600 °C; **c** 650 °C; **d** 700 °C; **e** enlarged SEM image of the interface between TC4 base metal and Ag foil; **f** elemental distributions across the entire joint bonded at 600 °C

Table 2 Elemental compositions of the selected points 1–5 (marked in Fig. 1)

Points	Element composition (at%)				Possible phases
	Ti	Ag	V	Al	
1	24.96	73.51	–	1.53	Ag (ss, Ti, Al)
2	41.66	57.69	–	0.66	TiAg (ss)
3	46.12	50.52	1.36	1.99	TiAg (ss, Al, V)
4	50.60	44.62	2.07	2.71	TiAg (ss, Al, V)
5	61.55	28.92	2.32	7.2	TC4 (ss, Ag)

From enlarged SEM image of the interface between TC4 base metal and Ag foil (Fig. 1e) and the EPMA analysis of the diffusion layer (Table 2), there are three regions at diffusion layer: Ag-rich solid solution, TiAg IMC and Ti-rich solid solution regions.

Shear Properties

Figure 2 displays the variation of shear strength of 304 SS/Ag foil/TC4 joints produced with different bonding temperatures. At lower bonding temperature of 550 °C, shear strength of the joint is less than 30 MPa, because of the fact that atomic diffusion at the 304 SS/Ag foil interface is inadequate, micro-voids remains existence at the interface. A maximum value of the average shear strength was 125 MPa at 600 °C. Elements were fully diffused at the interface and the joint was free of voids or cracks. However, when bonding temperature is above 650 °C, TiAg IMC layer forms at Ag foil/TC4 interface, which reduces bonding strength of joints.

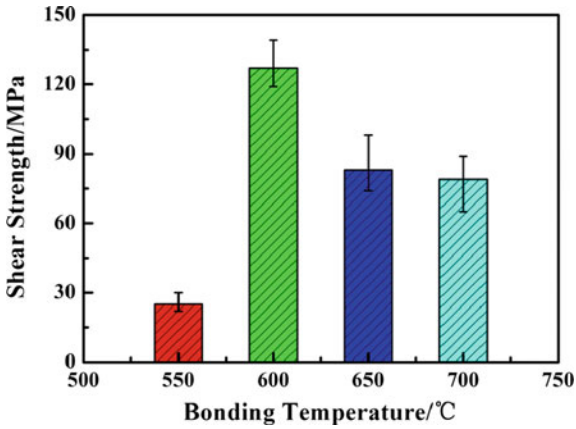

Fig. 2 Shear strength of 304 SS/Ag foil/TC4 joints bonded at different bonding temperatures (P = 10 MPa, t = 20 min)

Fracture Analysis

Figure 3 displays the representative XRD patterns of 304 SS/Ag foil/TC4 fracture surfaces. When the bonding temperature is 550 °C, the phase of 304 SS side is primarily Cr0.19Fe0.7Ni0.11 and the phase of TC4 side is Ag, indicating that the fracture failure of 304 SS/Ag foil/TC4 joint is mainly occurred at 304 SS/Ag foil interface. At 600 and 650 °C, the phase of 304 SS side is primarily Cr0.19Fe0.7Ni0.11 and Ag, the phase of TC4 side is Ag, while very weak peaks of TiAg are detected on both sides. It can be inferred that fracture of 304 SS/Ag foil/TC4 joint is occurred at 304 SS/Ag foil and Ag foil/TC4 interface. While, when the bonding temperature reaches 700 °C, phases of 304 SS and TC4 sides are TiAg and Ag, suggesting that fracture failure happens at TiAg IMC layer.

Figure 4 exhibits microstructure of 304 SS/Ag foil/TC4 fracture surfaces. In the Fig. 4a, fracture surface on 304 SS side can be separated into two areas in accordance with the pattern diversification. From high resolution topographies and EMPA analysis of two areas (Fig. 4b, c; Table 3), it can be found that the fracture failure is a mixture of ductile rupture in Ag and brittle rupture in TiAg IMC. By comparison, the fracture pattern of joints bonded at 700 °C is typical brittle fracture. And from XRD and EMPA results, the phrase is TiAg IMC dissolved with Cr, Ni, Al and V strengthening elements.

Bonding Process Analysis

Schematic illustrations of the diffusion layers appearing process are presented in Fig. 5. The interface reaction of 304 SS/Ag foil/TC4 bonded by plasma activated sintering process can be divided into three stages. The first stage is the formation of solid solution at 304 SS/Ag foil and Ag foil/TC4 interfaces. The second stage is the TiAg IMC nucleated at Ag foil/TC4 diffusion layer. And the last stage is the growth

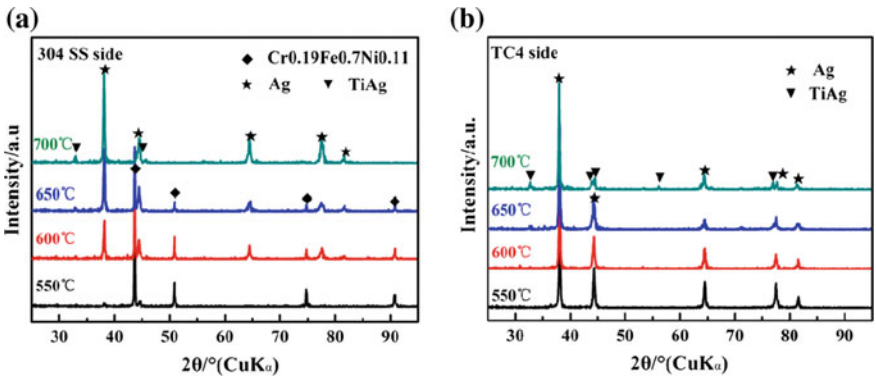

Fig. 3 XRD patterns of 304 SS/Ag foil/TC4 fracture surfaces: **a** 304 SS side; **b** TC4 side

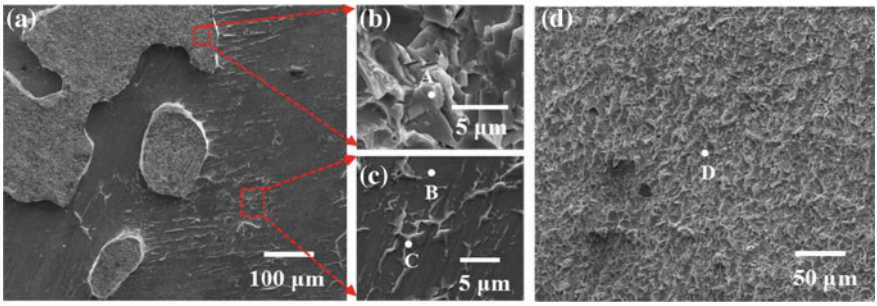

Fig. 4 Microstructure of 304 SS/Ag foil/TC4 fracture surfaces: **a** 600 °C, 304 SS side; **b**, **c** enlarged SEM image of fracture surfaces on 304 SS side; **d** 700 °C, 304 SS side

Table 3 Elemental compositions of the selected points 1–4 (marked in Fig. 4)

Points	Element composition (at%)							Possible phase
	Fe	Ti	Ag	Ni	Cr	V	Al	
A	–	44.49	51.18	–	–	–	4.34	TiAg (ss, Al)
B	72.04	–	–	7.33	20.62	–	–	Fe–Ni–Cr (ss)
C	17.06	–	77.94	–	5.01	–	–	Ag (ss, Fe, Cr)
D	–	43.04	46.96	3.97	6.03	6.04	4.96	TiAg (ss, Cr, Ni)

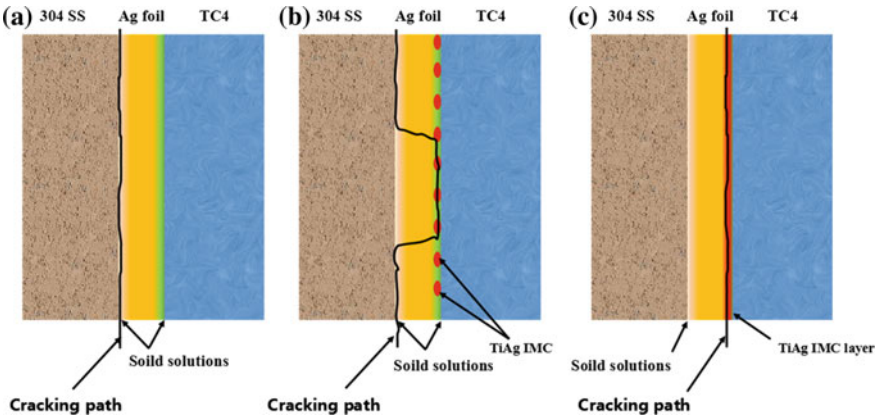

Fig. 5 Schematic illustration of the diffusion layers appearing process: **a** solid solutions form; **b** TiAg IMC particles appears; **c** TiAg IMC layer forms

of solid solution at 304 SS/Ag foil interfaces and the generation of TiAg IMC layer at Ag foil/TC4 interface.

When the bonding temperature is 550 °C, fracture failure is emerged at 304 SS/Ag foil solid solution layer (Fig. 5a). When the bonding temperature is

600 and 650 °C, TiAg IMC nucleated at Ag foil/TC4 interface, and fracture failure happens at both 304 SS/Ag foil and Ag foil/TC4 interfaces (Fig. 5b). As the bonding temperature is increased to 700 °C, TiAg IMC layer formed at Ag foil/TC4 interface, the fracture occurs at TiAg IMC layer (Fig. 5c). Therefore the formation of TiAg IMC layer at Ag foil/TC4 interface has side effects on bonding strength of joints.

Conclusions

(1) Dissimilar metals 304 stainless steel and TC4 alloy were bonded using Ag foil interlayer by plasma activated sintering. When bonding temperature is above 600 °C, the 304 SS/Ag foil/TC4 joints are free of voids or cracks, and TiAg IMC nucleates and grows at Ag foil/TC4 interface.
(2) Shear strength of joints increases first and then decreases with the rising of bonding temperature. A maximum value of the average shear strength is 125 MPa at 600 °C. The formation of TiAg IMC reduced the bonding strength of 304 SS/Ag foil/TC4 joints.
(3) When the bonding temperature is 550 °C, the fracture failure is emerged at 304 SS/Ag foil solid solution layer. When the bonding temperature is 600 and 650 °C, the fracture failure happens at both 304 SS/Ag foil and Ag foil/TC4 interfaces. The fracture failure of joint bonded at 700 °C is ductile fracture and occurs at TiAg IMC layer.

Acknowledgements This work has been supported by the National Natural Science Foundation of China (No. 51572208 and No. 51521001), the 111 Project (No. B13035), the Nature Science Foundation of Hubei Province (No. 2016CFA006), the Joint Fund (No. 6141A02022209) and Natural Science Foundation of Anhui Higher Education Institutions of China (No. KJ2015A314).

References

1. K. Campo, D. Lima, É. Lopes, R. Caram, On the selection of Ti–Cu alloys for thixoforming processes: phase diagram and microstructural evaluation. J. Mater. Sci. **50**, 8007–8017 (2015)
2. B. Sengupta, S. Shekhar, K. Kulkarni, A novel ultra-high strength and low-cost as-cast titanium alloy. Mater. Sci. Eng. A **696**, 478–481 (2017)
3. J. Huang, N. Warnken, J. Gebelin, M. Strangwood, R. Reed, On the mechanism of porosity formation during welding of titanium alloys. Acta Mater. **60**, 3215–3225 (2012)
4. K. Wang, S. Lua, M. Fu, X. Lia, X. Dong, Optimization of β/near–β forging process parameters of Ti–6.5Al–3.5Mo–1.5Zr–0.3Si by using processing maps. Mater. Charact. **60**, 492–498 (2009)
5. G. Li, Y. Li, F. Wang, H. Wang, Microstructure and performance of solid TC4 titanium alloy subjected to the high pulsed magnetic field treatment. J. Alloy. Compd. **644**, 750–756 (2015)

6. J. Lee, M. Lee, Microstructure and mechanical behavior of a titanium-to-stainless steel dissimilar joint brazed with Ag–Cu alloy filler and an Ag interlayer. Mater. Charact. **129**, 98–103 (2017)
7. T. Venkateswaran, X. Vincent, D. Sivakumar, P. Bhanu, R. Janaki, Brazing of stainless steels using Cu–Ag–Mn–Zn braze filler: studies on wettability, mechanical properties, and microstructural aspects. Mater Design. **121**, 213–228 (2017)
8. J. Lee, J. Lee, S. Hong, M. Lee, C.K. Rhee, Microstructure and bonding strength of titanium-to-stainless steel joints brazed using a Zr–Ti–Ni–Cu–Be amorphous filler alloy. J. Mater. Sci. **45**, 6837–6840 (2010)
9. M. Atabaki, J. Wati, A. Idris, Transient liquid phase diffusion brazing of stainless steel 304. Weld. J. **92**, 57–63 (2013)
10. M. Lee, J. Leea, Y. Choi, D. Kim, C. Rhee, Y. Lee, S. Hong, Interlayer engineering for dissimilar bonding of titanium to stainless steel. Mater. Lett. **64**, 1104–1108 (2010)
11. R. Tashia, S. Mousavia, M. Atabaki, Diffusion brazing of Ti–6Al–4V and austenitic stainless steel using silver-based interlayer. Mater. Design. **54**, 161–167 (2014)
12. M. Lee, J. Park, J. Lee, C. Rhee, Phase-dependent corrosion of titanium-to-stainless steel joints brazed by Ag–Cu eutectic alloy filler and Ag interlayer. J. Nucl. Mater. **439**, 168–173 (2013)
13. K. Morsi, K. Moon, S. Kassegne, R. Ugle, E. Villar, Novel current-activated tip-based sintering (CATS): localization of spark plasma sintering. Scr. Mater. **60**, 745–748 (2009)
14. Y. Wang, M. Rao, L. Li, G. Luo, Q. Shen, L. Zhang, Accelerated bonding of magnesium and aluminum with a CuNi/Ag/CuNi sandwich interlayer by plasma-activated sintering. Metall. Mater. Trans. A **47A**, 631–636 (2016)
15. R. Li, T. Yuan, X. Liu, K. Zhou, Enhanced atomic diffusion of Fe–Al diffusion couple during spark plasma sintering. Scr. Mater. **110**, 105–108 (2016)

Resistance Spot Welding Process and Properties of Hot Dip Galvanized DP590 High Strength Steel

Ruxia Liu, Mei Rao, Shulong Liu, Jian Zhang and Guoqiang Luo

Abstract Resistance spot welding of DP590 hot dip galvanized steel was investigated. The microstructure, shear force and current range of welded joints were studied. The results show that with the increasing of welding current or welding time, the shear force of the joints increased first and then decreased. The maximum value of shear force was 17.42 kN at the welding current of 9.5 kA and the welding time of 360 ms. The thinner of Zn layer thickness, the higher value of joint shear force under the same spot welding process. The spot welding current range is smaller with the increasing of Zn layer thickness.

Keywords Resistance spot welding · Hot dip galvanized steel
Zinc layer thickness · Shear force

Introduction

Resistance spot welding is the major production technology in automobile, which is widely used in low-carbon steel and coated steel [1, 2]. Compared with other metal connections, resistance spot welding has excellent techno-economic benefits such as low cost, high speed and suitability for automobile which make it an attraction choice in the future of the auto-body assemblies [3, 4].

With the development of the automobile lightweight, dual-phase (DP) steels are considered an attractive choice for automobile industry owing to their good mechanical properties, including low yield strength to tensile strength ratio, continuous yielding, high initial work hardening rate and superior crash performance

R. Liu · M. Rao · J. Zhang (✉) · G. Luo
State Key Lab of Advanced Technology for Materials Synthesis and Processing, Wuhan University of Technology, Wuhan 430070, China
e-mail: zhangjian178@whut.edu.cn

S. Liu
School of Physics and Electronic Information/Information College, Huaibei Normal University, Huaibei 235000, Anhui, China

© Springer Nature Singapore Pte Ltd. 2018

Y. Han (ed.), *Advances in Materials Processing*, Lecture Notes in Mechanical Engineering, https://doi.org/10.1007/978-981-13-0107-0_71

[5–7]. Compared with the ordinary steel sheets, the weldability of galvanized steel sheet is more demanding as the presence of Zn layer [8–10]. The contact resistance is small in the welding, and the welding current density is small, resulted in the poor performance of the spot welded joints [11]. This limits the application of galvanized steel sheets. To be able to successfully use galvanized steel, it is important to characterize and investigated the spot welding characteristics of galvanized steel sheets [12, 13].

The aim of this study was to investigate the weldability of DP590 hot hip galvanized steel. The microstructure and properties of the joint was studied, and the effect of Zn layer thickness on the quality of the joint also was discussed.

Experimental Procedures

The tested material used in the resistance spot welding experiments was hot dip galvanized DP590 dual-phase sheet with the thickness of 1.2 mm. The quality of Zn coated layer was 50, 80 and 100 g/m^2 respectively. The chemical composition of the tested materials was shown in Table 1. The sample was processed into the size of 1.2 mm × 40 mm × 110 mm by wire cutting. The specimens were ultrasonically cleaned in an acetone bath and then dried in air before welding. The RSW was conducted using an intermediate frequency DC machine (DBZ-160). A truncated class 2 electrode with 6.0 mm face diameter was used, and the weld force is 3 kN.

A weldability of test was conducted to determine weld lobes which produce acceptable weld quality over a range of current and time. The weld nugget size was measure by vernier caliper after peel test, the microstructure of the joint was investigated by metallographic microscope, the shear force of the joints was identified using universal machine, the sample size was shown in Fig. 1.

Table 1 Chemical composition of tested material (wt%)

Materials	C	Si	Mn	P	S	Cu	Al	Al_s	Cr	Mo
DP590	0.0968	0.017	1.735	0.010	0.0060	0.02	0.041	0.0399	0.250	0.138

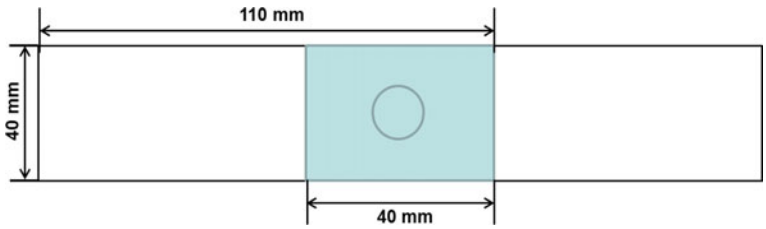

Fig. 1 Dimensions of spot welded tensile shear test specimens

Results and Discussion

Microstructure

Figure 2 shows the morphology of the DP590 steel spot welded joint at 9.5 kA and 360 ms. The joint can be divided into three areas: base metal, heat affected zone and fusion zone. Figure 2b shows the microstructure in the base metal basically consists of evenly distributed martensite within the ferrite. There are mainly martensite and ferrite in the HAZ (Fig. 2c). The martensite becomes larger and its volume fraction is higher in the HAZ than in the base metal. The weld metals are mostly full martensite as seen in Fig. 2d. This is due to the fact that when the grains are fine in the HAZ, the grain growth was restricted by the formation of martensite.

Figure 3 is schematic illustration of the EDS test location of spot nugget. There are three areas at welded joints: fusion zone (FZ), coarse grain heat affected zone (HAZ) and fine grain HAZ. It reveals that the content of Zn in FZ area is much lower than that of course grain HAZ and fine grain HAZ areas (Table 2). In the first stage of welding galvanized sheet, electric streamline shrinks at the interface of base metals, thus the current density is much higher at the edge of shrinking zone. The Zn coating first melts at shrinking zone and nucleates at the juncture of FZ and

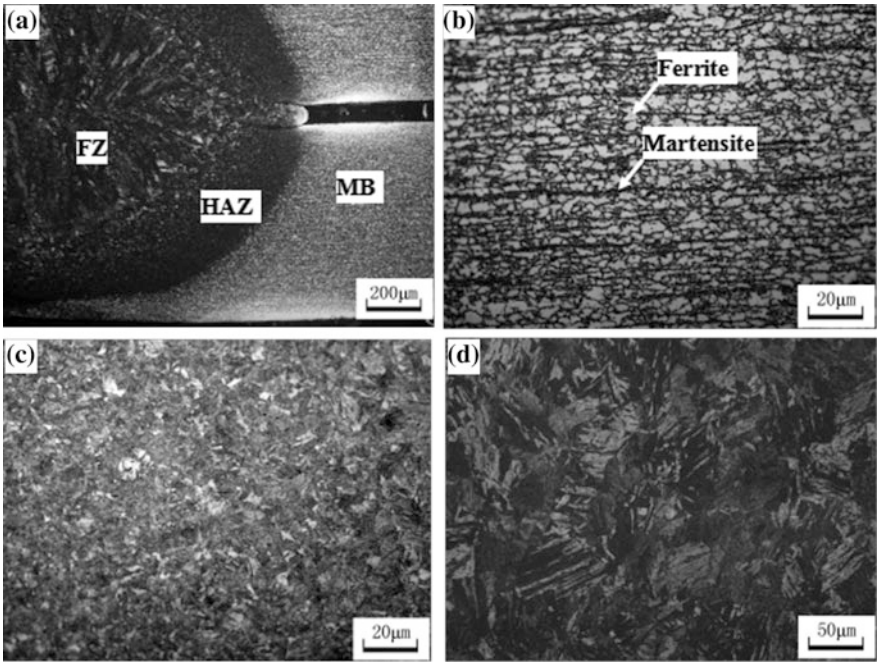

Fig. 2 Microstructure of welded joints. **a** Microstructure of welding joint **b** base metal **c** heat affected zone **d** nugget

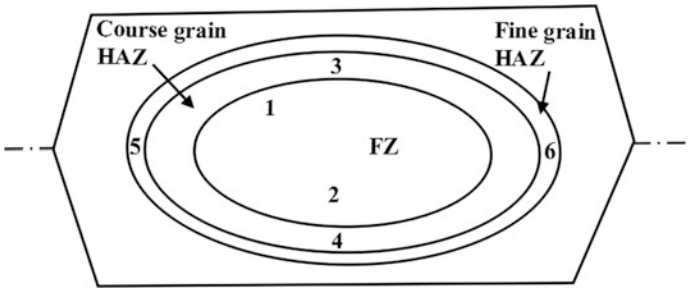

Fig. 3 EDS test location of spot nugget

Table 2 Content of Zn element (marked in Fig. 3)

Area		The content of Zn (at.%)
FZ	1	2.71
	2	3.03
Course grain HAZ	3	15.23
	4	15.32
Fine grain HAZ	5	20.83
	6	21.32

coarse grain HAZ. Zn element enriches at the boundary of HAZ which prevents the expansion of fusion zone. As a result the content of Zn element is higher in the center of welded joint, which decreases the welding quality of joints.

Tensile Properties

Static weld strength is obtained from the tensile shear test to quantify the static load-carrying capabilities. Figure 4 shows that with the increasing of the welding current, the shear force of the joints increases firstly and then decreases. Its maximum value obtains 17.42 kN at welding current of 9.5 kA. When the welding current is 7.0 kA, the nugget cannot be formed with low energy input, so the shear force of the joints is small. The fracture mode is interfacial fracture, as shown in Fig. 5a. With the welding current increases, the energy input of welding and the melting rate of metal in the contact surface increase, so the size of the nugget diameter grows. As a result, the shear force has a considerable improvement, which obtains 17.42 kN at 9.5 kA, and the fracture mode is button pull out, as shown in Fig. 5b. With a further increase of the welding current, the shear force of th*e joints* decreases due to the large amounts of spatter produced as shown in Fig. 5c.

It also can be seen in Fig. 4 that the shear force of the joints decreases with the increasing of the Zn layer thickness in the same welding process, that is, to get the same value of the shear force, the sheet with the thicker Zn layer required for

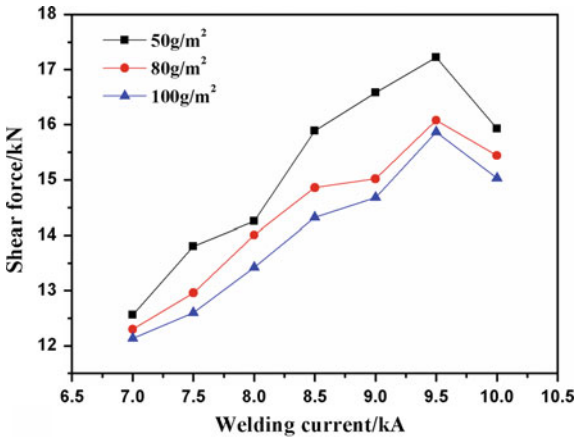

Fig. 4 Effect of welding current on the shear force of welded joints

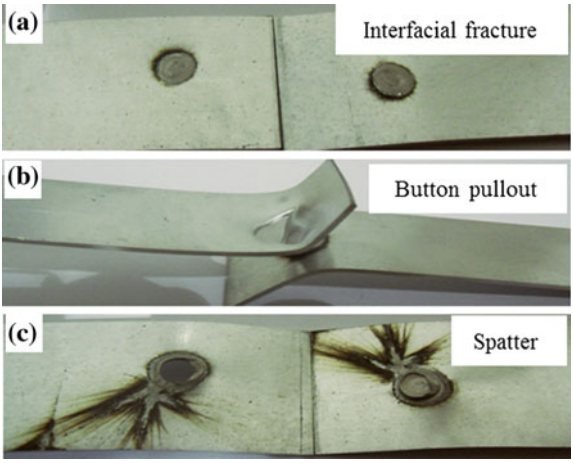

Fig. 5 Fracture mode of spot welded joints

the larger of the welding current. The Zn element will evaporate in the spot welding when the heat input is too big. With the increases of the welding current, the evaporation of Zn increases. Meanwhile, Zn in the molten state will be extruded out of the nugget under the electrode pressure, which results in the decreasing of the shear force.

Process Window

The minimum diameter of the nugget should be bigger than 4.25 t1/2, and it is the thickness of steel sheet. In this study t is 1.2 mm, so the minimum nugget size is 4.66 mm. The left border is the current obtain at the minimum nugget size, and the

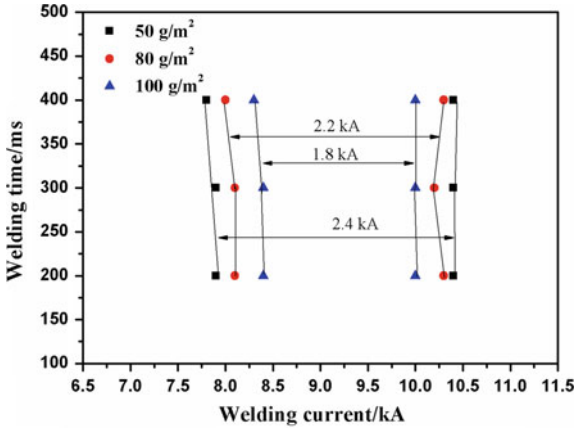

Fig. 6 Process window of spot welded joints

right boundary current obtains when the spatter generates during the welding. Figure 6 shows the process window of welding current at 200, 300 and 400 ms. It can be seen that when the mass of Zn coating is 100 g/m^2, the welding current is 1.8 kA. With the mass of Zn coating decreasing to 50 g/m^2, the welding current is 2.4 kA. Therefore, the larger of the Zn layer, the higher of welding current obtain at the same size of the nugget. On the other hand, the spatter occurs at lower current while the mass of Zn layer is larger.

Conclusions

(1) The DP590 spot welded joints can be divided into three areas: base metal, heat affected zone and fusion zone. There are mainly two phases of martensite and ferrite in the HAZ and mostly full martensite in weld metals.
(2) With the increment of the welding current, the evaporation of Zn increases, the shear force of the joints increases firstly and then decreases. The shear force decreases with the increasing Zn layer thickness in the same welding process.
(3) With the increasing Zn layer thickness by 50 g/m^2 to 100 g/m^2, the process window of welding current range reduces from 2.4 to 1.8 kA.

Acknowledgements This work has been supported by the Nature Science Foundation of Hubei Province (No. 2016CFA006), the Joint Fund (No. 6141A02022209) and Natural Science Foundation of Anhui Higher Education Institutions of China (No.KJ2015A314).

References

1. M. Pouranvari, Fracture toughness of martensitic stainless steel resistance spot welds. Mater. Sci. Eng., A **680**, 97–107 (2017)
2. C. Kwansoo, N. Wooram, Y. Xin, N. Heung, L. Myoung-Gyu, Practical failure analysis of resistance spot welded advanced high-strength steel sheets. Int. J. Polym. **94**, 122–147 (2017)
3. M. Wojciech, K. Alex, B. Nicholas, W. David, Use of modified electrode caps for surface quality welds in resistance spot welding. Mater. Manuf. Process. **22**, 60–73 (2016)
4. Y. Li, Y. Zhang, J. Bi, Z. Luo, Impact of electromagnetic stirring upon weld quality of Al/Ti dissimilar materials resistance spot welding. Mater. Des. **83**, 577–586 (2015)
5. H. Ashrafi, M. Shamanian, R. Emadi, N. Saeidi, A novel and simple technique for development of dual phase steels with excellent ductility. Mater. Sci. Eng., A **680**, 197–202 (2017)
6. L. Schemmanna, S. Zaefferera, D. Raabea, F. Friedelb, D. Mattissen, Alloying effects on microstructure formation of dual phase steels. Acta Mater. **95**, 386–398 (2015)
7. Y. Cao, J. Ahlström, B. Karlsson, The influence of temperatures and strain rates on the mechanical behavior of dual phase steel in different conditions. J. Mater. Sci. Technol. **4**, 68–74 (2015)
8. M. Marín-Sáncheza, P. Ocónb, A. Condea, I. Garcíaa, Electrodeposition of Zn-Mn coatings on steel from 1-ethyl-3-methylimidazolium bis (trifluoromethanesulfonyl) imide ionic liquid. Surf. Coat. Technol. **258**, 871–877 (2014)
9. H. Zhanga, X. Qiu, F. Xing, J. Bai, J. Chen, Failure analysis of dissimilar thickness resistance spot welded joints in dual-phase steels during tensile shear test. Mater. Des. **55**, 366–372 (2014)
10. G. Songa, T. Vystavelb, N. Persa, J. Hossonb, W. Sloof, Relation between microstructure and adhesion of hot dip galvanized zinc coatings on dual phase steel. Acta Mater. **60**, 2973–2981 (2012)
11. F. Hayat, I. Sevim, The effect of welding parameters on fracture toughness of resistance spot-welded galvanized DP600 automotive steel sheets. Int. J. Adv. Manuf. Technol. **58**, 1043–1050 (2012)
12. M. Spitza, M. Fleischanderlb, R. Sierlingerb, M. Reischauerb, F. Perndorferb, G. Fafilek, Surface lubrication influence on electrode degradation during resistance spot welding of hot dip galvanized steel sheets. J. Mater. Process. Technol. **216**, 339–347 (2015)
13. A. Macwan, A. Kumar, D. Chen, Ultrasonic spot welded 6111-T4 aluminum alloy to galvanized high-strength low-alloy steel: Microstructure and mechanical properties. Mater. Des. **113**, 284–296 (2017)

Surface Integrity of Nickel-Base Superalloy Materials by Electric Hot Machining

Jikun Yu, Shimin Geng, Shuo Liu, Xin Liu, MingYu Wu and Hongyou Zhang

Abstract Special equipment was established for electric hot machining (EHM). The Surface integrity of GH4169 nickel base superalloy by EHM was studied. The influences of cutting speed, cutting depth and current on the surface roughness were analyzed based on the experiments. The results showed that the surface with Ra 0.3429 μm of GH4169 could be achieved under the optimum process conditions by EHM. The rank of machining parameters' influence magnitude was cutting depth, current and cutting speed. The work hardening on the surface of GH4169 was obviously decreased compared with ordinary cutting. The residual stress was tensile stress.

Keywords Electric hot machining · Nickel-base superalloy · Surface integrity

J. Yu · M. Wu · H. Zhang
Applied Technology College of Dalian Ocean University, Dalian 116300, China
e-mail: 831022@126.com

M. Wu
e-mail: lnfxwmy@163.com

H. Zhang
e-mail: scxyzy@126.com

S. Liu · X. Liu (✉)
School of Mechanical Engineering, Dalian University of Technology, Dalian 116024, China
e-mail: xinliu@dlut.edu.cn

S. Liu
e-mail: 515418837@qq.com

S. Geng
CCTEG Shenyang Research Institute, Fushun, Liaoning 113122, China
e-mail: layer-abo@163.com

© Springer Nature Singapore Pte Ltd. 2018

Y. Han (ed.), *Advances in Materials Processing*, Lecture Notes in Mechanical Engineering, https://doi.org/10.1007/978-981-13-0107-0_72

Introduction

GH4169 nickel-base superalloy has good thermal intensity and thermal stability. The thermal intensity is the ability of resisting fracture and plastic deformation in high temperature environment. The thermal stability is the ability of resisting corrosion and oxidation. Therefore, it has a wide range of applications in space and aviation. The tensile strength of GH4169 nickel-base superalloy is up to 1393 MPa at room temperature. But the cutting coefficient is only 0.2, only 1/20 to 1/5 of 45 steel [1]. The plastic deformation and chilling phenomenon are serious. It is one of material which is most difficult to process [2].

At present, the processing technology of GH4169 nickel-base superalloy materials include grinding [3, 4], high speed cutting [5], cutting with laser heating [6]. But the higher requirements for processing tool and equipment performance limits the application of this technology.

EHM is the machining method of improving the cutting performance of materials [7], which can soften cutting area material by using the Joule thermal produced by the low voltage and large current formed in the loop among the machine tool, workpiece and cutting tool. EHM can be put into using by a simple transformation on the basis of machining equipment. The requirements of processing equipment and tool performance are relatively low, which can inhibit built-up edge and scale in the process of processing [8], and can reduce tool wear 5–100 times [9].

In this paper, GH4169 nickel-base superalloy is object of processing, whose surface integrity is studied by EHM, and the influence rule of surface roughness is analyzed.

Equipment and Condition

The basic principle of EHM is shown in Fig. 1. The positive electrode of the power supply is connected with the main shaft of the machine through an electric brush, and the negative electrode of the power supply is connected with the cutter. The tool and the tool post are insulated by a mica sheet. When the tool is in contact with the workpiece, a closed loop is formed among the machine, workpiece and the cutter. When the low voltage and high current are adopted, a large amount of Joule heat is generated in the cutting area so as to raise the temperature and soften the workpiece material. Thereby it improves the processing performance of the material.

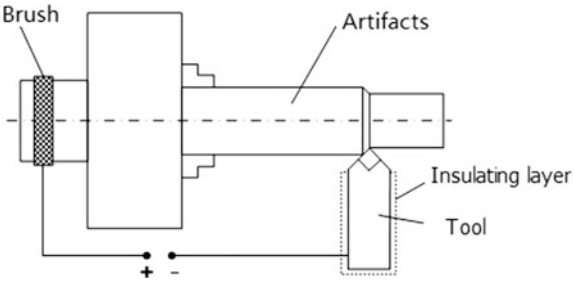

Fig. 1 Principle of EHM

Fig. 2 Experimental equipment of EHM

As shown in Fig. 2. The electric hot experimental equipment is transformed from the ordinary lathe. The test tool type is yt726 41305a. The workpiece is GH4169 nickel-base superalloy bar, whose diameter is 45 mm. Surface roughness measurements were performed by talysurf series 120 mm phase grating interferometer roughness profiler. Work hardening was measured using a digital micro hardness tester. The residual stresses were measured by using the X-ray diffractometer (Empyrean).

Experiment and Discussion

The influence of processing parameters on the surface roughness of GH4169 nickel-base superalloy material which is in EHM is explored through the single factor test.

Surface Roughness Experimental of Nickel-Base Superalloy Materials

According to the surface roughness theory, better surface roughness can be obtained with smaller feed rate [10]. In this paper, the feed is selected at 0.085 mm/r.

Other single factor test parameter selection is shown in Table 1. During the test, other factors are fixed as reference value. The factors were tested by selected reference value and level 1, 2, 3 and 4 respectively. In order to ensure the stability of the experimental results, each parameter combination was subjected to 3 sets tests. Each experiment was performed 3 times measurement of surface roughness and the average values were analyzed.

When no current is added in the experiment, the extrusion of the tool and the workpiece is louder, the shape of the chip is silvery white, short chips or broken chips, the vibration of cutting process is larger. After the current is applied, the extruding sound of the tool and workpiece decreases with the increase of the current. The contact area between the tool and the workpiece is bright red. The chips were purple and gold, and flow out in the form of plastic flow. The cutting process is smooth.

As shown in Fig. 3. When the cutting depth and the machining current are fixed, the change of surface roughness is not obvious with the increase of cutting speed.

Table 1 GH4169 single factor test parameter table of EHM

The processing parameters	At baseline	Level 1	Level 2	Level 3	Level 4
Cutting speed v (m/min)	12.723	7.686	21.206	28.274	X
Cutting depth a_P (mm)	0.25	0.15	0.2	0.3	0.35
Processing of current I (A)	150	120	180	200	X

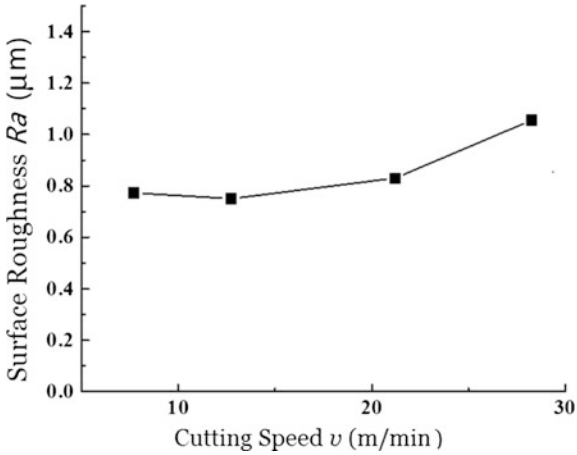

Fig. 3 Effect of cutting speed on surface roughness of GH4169 material

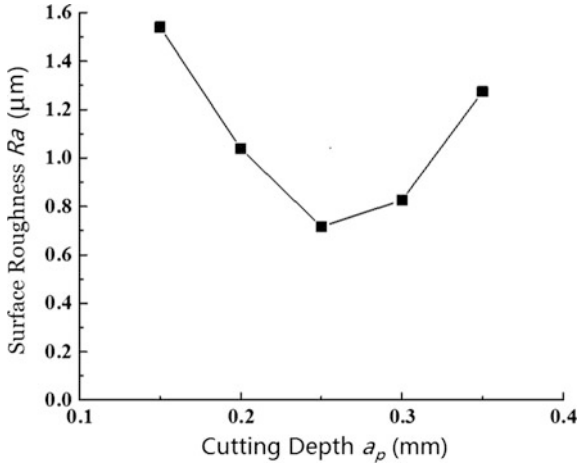

Fig. 4 Effect of cutting depth on GH4169 materials

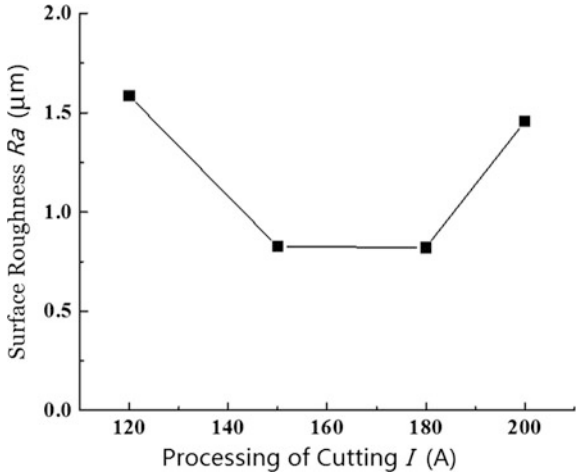

Fig. 5 Effect of current on GH4169 materials

The trend is decreasing first and then increasing. When the cutting speed is 12.723 m/min, the minimum average value of surface roughness is obvious. And the average value is Ra 0.7505 μm.

As shown in Fig. 4. When the cutting speed and machining current are fixed, the surface roughness decreases first and then increases with the increase of cutting depth. When the cutting depth is 0.25 mm, the minimum average value of surface roughness is obvious. And the average value is Ra 0.7168 μm.

As shown in Fig. 5. When the cutting speed and cutting depth are fixed, the surface roughness also decreases first and then increases with the increase of cutting

depth. When the cutting depth is 180A, the minimum average value of surface roughness is obvious. And the average value is Ra 0.8209 μm.

Taking the cutting depth v and the cutting depth a_p as the reference values, three groups of ordinary cutting tests were carried out on the GH4169 material and the surface roughness was measured. The average value of machined surface roughness is Ra 0.9133 μm, which is higher than that obtained in all single factor experiments.

The experimental results show that the surface roughness of GH4169 nickel-base superalloy can be improved by EHM. When other machining parameters are fixed, the surface roughness decreases first and then increases with the increase of cutting speed, cutting depth and processing current.

Hardening Experiment of Nickel-Base Superalloy Materials

Micro hardness measurements were carried out on ordinary turning workpieces and GH4169 workpieces by EHM with a surface roughness of 0.3429 μm, in order to study work hardening of GH4169 nickel-base superalloy by EHM.

The workpiece used in this paper is GH4169 nickel based high temperature material bar. Firstly, radial cutting of bars is carried out by using linear cutting machines, and the workpiece sample with thickness of 10 mm is obtained. Then, as shown in Fig. 6, the workpiece samples are cut at intervals of 120°, and 10 mm 5 mm × 5 mm specimens are obtained.

The specimens were embedded in epoxy resin, the specimen surfaces were coarsely grinded and fine grinded orderly by 400#, 800#, 1500#, 2000# water sand paper, and polished by polishing machine using the crystal phase. Finally, the final test sample is made through the corrosion of nitric acid alcohol with a concentration of 4%. The measurements and observations are made. As shown in Fig. 7, three measuring samples of GH4169 material by ordinary turning, G1, G2, G3 and three measuring samples of GH4169 material by EHM, G1′, G2′, G3′ are obtained.

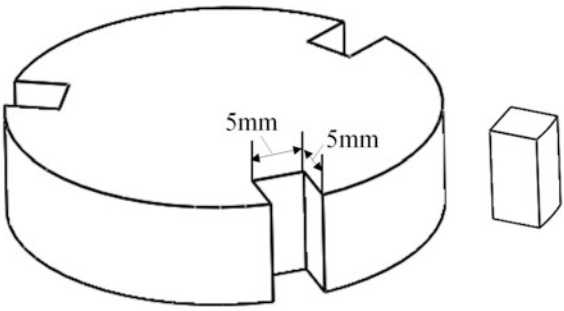

Fig. 6 Measuring sample of GH4169 material

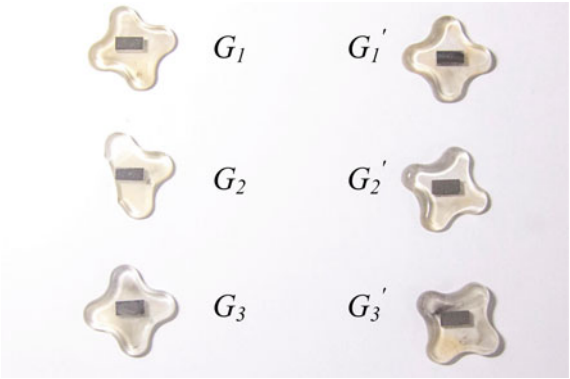

Fig. 7 Microhardness test sample of GH4169 material

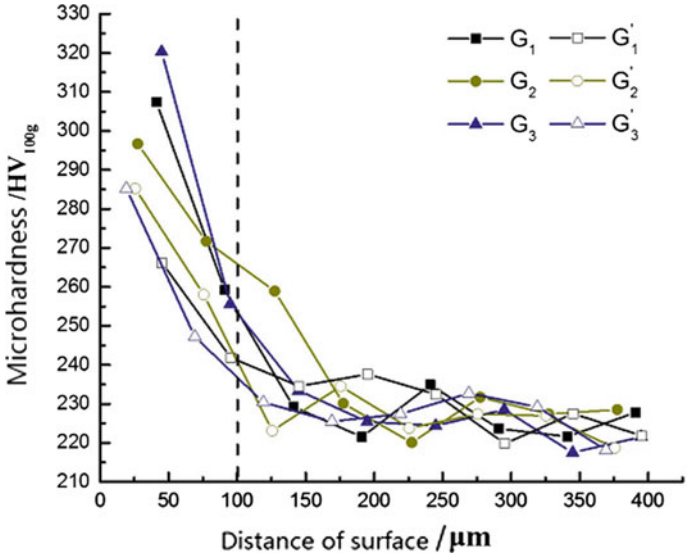

Fig. 8 Microhardness test sample of GH4169 material

The distance between the measuring point and the machined surface is X axis, and the microhardness is Y axis, GH4169 measurement results of the microhardness of the sample are shown in Fig. 8.

Within a surface depth layer of 100 μm from the machined surface, the microhardness of three groups of samples made of GH4169 material by EHM is obviously lower than that of ordinary turning samples, where the microhardness of

the material is more than that of the material, which is about 40–60% of the ordinary cutting. To cut GH4169 material by EHM is obviously less than ordinary turning hardening.

Residual Stress Experiment of Nickel-Base Superalloy Materials

The workpieces were measured by Empyrean X-ray diffractometers, which are from the ordinary turning workpieces and the GH4169 workpieces with surface roughness of 0.3429 μm by EHM. The measurement results show that the residual stress along the cutting direction of the ordinary cutting workpiece is tensile stress, the size is 70.6 MPa. The residual stress along the cutting direction on the surface of the GH4169 nickel-base superalloy by EHM is tensile stress. The size is 450.7 MPa, which is greater than that of the Ordinary cutting.

Conclusions

1. When other machining parameters are fixed, the surface roughness of GH4169 nickel-base superalloy by EHM decreases first and then increases with the increase of cutting speed, cutting depth and processing current.
2. The influence of processing parameters on the surface roughness of GH4169 nickel-base superalloy from the big to the small is the cutting depth, the machining current and the cutting speed.
3. With the cutting speed of 7.686 m/min, cutting depth of 0.25 mm, machining current of 150A and feed of 0.085 mm/r, the machined surface with surface roughness of Ra 0.3429 μm can be obtained.
4. The surface hardening of GH4169 nickel-base superalloy material by EHM is obviously less relative to ordinary cutting.
5. The residual stress along the cutting direction on the machining surface of the GH4169 nickel-base superalloy by EHM is tensile stress. The size is 450.7 MPa, which is greater than that of the Ordinary cutting.

Acknowledgements The financial support for this research provided by the General project of scientific research of LiaoNing Province in China No. L2015085 and L201613 are greatly appreciated.

References

1. T. Li, Analysis and research on cold air cutting performance of difficult to machine materials. (Xi'an Shiyou University, 2015)
2. L. Xu, Research on machinability analysis method of material machined difficultly. (Wuhan University of Technology, 2010)
3. X. Huang, D. Zhang, C. Yao, Influence of grinding parameters on surface integrity of nickel-base superalloy GH4169. J. Aerosp. Power **03**, 621–628 (2013)
4. M. Yang, Y. Li, X. Shi, Grinding performance and surface integrity of GH4169 superalloy by vitrified bond CBN grinding wheel. Tool Eng. **11**, 6–10 (1996)
5. S. Derrien, J. Vigneau, High speed milling of difficult to machine alloys (1997)
6. M. Anderson, R. Patwa, Y.C. Shin, Laser-assisted machining of Inconel 718 with an economic analysis. Int. J. Mach. Tools Manuf **46**(14), 1879–1891 (2006)
7. P. Sun, The basic research on electric heating cutting technology of Hardened steel. (Dalian University of Technology, 2005)
8. Z. Zhou, The scale spines in metal cutting. J. Mech. Eng. **3** (1960)
9. L. Li, Z. Chen, The development and present situation of heated cutting. J. Anhui Inst. Technol. **01**, 113–124 (1989)
10. R. Chen, *The Principles of Metal Cutting* (Machinery Industry Press, Beijing, 2002)

Analysis of the Spring-Back Properties of the TRIP/TWIP Steel Containing 0.035% RE

Lihui Wang, Hongchuan Zhu, Xiangdong Liu, Libo Pan and Tao Gong

Abstract The spring-back properties were analyzed for a comparison between the TRIP/TWIP (Transformation induced plasticity/Twinning induced plasticity) steel and the DP800 (dual phase) steel. The results showed that the spring-back amount of the steels was influenced importantly by the bending radius and the nominal tension force. The spring-back angle of the TRIP/TWIP steel was bigger than that of the DP800 steel when the R (bending radius) was 9.6 mm, at the same time the nominal tension force was not more than 0.66, and the nominal tension force was more than 0.66, the spring-back angle was smaller than that of the DP800 steel. The spring-back angle of the TRIP/TWIP steel was bigger than that of the DP800 steel when the R (bending radius) was 12.7 mm, at the same time the nominal tension force was not more than 0.73, in the same way, its spring-back angle was relatively small when the nominal tension force was more than 0.73. The spring-back angle of the TRIP/TWIP steel had little difference relative to that of the DP800 steel when the nominal tension force reached 1.0. The big die radius should be set in the stamping process, and the spring-back amount would be decreased.

Keywords TRIP/TWIP steel · Rare earth · Spring-back · Property

L. Wang (✉) · H. Zhu · X. Liu · L. Pan · T. Gong
Research and Development Center of Wuhan Iron and Steel Co., Ltd., Wuhan 430080, Hubei, China
e-mail: wlh337@163.com

H. Zhu
e-mail: axuezhu@163.com

X. Liu
e-mail: lxdneu@126.com

L. Pan
e-mail: pan97181@126.com

T. Gong
e-mail: gongtao98@163.com

© Springer Nature Singapore Pte Ltd. 2018

Y. Han (ed.), *Advances in Materials Processing*, Lecture Notes in Mechanical Engineering, https://doi.org/10.1007/978-981-13-0107-0_73

Introduction

The basic mechanical properties of TRIP/TWIP steels are excellent, especially the high strain hardening property of the TRIP/TWIP steels far beyond that of other ordinary high-strength steels. But there is a spring-back phenomenon inevitably in the stamping process of the steels. The interpretation of the reference [1] has been generally recognized, namely, when inside and outside surface of the sheets during the pressing have entered the state of plastic deformation, and the center plate layer still is in an elastic state. As the deformation of steel thickness direction is not synchronized, the steel sheet will produce elastic rebound phenomenon when the external load of the stamping die is removed, which is a spring-back phenomenon. The spring-back of high strength steels leads to the size accuracy of automotive parts bad in the course of the stamping, especially the high strength steels are used widely in recent years, and the steels spring-back problem becomes more obvious and it attracts people more and more attention. The spring-back is a major defect in sheet metal forming according to document [2], it is the most difficult to control relative to wrinkling and cracking. The formability of the TRIP/TWIP steel containing 0.035% RE (rare earth) was studied by the spring-back test in this paper, which may be very significant to the application of the test steel.

Experimental Materials and Methods

Experimental Materials

The ingots were prepared in 50 kg vacuum induction furnace of a model ZGJW0.05-100-2.5, then were forged, rolled, and subsequently cold-rolled into sheets for 1.5 mm thickness followed and annealed treatment in a nitrogen hydrogen atmosphere gradient furnace. The typical chemical composition (in mass percent) of the work materials contained C: 0.40, Mn:17.35, RE:0.035, Fe and impurity elements. In order to illustrate the spring-back property of TRIP/TWIP test steel, the DP800steel, in the composition (in mass percent), contained C:0.16, Mn:1.75, Si:0.55, Cr:0.67, Fe and impurity elements, with similar yield strength and the same thickness was contrasted to analyze. The mechanical properties of the test steels were shown in Table 1.

Table 1 Mechanical properties of the test steels

Type	Thick (mm)	$R_{p0.2}$ (MPa)	R_m (MPa)	A_{80mm} (%)
TRIP/TWIP	1.5	468	1030	49.5
DP800	1.5	479	815	17

Experimental Methods

The spring-back experimental method of the steels in this paper adopted the test method by R. H. Wagoner [3, 4] proposed, its working principle [3] was shown in Fig. 1. The spring-back experiment were done in the R&D department laboratory in Wuhan iron and steel Co. Ltd. Because of the same test equipment as the reference [5, 6], and the test methods [5, 6] are used on the steels, the test processing and the steps were similar to that of [5, 6]. In addition, the spring-back experimental method belongs to standard test method [5, 6]. As follows, the end of the test plate was clamped firstly and bent into the shape of 90° by the radius R working roll of the test machine, and then the other end of the specimen was clamped. According to Wagoner data [7], combined with the test equipment parameters in this paper, a tensile force was applied to the end of the sample and on the other end the test sample was pulled until 127 mm at a constant rate of 40 mm/s, these parameters were consistent with the reference [5, 6]. Then, the spring-back properties of the test steel and the DP800 steel were analyzed by measuring their spring-back angle size. The tensile force should be appropriately chosen according to their yield strength,

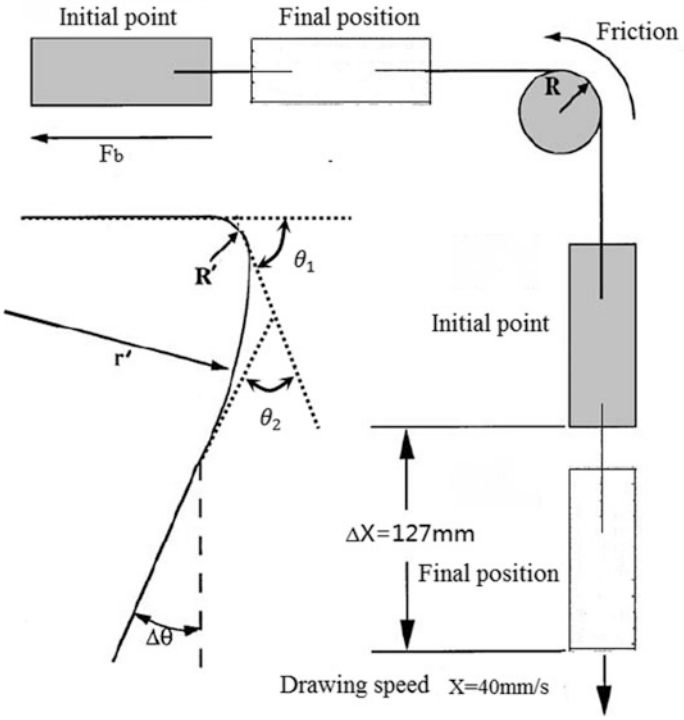

Fig. 1 Schematic diagram of spring-back test

and the actual tensile force was expressed by nominal tension. As followed the formula [4, 5] for calculating the nominal tensile force.

$$\overline{F_b} = \frac{F_b}{R_{eL} \times b \times t}. \tag{1}$$

$\overline{F_b}$ is nominal tensile force; F_b is actual tensile force; R_{eL} is yield strength; b is the samples width; t is the samples thickness.

The nominal tension force was a ratio for the actual tension force and the yield strength of the specimen. According to the stamping process of automobile parts, the nominal tension value of the test steels was 0.2–1.5, and these parameters was unified with document [5, 6]. After the test, the whole deformation process could be divided into 1–4 parts (Fig. 1). The first part was the drawing tension force, the test plate unloaded remained flat state. It was different between the radius R′ of the second part and the roll radius R for the spring-back of the test steel affected the round working roll region. The third part was an arc of radius R′, which was a reason that the steel was continuous bent and reversely bent. It was similar between the fourth part and the first part, the test plate shape was flat, what was caused a Δθ angle by bent and reversely bent on the fourth part of the specimen, i.e. the spring-back angle Δθ thus was produced. By the end of the steels spring-back test, what were measured that of the change of the arc radius r′ and Δθ after the steels spring-backed to illustrate the spring-back amount of the steels. As followed the spring-back angle Δθ [3, 4].

$$\Delta\theta = \frac{\pi}{2}\left(\frac{R}{R'} - 1\right) + \frac{127}{r'}. \tag{2}$$

Δθ is spring-back angle; R is roller radius; R′ is bending radius; r′ is arc radius after spring-back.

When the test samples were pre bent, the test parameters should be set up such as tensile force, drawing speed and drawing distance and so on. The test samples pre-bending and clamping process were completed, bending roller radius respectively represented die fillet radius value of the test plate forming [6]. The spring-back dimension of the test steel with different corner radius die could be simulated by the working roll radius. In this paper, 2 kinds of the bending radius, 9.6 and 12.7 mm, were chosen for the spring-back test. After the experiments were completed, the spring-back properties of the test steels were evaluated by measuring the spring-back angle of the test steels using digital image processing method.

Results and Discussion

First of all, two bending radius corresponded to five different tension force respectively (nominal tension were 0.22, 0.44, 0.66, 0.88 and 1.00) in the spring-back tests, and it was the same test equipment and methods as reference [5, 6], so the nominal tension was consistent with the reference [5, 6].

As shown in Fig. 2 for the samples shape after the experiment, the bending radius R of the TRIP/TWIP steels was 9.6 and 12.7 mm. The spring-back angle varied with the working roll radius and the tension force of the test machine, as shown in Fig. 3. It could be seen according to Fig. 3, when the bending radius was 9.6 mm, the spring-back angle of TRIP/TWIP steel was bigger than that of DP800 steel under the nominal tension was not more than 0.66 and the spring-back angle of TRIP/TWIP steel was smaller than that of DP800 steel under the nominal tension exceeds 0.66, when the bending radius increased to 12.7 mm, the spring-back angle of TRIP/TWIP steel decreases obviously, that was to say, the spring-back angle decreased with the bending radius increased, and the nominal tension force was lower than 0.73, the spring-back angle was bigger than that of DP800 steel, when the tension force was more than 0.73, the spring-back angle was smaller than that of DP800 steel. With the increasing of nominal tension force to 1.0, at the same time the bending radius was 12.7, the spring-back angle of the two kinds of steels had very little difference.

Comparing to the bending radius change on the TRIP/TWIP steel and the DP800 steel of industrial production under different tension force, the results of changing trend lines of the spring-back angle showed that the spring-back satisfied industrial application if a certain tension force and the right working roll were chosen.

Fig. 2 Tested samples of different bending radii

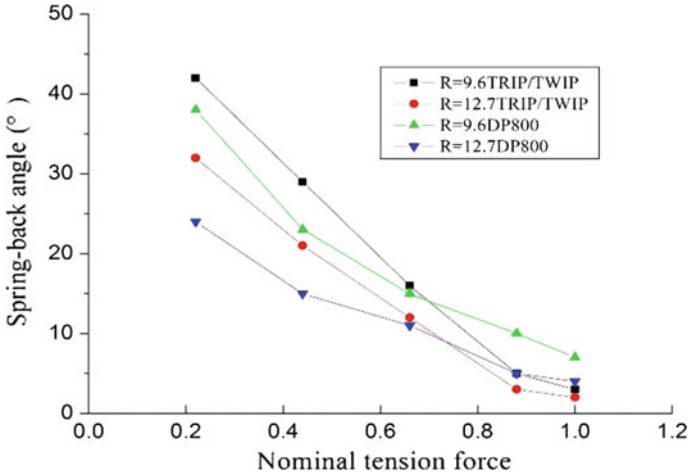

Fig. 3 Spring-back angle Δθ change of the steels

In the processing of TRIP/TWIP steel stamping, due to the nonlinear deformation processing, it was certain to produce elastic strain energy. According to the reference [1], the spring-back amount was direct-proportional relationship with the yield strength of the steels plate and inversely-proportional relationship with the strain hardening index of the steels plate. For the TRIP/TWIP steel had high strain hardening index in this paper, the spring-back was low relative to the other high strength steels. In order to control the dimension precision, TRIP/TWIP steels in stamping processing should be set large pressure side drawing force and large die radius, so the spring-back of the TRIP/TWIP steel would be lower than the spring-back amount of traditional DP800 steel of some industrial production, fully meet some stamping requirements. The spring-back phenomenon of the TRIP/TWIP was mainly occurred in unloading process after the test plates were bent and deformed. The inside and outside zone for the steels were influenced by the bending force and drawing force. Under the internal bending force, inside area of the steels produced the action of tangential compressive stress and strain and the external region of the steels produced tangential tensile stress and strain to lead to the test steels a certain spring-back phenomenon. It was a common phenomenon of all high strength steels. In the stamping process of the experiment steels, using of some common forming methods, such as increasing the die radius, reducing die gap, improving U steel blank-holder force, bending increasing, correcting radius of corner, anti tensile, restrained spring-back scale. The test steels had a good formability, a reinforcement could be set in non functional areas of the die to improve the rigid of opening piece [8–12]. Of course, the spring-back of the test steel in this paper also could be solved by the following methods, i.e. by measuring spring-back amount of TRIP/TWIP steel plate, and then according to the spring-back to stamp die stamping parts to compensate the spring-back to meet

justly the parts design to meet parts requirements. As described in reference [1, 13], the TRIP/TWIP test steel plate because of small spring-back could own good results by the first control method. If the spring-back of the traditional high strength steels are large, the die compensation method is used to correct the die, the result will be better, and the program and method should be chosen according to the actual conditions of the stamping parts.

Conclusions

(1) The spring-back experimental results of the steels show that when the bending radius R was 9.6 mm, the spring-back angle of TRIP/TWIP steel is bigger than that of DP800 steel under the nominal tension was not more than 0.66 and the spring-back angle of TRIP/TWIP steel is smaller than that of DP800 steel under the nominal tension beyond 0.66.
(2) When the bending radius increases to 12.7 mm and the tension force is more than 0.73, the spring-back angle of the test steelis smaller than that of the DP800 steel. When the nominal tension force reaches to 1.0, the spring-back angle of the two kinds of steels has very little difference.
(3) TRIP/TWIP steel should be set as far as possible on the large margin drawing force of the stamping and large mold radius, its spring-back angle will be less than that of DP800 steel.

References

1. G. Wei, R.H. Wagoner, Die design method for sheet springback, J. Int. J. Mech. Sci. **46**(7), 1097–1113 (2004)
2. Z. Dongxu, *The Numerical Simulation and Technology Optimization of the Stamping Forming of Automotive Lightweight Steel and Springback Characteristics* (Jilin University, D.Chang Chun, 2007)
3. K.P. Li, W.P. Carden, R.H. Wagoner, Simulation of springback. J. Int. J. Mech. Sci. **44**(112), 103–105 (2002)
4. T. Kuwabara, S. Takahashi, K. Akiyama et al., 2D springback analysis for stretch-bending processes based on total strain theory. M. SAE **950691**, 504–513 (1995)
5. W. Xing, Z. Hongchuan, P. Libo et al., Springback experimental study on stretch bending of advanced high strength dual phase steel. J. Forging Stamping Technol. **39**(11), 96–101 (2014)
6. L. An, Z. Hongchuan, H. Wenxiang, Analysis on drawbend of flanging cracking for automobile parts. J. Hot Working Technol. **144**(15), 236–238 (2015)
7. R.H. Wagoner, L. Hojun, G.L. Myoung, Advances in springback. J. Int. J. Plast. **45**, 3–20 (2013)
8. Y. Kang-kang, G. Wei, H. Ping, Springback prediction and control, compensation technique in sheet metal forming based on stamping CAE software KMAS. J. Jilin Univ. **35**(4), 409–414 (2005)

9. W.L. Xu, C.H. Ma, C.H. Li et al., Sensitive factors in springback simulation for sheet metal forming. J. Mater. Process. Technol. **151**(1), 217–222 (2004)
10. T.A. Lebedkina, M.A. Lebyodkin, J.P. Chateau et al., On the mechanism of unstable plastic flow in an austenitic Fe–Mn–C TWIP steel. Mater. Sci. Eng. A, **519**(s1–2), 147–154 (2009)
11. W. Gan, R.H. Wagoner, Design method for sheet springback. Int. J. Mech. Sci. **46**(7), 1097–1113 (2004)
12. B. Yidong, C. Wenliang, W. Hong, Fast springback simulation of bending forming based on one-step inverse analysis. Int. J. Mod. Phys. B **22**(31), 76 (2012)
13. F. Lan, J. Chen, J. Lin, A method of constructing smooth tool surfaces for Fe prediction of springback in sheet metal forming. J. Mater. Process. Technol. **177**(1–3), 382–385 (2006)

Polishing on Cubic Boron Nitride Abrasive Materials of Bearing Hollow Roller

Hongyou Zhang and Mingyu Wu

Abstract In order to solve the engineering problem for uniformly polishing the inner hole of the bearing hollow roller, the abrasive flow machining method was used to polish the hollow bearing of the large bearing with 46 mesh/220 mesh cubic boron nitride (CBN) abrasive. The experimental results showed that the difficult polished surface could be obtained by using various particle size of CBN abrasive under the same abrasive flow machine (AFM) parameters. Moreover, the polished surface matched with the used CBN abrasive. In addition, the polishing effect was better if the uniform precision polishing was performed in steps for polishing thicker oxide film machining surface.

Keywords Abrasive flow machine · Hollow pillar roller polishing
CBN abrasive

Introduction

Currently, the large rolling bearings which are shown in Fig. 1a are widely used in the field of rolling mills. Due to the large bearing load and poor working environment, the connecting form of large rolling bearings shown as Fig. 1b, c generally adopts hollow pillar roller connected with the cage through hinges. Thus, the polishing effect of the hollow pillar roller inner surface directly affects the rotation speed of the rolling body and the degree of sliding friction with the cage.

However, the main reason for the occurred failure of rolling bearings using hinges to connect the hollow pillar rollers is that the pillars of the cage which

H. Zhang (✉) · M. Wu
Application and Technology College of Dalian, Ocean University,
Dalian 116300, China
e-mail: scxyzy@126.com

M. Wu
e-mail: lnfxwmy@163.com

© Springer Nature Singapore Pte Ltd. 2018

Y. Han (ed.), *Advances in Materials Processing*, Lecture Notes in Mechanical Engineering, https://doi.org/10.1007/978-981-13-0107-0_74

(a) Rolling mill bearing (b) Assemble roller (c) Hollow roller

Fig. 1 Rolling mill bearing and the hollow pillar roller

connected with the hollow pillar roller are tilted or damaged. It also maybe the reason that the oxide film of the pillar roller inner hole is not clearly removed, the oxide film fell into the bearing raceway that causes bearing wear on the bearing raceway failure in the course of operation. Resulting in the machine stalled, even caused incalculable losses for the enterprise. Currently, since most of bearing companies use sandblasting method or manual polishing in the poor working environment, it is not only inefficient but also that the hole surface oxide film cannot be achieved evenly removed. Therefore, the rejection rate is extremely higher.

The abrasive flow machine (AFM) technology was firstly proposed by the United States in 1960s, and the relevant literature and patents formed in 1980s [1, 2]. The abrasive flow machine (AFM) mainly rely on two hydraulic cylinder symmetrical reciprocating extrusion semi-solid fluid abrasive media, crossing the sealing flow channel formed by between the work-piece and fixture, and then polishing the work-piece surface, shown as Fig. 2 [3]. It was a non-traditional machining process that can be used to deburr, polish and remove recast layers, and to produce compressive residual stresses [4, 5]. At the beginning, it was applied in the aerospace, automotive, electronics and die-making industries [6, 7]. However when AFM was applied in the parts of holes, thin sections and disks, the problem of non-uniform polishing can be discovered in these parts, just as “bell mouth”, “over polishing” and “chamfering” [8, 9].

At present, the technology has been applied to polish the complex surface and deep hole. Thus, some tests have been performed by using the abrasive flow machine (AFM) technology for polishing bearing hollow roller in this study.

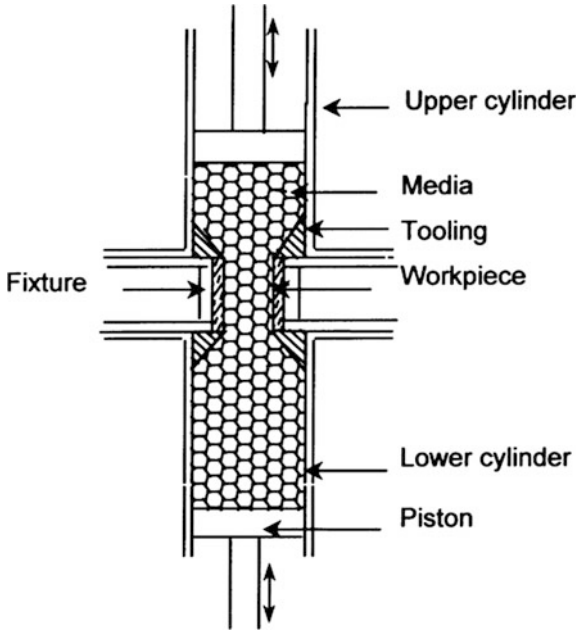

Fig. 2 Abrasive flow machine (AFM) process

Experiments and Equipment

At present, the four-row cylindrical roller bearings are widely used in the bearing factories. Its type code is fcdp92130470. In this study, we used abrasive flow machine equipment from Dalian University of Technology for polishing the thicker oxide layer of the hole generated from heat treatment of the fcdp92130470 hollow roller. The abrasive flow machine equipment is shown in Fig. 3.

Since the thicker oxide layer shown as Fig. 4 often generates on the inner hole after heat treatment the hollow pillar rollers are largely demanded in the bearing factories. The viscoelastic abrasive flow machine particles with various particle sizes were used for polishing.

Fig. 3 FCDP92130470 rolling mill bearing and abrasive flow machine equipment

Fig. 4 Hollow pillar roller and inner its surface

Polishing of abrasive flow machine provides the viscoelastic abrasive particle cutting technology a new opportunity because of its unique characteristics of flexibility, profiling, high efficiency and low damage. This viscoelastic abrasive will be focus on the problem of residual compressive stress formation mechanism of the by the force transmission and the abrasive movement and control of the abrasive grain group under the compression state in the micro surface abrasive cutting process. And based on grinding principle and the material abrasion theory of tribology, discover forming mechanism of residual stress on high pressure polishing surface of viscoelastic abrasive medium and influence regulation in the process of the viscoelastic abrasive flow expanding polishing. All kind of the hollow rolling bearing in wind power, high railway and key equipment, are tested to verify by the viscoelastic abrasive on the abrasive flowing machining equipment, within the scope of the mesoscopic scale, to explore surface roughness, residual stress and strain hardening behavior when the high service performance of bearing roller are in the process of fluid abrasive polishing. So the viscoelastic abrasive materials were beginning to take great effect. This kind of the viscoelastic abrasive materials would be composed of abrasive particle and adhesive. And this adhesive would be composed of polymer and plasticizer. Effect of temperature on shear viscosity for different volume percentage of plasticizer in the medium is shown in Fig. 5 [10]. Cubic boron nitride particles are chosen as a kind of polishing particles in this viscoelastic abrasive material that is shown in Fig. 6.

Results and Discussion

As the cutting abrasive of abrasive flow machine (AFM), the particle size and concentration has a great influence on the polishing effect. Therefore, the polishing abrasive should be firstly selected according to the different surface before the abrasive flow machine differential pressure regulating and sectional matching test. The domestic and foreign researchers have carried out a lot of research for the

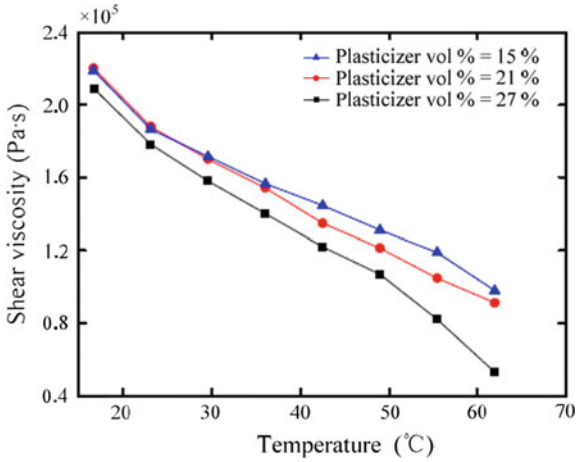

Fig. 5 Effect of temperature and shear viscosity

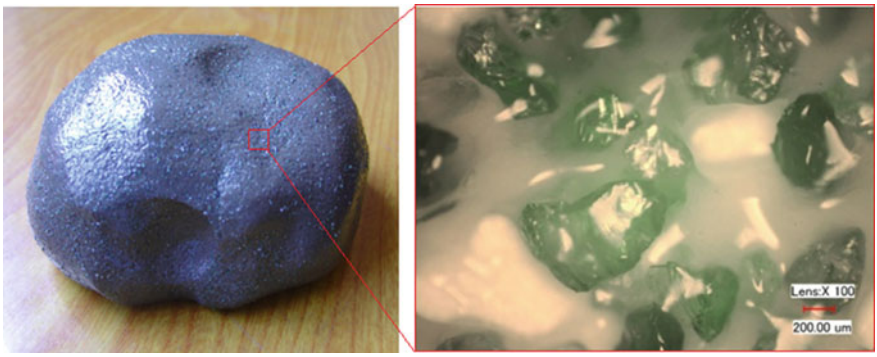

Fig. 6 Abrasive medium with CBN

abrasive grain abrasive properties. Among them, R. E. Williams verified the particle sizes of abrasive flow abrasive have a greater impact on the metal surface through a lot of tests Experiments show that using different polishing methods to obtain surface should choose different particle sizes of abrasive polishing. And the surface polishing effect is best through using abrasive flow machine (AFM) EDM processing [11–13]. However, the change in surface roughness tends to be constant even no further changes with the number of cycles increases [14]. The test parameters of abrasive polishing viscosity characteristics are shown in Table 1.

In order to verify the effect of abrasive particle sizes on the machined surface, we used two hollow rollers of the same type and analyzed abrasive flow machine (AFM) parameters and viscosity characteristics. Simultaneously, we also used 220 mesh/46 mesh CBN abrasive to polish the inner bore of the hollow roller. The extrusion pressure of stroke and return stroke was respectively set at 6.5 MPa, and

Table 1 Abrasive characteristic

Materials	Abrasive particle size [μm]	Abrasive concentration [wt%]	Viscosity temperature characteristic						
CBN	65	60	T [°C]	10	20	30	40	50	60
			Viscous torque [N cm]	2.4	2.2	2.0	2.2	2.0	1.3

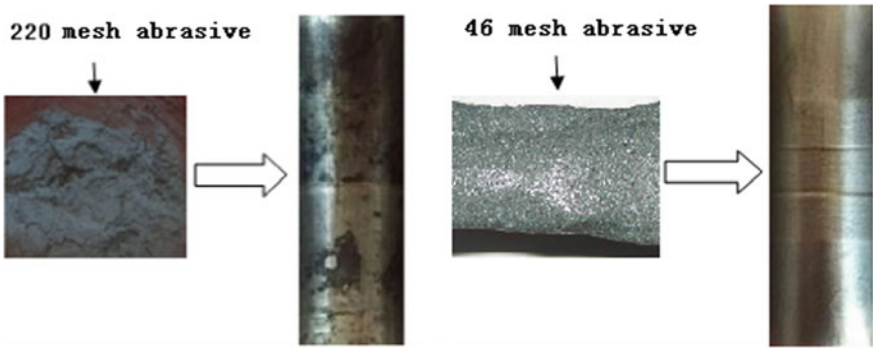

(a) 220 mesh abrasive polishing surface (b) 46 mesh abrasive polishing surface

Fig. 7 Hollow roller inner surface after different abrasive polishing

the back pressure was not increased (The back pressure of return stroke was zero). The rollers were cut by wire cutting after 50 cycles. Through experimental results, it can be seen that the polished surface is not uniform by using 220 mesh CBN abrasive and the oxide layer of polished surface cannot be completely removed. However, the oxide layer of polished surface can be completely removed by using 220 mesh CBN abrasive, and the polished surface is uniform. The comparative photos are shown in Fig. 7a, b.

Conclusions and Prospect

1. The experimental results prove that the abrasive material type and abrasive particle size are the essential factors for the polished surface quality.
2. The CBN abrasive grinding can be used for viscoelastic fluid abrasive of abrasive flow. Its machining efficiency is higher, and the precision polishing can be also achieved.
3. The viscoelastic CBN abrasive should match with the polished surface. If the polished surface is rough surface, the particle size of polishing abrasive should be bigger. If the polished surface is smooth, the particle size of polishing

abrasive should be smaller (abrasive particle size below 46 mesh). Moreover, the big particle size of polishing abrasive combined with the small particle size of polishing abrasive can be used for polishing roller inner surface with a little rough initial surface.

In this way, the abrasive flow machine (AFM) technology for bearing raceway may be further applied to other industrial areas for super-finishing, such as deep groove ball bearings, angular contact ball bearings, cylindrical roller bearings, double row or multi row tapered roller bearings and other types of bearing rings, and roller bearing raceways with larger sizes and more complex raceway surface curvature.

Acknowledgements The financial support for this research provided by the General project of scientific research of Liaoning Province in China No. L2015085 and No. L201613 and the abrasive flow machine equipment provided in the experiment by the of the Dalian university of technology are greatly appreciated.

References

1. J. Rhoads, Abrasive Flow Machining, Cutting Tool Engineering, pp. 75–78 (1988)
2. J. Rhoads, T. Kohut, N.N. Fick et al., Abrasive flow machining and polishing device: US. Patent 012335 (1994)
3. R.K. Jain, V.K. Jain, P.M. Dixit, Modelling of materials removal and surface roughness in abrasive flow machining process. Int. J. Mach. Tools Manuf **39**, 1903–1923 (1999)
4. L.J. Rhoades, Abrasive flow machining: a case study. J. Mater. Process. Technol. **28**, 107–116 (1991)
5. L.J. Rhoades, The development of abrasive flow machine in multitudinous production. Automobile manufacturing international symposium on equipment and technology and process set (1) (1999)
6. R.E. Williams, K.P. Rajurkar, Metal removal and surface finish characteristics in abrasive flow machining, in *Mechanics of Deburring and Surface Finishing Processes*. New york, ASME, 1989 93–106
7. G. Song, *Abrasive Flow Machining Technology of Theoretical Analysis and Experimental Study* (TaiYuan University of technology, TaiYuan, 2010)
8. S. Ji, B. Tang, D. Tan et al., Structured surface precision finishing soft abrasive flow machining method and abrasive flow mechanics numerical analysis. J. Mech. Eng. **46–48**(15), 178–184 (2010)
9. L.J. Rhoads, T. Kohut, N.N. Fick et al, Abrasive flow machining and polishing device: PCT/US1994/012335. China, CN1069859C (1994), pp. 10–24
10. M.R. Sankar, V.K. Jain, J. Ramkumar, Y.M. Joshi, Int. J. Mach. Tool Manu. **51**, 947 (2011)
11. R.E. Williams, Acoustic emission characteristics of abrasive flow machining. J. Manuf. Sci. Eng. **120**, 264–271 (1998)
12. P.J. Davices, A.J. Fletcher, J. Mech. Eng. Sci. **209**(6), 408–418 (1995)
13. A.J. Flectcher, A. Fioravanti, Proc. Inst. Mech. Eng. **210**, 254–265 (1996)
14. V.K. Gorana, V.K. Jain, G.K. Lal, Experimental investigation into cutting forces and active grain density during abrasive flow machining. Int. J. Mach. Tools Manuf **44**, 201–211 (2004)

Preparation of Large Size Monolayer MoS_2 by a Two-Step Heating Process by CVD

Fengjiao Lv, Yi Zeng, Bo Liu, Bin Tang and Qing Chen

Abstract Due to their fascinating properties, two-dimensional monolayer transition metal dichalcogenides (TMDs) have attracted a lot research interests in the recent years. Chemical vapor deposition (CVD) is the most effective way to grow monolayer TMDs in large area. However, to grow high quality monolayer TMDs controllably by CVD is still a challenge. Here, a two-step heating CVD process was developed to grow monolayer MoS_2, which the crystal size is obviously larger than that grown by traditional one-step heating CVD process. The effects of growing time and the distance from the Mo source to the size and density of MoS_2 crystals are also studied. The largest size of individual MoS_2 triangle reaches 62 μm in edge length.

Keywords MoS_2 · CVD · Monolayer · Growth · Heating process

Introduction

Two dimensional transition metal dichalcogenides (TMDs) have attracted a lot research interests in the recent years due to their fascinating properties [1–9]. Molybdenum disulfide (MoS_2), is a typical semiconductor TMD and is more suitable to be the channel material for logic devices and integrated circuits compared with graphene which normally does not have a band gap. The band gap of MoS_2 is tunable from 1.2 to 1.9 eV by changing the number of layers. Unlike its few-layer and bulk counterparts (which have indirect band gap), single layer or monolayer MoS_2 has a direct band gap being about 1.9 eV [10]. Other electrical and optical properties of MoS_2 are also influent by the number of layers and the defect condition including grain boundaries [11–14]. MoS_2 has been demonstrated to have a great potential in optoelectronics [15], photodetectors [16–19], transistors

F. Lv · Y. Zeng · B. Liu · B. Tang · Q. Chen (✉)
Key Laboratory for the Physics and Chemistry of Nanodevices,
Department of Electronics, Peking University, Beijing 100871, China
e-mail: qingchen@pku.edu.cn

© Springer Nature Singapore Pte Ltd. 2018

Y. Han (ed.), *Advances in Materials Processing*, Lecture Notes in Mechanical Engineering, https://doi.org/10.1007/978-981-13-0107-0_75

[20–23], valley electronics and flexible electronic devices [24]. Chemical vapor deposition (CVD) [25] is the most effective way to fabricate monolayer MoS_2 with large area [26–28]. Although many groups have successfully fabricated monolayer MoS_2 with large crystal size, the quality (especially the electronic properties) of CVD grown MoS_2 is still not as good as that prepared by mechanical exfoliation. On the other hand, it is still challenging to grow MoS_2 by CVD controllably.

In the literature, most of the CVD processes to grow MoS_2 use MoO_3 as the Mo source, and this Mo source is heated directly to the growing temperature. We call this kind process as one-step heating process. Here, a new two-step heating CVD process was used to fabricate monolayer MoS_2 under atmospheric pressure. The idea is to allow MoS_2 nucleation at a lower temperature first. The as-grown MoS_2 samples are characterized by optical microscopy, Raman spectrum and atomic force microscopy (AFM). The effects of growing time and distance from the Mo source to the size and density of the MoS_2 crystals are also studied.

Experimental Methods

The present CVD experiment setup is shown schematically in Fig. 1a. MoO_3 powder and S power are used as the Mo source and S source and are put into two separate quartz boats located at different temperature area in a quartz tube with inner diameter about 25 mm. In a typical experiment, 3 mg MoO_3 power is added in the quartz boat located in the center high temperature area of the furnace, enough amount S powder (about 2 g) is put into the boat about 20 cm away from the center of the furnace in the upper stream side. The temperature of S power is controlled by a thermal belt outside the furnace. Si substrate covered by a 300 nm oxide layer is first cleaned by O_2 plasma for 10 min and then placed on top of the MoO_3 powder in a facing-down mode. Horizontal or titled placing modes (as shown in the top two images in Fig. 1a) are used in different experiments, as described in detail in the following section. The CVD growth is performed under atmospheric pressure with the carrier gas of N_2. Before heating the furnace, the tube chamber is first pumped down to 0.06 kPa and stay there for 5 min. Then N_2 gas is introduced with 300 sccm flow and at the same time we keep pumping the tube by a vacuum pump to maintain a vacuum of the tube chamber at 0.27 kPa for 10 min in order to wash out the resident air. Then the vacuum pump is switched off while keeping the N_2 flow at 300 sccm. The pressure increases continuously until reaches the atmospheric pressure. Then heating process is started. The temperature change profiles at the MoO_3 powder area (upper curves) and S powder area (lower curves) during the CVD processes are shown in Figs. 1b, c. That shown in Fig. 1b is the traditional one-step heating process. The profile shown in Fig. 1c is for the new two-step heating process we developed presently. After 34 min from starting heating, the N_2 flow is changed from 300 to 15 sccm to obtain a suitable S vapor flow. After the high temperature growth at 760 °C, the heater is switched off and the N_2 flow is

changed from 15 sccm back to 300 sccm to allow quick cooling of the sample until the furnace temperature is back to the room temperature.

The morphologies of the MoS_2 samples are examined by optical microscope. AFM is used to measure the thickness of typical MoS_2 crystals. Raman spectrum is also taken from some samples to confirm the monolayer nature of the sample.

Results and Discussions

The growth results through two different heating processes are compared. Figure 1d shows the optical microscopy image of the best area in the sample grown by the one-step heating process as shown in Fig. 1b, e shows that grown by the two-step heating process as indicated in Fig. 1c. These two samples are grown with the substrate being placed horizontally. As can be seen, in the one-step heating process sample, the MoS_2 crystals have a truncated-triangle shape with the largest size around 10 μm (Fig. 1d). While the MoS_2 crystals grown by the two-step heating process have triangle shape and larger size up to 28 μm (Fig. 1e). The difference of the two samples can be explained as followed. At the lower temperature (660 °C) step in the two-step heating process, the evaporation rate of MoO_3 is lower than that at the high growing temperature (760 °C), so that the MoS_2 nucleation size and density are smaller, which allow the MoS_2 to grow out to a larger size single crystal at 760 °C growing temperature. Since the two-step heating process results better MoS_2 crystals, the following samples are all grown through this process.

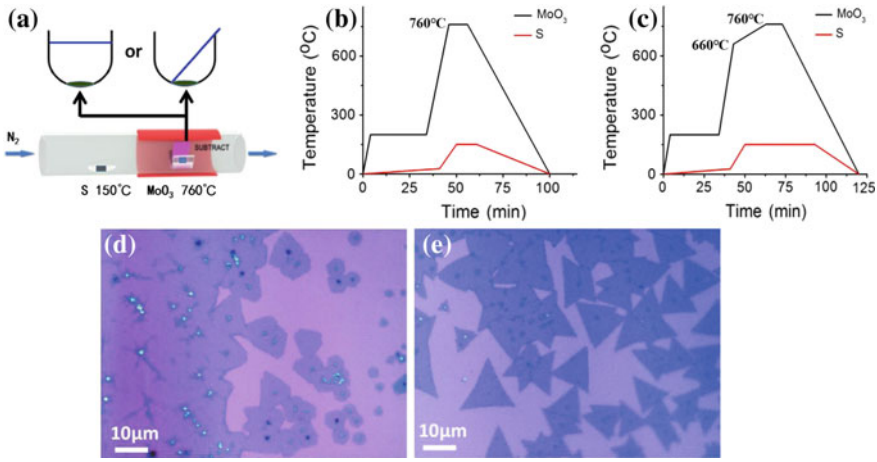

Fig. 1 **a** CVD experimental setup for MoS_2 growth. **b** The temperature change profile of the one-step heating process. **c** The temperature change profile of the two-step heating process. **d**–**e** The best area of the MoS_2 samples grown by one-step heating process **d** and two-step heating process **e**

Similar to other researcher's results, the MoS_2 crystal density is not uniform in the whole substrate chip. In the central part, the sample is thick and forms a continuous film due to the more-than-enough amount of Mo source, while the edge of the chip is not covered by any MoS_2 crystal due to the lack of the Mo supply. The best area is located just outside the continuous film. In order to enlarge the area with large and isolated MoS_2 single crystal, we place the substrate in a tilted mode as shown in the upper-right image in Fig. 1a. Figure 2a shows the best area of the sample grown for 8 min at 760 °C on a tilted-placed substrate. The largest triangular crystal size reaches 62 μm. Figure 3a is a low magnification image showing the fabricated MoS_2 on the substrate changes from a continuous film area (lower left part) to almost empty (top right part). The area covered by continuous film is nearer to the Mo source during growth, while the area covered by isolated MoS_2 single crystals (middle part) has longer distance from the Mo source during growth. When the distance is too long (for top right area), there is almost no MoS_2 growth.

To characterize the thickness of the MoS_2 single crystals, a typical triangle (as marked in Fig. 2a) is characterized by Raman and AFM. Figure 2b is the Raman spectrum of the sample showing two peaks at 386.0 and 405.9 cm^{-1} corresponding to E_{2g} mode peak and A_{1g} mode peak of MoS_2, respectively. The frequency difference between the two peaks is 19.9 cm^{-1}, indicating the MoS_2 has monolayer. Figure 2c is the AFM image and Fig. 2d is the line profile along the line in Fig. 2c. The thickness of the MoS_2 crystal is measured to be 0.9 nm, further confirming the MoS_2 is a monolayer MoS_2.

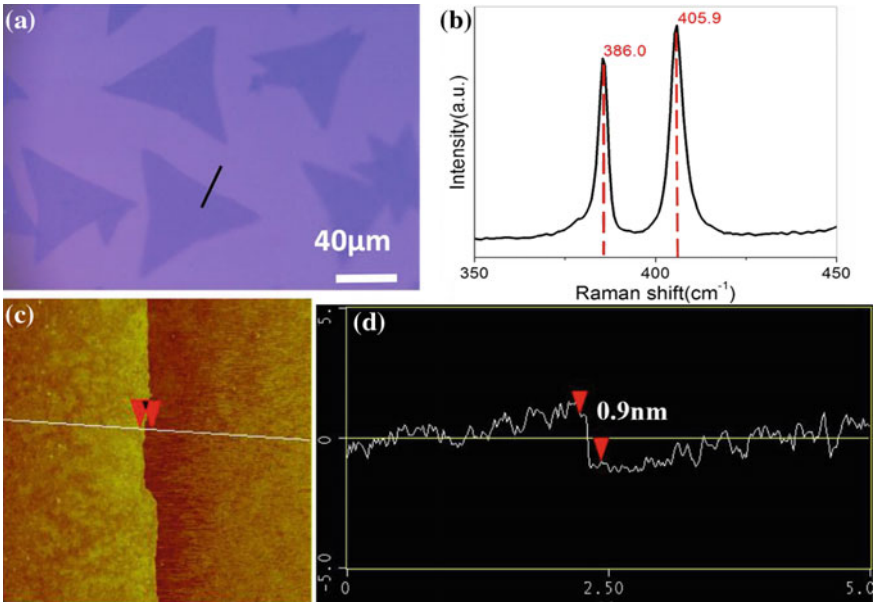

Fig. 2 **a** Optical images of the best area of a typical MoS_2 sample. **b** Raman spectrum of the MoS_2 crystals shown in **a**. **c**–**d** AFM image and height profile of the monolayer MoS_2 shown in **a**

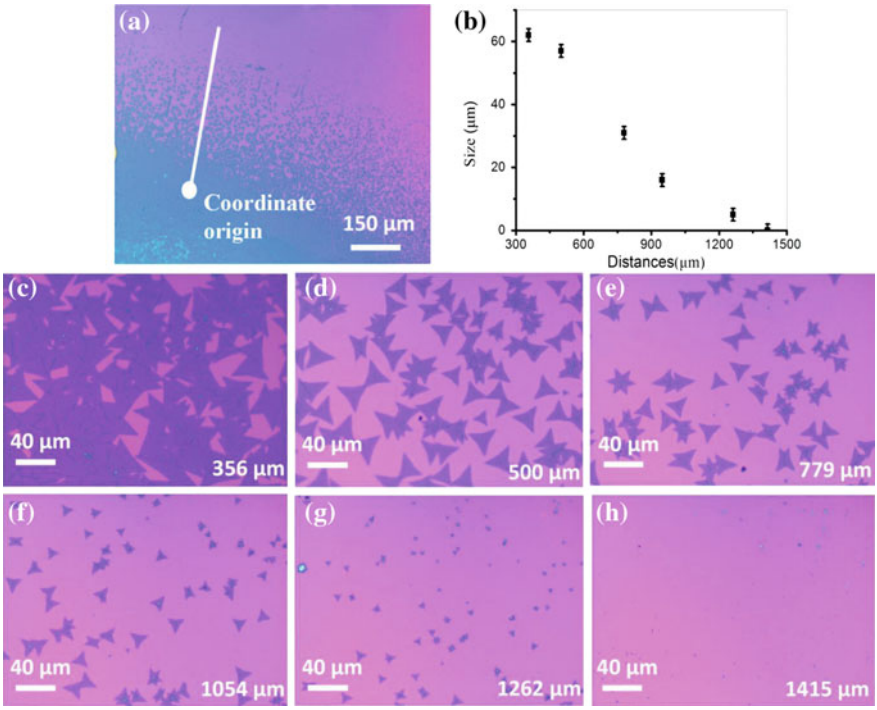

Fig. 3 **a** Low magnification optical microscopy image of a sample grown by two-step heating process. The distances noted in **b**–**h** are measured from the origin and along the line indicated in this image. **b** The measured average sizes of MoS_2 individual crystal at different position. **c**–**h** Optical microscopy image of the MoS_2 crystals at the position labled at the lower right corner

As shown in Fig. 3a, the MoS_2 crystals grown on different area of the substrate are obviously different, mostly due to the different distance of the substrate area from the Mo source. When the distance is short, the amount of Mo source arrived the substrate during growth is more than enough for growing one layer monolayer MoS_2, so that continuous film is formed. When the distance is too long, like that at the upper edge of the substrate shown in the upper right image in Fig. 3a, the amount of Mo source evaporated to the substrate is too small to grow MoS_2 crystals. The effect of the distance from the Mo source is studied in detail as followed. By using the edge of the continuous MoS_2 film as the origin (as indicated in Fig. 3a), the morphology of MoS_2 at different area is examined and some of the images are shown in Figs. 3c–h. When the distance from the origin on the substrate is 356 μm (Fig. 3c), the amount of Mo evaporated onto the substrate during growth is just about enough, individual MoS_2 triangle can be observed although a large number of the triangles are still connected due to the high nucleation density. When the distance on the substrate from the origin is about 500 μm toward the edge of the substrate, individual triangles are separated and the size is large (as shown in Fig. 3d). As the distance increases continuously, the size of single crystal

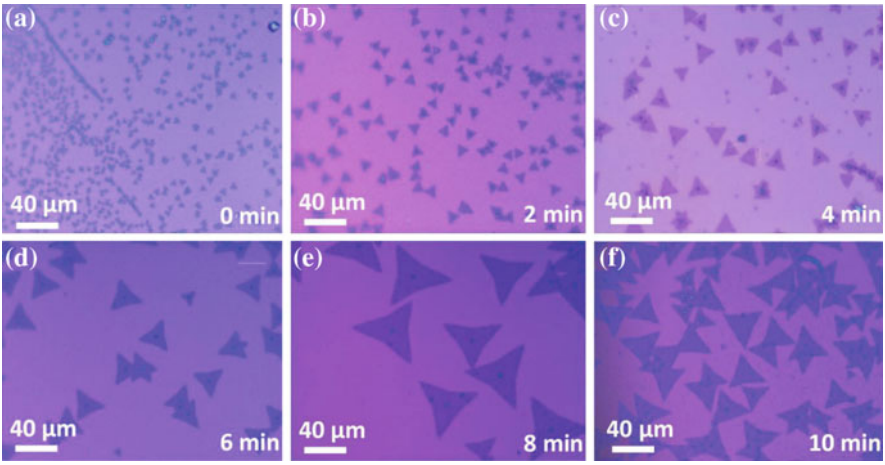

Fig. 4 **a–f** Images of the best area of the samples grown for different growing time. The growing time is marked at the lower right corner in each image

continuously decreases. And when the distance is 1054 μm, the average size of the crystal drops to around 14 μm (Fig. 3f). MoS_2 single crystal can hardly be observed when the distance on the substrate from the origin is 1415 μm (Fig. 3h). Figure 3b shows the quantitative measurement results.

The effect of growing time, which is the time staying at 760 °C, is also studied. Figure 4 shows the best area on the samples growing for different time. As shown in Fig. 4a, when the growing time is 0 min, there is only a nucleation point. After only 2 min growth, the triangle MoS_2 crystal can grow to about 10 μm, as shown in Fig. 4b. The size of the triangle crystals continuously increases and the density decreases while the growing time increases (shown in Fig. 4c–e). When the growing time is 8 min, the triangle MoS_2 crystals reach to the maximum size of 62 μm, but the edges of the triangle bend toward the center (Fig. 4e). If the growing time increases further, the size of the largest triangle crystals does not increase further, but more smaller triangles are observed and the density of the crystals increases, as shown in Fig. 4f. Importantly, although the size and morphology of the MoS_2 crystals changes when the growing time changes from 0 to 10 min, the crystals are all monolayer MoS_2.

Conclusions

A two-step heating CVD process to grow monolayer MoS_2 was developed. The MoS_2 grown by the two-step heating process has larger size and higher quality than that prepared through traditional one-step heating process. The largest size of individual single crystal MoS_2 we obtained is 62 μm. AFM and Raman spectrum

results confirm the crystals have monolayer. The effects of the distance from the Mo source and the growing time are studied in detail. The best sample is obtained with 8 min growth.

Acknowledgements This work was supported by NSF of China (Grant No. 61775006 and 11374022).

References

1. Y. Lee, J. Lee, H. Bark, I.K. Oh, G.H. Ryu, Z. Lee, H. Kim, J.H. Cho, J.H. Ahn, C. Lee, Synthesis of wafer-scale uniform molybdenum disulfide films with control over the layer number using a gas phase sulfur precursor. Nanoscale **6**(5), 2821–2826 (2014)
2. B. Radisavljevic, A. Radenovic, J. Brivio, V. Giacometti, A. Kis, Single-layer MoS_2 transistors. Nat. Nanotechnol. **6**(3), 147–150 (2011)
3. C.R. Dean, A.F. Young, I. Meric, C. Lee, L. Wang, S. Sorgenfrei, K. Watanabe, T. Taniguchi, P. Kim, K.L. Shepard, J. Hone, Boron nitride substrates for high-quality graphene electronics. Nat. Nanotechnol. **5**(10), 722–726 (2010)
4. W. Han, D. Nezich, K. Jing, T. Palacios, Graphene frequency multipliers. IEEE Electron Device Lett. **30**(5), 547–549 (2009)
5. Q.H. Wang, K. Kalantar-Zadeh, A. Kis, J.N. Coleman, M.S. Strano, Electronics and optoelectronics of two-dimensional transition metal dichalcogenides. Nat. Nanotechnol. **7** (11), 699–712 (2012)
6. J. Lee, S. Pak, P. Giraud, Y.W. Lee, Y. Cho, J. Hong, A.R. Jang, H.S. Chung, W.K. Hong, H. Y. Jeong, H.S. Shin, L.G. Occhipinti, S.M. Morris, S. Cha, J.I. Sohn, J.M. Kim, Thermodynamically stable synthesis of large-scale and highly crystalline transition metal dichalcogenide monolayers and their unipolar n-n heterojunction devices. Adv. Mater. **29**(33), 1702206 (2017)
7. H. Wang, T. Taychatanapat, A. Hsu, K. Watanabe, T. Taniguchi, P. Jarillo-Herrero, T. Palacios, BN/Graphene/BN transistors for RF applications. IEEE Electron Device Lett. **32**(9), 1209–1211 (2011)
8. H. Wang, L. Yu, Y.H. Lee, Y. Shi, A. Hsu, M.L. Chin, L.J. Li, M. Dubey, J. Kong, T. Palacios, Integrated circuits based on bilayer MoS_2 transistors. Nano Lett. **12**(9), 4674–4680 (2012)
9. A. Hsu, H. Wang, Y.C. Shin, B. Mailly, X. Zhang, L. Yu, Y. Shi, Y.H. Lee, M. Dubey, K.K. Kim, J. Kong, T. Palacios, Large-area 2-D electronics: materials, technology, and devices. Proc. IEEE **101**(7), 1638–1652 (2013)
10. H. Li, J. Wu, Z. Yin, H. Zhang, Preparation and applications of mechanically exfoliated single-layer and multilayer MoS_2 and WSe_2 nanosheets. Acc. Chem. Res. **47**(4), 1067–1075 (2014)
11. Y.H. Lee, X.Q. Zhang, W. Zhang, M.T. Chang, C.T. Lin, K.D. Chang, Y.C. Yu, J.T. Wang, C.S. Chang, L.J. Li, T.W. Lin, Synthesis of large-area MoS_2 atomic layers with chemical vapor deposition. Adv. Mater. **24**(17), 2320–2325 (2012)
12. S. Najmaei, Z. Liu, W. Zhou, X. Zou, G. Shi, S. Lei, B.I. Yakobson, J.C. Idrobo, P.M. Ajayan, J. Lou, Vapour phase growth and grain boundary structure of molybdenum disulphide atomic layers. Nat. Mater. **12**(8), 754–759 (2013)
13. Y. Xie, Z. Wang, Y. Zhan, P. Zhang, R. Wu, T. Jiang, S. Wu, H. Wang, Y. Zhao, T. Nan, X. Ma, Controllable growth of monolayer MoS_2 by chemical vapor deposition via close MoO_2 precursor for electrical and optical applications. Nanotechnology **28**(8), 084001 (2017)
14. H.M. Oh, G.H. Han, H. Kim, M.S. Jeong, Influence of residual promoter to photoluminescence of CVD grown MoS_2. Curr. Appl. Phys. **16**(9), 1223–1228 (2016)

15. Y. Shi, C. Hamsen, X. Jia, K.K. Kim, A. Reina, M. Hofmann, A.L. Hsu, K. Zhang, H. Li, Z. Y. Juang, M.S. Dresselhaus, L.J. Li, J. Kong, Synthesis of few-layer hexagonal boron nitride thin film by chemical vapor deposition. Nano Lett. **10**(10), 4134–4139 (2010)
16. Q. Ji, Y. Zhang, T. Gao, Y. Zhang, D. Ma, M. Liu, Y. Chen, X. Qiao, P.H. Tan, M. Kan, J. Feng, Q. Sun, Z. Liu, Epitaxial monolayer MoS_2 on mica with novel photoluminescence. Nano Lett. **13**(8), 3870–3877 (2013)
17. B. Radisavljevic, A. Kis, Mobility engineering and a metal-insulator transition in monolayer MoS_2. Nat. Mater. **12**(9), 815–820 (2013)
18. W. Liao, W. Wei, Y. Tong, W.K. Chim, C. Zhu, Electrical performance and low frequency noise in hexagonal boron nitride encapsulated $MoSe_2$ dual-gated field effect transistors. Appl. Phys. Lett. **111**(8), 082105 (2017)
19. X. Li, L. Yang, M. Si, S. Li, M. Huang, P. Ye, Y. Wu, Performance potential and limit of MoS_2 transistors. Adv. Mater. **27**(9), 1547–1552 (2015)
20. C. Ahn, J. Lee, H.U. Kim, H. Bark, M. Jeon, G.H. Ryu, Z. Lee, G.Y. Yeom, K. Kim, J. Jung, Y. Kim, C. Lee, T. Kim, Low-temperature synthesis of large-scale molybdenum disulfide thin films directly on a plastic substrate using plasma-enhanced chemical vapor deposition. Adv. Mater. **27**(35), 5223–5229 (2015)
21. K.F. Mak, C. Lee, J. Hone, J. Shan, T.F. Heinz, Atomically thin MoS_2: a new direct-gap semiconductor. Phys. Rev. Lett. **105**(13), 136805 (2010)
22. H.S. Lee, S.W. Min, Y.G. Chang, M.K. Park, T. Nam, H. Kim, J.H. Kim, S. Ryu, S. Im, MoS_2 nanosheet phototransistors with thickness-modulated optical energy gap. Nano Lett. **12** (7), 3695–3700 (2012)
23. S.W. Min, H.S. Lee, H.J. Choi, M.K. Park, T. Nam, H. Kim, S. Ryu, S. Im, Nanosheet thickness-modulated MoS_2 dielectric property evidenced by field-effect transistor performance. Nanoscale **5**(2), 548–551 (2013)
24. A.M. van der Zande, P.Y. Huang, D.A. Chenet, T.C. Berkelbach, Y. You, G.H. Lee, T.F. Heinz, D.R. Reichman, D.A. Muller, J.C. Hone, Grains and grain boundaries in highly crystalline monolayer molybdenum disulphide. Nat. Mater. **12**(6), 554–561 (2013)
25. X. Ling, Y.H. Lee, Y. Lin, W. Fang, L. Yu, M.S. Dresselhaus, J. Kong, Role of the seeding promoter in MoS_2 growth by chemical vapor deposition. Nano Lett. **14**(2), 464–472 (2014)
26. M. Bosi, Growth and synthesis of mono and few-layers transition metal dichalcogenides by vapour techniques: a review. RSC Adv. **5**(92), 75500–75518 (2015)
27. D. Cao, T. Shen, P. Liang, X. Chen, H. Shu, Role of Chemical potential in flake shape and edge properties of monolayer MoS_2. J. Phys. Chem. C **119**(8), 4294–4301 (2015)
28. R. Shahzad, T. Kim, S.W. Kang, Effects of temperature and pressure on sulfurization of molybdenum nano-sheets for MoS_2 synthesis. Thin Solid Films **641**, 79–86 (2017)

Influences of Initial Composition and Solid Back Diffusion on the Solidification Path of Al–Fe–Si Alloys

Guang Wei Zhao, Chong Ding, Xi Cong Ye and Cai Hua Huang

Abstract The influence of initial composition and the united solid back diffusion (SBD) effects on the calculated solidification paths (SP) of a series Al–Fe–Si ternary eutectic alloy were analyzed. The calculation programme was coupled with Thermo-Calc to calculate equilibrium for phase diagram information. The calculated results showed that initial compositions and SBD coefficient had important effects on SP of the Al–Fe–Si ternary eutectic alloys. The SP of the five Al–Fe–Si ternary alloys were divided into three categories: $L \rightarrow (L+\beta) \rightarrow (L+\alpha+\beta) \rightarrow (L+\alpha+\beta+\mathrm{Si})$, $L \rightarrow (L+\alpha) \rightarrow (L+\alpha+\beta) \rightarrow (L+\alpha+\beta+\mathrm{Si})$, and $L \rightarrow (L+\alpha) \rightarrow (L+\alpha+\mathrm{Si}) \rightarrow (L+\alpha+\beta+\mathrm{Si})$. It was found that the volume fraction of eutectic phase decreases obviously with the increase of the SBD coefficient. Solute distribution coefficients of K_{Fe} and K_{Si} in Al–0.08Fe–4.8Si alloy were also calculated and analyzed.

Keywords Al–Fe–Si · Solid back diffusion · Solidification path

G. W. Zhao (✉)
Hubei Key Laboratory of Hydroelectric Machinery Design & Maintenance, China Three Gorges University, Yichang, China
e-mail: zgwhit@163.com

G. W. Zhao · C. Ding · X. C. Ye · C. H. Huang
College of Mechanical and Power Engineering, China Three Gorges University, Yichang, China
e-mail: 691075509@qq.com

X. C. Ye
e-mail: 335778961@qq.com

C. H. Huang
e-mail: 4995991@qq.com

© Springer Nature Singapore Pte Ltd. 2018

Y. Han (ed.), *Advances in Materials Processing*, Lecture Notes in Mechanical Engineering, https://doi.org/10.1007/978-981-13-0107-0_76

Introduction

Because of the excellent castability, good hardness, and low thermal cracking tendency, Al–Si alloys are highly applied in foundry and manufacturing industry. Iron is the most common additives and/or impurities in this alloy and can affect the phase precipitation and properties [1, 2]. It is pretty time and energy consuming to develop Al–Fe–Si alloys using the traditional experiment method. If the SP of the investigated alloy system could be calculated in advance, it will be very helpful for the development and utilization of this alloy [3].

Ternary Al–Fe–Si alloys have been widely investigated by experiment research especially in the Al-rich zone of phase diagram [4–6], but very few works were carried out about the calculation or simulation of SP [7]. The influences of initial compositions on the SP of Al–Fe–Si ternary eutectic alloys will be analyzed in this work. In addition, the temperature versus solid phase fraction curves, the influences of the united SBD parameter on the liquid composition and the solute distribution coefficient of K_{Fe} and K_{Si} were also investigated.

Descriptions of Model

In this paper, a previously proposed model and the corresponding algorithm [8–10] which linked to Thermo-Calc software have been adopted to calculate the SP of Al–Fe–Si ternary eutectic alloy systems. This solute distribution micro-model and algorithm could be divided into three parts. This is because for a ternary Al–Fe–Si system, the solidification process could be divided into three steps: precipitation of the first solidified phase, precipitation of the eutectic of two and three phases. The expressions of this group of microsegregation models are shown in Eqs. (1)–(3) and more details can be seen in Refs. [8, 9].

$$C_{\mathrm{Li}}^{\alpha} = C_{0i}\left[1 - \left(1 - \Phi_i^{\alpha} k_i^{\alpha}\right) f_S\right]^{\frac{k_i^{\alpha}-1}{1-\Phi_i^{\alpha} k_i^{\alpha}}} \tag{1}$$

$$C_{Li}^{2E} = C_{0i}\left[1 - \left(1 - \Phi_i^{2E} k_i^{2E}\right) f_S\right]^{\frac{k_i^{2E}-1}{1-\Phi_i^{2E} k_i^{2E}}} \tag{2}$$

$$C_{Li}^{3E} \equiv C_{Li}^{TE} \tag{3}$$

Simulation Results and Analyze

Table 1 shows the initial compositions of five selected Al–Fe–Si alloys. The average solidification rate used in the calculation was 0.0036 [11]. The SBD coefficients of solute Si and Fe in the solid phase of α-Al used in this paper are referred to [12]. It can be seen in Fig. 1 that the three phases eutectic of all the selected alloys are $(\alpha - \mathrm{Al} + \mathrm{AlFeSi_}\beta + \mathrm{Diamond_A4})$, and can be abbreviated to $(\alpha + \beta + \mathrm{Si})$. The primary solidified phase of alloys A, B, C and D is phase α and the primary phase of alloy E is phase β. The two phases eutectic of A, B, C alloys are phases $(\alpha + \mathrm{Si})$ and the two phases eutectic of alloys D and E are phases $(\alpha + \beta)$. From the above analysis, we could know that the SP of alloys A, B and C are $L \rightarrow (L + \alpha) \rightarrow (L + \alpha + \mathrm{Si}) \rightarrow (L + \alpha + \beta + \mathrm{Si})$. The SP of alloy D is $L \rightarrow (L + \alpha) \rightarrow (L + \alpha + \beta) \rightarrow (L + \alpha + \beta + \mathrm{Si})$ which has a different two phases eutectic compared with alloy A, B and C. And the SP of alloy E is $L \rightarrow (L + \beta) \rightarrow (L + \beta + \alpha) \rightarrow (L + \alpha + \beta + \mathrm{Si})$.

Table 1 Initial compositions for the five selected Al–Fe–Si alloys

Alloys	A	B	C	D	E
Fe (wt%)	0.1	0.2	0.3	0.6	1.0
Si (wt%)	10.0	10.5	10.0	9.0	10.5

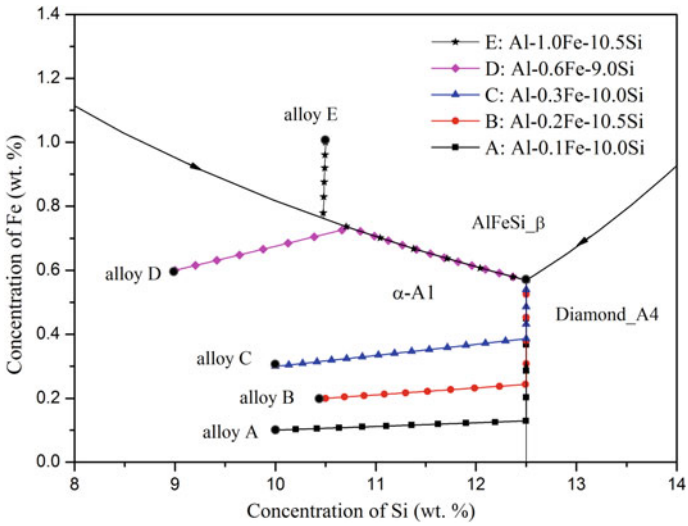

Fig. 1 Calculation results of SP for the selected Al–Fe–Si ternary eutectic alloys

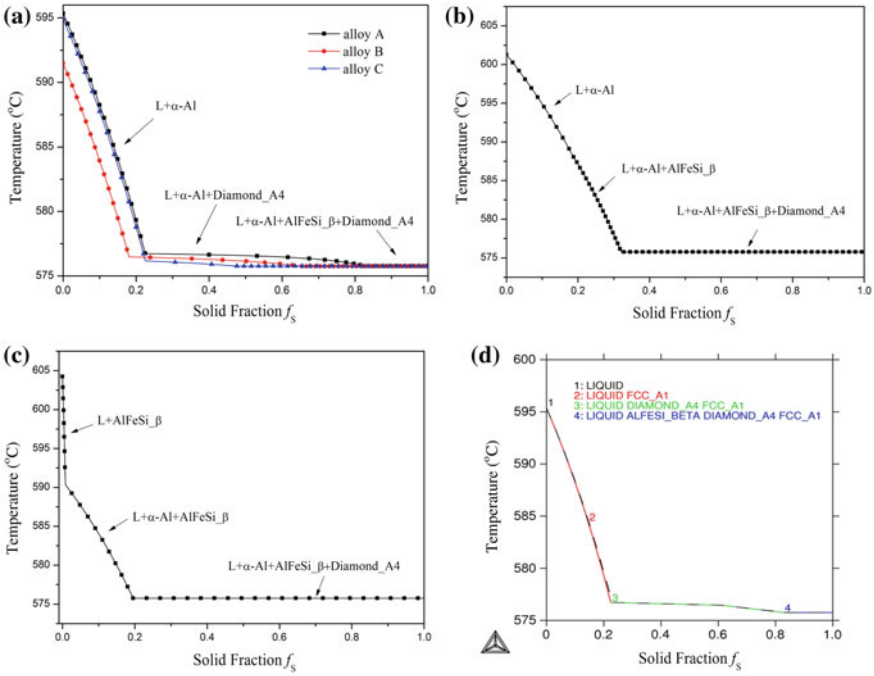

Fig. 2 Influences of initial compositions on the T–f_s curves (**a**)–(**c**) for the five selected Al–Fe–Si ternary eutectic alloys listed in Table 1 and the calculated results of alloy A using Thermo-Calc (**d**)

Figure 2a–c show the T–f_s curves for the five selected Al–Fe–Si alloys listed in Table 1. The T–f_s curves of Fig. 2a can be divided into three stages, corresponding to the three stages of the SP. Alloys A, B and C meet the binary trough at the temperature of 576.75, 576.54, 576.17 °C, respectively, and begin three phases solidification at T = 575.76 °C. The volume percent of phases in corresponding to the three stages of α-Al, (α-Al+ *Diamond_A4*) and (α-Al + AlFeSi_*β* + *Diamond_A4*) are (22.50, 63.33, 14.17%) of alloy A, and (18.00, 46.63, 35.37%) of alloy B, and (22.50, 24.78, 52.72%) of alloy C. And the temperature of alloy D and E reaching the binary trough as shown in Figs. 2b and c are 588.65 and 591.58 °C, and the phase volume of the three solidification stages are (18.00, 13.99, 68.01%) and (0.75, 18.70, 80.55%), respectively. Figure 2d shows the calculation results of alloy A using Thermo-Calc based on the Scheil (solid line) and Lever model (dotted line). It can be seen the SP alloy A is $L \rightarrow (L+\alpha) \rightarrow (L+\alpha+\mathrm{Si}) \rightarrow (L+\alpha+\beta+\mathrm{Si})$ and is consistent with the calculation results of this paper. In addition, the experiment results of Al–0.1Fe–10.0Si can be seen in Ref. [13] and can be compared with the calculation results of this paper, which can also validate the calculated result in this paper.

Figures 3 and 4 are the calculation results of Al–0.08Fe–4.8Si alloy calculated using different assumed Φ parameter, which represent the degree of SBD effects

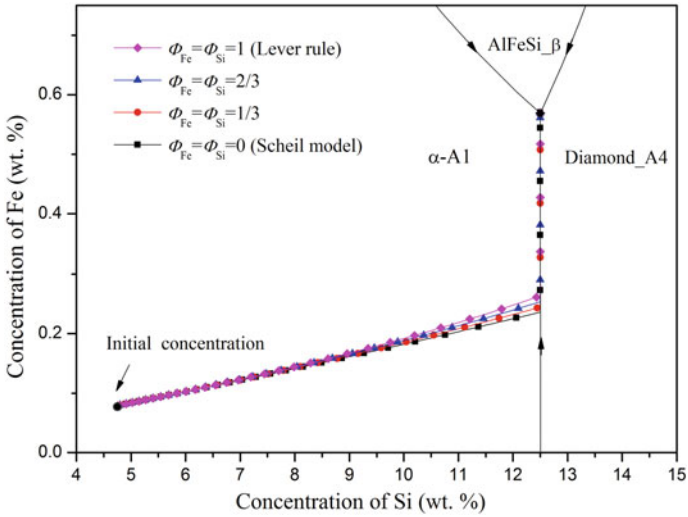

Fig. 3 Influences of the united SBD coefficient Φ on the SP of Al–0.08Fe–4.8Si alloy

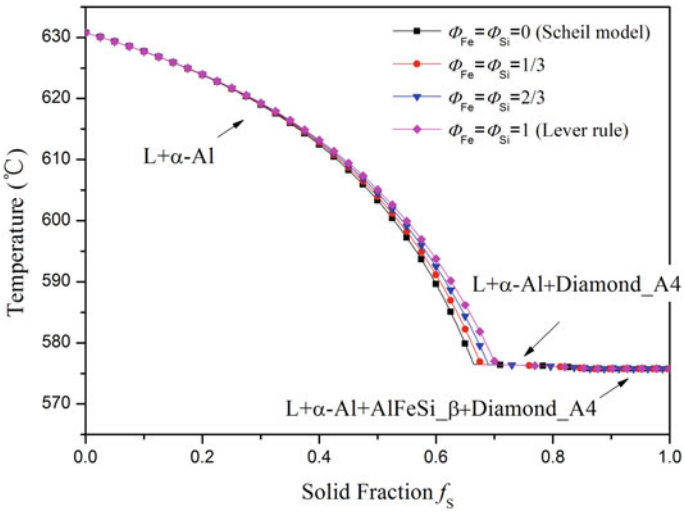

Fig. 4 Influences of the united SBD coefficient Φ on the T–f_s of Al–0.08Fe–4.8Si alloy

[8, 9]. From the calculation results, it can be known that united SBD parameter Φ affects the SP greatly and this is much more obviously in the solidification process of $(L+\alpha)$. The calculated results of Al–0.08Fe–4.8Si with different united SBD coefficient parameter conditions are $L \rightarrow (L+\alpha) \rightarrow (L+\alpha+\mathrm{Si}) \rightarrow (L+\alpha+\beta+\mathrm{Si})$, but the amounts of phases of the three stages are different. The alloys ended

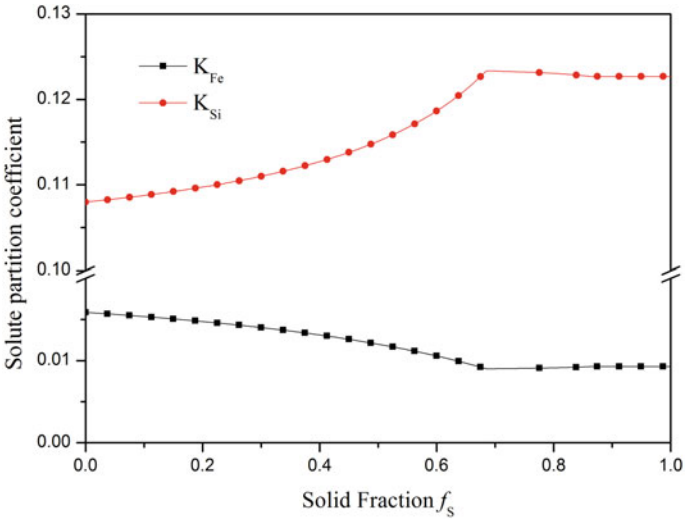

Fig. 5 Calculated solute distribution coefficient of K_{Si} and K_{Fe} of the Al–0.08Fe–4.8Si alloy

the first stage solidification at 576.96, 576.92, 576.90, 576.48 °C, and the volume percent of α-Al are 66.25, 67.50, 68.75, 70.25%, corresponding to condition of Lever-rule ($\Phi_{Fe} = \Phi_{Si} = 1$), $\Phi_{Fe} = \Phi_{Si} = 2/3$, $\Phi_{Fe} = \Phi_{Si} = 1/3$ and Scheil model ($\Phi_{Fe} = \Phi_{Si} = 0$), respectively. The calculated volume percent of two phases and three phases eutectic of the four above conditions are (19.53, 14.22%), (17.87, 14.63%), (17.42, 13.83%), (15.58, 14.17%), respectively. The volume percent of two phases eutectic and the sum of the eutectic are increased with the decreasing of the united SBD parameter of Φ. From the above calculation results it can be known that the SBD effects can affect the SP obviously. In addition, because the calculation results of the assumed conditions ($\Phi_{Fe} = \Phi_{Si} = 2/3$, $\Phi_{Fe} = \Phi_{Si} = 1/3$) are all between the two well known models of the Scheil ($\Phi_{Fe} = \Phi_{Si} = 0$) and the Lever-rule ($\Phi_{Fe} = \Phi_{Si} = 1$), therefore the calculated SP results can be considered reasonable.

Figure 5 displays the solute distribution coefficient of solute K_{Si} and K_{Fe} for the Al–0.08Fe–4.8Si alloy calculated using the same parameters of average solidification rate, second dendrite arm spacing and the diffusion coefficient as Fig. 1. In two phases eutectic solidification stage, Eq. (4) displays the united solute distribution coefficient of Fe and Si in two phases eutectic [8–10].

$$k_i^{2E} = g_\alpha^{2E*} k_i^\alpha + g_\beta^{2E*} k_i^\beta \tag{4}$$

Figure 5 displays that the calculated values of K_{Si} and K_{Fe} are not constant. K_{Fe} decreases from 0.0158 to 0.0090 at the first solidification stage, and the values of K_{Si} changed from the value of 0.1080 to 0.1233. For second solidifying step, solute distribution coefficient K_{Fe} increases slightly from 0.0090 to 0.0093, while the

solute partition coefficient of K_{Si} decreases slightly from 0.1233 to 0.1227. In the ternary eutectic solidification, because the composition of the solid and liquid phase remains unchanged, the solute partition coefficient of K_{Si} and K_{Fe} are 0.0093 and 0.1227, respectively.

Summary

The influences of initial compositions on the SP and T–f_s curves of Al–Fe–Si alloys were analyzed. It is found that the calculated SP for the five selected compositions of Al–Fe–Si ternary eutectic alloys could be divided into three categories. The calculated results of alloys A: Al–0.1Fe–10.0Si, B: Al–0.2Fe–10.5Si and C: Al–0.3Fe–10.0Si are $L \rightarrow (L+\alpha) \rightarrow (L+\alpha+\mathrm{Si}) \rightarrow (L+\alpha+\beta+\mathrm{Si})$, the SP of alloy D: Al–0.6Fe–9.0Si is $L \rightarrow (L+\alpha) \rightarrow (L+\alpha+\beta) \rightarrow (L+\alpha+\beta+\mathrm{Si})$, and the SP of alloy E: Al–1.0Fe–10.5Si is $L \rightarrow (L+\beta) \rightarrow (L+\alpha+\beta) \rightarrow (L+\alpha+\beta+\mathrm{Si})$. The calculate results of Al–0.08Fe–4.8Si alloy showed that united SBD parameters have obviously effects on the SP and T–f_s curves. The volume percent of two phases eutectic and the sum of the eutectic are increased with the decreasing of the united SBD parameter of Φ. It is found that the solute distribution coefficient of K_{Si} and K_{Fe} changed greatly in the first and second solidifying stages of a ternary eutectic alloy.

Acknowledgements We thank a lot for the financial support from the National Natural Science Foundation of China (Grant Nos. 51604162 and 51604161). We wish to thank Harbin Institute of Technology for providing the phase diagram information and data used in this paper. And we thank the opening fund of Hubei Key Laboratory of Hydroelectric Machinery Design & Maintenance (2017KJX12).

References

1. Z.K. Liu, Y.A. Chang, Thermodynamic assessment of the Al–Fe–Si system. Metall. Mater. Trans. A **30**, 1081–1095 (1999)
2. H.L. Chen, Q. Chen, Y. Du, J. Bratberg, A. Engström, Update of Al–Fe–Si, Al–Mn–Si and Al–Fe–Mn–Si thermodynamic descriptions. Trans. Nonferrous Met. Soc. China **24**, 2041–2053 (2014)
3. T.P. Battle, Mathematical modelling of solute segregation in solidifying materials. Int. Mater. Rev. **37**, 249–270 (1992)
4. C.Y. Ban, N. Liu, N. Wang, Y. Han, Q.X. Ba, J.Z. Cui, Influence of DC and AC magnetic fields on the solidification structures of Al–Fe–Si alloys. Rare Met. Mat. Eng. **40**, 102–106 (2011)
5. D.V. Malakhova, D. Panahi, M. Gallerneault, On the formation of intermetallics in rapidly solidifying Al–Fe–Si alloys. CALPHAD **34**, 159–166 (2010)
6. M. Shakiba, N. Parson, X.G. Chen, Effect of homogenization treatment and silicon content on the microstructure and hot work ability of dilute Al–Fe–Si alloys. Mater. Sci. Eng. A **619**, 180–189 (2014)

7. J.A. Taylor, G.B. Schaffer, D.H. Stjohn, The role of iron in the formation of porosity in Al–Si–Cu-based casting alloys: part II. A phase-diagram approach. Metall. Mater. Trans. A **30**, 1651–1655 (1999)
8. G.W. Zhao, D.M. Xu, M.H. Song, H.Z, Fu, D. Yong, Y.H. He, Thermo-Calc linked computations of solidification paths of ternary alloys using an extended unified microsegregation model. Acta Metall. Sin. **45**, 956–963 (2009)
9. G.W. Zhao, C. Ding, X.S. Gu, X.C. Ye, C.H. Huang, M.C. Gu, Solidification path calculations of Al–Zn–Mg alloys in Al-rich corner. China Foundry **14**, 443–448 (2017)
10. G.W. Zhao, X.C. Ye, W.J. Liu, M.C. Gu, Solidification path calculations of Al–Cu–Si alloys in Al-rich corner. Adv. Mater. Res. **503–504**, 374–377 (2012)
11. G.W. Zhao, D.M. Xu, X.Z. Li, J.J. Guo, H.Z. Fu, Y. Du, Y.H. He, Thermo-Calc based multicomponent microsegregation model and solidification paths calculations. China Foundry **8**, 269–274 (2011)
12. D. Yong, Y.A. Chang, B.Y. Huang, W.P. Gong, Z.P. Jin, H.H. Xu, Z.H. Yuan, Y. Liu, H.Y. He, F.Y. Xie, Diffusion coefficients of some solutes in fcc and liquid Al: critical evaluation and correlation. Mater. Sci. Eng. A **363**, 140–151 (2003)
13. J.A. Taylor, G.B. Schaffer, D.H. Stjohn, The role of iron in the formation of porosity in Al–Si–Cu-based casting alloys: part I. Initial experimental observations. Metall. Mater. Trans. A **30**, 1643–1650 (1999)

Influence of Mold Temperature on Microstructure and Shrinkage Porosity of the A357 Alloys in Gravity Die Casting

Longfei Li, Daquan Li, Junzhen Gao, Yongzhong Zhang and Yonglin Kang

Abstract In gravity die casting, mold temperature is a significant parameter during filling and solidification. The selection of mold temperature is commonly based on individual experience in production. No clear specification of mold temperature is pointed out in the international standard. Therefore, in this study the experimental and simulated methods were used to compare the effect of the mold temperature on microstructure and shrinkage porosity during solidification of the A357 alloys. The GB/T 1173-2013 standard mold was used at different temperature (150, 250, 350 °C). The microstructure of sample was compared in each condition. It was found that increasing the mold temperature, which influenced the cooling rate in solidification, increased the second dendritic arm space of α-Al phase and the size of Si particles in microstructure. Moreover, increasing the mold temperature also decreased the temperature gradient of sample during solidification and impaired the filling of the liquid in dendrites. When the mold temperature was 150 °C, no shrinkage porosity was observed in the microstructure. When the mold temperature increased to 350 °C, severe shrinkage defects were observed on the fracture of the samples. The simulated method was also applied to determine the tendency of shrinkage porosity and the results calculated by ProCAST agreed well with the experimental results.

Keywords Mold temperature · A357 aluminum alloy · Solidification Microstructure · Shrinkage porosity

L. Li · D. Li (✉) · J. Gao · Y. Zhang
General Research Institute for Nonferrous Metals, Beijing, China
e-mail: lidaquan@grinm.com

L. Li
e-mail: lilongfei_grinm@163.com

J. Gao
e-mail: gaojunzhen@163.com

Y. Zhang
e-mail: zhangyongzhong@grinm.com

L. Li · Y. Kang
University of Science and Technology Beijing, Beijing, China
e-mail: kangylin@ustb.edu.cn

© Springer Nature Singapore Pte Ltd. 2018

Y. Han (ed.), *Advances in Materials Processing*, Lecture Notes in Mechanical Engineering, https://doi.org/10.1007/978-981-13-0107-0_77

Introduction

Mold temperature is a critical parameter affecting the microstructure and mechanical property of castings during solidification [1, 2]. The grain size, phase distribution and casting defects are related to change of the die temperature field. When mold temperature is very low, the defect like cold shut can be observed on the surface of castings [3]. On the other hand, the prolonged solidification can be obtained with very high temperature of mold, which results to coarse grain structure and severe casting defects. Bichler et al. [4] found that mold temperature has significant influence on the later stage of solidification and referred that variations of mold temperature influence the casting porosity of the alloy. Huang et al. [5] investigated the influence of mold temperature on hot tearing susceptibility during casting magnesium components and suggested that the mold temperature is controlled to be ≥ 641 K for AZ91D alloy to achieve better hot tearing resistance. Rathi et al. [2] also studied the relationship between mold temperature and castability in Al–Si–Cu alloy and concluded that appropriate mold temperature results good refilling the material in later stage of solidification. Thus, it is important that the mold temperature should be carefully controlled to achieve defects-free castings during solidification.

In gravity die casting, shrinkage porosity is an unavoidable defect due to failure of effective feeding. Many researchers studied the mechanism of shrinkage porosity formation and searched for casting parameters including mold temperature to be an assessment of the shrinkage porosity formation. Mi et al. [6] improved the cooling capacity of the mold to reduce the shrinkage defects effectively. Zhang et al. [7] investigated that the thermal parameters including solidus velocity and cooling rate of ingot, which are influenced by die temperature field, can be developed to a new shrinkage porosity criterion for eliminating the centerline porosity in steel ingot. It is seen that the mold temperature influences the solidification of castings and the shrinkage porosity can be eliminated by controlling the mold temperature in a reasonable way.

Therefore, the influence of the mold temperature on microstructure and shrinkage porosity of the A357 alloys was investigated by optical and scanning electron microscopy. And the simulated method used by ProCAST was also applied to evaluate the tendency of shrinkage porosity.

Alloy Preparation, Test Methods and ProCAST Simulation

The GB/T 1173-2013 gravity mold (GB/T mold hereafter) shown in Fig. 1a was used in this experiment. The key dimensions of the casting (gauge diameter of 12 mm and gauge length of 60 mm) are shown in Fig. 1b.

Table 1 shows the composition of the A357 alloys used in experiment and simulation, which was measured by Inductively Coupled Plasma (ICP). Melt of

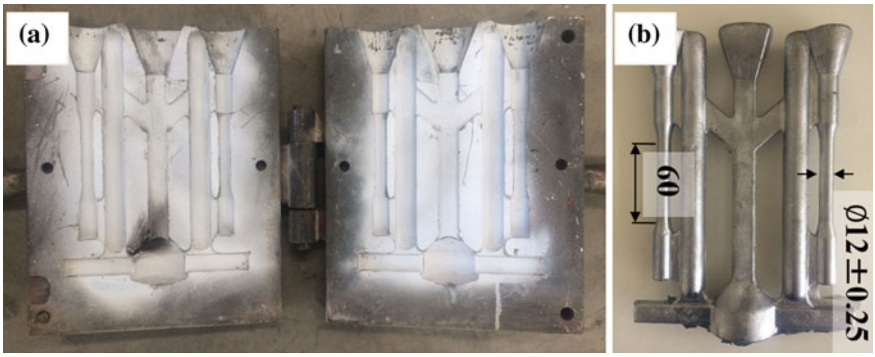

Fig. 1 GB/T 1173-2013 gravity mold and key dimensions of the casting

Table 1 Composition of the A357 alloys used in experiment and ProCAST simulation (wt%)

Alloy	Si	Mg	Cu	Sr	Fe	Ti	Al
A357	7.950	0.626	<0.0002	0.0187	0.116	<0.0002	Rem
A357 in ProCAST	8	0.6	–	–	–	–	

30 kg was prepared in clay-graphite crucible using an electric resistance furnace. The GB/T mold was placed in the furnace under different preheat temperature (150, 250 and 350 °C) for no less than 2 h. The A357 alloys were melted at 750 °C and then subjected to degassing with Argon for 30 min. The melt was subsequently homogenized in furnace for 30 min before taking reduced pressure tested (RPT) samples and K-value samples, which was used to evaluate melt cleanness in quantity. After degassing and skimming, the melt at 730 °C was manually poured into the GB/T mold. At least three castings with good surface were obtained in each condition of mold temperature. The microstructure of sample was examined using Zeiss optical microscope and the fracture of sample was observed using Field Emission Scanning Electron Microscopy (FESEM, JSM-6510). The ProCAST software (version 2016) was adopted to simulate the solidification process and evaluate the tendency of shrinkage porosity formation.

Experimental Results and Analysis

Influence of the Mold Temperature on Microstructure

Figure 2 shows the dendritic α-Al phase and eutectic Si phase under different mold temperature (150, 250 and 350 °C). The Si particles showed fibrous morphology

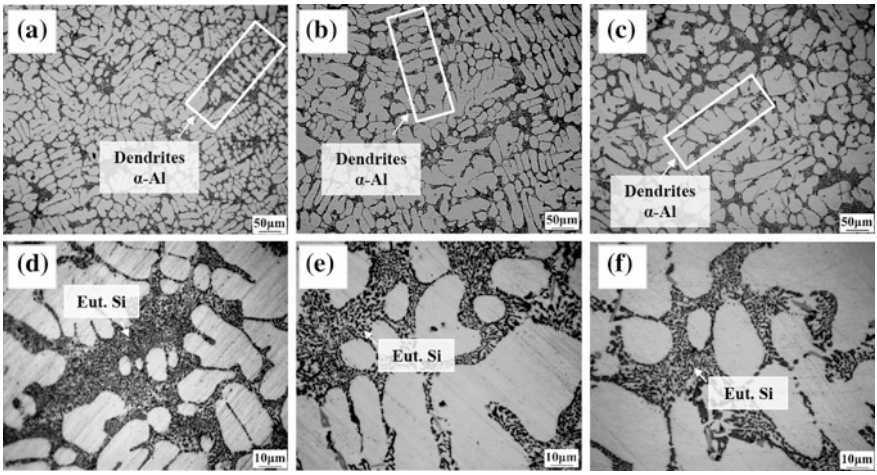

Fig. 2 Microstructure of dendrites α-Al and eutectic Si under different mold temperature at **a**, **d** 150 °C **b**, **e** 250 °C **c**, **f** 350 °C

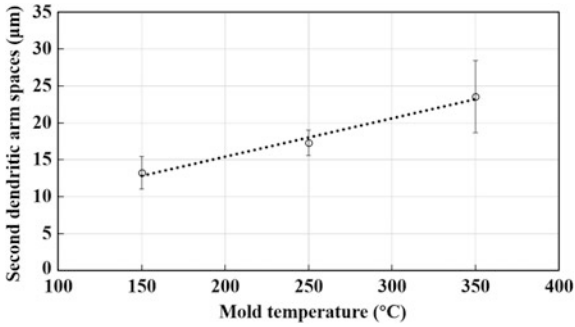

Fig. 3 Second dendritic arm spaces (SDAS) of dendrites α-Alunder different mold temperature

because of 0.0187 wt% strontium addition. The coarser dendritic α-Al phase and less fibrous Si particles were observed under the condition of higher mold temperature.

From measurement results in Fig. 3, the second dendritic arm space (SDAS) was decreased from 23.6, 17.3 to 13.2 μm when the mold temperature was 350, 250 and 150 °C. The mold temperature influenced the cooling condition during solidification. The simulation by ProCAST is widely used in casting industry, especially its practical application in metal filling and solidification process [8, 9]. In Fig. 4, cooling curves of point 1, which was located at the middle of the gauge length, were calculated by ProCAST under different mold temperature. The cooling curves were divided to three parts including liquid contraction (730–613 °C), solidification contraction (613–555 °C) and solid contraction (555 °C ∼ ambient temperature) [10]. The solidification contraction among three was the key process to obtain the

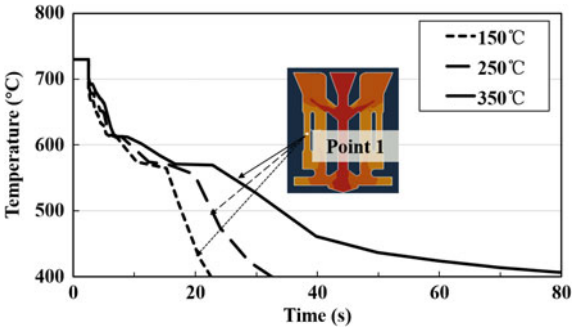

Fig. 4 Cooling curves calculated by ProCAST under different mold temperature

microstructure of the A357 alloys. The α-Al phase and eutectic Si phase were formed at temperature between liquidus (613 °C) and solidus (555 °C). The cooling rates, which were 9.22, 6.05, 4.47 °C/s for mold of 150, 250, 350 °C, were calculated based on the average slope between the liquidus and the solidus. It was concluded that the cooling rate of samples was reduced under increasing mold temperature, which resulted to increasing SDAS of α-Al phase and size of Si particles in microstructure.

Influence of the Mold Temperature on Shrinkage Porosity

Figure 5 shows the fracture of sample with 350 °C mold temperature. Figure 5a, b are respectively center and edge area of the fracture surface. It is seen that the grains at center showed equiaxed dendritic morphology, while the grains at edge showed columnar dendritic morphology. The morphology of grains showed that the melt was solidified in shell-mushy mode, which impaired the refilling of liquid in late

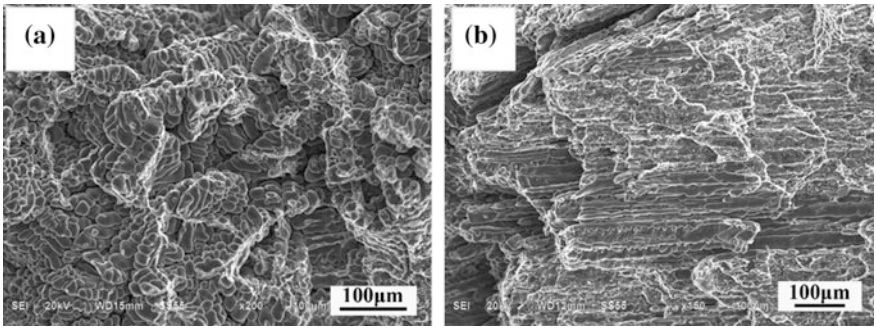

Fig. 5 **a** Center and **b** edge area of fracture surface under the mold temperature at 350 °C

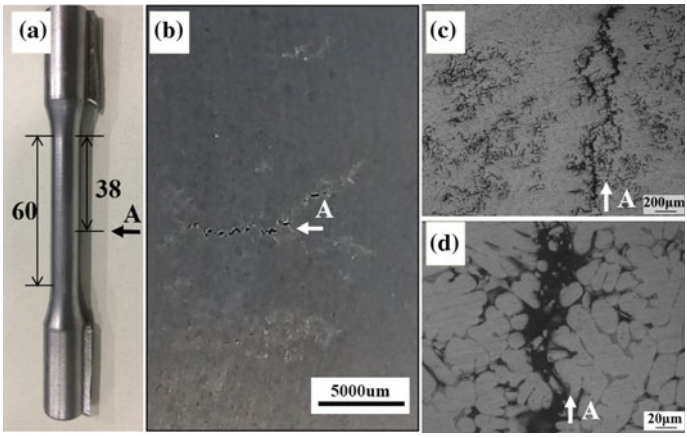

Fig. 6 **a–d** Longitudinal section of sample under the mold temperature at 350 °C

stage of solidification [10]. Moreover, shrinkage porosities with layer distribution were observed at longitudinal section of the sample under the mold temperature at 350 °C (Fig. 6).

To predict the tendency of shrinkage porosities, the ProCAST software was used to simulate the solidification process. The Niyama criteria was applied to evaluate the tendency of shrinkage porosities because of its good capability on predicting interdendritic microporosity [11, 12]. Figure 7 is the simulation showing shrinkage porosities under the mold temperature of 350 °C. Smaller Niyama value represented higher tendency to form shrinkage porosity. It is showed that the shrinkage porosities were distributed at both transverse (Fig. 7a) and longitudinal direction (Fig. 7b). The conditions of mold temperature with 150, 250 and 350 °C were also simulated and the results were shown in Fig. 8. It is clear seen that reduced mold temperature decreased the tendency of shrinkage porosities formation.

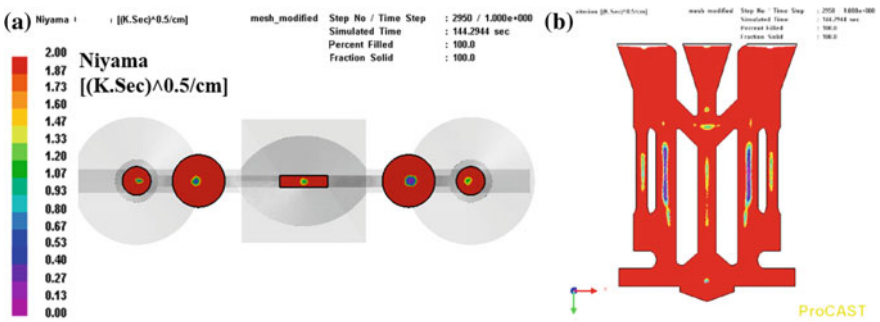

Fig. 7 Simulated results showing shrinkage porosity located at **a** transverse and **b** longitudinal direction of the castings under the mold temperature at 350 °C

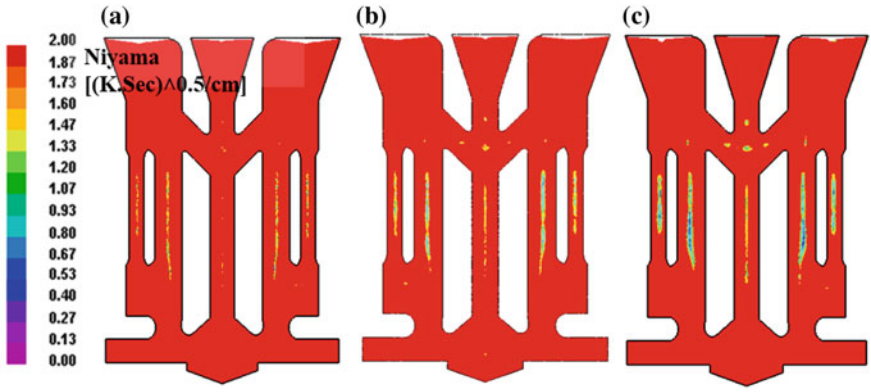

Fig. 8 Simulated results showing the influence of the mold temperature at **a** 150 °C **b** 250 °C **c** 350 °C on shrinkage porosity

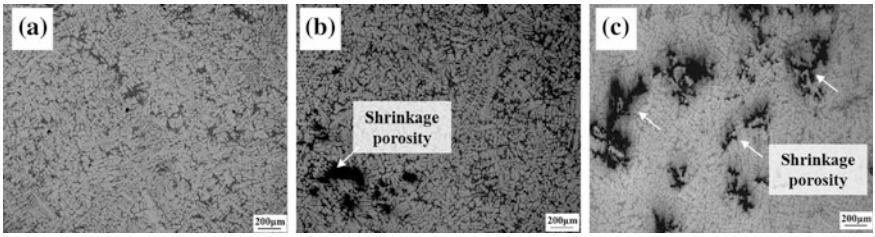

Fig. 9 Microstructure of the A357 alloys under different mold temperature at **a** 150 °C **b** 250 °C **c** 350 °C

Figure 9 shows the microstructure under different mold temperature. In condition of the mold temperature at 350 °C, severe shrinkage porosity formed in dispersive distribution. Fewer shrinkage porosities were observed with lower mold temperature (250 °C). When the mold temperature was 150 °C, microstructure with no shrinkage porosity was obtained.

During solidification, the mold temperature influenced the temperature gradient of the casting [10]. The temperature gradients of gauge length were calculated by ProCAST in the transverse and longitudinal direction. Figure 10 is the schematic of gauge length, of which the OA is at transverse direction and the OB is at longitudinal direction. The calculated results under different mold temperature are shown in Fig. 11. It is seen that the temperature gradient was changed with prolonged solidification. The mold temperature of 350 °C had the lowest temperature gradient (values were marked in Fig. 11) both in OA and OB. The low temperature gradient in castings enhanced the difficulty of liquid filling in dendrites and prompted the formation of shrinkage porosity [13]. Thus, severe shrinkage porosity was formed in microstructure under high mold temperature.

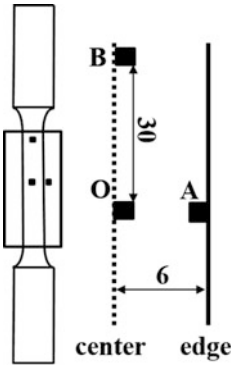

Fig. 10 Schematic of gauge length

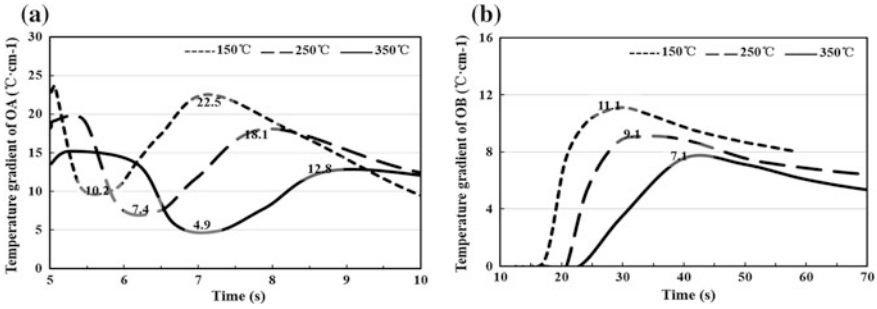

Fig. 11 Temperature gradient of **a** OA and **b** OB in gauge length under different mold temperature during solidification

Conclusion

(1) In gravity die casting, the cooling rate of the A357 alloys during solidification decreases with increasing mold temperature. The coarser α-Al phase and Si particles in microstructure are obtained under higher mold temperature.
(2) When the mold temperature is 150 °C, no shrinkage porosity forms in microstructure. Severe shrinkage porosityis observed on the transverse and longitudinal direction of sample when the mold temperature is 350 °C.
(3) The simulated results by ProCAST show that increasing the mold temperature can enhance the tendency of shrinkage porosity formation, which agrees well with the microstructure in experiment. The increasing mold temperature decreases the temperature gradient in gauge length of sample during solidification, which results to the formation of shrinkage porosity.

Acknowledgements This work was carried out with financial support from National Key Research and Development Program (2016YFB0301001): Production technology of high performance magnesium/aluminum alloy high quality castings. The financial support is gratefully acknowledged.

References

1. F. Wang, Q. Ma, M. Wen, Z. Han, Experimental study on the heat transfer behavior and contact pressure at the casting-mold interface in squeeze casting of aluminum alloy. Int. J. Heat Mass Transf. **112**, 1032–1043 (2017)
2. S.K. Rathi, A. Sharma, M.D. Sabatino, Effect of mould temperature, grain refinement and modification on hot tearing test in Al-7Si-3Cu alloy. Eng. Fail. Anal. **79**, 592–605 (2017)
3. V. Vazquez, A. Juarez-Hernandez, A. Mascarenas, P. Zambrano, Cold shut formation analysis on a free lead yellow brass tap. Eng. Fail. Anal. **17**, 1285–1289 (2010)
4. L. Bichler, A. Elsayed, K. Lee, C. Ravindran, Influence of mold and pouring temperatures on hot tearing susceptibility of AZ91D magnesium alloy. Int. J. Metalcast. Winter 43–54 (2008)
5. H. Huang, P. Fu, Y. Wang, L. Peng, H. Jiang, Effect of pouring and mold temperatures on hot tearing susceptibility of AZ91D and Mg–3Nd–0.2Zn–Zr Mg alloys. Trans. Nonferrous Met. Soc. China **24**, 922–929 (2014)
6. G.F. Mi, X.Y. Liu, K.F. Wang, H.Z. Fu, Numerical simulation of low pressuredie-casting aluminum wheel. China Foundry. **6**, 48–52 (2009)
7. C. Zhang, Y. Bao, M. Wang, L. Zhang, Shrinkage porosity criterion and its application to A 5.5 ton steel ingot. Arch. Foundry Eng. **16**, 27–32 (2016)
8. X.G. Hu, Q. Zhu, H.V. Atkinson, H.X. Lu, F. Zhang, H.B. Dong, Y.L. Kang, A time-dependent power law viscosity model and its application in modelling semi-solid die casting of 319s alloy. Acta Mater. **124**, 410–450 (2017)
9. W. Qu, F. Zhang, J. Wang, X. Hu, Q. Zhu, Effect of slurry temperature distribution on semi-solid die casting. Solid State Phenom. **256**, 107–112 (2016)
10. J. Campbell, Castings, second edition, Butterworth-Heinemann, 2003, pp. 205–230
11. E. Niyama, T. Uchida, M. Morikawa, S. Saito, A method of shrinkage prediction and its application to steel casting practice. AFS, Int. Cast Met. J. **9**, 52–63 (1982)
12. L. Pan, L. Zheng, H. Zhang, W. Gao, Applicability of shrinkage porosity prediction for casting with Niyama criterion. J. Beijing Univ. Aeronaut. Astronaut. **37**, 1534–1540 (2011)
13. N. Yu, L. Zhu, X.Q. Dong, The achievement and verification of the optimum temperature gradient of metal casting without shrinkage porosity defect. Spec. Cast. Nonferrous Alloy. **36**, 513–516 (2016)

Solidification Behavior and Mechanical Property of a Highly Undercooled Al–Si Alloys

Bo Dang, Zengyun Jian and Junfeng Xu

Abstract The solidification behavior of hypereutectic Al–Si alloys was investigated by electromagnetic levitation technique combining analysis of high-speed video and scanning electron microscopy. The results show that, with increasing degree of undercooling, the morphology of the primary Si transforms from dendrites to fragmented bulks and granular grains and then to equiaxed grains; the nucleation frequency increases exponentially, while the average grain size decreased exponentially. Furthermore, the effect of undercooling on microhardness was analyzed.

Keywords Growth morphology · Microstructure · Undercooling Microhardness

Introduction

Al–Si alloys have been widely used in various fields ranging from automotive to aerospace industries due to their excellent castability, low thermal expansion coefficient and high wear resistance [1–3]. The morphology, distribution and size of silicon plays a critical role in determining the properties and application of this alloy. Then, it has been shown that the morphology and size of primary Si are depended on solidification conditions (cooling rate) in highly undercooled solidification of the Al–Si alloy melt. Moreover, keeping a large undercooling state of melt can achieve spherical equiaxial crystals, which has a good result in improving their mechanical property [4, 5]. The EML (electromagnetic levitation) can undercool Al–Si alloy to a large degree and enable containerless solidification

B. Dang · Z. Jian (✉) · J. Xu
The School of Materials Science and Chemical Engineering,
Xi'an Technological University, Xi'an 710021, Shaanxi, China
e-mail: zengyunjian@xatu.edu.cn

B. Dang
e-mail: db19881019@163.com

© Springer Nature Singapore Pte Ltd. 2018

Y. Han (ed.), *Advances in Materials Processing*, Lecture Notes in Mechanical Engineering, https://doi.org/10.1007/978-981-13-0107-0_78

which can prevent heterogeneous nucleation [6, 7]. The EML is also convenient for investigating the dendrite growth through a high-speed video (HSV) during solidification.

In the study, the Al–80%Si alloy was melted by a continuous wave CO_2 laser, and then levitated via the EML technique (all alloy compositions are reported in wt % unless indicated otherwise). Afterwards, the influence of the undercooling on solidification behavior was investigated by observing the microstructure variations and measuring the nucleation frequency. Finally, the relationship between microhardness and undercooling of the Al–80%Si alloy was investigated to elucidate the strengthening mechanism of the alloy.

Experimental

The Al–80%Si alloy was prepared and melted with the pure Al (99.99%) and Si (99.9999%). The sample with a diameter of 10 mm was placed on the sintered boron nitride holder. The chamber was first evacuated to 5×10^{-4} Pa and filled purified Ar gas. Subsequently, the sample was melted above the liquidus temperature 300 K, and then cooled it through filled with purified He gas. The temperature of heating and cooling was measured with a monochromatic pyrometer with a 2 ms response time and 1.55 μm operating wavelengths. The HSV can reach 150,000 frames per second and with a maximum resolution of 1280×1024 pixels to record video.

The microstructure of the samples was analyzed by SEM (scanning electron microscopy). The hardness of the sample was measured by a Wilson 402MVD TM Digital Microhardness Tester.

Results and Disscusion

Microstructure Evolution

Figure 1 shows the solidification process of Al–80%Si alloys at different degree of undercooling.

If the degree of undercooling was $\Delta T = 52$ K, the primary Si of these alloys grew into dendrites with several branches. If the undercooling was increased to $\Delta T = 126$ K, the morphologies of primary Si still exhibited a dendritic structure. The length of the dendrites decreased compared with that in the undercooling of 52 K, and the branching of dendrites did not obviously decrease.

When the undercooling was increased to $\Delta T = 172$ K, the morphology of the primary Si showed fragmented and bulk shapes. When the undercooling was further increased to $\Delta T = 210$ K, the morphology of primary Si still exhibited fragmented

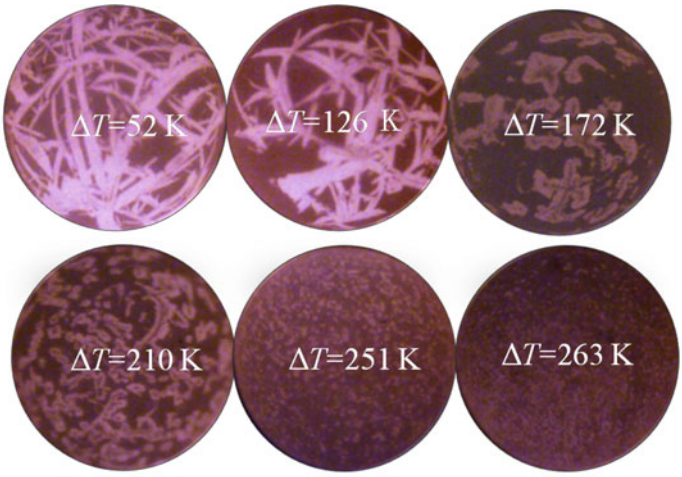

Fig. 1 The HSV image of the Al–80%Si alloy at different undercooling

and bulk shape. In the meantime, the size of the primary Si decreases, and the equiaxed grains was observed in the HSV image.

When the undercooling was increased to ΔT = 251 K, the primary Si showed equiaxed grains. When the undercooling was further increased to ΔT = 263 K, the morphology of primary Si shows as equiaxed grains with smaller size, and the size of primary Si further decreased.

In summary, three regions of growth for primary Si were observed: the dendrite at low undercooling, the fragmented and bulk shape at intermediate undercooling, and the equiaxed grains at large undercooling. Moreover, the undercooling had a significant effect on the growth of primary Si.

To further clarify the above conclusions, the SEM images of sample are shown in Fig. 2. Compared to Fig. 1, the morphologies of the primary Si in SEM images are similar to those observed in the HSV images. It indicates that the morphology transition recorded by HSV is indeed reflected in the sample surface. As can be seen from Fig. 2, primary Si grows as wafers or dendrites at low undercoolings (52 and 126 K). Mixture of bulks and equiaxed grains cover the sample surface at intermediate undercoolings (172 and 210 K). At large undercoolings (251 and 263 K), the primary Si shows as equiaxed grains, and the size decreases with increasing of undercoolings. Figure 4a–c showed the typical SEM images with high magnification of Al–80%Si alloys depict the morphologies transition of primary Si in three regions, and further confirm the microstructure evolution with undercooling.

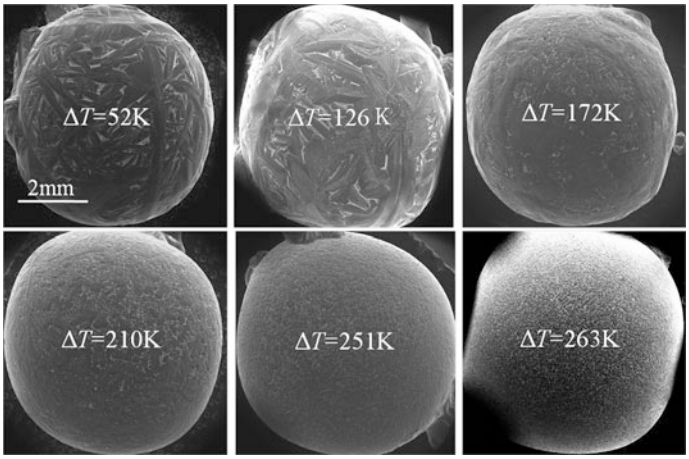

Fig. 2 SEM images of the Al–80%Si alloys at different undercoolings

Nucleation Rate

The nucleation frequency is measured according to classical nucleation theory, means the number of nucleus per unit area and unit time [8, 9]. So, if the nucleation number, the area of sample and the nucleation time are known, the nucleation frequency can be estimated as follows,

$$I = \frac{N}{S \cdot t} \tag{1}$$

where N is the nucleation number, S is area of the sample and t is the time for solidification.

The nucleation number can be estimated from the HSV images or SEM images. In Ref. [10], the authors distinguished and analyzed the advantages and disadvantages of HSV and SEM methods. The SEM method could describe the accurate number of nucleation points well. In this study, the nucleation number (N) and nucleation frequency (I) of the alloy are shown in Fig. 3a, b, respectively.

Furthermore, the average grain size can be estimated from the measured nucleation number. Assuming grain size as $r \times r$, then r could be estimated as follows,

$$r = \sqrt{\frac{A}{N}} = \sqrt{\frac{S}{N}} \tag{2}$$

The relationship of the average grain size and undercooling is plotted in Fig. 3c. The exponential relationship can fit the experiment results well especially in intermediate and large undercoolings. It may be because of that the small

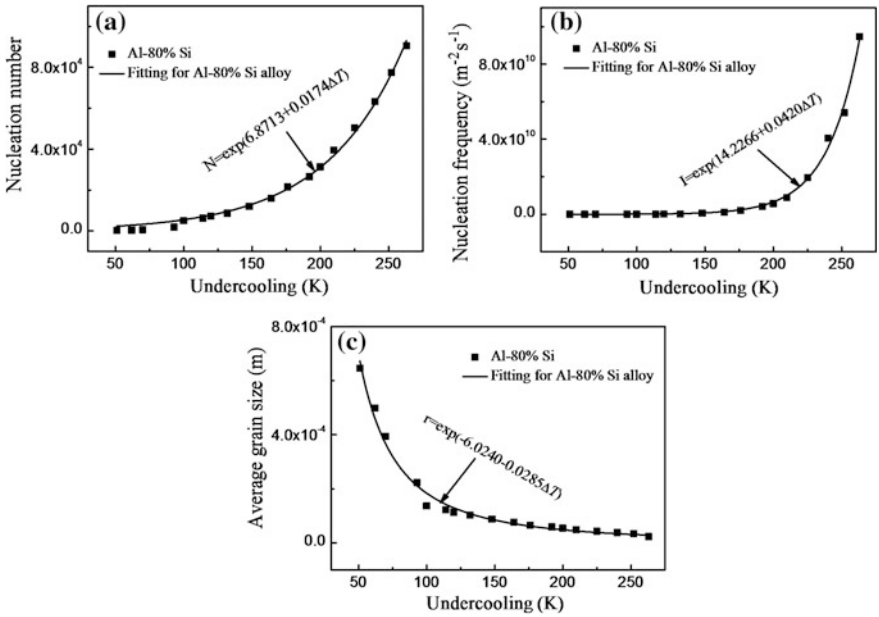

Fig. 3 The nucleation number (**a**), nucleation frequency (**b**) andgrain size (**c**) as a function of undercooling for the Al–80%Si alloys

undercooling region may be related to the faceted-wafer morphology of the primary silicon in these samples. But in intermediate and large undercoolings, the morphology of primary Si grew as nonfaceted equiaxed grains.

Microhardness

Figure 4d shows the measured values of the Vickers microhardness versus the undercooling of Al-80%Si alloy. The microhardness was acquired by using Eq. (3) [11],

$$HV = \frac{P}{D} = \frac{P\mathrm{Sin}(136^\circ/2)}{2d^2} = 0.436 \times \frac{P}{d^2} \tag{3}$$

where P is the load, d is diagonal length of the indentations.

Ruan et al. [12] found that there was a certain relation between Vickers microhardness and undercoolings. As undercooling increased, the microhardness increased with the linear correlation equation. In this study, with increasing undercooling, the microhardness increased from 870.2 to 1066.0 MN/m^2 (MPa) for Al–80%Si alloy. From the measured results, the change of microhardness for the

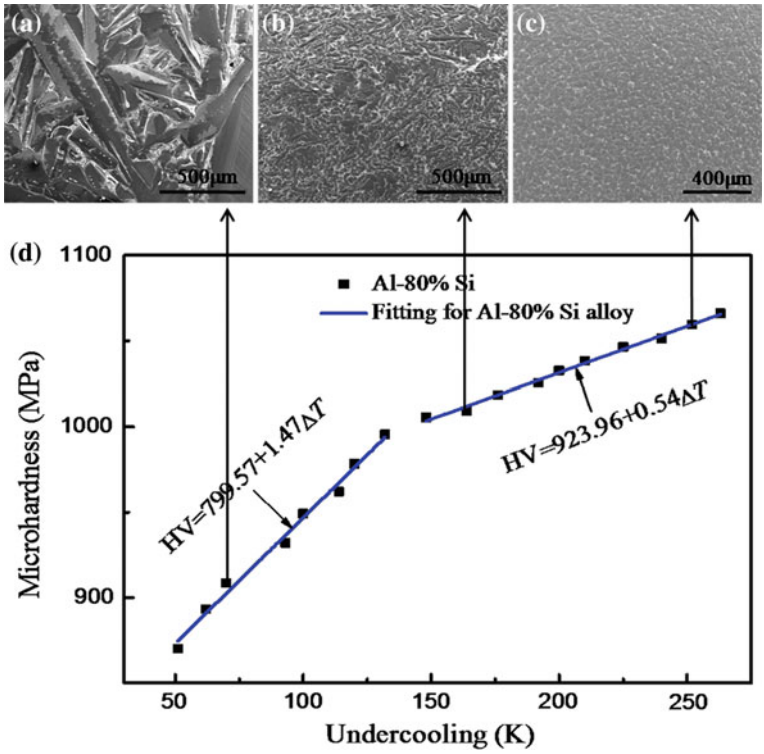

Fig. 4 Microstructure and microhardness of the Al–80%Si alloys with increasing of undercooling: SEM analysis with high magnification of **a** 52 K, **b** 172 K and **c** 251 K for the Al–80%Si alloy; **d** Microhardness variation along with undercooling

Al–80%Si alloys can be divided into two stages. For low undercoolings ($\Delta T \leq 132$ K), the variation of microhardness can be fitted by HV = 799.57 + 1.47ΔT. The second stage, according to intermediate and large undercoolings, was fitted by HV = 923.96 + 0.54ΔT.

As shown in Figs. 4a–c, at low undercoolings, the primary Si grows a dendritic or lath-shaped structure. For the properties, the primary Si plays a fiber refinement in alloy. In addition, the size of primary Si dendrite decreases with increasing degree of undercooling. Clearly, the refinement of the lath-shaped structure enhances the property of the Al–80%Si alloys at low undercooling. The microhardness increased with the decreasing amount of dendrites and increasing amount of equiaxed grains at intermediate and large undercoolings. With increasing of undercooling, the size of the primary Si decreased and the equiaxed Si grains increased, resulting in an increase in the microhardness. The difference in slope for the various microhardness stages can be attributed to the strengthening effect of fiber being stronger than that of equiaxed grains. So, the rate of increase of the microhardness at low undercooling was larger than that at intermediate and large

undercoolings. So, the property of the alloy was improved because of microstructure changes, and the strengthening mechanism was grain refinement strengthening.

Conclusions

The Al–80%Si alloy was investigated by the EML technique. The growth of primary Si was recorded using a high-speed video and the morphologies were examined by SEM. The results show as follows:

(1) The growth for primary Si in Al–80%Si alloy was the dendrite at low undercooling, the fragmented and bulk shape at intermediate undercooling, and the equiaxed grains at large undercooling.
(2) The nucleation number of the Al–80%Si alloy increases exponentially with increasing degree of undercooling and fitted by $N = \exp(6.8713 + 0.0174\Delta T)$. Besides, the nucleation frequency fitted by $I = \exp(14.2266 + 0.0420\Delta T)$. Finally, the grain size of primary Si decreases exponentially with undercooling and fitted by $r = \exp(-6.0240 - 0.0285\Delta T)$.
(3) As undercooling increased, the linear correlation equation of the form HV versus ΔT can be identified into two stages, corresponding to their microstructural evolutions. At low undercoolings ($\Delta T \leq 132$ K), the variation of microhardness fitted by $HV = 799.57 + 1.47\Delta T$. The second stage, corresponding to with intermediate and large undercoolings fitted by $HV = 923.96 + 0.54\Delta T$. The strengthening effect of the dendritic structure is stronger than that of equiaxed grains.

Acknowledgements The authors are grateful for the Natural Science Foundation of China (No. 51671151).

References

1. W.H. Yu, Y. Zhang, T.L. Yan, Y. Liu, A.L. Jiang, H.L. Zheng, X.L. Tian, Enhanced nucleation of primary Si in Al–20 wt. % Si alloy with Ni–Si inoculation. J. Alloy. Compd. **693**, 303–307 (2017)
2. H. Kaya, A. Aker, Effect of alloying elements and growth rates on microstructure and mechanical properties in the directionally solidified Al–Si–X alloys. J. Alloy. Compd. **694**, 145–154 (2017)
3. B. Dang, X. Zhang, Y.Z. Chen, C.X. Chen, H.T. Wang, F. Liu, Breaking through the strength ductility trade-off dilemma in an Al-Si-based casting alloy. Sci. Rep. **6**, 30874 (2016)
4. C. Panofen, D.M. Herlach, Solidification of highly undercooled Si and Si–Ge melts. Metall. Mater. Trans. A **449–451**, 699–703 (2007)

5. Y.K. Zhang, J. Gao, M. Kolbe, S. Klein, C. Yang, H. Yasuda, D.M. Herlach, ChA Gandin, Phase selection and microstructure formation in undercooled Co–61.8 at.% Si melts under various containerless processing conditions. Acta Mater. **61**, 4861–4873 (2013)
6. V. Metan, K. Eigenfeld, D. Räbiger, M. Leonhardt, S. Eckert, Grain size control in Al–Si alloys by grain refinement and electromagnetic stirring. J. Alloy. Compd. **487**, 163–172 (2009)
7. R.P. Liu, T. Volkmann, D.M. Herlach, Undercooling and solidification of Si by electromagnetic levitation. Acta Mater. **49**, 439–444 (2001)
8. D. Turnbull, Kinetics of solidification of supercooled liquid mercury droplets. J. Chem. Phys. **20**, 411–424 (1952)
9. Z.Y. Jian, W.Q. Jie, Criterion for judging the homogeneous and heterogeneous nucleation. Metall. Mater. Trans. A **32**, 391–395 (2001)
10. J.F. Xu, L. Diao, J.H. Yan, B. Dang, M. Zhu, F.E. Chang, Z.Y. Jian, In situ observations of the rapid solidification for undercooled $Al_{30}Si_{70}$ alloy melt. J. Mater. Res. **31**, 222–231 (2016)
11. H. Cheng, F.E. Chang, J.F. Xu, G.Q. Xue, Z.Y. Jian, Effects of heat treatment on the properties of $99.5Ge_{23}Se_{67}Sb_{10}$-0.5CsCl glass. Optik. **127**, 8379–8385 (2016)
12. Y. Ruan, X.J. Wang, S.Y. Chang, Two hardening mechanisms in high-level undercooled Al–Cu–Ge alloys. Acta Mater. **91**, 183–191 (2015)

Different Interfaces of Primary Transition and Eutectic Transition

Junfeng Xu, Dandan Fan, Bo Dang and Zengyun Jian

Abstract Solidification interfaces of the primary phase transition and eutectic transition for Ni–B alloy were investigated by high-speed video techniques. With increasing undercooling, the interface morphology for primary phase transition changes from single tip to multi-tip and to smooth plane, while for eutectic transition, it changes from multi-dendrite to single dendrite. The interface moving velocity of primary solidification is about a constant, but it is not the case for eutectic transition. This difference indicates that the primary phase transition is controlled by far-distance diffusion mechanism while the eutectic transition is controlled by short-distance diffusion mechanism. The different controlling mechanisms imply that under a similar undercooling, the velocity of an eutectic transition is much higher than that of a primary transition.

Keywords Undercooling · Solidification interface · Eutectic

Introduction

The solidification process can be handy observed by High-speed video (HSV) cinematography [1]. From HSV images, we can observe the morphology of solidification front across the sample surface, and measure dendrite tip velocity [2]. Aoyama et al. [3] studied the solid-liquid interface for highly pure Si and Ge growth by using HSV, and found that the growth mechanism can be classified into three categories: lateral growth at low undercooling, continuous growth at moderate undercooling and successive growth at high undercooling values, respectively. Using HSV, Nagashio [4], Nozaki [5] and Löser et al. [6] studied the metastable phases formation in solidification of $Nd_2Fe_{14}B$, Fe_2Si_5 and Fe–Ni melts.

J. Xu (✉) · D. Fan · B. Dang · Z. Jian
School of Materials and Chemical Engineering, Xi'an Technological University, Xi'an 710032, People's Republic of China
e-mail: xujunfeng@mail.nwpu.edu.cn

© Springer Nature Singapore Pte Ltd. 2018

Y. Han (ed.), *Advances in Materials Processing*, Lecture Notes in Mechanical Engineering, https://doi.org/10.1007/978-981-13-0107-0_79

In this study, the solidification interfaces of primary phase transition and eutectic transition of Ni–B hypoeutectic alloy were investigated by HSV. Furthermore, the different transition behaviors for primary phase and eutectic phase are discussed, which is helpful for multi-transition theory study.

Experiments

In order to investigate the solidification interfaces of primary and eutectic phases, the hypoeutectic alloy sample (100 g) was mixed by purity Ni (99.98 wt%) blocks and B (99.7 wt%) powder. It was arc-melted in the argon atmosphere by using a non-consumable tungsten electrode. To ensure the homogenization of the sample, the melting process was repeated several times. And then, by inductively coupled plasma atomic emission spectroscopy (ICP-AES) technique, the concentration of the sample was measured to be Ni-3.3 wt% B alloy. The sample (Ni-3.3 wt% B) weighed about 4 g, together with some pieces of B_2O_3 glass was placed into a quartz-glass crucible, which was placed in the middle-position of the high frequency induction coil located in a vacuum chamber. After the vacuum chamber was evacuated to 1×10^{-6} mbar and backfilled to 600 mbar with high purity Ar gas, the sample was cyclically superheated with a superheating of 100–200 K until a desired undercooling was achieved. Thermal history of every sample was monitored by a single wavelength pyrometer. The relative accuracy and response time are 10 K and 10 ms, respectively. In order to reveal what actually occurred during the rapid solidification, HSV instrumentation system with a high resolution of 1280×1024 pixels, OLYMPUS I-Speed 3 MONO, was used to observe the recalescence process for each transition. From HSV images, the time, Δt, needed by the envelope of the dendrite tips(interface front) to sweep across distance Δs is measured, and then the dendrite growth velocity is evaluated by the relation by $V = \Delta s/\Delta t$.

Result and Discussion

Figure 1 show the classical cooling curves for Ni-3.3 wt% B alloy. Generally, there are two recalescences, corresponding to primary phase transition and eutectic transition for Ni–B alloy. The primary phase transition undercooling can be defined as $\Delta T_p = T_L - T_n$, where T_L is the melting point (1450 K) and T_n is the initial nucleation point. The eutectic transition undercooling can be defined as $\Delta T_e = T_e - T_{en}$, where T_e is the equilibrium eutectic temperature (about 1366 K here) and T_{en} is the starting temperature of eutectic transition.

Figure 2a, b show respectively that the HSV images of the primary (L→α-Ni) and eutectic (L→Ni/Ni_3B) transition processes of Ni-3.3 wt% B alloy at different undercoolings, where undercooled melt is in the dark regions, and the growing solid

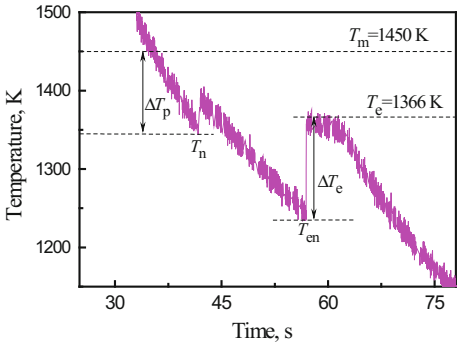

Fig. 1 Typical cooling curves of Ni-3.3 wt% B hypoeutectic alloy

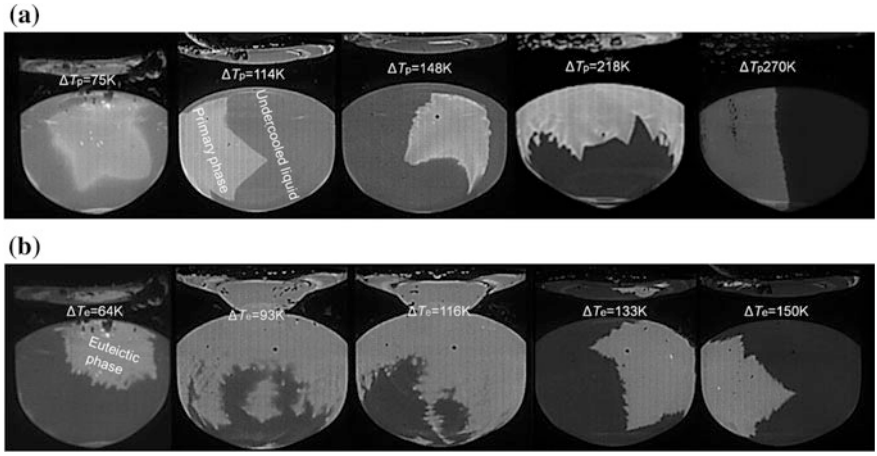

Fig. 2 HSV images for Ni-3.3 wt% B hypoeutectic alloy under different undercoolings: **a** primary transition; **b** eutectic transition

in, the bright regions. As can be seen, for primary transition, if ΔT_p = 75 K, the solidification interface shows as four dendritic tips. When the undercooling increases to ΔT_p = 148 K, the solidification interface shows as serrated shape. When the undercooling further increases to ΔT_p = 270 K, the solidification interface shows as smooth plane as shown in Fig. 2a. It suggests that nucleation of primary phase increases with undercooling. For eutectic transition, for the samples with ΔT_e = 64 K, the solidification interface looks like many small dendrites. For the samples with ΔT_e = 93 K, the interface also looks like dendrites, but the dendrite sizes increase. When the undercooling increases to ΔT_e = 133 K, mainly two dendritic tips grow in the interface, and if ΔT_e = 150 K, almost single large dendrite grows in the interface. It suggests that with the increase of undercooling, the

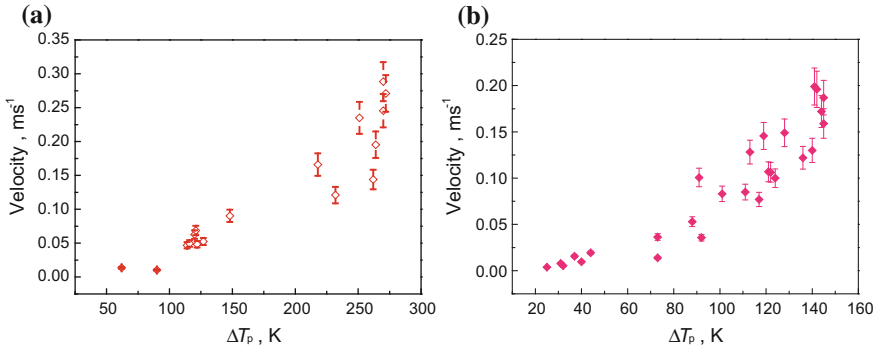

Fig. 3 Growth velocity as a function of undercooling: **a** V versus ΔT_p; **b** V versus ΔT_e

eutectic transition for off-eutectic alloy changes from couple growth to decoupled growth, and the nucleation number decreases with undercooling. Generally, from the classical nucleation theory [7], the nucleation rate increases with undercooling, so the present observation is opposite of the classical nucleation theory. In another words, the nucleation rate for eutectic transition decreases with undercooling. And not coincidentally, the report from Mingjun Li also shows that in Ni–Sn alloy, from HSV, the solidification interface changes from multipoint to a single smooth interface [8]. Jinfu Li's experiment for Co-24.0 at.% Sn alloys also shows that the anomalous-eutectic colony number reduces with increase of undercooling [9]. Clopet's report shows that a eutectic colony always corresponds to a nucleation point [10], so for a hypoeutectic Ni–B alloy, the nucleation rate of eutectic transition decreases with undercooling.

It can measure the growth velocity of solidification interface from HSV. Figure 3a, b show the measured growth velocities of primary transition and eutectic transition, respectively. As expected, the growth velocity increases with undercooling. However, the velocity of eutectic transition is larger than that of primary transition at a same undercooling.

To comprehend the growth velocity in the whole solidification process, Fig. 4 shows the interface moving distance (D) as a function of time (t) for the primary phase and eutectic transitions. In addition, for primary phase transition (taken the sample with $\Delta T_p = 75$ K as an example), there is an approximate linear relationship between D and t, which means that the interface speed is almost constant. However, for eutectic transition (taken the result of $\Delta T_e = 64$ K as an example), the plot of the distance versus time is not linear, and because of the instable interface, the process of the solidification front is spasmodic (a series of jumps and pauses). As a result, compared with eutectic transition, the interface front of primary transition is more stable and smooth. This may be due to alternating growth of Ni and Ni_3B phases, causing eutectic solidification of short-distance diffusion, so that the solid-liquid interface occurs a series of start-stop phenomenon.. This similar phenomenon also exists in Ag–Cu eutectic alloys studied by Clopet et al. [10, 11]. Therefore, eutectic

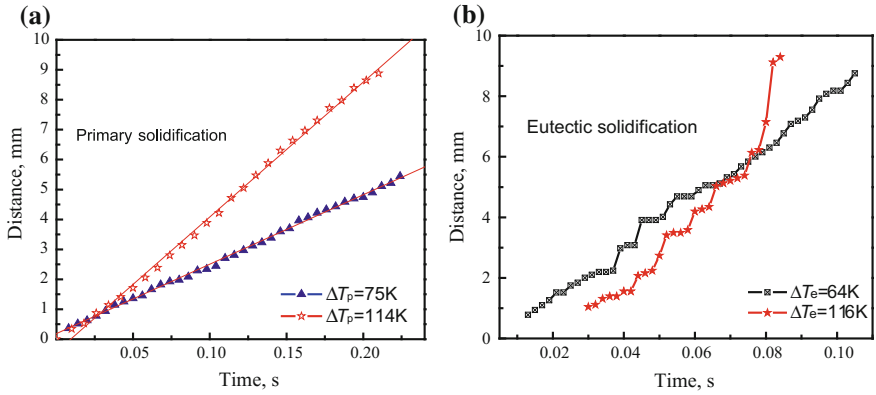

Fig. 4 Growth velocity as a function of time interval: **a** primary solidification interface; **b** eutectic solidification interface

solidification interface speed cannot be seen as a constant. In the present, the alternating growth phenomenon is not considered in any eutectic transition model, because the solidification process relates to the complicated diffusion problems [12–14].

Figure 5a shows the primary phase morphology at small undercooling of T_p = 40 K, it can be found that several large dendrites exist in the microstructure of the sample. Figure 5b shows the primary phase from large undercooling of ΔT_p = 262 K, where the small primary phase grains can be observed, and the growth direction is random. This evidences that at large undercooling, the many dendritic primary phase grow simultaneously. For the eutectic growth, if undercooling is small as show in Fig. 5a, it shows as lamellar eutectic. If undercooling is large as shown in Fig. 5c, it shows as mainly Ni_3B grains surrounding by network Ni phase. This indicates that for eutectic transition with large undercooling, the Ni_3B phase grows first, and then Ni phase is following. To further evidence the eutectic growth at large undercooling, a sample is quenched as the eutectic undercooling reaches to ΔT_e = 100 K, the microstructure is shown in Fig. 5d. It can be found that, there are many large Ni_3B dendrites distributed in the region of the lamellar eutectic. It indicates for the large undercooling of eutectic transition, the large Ni_3B dendrite nucleation and grow first, then the Ni phase follows, when the release latent makes the system rise to near eutectic point (recalescence process), the dendrite of Ni_3B was partly remelted, and the lamellar eutectic starts to form. Thus anomalous eutectic and lamellar eutectic can be observed. If the eutectic transition undercooling is large enough, the lamellar eutectic will not formed such as the microstructure in Fig. 5c.

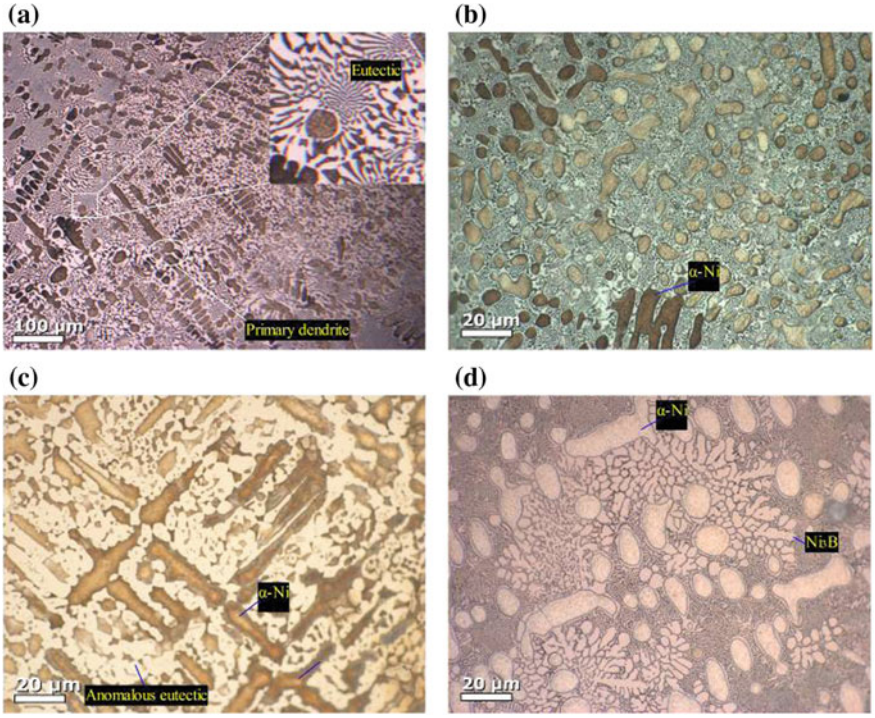

Fig. 5 The microstructure of the sample with different undercoolings: **a** $\Delta T_p = 40$ K, $\Delta T_e = 100$ K; **b** $\Delta T_p = 262$ K; **c** $\Delta T_p = 40$ K, $\Delta T_e = 145$ K; **d** $\Delta T_p = 50$ K, quenched at $\Delta T_e = 100$ K

Conclusions

Solidification interfaces of primary phase transition and eutectic transition for Ni-3.3 wt% B hypoeutectic alloy were observed by HSV techniques. For primary transition, the interface morphology changes from single tip to multi-tip and then to smooth plane with increasing undercooling. It suggests nucleation rate increases with undercooling. For eutectic transition, the interface morphology changes from multi-dendrite to single dendrite with increasing undercooling. It suggests nucleation rate decreases with undercooling. In addition, the growth velocity of primary phase shows a constant, and that of eutectic phase does not shows a constant, which can be explained as the primary transition controlled by far-distance diffusion mechanism but the eutectic transition controlled by short-distance diffusion mechanism. The different controlling mechanisms imply that under a similar undercooling, the velocity of eutectic transition is higher than that of primary transition.

Acknowledgements The authors are grateful for the Natural Science Foundation of China (Nos. 51401156 and 51671151) and the Science and Technology Program of Shaanxi Province (No. 2016KJXX-87).

References

1. J.F. Xu, F. Liu, D. Zhang, In situ observation of solidification of undercooled hypoeutectic Ni–Ni_3B alloy melt. J. Mater. Res. **28**, 1891–1902 (2013)
2. J.F. Xu, F. Liu, B. Dang, Phase selection in undercooled Ni-3.3 wt Pct B alloy melt. Metall. Mater. Trans. A **44**, 1401–1408 (2013)
3. T. Aoyama, K. Kuribayashi, Rapid solidification processes of semiconductors from highly undercooled melts. Metall. Mater. Trans. A **304–306**, 231–234 (2001)
4. K. Nagashio, M. Li, K. Kuribayashi, Containerless solidification and net shaping by splat quenching of undercooled $Nd_2Fe_{14}B$ melts. Mater. Trans. **44**, 853–860 (2003)
5. K. Nozaki, K. Nagashio, K. Kuribayashi, In-situ observation of solidification behaviour from undercooled α-Fe2Si5 melt using an electromagnetic levitator. Rev. Adv. Mater. Sci. **18**, 439–443 (2008)
6. W. Löser, T.G. Woodcock, O. Shuleshova, R. Hermann, H.G. Lindenkreuz, B. Gehrmann, S. Schneider, T. Volkmann, Metastable solidification in undercooled liquid droplets of Fe-Ni based soft-magnetic alloys under terrestrial and microgravity conditions. J. Phys: Conf. Ser. **327**, 111–118 (2011)
7. D.M. Herlach, B. Feuerbacher, Non-equilibrium solidification of undercooled metallic melts. Adv. Space Res. **4**, 255–262 (1991)
8. M. Li, K. Nagashio, K. Kuribayashi, Reexamination of the solidification behavior of undercooled Ni–Sn eutectic melts. Acta Mater. **50**, 3241–3252 (2002)
9. L. Liu, J.F. Liu, Y.H. Zhou, Solidification interface morphology pattern in the undercooled Co–24.0 at.% Sn eutectic melt. Acta Mater. **59**, 5558–5567 (2011)
10. C.R. Clopet, R.F. Cochrane, A.M. Mullis, Spasmodic growth during the rapid solidification of undercooled Ag-Cu eutectic melts. Appl. Phys. Lett. **102**, 384–393 (2013)
11. H.R. Peng, M.M. Gong, Y.Z. Chen, F. Liu, Thermal stability of nanocrystalline materials: thermodynamics and kinetics. Int. Mater. Rev. **66**, 303–333 (2017)
12. X.L. Xu, F. Liu, Nonequilibrium solidification, grain refinements, and recrystallization of deeply undercooled Ni-20 At. Pct Cu alloys effects of remelting and stress. Metall. Mater. Trans. A **10**, 4777–4785 (2017)
13. B. Dang, X. Zhang, Y.Z. Chen, C.X. Chen, H.T. Wang, F. Liu, Breaking through the strength ductility trade-off dilemma in an Al-Si-based casting alloy. Sci. Rep. **6**, 30874 (2016)
14. Y.Z. Chen, A. Herz, Y.J. Li, C. Borchers, P. Choi, D. Raabe, R. Kirchheim, Nanocrystalline Fe–C alloys produced by ball milling of iron and graphite. Acta Mater. **61**, 3172–3185 (2013)

Application of CAFÉ Method on Microstructure Simulation of Semi-solid Al–7%Si Alloy

Wenying Qu, Fan Zhang, Daquan Li, Min Luo, Zhiyu Yang and Yongzhong Zhang

Abstract Nucleation and growth of grains mainly happen in the stage of slurry preparation period during semi-solid die-casting process. The microstructure of slurry can directly influence the grain morphology and the mechanical properties of products. Thus, the prediction of semi-solid slurry microstructure is of vital importance for process optimization and products mechanical properties improvement. Cellular Automaton Finite Element (CAFÉ) method was adopted in this study to simulate the microstructure evolution of Al–7%Si alloy during semi-solid slurry preparation by using thermal equilibrium process. The models for interface heat transfer coefficient (IHTC) between slurry and crucible, and nucleation parameters under different pouring temperatures are the most important factors in this CAFÉ method, and they are the main tasks in this study. The results demonstrated that the cellular automaton model used in this article could directly display the details of microstructure evolution during slurry preparation process. The nucleation and growth patterns of grains were also analyzed according to the simulation results under different pouring temperature conditions. The control mechanism of thermal equilibrium process was obtained and it provided solid foundation for the popularization and application of thermal equilibrium semi-solid slurry preparation technique.

W. Qu · F. Zhang · D. Li (✉) · M. Luo · Z. Yang · Y. Zhang
General Research Institute for Nonferrous Metals, Beijing 100088, China
e-mail: lidaquan@grinm.com

W. Qu
e-mail: quwenying2008@163.com

F. Zhang
e-mail: zhangfan@grinm.com

M. Luo
e-mail: lm_grinm@163.com

Z. Yang
e-mail: yangzhiyu_grinm@163.com

Y. Zhang
e-mail: yyzhang@grinm.com

© Springer Nature Singapore Pte Ltd. 2018

Y. Han (ed.), *Advances in Materials Processing*, Lecture Notes in Mechanical Engineering, https://doi.org/10.1007/978-981-13-0107-0_80

Keywords Semi-solid · Al–7%Si alloy · Microstructure simulation CAFÉ method

Introduction

Semi-solid slurry of aluminum alloy is characterized by the co-existence of primary α-Al particles and eutectic silicon liquid, its solidification microstructure changes markedly from dendritic growth under conventional processing conditions to non-dendritic or globular growth under semi-solid slurry preparation conditions [1, 2]. The process of melt stirring influences the alloy distribution and boundary layer characteristics, many studies mostly concerned with columnar-equiaxed transition and the process of macro-segregation, and it was generally believed that fluid flow induced remelting, fragmentation, and normally disrupts dendritic solidification [3]. Also, the heterogeneous nucleation assumption was analyzed by many authors [4] too, they argued that stirring could provide continuous temperature fluctuating and shifted up nucleation temperature, the fluctuation activated more nucleation sites, so the microstructure was finer than conventional one. After nucleation, the growth of nuclei determined the morphology of grains, Nafisi et al. [5] reported that in the presence of forced convection, solute distribution was more uniform, by stirring, the thickness of the stagnant boundary layer which existed around the primary particles was decreased due to thermal-solutal homogenization, so the grains would grow isometrically.

But the evolution of microstructure cannot be observed by naked eyes due to the slurry and apparatus are opaque, so some physical modellings were designed to study the solidification process. Materials like succinonitrile-5 at.% water [6], succinonitrile-5 mol% acetone [7] were used to conduct physical simulations, also the solidification processes of steel, aluminum alloy, nitride alloy and copper alloy were simulated by methods of CAFÉ [8], phase field [9] and so on. However, different slurry preparation system has its own characteristic, it cannot only use the theories deduced in similar conditions to explain a certain one, they have different and subtle mechanisms. The CAFÉ stochastic model gives a wider window to study alloy solidification, in which the discrete and crystallographic aspects of grain growth are included, so, it is one of the most common methods in microstructure simulation.

In thermal equilibrium process [10], melt is poured into a well-designed crucible tilting at 45° and then swirled together with the crucible vertically placed until a desired semi-solid state is reached. The swirling motion, which is gentler, is different from conventional stirring movement by mechanical or electromagnetic, and the convection effect can affect the microstructure in a special way according to the rule of thermal equilibrium. The thermal equilibrium state is mainly achieved by heat transfer. Microstructure evolution is almost determined by initial nucleation and thermal state of slurry. So, in this paper, the most important boundary and initial conditions, including IHTC and nucleation parameters, are studied and

determined first, then the micro and macro simulations of Al–7%Si alloy are completed under different pouring temperatures to study the specific microstructure evolution during thermal equilibrium slurry preparation process by using CAFÉ model.

Setting of Simulation Parameters

Aluminum alloy Al–7%Si was taken as the objective material, and a well-designed crucible was used. The swirling motion effect of the thermal equilibrium process on heat transfer was considered by inversely calculating the IHTC between slurry and crucible, also the heat conductivity of Al–Si alloy according to the real temperature measurement. The temperature measurement apparatus and method can be seen in reference [11]. Material parameters of Al–7%Si alloy and crucible were calculated by Scheil method. The convection effect of mass flow will not be considered in this study. The process schematic diagram can be seen in Fig. 1.

The heat extraction from slurry to the outside is mainly done by crucible, so the determination of IHTC between slurry and crucible is critically important. The extracting heat includes contact conduction, air conduction between two surfaces and radiation, all of them are considered together by the same parameter IHTC [12]. The temperature results calculated by using reference value 3000 W/(m^2 K) cannot fit well with the measuring results, so the inverse calculation is essential. Also, the convection effect arising from swirling movement can change the heat conduction within the bulk liquid, and the heat conductivity vs temperature of the alloy is reduced to 80% of the original by inverse calculation, that means the swirling motion can make the heat transfer inside the bulk liquid slower.

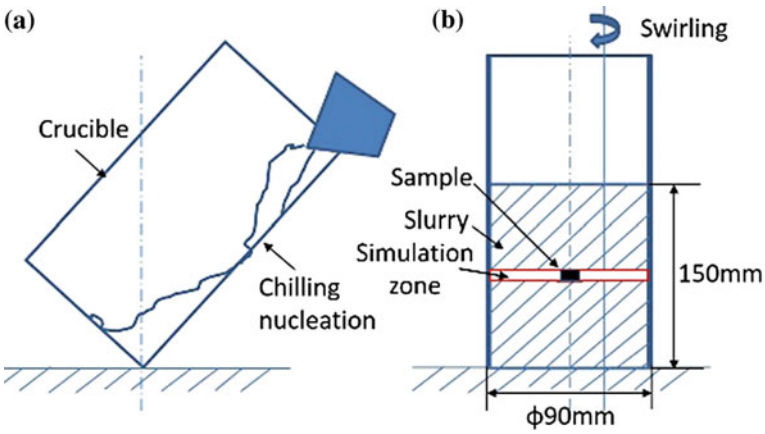

Fig. 1 Thermal equilibrium process for semi-solid slurry preparation, the crucible diameter is 90 mm, **a** pouring, **b** swirling

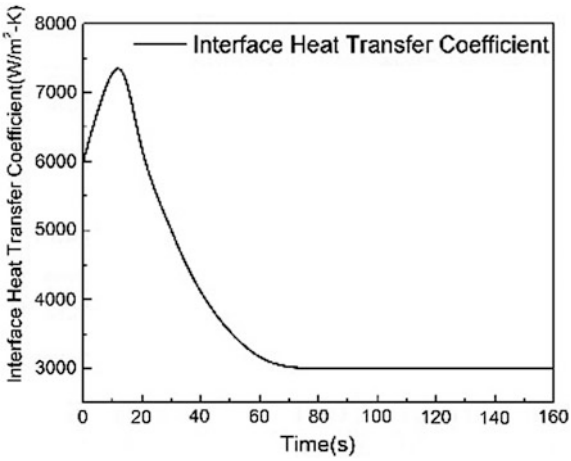

Fig. 2 Inverse calculated interface heat transfer coefficient versus time curve

Table 1 Parameters for microstructure simulation

Symbol	Definition	Value (units)
k_γ	Partition coefficient of silicon	0.1147
m_L	Liquidus slope	−6.79
Γ	Gibbs-Thomson coefficient	2×10^{-7}
c_P	Specific heat of liquid	963 (J/kg °C)
D_L	Diffusion coefficient in liquid	3×10^{-9}
T_P	Pouring temperature	690, 675, 660, 645, 630 (°C)
$H_{C\text{-}A}$	Heat transfer coefficient between crucible and air	60 (W/m^2 K)
$T_{crucible}$	Initial crucible temperature	25 (°C)

The inverse compute method will be simply introduced here. Firstly, temperature variations at 8 points in slurry, see Fig. 4, were measured by self-designed bracket with thermal-couples and recording instrument. Secondly, the measurement results were put into software, parameters were set as usual, initial IHTC versus time curve was given. Thirdly, inverse solver was chosen to calculate, and the solver would let the simulated temperature as close as possible to the measured one. The details can be seen in reference [12]. Then the IHTC versus time curve was determined, see Fig. 2. Other parameters can be seen in Table 1.

Governing Equations and Numerical Algorithm

Nucleation Model

In the bulk liquid and at the interface between liquid and mold, Gaussian distributions of nucleation sites were assumed to account for the heterogeneous nucleation in the present CAFÉ model. A continuous nucleation distribution function ($dn/d(\Delta T_N)$) described the variation of the grain density (dn), which was induced by an increase in undercooling ($d(\Delta T)$). Therefore, the total density of grains($n(\Delta T)$), which had been nucleated at a given undercooling (ΔT) was given by the following equations [13]:

$$n(\Delta T) = \int_0^{\Delta T} \frac{dn}{d(\Delta T_N)} d(\Delta T_N), \tag{1}$$

$$\frac{dn}{d(\Delta T_N)} = \frac{n_{max}}{\sqrt{2\pi}\Delta T_\sigma} \exp\left[-\frac{1}{2}\left(\frac{\Delta T - \Delta T_N}{\Delta T_\sigma}\right)^2\right] \tag{2}$$

where n_{max} was the maximum nucleation density, ΔT was the calculated local undercooling, ΔT_σ was the standard deviation, ΔT_N was the mean undercooling. These equations can be deduced from the relationships explained in reference [14].

Grain densities and undercoolings at different pouring temperature conditions were calculated according to the cooling curve and EBSD results, see Fig. 3. And the EBSD samples were selected from the center of the slurry, see Fig. 1. The ultimate values are listed in Table 2. It should be noted here that the statistics from metallographic structure is not accurate for its inability in distinguishing dendrites, see red circle in Fig. 3b, where more than 10 grains will be counted, but they belong to one dendrite in EBSD sight.

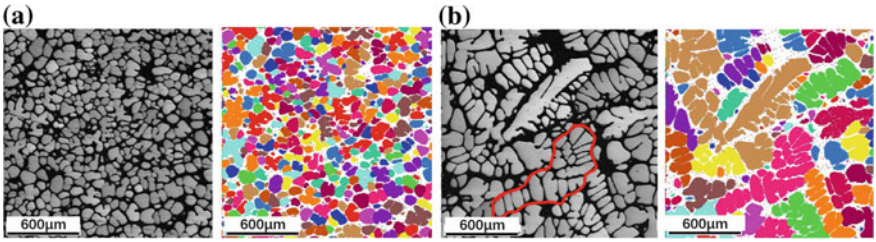

Fig. 3 Metallographicand EBSD observation results for different pouring temperature conditions, **a** 630 °C, **b** 690 °C

Table 2 Nucleation parameters calculated from experiment results

Pouring temperature (°C)	Grain number in EBSD result (/3.97 × 10^6 μm^2)	Cooling rate during 10–20 s from pouring begin (°C/s)	Volume n_{vmax} (m^{-3})	Surface n_{smax} (m^{-2})	ΔT_N	ΔT_σ
630	261	2.07	7.2251 × 10^{11}	8.0519 × 10^7	2	1
645	102	2.07	2.2266 × 10^{11}	3.6737 × 10^7	3	1
660	63	1.75	6.3115 × 10^{10}	1.5852 × 10^7	4	2
675	19	1.49	1.0453 × 10^{10}	4.7808 × 10^6	6	3
690	11	0.91	4.6048 × 10^9	2.7678 × 10^6	8	4

Growth Model

Growth kinetics parameters should be put into the CAFÉ model, including two parameters *a2* and *a3*, see the following equation:

$$v = a2 \times (\Delta T)^2 + a3 \times (\Delta T)^3 \tag{3}$$

The two parameters can be calculated by using the model presented by Kurz et al. [15]. The inputs of the model are liquidus temperature, Gibbs-Thompson coefficient Γ of the solvent, alloy concentration of each solute element, liquidus slope of each element, partition coefficient k of each element. And the calculation results of *a2* and *a3* are 3.4769e−007 and 2.1785e−007, respectively.

Results and Discussions

Eight corresponding points were selected to monitor the temperature variations during thermal simulation. The comparison between simulation and experiment results can be seen in Fig. 4, take case 630 °C for example, the other conditions are similar. It can see that, they can coincide with each other very well. It is obvious that the slurry preparation process has three well-defined stages, see Fig. 4. The molten liquid is cooled sharply at the first stage, here named chill nucleation period, plentiful nuclei are emerging in the bulk. And during the second stage, temperature is rising, this is due to the amount of latent heat release exceeds the heat loss to crucible, so temperature will increase for a certain time. In the third stage, it attains to an equilibrium state, and the heat transfer limit is between crucible and air, $H_{C\text{-}A}$, the IHTC has no more important effect. Now, the whole slug tends to have a homogeneous temperature distribution, and the semi-solid slurry is obtained at the end of thermal equilibrium process.

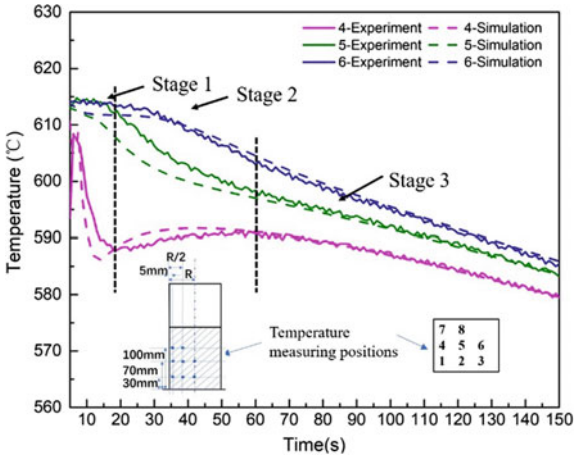

Fig. 4 Comparison of temperature variations vs time between experiment and simulation results under 630 °C pouring condition

The calculation zone for microstructure is shown in Fig. 1, it covers the whole horizontal cross section of the billet, the simulated grain size is coinciding well with the real one after correction, see Fig. 5. Corrections of the results in this article include two aspects. One is the experiment result, which will be reduced to 90% of the original value for the grain growth in quenching period [16]. The other one is the simulation result, which will be reduced to 65% of the original value for the model failure of considering eutectic phase, and the experimental result statistics shows that the solid fraction at the end of slurry preparation is 65%.

The chill effect of crucible on the bulk liquid is weakening with the pouring temperature increasing and less nuclei are formed, so these nuclei have enough space and proper adjacent environment to grow up, which can be seen from the evolution of microstructure in simulation, see Fig. 6. While under low pouring

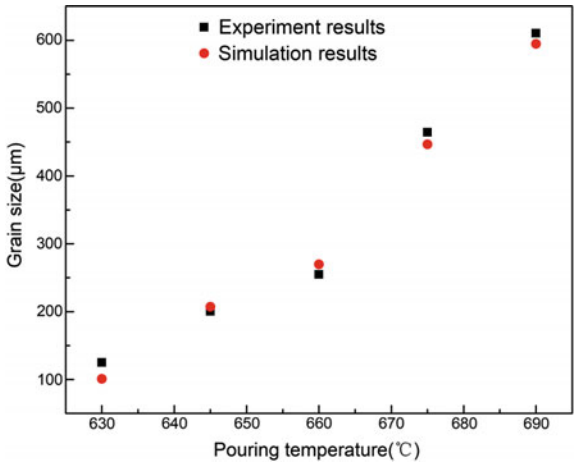

Fig. 5 Grain size comparison between experiment and simulation results

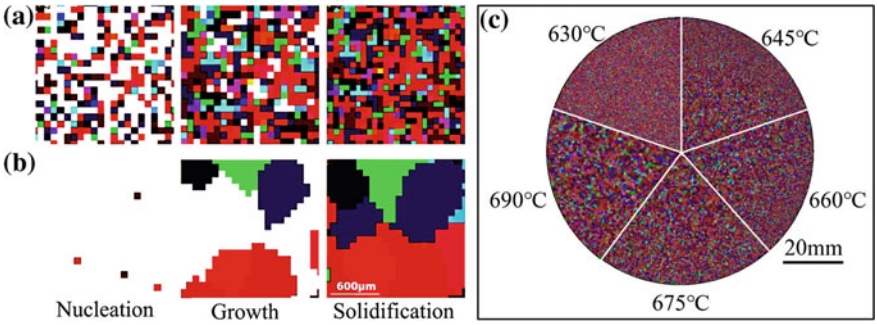

Fig. 6 Microstructure evolution under conditions of pouring temperature at **a** 630 °C and **b** 690 °C, the evolution is divided into three stages, from left to right, nucleation, growth and solidification, **c** is the solidified microstructure comparison between different pouring temperature conditions

temperature condition, more nuclei are formed during the first stage, and the growth of nuclei will be hindered by adjacent ones, so, grains are fine.

It can be seen from Fig. 6 that nucleation is bursting out and distributing homogeneously under 630 °C pouring condition, and it differs from the condition 690 °C. The simulation and experiment results indicate that this different will become bigger gradually with the pouring temperature increasing. It must be noted here that the alloy Al–7%Si is a binary phase material, the difference between α-Al phase and eutectic silicon phase cannot be considered in this CAFÉ model, so the simulation results must be corrected, which has been done already in the above section. This shortcoming of this model will be studied further in the next step.

Conclusions

1. The whole CAFÉ model used in this article can present the evolution and grain size of the microstructure under conditions of various pouring temperature very well, simulation results are verified by experiments.
2. The model of interface heat transfer coefficient between slurry and crucible established in this article can simulate the temperature field approximating reality.
3. The nucleation parameter model which is established based on practical experiment can predict the semi-solid microstructure accurately in grain size.
4. The pouring temperature has a very important effect on the microstructure evolution. The homogenous nucleation and fine grains are obtained under condition of lower pouring temperature 630 °C, the scattered nucleation and coarse grains are obtained under higher pouring temperature 690 °C.

Acknowledgements The authors would like to thank the financial support from the National Key Research and Development Program of China (No. 2016YFB0301001) and the Shenzhen Free Exploring Basic Research Project (JCYJ20170307110223452), and the assistance from Dr. Xiaokang Liang in experiment.

References

1. M.C. Flemings, Behavior of metal alloys in the semisolid state. Metall. Trans. A **22**, 957 (1991)
2. H.V. Atkinson, D. Liu, Microstructural coarsening of semi-solid aluminium alloys. Mater. Sci. Eng. A **496**, 439 (2008)
3. S. Nafisi, R. Ghomashchi, Semi-solid processing of aluminum alloys[M]. Springer International Publishing (2016)
4. Z. Fan, Semisolid metal processing. J. Int. Mater. Rev. **47**, 49–85 (2002)
5. S. Nafisi, R. Ghomashchi, Effect of stirring on solidification pattern and alloy distribution during semi-solid-metal casting. J. Mater. Sci. Eng. A **437**, 388–395 (2006)
6. T. Li, X. Lin, W. Huang, Morphological evolution during solidification under stirring. J. Acta Mater. **54**(18), 4815–4824 (2006)
7. M. Zhu, S. Pan, D. Sun, Modeling of microstructure evolution during alloy solidification, in *Advances in the Science and Engineering of Casting Solidification* ed. by L. Nastac, B.C. Liu (Springer International Publishing, 2015), pp. 183–190
8. W. Song, J. Zhang, S. Wang et al., Simulation of solidification microstructure of Fe-6.5% Si alloy using cellular automaton-finite element method. J. Cent. South Univ. **23**(9), 2156–2164 (2016)
9. P. Das, P. Dutta, Phase field modelling of microstructure evolution and ripening driven grain growth during cooling slope processing of A356 Al alloy. J. Comput. Mater. Sci. **125**, 8–19 (2016)
10. X.K. Liang et al., Comparison of Microstructure and mechanical properties of semi-solid castings produced using billets made by EMS and SEED. J. Solid State Phenom. **217**, 332–339 (2015)
11. W.Y. Qu, F. Zhang, J.J. Wang et al., Effect of slurry temperature distribution on semi-solid die casting. J. Solid State Phenom. **256**, 107–112 (2016)
12. X.B. Bu, L.X. Li, L.Q. Zhang et al., Microstructure simulation of Al-Cu alloy based on inverse identified interfacial heat transfer coefficient. J. Mater. Eng. Perform. **22**(9), 2451–2457 (2013)
13. M. Rappaz, ChA Gandin, Probabilistic modeling of microstructure formation in solidification process. J. Acta Metall. Mater. **41**, 345–360 (1993)
14. M. Rappaz, P. Thévoz, W. Kurz et al., *Micro-macroscopic Modelling of Equiaxed Solidification*, in 4th International Conference on Numerical Methods in Thermal Problems (LSMX-CONF-1985–002) (Pineridge Press, 1985), p. 251
15. W. Kurz, B. Giovanola, R. Trivedi, Theory of microstructure development during rapid solidification. J. Acta Mater. **34**(5), 823–830 (1986)
16. L. Gao, Y. Harada, S. Kumai, Microstructural characterization of aluminum alloys using Weck's reagent, part I: applications. J. Mater. Charact. **107**, 426–433 (2015)

Effects of Cooling Rate and Grain Refiner on Semi-solid Rheocasting Slurries of Al–Zn–Mg Alloy

Min Luo, Daquan Li, Wenying Qu, Xiaokang Liang and Jianzhong Fan

Abstract Swirled Equilibrium Enthalpy Device (SEED) process was used to make Al–4.8Zn–1Mg semi-solid slurries. The effects, about cooling rate and Al–5Ti–1B on semi-solid slurry microstructure and temperature field, were studied in detail. It was found that slow cooling rate was helpful to decrease slurry temperature gradient. The temperature difference between slurry centre and edge decreased from 8.3 to 4.1 °C when the cooling rate decreased from 1.63 to 0.69 °C/min. But low cooling rate also resulted in coarser grain. Grain morphology and size was modified by grain refiner. Trace amount of Al–5Ti–1B changed the grain morphology and size greatly, and improved the homogeneity of slurry microstructure. When the content of Ti increased from 0, 0.01 to 0.12%, the grain size was decreased from about 800 to 115 and 75 μm respectively. These results suggested that low cooling rate and grain refiner were necessary for making Al–4.8Zn–1Mg semisolid slurry.

Keywords Semi-solid rheocasting · Al–Zn–Mg alloy · Cooling rate Al–5Ti–1B · Microstructure

M. Luo · D. Li (✉) · W. Qu · X. Liang · J. Fan
General Research Institute for Nonferrous Metals, Beijing 101407, China
e-mail: lidaquan@grinm.com

M. Luo
e-mail: lm_grinm@163.com

W. Qu
e-mail: quwenying2008@163.com

X. Liang
e-mail: xiaokangcsu@163.com

J. Fan
e-mail: jzfan@grinm.com

© Springer Nature Singapore Pte Ltd. 2018

Y. Han (ed.), *Advances in Materials Processing*, Lecture Notes in Mechanical Engineering, https://doi.org/10.1007/978-981-13-0107-0_81

Introduction

Lots of work has been done to develop high-quality and cheap aluminum materials since H. C. Oenrsted produced aluminum metal in 1825. Composition optimizing and forming process developing are the two main methods to develop aluminum. Recently, B. Dang, X. Zhang et al. improved both strength and elongation of A356 through optimizing cast processing [1]. Appling cheap cast process to wrought alloy, like 7×××, 6××× and 2××× series aluminum alloys, is another way to develop cheap high-quality aluminum casts. But the fact is that those series alloy is difficult to cast due to hot tearing and low fluidity. Since semi-solid forming technology has been developed, many researchers think that semi-solid forming technology can overcome this problem [2, 3].

Semi-solid forming technology has been developed for over 40 years since Spencer et al. [5] found the special rheological behavior of semi-solid metal in 1972, and semi-solid diecasting technology is the most developed one. Until now, almost all commercial rheocasting is carried out with the conventional casting alloys, like A356, A357 and 319s. On the other hand, there are large demands of wrought aluminum parts, so lots of work has been done to apply semi-solid forming process to wrought aluminum alloys [6]. The final goal of all of the works about semisolid slurry is a slurry with well rheological properties, no matter for wrought alloys or for casting alloys. Flemings [7] and Bolouri et al. [8] found that rheological properties is strongly depend on solid fraction and solid particle feature (e.g. morphology and size). According to their study, slurry with low fraction solid and fine particles is easier to be deformed. Practical experience has highlighted several difficulties for wrought alloys semi-solid casting. One of the essential difficulties is the steep slope of the fraction liquid versus temperature curve for alloy [9], which affect the particle distribution in slurry. For A356, the temperature range between 40 and 60% of liquid is 18 °C [10], 12 °C for 7075 [8]. According to the curve of fraction liquid vs temperature (as shown in Fig. 1) of Al–4.8Zn–1Mg alloy measured by SPSC [4], the temperature range of this alloy is only 4.8 °C, which means that it is hard to obtain uniform slurries for Al–4.8Zn–1Mg. According to the Fourier's law of heat conduction, cooling rate and temperature gradient are proportional. Obviously, the uniform temperature field is significant for preparing Al–4.8Zn–1Mg semi-solid slurry. The second fact affecting slurry rheological properties is solid particle feature, which can be changed by grain refiner [11]. So, it is important to study how cooling rate and grain refiner affect Al–4.8Zn–1Mg alloy semi-solid slurry.

The objective of the present work was to prepare Al–4.8Zn–1Mg semisolid slurries by using SEED rheocasting process [12]. The effects of cooling rate and grain refiner on Al–4.8Zn–1Mg alloy semisolid slurries were studied in detail in this work.

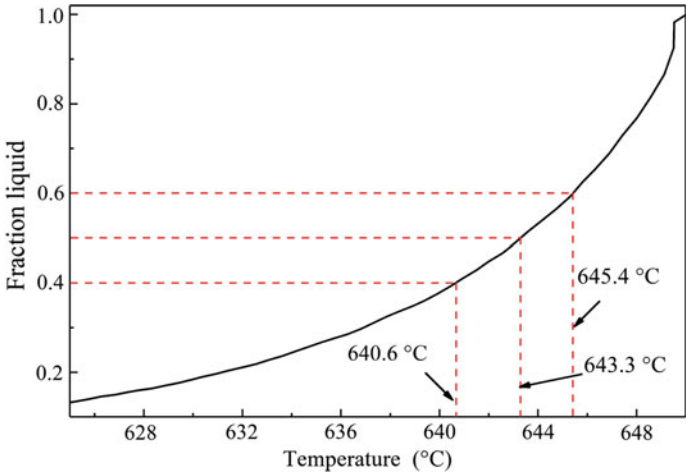

Fig. 1 Fraction liquid vs temperature curve for Al–4.8Zn–1Mg alloy measured by SPSC [4]

Experimental Procedures

The composition of Al–4.8Zn–1Mg aluminum alloy used in this study is given in Table 1. The SEED rheocasting process [12] was used to prepare semisolid slurries. Approximately 45 kg Al–4.8Zn–1Mg alloy was melted by electrical resistance furnace, and then about 2.3 kg melt was poured into the steel crucible at 680 °C. Subsequently, the eccentric rotary frequency 180 rpm was applied. When the temperature of point 3 in Fig. 2 was cooled to 645.4 °C, the rotation was stopped immediately. At last, the semisolid slurry was released from crucible and quenched in cold water. The dimensions of crucible were 90 mm in diameter and 250 mm in height. Two processes were used during the experiments, normal process [12] and modified process. For modified process, the crucible was coated with thermal insulation material on crucible outside surface, top and platform bottom, as shown in Fig. 2. The cooling rate of normal process and modified process, which were calculated based on the last 60 s temperature data of SEED process, were 1.63 and 0.69 °C/min respectively. In most of the tests, the slurry was refined with different weight of Al–5Ti–1B master alloy. The detail experimental parameters are shown in Table 2. The temperature variation of slurry was monitored by three K-type

Table 1 Chemical composition of Al–4.8Zn–1Mg

Element	Zn	Mg	Si	Mn	Fe	Ti	Al
Content (wt%)	4.82	1.06	0.01	0.003	0.06	<0.0002	Balance

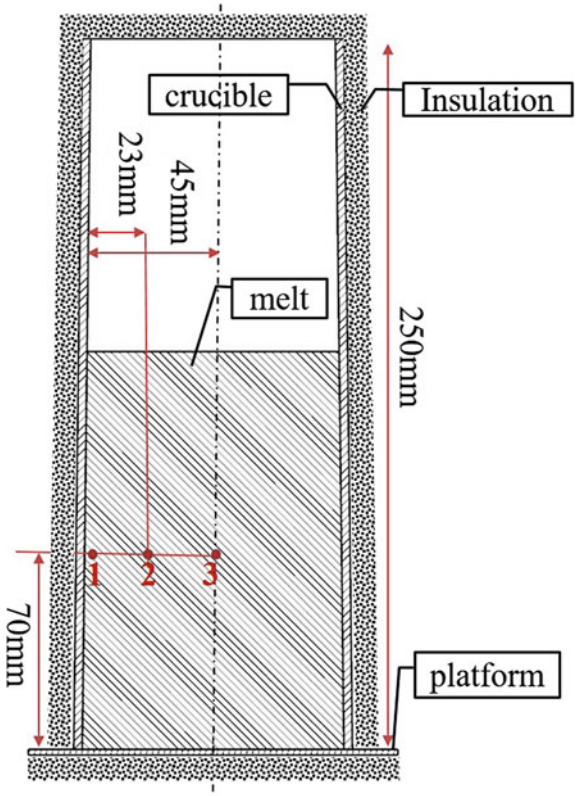

Fig. 2 Locations of the thermocouples and metallographic samples (1—Edge, 2—Middle, 3—Centre) and insulation coating schematic diagram

Table 2 Summary of the process parameters in this study

No.	1	2	3	4	5	6
Ti (wt%)	0	0.01	0.03	0.06	0.12	0.06
Cooling rate (°C/min)	0.69	0.69	0.69	0.69	0.69	1.63

Note Cooling rate was calculated according to measured temperature data

thermocouples, which were placed at edge, middle and center of the slurry, and their tips were at 70 mm height from the bottom of crucible, as shown in Fig. 2. Real-time temperature data were recorded by data logging system with a sampling rate of 1 Hz.

Metallographic examination samples were taken from the edge and center locations, which located at the height of 70 mm from the bottom of quenched billets, as illustrated in Fig. 2. Standard grinding and polishing processes were conducted, then the samples were anodized with Barker's reagent (5 mL

HBF_4 + 200 mL H_2O), (anodizing condition: voltage U = 30 V, current density J = 0.2 − 0.3 A/cm^2 for 30 s at room temperature). Subsequently, anodized samples were pictured by Carl Zeiss Axiovert 200MAT microscope under polarized light. Five micrographs were randomly taken from each sample for quantitative analysis. ASTM E112-10 [13] was employed to quantitative analysis of the microstructure.

Results and Discussion

Cooling Rate

Figure 3 presents the effect of cooling rate on temperature field. As shown in diagram, when the cooling rate decrease from 1.63 to 0.69 °C/min, the slurry temperature difference between centre and edge decrease from 8.3 to 4.1 °C, and the corresponding fraction liquid difference drops from 32 to 17%. Fourier's law of heat conduction can be used to explain the results. Simplified mathematical expression of Fourier's law of heat conduction is given as Eq. 1. The equation shows heat flux q and temperature difference ΔT are proportional, and the heat flux q and cooling rate are approximately proportional in this study. It is the reason why the temperature difference ΔT dropped to a half when the cooling rate was reduced to about a half.

$$q = \Delta T \frac{\lambda}{\delta} \tag{1}$$

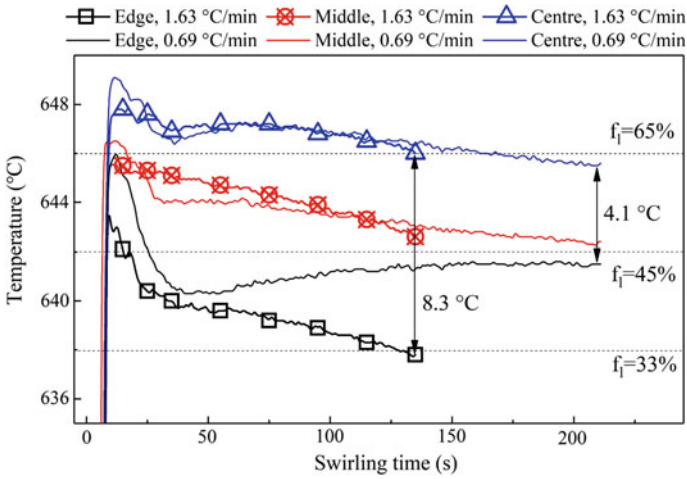

Fig. 3 Temperature field variation of slurry during solidification, f_l is fraction liquid, its value corresponds to the temperature of the dash line

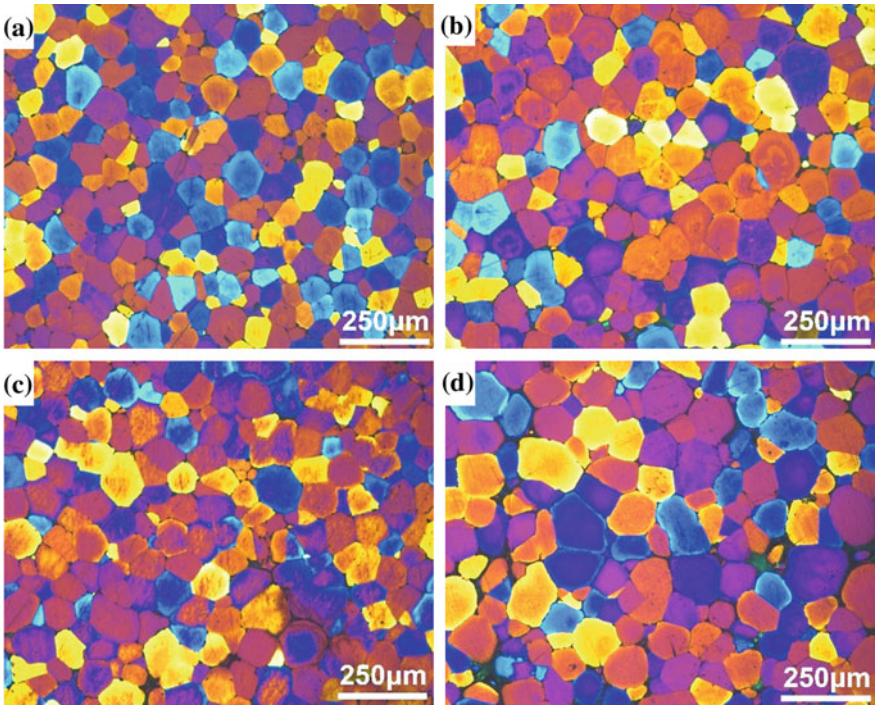

Fig. 4 Microstructure of billets centre and edge at different cooling rate, **a** edge, 1.63 °C/min, 0.06% Ti; **b** edge, 0.69 °C/min, 0.06% Ti; **c** centre, 1.63 °C/min, 0.06% Ti; **d** centre, 0.69 °C/min, 0.06% Ti

where q is heat flux, ΔT is temperature difference, λ is thermal conductivity, δ is thickness.

Figure 4 presents the microstructure of slurries solidified at different cooling rate. As shown, the grain size solidified at 1.63 °C/min is finer than that at 0.69 °C/min. The quantitative analysis, presented in Fig. 6 (the points of 0.06% Ti), shows slow cooling rate resulted in about 10 μm increasement in grain size no matter where. As Fig. 3 shows, the temperature curve of 0.69 °C/min is higher than that of 1.63 °C/min, which resulted in more solid particles nucleated during pouring process were melted during swirling stage. On the other hand, Fig. 3 shows that melt cooling at 0.69 °C/min take more 75 s to reach the target temperature, so the slurry solidified at 0.69 °C/min have more time to carry out Ostwald ripening process. That might be the reasons why the grain solidified at 1.63 °C/min is smaller than that at 0.69 °C/min.

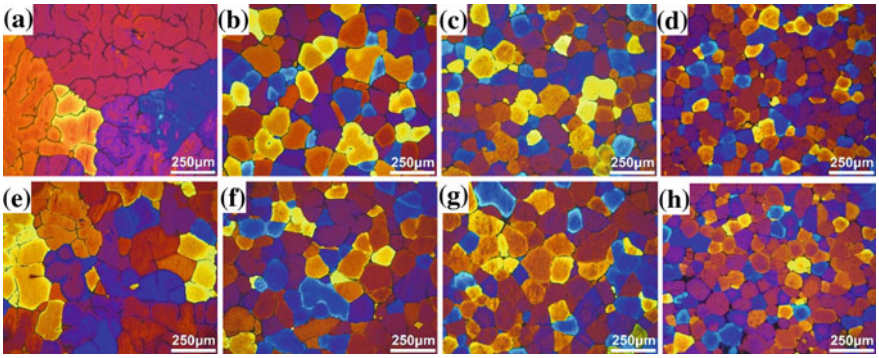

Fig. 5 Microstructure of billets centre and edge using various weight grain refiner **a** 0% Ti, edge; **b** 0.01% Ti, edge; **c** 0.03 %, edge; **d** 0.12% Ti, edge; **e** 0% Ti, centre; **f** 0.01% Ti, centre; **g** 0.03% Ti, centre; **h** 0.12% Ti, centre

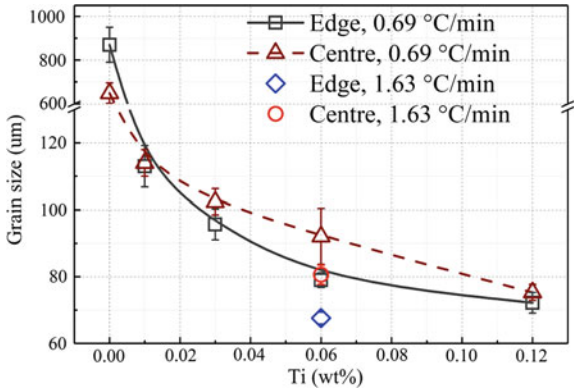

Fig. 6 Effect of Ti contents and cooling rate on grain size

Grain Refiner

Microstructure of slurries refined with various weight of grain refiner are presented in Fig. 5. The microstructure shows the grain morphology transformed from dendrite to fine globular structure after refining with Al–5Ti–1B, and the smaller grain obtained when more Al–5Ti–1B was used. Quantitative analysis (as shown in Fig. 6) shows huge difference in size existed between center (650 μm) and edge (870 μm). After 0.01% Ti in the form of Al–5Ti–1B was added, the grain size decreased to about 115 μm, and there was no obvious difference between slurry edge and centre in grain size and morphology. The more Al–5Ti–1B was added, the smaller grain was obtained. It's clearly that adding grain refiner made the slurry microstructure uniform and fine.

Desirable slurries are significant to semi-solid forming process. The fraction solid of slurry should be 40–60% and distribute uniformly, and the solid particals

should non-dendritic and small. According to the experiment results, low cooling rate increased the uniformity of fraction solid distribution, and grain refiner can eliminate dendritic and refine grain size. So, decreasing cooling rate and adding grain refiner are necessary for making Al–4.8Zn–1Mg semisolid slurry.

Conclusions

(1) When cooling rate decreases from 1.63 to 0.69 °C/min, the temperature difference between slurry centre and edge drops from 8.3 to 4.1 °C, and the corresponding fraction liquid difference decreases from 32 to 17%.
(2) The grain solidified at 1.63 °C/min condition is smaller about 10 μm than that at 0.69 °C/min.
(3) Grain refiner (Al–5Ti–1B master alloy) is useful for making Al–4.8Zn–1Mg alloy semisolid slurry. Trace amount of grain refiner can transform coarse dendrite structure to fine globular structure and improve the microstructure uniformity of the slurry greatly. When the Ti content increases from 0 to 0.01, 0.12%, the grain size decreases from about 800 to 115, 75 μm respectively.
(4) Low cooling rate and grain refiner are necessary for preparing Al–4.8Zn–1Mg alloy semisolid slurry.

Acknowledgements Financial support from the National Key Research and Development Program of China (N0.2016YFB0303001) and Shenzhen Free Exploring Basic Research Project (JCYJ20170307110223452) is gratefully acknowledged.

References

1. B. Dang, X. Zhang, Y.Z. Chen et al., Breaking through the strength-ductility trade-off dilemma in an Al-Si-based casting alloy. Sci. Prog. **6**, 30874 (2016)
2. S. Janudom, J. Wannasin, P. Kapranos et al., The effect of hot tearing in semi solid casting of aluminum A201 alloy. Adv. Mater. Res. **739**, 190–195 (2013)
3. J. Wannasin, D. Schwam, J. Yurko et al., Hot tearing susceptibility and fluidity of semi-solid gravity cast Al-Cu alloy. Solid State Phenom. **116**, 76–79 (2006)
4. H.B. Dong, J.D. Hunt, A. Novel, Single-pan scanning calorimeter. Measurement of thermophysical properties of metallic alloys. J. Therm. Anal. Calorim. **64**, 341–350 (2001)
5. D. Spencer, R. Mehrabian, M. Flemings, Rheological behavior of Sn-15 pct Pb in the crystallization range. Metall. Trans. **3**, 1925–1932 (1972)
6. U.A. Curle, H. Möller, G. Govender, R-HPDC in South Africa. Solid State Phenom. **192**, 3–15 (2013)
7. M.C. Flemings, Behavior of metal alloys in the semisolid state. Metall. Trans. B **22**, 269–293 (1991)
8. A. Bolouri, Q.F. Zhao, P. Côté et al., Microstructure and rheological properties of semi-solid 7075 slurries using SEED rheocasting process. Solid State Phenom. **256**, 288–293 (2016)
9. B. Hallstedt, E. Balitchev, H. Shimahara et al., Semi-solid processing of alloys: principles, thermodynamic selection criteria, applicability. ISIJ Int. **46**, 1852–1857 (2006)

10. D. Liu, H.V. Atkinson, H. Jones, Thermodynamic prediction of thixoformability in alloys based on the Al–Si–Cu and Al–Si–Cu–Mg systems. Acta Mater. **53**, 3807–3819 (2005)
11. B. Murty, S. Kori, M. Chakraborty, Grain refinement of aluminium and its alloys by heterogeneous nucleation and alloying. Int. Mater. Rev. **47**, 3–29 (2002)
12. M.E.L. Pascal Côté, X. Grant Chen, New Developments with the SEED technology. Solid State Phenom. **192–193**, 373–378 (2012)
13. ASTM E112-10, Standard test methods for determining average grain size. ASTM Int. (2010). (West Conshohocken, PA) www.astm.org

Microstructures and Mechanical Properties of 584 mm 7055 Alloy Billet by Direct Chill Casting Under Annular Electromagnetic Stirring Coupled with Intercooling

Yajun Luo, Zhifeng Zhang, Minwei Gao, Bao Li and Chunsheng Chen

Abstract Combined with annular electromagnetic stirring and intercooling, a uniform direct chill (UDC) casting was proposed and used to produce 7075 aluminum alloy billets of Φ584 mm. In this paper, the experiments were employed to investigate the solidification behavior of 7055 alloy during UDC casting process. The effect of the technology on the microstructures of the billets and mechanical property was studied. The results illustrated that the UDC could refine the microstructures of the billets of 7055 alloy and reduce macrosegregation. The billet prepared had better mechanical property compared to normal DC casting.

Keywords Direct chill casting · Electromagnetic stirring · 7055 alloy Intercooling

Y. Luo · Z. Zhang (✉) · M. Gao · B. Li · C. Chen
General Research Institute for Non-Ferrous Metals, Beijing, China
e-mail: zhangzf@grinm.com

Y. Luo
e-mail: ggluoyajun@qq.com

M. Gao
e-mail: gaomingwei1990@163.com

B. Li
e-mail: libao@grinm.com

C. Chen
e-mail: ccs@grinm.com

© Springer Nature Singapore Pte Ltd. 2018

Y. Han (ed.), *Advances in Materials Processing*, Lecture Notes in Mechanical Engineering, https://doi.org/10.1007/978-981-13-0107-0_82

Introduction

7055 alloy has been widely used in the aviation industry such as wing structures, keel beams and longerons, fuselage frames and fuselage stringers due to its high strength and low density [1, 2]. However, the fabrication process of the high quality large sized 7055 billet is very difficult because the high alloying element content under the relatively lower cooling speed [3]. Electromagnetic stirring (EMS) technology has been promoted as an effective method for grain refining in aluminium castings [4]. Based on EMS technology, an advanced melt treatment technology, namely, the annular electromagnetic stirring (A-EMS) process was developed, by which an intensively shearing force and a higher shearing rate could be achieved by specially designed annular chamber profiles [5]. However, as billet diameter increases to 500 mm, due to the cooling capacity of the mould and water spraying is limited, the heat in the sump centre could not be extracted in time, as a result, a larger temperature difference between central and periphery parts of the billet sump occurs, the fine and uniform microstructure could not be ensured by applying A-EMS alone in preparing the large-sized billet. To change the heat extraction pattern of the billet realized solely from the outer surface, a new uniform direct chill (UDC) casting was proposed by applying in-mould cooler and A-EMS in the DC casting process, which was designed to simultaneously cool the billet from both the centre and surface positions, and a multidimensional forced uniform solidification was realized [6].

In this study, the UDC technique was employed to produce 7055 billets, and alloy composition, microstructure features and mechanical properties were explored in detail. The formation mechanism of equiaxed grains in as-cast alloys was also discussed. The mechanical property was evaluated.

Experiment

Figure 1 shows the schematic of the UDC casting process, compared with the normal direct chill (NDC) casting process, an in-mould cooler with a cooling end made of highly pure graphite is added to realize inner cooling in the melt as well as an electromagnetic stirrer with the arrangement of six water-cooled cooper 72 turn coils fed with a three-phase electric current.

Pure aluminium, pure zinc, pure magnesium, pure copper and master alloy Al–4Zr were melted an induction furnace to obtain the experimental 7055 alloy, the chemical composition of which is Al–7.8Zn–2.0Mg–2.3Cu–0.18Zr–0.081Fe–0.024Si (wt%), subsequently, the melt was transferred into a holding furnace. After degassed and filtered, the melt was poured to the hot top of the preheated caster with a billet diameter of 584 mm. When the casting process proceeded at a stable stage, the electromagnetic stirring system was started and the in-mould cooler was inserted in the sump along the central vertical axis of the mould in the caster. The

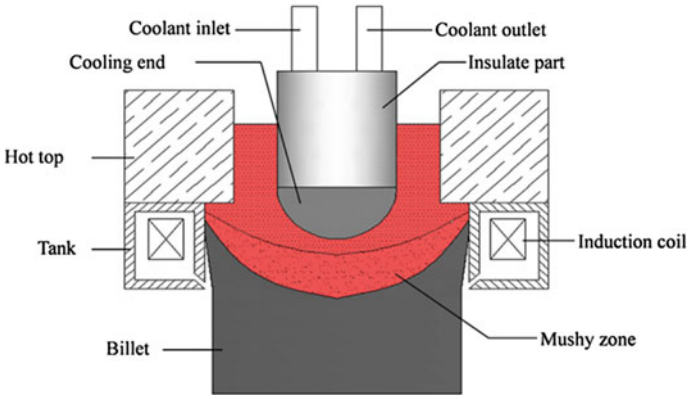

Fig. 1 Schematic view of the uniform direct chill (UDC) casting process

Table 1 Casting process parameters of NDC and UDC

Parameters	NDC	UDC
Pouring temperature (K)	1003–1033	1003–1033
Casting speed (mm min^{-1})	25–30	25–30
Cooling water (m^3 h^{-1})	8–10	8–10
Electromagnetic current (A)	None	90
Electromagnetic frequency (Hz)	None	3
Cooler diameter (mm)	None	200
Intercooling rate (W m^{-2} K^{-1})	None	500–1000

billets were homogenised treated for 12 h immediately after produced to avoid cracking. The NDC and UDC casting process parameters were shown in Table 1. The microstructures of the alloy were characterized using a polarized light optical microscope (Carl Zeiss Axiovert 200 MAT) and JSM-6510 scanning electron microscope/energy dispersive X-ray spectroscopy (SEM). The samples taken from the transverse cross-section of the billet for optical observation were electro-polished in 3% HBF4. The samples preparation for SEM observation were taken from 1/2 radius of billet. The chemical composition of the cross-section of billets was evaluated by means of FOUNDRY-MASTER Pro.

The Brinell hardness on location (0R, 0.5R and R) of billets obtained by NDC and UDC casting was measured after grinding and polishing. The Brinell hardness testing was performed on an HBE-3000A hardmeter with a load of 62.5 kgf and five measurements were made to obtain an average value.

Results and Discussion

In order to assess the quality of the billets prepared by UDC casting and NDC casting, the microstructures of the as-cast 7055 alloys were shown in Fig. 2. An equiaxed grain microstructure was distinctly observed in billets formed using UDC casting in contrast to a typical dendritic morphology of the primary phase often observed in billets formed using NDC casting. The average grain size in billets formed using UDC casting was 180 μm, while the average grain size of billets formed using NDC casting which was 773 μm, the former obvious finer than the later. The dominated factor that affects the grain size is the cooling rate, which mainly depends on cooling water, casting speed and billet size [7]. It is less than 10 K/s during NDC casting process. For this reason, there was no doubt that the grain size of NDC cast billet was relatively larger [8]. Efforts have been made to understand the microstructural evolution, especially upon the mechanisms of the equiaxed microstructure formation by stirring in DC casting [4, 9–11]. A-EMS with an intensively shearing force and a higher shearing rate, one of many ways of stirring, has effect on grain refining during 300 mm billets DC casting process [12]. For preparing billets larger than 500 mm, A-EMS has limited effect on grain refinement, because the heat extraction pattern is only realized through the outer mould, there is a large temperature difference along the radius direction of large-sized billet. Therefore the casting speed should be slow in case of melt leakage, but which allows enough time for nuclei to grow up. A-EMS coupled with intercooling by inserting an in-mould cooler into the melt sump can remove heat from the sump centre. As a result, the melt is chilled from the outer and inner simultaneously and both melt temperature and composition fields of the sump are

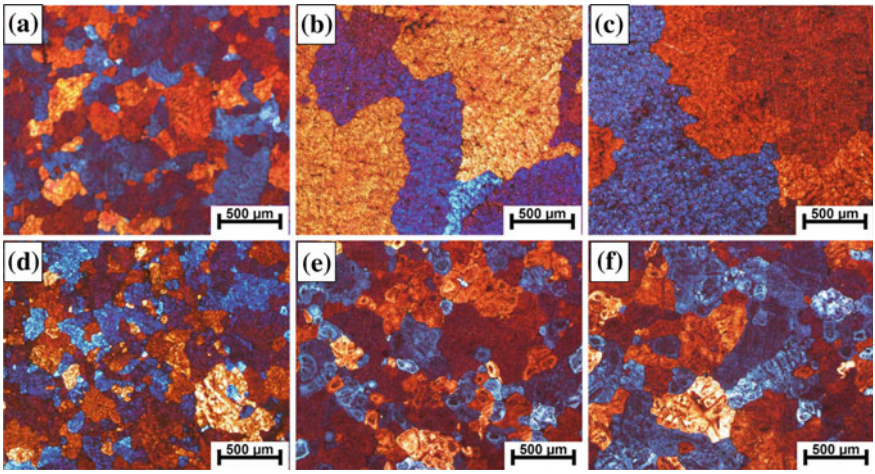

Fig. 2 Micrographs of radial cross sections of the edge (**a**, **d**), the 1/2 diameter (**b**, **e**) and the centre (**c**, **f**) of the 7055 billets prepared using NDC casting (**a**, **b** and **c**) and UDC casting (**d**, **e** and **f**)

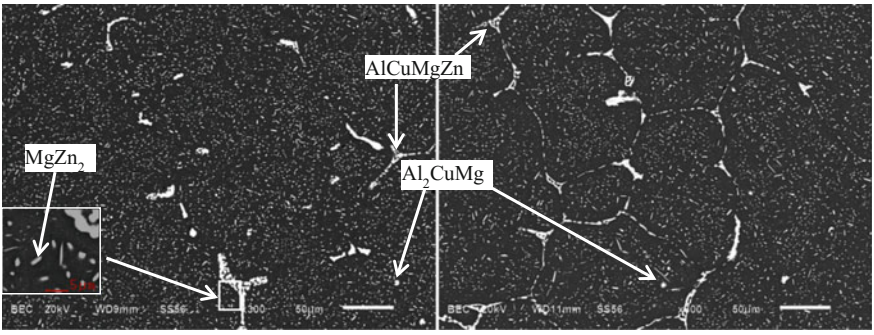

Fig. 3 Electron backscatter micrographs for the second-phase distribution of as-homogenised 7055 billets formed using by NDC casting (**a**) and UDC casting (**b**) processes

more uniform. Heterogeneous nucleation occurs continuously throughout the entire volume of the melt during the continuous cooling. All the nuclei could survive and contribute to the final microstructure [13]. Furthermore, electromagnetic force could break the primary dendrites into fragments that will become the nuclei [14]. All the nuclei grow spherically under intensive forced convection. The cooling effect of the in-mould cooler could increase the cooling rate of the billet, lots of nuclei without enough time to grow up. With increasing cooling rate of the billet, the structures are subjected to continuous refinement [15]. Due to the coupling effects of A-EMS combined with intercooling on the solidification of the billet, a fine microstructure throughout the billet can be achieved. Figure 3 represented back-scattered electron images obtained from billets formed using NDC and UDC casting. The needle shape phase distributed relatively uniformly throughout the alloy matrix is $\eta(MgZn_2)$. The small round phase located in the aluminium matrix is $S(Al_2CuMg)$. The phase in the grain boundary is AlZnMgCu quaternary phases that were not completely dissolved in the aluminium matrix. The quaternary phase of the NDC billets is larger than that of UDC billet. The fraction of second phase was higher after UDC processing than that after NDC processing because the grain size became smaller and the amount of boundary became higher. The result suggested that it would take more time for UDC billet in homogenization heat treatment.

Figure 4 showed the chemical composition at different positions on cross section of billets. Inverse macrosegregation exist in the surface of billets formed using NDC and UDC casting due to the quick chill on the billet surface by mould. This surface inverse macrosegregation could not be alleviated by intercooling or A-EMS. Because of low casting speed, large billet size and huge grain size, macrosegregation is quite serious in billet formed using NDC casting. However, element distributes very uniform in billets formed using UDC casing because the melt temperature and composition fields of the sump are more uniform due to A-EMS and intercooling.

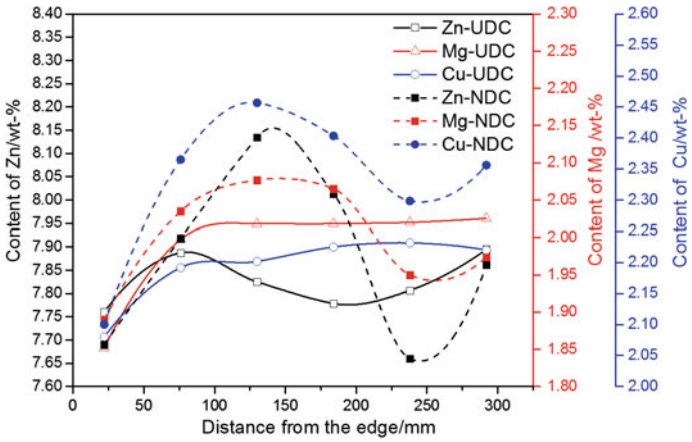

Fig. 4 Zn, Mg and Cu distribution along radical direction of billets prepared by NDC and UDC casting

Fig. 5 Brinell hardness of the billets formed using NDC and UDC casting

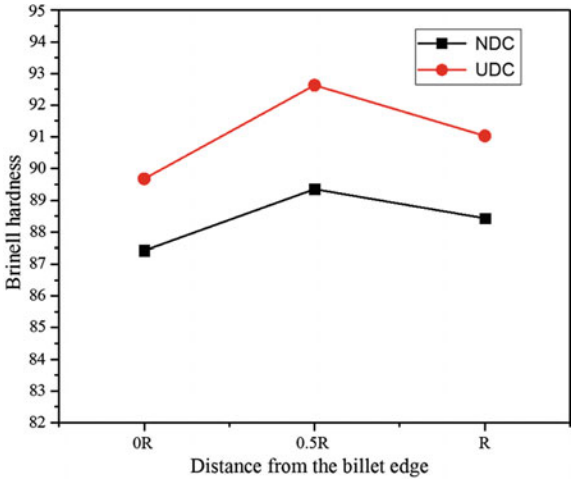

The Brinell hardness of billets formed using NDC and UDC casting was shown in Fig. 5. In NDC casting process, the hardness values of billet are relatively low. The Brinell hardness are 87, 89 and 88 at 0R 0.5 R and R, respectively. While under A-EMS coupled with intercooling, the Brinell hardness at corresponding location is higher and they are 89, 92 and 91, respectively. The large increase of hardness was contributed by the greatly refined grains and uniformly distributed composition.

Conclusion

The coupling effects of A-EMS combined with intercooling on the solidification of the billet can refine the microstructure. The average grain size of billets formed using UDC casting is about 180 μm and obvious finer than that of billets formed using NDC casting. The second phase is refined and distributes uniform. A-EMS coupled with intercooling can reduce macrosegregation of the billet, the composition distributes uniformly in the billet. But the surface inverse segregation can not be reduced by UDC casting. The Brinell hardness of billet increases because the microstructure greatly is refined and composition distributes uniformly.

Acknowledgements This work was financially supported by the International Science and Technology Cooperation Program of China (No. 2015DFA51230).

References

1. J.Z. Cui, H.T. Zhang, Y.B. Zuo, DC casting of large sized ingot of a high strength 7xxx alloy under the influence of electromagnetic field. C. Mater. Sci. Forum. **765**, 165–169 (2013)
2. B. Liu, Q. Lei, L. Xie, M. Wang, Z. Li, Microstructure and mechanical properties of high product of strength and elongation Al–Zn–Mg–Cu–Zr alloys fabricated by spray deposition. J. Mater. Des. **96**, 217–223 (2016)
3. H. Yu, M. Wang, X. Sheng, Z. Li, L. Chen, Q. Lei, C. Chen, Y. Jia, Z. Xiao, W. Chen, H. Wei, H. Zhang, X. Fan, Y. Wang, Microstructure and tensile properties of large-size 7055 aluminum billets fabricated by spray forming rapid solidification technology. J. Alloys Compd. **578**, 208–214 (2013)
4. C. Vives, Effects of electromagnetic vibrations on the microstructure of continuously cast aluminium alloys. J. Mater. Sci. Eng. A. **173**, 169–172 (1993)
5. J. Xu, H. Wang, M. Tang, Z. Zhang, Application research on DC casting process by annular electromagnetic stirring for a modified 7075 alloy. C. Mater. Sci. Forum. **765**, 175–179 (2013)
6. Y. Luo, Z. Zhang, B. Li, Y. Qiu, M. He, Effects of annular electromagnetic stirring coupled with intercooling on grain refinement and homogeneity during direct chill casting of large-sized 7005 alloy billet. J. JOM. 1–4 (2017)
7. D.G. Eskin, *Physical Metallurgy of Direct Chill Casting of Aluminum Alloys* (CRC Press, New York, 2008)
8. H.T. Li, M. Xia, P. Jarry, G.M. Scamans, Z. Fan, Grain refinement in a AlZnMgCuTi alloy by intensive melt shearing: a multi-step nucleation mechanism. J. Cryst. Growth **314**(1), 285–292 (2011)
9. Z. Fan, M. Xia, H. Zhang, G. Liu, J.B. Patel, Z. Bian, I. Bayandorian, Y. Wang, H.T. Li, G.M. Scamans, Melt conditioning by advanced shear technology (MCAST) for refining solidification microstructures. J. Int. J. Cast Met. Res. **22**(1), 103–107 (2009)
10. H. Zhang, H. Nagaumi, J. Cui, Coupled modeling of electromagnetic field, fluid flow, heat transfer and solidification during low frequency electromagnetic casting of 7XXX aluminum alloys. Part II: the effects of electromagnetic parameters on casting processes. J Mater. Sci. Eng. A. **448**(1–2), 177–188 (2007)
11. R. Haghayeghi, P. Kapranos, Grain refinement of AA7075 alloy under combined magnetic fields. J. Mater. Lett. **151**, 38–40 (2015)

12. Y. Luo, Z. Zhang, M. Gao, J. Xu, S. Zhang, Study on grain refinement and homogenization of large-sized DC casting ingot by A-EMS melt Treatment. C. Mater. Sci. Forum. **850**, 653–658 (2016)
13. Z. Fan, G. Li, Solidification behaviour of AZ91D alloy under intensive forced convection in the RDC process. J. Acta Mater. **53**(16), 4345–4357 (2005)
14. E. Liotti, A. Lui, R. Vincent, S. Kumara, Z. Guo, T. Connolley, I.P. Dolbnya, M. Hart, L. Arnberg, R.H. Mathiesen, P.S. Grant, A synchrotron X-ray radiography study of dendrite fragmentation induced by a pulsed electromagnetic field in an Al–15Cu alloy. J. Acta Mater. **70**, 228–239 (2014)
15. B. Dang, X. Zhang, Y.Z. Chen, C.X. Chen, H.T. Wang, F. Liu, Breaking through the strength-ductility trade-off dilemma in an Al–Si-based casting alloy. J. Sci. Rep. **6**, 30874 (2016)

Effects of Al–Ti–B–RE Grain Refiner on Microstructure of A357 Alloy

Chuanzheng Zhang, Yuelong Bai, Zhifeng Zhang, Bao Li and Chunsheng Chen

Abstract The refining effect of Al–5Ti–1B–1RE master alloy on as-cast microstructures of A357 alloy was studied by optical microscopy (OM) and scanning electron microscopy (SEM). The results showed that the Al–5Ti–1B–1RE master alloy could refine the A357 grain effectively. The grain refining effect achieved the best with 1.0 wt% Al–5Ti–1B–1RE master alloy addition level, dendrite was also remarkably refined. The addition of RE elements improved the wetting quality of the molten Al to TiB_2 and Al_3Ti phase, reduced the aggregation tendency of second phase particles, increased the number of nucleation particles and delayed the fading time. At the same time, RE elements is easily adsorbed on grain boundaries and phase interfaces, hindering the growth of Al_3Ti, which also increased the nucleation probability. In addition, A1–5Ti–1B–1RE could effectively modify the needle like iron-rich impurity phase to short rod/granular like. A1–5Ti–1B–1RE can get a better refining effect in A357 when compared with Al–5Ti–1B.

Keywords A357 alloy · Al–5Ti–1B–1RE grain refiner · Refining effect RE

C. Zhang · Y. Bai (✉) · Z. Zhang · B. Li · C. Chen
General Research Institute for Non-Ferrous Metals, Beijing 100088, China
e-mail: bai-yuelong@163.com

C. Zhang
e-mail: 17801127545@163.com

Z. Zhang
e-mail: zhangzf@grinm.com

B. Li
e-mail: libao@grinm.com

C. Chen
e-mail: ccs@grinm.com

© Springer Nature Singapore Pte Ltd. 2018

Y. Han (ed.), *Advances in Materials Processing*, Lecture Notes in Mechanical Engineering, https://doi.org/10.1007/978-981-13-0107-0_83

Introduction

A357 alloy is a hypoeutectic Al–Si alloy, widely used at home and abroad, aviation, aerospace and military industry [1–4] because of its excellent casting properties, high strength and toughness, good anti fatigue performance and corrosion resistance [5]. The performance of A357 alloy products can't meet the needs of some aerospace products. So the research of Al–Si alloy from different direction were studied, one of the key technology to improve the quality of aluminum products is aluminum melt processing technology, finding effective grain refinement treatment is an important way to improve the quality of aluminum. The most effective and simplest method is to add master alloy refiners into aluminum melt [6, 7]. At present, Al–5Ti–1B intermediate alloy is widely used as refiner in industry, but it's easy to lose effect due to the TiB_2 phase aggregation [8, 9]. In recent years, it has been proved that RE can improve this phenomenon [10–12], make refinement more stable, delay the fading time and basically eliminate the "poisoning" phenomenon. Lots of work has been done on Al–5Ti–1B refining A357, there are less researches on Al–5Ti–1B–RE refining A357. On the basis of the previous studies, this topic will further explore the refinement effect of Al–5Ti–1B–1RE refiners on A357 aluminum alloy and the role of RE.

Experimental

Experimental material:

A357 aluminum alloy and Al–5Ti–1B–1RE master alloy are all home-made, the composition was listed in Table 1. Put A357 aluminum alloy into a graphite crucible, with well crucible resistance furnace melting, heating-up to 760 °C, after the alloy has been completely melted, cooling down to 720 °C. Then 0.2, 0.5, 1.0, 2.0 wt% Al–5Ti–1B–1RE master alloy added into A357 alloy melts respectively at 720 ± 5 °C, after intermediate alloy completely melted, mix the melt. Then degas, slag after refining, heat preservation for a period of time, pour the mixed melt into TP-1 mold. Finally, prepare metallographic specimens.

Table 1 Composition of experimental material

Alloy	Si (wt%)	Mg (wt%)	Ti (wt%)	B (wt%)	Re (wt%)	Al (wt%)
A357	6.970	0.520	0.086			Bal.
Al–5Ti–1B–1RE			5.04	1.05	1.02(Ce/La = 6.5/3.5)	

Results and Discussion

Microstructure of Al–5Ti–1B–1RE Master Alloy

Scanning electron microscopy and energy spectrum analysis of the Al–5Ti–1B–1RE master alloy were carried out, and the result is shown as Fig. 1. The mainly second phase particles in the Al-5Ti-1B-1RE master alloy consist of Al_3Ti, TiB_2 and $Ti2Al_{20}RE$. The small black particles are TiB_2 phase, and TiB_2 phase is dispersive distribution. No needle like Al_3Ti was found in the intermediate alloy, RE elements enter into the Al_3Ti phase to form $Ti_2Al_{20}RE$ phase.

Al–5Ti–1B–1RE Refining Effect

Figure 2 shows the alloy microstructure of different amount of Al–5Ti–1B–1RE intermediate alloy. Figure 2a as cast A357, the α-Al phase shows a large dendrite, and the distribution was uneven, eutectic silicon was elongated, flaky or long needle like distribution around α-Al; Fig. 2b was add 0.2% Al–5Ti–1B–1RE, α-Al columnar crystal size decreases and distribution irregular, eutectic silicon flake or needle become smaller, the refining effect is obvious; Fig. 2c was add 0.5%Al–5Ti–1B–1RE, the columnar crystal has been further refined, the size of eutectic silicon moresmaller, the distribution becomes uniform; Fig. 2d was add 1% Al–5Ti–1B–1RE, α-Al grains become very small, and the distribution is more uniform, fine eutectic silicon phase distribution evenly, the most obvious effect of grain refinement is shown; Fig. 2e was add 2% Al–5Ti–1B–1RE, the grain of α-Al phase becomes larger and the distribution is more homogeneous. The eutectic silicon phase changes from elongated needle or flake to strip or rod, and the distribution is more concentrated, and the direction is more consistent. The secondary dendrite of

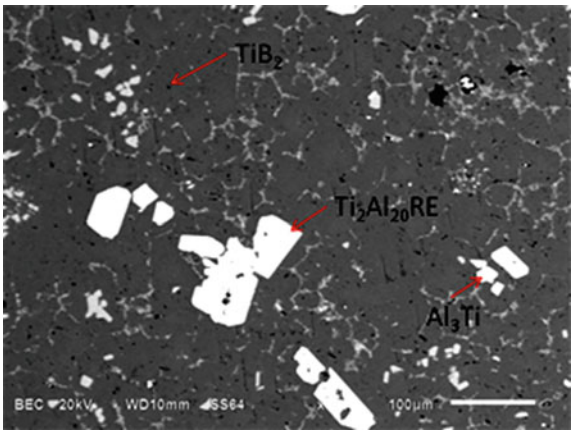

Fig. 1 SEM image of Al–5Ti–1B–1RE master alloy

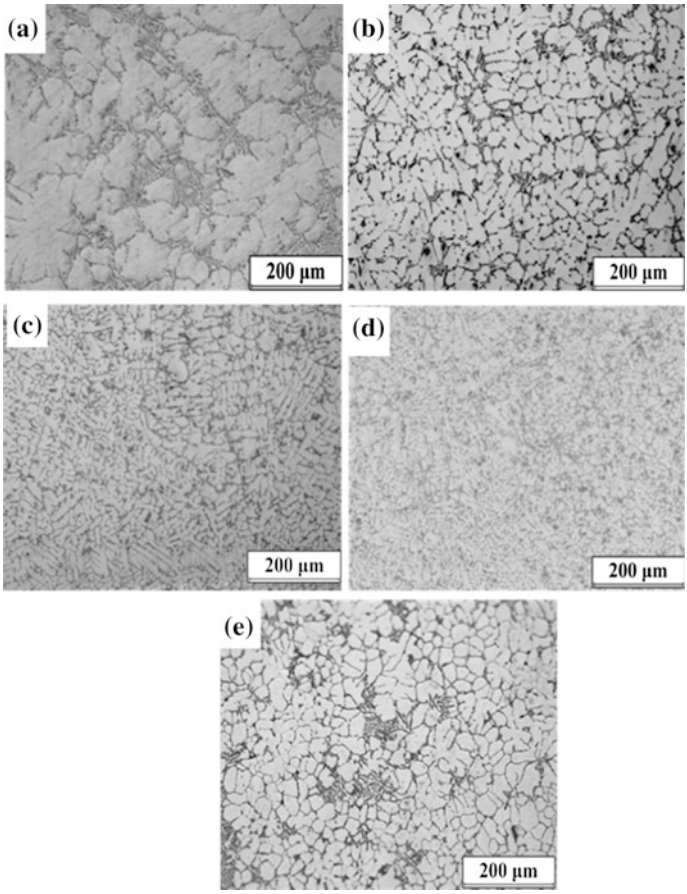

Fig. 2 Macrograph of A357 alloys refined by Al–5Ti–1B–1RE master alloys with different addition levels. **a** A357 **b** 0.2%Al–5Ti–1B–1RE **c** 0.5%Al–5Ti–1B–1RE **d** 1.0%Al–5Ti–1B–1RE **e** 2.0%Al–5Ti–1B–1RE

A357 alloy without addition of master alloy is very coarse. After the addition of the master alloy, the branch of dendrite become thinner, the dendrite microstructure become very fine, and the secondary dendrite spacing decrease obviously.

Analysis and Discussion

When Al–5Ti–1B–1RE alloy added to A357 melt, a large amount of second phase particles Al_3Ti, TiB_2 and $Ti_2Al_{20}RE$ are formed. $Ti_2Al_{20}RE$ compounds is unstable in the melt, quickly decomposed [13] ($L + Ti_2A1_{20}RE \leftrightharpoons \alpha\text{-Al (Ti)} + RE$), release RE atom, can not play the role of nucleation core, the effective nucleation

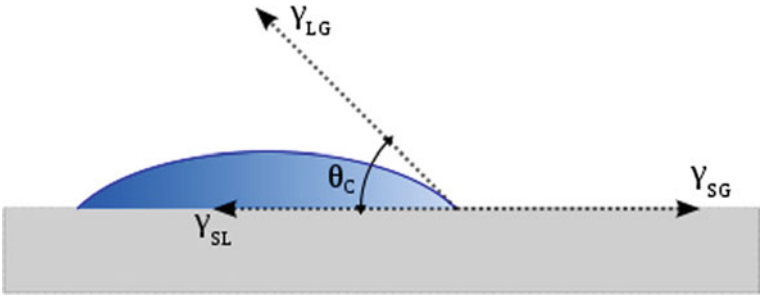

Fig. 3 Schematic diagram of wettability

particles are still $TiAl_3$ and TiB_2. RE is an active element that acts as dispersant, surfactant and catalyst in aluminum melt [14], it is easy to assemble at the crystal interface and phase interface of aluminum melt, increases the wettability of aluminum liquid to Al_3Ti and TiB_2 [15], as Fig. 3 shows that wetting angle (θ_c) becomes smaller. RE elements especially increased the spreading coefficient of aluminum liquid to TiB_2.

RE elements combine with the active point on second phase particles formed a "protective film", hinder particles contact, reduce the surface tension of interface, through coulomb force and steric stabilization to reduce the contact of second phase particles, produce repulsive force, the second phase particles distributed more evenly, difficult to assemble and grow up. Retard the fading time of refiners, make Al–5Ti–1B–1RE refiner has a longer effective time than Al–Ti–B refiner, the refining effect is more stable. At the same time, excess Ti in molten aluminum will cause TiB_2 particles to form more Al_3Ti laminae, thus obtaining more effective nucleation substrates.

In refining process, lots of second nucleation particles were released, the solidification process of the aluminum melt has been changed due to the presence of large number additional nucleation particles, these nucleation particles make the aluminum melt solidified at higher temperature, and higher than the grain growth temperature. After adding the fining agent, the released nucleation particles lead to the formation of new grains in front of grain growth, and these new grains hinder the growth of columnar crystals from the die wall, thus refining the grain structure.

When the addition amount of intermediate alloy reaches 2.0%, large number of Al_3Ti, $Ti_2Al_{20}RE$ and TiB_2 particles were formed, boundaries increased, in order to release the remaining interfacial energy, according to the Ostwald Ripening [16], at the end of primary intermetallic compound nucleation, the particle size always has a certain distribution, larger refiner particles grow further with smaller particles re-dissolving, the number of crystalline nuclear metal compound particles is greatly decreased, while the particle size increased, nucleation particles become larger, result in the enrichment and aggregation of nucleation particles, which reduces the effect of refining, as shown in Fig. 2e.

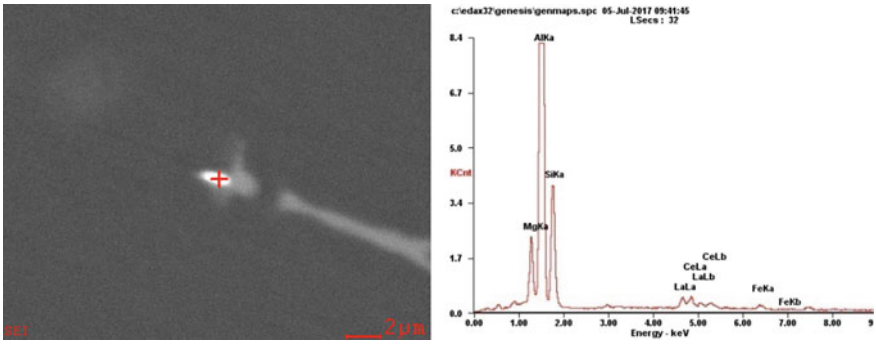

Fig. 4 SEM image of iron rich phase

In addition, it was found that the RE elements react with Fe and Si, produce many small compounds (as shown in Fig. 4), which greatly weaken the influence of iron rich phase. Literature [15] shows that these small compounds can play the role of heterogeneous nucleation. The addition of rare earth elements can lead to degassing and purification of intermediate alloys, guarantees the metallurgical quality of master alloy and aluminum melt [17], further enhance the refinement effect of the refiner.

Conclusion

(1) Add 1.0% Al-5Ti-1B-1RE refiner in A357, the grain is obviously refined, and the effect of dendrite refinement is remarkable.
(2) RE elements enhance the wettability of Al_3Ti and TiB_2 phases, prevent the aggregation and growth of the second phase particles, and delay the fading time of refiners.
(3) RE elements change the morphology of the iron rich phase, and reduce the influence of Fe element on the properties of the alloy.

References

1. F. Songjie, H. Guoqiu, L. Xiaoshan, Mechanical properties and microstructure of A356 aluminum alloy. Trans. Nonferrous Met. Soc. China **60**(4), 5–8 (2008)
2. B.A. Esgandari, B. Nami, M. Shahmiri. Trans. Nonferrous Met. Soc. China **23**(9), 2518 (2013)
3. Z. Jie, Z. Dongqi, W. Pengwei, W. Gang, D. Penglong, Numerical simulation research of investment casting for TiB_2/A356 aluminum base composite. Rare Metal Mater. Eng. **43**(1), 47 (2014)

4. G. Atxaga, A. Pelayo, A.M. Irisarri, Effect of microstructure on fatigue behaviour of cast Al–7Si–Mg alloy. Mater. Sci. Technol. **17**(44), 446–450 (2001)
5. B. Dang, X. Zhang, Y.Z. Chen, C.X. Chen, H.T. Wang, F. Liu, Breaking through the strength-ductility trade-off dilemma in an Al–Si-based casting alloy. Scientific Reports 2016, 6:30874
6. Y. Jiliang, L. Zhongkui, Z. Xin, Microstructural characteristics of TiAI intermetallic compounds prepared by different processes. Rare Metal Mater. Eng. **41**(11), 2054 (2012)
7. L. Yu, X. Liu, Z. Wang, Study on interfacial transition zone of TiC, TiB2/aluminum melt. J. Mater. Sci. **40**, 3865 (2005)
8. C. Yajun, X. Qingyan, H. Tianyou, Microstructure of AI–Ti–B–RE Master Alloy and Its Mechanism of Refining Pure Aluminum. J. Chin. Rare Earth Soc. **25**(5), 597 (2007)
9. U.K. Sotlz, F. Sommer, B.P. Sutttart, Aluminum **3**, 350 (1995)
10. H. Hui, L. Cheng, M. Huaming et al., Study on the preparation of new Mg–50%Al4C3–6%Ce intermediate alloy TiC, TiB2/aluminum melt interfacial transition zone and refinement mechanism of AZ91D alloy. Rare Metal Mater. Eng. **42**(1), 0028 (2013)
11. Z. Fan, Semi solid metal processing. Int. Mater. Rev. **47**(2), 49–85 (2002)
12. X. Tang, J. Peng, F. Huang, D. Xu, R. Du, Effect of mass fraction of mischmetal addition on microstructures of A356 alloy. Chin. J. Nonferrous Metals **1**, 2112–2116 (2010)
13. Y. Lan, The effect of rare earth on the refining property of the AI TI 13 RE intermediate alloy. Foundry Technol. **26**(9), 774–778 (2005)
14. Z. Wang, Research on a new type AI-Ti-B-Re master alloy for grain refiner of commercial pure aiuminum. Foundry Technol. **31**(8), 1021 (2010)
15. G. Fu, W. Chen, K. Qian, Refining effect of a new Al3Ti1B1RE master alloy on Al sheets used for can manufacture and behavior of rare earths in master alloy. J. Chin. Soc. Rare Earths **21**(5), (2003)
16. Z. Wang, Rare Mater. Eng. **41**(2), 577 (2012)
17. H. Chen, G. Fu, H. Liliang, W. Yan, Optimization of elements proportion and roles of RE in AlTiBRE master alloy, Foundry Technol. **57**(5), 436–441 (2008)

Effect of Cobalt on Microstructure and Mechanical Properties of Invar Alloy

Cuixin Chen, Baojun Ma, Sainan Miao and Baoxi Liu

Abstract Due to low coefficient of thermal expansion (CTE), Invar alloy is widely used in Liquefied Natural Gas (LNG) carrier, long distance transmission lines and so on. However, the coarse grain and low hardness restrict the further application. In the present study the samples were prepared by vacuum arc furnace. The effect of cobalt on microstructure and mechanical properties were explored. The results showed that the microstructure without cobalt was mainly composed of coarse columnar crystals with heterogeneous dimension distribution, and average grain area was 289 μm × 189 μm. For the sample with 0.2 wt% cobalt the microstructure was more uniform and the average grain area was 260 μm × 166 μm. In addition, lots of cellular substructure formed in the columnar dendrite with different shapes dislocation etch pits. The CTE decreased with the addition of cobalt, especially when the content of cobalt was 0.2 wt%. Compare to the sample without cobalt the microhardness with cobalt addition of 0.2 and 4 wt% are 193 and 170 HV, increased by 25 and 10% respectively. It can be concluded that the microstructure and mechanical properties can be changed by controlling the content of cobalt under the condition of rapidly cooling condition.

C. Chen (✉) · B. Ma · S. Miao
School of Materials Science and Engineering, Hebei University of Technology, Tianjin 300130, China
e-mail: karenccx@126.com

B. Ma
e-mail: 1255816583@qq.com

S. Miao
e-mail: 15225143723@163.com

C. Chen · B. Liu (✉)
Tianjin Key Laboratory of Laminating Fabrication and Interface Control Technology for Advanced Materials, Hebei University of Technology, Tianjin 300130, China
e-mail: liubaoxiliubo@126.com

C. Chen · B. Liu
Research Institute for Equipment Materials, Hebei University of Technology, Tianjin 300130, China

© Springer Nature Singapore Pte Ltd. 2018

Y. Han (ed.), *Advances in Materials Processing*, Lecture Notes in Mechanical Engineering, https://doi.org/10.1007/978-981-13-0107-0_84

Keywords Invar alloy · Vacuum arc melting · Crystalline organization
Grain area · Hardness

Introduction

Due to the lower average coefficient of thermal expansion (CTE) and good dimensional stability in a wide temperature range. Invar alloy has been widely used in precise instruments and cryogenic liquid storage such as Liquefied Natural Gas (LNG) carrier and moulds for aircraft [1–5]. However, cracks easily occur for a large amount of coarse columnar crystals in invar alloy. Adding alloy elements of titanium and manganese into invar alloy can solve this problem, but that have a bad effect on CTE [6, 7]. In addition, the low strength also limits the further use of the invar alloy [8]. So how to reduce the expansion coefficient of invar alloy with high strength has been paid more attention. Alloy elements were used to enhance the properties of Invar alloy in last few decades. The addition of W + Nb can refine microstructure and increase hardness, Ti and Al can improve the tensile strength but increase the CTE [9–12]. Most of the researches indicated that although alloy element additives can improve strength and hardness, it is inevitable to increase the CTE of Invar alloy simultaneously. C. E. Guillaume made it clear that the addition of some alloying elements, such as C, Mn, Cu, Cr, increased the CTE of Invar alloy [13].

As a ferromagnetic element, Ni has great effect on the expansibility of the alloy, and owing to the same characteristic, cobalt was used to replace Ni in our study. The samples with different cobalt content were prepared by vacuum arc melting. The purpose is to analyze the effect of cobalt on crystal structure, CTE and mechanical properties of invar alloy under rapid cooling.

Experimental Procedures

Invar alloys with different contents of cobalt, no cobalt added (alloy 1), 0.2 wt% (alloy 2), and 4 wt% (alloy 3) were melt in Vacuum arc furnace with the current of 150A and the holding time of 35 s under the argon circumstances. In order to ensure the composition uniformity, the samples were flipped and melted twice. The prepared samples were button-like samples and the diameter is about 2 cm. The chemical composition of the used Invar alloy is shown in Table 1.

Table 1 Chemical composition of the used Invar alloy (wt%)

Ni	Mn	Si	P	C	S	Fe
36.021	0.031	0.010	0.006	0.006	0.002	Bal.

After smelting, the samples were cut to cylinder with dimension Φ6 mm × 12 mm. DIL 402 thermal expansion instrument were used to measure CTE. The heating rate of this experiment was 3 °C/min, and the range of temperature was from 25 to 500 °C. The metallographic samples were polished and then etched by supersaturated ferric chloride solution for 15 s. LEICA, ICC50W, EVO MA15 scanning electron microscope (SEM) equipped with energy dispersive spectra (EDS) were used for the observation of morphology. The microhardness was tested on HMV-2T microscopic hardness meter with the load of 980 mN for 10 s. At least 10 points were selected randomly with the distance more than 500 μm to avoid the work hardening effect.

Results and Discussion

Effect of Cobalt on the Formation of Precipitates and Dislocations

Usually, dislocations form easily under the condition of deformation for metal material [14, 15]. However, in this study, a large quantity of the etch pits were obtained for the prepared invar alloy under rapid cooling process (as shown in Fig. 1). The shapes of dislocation etch pits are related to crystal type and crystal face. For invar alloy, the microstructure is face-centered austenite and the dislocation etch pits with different shapes are observed in different crystal faces. The shape in {111} crystal faces is a regular triangle and a rectangular in the {110} lattice planes (as shown in Fig. 2).

From Fig. 2, it can be found that the density of etch pits increase first and then drop with the increase of cobalt content (as shown in Fig. 2a–c). And the dislocation density is higher for the sample with 0.2 wt% cobalt addition (as shown in

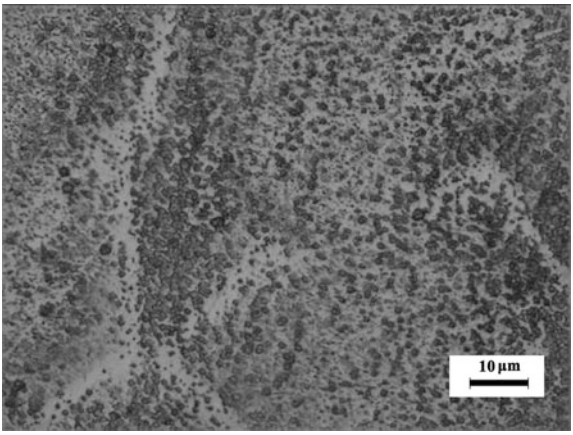

Fig. 1 Microstructure of etch pits

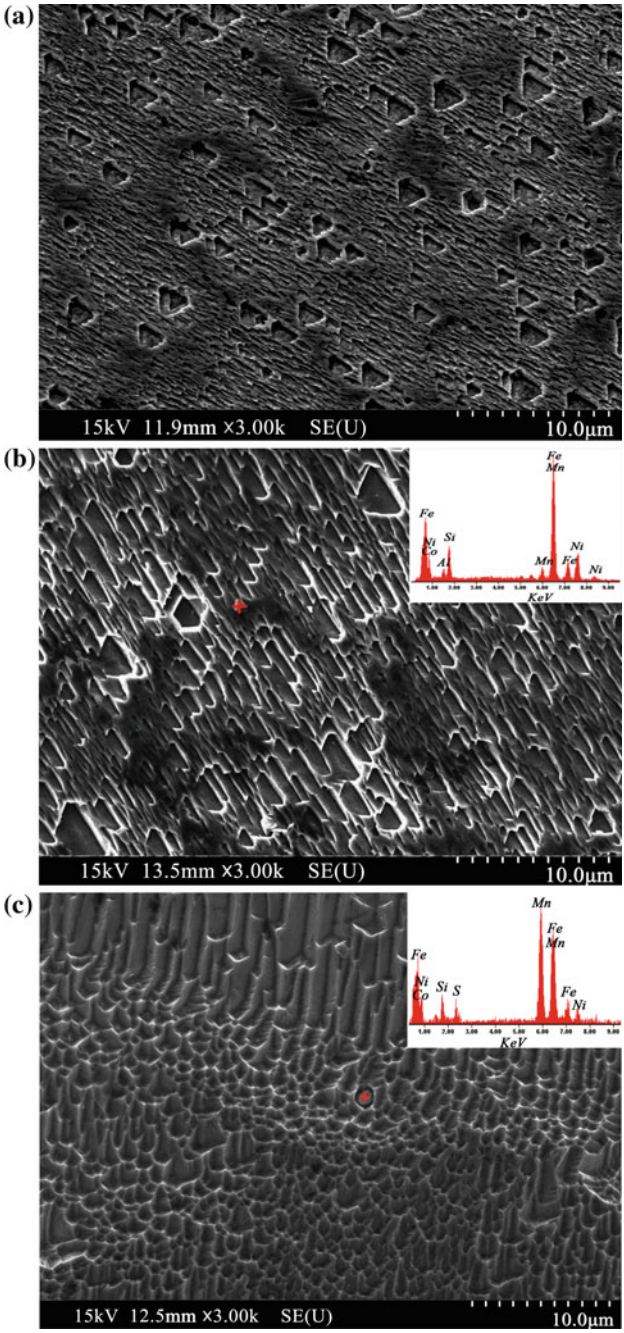

Fig. 2 Microstructure and precipitate evolution of alloys with different content of cobalt: **a** without cobalt (alloy 1); **b** 0.2 wt% cobalt (alloy 2); **c** 4 wt% cobalt (alloy 3)

Fig. 2b). Though the dislocation density in the alloy 3 reduces, it is still higher than the alloy 1 (as shown in Fig. 2c). Spherical or spherical-like Co–Ni–Si–Mn–Fe, Co–Ni–Si–Mn–S–Fe precipitates appear in alloy 2 and alloy 3. And the amount of precipitation in alloy 3 is higher than that of alloy 2.

The precipitate phases hinder the migration of dislocations, which lead to the increase of the density of dislocations. As the dislocation is the abnormal arrangement of atoms, there will appear a number of etch pits under the action of etching solution.

The Evolution of Microstructure of Invar Alloy

The constitutional undercooling has a great effect on the evolution of crystal microstructure. In this experiment, the solute concentration the addition of cobalt, lead to the change of the constitutional undercooling for the change of the solute concentration, resulting in different microstructure morphology. The results are shown in Fig. 3. The grains with a cellular substructure [2] are almost polygonal

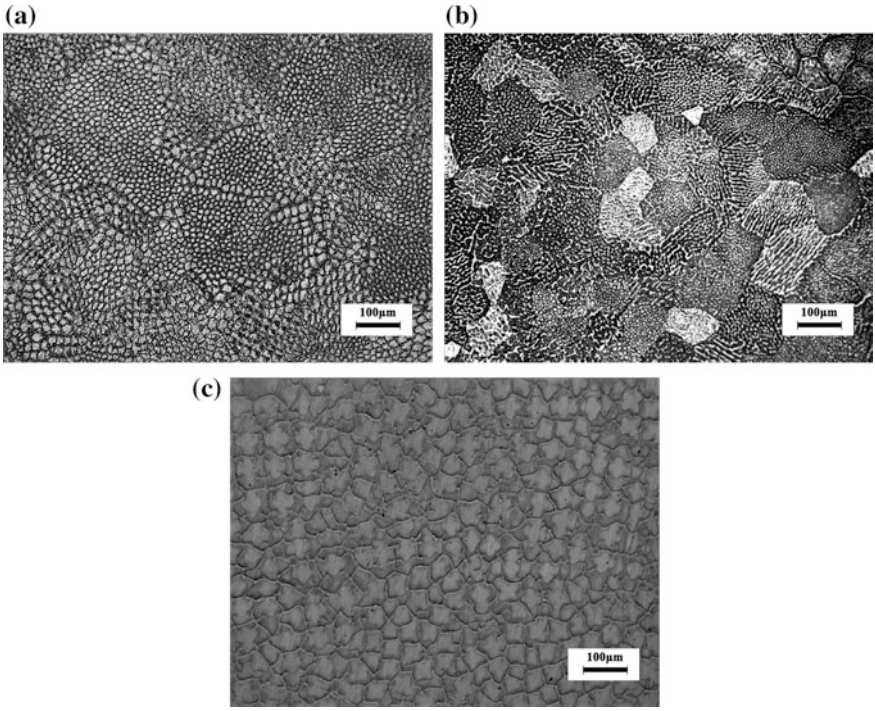

Fig. 3 Grain area evolution of alloys with different content of cobalt: **a** without cobalt (alloy 1); **b** 0.2 wt% cobalt (alloy 2); **c** 4 wt% cobalt (alloy 3)

and can be near to quadrilateral to measure the grain area. Figure 3 shows the evolution of microstructures of invar alloy with different cobalt content. The average grain area is 289 μm × 189 μm with uneven area distribution with no cobalt added (as shown in Fig. 3a) and the minimum grain area is 98 μm × 55 μm. In addition, cellular substructures in the grain can be seen obviously and it is evenly distributed inside the grain with a quite different area. With 0.2 wt% cobalt added (as shown in Fig. 3b), the grain area decreased with distribution homogeneously and the average grain area is 260 μm × 166 μm. Besides, cellular substructures became even finer.

Under the same etching conditions, it is difficult to observe the grain boundaries of the original grains with 4 wt% cobalt added (as shown in Fig. 3c), and the observed substance are replaced by well-area distributed cellular substructure, and the area of the cellular substructure is 87 μm × 57 μm. Due to the large amount of cobalt, the precipitated phase formed is larger (as shown in Fig. 2b, c), which is detrimental to refine the microstructure.

Generally, there are two kinds of nucleation mechanisms [16] in the process of solidification: homogeneous nucleation and non-homogeneous nucleation. The critical nucleation energy required for spontaneous nucleation non-spontaneous nucleation can expressed as E_k and E'_k respectively. The relationship between the E_k and E'_k can be expressed by the following equation

$$E'_k = \frac{1}{4} E_k \left(2 - 3\cos\theta + \cos^3\theta\right) \tag{1}$$

In which θ is wetting angle, it is obvious that the E'_k is lower than E_k and the former is the main form of nucleation. Cobalt is a high melting point (1495 °C). It can be seen from part 3.1 that the addition of cobalt can promote the formation of Co–Ni–Si–Mn–Fe or Co–Ni–Si–Mn–S–Fe precipitate, which can act as the non-homogeneous nucleation sites, which reduces the critical nucleation energy, and the number of effective core is improved, result in microstructure refinement. In addition, precipitation phase can hinder the movement of grain boundaries which plays a role in refining the microstructure.

It may be due to the addition of more cobalt in alloy 3, which has a great influence on the constitutional undercooling, so that it has a great influence on the microstructure, which has a great difference from other two samples. And the size of precipitate is too large to refine the microstructure.

CTE and the Microhardness

The CTE is measured by DIL 402 thermal expansion instrument. According to the ASTM E228-11, the CTE can be expressed by Eq. 2.

$$\overline{\alpha} = \frac{dL}{dT}\frac{1}{L_0} \tag{2}$$

where $\overline{\alpha}$ is CTE within a certain temperature range, dL is the dimension change, dT is the temperature difference, and L_0 is the original length of the sample. Taking into account the measurement error, it is needed to correct the measurement results. The correction coefficient is A_{Ti} [17].

$$A_{Ti} = [(\frac{\Delta L}{L_0})_t - (\frac{\Delta L}{L_0})_m]_{T_i} \tag{3}$$

where the $(\frac{\Delta L}{L_0})$ is true certified expansion of the sample, $(\frac{\Delta L}{L_0})_m$ is the measured certified expansion, T_i is the temperature at the length of L_i. So the CTE can be calculated by

$$[\overline{\alpha}]_{Ti} = \frac{1}{\Delta T}[(\frac{\Delta L}{L_0})_m + A]_{Ti} \tag{4}$$

According to the above equation, the measured CTEs of the three samples are shown in Fig. 4.

It can be seen from the figure that cobalt has a significant effect on CTE of the experimental material. The CTE value of alloy 1 is the highest in the measured temperature range. The CTE decreased with the addition of the cobalt content,

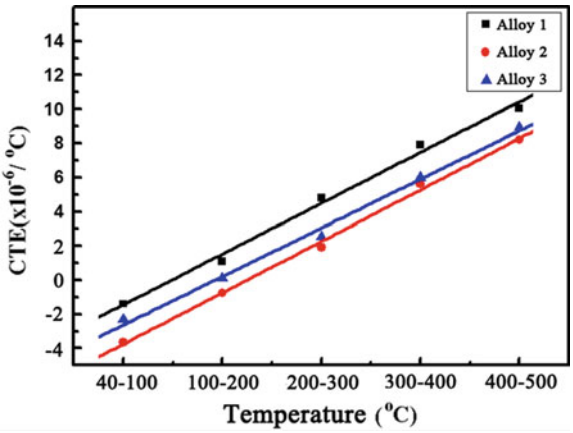

Fig. 4 Average CTEs of the alloys

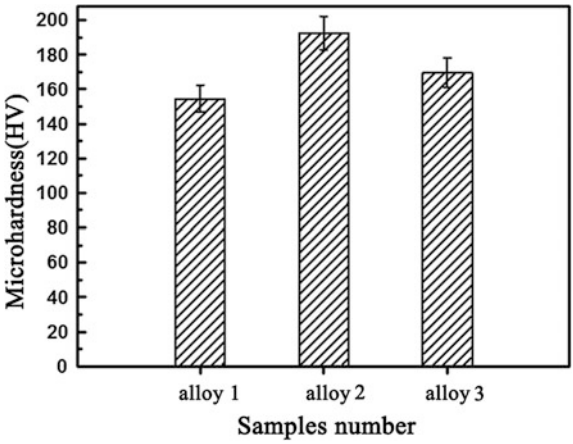

Fig. 5 Microhardness of the alloys

especially for the alloy 2, its CTE is lower and is negative from room temperature to 253 °C.

Figure 5 shows the measured microhardness. Compared to the alloy 1, the microhardness of alloy 2 is 193 HV, increasing by 25%, and the value of alloy 3 is 170 HV, increasing by 10%.

From the above results it can be found that the microhardness is positively correlated with the evolution of dislocation density. The dislocations are helpful for improving microhardness of Invar alloy. Higher dislocation density inside the matrix results in greater ability to resist deformation, and eventually leads to the higher hardness measured.

Summaries

1. Samples prepared under the rapid cooling conditions have a large number of dislocation pits after polished and etched without any deformation treatment. The density of dislocation pits has a close relationship with the content of cobalt. The number of dislocation pits reaches the peak highest with 0.2 wt% cobalt addition.
2. Cobalt can affect microstructure. For invar alloy without cobalt addition, the microstructure is composed of coarse columnar grains and the average grain area is 289 μm × 189 μm. Compared to the sample without cobalt, the grain area of sample with 0.2 wt% cobalt is 260 μm × 166 μm, with homogeneous area distribution. Fine cellular substructure form in sample with 4 wt% cobalt, and the area of the cellular substructure is 87 μm × 57 μm. In addition, Co–Ni–Si–Mn–Fe, Co–Ni–Si–Mn–S–Fe spherical or spherical-like precipitated phase appeared in the samples with cobalt addition.

3. Compared to the sample without cobalt, the CTE reduces with the addition of the cobalt. The CTE reduces more obviously with the addition of 0.2 wt% cobalt.
4. Microhardness of the matrix is improved with the addition of cobalt, the microhardness of sample with 0.2 and 4 wt% cobalt are 193 and 170 HV, increasing by 25 and 10%, respectively.

Acknowledgements The present authors are thankful for the financial support provided by National Natural Science Foundation of China (No 51304059).

Author Contributions

C. X. Chen: designing the experiment approach and executing part of the experiment processing; B. J. Ma: executing most part of the experiment processing; S. N. Miao: for mechanical property test; B. X. Liu: for theoretical analysis.

Conflicts of Interest

The authors declare no conflict of interest.

References

1. G.V. Adamova, V.M. Bukhanova, J.S. Colligonb, K.F. Minnebaeva, A.A. Nasretdinova, L.B. Shelyakina, V.E. Yurasovaa, EYu. Zykovaa, Secondary ion emission of Fe–Ni alloys in the temperature range including the curie point. Vacuum **73**, 47–52 (2004)
2. J.L. Corbacho, J.C. Suárez, F. Molleda, Grain coarsening and boundary migration during welding of invar Fe-36Ni alloy. Mater. Charact. **41**, 27–34 (1998)
3. S.W. Choi, J.U. Roh, M.S. Kim, W.I. Lee, Analysis of two main LNG CCS (cargo containment system) insulation boxes for leakage safety using experimentally defined thermal properties. Appl. Ocean Res. **37**, 72–89 (2012)
4. Y. Zhao, Y.S. Sato, H. Kokawa, A.P. Wu, Microstructure and properties of friction stir welded high strength Fe-36 wt%Ni alloy. Mater. Sci. Eng., A **528**, 7768–7773 (2011)
5. M. Inaba, Y. Honma, T. Hatanaka, Y. Otake, Effects of the annealing conditions on the oxidation behavior of Fe-36 Ni alloy. EAPPl. Surf. Sci. **27**, 164–179 (1986)
6. B. Mintz, S. Vue, J.J. Jonas, Hot ductility of steels and its relationship to the problem of transverse cracking during continuous casting. Int. Mater. Rev. **36**, 187–217 (1991)
7. Y. Maehara, K. Yasumoto, H. Tomono, T. Nagamichi, Y. Ohmori, Surface cracking mechanism of continuously cast low carbon low alloy steel slabs. J. Mater. Sci. Technol. **6**, 793–806 (2013)
8. J.M. Nan, G.X. Li, K.W. Xu, Yielding behavior of low expansion invar alloy at elevated temperature. J. Mater. Process. Technol. **114**, 36–40 (2001)
9. J.F. Zhang, Y.F. Tu, J. Xu, J.S. Zhang, J.L. Zhang, Effect of solid solution treatment on microstructure of Fe-Ni based high strength low thermal expansion alloy. J. Iron. Steel Res. Int. **15**, 75–78 (2008)
10. W. Chao, S.Q. Yuan, Z.J. Wang, Z.P. Feng, Effects of W + Nb on thermal expansion property and microhardness of Fe-Ni invar alloy. Rare Metal. Mat. Eng. **43**, 460–464 (2014)
11. Y.C. Yu, W.G. Chen, H.G. Zheng, Effects of Ti-Ce refiners on solidification structure and hot ductility of Fe-36Ni invar alloy. J. Rare Earth. **31**, 927–932 (2013)

12. S.H. Wang, J.T. Guo, W.H. Lai, Y.L. Ge, M.H. Tan, H. Li, Microstructure and mechanical properties of Fe-Ni-Co-Base superalloy after long-term aging at 650 °C. Acta Metall. Sin. **4**, 194–198 (1991)
13. C.E. Guillaume, The anomaly of the nickel-steels, J. Franklin I. **191**, 374–404 (1919)
14. D.Z. Lu, M.J. Wu, Observation of etch pits in Fe-36 wt%Ni Invar alloy. Int. J. Min. Met. Mater. **21**, 682–686 (2014)
15. I. Retat, T. Steffens, C. Schwink, Dislocation arrangement in FeNi-Invar single crystals. Phys. Status Solidi **92**, 507–510 (2010)
16. W.Y. Zhang, Basic principles of welding metallurgy, in *Molten Pool Solidification And Weld Solid Phase Transition* ed. by W. Y. Zhang (Mechanical Industry Press, Beijing, 2003), pp. 116–118
17. G. Li, M. Gao, C. Chen, C. Zhang, X.Y. Zeng, Characterisation comparison of laser and laser-arc hybrid welding of Invar 36 alloy. Sci. Technol. Weld. Joining **19**, 30–37 (2014)

Effect of Melt Treatment on Fe-Rich Phase in Al–25Si–2Fe–2Mn Alloy

Fan Xiao, Lu Li, Rongfeng Zhou, Yongkun Li, Yehua Jiang and Dehong Lu

Abstract The Al–25Si–2Fe–2Mn alloy melt was treated by using electromagnetic stirring, cooling slope and spray deposition technologies, respectively. By using various methods including SEM, EDS, XED and TEM, the solidification microstructure of Al–25Si–2Fe–2Mn alloys and the separation behavior and crystal structure of Fe-rich phase under different treatment modes of melts were analyzed. The result showed that under the three treatment modes, the hard phases in the microstructure of Al–25Si–2Fe–2Mn were all refined at different degrees. Among them, spray deposition yielded had the best refining effect, where the primary Si with the average diameter of about 5 μm were shown as tiny particles while granular Fe-rich phases with the average diameter of about 7 μm were dispersed into the microstructure. For the microstructure treated by cooling slope, the primary Si particles and the blocky Fe-rich phase exhibited the average diameters of about 30 and 40 μm, respectively and some Fe-rich phases were centered on the primary Si particles. In comparison, the electromagnetic stirring presented the worst refining effect. The primary Si particles, mainly appeared as blocks, showed an average

F. Xiao · L. Li (✉) · R. Zhou · Y. Li · Y. Jiang · D. Lu
Faculty of Material Science and Engineering, Kunming University of Science and Technology, Kunming 650093, China
e-mail: liluKust@126.com

F. Xiao
e-mail: 935836680@qq.com

R. Zhou
e-mail: zhourfchina@hotmail.com

Y. Li
e-mail: 717309098@qq.com

Y. Jiang
e-mail: 1742944769@qq.com

D. Lu
e-mail: ldhongkust@126.com

L. Li · R. Zhou
Research Center for Analysis and Measurement, Kunming University of Science and Technology, Kunming 650093, China

© Springer Nature Singapore Pte Ltd. 2018

Y. Han (ed.), *Advances in Materials Processing*, Lecture Notes in Mechanical Engineering, https://doi.org/10.1007/978-981-13-0107-0_85

diameter of about 50 μm and the blocky Fe-rich phase exhibited an average diameter of about 30 μm. In addition, some Fe-rich phases were bonded with the primary Si particles to distributed in the neighbor of latter. When the two materials were regarded as a whole, the average diameter were measured to be about 100 μm. Fe-rich phases treated by using the three treatment modes of melts were all stable α-$Al_{15}(Fe,Mn)_3Si_2$ phases, but their in the alloys undergoing different treatments shows significantly different morphologies and distributions.

Keywords Electromagnetic stirring · Cooling slope · Hypereutectic Al–Si alloys Fe-rich phase · Crystal structure

Introduction

Hypereutectic Al–Si alloys exhibit low thermal expansion coefficients, excellent wear resistance, and high hardness. Thus, they have been widely used to make wear resistant components in the automotive industry [1]. The addition of Fe to the hypereutectic Al–Si alloys can form Fe-contained intermetallic compounds (IMCs), which can improve the thermal stability. [2]. However, the IMCs with Fe (such as δ-Al_4FeSi_2 and β-Al_5FeSi) cast under conventional conditions are separated out in the long acicular shape, which cuts apart the alloy matrix and thereby greatly reduces the mechanical properties [3]. Mn in Al–Si–Fe alloy system is mainly used to neutralize acicular Fe-rich phase and improve the stability and corrosion resistance of hypereutectic Al–Si alloys at high temperature [4–10]. The research group led by Lin et al. [11] in Huazhong University of Science and Technology investigated the influence of additive amounts of Mn on the Fe-rich phase in the ultrasonically treated hypereutectic Al–Si alloys with 2% Fe. The result revealed that as the additive amount of Mn rises to 0.8%, the Fe-rich phase in the conventionally cast hypereutectic Al–Si alloys appear as Chinese script or granules from acicular or platy shapes. Moreover, Cai et al. [12] in University of Science and Technology Beijing studied the effect of Mn and Cr elements on the microstructures of spray-deposited hypereutectic Al–Si alloys containing Fe. The result illustrated that acicular Fe-rich phase can be transformed into granular Fe-rich phase under the effect of Mn and Cr. Moreover, Zhang et al. [13] studied the influence of Mn on Fe phase in spray-deposited hypereutectic Fe-containing Al–Si alloys. They found that when the ratio of Mn to Fe is 0.83 or 1, the Fe-rich phase in the alloys can appear in the form of α-$Al_{15}(Fe,Mn)_3Si_2$. Huang et al. [14] explored the effect of different ratios of Mn to Fe (mass ratio) on the microstructure of Fe-rich phase in solidification structures of cast Al–25Si–xFe–yMn alloys. They suggested that when the ratio of Mn and Fe is 1, the acicular Fe-rich phase is totally transformed into α-$Al_{15}(Fe,Mn)_3Si_2$ phase with dendritic crystals. To sum up, it can be seen that hypereutectic Al–Si alloys containing Fe and Mn are greatly influenced by the cooling rate and the morphologies and types of Fe-rich phase change under different solidification modes.

The Al–25Si–2Fe–2Mn alloy melts were treated by using electromagnetic stirring, Cooling slope and spray deposition technologies. Then, the authors analyzed the influence of different treatment modes of melts on morphology, size, quantity and distribution uniformity of primary Si, eutectic Si, and Fe-rich phase in Al–25Si–2Fe–2Mn alloys. Moreover, the influence of different solidification modes on microstructure, type, separation and crystal structure of Fe-rich phases in the solidification structure of Al–25Si–2Fe–2Mn alloys were systematically investigated. It provides a theoretical and practical basis for refining and improving the morphologies of primary Si and Fe-rich phases.

Experimental

The Al–25Si–2Fe–2Mn alloys were prepared by using Al–25Si–2Fe alloys and Mn agent with the content of 75% (*w*%). The alloy was smelted by using the resistance furnace. After the Al–25Si–2Fe alloys were heated to 850 °C in the furnace and completely fused, the Mn agents were added into the melts in batches and the mixture was fully stirred. After being preserved at the temperature for 30 min, C_2Cl_6 was added into the mixture for degassing and slag-skimming to obtain Al–25Si–2Fe–2Mn alloy melts, which was poured into the metal mold to attain square blanks (about 20 kg) after being cooled to 800 °C. The liquidus and solidus temperatures of the alloys were 770 and 570 °C, respectively measured through DSC.

The alloy melts were treated by using electromagnetic stirring, Cooling slope and spray deposition technologies. The electromagnetic stirring was carried out by using the self-made electromagnetic stirrer with a heating system and a cooling system for protecting coils. The solidification rate of melts inside the stirrer can be adjusted by using the heating system while the stirring force was regulated by adjusting the input currents (shown in Fig. 1a). The specific implementation steps were displayed as follows: the alloy melts obtained through smelting (superheat degree of about 30 °C) were rapidly poured into the stainless steel crucible preheated to 800 °C and then the crucible with melts was transferred to the stirring cavity of electromagnetic stirrer. Subsequently, the temperature of melts in the crucible was measured by using the K-thermocouple and then the melts were stirred at room temperature and the power was turned on until the temperature of melts were close to the liquidus. The input current of the stirrer was 25 A and the melts were rapidly poured into the high-purity graphite crucible to be cooled and cut into specimens for observation after the temperature of melts reached to the semi-solid range 690 °C of alloys.

Cooling slope casting process was completed by using the s unitized type cooling plates (shown in Fig. 1b). The upper and lower parts of the inclined plate were made of ordinary steel and high-purity graphite, respectively. The molten metal dropped to the lower graphite flowing through the upper steel plate under the effect of gravity and finally entered into the crucible. Learning from previous experience, the original casting temperature of melts was 790 °C while the inclined

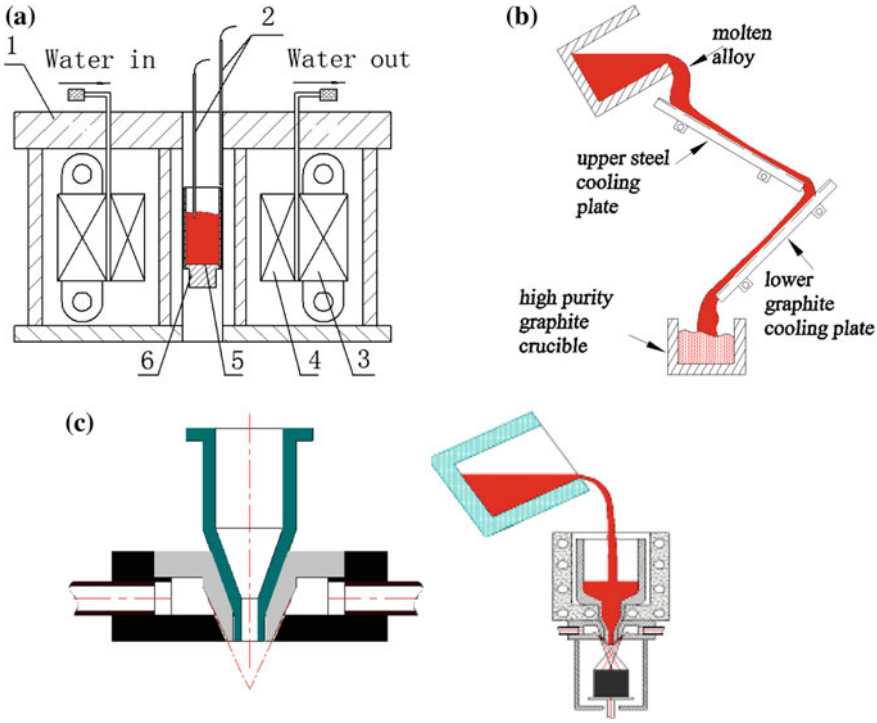

Fig. 1 **a** Electromagnetic stirring structure schematic 1. cover, 2. K-type thermocouple, 3. three phases AC coil, 4. resistance heater, 5. molten Al alloy, 6. stainless steel crucible **b** CS casting unit used in the present work 1. graphite crucible, 2. metallic solution, 3. inclined plate, 4. pin, 5. graphite crucible, 6. gas protection case **c** schematic diagram of the spray equipment and nozzle

angles of the upper steel plate and the lower graphite were 30° and 50°, showing the effective length of each plate was 300 mm. Under this condition, the primary tiny Si particles in a regular shape can be obtained.

A single-deck and cellular air-blast atomizing nozzle (Fig. 1c) were applied in spray deposition treatment. The high-purity nitrogen was used as atomizing gas and the reception distance was 600 mm. The pressure of atomizing gas was controlled in the range of 0.4–0.6 MPa and superheat degree of melts was limited about 200 °C. By using the process, the final yield of the alloy was 70%.

The specimens treated through different methods were corroded by etching 0.5% HF aqueous solution after coarsening, grinding and polishing. Next, the microstructure of the specimens was analyzed by using the optical microscope (Leica), the TESCAN VEGA3 SBH scanning electron microscope (SEM), the energy dispersive spectrometer (EDS) (Thermal), the transmission electron microscope (TEM) (TecnaiG2 F30 S-TWIN) and the X-ray diffractometer (XRD, D/max-3B, Ricoh Co). The solidus and liquidus of alloys were measured by employing the simultaneous thermal analyzer (NETZSCH STA 499F3).

Results and Discussion

Effect of Electromagnetic Stirring on Microstructure of Al–25Si–2Fe–2Mn Alloys

Figure 2 displays the microstructure of Al–25Si–2Fe–2Mn alloys separately prepared through conventional casting and electromagnetic stirring. Figure 2a displays the solidification structure of conventionally cast Al–25Si–2Fe–2Mn alloys. The primary Si particles showed an average diameter of about 60 ± 10 μm and Fe-rich phase exhibited poor distribution uniformity, parts of them were shown as irregular polygon or slender particles and others appeared in the shape of coarse fishbone (see remarks in the figure). Fe-rich phase shown as blocky irregular polygon exhibited an average diameter of about 40 μm while the remarked structure appeared in the shape of coarse fishbone had the overall length and width of about 100 and 30 μm, respectively. The solidification structure of Al−25Si–2Fe–2Mn alloy prepared through electromagnetic stirring is shown in Fig. 2b. The primary Si particles, mainly found to be blocks, showed an average diameter of about 50 μm. The black Fe-rich phase was shown as blocks and parts of Fe-rich phase with the average diameter around 30 μm were attached to the depression of primary Si particles and distributed in the neighbor of primary Si particles. The primary Si particles and Fe-rich phase bonded together were regarded as a whole whose average diameter was measured to be about 100 μm.

The XRD pattern of Al–25Si–2Fe–2Mn alloys obtained through electromagnetic stirring is shown in Fig. 3a. The result shows that Al–25Si–2Fe–2Mn alloys prepared through electromagnetic stirring contain α-Al, Si, δ-Al_4 $(Fe,Mn)Si_2$ and α-$Al_{15}(Fe,Mn)_3Si_2$. There is only one diffraction peak of δ-$Al_4(Fe,Mn)Si_2$ phase in the XRD pattern of alloys while α-$Al_{15}(Fe,Mn)_3Si_2$ phase exhibits numerous

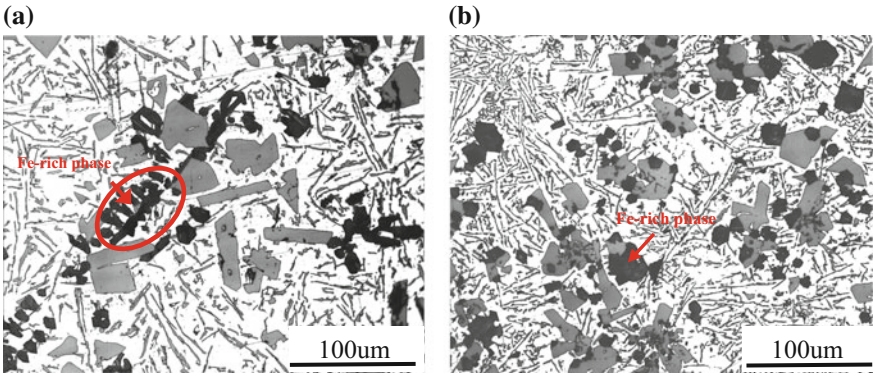

Fig. 2 As-cast and EMS microstructures of Al–25Si–2Fe–2Mn alloy. **a** Without EMS; **b** with EMS

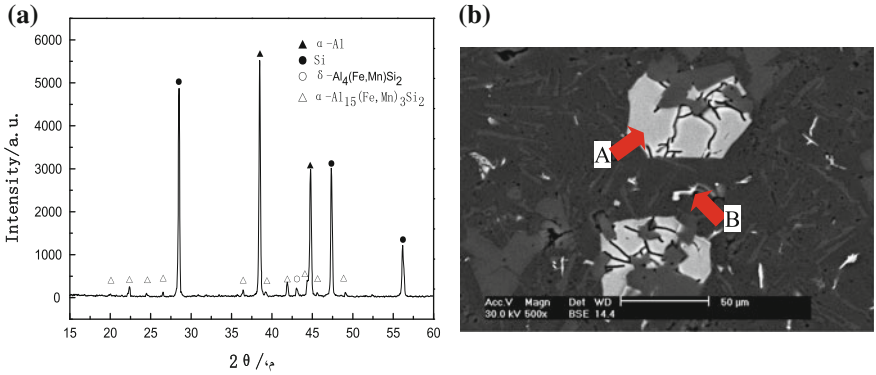

Fig. 3 XRD pattern **a** and BSE **b** image of Al–25Si–2Fe–2Mn alloy treated by EMS (**b**)

Table 1 EDS results of Al–22Si–2Fe–2Mn alloys treated by EMS

Phase marked	Al (%)	Si (%)	Fe (%)	Mn (%)	Mn/Fe
"A"	70.35	12.96	08.38	08.32	$Al_{12.63}(Fe,Mn)_3Si_{2.33}$
"B"	77.26	8.57	12.14	1.77	$Al_{16.65}(Fe,Mn)_3Si_{1.85}$

diffraction peaks. It indicated that the Fe-rich phase of the solidification structure of alloy prepared through electromagnetic stirring was mainly shown as α-Al_{15} (Fe, Mn)$_3Si_2$ phase.

Figure 3b displays the blocky Fe-rich phase in the solidification structure of Al–25Si–2Fe–2Mn alloys attained through electromagnetic stirring. In the BSE image of the solidification structure of Al–25Si–2Fe–2Mn alloys through electromagnetic stirring, the blocky light-white Fe-rich phase was marked as A, on the surface of which plenty of cracks are found. The Fe-rich phase shown as tiny Chinese script shape mostly distributed in eutectic structure was marked as B (Fig. 3b) and the EDS results of the two kinds of Fe-rich phases are displayed in Table 1. The result shows that the molecular formula of regular blocky and tiny Chinese-character Fe-rich phases obtained are $Al_{12.63}(Fe,Mn)_3Si_{2.33}$ and $Al_{16.65}(Fe,Mn)_3Si_{1.85}$ according to the atomic percent, respectively. The molecular formula of the two kinds of Fe-rich phases are close to α-$Al_{15}(Fe,Mn)_3Si_2$ phase.

A few of slender Fe-rich phases are found in the solidification structure of conventionally cast Al–25Si–2Fe–2Mn alloys, and analyzed in terms of element area distribution (Fig. 4). Obviously, it can be seen that the outer sphere of the slender Fe-rich phase covers the inner sphere. Figure 4b–e show the distributions of Al, Si, Mn and Fe in slender Fe-rich phase. By analyzing the scanning result of element area, Al is mostly distributed in outer sphere of slender Fe-rich phase and slightly in the inner sphere while Si is opposite to Al. Moreover, Fe and Mn elements are basically equivalent in the inner and outer spheres of slender Fe-rich phase.

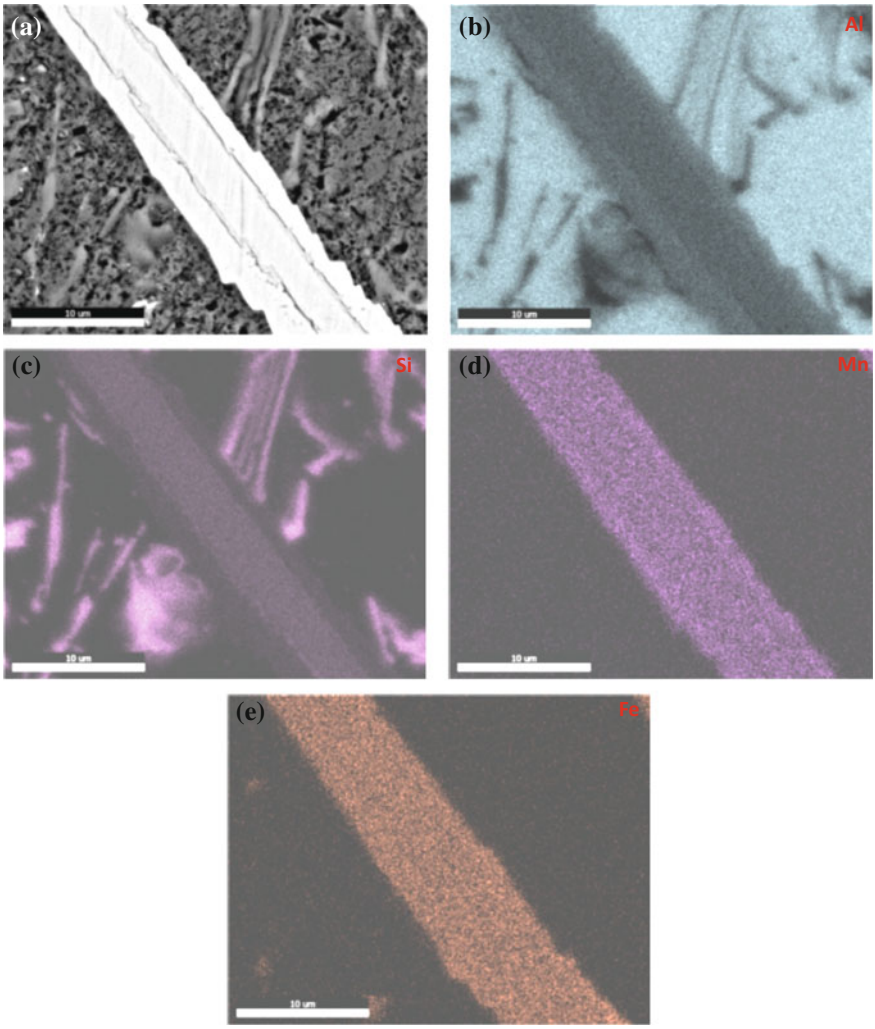

Fig. 4 Area scanning image of rod-like Fe-rich phases in conventional casting Al–25Si–2Fe–2Mn alloy

Additionally, EDS point analysis is conducted on the inner and outer spheres of slender Fe-rich phase (shown in Fig. 5). The calculated molecular formula of point A is $Al_{3.67}(Fe,Mn)Si_{1.85}$ based on atomic percent, which is close to that of pδ-$Al_4(Fe,Mn)Si_2$ phase. The calculated molecular formula of point B is $Al_{12.27}(Fe,Mn)_3Si_{1.99}$ based on atomic percent, which is close to that of α-$Al_{15}(Fe,Mn)_3Si_2$ phase. It can be seen that inner δ-$Al_4(Fe,Mn)Si_2$ phase is packed by outer α-$Al_{15}(Fe,Mn)_3Si_2$ phase. Furthermore, it can be speculated that δ-$Al_4(Fe,Mn)Si_2$ phase is likely to transform into α-$Al_{15}(Fe,Mn)_3Si_2$ phase during solidification.

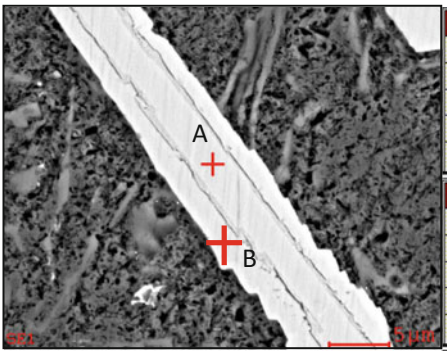

Element	Wt%	At%
AlK	47.94	56.25
SiK	25.21	28.42
MnK	11.44	06.59
FeK	15.42	08.74
Matrix	Correction	ZAF

Element	Wt%	At%
AlK	59.98	71.19
SiK	10.08	11.50
MnK	14.53	08.47
FeK	15.41	08.84
Matrix	Correction	ZAF

Fig. 5 EDS results of rod-like Fe-rich phase

Effect of Cooling Slope on Microstructure of Al–25Si–2Fe–2Mn Alloys

Figure 6 presents the structures of Al–25Si–2Fe–2Mn alloys treated separately through conventional casting and cooling slope casting. Figure 6a shows the BSE image of Al–25Si–2Fe–2Mn alloys treated through conventional casting, and it can be seen from the figure that Fe-rich phase in the alloys treated through conventional casting is in the shapes of fishbone (dendritic crystals) and tiny Chinese-script. Figure 6b shows the BSE image of Al–25Si–2Fe–2Mn alloys treated through Cooling slope process, in which blocky black phase in the structure is the primary Si particle with the average diameter of 30 μm while parts of blocky bright-white Fe-rich phase with the average diameter of 40 μm are centered on the primary Si particles. Additionally, plenty of tiny Chinese-character Fe-rich phases are uniformly distributed in the solidification structure of the alloys. By comparing

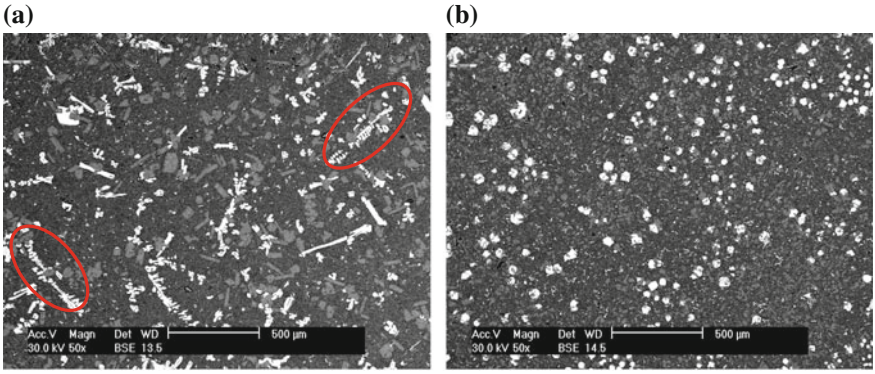

Fig. 6 Microstructures of Al–25Si–2Fe–2Mn alloy **a** conventional casting, **b** cooling slope casting

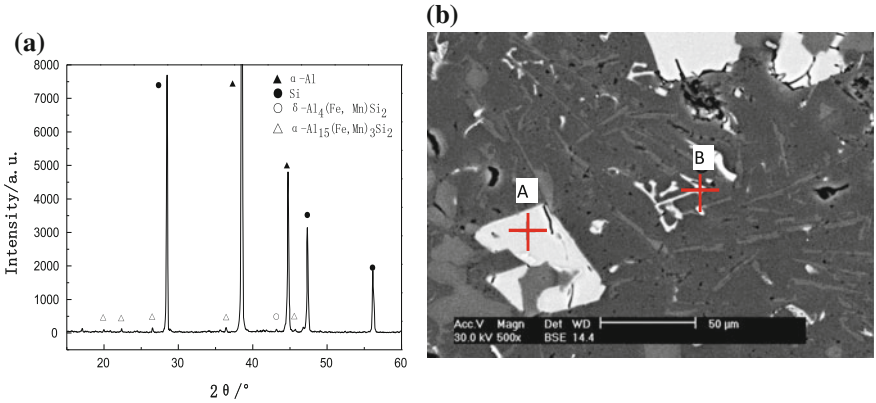

Fig. 7 XRD pattern **a** and BSE images of Fe-rich phases **b** in Al–25Si–2Fe–2Mn alloy treated by cooling slope

Table 2 EDS results of Fe-rich phases in cooling slope casting Al–25Si–2Fe–2Mn alloys

Phase marked	Al (%)	Si (%)	Fe (%)	Mn (%)	Mn/Fe
"A"	69.63	13.65	08.51	08.21	$Al_{12.48}(Fe,Mn)_3Si_{2.46}$
"B"	73.57	10.08	12.72	03.64	$Al_{13.49}(Fe,Mn)_3Si_{1.85}$

Fig. 6a, b, the primary Si treated through Cooling slope is significantly refined and fishbone-like Fe-rich phase obtained through conventional casting is transformed into blocky Fe-rich phase.

Figure 7a shows the XRD pattern of the solidification structure of Al–25Si–2Fe–2Mn alloys treated through cooling slope. The solidification structure of the alloys contains Si, α-Al, δ-Al_4FeSi_2 and α-$Al_{15}(Fe,Mn)_3Si_2$ phases. There is only one diffraction peak of δ-$Al_4(Fe,Mn)Si_2$ phase, implying that a few δ-$Al_4(Fe,Mn)Si_2$ phases are found in the solidification structure of the Al–25Si–2Fe–2Mn alloy. Figure 7b shows the BSE image of Fe-rich phase of the Al–25Si–2Fe–2Mn alloys treated by using Cooling slope. The blocky and tiny Chinese-script Fe-rich phases (marked as A and B separately) are centered on the primary Si particles.

The EDS results for the two kinds of Fe-rich phases are listed in Table 2. The result indicates that the molecular formula of blocky and tiny Chinese script Fe-rich phases in Fig. 5b obtained are $Al_{12.48}(Fe,Mn)_3Si_{2.46}$ and $Al_{13.49}(Fe,Mn)_3Si_{1.85}$, respectively based on the atomic percent, which are close to the molecular formula of α-$Al_{15}(Fe,Mn)_3Si_2$ phase.

Effect of Spray Deposition on Microstructure of Al–25Si–2Fe–2Mn Alloys

Figure 8a shows the microstructure of Al–25Si–2Fe–2Mn treated by using spray deposition technologies, indicating that gray primary Si particles and bright polygonal particles of Fe-rich phases exhibit the average diameters of 7 and 5 μm, respectively. Moreover, there is no significant eutectic structure in the microstructure obtained through gas atomization and spray deposition technology. Figure 8b shows a BSE image which illustrates that apart from granular Fe-rich phase, plenty of tiny Chinese script Fe-rich phases are uniformly distributed in α-Al matrix.

Figure 9 presents the XRD spectrum of Al–25Si–2Fe–2Mn alloys treated through spray-deposited, implying that the solidification structure of the alloys

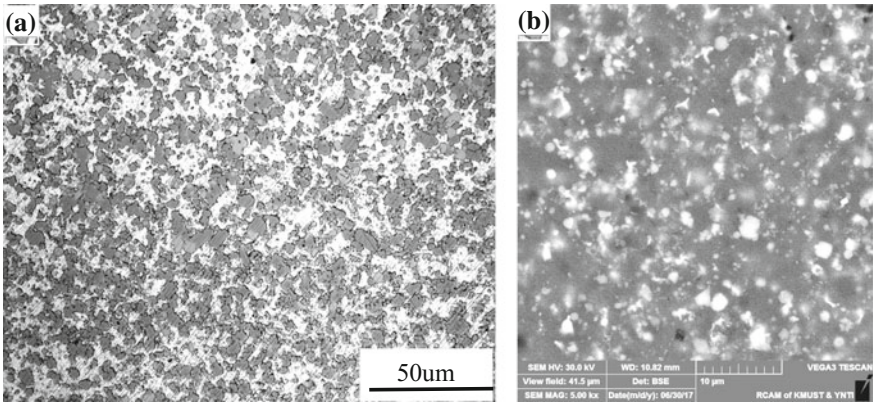

Fig. 8 OM and BSE microscopies of spray-formed Al–22Si–2Fe–2Mn alloys

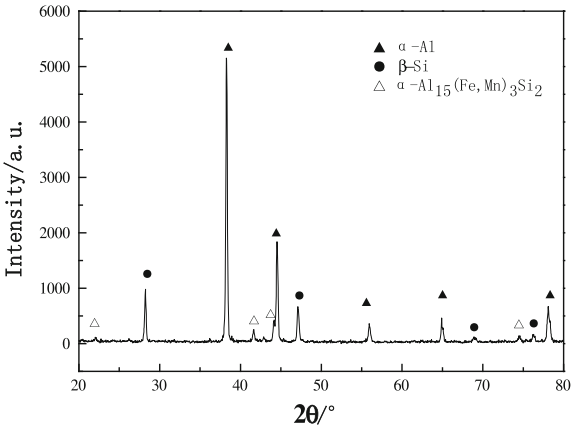

Fig. 9 XRD pattern in Al–25Si–2Fe–2Mn alloy treated by spray formed

contains Si, α-Al and α-$Al_{15}(Fe,Mn)_3Si_2$ phases in which Fe-rich phase only exhibits a diffraction peak of α-$Al_{15}(Fe,Mn)_3Si_2$ phase.

Figure 10 displays the element distribution condition of the microstructure of the spray-deposited alloys. The figure reveals that the dispersed tiny particles due to spray deposition are mainly composed of Al, Si, Fe and Mn, which are uniformly distributed in the microstructure. Moreover, the distribution of Fe element is

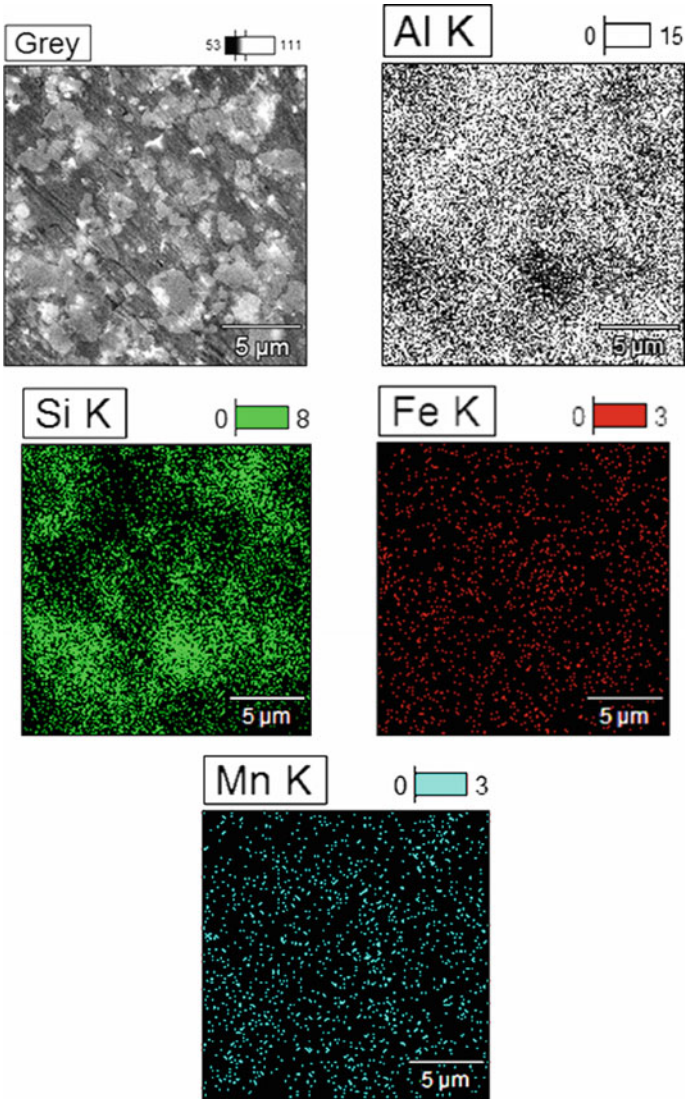

Fig. 10 X-ray mapping of Al–22Si–2Fe–2Mn alloys

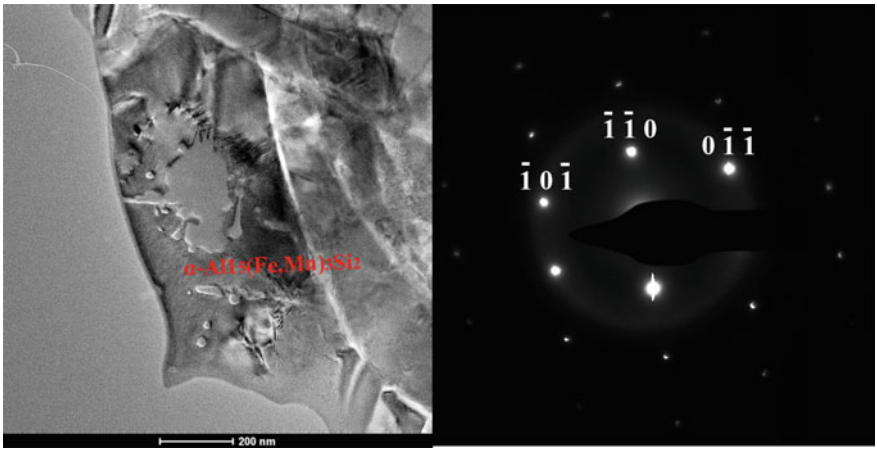

Fig. 11 TEM image and diffraction pattern along [−111] zone axis of α-$Al_{15}(Fe,Mn)_3Si_2$ phase

basically the same as that of Mn element, which is consistent with the distribution condition of bright-white Fe-rich phase.

According to the above test results, the Fe-rich phases in the Al–25Si–2Fe–2Mn alloys treated by using three methods are mainly found to be α-$Al_{15}(Fe,Mn)_3Si_2$. The TEM image and the selected-area diffraction pattern of the α-$Al_{15}(Fe,Mn)_3Si_2$ phase in the solidification structure of the Al–25Si–2Fe–2Mn alloys treated by cooling slope casting are shown in Fig. 11. Through the analysis, the phase is in the body-centered cubic structure with the lattice constants of a = 0.75198 nm and c = 0.77688 nm.

The Mechanism Analysis for the Fe-Rich Phases During Melt Treatment Process

Based on the aforementioned results, the primary Si particles in the solidification structure of the alloys obtained by using electromagnetic stirring and spray deposition exhibit the largest and smallest sizes, respectively. It is worth noting that Fe-rich phase in the alloys undergoing different treatments shows significantly different morphologies and distributions.

Fe-rich phase in the solidification structure of the alloys treated by using electromagnetic stirring does not exhibit the phase structure that outer sphere covers the inner sphere in the cast alloys. According to the judgment on the structure in the above content, it can be seen that when the Al–25Si–2Fe–2Mn alloys were treated through electromagnetic stirring, primary Si particles and a few δ-$Al_4(Fe,Mn)Si_2$ phase were produced first, followed by the generation of large amounts of α-$Al_{15}(Fe,Mn)_3Si_2$ phase. In the subsequent electromagnetic stirring, the

homogenization of the temperature field of melts and solute distribution enables the sufficient reaction of L + δ-$Al_4(Fe,Mn)Si_2$ → α-$Al_{15}(Fe,Mn)_3Si_2$. Moreover, it is difficult to find the phase structure that outer sphere covers inner sphere in the solidification structure under electromagnetic stirring while a few δ-$Al_4(Fe,Mn)Si_2$ phases were still detected in the XRD result. Therefore, the Fe-rich phase in the solidification structure through electromagnetic stirring mainly appeared as blocky and tiny Chinese-character α-$Al_{15}(Fe,Mn)_3Si_2$ phase. Moreover, the blocky α-$Al_{15}(Fe,Mn)_3Si_2$ phase was mainly circled around primary Si particles in the Al–25Si–2Fe–2Mn alloys. According to the WHS principle illustrated by Van de Waal [15], nuclear layer probably extends in the internal groove of the internal corner and the surface nucleation and growth are considered as the main mechanism. Wu [16] also found the phenomenon while studying the growth process of Fe-rich phase in the near-eutectic Al–Si alloys. In the solidification process, primary Si particles were first nucleated and blocky α-$Al_{15}(Fe,Mn)_3Si_2$ phase was separated out at about 740 or 690 °C. Moreover, the previously nucleated primary Si particles served as the nucleation substrate of α-$Al_{15}(Fe,Mn)_3Si_2$ phase. The surface nucleation mechanism play an important role in the growth of α-$Al_{15}(Fe,Mn)_3Si_2$ phase. In the final solidification structure, α-$Al_{15}(Fe,Mn)_3Si_2$ phase was centered on primary Si particles. Another explanation is that primary Si particles first nucleated during solidification and then α-$Al_{15}(Fe,Mn)_3Si_2$ phase was gradually nucleated and separated out with the fall of temperature. Moreover, molten metal showed a dramatic stirring effect during electromagnetic stirring or Cooling slope, so that the nucleated particles were mutually crashed in the rotating or flowing molten metal. The particles were bonded in the collision process just like primary Si particles agglomerated due to collision, which caused that the two particles inter-depended in the solidification structure.

Due to the addition of Mn element, the precipitation temperature range of the metastable δ-$Al_4(Fe,Mn)Si_2$ phase narrowed while the temperature for separating α-$Al_{15}(Fe,Mn)_3Si_2$ phase rose and therefore the temperature range broadened. Moreover, less δ-$Al_4(Fe,Mn)Si_2$ phase was separated out during treatment using cooling slope casting. Due to separation of various phases, the alloy melts released amounts of latent heat of crystallization [17, 18], that is, the recalescence phenomenon effect in the flowing process, resulting in the rising temperature of the melt. In the high-temperature melt, the metastable δ-$Al_4(Fe,Mn)Si_2$ phase was remolten in the liquid phase to produce more stable blocky α-$Al_{15}(Fe,Mn)_3Si_2$ phase. According to researches [19], Al alloy melts contain short-range and medium-range ordered structures with different sizes. For example, various alloys melts including Al–Fe and Al–Ni contain plenty of ordered medium-range atomic clusters [20, 21]. Additionally, there are plenty of atomic clusters in the local Al–Si alloy melt after adding various alloys including Fe and Mn, which can stably exist in the melt within a certain temperature range and time. Moreover, the proportion of different elements in the clusters has a certain relationship with the mass ratio of different alloys in the melt. After the mass fraction of Mn in alloys reaches to a certain number, the atomic mass ratio of atomic clusters in the melt probably reaches to the atomic mass ratio of α-$Al_{15}(Fe,Mn)_3Si_2$ phase instantaneously.

Therefore, the high solidification rate during the treatment using inclined plates inhibits the diffusion of atoms and facilitates the nucleation of these clusters to produce stable α-$Al_{15}(Fe,Mn)_3Si_2$ phase.

A great mount of granular α-$Al_{15}(Fe,Mn)_3Si_2$ phase in emerges spray-deposited Al–25Si–2Fe–2Mn alloys. In the process of spray deposition, a large number of fight droplets at high cooling rate will be released latent heat-the recalescence phenomenon, so that the metastable δ-$Al_4(Fe,Mn)Si_2$ phase will transformed to stable phase α-$Al_{15}(Fe,Mn)_3Si_2$ or remelted into the liquid phase [17, 18]. After that, the atomized droplets collide with the Semi-solid deposited billet, which is converted to a large number of granular phase α-$Al_{15}(Fe,Mn)_3Si_2$ in the high temperature annealing of the Semi-solid deposited billet [22]. In addition, after the Mn mass fraction reaches a certain amount in the alloy, the atomic mass ratio of the atomic clusters in the alloy melt satisfied synchronously that of the α-$Al_{15}(Fe,Mn)_3Si_2$ phase, which will promote the formation of α-$Al_{15}(Fe,Mn)_3Si_2$ phase during the rapid instantaneous solidification process. Compare with cooling slope, overheated alloys melt exhibits more dispersed and tiny atomic clusters in the spray treatment. During solidification process at a higher cooling rate, α-$Al_{15}(Fe,Mn)_3Si_2$ phase is instantaneously separated out and subsequently elements cannot be diffused to promote the growth of phase. Thus, Fe-rich phase in the solidification structure treated by using spray deposition is mainly shown as tiny α-$Al_{15}(Fe,Mn)_3Si_2$ phase.

Conclusions

1. Under the three treatment modes, the hard phases in the microstructure of Al–25Si–2Fe–2Mn are all refined at different degrees. Among them, the spray deposition yields the best refining effect where the primary Si and Fe-rich phase are dispersed into the microstructure. For the second refining effect using cooling slope, the primary Si particles and the Fe-rich phase are blocky which uniformly distribute in the solidification structure of the alloys. In comparison, the electromagnetic stirring presents the worst refining effect, some Fe-rich phases are bonded with the primary Si particles to distribute in the neighbor of latter. When the two phases are regarded as a whole, the average diameter is measured to be about 100 μm.
2. Fe-rich phases treated by using the three treatment modes of melts are all stable α-$Al_{15}(Fe,Mn)_3Si_2$ phases, but their in the alloys undergoing different treatments show significantly different morphologies and distributions.

Acknowledgements The authors acknowledge funding for the research from National Science Foundation of China (51505205) and (E050802), Science and Technology Project Foundation of Yunnan Province of China (KKZ3201532005). This work is supported by the Advanced Solidification forming and Equipment Technology National Joint Local Engineering Laboratory, Kunming University of Science and Technology, Kunming, China.

References

1. W. Zhang, F. Yang, W.P. Gan et al., Study of the hot deformation behavior of the Al-35Si high silicon aluminum alloy. J. Mater. Rev. **19**, 136–138 (2005)
2. Y.S. Choi, J.S. Lee, W.T. Kim et al., Solidification behavior of Al-Si-Fe alloys and phase transformation of metastable intermetallic compound by heat treatment. J. Mater. Sci. **34**, 2163–2168 (1999)
3. P. Kapranos, D.H. Kirkwood, H.V. Atkinson et al., Thixoforming of an automotive part in A390 hypereutectic Al-Si alloy. J. Mater. Process Technol. **135**, 271–277 (2003)
4. B.Q. Chen, J.B. Peng, E. Miao, The influence of Mn on Fe-phase aspect in Al-Si alloy. J. Wuhan Univ. Technol. **26**, 485–487 (2002)
5. X.M. Fan, J.F. Liu, H.Y. Wen, Effects of manganese on the morphology of iron phase and mechanical properties of Al-Si alloy with high Fe content. J. Spec. Cast. Nonferrous Alloys. **28**, 594–596 (2008)
6. Y. Jia, P. Zhao, Effects of Al-Si-Mn-Fe Phase in hypereutectic Al-Si alloy. J. ChengDu. Univ. Technol. **28**, 214 (2001)
7. H.Y. Kim, T.Y. Park, S.W. Han et al., Effects of Mn on the crystal structure of α-Al(Mn, Fe) Si particles in A356 alloys. J. Cryst. Growth. **291**, 207–211 (2006)
8. L.G. Hou, H. Cui, Y.H. Cai, J.S. Zhang, Microstructures and phase formation of cast and spray-formed Al-25Si-5Fe-3Cu alloys. J. Univ. Sci. Technol. B. **31**, 1006–1012 (2009)
9. L. Li, R. Zhou, Y. Jiang et al., Effect of manganese on the formation of Fe-rich phases in electromagnetic stirred hypereutectic Al-22Si alloy with 2% Fe. J. Trans. Indian Inst. Met. **67**, 861–867 (2014)
10. B. Dang, X. Zhang, Y.Z. Chen et al., Breaking through the strength-ductility trade-off dilemma in an Al-Si-based casting alloy. J. Sci. Rep. **6**, 30874 (2016)
11. C. Lin, S. Wu, S. Lü et al., Effects of ultrasonic vibration and manganese on microstructure and mechanical properties of hypereutectic Al-Si alloy with 2% Fe. J. Intermetallics. **32**, 176–183 (2013)
12. Y. Cai, R. Liang, L. Hou et al., Effect of Cr and Mn on the microstructure of spray-formed Al-25Si-5Fe-3Cu alloy. J. Mater. Sci. Eng. A. **528**, 4248–4254 (2011)
13. H.J. Hung, J.S. Zhang, H. Feng, Effect of Mn on Fe phases in spray-deposited Al-25Si-xFe-yMn alloys. J. Univ. Sci. Technol. B. **32**, 219–233 (2010)
14. H.J. Hung, H. Feng, J.S. Zhang, Solidification structure of cast Al-25Si-xFe-yMn alloy. J. Spec. Cast. Nonferrous Alloys. **30**, 766–769 (2010)
15. B.W. Van de Waal, Cross-twinning model of FCC crystal growth. J. Cryst Growth **158**, 153–165 (1996)
16. Y.Y. Wu, X.F. Liu, B.G. Jiang et al., Four-branched compounds coupled Si and iron-rich intermetallics in near eutectic Al-Si alloys. J. Alloys Compd. **437**, 80–83 (2007)
17. U. Fritsching, *Spray Simulation* (M. Cambridge University Press, New York, 2004)
18. Q. Xu, E.J. Lavernia, Influence of nucleation and growth phenomena on microstructure evolution during droplet-based deposition. J. Acta Mater. **49**, 3849–3861 (2001)
19. D. Holland-Moritz, T. Schenk, V. Simonet et al., Short-range order in undercooled and stables melts forming quasi crystals and approximants and its influence on nucleation. J. Philos. Mag. **86**, 255–262 (2006)
20. J. Brillo, A. Bytchkov, I. Egry et al., Local structure in liquid binary Al-Cu and Al-Ni alloys. J. Non Cryst Solids **352**, 4008–4012 (2006)
21. I. Egry, L. Hennet, M. Kehr et al., Chemical short-range order in liquid Al-Ni alloys. J. Chem. Phys. **129**, 064508 (2008)
22. L.G. Hou, C. Cui, J.S. Zhang, Optimizing microstructures of hypereutectic Al–Si alloys with high Fe content via spray forming technique. J. Mater. Sci. Eng. A **527**, 6400–6412 (2010)

An Overview of Phase Diagram and Thermodynamic Parameters of Pt–Au–Sn System

Jieqiong Hu, Ming Xie, Song Chen, Aikun Li, Saibei Wang and Yongtai Chen

Abstract Rare and precious metals materials with unique physical and chemical properties are widely used in aviation, aerospace, navigation, electronic, electric, petroleum chemical industry, glass fiber, waste gas purification, metallurgical and other industries, which are known as "the vitamin of modern industry". In this article, the development and application of Pt–Au–Sn system, the binary and ternary alloy phase diagrams in the Pt–Au–Sn system, and the related thermodynamic parameters, including phase structure and formation enthalpy of alloy, the cohesive energy and the Gibbs free energy of Pt–Au–Sn system were reviewed, at the same time, the further research interests and the experimental verification of phase diagram of Pt–Au–Sn system were also discussed, which could provide necessary theoretical support for the alloy composition design and industrial applications in the future.

Keywords Pt–Au–Sn system · Phase diagram · Thermodynamic parameters Phase structure

J. Hu · M. Xie (✉) · S. Chen · S. Wang · Y. Chen
School of Materials Science and Engineering, Kunming University of Science and Technology, Kunming 650093, China
e-mail: powder@ipm.com.cn

J. Hu
e-mail: hujq@ipm.com.cn

S. Chen
e-mail: cs@ipm.com.cn

S. Wang
e-mail: wsb@ipm.com.cn

Y. Chen
e-mail: cyt@ipm.com.cn

J. Hu · M. Xie · S. Chen · A. Li · S. Wang · Y. Chen
Kunming Institute of Precious Metals, Kunming 650106, China
e-mail: lak@ipm.com.cn

© Springer Nature Singapore Pte Ltd. 2018

Y. Han (ed.), *Advances in Materials Processing*, Lecture Notes in Mechanical Engineering, https://doi.org/10.1007/978-981-13-0107-0_86

Introduction

Rare metals alloys have the unique physical and chemical properties, which make it widely used in aviation, spaceflight, navigation, missile, rocket, atomic energy, microelectronics, chemical, petrochemical, glass fiber, exhaust gas purification and metallurgical industry, therefore it is called "the vitamin of modern industry" and "modern new metals" [1–3]. The Au–Sn alloy has been widely used as the high temperature solder due to its excellent thermal and mechanical properties as well as its potential to be reflowed without flux [4, 5]. Moreover, the high re-melting temperatures of the Au-rich compounds enable Au–Sn to be a potential transient liquid phase bonding material [6]. However, the robustness of the bond depends not only on the appropriate selection of the solder system and bonding characteristics but also on the interfacial reaction between the solder and contact metallization. And the thermally stable interconnections have been considered as one of the main requirements for packaging semiconductor electronic devices. Therefore, it is necessary to acquire a thorough understanding on the relevant microstructure evolution and phase stability of the interconnections.

Au and Pt alloy are the most widely used catalyst, which have better catalytic effect on many reactions, such as catalytic hydrogenation, dehydrogenation, isomerization, cyclization, dewatering, dehalogenation, oxidation and cracking reaction [7]. Using Pt catalyst reforming naphtha can improve the octane number of gasoline products. The another important applications of Pt catalysts are as electrode material in proton membrane fuel cell, methanol fuel cells, formic acid fuel cell and so on [8–10]. Compared with Pt catalyst, Au as electrode materials of methanol oxidation does not produce toxic intermediates, so the catalytic properties of Au catalyst is greatly improved in the modified electrode structure [11].

In the chemical industry, isobutane as raw material for making isobutylene is the solution of isobutylene scarcity and isobutane waste, the main problem of isobutane dehydrogenation is the catalyst research and development. A large number of research at home and abroad using Pt–Sn as an active component, but it has some problems such as conversion rate is low and easy to deactivation. Prophase research [12] shows that using volume immersion method to prepare Pt–Au–Sn catalyst could enhance the activity of catalyst, and when n (Au): n (Pt) = 1.0, isobutylene yield is greater than 40%.

So far, binary or ternary system phase diagram including single precious metal elements has been basically completed. However, ternary system containing two precious metals elements and other multi-component system phase diagram are extremely rare [13, 14]. In the precious metal alloys, Pt–Au have good catalytic effect, which is a typical representative of the platinum group metal alloy. In order to make better use of limited resources, and develop more excellent new precious metal materials, this paper summarizes the related thermodynamic parameters and phase diagram study status of Pt–Au–Sn system at home and abroad, so as to provide certain guidance for the alloy system application in the brazing and the chemical catalytic industry.

Pt–Sn System

Pt–Sn binary system is early studied by Su [15] with Pandat software [16], such as calculation and optimization, optimization of Pt–Sn binary phase diagram is shown in Fig. 1, it can be seen from Fig. 1 that in the tin-rich area, the miscibility phenomenon exist in liquid region. But this area of miscibility is actually not exist, and no related experiment validate. But there are still some reports and studies [17] about the typical pseudo miscibility area.

Vincent [18] also uses calculation method to study the phase diagrams and thermodynamic parameters of Pt–Sn system. They compiled some of the thermodynamic experiment data for further optimization of the thermodynamic model of Pt–Sn system.

Gibbs Free Energy of Pure Components

Gibbs free energy expression of pure components use $G_i^{0,\phi}(T) = G_i^{\phi}(T) - H_i^{SER}$, which element i (i = Pt, Sn) is component of Φ phase (Φ = FCC (Pt, Sn), BCT Sn and liquid), the relationship between free energy and the temperature is:

$$G_i^{0,\phi}(T) = a + bT + cT\ \ln\ T + dT^2 + eT^3 + fT^{-1} + gT^7 + hT^{-9} \qquad (1)$$

where the H_i^{SER} is the molar enthalpy of pure element i at 298.15 K and under 1 atmospheric pressure, T is the absolute temperature, a, b, c, d, e, f… is the fitting undetermined coefficients, Gibbs free energy expression of pure component (Pt and Sn) use SGTE (Science Group Thermodata Europe) expression in the database [19].

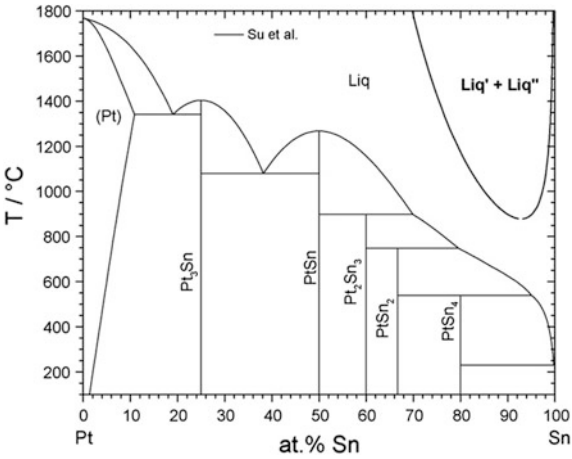

Fig. 1 The phase diagram of Pt–Sn system calculated by Su [15]

Thermodynamics Model of Liquid Phase

In the actual solution, atoms binding energy are often influenced by temperature, composition and other factors, the interaction parameters is not always the constant, therefore, to modify the interaction parameters, often using the function related to the temperature and composition. In order to achieve the more accurate description of liquid phase and the FCC phase in Pt–Sn system, choose the subregular solution model to describe the Gibbs free energy, the Gibbs free energy expression is:

$$G^L(T,\{y_i\}) = \sum_i y_i G_i^{0,L}(T) + RT\sum_i y_i \ln y_i + \sum_{i,j>i} y_i y_j \sum_v L_{i,j}^{L,v}(y_i - y_j)^v \quad (2)$$

where the y_i is the mole fraction in the liquid phase of element i, i(j) on behalf of each phase, namely Pt, Sn and PtSn. $G_{Pt}^{0,L}(T)$ and $G_{Sn}^{0,L}(T)$ in formula (2) is the Gibbs free energy of Pt and Sn liquid phase, adopts the SGTE database expression [20]. The Gibbs free energy $G_{PtSn}^{0,L}(T)$ using the following formula:

$$G_{PtSn}^{0,L}(T) = G_{Pt}^{0,L}(T) + G_{Sn}^{0,L}(T) + a_{PtSn}^L + b_{PtSn}^L T \quad (3)$$

Type a_{PtSn}^L and b_{PtSn}^L is formation enthalpy and entropy of PtSn respectively, the two parameters were optimized.

The Thermodynamic Model of Solid Phase (Pt)

The computation formula Gibbs free energy of face-centered cubic phase Pt is as follow:

$$G^{(Pt)} = x_{Pt} G_{Pt}^{0,fcc} + x_{Sn} G_{Sn}^{0,fcc} + RT(x_{Pt}\ln x_{Pt} + x_{Sn}\ln x_{Sn}) + x_{Pt}x_{Sn}L_{Pt,Sn}^{0,(Pt)} \quad (4)$$

Thermodynamics Model of Intermediate Phase

Pt–Sn system have five intermediate phases, namely PtSn, $PtSn_2$, Pt_2Sn_3, Pt_3Sn and $PtSn_4$, among them PtSn crystal structure belongs to the hexagonal system, which has the NiAs type structure, the space group is P63/mmc, crystal parameters are a = b = 4.104 Å, c = 5.436 Å, α = β = 90°, γ = 120°, cell contains four atoms; Crystal structure of $PtSn_2$ belongs to the cubic system, the space group is Fm-3m, crystal parameters are a = b = c = 6.4331Å, α = β = γ = 90°, cell contains 12 atoms; Pt_2Sn_3 crystal structure belongs to the hexagonal system, the space group is P63/mmc, crystal cell parameters are a = b = 4.325Å, c = 12.934 Å, α = β = 90°,

$\gamma = 120°$, the cell contains 10 atoms; Pt_3Sn crystal structure belong to cubic system, with $AuCu_3$ type structure, space group is Pm-3m, crystal cell parameters are a = b = c = 4Å, $\alpha = \beta = \gamma = 90°$, the cell contains 4 atoms; $PtSn_4$ crystal structure belongs to the orthogonal system, space group is ABA2, crystal cell parameters are a = 6.397Å, b = 6.426Å, c = 11.381Å, $\alpha = \beta = \gamma = 90°$, the cell contains 20 atoms [21–24]. The computation formula of Gibbs free energy of five intermediate phase is:

$$G^{Pt_pSn_q}(T) = \frac{p}{p+q} G_{Pt}^{0,fcc}(T) + \frac{q}{p+q} G_{Sn}^{0,bct}(T) + A' + B'T \tag{5}$$

Type A′ and B′ is optimized parameters.

The Optimized and Calculated Thermodynamic Parameters

PanOptimizer is the parameters module in C/C++ software environment, which evaluated the experiment thermodynamics, kinetics and thermal physical model, not only used as a thermodynamic model parameters optimization tools, as well as optimizing the thermal physical properties and dynamic model parameters. Using the recent related experimental data, and combined with PanOptimizer optimization platform, optimized each phase parameters. Doerinckel [25], Durussel et al. [26] and Anres et al. [27] successively carry on the experiment and thermodynamics calculation for Pt–Sn binary system. The phase diagram calculated by different research group was shown in Fig. 2, It can be seen from Fig. 2 that the work of Vincent Grolier and Durussel are more comprehensive and reliable, so optimization mainly chose their experimental data and SGTE proposed data in 2010.

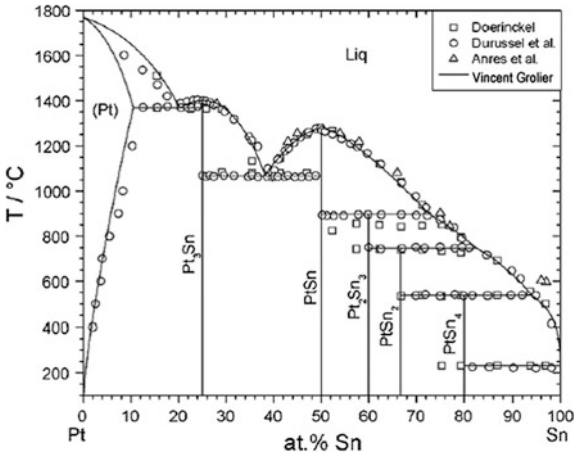

Fig. 2 The phase diagram of Pt–Sn system calculated by Doerinckel [25], Durussel et al. [26], Anres et al. [27] and Vincent [18]

Table 1 Evaluated thermodynamic parameters for Pt–Sn system [18]

Phase type	Phase	Thermodynamic parameters (J/mol)
Solid solution phase	Liquid	$G^{0,Liq}_{PtSn} = -94{,}663.3 + G^{0,Liq}_{Pt} + G^{0,Liq}_{Sn}$
		$L^{0,Liq}_{Pt,PtSn} = -71{,}062.3 + 25.6461T$
		$L^{1,Liq}_{Pt,PtSn} = -10{,}754.4$
		$L^{0,Liq}_{PtSn,Sn} = -33{,}610.0 + 18.8021T$
	Pt	$L^{0,(Pt)}_{Pt,Sn} = -125{,}000 - 2T$
Intermediate phase	Pt_3Sn	$G^{Pt_3Sn} = -35{,}826.2 - 0.5T + (\frac{3}{4})G^{0,fcc}_{Pt} + (\frac{1}{4})G^{0,bct}_{Sn}$
	PtSn	$G^{PtSn} = -59{,}500 + 4.3833T + (\frac{1}{2})G^{0,fcc}_{Pt} + (\frac{1}{2})G^{0,bct}_{Sn}$
	Pt_2Sn_3	$G^{Pt_2Sn_3} = -52{,}240 + 4.83T + (\frac{2}{5})G^{0,fcc}_{Pt} + (\frac{3}{5})G^{0,bct}_{Sn}$
	$PtSn_2$	$G^{PtSn_2} = -45{,}160 + 4.02T + (\frac{1}{3})G^{0,fcc}_{Pt} + (\frac{2}{3})G^{0,bct}_{Sn}$
	$PtSn_4$	$G^{PtSn_4} = -29{,}000 + 2.4T + (\frac{1}{5})G^{0,fcc}_{Pt} + (\frac{4}{5})G^{0,bct}_{Sn}$

Optimization carried out by PanOptimizer program. First, optimization the phase parameters one by one, and then overall optimization. The Optimized parameters of Pt–Sn system by Vincent [18] are shown in Table 1.

Au–Sn System

According to the Au–Sn binary alloy phase diagram (Fig. 3) [28], and related research reports [28, 29], Au–Sn system have four intermediate phases, namely AuSn, $AuSn_2$, $AuSn_4$ and Au_5Sn. The crystal structure of AuSn belongs to the hexagonal system, which has the NiAs type structure, the space group is P63/mmc,

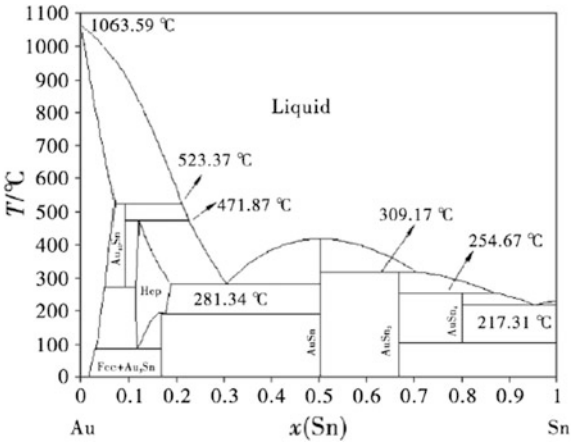

Fig. 3 The phase diagram of Au–Sn system [28]

crystal parameters are a = b = 4.3218 Å, c = 5.5230 Å, $\alpha = \beta = 90°$, $\gamma = 120°$; $AuSn_2$ belongs to the orthogonal crystal system, space group is PBCA, crystal parameters are a = 6.898Å, b = 7.011 Å, c = 11.773 Å, $\alpha = \beta = \gamma = 90°$, the cell contains 24 atoms; $AuSn_4$ crystal structure belongs to the orthogonal system, with $PtSn_4$ type structure, the space group is ABA2, crystal parameters are a = 6.512Å, b = 6.516Å, c = 11.707 Å, $\alpha = \beta = \gamma = 90°$, the cell contains 20 atoms; Au_5Sn crystal structure belongs to trigonal system, the space group is R3H, crystal parameters are a = b = 5.092Å, c = 14.333Å, $\alpha = \beta = 90°$, $\gamma = 120°$, the cell contains 18 atoms.

Chevalier [30] evaluated the thermodynamics of Au–Sn system and calculated the phase diagram of this system. Liu et al. [31] and Grolie et al. [32] also optimized the thermodynamic parameters of Au–Sn system, the calculated phase diagram is in good agreement with the experimental data. Among them, Liu [31] has more consideration on the relationship between liquid phase mixing enthalpy and temperature in the process of optimization. However, besides phase formation enthalpy of AuSn, there is few reports on formation enthalpy of intermetallic compounds [33]. Therefore, in order to get more reasonable description of Au–Sn binary system, Liu [34] in central south university obtained phase formation enthalpy of AuSn and $AuSn_4$ intermetallic compound by using the first principles calculations, which made the further correction of Liu's [31] thermodynamic parameters. A. Dębski et al. [35] use the experimental method to determining the formation enthalpy of four intermetallic compound in Au–Sn system, the formation enthalpy of AuSn, $AuSn_2$, $AuSn_4$ and Au_5Sn are -15.3 ± 0.3, -14.2 ± 0.3, -7.9 ± 0.6, -5.8 ± 0.3 kJ/mol.

Our team [36] also used plane wave pseudo potential method based on the density function theory, calculated the formation enthalpy, cohesive energy, electronic structure, elastic properties and structural stability of Au–Sn system, through comparing formation enthalpy and the cohesive energy, come to the conclusion that formation enthalpy of Au_5Sn alloy is the minimum, which indicated that Au_5Sn is easy to generate, and the cohesive energy of Au_5Sn is the largest, so Au_5Sn is the most unstable alloy.

Pt–Au System

Pt–Au system is the isomorphous system, there is no intermediate phase in Pt–Au system. Xu et al. [37] in Northeastern University based on the recent experiment phase equilibrium data of Au–Pt system, using the Calphad method to evaluate the thermodynamic parameters of Pt–Au binary system. Using the sub-regular solution model Redlich-Kister equation describing Gibbs free energy of liquid and FCC phases. Considering the limitation of thermodynamics third law, Xu et al. [37] reevaluated the solid phase thermodynamic properties and phase equilibrium data, including activity and mixing enthalpy, and then optimizing the thermodynamic parameters of Pt–Au system. The optimization results show that the clearance

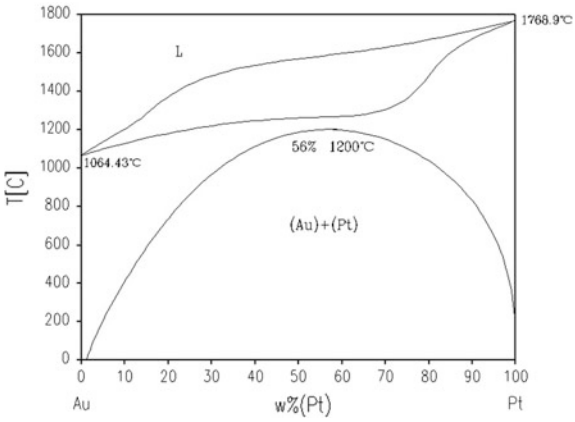

Fig. 4 The phase diagram of Pt–Au system [37]

Table 2 Optimized thermodynamic parameters of Pt–Au system by Xu [37]

Phase type	i	Thermodynamic parameters	
		${}^{i}A^{\alpha}_{Au,Pt}/(\mathrm{J\,mol^{-1}\,atom^{-1}})$	${}^{i}B^{\alpha}_{Au,Pt}/(\mathrm{J\,mol^{-1}\,atom^{-1}})$
Liquid	0	12,800	7.00
FCC	0	15,000	6.10
FCC	1	−7600	3.55

boundary solubility of Pt–Au alloy system migration for Au rich area, the vertex positions at 1200 °C, Au-56%Pt, the optimized phase diagram is shown in Fig. 4, (Table 2).

Pt–Au–Sn System

Alexandra et al. [38] use the experiment method to study the 400 °C isothermal section of tin-rich part (Sn $\geq$ 50 at.%) of Pt–Au–Sn ternary system. The phase relations in the Sn-rich section of the Pt–Au–Sn system have been studied by XRD, metallography, electron microprobe analysis and thermal analysis. A new ternary phase ($AuPt_2Sn_4$) has been discovered, with a homogeneity range in the Au–Pt dimension between $Au_{137}Pt_{293}Sn_{570}$ and $Au_{196}Pt_{241}Sn_{563}$. The new ternary alloy $AuPt_2Sn_4$ is C-centered monoclinic with unit-cell dimensions a = 543.1 pm, b = 527.4 pm, c = 931.3 pm, β = 101.17°. It is worth noting that $AuPt_2Sn_4$ is stable up to 490 °C, then it decomposes according to the reaction: $AuPt_2Sn_4 \rightarrow L + Pt_2Sn_3$. The isothermal section of Pt–Au–Sn system at (or near) 400 °C is shown in Fig. 5.

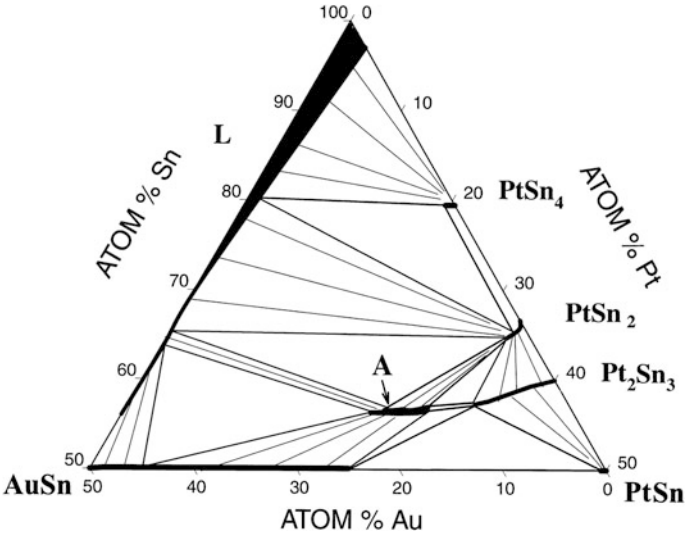

Fig. 5 Isothermal cross-section of the Pt–Au–Sn system at (or near) 400 °C [38]

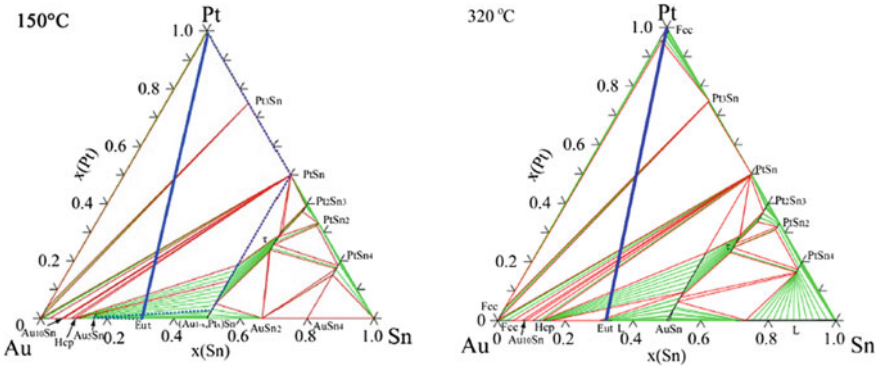

Fig. 6 Isothermal section of Pt–Au–Sn at 150 and 320 °C, with reaction path superimposed on the dotted blue line [39]

Dong et al. [39] use Calphad method to description the Pt–Au–Sn ternary system by remodeling the ternary compound and the solubility of the third elements in relevant binary compounds. The calculated isothermal section of Pt–Au–Sn at 150 and 320 °C are shown in Fig. 6, and the reassessed thermodynamic parameters of Pt–Au–Sn system are shown in Table 3. It can be seen from Table 3 that the binary compounds AuSn, PtSn, Au_5Sn, Pt_3Sn, Pt_2Sn_3, $PtSn_2$ and $PtSn_4$ with the solubility of the third elements are all redefined, and the ternary compound τ is also redefined. These obtained consistent parameters could reproduce most of the experimental results. In addition, the microstructures of Au-20wt%Sn-Pt reaction couples are

Table 3 Reassessed thermodynamic parameters of the ternary Pt–Au–Sn system by Dong [39]

Defined phases	Parameters
NiAs (representing AuSn and PtSn): $(Sn)_1$:(Sn,Va):(Au,Pt)	${}^{0}L^{NiAs}_{Sn:Va:(Au,Pt)} = +2000$
	${}^{1}L^{NiAs}_{Sn:Va:(Au,Pt)} = -14{,}000$
Au_5Sn:(Au, Pt)$_{0.84}$:$Sn_{0.16}$	$G^{Au_5Sn}_{Pt:Sn} = -23{,}130.9668 + 7.4018 * T + 0.84 * GHSERPT + 0.16 * GHSERSN$
	${}^{0}L^{Au_5Sn}_{(Au,Pt):Sn} = -28{,}980.8006 + 11.4109 * T$
	${}^{1}L^{Au_5Sn}_{(Au,Pt):Sn} = -31{,}906.3444 + 14.1994 * T$
Pt_3Sn:(Au, Pt)$_{0.75}$:$Sn_{0.25}$	$G^{Pt_3Sn}_{Au::Sn} = -5000 - 1.5 * T + 0.75 * GHSERAU + 0.25 * GHSERSN$
	${}^{0}L^{Pt_3Sn}_{(Pt,Au):Sn} = -1000$
Pt_2Sn_3:(Pt, Au)$_{0.4}$:$Sn_{0.6}$	$G^{Pt_2Sn_3}_{Au::Sn} = -4500 + 0.4 * GHSERAU + 0.6 * GHSERSN$
	${}^{0}L^{Pt_2Sn_3}_{(Pt,Au):Sn} = -10{,}200$
$PtSn_2$:(Pt, Au)$_{0.333333}$: $Sn_{0.666667}$	$G^{PtSn_3}_{Au::Sn} = -4300 + 0.333333 * GHSERAU + 0.666667 * GHSERSN$
	${}^{0}L^{PtSn_2}_{(Pt,Au):Sn} = -5000$
$PtSn_4$:(Pt,Au)$_{0.2}$: $Sn_{0.8}$	$G^{PtSn_4}_{Au::Sn} = -3000 + 0.2 * GHSERAU + 0.8 * GHSERSN$
	${}^{0}L^{PtSn_4}_{(Pt,Au):Sn} = -6000$
τ:(Au,Pt)$_3$:Sn_4	$G^{\tau}_{Au::Sn} = -47{,}957.4292 + 14.6569 * T + 3 * GHSERAU + 4 * GHSERSN$
	$G^{\tau}_{Pt::Sn} = -377{,}257.444 + 62.4101 * T + 3 * GHSERPT + 4 * GHSERSN$
	${}^{0}L^{\tau}_{(Au,Pt):Sn} = -162{,}981.9235 + 10.3167 * T$

characterized by using SEM with energy-dispersive X-ray microanalysis, as well as scanning transmission electron microscopy with EDS. The results show that the Au-20wt%Sn-Pt reaction couples have good thermal stability at 150 °C.

Summary

The Pt–Au–Sn phase diagram has been investigated extensively, because of the potential application in the electrode wire, catalyst, soldering and chemical industry, as well as the experimental and theoretical interest in the miscibility gap occurring in the solid solution field. The previous work have reassessed the thermodynamic description of the Pt–Au–Sn system by redefining the ternary compound, AuSn, PtSn and the solubility of the third elements in relevant binary compounds. The self-consistent thermodynamic parameters obtained there can reproduce most of the experimental data. But there are still few research reports on the alloying effects on

the precipitation of G.P. zones and a valid strengthening mechanism for Pt–Au–Sn system, so the further studies on Pt–Au–Sn system will be mainly put on the miscibility gap in precious metals as well as its alloying for the applications in the strengthening of precious metals and the microstructure control of Pt–Au–Sn system, in addition, the thermodynamic database of Pt–Au–Sn system need to be established. The research results can accelerate the developments of advanced precious metal materials and provide necessary theoretical support for the alloy composition design and industrial applications in the future.

Acknowledgements This work was financially supported by the Nature Science Foundation of China (U1602275, U1602271, U1302272, 51267007, 51461023, 51507075); Institutes Special Technology Development Project of Yunnan (2013DC016); Fund of the Collaborative Innovation Center of Rare and Precious Metals Advanced Materials (2014XT02). Finally, we also wish to thank referee for useful suggestions and comments.

References

1. C. Xu, Y. Xu, Y. Yang et al., Au/Sn eutectic bonding technology in the application of MEMS packaging. Micro Nanoelectronic Technol. **51**, 131–135 (2014)
2. J. Ma, H. Sun, H. Z et al., Electrocatalytic performance of carbon supported Pt-Sn catalyst prepared with direct thermo-decomposition method for ethanol oxidation. Chem. J. Chin. Univ. **32**, 2856–2860 (2011)
3. J. Cai, F. Yang, K. Qiu et al., Novel electrical contact materials Ag/$La_{1-x}Sr_xCoO_3$. Electron. Compon. Mater. **33**, 1–3 (2014)
4. W. L, Y. Huang, Y. Ma, Research progress in preparation and application of Au80Sn20 solder alloy. Mater. Rev. **27**, 1–6 (2013)
5. H. Oppermann, E. Zschech, C. Whelan et al., *Materials for Information Technology* (Springer, London, 2005), pp. 377–390
6. G.S. Zhang, H.Y. Jing, L.Y. Xu et al., Creep behavior of eutectic 80Au/20Sn solder alloy. J. Alloys Compd. **476**, 138–141 (2009)
7. L. Wang, Y. Wang, W. Liao et al., Ethanol electrocatalytic oxidation performance of carbon black-supported Pt-Sn bimetallic catalysts. J. Mol. Catal. **39**, 35–44 (2014)
8. Z. Chen, D. Chen, J. Qin et al., Electrocatalytic effect of polyaniline electrode modified by platinum microparticles on oxidation of formaldehyde. Mater. Rev. **28**, 36–39 (2014)
9. S. Sun, P. Mu, Influence of nafion and the proportion of water and isopropyl alcohol on activity of Pt/C catalyst. Mater. Rev. **28**, 36–39 (2014)
10. X. Ma, X. Ge, Q. Yuan, Research of direct methanol fuel cell catalysts. Sci. Technol. Vision **14**, 101–102 (2015)
11. J. Li, X. Wang, L. Yi et al., Research of Au-based anode electrocatalysts materials and reaction mechanism for direct borohydride fuel cell. Chin. J. Power Sources **38**, 181–184 (2014)
12. L. Liu, D. Fang, W. Ren et al., Preparation of Au-Pt-Sn catalysts for isobutane dehydrogenation. Ind. Catal. **22**, 293–296 (2014)
13. L. Liu, *Phase Diagram Thermodynamic Calculation and Experimental Study of Au-Pd-Zr Ternary Alloy* (Kunming University of Science and Technology, Kunming, 2011)
14. Y. Wu, *Thermodynamic Optimization and Calculation of Pt-Zr-X (X=Ir, Au) System* (Kunming University of Science and Technology, Kunming, 2014)
15. X. Su, F. Yin, M. Huang, Z. Li, C. Chen, J. Alloys Compd. **325**, 109–112 (2001)

16. S.-L. Chen, S. Daniel, F. Zhang, Y.A. Chang, W.A. Oates, R. Schmid-Fetzer, J. Phase Equilib. Diff. **22**, 373–378 (2001)
17. R. Schmid-Fetzer, A. Kozlov, Thermodynamic aspects of grain growth restriction in multicomponent alloy solidification. Acta Mater. **59**, 6133–6144 (2011)
18. G. Vincent, S.F. Rainer, Thermodynamic analysis of the Pt–Sn system. J. Alloy. Compd. **450**, 264–271 (2008)
19. A.T. Dinsdale, Calphad **15**(4), 317–425 (1991)
20. R. Schmid, Y.A. Chang, Calphad **9**(4), 363–382 (1985)
21. W. Zhou, L. Liu, B. Li et al., Structural, elastic and electronic properties of intermetallics in the Pt–Sn system: a density functional investigation. Comput. Mater. Sci. **46**, 921–931 (2009)
22. K.L. Shelton, P.A. Merewether, B.J. Skinner, Phases and phase relations in the system Pd-Pt-Sn. Can. Mineral **19**, 599–605 (1981)
23. J.S. Charlton, H.M. Cordey, I.R. Harris, A study of the 119Sn Moessbauer isomer shifts in some platinum-tin and gold-tin alloys. J. Less-Common Metals **20**, 105–112 (1970)
24. K. Schubert, H. Pfisterer, Die Kristallstruktur von Pt_2Sn_3. Z. Metallkd. **40**, 105–112 (1949)
25. F. Doerinckel, Z. Anorg. Chem. **54**, 333–366 (1907)
26. P.H. Durussel, R. Massara, P. Feschotte, J. Alloy. Compd. **215**, 175–179 (1994)
27. P. Anres, M. Gaune-Escard, J.P. Bros, E. Hayer, J. Alloy. Compd. **280**, 158–167 (1998)
28. J.S. Charlton, M. Cordey-Hayes, I.R. Harris, A study of the ^{119}Sn mössbauer isomer shifts in some platinum-tin and gold-tin alloys. J. Les. Comm. Met. **20**, 105–112 (1970)
29. U.C. Rodewald, R.D. Hoffmann, Z. Wu et al., Structure refinement of $AuSn_2$. Z. Naturforsch. **61**, 108–110 (2006)
30. P.Y. Chevalier, A thermodynamic evaluation of the Au-Sn system. Thermochim. Acta **130**, 1–13 (1988)
31. L.C. Liu, H.S. Liu, K. Ishida et al., Thermodynamic modeling of the Au-In-Sn system. J. Electron. Mater. **32**, 1290–1296 (2003)
32. V. Grolier, R.F. Schmid, Experimental study of Au-Pt-Sn phase equilibria and thermodynamic assessment of the Au-Pt and Au-Pt-Sn systems. J. Electron. Mater. **37**, 264–278 (2008)
33. A. Jena, M. Bever, On the thermodynamic properties of the phases Zeta and AuSn in the system Au-Sn. Metall. Mater. Trans. B **10**, 545–549 (1979)
34. H. Dong, *Thermodynamic Optimization and Calculation of Au-Sn-X(X=Co, La, Er) System* (Central South University, Chamgsha, 2010)
35. A. Dębski, W. Gąsior, Z. Moser, R. Major, Enthalpy of formation of intermetallic phases from the Au-Sn system. J. Alloy. Compd. **491**, 173–177 (2010)
36. J. Hu, M. Xie, J. Zhang et al., First principles study of Au-Sn intermetallic compounds. Acta Phys. Sinica **62**, 247102 (2013)
37. X. Xu, Y. Ren, C. Li et al., Thermodynamic assessment of Au–Pt system. Trans. Nonferrous Metals Soc. China **22**, 1432–1436 (2012)
38. N.T. Alexandra, O. Laila, A. Kjekshus et al., The tin-rich part of the Au-Pt-Sn system. J. Alloys Compd. **314**, 92–95 (2001)
39. H. Dong, V. Vuorinen, M. Broas, M. Paulasto-Kr€ockel, Thermodynamic reassessment of the Au-Pt-Sn system and microstructural evolution of the (AuSn)eut-Pt interconnection. J. Alloy. Compd. **688**, 388–398 (2016)

Failure Mechanisms of Ti–Al_3Ti Metal-Intermetallic Laminate Composites

Yuan Meini, Li Yao, Li Lizhou, Chen Hehe and Huang Bin

Abstract Ti–Al_3Ti Metal-Intermetallic Laminate (MIL) composites were fabricated by vacuum hot pressing. The failure mechanisms of Ti–Al_3Ti MIL composites under the bending load and dynamic loading conditions were analyzed by three points bending test and finite element analysis respectively. The results indicated that the vertical crack existed in the as-deposited state Ti–Al_3Ti MIL composites in the Al_3Ti layers resulted by the thermal residual stress. The three points bending load- displacement curves of Ti–Al_3Ti MIL composites embraced a long plateau region, indicating that Ti–Al_3Ti MIL composites have excellent damage tolerance. Ti–Al_3Ti MIL composites under high-speed impact was mostly under the tensile stress. In the high-speed impact period, the transverse, inclined, and vertical cracks which dramatically absorb the projectile kinetic energy formed in Al_3Ti phase.

Keywords Metal-intermetallic laminate composites · Three points bending Finite element method · High-speed impact

Introduction

Ti–Al_3Ti Metal-Intermetallic Laminate (MIL) composites have great potential in lightweight armor materials due to their high hardness, compressive strength and some level of ductility at a lower density [1–4]. In the last two decades, researchers have concentrated on the fabrication process, the mechanical properties and fracture behavior of Ti–Al_3Ti MIL composites. The fabrication process and mechanical

Y. Meini (✉) · L. Yao · L. Lizhou · C. Hehe
College of Mechanical and Electrical Engineering,
North University of China, Taiyuan 030051, China
e-mail: mnyuan@126.com

Y. Meini · H. Bin
State Key Laboratory of Solidification Processing,
Northwestern Polytechnical University, Xi'an 710072, China

© Springer Nature Singapore Pte Ltd. 2018

Y. Han (ed.), *Advances in Materials Processing*, Lecture Notes in Mechanical Engineering, https://doi.org/10.1007/978-981-13-0107-0_87

properties of Ti–Al_3Ti MIL composites have been investigated thoroughly [5–7]. However, limited researches were conducted on characterizing the failure mechanisms of Ti–Al_3Ti MIL composites. In order to better design and application Ti–Al_3Ti MIL composites in armor materials, it is critical to acquire more information on the failure mechanisms of Ti–Al_3Ti MIL composites. Cao et al. [3] investigated the failure mode and damage mechanisms of Ti–Al_3Ti MIL composites under high impact. Li et al. [8] investigated the crack propagation in Ti–Al_3Ti MIL composites at different strain rates (0.0001 and 800–2000 s^{-1}).

In this paper, Ti–Al_3Ti MIL composites was fabricated by vacuum hot pressing. Moreover, the failure mechanisms of Ti–Al_3Ti MIL composites under three-point bending load and high impact load were investigated.

Experimental Procedure

Material Fabrication

Ti–Al_3Ti MIL composites were fabricated using pure Al and Ti–6Al–4V alloy foils by vacuum hot pressing. The dimensions of the pure Al and Ti–6Al–4V foils were 38 mm × 68 mm × 0.1 mm. First, the surface of both foils were grinded by silicon carbide papers and cleaned in alcohol bath using ultrasonic cleaning machine to remove the contaminations and oxide layers. Then, the cleaned foils were dried rapidly. Last, the cleaned foils were stacked in alternate and placed in a vacuum furnace to sinter under appropriate temperature, pressure, and time. Ti–Al_3Ti MIL composites in this study have 52 layers in total, including 18 layers of ductile Ti–6Al–4V,17 layers of ductile Al, and 17 layers of brittle intermetallic Al_3Ti.

Three-Point Bending Test

The three-points bending test was conducted using Instron5505 universal testing machine. The under press rate of cross head is 1 mm/miu. Figure 1 shows the

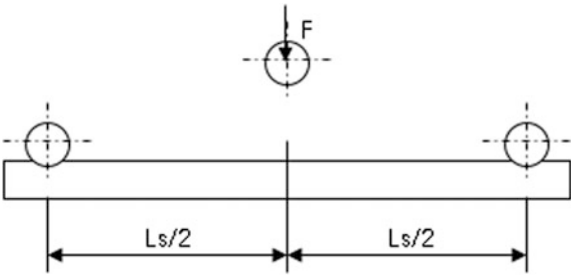

Fig. 1 Schematic diagram of the three-point bending test

diagram of three-point bending specimen, in which F represents as load, Ls is the span of 26 mm for supporting the specimen.

High Impact Test

The 2D axisymmetric model was adopted to analyze the high impact test on Ti–Al_3Ti MIL composites, as shown in Fig. 2, which consisted of a projectile with initial velocity and a Ti–Al_3Ti MIL composite target. Ti–Al_3Ti MIL composites consisted of 18 layers of Ti and 17 layers of Al_3Ti, the thickness of Ti and Al_3Ti layers were $\sim$0.23 and $\sim$0.94 mm, respectively. The projectile was a rod of 6.15 mm diameter and 23 mm length, which was made of a tungsten alloy with a density of $\sim$18.5 g/cm^3. The impact velocity of the projectile was 900 m/s. The tungsten alloy projectile, Ti and Al_3Ti layers in MIL composites were meshed with 2D axisymmetric quadratic shell. The projectile elements size was 0.5 mm $\times$ 0.5 mm, and the MIL composite element size was 0.5 mm $\times$ 0.2 mm. The total numbers of elements and nodes were 66,309 and 67,075, respectively.

The model considered realistic boundary conditions during the high impact process. A zero values are imposed to the rotations in x and y directions for all the elements, also the edges of composites were fixed. CONTACT_ERODING_SURFACE_TO_SURFACE contact model was defined between the projectile and Ti–Al_3Ti MIL composites. This contact model allowed elements to be eroded from both of the projectile and composites when certain failure criteria were met.

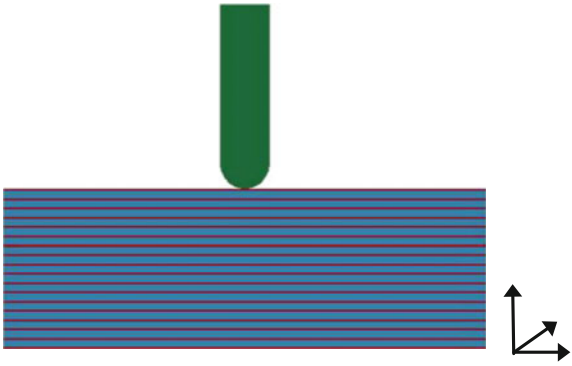

Fig. 2 2D axisymmetric model of projectile and Ti–Al_3Ti MIL composites

Materials Models

In the simulation, the titanium layers and the tungsten alloy projectile were modeled using the Johnson–Cook (JC) material model and the JC fracture criterion. The material parameters were given in Table 1 [9]. In the JC model, the equivalent stress σ_{eq} can be expressed as [10]:

$$\sigma_{eq} = [A + B\varepsilon^{n}][1 + C\ln\varepsilon^{*}][1 - T^{*m}]. \tag{1}$$

where A, B, n, C and m are the material constants, ε is the equivalent plastic strain, the dimensionless plastic strain rate ε* equals to $\varepsilon/\varepsilon^{0}$, The homologous temperature T* is defined as follows:

$$T^{*} = (T - 298)/(T_{melt} - 298). \tag{2}$$

where T and T_{melt} are absolute temperature and melting temperature, respectively.

The damage parameter, D, (0 < D < 1) in the JC fracture criterion describes the degree of damage, which is written as follows:

$$D = \Sigma\left(\Delta\varepsilon/\varepsilon^{f}\right). \tag{3}$$

The equivalent fracture strain is given by:

$$\varepsilon_{f} = [D_1 + D_2\exp(D_3\sigma^{*})][1 + D_4\ln\varepsilon^{*}][1 + D_5T^{*}] \tag{4}$$

where D_1, D_2, D_3, D_4 and D_5 are material constants, σ_m is the hydrostatic stress, and $\sigma^* = \sigma_m/\sigma_{eq}$ is the stress triaxiality.

When the JC model was used to simulate the material's dynamic response, Gruneisen's Equation of State describes the relationship between pressure and volume difference. Gruneisen's Equation of State has the following form [11]:

$$p = \frac{\rho_0 C_{\mu}^{2}[1 + \left(1 - \frac{\gamma_0}{2}\right)\mu - \frac{a}{2}\mu^{2}]}{[1 - (S_1 - 1)\mu - S_2\frac{\mu^{2}}{\mu+1} - S_2\frac{\mu^{2}}{(\mu+1)^{2}}]^{2}}. \tag{5}$$

where P is pressure, μ is the volume difference, C is material sound velocity and S1, S2 and S3 are fluid state equation coefficients. The Johnson-Holmquist-Ceramics (JH-2) model was applicable for the constitutive relation of intermetallic Al_3Ti. Table 2 listed the necessary material constants for Al_3Ti used in the JH-2 model, some of which were taken from aluminum nitride [12] due to lack of the data for the Al_3Ti intermetallic. And the effectiveness of these parameters was confirmed by Li et al. [8].

Table 1 Parameters of Tungsten and Titanium in Johnson-Cook constitutive equation

Material	ρ	E(GPa)	E	PR	A	B	N	C	M	T_M	T_R	EPSO
Tungsten	18.50	1.60	3.10	0.30	1.506E−02	0.177E−02	0.12	0.016	1.1	1752	293	0.1E−05
Titanium	4.428	0.434	1.14	0.34	1.098E−02	1.092E−02	0.93	0.014	1.1	1878	293	0.1E−05

Table 2 Parameters of $A1_3Ti$ in JH-2 constitutive equation

ρ	E(GPa)	A	B	C	M	N	E_{PSI}	T
3.38	215	0.85	0.31	0.013	0.21	0.29	1.0	0.0022

H_{EL}	P_{HEL}	B_{ETA}	D1	D2	K1	K2	K3	FS
0.10	0.03049	1.0	0.020	1.85	2.01	2.6	0.0	1.00

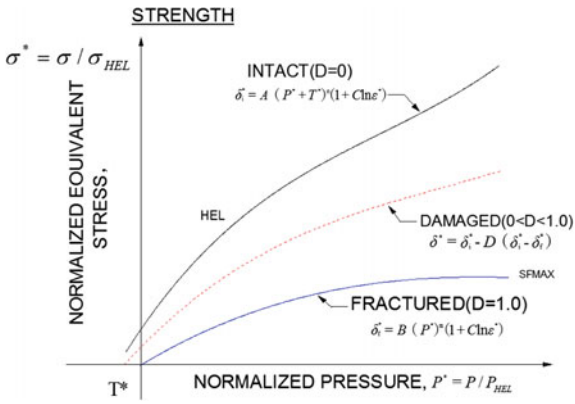

Fig. 3 Description of the JH-2 model

When the JH-2 model was used to simulate the intermetallic Al_3Ti, the damage parameter D for Al_3Ti was defined as the ratio of equivalent plastic strain increment to fracture strain. Different strength models corresponding to different damage degrees (Fig. 3) can be employed as follows [13]:

$$D' = 0 \tag{6}$$

$$D' = 1 \tag{7}$$

$$(0, 1).D'(0, 1) \tag{8}$$

where A, N, C, B and m are material constants measured by quasi-static and dynamic compression tests, and p* and T* are current and maximum hydrostatic pressures, respectively. Both hydrostatic pressures are normalized by the pressure at the Hugoniot elastic limit (HEL). The current material strength (σ*) is dependent upon its initial strength (σ i*) and fracture strength (σ f*). All the strengths mentioned above are normalized by equivalent stress at the HEL measured by plate impact tests. The JH-2 constitutive model requires several material constants to completely describe the response of Al_3Ti material. Based on the material deformation, μ (Eq. 9) and corresponding pressure (Eqs. 10a and 10b) can be calculated.

$$\mu = \rho/\rho_0 - 1. \tag{9}$$

$$P = K_1\mu + k_2\mu^2 + K_3\mu^3 + \Delta P_{n-1}. \quad \text{compression} \tag{10a}$$

$$P = K_1\mu. \quad \text{tension} \tag{10b}$$

In Eq. (10a), P corresponds to the compressive pressure and is determined by the accumulated damage. Under the compressive loading, damage begins to accumulate within the material when the stress exceeds a critical value. This damage accumulation is tracked via a damage parameter (ranging from 0 to 1.0). The pressure is normalized by the equivalent pressure at the HEL. When subjected to tensile pressure (10b), the material responds elastically until brittle failure at a specified stress value. This corresponds to complete instantaneous damage.

Results and Discussion

Microstructure of Ti–Al_3Ti MIL Composites

Figure 4 showed the SEM image of Ti–Al_3Ti MIL composites fabricated by vacuum hot pressing. It showed that Ti–Al_3Ti MIL composites were well-bonded, nearly fully dense and readily designed and controlled. Ti–Al_3Ti MIL composites consisted of three different phases, including Al (dark regions), intermetallic Al_3Ti (grey regions) and Ti (white regions) layers. The intermetallic phases Al_3Ti provided high hardness and compressive strength to Ti–Al_3Ti MIL composites, while the ductile metal Ti and Al layers provided the necessary ductility, which serve to constrain and connect Al_3Ti layers together. In additional, some cracks were originated in Al_3Ti layers and perpendicular to the interface. This was attributed to the development of residual stresses during the cooling process of Ti–Al_3Ti MIL composites.

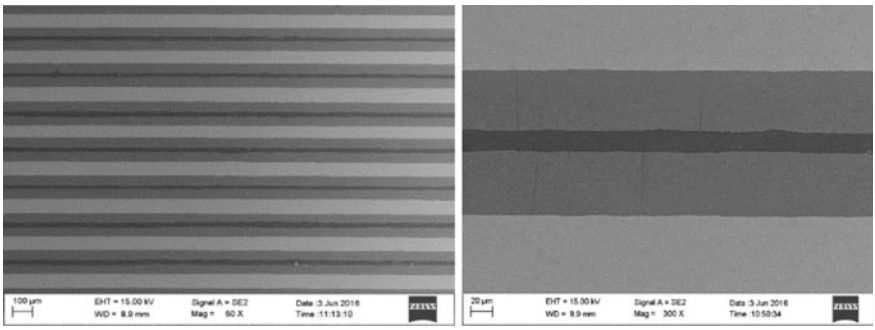

Fig. 4 The SEM micrograph of Ti–Al_3Ti laminate composites

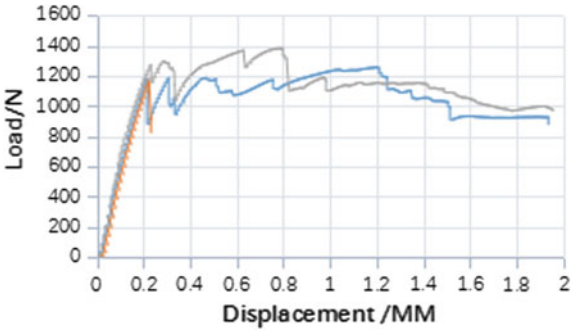

Fig. 5 Load-displacement curves for three-point bending specimens of Ti–Al_3Ti laminated composites

Three-Point Bending Curves

Figure 5 showed the typical three-point bending load-displacement curves of un-notched Ti–Al_3Ti MIL composite specimen at 1 mm/miu loading rate. As shown, the curve remained nearly linear up to the peak load 1200 Mpa, at which point a crack initiated from some defect and extended gradually in the through-thickness, giving rise to the peak load drop. It was noted that the load-displacement curves of un-notched Ti–Al_3Ti MIL composite specimen showed the strain platform in a wide range, due to numerous cracks originating in Al_3Ti regions. It also demonstrates that Ti–Al_3Ti MIL composites have good energy dissipation and anti-shock performance, and MIL composite is effective to enhance the ductility and keep the strength of intermetallic Al_3Ti. Dang et al. [14] employed rapid solidification post-solidification heat treatment to break through the strength-ductility trade-off dilemma in casting alloys. Figure 6 showed the side morphology of Ti–Al_3Ti MIL composites under the three-point bending loading. The failure modes of Ti–Al_3Ti MIL composites under the three-point bending load was titanium alloy yielding, Al_3Ti crushing, and interface debonding. Crack originated in the Al_3Ti regions and propagated in the vertical direction of the interface.

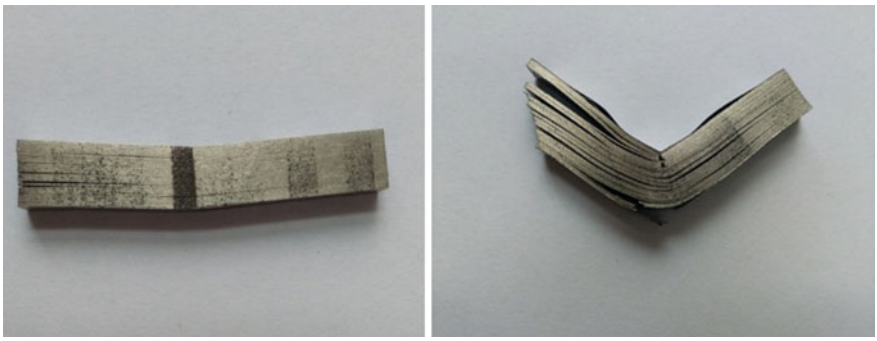

Fig. 6 Side micrograph of Ti–Al_3Ti laminate composites under three-point bending loading

Then crack deflected along the Ti/Al_3Ti interface, which also demonstrates the MIL composites had excellent damage tolerance because of the high energy-absorbing mechanisms.

Damage Evaluation

Figure 7 shows the failure mode and damage evaluation of the Ti–Al_3Ti MIL composite was impacted by a tungsten alloy projectile with an impact velocity of 900 m/s. The tungsten alloy projectile impacted on the Ti–Al_3Ti MIL composite, and produced a crater and Al_3Ti fragments. The Ti layer prevented Al_3Ti fragments ejecting effectively from the crater, and forced the fragments to act with the projectile, which reduced largely the kinetic energy of projectile and decelerated the projectile.

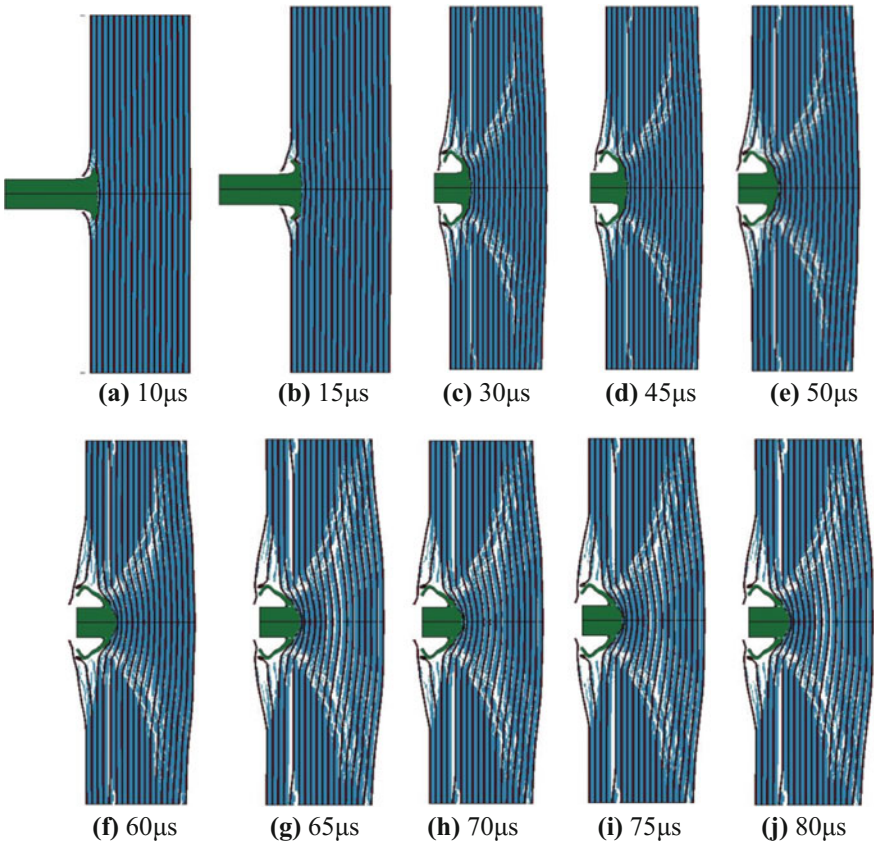

Fig. 7 Damage evaluation of the MIL target impacted by a tungsten projectile

The simulated image at 10 μs (Fig. 7a) showed evidently that there was a crater on the top surface of Ti–Al_3Ti MIL composites. Moreover, a crack concentration zone existed between the projectile and the composite, and there was almost no cracking beyond the crack concentration area. When the tungsten alloy projectile penetrated Ti–Al_3Ti MIL composite, the front end of the tungsten alloy projectile was squeezed by the MIL composite, and the high normal contact stress occurred in the region between the projectile and the composite. The normal contact stress was more than the compressive strength of Al_3Ti, which result in the crushing of Al_3Ti phase. Several studies [15–17] demonstrated that in Ti–Al_3Ti MIL composites the failure always initiated from the Al_3Ti intermetallic compound.

At 15 μs, there were a little vertical cracks originally occurring on the sixth, seventh and eighth layers, as shown in Fig. 7b. Such a unique failure feature was observed only in Ti–Al_3Ti MIL composite under high velocity impact. Tan et al. [18] also researched that when the tensile stress, caused by the deflection of the support plate, exceeded the composite strength, the petal cracks would occur in the bottom surface of support plate.

In the period of 20–50 μs (Fig. 7c–e), the transverse, inclined, and vertical cracks formed in Al_3Ti phase under the combined effect of tensile and compressive stress. The brittle micro-cracks density increased with increasing the penetration time, and these brittle micro-cracks were grown the main crack along an inclined angle direction. In other words, a ceramic cone occurred in Ti–Al_3Ti MIL composites. The angle of ceramic cone was about 60 degree, which agreed with the results in Refs. [18, 19].

During the final penetration time 60–80 μs (Fig. 7f–j), the delamination cracks continued to occur under the reflected tensile stress wave. The depth and diameter of the ceramic cone was becoming smaller and smaller. The projectile penetrated into the ceramic cone, which also resulted in producing new small ceramic cone, this was also mentioned in Ref. [19]. Such penetration would repeat until the diameter of the new small ceramic cone was close to the diameter of projectile. Then, the new small ceramic cone was compressed by the projectile and separated from the surrounding ceramic fragments [20].

Conclusion

The failure mechanism of Ti–Al_3Ti in the as-deposited state, the three-point bending and the high impact has been studied. In the as-deposited state, some cracks originate in the Al_3Ti layers due to the development of residual stresses during the cooling process of Ti–Al_3Ti MIL composites. Under the three-points bending loading the failure modes of Ti–Al_3Ti MIL composites is titanium alloy yielding, Al_3Ti crushing, and interface debonding. The cracks originate in the Al_3Ti regions and propagate in the vertical direction of the interface. Then the crack deflectes along the Ti/Al_3Ti interface; When the Ti–Al_3Ti composite is impacted by a tungsten projectile at about 9000 m/s, the transverse, inclined, and vertical cracks

form in Al_3Ti phase under the combined effect of tensile and compressive stress, and these transverse, inclined, and vertical cracks dramatically absorb the projectile kinetic energy.

Acknowledgements The authors acknowledge the financial support provided by the Natural Science of China (51201155), the Natural Science of Shanxi province (2012011019-1, 2012011007-1), and the Chinese Education Ministry Foundation for Doctors (20101420120006).

References

1. D.J. Harach, K.S. Vecchio, Microstructure evolution in metal-intermetallic laminate (MIL) composites synthesized by reactive foil sintering in air. Metall. Mater. Trans. A **32** (6), 1493–1505 (2001)
2. J.G. Luo, V.L. Acoff, Using cold roll bonding and annealing to process Ti/Al multilayered composites from element foils. Mater. Sci. Eng., A **379**(1/2), 164–172 (2004)
3. Y. Cao, C.H. Guo, S.F. Zhu et al., Fracture behavior of Ti/Al_3Ti metal-intermetallic laminate (MIL) composite under dynamic loading. Mater. Sci. Eng., A **637**, 235–242 (2005)
4. S.A. Zelepugin, S.S. Shpakov, Failure of metallic-intermetallic multilayered composite under high-velocity impact. J. Comp. Mech. Design **15**(3), 369–382 (2009)
5. P.J. Zhou, C.H. Guo, E.H. Wang et al., Interface tensile and fracture behavior of the Ti/Al_3Ti Metal-Intermetallic Laminate (MIL) composite under quasi-static and high strain rates. Mater. Sci. Eng., A **665**, 66–75 (2016)
6. F. Jiang, R.M. Kulin, K.S. Vecchio, Use of Brazilian disk test to determine properties of metallic-intermetallic laminate composites. J. Min. Met. Mater. Soc. **62**(1), 35–40 (2010)
7. A. Rohatgi, D.J. Harach, K.S. Vecchio, K.P. Harvey, Resistance-curve and fracture behavior of Ti-Al_3Ti metallic-intermetallic laminate (MIL) composites. Acta Mater. **51**, 2933–2957 (2003)
8. T.Z. Li, F. Grignon, D.J. Benson, K.S. Vecchio et al., Modeling the elastic properties and damage evolution in Ti-Al_3Ti metal-intermetallic laminate (MIL) composite. Mater. Sci. Eng., A **374**(1–2), 10–26 (2004)
9. D.R. Leseur, Experimental investigations of material models for Ti-6Al-4V titanium and 2024-T3 aluminum. Technical Report DOT/FAA/AR-00/25. US department of Transportation. Federal Aviation Administration, September 2000
10. G. Kay, Failure modeling of titanium 6Al-4V and aluminum 2024-T3 with the Johnson-Cook material model. Technical Report DOT/FAA/AR-03/57. US department of Transportation, Federal Aviation Administration, September 2003
11. Y. Cao, S.F. Zhu, C.H. Guo, K.S. Vecchio, Numerical investigation of the ballistic performance of metal-intermetallic laminate composites. Appl. Compos. Mater. **22**, 437–456 (2015)
12. D.S. Cronin, K. Bui, C. Kaufmann, G. McIntosh, T. Berstad, Implementation and validation of the Johnson-Holmquist ceramic material model in LS-DYNA, in *4th European LS-dyna Users Conference*, 2003, pp. 47–60
13. T.J. Holmquist, G.R. Johnson, Modeling prestressed ceramic and its effect on ballistic performance. Int. J. Impact Eng. **31**(2), 113–127 (2005)
14. B. Dang, X. Zhang, Y.Z. Chen et al., Breaking through the strength-ductility trade-off dilemma in an Al-Si-based casting alloy. Scientific Reports, 6(30874) (2016), pp. 1–10
15. D.R. Hartman, S.J. Bless, S.J. Hanchak, Ballistic performance of thick S-2 glass composites, in *Proceedings of the Symposium on Composite Materials in Armament Applications*, UDR-TR-85-88a, 20–22 August 1985

16. D. Sherman, T. Ben-Shushan, Quasi-static impact damage in confined ceramic tiles. Int. J. Impact Eng. **21**(4), 245e65 (1998)
17. N.A. Fellows, P.C. Barton, Development of impact model for ceramic faced semi-infinite armour. Int. J. Impact Eng. **22**, 793–811 (1999)
18. Z.H. Tan, X. Han, W. Zhang, S.H. Luo, An investigation on failure mechanisms of ceramic/metal armour subjected to the impact of tungsten projectile. Int. J. Impact Eng. **37**, 1162–1169 (2010)
19. R. Yahaya, S.M. Sapuan, M. Jawaid et al., Measurement of ballistic impact properties of woven kenaf-aramid hybrid composites. Measurement **77**, 335–343 (2016)
20. W.L. Cheng, S. Langlie, S. Itoh, High Velocity impact of thick composites. Int. J. Impact Eng. **29**, 167–184 (2003)

Microstructures and Properties of High Performance Cast Irons Applied in Automobile Flywheels

Xianfei Ding, Hong Huang, Xiaozheng Li, Warkentin Matthias, Shiyao Huang and Qiang Feng

Abstract High performance cast iron (HPCI) with improved mechanical properties and balanced thermal conductivity is a strong candidate to replace ductile iron in the application of automobile flywheel. In this work, the relationship between microstructures and properties, including mechanical and thermal properties, of the grey cast iron were investigated by analysing some commercial flywheels. The results showed that the content of graphite was dependent on the content of carbon in the grey cast irons, and the simulation results indicated that most of carbon directly formed into graphite at room temperature (RT). High ultimate tensile strength (UTS) is caused by low area fraction and short length of the graphite. The thermal conductivity increased with increase of the area fraction of graphite. The short length of graphite would also contribute to thermal conductivity since a large number of the short graphite flakes formed under the circumstance of the similar area fraction of graphite. In order to get HPCI, the microstructures with a moderate area fraction and short length of graphite should be controlled.

X. Ding (✉)
Beijing Institute of Aeronautical Materials, Beijing 100095, China
e-mail: xfding@ustb.edu.cn

X. Ding · H. Huang
National Center for Materials Service Safety, University of Science and Technology Beijing, Beijing 100083, China

X. Li · Q. Feng
State Key Laboratory for Advanced Metals and Materials, University of Science and Technology Beijing, Beijing 100083, China

W. Matthias
Ford Research & Advanced Engineering Europe, Ford Werke GmbH, Süsterfeldstr. 200, 52072 Aachen, Germany

S. Huang
Materials and Process Research, Ford Motor Research and Engineering Center, Nanjing 211100, China

Q. Feng
Beijing Key Laboratory of Special Melting and Preparation of High-End Metal, University of Science and Technology Beijing, Beijing 100083, China

© Springer Nature Singapore Pte Ltd. 2018

Y. Han (ed.), *Advances in Materials Processing*, Lecture Notes in Mechanical Engineering, https://doi.org/10.1007/978-981-13-0107-0_88

Keywords High performance cast iron (HPCI) · Grey cast iron Microstructure · Type A graphite · Thermal conductivity · Ultimate tensile strength

Introduction

Grey cast iron is one of the most significant casting materials, which has been widely used in modern industries [1]. Due to its excellent damping and thermal transport properties, grey cast iron is the primary material for vehicle discs, brake rotors as well as flywheels [2]. However, for advanced automobile engines, increased loading for flywheels is necessary and conventional grey cast iron cannot meet the performance requirements. Therefore, high performance cast iron (HPCI) with improved mechanical properties and balanced thermal conductivity is developed to replace the high-cost ductile iron in flywheel application.

It's known to all that both of the mechanical properties and thermal properties are closely related to the graphite morphology in cast iron [3, 4]. For grey cast iron, graphite flake breaks the continuity of matrix, which could decrease the tensile strength of grey cast iron [5]. However, the graphite is beneficial to thermal conductivity. It was reported that a higher amount of flake graphite leads to a higher thermal conductivity [6]. Thus, to find out appropriate amount and morphology of graphite is important to develop HPCI with good thermal conductivity while maintaining high strength to replace the commercial ductile iron. Nevertheless, the relationship between microstructure and properties is a major challenge to achieve HPCI.

This paper mainly focuses on promoting microstructures in grey cast iron with high properties. The relationship between microstructure and properties, especially thermal properties of grey cast iron will be investigated by analysing some commercial flywheels. The data conducted would lay a foundation to develop HPCI.

Experimental

All the specimens for microstructure observation and properties testing were directly cut from the commercial flywheel productions labelled as CI-1, CI-2, CI-3 and CI-4. Figure 1a shows the exterior appearance of typical flywheel samples. The diameters of the flywheels were around 300 mm, and the chemical compositions of all these samples were detected and listed in Table 1. The specimen locations for the microstructure observation, thermal properties and tensile properties testing were shown in Fig. 1b.

J-mat Pro was used to simulate the phase transformations with temperature changes according to the compositions of these four samples. Microstructures of graphite and matrix were characterized by an optical microscope (OM, ZEISS Axio

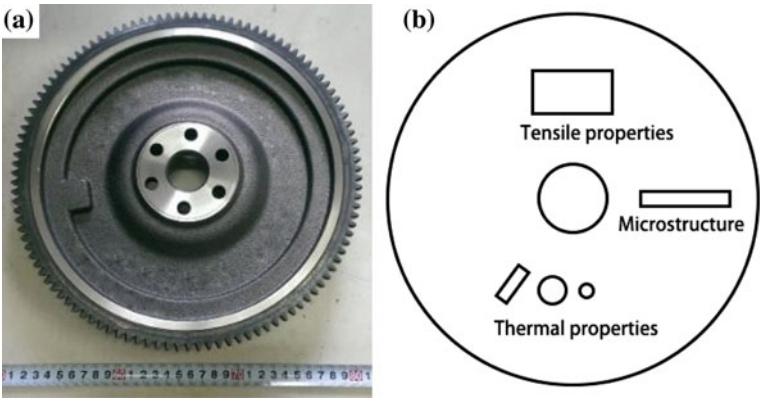

Fig. 1 Exterior appearance of typical flywheel sample (**a**) and the specimen positions for microstructure observation, tensile properties and thermal properties testing (**b**)

Table 1 Measured chemical compositions for all samples (wt%)

Sample	Fe [%]	C [%]	Si [%]	Cr [%]	Mo [%]	Mn [%]	P [%]	S [%]
CI-1	Bal.	3.10	1.92	0.14	0.019	0.87	0.067	0.063
CI-2	Bal.	3.29	1.99	0.24	0.014	0.65	0.017	0.044
CI-3	Bal.	3.51	1.32	0.10	0.21	0.50	0.018	0.028
CI-4	Bal.	3.65	1.18	0.089	0.29	0.47	0.020	0.034

Imager A2m) and a scanning electron microscope (SEM, ZEISS SUPRA 55). Graphite type and classification were determined according to EN ISO 945-1 2008 [7]. Statistical analysis on the area fraction and size of graphite was conducted by Image J software, and more than ten images were used to calculate the average value and error for the final results. After measurement on more than three images, the curved graphite length and classification were determined by the average length value of three longest graphite flakes. Schematic diagram of the curved graphite length measurement was illustrated in Fig. 2.

Tensile properties were tested at 25, 200, 400, 500 and 800 °C for three times at every temperature. The tensile samples were 65 mm length, with a gauge in diameter of 3 mm. Dimension and outline drawing of the tensile specimens are shown in Fig. 3a and b, respectively. After testing the tensile properties, the fracture features were also characterized by using the SEM.

Thermal conductivity was calculated by the following equation [8, 9]

$$\lambda(T) = a(T) * Cp(T) * \rho(T) \tag{1}$$

where $\lambda(T)$ is thermal conductivity, $a(T)$ is thermal diffusivity, $C_p(T)$ is specific heat capacity and $\rho(T)$ is density. With increase of the temperature, the density

Fig. 2 Schematic diagram of the curved graphite length measurement using Image J software

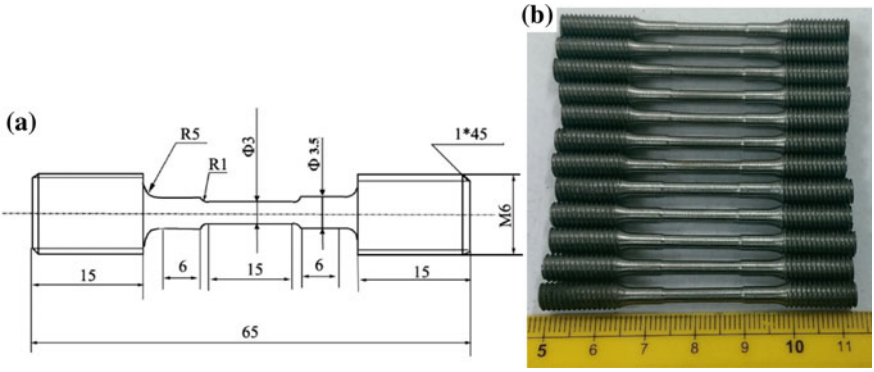

Fig. 3 Dimension drawing (**a**) and outline (**b**) of the tensile specimens

decreases all the way due to thermal expansion, and their relationship can be expressed as follow:

$$\rho(T) = \rho RT/(1 + 3a\,\Delta\,T) \tag{2}$$

where ρ_{RT} is density at room temperature (RT), ρ(T) is density at temperature of T, α is thermal expansion coefficient and ΔT is the temperature gradient between T and RT.

Thermal properties were obtained at 25 °C and at range from 100 to 800 °C with intervals of every 100 °C. The specimen dimensions for thermal diffusivity test were Φ12.7 mm × (1–2) mm, using a laser flash equipment, Netzsch LFA 427. The special heat capacities, $C_p(T)$, were calculated by theory according to the Neumann-Kopp rule [10]. The specimen length for thermal expansion coefficient

was 25 mm, with a diameter of 6 mm, which was measured by using a dilatometry, NETZSCH DIL402C. The densities of the samples were measured by Archimedes' method [11].

Results and Discussion

Typical J-mat Pro simulation on phase transitions of the grey cast irons is illustrated in Fig. 4. CI-2 is taken as an example for that they are nearly the same. And their differences are dependent on the content of graphite at low temperature and the precipitation temperature of austenite, as shown in Table 2. With decreasing carbon content or increasing manganese content, the precipitation temperature of austenite increases. Another fact that should be paid attention to is that, the graphite content calculated by J-mat Pro is a little less than the carbon content from the measured results, which means that most of the carbon is transformed into graphite at low temperature. It is suggested that the graphite content can be controlled by modifying the content of carbon.

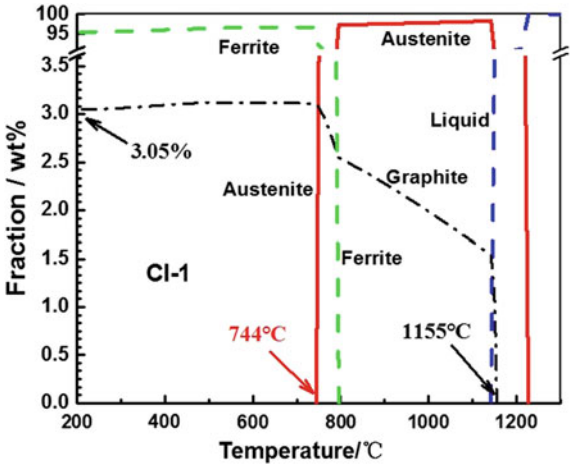

Fig. 4 Typical J-mat Pro simulation on phase transitions of grey cast iron CI-1

Table 2 Simulation results on austenite precipitation temperature and graphite content

Sample	Precipitation T of austenite [°C]	Graphite content [%]
CI-1	1227	3.05
CI-2	1210	3.22
CI-3	1203	3.45
CI-4	1191	3.59

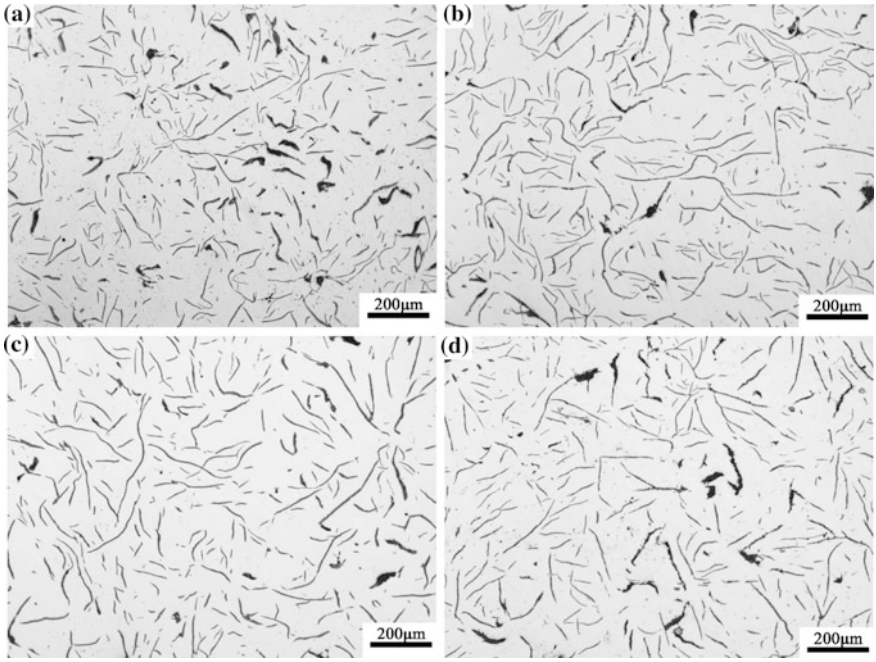

Fig. 5 Morphology of graphite observed by OM at ×100 magnification: **a** CI-1 **b** CI-2 **c** CI-3 **d** CI-4

Figure 5 shows the typical morphology of graphite observed by OM for each samples without etching. All of the graphite morphologies are classed as Type A according to EN ISO 945-1 [7]. The dark area is flake graphite while the bright area is the matrix. Obviously, CI-1 has smaller graphite from the point of two-dimension's view.

Figure 6 illustrates the morphology of matrix for the samples after etching by 4% nital. The matrix in all samples almost consists of the laminar pearlite and no any other precipitates are observed. The interlamellar spacing of these pearlite colonies is inhomogeneous and the sizes of lamellar colonies are close to each other in all samples, which suggest that it is no preferred orientation and these grey cast irons should be experienced by the similar casting processing conditions.

Statistic results on the length, area fraction and classification of graphite are listed in Table 3. Obviously, CI-4 and CI-1 have lower area fractions and shorter length of graphite while CI-3 has both the highest area fraction and largest graphite length, which is consistent with the graphite morphology shown in Fig. 5.

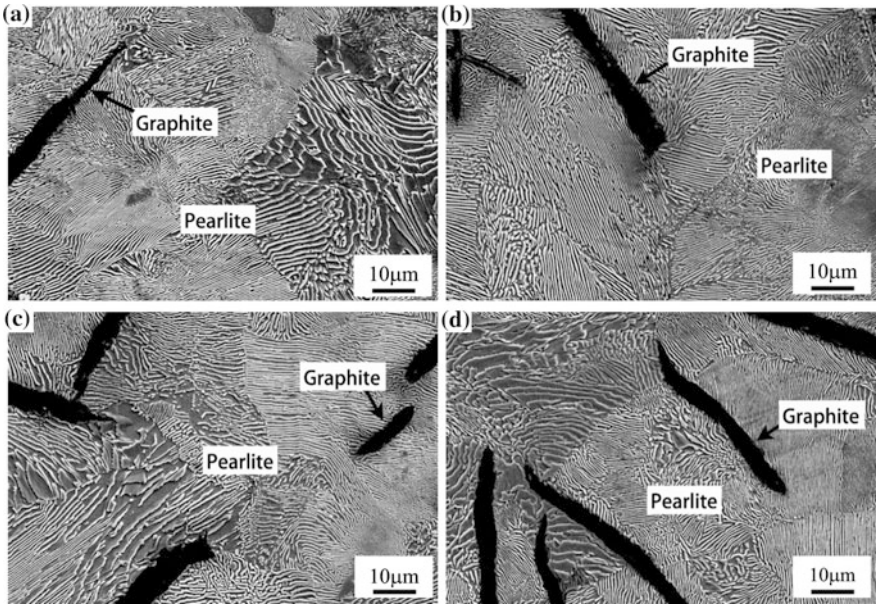

Fig. 6 Morphology of the matrix observed by SEM after etching by 4% nital. **a** CI-1 **b** CI-2 **c** CI-3 **d** CI-4

Table 3 Detailed parameters of graphite microstructures observed by OM at ×100 magnification

Sample	Area fraction of graphite	Length of graphite [μm]	Length classification
CI-1	7.6% ± 0.9%	244.0 ± 29.2	3/4
CI-2	8.5% ± 0.7%	316.6 ± 31.9	3
CI-3	9.5% ± 0.6%	329.4 ± 50.7	3
CI-4	7.6% ± 0.5%	310.4 ± 65.9	3

Figure 7 shows typical stress-strain curves of the tensile tests at RT. The strains of CI-2, CI-3 and CI-4 are only less than 1%, while CI-1 is almost 3 times larger than that of other specimens. It is clearly that CI-1 has larger elongation rate and relatively high ultimate tensile strength (UTS) value than other samples. Figure 8 presents UTS for all samples at temperatures from RT to 800 °C. It is shown that CI-1 always has higher UTS values than other samples at different temperatures, which reaches to about 313 MPa at RT.

Combined with the microstructures aforementioned, a conclusion could be drawn that low area fraction of graphite leads to high UTS value, and short length of graphite would also increase the value. This could be explained by that the graphite, especially with large length, breaks continuity of matrix. In other words, cracks could expand easily along the graphite flakes. As a result, tensile strength of the sample decreases a lot. These results are in agreement with that in other studies

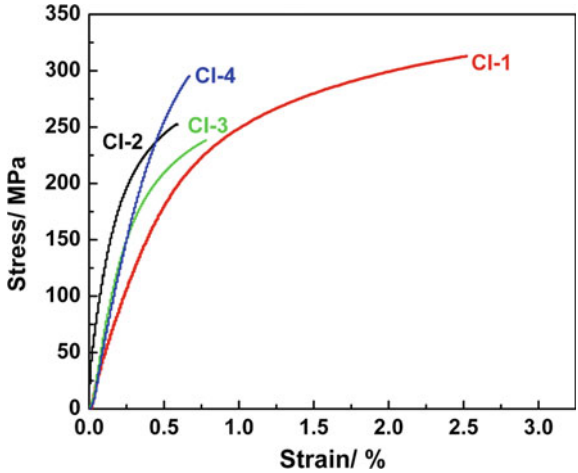

Fig. 7 Stress-strain curves of tensile tests for the samples at RT

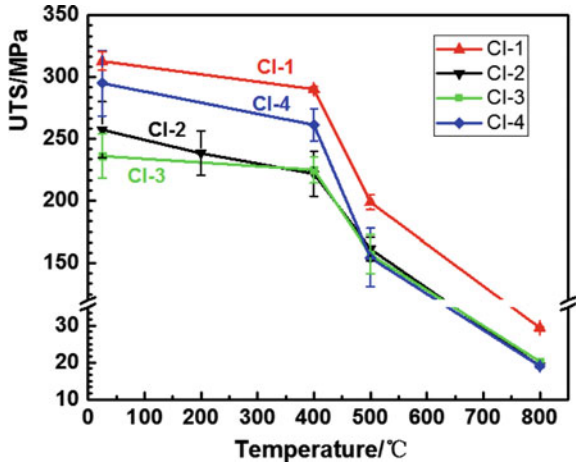

Fig. 8 Ultimate tensile strength for the samples at temperatures from RT to 800 °C

[4, 12, 13]. For all samples, the UTS values at 800 °C are all very low, around 20–30 MPa, which may be caused by strength decrease of the matrix changed from pearlite to austenite at high temperature.

Figure 9 illustrates the fracture structures for the samples after the tensile test at RT. The morphology of graphite flake can be clearly observed on the fracture surfaces of every sample. As shown in Fig. 9a–c, some of the flake graphite has been pulled out of the matrix during failure, leaving indentations on the fracture surface. The inside surfaces of the indentations in CI-2 and CI-3 are more smooth than that in CI-4, which suggests that a faster debonding process along the interface between the graphite and the matrix in CI-2 and CI-3. However, as shown in Fig. 9d, CI-1 has relatively smaller graphite and most of flake graphite was

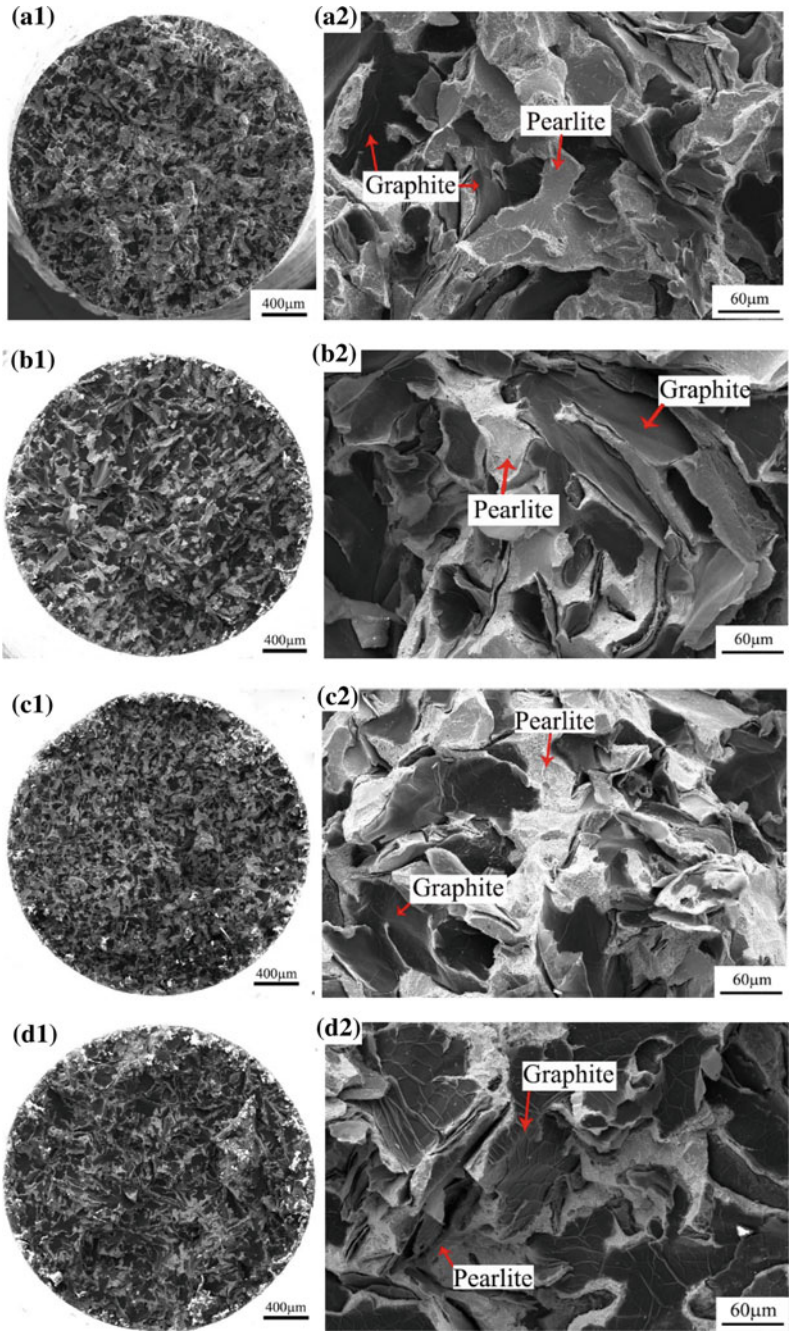

Fig. 9 Structures of fractures for the samples after tensile test at RT: **a** CI-1 **b** CI-2 **c** CI-3 **d** CI-4

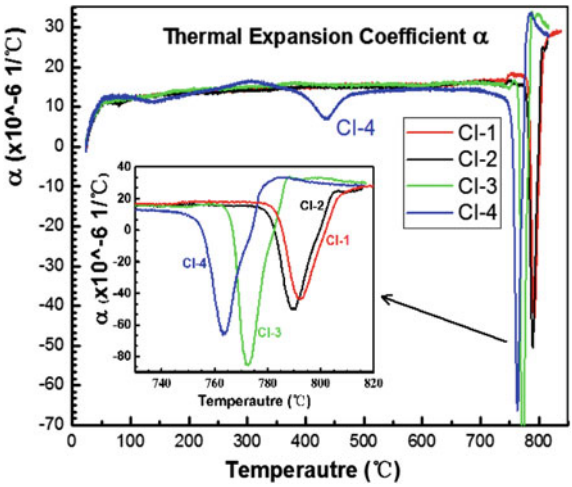

Fig. 10 Thermal expansion coefficients for different samples at temperatures from RT to 800 °C

fractured intergranularly, which suggests a slowly compatible deformation during tension. It is evidenced that CI-1 had higher UTS value than other samples.

Thermal properties are important properties to the cast irons applied in automobile flywheels. Three parameters, thermal expansion coefficient, density and thermal diffusivity were measured to calculate thermal conductivity. Figure 10 shows the expansion coefficient of different samples at temperatures from RT to 800 °C. The thermal expansion coefficient values are all about 1.2×10^{-5} °C^{-1} and very close to each other in all these samples except CI-4's low peak at around 450 °C resulted by unknown reason. A large peak at about 770 °C for all samples is induced by the phase transformation of ferrite and austenite, which makes it difficult to measure the accurate thermal capacity at 800 °C.

Table 4 lists the bulk densities for different samples at RT, and all of which are about 7.2 g/cm^3. Combined with the measured thermal diffusivity, the calculated results of thermal conductivities for all samples at different temperatures are shown in Fig. 11. A raise from 700 to 800 °C is caused by the phase transformation as explained before. As shown in Fig. 11, CI-3 has the highest thermal conductivity value than other samples, which might be ascribed to its large area fraction and long length of graphite. Although the area fraction of CI-2 is larger than that of CI-4 and CI-1, a considerable lower thermal conductivity is found in CI-2, which is at same level of CI-4 and CI-1. Thus, for grey cast iron, it could be deduced that when the content of graphite reaches at some extent, a huge promotion of thermal conductivity would eventually be achieved.

Usually, there should exist a large span of interconnected graphite, which has decisive effect on the dissipation of heat. As shown in Table 3, CI-4 and CI-1 have similar area fraction of graphite, but CI-1 has higher thermal conductivity than CI-4 at every test temperature, which should be related to a shorter length of graphite in CI-1. So it could be inferred that low carbon content could also contribute to thermal conductivity. That is, if grey cast irons have similar area fraction of

Table 4 Densities for the samples at RT

	CI-1	CI-2	CI-3	CI-4
Density [RT, g/cm^3]	7.17	7.20	7.22	7.19

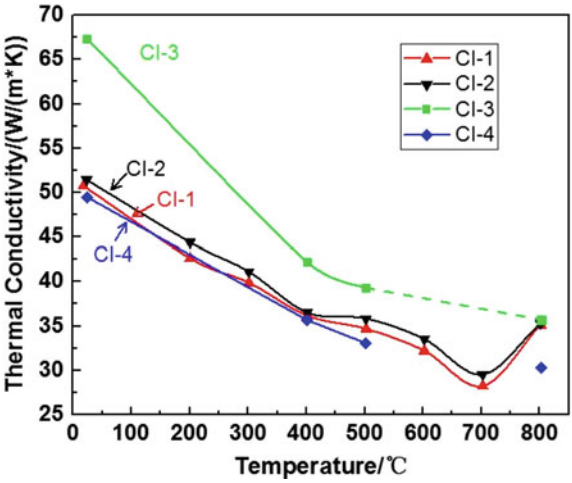

Fig. 11 Thermal conductivities for different samples at temperatures from RT to 800 °C

graphite, shorter length of graphite could lead to a larger number of graphite flakes, which would contribute to the heat conduction.

In summary, for mechanical properties, the combined low area fraction and short length of graphite can lead to high UTS value, but for thermal properties, the combined high area fraction and large length of graphite will induce to high thermal conductivity. Short length of graphite should also contribute to thermal conductivity under the circumstance of the similar area fraction of graphite since a large number of the short graphite flakes can be formed. Therefore, in order to develop HPCI with balanced UTS and thermal conductivity, the graphite microstructures with moderate area fraction and shorter length of graphite flakes should be controlled.

Conclusions

Microstructures, mechanical properties as well as thermal properties of the grey cast irons have been investigated by analysing some commercial flywheels. The following conclusions can be drawn from the results:

(1) The content of graphite is depended on the content of carbon in the grey cast irons, and the simulation results show that most of carbon directly formed into graphite at RT.

(2) As the temperature increase, UTS decreases at all testing temperature. CI-1 has higher UTS values than other samples it has the lowest area fraction of graphite and the shortest graphite length.
(3) Thermal conductivity increases with increase of the area fraction of graphite. Short length of graphite also contributes to the thermal conductivity since a large number of the short graphite flakes can be formed under the circumstance of the similar area fraction of graphite.
(4) In order to get HPCI, microstructure with moderate area fraction and short length of graphite should be considered.

Acknowledgements The authors would like to acknowledge W. Y. Yang and Y. R. Zheng for the assistance of useful discussions. The financial support provided by Ford Motor Company (University Research Program, 2014-5121R) is also acknowledged.

References

1. O. Oloyede, T.D. Bigg, R.F. Cochrane, A.M. Mullis, Microstructure evolution and mechanical properties of drop-tube processed, rapidly solidified grey cast iron. J. Mater. Sci. Eng. A **654**, 143–150 (2016)
2. R.J. Brown, *Foseco Ferrous Foundryman's Handbook*, 11th edn. (Butterworth-Heinemann, 2000)
3. A. Velichko, A. Wiegmann, F. Mücklich, Structure and property studies on austempered and as-cast ausferritic gray cast irons. J. Acta Mater. **57**, 5023–5035 (2009)
4. P. Lan, J. Zhang, Strength, microstructure and chemistry of ingot mould grey iron after different cycles of low frequency high temperature loads. J. Mater. Des. **54**, 112–120 (2014)
5. M. Moonesana, A. Honarbakhsh Raoufa, F. Madahb, A. Habibollah Zadeh, Effect of alloying elements on thermal shock resistance of gray cast iron. J. Alloys Compd. **520**, 226–231 (2012)
6. M.C. Rukadikar, G. Reddy, Influence of chemical composition and microstructure on thermal conductivity of alloyed pearlitic flake graphite cast irons. J. Mater. Sci. **21**, 4403–4410 (1986)
7. EN ISO 945-1: 2008. Microstructure of cast irons–Part 1, 2010
8. D. Holmgren, R. Källbom, I.L. Svensson, Influences of the graphite growth direction on the thermal conductivity of cast iron. J. Metall. Mater. Trans. A **38**, 268–275 (2007)
9. D. Holmgren, I.L. Svensson, Thermal conductivity–structure relationships in grey cast iron. Int. J. Cast Metals Res. **18**, 321–330 (2005)
10. J. Leitner, P. Chuchvalec, D. Sedmidubský, A. Strejc, P. Abrman, Application of Neumann-Kopp rule for the estimation of heat capacity of mixed oxides. J. Thermochim. Acta **395**, 27–46 (2002)
11. C.L. Zhang, Y.L. Pei, L.D. Zhao, D. Berardan, N. Dragoe, S.K. Gong, H.B. Guo, The phase stability and thermophysical properties of InFeO3(ZnO)m (m = 2, 3, 4, 5). J. Eur. Ceram. Soc. **34**, 63–68 (2014)
12. L. Collini, G. Nicoletto, R. Konečná, Microstructure and mechanical properties of pearlitic gray cast iron. J. Mater. Sci. Eng. A **488**, 529–539 (2008)
13. A. Vadiraj, G. Balachandran, M. Kamaraj, Structure–property correlation in austempered alloyed hypereutectic gray cast irons. J. Mater. Design **30**, 4488–4492 (2009)

P110T Casing Material's Relation of Creep and Relaxation for the Sealing Surface of Premium Connection in High Temperature Gas Well

Ying Zhang, Zhanghua Lian, Mi Zhou and Tiejun Lin

Abstract Creep or stress relaxation is considered as a mainly factor of reducing the contact pressure on the sealing surface of premium connection, causing the gas leakage in the high temperature gas well. In this paper, the creep tests of P110T casing material were conducted under different temperatures (120, 200, 300 °C). According to the experimental data, the fitting mathematical model of P110T casing material's steady creep strain rate was obtained under the different temperature and loading by the Least Square method. Then, the relation of creep and relaxation was presented, and an innovation stress relaxation model was put forward from the creep strain rate. Finally, applying with the stress relaxation model, P110T casing material's stress relaxation varying with time was obtained. The results show that, the stress relaxation was obvious in the initial phase and it decreased with time increasing. The stress decreased significantly and tended to a stable value. And the environmental temperature and initial stress had a significant influence on the stress relaxation. This study can be used for the designing of the premium connection's structure, or prediction their service life in the high temperature gas well.

Keywords Premium connection · Contact pressure · Sealing mechanism Creep · Stress relaxation

Y. Zhang · Z. Lian · T. Lin
State Key Laboratory of Oil and Gas Reservoir Geology and Exploitation, Southwest Petroleum University, Chengdu 610500, Sichuan, China
e-mail: Hello_913@126.com

Z. Lian
e-mail: cwctlzh@swpu.edu.cn

T. Lin
e-mail: cwctltj@swpu.edu.cn

M. Zhou (✉)
Sichuan University of Science and Engineering, Zigong 643000, Sichuan, China
e-mail: zhoumi326@163.com

© Springer Nature Singapore Pte Ltd. 2018

Y. Han (ed.), *Advances in Materials Processing*, Lecture Notes in Mechanical Engineering, https://doi.org/10.1007/978-981-13-0107-0_89

Introduction

In recent years, with development of petroleum exploration toward the deeper formation and offshore, wellbore integrity is put forward as a critical problem in the high pressure and high temperature (HPHT) gas wells. The key of the wellbore integrity is about casing strings. The casing strings, used in almost all oil and gas wells, employ threaded connections, which are expected to provide both structural and leakage integrity under service environment [1]. However, the risk of the casing string leakage increases with well temperature and pressure. A significant gas leak from even a single connection can constitute a completion failure. Connection leakage or failures can lead to serious safety consequences: the sustained casing gas pressure; exposure of unprotected equipment to corrosive fluids; external pressure buildup leading to casing collapse; and abandonment concerns. These problems are the most critical in HPHT gas wells, and offshore platform or subsea gas wells.

The premium connection is designed for the casing and tubing connections, achieving high levels of seal integrity and structural strength in the thermal and HPHT wells. Whereas the premium connections incorporate mating sealing surfaces in pin/box component, which are pre-stressed during make-up to provide a direct gas sealing mechanism [2, 3]. As is shown in Fig. 1. Figure 1 presents a sketch of premium connection and its enlarged view of the sealing surface. It shows the commonly used gas sealing mechanism method in the premium connection, defined as contacted sealing mechanism with metal-to-metal. When the connection is made-up, a high contact pressure on the sealing surface will be generated by an interference fit between the box and the pin. And if the contact pressure is higher than the gas pressure, the connection can prevent the gas leakage efficiently [4, 5]. Therefore, one of the most important concerns in designing a premium connection is the contact pressure. Considerable factors include the right geometry of the

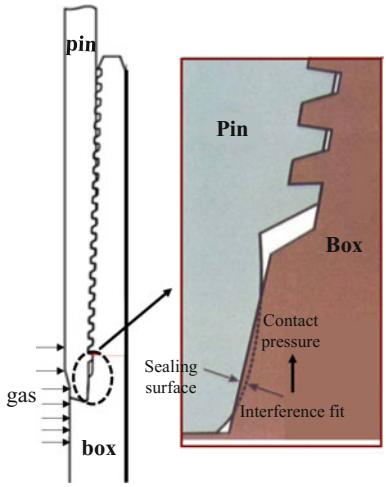

Fig. 1 Gas sealing mechanism of premium connection

contact surface, and selecting an alloy with the necessary strength. The well-designed premium connections could bear high pressure gas in the downhole and provide structure integrity. However, the gas leakage problem may appear after two years of gas production in some HTHP wells, which is far less than the normal service life of most gas wells. That is because, the connections will experience creep strain, and the sealing surface will lose a significant amount of its initial contact pressure over time in the HPHT wells. This decay of contact pressure is called stress relaxation. When the sealing surface's contact pressure is reduced to less than the gas pressure or the wellbore pressure, the gas leakage is likely to happen, which will reduce the service life of the gas well, causing economic loss. Therefore, it is of great importance to study the casing material's creep behavior, and investigate the relaxation of sealing surface's contact pressure under different temperatures. This would benefit the operators to design the sealing surface's contact pressure in the premium connection and select a suitable casing material for the HPHT wells.

Research on the thread connection's mechanical design and its safety evaluation, has been conducted from various perspectives. Masaaki developed a high performance premium connection, which was conducted by Finite Element method and prototype physical testing [6]. Several new types of premium connections, with high strength and high seal integrity, were developed to comply with the severest protocol of ISO13679 CAL IV in the HTHP gas field. ISO13679 is the international standard detailing the testing procedures for casing and tubing connections [7]. Several studies have been performed on the metal-to-metal seals of a premium threaded connections. And laboratory experiment was conducted to evaluate the sealability of the connection [8–10]. Some researchers also investigated the fatigue failure mechanism in the connection, and evaluated the stress concentration of the thread root to predict the fatigue life of the connections [11, 12]. However, the sealing mechanism of the premium connections has not been completely investigated, especially in the creep and relaxation characterizations of the casing material in high temperature.

The contact pressure on the sealing surface of the premium connection is the key affecting the gas leak. Furthermore, the relaxation behavior of casing material is a critical factor for the contact pressure decreasing with time. As many operators lack the knowledge of the relaxation mechanical property of the casing material under different temperatures, they cannot accurately evaluate the connection's safety service life. In this paper, a tension creep test for the casing material P110T is employed under different temperature. Using the creep experimental results data, the creep strain rate model of the casing material under different temperature and tension loading is obtained by the least square method. And the interrelation model of stress creep and relaxation is established by the recurrence equation. Then the stress relaxation's mathematic model is used to study the sealing surface's contact pressure varying with time, which can predict its service life under different temperature.

Experimental Material Tests

Experimental Apparatus and Procedure

P110T casing material is applied to the creep experiment under the different temperature to investigate the material's creep behavior. As is shown in Fig. 2a, the creep experiment apparatus is composed of oven, temperature sensor, displacement senor, tension tester, and specimen. The geometry of the specimen is shown in Fig. 2b. And its chemical composition is listed in Table 1. As the alloy's creep experiment is time consuming, a set of constant tension load tests are carried out within 600 h under 120, 200, and 300 °C, respectively. The environmental temperature 120 °C represents the high temperature wells. The 200 °C represents the extra-high temperature situation in the wellbore. And the 300 °C represents environmental temperature in thermal production wells or geothermal wells.

Experimental Result

Table 2 shows the creep experimental conditions, the constant tension loading, experimental temperature, and experimental testing time. Notice that, in test #1 and

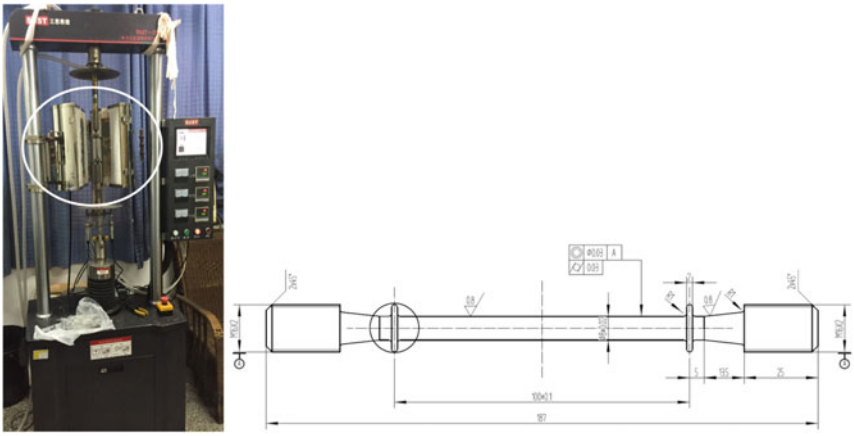

(a) Creep experiment apparatus (b) size of specimen (unit: mm)

Fig. 2 Computer control high temperature electronic creep experiment apparatus

Table 1 Main chemical composition of P110T alloy (mass fraction, %)

C	Si	Mn	P	S	Cr	Al
0.24	0.23	1.48	0.008	0.002	0.06	0.013

Table 2 Creep experimental data of casing material P110T

Test No.	Environmental temperature	Tension stress (MPa)	Experimental time (h)
#1	300	680	570 (fracture)
#2	300	756	340 (fracture)
#3	200	665	600
#4	200	830	600
#5	120	680	590
#6	120	907	600

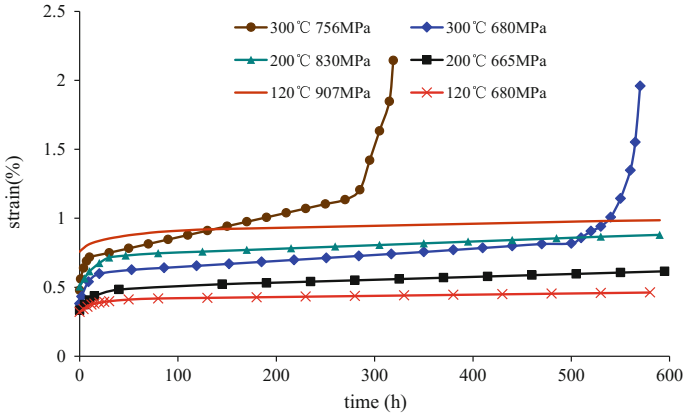

Fig. 3 Creep experiment results under different temperature and tension stress

#2, under 300 °C, both of the specimen were broken at 570 and 340 h in different tension stress, respectively. However, at a lower temperature environment, the specimen did not fracture. It shows that the material's creep behavior at 300 °C is more obvious than at lower temperatures. The creep curves in the experiment are shown in Fig. 3. The strain-time curves at the 300 °C consist from three-creep stages, primary, secondary, and tertiary stage. In the primary stage, the strain rate is relatively high, but slows with time. Then, the strain rate eventually reaches a minimum and becomes near constant at secondary stage. Finally, in the tertiary stage, the strain rate exponentially increases with time, and the specimen is broken at last, which is mainly caused by necking phenomena, as is shown in Fig. 4. However, for the creep experiment at 120 and 200 °C, the fracture is not happen, and there are only 2 stages, primary stage and secondary stage. Therefore, creep is mainly dependent on the temperature and stress, and temperature is dominant in the creep. The material's creep characterization should be deeply investigated in aspect of the temperature and stress.

Fig. 4 Creep test under 300 °C

Material Characterization

Creep Strain Rate

In the design for structural integrity, one of the most interested is the steady stage of creep strain rate, since the steady state belongs to a long-term in the whole creep process, and the creep strain rate in this process is a constant value. The creep strain rate is defined as the change in creep strain with respect to time,

$$\dot{\varepsilon} = \frac{\Delta\varepsilon}{\Delta t} \tag{1}$$

where, $\dot{\varepsilon}$ is the creep strain rate, $\Delta\varepsilon$ is the changing strain, and Δt is the changing time. According to the P110T casing material's creep tests result, the steady creep strain rate can be obtained through Eq. 1, as is shown in Table 3.

It has been verified that most of the metal material's creep property can be described by the Norton's equation, and its equation governing the rate of steady creep strain rate is [13]:

$$\dot{\varepsilon} = a\sigma^b e^{-\frac{c}{T}} \tag{2}$$

where, σ is stress, T is the absolute temperature, a, b, c are material's creep coefficient, respectively. It was assumed that, in any volume element, the creep rate given by Eq. 2, for the local stress or temperature, is instantaneously adopted at any point during the test. And it also presents the creep behavior is affected by the

Table 3 Steady creep strain rate under different temperature and tension loading

Test No.	Temperature (°C)	Tension loading (MPa)	Steady creep strain rate (10^{-6}/h)
1#	300	680	10.3
2#	300	756	16.06
3#	200	665	1.57
4#	200	830	1.733
5#	120	680	0.223
6#	120	907	0.665

changing condition of environmental temperature and loading. According to the steady creep strain rate data in Table 3 and the creep strain rate equation, 6 sets of equations for the creep strain rate can be established. However, there only exists three undetermined creep coefficient in Eq. 2. So it belongs to an overdetermined and inconsistent equation. And it can be solved by the Least Square method, and the creep strain rate under different temperature and loading can be presented by the fitting function [14].

Equation 2 can be rearranged into the form:

$$\ln \dot{\varepsilon}_2 = \ln a + b \ln \sigma + \left(-\frac{c}{T}\right) \tag{3a}$$

or,

$$\ln a + b \ln \sigma + \left(-\frac{1}{T}\right) c = \ln \dot{\varepsilon}_2 \tag{3b}$$

and Eq. 3b can be expressed in the matrix equation,

$$\mathbf{AX} = \mathbf{f} \tag{4}$$

where,

$$\mathbf{A} = \left\{ \mathbf{1} \;\; \ln 2\boldsymbol{\sigma} - \frac{1}{2\mathbf{T}} \right\} = \begin{bmatrix} 1 & \ln 680 - \frac{1}{573} \\ 1 & \ln 756 - \frac{1}{573} \\ 1 & \ln 665 - \frac{1}{473} \\ 1 & \ln 830 - \frac{1}{473} \\ 1 & \ln 680 - \frac{1}{393} \\ 1 & \ln 907 - \frac{1}{393} \end{bmatrix}; \quad \mathbf{X} = \begin{bmatrix} x_1 \\ x_2 \\ x_3 \end{bmatrix};$$

$$\mathbf{f} = \begin{bmatrix} \ln\left(10.3 \times 10^{-6}\right) \\ \ln\left(16.06 \times 10^{-6}\right) \\ \ln\left(1.57 \times 10^{-6}\right) \\ \ln\left(1.733 \times 10^{-6}\right) \\ \ln\left(0.223 \times 10^{-6}\right) \\ \ln\left(0.665 \times 10^{-6}\right) \end{bmatrix},$$

Matrix **A** is a 6 × 3 matrix, containing creep test loading and temperature. Matrix **X** is a 3 × 1 matrix, representing material's undetermined creep coefficients. Matrix **f** is a 6 × 1 matrix, containing the creep strain rate under different pressure and temperature. And Eq. 4 can be solved by the Least Square method,

$$\boldsymbol{X} = \left(\boldsymbol{A}^{\mathrm{T}}\boldsymbol{A}\right)^{-1}\boldsymbol{A}^{\mathrm{T}}\boldsymbol{f} \tag{5}$$

where, $\boldsymbol{A}^{\mathrm{T}}$ is a transpose of matrix **A**. And the matrix **X** is,

$$\begin{cases} x_1 = \ln a \\ x_2 = b \\ x_3 = c \end{cases} \tag{6}$$

Applying the matrix multiplication method, the solution of matrix **X** is that,

$$\mathbf{X} = (-21.34, 2.75, 4659)$$

Then, the undetermined creep coefficients, a, b, and c in Eq. 6, can be obtained, respectively.

$$a = 5.37 \times 10^{-10}, \quad \mathrm{b} = 2.75, \quad \mathrm{c} = 4659.$$

Submitting the undetermined creep coefficients into Eq. 2, the steady creep strain rate, under different temperature and tension stress, can be obtained,

$$\dot{\varepsilon} = 5.37 \times 10^{-10}\sigma^{2.75}\mathrm{e}^{-\frac{4659}{T}} \tag{7}$$

Equation 7 is the mathematical model of the P110T casing material's steady creep strain rate under the different temperature and tension stress. Basing on the established mathematical model, the 3D surface plot is drawn in Fig. 5, describing the P110T casing material's steady creep strain rate changing with the temperature and tension stress. It shows that, the steady creep strain rate is increased along with the increasing of the temperature and stress, and the temperature is dominance in the creep strain rate. In the low temperature environment, when the temperature is below 140 °C, the creep strain rate is very small, which means the creep is not obvious, and phenomenon of creep is very slow under that temperature condition. While, when the temperature exceeds 160 °C, the creep strain rate increases sharply, especially with a high loading. Therefore, when the P110T casing material is applied in the over 180 °C temperature wellbore, the material's creep behavior should be considered. And the mathematical model of creep strain rate is helpful for the engineer to select casing material and design the contact stress on the premium connection, which could avoid the high creep strain rate, leading to the sealing failure or the casing fracture.

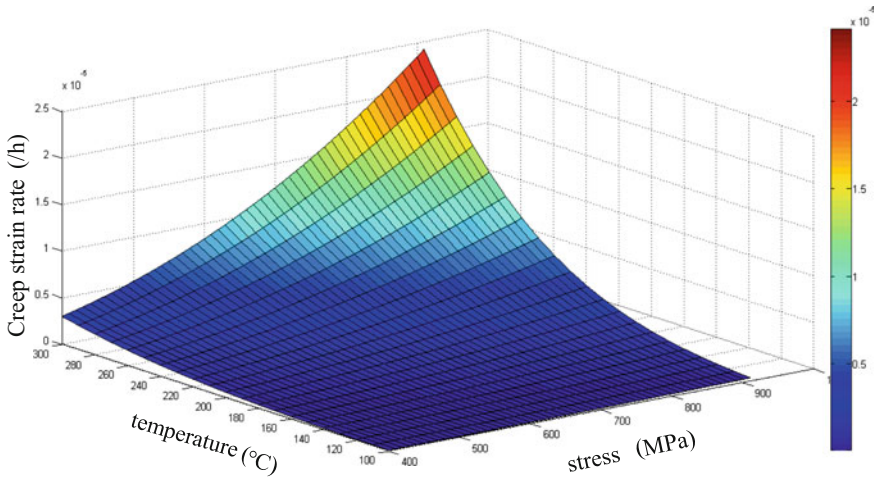

Fig. 5 Fitting surface of P110T casing material's steady creep rate

Interrelation of the Stress Relaxation and Creep

The creep and stress relaxation are two characteristics in response of the material to static load. The creep and stress relaxation are related but are not exactly the phenomenon. The creep is the tendency of a material to progressively deform over time under a constant load. While, the stress relaxation is a decrease of stress in material under constant strain. In this paper, the interrelation of the stress relaxation and creep is investigated in theory. For the stress relaxation, the elastic strain is decreased by the decreasing stress, and a part of elastic strain turn into the plastic strain. What's more, the plastic strain cannot be recovered. Therefore, the stress relaxation can be regarded as creep in small increment of time. And the relaxation characterization is presented as follows,

$$\varepsilon_e + \varepsilon_p = \varepsilon_0 \tag{8}$$

where, ε_0 is the initial strain loads, and ε_0 is also a constant strain in the relaxation, $\varepsilon_0 = \frac{\sigma_0}{E}$; σ_0 is the initial stress in the relaxation; ε_e is residual elastic strain in the relaxation; ε_p is plastic strain in the relaxation, $\varepsilon_p = \dot{\varepsilon}t$; $\dot{\varepsilon}$ is the creep strain rate.

So Eq. 8 can be rewritten as,

$$\frac{\sigma_s}{E} + \dot{\varepsilon}t = \varepsilon_0 \tag{9}$$

where, σ_s is the stress relaxation during the relaxation; E is elasticity modulus, t is the relaxation time.

When the time, t = 0, the stress relaxation is the initial stress, $\sigma_s = \sigma_0$, and this belongs to the Hook law. Equation 9 can be expressed by, $\frac{\sigma_0}{E} = \varepsilon_0$.

Set the whole relaxation time t into n individuals, from time t_1, t_2, t_3 … t_n. Each of the time segments is $\Delta t = \frac{t}{n}$. And at the time t_1, the mathematical model of the stress relaxation is,

$$\frac{\sigma_1}{E} + \dot{\varepsilon}_1 \Delta t = \frac{\sigma_0}{E} \tag{10}$$

Furthermore, the stress relaxation changing with the relaxation time can be expressed as

$$\begin{cases} \frac{\sigma_1}{E} + \dot{\varepsilon}_1 \Delta t = \frac{\sigma_0}{E} \\ \frac{\sigma_2}{E} + \dot{\varepsilon}_1 \Delta t + \dot{\varepsilon}_2 \Delta t = \frac{\sigma_0}{E} \\ \frac{\sigma_3}{E} + \dot{\varepsilon}_1 \Delta t + \dot{\varepsilon}_2 \Delta t + \dot{\varepsilon}_3 \Delta t = \frac{\sigma_0}{E} \\ \cdots \\ \frac{\sigma_n}{E} + \sum_{i=1}^{n} \dot{\varepsilon}_i \Delta t = \frac{\sigma_0}{E} \end{cases}, \tag{11}$$

where, σ_i and $\dot{\varepsilon}_l$ are the stress relaxation and the creep strain rate at the time t_i, respectively. Δt is the increment time.

According to Eq. 7, the creep strain rate can be written as a function form with the stress relaxation and temperature. As is shown in Eq. 12.

$$\dot{\varepsilon}_i = f(\sigma_i, T) = 5.37 \times 10^{-10} \sigma^{2.75} \mathrm{e}^{-\frac{4659}{T}} \tag{12}$$

Submitting Eq. 12 to Eq. 11, the relationship of the stress relaxation and time is that,

$$\frac{\sigma_n}{E} + \sum_{i=1}^{n} f(\sigma_i, T) \Delta t = \frac{\sigma_0}{E} \tag{13}$$

It can be rewritten as,

$$\frac{\sigma_n}{E} + \sum_{i=1}^{n-1} f(\sigma_i, T) \Delta t + f(\sigma_n, T) \Delta t = \frac{\sigma_0}{E} \tag{14}$$

And the whole relaxation time t is expressed by,

$$\mathrm{t} = \mathrm{n} \Delta t \tag{15}$$

In Eq. 14, the σ_n is the stress relaxation at the time t_n, which needs to be solved. And it can be obtained by recurrence relations in Eq. 11.

Stress Relaxation Analysis

By the commonly-employed methodology for the creep strain rate's parameters, the mathematical model of stress relaxation behavior of the P110T casing material, under different temperature and loading stress, is established in Eq. 14. And it can be rewritten as Eq. 16, which includes the influence of temperature, relaxation time and initial stress. As for Eq. 16 belongs to a high-order equation, and needs numbers of iteration to solve the stress relaxation. Applying with MATLAB software, the stress relaxation versus time can be obtained, as is shown in Figs. 6 and 7.

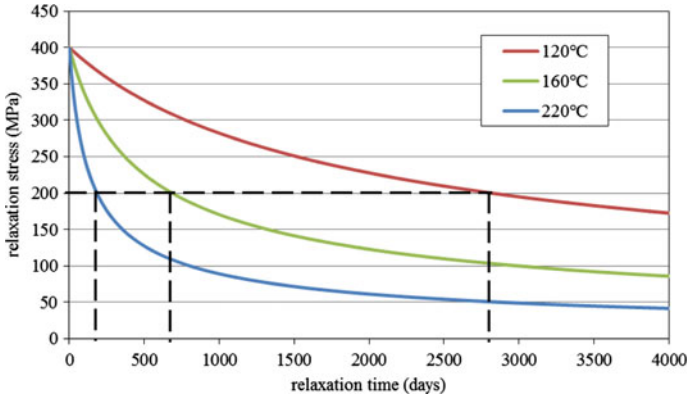

Fig. 6 Stress relaxation versus time under the different temperature

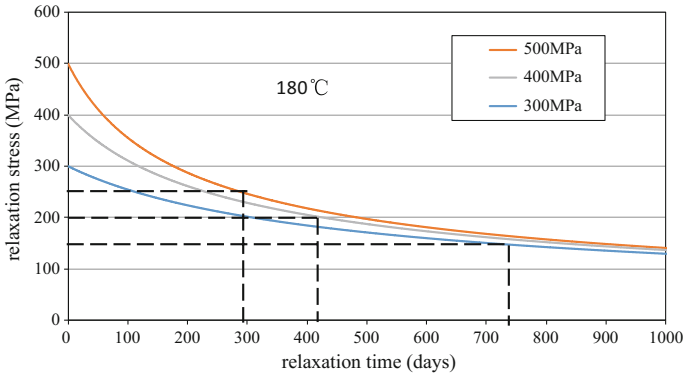

Fig. 7 Stress relaxation versus time in the different initial stress

$$\frac{\sigma_n}{E} + 5.37 \times 10^{-10} \sum_{i=1}^{n-1} \sigma_i^{2.75} e^{-\frac{4659}{T}} \Delta t + 5.37 \times 10^{-10} \sigma_n^{2.75} e^{-\frac{4659}{T}} \Delta t = \frac{\sigma_0}{E} \quad (16)$$

Figure 6 shows the P110T casing material's stress relaxation versus time under 120, 160, 220 °C, respectively. In Fig. 6, the initial stress is 400 MPa, the period of stress relaxation will take around 200 days to reduce to a half, 200 MPa under 220 °C. And it will take around 600 days, 2800 days under 160 and 120 °C, respectively. Therefore, the higher environment temperature is, the faster stress relaxation is. And under the 220 °C, the stress relaxation decreased most rapidly at first, and tend to be smooth when decreased to 50 MPa. The stress relaxation under the high temperature environment is obviously.

Figure 7 shows the stress relaxation varying with time under the same temperature 180 °C, but the initial stress is different. Their initial stress are 500, 400 and 300 MPa, respectively. From Fig. 7, it shows that, when the stress relaxation decreased by half of the initial stress, it will take around 290, 410, and 770 days, respectively. It presents that the higher initial stress is, the faster decreased in the stress relaxation. However, the stress relaxation will tend to be the same in the end. This is because that, the creep strain rate is higher under a higher loading stress, and the stress relaxation will decrease faster, accompanying with the decease of creep strain rate. And when the stress reach a same level, under the same temperature environment, the creep strain rate will turn into the same, and the relaxation stress tend to be the same.

Conclusions

The following conclusions can be drawn from this work.

1. The P110T casing material's creep experiment has been carried out under different high temperature, within 600 h. And the necking phenomenon is observed in the fractured specimen under 300 °C. The creep experiment shows that temperature and loading can affect the creep behavior of material, and temperature is a dominant factor.
2. The P110T casing material's creep behavior has been characterized by using a previously-proposed functional form the creep strain rate. And the Least Square method is applied to fit the set of parameter values, and the 3D plot is obtained for describing the creep strain rate under the different temperature and loading. Result shows, when the temperature is below 140 °C, the creep strain rate is small. And when the temperature exceeds 160 °C, the creep strain increases rapidly.
3. Basing on the interrelation of relaxation and creep, the mathematical model of stress relaxation is established from the creep strain rate. Applying this model, stress relaxation can be predicted under the different temperature and loading.

4. The higher temperature is, the more obvious relaxation is. Meanwhile, under the same temperature, the stress relaxation rate decreased with the deceased stress.

Acknowledgements The authors are grateful to the support from the National Natural Science Foundation of China (No. 51574198) and Research Fund for the Doctoral Program of Higher Education of China (No. 20135121110005).

References

1. C. Teodoriu, C. Kosinowski, M. Amani et al., Wellbore integrity and cement failure at HPHT conditions. Int. J. Eng. Appl. Sci. **2**, 1–13 (2013)
2. J. Takano, M. Yamaguchi, H. Kunishige, Development of premium connection "KSBEAR" for withstanding high compression, high external pressure, and sever bending. Kawasaki Steel Tech. Rep. **47**, 14–22 (2001)
3. K. Inose, M. Sugino, K. Goto, Influence of grease on high pressure gas tightness by metal-to-metal seals of premium threaded connections. Tribol. Online **11**, 227–234 (2016)
4. J. Wang, Y. Feng, K. Lin et al., Comparison analysis of premium connection's seal structure. J. China Univ. Petrol. **34**(5), 125–129 (2010)
5. E.P. Cernocky, G.A. Valigura, F.C. Scholibo et al., *A standardized approach to finite element analysis of casing-tubing connections to establish relative sealing performance as a function of design geometry, machining tolerances, and applied loads* (Computational mechanics, CIMNE, Barcelona, Spain, 1998), pp. 1–19
6. M. Sugino, K. Nakamura, S. Yamaguchi et al., *Development of an innovative high-performance premium threaded connection for OCTG*, in Offshore Technology Conference (Houston, Texas, USA, May 2010)
7. G. Carcagno, The design of tubing and casing premium connections for HTHP wells, in SPE High Pressure/High Temperature Sour Well Design Applied Technology Workshop Conference (The Woodlands, Texas, 2005, SPE-97584-MS)
8. G. Ong, S. Yamaguchi, R. Imai, Successful casing drilling experience with premium connection for production casing application on a subsea well, in Proceeding of the SPE Asia Pacific Oil & Gas Conference and Exhibition (2013)
9. N. Matsuki, Y. Morita, H. Kawashima, Evaluation of premium connection design conditions, in ASME ETCE Drilling and Production Symposium (Feb 1985), pp. 73–85
10. G. Murtagian, V. Fanelli, J. Villasante, D. Johnson et al., Sealability of stationary metal-to-metal seals. J. Tribol. **126**, 591–596 (2004)
11. T. Lin, Q. Zhang, Z. Lian et al., Multi-axial fatigue life prediction of drill collar thread in gas drilling. Eng. Fail. Anal. **59**, 151–160 (2016)
12. Ali Cetin, G. Harkegard, Fatigue life prediction for large threaded components. Proc. Eng. **2**, 1225–1233 (2010)
13. J. Dean, A. Bradbury, G. Aldrich-Smith et al., A procedure for extracting primary and secondary creep parameters from nano-indentation data. Mech. Mater. **65**, 124–134 (2012)
14. D. Zhang, F. Wei, Exposition and argumentation on constrained least square method. Journal of computational mechanics. **11**, 398–403 (2000)

Aluminum Alloy Pipe Design and Mechanical Property Analysis

Shangyu Yang, Chun Feng, Yaorong Feng and Lihong Han

Abstract Since the pipes of aluminum alloy have many advantages over traditional carbon steel pipes, the aluminum alloy pipes are gaining their shares in applications in petroleum development. Considering the complexity of the structure of deep and ultra-deep well, the laboratory experimental studies were conducted on the mechanical property, such as tensile strength, and elastic modulus of the steel pipe, aluminum pipe and titanium alloy pipe. A theoretical relationship between aluminum alloy pipe diameter, wall thickness, and tensile strength was established. For field study, a 7000 m deep well in Tarim oilfield was carried on the detailed design, and the results showed that the aluminum alloy pipe down to 7000 m had a safety factor of hook load greater than 1.94, and the safety coefficient of torque value was greater than 1.62. At the same time, the design requirements could be well met; when aluminum pipe was adopted to improve the design, the maximum tension of drill pipe was much bigger than that of a steel pipe's maximum permissible stress as the steel pipe's mechanical properties could not meet the requirement of drill pipe string design.

Keywords Deep and ultra-deep well · Aluminum alloy pipe · Steel pipe Safety coefficient

Introduction

Compared with the traditional steel drill pipe, the high strength aluminum alloy pipes have the characteristics of light weight, good corrosion resistance and fatigue resistance, and are suitable for drilling deep wells, ultra-deep wells, large displacement horizontal wells and wells in acid oil and gas field. In Tarim oil field,

S. Yang (✉) · C. Feng · Y. Feng · L. Han
State Key Laboratory of Performance and Structural Safety for Petroleum Tubular Goods and Equipment Materials, CNPC Key Lab for Petroleum Tubular Goods Engineering, Tubular Goods Research Institute, Xi'an 710077, Shaanxi, China
e-mail: shangyuy@163.com

© Springer Nature Singapore Pte Ltd. 2018

Y. Han (ed.), *Advances in Materials Processing*, Lecture Notes in Mechanical Engineering, https://doi.org/10.1007/978-981-13-0107-0_90

Southwest oil field in China and Gulf of Mexico, high strength aluminum alloy pipes have been widely used. In United States, Russia and other countries, high-tech and high quality aluminum alloy pipes can be produced and supplied, and the technology is mature. However, using aluminum alloy drilling pipe has a lead order and is usually expensive. In view of the present situation that research and development of aluminum alloy pipes in China is at the starting age, it is of great significance to study the use characteristic of aluminum alloy pipes [1, 2]. Scholars [3–5] studied the relationship between the density of drilling fluid and aluminum alloy pipes setting depth based on the material, and literature survey [6, 7] shows the following advantages of aluminum alloy pipes: ① light weight, good flexibility and small friction; ② great resistance of H_2S and CO_2 corrosion; ③ during the drilling process of deep and large displacement wells, the use of aluminum alloy pipes can reduce the weight of drilling pipes and friction, shorten trip durations, decrease torque and pressure, optimize drilling pressure, and significantly raise the drilling efficiency; ④ aluminum alloy pipes are more suitable for directional and horizontal wells with large curvature, and can reduce hook-load; ⑤ The wider range of temperature that aluminum alloy pipes can be used, the deeper that wells can be drilled. Gelfgat et al. [8] compared the relationship between different yield strength of aluminum alloy pipes, titanium alloy pipes, steel pipes and maximum setting depth when using different drilling fluids. Yu et al. [9], Wu et al. [10], Tang et al. [11] studied the wear resistance of aluminum alloy pipes and its potential applications in the future. However, the authors did not find any study on the design method of aluminum alloy pipes for the actual field well condition. Feng et al. [12–17] successfully developed high strength aluminum alloy pipes with independent intellectual property rights based on field applications, laboratory experiments and materials study. According to the Tarim oil field application and laboratory experiments, the performance of the domestic high strength aluminum alloy pipe fully conforms to the expectations and actual working conditions, and achieves an advanced level of similar products in international markets. Moreover, mechanical properties, heat resistance and surface quality are even better than the counterparts of carbon steel.

Based on the technical advantages and potential wide applications of aluminum alloy drill pipes, we derived an mathematical model to estimate the maximum setting depth of drill pipes for different materials and sizes in this paper. Combined with the drilling and completion conditions in the field, the downhole design of drilling pipes in L-shape well is carried out with the considerations of the tensile and torsional characteristics of the aluminum alloy pipes. Furthermore, the relationship between frictional resistance and drilling depth of drilling pipes with different materials are studied and developed, which could provide technical guideline for the field application.

Experimental

Theoretical and field studies show that the influencing factors to the safety of drilling includes drill pipe tensile strength, density, O.D, wall thickness and elastic modulus. In order to evaluate the safety performance of drilling pipe, the physical/mechanical characteristics need to be considered. These parameters are shown in Table 1.

During the process of drilling and tripping, the maximum load of drill pipes is tensile force, so the design of drill pipes mainly includes the tensile load due to self weight and dynamic loading. Other forces can be included using a certain safety factor.

In the study example, the O.D. is 139.7 mm, the wall thickness is 10.54 mm, safety hook-load is 50 ton and the safety factor is 1.5. The influence of three different materials of drill pipes on setting depth is shown in Fig. 1. From Fig. 1, in the same situation, although the yield strength for drill pipes with three different materials ranges from 490 to 1080 Mpa and $\sigma_{s\mathrm{Al-alloy}} < \sigma_{sSteel} < \sigma_{s\mathrm{Ti-alloy}}$, the setting depth for aluminum alloy pipes is the largest, and the setting depth for titanium alloy pipes is the second largest. For steel alloy, the setting depth is only one third of aluminum alloy pipes' setting depth.

When the density of drilling fluid is 2 g/cm^3, the relationship between wall thickness and theoretical setting depth is shown in Fig. 2.

From the calculating result of Fig. 2, when the wall thickness of drill pipes, 138.7 mm O.D, increasing from 9.17 to 10.54 mm, the increasing for maximum setting depth of aluminum alloy pipes, titanium alloy pipes and steel pipes are 3.1, 0.96 and 0.41 km.

Theoretical Analysis—The Length of Drill Pipes

Calculation of the Length of Drill Pipes

In deep or Ultra-deep wells, the composite drill pipes are usually used. The composite drill pipes mean that drill pipes consist of pipes with different size, wall thickness and steel grade. In the design of composite drill pipes, the length of pipe in each section should be calculated from bottom to up. The lower carrying capacity be placed above drill collars. The drill pipes above drill collars should be divided into different section. One section means the geometry size is the same. And the section should be tagged from bottom to up (1, 2, …, i, …, n). In each section, the maximum length L_{dpi} can be calculated by:

$$L_{dpi} = \frac{\sigma_t(\pi Dt - \pi t^2) - 1000nTg}{(1 - \frac{\rho_k}{\rho_d})q_{dpi}} - \frac{1}{q_{dpi}}\left(q_c L_c + \sum_{j=1}^{i-1} q_{dpj} L_{dpj}\right). \quad (1)$$

where q_{dpi}—the weight of i—section pipe in the air each unit length, kN/m.

Table 1 Physical/mechanical properties of drill pipes (20 °C)

Material	Density (g/cm^3)	Elastic modulus (GPa)	Shear modulus (GPa)	Poisson ratio	Thermal expansion coefficient (10^{-6}/°C)	Specific heat capacity (J/(kg °C))	Yield strength (MPa)	Specific strength, (N m/kg)
Steel	7.85	210	79	0.27	11.4	500	517–931	65,860–118,600
Titanium alloy	4.54	110	42	0.28	8.4	460	517–724	121,366–159,471
Aluminum alloy	2.78	71	27	0.3	22.6	840	325–550	116,906–197,842

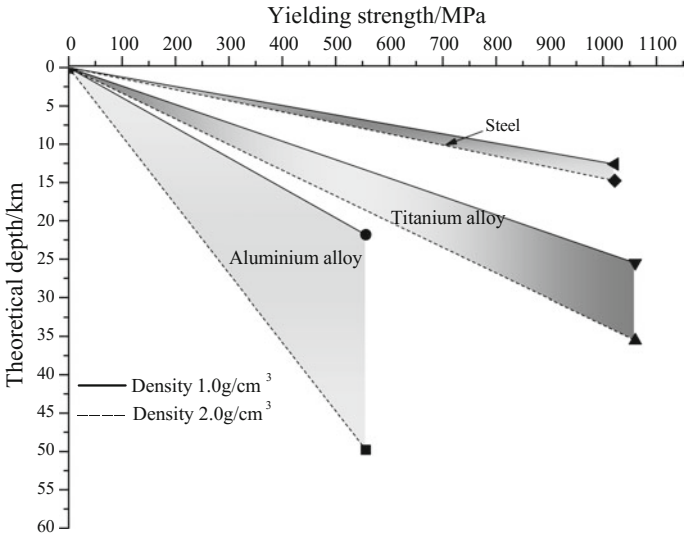

Fig. 1 Drill fluid and setting depth of 5.5 in. drill pipes

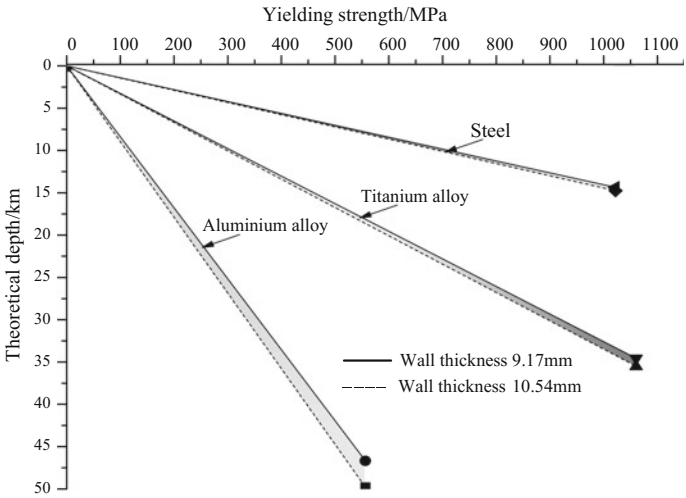

Fig. 2 Wall thickness and setting depth of 5.5 in. drill pipes

Torsional Properties of Drill Pipes

From the result of mechanics of materials and theoretical mechanics study, the torque on drill pipe can be calculated by:

$$M = \frac{30}{\pi}\frac{P}{n} = 9.549\frac{P}{n}. \quad (2)$$

where M-torque on drill pipes, kN m; P-rotating power of drill pipes, kw; n-rotating speed of drill pipes, rpm.

Result and Discussion

Aluminum Alloy Pipe Length Design

In the example of "L" well, the measure depth is 7000 m, drilling fluid density is 1.2 g/cc, the down hole design for L well includes three different common size drill pipes which conform to the requirements of drilling. From the laboratory experiments, physical/mechanical parameters of these pipes are shown in Table 2. Assuming friction factor of steel pipe is 0.24, aluminum alloy pipe friction factor is 0.22, rotating speed is 60 rpm, the drill pipes design for L well is shown in Tables 3 and 4.

Under the same design standard and size of drill pipes, the maximum tensile force along axial direction is 3200 kN when all drill pipe size changed to 5.5 in. and material of drill collar remaining the same. This is close to Steel139.7×10.54-S allowable tensile force. When using aluminum pipes instead of steel pipes, this design composite drill pipes' safety factor of tensile ranges from 1.94 to 9.89 and the safety factor of torque ranges from 2.53 to 10.48. This design can significantly increase the service life of drill pipes, raise the efficiency of drilling process, and fulfil field requirements.

Table 2 Aluminum alloy pipe mechanical properties

	Aluminum alloy pipe physical/mechanical properties	Different aluminum alloy pipe		
		D16T	1953T1	AK41T1
1	Yield strength (MPa)	330	480	350
2	Tensile strength (MPa)	450	540	410
3	Hardness (HB)	120	120–130	130
4	Elongation (%)	10–11	7–8	11–12
5	Reduction of area (%)	18–20	14–15	24–26
6	Density (g/cm^3)	2.8	2.8	2.8
7	Elastic modulus (GPa)	72	70	73
8	Shear modulus (GPa)	26	27.5	27.5

Table 3 Design for drill pipes considering torque (0–6000 m) Wellbore diameter (215.9 mm)

Design of drill pipes	Cross-section length (m)	Total length (m)	Cross-section weight (kN)	Total weight (kN)	Friction force (kN)	Tensile force of upper cross-section (kN)	Torque (kN m)	Allowable tensile force (kN)	Allowable torque (kN m)	Safety factor	
										Tensile	Torque
BHA	10	10	12.75	12.75	3.44	16.19	–	–	–	–	–
HWA150×25-D16T	25	35	6.73	19.48	1.82	21.3	–	–	–	–	–
LAIDP103×9-1953	3500	3535	255.25	274.73	68.92	343.65	8.9	864	22.5	2.51	2.53
LAIDP131×13-1953	2000	5535	631.93	906.66	170.62	1077.28	18.4	2090	72	1.94	3.91
HWA150×25-1953	25	5560	6.73	913.39	1.82	915.21	19.5	2900	96	3.17	4.92
Steel139.7×10.54-S	250	5810	81.73	995.12	22.07	1017.19	20.8	3380	138	3.32	6.63
DC 177.8×71.4-G	190	6000	346.63	1341.75	93.59	1435.34	21	14,200	220	9.89	10.48

Table 4 Design for drill pipes considering torque (6000–7053 m), Wellbore diameter (215.9 mm)

Design of drill pipes	Cross-section length (m)	Total length (m)	Cross-section weight (kN)	Total weight (kN)	Friction force (kN)	Tensile force of upper cross-section (kN)	Torque (kN m)	Allowable tensile force (kN)	Allowable torque (kN m)	Safety factor	
										Tensile	Torque
BHA	10	10	12.75	12.75	3.44	16.19					
HWA120×30-D16T	25	35	5.82	18.57	1.57	20.14					
LAIDP103×9-1953	4000	4035	291.72	310.29	78.76	389.05	12.6	864	22.5	2.22	1.79
LAIDP114×10-1953	1500	5535	134.48	444.77	36.31	481.08	16.5	1230	26.8	2.56	1.62
HWA120×30-D16T	500	6035	116.38	561.15	31.42	592.57	18.4	1650	46	2.78	2.5
Steel101.6×9.65-S	500	6535	106.54	667.69	28.77	696.46	23.5	2230	72.2	3.2	3.07
DC 120.6×57.1-G	465	7000	404.89	1072.58	109.32	1181.9	25	5900	115	4.99	4.6

BHA Bottom hole assembly, *Steel* steel pipes, *DC* drill collar

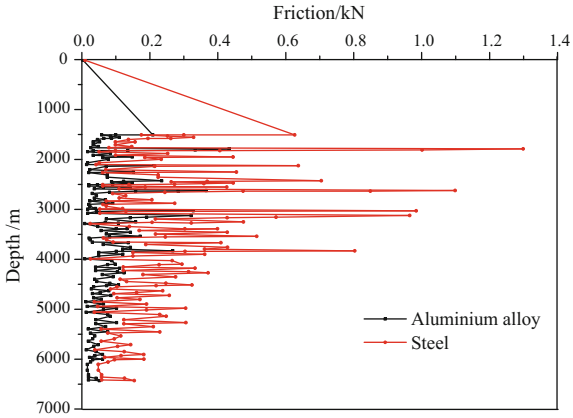

Fig. 3 Friction resistance and depth of different material drill pipes

Friction

The friction resistance during drilling process mainly includes axial friction force and axial friction torque. Generally, the drill pipes structure of horizontal wells is complex, and the rigidity of bottom hole assembly is strong and O.D is large. Due to the gravitational effect, drill pipes would contact bottom wall of the well. This will lead to a bad influence on the flow of drilling fluid and sand return process. During the process of drilling in oil zone, there is a lot of sandstone layer and the porosity of the formation is large. These will lower the tripping speeds. In directional wells with large curvature and horizontal wells, correct prediction of friction problem and low friction resistance are the key factor.

Since the density of aluminum is low, the relationship between the friction resistance and depth of different material drill pipes show: ① when using aluminum alloy instead of steel, friction resistance will be reduced to 35.84% of original friction; ② in the aspect of friction, aluminum alloy pipes are more suitable for directional wells with large curvature and horizontal wells (Fig. 3).

Conclusions

(1) The maximum setting depth of 5.5 in. aluminum alloy pipes, titanium alloy pipes and steel pipes is studied. The advantages of aluminum pipes over traditional ones are presented. The density of drilling fluid has a significant influence on the setting depth;
(2) Based on the design of drill pipes for L wells, the use of aluminum alloy in drill pipes can reduce drilling accidents and increase drilling efficiency when the depth of the well is larger than 7000 m;

(3) Since aluminum alloy pipes have a low density, light weight and small friction resistance, there are more studies should be done towards design method of drill pipes in large displacement horizontal wells.

Acknowledgements The authors gratefully acknowledge the financial support from the post-doctoral research project and industrial breakthrough project (2015GY119) in Shaanxi province, and National key research and development plan (2016YFB0300904).

References

1. Lv. Shuanlu, L. Faqian, Z. Jie et al., Prospects of aluminum alloy drill pipe in Tarim oilfield. Petrol. Drill. Technol. **37**(3), 74–77 (2009)
2. V.I. Gulyayev, N.V. Shlyun, Global analysis of drill string buckling in the channel of a curvilinear bore-hole. J. Nat. Gas Sci. Eng. **40**, 168–178 (2017)
3. L. Sun, C. Bu, P. Hu et al., The transient impact of the resonant flexible drill string of a sonic drill on rock. Int. J. Mech. Sci. **122**, 29–36 (2017)
4. Y. Liu, D. Gao, A nonlinear dynamic model for characterizing downhole motions of drill string in a deviated well. J. Nat. Gas Sci. Eng. **38**, 466–474 (2017)
5. Z. Lian, Q. Zhang, T. Lin et al., Experimental and numerical study of drill string dynamics in gas drilling of horizontal wells. J. Nat. Gas Sci. Eng. **27**, 1412–1420 (2017)
6. National standards of the People's Republic of China. GB/T20659-2006/ISO15546-2002. Oil and gas industry aluminum alloy drill pipe (China Standards Press, Beijing, 2007)
7. T.G. Ritto, M.R. Escalante, R. Sampaio et al., Drill string horizontal dynamics with uncertainty on the frictional force. J. Sound Vib. **332**, 145–153 (2013)
8. M.Y. Gelfgat, V.S. Basovich, V.S. Tikhonov et al., Drillstring with aluminum alloy pipes design and practices. SPE79873 (2003)
9. R. Yu, P. Yuan, Aluminum drill pipe characteristics and potential applications. Oil Field Equip. **40**(3), 81–85 (2011)
10. T. Wu, W. Xue, C. Lu, Superiorities of aluminum alloy drilling pipe and its application prospects in deep holes for geological exploration. Explor. Eng. **37**(2), 27–29 (2010)
11. J. Tang, Q. Di, Y. Hu et al., Analysis on dynamic characteristics and wear mechanism of aluminum alloy drill pipe. Acta Petrolei Sin. **31**(4), 684–688 (2010)
12. C. Feng, Domestic researched Aluminum alloy drilling pipe drilled in the Tarim oilfield for the first time. China Petroleum Daily
13. C. Feng, W. Shou, H. Liu et al., Microstructure and mechanical properties of high strength Al–Zn–Mg–Cu alloys used for oil drill pipes. Trans. Nonferr. Metals Soc. China **25**(11), 3515–3522 (2015)
14. C. Feng, Z. Liu, A. Ning et al., Retrogression and re-aging treatment of Al-9.99%Zn-1.72% Cu-2.5%Mg-0.13%Zr aluminum alloy. Trans. Nonferr. Metals Soc. China **16**(10), 1163–1170 (2006)
15. S. Yang, C. Feng, Aluminum alloy pipe design with the deep & ultra deep well, in International Conference on Oil Country Tubular Goods and Tubular String (2016)
16. V. Tikhonov, K. Valiullin, A. Nurgaleev et al., Dynamic model for stiff string torque and drag. SPE 163566 (2015)
17. C. Raap, A.D. Craig, R. Graham, Drill pipe dynamic measurements provide valuable insight into drill string dysfunctions. SPE 145910 (2011)

Experimental Validation of Constraint Effects on Toughness Test of Pipeline Girth Welds

Lin Chen, Jianwu Liu, Ling Wang and Dengzun Yao

Abstract In the structural integrity assessment or ECA (Engineering Critical Assessment) of pipeline weld defects, one of the most critical inputs is material's fracture toughness. This toughness is often obtained from standardized fracture toughness tests, such as the CTOD (Crack Tip Opening Displacement) toughness tests frequently used in the oil and gas industries. Given how the specimens are tested, the fracture toughness values from these standardized tests can be lower than the apparent toughness of welds under typical pipeline loading. Consequently, weld integrity assessment using these toughness values can be overly conservative. The difference in toughness between the standardized specimens and pipeline welds can be partly attributed to the constraint effects. In this paper, the constraint effect of X80 pipeline girth weld was studied using SENB (Single edge notch bending), SENT (Single notch tensile) and CWP (Curved wide plate test). The results showed that the level of constraint was affected by the crack depth and loading configuration of the test sample. And the toughness obtained by SENB was more conservative than that achieved by CWP and SENT. In the field of toughness test for pipeline girth welds, CWP and SENT are recommend to be chosen.

Keywords Pipeline steel · Constraint effects · Girth weld · Toughness ECA

L. Chen · J. Liu
Sinopec Petroleum Engineering Corporation, Dongying 257026, Shandong, China

L. Wang
Southeast (South–East) Asia Division of CPP, Langfang 065000, Hebei, China

D. Yao (✉)
Pipeline Research Institute of CNPC, Langfang 065000, Hebei, China
e-mail: yaodengzun@163.com

© Springer Nature Singapore Pte Ltd. 2018

Y. Han (ed.), *Advances in Materials Processing*, Lecture Notes in Mechanical Engineering, https://doi.org/10.1007/978-981-13-0107-0_91

Introduction

Structural integrity assessment or ECA (Engineering Critical Assessment), such as BS7910, API 579 or API 1104, provides a method for pipeline weld assessment. However, these schemes usually use the fracture toughness data from deeply cracked bend specimens. Although this approach is safe, it is conservative, and may lead to the imposition of prohibitive repair. Removal of this latter conservatism by consideration of constraint effects has been the subject of much worldwide research. And constraint is then accommodated in BS7910 by making the failure assessment curve a function of structural constraint. So it is very important to confirm the influence of the constraint effect on pipeline girth weld toughness for pipeline defect assessment.

Experiments have shown that the crack depth, section thickness, specimen size, crack geometry and loading configuration all can have a strong effect on the fracture toughness measurements (K, G, J and d). These effects are referred to as constraint effect. Materials loaded in tension, such as girth welds in a pipeline, exhibit higher apparent toughness than the same materials loaded in bending, which is adapted in the standardized fracture mechanics tests [1].

The constraint effects was firstly noted by Prof. Frank McClintock at the Massachusetts Institute of Technology (MIT) in the late 1960s when he examined the slip-line fields of bend and tension loaded specimens [2]. The current theoretical understanding of the constraint effects started in part by the pioneer work of Prof. John Hancock at the University of Glasgow [3]. Recently, extensive work has been done to characterize the constraint effect on the fracture toughness by introducing a second parameter, such as in the J–T theory [3, 4], J–Q theory [5, 6] and J–A2 theory [7].

Recently, the test methods and codes of the fracture toughness for pipeline girth welds have also developed with the recognition of constraint effects. Different test methods, such as SENB, SENT and CWP, have been used in assessing the property of girth welds. However, the relationship between these test methods has not been fully understood and characterized, which limits the usage of incorporating the constraint effects in girth weld integrity assessment procedures.

The present work focuses on the effects of the constraint effects on the CTOD fracture toughness of pipeline girth welds. The effects of crack depth on constraint and on fracture toughness have been studied by SENT and SENB samples. And the relationship between different test methods has also been revealed. These data should be helpful in quantitatively determining the constraint effects on fracture toughness.

Modern Constraint Theories

T-Stress as a Constraint Parameter

In linear elastic fracture mechanics, the effects of specimen geometry and loading condition can be characterized by the T-stress, while the intensity of the asymptotic crack-tip fields is characterized by the stress intensity factor K_I [8, 9]. The T-stress is the second term in Williams Eigen-expansion of near crack-tip elastic field,

$$\sigma_{ij}(r,\theta) = \frac{K_I}{\sqrt{2\pi r}} f_{ij}(\theta) + T\delta_{1i}\delta_{1j} \tag{1}$$

where i and j vary from 1 to 2, (r, θ) are polar coordinates with the origin at the crack tip, K_I is the stress intensity factor, $f_{ij}(\theta)$ are nondimensional angular functions, the T-stress is a uniform stress parallel to the crack face, and δ_{ij} are Kronecker delta.

Q-Stress as a Constraint Parameter

For power-law hardening materials, Sharma and Aravas obtained the two-term expansion of near crack-tip elastic plastic field [10]. A simpler form of the solution was later adopted by O'Dowd and Shih [6, 11]

$$\sigma_{ij} = \sigma_{yy}^{HRR} + \sigma_0 Q \delta_{ij}. \tag{2}$$

where Q is the hydrostatic stress defined by the difference between HRR stress fields and the actual (geometry and loading mode specific) stress fields. O'Dowd and Shih further define Q as,

$$Q = \frac{\sigma_{yy} - \sigma_{yy}^{HRR}}{\sigma_0}. \tag{3}$$

Other Constraint Parameters

The T-stress and Q-stress are the most widely used constraint parameters. Chao and his coworkers have proposed the constraint parameter A2 [12, 13]. Others have proposed hydrostatic stress or the ratio of hydrostatic stress over Mises stress as the constraint parameters. All the constraint parameters have their advantages and limitations. It is critical that they be used within their range of validity.

Materials and Experimental Procedure

Materials

In this study, an X80 grade helical seam submerged-arc welded pipe steel with a thickness of 18.4 mm is used. The Surface Tension Transfer (STT) by Lincoln Electric has been used for root pass welding, while the Self Shielded Flux Cored Arc Welding and Lincoln NR207 welding wire consumable is used for the hot, fill and cap passes of the girth weld. The small-scale samples and CWP samples are taken from the fabricated weld for fracture toughness tests. Table 1 shows the mechanical property of the pipe and the weld.

Experimental Procedure

For better understand the constraint effects, three different toughness test methods, SENT, SENB, and CWP, have been used in this paper. Firstly, the toughness of pipe parent material has been tested by SENT and SENB with different crack depth to identify that the difference among the test results are because of the constraint effects but not the difference of material property. The size of the tested specimens and cracks are given in Table 2 for SENB and SENT for pipe parent material.

For girth weld, three toughness test methods have been used. The detail of CWP sample, test method and the results can be found in the other articles [14]. While the size of SENB and SENT samples for girth weld is also present in Table 2. SENB sample and test are according to ASTM E1820-05 and the requirement of SENT

Table 1 Material property of the X80 grade pipe and the fabricated girth weld

Property	Direction	Yield strength (MPa)	Tensile strength (MPa)	Elongation (%)
Tensile test	Pipe axial	650.00	710.00	19.00
		637.02	701.00	19.00
	Pipe hoop	600.53	696.00	20.00
		611.71	699.00	20.50
Charpy impact toughness	Location	Test temperature (°C)	Energy (J)	
			Single	Average
	Weld	0 °C	48.67	66.40
			37.04	
			113.5	
		−10 °C	87.76	58.51
			69.68	
			18.11	

Table 2 Size of the tested specimens and cracks for SENB and SENT

Specimen No.	Specimen type	a0 (mm)	B (mm)	W (mm)	H (mm)	Test position	Testing method
T-1	SENT	6.95	16	16	16	Pipe parent	Unloading compliance
T-2	SENT	7.24	16	16	16	Pipe parent	Unloading compliance
T-3	SENT	8.70	16	16	16	Pipe parent	Unloading compliance
T-4	SENT	8.23	16	16	16	Pipe parent	Unloading compliance
B-1	SENB	4.78	8	16	16	Pipe parent	Unloading compliance
B-2	SENB	5.30	8	16	16	Pipe parent	Unloading compliance
B-3	SENB	7.06	8	16	16	Pipe parent	Unloading compliance
B-4	SENB	7.06	8	16	16	Pipe parent	Unloading compliance
B-5	SENB	8.48	8	16	16	Pipe parent	Unloading compliance
B-6	SENB	8.64	8	16	16	Pipe parent	Unloading compliance
WT-1	SENT	8.71	16	16	16	Girth weld	Unloading compliance
WB-1	SENT	11.06	16	16	16	Girth weld	Unloading compliance
WB-2	SENB	10.39	8	16	16	Girth weld	Unloading compliance
WB-3	SENB	10.94	8	16	16	Girth weld	Unloading compliance

sample and test can be find in the BMT Fleet Technology's test protocol [15]. Furthermore, the test temperature is 0 °C in this work.

Results and Discussion

Figure 1 is the test result of SENT samples for X80 pipe parent material. It can be seen that the toughness decreased with the crack depth increasing. And the shallowest crack shows the best toughness, while the deepest crack gives the worst.

Figure 2 is the test result of SENB samples for X80 pipe parent material. It can be seen the tendency of the results is same with that of SENT. Also the shallowest

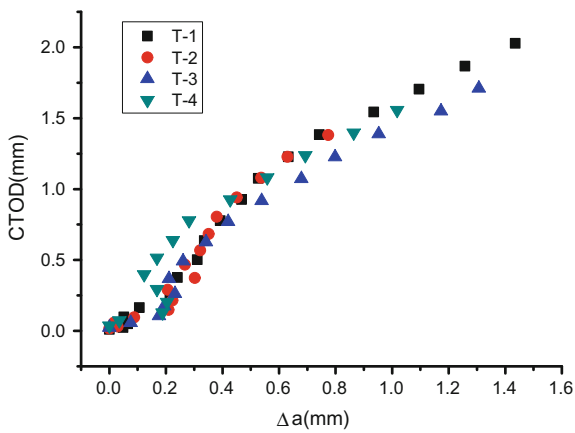

Fig. 1 Measured CTOD R-curves for SENT samples for X80 pipe parent material

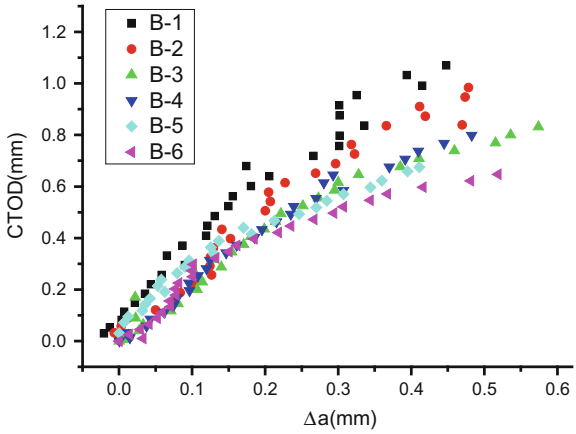

Fig. 2 Measured CTOD R-curves for SENB samples for X80 pipe parent material

crack (4.78 mm) shows the best toughness, while the deepest crack (8.64 mm) gives the worst. Compared to the results of SENT, it can also get that the toughness of SENT is higher than that of SENB.

In this work, the X80 pipe parent material property difference can be ignored because the test samples are cut from the pipe in the same direction and near to each other. So from the results of Figs. 1 and 2, it can be concluded that the difference between the toughness test results are due to the constraint effects, which is related to crack depth, section thickness, specimen size and loading configuration. From Figs. 1 and 2, it also can be reached that for the same crack depth, SENT shows much less constraint level than that of SENB.

Same results can be found in other papers [16, 17]. Figure 3 is the toughness test results of an RAFM Eurofer steel [16]. In that paper, SENB samples with different

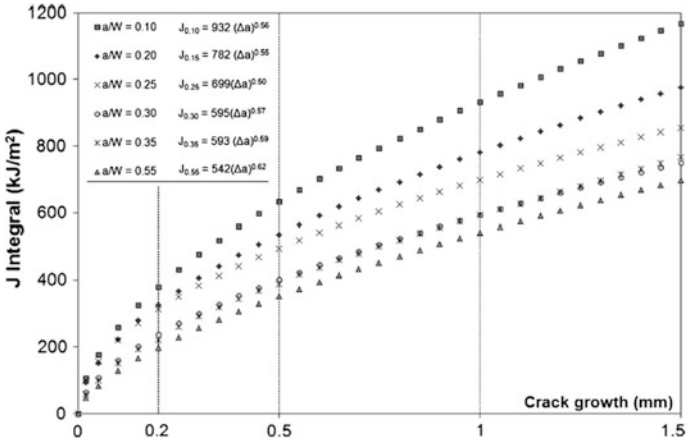

Fig. 3 Measured CTOD R-curves for SENB samples for X80 pipe parent material [16]

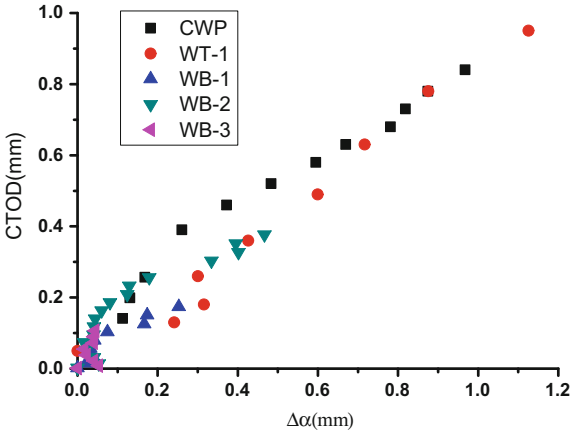

Fig. 4 Measured CTOD R-curves for CWP, SENT and SENB samples for X80 pipe girth weld

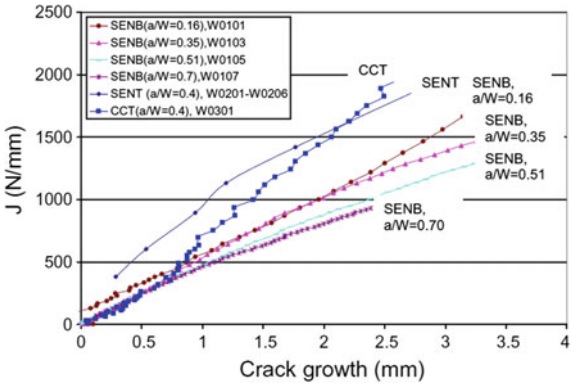

Fig. 5 Measured J–R curves for weld metal in X65 pipeline using SENB, SENT and CCT specimens [16]

crack length have been used in order to get different levels of constraint. It also can be seen that with the depth of crack increasing, the toughness of the pipe parent decreases. And the deepest crack shows the worst toughness, while the shallowest crack gives the highest toughness. This is coincident with the results in this paper.

Figure 4 gives the toughness test results of the girth weld by CWP [14], SENT and SENB. From the picture it can be seen that the test result of CWP is similar to that of SENT, while the results of SENB are much lower than that of CWP and SENT. So it can be concluded that for the girth weld, the constraint effect is also applicable.

Figure 5 shows the toughness test results of X65 pipeline girth weld from other research [17]. It can be seen that CCT gives the highest toughness value, while SENB gives the lowest value. The result from this research is agreed with our work.

Conclusions

The constraint effect on pipeline girth welds has been extensively studied. SENB, SENT and CWP have been used to prove the constraint effect. The conclusions are as follows:

1. There is constraint effect which affects the results of material toughness test.
2. The level of constraint is affected by the crack depth and loading configuration of the test sample.
3. The toughness obtained by SENB is more conservative than that achieved by CWP and SENT. In the field of toughness test for pipeline girth welds, CWP and SENT are recommend to be chosen.

References

1. Y.-Y. Wang, D. Rudland, M. Liu, *Experimental Validation of Constraint Effects* (Gas Research Institute, GRI-04/0147, 2005)
2. F.A. McClintock, *Slip Line Fracture Mechanics: A New Regime of Fracture Mechanics* (2003)
3. C. Betegón, J.W. Hancock, Two-parameter characterization of elastic-plastic crack-tip fields. J. Appl. Mech. **58**, 104–110 (1991)
4. A.M. Al-Ani, J.W. Hancock, J-dominance of short cracks in tension and bending. J. Mech. Phys. Solids **39**, 23–43 (1991)
5. N.P. O'Dowd, C.F. Shih, Family of crack-tip fields characterized by a triaxiality parameter—I. Structures of fields. J. Mech. Phys. Solids **39**, 989–1015 (1992)
6. N.P. O'Dowd, C.F. Shih, Family of crack-tip fields characterized by a triaxiality parameter—II. Fracture applications. J. Mech. Phys. Solids **40**, 939–963 (1992)
7. Y.J. Chao, X.K. Zhu, J-A2 characterization of crack-tip fields: extent of J–A2 dominance and size requirements. Int. J. Fract. **89**, 285–307 (1998)
8. S.G. Larsson, A.J. Carlsson, Influence of non-singular stress terms and specimen geometry on small-scale yielding at crack tips in elastic-plastic material. J. Mech. Phys. Solids **21**, 263–277 (1973)
9. B.A. Bilby et al., *A Finite Element Investigation of the Effect of Specimen Geometry on the Fields of Stress and Strain at the Tips of Stationary Cracks, in Size Effects in Fracture* (The Institution of Mechanical Engineers, London, 1986), pp. 37–46
10. S.M. Sharma, N. Aravas, Determination of higher-order terms in asymptotic elastoplastic crack tip solutions. J. Mech. Phys. Solids **39**, 1043–1072 (1991)
11. N.P. O'Dowd, C.F. Shih, Family of crack-tip fields characterized by a triaxiality parameter—I. Structure of fields. J. Mech. Phys. Solids **39**, 989–1015 (1991)
12. S. Yang, Y.J. Chao, M.A. Sutton, Complete theoretical analysis for higher order asymptotic terms and the HRR zone at a crack tip for mode I and mode II loading of a hardening material. Acta Mech. **98**, 79–98 (1993)
13. S. Yang, Y.J. Chao, M.A. Sutton, Higher order asymptotic fields in a power law hardening material. Eng. Fract. Mech. **45**, 1–20 (1993)
14. D.Z. Yao, L. Zhang, Y.R. Fan, T.Q. Wang, Y. Zhou, Toughness of X80 grade pipe steel girth welds by curved wide plate testing. Mater. Sci. Forum **850**, 873–880 (2016)

15. N. Pussegoda, S. Tiku, B. Tyson, *Consultant Measurement of Crack-Tip Opening Displacement (CTOD) and J-Fracture Resistance Curves Using Single-Edge Notched Tension (SENT) Specimens* (BMT Fleet Technology, 2013)
16. C. Rodriguez, F.J. Belzunce, T.E. Garcia, I. Peñuelas, Constraint dependence of the fracture toughness of reduced activation ferritic–martensitic Eurofer steel plates. Eng. Fract. Mech. **103**, 60–68 (2013)
17. D.W. Zhou, Measurement and modelling of R-curves for low-constraint specimens. Eng. Fract. Mech. **78**, 605–622 (2011)

Material Identification and Safety Evaluation of Defective 15Cr1Mo1V Steel

Xianxi Xia, Guodong Zhang, Fei Xue and Qinzheng Ma

Abstract Main steam pipe and reheat steam pipe of Russian unit boiler are mostly made of 15Cr1Mo1V steel. It is a common problem that a large number of inclusions defects were found in the pipeline overhaul census. In this paper 15Cr1Mo1V steel pipe containing defects was studied by material identification and safety assessment. The results showed that the pipe microstructure was bainite + ferrite + carbide particles, aging at level 3. There were a large number of string-like and granular inclusions inside the material, mainly composed of manganese sulfide inclusions. Minimum longitudinal impact energy and lateral impact energy were both at lower level. The pipe crack was exempt from fatigue fracture assessment. The pipeline creep loss was 0.616, pipeline fatigue loss was 2.23×10^{-6}, the main loss of pipeline was creep damage, and therefore more attention should be paid to pipeline operating temperature and pressure in the follow-up operation to avoid over-temperature creep resulting in accelerated failure.

Keywords Inclusion defects · Material identification · Safety evaluation
Life prediction

Introduction

The safety and life study of high temperature and high pressure pipeline is an important part of the safety and life study of power plant components. A lot of researches on material safety evaluation and life assessment of the defective pipeline and equipment have been done abroad, forming the corresponding assessment criteria and norms. The introduction time of China's supercritical units is the beginning of 1990s, and the running time of more and more supercritical units is close to or more than 100,000 h. As crew service time increasing, the probability of defect degradation will be greatly increased. Creep and fatigue fracture of metal

X. Xia (✉) · G. Zhang · F. Xue · Q. Ma
Suzhou Nuclear Power Institute, Suzhou, China
e-mail: xiaxianxi@cgnpc.com.cn

© Springer Nature Singapore Pte Ltd. 2018

Y. Han (ed.), *Advances in Materials Processing*, Lecture Notes in Mechanical Engineering, https://doi.org/10.1007/978-981-13-0107-0_92

structures become the main failure forms under high temperature [1], and about 30% failure of boiler and high temperature cracking reforming devices are caused by creep rupture [2–6]. The key challenge of creep and fatigue interactions [7–11] is that damage gradually accumulates within the material, often without obvious signs of sudden destruction, leading to serious production losses and even heavy consequences.

In this paper the study of high temperature and high pressure pipeline safety evaluation and life assessment was carried out on Russian 500 MW unit. 15Cr1Mo1V is followed by the former Soviet Union 15X1M1∅, chromium is added to steel to improve the oxidation resistance of steel, while molybdenum and vanadium are added in order to improve the heat resistance of steel. 15Cr1Mo1V steel which is mainly used in main steam pipe and header which wall temperature ≤ 580 °C under long-term work is of long-term organizational stability and good oxidation resistance. But sometimes impact value of some 15Cr1Mo1V steel is below the standard requirements, besides steel contains 0.013–0.08% residual aluminum, which will have a negative impact to the steel thermal performance and durable plastic [12]. In recent years a large number of inclusions defects common problems were found in pipeline overhaul census, therefore, it is necessary to lucubrate on the material state to ensure the safe operation of the pipeline. The size of pipeline is ∅325 × 60 mm, a total of 118,000 h run, operating temperature 545 °C, pressure of 25 MPa.

Material Performance Evaluation

Chemical Analysis

15Cr1Mo1V steel chemical composition meets the standards for the corresponding requirements (Table 1).

Table 1 Results of chemical composition (15Cr1Mo1V)

No.	Chemical composition (wt%)								
	C	S	P	Si	Mn	V	Cr	Mo	Ni
TY14-3-460-75	0.1–0.5	≤ 0.025	≤ 0.025	0.17–0.37	0.40–0.70	0.20–0.35	1.10–1.40	0.9–1.1	≤ 0.25
Sample	0.164	0.0198	0.0121	0.367	0.652	0.237	1.18	1.04	0.0909

Table 2 Room temperature and high temperature tensile strength test results

No.	R_m (MPa)	$R_{P0.2}$ (MPa)	R_{eL} (MPa)	Z (%)	A (%)	Experiment method
R1	538	–	287	67	26.0	Room temperature 20 °C
R2	537	–	300	66	26.0	
R3	537	–	297	66	27.0	
H1	285	225	–	83.5	45.5	545 °C
H2	285	225	–	82.0	34.5	
H3	285	230	–	83.5	47.0	
China 15Cr1Mo1V	550–770	–	≥ 350	≥ 50	≥ 18	Longitudinal
				≥ 45	≥ 16	Lateral
The Soviet Union 15X1M1∅	≥ 500	–	≥ 320	≥ 50	≥ 18	Longitudinal
				≥ 45	≥ 16	Lateral
The Soviet Union 15X1M1∅	410	310	–	79	19	550 °C
	470	310	–	76	19	500 °C
	404	310	–	78.7	19	545 °C

Where: R_m—tensile strength; $R_{p0.2}$—non-proportional extension strength; R_{eL}—lower yield strength; A—percentage elongation; Z—percentage reduction

Room Temperature and High Temperature Mechanical Properties

(1) 15Cr1Mo1V steel room temperature tensile strength, percentage elongation and reduction meet the requirements of China and the former Soviet Union standards, the room temperature yield strength is lower than China and the former Soviet Union standards
(2) 15Cr1Mo1V steel high temperature tensile and yield strength are lower than China and the former Soviet Union standards, percentage elongation and reduction of area meet the standards (Table 2).

Hardness Testing

Inspection pipe hardness is relatively uniform, and meets the corresponding steel hardness requirements of GB5310 and DL/T438 standards (Table 3).

Table 3 15Cr1Mo1V steel hardness test results

Material	Test position	Hardness (HBW)			Average
15Cr1Mo1V	Outer wall side	159	159	161	160
	Center side	162	162	161	162
	Inner wall side	162	162	163	163

DL/T438 and GB5310 15Cr1Mo1V steel hardness control 135-180HBW
Note Hardness test was carried out in the lateral surface of the metallographic examination

Impact Performance Test

Room temperature longitudinal and lateral impact energy is much lower than China and the former Soviet Union standards (Table 4).

Metallographic Examination

Microstructure test found that there is a lot of string-like and granular inclusions inside the material, tissue aging at level 3, grain size at level 6–7, the inclusion content does not meet GB5310 inclusion requirements (no greater than 2.5) (Table 5; Fig. 1).

Oxide SEM Analysis

Inclusions content of the inspection pipe is large, and size is big. Inclusions are mainly composed of manganese sulfide (Table 6; Fig. 2).

Table 4 15Cr1Mo1V steel Charpy V impact (10 × 10 × 55) test results

No.	KV_2 (J)	Remark
Z1	20.0	Longitudinal impact
Z2	13.5	
Z3	10.0	
H1	9.0	Lateral impact
H2	10.5	
H3	5.0	
China 15Cr1Mo1V	Longitudinal	40 J
	Lateral	32 J
The Soviet Union 15X1M1∅	Longitudinal	40 J
	Lateral	32 J

Table 5 Metallurgical test results

Photo	Position	Explanation
1	Longitudinal inclusions	Test on the entire polishing surface using A method,inclusion level: A3, D1
2	Outer wall side	Bainite + ferrite + carbides, the number of carbide Particles inside bainite reducing, and size coarse. Bainite features gradually disappearing, local grain boundary separating out Chain carbide, aging at level 3, grain size of 6–7, longitudinal inclusions mostly being long string-like features
3	Center side	
4	Inner wall side	

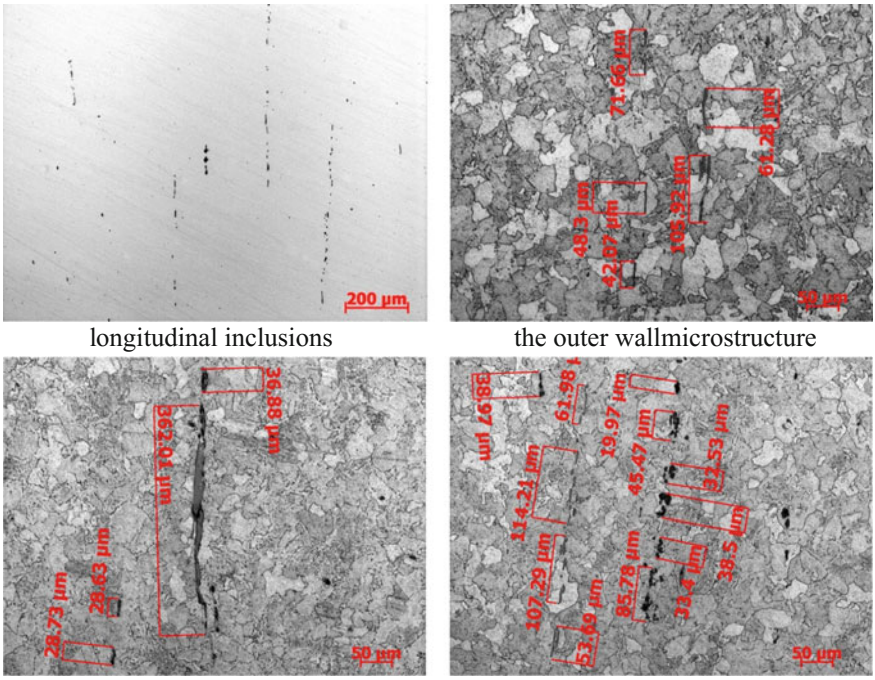

longitudinal inclusions

the outer wallmicrostructure

the centermicrostructure

the inner wallmicrostructure

Fig. 1 Metallographic structure

Table 6 Inclusions spectral component

Element	S	Mn
Mass percentage (wt%)	38.63	61.37
Atomic percentage (at.%)	51.89	48.11

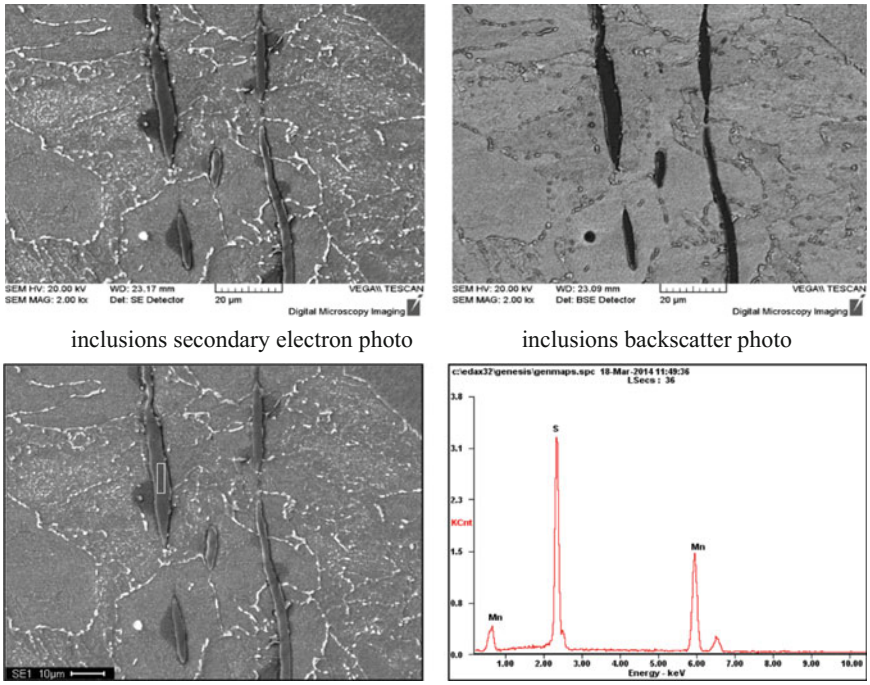

inclusions secondary electron photo

inclusions backscatter photo

longitudinal inclusions spectrum scan area

longitudinal inclusion linespectrum diagram

Fig. 2 Inclusions spectrum analysis

Remaining Life Assessment

Component which creep as the main failure mode, can be life evaluated with isothermal line extrapolation [13, 14].

According to persistent strength curve of the material $\tau = A\sigma^{-B}$.

Make $\tau 1 = 10^5$ h, $\tau 2 = 10^4$ h, $\tau 3$ as the rupture time under $\sigma 3 = n\sigma_\theta$, $\sigma 1$, $\sigma 2$ respectively as the corresponding enduring strength, then:

$$\lg \frac{\tau_3}{10^4} = \varnothing \frac{\lg \frac{\sigma_3}{\sigma_2}}{\lg \frac{\sigma_1}{\sigma_2}} = \frac{\lg \frac{n\sigma_\theta}{\sigma_{10^4}}}{\lg \frac{\sigma_{10^5}}{\sigma_{10^4}}} \tag{1}$$

For the remaining life of the pipe, directly use the enduring strength to extrapolate, without considering the strength dispersion, the stress safety factor of n is 1.5, the minimum wall thickness for sampling, 545 °C, 25 MPa under creep residual life calculations as follows in Table 7.

Without considering the dispersion of rupture strength, the stress safety factor n takes 1.5, the remaining life of the pipeline is 98,000 h.

Table 7 Remaining life assessment

τ_1 (h)	τ_2 (h)	$\sigma_{10^5}^{545\,^\circ C}$ (MPa)	σ_θ	$\sigma_{10^4}^{545\,^\circ C}$ (MPa)	N	Residual life (ten thousand hours)
10^5	10^4	88.9	59.3	106.1	1.5	9.8

Fatigue Fracture Assessment

Two CT sample testing *Kq* (conditions fracture toughness) values are 44.63 and 52.46 MPam$^{1/2}$, Use the validity conditions of Eqs. (2)–(5) to test *Kq* values validation:

$$2.5\left(K_q/R_{p0.2}\right)^2 > B \tag{2}$$

$$2.5\left(K_q/R_{p0.2}\right)^2 > W - a \tag{3}$$

$$2.5\left(K_q/R_{p0.2}\right)^2 > a \tag{4}$$

$$F_{max}/F_Q > 1.1 \tag{5}$$

After calculation fracture toughness *Kq* does not satisfy the validation conditions, and therefore *Kq* cannot be considered as valid K_{IC} [15, 16]. As the fracture toughness K_{IC} is invalid, therefore the stress intensity factor range ΔK need to be calculated, stress intensity factor expression is:

$$K_I = (Y\sigma)\sqrt{\pi a} \tag{6}$$

For the assessment of fatigue, stress intensity factor range is:

$$\Delta K_I = Y(\Delta\sigma)\sqrt{\pi a} \tag{7}$$

$$(Y\sigma) = (Y\sigma)_p + (Y\sigma)_s \tag{8}$$

Which $(Y\sigma)_p$ is primary stress, $(Y\sigma)_s$ is secondary stress, secondary stress is normal stress or shear stress which meet the external constraint or structure itself continuous deformation requirements, the structure of the paper is no need to consider the impact of secondary stress, Therefore, in the calculation of the stress intensity factor, primary stress can be calculated only once.

Crack regularization treatment length 2c = 0.475 mm, depth a = 0.166 mm, θ = π, shown in Fig. 3, crack defect analysis shown in Fig. 4.

The calculated stress intensity factor range ΔK in Table 8:

According to DL/T654-2009, the stress intensity factor range threshold ΔK_{th} of alloy steel in air fatigue crack growth can be calculated as follows:

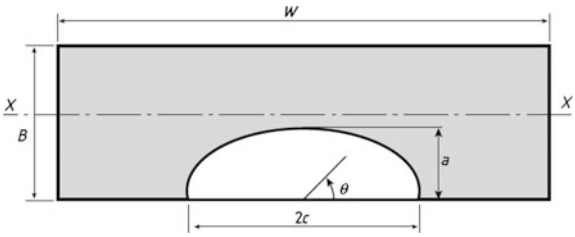

Fig. 3 Crack regularization treatment diagram

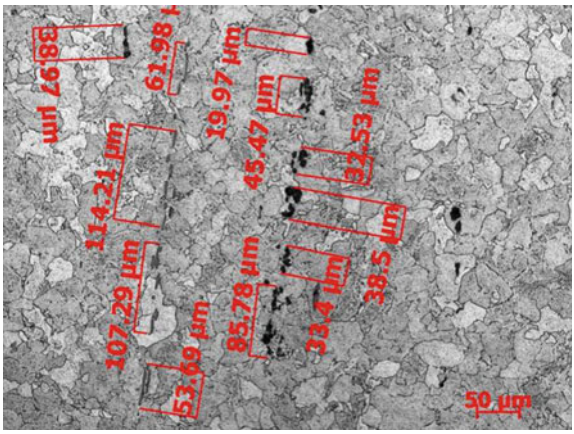

Fig. 4 Crack defect

Table 8 Stress intensity factor range

P_b (MPa)	P_m (MPa)	M_b	M_m	ΔK (MPa $m^{1/2}$)
11.2	44.7	0.73	1.346	1.58

$$\Delta K_{th} = 2221 - 0.85\mathrm{r}, \quad \mathrm{r} > 0.1 \tag{9}$$

$$\Delta K_{th} = 191, \quad \mathrm{r} \leq 0.1 \tag{10}$$

where r is the stress ratio which is the ratio of stress cycles minimum stress and maximum stress. The calculated stress intensity factor range ΔK is far less than the threshold value ΔK_{th}, so the crack defect is exempt from fatigue fracture assessment.

Creep Fatigue Interaction Assessment

Low cycle fatigue experiments on 100 kN MTS 810 250 kN electro-hydraulic servo fatigue testing system, the experiment using strain control method, load waveform using triangular wave, material strain rate: 4×10^{-3} s^{-1}, the sample

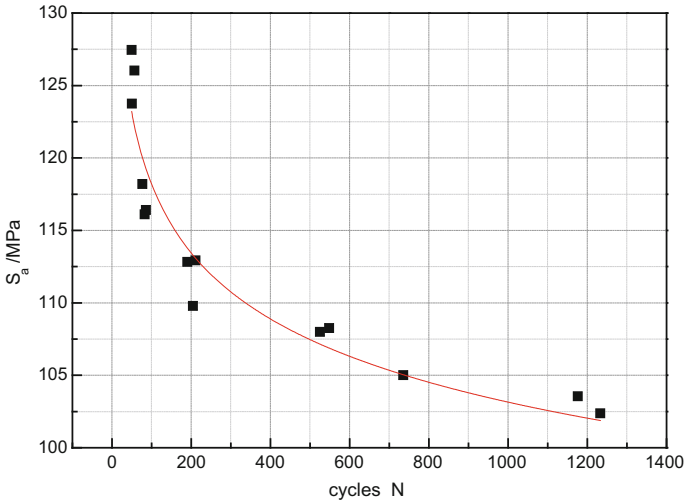

Fig. 5 Fatigue life curve

fracture is judged by load down 10%, material S-N curve based on the experimental test results, as shown in Fig. 5.

Calculation formula of stress hoop stress of pipe pressure conversion is:

$$\sigma_\theta = \frac{P(D_o - S)}{2S} \tag{11}$$

where:

P rated working pressure, 1.05 × 25 MPa
D_o pipe outside diameter, measured outside diameter
S pipe wall thickness.

Put the relevant data into Eq. (11), you can get inner conversion stress of straight pipe:

$$\sigma_\theta = 57.96\,\text{MPa}$$

According σ_θ value of the pipeline, its corresponding fatigue life can be found in the fatigue curves $N_f = 1.3 \times 10^7$.

The pipe running record shows that from 2007 to now the pipe has accumulated 60,371 h operation, start and stop 29, the remaining life of the parent metal pipe cut in 2007 is 98,000 h.

According to the standard DL/T654-2009, linear cumulative damage rule is used to assess the life loss of the main steam pipe under fatigue–creep interaction loads, fatigue–creep interaction life loss as follows:

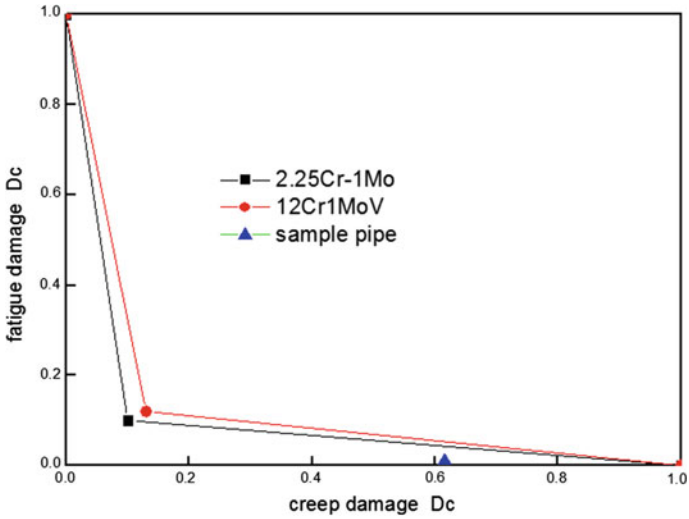

Fig. 6 Common fatigue–creep interaction curve

$$D = \sum_{i=1}^{n} \frac{n_i}{N_{fi}} + \sum_{i=1}^{n} \frac{t_i}{t_{ri}} \tag{12}$$

where:

n_i, N_{fi} i condition of actual cycles and the fatigue failure cycles;
t_i, t_{ri} i condition part uptime and lasting break time;
D value related to the share of fatigue, creep damage

Steam pipes steel commonly used fatigue–creep interaction curve shown in Fig. 6.

Linear cumulative damage rule shows that pipeline creep loss of 0.616, pipeline fatigue loss of 2.23×10^{-6}, the linear cumulative loss of pipeline in the envelope.

Conclusions

15Cr1Mo1V steel pipe containing defects has been studied by material identification and safety assessment. The main conclusions are as follows:

(1) 15Cr1Mo1V steel pipe chemical composition, hardness and strength (room temperature tensile) index meet the relevant standards.
(2) The microstructure is bainite + ferrite + carbide particles, aging at level 3, uniform hardness. But there are a large number of string-like and granular

inclusions inside the material, mainly composed of manganese sulfide inclusions, and inclusions content exceeds GB5310 requirements.

(3) The minimum longitudinal impact energy value 10 J and the minimum lateral impact energy 5 J are below the standard requirements.

(4) The pipe crack is exempt from fatigue fracture assessment. Pipeline creep loss is 0.616, pipeline fatigue loss is 2.23×10^{-6}, the main loss of pipeline is creep damage, therefore more attention should be paid to the pipeline operating temperature and pressure in the follow-up operation to avoid over-temperature creep resulting in accelerated failure.

References

1. R. Viswanathan, J. Stringer, Failure mechanisms of high temperature components in power plants. J. Eng. Mater. Technol. **122**, 246–255 (2000)
2. D. Jones, Creep failures of overheated boiler, superheater and reformer tubes. Eng. Fail. Anal. **11**, 873–893 (2004)
3. T.H. Hyde, A.A. Becker, W. Sun et al., Finite-element creep damage analyses of P91 pipes. Int. J. Press. Vessels Pip. **83**(11–12), 853–863 (2006)
4. Zhang Guodong, Zhou Changyu, Finite element simulations of welding residual stress and creep damage for welded joint. Acta Metall. Sin. **44**(7), 848–852 (2008)
5. T.H. Hyde, W. Sun, Effect of bending load on creep failure behavior of a pressurised thick walled CrMoV pipe weldment. Int. J. Press. Vessels Pip. **79**(5), 331–339 (2002)
6. T.H. Hyde, W. Sun, J.A. Williams, Life estimation of pressurised pipe bends using steady-state creep reference rupture stresses. Int. J. Press. Vessels Pip. **79**(12), 799–805 (2002)
7. S. Khodamorad, D. Haghshenas Fatmehsari, H. Rezaie, A. Sadeghipour, Analysis of ethylene cracking furnace tubes. Eng. Fail. Anal. **21**, 1–8 (2012)
8. P. Auerkari, J. Salonen, S. Holmström, A. Laukkanen, J. Rantala, R. Nikkarila, Creep damage and long term life modelling of an X20 steam line component. Eng. Fail. Anal. **35**, 508–515 (2013)
9. X.H. Yang, N. Li, Z.H. Jin, T.J. Wang, A continuous low cycle fatigue damage model and its application in engineering materials. Int. J. Fatigue **19**(10), 687–692 (1997)
10. J.P. Jing, Y. Sun, S.B. Xia et al., A continuum damage mechanics model on low cycle fatigue life assessment of steam turbine rotor. Int. J. Press. Vessels Pip. **78**(1), 59–64 (2001)
11. G.D. Zhang, Y.F. Zhao, F. Xue et al., Creep–fatigue interaction damage model and its application in modified 9Cr–1Mo steel. Nucl. Eng. Des. **241**(12), 4856–4861 (2011)
12. Q. Jiang, J. Wang, *Thermal Power Metal Materials Handbook* (China Electric Power Press, Beijing, 2000)
13. DL/T654-2009, Thermal Power Life Assessment Technology Guidelines
14. DL/T940-2005, Thermal power Plant Steam Pipe Life Assessment Technology Guidelines
15. BS7910-2005, Guide to Methods for Assessing the Acceptability of Flaws in Metallic Structures
16. GB/T19624-2004, The Safety Assessment of Containing Defects Pressure Vessels in Service

Permeation Characteristic and Mechanism of CO_2 in High Density Polyethylene

Houbu Li, Dongming Yang, Dongna Zhang, Yuanyuan Zhu, Pengli Ge, Dongtao Qi and Zhihong Zhang

Abstract Thermoplastic lined composite pipes are broadly employed in transporting the oil and gas which contains H_2S/CO_2 due to its good corrosion resistance. However, permeation of gases of the frequently-used thermoplastics makes the liner at the risk of blister. This brings a hidden danger for safety of pipelines and environment. In order to understand the permeation behavior and mechanism of gases in thermoplastics and to present effective methods to prevent permeation, this paper studies the permeation behavior of a typical acid gas CO_2 in high density polyethylene (HPDE), which is a widely used liner in composite pipes. Combined with analysis of morphology, composition and thermal resistance of the penetrated samples, the permeation mechanism was systematically investigated. The results showed that permeation coefficient of CO_2 in HDPE increased with the increasing temperature. It is reveal that the mode of gas permeation was mainly physical process rather than chemical attack, because morphology, the composition and

H. Li (✉) · D. Zhang · D. Qi
State Key Laboratory of Performance and Structural Safety for Petroleum Tubular Goods and Equipment Materials, CNPC Tubular Goods Research Institute, Xi'an 710077, China
e-mail: lihoubu@cnpc.com.cn

D. Zhang
e-mail: zhangdongna@cnpc.com.cn

D. Qi
e-mail: qidtao@cnpc.com.cn

D. Yang · Y. Zhu · P. Ge · Z. Zhang
Engineering and Technology Research Institute of Sinopec Northwest Oilfield Company, Urumqi 830011, Xin-Jiang, China
e-mail: ydmxbj@163.com

Y. Zhu
e-mail: zhuyuanyuan@163.com

P. Ge
e-mail: gepli@163.com

Z. Zhang
e-mail: zhangzh@163.com

© Springer Nature Singapore Pte Ltd. 2018

Y. Han (ed.), *Advances in Materials Processing*, Lecture Notes in Mechanical Engineering, https://doi.org/10.1007/978-981-13-0107-0_93

thermal resistance of the samples were not change obviously after the gas permeation. The diffusion coefficient obtained by molecular dynamics simulation was identical with the tested one, revealing that diffusion of CO_2 in HDPE belongs to a normal diffusion (jumping between the cavities).

Keywords HDPE · Permeation · Oil field · Diffuse · Gathering and transportation

Introduction

Natural gas which contains H_2S has become a very important natural gas resource in China [1]. As the transported pipeline, steel pipe suffers serious corrosion in such acid environment containing H_2S/CO_2. In recent years, reinforced thermoplastic pipes (RTPs) become a very important selection to transport the acid gas due to their good corrosion resistance, flexibility, fatigue resistance, easy installation, et al. RTPs have been widely used in Tarim Oilfield, Tahe Oilfield, Xinjiang Oilfield, et al. [2–5]. Generally, RTPs have three typical layers, including the liner, the reinforced layer and the outer layer, respectively. The liner and outer layer are normally thermoplastic materials, while the reinforced layer can either be metal such as steel wire or steel belt, or be non-metallic materials such as continuous fibers. Till now, the widely used liner of RTPs in China is high density polyethylene (HDPE) [1–5]. However, in view of the essential characteristics of thermoplastics, gas molecules would inevitably be absorbed on the inner face of thermoplastic material, and subsequently diffuse into the liner due to their free movement. Such permeation can not only waste the transported gas, but also result in blister and collapse of the liner [6–8]. Moreover, the penetrated gas will diffuse along the radial direction of the liner, which increases the failure risk of the reinforcements especially the metal reinforcement. Thus, pressure resistance and service life of RTPs would be decreased.

In order to avoid damage or destroy of the HDPE liner due to gas permeation, and to reduce failure risk of RTPs, it is essentially to understand the permeation characteristic and mechanism of gases in HDPE. Effective methods can thus be provided to prevent gas permeation. It is also helpful to put forward some direct guidance to improve the barrier property of HDPE. This paper studies the permeation behavior of a typical acid gas CO_2 in high density polyethylene (HPDE) at different temperatures according to GB/T 1038-2000 [9] by using the gas permeability tester. Combined with analysis of morphology, composition and thermal resistance of the penetrated samples, permeation mechanism of CO_2 in HDPE is systematically investigated. It is benefit to verify and control the permeation property of coupled oil and gas in thermoplastics.

Experimental Procedure

The HDPE samples used were extruded circular thin film. Their diameter and thickness were 60 mm and 300 μm, respectively. Permeability coefficient of CO_2 in HDPE was tested by using a VAC-V2 gas permeability tester. The test temperatures were 30, 40, 60 and 80 °C, respectively. At least three samples were tested in each condition.

Surface morphologies of penetrated samples were detected by a Hitachi S-4800 scanning electron microscope (SEM). To check any significant chemical modification of the sample, the samples were characterized by Fourier transform infrared spectroscopy (FT-IR), which was obtained by using a VERTEX 70 Spectrometer. The thermal analysis for the sample was conducted on thermal gravimetric analysis-differential scanning calormetry (TG-DSC) (Netzsch STA 409C) in argon gas with a ramping rate of 10 °C/min. Permeation mechanism of CO_2 in HDPE was analyzed by using a software of Material Studio 6.0 and Visual studio.

Results

Permeability Coefficient of CO_2 in HDPE

The permeability coefficient of CO_2 in HDPE at different temperatures is shown in Fig. 1. With the increase of temperature, the permeability coefficient of CO_2 in HDPE is increasing. At constant pressure, the effect of temperature on the diffusion coefficient of gas in polymer follows the Arrhenius equation [10, 11]. According to the free volume model, the free volume of the material decreases and the activation energy increases at low temperatures (such as near or below the glass transition temperature of the polymer material). As the temperature increases, the total free

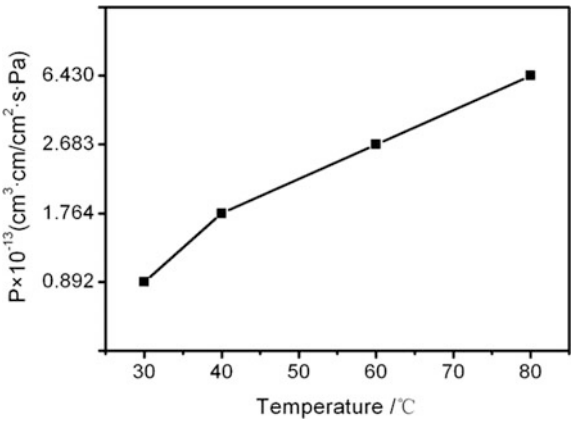

Fig. 1 The permeability coefficient of CO_2 in HDPE at different temperatures

volume increases, and the permeate gas molecules can move more freely in the amorphous material. At this time, the medium molecules follow the "liquid-like" permeation mechanism, in which the activation energy is lower and the gas permeability coefficient is increasing [10].

Performance Analysis of the Penetrated Sample

Microstructure Analysis

The SEM microstructure of the original HDPE sample is shown in Fig. 2. It can be seen that the sample surface is flat, and there is no obvious cracks, holes and other defects but with extruded pultrusion marks on the surface. The morphology of HDPE sample after CO_2 gas penetration at different temperatures is shown in Fig. 3. Compared with the original morphology of HDPE (Fig. 2), the microstructure of the sample after CO_2 gas penetration at different temperatures did not change significantly. There was also no crack, and other defects except the clear extrusion traces.

The above results indicate that the penetration of CO_2 gas did not have a significant effect on the microstructure of HDPE. Although the increase of temperature accelerates the permeation rate of CO_2 gas in HDPE, the acceleration of gas permeation process does not destroy the microstructure of HDPE samples. It can be inferred that the CO_2 gas permeation process does not produce significant physical or chemical damage to HDPE.

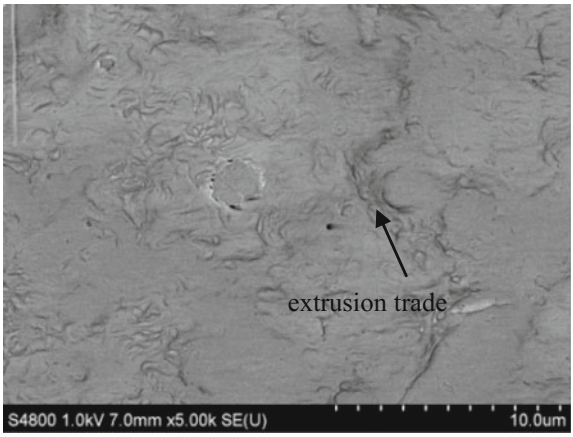

Fig. 2 SEM of the original sample HDPE

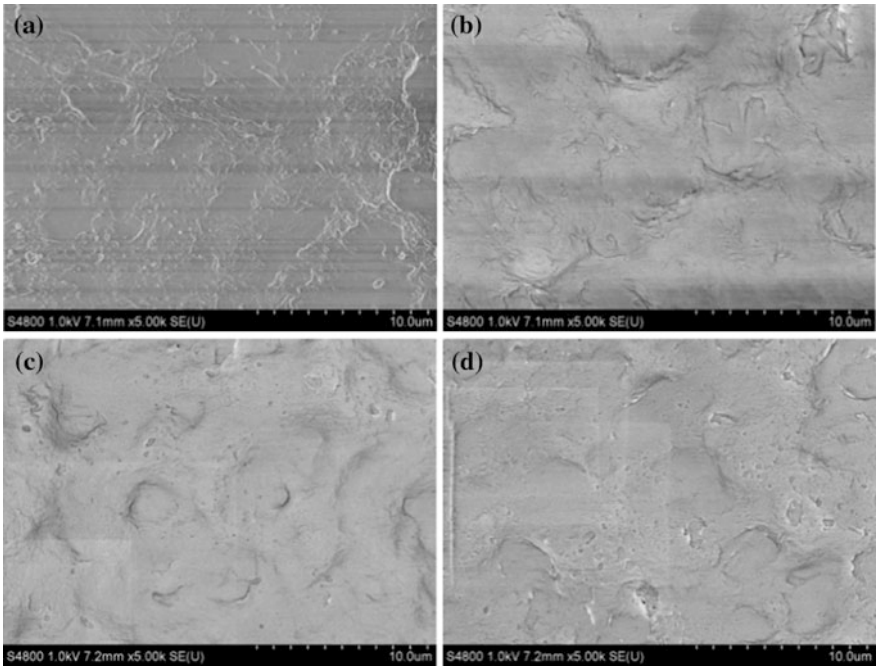

Fig. 3 Morphology of HDPE sample after CO_2 gas penetration at different temperatures: **a** 30 °C **b** 40 °C **c** 60 °C **d** 80 °C

Composition Analysis

The FTIR pattern of HDPE samples before and after CO_2 gas penetration is shown in Fig. 4. The chemical formula of HDPE is $–[CH_2–CH_2]_n–$. It can be seen from Fig. 4 that the characteristic absorption peaks of FTIR spectra of the original HDPE sample are at 2912, 2854, 1465 and 721 cm^{-1}, respectively, where 2912, 2854 cm^{-1} is the asymmetric and symmetric stretching vibration absorption peak of $–CH_2$, 1465 cm^{-1} is the symmetrical bending vibration absorption peak of $–CH_2$, 721 cm^{-1} is the swing vibration absorption peak in the plane of $–CH_2$ [12]. Compared with the FTIR spectra of the original HDPE sample, the characteristic absorption peak position and peak intensity of the FTIR spectra of the samples after CO_2 gas permeation at different temperatures did not change significantly (Fig. 4), which indicated that the structure of the HDPE sample did not be damaged after gas permeation at different temperatures. It can be deduced that the process of gas permeation in HDPE is a simple physical penetration, which does not cause obvious erosion and damage to its molecular structure and element composition.

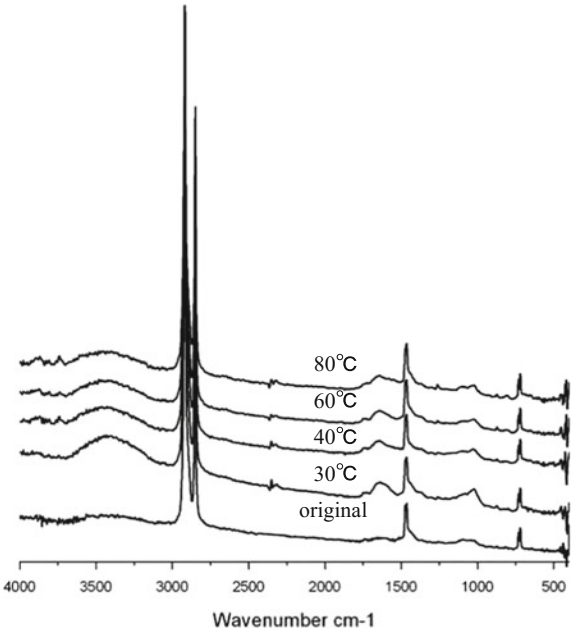

Fig. 4 FTIR of HDPE samples before and after CO_2 gas penetration

Thermal Resistance Analysis

The TG-DSC pattern of HDPE samples before and after CO_2 gas penetration is shown in Fig. 5. It can be seen that the initial weight loss temperature of HDPE is 464.9 °C, the temperature at the inflection point (which is the maximum weight loss rate) is 483.9 °C and the weight loss termination temperature is 494.7 °C. The total mass loss is 96.1%. The first endothermic peak of original HDPE sample occurs at 135.0 °C, which is the melting peak of HDPE, indicating that the resin begin to melt at this temperature. Subsequently, the small molecules of side chain of polymer resin become fracture and then escape during the heating process, which resulting in a slow exothermal curve. A significant exothermic peak occurs at 483.0 °C (near the weight loss inflection point) due to the breakage of the macromolecule chains of the resin. With the weight loss of HDPE resin tends to be flat, thermal changes close to be steady. A new exothermic peak occurs at about 717.3 °C. This is because that the thermal radiation and absorption of the sample cannot be shielded by alumina crucible at this temperature, which results in the DSC baseline drifting to the endothermic direction at high temperature, and disturbing DSC signal of the sample [7].

After CO_2 gas penetrated at different temperatures (30, 40, 60, 80 °C), the location and intensity of the endothermic peak and exothermic peak were consistent with the original one, and no other endothermic or exothermic peaks were observed, indicating that CO_2 gas penetration at different temperatures did not affect the thermal resistance and pyrolysis behavior of HDPE samples.

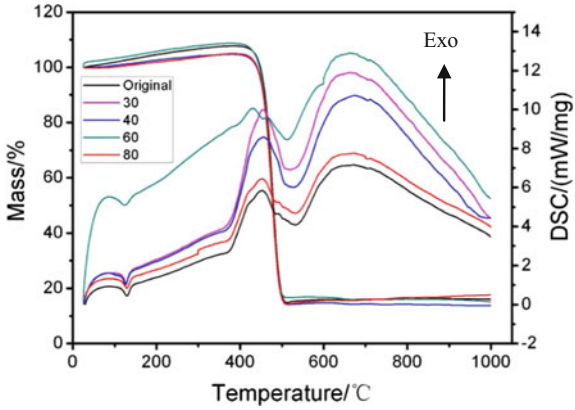

Fig. 5 TG-DSC of HDPE samples before and after CO_2 gas penetration

Molecular Dynamics Simulation of CO_2 Permeation in HDPE

The permeation process of gas in polymer usually can be described by the dissolution-diffusion mechanism, which is the most widely accepted mechanism model for the past several decades [11]. That is, high-pressure gas adsorb (dissolve) into the high-pressure side surface of the materials; permeable gas molecules diffuse to the internal materials due to the pressure difference, and finally desorb from the low pressure side surface. Therefore, it is significant to study the diffusion process, which is an important part of the permeation process. In this paper, the diffusion behavior of CO_2 gas molecules in HDPE at 30 °C was studied by molecular dynamics simulation to obtain the corresponding diffusion coefficients. The feasibility of the molecular simulation method was verified by comparison with the experimental results, and the diffusion mechanism was analyzed.

Modeling and Diffusion Process Simulation

HDPE monomer and CO_2 diffusion molecular structure were constructed firstly, and then the diffusion unit cell model of CO_2 molecule in HDPE was constructed, which was optimized to obtain a relatively stable lattice structure. The optimized HDPE unit cell containing CO_2 molecules is shown in Fig. 6.

For the optimized model, the system was equilibrated by NVT + NVE dynamic simulation, and then NVE full-track dynamics was simulated. The atom-based method was used to calculate van der Waals interaction force and Ewald method was used to calculate the electrostatic interaction force.

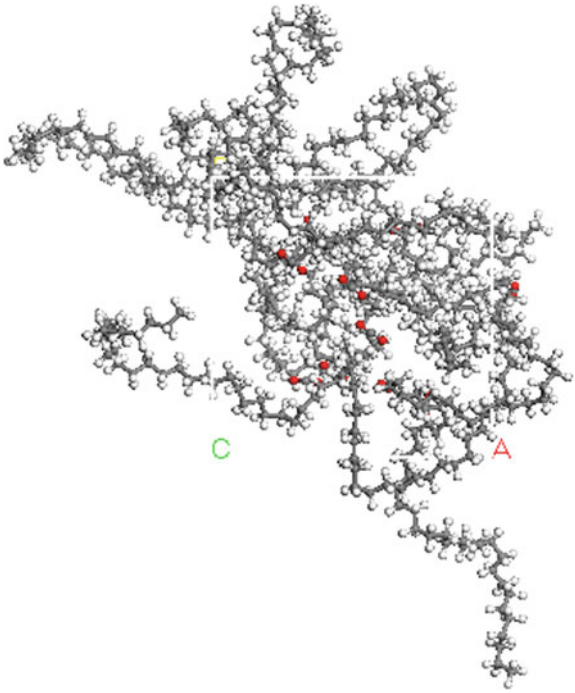

Fig. 6 Optimized HDPE unit cell containing CO_2 molecules

Simulation Results

A series of optimized and system equilibrium of HDPE unit cell containing CO_2 molecules were conducted. NVE simulation was then carried out and all of the trajectories were preserved. MSD analysis was performed to obtain the mean square displacement curve of CO_2 molecule in HDPE unit cell system (Fig. 7). It can be seen that the mean square displacement curves of CO_2 molecules exhibit good linear relationship. There are obvious displacements at all of the X-axis, Y-axis and Z-axis directions but little difference among them, which means the diffusion of CO_2 molecules in the system is relatively stable. The diffusion coefficient is calculated by Einstein method, which correlates the diffusion coefficient D with the mean square displacement (MSD) of the molecule [13], i.e. D = m/6. Where m is the slope of the MSD versus time curve fitted by the least squares method. As shown in Fig. 8, the slope of the straight line m is 0.9694 obtained by the fitted log (MSD)–log(time). Therefore, the diffusion coefficient of CO_2 in HDPE is 0.14493 (10^{-6} cm^2 s^{-1}) at 30 °C, which is close to the experimental value of 0.16341 (10^{-6} cm^2 s^{-1}), indicating that the established model is reliable.

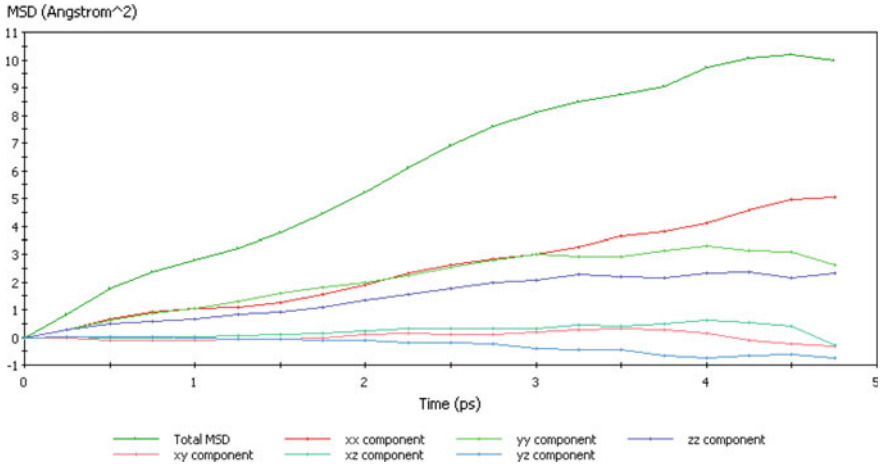

Fig. 7 Mean square displacement curves of CO_2 molecule diffusion in HDPE

Fig. 8 Fitting curves of log (MSD) to log (time)

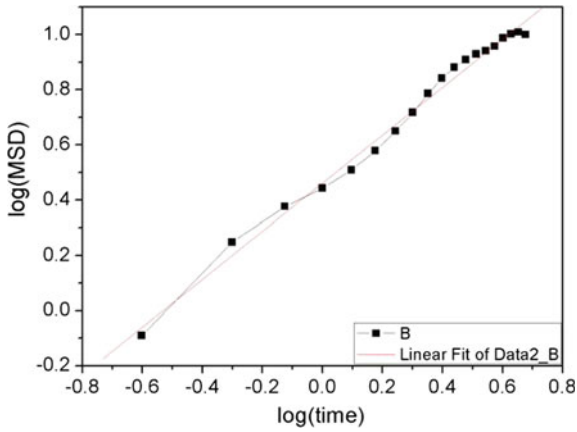

Discuss of the Diffusion Mechanism

The polymer volume consists of the occupied volume and the unoccupied free volume. The size and shape of the free volume existing in the form of cavities play an important role in the diffusion behavior of the permeation molecule in the polymer, which provides the necessary space for the chain motion and the diffusion space of the small molecule. Small molecules are constantly moving in the polymer, in most cases the movement amplitude is small and can be regarded as vibration. Occasionally a major transition occurs, jumping to another area to continue small vibration, so that a region is a cavity, that is, free volume. When the gas molecular vibrates to a certain position within the cavity, the polymer chains shift or relative

motion providing the channel for a major leap of small molecules, so small molecules jump to another cavity to vibration.

The mean square displacement curve (MSD) of CO_2 molecules in HDPE was obtained by above molecular dynamics simulation and the slope m of log (MSD)–log (time) curve can be used to determine the diffusion of small molecules. If $m < 1$, it means that the diffusion is non-normal diffusion (motion within the cavity); if m is close to 1, it means that the diffusion belongs to the normal diffusion (jump between the cavities) [9]. In this paper, the m obtained by simulation is 0.9694, close to 1, indicating that the diffusion of CO_2 in HDPE is a normal diffusion, which diffusion trajectory can be expressed as [14]: (1) Within a certain period of time, the gas molecules jump in a small space where the center is a certain point, but not exceed this "quasi-stable" area; (2) The "quasi-stable" area is broken and the gas molecules jump quickly from one "quasi-stable" area into another "quasi-stable" area. Such a "quasi-stable" area is actually a cavity and the gas molecules move in the cavity near the original one before moving to another cavity.

Summary

(1) The permeability coefficient of CO_2 gas in HDPE increases with the increase of temperature, which follows the Arrhenius equation.
(2) The microstructure, composition and thermal resistance of the penetrated samples do not change significantly, indicating that the main mode of permeation of CO_2 in HDPE is physical permeation process rather than chemical attack.
(3) The diffusion coefficient obtained by molecular dynamics simulation is in good agreement with the experimental results. The diffusion coefficient calculation results show that the diffusion of CO_2 in HDPE belongs to normal diffusion (jump between the cavities).

References

1. G.Y. Zhu, S.C. Zhang, Y.B. Liang, Y.S. Ma, T.L. Guo, G.Y. Zhou, Distribution of high H_2S-bearing natural gas and evidence of TSR origin in the Sichuan Basin. Acta Geol. Sin Engl. **80**, 1208–1218 (2006)
2. L.H. Li, H. Li, H.B. Tu, S.L. Zhang, H. Mou, Internal anticorrosion techniques for oil and gas pipelines. Shanghai Coat. **49**, 31–33 (2011)
3. D.T. Qi, M.L. Yan, N. Ding, X.H. Cai, H.B. Li, S.H. Zhang, Application of polymer composite pipes in oilfields in China, in *The 7th Internatioanl MERL Oilfield Engineering with Polymers Conference, 20–22 Sept 2010, London, UK* (SPE, New-York, 2010)
4. Z. Li, H.J. Wang, J. Wei, The applicaiton of plastic pipelines in pil gathering system of tarim oil field. Oil Gas Stor. Trans. **22**, 37–39 (2003)

5. F.Y. Han, J.Y. Ding, T.M. Sun, Y. Yang, Application of the nonmetallic pipeline technologies to the oil and gas field. Petro. Plan. Eng. **23**, 5–9 (2012)
6. H.B. Li, X.M. Zhang, X.Q. Mao, D.T. Qi, Z.L. Li, M.C. Wang, Research and advise on permeation of thermoplastics used in oil and gas transportation. Nat. Gas Oil. **34**, 84–88 (2016)
7. D.T. Qi, J.H. Ren, H.B. Li, P.G. Ren, H. Zhang, The permeation law of hydrogen sulfide in multilayer polymer composited oil/gas pipes. Nat. Gas. Ind. **34**, 126–130 (2014)
8. B. Wei, D.T. Qi, H.B. Li, G.Q. Qi, X.H. Cai, N. Ding, Corrosion resistance of reinforced thermoplastic pipes in a sour environment. Nat. Gas. Ind. **35**, 87–91 (2015)
9. The State Bureau of Quality and Technical Supervision, *GB/T 1038-2000 Plastics—Film and sheeting—Determination of gas transmission—Differential-Pressure Method* (Standards Press of China, Beijing, 2000)
10. F. Mozaffari, H. Eslami, J. Moghadasi, Molecular dynamics simulation of diffusion and permeation of gases in polystyrene. Polymer **51**, 300–307 (2010)
11. C.G. Soney, S. Thomas, Transport phenomena through polymeric systems. Prog. Polymer. Sci. **26**, 985–1017 (2001)
12. H.B. Li, M.L. Yan, D.T. Qi, Failure analysis of steel wire reinforced thermoplastics composite pipe. Eng. Fail. Anal. **20**, 88–96 (2012)
13. X.L. Ren, J.Z. Ren, M.C. Deng, Poly(amide-6-b-ethylene oxide) membranes for sour gas separation. Sepa. Puri. Tech. **89**, 1–8 (2012)
14. R. Scheichl, M.H. Klopffer, Z. Benjelloun-Dabaghi, B. Flaconnèche, Permeation of gases in polymers: parameter identification and nonlinear regression analysis. J. Membr. Sci. **254**, 275–293 (2005)

Dropout Failure Analysis for Long Round Thread Connection at Mill End

Zhiyong Pan, Yaorong Feng, Lihong Han, Jianjun Wang, Xianren Kuang, Peng Yang, Chengli Song, Han Ding and Shen Cong

Abstract Round thread casing connection may be dropout failure due to main reasons of material's property, thread parameter, make-up position or make-up torque, field operation problems etc. Thread connection is easy to dropout at field end because of complex condition in oil field. In the present study the cause of thread connection dropout at mill end was analyzed by combining relative theory with test in this paper. The macroscopic analysis was done for failure sample. The material's physical and chemical properties were checked. The measurement and comparative analysis was carried out for dropout coupling's outside diameter and thread taper. Full scale tension test was done for two lots of casing connection simples. The finite element simulation analysis on interference thread connection was carried out under axial tensile loading according to calculation. The results

Z. Pan (✉) · Y. Feng · L. Han · J. Wang · X. Kuang · P. Yang · C. Song · H. Ding · S. Cong
Tubular Goods Research Institute of China National Petroleum Corporation,
Xi'an 710089, Shaanxi, China
e-mail: panzy@cnpc.com.cn

Y. Feng
e-mail: fengyr@cnpc.com.cn

L. Han
e-mail: hanlihong@cnpc.com.cn

J. Wang
e-mail: wangjianjun005@cnpc.com.cn

X. Kuang
e-mail: kuangxr@cnpc.com.cn

P. Yang
e-mail: yangpeng002@cnpc.com.cn

C. Song
e-mail: songcl@cnpc.com.cn

H. Ding
e-mail: dinghan@cnpc.com.cn

S. Cong
e-mail: congshen@cnpc.com.cn

© Springer Nature Singapore Pte Ltd. 2018

Y. Han (ed.), *Advances in Materials Processing*, Lecture Notes in Mechanical Engineering, https://doi.org/10.1007/978-981-13-0107-0_94

showed that the casing material's yield strength was lower than standard value. The thread connection's make-up trace location at mill end was in accordance with corresponding standard. Dropout coupling's outside diameter at different axial location had a good consistent and is little difference. The variation scope of dropout couple's thread taper at mill end was high. The finite element force simulation result refer thread connection at mill end could not dropout at make-up trace location. The final results showed that dropout failure was ascribe to unqualified casing material's yield strength and thread connection break-out because of float make-up in oil field.

Keywords Round thread · Casing connection · Dropout · Mill end
Yield strength · Finite element · Float make-up · Failure analysis

Introduction

The API round thread and buttress thread are the most common thread type in oil and natural gas industry. The axial tensile strength and axial compression strength of buttress thread is very strong, and the buttress thread connection strength can almost reach the tensile strength of the pipe, while its sealing performance is poor due to non-intact threads and multiple helical channels. Round thread type is triangle, and the thread profile angle is 60°, the bisector line of thread profile angle is perpendicular to the axis of pipe. The top profile and bottom profile of round thread is round arc. The pin thread's guide flank and load flank are closely contact with box thread after the connection was made up. Packed with thread compound between the bottom and top of the round thread, the thread connection has good sealing performance. The round thread is suitable to be used in low or middle pressure gas well or oil well. The round thread is prone to deformation under axial load because of thread characteristics. The round thread connection's tension strength is only the 60–80% body strength. The round thread connection is easy to dropout at field end because of complex condition in oil field. A great number of studies had been conducted on connection dropout failure at field end in order to reduce or avoid the dropout case [1–7]. The cause of thread connection dropout at mill end was analyzed by combining relative theory with test in this paper. The vertical well depth is 3710 m, the failure casing specification is Φ139.7 × 9.17 mm P110 LC, the fish length is 3695 m.

Macroscopic Examination

The guide flank morphology at mill end of pullout coupling is shown in Fig. 1. The friction trace on guide flank is obvious and the trace extends to the 22nd thread. The load flank morphology at factory end of pullout coupling is shown in Fig. 2.

Fig. 1 Guide flank morphology

The friction trace on load flank extends to the 22nd thread also. It can be deduced that the box thread's make-up position at mill end is the position of 22nd thread according to the above results.

The dropout pin thread morphology at mill end of pullout coupling is shown in Fig. 3. The friction trace on guide flank and load flank is bright and the trace extends to the 22nd thread. The rust and thread compound hardened on thread had been found on thread more than 22nd thread. It can be deduced that the pin thread's make-up position at mill end is the position of 22nd thread according to the above analysis. The end face morphology at mill end of dropout coupling is shown in Fig. 4, the surface was worn visibly and the surface is smooth and shiny, indicating that extrusion and relative slip had taken place on end face.

Geometric Measurement

The dropout coupling was divided into 9 evenly from mill end to field end along the axial of coupling. The each segment's outside diameter was measured in 0° direction, 45° direction, 90° direction and 145° direction. Dropout coupling's

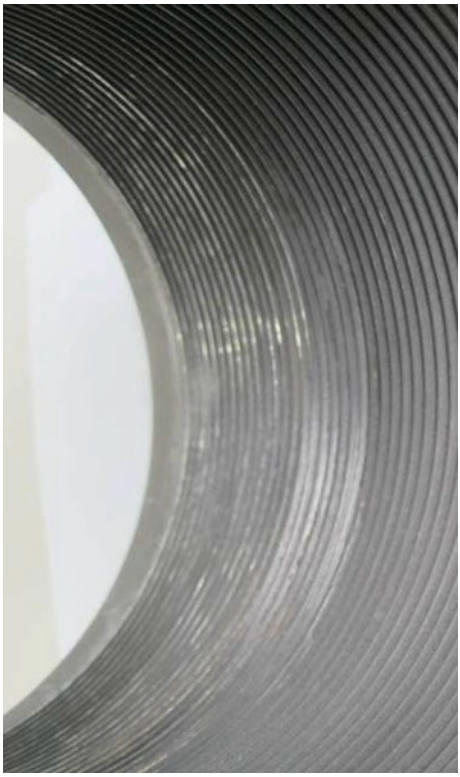

Fig. 2 Load flank morphology

outside diameter at different axial location is in accordance with API Spec 5CT [8] and it has a good consistent and is little difference. The morphology of partial bulge can't be found.

The thread taper at mill end and field end of dropout coupling was measured in 0° direction and 90° direction. The thread taper at field end is in accordance with API Spec 5B [9]. The thread taper at mill end isn't in accordance with API Spec 5B, and variation scope of different thread taper is high.

Material Test

The oil casing was classified according to the grade of steel and some chemical elements were limited in material. The chemical composition of material of the pullout coupling and pipe is shown in Table 1, and the chemical composition of material is in accordance with API Spec 5CT.

The tensile test was carried out on longitudinal round bar with a diameter of 6.25 mm processed in dropout coupling at room temperature, the result is shown in Table 2 and the result is in accordance with API Spec 5CT. The tensile test was

Fig. 3 Dropout pin thread morphology

Fig. 4 Eend face morphology

carried out on longitudinal plate bar with a gauge width of 25.4 mm processed in dropout casing at room temperature, the result is shown in Table 2 and the yield strength is lower than standard value.

Table 1 Chemical composition of material of pipe and coupling (wt, %)

Element	C	Si	Mn	P	S	Cr	Mo	Ni	Nb	V	Ti	Cu	B
Coupling	0.24	0.21	1.62	0.012	0.0032	0.069	0.0089	0.11	<0.005	0.079	0.0018	0.14	0.0008
Pipe	0.26	0.25	1.33	0.0097	0.0047	0.060	0.020	0.10	<0.005	<0.005	0.0022	0.087	0.0006
API Spec 5CT requirement	/	/	/	≤ 0.030	≤ 0.030	/	/	/	/	/	/	/	/

Table 2 Mechanical property of material of pipe and coupling

Subject		Tensile strength Rm (MPa)	Yield strength Rt 0.6 (MPa)
Coupling	Test value	934 933 929	823 821 817
	Average	932	820
Pipe	Test value	936 936 937	741 739 756
	average	936	747
API Spec 5CT requirement		≥ 862	758–965

Finite Element Simulation

The finite element simulation analysis was carried out on thread connection under tensile loading. Two-dimensional axisymmetric model is adopted. The coupling's middle cross section was fixed in axial direction and free in radial direction. The friction coefficient is 0.02. The actual strength data is adopted in model. The ideal elastic-plastic model is analyzed under interference and load conditions shown in Table 3.

The number code of axial thread position in which the radial distance is far between the top of the thread and the bottom of the thread is shown in Fig. 5. The axial position is the x-coordinate, the radial distance between the thread top and bottom is the vertical coordinate, and the radial distance contrast under four conditions is shown in Fig. 6. Visibly, the separation distance in case c and d is greater than the separation distance in case a, this means that the connection in case c and d is prone to dropout, and the failure risk in case d is the biggest. Therefore, the connection strength will be reduced greatly when the thread connection is fitted loosely, which can easily lead to the occurrence of dropout.

The connection's stress distribution and deformation under the condition of case a is shown in Fig. 7. Visibly, the biggest radial deformation located at 18th thread

Table 3 Interference and load conditions

Load code	Interference turns	Axial tension strength (kN)	Load source
a	2	2437	Minimum connection strength according to standard
b	1	1050	Fish weight
c	0	1050	Fish weight
d	−1	1050	Fish weight

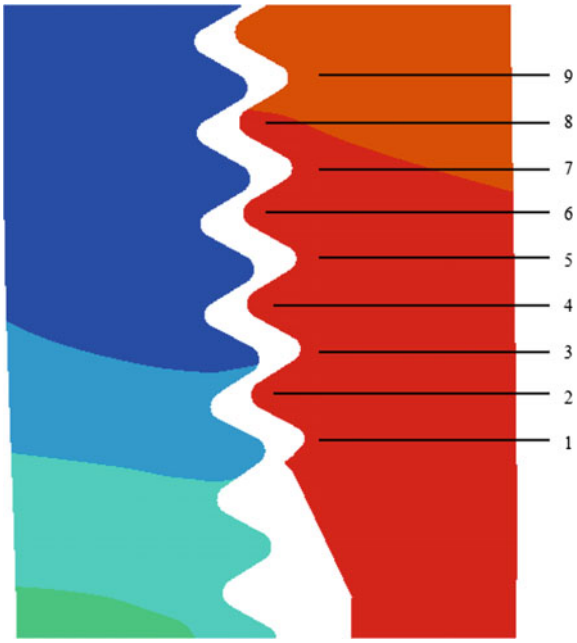

Fig. 5 Position number

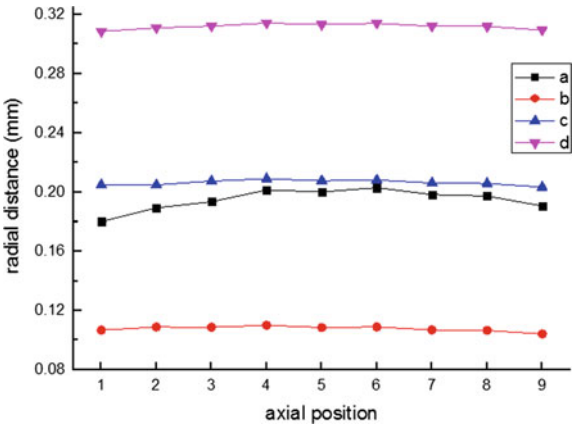

Fig. 6 Radial distance contrast

to 19th thread in pin thread, and the coupling's radial maximum deformation occurred in the transition boundary between boring and thread. If the thread connection dropout under the condition of case a, the maximum radial plastic deformation will occur in the corresponding position. The depression deformation can't be found in outside surface profile of pin thread connection, and the ballooning deformation can't be found in outside surface of coupling. Therefore the make-up position at mill end is not in the 22nd thread when the thread connection dropout.

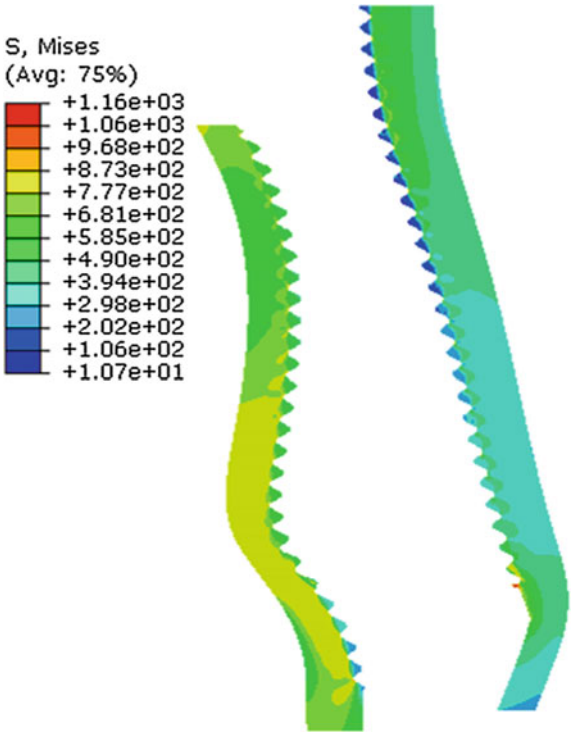

Fig. 7 Stress distribution and deformation

Comprehensive Analysis

The same lots sample's thread parameter is met with API Spec 5B in oil field. Full scale tension to failure tests were done for two connection simples according to ISO 13679 [10] at room temperature. One simple was made up according to location on which three pin thread pitch exceed the coupling end side, and the other was made up according to minimum torque. The all results are in accordance with ISO/TR 10400 [11]. Therefore, the thread connection joint strength is lower than standard value only if the situation on which the thread connection is fitted loosely.

The conclusion can be got that the make-up position at mill end is not in the 22nd thread when the thread connection dropout according to the finite element simulation analysis, and the failure strength is lower. It also can be reduced that the make-up position at mill end is not in the 22nd thread when the thread connection dropout according to measurement result of dropout coupling. While it is shown that the dropout thread's make-up position at mill end is the position of 22nd thread according to the macroscopic Examination results. Therefore, it can be concluded that dropout failure took place after the thread connection was broke up. Lower yield strength of casing material is helpful for thread connection dropout.

Float make-up was used in oil field and coupling didn't be held in the course of making up. It can be reduced that relative slip had taken place between coupling and elevator according to end face morphology of coupling. It is that the whole casing string was rotary in the course of making up.

Due to wall friction resistance and mud viscous resistance, casing string like a torsion spring in the wall. Mechanical deformation energy will be stored in casing string in the course of rotation. The casing string will be reversal rotate abruptly when the energy lead to limits.

Because resistance is maximum value in elevator, the break-out torque is maximum to the thread connection at mill end. It will easily lead to the occurrence of dropout.

Conclusions

The dropout failure was ascribe to unqualified casing material's yield strength and thread connection break-out due to float make-up in oil field. Finite element simulation analysis is an important method to study the stress state of thread connection.

References

1. S. Lu, Y. Han, C.Q. Terry et al., Analysis of well casing connection pullout. J. Eng. Fail. Anal. **13**(4), 638–645 (2006)
2. Zhiyong Pan, Peng Chen, Jianjun Wang et al., Pullout cause analysis of buttress thread connection for a well. J. Heat Treat. Metals. **37**(4), 124–127 (2012)
3. Zhiyong Pan, Zhu Yan, Wenhong Liu et al., Two typical cases analysis of casing connection pullout. J. Drilling Prod. Technol. **35**(5), 83–86 (2012)
4. Z. Pan, S. Song, W. Liu et al., Round thread casing connection dropout accident analysis for a well. J. Oil Field Equip. **40**(12), 20–24 (2011)
5. Z. Shen, Influence of material deformation strengthening and friction coefficient on round thread connection pull-out. J. Chin. J. Appl. Mech. **25**(2), 293–295 (2008)
6. L. Gao, J. Shi, Y. Jin, Influence of make-up torque on the connection strength of round thread casing. J. Nat. Gas Ind. **25**(2), 87–89 (2005)
7. J. Qi, We. Luo, Z. Hong et al., Numerical simulation of screw-on and jump-out behavior of threaded casing connection. J. Univ. Pet. China **24**(4), 68–71 (1998)
8. International Organization for Standardization, *Petroleum and Natural Gas Industries—Steel Pipes for Use as Casing or Tubing for Wells* (ISO, Switzerland, 2014)
9. American Petroleum Institute, *Specification for Threading, Gauging, and Thread Inspection of Casing, Tubing, and Line Pipe Threads* (API, Washington, 2008)
10. International Organization for Standardization, *Petroleum and Natural Gas Industries-Procedures for Testing Casing and Tubing Connections* (ISO, Switzerland, 2002)
11. International Organization for Standardization, *Petroleum and Natural Gas Industries-Equations and Calculations for the Properties of Casing, Tubing, Drill Pipe and Line Pipe used as Casing or Tubing* (ISO, Switzerland, 2007)

Coupling Effect of Transient Temperature-Pressure on Casing String During Volume Fracturing in Shale Gas Wells

Yan Xi, Jun Li, Yang Yu, Zongyuan Li and Bowen Mei

Abstract Casing deformation has been found to be a very significant issue in the development process of shale gas in China, while the coupling effect of transient temperature-pressure has a significant impact on casing stress, and worthy of study. This paper presented a new numerical investigation to understand the coupling effect of transient temperature-pressure on casing string during volume fracturing. A wellbore temperature model was established to obtain the required input parameters of dynamic temperature boundary. The numerical model considers the coupling effect of transient temperature-pressure and the various cement sheath shapes. The results showed that the temperature of casing changed drastically during fracturing. Under the influence of the coupling effect of transient temperature-pressure, (a) when the cement sheath shape was integrity, the casing stress increased greatly and showed dynamic changes: first increased and then decreased, (b) when there was deficiency in cement sheath, with the increase of the eccentric distance or deficiency angle, the casing stress increased aggravating risk of casing deformation. Rotating the casing string during the cementing process to avoid the deficiency in cement sheath or using warm fracturing fluids to minimize the influence of the coupling effect of transient temperature-pressure are possible innovative strategies to solve these difficult problems.

Y. Xi (✉) · J. Li · Y. Yu · Z. Li
China University of Petroleum-Beijing, Beijing 102249, China
e-mail: garfield0510@163.com

J. Li
e-mail: lijun446@vip.163.com

Y. Yu
e-mail: 2281063450@qq.com

Z. Li
e-mail: 1504559953@qq.com

B. Mei
China Petroleum Materials Corporation, Beijing 100029, China
e-mail: 348283009@qq.com

© Springer Nature Singapore Pte Ltd. 2018

Y. Han (ed.), *Advances in Materials Processing*, Lecture Notes in Mechanical Engineering, https://doi.org/10.1007/978-981-13-0107-0_95

Keywords Volume fracturing · Shale gas · Wellbore temperature field model Coupled thermal-mechanical effect · Semi-analytical method

Introduction

Due to the ultra-low permeability in shale gas reservoir, volume fracturing technology becomes the fundamental technology to unlock shale gas from the tight formation by creating complex fracture networks within them [1, 2]. Nevertheless, during the volume fracturing process, the casing must endure the extremely high casing pressure and abrupt temperature change in the down hole. Numerous studies [3–6] have shown that the temperature-pressure coupling effect is one of the main factors resulting in casing deformation.

The effect of temperature on casing stress is obvious in modern fracturing operations and it is worth studying [7–9]. Wellbore temperature decreases for the reason of cooling induced by volume fracturing, and it brings about the problem of thermal shrinkage of the casing, changing its stress state. Some studies have shown that the effect of thermal loading caused by hydraulic fracturing in shale gas wells on casing strings was very significant [10–13], but most of them were based on the analysis of steady state heat conduction, and did not consider the coupling effect of transient temperature-pressure on casing string.

In this work, wellbore temperature field model during volume fracturing was established on the basis of engineering practice, and the effect of fracturing fluid displacement on heat transfer coefficient and friction heat of liquid were both considered in the model. The calculated variation of time-dependent wellbore temperature is input into Finite Element Model (FEM) comprised of casing-cement-formation as function parameter. Then the coupling effect of transient temperature-pressure on casing stress was calculated and analyzed by using semi-analytical method, considering the different shape of cement sheath.

Wellbore Temperature Field Model During Fracturing

Some scholars [14, 15] have calculated the casing temperature without considering the effect of displacement on heat transfer coefficient and friction heat of liquid. Both of the two factors are considered in the wellbore temperature field model established in this paper.

The following assumptions are made before the establishment of the wellbore temperature field model: ① The influence of temperature on specific heat, density, and coefficient of heat conduction is neglected. ② The fluid in casing is in a turbulent state. Therefore, there is no radial temperature gradient. ③ The heat generated by viscous dissipation of fluid can be neglected. ④ There is a linear relationship between the formation temperature and depth:

$$T_z = T_b + \alpha(z - b) \tag{1}$$

where T represents formation temperature at a certain depth (°C), T_b represents land surface temperature (°C), α represents the geothermal gradient (°C/m), z represents reservoir depth (m) and b represents the benchmark depth (m).

Based on the theorem of energy conservation, a model of the wellbore temperature field during fracturing is established. The wellbore is divided into equal parts axially and into equal parts along the wellbore wall to an infinite distance in the stratum. The conservation of energy of fluid in wellbore is calculated according to Eqs. (2) and (3):

$$\begin{aligned} &Q\rho_0 C_0 T_{0,j-1}^{n+1} - Q\rho_0 C_0 T_{0,j}^{n+1} + 2\pi r_0 \Delta H_j U\left(T_{1,j}^{n+1} - T_{0,j-\frac{1}{2}}^{n+1}\right) + W_j \\ &= \pi r_0^2 \Delta H_j \rho_0 C_0 \frac{T_{0,j-\frac{1}{2}}^{n+1} - T_{0,j-\frac{1}{2}}^{n}}{\Delta t}. \end{aligned} \tag{2}$$

$$W_j = \lambda_{fj} \frac{\Delta H_j}{r_0} \frac{\rho_0}{2} \frac{Q^3}{\pi^2 r_0^2}. \tag{3}$$

$$\frac{T_{0,j}^{n+1} - T_{0,j-1}^{n+1}}{2} = T_{0,j-\frac{1}{2}}^{n+1}$$

The conservation of energy of solid elements with a fluid foundation, and for solid elements is shown in Eqs. (4) and (5), respectively:

$$\begin{aligned} &-2\pi r_0 \Delta H_j U\left(T_{1,j}^{n+1} - T_{0,j-\frac{1}{2}}^{n+1}\right) + 2\pi r_1 \Delta H_j K_1 \frac{T_{2,j}^{n+1} - T_{1,j}^{n+1}}{\frac{r_2 - r_0}{2}} \\ &= \pi\left(r_1^2 - r_0^2\right) \Delta H_j \rho_1 C_1 \frac{T_{1,j}^{n+1} - T_{1,j}^{n}}{\Delta t}. \end{aligned} \tag{4}$$

$$\begin{aligned} &\frac{4\pi r_{i-1} \Delta H_j K_{i-1}}{r_i - r_{i-2}} T_{i-1,j}^{n+1} + \left(-\frac{4\pi r_{i-1} \Delta H_j K_{i-1}}{r_i - r_{i-2}} - \frac{4\pi r_i \Delta H_j K_i}{r_{i+1} - r_{i-1}} - \frac{\pi\left(r_i^2 - r_{i-1}^2\right) \Delta H_j \rho_i C_i}{\Delta t}\right) T_{i,j}^{n+1} \\ &+ \frac{4\pi r_i \Delta H_j K_i}{r_{i+1} - r_{i-1}} T_{i+1,j}^{n+1} = -\frac{\pi\left(r_i^2 - r_{i-1}^2\right) \Delta H_j \rho_i C_i}{\Delta t} T_{i,j}^{n+1} \end{aligned} \tag{5}$$

where, W_j represents the heat generated by friction between the fracturing fluid and casing wall (J), Q represents the displacement of fracturing fluid (m^3/min), ρ represents density (kg/m^3), C represents specific heat [J/(kg °C)], r is the radius (m), ΔH_j represents the height of the control unit body (m), U represents the convective heat transfer coefficient between the fracturing fluid and casing wall [J/(m^2 s K)] and λ_{fj} represents the casing friction coefficient (dimensionless). According to the meshing, when $i = 0$, $1 \le i < n$, $n \le i < m$, $m \le i < k$, ρ, C, K represents the

density, specific heat, and heat conductivity coefficient of fracturing fluid, casing, cement sheath, and formation. n, m, k represents mesh counts (dimensionless).

Calculation shows that the flow pattern in the wellbore is turbulent and hence the convective heat transfer coefficient of the casing wall, at different displacements, can be obtained from Eqs. (6)–(8):

$$U = \frac{S_t K_0}{2r_0} \tag{6}$$

where

$$S_t = 0.0107 Re^{0.67} Pr^{0.33} \tag{7}$$

$$Pr = \frac{\gamma C_0}{K_0} \tag{8}$$

where S_t is the Stanton number (dimensionless), Re is the Reynolds number (dimensionless), Pr represents the Prandtl number (dimensionless), γ represents apparent viscosity of the fracturing fluid (Pa s) and C_0 represents the specific heat of the fracturing fluid [J/(kg K)].

According to Eqs. (1)–(8), the fracturing fluid temperature changes can be calculated and also the temperature history of any position along the horizontal section can be expressed as functions that are used as the basic parameters in the finite element model:

$$T_l^Q = g(Q, l, t). \tag{9}$$

Numerical Simulation

Finite Element Modeling and Meshing

A 2-D computational domain of a shale gas well section comprised of casing-cement-formation is considered. The specifics of the numerical model are as follows:

- The materials are linearly elastic. This assumption is aligned with the interest to identify the likelihood of having a certain failure mode rather than rigorously modeling it. Therefore, the computational costs of modeling plastic deformation that may occur at the cement sheath and near borehole are evaded.
- To calculate the combined effects of pressure and thermal loads, the model considers multi-step thermal and mechanical analysis, as shown in Fig. 1. First, the position of casing deformation in the horizontal segment is selected as research object, and the temperature of fracturing fluid flowing through the

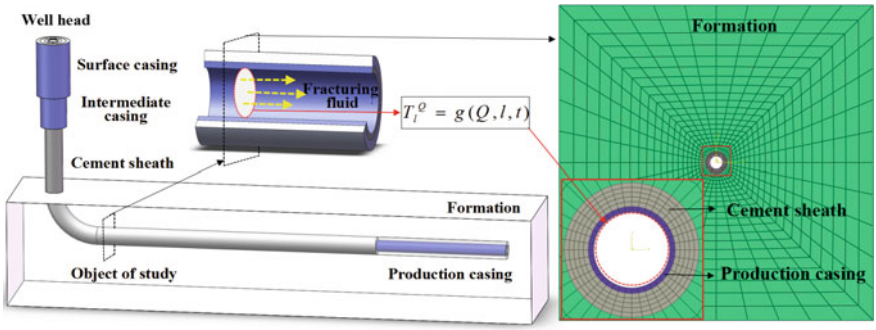

Fig. 1 Numerical model

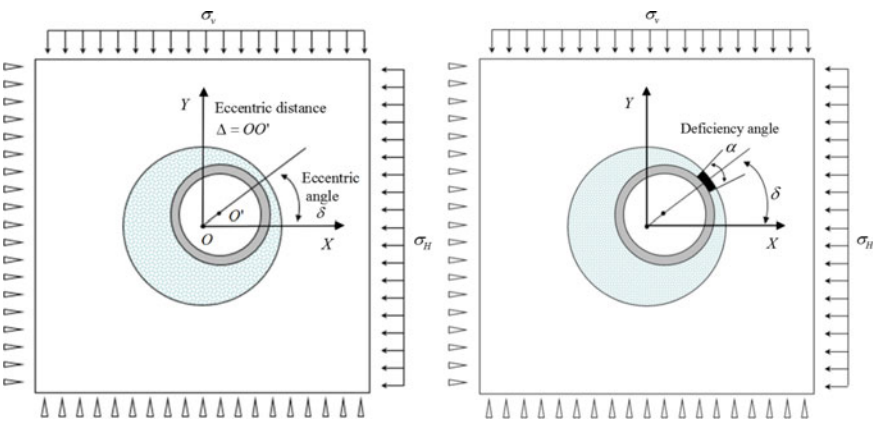

Fig. 2 Numerical model of different cement sheath shape

research object is calculated on the basis of wellbore temperature field model. Second, the variation of time-dependent temperature is input to numerical model as function parameter, then the wellbore temperature variations are calculated and the calculated temperature distribution and casing internal pressure are applied, computing the mechanical response of the well section thereafter.

- The outer edges of the formation material are fixed in displacement. Thus, the variations of in situ stresses around the borehole are only a consequence of the pressure/thermal loads applied from inside the casing. According to Saint venant theorem the formation material side length is 3 m × 3 m which is about ten times of the borehole diameter. In order to reduce the errors, while dividing the finite element net of the model, structured grid and variable density meshing method is applied at gridding drawing process.

- In order to make the conditions similar to the downhole, under the condition of coupled thermal-mechanical effect cement sheath shape is taken into account in the FEM, as shown in Fig. 2. σ_H is the maximum horizontal in situ stress, MPa; σ_v is vertical stress, MPa; Δ is eccentric distance, mm; δ is eccentric angle, °; α is deficiency angle, °.

Geometry and Mechanics Parameters

W1-h well is a shale gas horizontal well located in the west of China. The total drilled depth is 2767 m, and the horizontal segment is 1059 m. The reservoir is Longmaxi Formation, dominated by grey shale. The geothermal gradient is 3.71 °C/100 m. The maximum, minimum and vertical principal stress are 48, 29 and 35 MPa, respectively. The pumping pressure is 60 MPa and the displacement is 16 m^3/min, the duration of fracturing is 4 h. The size of horizontal segment casing is 139.70 mm × 9.17 mm, and its rigidity grade is TP95S, yield strength is 658 MPa. The geometric and mechanical parameters of casing-cement sheath-formation assembly are as shown in Table 1.

Results and Discussion

Changes of Wellbore Temperature During Volume Fracturing

For purpose of analyzing and comparing the change of wellbore temperature under different fracturing fluid displacement, the displacement of 8, 12, 20 m^3/min are selected with the comparison of W-1 h well. The initial temperature of fracturing fluid in summer and winter are 20 and 3 °C respectively.

Table 1 The geometric and mechanical parameters of casing-cement sheath-formation assembly

	Outer diameter (mm)	Modulus of elasticity (GPa)	Poisson's ratio	Coefficient of heat conduction [W (kg °C)$^{-1}$]	Specific heat [J (kg °C)$^{-1}$]	Density (kg m^{-3})	Coefficient of thermal expansion (10^{-6} °C^{-1})
Casing	139.7	210	0.3	45	461	7800	13
Cement sheath	215.9	10	0.17	0.98	837	3100	11
Formation	\	22	0.23	1.59	1256	2600	10.5

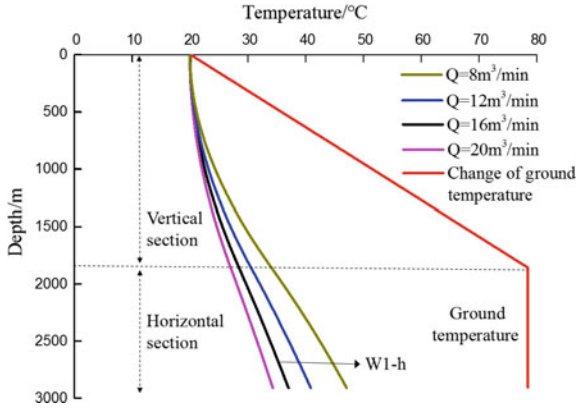

Fig. 3 Change of wellbore temperature in summer

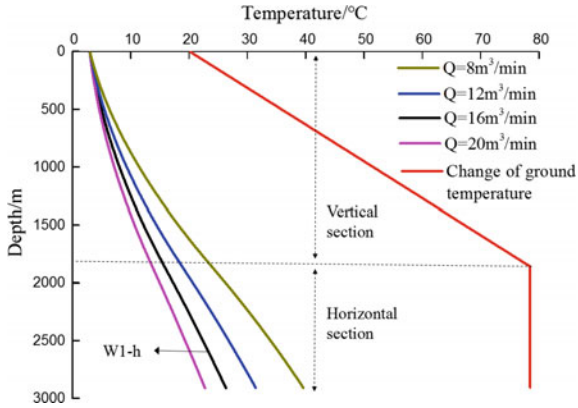

Fig. 4 Change of wellbore temperature in winter

Figure 3 shows the wellbore temperature after fracturing for 4 h under the displacement of 8, 12, 16, 20 m^3/min in summer. The drop of temperature are 44.3, 48.5, 50, 51.4 °C in the heel of horizontal segment, and 31.4, 37.7, 41.5, 44.2 °C in the toe-end. It can be known that the larger the displacement, the greater the temperature drop.

The initial temperature of fracturing fluid is one of the main factors affects the wellbore temperature. Figure 4 shows wellbore temperature after fracturing for 4 h under the different displacement in winter. The drop of temperature are 54.5, 59.6, 62.7, 64.7 °C in the heel of horizontal segment, and 38.9, 47.1, 52.2, 55.8 °C in the toe-end. By comparison of curves between Figs. 3 and 4, it can be found that the change rule in winter is similar to it in summer. At the same displacement, the lower the initial temperature of fracturing fluid, the lower the wellbore temperature in the same position of the well.

As shown in Figs. 3 and 4, the wellbore temperature in the heel of horizontal segment is significantly higher than in toe-end. Figure 5 describes transient changes

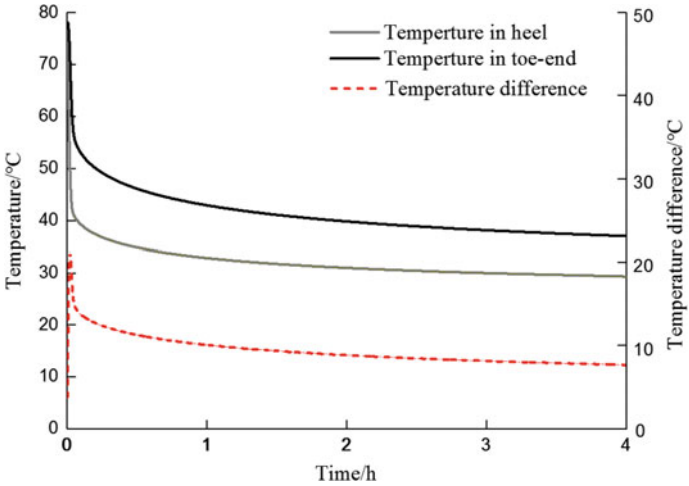

Fig. 5 Transient change of temperature in the heel and toe-end (Q = 16 m^3/min, summer)

of the wellbore temperature in heel and toe-end during volume fracturing. The initial temperature of wellbore in the two positions is equal to the reservoir temperature. At the beginning of volume fracturing, the temperature decreases fast and sharply and after some time it descends slowly. The cooling is rapid and 90% of the temperature decline occurs within the first half hour of pumping and near steady state conditions are reached within the first hour, Catherine et al. have come to the same conclusion [16].

Coupling Effect of Transient Temperature-Pressure on Casing Stress

Three casing deformation points which occurred in the horizontal segment of W1-h well during the fracturing process were selected as research objects. The positions of them are located in 1882, 2331 and 2535 m, and are named D_1, D_2, and D_3. From the above analysis, it can be known that the temperature variation functions of fracturing fluid flowing through these three positions are as follows:

$$\begin{aligned} &\mathrm{D1}: T_l^Q(D_1) = g(16,985,t), \quad 0 \le t \le 4 \\ &\mathrm{D2}: T_l^Q(D_2) = g(16,476,t), \quad 0 \le t \le 4 \\ &\mathrm{D3}: T_l^Q(D_3) = g(16,232,t), \quad 0 \le t \le 4 \end{aligned}$$

Under the Condition of Integrated Cement Sheath

Figure 6 is the imaging logging result of T1. The cement sheath in this area is integrated. Figure 7 shows the change of the maximum stress of the casing inner wall under coupled thermal-mechanical effect during volume fracturing at the position of T1. S_M represents the latter, MPa; S_{M+T} represents the former, MPa. As shown in the figure, when the coupling effect of transient temperature-pressure is not considered, casing stress keeps constant during volume fracturing, and it is 234.6 MPa. But when it is considered, for the reason that the temperature of casing/cement sheath/formation assembly continuously changes, the coupled thermal-mechanical effect on casing stress changed with time, resulting in dynamic change of casing stress. As shown in the figure, the stress increases first and then decreases continuously with continuing heat conduction. The maximum stress of casing reaches the maximum value at t_1 = 0.13 h (485 s) and it is 452.4 MPa, which increases by 92.8% compared with only considering the influence of casing internal pressure and non-uniform in situ stress.

When the coupling effect of transient temperature-pressure is considered, the distributions of casing stress of the inner wall in circumference at the time of t_1, t_2 and t_3 are compared with the stress distribution without considering this effect, as shown in Fig. 8. Without considering the coupled effect or only considering the casing internal pressure and non-uniform in situ stress, the maximum value appears in horizontal direction, and the difference between the maximum and minimums

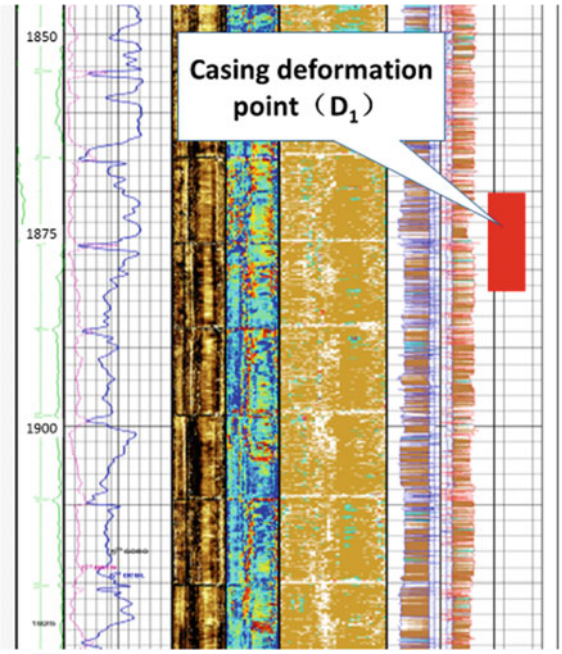

Fig. 6 Imaging logging of D_1

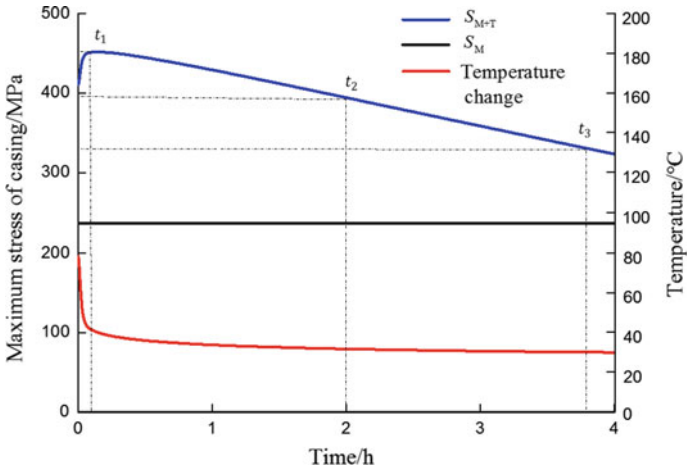

Fig. 7 Transient change of the casing maximum stress

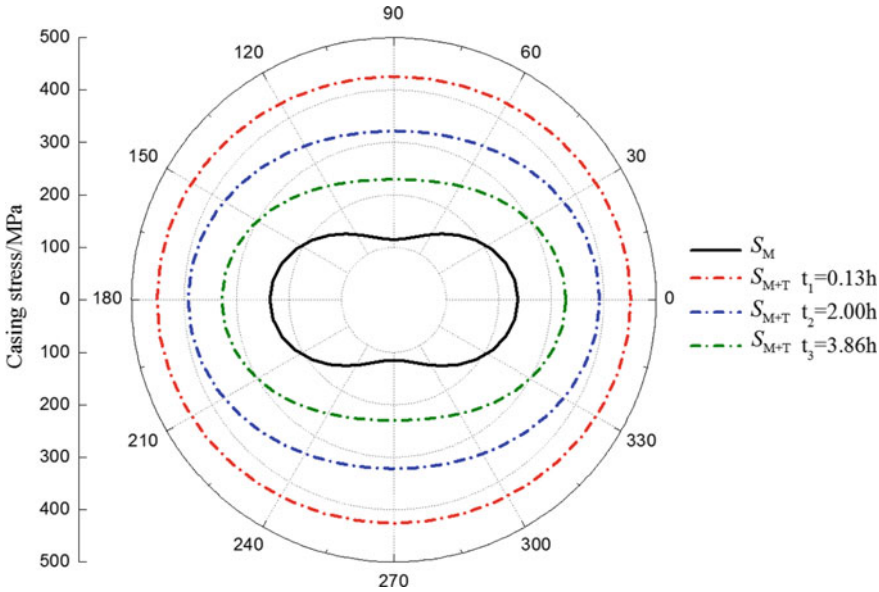

Fig. 8 Distributions of casing stress in circumference

value is obvious. When the coupled effect is taken into account, the stress increases significantly and the difference between the maximum and minimums value is smaller.

Under the Condition of Casing Eccentricity

The horizontal section of the shale gas well is relatively long, and casing strings can not always be centered. Figure 9 shows the picture of imaging logging at the position of D_3. Casing eccentricity is obvious with discontinuous channeling. According to the above analysis casing stress changes all the time under coupled thermal-mechanical effect, so the time when the casing stress is maximum ($t = t_1$) is selected.

Figure 10 shows the distribution of casing stress in circumference under the condition of casing eccentricity. S_{M+Ans} represents the distribution of casing stress in circumference under the condition of casing eccentricity, MPa; $S_{M+Ans+T}$ represents the distribution under considering casing eccentricity and the coupling effect of transient temperature-pressure. When the coupling effect is not taken into account, the maximum casing stress under the condition of casing eccentricity is higher than no casing eccentricity, but the difference between the two can be ignored. Casing stress increases significantly when the coupled thermal-mechanical effect is considered, and the rules are as follows: (1) When the eccentric angle is 0°, with the increase of the eccentric distance, the maximum stress becomes greater and (2) when the eccentric distance is 30 mm, the maximum stress decreases with the increase of the eccentric angle ($0° \leq \delta \leq 90°$).

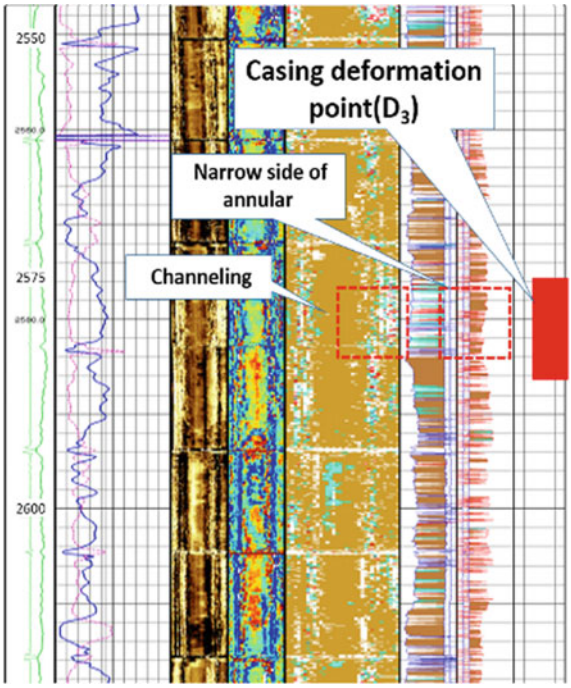

Fig. 9 Imaging logging of D_3

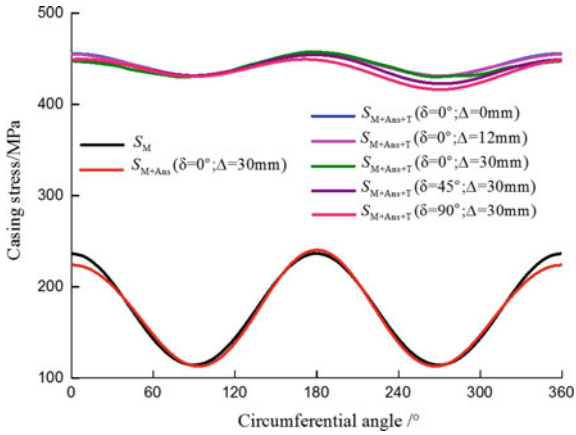

Fig. 10 Distributions of casing stress in circumference

Under the Condition of the Deficiency of Cement Sheath

Casing eccentricity leads to uneven circumferential gap, resulting in uneven circumferential velocity distribution during cementing operation, and the displacement efficiency at narrow gap decreases sharply. Also, the oil-based mud is not easy to be washed and replaced, the cement channeling which will bring about deficiency of cement sheath is likely to occur. According to the data of imaging logs, the deficiency of cement sheath occurs at the position of D_2 and coexists with casing eccentricity, as shown in Fig. 11. Moreover, due to the liquid phase material at the channeling, the change of wellbore temperature will significantly increase trapped pressure and the risk of casing deformation. In order to facilitate the calculation, the water is adopted as the substitution of the liquid phase material filled in the deficiency of the cement sheath, and the value of thermal expansion coefficient is changing with temperature.

Figure 12 shows the distribution of casing stress in circumference under the condition of the deficiency of cement sheath. S_{M+Def} represents the distribution of casing stress in circumference under the condition of the deficiency of cement sheath, MPa; $S_{M+Def+T}$ represents the distribution under considering the deficiency of cement sheath and the coupling effect of transient temperature-pressure. When the coupling effect is not considered, the casing stress increases obviously in the deficiency location of the cement sheath. When the coupling effect is taken into account, the maximum stress increases obviously and the rules are as follows: (1) when the eccentric distance is 0 mm, with the increase of the deficiency angle, the maximum stress is continuously increasing and (2) when the deficiency angle is 30°, with the increase of the eccentric distance, the maximum stress of the casing is increasing.

In conclusion, the maximum stress of casing appears at the beginning of fracturing. The increase of stress under the coupling effect of transient temperature-pressure when the cement sheath shapes are different are as shown in

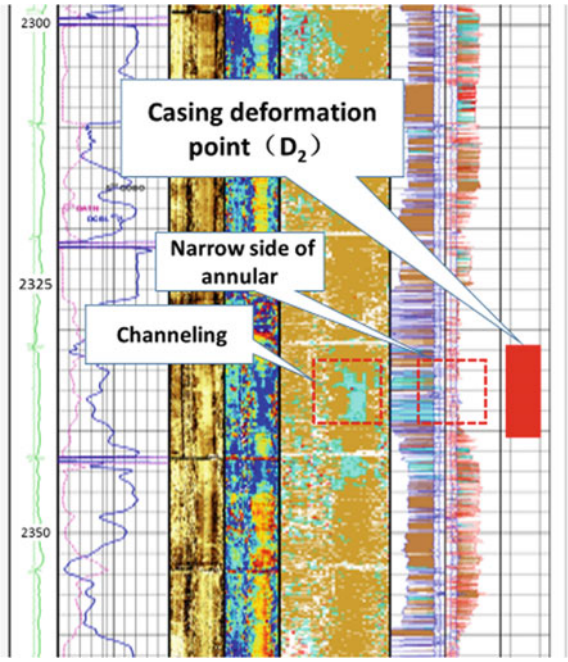

Fig. 11 Imaging logging of D_2

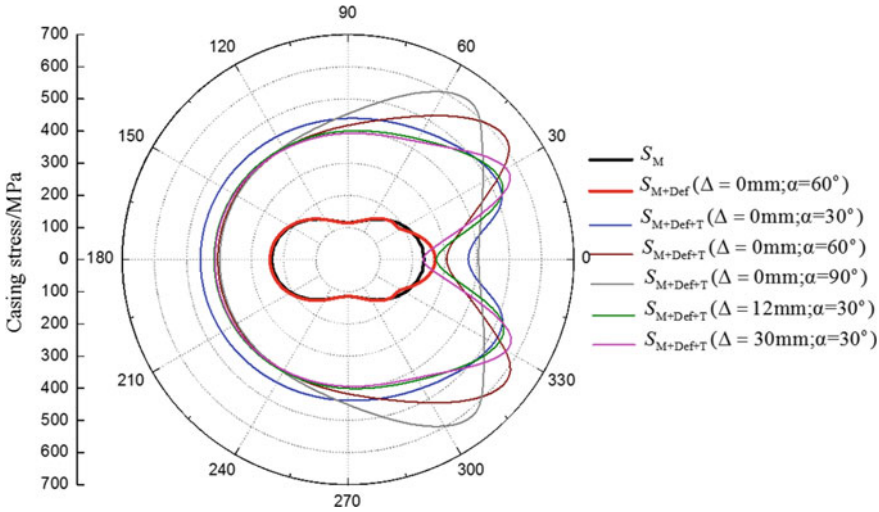

Fig. 12 Distributions of casing stress in circumference

Table 2 The comparison of results calculated between conventional and new model

	Wellbore conditions	Conventional model	New model	Rate of increase (%)
1	Integrated cement sheath	234.6	452.4	92.8
2	Δ = 30 mm; δ = 90°	245.3	465.8	89.8
3	Δ = 30 mm; δ = 30°; α = 90°	272.4	625.4	127.9

Table 2. The calculated data shows that when the cement sheath is integrated, the increase of casing stress under coupled thermal-mechanical effect is 92.8% comparing without considering it. When the eccentric angle is 30°, the deficiency angle is 90°, the growth can reach 129.5%. Casing stress is 625.4 MPa and it is close to the yield strength, greatly enhancing the risk of casing deformation.

Conclusion

The coupling effect of transient temperature-pressure on casing string during volume fracturing in shale gas wells has been studied, and the main conclusions are as follows:

(1) In the process of volume fracturing the wellbore temperature changes greatly, which is significantly related with fracturing fluid displacement and initial temperature. In the same position of the well, the greater the displacement, the greater the temperature drop; the lower the initial temperature of fracturing fluid, the lower the wellbore temperature.
(2) Under the coupling effect of transient temperature-pressure, when the cement sheath shape is integrity, the transient temperature-pressure coupling effect on casing stress is significant, casing stress first increases and then decreases, the maximum casing stress appears at the beginning of fracturing; when there is deficiency in cement sheath, with the increase of the eccentric distance or deficiency angle, casing stress increases.
(3) It is recommended that the cementing quality should be improved. Rotating the casing string at a low speed (e.g. 15–20 rpm) during cementing operation might be helpful in avoiding cement defect forming. It is also recommended to raise the temperature of the fracturing fluids on the ground to minimize the influence of temperature.

Acknowledgements The authors thank the National Natural Science Foundation "Study on optimization of un-uniform clustering perforation for long horizontal inhomogeneous shale formation" (Item No. 51674272), National Science and Technology Major Project "Optimizing technology of cluster perforation completion design in complicated structure wells" (Item No. 2017ZX05009), the Science Foundation of China University of Petroleum (Beijing) "Research on optimization method of cluster perforation parameters in anisotropy shale gas reservoirs" (Item No. 2462015QZDX05), and the State Key Laboratory of Shale Oil and Gas Enrichment Mechanisms and Effective Development "Research on casing loading spectrum under multi-factor coupling effect in shale gas wells", for contributions to this paper.

References

1. D. Zhou, P. Zhang, P. He, Peng Jiao, Hydraulic fracture propagation direction during volume fracturing in unconventional reservoirs. J. Petrol. Sci. Eng. **141**, 82–89 (2016)
2. A. Kreuzea, C. Schellya, E. Norman, To frack or not to frack: Perceptions of the risks and opportunities of high-volume hydraulic fracturing in the United States. Energy Res. Soc. Sci. **20**, 45–54 (2016)
3. A.A. Daneshy, Impact of off-balance fracturing on borehole stability & casing failure, in *Presented at the 2005 SPE Western Regional Meeting held in Irvine, CA., U.S.A.,* 30 Mar–1 Apr (2005)
4. G.S. Kaldal, M.T. Jonsson, H. Palsson, S.N. Karlsdottir, Structural modeling of the casings in high temperature geothermal wells. Geothermics **55**, 126–137 (2015)
5. W. Wang, H. Zhang, P. Liu, Z. Li, W. Ni, H. Uechi, T. Matsumura, A finite element method approach to the temperature distribution in the inner casing of a steam turbine in a combined cycle power plant. Appl. Therm. Eng. **105**, 18–27 (2016)
6. Z. Bo, Z. Guan, A.R. Hasan, N. Lu, Q. Wang, Y. Xu, Z. Qi, Y. Liu, Development and design of new casing to mitigate trapped annular pressure caused by thermal expansion in oil and gas wells. Appl. Thermal Eng. **118**, 292–298 (2017)
7. J.A. Wheeler, Analytical calculations of heat transfer from fractures, in *Presented at the Improved Oil Recovery Symposium held in Tulsa*, Apr 12–13 (1962)
8. M.A. Biot, L. Masse, W.L. Medlin, Temperature analysis in hydraulic fracturing. J. Petrol. Technol. **27**, 1389–1397 (1987)
9. C.E. Cohen, X. Weng, O. Kresse, Influence of fracturing fluid and reservoir temperature on production complex hydraulic fracture network in shale gas reservoir, in *Presented at the SPE Unconventional Resources Conference and Exhibition-Asia Pacific held in Brisbane, Australia*, Nov 11–13 (2013)
10. W. Yan, L. Zou, H. Li, J. Deng, H. Ge, H. Wang, Investigation of casing deformation during hydraulic fracturing in high geo-stress shale gas play. J. Petrol. Sci. Eng. **150**, 22–29 (2017)
11. Y. Hu, Y. Zhang, A quantitative evaluation method for the effect of temperature on casing collapsing strength: a case study of lagge scale hydraulic fracturing in shale gas horizonal wells. J. Nat. Gas Sci. Eng. **36**, 73–77 (2016)
12. Y. Xi, J. Li, G. Liu, Y. Fu, Y. Li, Sensitivity study of shale reservoir anisotropy on casing stress. Spec. Oil Gas Reservoir **23**, 128–132 (2016)

13. K. Jiang, Q. Lian, Y. Chen, G.X. Fu, Y. Li Jun, Influence of cementing quality on casing failures in horizontal shale gas wells. J. Nat. Gas Sci. Eng. **35**, 77–82 (2015)
14. W. Dong, R. Shen, Q. Liang, H. Zhang, D. Yu, Calculation and analysis of casing thermal stress during stimulated reservoir volume fracturing. Fault Block Oil Gas Field **23**, 673–675 (2016)
15. Z. Tian, L. Shi, L. Qiao, Research of and countermeasure for wellbore integrity of shale gas horizontal well. Nat. Gas. Ind. **35**, 70–77 (2015)
16. C. Sugden, J. Johnson, M. Chambers, G. Ring, P.V. Suryanarayana, Special considerations in the design optimization of high rate, multistage fractured shale wells, in *IADC/SPE Presented at the 2012 IADC/SPE Drilling Conference and Exhibition, San Diego, California, USA*, March 6–8 (2012)

Application of Titanium Alloy Tubing in HPHT Gas Wells to Reduce Vibration and Buckling

Qiang Zhang, Zhanghua Lian, Taihe Shi and Yisheng Mou

Abstract Tubing string vibration and buckling are primary causes of tubing string failure, sustained casing pressure and production casing wear in HPHT gas wells. In order to obtain an improved understanding of tubing string vibration and buckling, finite element analysis is carried out in this paper. Typical tubing string failures in HPHT gas wells are analyzed, and fracture surfaces are tested. The vibration and buckling characteristics of original nickel-base alloy tubing string and modified tubing string with Titanium alloy tubing are calculated and compared. The results indicate that the application of Titanium alloy tubing can effectively reduce tubing string vibration and buckling. Titanium alloy tubing has lower elasticity modulus, so it transforms more energy into deformation energy rather displacement energy. Therefore, it is concluded that Titanium alloy tubing can effectively reduce tubing axial vibration displacement, so as to prevent tubing fatigue and thread looseness. Original tubing string has contacted with the wellbore under sinusoidal buckling. The sinusoidal buckling of modified tubing string is much slighter and tubing doesn't contact with the wellbore. The work presented in this paper can provide a technological basis for the reduction of tubing string vibration and buckling, as well as application of Titanium alloy tubing.

Keywords Tubing string vibration · Tubing string buckling · Titanium alloy tubing · HPHT gas well · Fluid-structure coupling vibration

Q. Zhang (✉) · Z. Lian · T. Shi · Y. Mou
State Key Laboratory of Oil and Gas Reservoir Geology and Exploitation, Southwest Petroleum University, Chengdu 610500, China
e-mail: zhangqiang_a301@163.com

Z. Lian
e-mail: milsu1964@163.com

T. Shi
e-mail: taiheshi@126.com

Y. Mou
e-mail: 479824223@qq.com

© Springer Nature Singapore Pte Ltd. 2018

Y. Han (ed.), *Advances in Materials Processing*, Lecture Notes in Mechanical Engineering, https://doi.org/10.1007/978-981-13-0107-0_96

Introduction

In the production process of HPHT (high-pressure, high-temperature) gas wells, sudden fluctuation of production rate and pressure as well as change of flow channel will induce fluid-structure coupling vibration of tubing string [1]. Moreover, packer-to-tubing compression force caused by change of downhole temperature and pressure will lead to tubing buckling above packer location. Tubing string vibration and buckling in HPHT gas wells can result in fatigue failure, thread looseness, and connection wear [2, 3]. Therefore, it is urgent to resolve these problems and assure safe working conditions for tubing string.

There is currently significant interest in Titanium alloys as a new class of materials for downhole tubular and components [4]. The Young's modulus and thermal expansion coefficient of Titanium are smaller, compared to nickel-based alloys. As a result, the minimum yield strength of Titanium will not be exceeded during different conditions [5]. Moreover, Titanium alloy tubing has shown good resistance to stress corrosion cracking and environmental sensitive fracture during fracturing, production and other conditions. In China, the first Titanium alloy tubing was used in Yuanba high sour gas well. Titanium shows a good fulfillment to the requirement of corrosion resistance, mechanical property and sealing property.

Fluid-structure coupling vibration of tubing string has attracted many investigators to conduct physical or numerical modeling. Huang [6] put forward an opinion that the vibration of tubing string will influence service life. Adnan [7] addressed the VIV (Vortex induced vibration) that could occur to tubing and piping with non-linear geometry. Deng [8] analyzed the mechanism of tubing string vibration in high production gas wells. The excitation force of natural gas was obtained and dynamical analysis of tubing vibration was also conducted.

In the last 20 years, researches on tubing buckling have been conducted from various perspectives. Lubinski and Althouse [9] developed the first commonly used theory for tubing buckling analysis. The theory has been applied in many other areas. Dawson and Paslay [10] established a mathematical model to calculate the critical condition of lateral buckling of tubing string. The research has pushed forward the advancement of tubing buckling analysis. Chen et al. [11] went a step further and studied the helical buckling condition in deviated wells. Mitchell [12–14] considered the contact of tubing and casing, and used the beam-column equations to calculate tubing buckling.

Despite these studies, to the best of our knowledge, studies focusing on vibration and buckling of Titanium alloy tubing are not adequate. In this paper, the vibration and buckling characteristics of original nickel-base alloy tubing string and modified tubing string with Titanium alloy tubing are calculated and compared.

Tubing String Failure Analysis

According to Schlumberger, HPHT gas wells are categorized as gas wells with bottom hole pressure more than 70 MPa and bottom hole temperature more than 150 °C. Service condition of tubing string is extremely harsh in HPHT gas wells and tubing string failures happens frequently.

Figure 1 shows a typical fracture morphology and fluorescent detection of tubing string. Tubing string fracture happens at the depth of 4810 m. Fluorescent magnetic particle flaw detection fins that numerous longitudinal cracks exist at the outer wall of tubing. Corrosion pits distribute intensively at the outer wall of tubing. Back to the working condition of tubing string, it is found that pressure supplement and relief operations are conducted frequently, leading to alternating stress on tubing string. Therefore, the fracture of tubing results from corrosion and alternating stress.

Figure 2 shows a failure morphology of tubing string. Tubing string fracture happens at the depth of 1681 m. Corrosion pits distribute intensively at the outer wall of tubing near pin thread. Micro-cracks are generated at some corrosion pits and crack propagation finally leads to tubing fracture.

Fig. 1 Fracture morphology and fluorescent detection of tubing string

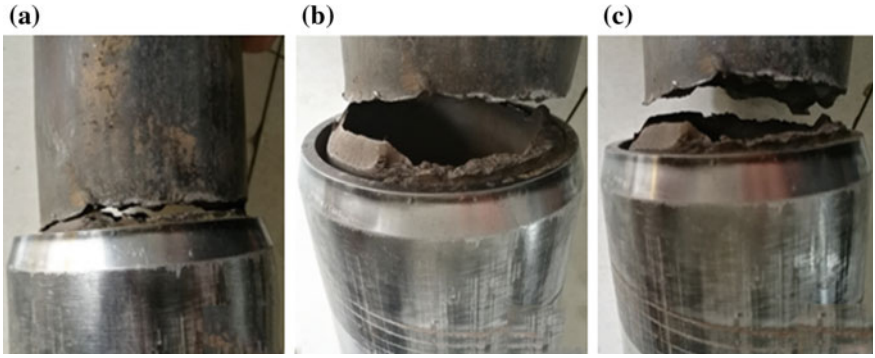

Fig. 2 Failure morphology of tubing string

Fluid-Structure Coupling Vibration of Tubing String

Fluid-Structure Coupling Vibration Model

When flow parameters of natural gas in tubing string are uniform at the same flow section don't change with time, tubing string vibration will not happen. However, in actual field condition, production parameters (including production rate, pressure and temperature) will change, the flow of natural gas belongs to one-dimensional unsteady flow. The formation of transient pressure and pressure wave propagation will induce fluid-structure coupling vibration, during the transformation of fluctuation energy to mechanical vibration energy.

A physical model of tubing string with both ends fixed is shown in Fig. 3. The outer diameter is d_o, inner diameter is d_i and tubing string length is l. Tubing string is fully constrained at packer location (point A) and wellhead (point B). According to Hamilton principle [15], Eq. (1) can be obtained.

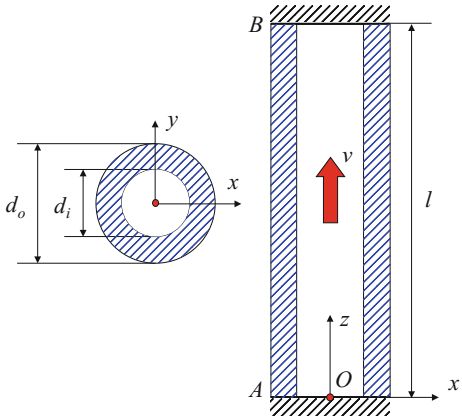

Fig. 3 Fluid-structure coupling vibration model of tubing string

$$\int_{t_1}^{t_2} \delta(T - V)\mathrm{d}t + \int_{t_1}^{t_2} \delta W \mathrm{d}t = 0, \tag{1}$$

where, T is kinetic energy of tubing element; V is potential energy of tubing element; δW is the done by non-conservative force on the virtual displacement.

With high flow velocity, the effect of Coriolis force and centrifugal force on tubing vibration is significant. We ignore the effect of gravity and structural damping, and obtain the differential equations of three-dimensional tubing vibration induced by axial gas flow [16]:

$$EA\frac{\partial^2 u_z}{\partial z^2} + c_1\frac{\partial u_z}{\partial z} + \left(m_p + m_f\right)\frac{\partial^2 u_z}{\partial t^2} = 0, \tag{2}$$

$$EI\frac{\partial^4 u_y}{\partial z^4} + c_1\frac{\partial u_y}{\partial z} + \left(Ap + m_f v^2\right)\frac{\partial^2 u_y}{\partial xz^2} + 2m_f\frac{\partial^2 u_y}{\partial z\partial t} + \left(m_p + m_f\right)\frac{\partial^2 u_y}{\partial t^2} = 0, \tag{3}$$

$$EI\frac{\partial^4 u_x}{\partial z^4} + c_1\frac{\partial u_x}{\partial z} + \left(Ap + m_f v^2\right)\frac{\partial^2 u_x}{\partial z^2} + 2m_f\frac{\partial^2 u_x}{\partial z\partial t} + \left(m_p + m_f\right)\frac{\partial^2 u_x}{\partial t^2} = 0, \tag{4}$$

where, E is elasticity modulus of tubing; A is cross-sectional area of tubing; I is inertia moment of tubing; u_x, u_y and u_z are tubing displacement at x, y and z direction respectively; m_p is tubing mass per unit length; m_f is gas mass per unit length; v is gas flow velocity; p is gas pressure.

Equation (2) is the differential equation of axial tubing vibration, while Eqs. (3) and (4) are the differential equations of lateral tubing vibration.

One-dimensional unsteady flow equations of natural gas is expressed as [17]:

$$\left.\begin{array}{c} \frac{\partial(\rho v)}{\partial t} + \frac{\partial\left(\rho v^2\right)}{\partial z} + \frac{\partial p}{\partial z} + \rho g + \rho\frac{\lambda}{d_i}\frac{v^2}{2} = 0 \\ \frac{\partial \rho}{\partial t} + \frac{\partial(\rho v)}{\partial z} = 0 \\ p = Z\rho RT \end{array}\right\} \tag{5}$$

where, ρ is density of natural gas; λ is coefficient of friction resistance; d_i is inner diameter of tubing; Z is compressibility factor of natural gas; R is perfect gas constant; T is temperature.

To understand the vibration of downhole tubing string, Eqs. (1)–(5) must be combined. However, the change of gas flow rate is rapid, let alone the complicated tubing string structure in HPHT gas wells, it is difficult to obtain accurate vibration characteristics of tubing string via analytic method. Therefore, this paper uses finite element method to study fluid-structure coupling vibration of tubing string in HPHT gas wells.

Finite Element Simulation

According to the details of tubing string structure of KeS8-5 well (Table 1), this paper establishes a finite element model for fluid-structure coupling vibration, as shown in Fig. 4. Tubing string is fixed at both ends, fully constrained at packer location and wellhead. After packer setting, there will be a packer-to-tubing force due to downhole pressure and temperature change. If packer-to-tubing force is an axial compressive force for tubing, there exists a "neutral point" inside tubing string. Tubing above neutral point is under tension, with the largest tension at wellhead; tubing below neutral point is under compression, with the largest compression at packer location.

In static analysis, the forces on tubing mainly include: tension Fwh at wellhead (point A), compression Fb at packer location (point B), buoyant weight W and fluid pressure inside and outside tubing. The studied production rate is 50E4 m^3/d, where oil pressure is 95 MPa, casing pressure is 0, fluid density outside tubing is 1.4 g/cm^3, and bottom hole temperature is 158 °C.

Excessive bottom compression may cause buckling and instability of tubing above packer location. Vibration of buckled tubing will cause impact with production casing, which aggravates fatigue failure, thread looseness and connection wear. Therefore, to reduce bottom compression of tubing is of great significance for the prevention of tubing buckling and vibration. The use of Titanium alloy tubing can effectively reduce bottom compression because of low density, elasticity modulus, as well as thermal expansion coefficient.

This paper studies the vibration characteristics of original tubing string structure (Table 2) and modified tubing string structure (replacing the last 2000 m tubing with Titanium alloy tubing of the same grade). The comparison of vibration mode of two tubing string structures is shown in Fig. 5. Lateral displacements of the first three order is relatively small, within ±10 mm. With lower elasticity modulus, the deformation of Titanium alloy tubing is larger under the same load level. Therefore,

Table 1 Details of tubing string structure

Outer diameter (mm)	Thickness (mm)	Depth (m)	Material and steel grade	Weight (kg/m)	Burst strength (MPa)	Collapse strength (MPa)
114.3	12.7	700	S13Cr110	32	147.5	149.8
114.3	9.65	1500	S13Cr110	25.3	112.1	117.3
114.3	8.56	2100	S13Cr110	22.32	99.4	98.9
88.9	9.52	2700	S13Cr110	18.9	142.2	145.1
88.9	7.34	3300	S13Cr110	15.18	109.6	114.9
88.9	6.45	6250	S13Cr110	13.69	96.3	93.3
Packer		6250	–	–	109.35	103.42
73.02	7.01	6800	S13Cr110	11.611	127.4	131.6

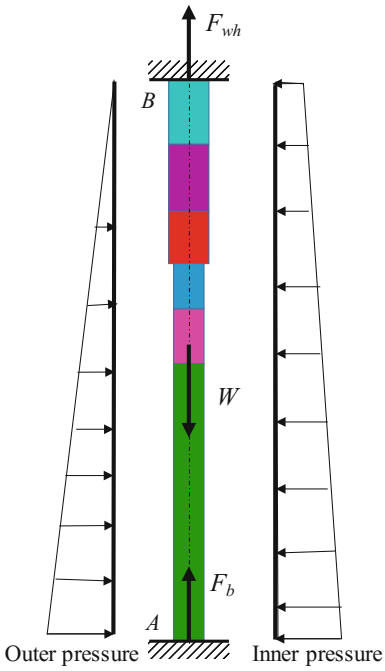

Fig. 4 Finite element model for fluid-structure coupling vibration

Table 2 Tubing material characteristics

Tubing material	Elasticity modulus (MPa)	Poisson's ratio	Thermal expansion coefficient (°C^{-1})	Density (kg/m^3)
S13Cr110	2.10e5	0.3	1.2e−5	7855
Titanium alloy	1.07e5	0.34	0.9e−5	4420

lateral displacement of modified tubing string at Titanium alloy tubing is larger than that of original tubing string.

The comparison of axial displacement of two tubing string structures is shown in Fig. 6. The maximum axial displacement of original tubing string is 2.2 m, while the maximum axial displacement of modified tubing string is 1.5 m. Titanium alloy tubing has lower elasticity modulus, so it transforms more energy into deformation energy rather displacement energy. Therefore, it is concluded that Titanium alloy tubing can effectively reduce tubing axial vibration displacement, so as to prevent tubing fatigue and thread looseness.

Tubing string vibration will change axial force distribution as well as neutral point location. The comparison of axial force distribution of two tubing string

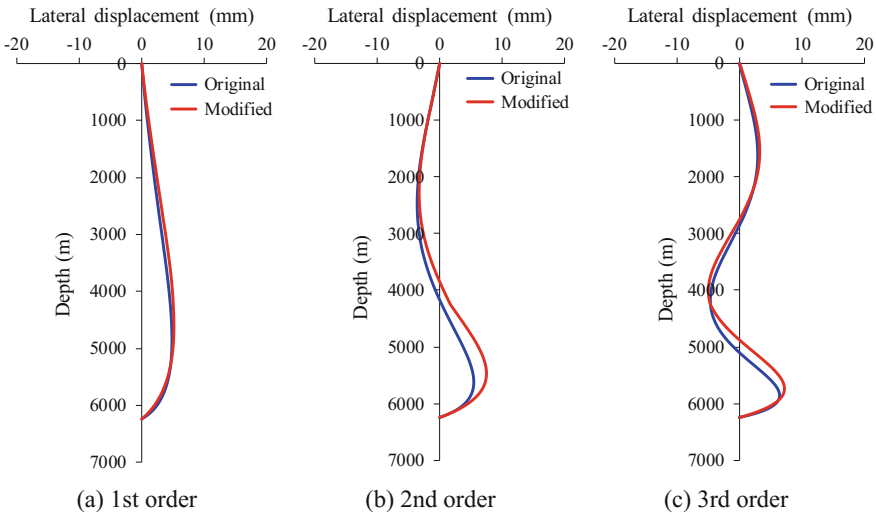

Fig. 5 Comparison of vibration mode

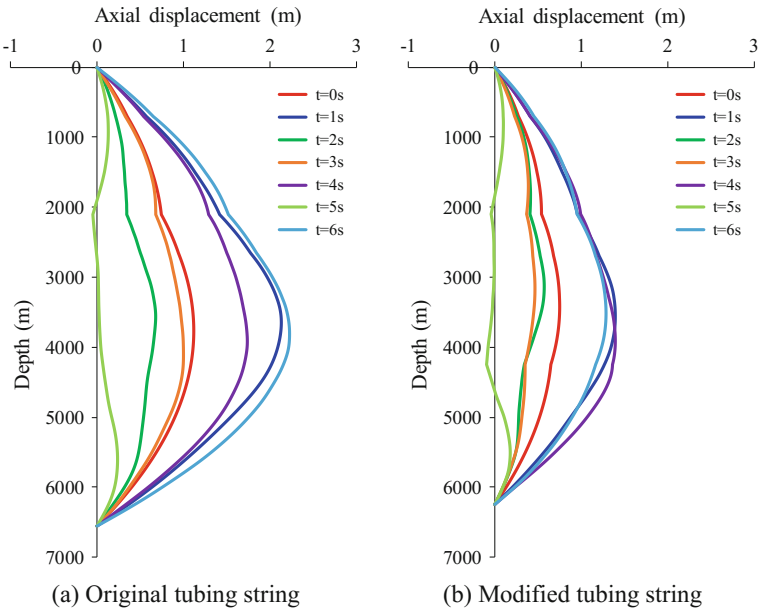

Fig. 6 Comparison of axial displacement

structures is shown in Fig. 7. Neutral point of original tubing string varies from 4228 to 6418 m, while neutral point of modified tubing string varies from 4692 to 6164 m.

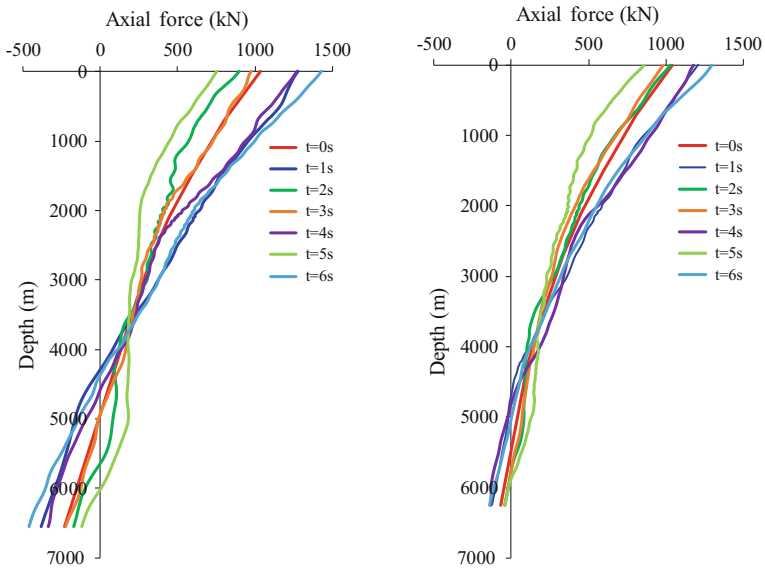

(a) Original tubing string (b) Modified tubing string

Fig. 7 Comparison of axial force

Buckling Analysis of Tubing String

Tubing String Buckling Model

Tubing buckling analysis is an important part of tubing design and wellbore integrity. Since Lubinski's analysis of tubing buckling, Hammerlindl [18–20] applied tubing buckling theory to other problems. This paper establishes a mathematical model to analyze tubing string buckling. The established mechanical model are shown in Fig. 8.

The geometry of the helix (see Fig. 8) is described by the equations.

$$u_1 = r\cos\theta, \tag{6}$$

$$u_2 = r\sin\theta, \tag{7}$$

$$\theta = \frac{2\pi z}{P}, \tag{8}$$

where r is the radial clearance of tubing and casing; u_1 and u_2 are tubing centerline locations in x and y directions, respectively; θ is angular coordinate; P is helix pitch.

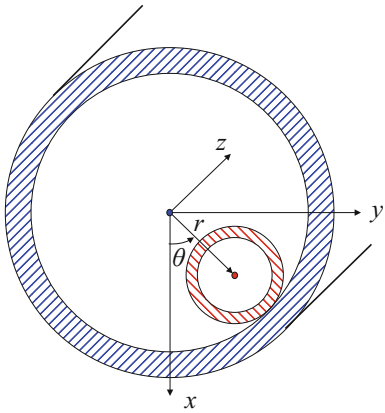

Fig. 8 Tubing string buckling model

The following equation indicates the principle of virtual work relates P to F_f:

$$P^2 = \frac{8\pi^2 EI}{F_f}. \tag{9}$$

The differential equation of tubular-string buckling is expressed by (Mitchell [13]):

$$\frac{\mathrm{d}^4\theta}{\mathrm{d}z^4} + \left[\frac{F}{EI} - 6\left(\frac{\mathrm{d}\theta}{\mathrm{d}z}\right)^2\right]\frac{\mathrm{d}^2\theta}{\mathrm{d}z^2} = 0. \tag{10}$$

Assuming that the full helical-buckling configuration is $\theta = \omega \cdot z$, Eq. (10) is transformed into

$$2\omega^3 - \frac{F}{EI}\omega + C_0 = 0. \tag{11}$$

When $C_0 = 0$ is satisfied, the buckling solution from Eq. (11) is expressed by

$$\theta = \pm\sqrt{\frac{F}{2EI}}z \tag{12}$$

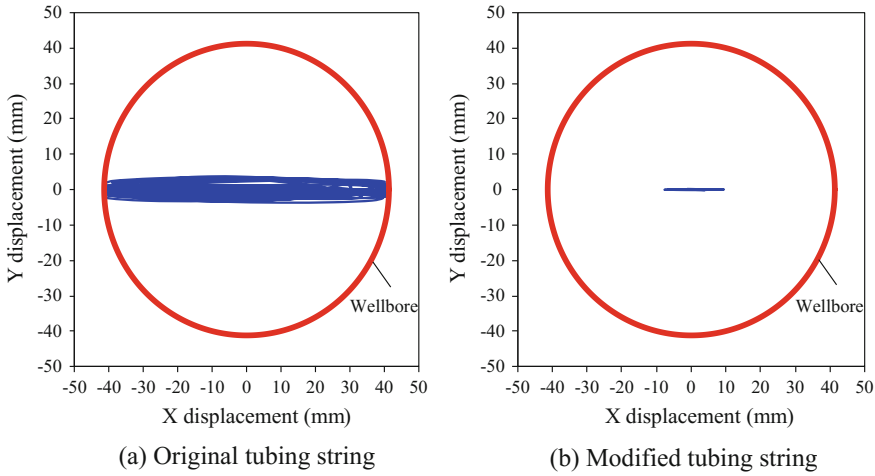

Fig. 9 Projection drawing of buckled tubing shape

Fig. 10 Contact force distribution

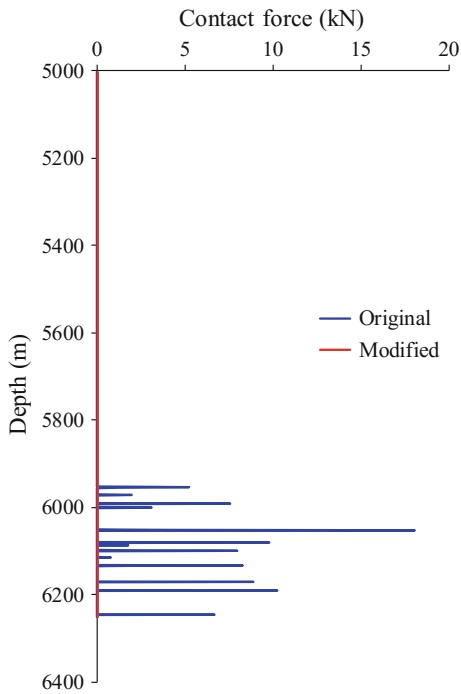

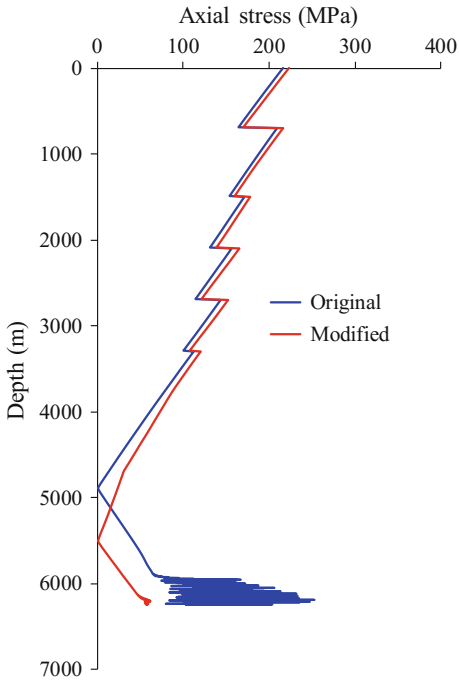

Fig. 11 Axial stress distribution

Finite Element Simulation

Based on the finite element model established in Fig. 4, this paper carries out simulation on tubing buckling for two different tubing string structures. The projection drawing of buckled tubing shape is shown in Fig. 9. The annulus clearance between bottom tubing and casing inner wall is 41.275 mm. Original tubing string has contacted with the wellbore under sinusoidal buckling. The sinusoidal buckling of modified tubing string is much slighter and tubing doesn't contact with the wellbore.

Figure 10 shows the distribution of contact fore for the two different tubing string structures. Modified tubing string doesn't contact with the wellbore, so its contact force remains zero along well depth. Original tubing string contacts with the wellbore and the maximum contact force reaches up to 18 kN.

Figure 11 shows the distribution of axial stress for the two different tubing string structures. The distribution of axial stress changes suddenly when tubing cross-sectional area changes. Axial stress of original tubing string fluctuates a lot in the buckling section and the mean valve is larger than that of modified tubing string. Therefore, tubing buckling will add axial stress and form a more dangerous working condition for tubing string. Titanium alloy tubing can effectively reduce tubing buckling and improve working condition of tubing string.

Conclusions

Typical tubing string failures in HPHT gas wells are analyzed, and fracture surfaces are tested. Vibration and buckling characteristics of original nickel-base alloy tubing string and modified tubing string with Titanium alloy tubing are studied systematically in this paper, based on finite element simulation. Comparison indicates that the application of Titanium alloy tubing can effectively reduce tubing string vibration and buckling. The Young's modulus and thermal expansion coefficient of Titanium are smaller, compared to nickel-based alloys. As a result Titanium alloy tubing transforms more energy into deformation energy rather displacement energy. Therefore, it is concluded that Titanium alloy tubing can effectively reduce tubing axial vibration displacement, so as to prevent tubing fatigue and thread looseness. Original tubing string has contacted with the wellbore under sinusoidal buckling. The sinusoidal buckling of modified tubing string is much slighter and tubing doesn't contact with the wellbore.

Acknowledgements This research was made possible by financial support from National Natural Science Foundation of China (No. 51574198).

References

1. Q. Ju, S. Tong, Longitudinal vibration characteristics analysis of completion tubing string in high gas rate well. Drilling Prod. Technol. **37**(2), 79–82 (2014)
2. M. Yang, H. Li, R. Jiang, et al., Research on vibration damage of completion string in Yolotan high-yield gas well. J. Southwest Petrol. Univ. (Sci. Technol. Ed.) **38**(1), 158–163 (2016)
3. Y. Dou, L. Wang, J. Liu, Safety analysis of completion tubing considering the vibration during wll startup or shutdown. Oil Field Equip. **44**(10), 11–15 (2015)
4. R.D. Kane, S. Craig, A. Venkatesh, *Titanium alloys for oil and gas service: a review*. NACE Conference Paper (2009)
5. B. Hargrave, M. Gonzalez, K. Maskos, et al., *Titanium alloy tubing for HPHT OCTG applications*. NACE Conference Paper (2010)
6. Z. Huang, The research of vibration mechanism and analysis of dynamic response for tubing string. Southwest Petrol. Univ. (2005)
7. S. Adnan, Y.C. Chen, P. Chen, Vortex-induced vibration of tubings and pipings with nonlinear geometry (SPE 100173, 2006)
8. Y. Deng, Tubing string vibration mechanism analysis and fatigue life prediction in high production gas well. Southwest Petrol. Univ. (2006)
9. A. Lubinski, W.S. Althouse, Helical buckling of tubing sealed in packers. J. Petrol. Technol. **14**(6), 655–670 (1962)
10. R. Dawson, P.R. Paslay, Drill pipe buckling in inclined holes. J. Petrol. Technol. **36**(11), 1734–1738 (1984)
11. Y.C. Chen, Y.H. Lin, J.B. Cheatham, Tubing and casing buckling in horizontal well (SPE 19176, 1990)
12. R.F. Mitchell, Effects of well deviation on helical buckling (SPE 29462, 1997)
13. R.F. Mitchell, New concepts for helical buckling (SPE 15470, 1988)
14. R.F. Mitchell, Helical buckling of pipe with connectors in vertical wells (SPE 65098, 2000)

15. A.K. Kohli, B.C. Nakra, Vibration analysis of straight and curved tubes conveying fluid by means of straight beam finite elements. J. Sound Vib. **93**, 307–311 (1984)
16. Y. Yao, Analysis of fluid-filled pipe dynamic modeling and vibration characteristic (Shanghai Jiao Tong University, 2011)
17. C. Li, Y. Wang, Y. Wang, Analysis of the vibration in gas pipeline system. Nat. Gas. Ind. **20** (2), 80–83 (2000)
18. D.J. Harnmerlindl, Movement, forces, and stresses associated with combination tubing strings sealed in packers (SPE 5143, 1977)
19. D.J. Harnmerlindl, Basic fluid and pressure forces on oil well tubulars (SPE 7594, 1980)
20. D.J. Hammerlindl, Packer-to-tubing forces for intermediate packers (SPE 7552, 1980)

Stress Analysis of Tubing Thread of the Gas Seal Test in Deep Gas Well

Yisheng Mou, Zhanghua Lian, Qiang Zhang and Taihe Shi

Abstract Seal test of tubing thread in high pressure gas well is a new technology currently, but there is no uniform standard regarding the accurate sealing test pressure, frequently improper sealing test pressure can easily lead to damage and fatigue failure of tubing threads. In order to solve the above problems, in this paper the axisymmetric finite element mechanical model of the BEAR threads based on the theory of elastic-plastic mechanics was established, and the finite element software used to calculate the results. The results showed that when the test pressure was equal to 100 and 50% of the RIP (Resistance to internal pressure) of tubing, the plastic deformation of the tubing thread occurred, and the plastic deformation area generated in the roots of the last three buckle, when the test pressure was equal to 25% of the RIP of the tubing, the maximum stress of all types of tubing threads was less than the yield strength. Based on this model, the stress of the tubing thread of the high-pressure gas well can be quantitatively and fully evaluated, and the gas seal test technology can be provided with theoretical reference.

Keywords Gas seal test · Deep gas well · Tubing thread · Finite element analysis

Y. Mou (✉) · Z. Lian · Q. Zhang · T. Shi
State Key Laboratory of Oil and Gas Reservoir Geology and Exploitation, Southwest Petroleum University, Chengdu 610500, Sichuan, China
e-mail: 479824223@qq.com

Z. Lian
e-mail: 2090908592@qq.com

Q. Zhang
e-mail: zqiang1110@foxmail.com

T. Shi
e-mail: 1043050179@qq.com

© Springer Nature Singapore Pte Ltd. 2018

Y. Han (ed.), *Advances in Materials Processing*, Lecture Notes in Mechanical Engineering, https://doi.org/10.1007/978-981-13-0107-0_97

Introduction

At present, with the increasing of oil and gas reservoir development, the difficult oil well is rapidly developed and put into production, such as the "three ultra" oil and gas well (ultra-high temperature and ultra-high pressure and ultra-deep well). So the working conditions are very harsh [1]. The study found that the tubing string's position of leaking and even breaking mostly at the thread of the tubing connections. Thus it can be seen that the joint thread is the easy failure position of the tubing string, so the joint thread is an important research object to ensure downhole production safety and wellbore integrity.

In the light of the research methods of tubing thread joint, scholars at home and abroad have made corresponding research, mainly divided into three research methods: Analytic method, experimental method and finite element method. In terms of analytic methods, based on the stress characteristics of thread, Wang and Peng [2] and others in China have deduced the analytical formula of hoop stress and radial stress. Foreign Yoshihiro, Tsuru and others [3–5], deduced the contact pressure calculation formula and the calculation formula of the joint thread force. In the study of experimental methods. Dou, Wang, and others [6, 7] pointed out the static load to evaluate the detection performance of thread. Mao Dongfeng, Li Xuchun used dynamic load to evaluate the detection performance of thread. However, the analytical method and the experimental method has its limitations, the premise is to calculate all of the deformation are in the range of elastic deformation, simple calculation; experimental method is difficult to accurately study in the thread in the stress exceeds the allowed stress strain after stress. With the development of the finite element theory, the method has been widely used to study the structural problems of threaded joints. In 1994, Gao, Zhang [8, 9] and others studied the anti-leakage performance of the threaded joint by the finite element method. In 2000, Wang [10] and others studied the force of casing thread based on the finite element method and elastic-plastic theory. In 2016, Lian et al. [11] through the finite element method of fatigue fracture analysis of various types of thread. Foreign Pai, Hess and others [12–14] and others use three-dimensional finite element to analyze the fatigue problems of threaded joints, and a large amount of stress analysis has been done on the safety service of the thread.

The domestic and foreign scholars have acquired some classical formulas and rules, which has important significance to study the thread, but gas seal test technology as a new technology, both at home and abroad for the research is used very few. Because of the lack of theoretical support, the field detection of test pressure often be used improperly. To solve the above problems, based on the elastic-plastic mechanics and finite element theory, an axisymmetric finite element model of Bear thread is established, which are used to calculate the thread internal stress distribution. Finally, a scientific basis and reference for the follow-up of the safety assessment of gas seal and thread detection connector are provided.

Results and Discussion

Failure Analysis of Threaded Joint

Case Analysis

Under the work-over operation of an ultra-deep gas well in an oilfield, two cases of lateral fracture of tubing occurred. The tubing size of the fracture location is 3-1/2″× wall thickness is 6.45 mm, and the fracture tubing is shown in the figure (refer with: Fig. 1). It is concluded that the fracture location is brought about by stress corrosion cracking, and the initial crack occurs in outside of tubing thread.

According to the analysis of site conditions: during the testing process, the tubing under high internal pressure, at the same time, the lower part of the tubing under tubing gravity is large, which may cause damage to the tubing, so gas seal test can also be used as a mechanism of tubing failure. The theory of elastic-plastic mechanics and the finite element method is used to analyze the stress distribution in the tubing thread of gas seal test in this paper. The relevant rules are obtained, which could provide the reference and basis for the gas seal test in the future.

Von Mises Yield Criterion

The object of this study is the internal stress of the thread when the seal is tested, the radial deformation of tubing thread is emphatically analyzed, according to elasticity and plasticity, it can be simplified as axisymmetric mechanics model. Judging whether plastic strain occurring in the tubing, it can be judged by the equation (refer with: Eq. 1):

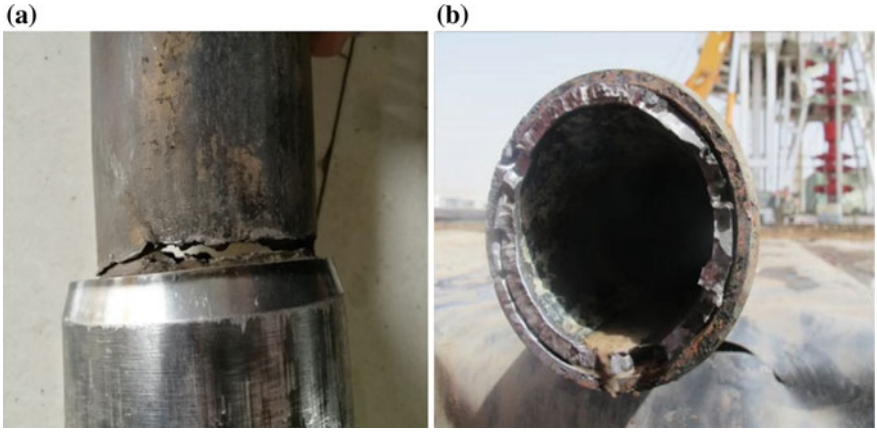

Fig. 1 Tubing fracture figure

$$f(\sigma) = \sigma_y \tag{1}$$

where, $f(\sigma)$ is a scalar function of the state of stress; σ_y is uniaxial yield stress.

When the function exceeds the yield stress, there is a plastic strain.

The Von Mises yield criterion is defined as the equivalent stress $f(\sigma)$ and σ_e, it can be judged by the equation (refer with: Eq. 2):

$$f(\sigma) = \sigma_e = \left[\frac{3}{2}\{s\}^T[M]\{s\}\right]^{\frac{1}{2}} \tag{2}$$

where, {s} is stress deviator vector.

The equation of {s} can be judged by the equation (refer with: Eq. 3):

$$\{s\} = \left\{\sigma_x\ \sigma_y\ \sigma_z\ \sigma_{xy}\ \sigma_{yz}\ \sigma_{xx}\right\} - \{\sigma_m\ \sigma_m\ \sigma_m\ 0\ 0\ 0\}^T \tag{3}$$

where, σ_m can be judged by the equation (refer with: Eq. 4):

$$\sigma_m = \left(\sigma_x + \sigma_y + \sigma_z\right)/3 \tag{4}$$

The equivalent stress can also be determined by the principal stress component, it can be judged by the equation (refer with: Eq. 5):

$$\sigma_e = \sqrt{\frac{1}{2}\left[(\sigma_1 - \sigma_2)^2 + (\sigma_2 - \sigma_3)^2 + (\sigma_3 - \sigma_1)^2\right]} \tag{5}$$

where, σ_1, σ_2, σ_3 are the first, second and third principal stresses.

The Von Mises yield criterion can be described as: If the equivalent stress reaches the yield stress of the material, the yielding occurs, as shown in the equation (refer with: Eq. 6):

$$\left[\frac{3}{2}\{s\}^T[M]\{s\}\right]^{\frac{1}{2}} = \sigma_y \tag{6}$$

In Eq. 6, [M] can be judged by the equation (refer with: Eq. 7):

$$[M] = \begin{bmatrix} 1 & 0 & 0 & 0 & 0 & 0 \\ 0 & 1 & 0 & 0 & 0 & 0 \\ 0 & 0 & 1 & 0 & 0 & 0 \\ 0 & 0 & 0 & 2 & 0 & 0 \\ 0 & 0 & 0 & 0 & 2 & 0 \\ 0 & 0 & 0 & 0 & 0 & 2 \end{bmatrix} \tag{7}$$

In the uniaxial stress state, the equivalent stress is equal to the uniaxial stress, the stress tends to yield. In the complex three axis stress state, the equivalent stress becomes a combination of stress components. In the three principal stress state, the yield surface becomes a cylindrical surface. Any stress state within this yield surface is elastic, any stress state outside this yield surface will cause plastic strain.

Finite Element Analysis of Tubing Thread

Mechanical Model of Tubing Thread

The figure (refer with: Fig. 2) is a seal testing tool. When the test operation starts, place the tool inside the tubing, rubber cylinder internal pressure bulging, the both ends of the joint seal, the helium is characterized in that the small molecular diameter and non-corrosive. At the same time, a high sensitivity He molecular monitoring instrument is arranged outside the oil pipe, when the helium leaks, the instrument alarms.

The size of tool is selected according to the tubing dimensions being checked, such as 68-tools, the outer diameter of 68 mm, which is matching the 3-1/2″ tubing testing tools, the outer diameter of the rubber cylinder is 64–72 mm. And 90-tool, the outer diameter is 90 mm, which is matching the 4-1/2″ tubing testing tool, the outer diameter of the rubber cylinder is 83–97 mm. Matching principle: smaller than the diameter of the tubing 4–10 mm. The schematic diagram of the two kinds of tools is shown in the figure (refer with: Fig. 3).

According to the actual working conditions of the scene, the tubing shall bear the tubing gravity F_G. In the process of pressure detection, the rubber cylinder first expands inside the tubing, making the tubing internal to bear the extrusion pressure.

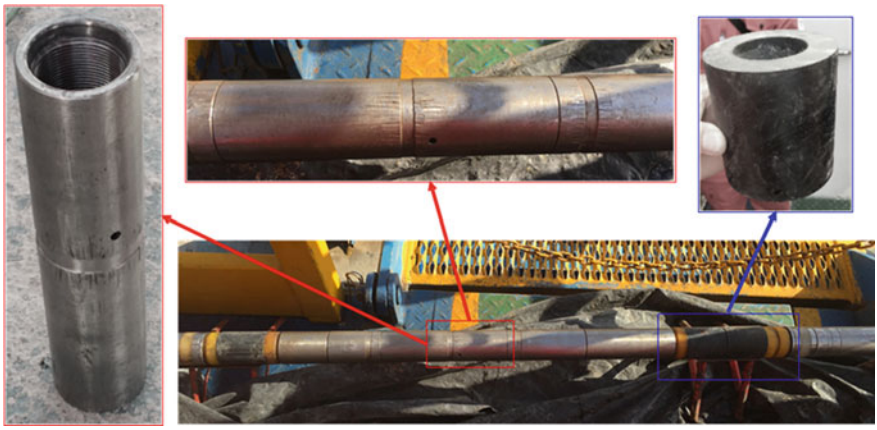

Fig. 2 Gas seal tool for oil field

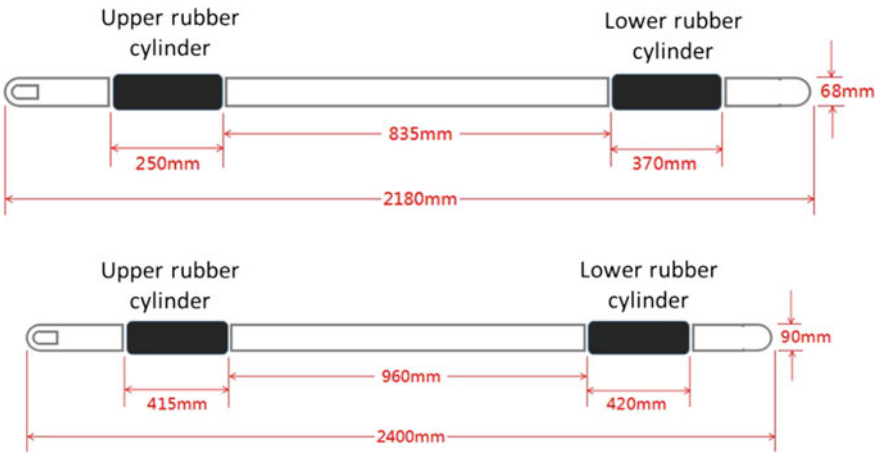

Fig. 3 Schematic diagram of gas seal tool

When the rubber cylinder expands, the helium gas will generate the piston power F_P on the cylinder. The tubing is subjected to the sealing test pressure P_i. Therefore, in the test process, the tubing is coupled by four forces, especially the large pulling force and the detection pressure, which will make the environment of the tubing joint at the test lower than the service environment of the lower well. For example, when the oil pipe with 3800 m 3-1/2″ is hung at the bottom, the internal pressure is 96.0 MPa, the extruding force of the rubber cylinder is 10 MPa, the axial pulling force is 55 t and the upper torque is 5694 N m.

According to the stress of the tubing thread, the mechanical model is shown in the figure (refer with: Fig. 4). Different colors represent different parts, including thread buckle, thread button seal detecting tool and rubber cylinder. The boundary conditions of the detection of tubing screw gas seal are as follows: The top of the thread buckle is fully restrained; The bottom of the thread buckle is subjected to the gravity F_G from the lower tubing; The inside of the thread buckle is tested under sealing test pressure P_i; The inside of the thread buckle is subjected to extrusion pressure in the cylinder position F_E; Sealing test pressure squeeze rubber cylinder to produce piston force F_P. The established mechanical model only considers the strength theory, and evaluating the safety of tubing thread through strength theory.

JFE BEAR as a new type of screwed joint which has basically replaced FOX. This type of screwed has some improved parameters such as guide surface, bearing surface angle and tooth width, so it has better sealing effect. According to the JFE BEAR thread for solid modeling, the outer diameter of tubing is 88.9 mm, its wall thickness is 6.45 mm, bearing tooth side angle is −5°, guide tooth side angle is 25°, thread taper is 1:16, finite element model is shown in the figure (refer with: Fig. 5).

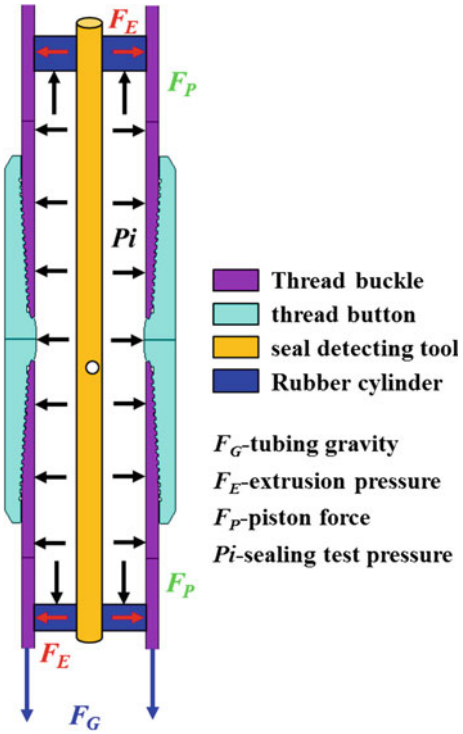

Fig. 4 Mechanical model of gas seal test

Stress Analysis of Tubing Thread Under Different Pressures

According to gas seal test in the oil field, the measures taken are shown in the table (refer with: Table 1), the steel grades of tubing in the table are all 13Cr110, and the buckle types are JFE BEAR.

After the analysis of the tubing in the serial number 1 in Table 1, the stress distribution of the gas seal test of the tubing thread is shown in the figure (refer with: Fig. 6). The lower part of the thread buckle is suspended with 55 tons of tubing, the buckle type is JFE BEAR, the outside diameter (OD) of tubing is 88.9 mm, the wall thickness (WT) of tubing is 6.45 mm, the RIP of the tubing is 96.3 MPa, and the sealing test pressure selects 100% (93.6 MPa) of the RIP, and the corresponding torque is 5694 N m.

The figure (refer with: Fig. 7) is the stress of thread buckle under 100% of the RIP. It can be seen from Fig. 7 that the position of the maximum Von Mises stress inside the threaded joint in the gas seal test takes place in the roots of the last three buttons of the external thread. The yield stress of the tubing material is 758 MPa, so in the red region, the plastic deformation of the tubing thread has occurred, and the thread in the middle of the last three buttons has the largest plastic deformation range. The initial crack of the tubing can easily occur after working with the tubing with plastic defects. In the harsh environment, the initial crack can be extended to the wall of the tubing, resulting in the failure of the tubing fracture.

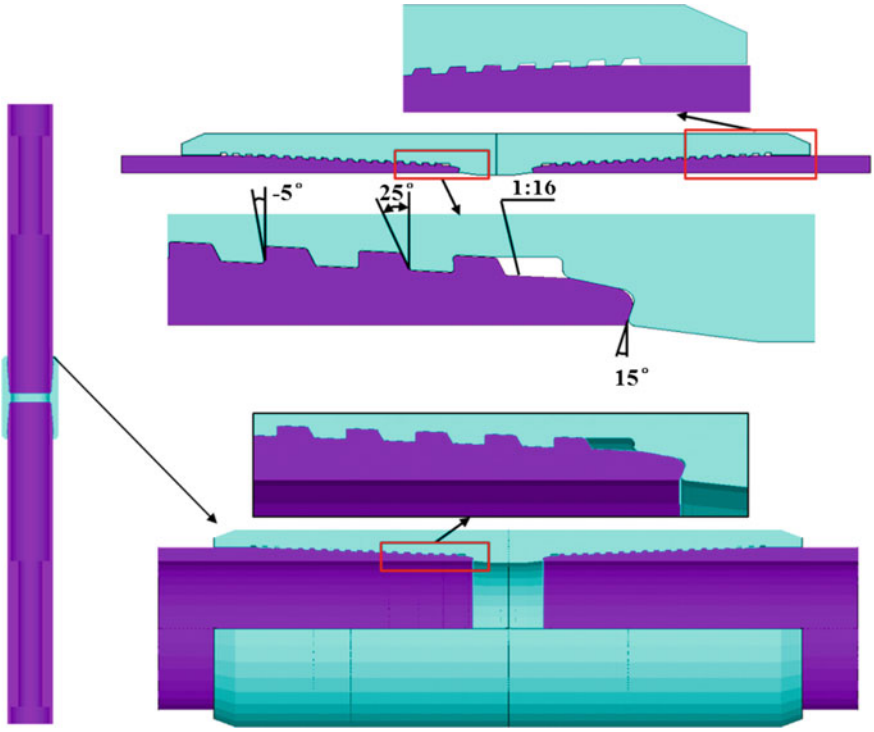

Fig. 5 Finite element model of JFE BEAR thread

Table 1 6 types of tubing for oil field

	Tubing specifications	OD (mm)	WT (mm)	RIP (MPa)	Test pressure (MPa)
1	3-1/2″	88.9	6.45	96.3	48
2	3-1/2″	88.9	7.34	109.6	55
3	3-1/2″	88.9	9.52	142.2	70
4	4-1/2″	114.3	8.56	99.4	50
5	4-1/2″	114.3	9.65	112.1	56
6	4-1/2″	114.3	12.7	147.5	74

The figure (refer with: Fig. 8) is the stress of thread buckle under 50% of the RIP. It can be seen from Fig. 8 that when the sealing test pressure is equal to 50% of the RIP of the tubing (48 MPa), other force (P_i, F_E and F_P) conditions remain unchanged. It can be seen from Fig. 8 that the position of the maximum stress also occurred in the roots of the last three buttons of the external thread, and the thread in the middle of the last three buttons also has the largest plastic deformation range, the red region is the place where plastic deformation has occurred. Overall, however, the overall plastic range decreased significantly, and the maximum stress at the last three buckles is reduced from 875.178 to 861.027 MPa.

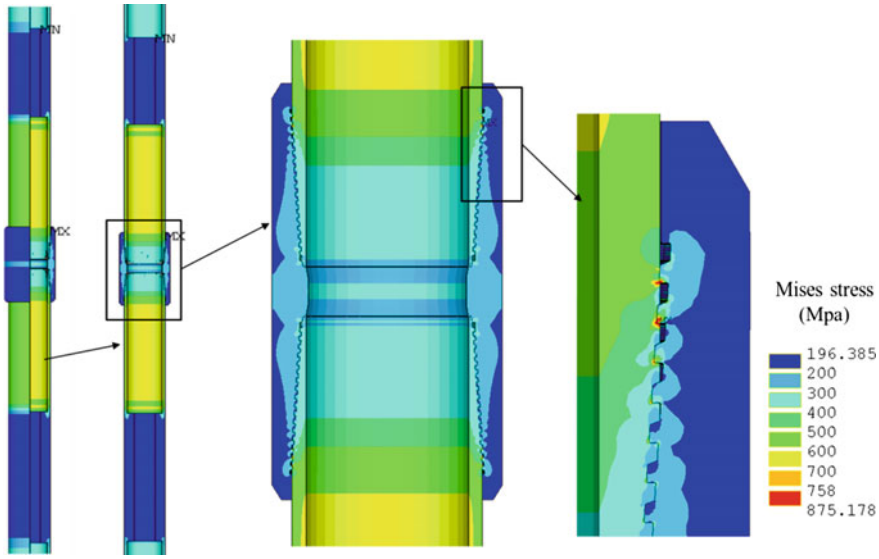

Fig. 6 Stress distribution diagram of thread under 100% of the RIP

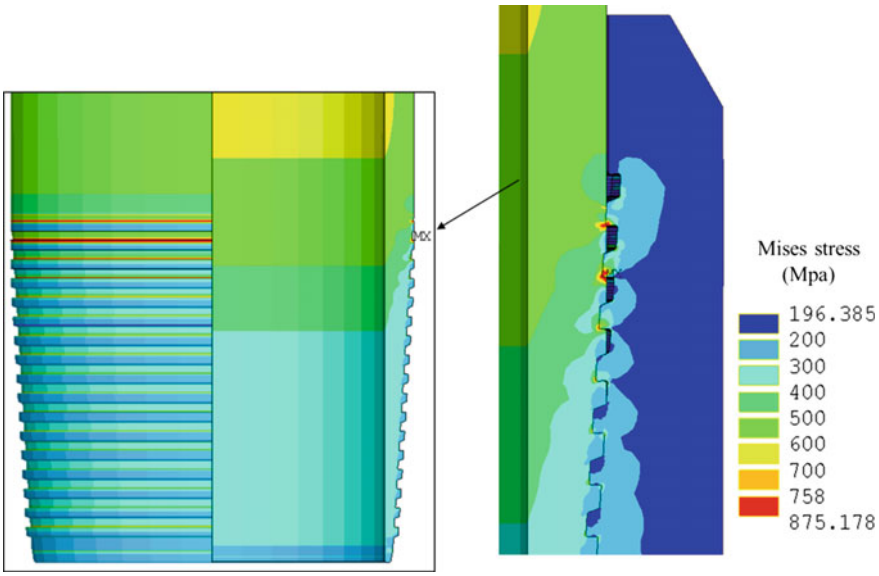

Fig. 7 Stress distribution diagram of thread buckle under 100% of the RIP

The figure (refer with: Fig. 9) is the Von Mises stress distribution on the root surface of the external thread. As can be seen from Fig. 9, the other force (P_i, F_E and F_P) conditions are unchanged, when the sealing test pressure drops from 96 to

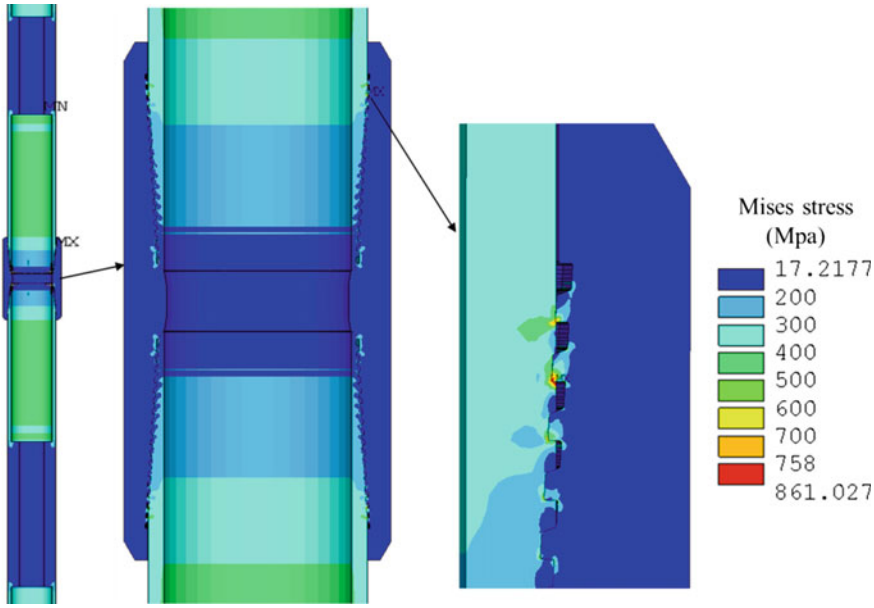

Fig. 8 Stress distribution diagram of thread under 50% of the RIP

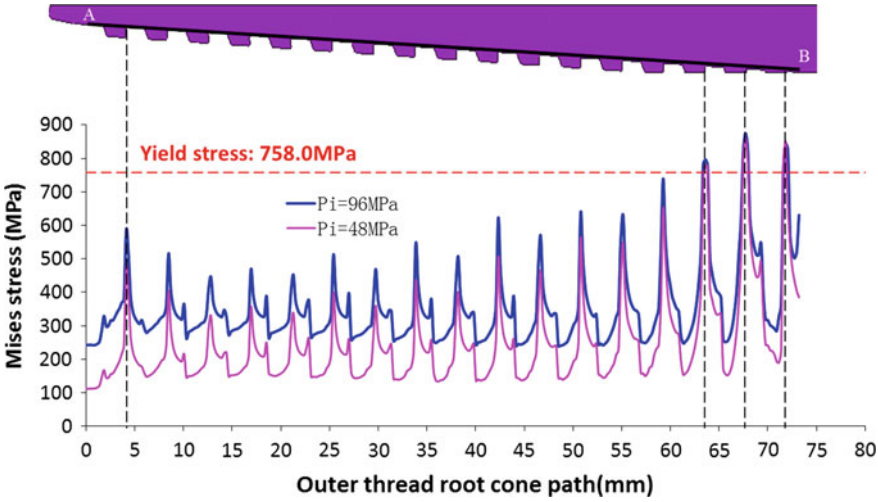

Fig. 9 Von Mises stress at the root of external thread under different testing pressure

48 MPa, the stress on the small side of the tubing thread decreases significantly. Whether 96 MPa (100% of the RIP) or 48 MPa (50% of the RIP), the roots of the last three buttons of the external thread occur plastic deformation. The analysis shows that improper sealing test pressure can cause plastic deformation of tubing threads. Tubing after service, the initial crack is easily produced in the position of

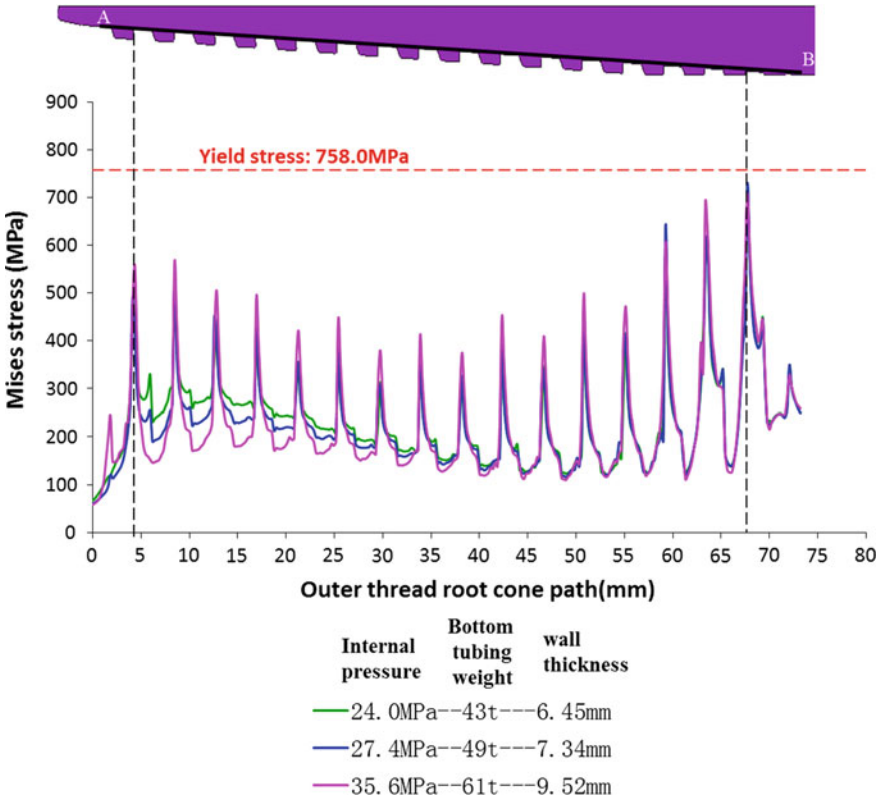

Fig. 10 The Von Mises stress diagram of the root of external thread under different internal pressure, bottom tubing weight and wall thickness

plastic deformation. Under the condition of turbulence, the initial crack propagation can cause the fracture under the low stress level, which is also the important reason for the serious failure of the tubing in the oil field.

Measures to Prevent Plastic Damage of Tubing Thread

Stress Analysis of Tubing Thread After Optimizing Inspection Pressure

Analyzed by Figs. 7, 8 and 9, the value of gas sealing test pressure is an important factor affecting the integrity of the following tubing. If the pressure value is not properly chosen, plastic damage will be caused to the tubing, through a large number of finite element calculations, it is suggested that 25% of the RIP of the tubing is taken as the sealing test pressure. 6 kinds of tubing in Table 1 are calculated by finite element method, and then used as verification.

Improvement of Gas Seal Inspection Pressure Scheme

From Figs. 10 and 11 analysis can be seen, without affecting the detection effect of gas seal, when the sealing test pressure is 25% of the RIP, the stress in the thread of 6 kinds of the tubing decreases obviously under the same force (P_i, F_E and F_P) conditions. The maximum stress in the joint shall not exceed its yield stress

Table 2 Prevention and control scheme of tubing thread for gas seal test

	Tubing specifications	OD (mm)	WT (mm)	RIP (MPa)	Test pressure (MPa)
1	3-1/2″	88.9	6.45	96.3	24.1
2	3-1/2″	88.9	7.34	109.6	27.4
3	3-1/2″	88.9	9.52	142.2	35.6
4	4-1/2″	114.3	8.56	99.4	24.9
5	4-1/2″	114.3	9.65	112.1	28
6	4-1/2″	114.3	12.7	147.5	36.9

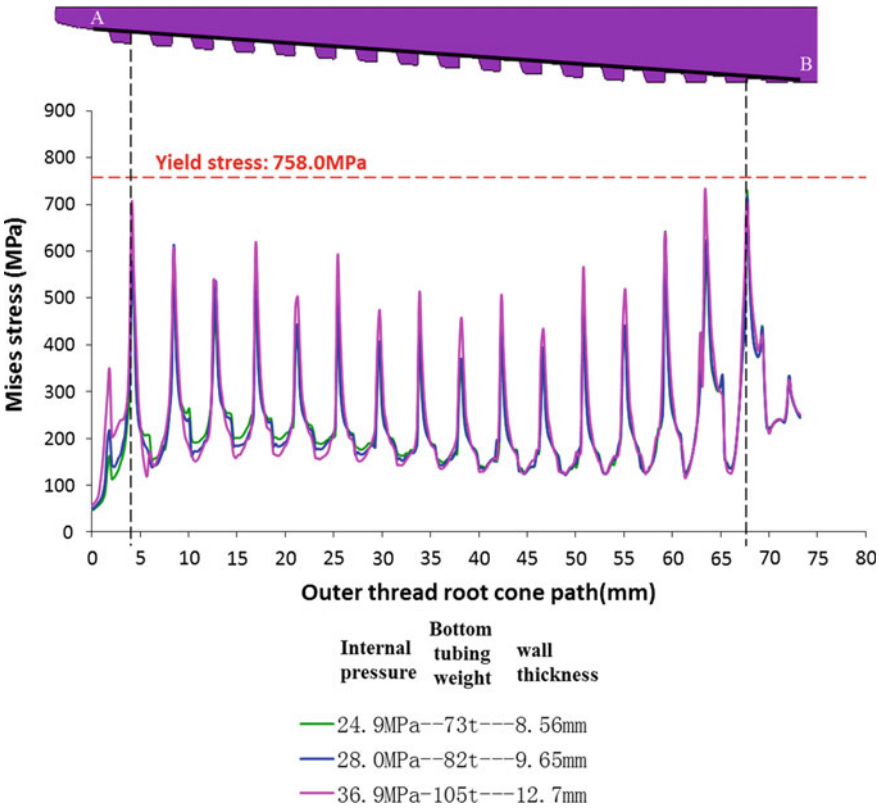

Fig. 11 The Von Mises stress diagram of the root of external thread under different internal pressure, bottom tubing weight and wall thickness

(758.0 MPa). According to the above analysis, it is suggested that the scheme used to prevent the plastic deformation of tubing during gas seal testing is shown in the table (refer with: Table 2).

Summary

(1) When the test pressure is equal to 100 and 50% of the RIP of tubing, the plastic deformation of the tubing thread occurs, and the plastic deformation area appears in the last three buckle roots; after servicing in the well, the initial crack occurs from this location due to the harsh conditions, which may cause fatigue fracture under low stress level.
(2) When the test pressure is equal to 25% of the RIP of the tubing, the plastic deformation area appears in the last three buckle roots, but the maximum stress of all types of tubing threads is less than the yield strength (758 MPa).
(3) Through simulation, the selection pressure scheme of gas seal test for six specifications of tubing is designed.
(4) Based on the finite element model, the stress of the tubing thread of the high-pressure gas well can be quantitatively and fully evaluated, and the gas seal detection technology can be provided with theoretical reference.

References

1. S. Wang, N. Peng, B. Liu, Selection of premium connection as used in HPHT well and relevant evaluation test methods. J. Steel Pipe **45**(01), 64–71 (2016)
2. J. Xiao, S. Peng, F.Q. Cheng et al., Effect of internal pressure strength of buttress and collapse pressure on limit casing thread connection. J. Oil Field Equip. **37**(06), 55–57 (2008)
3. N. Yoshihiro, F. Minoru, N. Norihiko, Designing and proof testing of special joints for high pressure oil-well casing. J. Sumitomo Search **12**, 85–91 (1974)
4. N. Yoshihiro, N. Seiichi, K. Tetsuro, Leak-proof tests of special joints for oil country tubular goods. J. Sumitomo Met. **26**(1), 97–105 (1974)
5. E. Tsuru, M. Ueno, M. Ogasawara, Performance of tubular connections under the loading conditions of horizontal wells. J. SPE Drill. Completion 242–248 (1996)
6. Y. Dou, A. Xu, G. Zhang et al., Influence of thread parameter tolerance on connection strength of tubing thread. J. China Petrol. Mach. **35**(01), 13–15 (2007)
7. S. Wang, P. Cheng, X. Shi et al., Influence of temperature on contact pressure of casing joints. J. Southwest Petrol. Inst. **04**, 63–65 (2005)
8. X. Gao, Z. Zhang, H. Zhao et al., Calculation and analysis of tooth force of two stage cylindrical thread casing coupling. J. Univ. Petrol. **05**, 70–73 (1994)
9. X. Gao, Z. Zhang, Distribution and calculation of buckle force of variable pitch sleeve thread under axial tension. J. Petrol. Drill. Tech. **01**, 55–56 (1994)
10. L. Wang, Z. Chen, R. Zhang et al., Analysis of sealing performance on api round thread casing connection for thread compound. J. Shanghai Jiaotong Univ. **35**(07), 1053–1056 (2001)

11. Z. Lian, H. Liang, T. Shi, Q. Lu, Y. Wang, S. Feng, Development and application of screw structure of miniature drilling tool for super-deep wells. J. Oil Drill. Prod. Technol. **38**(02), 160–165 (2016)
12. N.G. Pai, D.P. Hess, Three-dimensional finite element analysis of threaded fastener loosening due to dynamic shear load. J. Eng. Fail. Anal. **9**, 383–402 (2002)
13. S. Izumi, T. Yokoyama, A. Iwasaki, S. Sakai, Three-dimensional finite element analysis of tightening and loosening mechanism of threaded fastene. J. Eng. Fail. Anal. **12**, 604–615 (2005)
14. J.A. Sanclemente, D.P. Hess, Parametric study of threaded fastener loosening due to cyclic transverse loads. J. Eng. Fail. Anal. **14**, 239–249 (2007)

Assessment Methods for the Dented Pipe of Grade X80

Qiaofei Sun, Lei Guo, Dahai Zheng, Leilei Wang and Yi Liu

Abstract Dents are common defects in pipeline, and may occur during pipeline construction or in service. The dents may threaten the integrity of pipelines. To guarantee the safety operation, the assessment of plain dents is mainly based on the depth or the strain criterion. This paper reviews the basis of the criteria in different codes and the recent research of plain dents. In addition, comparisons are made between different grades of the steel in terms of mechanical properties. With the increasing grade, the strength and the yield ratio increase, but the plastic property decreases. The average UEL of X80 is only 6.2%. When the strain-based criterion is applied to the X80 pipe with dents, it needs to be demonstrated by engineering analysis.

Keywords Plain dents · Burst strength · Depth-based criterion
Strain-based criterion · Fatigue life

Q. Sun (✉)
China Petroleum Pipeline Research Institute Co. Ltd., Langfang 065000, Hebei, China
e-mail: sunqiaofei137@163.com

L. Guo · L. Wang · Y. Liu
Sci-Tech Information Center, PetroChina West to East Gas Pipeline Company, Wuhan 430073, Hubei, China
e-mail: gdguolei@petrochina.com.cn

L. Wang
e-mail: szhwll@petrochina.com.cn

Y. Liu
e-mail: hzliuyi@petrochina.com.cn

D. Zheng
Piping Department, PetroChina West to East Gas Pipeline Company, Wuhan 430073, Hubei, China
e-mail: zhangdahai@petrochina.com.cn

© Springer Nature Singapore Pte Ltd. 2018

Y. Han (ed.), *Advances in Materials Processing*, Lecture Notes in Mechanical Engineering, https://doi.org/10.1007/978-981-13-0107-0_98

Introduction

Dents are common defects in pipeline, and may occur during different stages. During pipeline construction, dents may be caused by the hard rocks or the handling of pipe; and in-service, they may be caused by excavator impact. The dents will threaten the integrity of pipelines. How to rank the severity of the dents is much more concerned.

Over the past few decades, lots of studies were made to study the structural behavior of the dents. Accordingly, some recommendations were made for assessment of dent severity and adopted by some standards and codes. However, the high grade steel are widely used with the increasing demands of gas in China in recent years, and in the second line of China's west-to-east gas transmission pipelines are mainly X80. Whether the assessment methods can be suitable for the high grade steel pipe with plain dents needs to be demonstrated.

In the paper, a detailed review of the guidelines and recent research was made, to determine the basis of the acceptance criteria and the model for predicting the fatigue life. The basis may explain what grade steel it can cover.

Definition of the Dents

A dent in a pipeline is a permanent plastic deformation of the circular cross section of the pipe [1]. Dent depth is defined as the maximum reduction in the diameter of the pipe compared to the original diameter, considering the influence of out-of-roundness.

Since the acceptance criteria are different between different kinds of dents, the definition of dents are described firstly:

Smooth Dent a dent which causes a smooth change in the curvature of the pipe wall.

Kinked/Sharp Dent a dent which causes an abrupt change in the curvature of the pipe wall (radius of curvature of the sharpest part of the dent is less than five times the wall thickness, or the length to depth ratio is less than 20).

Plain Dent a smooth dent without stress concentrations (such as a gouge/crack or other defects).

Unrestrained Dent a dent that is free to spring back when the indenter is removed, and is free to re-round as the internal pressure changes.

Restrained Dent a dent that is not free to spring back or re-round, for example of a dent induced by rocks.

Burst Strength of the Plain Dents

Summary of the Assessment of the Dents

Table 1 summarizes the Chinese and international code related with the acceptance criteria of dents in oil and gas pipelines [1–6]. The acceptance criteria are provided for plain dents, kinked dents, dents with crack or gouge, dents at welds, dents with corrosion, which are only applicable to the conditions of static internal pressure.

The assessment of plain dents is mainly based on the dent depth, and generally the limit 7%D for plain dents is permitted, such as SY/T 6996, ASME B318. However, PDAM suggests the limit 7%D and 10%D respectively for unrestrained dents and restrained dents. In addition, ASME B31.8 and CSA Z662 provide strain acceptance criterion with the threshold of 6% for plain dents.

For kinked/sharp dents, PDAM do not permit this kind of dents.

Dents with crack are not permitted in any codes and an immediate repair is recommended.

Dents with gouge are not permitted in most codes. However, API 579 suggests the assessment methods for this kind of dents.

For dents with corrosion, several codes allow the corrosion to be assessed independently, which is different form dents with gouge.

The acceptance criteria for dents at welds are stricter than those for plain dents, and even they are not permitted in some codes such as PDAM and ASME B31.4, because crack may exist in the welds, and then threaten the integrity [7].

Depth Based Criterion for Plain Dents

Since 1950s, full scale burst tests have been carried out to determine whether the plain dents will reduce the burst strength or not. Battle carried out 39 tests, and stated plain dents of less than 8%OD will not reduce the bust strength [8]. For the rock dents, the limited burst tests demonstrated that the burst strength of the rock dents is at least equivalent to that of an unrestrained dent, and the restrained dent will threaten pipeline integrity, leading to puncture of the pipe if the restraining object is hard enough and sharp enough [9]. In addition, other institutes also carried out some burst tests [10–13]. All of the early tests showed that plain dents do not significantly reduce the pressure carrying capacity of the pipe, unless they are very deep. But few analytical methods were published for assessing the pressure carrying capacity of a plain dent. So, present criteria in depth were based originally on the basis of these tests and also take into account the safe passage requirements of in-line tools.

In 2003, PDAM was developed and published by a Joint Industry Project, which has been sponsored by fifteen international oil and gas companies. PDAM suggested the plain dent limits based on the published full-scale test data, which were used to develop and validate existing assessment methods. Table 2 shows the range of the test

Table 1 Summary of the acceptance criteria of the dents

Guidance	Plain dent	Kinked/sharp dent	Dent with gouge	Dent with crack	Dent at welds	Dents with corrosion
SY/T 6996	Up to 6%OD or unlimited if strain <6%	Not allowed	Not allowed	Not allowed	Up to 2%OD or unlimited if strain <4%	As per SY/T 6151 limits
PDAM	Up to 7%OD (unrestrained); Up to 10% OD (restrained)	Not allowed	Method provided	Not allowed	Not allowed	Not allowed
CSA Z662	Up to 6 mm when OD $\leq$ 101.6 mm; Up to 6%OD when OD >101.6 mm or unlimited if strain <6%	A length to depth ratio >20 or unlimited if strain <6%	Not allowed	Not allowed	Up to 6 mm when OD $\leq$ 323.9 mm; Up to 4%OD when OD > 323.9 mm	As per ASME B31G limits
API 579	Up to 7%OD	–	Method	–	–	–
ASME B31.8	Up to 6%OD or unlimited if strain <6%	–	Not allowed	Not allowed	Up to 6%OD or unlimited if strain <4% for ductile welds; Not allowed for brittle welds	As per ASME B31G limits
ASME B31.4	Up to 6 mm when OD $\leq$ 101.6 mm; Up to 6%OD when OD > 101.6 mm	–	Not allowed	Not allowed	Not allowed	Corrosion <87.5%t

Table 2 The range of the full scale burst tests of the plain dents

Pipe diameter (mm)	168–914.4	Grade (API 5L)	X42–X60
Wall thickness (mm)	4.78–12.7	Yield strength (MPa)	371.6–485.4
Dent depth (mm)	2.72–327.7	Tensile strength (MPa)	483.3–639.2
H/D	0.005–0.43	Yield to tensile ratio	0.7–0.85

data [1]. All of the tests are based on the pipe of the grade X42–X60. Caution should be exercised when assessing the plain dents that fall outside of these limits.

Strain Based Criterion for Plain Dents

Although the dents with the depth of less than 6%OD will not reduce the burst strength, real life exceptions do exist: at least one rock puncture in service, as well as two simulated rock puncture tests where indentations were less than 6% of the pipe diameter [14]. Since metal damage caused by plastic deformation is related to strain, ASME B31.8 and CSA Z662 provide a method based on strain criteria with the threshold of 6% and ASME B31.8 provides non-mandatory formulas for strain calculation in Appendix R.

The critical strain of 6% is taken from 3 to 12% [15]. 3% is the strain limit of cold field bends, which is not concerned. It has been observed that puncture in dents and cracking in pipe deformations such as buckles seem likely to occur, when material strain exceeds around 12%. Thus a strain threshold between 3 and 12% would be suitable. The criterion of 6% is obtained with a safety factor of 2 [16].

The method presented in Appendix R of ASME B31.8 Code offers relatively simple non-mandatory equations to evaluate each strain component separately and the equivalent strain. The maximum equivalent strain at the OD and ID surfaces are regarded as the strain of dents, and then compared to 6% to determine whether the dent is allowable. The equations are as follows.

The Bending Strain in the Circumferential Direction

$$\varepsilon_1 = \frac{t}{2}(1/R_0 - 1/R_1) \tag{1}$$

The Bending Strain in the Longitudinal Direction

$$\varepsilon_2 = -t/(2R_2) \tag{2}$$

The Extensional Strain in the Longitudinal Direction

$$\varepsilon_3 = \frac{1}{2}(d/L)^2 \tag{3}$$

The Strain on the Inside Pipe Surface

$$\varepsilon_i = \sqrt{\varepsilon_1^2 - \varepsilon_1(\varepsilon_2 + \varepsilon_3) + (\varepsilon_2 + \varepsilon_3)^2} \tag{4}$$

The Strain on the Outside Pipe Surface

$$\varepsilon_o = \sqrt{\varepsilon_1^2 + \varepsilon_1(-\varepsilon_2 + \varepsilon_3) + (-\varepsilon_2 + \varepsilon_3)^2} \tag{5}$$

Since ASME B31.8 proposed the strain criterion firstly in 2003, large number of studies has been made.

The equations of the bending strain and the extensional strain in the longitudinal direction were corrected in 2007, and were demonstrated by Noronha et al. [17].

The longitudinal extensional strain depends on the depth and the length of dents. The equations were obtained from an empirical estimation based on a limited number of finite element analyses [18]. However, when the length is defined differently, the stain is significantly different. Studies demonstrated that the strain is accurate using the distance measured at the dent half-depth [19].

In the published literature, there are no explanations how the equivalent strain was established. The strains in Eqs. (4) and (5) are similar to those for a plane strain condition without having a preceded constant 2/3, or analogous to Von Mises stress for a plane stress condition [18]. The equation is expressed as follow.

The Equivalent Strain

$$\varepsilon_{equivalent} = \sqrt{\varepsilon_{\mathrm{I}}^2 - \varepsilon_{\mathrm{I}}\varepsilon_{\mathrm{II}} + \varepsilon_{\mathrm{II}}^2} \tag{6}$$

where, ε_{I} and $\varepsilon_{\mathrm{II}}$ are respectively principal strain.

In the equation, both the circumferential membrane strain and the radial strain are negligible [20]. However, it is doubtful that the radial strains are negligible, because the pipe at the dent region is not in a plane strain state. Other researches indicate that Eq. (6) may results in an un-conservative results, which means dents that may actually fail the current strain limit criterion could remain unrepaired in pipelines. A new equation for calculating the equivalent is suggested as Eq. (7) [21]. The method may need to be further verified and revised.

$$\varepsilon_{equivalent} = \frac{2}{\sqrt{3}}\sqrt{\varepsilon_{\mathrm{I}}^2 + \varepsilon_{\mathrm{I}}\varepsilon_{\mathrm{II}} + \varepsilon_{\mathrm{II}}^2} \tag{7}$$

Fatigue Life of the Plain Dents

The main concern with unrestrained plain dents is fatigue driven by the cyclical radial fluctuation of the dent in response to operating pressure cycles. High local bending stress cycles are associated with the fluctuation of the dent, leading to fatigue after a sufficient number of pressure cycles. A significant proportion of the research effort has been made to predict the pressure-fatigue characteristics of dent. All the researches are based on the laboratory test utilized with FEA analysis. All of fatigue life assessment methods are a stress-life based assessment approach, including models by EPRG [22], SES [23], Kiefner & Associates [24].

The dents are assumed to be unrestrained in all of the methods. It is generally conservative as unrestrained dents tend to have a lower fatigue life than equivalent or even deeper restrained dents. The limited experiment tests demonstrated that the fatigue life of a restrained plain dent will be at least equivalent to that of an unrestrained plain dent of the same depth.

The models proposed by SES and Kiefner & Associates need to determine the cyclic stress range at the dent by FEA or experiment. Thus the EPRG model are used widely and adopted by PDAM and API 579 in different forms [1, 5]. The model accounts for the stress concentration at the dent, which depends on the dent depth with a simple formula.

However, large scatter is present in the accuracy of the four fatigue life prediction models when compared to experimental data [1]. That may be because that the dent depth is generally not the only factor to determine the severity of the dent in terms of its impact on the fatigue life of a pipe. Studies indicate that the local stress-strain state at the dent region, and hence fatigue life, is affected by a number of parameters, including: dent depth, dent length, dent width, length to depth ratio [25]. Thus the application of the model need to be further improved.

The Fitness of the Assessment Methods for Steel of Grade X80

The high grade steels are widely used with the increasing demands of gas in China in recent years. And in the second line of China's west-to-east gas transmission pipelines are mainly X80. In the previous section, the conclusion was draw that the assessment criterion is based on low grade steel. However, the properties

Table 3 Average value of the properties of different steels

Grade	$R_{t0.5}$	R_m	$R_{t0.5}/R_m$	δ (%)
X52	412	552	0.75	39.7
X60	448	571	0.79	38.2
X70	536	623	0.86	38
X80	601	667	0.90	26

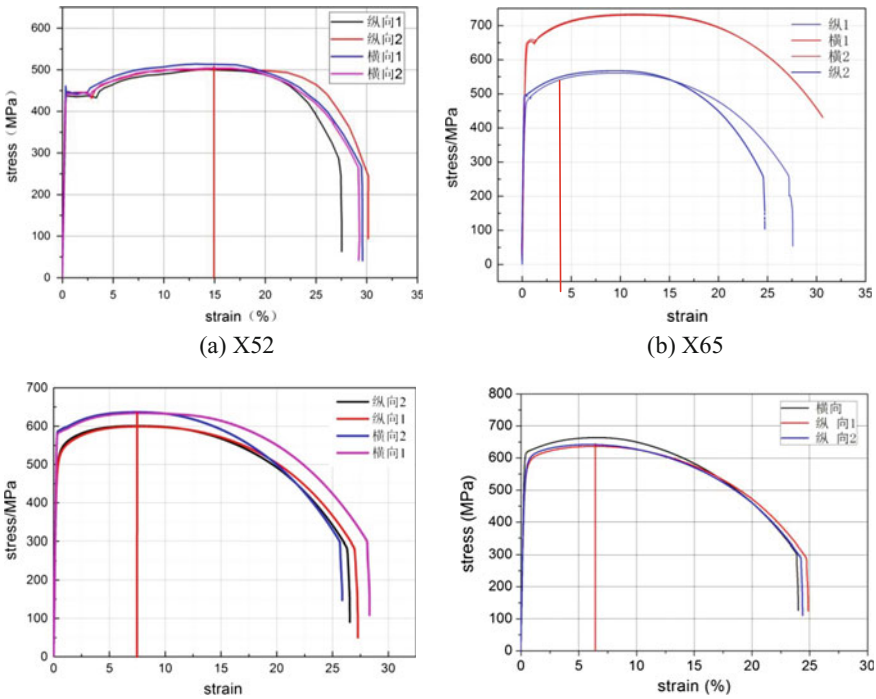

(a) X52 (b) X65

(c) X70 (d) X80

Fig. 1 Stress-strain curve of different grade steels

change significantly with the increasing grade. Whether the criterion is accurate for the assessment of the dented pipe of high grade needs to be demonstrated.

Since the metal damage is related with the properties, we compared the properties of different grade steel. In API 5L, the properties are required, including yield strength, ultimate tensile strength, yield to tensile ratio and elongation. Table 3 shows the statistical results of the average value. Compared to the low grade steel, the yield strength, ultimate tensile strength and yield to tensile ratio of high grade steels increase, while the elongation changes little when the grade less than X70, and decreases with the grade of X80. This indicates that the plastic deformation capacity of X80 steel decreases.

Figure 1 shows the stress-strain curves of different steel. It shows that the uniform elongation decreases significantly with the grade increasing. The uniform elongation of X80 is 6.4%, less than half of that of X52. In addition, the uniform elongation of X80 from 68 tests is averagely 6.2%, with the range of 2.7–8.5. In the uniaxial tensile test, when the strain is up to the uniform elongation, the specimen starts necking, which means that microporous form, grow up and gather to form cracks, and finally fracture. In other words, when the strain criterion of 6% is applied to the assessment of X80 pipe with a plain dent, the strain at the dent may

reach up to the uniform elongation, and even much more than the uniform elongation. Finally it will fail as the uniaxial tensile test. When the criterion in current guidance and codes is applied to X80, it may result in an unconservative assessment, and the dent which needs to be repaired still remains in the pipeline.

Conclusions

(1) The current assessment methods of plain dents in codes are mainly based on full scale burst test of low grade steel with a range of X42–X60.
(2) The EPRG model for predicting the fatigue life of plain dents is an empirical method dependent on the dent depth, with a large amount of scatter when compared to experimental data. The application of the model need to be further improved.
(3) Compared to low grade steels, the properties of X80 changed significantly, especially the uniform elongation. If the current criterion is applied to X80, it may result in an un-conservative assessment. It needs detailed analysis or experiment to demonstrate the fitness of the assessment method.

References

1. PDAM-2006. *Pipeline Defect Assessment Manual* (2006)
2. SY/T 6996-2014. Assessment of steel oil & gas pipeline with dent (2014)
3. ASME B31.8-2012. Gas transmission and distribution piping systems (2012)
4. ASME B31.4-2006. Pipeline transportation systems for liquid hydrocarbons and other liquids (2006)
5. API 579-2016. Fitness for service (2016)
6. CSA Z662-2015. Oil and gas pipeline systems (2015)
7. M.J. Rosenfeld, Toward an acceptance criterion for shallow dents affecting girth welds in gas transmission pipelines in *ASME Pressure Vessel and Piping Conference*, vol. **353** (1997)
8. R.J. Eiber, W.A. Maxey, C.W. Bert, G. McGlure, The effects of dents on the failure characteristics of line pipe. Battelle Report to A.G.A. Pipeline Research Committee, L51403 (1981), p. 38
9. C.R. Alexander, J.F. Kiefner, *Effects of Smooth and Rock Dents on Liquid Petroleum Pipelines* (API Publication, 1997), p. 1156
10. P. Hopkins, I. Corder, P. Corbin, Paper VIII-3, in *International Conference on Pipeline Reliability* (Calgary, Canada, June 1992)
11. O.H. Bjørnøy, O. Rengård, S. Fredheim, P. Bruce, Residual strength of dented pipelines, DNV test results, in *Tenth International Conference on Offshore and Polar Engineering* (ISOPE 2000)
12. G. Jonesd, *The Significance of Mechanical Damage in Pipelines*, 3R International, 21, Jahrgang, Heft, 7, July 1982
13. P. Hopkins, D.G. Jones, A.C. Clyne, Paper C376/049, in *Proceedings of International Conference on Pipework, Engineering and Operation* (Institution of Mechanical Engineers, London, 1989)

14. J.F. Kiefner, C.R. Alexander, *Effects of Smooth and Rock Dents on Liquid Petroleum Pipelines (Phase 2)* (Addendum to API Publication, 1999), p. 1156
15. M.J. Rosenfeld, J.W. Pepper, K. Leewis, Basis of the new criteria in ASME B31.8 for prioritization and repair of mechanical damage, in *4th International Pipeline Conference*, Calgary, Alberta, Canada (2002)
16. J.F. Kiefner, L. Keith, *Guidance for the Assessment of Pipeline Defects, PR218-05404, PRCI* (2010)
17. D.B. Noronha, R. Martins, B. Jacob, E. Souza, The use of B-splines in the assessment of strain levels associated with plain dents, in *Rio Pipeline Conference & Exposition*, PaperNo. IBP 1245_05 (2005)
18. M. Baker, Dent Study, Final Report, TTO Number 10, Integrity Management Program, Delivery Order DTRS56-02-D-70036, DOT Research and Special Programs Administration, Office of Pipeline Safety (2004)
19. D.B. Noronha,R.R. Martins, B.P. Jacob et al., Some remarks on the strain based assessment of pipeline dents, in *The 7th International Pipeline Conference* (2008)
20. M. Gao, R. Mcnealy, R. Krishnamurthy, Strain-based models for dent assessment—a review, in *The 7th International Pipeline Conference* (2008)
21. S.A. Lukasiewicz, J.A. Czyz, C. Sun et al., *2006 International Pipeline Conference*, Calgary, Alberta (2006)
22. I. Corder, P. Chatain, in *Proceeding of the EPRG/PRC 10th Biennial Joint Technical Meeting on Line Pipe Research*, Cambridge, UK, April 1995
23. J.R. Fowler, C.R. Alexander, P.J. Kovach, L.M. Connelly, Report PR-201-927 and PR-201-9324, Pipeline Research Council International, AGA, June 1994
24. M.J. Rosenfeld, *Development of a Model for Fatigue Rating Shallow Unrestrained Dents*. PR-218-9405, Pipeline Research Council International, KAI, L51741 (1997)
25. A. Dinovitzer, R. Lazor, L.B. Caroll et al., Geometric dent characterization, in *International Pipeline Conference*, Calgary, Alberta (2002)

Influence of Cement Defection on Casing Stress Under Cyclic Loading During Multi-stage Hydro-Fracturing

Xueli Guo, Jun Li, Yang Yu and Gonghui Liu

Abstract The casing integrity problem presents severe challenges for shale gas wells regarding the multi-stage fracturing operation. Multiple factors during fracturing process may have individual or combined influence on it. However, most of the researchers only studied one fracturing stage. The influence of cyclic fracturing loading on casing of shale gas well has been rarely studied. This paper presents a finite element model approach to simulate the multi-stage fracturing operations. Based on the theory of elasto-plasticity, the nonlinear isotropic/kinematic hardening material was used to simulate the response of the casing under cyclic loading. The transient temperature-pressure coupling model of casing-cement sheath-formation (CCF) was established. Multiple analysis steps were used to simulate the multi-stage fracturing processes. The cement channel angle, pump rate, and fracturing fluid temperature were the variables taken into account. An attempt was made to reveal how the factors affect the casing stress. Sensitivity analyses showed that the cement channel had the greatest influence on casing stress. The casing had the highest Von Mises stress and equivalent plastic strain (PEEQ) at the channel angle between 60° and 90°. The stress could be easy to exceed the casing yield stress, causing the casing failure. The more the fracturing stage was, the larger the Von Mises stress and PEEQ of casing were. Larger pump rate tended to dramatically reduce the downhole temperature. The lower the temperature of the fracturing

X. Guo · J. Li (✉) · Y. Yu · G. Liu
China University of Petroleum-Beijing, 18 Fuxue Road, Changping
Beijing 102249, China
e-mail: lijun446@vip.163.com

X. Guo
e-mail: clouder0713@163.com

Y. Yu
e-mail: 2281063450@qq.com

G. Liu
e-mail: lgh_1029@163.com

G. Liu
Beijing University of Technology, 100 Pingle Park, Chaoyang
Beijing 100124, China

© Springer Nature Singapore Pte Ltd. 2018

Y. Han (ed.), *Advances in Materials Processing*, Lecture Notes in Mechanical Engineering, https://doi.org/10.1007/978-981-13-0107-0_99

fluid was, the greater the reduction of the downhole temperature was. When the cement channel angle was smaller than 60°, the casing had the higher Von Mises stress and PEEQ for the larger pump rate and lower fracturing fluid temperature. The results indicated that good cement sheath was the basic requirement to ensure the safety of casing. The pump rate and fracturing fluid temperature should be in a reasonable range. During multi-stage fracturing construction, the pressure should be not too high to reduce the casing stress, avoiding the risk of casing deformation.

Keywords Casing stress · Cyclic loading · Multi-stage fracturing
Shale gas well

Introduction

With the exploration of Changning-Weiyuan Shale Gas National Demonstration Zone of Sichuan basin in China in 2013, there were some problems with the well integrity in several shale gas wells. For examples, casing string could hardly be set into the well hole, and cement ring could not seal completely. Even worse, the casing in horizontal section collapsed during multi-stage hydro-fracturing. If this happened, the bridge plug could not be seated in the right section through the casing string or not be drilled by grind tool which was set into the hole through the coiled tube. What's more, some fracturing sections would have to be abandoned. All of these troubles had seriously affected the production of single shale gas well and restricted the shale gas exploration [1–3].

From now on, the wellbore integrity have raised among many scholars. As discovered by K. J. Goodwin, exposure of steel casing to excessive temperature increases or internal test pressures caused diametrical and circumferential casing expansion. This circumferential force created a shearing force at the cement/casing interface, causing failure at the cement/casing interface or radial fracturing of the cement sheath from the inner casing surface to the outer casing (or borehole) surface [4].

Through the finite element studies, A. Berger presented the presence of voids in the formation or cement would result in a reduction of the collapse resistance of casing up to 60%. But the eccentricity had a minor effect on the collapse resistance of casing [5].

By using the finite element method to build a three dimension simulation model. Zhaoguang Yuan presented that, in the cement channeling, the casing had highest von Mises stress at the hole angle of 90°, and the cement tended to fail in tension. The casing eccentricity tended to reduce cement shear stress and tensile stress, but increase cement compressive stress. The cement had the highest compressive failure probability in casing eccentricity condition [6].

George E. King pointed out almost all of the failures of fracture and re-fracture treatments and separated into a few major categories: (1) Design, (2) Drilling issues, (3) Mechanical failures, (4) Application failures, (5) Cement sheath failure,

(6) Production or Completion damage, (7) Geologic forces, (8) Unknowns. Even though, the author considered that no one-size-fits-all check list of damage potential or risk could be offered to accurately address all damage mechanical. Therefore, specific type of collapse must be discussed [7].

In this paper, the actual casing damage of shale gas plays in Sichuan is investigated, and the cementing quality of fracturing section is statistically analyzed. The results show that there is a great correlation between poor cementing quality and casing damage [8–11]. The main manifestation of poor quality of wells is the cement ring channeling [12].

Model Establishment

Heat Transfer Coefficient Model

The slippery water used in the fracturing process is generally a non-Newtonian power law fluid [13]. The rheological properties equation is as the following.

$$\tau = K\gamma^n. \tag{1}$$

where K is the consistency coefficient, Pa s^{-n}; n is the flow index, $n < 1$ referring to pseudo-plastic fluid, $n > 1$ referring to expansive fluid, for fracturing fluid, $n < 1$, meaning pseudo-plastic fluid; γ is shear rate, s^{-1}.

When the fracturing fluid is pumped into the wellbore with large rate, it is in the turbulent state. The heat transfer coefficient between the fracturing fluid and the casing inner wall can be calculated by Marshall Model [14].

$$h = \frac{N_u k_m}{D}. \tag{2}$$

$$N_u(S_t) = 0.0107 R_{eg}^{0.67} P_r^{0.33}. \tag{3}$$

$$\mu_{w,app} = K\left(\frac{3n+1}{4n}\right)^n \left(\frac{8v}{D}\right)^{n-1}. \tag{4}$$

$$R_{eg} = \frac{\rho_a D_{eff} v}{\mu_{w.app}}. \tag{5}$$

$$P_r = \frac{\mu_{w,app} C_m}{k_m}. \tag{6}$$

$$v = \frac{q}{15\pi D^2}. \tag{7}$$

where: h is the heat transfer coefficient between casing wall and fluid, W/(m^2 °C); N_u is the Nusselt number; D is the casing diameter, m; D_{eff} is the equivalent diameter, m; ρ_a mud density, kg/m^3; $\mu_{w,app}$ is the apparent viscosity, Pa s; v is the fluid speed, m/s; q is the pump rate, m^3/min; C_m is the specific heat capacity, kg °C.

The convective heat transfer coefficient between the fracturing fluid and the casing inner wall under different pump rate can be calculated by the above equations, and then the bottom-hole temperature change can be calculated.

Transient Thermal-Pressure Coupling Model

After the cement slurry is solidified, the casing, the cement sheath and the surrounding rock will be consolidated as a whole. Assuming that the cement is well, without sliding. The three parts are uniform homogeneous thermos-elastic [15, 16]. The combination of temperature-pressure coupling model is established based on the theory of thermos-elasticity, as shown in Fig. 1.

Since the axial dimension of the assembly is much larger than the radial dimension, the assembly can be simplified as a planar strain model [17]. That is, there is strain in the radial direction and no strain in the axial direction. For the transient temperature stress calculation, since the thermal parameters do not change with time in the considered temperature range, it is possible to superimpose the mechanical analysis step after the whole transient temperature field analysis is completed. In this way, the stress of the CCF can be calculate under the effect of thermal-pressure coupling.

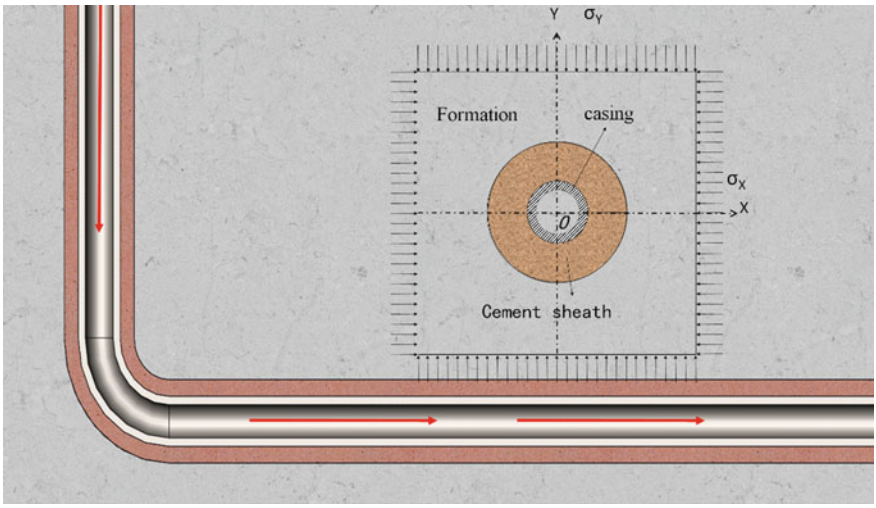

Fig. 1 Thermal-pressure coupling model

Cement Conditions

By statistically analyzing the cementing quality of X shale gas well in Sichuan, the cementing quality in casing failure section is obtained, as shown in Figs. 2 and 3. Several casing deformation occur at which the cement quality is poor.

The typical characteristic of poor cementing quality is the cement channeling. The size of the cement channel is described by the cement channel angle α (Fig. 4) with range between 0° and 360°.

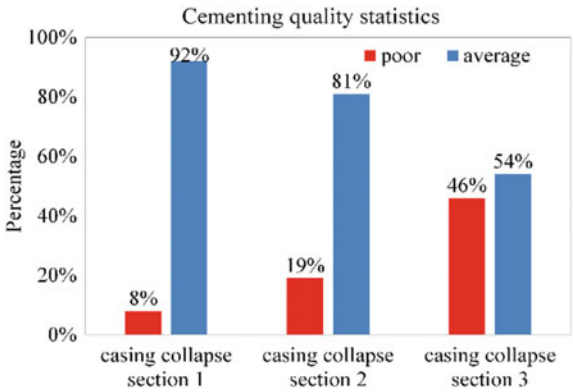

Fig. 2 Cementing quality statistics of X shale gas

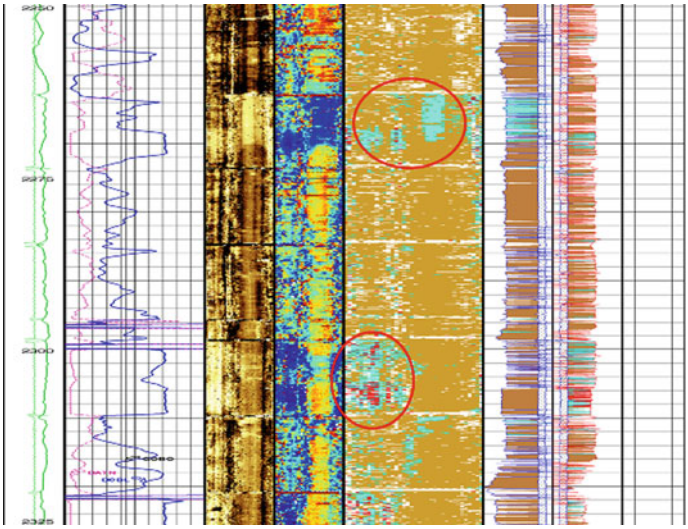

Fig. 3 SLG imaging of X shale well

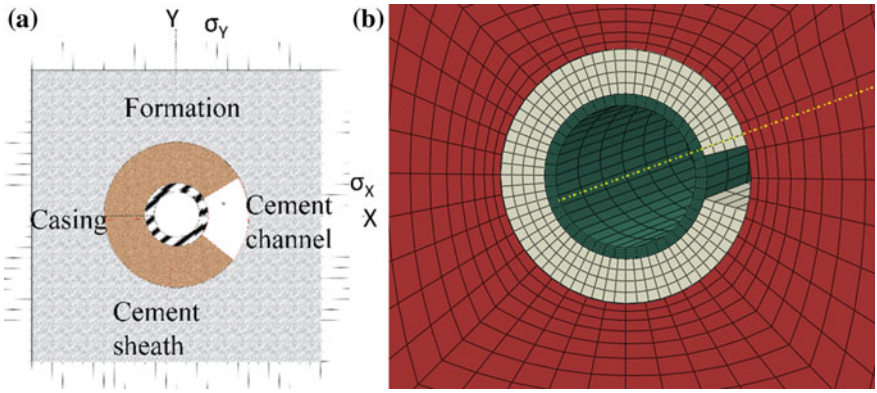

Fig. 4 Cement channel model

Parameters Setting

Basic Parameters

(See Table 1).

Casing Plastic Harden Parameter

The model has two features to simulate plastic hardening in cyclic loading conditions: the centre of the yield surface moves in stress space (kinematic hardening behaviour), and the size of the yield surface evolves with inelastic deformation (isotropic hardening behaviour). This combination of kinematic and isotropic hardening components is introduced to model the Bauschinger effect and other phenomena such as plastic shakedown, ratchetting, and relaxation of the mean stress.

The nonlinear evolution of the centre of the yield surface is defined by the equation:

$$\dot{\alpha} = C\frac{1}{\sigma^0}(\boldsymbol{\sigma} - \boldsymbol{\alpha})\dot{\bar{\varepsilon}}^{\mathrm{pl}} - \gamma\boldsymbol{\alpha}\dot{\bar{\varepsilon}}^{\mathrm{pl}}. \tag{8}$$

where: is the back stress, MPa; σ^0 is the size of the yield surface (size of the elastic range), MPa; $\bar{\varepsilon}^{\mathrm{pl}} = \int \mathrm{d}\bar{\varepsilon}^{\mathrm{pl}} = \int (\frac{2}{3}\mathrm{d}\varepsilon_{ij}^{\mathrm{pl}} \cdot \mathrm{d}\varepsilon_{ij}^{\mathrm{pl}})^{1/2}$ is the equivalent plastic strain, C is the initial hardening modulus, MPa, γ is the rate at which the hardening modulus decreases with increasing plastic strain; $\bar{\alpha} = \sqrt{\boldsymbol{\alpha}^{dev} : \boldsymbol{\alpha}^{dev}}$ is the limiting value of the

Table 1 Basic parameters

Parameters	Value	Parameters	Value
Wellbore diameter [mm]	215.9	Maximum horizontal stress σ_H [Mpa]	48
Casing diameter [mm]	139.7	Minimum horizontal stress σ_h [Mpa]	29
Casing thickness [mm]	9.17	Vertical stress σ_v [Mpa]	35
Boundary diameter [mm]	3000	Vertical stress gradient [MPa/m]	0.023
Casing elastic module E [GPa]	210	Geothermal gradient [K/m]	0.025
Casing Poisson's ratio μ	0.3	Pump rate q [m^3/min]	1–20
Casing thermal expansion coefficient $\alpha \times 10^{-5}$ [K]	1.06	Consistency coefficient K [$Pa\ s^{-n}$]	0.01–1
Cement elastic module E [GPa]	10	Flow index n [s^n]	0.1–1
Cement Poisson's ratio μ	0.17	Fracturing fluid temperature [° C]	100
Cement thermal expansion coefficient $\alpha \times 10^{-5}$ [K]	1.0	Specific heat capacity C_{pi} [J/(kg K) (i = 0,1,2,3)]	3935, 460, 1830, 1043
Formation elastic module E [GPa]	22	Thermal conductivity K_i/[J/(m s K) (i = 0,1,2,3)]	1.73, 58.2, 1.74, 1.0
Formation Poisson's ratio μ	0.23	Density ρ_i [kg/m^3 (i = 0,1,2,3)]	1080, 7850, 1800, 2500
Formation thermal expansion coefficient $\alpha \times 10^{-5}$ [K]	1.02	Vertical depth [m]	1500

Table 2 Kinematic hardening behavior parameters

σ_O [MPa]	C [GPa]	γ
550	25.5	81

equivalent back stress, MPa; $\sqrt{2/3}C/\gamma$ defines the $\bar{\alpha}$; further hardening is possible only through changing the size of the yield surface (isotropic hardening) (Table 2).

The isotropic hardening behavior of this material is modeled with the exponential law:

$$\sigma^0 = \sigma|_0 + Q_\infty(1 - e^{-b\bar{\varepsilon}^{pl}}). \tag{9}$$

where $\sigma|_0$ is the initial yield surface, MPa. Q_∞ is the maximum increase in the elastic range, and b defines the rate at which the maximum size is reached as plastic straining develops. The material hardened state is represented by specifying an initial equivalent plastic strain $\bar{\varepsilon}^{pl}|_0$ (so that σ^0=761 MPa for $\sigma|_0$=550 MPa) (Table 3).

Table 3 Isotropic hardening behavior parameters

Q_∞ [MPa]	b	ε_0^{pl}
2000	0.26	0.43

Table 4 Isotropic hardening behavior parameters

α_{01} [MPa]	α_{02} [MPa]	α_{03} [MPa]
128	−181	53

The back stress is defined by $\dot{\alpha}_k = C_k \frac{1}{\sigma^0}(\boldsymbol{\sigma} - \boldsymbol{\alpha})\dot{\bar{\varepsilon}}^{pl} - \gamma_k \boldsymbol{\alpha}_k \dot{\bar{\varepsilon}}^{pl}$, and the initial back stress tensor is shown in Table 4.

When the Von Mises stress of the casing reaches the casing yielding stress, the casing tends to be failure. Casing yielding failure is expressed in Eq. 10.

Yielding failure:

$$f(J_2, k) = \sqrt{J_2} - k(\kappa) = 0. \tag{10}$$

$$J_2 = \frac{1}{2} s_{ij} s_{ij}. \tag{11}$$

where $s_{ij} = \sigma_{ij} - \frac{1}{3}\sigma_{kk}\delta_{ij}$ is the deviatoric stress tensor, MPa; σ_{ij} is the stress tensor, MPa; σ_{kk} is the average stress tensor, MPa; δ_{ij} is the Kronecker sign, $i = j, \delta_{ij}$=1, $i \neq j, \delta_{ij}$= 0.

Hydraulic Fracturing Pressure

Typical pressures during hydraulic fracturing operation are shown in Fig. 5.

From Fig. 5, it can be seen that the pressure increases with the increase of the number of fracturing stage. Every fracturing stage can last more than one hour. So this time could be set as the fracturing time in the finite model. And to simulate the increasing pressure, the pressure in the analysis steps are shown in Fig. 6. It can be seen as the cyclic loading conditions for asymmetric equal—amplitude stress control.

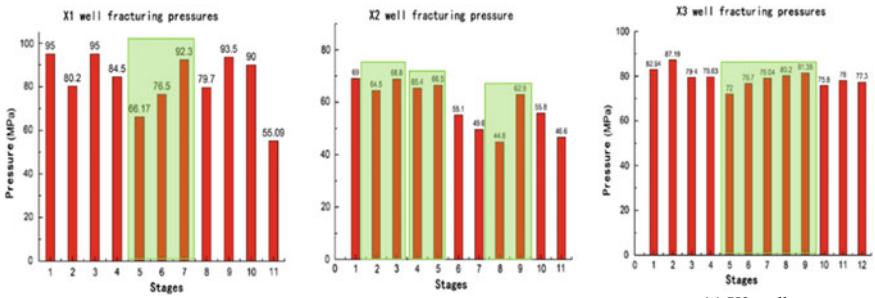

(a) X1 well (b) X2 well (c) X3 well

Fig. 5 Multi-stage fracturing pressure **a** X1 well **b** X2 well **c** X3 well

Fig. 6 Multi-stage fracturing pressure in finite model

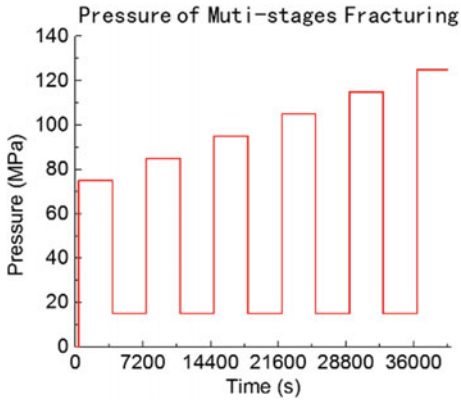

Model Validation

For the reason of complexity of 3D model, the plane strain model is used to validate the numerical solutions. The basic parameters are shown in the Table 1. CCF stresses with cement channel angle of 0° are calculated by the theoretical and numerical method. The comparisons of radial stress and hoop stress are shown in the Fig. 7.

It is clearly shown from Fig. 7 that solutions obtained by the numerical method are in good agreement with that by the theoretical method, validating the correction of the numerical method. It also shows that radial stress is compressive stress. The absolute value of the radial compressive stress decreases along the radius of casing and cement, while increasing along the radius of formation. The casing hoop stress is positive and the biggest among the three sections. Using this FEM model, the influences of different factors are analyzed to reveal how those factors affect the casing stress.

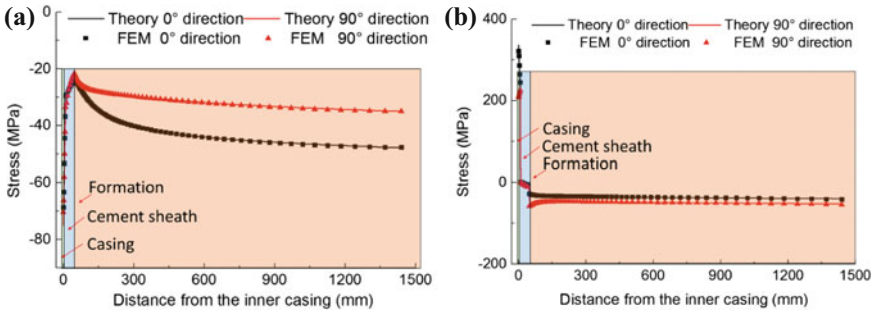

Fig. 7 Comparison of radial stress and hoop stress with the theoretical and numerical method **a** radial stress **b** hoop stress

Results Analysis

Heat Transfer Coefficient

The rheological parameter and pump rate will affect the heat transfer coefficient. From the Eqs. 2–7, the heat transfer coefficient can be calculated under different rheological parameters and pump rate during fracturing operation.

Figure 8 presents the effect of n (the consistency coefficient) and K (the flow index) on the heat transfer coefficient (h). For $n = 0.8$, the h increases with the increase of Q (the pump rate), and decreases with the increase of the K. For $K = 0.08$, the h increases with the increase of Q and n. Therefore the appropriate heat transfer coefficient can be obtained through adjusting the rheological parameters and pump rate.

The rheological parameters of the fracturing fluid are $K = 0.08$, $n = 0.8$. The fracturing pump rates are 0/1//3/6/20 m^3/min, and the corresponding heat transfer coefficient can be calculated as following (Table 5).

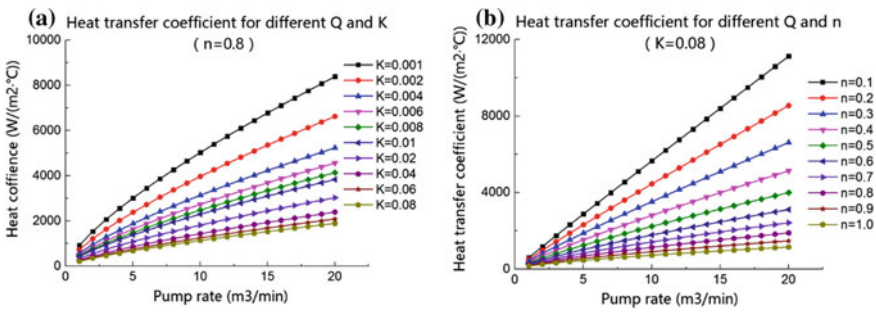

Fig. 8 Variation curve of h under different rheological parameters

Table 5 Heat transfer coefficient for different pump rates

K [s^n]	n [Pa/s^n]	Q [m^3/min]	h [W/(m^2 K)]
0.08	0.8	0	50
		1	107
		3	466
		6	777
		20	1890

Effect of Pump Rate

Transient Temperature

The cement channel is serious in shale gas horizontal wells. The channel alone has some effects on the casing transient temperature. Figure 9 shows that the transient temperature decreases dramatically, then increases slowly to the formation temperature during multi-fracturing construction. For small pump rate, the lowest temperature for 60 channel angle is 10 °C lower than that of 0 channel angle. When the pump rate is large enough, the temperatures for 0° and 60° are almost the same.

Casing Stress and Strain

It is shown in Fig. 10 that with the same fracturing stage, the casing maximum Von Mises stress and PEEQ (Equivalent plastic strain) happens at the pump rate between 3 and 6 m^3/min. At the pump rate beyond 6 m^3/min, the casing maximum Von Mises stress and PEEQ remain constant. It is interesting that for the same pump rate, the casing maximum Von Mises stress increases with the increase of the number of fracturing stage. During the 6 cyclic fracturing process, the maximum

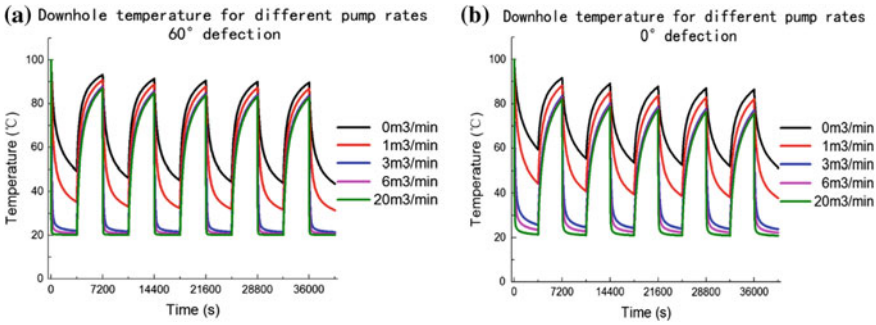

Fig. 9 Temperature for different pump rate with cement channel

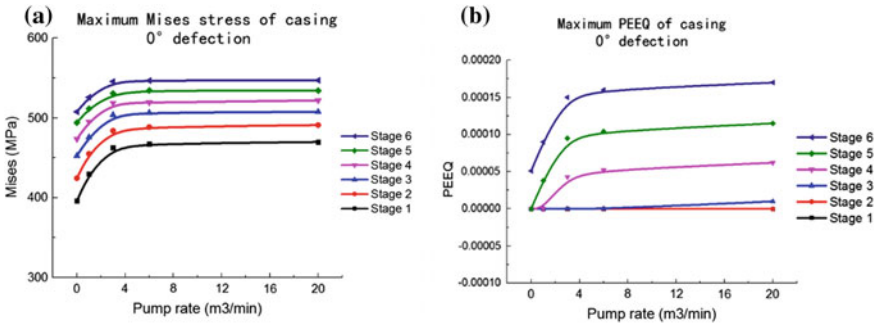

Fig. 10 Von Mises stress and PEEQ of casing for different pump rate

Von Mises stress reaches 550 MPa, which has already reached the plastic state. From the 4th stage, casing PEEQ begins to appear and the law of the casing PEEQ increase is similar to the Von Mises.

Effect of Fluid Temperature

Transient Temperature

Figure 11 shows that, when large amount of low temperature fluid are pumped into the wellbore, the downhole temperature can quickly reduce to be the same as the pumping fluid temperature in very short time. The lower the fluid temperature is, the lower the degree of downhole temperature reduction will be. No matter what the cement channel angle is, the transient temperature for different fluid temperature are almost the same during multi-stage fracturing construction.

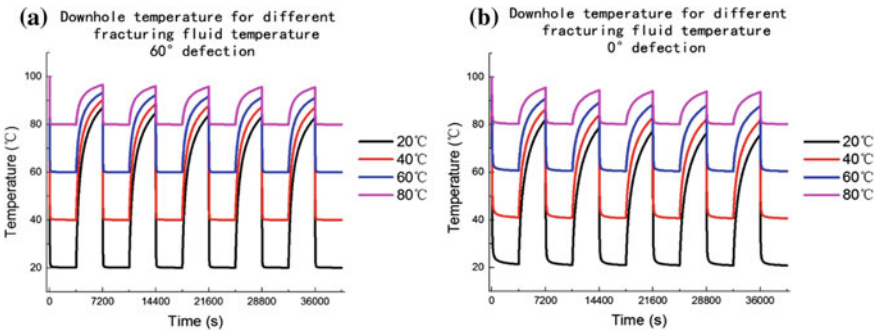

Fig. 11 Casing inner transient temperature for different fracturing fluid temperature

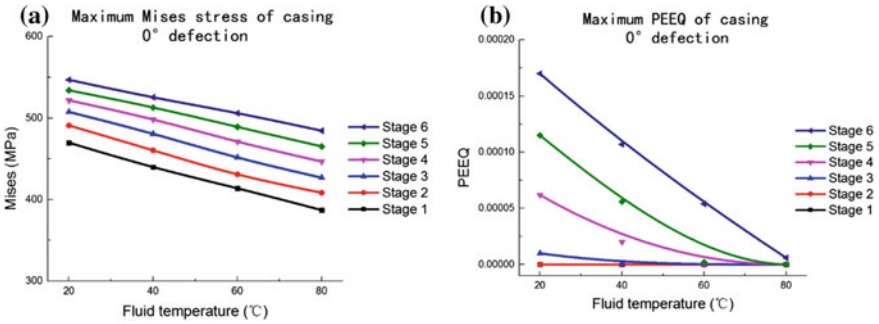

Fig. 12 Von Mises stress and PEEQ of casing for different fluid temperature

Casing Stress and Strain

Figure 12 presents that lower fracturing fluid temperature tends to increase casing stress and PEEQ. In the same stage, with the fluid temperature decreasing, the Von Mises and PEEQ increases for the reason that lower temperature produces more thermal stress. In stage 1, the casing Von Mises stress for 20 °C fluid can be almost 83 MPa larger than that for 80 °C fluid. The casing stress and PEEQ can increase with the increasing of the fracturing stage. When the fluid temperature reaches 80 °C, the casing PEEQ is almost zero for different fracturing stages.

Effect of Cement Channel Angle

Transient Temperature

Figure 13 shows that at the fluid temperature of 20 °C, the transient downhole temperatures are the almost the same for different channel angles when the fluid is

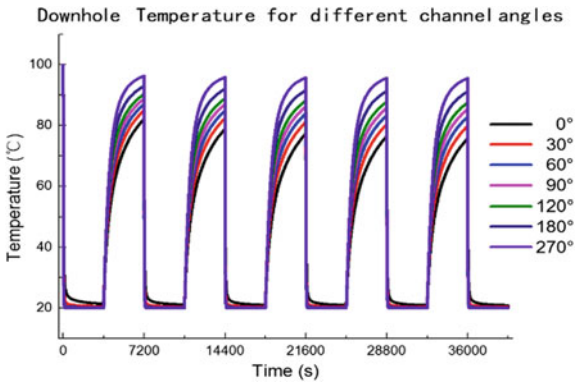

Fig. 13 Temperature for different cement channel angles

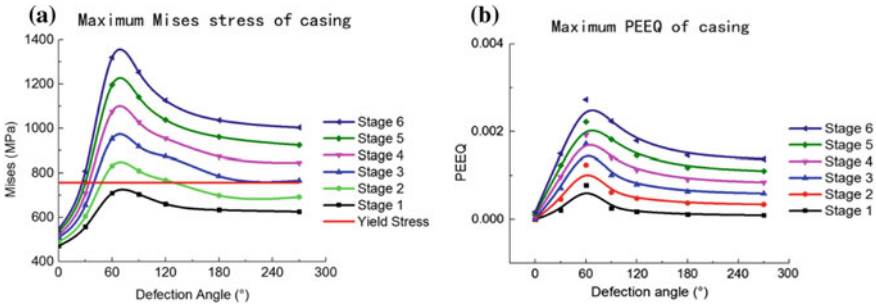

Fig. 14 Von Mises stress and PEEQ of casing for different defection angles

pumped into the wellbore at the rate of 20 m^3/min. After one stage fracturing, the temperature return slowly to the formation temperature. The greater the channel angle is, the closer the downhole temperature to the formation temperature will be.

Casing Stress and Strain

Figure 14 shows that at the cement channel angle from between 60° and 90°, the casing has the highest Von Mises stress and PEEQ. At stage 1, the maximum stress is 50% larger than that of good cement, and 140% larger than that at stage 6. The fracturing pressure also tends to increase casing Von Mises and PEEQ, which is clear in the previous researches. For the casing of P110 steel grade, the yield stress is 758 MPa. At the stage 2, the casing stress will exceed the yield stress at the cement channel angle between 60° and 120°, which means casing failure, as the Fig. 14a. In the following fracturing stage, casing stress gets much larger than the first stage.

Conclusions

This paper presents the sensitivities of the variables and gives a better understanding of the effect of cement complications and fracturing parameters on the shale gas well integrity. Transient thermal-pressure coupling finite element model is established to simulate the influence of pump rate, fluid temperature and cement channeling on casing stress. It can be concluded from the results that:

(1) Among all the factors, the cement channel has the greatest influence on casing stress. At the cement channel angle from between 60° and 90°, the Von Mises stress and PEEQ of casing are the highest. The fracturing pressure also tends to increase casing Von Mises stress and PEEQ.

(2) While the transient temperature drops dramatically, a certain thermal stress is generated in the casing. The maximum casing Von Mises stress and PEEQ appear at the pump rate between 3 and 6 m^3/min. At the pump rate beyond 6 m^3/min, the stress and PEEQ remain constant. For the same pump rate, the more the fracturing stage is, the larger the casing stress and PEEQ are.
(3) Lower fracturing fluid temperature tends to increase casing stress and PEEQ. At the same stage, the Von Mises stress and PEEQ increase with the fluid temperature decreasing. The more the fracturing stage is, the larger the casing stress and PEEQ are.

Good cement sheath is the basic requirement to ensure the safety of casing. The pump rate and fluid temperature should be in a reasonable range. During multi-stage fracturing process, pressure should also not be too high to avoid increasing stress and PEEQ of the casing.

Acknowledgements The authors thank the National Natural Science Foundation "Study on optimization of un-uniform clustering perforation for long horizontal inhomogeneous shale formation" (Item No. 51674272), National Science and Technology Major Project "Optimizing technology of cluster perforation completion design in complicated structure wells" (Item No. 2017ZX05009), the Science Foundation of China University of Petroleum (Beijing) "Research on optimization method of cluster perforation parameters in anisotropy shale gas reservoirs" (Item No. 2462015QZDX05), and the State Key Laboratory of Shale Oil and Gas Enrichment Mechanisms and Effective Development "Research on casing loading spectrum under multi-factor coupling effect in shale gas wells", for contributions to this paper.

References

1. T. Zhonglan, S. Lin, Q. Lei, Research of and countermeasure for wellbore integrity of shale gas horizontal well. Nat. Gas. Ind. **35**(09), 70–76 (2015)
2. N.C. Last, S. Mujica, P.D. Pattillo et al., Evaluation, impact, and management of casing deformation caused by tectonic forces in the Andean foothills, Colombia. SPE Drill. Completion **21**(02), 116–124 (2006)
3. L. Zhanghua, Y. Hao, L. Tie et al., A study on casing deformation failure during multi-stage hydraulic fracturing for the stimulated reservoir volume of horizontal shale wells. J. Nat. Gas Sci. Eng. **23**, 538–546 (2015)
4. K.J. Goodwin, R.J. Crook, Cement sheath stress failure. SPE Drill. Eng. **7**(04), 291–296 (1992)
5. A. Berger, W.W. Fleckenstein, A.W. Eustes, et al., Effect of eccentricity, voids, cement channels, and pore pressure decline on collapse resistance of casing. SPE 90045 (2004)
6. Y. Zhaoguang, J.J. Schubert, C. Teodoriu, The effect of hole angle and cementing complications on HPHT well integrity. SPE 162839 (2012)
7. G.E. King, R.L. Valencia, Well integrity for fracturing and re-fracturing: what is needed and why? SPE Hydraulic Fracturing Technology Conference. Society of Petroleum Engineers (2016)
8. J. De Andrade, M. Torsæter, J. Todorovic, et al., Influence of casing centralization on cement sheath integrity during thermal cycling. IADC/SPE Drilling Conference and Exhibition. Society of Petroleum Engineers (2014)

9. P. Quanlin, H. Shiming, Z. Jingcheng, Research on the influence of defective cement ring on casing strength. Drill. Prod. Technol. **40**(04), 35–37 (2015)
10. Y. Hao, L. Zhanghua, X. Xiaoling et al., An analysis of hydraulic fracturing technology in shale gas wells and its application. China Pet. Mach. **43**(03), 73–77 (2015)
11. F. Mingtao, L. Gonghui, L. Jun et al., Effect of cementing quality on casing stress of shale gas well under heat-mechanical coupling. China Pet. Mach. **44**(08), 1–5 (2016)
12. L. Jun, C. Mian, Z. Hui et al., Influence of cement sheath shape on casing stress under different ground stress conditions. Nat. Gas. Ind. **24**(08), 50–52 (2004)
13. L. Jun, C. Mian, L. Gonghui et al., Elastic-plastic analysis of casing-concrete sheath-rock combination. Acta Petrolei Sin. **26**(06), 99–103 (2005)
14. Y. Hao, L. Zhanghua, L. Tiejun, Finite element analysis of failure mechanism of casing during shale gas fracturing. China Pet. Mach. **42**(08), 84–88, 93 (2014)
15. C. Sugden, J. Johnson, M. Chambers, et al., Special considerations in the design optimization of high rate, multistage fractured shale wells. Society of Petroleum Engineers. SPE 151470 (2012)
16. L. Kui, W. Yanbin, G. Deli et al., Effects of hydraulic fracturing on horizontal wellbore for shale gas. Acta Petrolei Sin. **37**(03), 406–414 (2015)
17. Z. Xinbo, H. Shengchao, Y. Xiujuan et al., Mechanical characteristics analysis of casing-cement sheath—formation multilayer composite system with thermo-structural coupling effects. J. Cent. S. Univ. (Sci. Technol.) **48**(03), 837–843 (2017)

Simulation Analysis of the Strain Behaviour of X80 Girth Weld Joint

Shixin Wang, Zhiwen Li, Zhenglong Li, Zhaojun Zhang and Changchai Han

Abstract As the service environment of the pipeline is becoming worse and worse, large plastic deformation may occur at any time when the pipeline through the poor geological area. The load of the pipeline consists of the tension load and the internal pressure load while the main failure mode of the high-grade steel is ductile fracture. In order to study the influence of the tension load and the internal pressure load on the strain capacity of the X80 high deformation steel with circumferential cracks, the GTN (Gurson–Tvergaard–Needleman) model was adopted for analysis with both X80 high deformation steel wide plate and pipe. The results showed that the crack propagation could be divided into the blunting stage, the unstable flaw growth stage and the stable flaw growth stage. CTOD increased with the crack propagation in the process, the softening of weld heat affected zone could lead to the weak of the strain capacity. The toughness of the X80 high deformation steel under a certain crack size became worse gradually with the increase of softening degree.

Keywords X80 high deformation steel · Ductile fracture · Strain capacity

S. Wang
Hebei Technical College of Petroleum Profession, Langfang, Hebei 065000, China
e-mail: 244734815@qq.com

Z. Li · C. Han
Sci-Tech Information Center, PetroChina West to East Gas Pipeline Company, Wuhan, Hubei 430073, China
e-mail: ywguolei@petrochina.com.cn

C. Han
e-mail: hanchangchai@petrochina.com.cn

Z. Li (✉)
China Petroleum Pipeline Research Institute Co. Ltd., Langfang, Hebei 065000, China
e-mail: upc_lzl@163.com

Z. Zhang
Yinchuan Management Office, PetroChina West to East Gas Pipeline Company, Yinchuan, Ningxia 750000, China
e-mail: XQDSZZJ@126.com

© Springer Nature Singapore Pte Ltd. 2018

Y. Han (ed.), *Advances in Materials Processing*, Lecture Notes in Mechanical Engineering, https://doi.org/10.1007/978-981-13-0107-0_100

Introduction

As one of the most economical modes for oil and natural gas transportation, the pipeline transportation has gradually developed into more remote areas in the world, which have a large number of poor geological areas such as landslides, floods, frozen soil, etc. making the service environment of pipelines worse and worse. And large plastic deformation may occur at any time in these areas. High deformation pipeline steel has become the preferred material in these areas because of its lower yield ratio, higher deformation hardening index and greater uniform elongation.

During the pipeline operation, the load of the pipeline consists of the tension load and the internal pressure load while the main failure mode of the high-grade steel is ductile fracture. So, study on the strain-based fracture assessment of the X80 high deformation (X80HD) pipeline and analyze the variation of its strain capacity are of great significance for the safe operation of pipelines.

Theoretical Model

Ductile tearing process of the metal material mainly consists of the nucleation of pores, the growth of pores and the aggregation of pores forming macroscopic cracks. The best model for the pore theory was proposed by Gurson and improved by Tvergaard and Needleman which is called the Gurson–Tvergaard–Needleman (GTN) model [1–3]. Its specific expression form is as follows.

$$\Phi = (\sigma_\varepsilon/\sigma_f)^2 + 2\,q_1 f cosh(3\,q_2\sigma_m/2\sigma_f) - 1 - (q_3 f^*)^2 = 0 \tag{1}$$

In Eq. 1, σ_ε is the Von Mises equivalent stress, σ_f is the flow stress of the base metal, f is the volume fraction of the pores, σ_m is the mean normal stress of the pores, q_1, q_2, and q_3 are constants, f^* is the active volume fraction of the pores expressing as follows.

$$\text{For}\, f \leqslant f_c, f^* = f \tag{2}$$

$$\text{For}\, f_c \leqslant f \leqslant f_F, f^* = f_c + (f^* u - f_c)(f - f_c)/(f_F - f_c) \tag{3}$$

$$\text{For}\, f \geqslant f_F, f^* = f_F \tag{4}$$

In Eq. 2, if $f > f_c$ and $f^* u = 1/q_1$, f_c represents the critical volume fraction of the pores when the pores begin to aggregate, f_F is the critical volume fraction of the pores when the material breaks.

Finite Element Model

Basic Assumption

The analysis in the paper are based on the following simplifications or assumptions.

(1) The whole heat affected zone (HAZ) material of the welded joint is assumed to be coincident. That is to say, the material softening level of the HAZ is uniform in the model. The yield strength and tensile strength of the HAZ material are entirety decreased based on the softening level while its elasticity modulus and Poisson ratio keep in line with the base metal.
(2) The depth of the internal surface crack is assumed to be uniform. The size is 4 mm and its circumferential length is 50 mm. A 4 mm diameter arc transition is used at both ends of the crack. This shape of the crack can well represent the shape of the actual annular weld crack [4–6]. All the softening zone widths are fixed to be 5 mm while its influence is ignored.
(3) It is assumed that softening does not change the distribution and spacing of the second phase particles or inclusions in the HAZ material, hence the fracture mechanics parameters in this paper are still valid for HAZ materials.
(4) The effect of mismatch of weld strength on heat affected zone is not studied. For convenience of calculation, it is assumed that the strength of welded metal is the same as that of base metal.

Modeling

1/2 model of the Φ1219 × 26.4 mm wide plate and pipe are established on the basic of the assumptions. The circumferential width (W) of the wide plate is 600 mm while its length is 4.5 W. The crack has a circumferential length of 50 mm and a depth of 4 mm as it is showed in Fig. 1. The length and crack size of the pipe model are the same as the wide plate. Crack on the girth weld center and the HAZ are both simulated, and their locations are showed in Fig. 2.

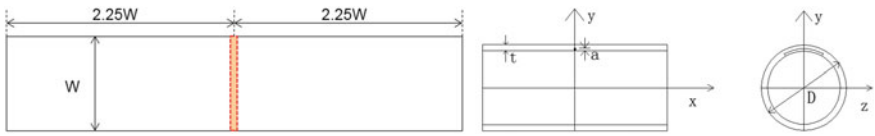

(a) Geometric dimension of the wide plate (b) Geometric dimension of the pipe

Fig. 1 Geometric dimension of the plate and the pipe

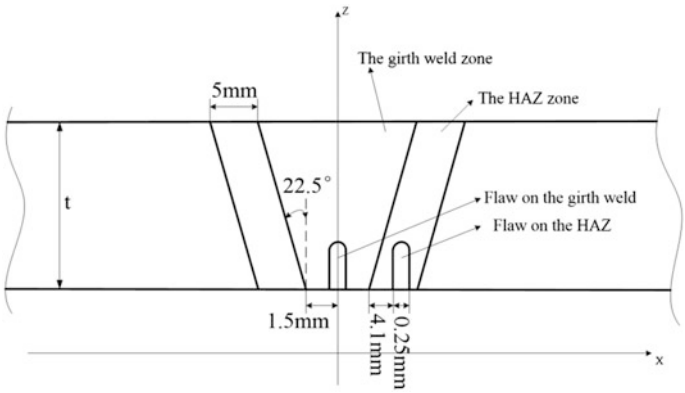

Fig. 2 Crack location of the plate and the pipe

Set of Parameters

In the ABAQUS simulations, the metal property consists of the elastoplastic metal property and the porous metal plasticity. The R–O (Ramberg–Osgood) model is used to describe the elastoplastic metal property while the GTN model is used to describe the porous metal plasticity. Their parameter values are showed in Tables 1 and 2 separately.

Because of the asymmetry of geometry and boundary condition, the axial displacement is applied at one end of the model far from the crack, and the whole constraint is applied at the other end, and the symmetry constraint is applied to the symmetry surface. In addition to the above constraints, a 12 MPa internal pressure should be applied to the inner surface of the pipe and the inner surface of the crack. The loads and boundary conditions of the models are shown in Fig. 3.

Table 1 Pipe characteristic and the R–O model parameters

Steel grade	Thickness [mm]	Modulus of elasticity [GPa]	Yield strength [MPa]	Tensile strength [MPa]	Ultimate strain [100%]	Yield offset, α
X80HD	26.4	206	566	726	4.24	22.54

Table 2 GTN model parameters

q_1	q_2	q_3	f_0	f_c	f_F
1.5	1	2.25	0.00015	0.013	0.1503

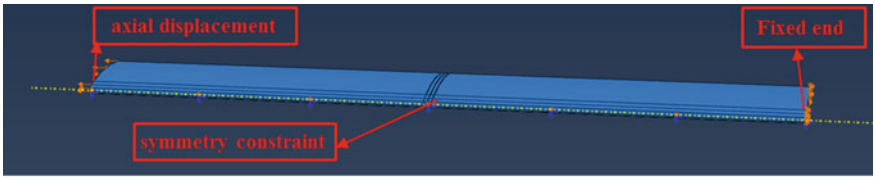

(a) 1/2 wide plate model with crack on the weld center

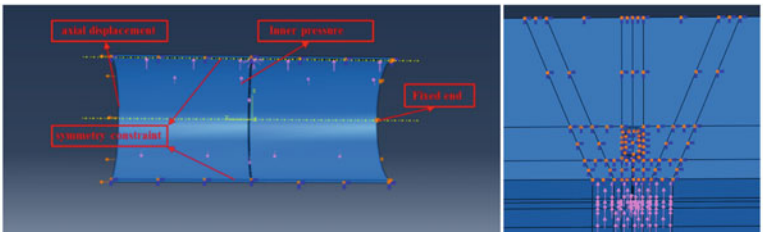

(b) 1/2 pipe model with crack on the weld center

Fig. 3 Loads and boundary conditions of the models

A C3D8R reduced integration unit is used in the finite element model. The crack propagation region of the cell size is fixed at 0.125 mm, and a transition sketch mode is used for the units away from the crack tip to realize the mesh sketch transition from coarse to fine. Crack tip structure of semicircle arc is used to simulate the blunting process of the crack tip which can obtain a coincident crack growth resistance curve with the actual experiment results. The mesh of the model is showed in Fig. 4.

Analysis of the Simulation Results

Characterization of the Fracture Parameters

Characterization of the crack tip opening displacement (CTOD) is showed in Fig. 5. The CTOD value is fixed as the displacement of the end of the ¼ arc after the initiation of the crack tip when calculating the CTOD—Δa crack growth resistance curve.

In the post-processing of ABAQUS software, the color change of stress nephogram reflects the change of stress condition of the material in the model. The stress level decreases in turn from red to orange to green to blue.

In the simulation, the stress level at the crack tip of the X80HD wide plate begins to increase due to the far end stretching displacement, and the color of the crack tip changes from blue to red gradually. When the pore volume fraction value of a crack tip element runs up to the critical pore volume fraction (f_F), the element loses the

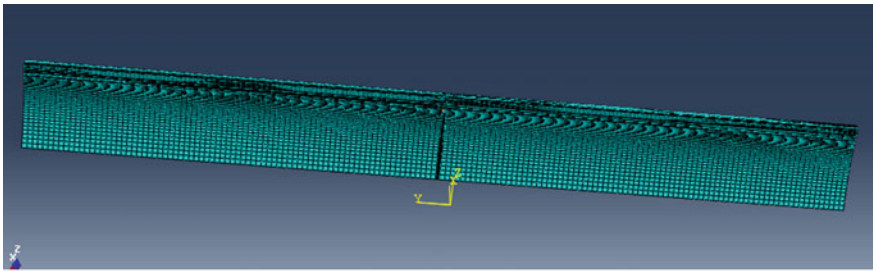

(a) Mesh of the 1/2 wide plate model with crack on the weld center

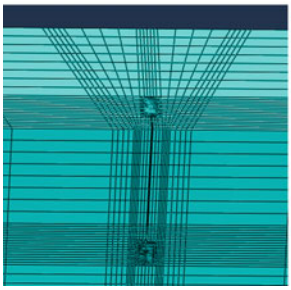

(b) Local mesh of crack tip

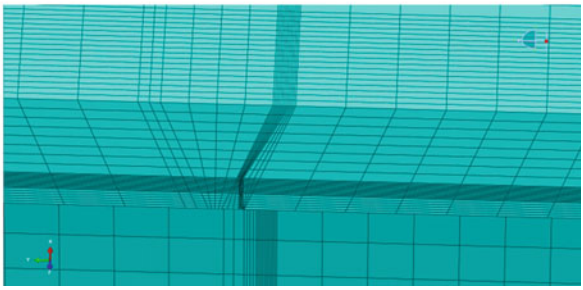

(c) Local mesh of the 1/2 pipe model with crack on the HAZ

Fig. 4 Mesh of the finite element models

Fig. 5 Characterization of CTOD (the left figure)

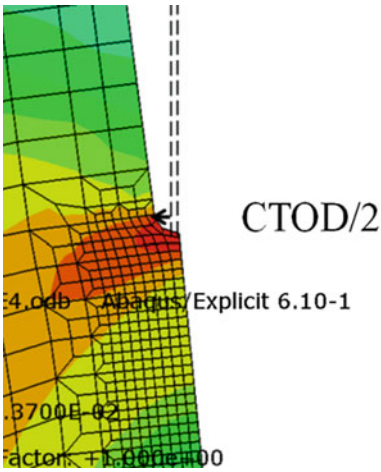

load carrying capacity and begins to release with its color changing from red to blue gradually and eventually disappear. At the same time, the crack tip extends forwards which can simulate the fracture effect.

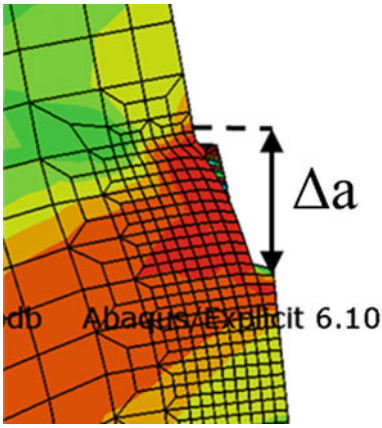

Fig. 6 Characterization of the crack propagation length Δa (the right figure)

The crack propagation length (Δa) is the length between the crack tip and the point of the initial crack as it is showed in Fig. 6. The values of CTOD and Δa are taken at the previous increment step.

Analysis of the Simulation Results

In order to study the influence of circumferential surface crack defects on the strain capacity of pipelines, ½ model of the wide plate and pipe with circumferential surface crack on the weld center and the HAZ are established separately. And the HAZ softening at 0, 5, 10, 15% are simulated. The results are showed in Figs. 7 and 8. In the figures, the CWP-HAZ represent the wide plate model with crack on the

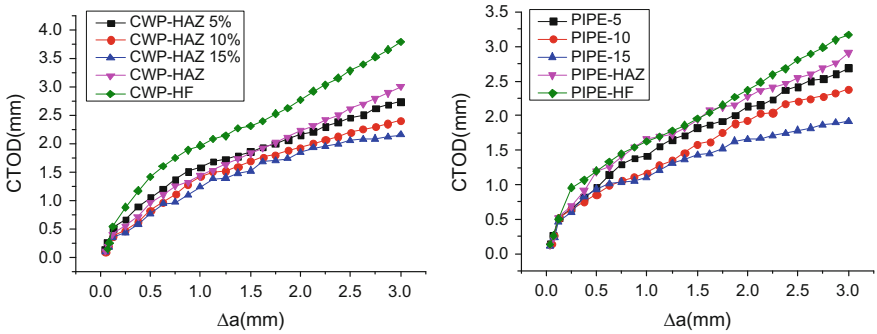

(a) CTOD-Δa curve of the wide plate (b) CTOD-Δa curve of the pipe

Fig. 7 CTOD-Δa curves of the X80HD wide plate and pipe at different softening levels

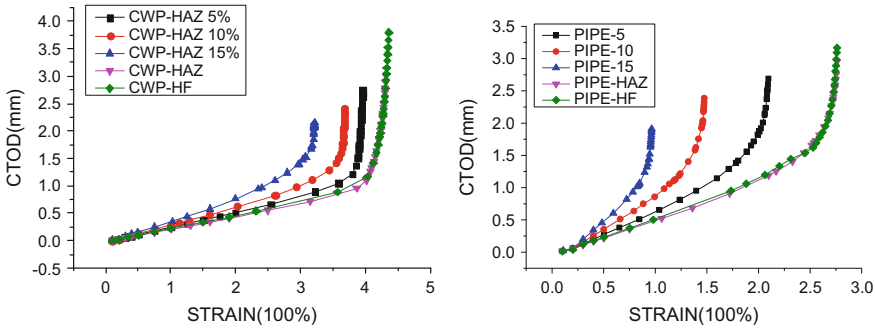

(a) Strain-CTOD curve of the wide plate (b) Strain-CTOD curve of the pipe

Fig. 8 Strain-CTOD curves of the X80HD wide plate and pipe at different softening levels

HAZ, the CWP-HF represent the wide plate model with crack on the weld center, the PIPE-HAZ represent the pipe model with crack on the HAZ, the PIPE-HF represent the pipe model with crack on the weld center, and 5, 10, and 15 represent the degrees of softening.

Figure 7 showed the CTOD-Δa curves of the X80HD wide plate and pipe at different softening levels.

From Fig. 7 it can be seen that:

(1) CTOD increases with the crack propagation in the process, and the crack propagation can be divided into the blunting stage, the unstable flaw growth stage and the stable flaw growth stage. The corresponding curve slope of CTOD-Δa first increases, then decreases, and eventually remains constant.
(2) Softening of HAZ can remarkably affect the CTOD-Δa curve. The toughness of the X80HD wide plate and pipe under a certain crack size becomes worse gradually with the increase of softening degree.

Figure 8 showed the Strain-CTOD curves of the X80HD wide plate and pipe at different softening levels.

From Fig. 8 it can be seen that:

(1) With the increase of the strain, CTOD firstly increases steadily and linearly. When the strain reaches a certain value, CTOD increases sharply, indicating that the width plate and the pipe have failed. The slope of the Strain-CTOD curve undergoes a linear increase followed by a gradual increase.
(2) The location of the crack has no effect on the Strain-CTOD curve, but with the increase of the softening level, the strain capacity of the wide plate and pipe is worse.
(3) The CTOD values of the cracked wide plate and pipe increase with the increase of softening level when the strain is certain. Cracked wide plate and pipe at high softening level fail at first because softening leads to strain capacity deterioration.

There are two main reasons of the above phenomenon. First, the HAZ softening results in a decrease in the properties of the HAZ material, when the wide plate or pipe is subjected to a tensile load, HAZ defects first leads to the strain concentration, and then the crack begins to expand rapidly. Second, as the material properties of HAZ have a trend of step change, but this paper assumes the HAZ has softened at the same level which increase the width of HAZ in a sense leading to the increasing of the HAZ strain concentration coefficient and rapid expansion of cracks.

Conclusion

The crack has a same impact on the X80HD wide plate and pipe. In the process of the crack propagation, the crack tip has gone through the blunting stage, the unstable flaw growth stage and the stable flaw growth stage. The toughness of the X80HD wide plate and pipe under a certain crack size becomes worse gradually with the increase of softening degree.

References

1. V. Tvergaard, Influence of voids on shear band instabilities under plane strain conditions. Int. J. Fract. **17**, 389–407 (1981)
2. V. Tvergaard, On localization in ductile materials containing spherical voids. Int. J. Fract. **18**, 237–252 (1982)
3. V. Tvergaard, A. Needleman, Analysis of the cup-cone fracture in a round tensile bar. Acta Metall. **32**, 157–169 (1984)
4. E. Østby, M. Hauge, et al., Strain capacity of SENT specimens—influence of weld metal mismatch and ductile tearing resistance, in Proceedings of the Eighteenth (2008) International Offshore and Polar Engineering Conference (Vancouver, BC, Canada, 2008 July 6–11)
5. S. Cravero, R.E. Bravo, H.A. Ernst, Constraint evaluation and effects on J–R resistance curves for Pipes under combined load conditions, in Proceedings of the Eighteenth (2008) International Offshore and Polar Engineering Conference (Vancouver, BC, Canada, 2008 July 6–11), pp 149–156
6. L. Xia, C.F. Shih, J.W. Hutchinson, A computational approach to ductile crack growth under large scale yielding conditions. J. Mech. Phys. Solids **43**, 389–413 (1995)

Toughness Scatter About FCAW-S Girth Weld for X80 Pipeline Steel

Youxiao Xu, Feng Wang, Lin Chen, Ziyun Wei and Weichen Song

Abstract The toughness scatter about Flux-Cored Arc Welding Self for X80 pipeline steel was investigated to explore the reason that causes toughness scatter, and how to improve the toughness scatter. The type of the metallography, the volume fraction and the pattern distribution of M/A constituents, and the effects of them to the weld toughness were studied by weld thermal-cycle curves measurement, thermal simulation experiments, Charpy Impact Test, optical microscope observation and SEM. The results showed that the toughness scatter was observed in temperature region of A_{c1}–A_{c3}, MA constituent directly related to the charpy impact toughness, toughness decreased with increasing of the volume fraction of MA constituent. It is considered that bacilliform MA is the main reason that cause toughness scatter, bulk MA is another reason that cause low toughness.

Keywords X80 pipeline · Flux-Cored arc welding self · Girth weld
Toughness scatter · MA constituent

Introduction

The second west-to-east gas transmission pipeline project marked the domestic X80 pipeline steel's first engineering application. However, on the one hand, with the improvements of steel rolling process and pipe manufacturing technique, the new-produced X80 steels are somewhat different than before, on the other hand, more and more steel mills and pipe plants joining into X80 engineering application research in recent years, and each company's manufacture technology is different

Y. Xu · L. Chen · Z. Wei · W. Song
Sinopec Petroleum Engineering Co., Ltd., 49 Jinnan Road, Yingkou 257026, China
e-mail: slecccl@163.com

F. Wang (✉)
China Petroleum Pipeline Research Institute Co., Ltd., 44 Jinguang Road,
Langfang 065000, China
e-mail: jyjwangfeng@163.com

© Springer Nature Singapore Pte Ltd. 2018

Y. Han (ed.), *Advances in Materials Processing*, Lecture Notes in Mechanical Engineering, https://doi.org/10.1007/978-981-13-0107-0_101

than others, the new-produced X80 steels are different from each other, thus, the problem of toughness scatter of X80 girth weld is more prominent. As Flux-Cored Arc Welding Self (abbreviated as FCAW-S) weld still will be a main weld process in China, toughness scatter of SSFC weld for X80 pipeline steel is studied in this paper, the aim is to explore the reason that causes toughness scatter, and how to improve.

The toughness, the volume fraction and the pattern distribution of M/A constituents, and the correlation between them was studied by thermal simulation experiments, the results will be beneficial to improve toughness scatter of X80 girth weld.

Experimental

The pipe grade used for study is X80, it's chemical compositions are shown in Table 1, the welding process is Shielded Metal Arc Welding Flux-Cored Arc Welding Self (abbreviated as SMAW-FCAW-S) refers to "Welding Procedure Specification for The 2nd West-to-East Gas Transmission Pipeline Project" [1], the welding consumable for root welding and filling & caping is KOBE LB52U and JC30 respectively, the chemical composition of the deposited metal is shown in Table 2, chemical composition of weld metal is shown in Table 3.

In the process of welding, the weld thermal-cycle curves were recorded by OMEGA DAQ-USB-2401 to obtain thermal-cycle parameters for thermal simulation experiment. In order to ensure the study weld metal undergoes the same original thermal-cycle and the thickness of the weld metal is thick enough for sampling, the last fill layer thickness is about 5 mm. (The last fill layer thickness is not according to reference [1], which is purely designed for research convenience, and it is the only layer which is not according to reference [1].) Sampling schematic diagram for thermal simulation is shown in Fig. 1. Then the thermal simulated speciments were sampled for Charpy impact test and optical microscope observation and SEM analysis, sampling schematic diagrams are shown in Fig. 2.

Table 1 Chemical composition of X80 pipe

Mass fraction [%]								
C	Si	Mn	P	S	V	Nb	Ti	V + Nb + Ti
0.074	0.184	1.839	0.015	0.008	0.019	0.097	0.011	0.127
Cu	Ni	Cr	Mo	Al	B	Pcm	/	
0.213	0.223	0.099	0.264	0.035	0.001	0.218	/	

Table 2 Chemical composition for deposited metal

Mass fraction [%]								
C	Si	Mn	P	S	V	Nb	Ti	V + Nb + Ti
0.033	0.184	1.440	0.009	0.003	0.003	0.005	0.004	0.012
Cu	Ni	Cr	Mo	Al	B	Pcm	/	
0.011	1.660	0.025	0.006	1.090	/	0.140	/	

Table 3 Chemical composition for weld metal

Mass fraction [%]								
C	Si	Mn	P	S	V	Nb	Ti	V + Nb + Ti
0.0441	0.1970	1.530	0.008	0.004	0.007	0.010	0.007	0.024
Cu	Ni	Cr	Mo	Al	B	Pcm	/	
0.025	1.48	0.070	0.033	0.815	0.002	0.161	/	

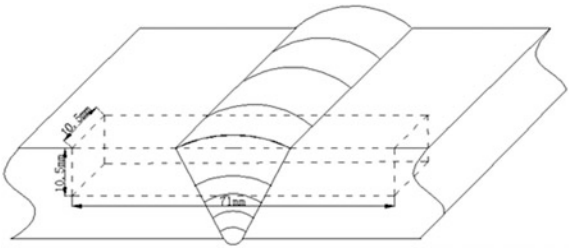

Fig. 1 Schematic diagram for thermal simulation sampling

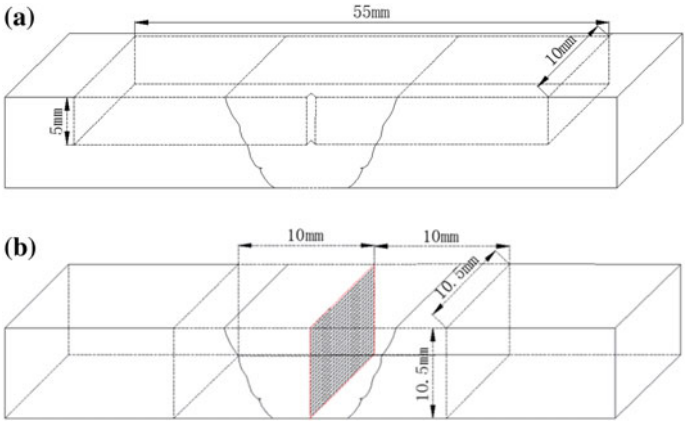

Fig. 2 Schematic diagram for thermal simulated speciments sampling **a** charpy impact sample, **b** metallographic analysis sample

On the basis of the thermal-cycle parameters tested, the thermal simulation of X80 FCAW-S task was carried out on Gleeble 3500. Lepera agentia (1% picric acid: ethyl alcohol & 4% sodium bisulfite: purified water mix with 1:1) was used to show MA constituents.

In addition, the transformation temperature and the CCT curves of JC30 are also tested for use by thermal dilation method.

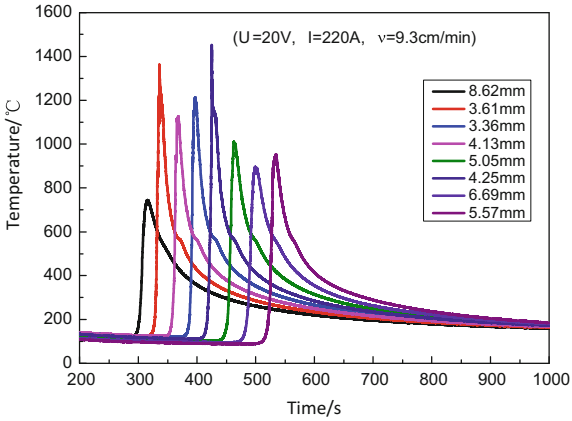

Fig. 3 Measured thermal-cycle curves

Results

Thermal-Cycle Curves

The obtained thermal-cycle curves are shown in Fig. 3, thermal-cycle curves of the tested points with different distance from the heat source are presented with different colors.

Transformation Temperature

The transformation temperatures and CCT curves of JC30 are shown in Fig. 4. A_{c1} is about 700 °C and A_{c3} is about 880 °C for JC30.

On the basis of thermal-cycle curves, transformation temperatures and CCT curves, the thermal simulation parameters were determined, which are shown in Table 4, where T_m is the maximum temperature during thermal simulation.

Charpy Impact Toughness

Charpy impact toughness was tested at −20 °C, the obtained results is shown in Table 5.

Charpy impact toughness of specimens T_{m1} = 800 °C is obviously low, and far below than others, then is specimens T_{m1} = 950 °C, besides low toughness, toughness scatter is also displayed between specimens T_{m1} = 950 °C.

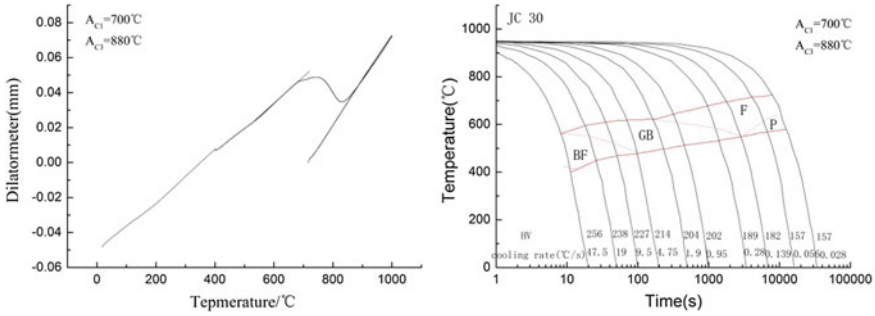

Fig. 4 Transformation temperature and CCT curves of JC30

Table 4 Thermal simulation parameters

T_m [°C]	Heating rate [°C/s]	t_H [s]	$t_{8/5}$ [s]	$t_{5/3}$ [s]
700	150	0	20	80
800	150	0	20	80
900	150	7.0	20	80
950	150	7.5	20	80
1000	150	10.3	20	80
1050	150	10.7	20	80
1100	150	15.0	20	80
1200	150	16.7	20	80
1300	150	18.3	20	80

Table 5 Charpy impact toughness

T_m [°C]	Single [J]	Ave. [J]
700	108.0, 92.0, 101.5	100.5
800	17.5, 10.5, 16.5	14.8
900	115.5, 119.0, 76.0	103.5
950	62.0, 61.5, 18.5	47.3
1000	104.5, 112.5, 115.0	110.5
1050	108.0, 111.5, 111.0	110.0
1100	111.0, 102.5, 113.5	109.0
1200	93.0, 101.5, 107.5	100.5
1300	77.5, 76.5, 97.0	83.5

Microstructure

Microstructure of thermal simulated samples is shown in Fig. 5.

Generally, the microstructures of simulated samples are BF and GB. Microstructure of T_m = 700 °C remains as-welded status, as phase transformation did not occur. As in critical phase transformation region, the grain boundary of

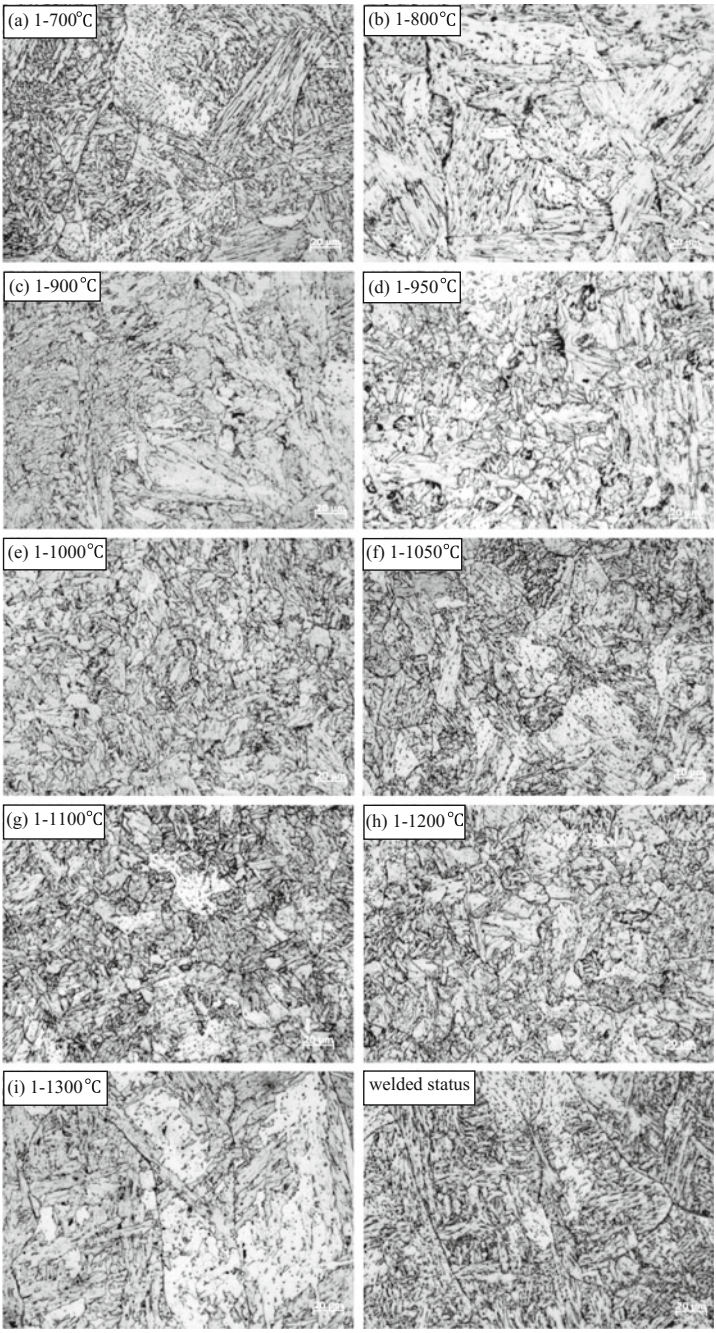

Fig. 5 Microstructure of simulated samples (500×)

microstructure and the orientation of lath-like for BF of T_m between A_{c1} and A_{c3} become more and more indistinct as T_m is higher, meanwhile the grain size is nonuniform, and GB appears. Particularly, chain-like phase is seen in the grain boundary of T_m = 800 °C. While T_m is higher than A_{c3} but lower than 1300 °C, the grain boundary of microstructure and the orientation of lath-like for BF becomes distinct, and the grain size is relatively fine. As high maximum temperature, gain size of T_m = 1300 °C is coarser than others.

MA Constituent

Morphology and distribution of MA constituent for thermal simulated samples are shown in Fig. 6.

The morphology of MA constituent is bulk & spotty, and bulk MA is mainly distributed at grain boundary, spotty MA is mainly distributed in grain. There are some bacilliform MA between lath beam of BF for T_m = 800 °C. The result of MA constituent volume fraction analysis is shown in Table 6.

Discussions

For the convenience of discussion intuitively, the results of charpy impact toughness and volume fraction of MA constituent of all samples are illustrated in Fig. 7.

From Fig. 7, it can be seen that toughness scatter is obvious with T_m in temperature region of 700–950 °C, which is nearly in the region of A_{c1}–A_{c3}, while T_m is higher than 950 °C, toughness scatter disappear, moreover toughnesses are high for them. And the volume fraction of MA constituent with T_m in temperature region of 700–950 °C is higher than that of $T_m \geq 950$ °C.

This is because of microstructure of samples with T_m in temperature region of 700–950 °C is ICCGHAZ (Inter-critically Coarse-Grained HAZ). Research results of H. K. D. H. Bhadeshia [2], S. Aihara [3], D. P. Fairchild [4], A. M. Guo [5] show that as existence of coarse MA constituent worsen the toughness of ICCGHAZ. As a harden structure, MA constituent would like to form stress concentration during distortion, and in addition to residual stress formed in phase transformation, the brittle fracture will be easy to initiation and propagation [6]. Li Y found that different morphology of MA constituent has different effect to toughness, bacilliform MA is the worst, then is bulk MA [7–10].

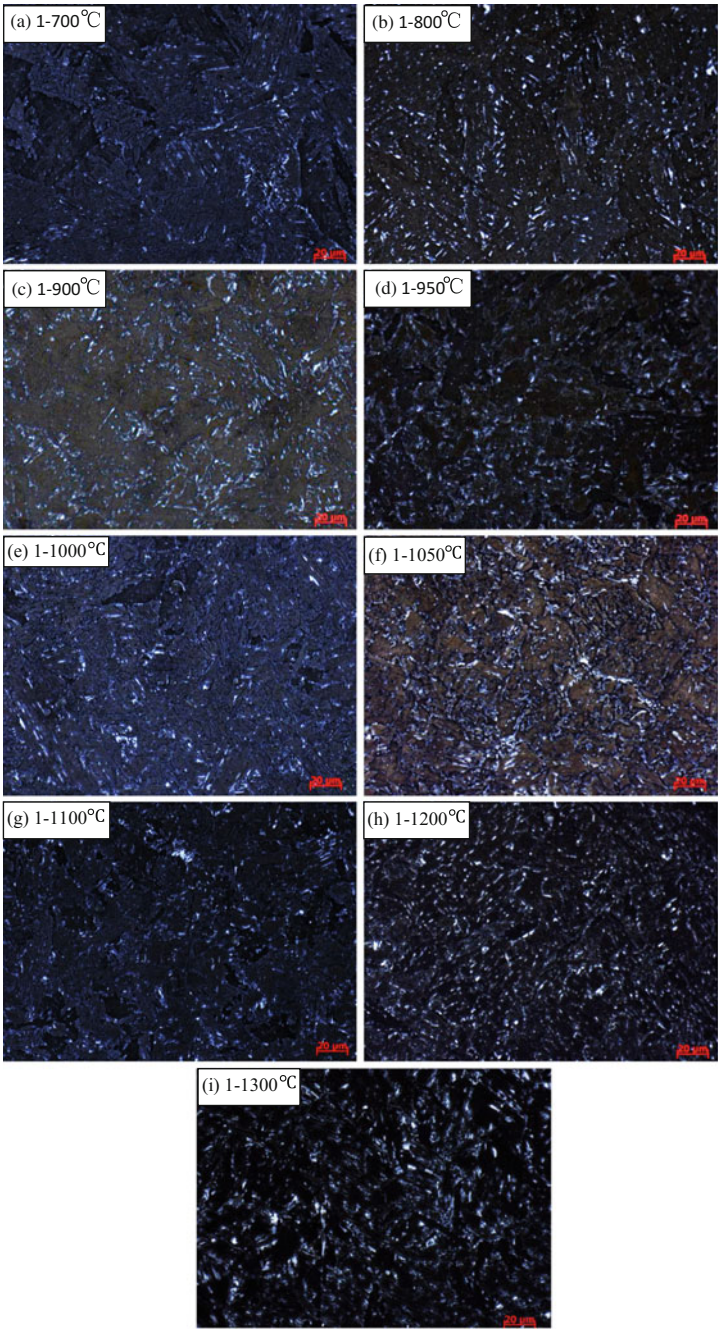

Fig. 6 MA constituent of simulated samples (500×)

Table 6 Results of volume fraction of MA constituent

T_m [°C]	700	800	900	950	1000	1050	1100	1200	1300
MA [%]	4.13	5.04	4.84	4.5	3.63	4.04	3.93	3.49	5.22

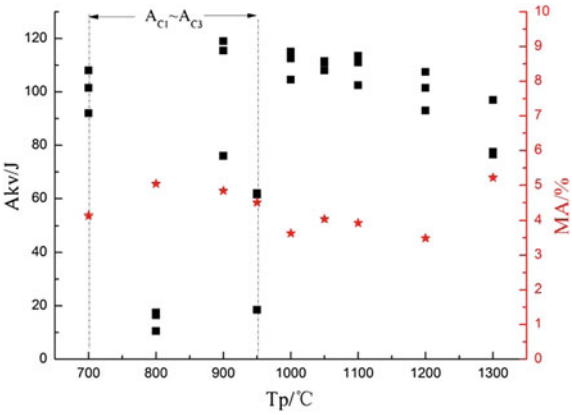

Fig. 7 Illustration for results analysis

Conclusions

(1) The volume fraction of MA directly relates to the charpy impact toughness, the toughness decreases with increasing of the volume fraction of MA;
(2) Bacilliform MA is the main reason to cause the toughness scatter, and bulk MA is another reason to cause low toughness;
(3) The volume fraction of MA is higher than others when the specimen undergoes the temperature between the range of A_{c1}–A_{c3};
(4) Besides MA constituent, the structural constitution and the grain size of metallography should also be considered for X80 girth weld toughness;
(5) The decrease of the temperature range of A_{c1}–A_{c3} by chemical composition matching of base metal and weld consumable maybe a solution for FCAW-S for X80 girth weld engineering application, but there still is a far way to go.

References

1. Q/SY-GJX 0110-2007, Mainline welding technical specification for second west-east natural gas transmission pipeline project
2. H.K.D.H. Bhadeshia, About calculating the characteristics of the martensite-austenite constituent, in Proceedings of the International Seminar on Welding of High Strength Pipeline Steel (TMS, Araxa, Brazil, 2011)
3. S. Aihara, K. Okamoto, Influence of local brittle zone on HAZ toughness of TMCP steels, in International Conference on The Metallurgy, Welding, and Qualification of Microalloyed (HSLA) Steel Weldments (Houston, USA, 1990)

4. D.P. Fairchild, Local brittle zones in structural welds, in Welding Metallurgy of Structural Steels (Warrendale, USA, TMS–AIME, 1987)
5. A.M. Guo, S.R. Li, J. Guo et al., Effect of zirconium addition on the impact toughness of the heat affected zone in a high strength low alloy pipeline steel. Mater. Charact. **59**(2), 134–139 (2008)
6. H.K.D.H. Bhadeshia, Reliability of weld microstructure and properties calculations. Weld. J. **83**(9), 237–243 (2004)
7. Y. Li, T.N. Baker, Effect of morphology of martensite–austenite phase on fracture of weld heat affected zone in vanadium and niobium microalloyed steels. Mater. Sci. Technol. **26**, 1029–1040 (2010)
8. P. Mohseni, J.K. Solberg, M. Karlsen, O.M. Akselsen, E. Østby, Cleavage fracture initiation at M–A constituents in intercritically coarse-grained heat-affected zone. Metall. Mater. Trans. **45**A, 384–394 (2014)
9. C.L. Davis, Cleavage initiation in the intercritically reheated coarse grained heat affected zone of steels, Ph.D. thesis, University of Cambridge, Cambridge, U. K. (1994)
10. C.L. Davis, J.E. King, Effect of cooling rate on intercritically reheated microstructure and toughness in high strength low alloy steel. Mater. Sci. Technol. **9**, 8–15 (1993)

Graphene Modified Epoxy Coating Tubing Applied in the Water Injection Wells

Caihong Lu, Chun Feng, Lijuan Zhu, Long Jiang, Guhui Gao, Lihong Han and Yaorong Feng

Abstract Epoxy coatings (EP coating) with or without 0.5% graphene were prepared on the N80 tubing in order to improve its corrosion resistance in the water injection well. The performance of ordinary epoxy coating and graphene modified epoxy coating was compared by thickness measurement, adhesion test, abrasion resistance test, impact resistance test, coating microstructure analysis, corrosion test in extreme corrosive injection water of one oilfield and electrochemical test. The results indicated that adding 0.5% graphene greatly improved the density, abrasion resistance, corrosion resistance and decreased the surface roughness of the ordinary epoxy coating, due to the small size effect, self-lubricating and hydrophobicity of the grapheme. Therefore, the graphene modified epoxy coating might be an effective way of solving the corrosion and scaling of tubing in the water injection well.

C. Lu · C. Feng (✉) · L. Zhu · L. Jiang · L. Han · Y. Feng
State Key Laboratory for Performance and Structure Safety of Petroleum Tubular Goods and Equipment Materials, Xi'an, Shaanxi 710077, China
e-mail: fengchun003@cnpc.com.cn

C. Lu
e-mail: lucaihong@cnpc.com.cn

L. Zhu
e-mail: zhulijuan1986@cnpc.com.cn

L. Jiang
e-mail: jianglong003@cnpc.com.cn

L. Han
e-mail: hanlihong@cnpc.com.cn

Y. Feng
e-mail: fengyr@cnpc.com.cn

C. Lu · L. Zhu · L. Jiang · L. Han · Y. Feng
CNPC Tubular Goods Research Institute, Xi'an, Shaanxi 710077, China

G. Gao
Redbud Innovation Institute, Baodi, Tianjin, China
e-mail: gaogh@bjtu.edu.cn

© Springer Nature Singapore Pte Ltd. 2018

Y. Han (ed.), *Advances in Materials Processing*, Lecture Notes in Mechanical Engineering, https://doi.org/10.1007/978-981-13-0107-0_102

Keywords Water injection well tubing coating · Epoxy (EP) coating
Graphene modified epoxy coating (G-EP) · Microstructure · Corrosion resistance

Introduction

With the deepening of oilfield development, the number of water injection wells is increasing, and the internal corrosion of water injection tubing is becoming more and more serious. Because of the large amount of dissolved oxygen, microbial (sulfate-reducing bacteria, iron bacteria), mineralized ions (Cl^-, Ca^{2+}, Mg^{2+}, etc.), and corrosive gases such as CO_2 and H_2S existed in the injection water, as well as the higher formation temperature, etc., dissolved oxygen corrosion, scale corrosion, microbial corrosion, electrochemical corrosion and temperature corrosion of inner wall of tubing are prone to occur [1–3]. In order to reduce the corrosion within the tubing, the injection water tubing was treated with epoxy coating on the inner wall, due to its simple process, low cost and good adhesion of the coating. However, in some harsh water quality, the EP coating would be bubbling and peeling (see Figs. 1 and 2). It is necessary to improve the EP coating for the water injection tubing.

In the recent years, the graphene modified coating has attracted much attention due to its outstanding performance. As we all know, the graphene is present as a structural unit of a stable carbon six-membered ring, and the graphene monolithic layer presents a two-dimensional periodic honeycomb lattice structure (see Fig. 3). It has the advantages of conductive, thermal conductivity, high specific surface area, stable chemical properties and outstanding mechanical properties. Especially, the graphene has strong hydrophobicity, which makes the graphene modified anticorrosive coating have wide application prospect [4–7]. Adding 0.5% graphene into epoxy coating, the properties of coating were investigated.

In this study, the N80 tubing was inner coated by the modified epoxy coating with nano-graphene for the water injection well in the oil field, and the preliminary

Fig. 1 Coating bubbling of tubing

Fig. 2 Coating peeling of tubing

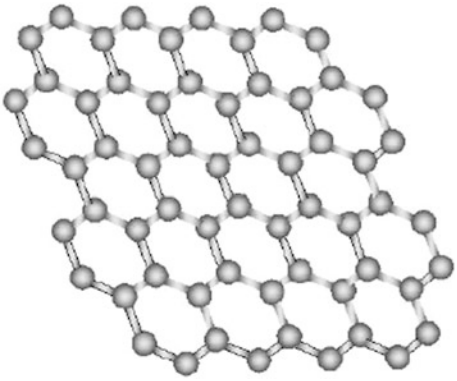

Fig. 3 Single layer graphene

comparison analysis between general epoxy coating and the graphene modified epoxy coating tubing was investigated.

Materials and Experimental

The N80 tubing with an outer diameter of 73.02 mm and a wall thickness of 5.51 mm was used as the substrate in the preparation of the experimental material. Two kinds of inner coatings were prepared on the inner wall of the tubing. One is the three-layer composite epoxy coating prepared by the manufacturer A and the other is graphene modified epoxy coating with 0.5% graphene prepared by Plant B (see Fig. 4).

The following comparison tests were carried out on the two kinds of tubing coatings:

The thickness of the inner coating of the tubing was measured by minitest 3100–4100 cladding thickness gauge; The adhesion analysis of the two coatings was carried out using the standard method specified in Appendix B of the standard SY/T

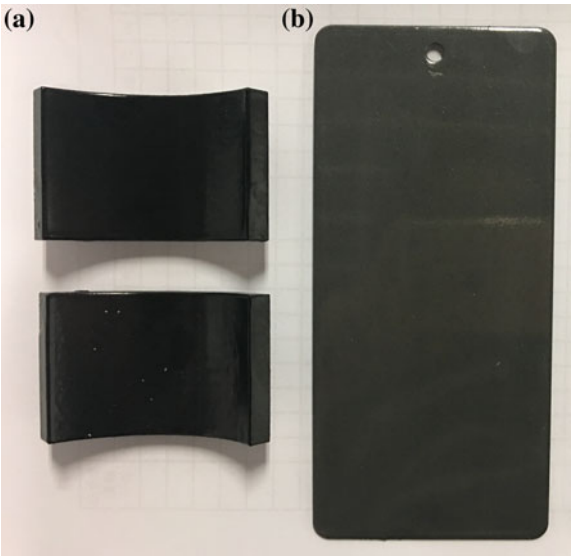

Fig. 4 EP coating (**a**) and G-EP coating (**b**)

6167-2008 "Specification of internal coating for tubing and casing" [8]; The wear resistance test was according to GB/T 23988-2009. The total sand content was 20L, flow rate was 21 s out of 2L, the coating thickness was measured before and after test, and calculated as Eq. 1:

$$A = V/(T_{before} - T_{after}) \tag{1}$$

where:

A wear resistance in L/μm;
V Abrasive Usage, in L;
T_{before} the coating thickness before test, in μm;
T_{after} the thickness of the coating after the sand test, in μm.

The QJL impact testing machine was used to carry out a series of impact toughness tests on the two coatings. The sample size was 200 mm × 25 mm. The microstructures and cross sections of the two coatings were observed by TESCAN VEGA II scanning electron microscopy. The cathodic polarization curves of the coatings after 5 days corrosion in the injected water were investigated by the electrochemical work station. The water quality parameters of the injected water were shown in Table 1.

Table 1 Soaking test condition (extreme condition injection water)

Temperature [°C]	Mineralization degree [mg/L]	Cl^- [mg/L]	HCO^{3-} [mg/L]	CO_3^{2-} [mg/L]	SO_4^{2-} [mg/L]	Ca^{2+} [mg/L]	Mg^{2+} [mg/L]	K^+Na^+ [mg/L]
104	38,218	18,351	3853	156	2491	1023	194	12,150
	SRB [CFU/ml]	Iron bacteria [CFU/ml]	Saprophytic Bacteria [CFU/ml]		Dissolved oxygen [CFU/ml]			
	25,000	60	1,100,000		None			

Results and Discussion

The thickness of both coatings is greater than 125 μm (see Table 2). According to SY/T 6167-2008 standard, the adhesion of both coatings met the requirement of A level which investigated by knife engraving method. However, the ordinary epoxy coating peeled after the compression test in which the tubing pressed to 43% of the diameter, while only a small amount of bubble occurred on the graphene modified epoxy coating, as shown in Fig. 5.

The wear resistance of graphene epoxy coating was twice as large as ordinary epoxy coating (see Table 3), the toughness of the graphene modified epoxy coating and the ordinary epoxy coating toughness were 6 and 2 J respectively. As shown in

Table 2 Thickness of two coatings [μm]

Coating	Max	Min	Average
Epoxy coating	201	152	180
Graphene modified epoxy coating	205	152	185

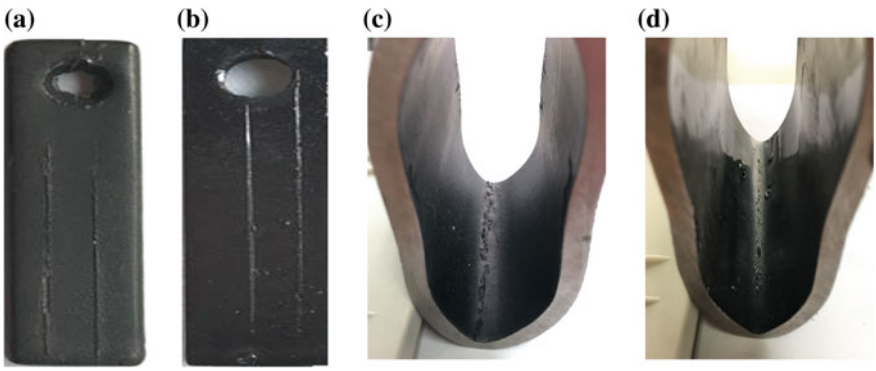

Fig. 5 Adhesion test results of EP coating (**a**) and G-EP coating (**b**)

Table 3 Wear resistance of two coating

Coating	Thickness of coating [μm]		Amount of falling sand [L]	Wear quantity [L/μm]
	Before	After		
Epoxy coating	145	95.7	20	0.41
Graphene modified epoxy coating	140.5	114.6	20	0.77

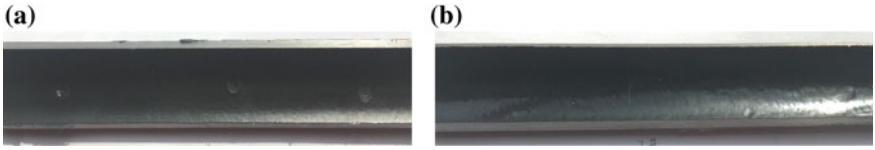

Fig. 6 Impact toughness test (6 J) of EP coating (**a**) and G-EP coating (**b**)

Fig. 6, cracks were obvious on the surface of the EP coating after impact test with 6 J impact energy, while no crack occurred on the graphene modified epoxy coating.

There are obvious holes in the ordinary epoxy coating, and the pores and defects in the graphene modified epoxy coating are obviously reduced, nano-scale graphene dispersed uniformly in the holes and filled in other defects of the coating (Fig. 7).

The self-corrosion current densities of the graphene-modified epoxy coating and ordinary epoxy coating are 9.7522E-8 and 4.7554E-6 i/cm^2 respectively, the corresponding corrosion potential are −0.6179 and −0.6736 V, as shown in Fig. 8. The corrosion current density of graphene epoxy coating is lower than that of the conventional epoxy coating by two orders of magnitude. The corrosion potential is also increased by about 0.06 V. The results indicated that the addition of graphene improved the protection performance of epoxy coating for metal substrate.

In conclusion, the corrosion resistance and the physical properties of the graphene modified epoxy coating is better than the EP coating, which is mainly due to the following main reasons:

(1) The hydrophobicity of graphene. The surface effect of graphene makes the contact angle between the graphene and water very large and poor water infiltration, water molecules are difficult to be absorbed by graphene. When graphene is added to the epoxy coating, the hydrophobicity of the graphene prevents the water molecules from entering the surface of the metal substrate through the coating, thereby reducing the corrosion of the metal surface.
(2) Small size effect of graphene and two-dimensional lamellar structure. The small size of graphene allows graphene to be filled into the pores and defects of the coating, and due to the two-dimensional lamellar structure of the graphene

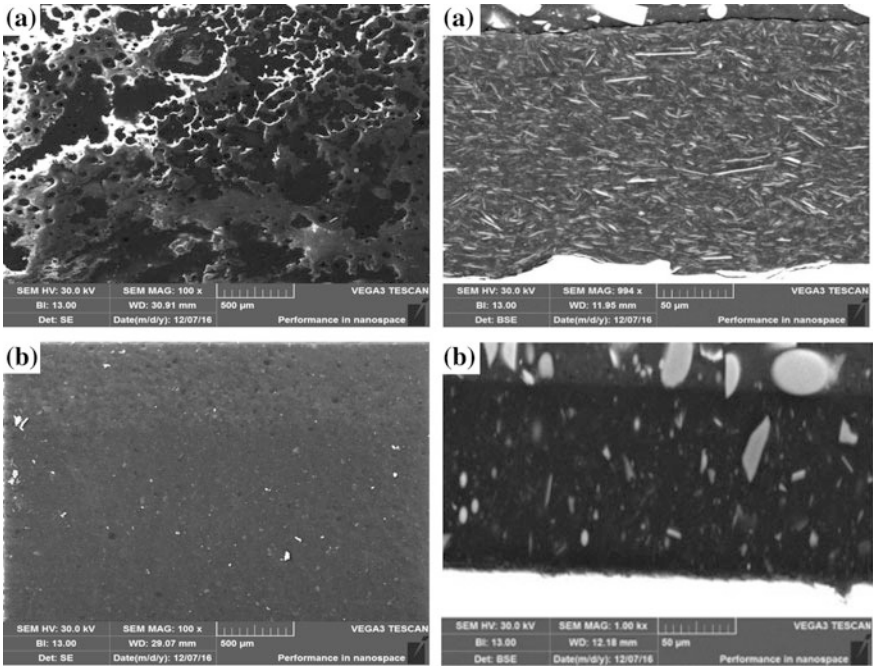

Fig. 7 Microstructure analysis of coating of EP coating (**a**) and G-EP coating (**b**)

Fig. 8 Polarization curve of two coatings

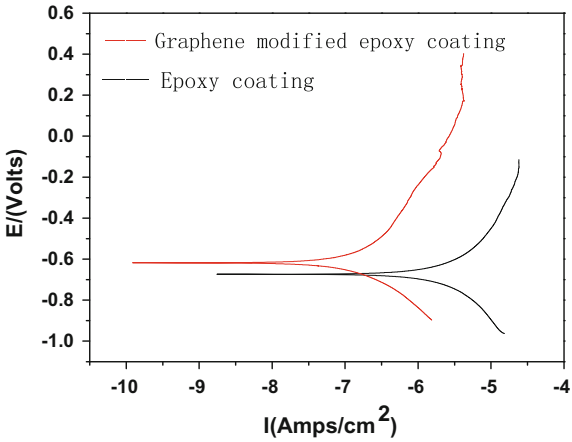

itself, the layers are superimposed on the coating to form a dense physical barrier, thus preventing and delaying the permeation of H_2O, O_2, $C1^-$ and other small molecules corrosive media into the metal matrix. This enhanced the physical isolation and corrosion resistance of the coating.

Summary

(1) Adding 0.5 wt% graphene in the ordinary epoxy coating greatly increases the adhesion, the density, wear resistance and impact resistance of the coating.
(2) The corrosion resistance of the coating is greatly improved by adding graphene. The corrosion current density of the graphene epoxy coating is 2 orders of magnitude lower than that of the conventional epoxy coating, and the corrosion potential is also increased by about 0.06 V, mainly due to the hydrophobicity, small size effect and a two-dimensional Lamellar structure of graphene, which prevent the water molecules penetrate the coating to the metal substrate. In addition, the dense physical isolation graphene modified coating effectively isolates the small size corrosive media (Cl^-, H2O, O2, etc.), resulting to better corrosion resistance than the conventional EP coating.

Acknowledgements This work is sponsored by the Foundation Research and Strategic Reserve Technology Research Fund Project of China National Petroleum Corporation under Grant No. 2017Z-04.

References

1. F. Huang, J. Hu, W. Li, J. Xia, Corrosion of produced water in oilfield and prevention. Corros. Prot. Petrochemical Indus. **27**(1), 44 (2010)
2. J. Wang, Application of water injection tubing anticorrosion Technology in Qinghai Oilfield. Oil Field Equip., **44**(9), 89–92 (2015)
3. R. Li, Water injection string erosion mechanism and its control. **36**(4), 64–66 (2008)
4. F. Wu, W. Zhao, Z. Zeng, Improving the anticorrosion performance of epoxy resin coating by incorporation of modified graphene and graphene oxide, in 2014 Conference for Corrosion and Protection of Marine Materials, (2014), pp. 285–290
5. Y. Wang, The synthesis and application of polyaniline and graphene nanosheets in anti-corrosion coatings, Dissertation for the Master Degree in Engineering, 2012
6. G. Wu, Application of silicon powder in wear and high temperature resistant coatings on metal surface, Dissertation for the Master Degree in Engineering, 2015
7. Q. Wang, X. Wang, J. Fang, Application of graphene in epoxy zinc rich primer, paint and coatings industry, **46**(12), 42–46 (2016)
8. F. Huang, G. Zhang, Z. Liu, SY/T 6167-2008, Specification of internal coating for tubing and casing, National Development and Reform Commission

Corrosion Behavior of Ni–P Alloy Coated Carbon Steel Tubing in Water Injection Wells

Lijuan Zhu, Chun Feng, Caihong Lu, Long Jiang, Juntao Yuan, Tao Tian and Xin Xu

Abstract The cause of severe local corrosion on N80 carbon steel tubing with Ni–P plating after 23 months of service has been analyzed in the present work. Measurements and inspection were performed on the chemical composition and metallographic structure of the tubing. The morphology and composition of the corrosion products were characterized by scanning electron microscopy (SEM), energy dispersive spectroscopy (EDS) and X-ray power diffraction (XRD). The results indicated that serious scaling and heavy Ni–P plating spalling occurred on the internal surface of the tubing; corrosion failure at the end of the threaded joint was obvious. The Ni–P plating failure was mainly attributed to the poor pretreatment technique and the too thin thickness of the Ni–P plating. The poor protective Ni–P plating gradually failed and flaked off with the effect of the corrosive media and therefore the N80 carbon steel tubing was largely corrupted. The corrosion mechanisms were mainly corrosion under scale, galvanic corrosion, and corrosion induced by dissolved oxygen, Cl^- and CO_2.

L. Zhu (✉) · C. Feng (✉) · C. Lu · L. Jiang · J. Yuan · T. Tian · X. Xu
State Key Lab for Performance and Structure Safety of Petroleum Tubular Goods and Equipment Materials, Tubular Goods Research Institute of China National Petroleum Corporation, No. 89 Jinyeer Road, Xi'an, Shaanxi 710077, China
e-mail: zhulijuan1986@cnpc.com.cn

C. Feng
e-mail: fengchun003@cnpc.com.cn

C. Lu
e-mail: lucaihong@cnpc.com.cn

L. Jiang
e-mail: jianglong003@cnpc.com.cn

J. Yuan
e-mail: yuanjt@cnpc.com.cn

T. Tian
e-mail: tiantao001@cnpc.com.cn

X. Xu
e-mail: xuxin010@cnpc.com.cn

© Springer Nature Singapore Pte Ltd. 2018

Y. Han (ed.), *Advances in Materials Processing*, Lecture Notes in Mechanical Engineering, https://doi.org/10.1007/978-981-13-0107-0_103

Keywords Water injection · Ni–P plating · Tubing · Corrosion Failure

Introduction

With the exploration of the oilfield, the water cut increases in the process of water flooding development and the injected water quality worsens obviously, which result in serious corrosion and scale buildup of the water injection tubing [1–3]. In order to improve the water injection effect, a variety of anti-corrosion measures have been adopted in oilfields. Typical measures are: chemical preservatives (corrosion inhibitor [4], fungicides [5], deoxidizing agent [5], incrustation inhibitor [5]), cathodic protection [4], coating protection [2, 6, 7] surface nitriding [8] and fiberglass tubing [7]. Application of protective coatings is widely used due to its economic effectiveness. However, tubing failure induced by quality varies, improper selection and improper construction of the protective coatings used in the oilfields occurred frequently in the recent years.

Severe local corrosion occurred on N80 carbon steel tubing with Ni–P plating after 23 months of service in a water injection well. Serious scaling and heavy Ni–P plating spalling occurred on the internal surface of the tubing; corrosion failure at the end of the threaded joint was obvious. No removing dissolved oxygen measure was carried out for the injected water. The type of injected water was sodium bicarbonate; the volume of injected water was 45 m^3/d; pH was 6.4; the content of suspended particles was 120 mg/L. The results of water quality analysis are shown in Table 1. In addition, there is a certain amount of saprophytic bacteria, iron bacteria and sulfate reducing bacteria in the injected water. The tubing samples are taken from the water injection well at a depth of about 200 m with a water injection pressure of 14.2 MPa and a water injection temperature of 22 °C. As mentioned in the orders technical agreement, the tubing with Ni–P plating was ordered to meet the requirements of API SPEC 5CT-2012 standard (Specification for Casing and Tubing) and GB/T 13913-2008 standard (Metallic coatings-Autocatalytic (Electroless) nickel-phosphorus alloy coatings-Specification and test methods).

In the present work, the morphology and composition of the corrosion products were characterized by scanning electron microscopy (SEM), energy-dispersive spectroscopy (EDS) and X-ray power diffraction (XRD). The failure cause of the Ni–P plating and the corrosion mechanism of the N80 carbon steel tubing were analyzed.

Table 1 The results of water quality analysis (mg/L)

Cl^-	Mg^{2+}	Ca^{2+}	HCO^{3-}	SO_4^{2-}	Na^+, K^+
9912.4	104.2	110.8	1107.2	4.9	Balanced

Experimental Procedure

In order to investigate the failure cause of the Ni–P plating tubing, the macro morphology, micro morphology, metallographic structure, remainder wall thickness, chemical composition and corrosion products of the Ni–P plating tubing were observed and analyzed. Crack detection was carried out by fluorescent magnetic particle detection. The remainder wall thickness was measured by ultrasonic thickness measuring meter. The morphology and composition of the corrosion products were characterized by metallographic microscope, scanning electron microscopy (SEM), energy-dispersive spectroscopy (EDS) and X-ray power diffraction (XRD).

Results

Morphologies

As shown in Fig. 1, severe local corrosion and scaling occurred on the internal surface of the Ni–P plating tubing. After cleaning the tubing, corrosion failure at the end of the thread joint and a large surface spalling of the Ni–P plating was observed. No crack was detected by the fluorescent magnetic particle detection. However, the minimum remainder wall thickness of the tubing with a nominal thickness of 5.51 mm is only 3.1 mm, far below the allowed level in the API SPEC 5CT standard. The maximum pitting corrosion rate is 1.26 mm/a, far more than the allowed level, 0.20 mm/a in the NACE Standard RP 0775 (Preparation, Installation, Analysis, and Interpretation of Corrosion Coupons in Oilfield Operations).

Compositions

The chemical composition of the N80 tubing and the Ni–P plating are shown in Tables 2 and 3 respectively. The results showed that the chemical composition of the N80 tubing and the Ni–P plating conformed to the API Spec 5CT-2012 standard and the GB/T 13913-2008 standard respectively.

Metallographic Analysis

Cross-sectional morphologies of the tubing with Ni–P plating after 23 months service in the water injection well and the prepared tubing with Ni–P plating in the same batch are displayed in Fig. 2. As shown in Fig. 2a, corrosion pits and

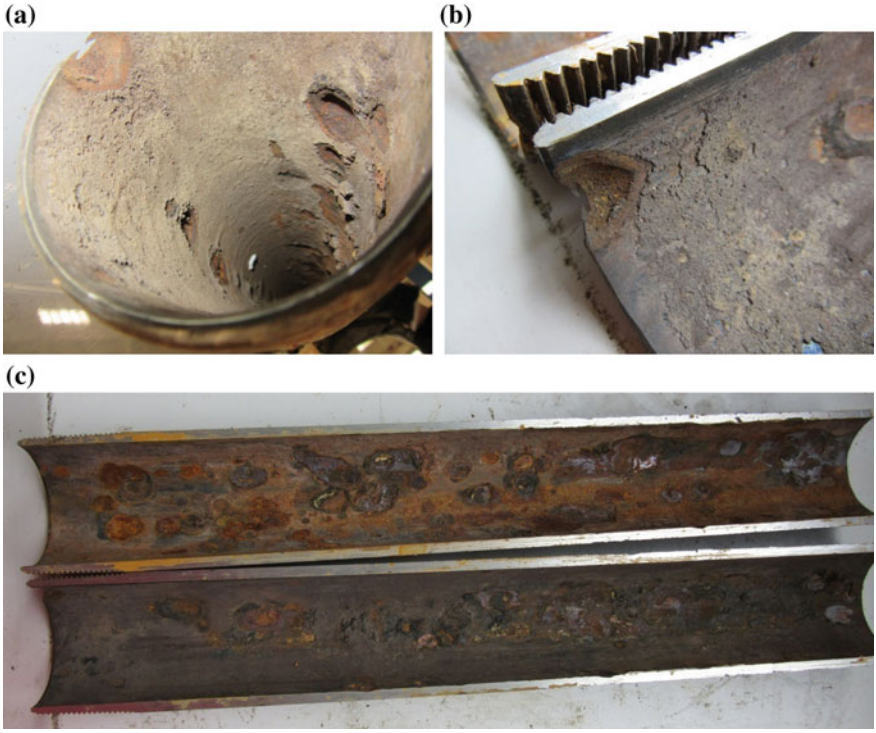

Fig. 1 Morphologies of the Ni–P plating tubing

Table 2 Chemical compositions of the N80 tubing (wt%)

Elements	C	Si	Mn	P	S	Cr	Mo	V
Tubing	0.33	0.24	1.68	0.016	0.011	0.19	≤ 0.005	0.091
API Spec 5CT-2012	–	–	–	≤ 0.030	≤ 0.030	–	–	–

Table 3 Chemical compositions of the Ni-P plating (wt%)

Elements	C	P	Fe	Ni
Ni–P coating		8.33	2.28	89.39
GB/T 13913-2008	–	5–9	–	–

corrosion products at the interface between the Ni–P plating and N80 carbon steel for the tubing with Ni–P plating after 23 months service in the water injection well were observed; the thickness of the Ni–P plating was in a range from 5.3 to 9.8 μm. As shown in Fig. 2b, inclusions at the interface between the Ni–P plating and

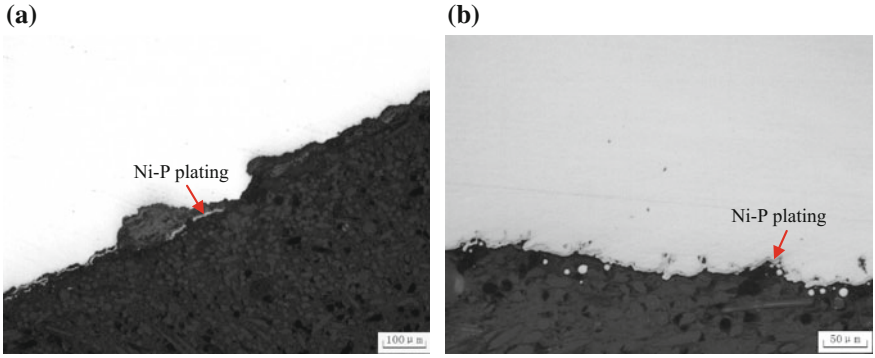

Fig. 2 Cross-sectional morphologies of **a** the tubing with Ni–P plating after 23 months service in the water injection well and **b** the prepared tubing with Ni–P plating in the same batch

N80 carbon steel for the prepared tubing with Ni–P plating in the same batch was observed; the thickness of the Ni–P plating was in a range from 2 to 4 μm, far below 15 μm that required in the orders technical agreement.

Corrosion Products

The composition of the corrosion products as shown in Fig. 2a is displayed in Table 4. The outer layer corrosion products for the N80 tubing mainly include C, O and Fe, and with a very small amount of S, Cr and Si elements; while the inner layer mainly dominated by O and Fe, Cl with 0.9 wt% was also detected. In addition, the scaling layer are mainly composed by Ca, Mg, O and C.

XRD patterns of the corrosion products for the N80 tubing and the Ni–P plating after 23 months service in the water injection well are displayed in Fig. 3. The corrosion products for the N80 tubing were composed of $FeCO_3$, FeO, Fe_3O_4 and Fe_2O_3 (Fig. 3a), while no corrosion product was detected on the Ni–P plating, only Ni for the Ni–P plating and Fe for the N80 substrate were detected.

Table 4 Elements analysis for corrosion products in Fig. 2a (wt%)

	C	O	Si	P	Cl	S	Cr	Fe	Ni
Outer layer	10.91	26.71	0.28	2.79		0.48	0.70	55.35	2.77
Inner layer		18.25		2.43	0.9			49.49	28.93

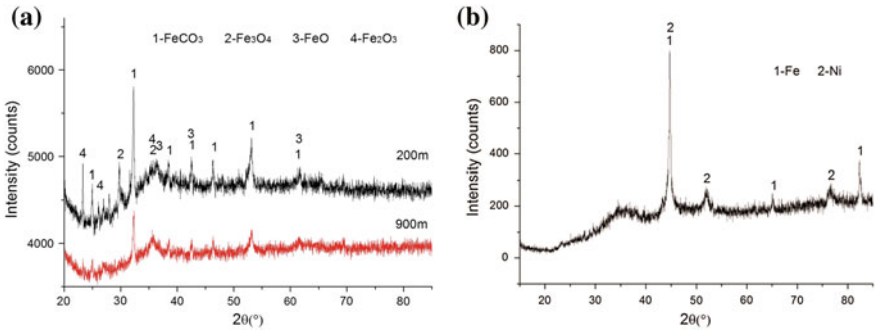

Fig. 3 XRD patterns for the corrosion products (**a**) and Ni–P plating (**b**) on the N80 tubing after 23 months service in the water injection well

Discussion

Failure Analysis of the Ni–P Coating

The composition of the Ni–P plating conformed to the GB/T 13913-2008 standard. However, the thickness of the Ni–P plating after 23 months service in the water injection well was in a range from 5.3 to 9.8 μm; and the thickness of the Ni–P plating on the prepared tubing in the same batch was in a range from 2 to 4 μm, far below 15 μm that required in the orders technical agreement. In addition, inclusions which greatly decreased the adhesion of the Ni–P plating at the interface between the Ni–P plating and N80 carbon steel for the prepared tubing with Ni–P plating in the same batch was observed. It indicated that a poor pretreatment was carried out during the Ni–P plating preparation. Therefore, The Ni–P plating failure was mainly attributed to the poor pretreatment technique and the too thin thickness of the Ni–P plating.

In addition, it is inevitable to avoid coating porosity for the electroplating coating [9]. The preferred corrosion induced by Cl^- and other corrosive media on the pores distributed on the surface of the Ni–P coating led to local corrosion. Song indicated that [10] chloride ions can be easily adsorbed on the pores, grain boundaries and other defects, and destroys the dynamic balance of $Ni = Ni^+ + e^-$:

$$Ni^{2+} + 2Cl^- \leftrightarrow NiCl_2 \tag{1}$$

This is an autocatalytic reaction. Therefore, the pitting will go deep into the coating. In the present work, the content of Cl^- in the injected water was 9912.4 mg/L. Under the action of the autocatalytic reaction, the preferential failure of the Ni–P plating occurred on the surface with defects and with too thin thickness of Ni–P plating.

On the other hand, serve scaling occurred on the internal surface of the tubing, which resulted in serious corrosion under the scale and galvanic corrosion.

As the corrosion went deep into the coating, the corrosion products accumulated at the interface between the N80 carbon steel and the Ni–P plating, which resulted to large surface spalling of the Ni–P coating.

Corrosion Mechanism of the N80 Tubing

The poor protective Ni–P plating gradually failed and flaked off with the effect of the corrosive media and therefore the N80 carbon steel contact with the corrosive media directly.

It showed that the outer layer corrosion products for the N80 tubing mainly include C, O and Fe, and the corrosion products contain $FeCO_3$. The HCO_3^- detected in the injected water reached 1107 mg/L. Therefore, corrosion induced by CO_2 occurred on the N80 carbon steel. The generally recognized corrosion mechanism induced by CO_2 is as follows [11–13]:

$$CO_2 + H_2O \leftrightarrow H_2CO_3 \tag{2}$$

$$H_2CO_3 \leftrightarrow H^+ + HCO_3^- \tag{3}$$

$$HCO_3^- \leftrightarrow H^+ + CO_3^- \tag{4}$$

$$2H^+ + Fe \leftrightarrow Fe^{2+} + H_2 \tag{5}$$

$$Fe^{2+} + CO_3^2 \leftrightarrow FeCO_3 \tag{6}$$

That is:

$$CO_2 + H_2O + Fe \leftrightarrow FeCO_3 + H_2 \tag{7}$$

The corrosion products also contain FeO, Fe_3O_4 and Fe_2O_3. No removing dissolved oxygen measure was carried out for the injected water. Therefore, corrosion induced by dissolved oxygen also occurred on the N80 carbon steel. Research shows that the corrosion rate of carbon steel increases with the increase of dissolved oxygen content [14, 15], even if the oxygen concentration is very low, it still has a significant impact on the corrosion of carbon steel [16]. The corrosion mechanism is as follows:

$$Fe - 2e \leftrightarrow Fe^{2+} \tag{8}$$

$$O_2 + 2H_2O + 4e \leftrightarrow 4OH^- \tag{9}$$

That is

$$2Fe + O_2 + 2H_2O \leftrightarrow 2Fe^{2+} + 4OH^- \quad (10)$$

Fe^{2+} subsequently hydrolyzed into α-FeO (OH):

$$O_2 + 6H_2O + 4Fe^{2+} \leftrightarrow 4FeO(OH) + 8H^+ \quad (11)$$

As the dehydration of the FeO (OH), Fe_2O_3 formed. The formation of Fe_3O_4, FeO and other corrosion products occurred in the subsequent reaction.

On the other hand, serve scaling induced by Ca^{2+} and Mg^{2+} occurred on the internal surface of the tubing, which resulted in serious corrosion under the scale. In addition, galvanic corrosion occurred between the surface of the tubing and the surface with scaling [17].

Cl^- with 0.9 wt% was detected in the inner layer of the corrosion products on the surface of the N80 tubing, and the content of Cl^- in the injected water was up to 9912.4 mg/L. Yi et al. [18] and Ma et al. [17] indicated that Cl^- could induce and accelerate the pitting corrosion of carbon steel; In oil and gas wells, Cl^- can accelerate the anodic reaction of corrosion induced by CO_2, destroy the corrosion products film [19]. Wan et al. [20] indicated that the corrosion rate of carbon steel increased with the increase of content of Cl^- in solution. Therefore, Cl^- in the injected water accelerated the corrosion of the N80 tubing.

In addition, there is a certain amount of saprophytic bacteria, iron bacteria and sulfate reducing bacteria in the injected water, which also accelerated the corrosion of the tubing to some extent.

Conclusions

(1) Serious scaling and heavy Ni–P plating spalling occur on the internal surface of the tubing; corrosion failure at the end of the threaded joint is obvious. The Ni–P plating failure is mainly attributed to the poor pretreatment technique and the too thin thickness of the Ni–P plating. The poor protective Ni–P plating gradually fails and flaks off with the effect of the corrosive media and therefore the N80 carbon steel tubing is largely corrupted.
(2) The corrosion mechanisms are mainly corrosion under scale, galvanic corrosion, and the corrosion is induced by dissolved oxygen, Cl^- and CO_2.

Acknowledgements This work is sponsored by the Foundation Research and Strategic Reserve Technology Research Fund Project of China National Petroleum Corporation under Grant No. 2017Z-04.

References

1. B. Wang, H.Z. Ma, G.L. Huang, R.Q. Sun, L.B. Jia, On oilfield water injection corrosion. J. Xi'an Pet. Inst. (Natural Science Edition), **16** (2), 39 (2001). (in Chinese)
2. F. Huang, J.X. Huang, W.T. Li, J. Xia, Corrosion of produced water in oilfield and prevention. Corros. Protect. Petrochem. Ind. **27**(4), 44 (2010). (in Chinese)
3. Y.G. Liu, Effect analysis of anti-corrosion measures for tubes of water injection well in Shengli oilfield. Corros. Protect. **24** (8), 361 (2003). (In Chinese)
4. F.L. Zhao, J.N. Yan, H.H. Hu, Corrosion and protection technology of water injection system. Oil Gas Surf. Eng. **21**(6), 19 (2002). (in Chinese)
5. Y.N. Xu, Ni-P alloy coated plating tubing and its anti-corrosion technology. Xinjiang Pet. Sci. Technol. **10**(1), 21 (2000). (in Chinese)
6. C.Y. Ye, Z.B. Wang, C.Q. Ren, P.Q. Li, Study on CO_2 corrosion resistance of oil steel J 55 and Its Ni-P coating. Oil Field Equip. **33**(2), 25 (2004). (in Chinese)
7. R.Q. Li, Water injection string erosion mechanism and its control. Pet. Drill. Tech. **36**(4), 64 (2008). (in Chinese)
8. R.Q. Li, L.J. Wei, S.W. Wang, B. Li, Experimental study on corrosion prevention of water injection string. J. Pet. Nat. Gas **30**(1), 369 (2008). (in Chinese)
9. F.C. Walsh, C. Ponce de León, C. Kerr, S. Court, B.D. Barker, Electrochemical characterisation of the porosity and corrosion resistance of electrochemically deposited metal coatings. Surf. Coat. Technol. **202**, 5092 (2008)
10. Y.W. Song, D.Y. Shan, E.H. Han, High corrosion resistance of electroless composite plating coatings on AZ91D magnesium alloys. Electrochim. Acta **53**, 2135 (2008)
11. Q.N. Li, Q. Zhang, J.B. Wen, Z.Q. Bai, Prediction and prevention of CO_2 corrosion of oil tubular goods. Corros. Sci. Protect. Technol. **6**(16), 381 (2004). (in Chinese)
12. G. Fierro, G.M. Ingo, F. Mancla, XPS - investigation on the corrosion behavior of 13Cr2martensitic stainless steel in CO_2-H_2S-Cl^- environments. Corrosion **10**, 814 (1989)
13. J.K. Heuer, J.F. Stubbins, An XPS characterization of $FeCO_3$ films from CO_2 corrosion. Corros. Sci. **41**, 1231 (1999)
14. D.A. Jones, *Principles and Prevention of Corrosion*, 2nd edn. (Prentice Hall, Upper Saddle River, NJ, 1996)
15. H.H. Uhlig, H.H. Triadis, M. Stern, Effect of oxygen, chlorides, and calcium ion on corrosion inhibition of iron by polyphosphates. Electrochem. Soc. **102**, 59 (1995)
16. N.R. Rosli, Y.S. Choi, D. Young, Impact of oxygen ingress in CO_2 corrosion of mild steel. Corrosion **1**, 4299 (2014)
17. H.Y. Ma, C. Yang, G.Y. Li, W.J. Guo, S.H. Chen, J.L. Luo, Influence of nitrate and chloride ions on the corrosion of iron. Corrosion **59**(12), 1112 (2003)
18. C.G. Yi, J. Gong, Y. Yang, X.D. Li, Optimal selection of steel pipes for gathering pipelines transporting CO_2-contained natural gas. OGST **28**(6), 76 (2009). (in Chinese)
19. Q.Y. Liu, L.J. Ma, S.W. Zhou, Effects of chloride content on CO_2 corrosion of Carbon steel in simulated oil and gas well environments. Corros. Sci. **84**, 165 (2014)
20. L.P. Wan, Y.F. Meng, C.X. Wang, L. Yang, Mechanism of corrosion and scale deposit of tubes in western oilfield. J. Chin. Soc. Corros. Protect. **27**(4), 247 (2007). (in Chinese)

Ultrafast Precipitation Kinetics in an Ultrafine-Grained Al–Cu Alloy Used for Oil Drill Pipes

Long Jiang, Chun Feng, Lihong Han, Yaorong Feng, Caihong Lu, Lijuan Zhu, Hang Wang, Gang Liu and Jun Sun

Abstract In the ultrafine-grained (UFG, <1 μm) Al–Cu alloys having very poor thermal stability, only intergranular equilibrium θ-Al_2Cu precipitates were found after aging treatment, which means that the precipitation was greatly accelerated even at room temperature and has directly transformed to equilibrium θ phases while bypassed the metastable phases GP zones, θ'' and θ' as usually seen in representative precipitation transition sequence of coarse grained (CG, >10 m) Al–Cu alloy. It was found the precipitation kinetics of θ phases in the UFG Al–Cu alloy occurred at several orders of magnitude faster than that can be predicted by conventional grain boundary precipitation theory. Considering ultrafast solute diffusion at the UFG length-scale, a developed/modified precipitation kinetics model at the UFG length-scale has been established. It yields predictions in satisfied accordance with experimental aging precipitation process/parameters of UFG Al–Cu alloys.

Keywords Al–Cu alloys · Ultrafine grain · Precipitation behavior Thermodynamic-kinetic models

L. Jiang (✉) · C. Feng · L. Han · Y. Feng · C. Lu · L. Zhu · H. Wang
CNPC Tubular Goods Research Institute, State Key Laboratory for Performance and Structure Safety of Petroleum Tubular Goods and Equipment Materials, 89 Jinye Second Road, Xi'an 710077, Shaanxi, China
e-mail: jianglong003@cnpc.com.cn

G. Liu (✉) · J. Sun (✉)
State Key Laboratory for Mechanical Behavior of Materials, Xi'an Jiaotong University, Xi'an 710049, China
e-mail: lgsammer@mail.xjtu.edu.cn

J. Sun
e-mail: junsun@mail.xjtu.edu.cn

© Springer Nature Singapore Pte Ltd. 2018

Y. Han (ed.), *Advances in Materials Processing*, Lecture Notes in Mechanical Engineering, https://doi.org/10.1007/978-981-13-0107-0_104

Introduction

Severe plastic deformation (SPD)-processed ultrafine grained Aluminum alloy has outstanding mechanical properties, e.g. high strength with superior superplasticity at lower temperature [1–5]. Particularly in heat treatable UFG Al alloys, with the goal of obtaining more higher strength acquired from both precipitation particles and small grain size, e.g. yield strength $\sim$1 GPa and uniform elongation $\sim$5% have been obtained in an SPD-processed 7XXX alloy with a nanostructured hierarchy [2, 3]. The significant different precipitation characteristic (i.e. accelerative precipitation kinetics [5–8], alterative morphology and sequence of precipitation [8–10]) are being attracted growing attention in the precipitation-strengthened UFG alloys [7]. Zhao et al. [5] investigated the precipitation process in naturally aged UFG Al–Zn–Mg–X alloy and found that, although the precipitation kinetics was accelerated, the precipitation sequence was not changed, i.e., the same sequence of supersaturated solid solution $\rightarrow$ GP zones $\rightarrow$ $\eta'(MgZn_2)$ $\rightarrow$ $\eta(MgZn_2)$ as observed in the CG alloys.

Extensive studies [7, 11–15] have been implemented on precipitation thermodynamics and kinetics in CG alloys. However, precipitation behavior of UFG alloys is difficult to be quantitatively modeled [6–8] due to a great deal of dislocations and grain boundaries make precipitation very different from the CG counterparts. It is challengeable to apply conventional thermodynamic/kinetic models to the UFG Al alloy [7]. Thus, this paper will concentrate on quantifying the aging precipitation kinetics of UFG Al–Cu alloy, to explain the abnormal aging behavior and ultimately tailor microstructure of advanced UFG precipitation-strengthened Al alloy to achieve excellent mechanical properties.

Experimental Procedures

Material Preparation and Heat Treatments

The used materials are Al–2.5 wt% Cu (Al–Cu) alloys. After homogenization treatment at 723 K for 4 h, the billet (100 mm $\times$ Ø 10 mm) was machined [4, 7]. Subsequently, billets were solution treated at 853 K for 3 h then subsequently subjected to equal-channel angular pressing (ECAP) [4, 7]. To obtain UFG alloys, samples were processed by 12-passes route B_c [2]. After ECAP, samples were aged for 240 h at room temperature (298 K) or aged for 10, 20, 30 and 40 h at 398 K [4].

Microstructural Characterizations

The deformed microstructures of ECAP-processed samples were characterized by electron backscattered diffraction (EBSD), which was carried out on a JSM 7001F equipped with Pegasus XM2–EBSD system [4]. The EBSD specimen was prepared by electro-polishing (an electrolyte of 75% methanol and 25% nitric acid) at 252 K at voltage of 15 V [4, 7]. Transmission electron microscopy (TEM) was performed by JEOL 2100F [7]. The precipitations volume fraction was calculated by corrected projection method [2, 4, 7, 14, 16].

The dislocation density was counted in the high-resolution TEM images [7]. Meanwhile, the dislocations density was determined from XRD peak broadening by Williamson-Hall models [7, 17], following others' work [5, 18, 19]. Quantitative X-ray Diffraction measurement was implemented by a Rigaku D/max-RB X-ray diffractometer [7].

Results and Discussions

Deformation Structures

Figure 1 presents the TEM image (Fig. 1a) and EBSD orientation map (Fig. 1b) of the 12-passes ECAP processed UFG Al–Cu alloys. The mean grain size is $\sim$460 nm. The dislocation density of the as-deformed UFG Al–Cu alloys is shown in Fig. 1c. EBSD analyses (Fig. 1b, d) show, in the UFG Al–Cu alloy, the grain boundaries (GBs) are mainly (>85%) high angle grain boundaries (HAGBs $\geq$ 51°). As discussed later, the HAGBs play very important role in GBs precipitation nucleation.

Precipitation Behaviors

Figure 2a shows representative precipitation morphology of naturally aged UFG Al–Cu alloy. Precipitations with diameter of $\sim$35 nm, are clearly observed at the GBs. Based on HRTEM (inserts of Fig. 2a) and FFT analyses, these GBs particles were soundly proven to be equilibrium θ-Al_2Cu precipitates. No other intragranular second phase particle was found. In UFG Al–Cu alloy, precipitation even at natural aging treatment, has directly transformed to equilibrium θ phase skipped of traditional metastable sequence of GP zones, θ'' and θ' as usually seen in the CG Al–Cu alloys [4]. These results are close to precipitation in UFG Al–4 wt% Cu alloy [6] that was also subjected to natural aging treatment but has smaller grain size of $\sim$100 nm in width.

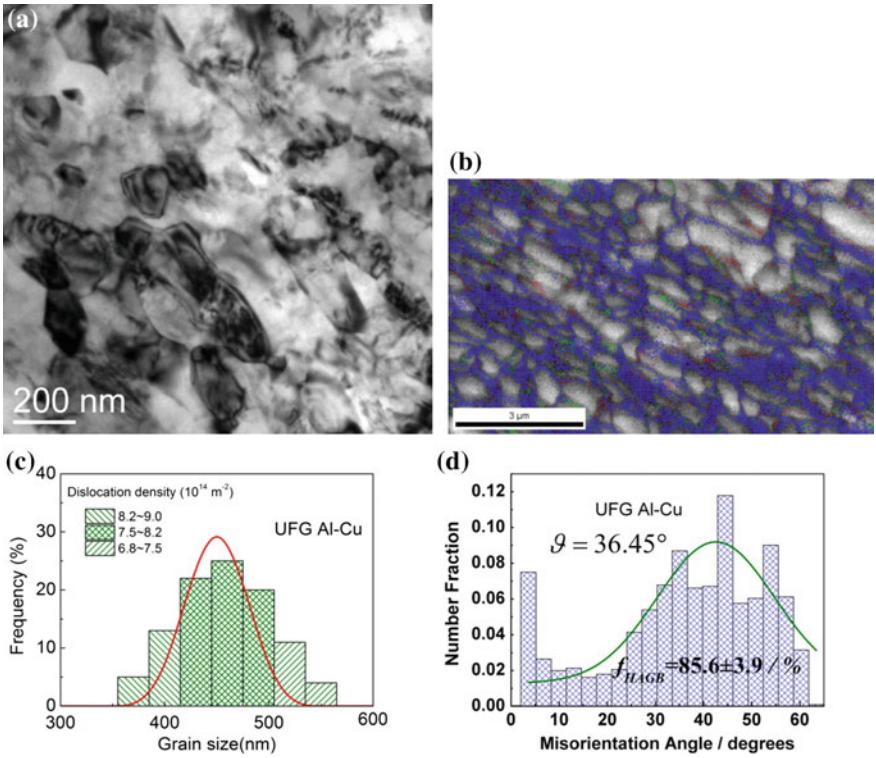

Fig. 1 Representative TEM images **a** and EBSD orientation maps **b** showing the microstructures of as—ECAP processed UFG Al–Cu alloy. The blue lines indicated HAGBs ($\geq 15°$). **c** The grain size and dislocation density distribution [2, 4]. **d** EBSD analyzed misorientation angel statistical results [2]

However, after aging at the same condition, there was no precipitation in CG (~ 10 μm) Al–Cu alloy (Fig. 2b) [2, 11–15]. The above results illustrate precipitation kinetics is accelerative at the UFG grain length-scale. The suggested reasons for the unusual θ at room temperature (RT) include [2, 4, 20] (i) the HAGBs provide preferential nucleation sites for precipitates due to the reduction in energy barrier; (ii) the θ precipitations, having high energetic incoherent interfaces with the matrix, benefit by nucleating at GBs, conversely semi-coherent θ'' and θ' precipitations cannot nucleate on GBs due to difficult to maintain habit relationships; and (iii) the diffusion should be extremely accelerated by the HAGBs which makes it probable for the RT growing of θ phases. In Comparison with equilibrium concentration ($\sim 10^{-10}$), concentration of vacancy is superhigh in UFG alloy [7, 21], that is as large as $\sim 10^{-4}$ immediately after SPD [22]. The intragranular Cu-vacancy pairs are not stable enough because of the weak interaction (the binding energy between Cu atom and vacancy is <0.10 eV [2, 23]). Strongly "attracted" by

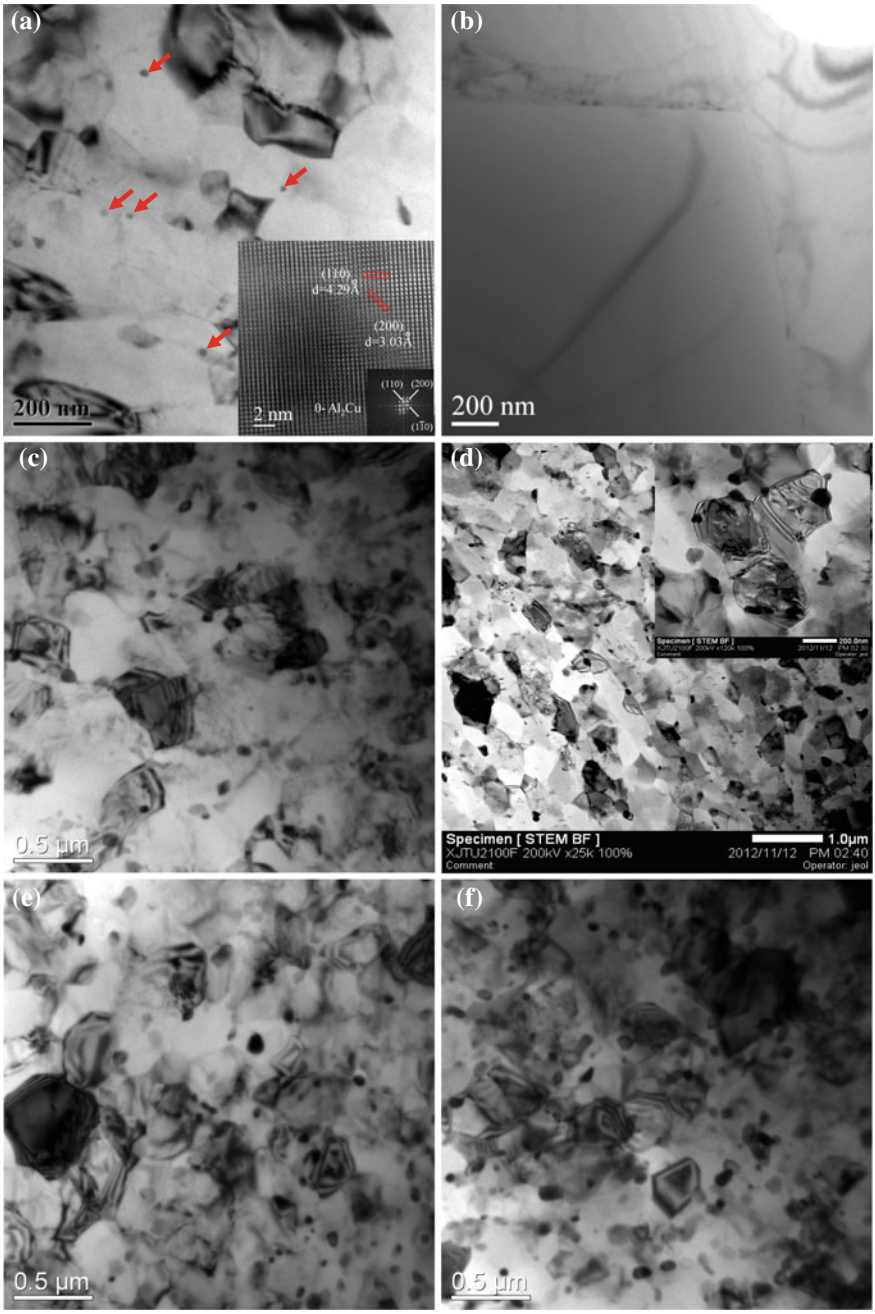

Fig. 2 TEM and STEM(d) images in aged Al-Cu alloys: **a** UFG, 298 K/240 h; **b** CG, 398 K/20 h [2]; **c** UFG, 398 K/10 h; **d** UFG, 398 K/20 h; **e** UFG, 398 K/30 h; **f** UFG, 398 K/40 h. Note red arrows in (**a**) indicate θ-Al_2Cu precipitates along the grain boundaries at RT. However, in the CG Al–Cu alloy, precipitation was not observed (**b**). The structural analyses of θ phases are shown in HRTEM/FFT images of (a)

GBs, vacancies and Cu solutes are both diffused to support the GBs θ precipitation, inhibiting intragranular precipitation.

When the UFG Al–Cu alloy was artificially aged at 398 K, similar precipitation behaviors were observed that only θ phases was precipitated at grain boundaries and no other second phases formed within grain interior (see Fig. 2c–f). The diffusion of Cu dilutes from grain interior to GBs θ precipitates is remarkably enhanced by the large number of dislocations, diminishing the supersaturation of Cu and hence suppressing the precipitation of metastable phases in grain interior [2]. Figure 2c–f respectively shows detailed precipitation morphology of θ-Al_2Cu aged at 398 K for 10, 20, 30 and 40 h. From these TEM images, it can be seen that the precipitate radius increases with aging times, however, the number density decreases after 20 h while volume fraction increases at a diminishing rate. Compared with those in the naturally aged counterpart, the grain-boundary θ phases in the artificially aged UFG Al–Cu alloy has larger density and larger size ($\sim$95 nm in diameter), indicating that the Cu diffusion to grain boundaries and along grain boundaries can be further promoted at the elevated temperature.

Modeling of Precipitation Thermodynamic/Kinetics

The Al–Cu eutectic phase diagram is presented in Fig. 3a in which the solvus lines of metastable precipitations are shown [2, 24]. At the CG length-scale, to directly precipitate equilibrium θ phases in CG Al–2.5 wt% Cu alloy, the aging temperature is beyond 643 K. While at the UFG length-scale, above results show θ phases can precipitate even at RT (blue dot). It means the solvus line of heat-treatable UFG Al alloy is undoubtedly different with that of its CG counterpart and related diagrams need to be revised.

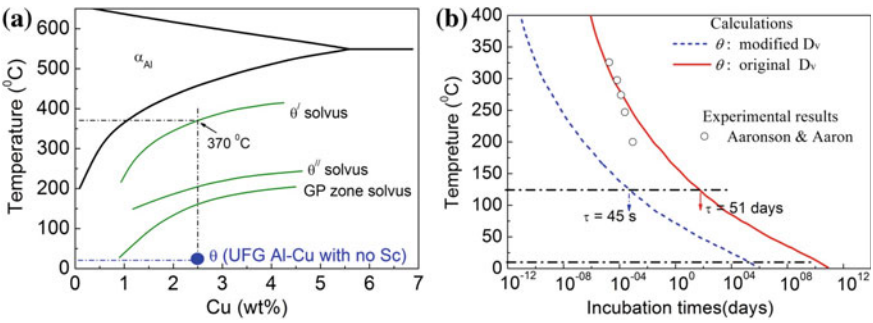

Fig. 3 **a** The Al–Cu eutectic phase diagram [2, 4]. **b** Estimated nucleation incubation times of θ-Al_2Cu precipitations transform with temperature. Some available experimental results from Aaron and Aaronson [25] are depicted in this figure

Next, we present calculations to quantitatively describe the unusual precipitation behaviors in UFG Al–Cu alloys. The incubation time of grain boundary nucleating is given in [6].

$$\tau = \frac{kT\sigma_{\alpha p}a^4}{V_\alpha^2 \Delta G_v^2 D_v \bar{c}} \frac{(2 - 3\cos\psi + \cos^3\psi)}{(1 - \cos\psi)}, \tag{1}$$

k is the Boltzmann's constant, T—absolute temperature, $\sigma_{\alpha p}$—the nucleus/matrix interfacial energy, a—the Al lattice parameter, V_α—the Cu atom volume, ΔG_v—the volume free energy variety during θ formation, D_v—the Cu diffusion coefficient in the matrix, $\bar{c}$—the Cu mole fraction in Al matrix, and ψ—the contact angle of nucleus [4, 6].

For quantitative purposes, the nucleus interfacial energy is estimated to be $\sigma_{\alpha p} = 0.1\,\mathrm{Jm}^{-2}$ and contact angle $\psi = 15°$, as proposed by Huang et al. [6]. Values for other parameters can be referred to [25] and [26]. D_v is firstly evaluated by

$$D_v = 4.44 \times 10^{-5} \exp(-333,900/RT) \tag{2}$$

which is an expression for Cu diffusion in coarse grained Al alloys [27]. The usage of Eq. 2 results in the Temperature-Incubation relationship as shown in the right solid red curve of Fig. 3b. As to natural aging, the incubation time for θ precipitation is predicted to be more than 1.7×10^7 years (Fig. 3b). This is disagreeable with present results that the θ precipitations were observed after 10 days in the naturally-aged UFG Al–Cu samples. For artificial aging at 398 K, the incubation time is predicted to be 51 days, much longer than practical observations.

The predominant reason of the discrepancy is Eq. 2 underestimates D_v too much [2]. Actually, the presence of HAGBs and dislocations will extraordinarily improve the solute diffusion coefficient in the UFG alloy by orders. For instance, the diffusion coefficient of Cu solutes at GBs in ECAP-processed Ni is estimated 10^4–10^5 times larger than that in CG counterpart [28, 29]. Modifying Eq. 2 by multiplying an adjust factor, a more reasonable curve can be obtained, see the left blue dash curve in Fig. 3b. From this curve, the incubation time is predicted to be 45 s when aged at 398 K, which is more reasonable and close to the experimental results that θ phases have been found after 10 h. However, the room temperature precipitation of θ phases is not satisfactorily modeled yet. Another influence should be considered is that "non-equilibrium" GBs [29] in UFG alloys can not only enhance the solute diffusion along grain boundaries but also increase the chemical driving force for nucleation. The "non-equilibrium" GBs, defined in UFG alloys [29], are featured by excess of GBs energy, correspondingly high density of near GBs dislocations, large residual micro strain, the long-range elastic stress and intensive free volumes. These high-energy conditions aid the solute atoms highly segregated at the "non-equilibrium" GBs, increasing the supersaturation at GBs and hence increasing ΔG_v.

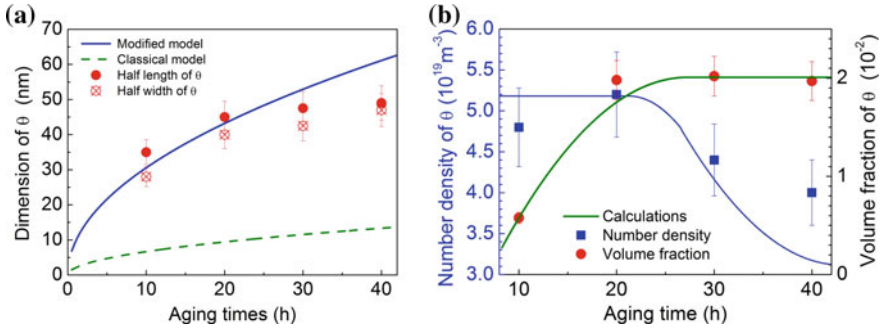

Fig. 4 Predictions and experimental data on the evolution of precipitations half length and width (**a**), number density and volume fraction at 398 K (**b**) as a function of aging time (t) in the UFG Al–Cu alloy. Predictions before (dash curves) and after (solid curves) modification on thermodynamic/kinetic models are indicated, respectively

The growth rates of the θ phase have the following expression [6, 30]:

$$\frac{d\,r_p^{\mathrm{inter}}}{dt} = \frac{A_v\sqrt{D_v}(C - C_e)}{3\pi^{3/2}f(\psi)\left(C_{\mathrm{p}} - C_e\right)}\frac{\sqrt{t}}{\left(r_p^{\mathrm{inter}}\right)^2} \tag{3}$$

In which A_v is the area of collector plate, C_e—the precipitate/matrix interfacial Cu concentration for curvature, C_p—the Cu-solute concentration in precipitates, $f(\psi)$—geometric factors, r_p^{inter}—the precipitate half length and t aging time.

Inputting the CG-based parameter values (some critical values given in [6, 23, 25, 26]) into Eq. 3, the predictions underestimate the experimental θ size considerably; see the comparison in Fig. 4a. After modifying the diffusion-related parameters, The Eq. 3 reasonably reproduces the precipitation parameters of θ size, as solid blue curve in Fig. 4a. The further calculations of intergranular θ number density and volume fraction are also in satisfied accordance with experimental ones (Fig. 4b).

Conclusions

In summary, unusual precipitation behaviors have been experimentally found in UFG Al–Cu alloy. And, the precipitation kinetics occurs at several orders of magnitude faster than can be predicted by traditional grain boundary precipitation models. The accelerated equilibrium θ-Al_2Cu precipitation is exclusively at grain boundaries in the UFG Al–Cu alloy, that is attributed to the extremely enhanced Cu

atomic diffusion, increased supersaturation, and strongly Cu atomic segregation at the high angle grain boundaries. These results should be useful for further understanding on the precipitation behavior in UFG alloys, with which the target of achieving superior mechanical properties of heat-treatable UFG alloys by artificially manipulating could be realized.

Acknowledgements Present work was supported by the National Basic Research Program of China (Grant No. 2010CB631003, 2012CB619600 & 2016YFB0300904), National Science and Technology Major Project (2016ZX05020-002) and the National Natural Science Foundation (51201133, 51321003, 51171142 & 51322104).

References

1. R.Z. Valiev, R.K. Islamgaliev, I.V. Alexandrov, Prog. Mater. Sci. **45**, 103 (2000)
2. L. Jiang, J.K. Li, P.M. Cheng, G. Liu, R.H. Wang, B.A. Chen, J.Y. Zhang, J. Sun, M.X. Yang, G. Yang, Mater. Sci. Eng. A **A637**, 139–154 (2015)
3. P.V. Liddicoat, X.Z. Liao, Y.H. Zhao, Y.T. Zhu, M.Y. Murashkin, E. Lavernia, R.Z. Valiev, S.P. Ringer, Nature Commun. **1**, 63 (2010)
4. L. Jiang, J.K. Li, P.M. Cheng, G. Liu, R.H. Wang, B.A. Chen, J.Y. Zhang, J. Sun, M.X. Yang, G. Yang, Sci. Rep. **4**, 3605 (2014). https://doi.org/10.1038/srep03605
5. Y.H. Zhao, X.Z. Liao, Z. Jin, R.Z. Valiev, Y.T. Zhu, Acta Mater. **52**, 4589 (2004)
6. Y. Huang, J.D. Robson, P.B. Prangnell, Acta Mater. **58**, 1643 (2010)
7. L. Jiang, J.K. Li, P.M. Cheng, G. Liu, R.H. Wang, B.A. Chen, J.Y. Zhang, J. Sun, M.X. Yang, G. Yang, Mater. Sci. Eng. A **A607**, 596–604 (2014)
8. T. Hu, K. Ma, T.D. Topping, J.M. Schoenung, E.J. Lavernia, Acta Mater. **61**, 2163 (2013)
9. G. Sha, Y.B. Wang, X.Z. Liao, Z.C. Duan, S.P. Ringer, T.G. Langdon, Acta Mater. **57**, 3123 (2009)
10. M. Murayama, Z. Horita, K. Hono, Acta Mater. **49**, 21 (2001)
11. J.F. Nie, B.C. Muddle, Acta Mater. **56**, 3490 (2008)
12. J. da Costa Teixeira, D.G. Cram, L. Bourgeois, T.J. Bastow, A.J. Hill, C.R. Hutchinson, Acta Mater. **56**, 6109 (2008)
13. J. da Costa Teixeira, L. Bourgeois, C.W. Sinclair, C.R. Hutchinson, Acta Mater. **57**, 6075 (2009)
14. G. Liu, G.J. Zhang, X.D. Ding, J. Sun, K.H. Chen, Mater. Sci. Eng., A **344**, 113 (2003)
15. A.W. Zhu Jr., E.A. Starke, Acta Mater. **49**, 3063 (2001)
16. D.L. Gilmore Jr., E.A. Starke, Metall. Mater. Trans. A **28**, 1399 (1997)
17. G.K. Williamson, R.E. Smallman, Philos. Mag. **1**, 34 (1956)
18. J. Gubicza, I. Schiller, N.Q. Chinh, J. Illy, Z. Horita, T.G. Langdon, Mater. Sci. Eng., A **460–461**, 77 (2007)
19. K.K. Ma, H.M. Wen, T. Hu, T.D. Topping, D. Isheim, D.N. Seidman, E.J. Lavernia, J.M. Schoenung, Acta Mater. **62**, 141–155 (2014)
20. Y. Huang, J.D. Robson, P.B. Prangnell, J. Mater. Sci. **45**, 4851–4857 (2010)
21. W. Lechner, W. Puff, B. Mingler, M.J. Zehetbauer, R. Würschum, Scr. Mater. **61**, 383 (2009)
22. D. Altenpohl, Aluminium **37**, 401 (1961)
23. R.W. Balluffi, P.S. Ho, *Diffusion* (Metals Park, American Society of Metals, OH, 1973), p. 83
24. J.L. Murray, Int. Met. Rev. **30**, 211 (1985)

25. H.B. Aaron, H.A. Aaronson, Acta Metall. **16**, 789 (1968)
26. K.C. Russell, Acta Metall. **7**, 1123 (1969)
27. Y. Du, Y.A. Chang, B. Huang, W. Gong, Z. Jin, H. Xu, Mater. Sci. Eng., A **363**, 140 (2003)
28. Y.R. Kolobov, G.P. Grabovetskaya, M.B. Ivanov, A.P. Zhilyaev, R.Z. Valiev, Scr. Mater. **44**, 873 (2001)
29. X. Sauvage, G. Wilde, S.V. Divinski, Z. Horita, R.Z. Valiev, Mater. Sci. Eng., A **540**, 1 (2012)
30. R.A. Carolan, R.G. Faulkner, Acta Metall. **36**, 257 (1988)

Creep Behavior and Mechanism of Casing in Thermal Well Under Cyclic Steam Stimulation at Medium Temperature

Hang Wang, Lihong Han, Shangyu Yang, Tao Tian, Long Jiang and Wei Chen

Abstract Based on traditional theory, creep behavior does not occur unless operation temperature exceeds the 30% melting point of steel (i.e. 450 °C). Whereas, The casing damage in heavy oil recovery well demonstrated that creep occurred obviously for casing materials during long term service at 280–350 °C. In the present study the creep behavior, precipitation feature and deformation substructure were investigated in C–Mn steel with low carbon and Cr–Mo steel with low alloy during creep at 350 °C comparatively. The results showed that creep rate decreased initially, then remained stabilization. The creep rate reduced significantly for Cr–Mo steel with low alloy. TEM examination revealed that the carbide precipitation distributed along grain boundary in C–Mn steel with low carbon as-received condition. The typical morphology evolved from pile-up dislocation to nets during creep. However, both spherical precipitation with nanometer and rod-like one with micrometer were observed in Cr–Mo steel with low alloy

H. Wang (✉) · L. Han · S. Yang · T. Tian · L. Jiang
Tubular Goods Research Institute of China National Petroleum Corporation, Xi'an, Shaanxi 710077, China
e-mail: wanghang008@cnpc.com.cn

L. Han
e-mail: hanlihong@cnpc.com.cn

S. Yang
e-mail: yangshangyu@cnpc.com.cn

T. Tian
e-mail: tiantao001@cnpc.com.cn

L. Jiang
e-mail: jianglong003@cnpc.com.cn

H. Wang · L. Han · S. Yang · T. Tian · L. Jiang
State Key Laboratory of Performance and Structural Safety for Petroleum Tubular Goods and Equipment Materials, Xi'an, Shaanxi 710077, China

W. Chen
State Key Laboratory for Mechanical Behavior of Materials, Xi'an Jiaotong University, Xi'an 710049, China
e-mail: weichen813@mail.xjtu.edu.cn

© Springer Nature Singapore Pte Ltd. 2018

Y. Han (ed.), *Advances in Materials Processing*, Lecture Notes in Mechanical Engineering, https://doi.org/10.1007/978-981-13-0107-0_105

as-received condition simultaneously. The strong carbide containing Nb and V sheared glide dislocation, then stacking faults and microtwins formed gradually during creep. The transition of creep mechanism could be attributed to the reduction of stacking fault energy (SFE) due to addition of alloy element, which leaded to improve in creep resistance finally.

Keywords Creep · Thermal casing · Heat resistant · Dislocation
Stacking faults

Introduction

Thermal recovery technology included cyclic steam stimulation (CSS), steam stimulation (SS) and steam assisted gravity drainage (SAGD), their operation temperature was always in the range of 280–350 °C. According to traditional theory, creep would not occur obviously unless operation temperature exceeds the 30% melting point of steel (i.e. 450 °C). Therefore, the heat resistance was usually not to design for thermal casing. However, the investigation showed that casing damage occurred in the form of creep and rupture frequently. The heat resistance steel at high temperature of 560–650 °C consisted of ferritic one with medium alloy (9–12%) and austenitic one with high alloy (more than 30%) [1–4]. It is believed that the steel with 9–12%Cr held the highest creep strength in ferritic heat resistance steel. The results implied that both MX and M23C6 were dominant mechanism for creep strength at 560–650 °C [3, 4]. The C–Mn steel was used in thermal well, resulted in a large amount of casing damage. Currently, heat resistance improved significantly via addition of Cr and Mo elements at medium temperature, such as BG80H and TP90H.

The content of alloy element was much lower in heat resistance steel with low alloy, then the heat resistance and associated deformation mechanism were different significantly, compared with the one with high alloy element. In this case, Xie etc. [5] proposed the performance requirement for thermal steel. Han etc. [6] put forword the technology index for casing selection material. Wang etc. [7] pointed out that strong carbide caused improvement in creep resistance in Cr–Mo steel with low alloy. However, the creep mechanism has been still unclear so far. The feature of precipitation and deformation substructure would be characterized in C–Mn steel with low carbon and Cr–Mo steel with low alloy comparatively, which would be theoretical foundation for composition design and performance improvement.

Experimental Procedure

The C–Mn steel with low carbon and Cr–Mo steel with low alloy were selected, their composition listed in Table 1. Creep test was performed using high-precision creep electron testing machine with Instron-8862 at 350 °C, of which tension loading was set to 450, 475, 500, 520, 530 MPa. Firstly, the microstructure as-received condition would be examined comparatively, and then the typical substructure was observed after creep. The specimen for TEM was cut along cross section using wire-electrode cutting, then reduction thickness by means of mechanical and two-jet. The feature of precipitation and deformation substructure would be characterized using transmission electron microscopy (TEM) with JEM-200CX at 120 kV.

Results

The creep versus time curve was plotted, as shown in Fig. 1. It can be seen that creep rate decreased initially, then remained constant for these two types of steel. Particularly, the curve for Cr–Mo steel with low alloy located under that for C–Mn steel, as shown in Fig. 2. This result indicated that the former steel had the lower creep rate, the similar trendency was also reported under compression loading [7].

Table 1 Chemical composition of C–Mn steel and Cr–Mo steel (wt, %)

	C	Si	Mn	P	S	Cr	Mo	Ni	Nb V Ti	Cu	Al	Fe
C–Mn	0.26	0.24	1.27	0.015	0.0018	0.042	0.008	0.02	0.007	0.053	0.016	Bal
Cr–Mo	0.17	0.24	0.98	0.011	0.0034	0.99	0.33	0.059	0.061	0.21	0.017	Bal

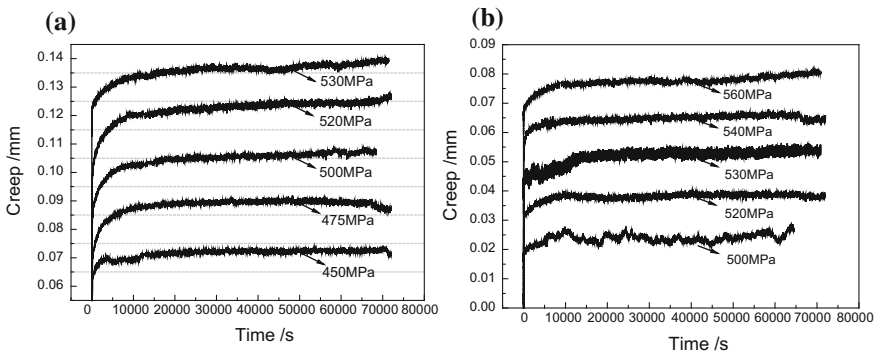

Fig. 1 Creep curve: **a** C–Mn steel, **b** Cr–Mo steel

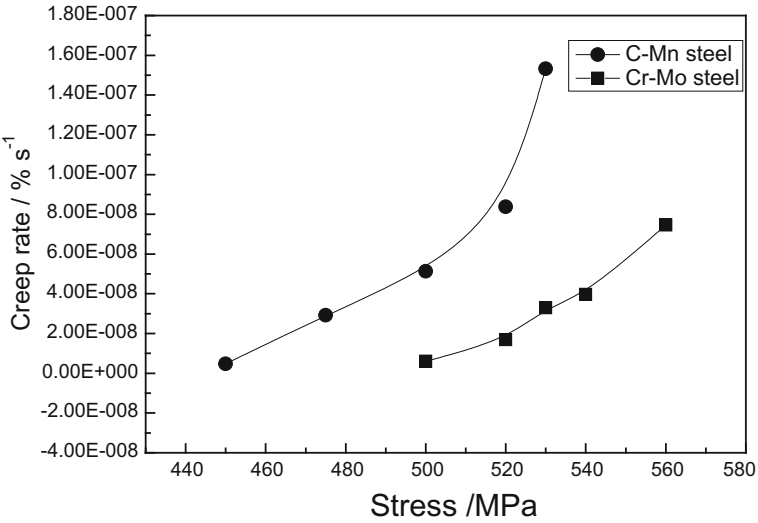

Fig. 2 Creep rate curve of C–Mn steel and Cr–Mo steel

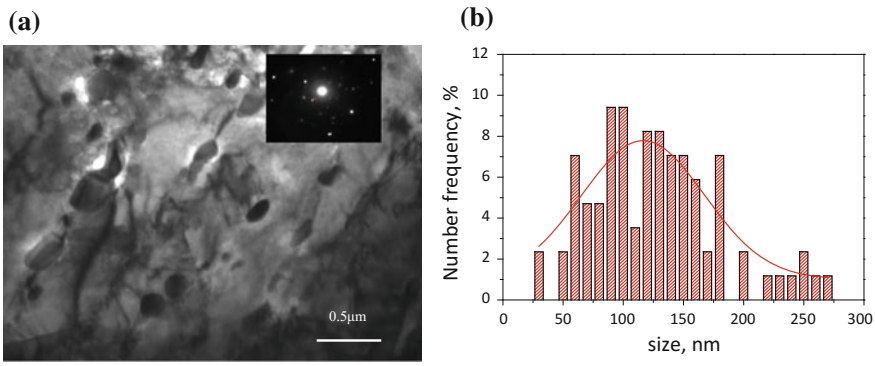

Fig. 3 Precipitation features in C–Mn steel as-received condition. **a** Shape, **b** size distribution

The precipitation feature was observed in C–Mn steel as-received condition, as shown in Fig. 3.

Carbide appeared in the form of spherical, which distributed along grain boundary, its size was about the range of 100–150 nm. Meanwhile, high density dislocation piled up during early stage of creep, as shown in Fig. 4a, indicating the strong impede to dislocation glide from the interface of carbide precipitation. At steady stage of creep, dislocation nets was observed around the area of interface and grain boundary, as shown in Fig. 4b. It was speculated that slip dislocation intersected and tangled mutually, which accumulated continuously along interface and then formed dislocation nets gradually. These nets eventually became into sub-grain

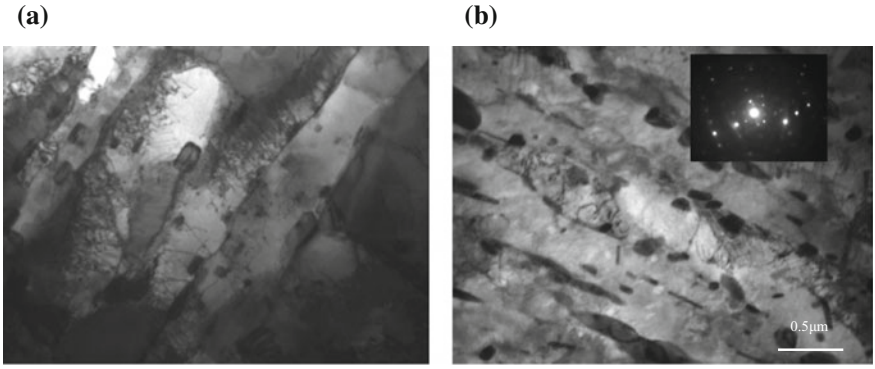

Fig. 4 Dislocation substructure in C–Mn steel: **a** at initial stage, **b** at steady state ($\vec{g} = (\bar{2}00)$, $B = [013]$)

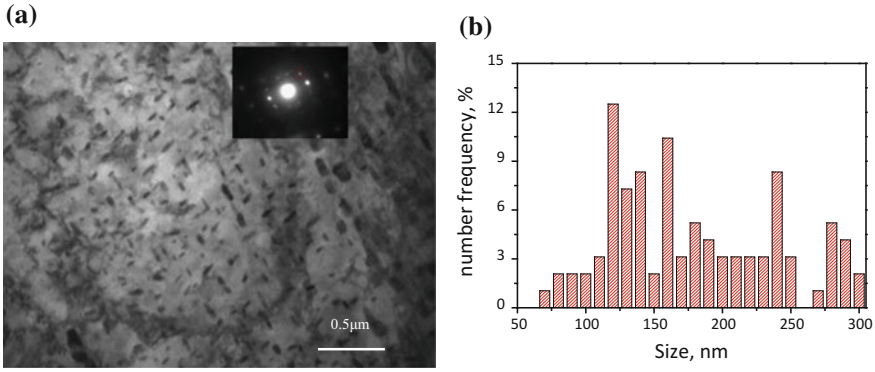

Fig. 5 Precipitation features in Cr–Mo steel as-received condition: **a** shape, **b** size distribution

structure. As a result, single dislocation line and pile-up dislocation evolved into dislocation nets and sub-grain during creep. The interface of carbide precipitation and net-like subgrain were dominant mechanism in C–Mn steel with low carbon.

The feature of precipitation was observed in Cr–Mo steel with low alloy as-received condition. Both spherical precipitation with nanometer and rod-like one with micrometer appeared, indicating the duplex characteristics in term of shape and size, as shown in Fig. 5. Precipitation distributed homogeneously, accompanying cross feature in local area. The results pointed out that this type of precipitation was the strong carbide containing micro-alloy such as Nb, V elements [7].

During early stage of creep, strong carbide impeded dislocation glide, as shown in Fig. 6a. Moreover, deformation substructure was characterized with planar dislocation, as shown in Fig. 6b. At steady stage of creep, stacking faults formed in the area of high-density dislocation, as well as microtwin, as shown in Fig. 7.

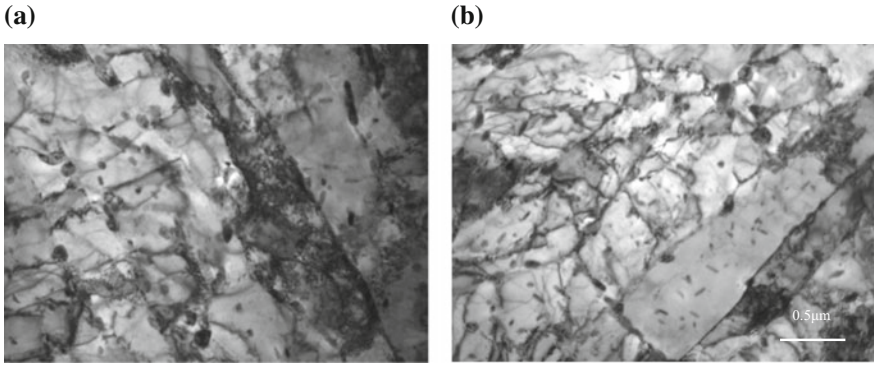

Fig. 6 Interaction between precipitation and glide dislocation in Cr–Mo steel: **a** local magnification, **b** dislocation configuration

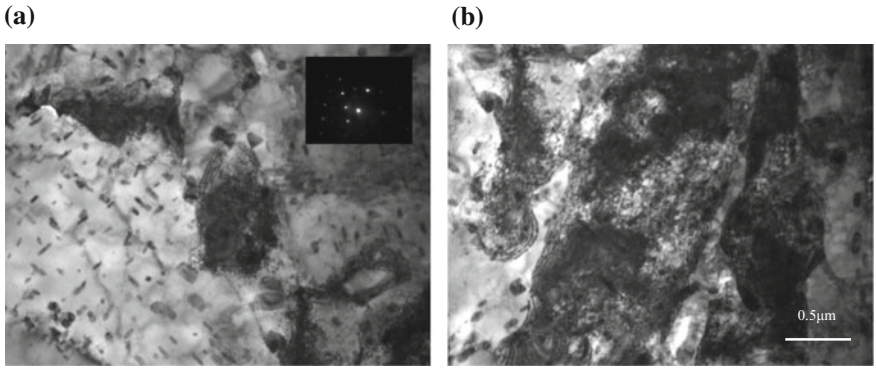

Fig. 7 Evolution of substructure in Cr–Mo steel with low alloy($\vec{g} = (\bar{2}00)$, $B = [012]$). **a** SFs, **b** microtwins

Consequently, strong carbide precipitation was the dominant mechanism in Cr–Mo steel with low alloy during long term service at 350 °C.

Discussion

As for C–Mn steel with low carbon, both grain boundary and net-like subgrain were the dominant mechanism during creep, which implied the closely relationship between creep rate and subgrain. Creep rate can be shown using Orowan relationship:

$$\dot{\varepsilon} = \rho_m b \cdot \frac{L}{d} V_c. \tag{1}$$

ρ_m is density of glide dislocation, b is Burger vector, d is distance to climb of dislocation, V_c is distance to climb, L is the free path for dislocation glide. Of which glide dislocation density is proportional with both total dislocation density and density at thermal activation location, the density of this glide dislocation can be expressed as follow:

$$\rho_m = \alpha_1 \rho_t N_m. \tag{2}$$

ρ_t denotes the total dislocation density inside grain, N_m denotes the density at thermal activation location (defined as activation count per unit volume).

Microstructure observation exhibited that slip dislocation was inhibited by subgrain boundary, and then climbed through thermal activation. Hence, free path for dislocation can be characterized with average size of subgrain, and point density of thermal activation is in direct proportion with area of subgrain boundary per unit volume, that is

$$N_m = \alpha_2 L^2 / L^3 = \alpha_2 / L. \tag{3}$$

Of which α_2 is a proportional constant, which related with dislocation property and shape of subgrain in subgrain boundary. Based on (1), (2), (3) formulation, creep rate at stage of steady can also be expressed:

$$\dot{\varepsilon} = \alpha \rho_t b V_c / d. \tag{4}$$

Glide dislocation interacted with unlike dislocation inside subgrain boundary during climb [8, 9], therefore, the distance to climb for dislocation d is in direct proportion to size of dislocation mesh around subgrain boundary, or space between dislocation in subgrain boundary, so

$$\dot{\varepsilon} = \alpha' \rho_t b V_c / h. \tag{5}$$

Then, creep rate at stage of steady is directly correlated with parameter of dislocation substructure (such as size of dislocation mesh). Moreover, misorientation θ of subgrain can replaces the size of dislocation mesh around subgrain boundary h, of which the more bigger for the size of dislocation mesh, the more smaller for misorientation of subgrain (its relationship can be expressed $\theta = b/h$). As a result, the key parameter is the size of dislocation mesh or misorientation.

At early stage of creep, the key parameter for creep rate was grain boundary, which impeded glide dislocation significantly. During steady stage of creep, dislocation nets occurred close to grain boundary. Therefore, misorientation changed as typical deformation structure evolved from grain boundary to dislocation nets, which leaded to decrease in creep rate during creep.

A large amount of precipitation occurred in Cr–Mo steel with low alloy, and glide dislocation cut precipitation. Stacking faults formed, as well as deformation twinning during creep. It is suggested [10, 11] that the formation of stacking faults can be explained in term of dissociation of perfect dislocation $a/2\langle 110\rangle$, which divided into partial dislocation of $a/3\langle 1\bar{2}1\rangle$ and $a/6\langle 11\bar{2}\rangle$. Of which partial dislocation of $a/3\langle 1\bar{2}1\rangle$ cut into precipitation. Meanwhile, partial dislocation $a/6\langle 11\bar{2}\rangle$ remained the interface between precipitation and the matrix, and formed stacking faults. This process can be expressed as follow:

$$1/2[110] \rightarrow 1/3[1\bar{2}1] + \mathrm{SF} + 1/6[11\bar{2}]. \tag{6}$$

Perfect dislocation divided into two Shockly dislocations, accompanying with stacking faults. For an extended dislocation, there existed the repulsive and attractive force between the two partials. The former originated from interaction of the partial dislocations themselves, whereas the latter was exerted by SF. Assuming that the two forces were in balance, the SFE can therefore be expressed using the following equation [11]:

$$\gamma_{\mathrm{SF}} = \frac{Gb^2 \cdot (2-\nu)}{8\pi \cdot d \cdot (1-\nu)} \cdot 1 - \frac{2\nu \cdot \cos 2\varphi}{2-\nu}. \tag{7}$$

where γ_{SF} is the SFE, G is the shear modulus, ν is the Poisson's ratio, b is the Burges vector of partial dislocation, d is the separation width of two partials (SF width), and φ is the angle between line direction of the undissociated dislocation and the Burges vector. The schematic drawing was showed in Fig. 8.

The stacking fault energy (SFE) is an important intrinsic parameter of materials, which is closely associated with the deformation mechanism, such as dislocation dissociation, cross-slip, and deformation twinning. It is considered that SFE is a parameter controlling the formation of twins in materials, and the tendency for twinning is higher in metals and alloys with low SFE, and vice versa [10, 11]. Low SFE promotes the dissociation of perfect dislocation, accompanying with the formation of stacking faults. The study on Ni–Co base alloy [12] indicated that the SFE decreased with increasing Co content and reached the lowest value, which is 19.9 + 2.5 mJ/m^2 in the γ matrix of TMW-4M3 alloy with Co content of 34.0 at.%.

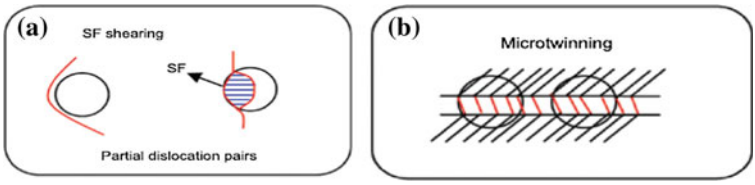

Fig. 8 The schematic drawing of creep mechanism in Cr–Mo steel with low alloy at medium temperature [13]

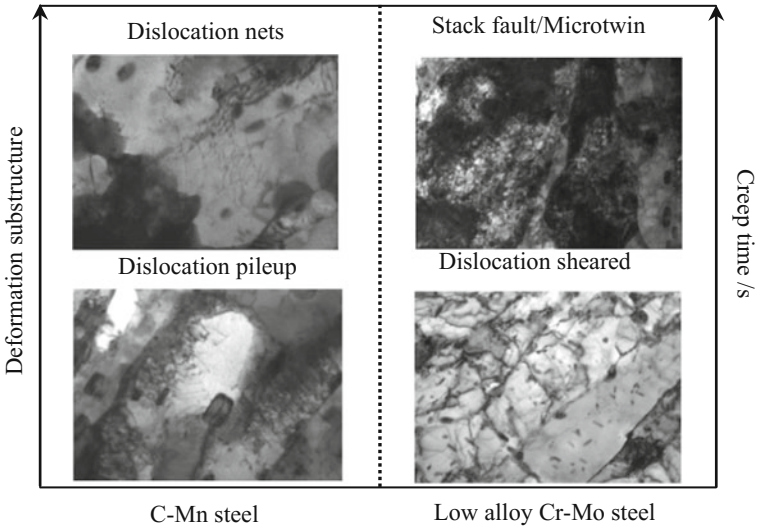

Fig. 9 Evolution of deformation substructure in C–Mn and Cr–Mo steel at 350 °C

As for Cr–Mo steel with low alloy, the SFE decreased with addition of Cr and Mo alloy elements, which resulted in perfect dislocation dissociated easily. Therefore, stacking faults occurred, as well as micro-twins. Dislocation nets was the dominant mechanism in C–Mn steel with low carbon. whereas, creep mechanism changed into stacking faults and microtwins in Cr–Mo steel with low alloy, the evolution of deformation substructure was showed in Fig. 9.

Summary

Carbide precipitation mainly distributes along ferritic boundary in C–Mn steel with low carbon as-received condition. Whereas, both spherical precipitation with nanometer and rod-like one with micrometer appears in Cr–Mo steel with low alloy. The typical deformation substructure evolves from dislocation piled up to nets in C–Mn steel with low carbon. Whereas, both stacking faults and microtwin occur in Cr–Mo steel with low alloy during creep at 350 °C. The transition of creep mechanism can be attributed to reduction in SFE and strong carbide precipitation due to addition of Cr and Mo alloy elements.

Acknowledgements We would like to thank for financial support from NSFC (No. 51574278) and CNPC (2016A-3905).

References

1. A. Schneider, G. Inden, Simulation of the kinetics of precipitation reactions in ferritic steels. Acta Mater. **53**, 519–531 (2005)
2. A. Aghajani, F. Richter, C. Somsen, S.G. Fries, I. Steinbach, G. Eggeler, On the formation and growth of Mo-rich laves phase particles during long-term creep of a 12% chromium tempered martensite ferritic steel. Scripta Mater. **61**, 1068–1071 (2009)
3. A. Kostka, K.-G. Tak, G. Eggeler, On the effect of equal-channel angular pressing on creep of tempered martensite ferriitic steels. Mater. Sci. Eng. A **481–482**, 723–726 (2008)
4. M. Taneike, F. Abe, K. Sawada, Creep strengthening of steel at high temperatures using nano-sized carbonitride dispersions. Nature **424**, 294–301 (2003)
5. J. Xie, in *Casing Design and Analysis for Heavy Oil Wells*. World Heavy Oil Conference, vol. 415 (2006)
6. L.H. Han, J.J. Wang, H. Wang, C.Y. Qin, Y.R. Feng, *Strain Based Design and Material Selection Technology for Thermal Well.* International Petroleum Technology Conference, IPTC 16739 (2013)
7. H. Wang, J.J. Wang, L.H. Han, Z.H. Tian, B. Xie, Creep behavior and microstructure of low alloy heat resistant steels at medium temperature. Trans. Mater. Heat Treat. **35**, 131–136 (2014)
8. M.A. Morris, J.L. Martin, The effect of low-angle and high-angle grain boundaries. Acta Metall. **32**, 1609–1614 (1984)
9. D. Cailard, J.L. Martin, Effect of grain size on plasticity in ultra-fine grain size steels. Acta Metall. **31**, 813–821 (1983)
10. B. Décamps, A.J. Morton, M. Condat, On the mechanism of shear of precipitates by single (α/2) dissociated matrix dislocations in Ni-based superalloys. Philos Mag. **64A**, 641 (1991)
11. M. Condat, B. Décamps, Some deformation micromechanism in Ni-Based super- alloys evidenced using TEM experiments. Scripta Metall. **21**, 607 (1987)
12. Y. Yuan, Y.F. Gu, C.Y. Cui, T. Osada, Z.H. Zhong, T. Tetsui, T. Yokokawa, H. Harada, Influence of Co content on stacking fault energy in Ni-Co base disk superalloys. J. Mater. Res. **26**, 2833 (2011)
13. L. Xu, Z.K. Chu, C.Y. Cui, Y.F. Gu, X.F. Sun, Creep Mechanism of a Ni-Co base wrought superalloy. Acta Metall. Sin. **49**, 863–870 (2013)

Evaluating the Compatibility of PA11 Pipe with Oil Field Media Based on Tensile Tests

Nan Ding, Meng Zhang, Houbu Li, Xiang Zhang, Ke Cai and Bin Wei

Abstract In recent years, a large number of thermoplastic pipes have been used in onshore oil fields of china in order to solve the corrosion problem of traditional carbon steel pipelines. However the domestic investigations on compatibility evaluation of thermoplastic materials with oil field media are just at the preliminary stage. Therefore, PA11 was chosen to study compatibility according to ISO 23936-1 standard. And influences of various factors on tensile test results were analyzed in order to optimize test parameters. Exposure tests were carried out in five kinds of simulated environments that were representative in the oil field service, and tensile tests were carry out in accordance with ISO 527 standard. The results showed that: ISO 23936-1 standard was confirmed to be an effective method of evaluating compatibilities of thermoplastic materials quantitatively; the tensile properties obtained from original PA11 material were in agreement with the data released by material supplier; the elongation of specimens decreased significantly after exposure tests, which indicates that the material's toughness decreased; PA11 was compatible to all the test environments except the H_2S-containing, judged by changes of tensile properties. RSDs (relative standard deviation) of test data showed

N. Ding (✉) · H. Li · X. Zhang · K. Cai · B. Wei
CNPC Tubular Goods Research Institute, State Key Laboratory of Performance and Structural Safety for Petroleum Tubular Goods and Equipment Materials, Xi'an 710077, Shaanxi, China
e-mail: dingnan@cnpc.com.cn

H. Li
e-mail: lihoubu@cnpc.com.cn

X. Zhang
e-mail: zhangxiang003@cnpc.com.cn

K. Cai
e-mail: caike@cnpc.com.cn

B. Wei
e-mail: weibin06@cnpc.com.cn

M. Zhang
Xi'an Shiyou University, Xi'an 710065, Shaanxi, China
e-mail: 2516228010@qq.com

© Springer Nature Singapore Pte Ltd. 2018

Y. Han (ed.), *Advances in Materials Processing*, Lecture Notes in Mechanical Engineering, https://doi.org/10.1007/978-981-13-0107-0_106

that stress test precision of specimens was better than that of strain and modulus. And suggestions for tensile test were given as the following: (1) specimens should be flat and straight in order to ensure the precision of strain test; (2) low test speed, such as 1 mm/min should be used to ensure that modulus could be calculated precisely.

Keywords PA11 · Thermoplastic · Compatibility · Oil field · Tensile test

Introduction

Nowadays, onshore oil fields of China commonly face to the serious problem of internal corrosion of traditional carbon steel pipes, especially in some areas where transmission media characterized as high content of H_2O, CO_2, H_2S and Cl^- and low pH value. Therefore, the integrated corrosion management is in urgent need in the aim of production safety and environment protection. Main treatment measures are coatings, inhibitors, corrosion-resistant alloys and non-metallic pipes. Compared with other measures, the main advantage of using non-metallic pipes is to avoid corrosion problem completely at a relatively low cost, and without supporting facilities or continuous consumables. Based on the current level of non-metallic pipes manufacturing technology, it is difficult to achieve large diameter for high pressure service, so non-metallic pipes are widely used as single well or gathering pipelines now.

The thermoplastic is a kind of widely used non-metallic materials. It can be made into homogeneous pipes and used alone, and can also be used as the liner or the matrix material of composite pipes. During the service life, thermoplastic materials seal, isolate and contact with transmission media.

Although polymer materials are corrosion-free, transmission media might lead to the degradation [1, 2]: firstly, media can change the properties of polymer materials by attacking the molecule chain directly through chemical reactions, such as the hydrolysis; secondly, through physical reactions, such as the swelling and the permeation, media can result in the loss stability of the pipe geometry even blistering or collapse failures; thirdly, media can extract the additives from plastics, which may result in changes of material properties. The design life of plastic pipes is usually more than twenty years, during such a long time these chemical and physical effects will change the composition and the structure of materials gradually. And elevated temperature can accelerate these effects and cause the degradation of pipe mechanical properties. Therefore, prior to the practical application, sufficient data should be provided to demonstrate the compatibility of thermoplastics.

At the present time, a commonly recognized method for determining the service pressure of thermoplastic pipes is based on the long-term hydrostatic test and the standard extrapolation calculation method. Although a service life of fifty years can be obtained by using this method, the test period is very long (10,000 h) and the

cost is considerable [3, 4]. In addition, only mechanical properties of pipes are concerned in this method, and the service condition may be complicated and cannot be represented by using some experiential factors. Therefore, it is essential to evaluate the compatibility of thermoplastic materials for the pipeline design and the material selection.

The laboratory compatibility test contains two stages: the first stage is to expose specimens in simulated environments; and the second stage is to test the performance changes of specimens experienced exposures.

Initially, non-metallic pipes used in onshore oil field of China were mainly fiber glass-reinforced plastic (FRP) pipes. During this period, the thermoplastic pipes were seldom used because of their low pressure rating. Therefore, the initial research work on compatibility of thermoplastic pipes was reference to the method used for FRPs according to NACE TM0298 [5] standard: this method includes exposing ring-shaped specimens cut from pipes to simulated oilfield environments in autoclaves, and determining the comparative apparent tensile strength of specimens experienced exposures and the blank. Figure 1 shows specimens and tensile test fixtures used in NACE TM0298.

The advantages of this method are: specimens can be prepared easily, and the apparent tensile strength corresponds to the internal pressure of pipes. But its disadvantages are also obvious: the results have no direct relation to service performances, and the significance of the results can be determined only by each laboratory for its particular application. So this method shall be considered as a screening method.

Since year 2008, with the development of the lining technology and reinforced thermoplastic pipes (RTP), the usage of thermoplastic materials has increased significantly. In recent years, RTPs designed for elevated temperature and/or H_2S-containing environments and/or gas transmission services have been manufactured and been on trial in onshore oil fields. And at the same time, flexible risers designed for offshore services have also become a research focus. Under this background, traditional thermoplastic materials, such as PE and PVC/C-PVC alloy, may not competent, so some advanced polymer materials, such as PVDF and PEX have been used, and there are also some other materials, such as PA11, PA612 and

Fig. 1 Ring-shape specimens (left) and tensile test fixture (right)

POK are going to enter the Chinese oil field marker. Therefore, it is necessary to establish a standard test method to evaluate compatibility of thermoplastic materials.

Internationally, ISO 23936-1 standard provides requirements and recommendations for the selection and qualification of thermoplastic materials in contact with media related to oil and gas production. Similar to NACE TM0298, ISO 23936-1 carries out exposures in simulated oil field media environments using autoclaves. But according to ISO 23936-1, the dumbbell-shaped specimens are used, and after exposures the changes of specimens in size, quality, tensile property and thermal stability (oxidation induction temperature) are tested and calculated, and the compatibility is evaluated according to general acceptance criteria [6].

At the present time, laboratories, oil field users and pipe manufactures of China are all lack of experience on the test method of ISO 23936-1. Therefore, PA11 was chosen to study the test method of compatibility evaluation. Compared with other tests, tensile test is much more complex, and affected by several factors, so the discussion was focused on the results of tensile tests.

Experiment

Specimens

Mainly in offshore oil fields, PA11 (polyamide 11) has been successfully used for more than twenty years, and it is also one of the liner thermoplastic materials recommended in ISO 23936-1. Therefore, choosing PA11 as the study object, the test results can be compared with the existing data in order to verify material compatibilities with media, and discuss the optimization of the test method.

Dumbbell-shaped specimens described in ISO 527-2 [7] were used according to ISO 23936-1, and this type of specimen should be flat and straight, and be prepared by moulding, extrusion and cast from raw material. Considering the heat history specimens experienced during preparation, and even the additive components, may be different from the final product, so all specimens used in this study were machined from pipe in order to simulate the actual application to the maximum extent. Pipe samples were PA11 (Rilsan® BESNO P40TLX) supplied by ARKEMA, which size is OD (outside diameter) 90 mm and WT (wall thickness) 7 mm. Test specimens of 1B type were machined from PA11 pipes in the way that the length direction of specimens was along the axial direction of pipes and the thickness was reduced into the standard size from the outside of the pipe wall. Figure 2 shows the morphology of test specimens. Thirty specimens were prepared and divided into six groups in the way that each group contained five specimens. Five groups (Group 2–6) experienced exposure tests in simulated environments, and one group (Group 1) was blank.

Fig. 2 Morphology of test specimen

Exposure

As shown in Table 1, five kinds of simulated environments were selected for exposure tests. For all these five environments, test temperature was maintained at 70 °C and test period lasted 90 days. As shown in Fig. 3, the exposure tests without high pressure gas were carried out in a oil-bath, and high-pressure exposure tests were carried out in autoclaves.

When exposure tests were completed, specimens were ultrasonic cleaning in de-ionized water and followed by drying in 40 °C air, and then examined by visual inspection. It is found that all exposure specimens were discolored in various degrees depended on exposure environment, but no macroscopic morphology changes were observed. Tensile tests were then carried out.

Table 1 Test fluids of simulated environments selected for exposure tests

Group No.	Environment	Initial composition	Specimen No.
1	Blank	–	1–5#
2	Brine	3.5% wt NaCl aqueous solution	6–10#
3	Hydrocarbon	0# diesel oil	11–15#
4	Crude oil	Light crude (pH = 5–6)	16–20#
5	Inhibited brine condition	Gasp phase (30% volume): N_2, 10 ± 1 MPa at room temperature; Liquid phase (70% volume): brine (3% wt NaCl + 0.5% wt hexadecyltrimethylammonium chloride)	21–25#
6	Sweet service condition	Gasp phase (30% volume): 5% CO_2 + 10% H_2S + 85% N_2, 10 ± 1 MPa at room temperature; Water phase (10% volume): de-ionized water (conductivity < 5μS); Oil phase (10% volume): 0# diesel oil	26–30#

Fig. 3 Exposure test equipment: oil-bath (left two) and autoclaves (right two)

Tensile Test

Tensile tests were carried out in according with ISO 527-1 [8] and ISO 527-2. Tests were carried out at room temperature, and gauge length was 50 mm. Instead of 1 mm/min recommended in ISO 527, a faster test speed 5 mm/min was selected for a higher efficiency. As shown in Fig. 4, a CMT-4101 universal testing machine was used as the test equipment, and a large deformation extensometer was used for the strain measure.

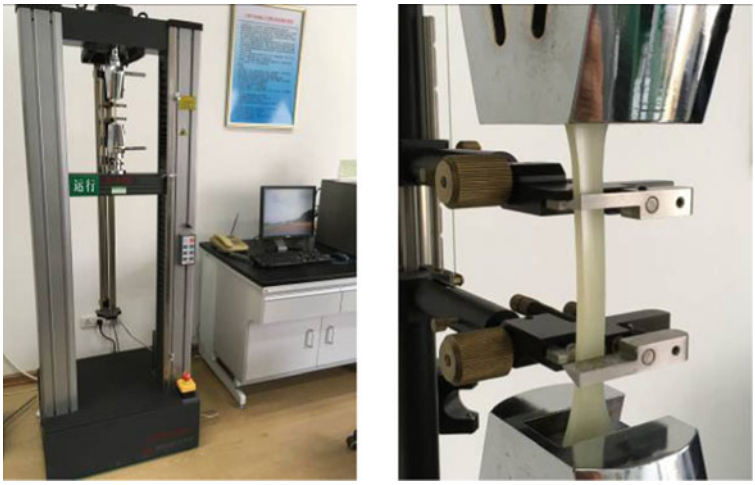

Fig. 4 Tensile test equipment (left) and large deformation extensometer (right)

Result and Discussion

Figure 5 shows tensile test curves of all PA11 specimens. Curves of blank specimens (No. 1–5#) can be roughly divided into three stages: first, the slope is large at the initial, and the stress increases rapidly with the increase of strain; followed by a gentle stage with a lower slope, but there is no obvious yield, and this stage corresponds to the necking period of specimens; then the slope rises up again and maintains to a relatively stable level until the specimen fracture. Compared with blank specimens, exposed specimens (6–30#) shows differences on tensile curves: the first stage possesses a higher slope, and it terminates in a higher stress although the strain corresponding remains at the level of blank, and it appears obvious yield phenomenon; the third stage becomes shorter or even disappears, and the fracture strain reduces significantly, especially for the specimens (26–30#) exposed in H_2S-containing environment. These indicate that, after exposure, the strength of PA11 does not change obviously, but the toughness reduces significantly. Treating the transition zone between the first and the second stages of tensile curves as yield, the blank specimens' yield stress and yield strain are calculated, and the results obtained are consistent with the data of PA11 (Rilsan® BESNO P40TL) [9] released by material supplier: σ_e = 27 MPa, and ε_e = 30%.

In ISO 23936-1, tensile properties for determining whether or not the material compatibility is qualified are the tensile strength (stress at break), the elongation (strain at break) and the E-modulus, and their general acceptance criteria are shown in Table 2. Data of tensile test results are given in Table 3: every figure is the arithmetic mean of five values obtained from specimens of each group, and the stress at break (σ_B) and the tensile modulus (E_t) are calculated to three significant figures and the strain at break (ε_B) is calculated to two significant figures. As shown in Table 3, values of ε_B and E_t of blank specimens are consistent with the data of PA11 (Rilsan® BESNO P40TL) released by material supplier: nominal break >50% at strain, and tensile modulus is 360 MPa. Compared with blank specimens, after exposure the σ_B does not show obvious changes; but ε_B significantly decreases which indicates the decrease of toughness; and as to E_t, it changes irregularly. The σ_B, ε_B and E_t of specimens exposed in the H_2S-containing environment (Group 6) are all changed too much and exceeded the allowable range listed in Table 2, and the E_t of specimens exposed in the brine (Group 2) is the same. The Group 6 is a H_2S-containing environment, and the H_2S has already been confirmed to be harmful to thermoplastic materials by previous studies [10]. As to Group 2, the test temperature 70 °C is almost the maximum service temperature recommended for PA when water existing, because of the potential risk of material hydrolysis, and this is why PA materials are commonly used in hydrocarbon environment rather than aqueous. But Group 5 is also water-containing, and is compatible with PA11 according to Table 3. This shows that the effect of hydrolysis in brine should be slight in this study. So the cause of Group 2 "ΔE_t" unqualified should be reconsidered.

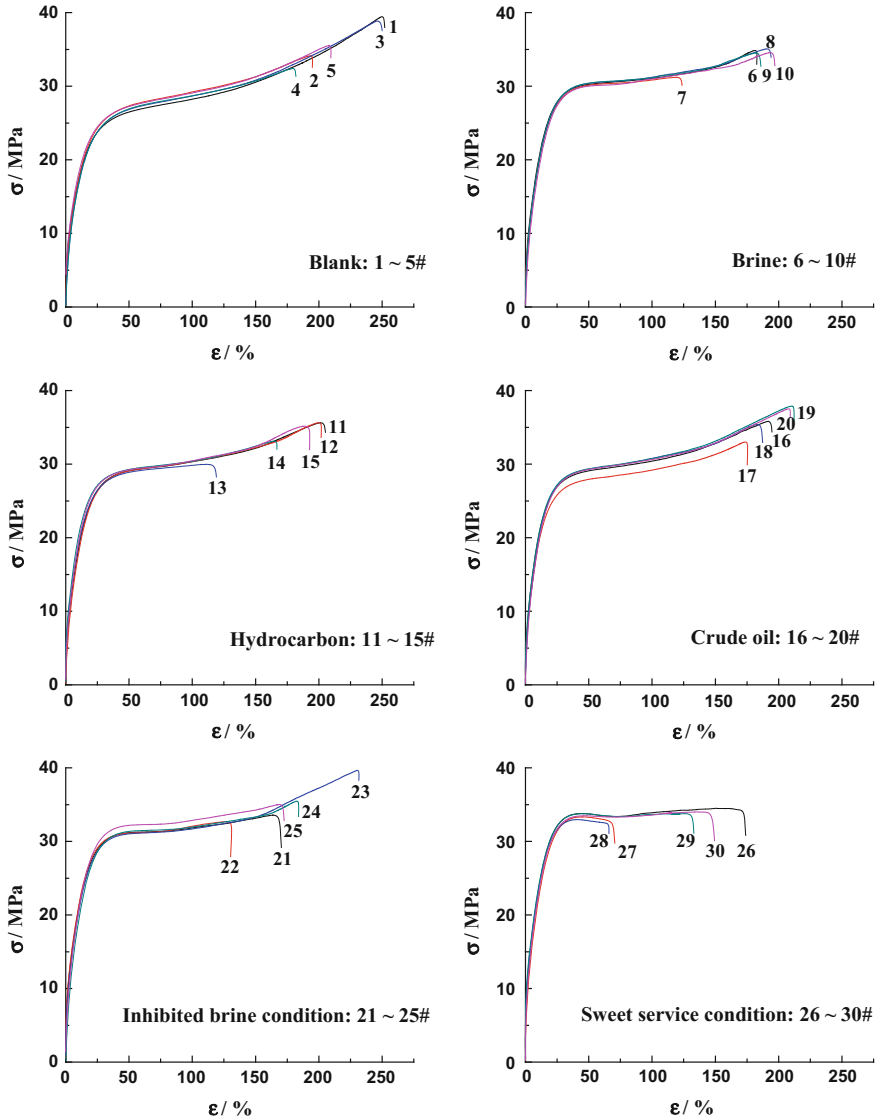

Fig. 5 Tensile test stress-strain curves of all specimens (x-axis: strain; y-axis: stress)

Table 2 General acceptance criteria

Tensile strength (Break) σ_B/MPa	Elongation ε_B/%	E-modulus E_t/MPa
±20	±30	±20

Table 3 Tensile test results of σ_B, ε_B and E_t

Group No.	σ_B/MPa	$\Delta\sigma_B$/%	ε_B	$\Delta\varepsilon_B$/%	E_t	ΔE_t/%
1	33.4	–	220	–	354	–
2	29.6	−11	180	−18	454	+28
3	30.1	−10	180	−18	342	−3
4	31.6	−5	200	−9	400	+13
5	30.7	−8	180	−18	425	+20
6	26.3	−21	120	−45	577	+63

RSD (relative standard deviation) is commonly used to represent the accuracy of test result, and it is calculated by following equations (Eqs. 1 and 2):

$$S = \sqrt{\frac{\sum_{i=1}^{n}(x_i - \bar{x})^2}{n-1}} \tag{1}$$

$$RSD = \frac{S}{\bar{x}} \times 100\% \tag{2}$$

where S is the standard deviation, $\bar{x}$ is the arithmetic mean and RSD is the relative standard deviation.

Figure 6 shows the RSD of test data of three kinds of parameters, it can be seen that: the RSD of σ_B was relatively small, and the values of different groups were basically the same, which indicates that the dispersion of stress values measured is relatively small, and the dispersion levels of the six groups are basically the same; RSDs of ε_B and E_t are greater, and figures are different between each group, which indicates that the dispersions of strain and modulus are great. Therefore, the stress test results are considered to be reliable, while the accuracies of strain and modulus test results are unsatisfactory. The reasons are as follows:

(1) The test results of stress are seldom affected by external factors. It is because that the force value is collected by load sensor directly, and the cross-sectional

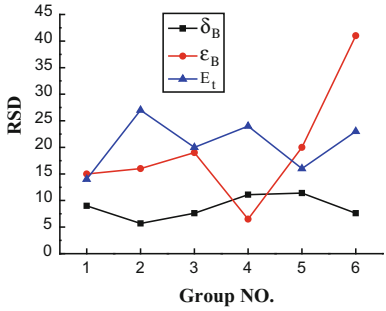

Fig. 6 RSD of σ_B, ε_B and E_t of each groups

area of specimen is measured prior tensile test and can be treated as a constant for each specimen. And all specimens are tested under the same test speed. Therefore, it can be concluded that as long as specimens were fixed tightly, the load sensor was in good condition and area values were calculated correctly, stress results would be not affected by external factors in this study.

(2) The strains are measured by a large deformation extensometer (LDE) that can clamp to specimens by blades and elongate together with the specimens during tests, as shown in Fig. 4. The reliability of LDE clamped to specimens can affect the elongation consistency. As shown in Fig. 2, the specimens prepared from pipes are curved in the width direction, which has adverse effect on fixing the LDE. In addition, the plastic surface is smooth and soft, so the blades of LDE may skid on the specimens. Therefore, all these factors can affect the strain test results.

(3) The E_t is defined as the slope of the $\sigma(\varepsilon)$ curve in strain interval between $\varepsilon_1 = 0.05\%$ and $\varepsilon_2 = 0.25\%$, so the linearity of initial section on the $\sigma(\varepsilon)$ curve is essential for calculation. Unfortunately, the curves obtained by tensile tests are not smooth and step-shaped in the initial sections. So the results of E_t are considered to be doubtable, despite calculated by computer with the help of test software. Two main reasons are thought to result in the micro-steps, the excessive test speed and the bending of specimens in the length direction. The recommended test speed 1 mm/min shall be used for modulus measure although is inefficient. But the bending of specimens is the result of residual stress [11, 12] release. Residual stresses are mainly caused by the temperature gradient distributing along the thickness direction of pipe wall, and temperature gradients are resulted from the cooling method used during extrusion process [13–16]. Therefore, when cut off from PA11 pipes, specimens bent along the length direction with the release of axial residual stress and cannot be corrected easily. And specimens may still be un-straight even fixed on grips, so the initial section on $\sigma(\varepsilon)$ curves may correspond to the straighten of specimens rather than the elastic deformation. As the residual stresses are created during extrusion process, the length direction bending of specimens machined from pipes cannot be avoided. Molding specimens can be used for modulus test, as they are flat and straight.

Conclusions

In accordance with ISO 527-1 standard, an evaluation of PA11 compatibility with oil/gas environments has been successfully carried out, which is based on comparison of tensile test properties of specimens prior and after exposure tests.

The original material tensile property of PA11 specimens determined are in agreement with the data released by material supplier, and the changes of tensile property of PA11 after exposure are reasonable according to material characteristics.

The ISO 23936-1 standard is confirmed to be an effective method, which can be used to evaluate the compatibility of thermoplastic materials quantitatively. And some suggestions for tensile tests are given as the following: (a) specimens should be flat and straight in order to ensure the precision of strain test; (b) low test speeds, such as 1 mm/min recommended in ISO 527, should be used for tensile tests in order to ensure that the modulus could be calculated precisely.

Acknowledgements The authors wish to thank ARKEM for supply sample pipes for this investigation.

References

1. L. Simon, R. MacDonald, K. Goerz, M. Grigis, Corrosion failure in a lined sour gas pipeline —part 1: case history of incident. Paper presented at NACE NAWC 2010, Calgary, Alberta, Canada, 15–18 February 2010
2. G.R. Ruschau, Novel polymers for applications as liners. Paper NACE00780 presented at the 55th annual conference and exposition, Orlando, Florida, USA, 26–31 March 2000
3. American Society for Testing and Materials, *ASTM D2837-13e1 Standard Test Method for Obtaining Hydrostatic Design Basis for Thermoplastic Pipe Materials or Pressure Design Basis for Thermoplastic Pipe Products* (ASTM International, West Conshohocken, PA, United States, 2013)
4. International Organization for Standardization, *ISO 9080:2012 Plastics Piping and Ducting Systems—Determination of the Long-term Hydrostatic Strength of Thermoplastics Materials in Pipe Form by Extrapolation*, 2nd edn. (ISO, Geneva, Switzerland, 2012)
5. NACE International, *NACE TM0298-2003 Standard Test Method Evaluating the Compatibility of FRP Pipe and Tubular with Oilfield Environments*, 1st edn. (NACE International, Houston, Texas, United States, 2003)
6. International Organization for Standardization, *ISO 23936-1:2009 Petroleum, Petrochemical and Natural Gas Industries—Non-metallic Materials in Contact with Media Related to Oil and Gas Production—Part 1: Thermoplastics*, 1st edn. (ISO, Geneva, Switzerland, 2012)
7. International Organization for Standardization, *ISO 527-2:2012 Plastics—Determination of Tensile Properties—Part 2: Test Conditions for Moulding and Extrusion Plastics*, 2nd edn. (ISO, Geneva, Switzerland, 2012)
8. International Organization for Standardization, *ISO 527-1:2012 Plastics—Determination of Tensile Properties—Part 1: General Principles*, 2nd edn. (ISO, Geneva, Switzerland, 2012)
9. http://www.extremematerials-arkema.com/en/materials-database/
10. N. Ding, K. Cai, X. Zhang, H. Li, Research on applicability of plastic alloy in oilfield sour aqueous environment. China Plast. Ind. **45**(1), 25–27, 52 (2016)
11. J. Poduška, P. Hutař, J. Kučera, A. Frank, J. Sadílek, G. Pinter, L. Náhlík, Residual stress in polyethylene pipes. Polym. Test. **54**, 288–295 (2016)
12. J. Poduška, J. Kučera, P. Hutař, M. Ševčík, J. Křivánek, L. Náhlík, Residual stress distribution in extruded polypropylene pipes. Polym. Test. **40**, 88–98 (2014)
13. L.E. Janson, *Plastic Pipes for Water Supply and Sewage Disposal*, 3rd edn. (Stockholm, Borealis, 1999)

14. J.G. Williams, J.M. Hodgkinson, A. Gray, The determination of residual stresses in plastic pipe and their role in fracture. Polym. Eng. Sci. **21**(13), 822–828 (1981)
15. E.Q. Clutton, J.G. Williams, On the measurement of residual stress in plastic pipes. Polym. Eng. Sci. **35**(17), 1381–1386 (1995)
16. K. Chaoui, A. Chudnowsky, A. Moet, Effect of residual stress on crack propagation in MDPE pipes. J. Mater. Sci. **22**(11), 3873–3879 (1987)

Impact Fracture Behavior of Large-Diameter X80 Line Pipes

Hui Feng, Hao Ding, Yiming Zhang and He Li

Abstract Pendulum instrumented impact test and Charpy impact test were employed to investigate the fractural behaviors of the large diameter X80 line pipes. The results revealed that the pendulum instrumented impact absorbed energy decreased significantly as the testing temperature lowered down, and the brittle appearance arose on the impact fracture morphology as well. However, the Charpy impact test result showed little difference when tested at the given temperatures, it is deduced that the increase of the specimen thickness improves the fracture sensibility of the pipeline steel on temperature, which makes great contribution to the difference between pendulum instrumented impact test result and Charpy impact test result.

Keywords X80 line pipe · Pendulum instrumented impact test
Fracture property · Fracture morphology

H. Feng (✉) · H. Ding · Y. Zhang · H. Li
Tubular Goods Research Institute of China National Petroleum Corporation, Xi'an, Shannxi, China
e-mail: rainfal012003@126.com

H. Ding
e-mail: dinghao01@cnpc.com.cn

Y. Zhang
e-mail: zhangym3@cnpc.com.cn

H. Li
e-mail: lihe008@cnpc.com.cn

H. Feng · H. Li
State Key Laboratory for Performance and Structural Safety of Oil Industry Equipment Materials, Xi'an, Shaanxi, China

© Springer Nature Singapore Pte Ltd. 2018

Y. Han (ed.), *Advances in Materials Processing*, Lecture Notes in Mechanical Engineering, https://doi.org/10.1007/978-981-13-0107-0_107

Introduction

To ensure the supply of natural gas to meet the needs of national economic development, high grade, large diameter and long-distance transportation has become the inevitable trend of China's natural gas pipeline technology development, yet the pipeline material must be of high strength and high toughness to guarantee the safe operation of line pipes. At present, X80 grade pipeline steel has been largely used in the 2nd West-east pipeline project by industrial production, and the fracture control as well as the fracture properties are reported in many literatures [1–4]. However, in the upcoming construction of China-Russia natural gas pipeline [5, 6], the X80 line pipe in large diameter of 1422 mm with higher transfer capacity and working in lower environment temperature puts forward higher requirements on the fracture properties of pipeline steel.

Charpy impact V-notch test (CVN) and Drop weight tearing test (DWTT) as well as Charpy instrumented impact test developing based on the traditional CVN test are the main test methods to determine the toughness of pipeline steel, according to which much work has been done to test the pipeline toughness. However, the traditional CVN and DWTT test methods only give the impact absorption energy, and cannot reflect the crack initiation and propagation process during deforming. As for Charpy instrumented impact test, the crack initiation and propagation process could be obtained while the ligament width of tested specimen is only 8 mm, far smaller than the actual wall thickness of large diameter X80 line pipe, resulting in inaccurate toughness properties crossing the whole wall thickness. In this study, pendulum instrumented impact test was employed to study the fracture properties of large diameter X80 line pipe with full wall thickness specimens, and the fracture behavior was investigated as well, to provide theoretical support for the safe operation of natural gas transportation pipe lines.

Experimental Procedure

OD1422 mm X80 submerged-arc helical welded pipe (SAWH) with wall thickness of 21.4 mm was used in this study, and the chemical composition is listed in Table 1. Rod tensile specimens along transvers direction with gauge length of

Table 1 Chemical composition of the tested line pipe (mass fraction, %)

Grade	Mass fraction								
	C	Si	Mn	P	S	Cr	Mo	Ni	Cu
X80	0.06	0.2	1.77	0.011	0.0018	0.27	0.18	0.2	0.2

Table 2 Tensile results of tested X80 line pipe

	No.	Rt 0.5 (MPa)	Rm (MPa)	A (%)
X80 line pipe	1	556	654	29
	2	578	667	24
	3	567	660	28
	Average value	567	660	27

50 mm and diameter of 12.7 mm were sampled on the SSAW pipe 180° from the weld. The tensile test was carried out using UTM5305 test machine according to ASTM A370-2012 with stretching rate of 2 mm/min. The tensile results are shown in Table 2.

Charpy V-notch specimens were machined in accordance with ASTM A370 recommended dimensions (10 mm × 10 mm × 55 mm), and Charpy impact test was performed using the ZBC 2752-B instrumented testing machine. The microstructural characterization was performed on MEF4 M optical microscopy.

Pendulum instrumented impact test is conducted in this study using the Zwick HIT50KP high energy pendulum impact test machine, with the maximum impact capacity of up to 50,000 J, and the whole process of real-time data acquisition could be completed with the help of instrumented test system, which provides the load-time, displacement-time and load-displacement curves. Tested specimens with length of 305 mm and width of 76.2 mm were sampled on the SSAW pipe 180° from the weld, and the thickness of the specimens was 21.4 mm, which is the full wall thickness. The notch is pre-pressed in the center of the specimen along the length direction.

Results

Microstructure

The microstructure of X80 SSAW line pipe mainly consist of acicular ferrite (AF), small fraction of quasi-polygonal ferrite (QF) and martensite/austenite (M/A) islands, as shown in Fig. 1. Besides, the grains on the surface are finer due to the more severe deformation during the rolling process while the microstructure in the center contains more QF with slightly larger grain size. Thermo-Mechanical Control Process (TMCP) technology was employed for the micro-alloyed pipeline steel to restrain the proeutectoid ferrite and pearlite transformation, therefore, AF structure is formed in the whole wall thickness range, which makes contribution to the high strength and ductility of the material.

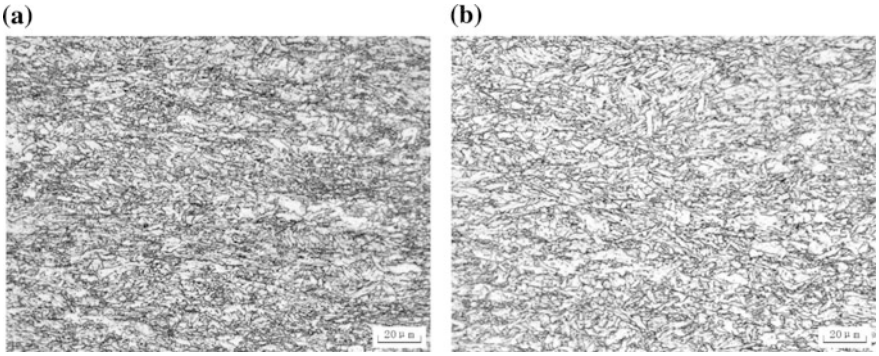

Fig. 1 Microstructure of the experimental pipeline steel on the surface (**a**) and in the center (**b**)

Impact Fracture Properties

The crack initiation and propagation of the X80 pipeline steel during fracture process were systematically investigated using the pendulum instrumented impact test machine in this study. The instrumented Charpy impact curves (Load/Impact energy versus Displacement) of the tested material at different temperatures are shown in Fig. 2. The physical meanings of each symbol in the figure are as follows [7, 8]: E1: the induced crack initiating energy, E2: ductile fracture absorbing energy, E3: brittle fracture absorbing energy, E4: absorbed energy after brittle fracture, Pm: maximum load, Pf: load at the brittle fracture initiating, Pe: load after brittle fracture, d0: displacement after impact test.

It can be seen in Fig. 2 that the pendulum impact fracture process could be divided into induced crack initiating stage, ductile fracture stage and brittle fracture stage. The absorbing energy during crack initiating stage and ductile fracture stage (E1 + E2) of the specimens tested at 10 and −10 °C make little difference, while

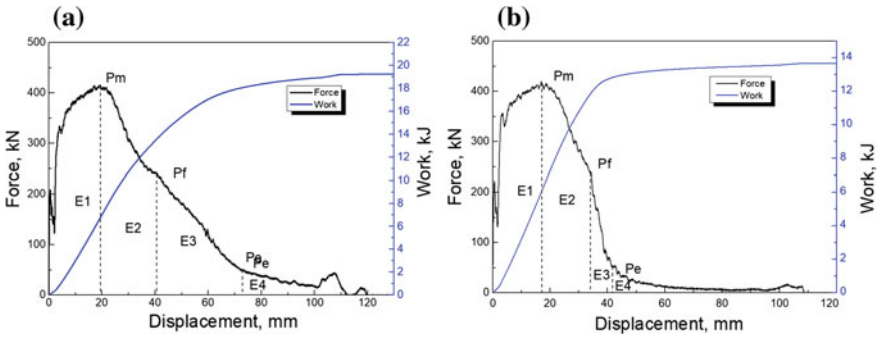

Fig. 2 Pendulum instrumented impact test curves of X80 pipeline steel tested at 10 °C (**a**) and at −10 °C (**b**)

Table 3 Impact fractural properties of X80 pipeline steel tested at different temperatures

	Testing temperature °C	Impacting energy, kJ			Slope of the load-displacement curve, K
		1	2	Average value	
X80 line Pipe	10	26.7	19.2	23.0	−6.0
	−10	13.6	14.7	14.2	−26.6

both the absorbing energy at brittle fracture stage (E3) and the energy after brittle fracture (E4) at 10 °C are higher than those tested at –10 °C. From the impact load-displacement curve, the Pf-Pe segment belongs to a brittle fracture stage, and the slope of the load-displacement curve, K, represents the ability of the material to prevent the cracking. The smaller the absolute value of K, the slower the crack propagating, indicating that the brittle fracture process of the specimen is strongly restrained. On the contrary, if the material could not resist the crack propagation effectively, the brittle crack spreads rapidly, resulting in a higher absolute value of K. In the test, the absolute value of K tested at −10 °C is 26.6, far higher than that tested at 10 °C, 6.0, as shown in Table 3. Thus, it can be deduced that the crack arresting ability of the experimental X80 line pipe decreases significantly as the testing temperature lowers down from 10 °C to −10 °C.

Figure 3 shows the fracture morphology of the X80 pipeline steel after pendulum impact test. The fracture morphology demonstrates ductile fracture feature, and large deformation could be seen at the end of the crack propagating (upper part in Fig. 3); however, the fracture morphology of the specimen tested at −10 °C shows obvious cleavage feature in the middle part of the fracture, and the deformation at the end of the crack propagating is slighter than that shown in Fig. 3a. These characteristics agree well with the fact that the absolute value of K tested at −10 °C is higher than that tested at 10 °C. Thus the crack arresting ability of X80 line pipe at −10 °C is lower comparing with the crack arresting ability at 10 °C.

Discussion

Influence of Testing Temperature on the Impact Fracture Properties

The influence of test temperature on the fracture toughness of pipeline steel mainly includes the influence of crack initiation and crack propagation. For X80 pipeline steel, the nucleation site of the crack is located at the interface of inclusions, the interface between the bainite lath and the M/A island and the interior of the M/A islands. At the early stage of loading, the stress concentration arises when there is significant difference between the stiffness of non-metallic inclusions and that of the matrix, leading to the formation of micro cracks at the interface if the bonding force

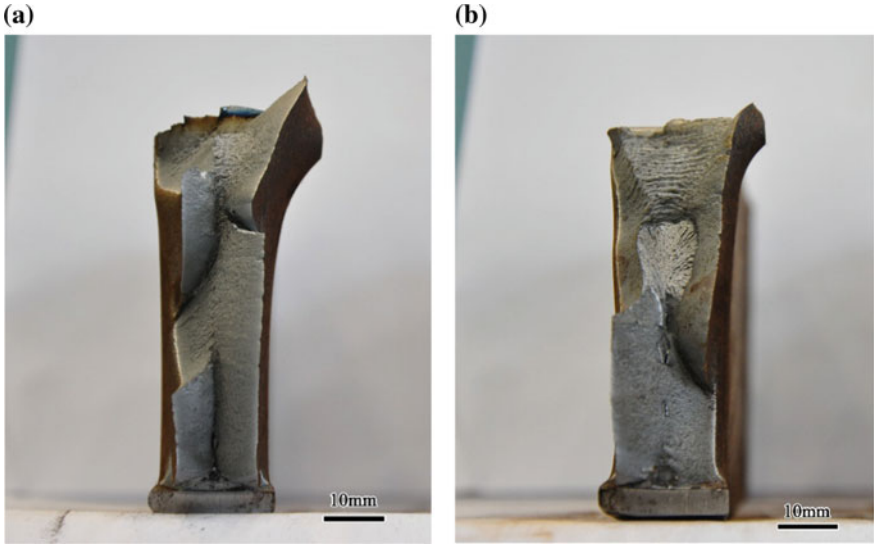

Fig. 3 Fracture morphology of X80 pipeline steel tested at 10 °C (**a**) and at −10 °C (**b**)

is poor. In addition, dislocations pile up at the phase boundaries due to the obstruction of M/A islands, which results in stress concentration. Once the shear stress at the interface component equals to the interface strength, the interface debonds and microcrack initiates. The crack propagation is mainly effected by the normal stress. After the crack initiation, under the impact bending load, the micro cracks propagate through connecting with each other with the increase of strain rate [9, 10]. In this experiment, the temperature difference between 10 and −10 °C has little effect on the crack initiation and the plastic propagation stage. However, the impacting absorbing energy at brittle fracture stage tested at −10 °C is lower than that of 10 °C. The decrease of testing temperature increases the dislocation slip difficulty during impact deformation process, making it more easily for dislocation piling up and stress concentrating, thereby the impact fracture properties of the material decreases accordingly.

Thickness Effect on Impact Fracture Properties

In addition to the pendulum impact test, Charpy impact test is another traditional method to characterize the impact fracture properties, yet the specimen used for Charpy impact test is 10 mm × 10 mm × 55 mm in dimension, which is different from that of pendulum impact test. Thus, the impact fracture properties tested with specimens of variant wall thickness are different. Table 4 shows the Charpy impact fracture properties of X80 pipeline steel tested at 10 and −10 °C. It can be seen that

Table 4 Charpy impact fractural properties of X80 pipeline steel tested at different temperatures

	No.	10 °C		−10 °C	
		Impact energy (J)	Shearing area (%)	Impact energy (J)	Shearing area(%)
X80 line pipe	1	342	100	397	100
	2	396	100	328	100
	3	362	100	345	100
	Average value	367	100	357	100

the fracture shearing area of both specimens is 100%. Besides, the Charpy impact energy tested at 10 °C is 367 J and 357 J at −10 °C, thus the difference is less than 5%, indicating that the difference of testing temperature between 10 and −10 °C has slight effect on the Charpy impact energy. While for pendulum impact test, the absorbing energy at 10 °C is 23.0 and 14.2 kJ at −10 °C, thus the difference is about 40%, as shown in Table 3, indicating that the difference of testing temperature between 10 and −10 °C has significant effect on the pendulum impact energy.

Generally, if the wall thickness of the specimen is small such as the Charpy specimen, the area near crack tip is under plain stress condition during impact fracture process; while if the wall thickness of the specimen is large such as the pendulum impact specimen, the area near crack tip is under plain strain condition during impact fracture process, therefore the plastic deformation at the crack tip is suppressed and the brittle fracture characteristic is observed [11–13]. These results reveal that the increase of wall thickness of specimens significantly improved the sensitivity of testing temperature on the pendulum impact fracture properties of the X80 pipeline steel, leading to a sharp reduction of impact absorbing energy for about 40% and the obvious brittle fracture feature in the middle of the fracture despite the testing temperature lowered down just from 10 to −10 °C.

Conclusion

The impact fracture behavior of large diameter X80 pipe line has been investigated.

(1) The pendulum instrumented impact absorbing energy decreases sharply as the testing temperature lower down, and brittle characteristic is observed in the fracture. The decrease of testing temperature increases the dislocation slip difficulty during impact deformation process, making it more easily for dislocation piling up and stress concentrating, thereby the impact fracture properties of the material decreases accordingly.

(2) Different from the pendulum impact result, the Charpy impact energy remains almost unchanged with testing temperature lowering down. The increase of wall thickness of specimens significantly improved the sensitivity of testing temperature on the impact fracture properties of the X80 pipeline steel, which makes great contribution to the difference between pendulum impact result and Charpy impact result.

Acknowledgements The authors would like to acknowledge China National Petroleum Corporation (CNPC), Key Lab of Oil Tubular and Environmental Behavior of CNPC for the financial assistance and allowing the publication of the paper.

References

1. C. Huo, H. Li, W. Zhang, K. Yang, Q. Chi, Q. Ma, Crack control technology for the X80 large OD 1422 mm line pipes. Nat. Gas Ind. B **3**(5), 479–484 (2016)
2. T. Sadasue, S. Igi, T. Kubo, N. Ishikawa, S. Endo, A. Glover et al., Ductile cracking evaluation of X80/X100 high strength linepipes. Int. Pipeline Conf. 1661–1669(2004)
3. H. Li, W. Zhang, Y. Li, C. Huo, Y. Feng, L. Ji, Comparison of BTC, RBTC and HLP models in the calculation of the dynamic ductile fracture propagation velocities based on the X80 full-scale burst test. Int. Conf. Pipelines Trenchless Technol. 1196–1203 (2013)
4. K.B. Kang, S.H. Chon, J.Y. Yoo, Microstructures and mechanical properties of heavy gauge API-X80 linepipe steel for arctic application. Mater. Trans. **50**(1), 1–5 (2012)
5. B. Wang, J. Lian, Effect of microstructure on low-temperature toughness of a low carbon Nb–V–Ti microalloyed pipeline steel. Mater. Sci. Eng., A **592**, 50–56 (2014)
6. W. Ding, Z. Jiang, J. Li, S. Li, C. Zha, X. Bai et al., Research and development into low temperature toughness of large diameter heavy wall X80 pipeline steel at Shougang steel. Int. Pipeline Conf. 285–291 (2012)
7. J. Fang, J.W. Zhang, L. Wang, An energy based regression method to evaluate critical CTOA of pipeline steels by instrumented drop weight tear tests. Int. J. Fract. **187**, 123–131 (2014)
8. H. Liu, H.L. Gao, Effect of pre-heating temperature at organization and performance of X80 pipeline steel. Welded Pipe Tube **30**(3), 27–29 (2007)
9. X.L. Zhang, C.J. Zhuang, Y.R. Feng, W.Z. Zhao, C.Y. Huo, Local brittleness of heat-affected zone of X80 pipeline steel. Iron Steel **42**, 69–72 (2007)
10. Z.P. Zhao, G.Y. Qiao, L. Tang, H.W. Zhu, B. Liao, F.R. Xiao, Fatigue properties of X80 pipeline steels with ferrite/bainite dual-phase microstructure. Mater. Sci. Eng., A **657**, 96–103 (2016)
11. Y.S. Shin, Effects of microstructure on tensile, charpy impact, and crack tip; opening displacement properties of two API X80 pipeline steels. Metall. Mater. Trans. A **44**, 2613–2624 (2013)
12. X.B. Liu, Q.Q. Duan, B.D. Wang, H. Zhang, Critical crack tip opening displacement for X70 and X80 steels—a parametric study. Mater. Sci. Forum **898**, 719–724 (2017)
13. P. Wang, E. Dang, L.U. Cai-Hong, L.I. Lei, Z.X. Shen, X.H. Wang et al., Research on crack tip opening displacement (CTOD) Experiment of X80 marine riser submerged arc welding joint. Welded Pipe Tube **04**, 17–22 (2011)

Hydrostatic Experimental Study and Failure Mechanism of Glass Fiber Reinforced Thermoplastic Pipes Used for Oilfields

Guoquan Qi, Dongtao Qi, Nan Ding and Xiaodong Shao

Abstract The traditional carbon steel pipe has been unable to meet the needs of high corrosive media oil and gas production since the gradual increase of the moisture content, and the increasingly severe corrosion environment during the deepening of the oil and gas field development process. In such situation, the reinforced thermoplastic pipe, as a typical non-metallic pipe, has become important solution for corrosion protection, and used in oil and gas gathering and transportation widely. In this study, the residual strength of reinforced thermoplastic pipe for oil and gas gathering and transportation was studied by using hydrostatic pressure residual strength method based on linear regression using pressure composite device with inner lining of PVDF and reinforced layer of glass fiber reinforced resin tape. The damage mechanism of the flexible composite pipe was studied by means of scanning electron microscopy. The results showed that the residual strength of the flexible composite pipe decreased with the increase of service time, and the logarithmic value was linear with the service time. The damage mechanism of the reinforcement layer was similar to that of the composite material, which was composed of four stages: matrix cracking, crack propagation, delaminating and fiber fracture.

Keywords Gathering and transportation · Reinforced thermoplastic pipe
Hydrostatic pressure-residual strength · Linear regression · Damage mechanism

G. Qi · D. Qi (✉) · N. Ding · X. Shao
State Key Laboratory for Performance and Structure Safety of Petroleum Tubular Goods and Equipment Materials, CNPC Tubular Goods Research Institute, Xi'an 710077, China
e-mail: qidt@cnpc.com.cn

G. Qi
e-mail: qgqstar@163.com

N. Ding
e-mail: dingnan@cnpc.com.cn

X. Shao
e-mail: shaoxd@cnpc.com.cn

G. Qi
Northwestern Polytechnical University, Xi'an 710029, China

© Springer Nature Singapore Pte Ltd. 2018

Y. Han (ed.), *Advances in Materials Processing*, Lecture Notes in Mechanical Engineering, https://doi.org/10.1007/978-981-13-0107-0_108

Introduction

In recent years, reinforced thermoplastic pipe has been used widely in the oil and gas field construction projects with the properties of excellent corrosion resistance and low hydraulic friction. This has played an important role in slowing corrosion of steel pipelines, saving ground investment and reducing maintenance costs. At present, the reinforced thermoplastic pipe has been applied to the oil and gas gathering and transportation, water supply and water injection system with the length of more than 20,000 km, accounting more than 10% of the total pipeline for oil and gas field surface engineering [1–3].

There is pressure inside the pipe body during the oil and gas transportation process, especially under certain special conditions. In order to ensure the safety of pipeline transportation and the smooth progress of production, it is necessary to ensure that the pipeline is subjected to the internal pressure requirements caused by conveying medium.

However, the production of reinforced thermoplastic pipe history is not long, and the domestic product does not have a unified official name, currently. The conditions of domestic manufacturers are different, some introduce foreign mature production technology, some design their own production processes, some use of high-performance materials to produce high-end products, while others use relatively low-grade materials to take the economic route. So, the market of d thermoplastic pipe can be described as a variety of products, different performance at present. For different types of products, some manufacturers do not strictly in accordance with the relevant standards for product evaluation, and some do not have long-term hydrostatic test conditions even more [4].

Accurate fatigue life estimation has important theoretical significance and engineering value for eliminating accidents, developing effective maintenance plans and extending the service life [5]. The long-term hydrostatic strength extrapolation of thermoplastic plastic pipe is used for aging prediction, which is mentioned in GB/T 18252-2000 [6]. Although this standard saves a lot of time, but still need one year for determination, and another drawback is that too many experimental data acquisition points, more than 18 points, cause inconvenience to actual operation. Faced with the rapid development of flexible composite pipe industry, very few suppliers or buyers implement this standard. In this study, a new method for predicting the life of reinforced thermoplastic pipe has been developed and tested.

Experiment

Selection of Samples

The sample selected in this test is the reinforced thermoplastic pipe for high pressure transmission, the structure shown in Fig. 1.

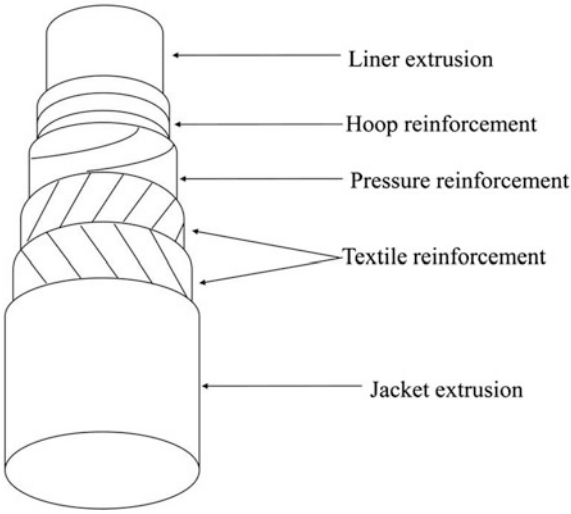

Fig. 1 The structure of reinforced thermoplastic pipe

Specifications: Diameter: 80 mm; Pressure endurance: 16 MPa;
Liner material: PVDF;
Material of reinforcement layer: Glass fiber reinforced resin tape;
Material of external protection layer: PE.

Experimental Procedures

Using the reinforced thermoplastic pipe mentioned in 1.1 above, the 90 °C blasting test and the long-term hydrostatic pressure-remaining blasting test were carried out. The specific test plan is shown in Table 1.

Table 1 Test program for long service performance evaluation of reinforced thermoplastic pipe

Test items	Test conditions			Sample requirements		
	Temperature/ °C	Hydrostatic pressure/ MPa	Hydrostatic time/h	Specification	Nominal pressure/ MPa	Sample quantity
Hydrostatic pressure residual bursting strength	90	20	1 100 200 500 700 1000	DN80 PN16 MPa	16	10

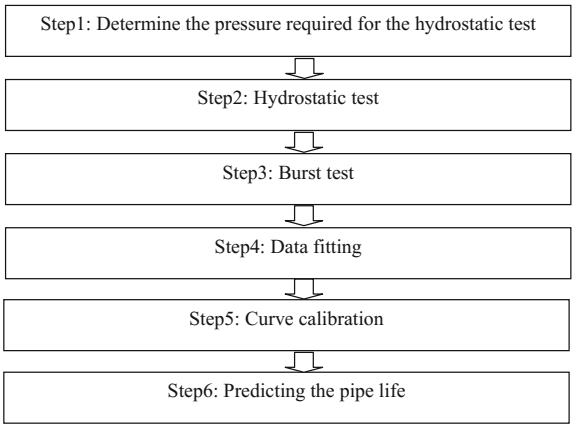

Fig. 2 The flow of hydrostatic experimental study

The test method is summarized as Fig. 2, and the detail of this method is shown as follows.

(1) Determine the Pressure Required for the Hydrostatic Test. Hydrostatic pressure test was carried out on the selected pipes according to GB/T 6111-2003 [7]. The test temperature is 90 °C and water bath heating method was adopted. The hydrostatic pressure value is determined by a lower confidence limit (LCL), which is calculated according to the method specified in SY/T 6794-2010 [8]. Where: MSP = 16 MPa; pressure safety factor, PSF = 0.67; cycle work reduction factor, $f_{cyclic} = 1$; fluid reduction factor, $f_{Fluid} = 0.67$. In addition, combined with the Arrhenius formula, the final hydrostatic pressure value is determined to be 20 MPa.

(2) Hydrostatic Test. The pipe samples of 10 selected in the same batch randomly, and divided into five groups with two samples in each group, respectively. Hydrostatic pressure test is carried out with the pressure of 20 MPa and the temperature of 90 °C, and hydrostatic pressure is selected at five discrete points within 1000 h.

(3) Burst Test. The test is carried out in accordance with the standard of GB/T 15560-1995 [9] to test the remaining burst strength after hydrostatic test. And then, analyze the data to determine whether the data is normal with calculating the relative deviation values according to the following formula (Eq. 1).

$$\text{relative deviation} = [(\text{measured value} - \text{average value})/\text{average value}] * 100\% \tag{1}$$

when the relative deviation of each group data within the range of −10 to 10%, the data can be used, otherwise the group test needs to be re carried out.

(4) Data Fitting. Data fitting is used to obtain the residual strength of pipe during 20 years' operation. The logarithm of the hydrostatic time and the logarithm of

the residual pressure are taken as the horizontal and vertical coordinates respectively. The fitting equation, $y = ax + b$, is obtained by linear regression method.

(5) Curve Calibration. If the test points with the larger offset are discarded and the test is repeated from step (1) to (5). Then, final fitting equation $y = a_1x + b_1$ is obtained, ultimately. This step is not performed if the point distribution conforms to the linear regression requirement.

(6) Predicting the pipe life. The life-pressure (δ_{end}) is 1.5 times the value of the nominal pressure. The corresponding life time value is obtained by the known life pressure value in the equation $y = a_1x + b_1$, which is the life time of the batch pipe, finally.

After the completion of the life prediction of the composite pipe, the microstructure of the reinforcement layer was observed by JEOL-6700F scanning electron microscope, and the damage mechanism was analyzed.

Results and Analysis

Hydrostatic Pressure Residual Strength Test Results

The hydrostatic pressure residual strength test results are shown in Table 2, and the regression curve of the fitting result is shown in Fig. 3. It can be seen from Fig. 4 that the relationship between Y (the residual strength value) and X (the pipe life time) is $Y = 78.865 - 4.493 \ln (X)$. When the residual strength value is 1.5 times (24 MPa) of the maximum working pressure, the value of X is 201,032 h, totaling about 22.9 years. That is to say, the life of the pipe at a temperature of 90 °C and pressure of 20 MPa is 22.9 years. It is inferred that the pipe can be safely operated in 20 years (pipe design life) when the internal pressure and temperature are less than 20 MPa and 90 °C, respectively, in the case of failure caused by external factors.

However, in the actual service process, the pipe is not only affected by the temperature and pressure, but also will withstand the gas medium infiltration,

Table 2 Bursting strength of composite pipe after 90 °C hydrostatic test

Hydrostatic time, h	Bursting strength, MPa		
	Sample 1	Sample 2	Average value
1	77.3	77.9	77.6
100	61.2	60.6	60.9
200	56.5	55.7	56.1
500	51.8	53	52.4
700	49.4	48.2	48.8
1000	46.7	42.3	44.5

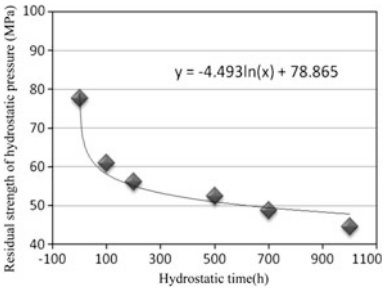

Fig. 3 Numerical fitting of hydrostatic pressure residual strength test results

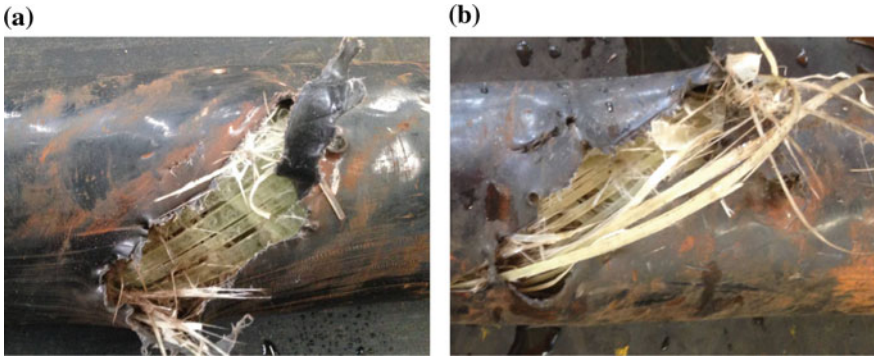

Fig. 4 Morphology of the sample after bursting

alternating pressure changes caused by pipe fatigue, external complex situations such as the destruction of human factors.

In this test, only the constant temperature and pressure factors are considered and can be used as a sufficient condition for the pipe to be used for the same or lower temperature and pressure conditions required by the test. If the conditions are complex, it should be considered comprehensively [10].

Analysis of the Pipe Damage Mechanism

After bursting test, the shape of the specimen is shown in Fig. 4. The bursting position is located in the pipe body. The crack extends along the winding angle of the reinforcing layer, and the angle is 60° to the axial direction of the pipe.

In order to further clarify the failure mechanism of the bursting of the composite pipe, the damage mechanism of the main bearing of the internal pressure is analyzed. Through the observation of the original glass fiber reinforced plastic tape (Fig. 5), it can be found that the glass fiber reinforced resin tape consists of three

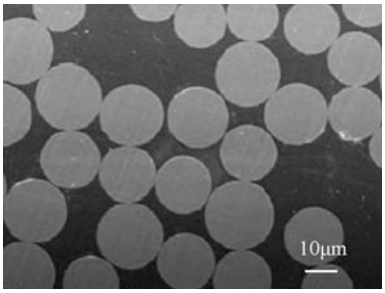

Fig. 5 Morphology of original glass fiber reinforced resin tape

physical phases, fiber phase, matrix phase and interfacial phase between them. The elastic modulus of the three phase are different, the modulus of elasticity of the fiber is the biggest, the one of interface phase is second, and the one of matrix is the smallest.

Glass fiber to bear the glass fiber reinforced resin tape with more than 95% of the load; and the main role of the matrix is to connect and fix the fiber, to withstand compressive stress and shear stress; The interface is the connection between the fiber and the substrate, the main role of which is to stress from the matrix to the fiber [11–13].

In the process of damage to the glass fiber reinforced resin tape, the first step is the occurrence of matrix cracking (Fig. 6a), that is, the plastic material under stress caused by plastic deformation eventually lead to cracking. The crack begins and expands at the defect in the matrix until it collides with the interface [14, 15]. With the further occurrence of cracking, crack propagating and extending to the interface. The interfacial strength is limited by the characteristics of the weaker phase material and also the manufacturing process, which has a great influence on the strength and toughness of the composite [16]. Finally, the fiber breaks and the reinforcement layer material fails (Fig. 6b), resulting in bursting of the pipe (Fig. 4). Due to the overload of single fiber breakage, the fiber can be damaged in the weak point or the

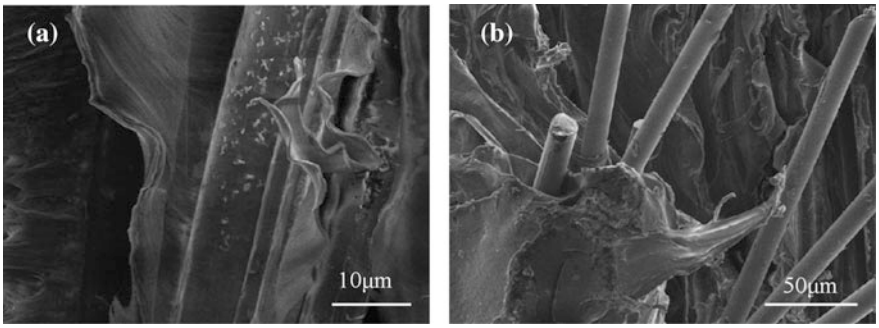

Fig. 6 Morphology of specimen after stretching

stress concentration. The voids present in the matrix will increase the local tensile stress to cause lateral cracking [17].

In addition, the temperature effect on the failure of the reinforcement layer is also critical. Previous studies have shown that with the increase of temperature (room temperature to 90 °C), the average value of blasting strength of flexible composite pipe declines by about 15%. The reason is that, with the increase of temperature, the solution orientation and crystallization occur during molecular thermal motion, and then the amorphous orientation decreases, while the crystallinity and the factor of crystal orientation increasing gradually.

Therefore, with the size and content of the micro porous in fiber increasing, part of the macromolecule fracture begin to appear, and its bearing capacity is obviously reduced, which leads to the decrease of the pipe pressure performance finally.

Conclusion

(1) In the process of pipeline service the pressure bearing capacity is mainly supported by the reinforced layer material. With the increase of service time the pressure bearing capacity of reinforced thermoplastic pipe is reduced, which is due to the aging of reinforced layer material with the increase of service time. The results show that the predicted life of the composite pipe is about 22.9 years, which satisfies the requirement of 20 years of design life.

(2) The study on the damage mechanism of the glass fiber reinforced resin tape has been investigated. The damage behavior is divided into three processes: first, the matrix cracking, that is, the resin lead to cracking under the action of plastic deformation occurs eventually; secondly, with the further occurrence of cracking, the crack appear to propagation and coupling. When it extended to the interface the glass fibers de-bond away from the matrix; finally, the overall failure of the material layer occurs, which is caused by the fiber fracture, and hence, the body burst.

Acknowledgements The project was supported by the National Natural Science Foundation of China (Grant No. 51304236).

References

1. A.G. Andreopoules, A new coupling agent for aramid fibres. J. Appl. Polym. Sci. **38**, 1053–1064 (1989)
2. Q.I. Dongtao, L.I. Houbu, *Application and qualification of reinforced thermoplastic pipes in Chinese oilfields*. International Conference on Pipelines and Trenchless Technology (ICPTT) (ASCE, Reston, Beijing, China, 2011), 26–29 October 2011
3. Wei Bin, Qi Dongtao, Li Houbu et al., Corrosion resistance of reinforced thermoplastic pipe in the sour environment. Nat. Gas Ind. **35**(06), 87–92 (2015)

4. G. Qi, Y. Wu, D. Qi et al., Experimental study on the thermostable property of aramid fiber reinforced PE-RT pipes. Nat. Gas Ind. B **2**(5), 461–466 (2015)
5. E.H. Fisher, A.G. Gibson, Continuous fiber reinforced thermoplastic pipes for transport and distribution of fluids for the oil and gas industries. Plast. Rubber Compos. **27**(10), 447–451 (1999)
6. GB/T 18252-2000, Plastic piping and ducting systems-determination of the long-term hydrostatic strength of thermoplastics materials in pipe form by extrapolation
7. GB/T 6111-2003, Thermoplastics pipes for the conveyance of fluids-resistance to internal pressure-test method
8. SY/T 6794-2010, Qualification of spoolable reinforced plastic line pipe
9. GB/T 15560-1995, Standard test method for short-time hydraulic failure and resistance to constant internal pressure of the plastics pipes for the transport of fluids
10. H. Faria, R.M. Guedes, Long-term behaviour of GFRP pipes: reducing the prediction test duration. Polym. Test. **29**(3), 337–345 (2010)
11. L.I. Houbu, Z.H.A.N.G. Xuemin, Q.I. Dongtao et al., Corrosion resistance of E6-glass fibre in simulated oilfield environments. J. Reinf. Plast. Compos. **32**(8), 563–572 (2012)
12. K. El-Egili, Infrared studies of Na2O-B2O3-SiO2 and Al2O3-Na2O-B2O3-SiO2 glasses. Phys. B **325**, 340–348 (2003)
13. N.J. Jin, H.G. Hwang, J.H. Yeon, Structural analysis and optimum design of GRP pipes based on properties of materials. Constr. Build. Mater. **38**, 316–326 (2013)
14. R. Rafiee, Experimental and theoretical investigations on the failure of filament wound GRP pipes. Compos. Part B **45**(1), 257–267 (2013)
15. Q. Qiu, M. Kumosa, Corrosion of E-glass fibres in acidic environments. Compos. Sci. Technol. **57**(5), 497–507 (1997)
16. M. Farshad, A. Necola, Strain corrosion of glass fibre-reinforced plastics pipes. Polym. Test. **23**(5), 517–521 (2004)
17. M. Farshad, A. Necola, Effect of aqueous environment on the long-term behavior of glass fiber-reinforced plastic pipes. Polym. Test. **23**(2), 163–167 (2004)

Girth Welding on Oil and Gas Pipeline Projects in China

Yongli Sui

Abstract This paper introduces development of girth welding of long-distance oil and gas transmission pipelines in China, focusing on automatic welding equipment researches and application. Based on characteristics of high strength line pipes, the paper points out a few technical difficulties in girth welding, including the wide range of line pipes, various composition of alloy, refinement of grain and increase of carbon equivalent. It also describes the girth welding processing and grooving of China's high strength line pipes, indicating that the reliability, adaptability and stability of CPP automatic welding system in China's pipeline construction have been highly recognized. This paper argues that self-shielded flux cored arc welding (FCAW-S) and low hydrogen electrode manual welding (SMAW) will still be choices for oil and gas pipeline construction, while automatic welding will be the major method in the future.

Keywords Transmission pipeline · Girth welding · Welding technology Welding quality

Introduction

So far, the total length of oil and gas transmission pipelines in China has accumulated to nearly 110,000 km, forming a pipeline system which covers the whole China and connects overseas. Therefore, it becomes an energy artery that promotes economic returns and benefits nearly 1 billion people. As transmission capacity and distance continuously increase, line pipes of large diameter, high strength and high toughness designing for high pressure are applied more and more in construction. Among them, X70 pipes have reached about 14,600 km, and these pipes whose

Y. Sui (✉)
National Engineering Laboratory for Pipeline Safety, Langfang, Hebei, China
e-mail: cnpcsuiyongli@sina.com

Y. Sui
China Petroleum Pipeline Research Institute Co., Longfang, China

© Springer Nature Singapore Pte Ltd. 2018

Y. Han (ed.), *Advances in Materials Processing*, Lecture Notes in Mechanical Engineering, https://doi.org/10.1007/978-981-13-0107-0_109

diameters are 1016 mm have design pressure of 10 MPa. Meanwhile, X80 pipes, whose diameters are 1219 mm and have design pressure on 12 MPa, have reached about 12,200 km. This brings new challenges to girth welding in transmission pipeline and makes girth welding on high-grade line pipes become a bottleneck that restricts its progress.

Development of Girth Welding

Girth welding has undergone several major changes in China. In the 1970s, the traditional welding method, namely low hydrogen electrode arc welding with vertical up direction, was mostly applied. It is easy and flexible to operate, and can adapt to various construction environments. However, it also suffers from larger groove gaps, thicker beads, and lower speed, efficiency and quality. Therefore, it is used mainly in welding small diameter pipeline and repair welding.

Vertical down arc welding using cellulose or low hydrogen electrodes was promoted in the 1980s. This method needs to be operated with high-current, multilayer and rapid welding, not only narrowing layers' thickness and groove gaps, but also increasing welding efficiency. Shielded metal arc welding (SMAW) enjoys high flexibility, convenience and applicability. Its deposition efficiency and mechanical properties still can meet the needs of pipeline construction today because of the continuous improvement of processing property.

In the 1990s, self-shielded flux cored arc welding (FCAW-S) arose. Since this method has good wind resistance, no protective atmosphere is required. A semi-automatic welding torch is used while the wire feeder continuously feeds electrodes. FCAW-S applies much higher welding current and speed than SMAW, therefore it improves welding efficiency and reduces joints, greatly raising the qualification rate. It develops the most quickly in pipeline construction in China since it has little investment in equipment, high utilization rate, short payback period, and is cost-effective in quality, efficiency, material consumption and energy-usage, conforming to low-cost automatic welding.

Automatic gas metal arc welding (GMAW) has been gradually applied since 2000, with the increase of strength grade, diameter and thickness of pipe. The characteristics of this method are listed as below: excellent joint performance, high requirement for construction management, little affected by human, high welding efficiency, low labor intensity, adaptability to adverse weather condition, and great potential for constructing large diameter and thick wall pipes. As automatic welding platforms gradually mature, automatic welding will improve continuously in both quality and economic benefit, and gradually become the leading field welding method [1].

Development of Automatic Welding in China

It is in 1999 that China recorded the first automatic welding application in Hong Kong-Beijing gas pipeline and Zhengzhou-Yima gas pipeline, where the total girth welding amount by automatic external welding machines reached 8.8 km. Automatic welding began to expand since the West-East Gas Pipeline Project began to construct in 2001. Now the total length of pipeline welded by automatic welder is about 2600 km (Table 1).

Today, China has formed CPP pipeline automatic welding system, consisting of beveling machine, internal welding machine, single-torch or double-torches welding machine that are all made in China. The beveling machine has been developed and designed since the 1990s, and now the CPP900-FM beveling machine can

Table 1 Automatic welding in China's pipeline projects [2]

Time to construct	Project name	Pipe grade	Diameter (mm)	Wall thickness (mm)	Welding length (km)
1999	Hong Kong-Beijing Gas Pipeline	X65	711	7.1	1.3
1999	Zhengzhou-Yima Gas Pipeline	16Mn	426	7.8	7.5
2000	Zhangzhou Water Pipeline	Q235	1220	14	1.0
2000	Sebei-Xining-Lanzhou Gas Pipeline	X70	660	10.3	8.5
2001–2002	West-East Gas Pipeline Project	X70	1016	14.6, 21	704
2005	Jining Branch Pipeline of West-East Pipeline Project	X80	1016	15.3	7.8
2005–2006	India East-West Gas Pipeline Project	X70	1219	17.2, 20.7	50
2007–2008	Eastern Siberia-Pacific Ocean (ESPO) Pipeline in Russia	K60	1220	19,24	54.3
2008–2009	The Second West-East Gas Pipeline Project	X80	1219	15.3, 18.4, 22	662
2008–2009	Branch A/B of China-Central Asia Gas Pipeline Project	X70	1067	15.9, 19.1	605
2012–2013	Branch C of China-Central Asia Gas Pipeline Project	X80	1219	17.5	277
2013	The 3rd West-East Gas Pipeline Project	X80	1219	16.5	239.4
Total length					2617.8

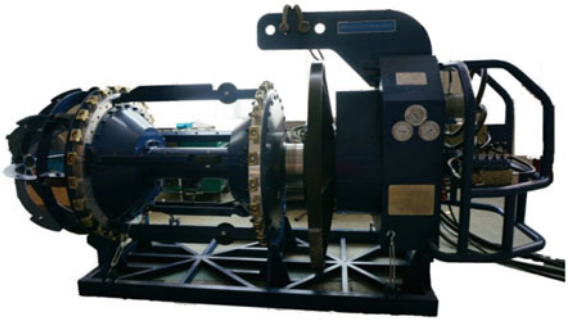

Fig. 1 CPP900-FM beveling machine

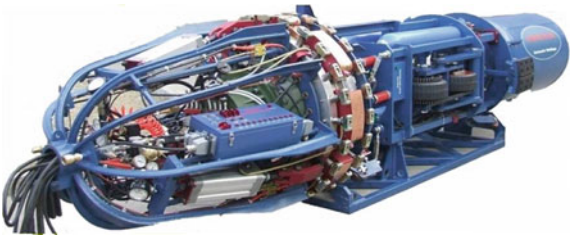

Fig. 2 CPP900-IIW internal welding machine

process shape V, U, X and compound grooves. This equipment enjoys easy operation, high processing precision, good groove shape and can process a single groove within 2 min. In 2000, research and development of the internal welding machine began, and the CPP900-IIW internal welding machine today can not only precisely joint the ends of pipes, completing inner circumferential welding on the roots within 90 s, but also achieve wireless remote welding and adjust the groove gap. The single-torch external welding machine launched in 1995, while the double-torches external welding machine in 2002. Today the CPP900-W1 and CPP900-W2 external welding machines combine functions of traditional automatic welding machine and innovative achievements on automatic control and mechanical transmission. They realize double-axes automatic tracking on the X–Y weld seam with convenient and easy operation. After nearly 20 years of applications, the CPP system gains highly recognition in pipeline project construction due to its reliability, stability and environmental adaptability (Figs. 1, 2, 3 and 4).

Till now laser-arc hybrid automatic welding technology and equipment have been in the research and development and design. Since this technology has high penetration and efficiency, it is regarded as an industrial innovation. This method has been successfully implemented in the laboratory on all position root welding on line pipes with 8 mm root face, and the laser generator and cooling system are under research of its on-site adaptability. The technology and equipment need continuous improvement during the process to meet the requirements of field welding.

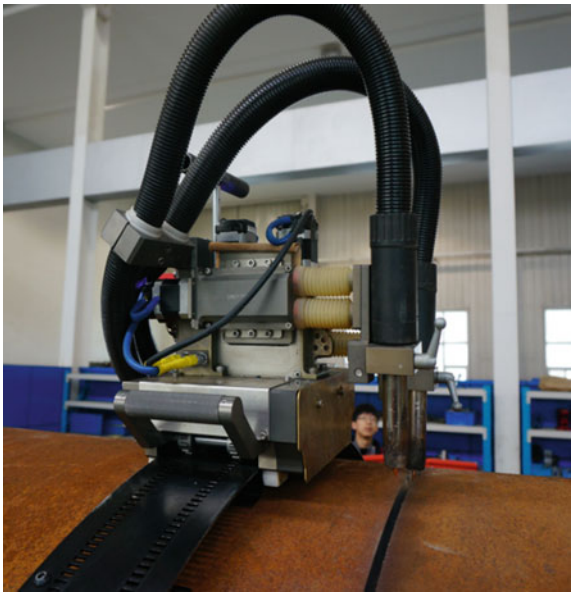

Fig. 3 CPP900-W1 single-torch machine

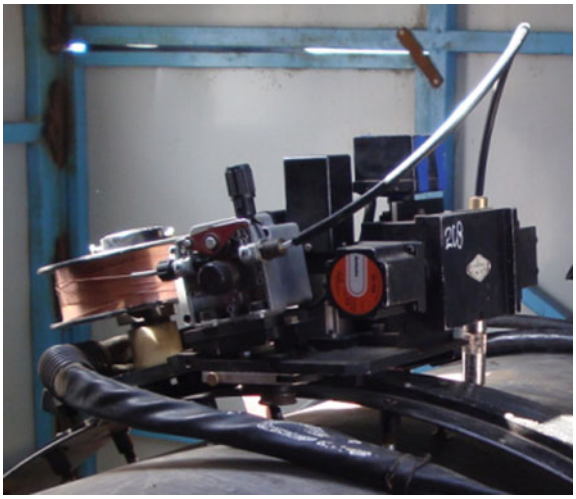

Fig. 4 CPP900-W2 double-torches machine

Major Technical Difficulties of High Grade Line Pipe Girth Welding

There are two ways to raise line pipe intensity revealed in its long-time application. One is to carefully design the metallurgical composition and precisely control alloy composition in smelting. The other is to accurately control the cooling rate in

rolling. These excellently protect high intensity pipeline steel from cold cracks and the brittleness of HAZ. However, there appear to be some new technical difficulties in welding.

Joints Strength and Toughness Matching Due to Increasing Strength and Wide Range of Actual Strength of the Steel Pipe

On the one hand, to balance strength and toughness in weld metal is more difficult than in pipe steel that has gone through TMCP, since the metal is an as-cast structure formed in heating, melting and solidification. The higher the strength grade of pipe steel is, the more difficult it is to gain balance in weld metal. On the other hand, the wide range of the actual strength of steel pipe makes it difficult to realize a standard higher or equal strength match. Although the tensile strength of girth-welded joints is not lower than the minimum specified tensile strength of the pipe, the girth-welded joint is matched with an equal or lower strength compared with the actual strength of the steel pipe, which requires a rigorous selection of welding materials and process (Fig. 5).

Decreasing Weldability of Girth-Welded Joints Due to Increasing Alloying Elements and the Wide Range of the Actual Alloy

It is necessary to add some alloying elements and few micro-alloying elements to raise the strength of line pipe, as shown in Table 2. Actual alloying elements vary greatly, affecting the fusion ratio of the base metal in welding, therefore, they will influence the stability of welding and integrated performance of HAZ and weld

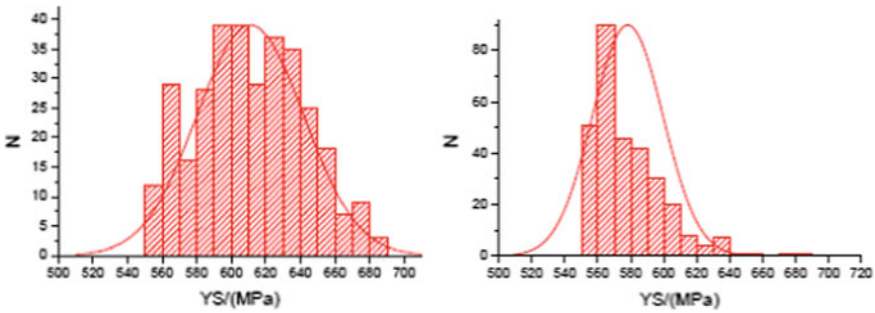

(a) Pipe Strength Distribution in Plant A (b) Pipe Strength Distribution in Plant B

Fig. 5 Strength distribution of pipes from different sources in a X80 pipeline project

Table 2 Metallurgical composition and microstructure design of pipeline steel

Strength grade	Base metal	Additional alloying elements	Additional micro-alloying elements	Final structure	Remark
B and X42	C–Mn–Si			Ferritic + Pearlitic	
X52–X70	C–Mn–Si	Cu, Ni, Mo	Nb < 0.06%	Ferritic + Pearlitic	
X65, X70 and X80	C–Mn–Si	Cr, Mo	Nb < 0.11%	Ferrite/Acicular Ferrite	Low finishing temperature
	C–Mn–Si	Cu, Ni, Cr, Mo	Nb < 0.07%	Ferrite/Acicular Ferrite	High finishing temperature

metal, such as strength, toughness and hardness. Higher requirements are put forward for selecting groove type, welding parameters and welding materials.

As shown in Table 3 and Fig. 6, the base metal molten into the weld metal will put different effects on the alloy composition and microstructure of the weld metal when the actual alloy elements of the pipeline change widely. Meanwhile, the factors that affect the cooling rate, such as the welding parameters and the construction environment temperature, will influence the mechanical properties of the girth welds. This makes joints of FCAW-S, FCAW-G and SMAW show a greater dispersion of the Charpy impact energy.

Significant Softening of HAZ Due to Steel Grain Refining

The HAZ of high strength pipeline steel softens because of the lower cooling speed after welding compared with that of rolling, grain growth and the dissolution of second phase particles formed by micro-alloying elements. Therefore, tensile fractures mostly occur at HAZ, especially for semi-automatic welding and SMAW which input large amount of heat, as shown in Fig. 7. The interpass temperature, the number of passes and the welding sequence need to be controlled strictly to ensure a small amount of the welding heat input.

Root Welding—The Key to Control Welding Quality and Construction Efficiency

The sensitivity of welding cold crack increases according to the significant raise of carbon equivalent as the strength grade of pipeline steel improves. When high

Table 3 Chemical composition of X80 pipe and semi-automatic FCAW-S welds

A Steel	C	Si	Mn	P	S	Cr	Mo	Ni	Al	Cu	Nb	Ti	V
Pipe	0.05	0.21	1.69	0.011	0.003	0.19	0.006	0.01	0.031	0.095	0.041	0.016	0.003
Welding	0.05	0.12	1.49	0.012	0.004	0.06	0.007	1.80	0.891	0.036	0.013	0.006	0.002
B Steel													
Pipe	0.05	0.20	1.78	0.008	0.003	0.32	0.18	0.008	0.04	0.009	0.086	0.014	0.03
Welding	0.05	0.12	1.52	0.011	0.004	0.084	0.047	1.86	0.973	0.014	0.022	0.006	0.001

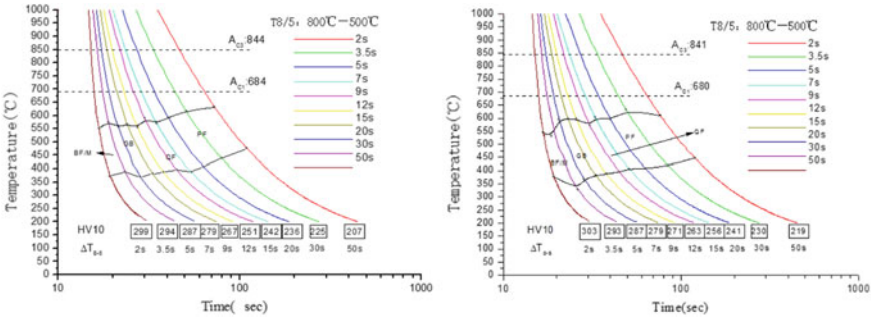

(a) Plant A (b) Plant B

Fig. 6 CCT curve of FCW-S welds

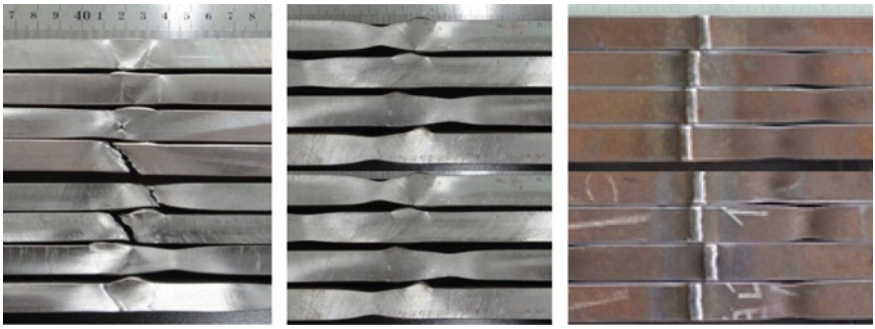

(a) SMAW (b) Semi-automatic FCW-S (c) GMAWAutomatic Welding

Fig. 7 Transverse tensile samples of girth-welded joints with different heat input

strength steel pipes are fitted on site, it is the most important to ensure that root welding can effectively avoid the welding crack, and has good performance and efficiency. Through cold crack sensitivity tests and analyses of X80 steel pipes, it is considered that root welding with cellulose electrodes tends to leave larger cold cracks. In this connection, it is recommended to use low hydrogen electrode manual welding or semi-automatic welding with solid wire or metal powder cored wire in X80 steel pipe root welding. This has been applied and implemented in fitting X80 steel pipeline in china.

Application of Girth Welding on High Grade Pipeline

Aiming at resolving above difficulties in girth welding on high strength line pipes, below list several girth welding technologies that are applied in oil and gas pipeline projects, of which automatic welding will gradually become the major method in future construction of high strength pipeline.

Combined Semi-automatic Welding of "Gas Shielded Solid Wire or Metal Powder Cored Wire + Self-Shielded Flux Cored Wire" (PGMAW + FCAW-S)

Semi-automatic welding using solid wire and metal powder cored wire is root welding that adopts STT or RMD to complete the melt-through bead welding. The self-shielded flux cored semi-automatic welding is applied in filling and cover welding, whose groove types are shown in Fig. 8a and d. This combined process is flexible to operate and easy to adapt to environment, therefore, it is suitable for fitting in complex terrains, such as hills, slopes, water networks and other areas that are not accessible to large-scale equipment.

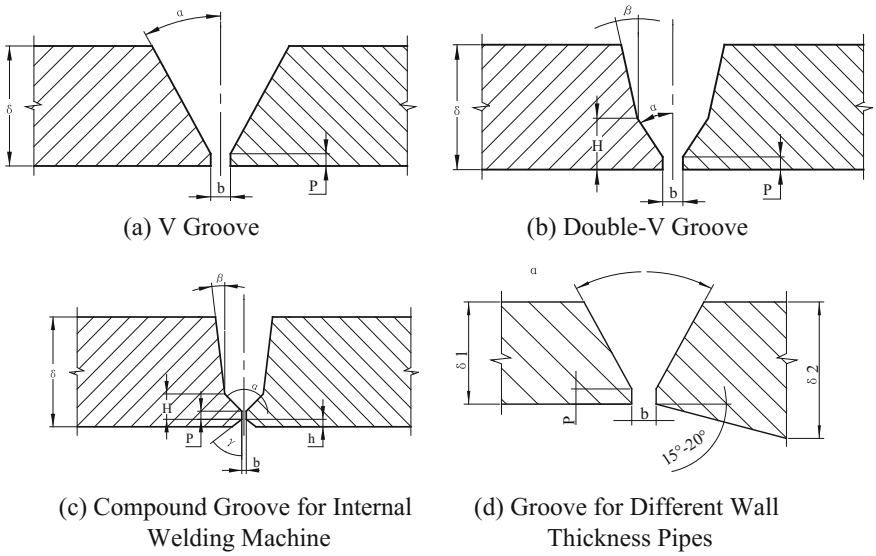

(a) V Groove

(b) Double-V Groove

(c) Compound Groove for Internal Welding Machine

(d) Groove for Different Wall Thickness Pipes

Fig. 8 Groove types

Manual Welding of Low Hydrogen Electrode (SMAW)

In this process, low hydrogen electrodes which are suitable for one side welding both sides formation are selected in vertical-up root welding. High strength and toughness ones are chosen in filling and cover welding, either vertical-up or down. The groove types are shown in Fig. 8a and d. This method is mainly used for repair welding of welds, tie-in welding, and so on.

Combined Automatic Welding of "Internal Welding + Single-Torch External Welding + Double-Torches Welding"

Automatic root welding using inner welding machine and gas shielded solid wire is done from inside steel pipes to realize DC constant voltage CO_2 short-circuit transfer. From outside, double-torches external welding machine and gas shielded solid wire are selected in hot, filling and cover welding to achieve DC pulsed spray transfer (PGMAW). The groove type is shown in Fig. 8c. This combined process is the main method in China's oil and gas pipeline construction, since it has high efficiency and good quality.

Combined Automatic Welding of "Internal Welding + Single-Torch External Welding"

Automatic root welding using inner welding machine and gas shielded solid wire is done from inside steel pipes. From outside, single-torch external welding machine and gas shielded solid wire are selected in hot, filling and cover welding. The groove type is shown in Fig. 8c. This combined process is the main method in China's oil and gas pipeline construction, since it has high efficiency and good quality.

Combined Welding of "Gas Shielded Solid Wire or Metal Powder Cored Wire Semi-automatic Welding + Single-Torch Automatic Welding with Gas Shielded Flux Cored Wire" (GMAW)

Semi-automatic welding using solid wire and metal powder cored wire adopts STT or RMD to complete one side welding both sides formation root welding.

Single-torch external welding machine and as shielded flux cored wire from outside of pipes are selected in hot, filling and cover welding to achieve DC constant voltage CO_2 short-circuit transfer. Groove types are shown in Fig. 8a, b and d. This method is mainly used in fitting in complex terrains and girth welding on complex butts.

Conclusions

(1) China has undergone several major changes in pipeline girth welding. With increases in steel strength grade, pipe's diameter and wall thickness, vertical up or down manual welding gradually transfers to semi-automatic and automatic welding. However, semi-automatic and manual welding will remain to be choices, considering different topography and all weathers.
(2) CPP automatic welding system consists beveling machine, internal welding machine, single-torch and double-torched external welding machine. After nearly 20 years' development, CPP system gains highly recognition in pipeline project construction due to its reliability, stability and environmental adaptability.
(3) Improvements in high grade pipeline steel excellently resolve cold cracks and HAZ brittleness while bring new technical difficulties in welding. Therefore, satisfactory mechanical properties of girth-welded joints are ensured by strictly selecting groove types, welding process parameters and welding materials to guarantee little welding heat input.
(4) Welding and groove types of high grade steel pipe have undergone strict evaluation and plentiful practical application. For this reason, it conforms to characteristics of long-distance pipeline construction and requirements of design documents and standards, performing good welding quality.

References

1. Y. Sui, R. Guo, J. Zhang, Comparison of the semi-automatic and automatic technology on pipeline girth welding. Welded Pipe Tube **36**(9), 38–47 (2013)
2. Y. Sui, H. Wu, Development and application of automatic welding on transmission pipeline at home. Oil Gas Storage Transp. **36**(9), 1–9 (2014)

Cigarette Butts Water Extracts as Corrosion Inhibitor in Oil Field Acidizing Fracture Using Different Metal Chlorides Intensifiers

Xunji Li, Juantao Zhang, Wenwen Song, Zeliang Chang, Yan Han and Rui Cai

Abstract The corrosion inhibitive effect of four metal chlorides ($CoCl_2$, $NiCl_2$, $CrCl_2$ and $CuCl_2$) intensifiers in cigarette butts extracts are contrasted in 15% (wt%) hydrochloric acid with N80 steel at 90 °C. Weight loss, polarization, impedance, electrochemical noise and scanning electron microscopy results are all shown that the most corrosion inhibitive effect of inhibitors is $CuCl_2$ intensifiers, the next is $CrCl_2$, $NiCl_2$ and $CoCl_2$, and the last is cigarette butts extracts. The corrosion inhibitive efficiency of $CuCl_2$ intensifiers can reach 94.2% with the addition of 5% (wt%) and the four metal chlorides all do their intensive job.

Keywords Cigarette butts water extracts · Metal chlorides intensifiers N80 oil tube steel · Acid corrosion

Introduction

Cigarette butt is a tiny trash containing hazardous chemicals and needs treatment. A new study indicates that cigarette butts can be water extracted as corrosion inhibitor for N80 steel in oil field. In that paper, a series of the organic amine play a significant role [1]. They are included nicotine, continine, N-nitroso-nornicotine. The reports write by Moreover and Cizek [2] show that the soluble copper metal salt may be present as co-intensifier, such as acetate, chloride, nitrate, formate, and mixtures thereof. According to the two reports, the different metal chlorides are investigated as intensifiers of the cigarette butts extracts.

X. Li · W. Song · Z. Chang
Tarim Oilfield Company, Petro China, Korla 841000, Xinjiang, China

J. Zhang (✉) · Y. Han · R. Cai
State Key Laboratory for Performance and Structure Safety of Petroleum Tubular Goods and Equipment Materials, Xi'an 710065, People's Republic of China
e-mail: zhangjuantao@cnpc.com.cn

© Springer Nature Singapore Pte Ltd. 2018

Y. Han (ed.), *Advances in Materials Processing*, Lecture Notes in Mechanical Engineering, https://doi.org/10.1007/978-981-13-0107-0_110

In this research, four metal chlorides ($CoCl_2$, $NiCl_2$, $CrCl_2$ and $CuCl_2$) intensifiers are provided to inhibit corrosion in conjunction with cigarette butts water extract when a steel surface is present in an acid environment. These four chlorides as co-intensifiers in cigarette butts extracts are contrasted in 15% (wt%) hydrochloric acid with N80 steel at 90 °C. Weight loss, electrochemical impedance, electrochemical noise (EN) and polarization are used to analyze corrosion inhibitive effect of different metal chlorides intensifiers in cigarette butts water extracts. The scanning electron microscopy (SEM) is used to view the N80 steel morphology in 15% hydrochloric acid with cigarette butts extracts and its intensive inhibitors.

Experimental

The N80 oil tube steel discs are used as the testing material with the elemental composition of Si 0.22, C 0.24, P 0.013, Mn 1.19, S 0.004, Nb 0.006, Cr 0.036, Mo 0.021, Cu 0.019, V 0.017, Ni 0.028, Ti 0.011 and the rest of Fe. Before the corrosion inhibition test, the surfaces of the oil tube steel discs are mechanically polished by grit sandpaper form 300# up to 1200# progressively, then rinsed with alcohol and last stove-dried.

The cigarette butts extracts intensive inhibitors preparation: adding 50 cigarette butts into 1000 ml distilled water and continuous aging for 24 h. Then the aged extracts solution is divided into five same parts. The first part is directly used as cigarette butts water extracts inhibitor. The other four parts are added in 1.0 g $CoCl_2$, $CrCl_2$, $NiCl_2$ and $CuCl_2$ respectively. The four kinds of solution are then used as cigarette butts water extracts intensive inhibitors.

The instruments used in this paper are as follows: The electrochemical impedance, noise, and potentiodynamic polarization are analyzed by M273A potentiostat and M5210 lock-in amplifier all made in USA. The Quanta 200 SEM is made in FEI Co. In electrochemical test, the specimen exposed surface area to electrolyte is 0.785 cm^2. The analytical grade 37% HCl is diluted to the aggressive solutions (15% HCl, wt%). The platinum electrode is used as counter electrode and the saturated calomel electrode (SCE) is the reference electrode. Polarization is worked from −150 to +150 mV with 2 mV/s scanning rate contrasted to the corrosion potential. The impedance testing frequency range is from 0.01 to 100 kHz. All teats are performed at 90 °C in atmospheric condition.

Results and Discussion

Weight Loss and Polarization Results

The same concentration (5%, wt%) of cigarette butts extracts and cigarette butts extracts intensive inhibitors are added into HCl solution with N80 steel to study the corrosion inhibition. Weight loss test is lasting 4 h at 90 °C in HCl solution. The used N80 steel specimens size is 50 mm × 10 mm × 3 mm. The corrosion inhibition efficiencies (*IE*) detected by weight loss and polarization are calculated by Eqs. (1) and (2) [3–5]:

$$IE(\%) = \frac{W_0 - W_i}{W_0} \times 100 \tag{1}$$

$$IE(\%) = \left(\frac{I_{corr} - I'_{corr}}{I_{corr}}\right) \times 100 \tag{2}$$

In the equations, W_i and W_0 represent the weight loss values in presence and in absence of inhibitor, I'_{corr} and I_{corr} represent the inhibited and uninhibited corrosion current densities. The weight loss and polarization results are shown in Table 1, where E_{corr} is corrosion potential, I_{corr} is corrosion current density, b_a is anode Tafel slopes and b_c is cathodic Tafel slopes. Figure 1 shows polarization curves for cigarette butts extracts and cigarette butts extracts intensive inhibitors in 15% HCl with N80 steel.

From Table 1 and Fig. 1, the anodic branches of cigarette butts extracts and its intensive inhibitors are shifted to more positive and the cathodic branches are moved to more passive direction by comparing to the blank solution. In the copper intensive inhibitor anodic branches, appear slight passivation. The I_{corr}, b_a and $-b_c$ all diminish in the presence of the cigarette butts extracts and its intensive inhibitors. These results indicate that the cigarette butts extracts and its intensive inhibitors are mixed type inhibitor. Compared the *IE* obtained from polarization curves and weight loss, the cigarette butts extracts intensive inhibitors are all more excellent than cigarette butts extracts. And the inhibition efficiency order of the cigarette butts water extracts intensive inhibitors is $CuCl_2 > CrCl_2 > NiCl_2 > CoCl_2$.

Impedance

The impedance of N80 steel in 15% HCl with the same concentration of cigarette butts extracts and its intensive inhibitors have been tested. The contrastive Nyquist picture and corresponding equivalent circuit diagram are demonstrated in Fig. 2. And the calculated results are presented in Table 2, where R_s is solution resistance, CPE is the constant phase element [6–8], R_t is charge transfer resistance [9–11], L is

Table 1 Polarization and weight loss results of 5% cigarette butts extracts and its intensive inhibitors in 15% HCl solution with N80 steel at 90 °C

Inhibitors with the same concentration of 5% (wt%)		Method						
		Polarization					Weight loss	
		$-E_{corr}$ versus SCE (mV)	b_a (mV dec^{-1})	$-b_c$ (mV dec^{-1})	I_{corr} (mA cm^{-2})	*IE* (%)	W_{corr} (mg cm^{-2} h^{-1})	*IE* (%)
Blank		419	107.42	149.02	19.27	–	37.08	–
Cigarette butts water extracts		424	66.44	68.53	1.89	90.2	4.04	89.1
Cigarette butts extracts intensive inhibitors	$CoCl_2$	436	65.45	67.92	1.81	90.6	3.93	89.4
	$NiCl_2$	443	73.85	87.46	1.64	91.5	3.49	90.6
	$CrCl_2$	451	84.42	102.31	1.39	92.8	3.26	91.2
	$CuCl_2$	424	70.48	91.7	1.27	93.4	2.15	94.2

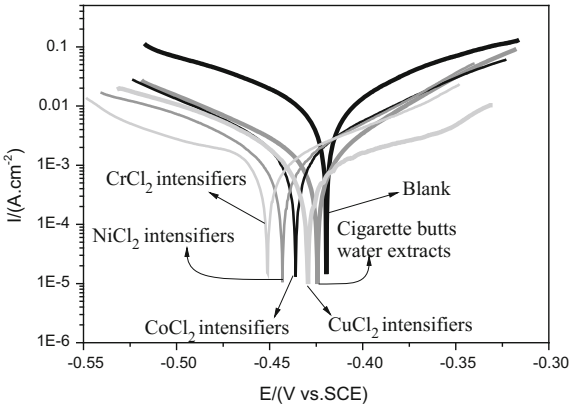

Fig. 1 Polarization curves of 5% cigarette butts extracts and its intensive inhibitors in 15% HCl with N80 steel at 90 °C

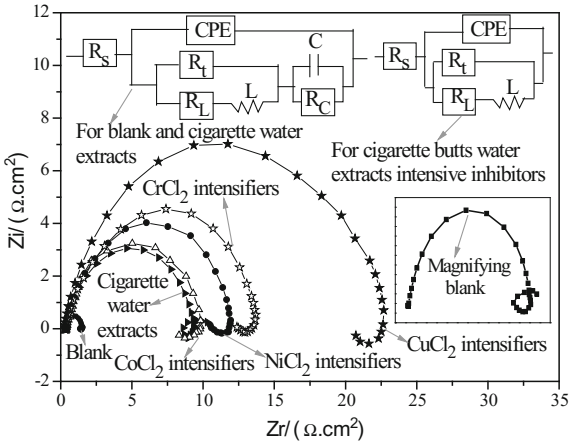

Fig. 2 Impedance of 5% cigarette butts extracts and its intensive inhibitors in 15% HCl with N80 steel at 90 °C

inductive reactance [12, 13], R_L is the inductive resistance, R_C is the resistance of corrosion film and C is the constant phase element of capacity. The impedance of CPE is given as follows [6–8]:

$$Z_{CPE} = \frac{1}{Y_0} \times \frac{1}{(j\omega)^n} \tag{3}$$

In Eq. (3), Y_0 is the CPE magnitude, n is the CPE exponent, ω is the angular frequency and j is the imaginary unit. The correction of capacity to its real values is calculated from the Eq. (4) [14–16]:

$$C_{dl} = Y_0(\omega_{\max})^{n-1} \tag{4}$$

Table 2 Impedance results of 5% cigarette butts extracts and its intensive inhibitors in 15% HCl with N80 steel at 90°C

Parameters		Inhibitors with the same concentration of 5% (wt%)					
		Blank	Cigarette butts extracts	Cigarette butts extracts intensive inhibitors			
				$CoCl_2$	$NiCl_2$	$CrCl_2$	$CuCl_2$
R_s (Ω cm^2)		0.33	0.39	0.36	0.34	0.36	0.28
Q	$Y_0\times 10^{-4}$ (S sec^ncm^{-2})	4.56	7.55	8.92	3.73	5.00	8.07
	n	0.89	0.85	0.80	0.80	0.78	0.81
C_{dl} (μF cm^{-2})		561.79	178.06	58.04	52.91	48.73	38.25
R_t (Ω cm^2)		1.18	4.53	10.56	11.24	12.99	20.54
R_L (Ω cm^2)		0.65	31.59	4.14	2.23	1.16	1.17
L (μH cm^2)		1629.51	257.67	31.63	38.98	41.72	49.94
R_C (Ω cm^2)		0.23	6.23	–	–	–	–
C (μF cm^{-2})		1025.23	94.82	–	–	–	–
R_P (Ω cm^2)		0.98	10.53	10.92	11.58	12.99	21.82
IE (%)		–	90.7	91.0	91.5	92.7	95.5

where $\omega_{\max}$ is the frequency at which the imaginary part of impedance (−Zi) has a maximum. According to the equivalent circuit model in Fig. 2, the impedances of the electrodes for blank and cigarette butts water extracts are given by Eq. (5):

$$Z(\omega) = \mathrm{R_S} + \left\langle \left\{ \left[\mathrm{R_t}^{-1} + (R_L + j\omega L)^{-1} \right]^{-1} + (R_C^{-1} + j\omega C)^{-1} \right\}^{-1} + j\omega C_{dl} \right\rangle^{-1} \tag{5}$$

The inhibition efficiency IE (%) is calculated as follows [14–16]:

$$IE(\%) = \frac{1/R_P - 1/R'_p}{1/R_p} \times 100 \tag{6}$$

$$R_p = Z(\omega = 0) \tag{7}$$

where R'_p and R_p are inhibited and uninhibited polarization resistances. The impedances of the electrodes for various cigarette butts extracts intensive inhibitors are given by Eq. (8):

$$Z(\omega) = \mathrm{R_S} + \left\{ \left[\mathrm{R_t}^{-1} + (R_L + j\omega L)^{-1} \right]^{-1} + j\omega C_{dl} \right\}^{-1} \tag{8}$$

The Eq. (8) can be simplified as Eq. (9) when ω = 0. Coupled with the value of $R_t^{-1} + R_L^{-1}$ is always far less than R_t, the electrodes impedances R_p of the intensive inhibitors could be presented by Eq. (10) [17, 18].

$$Z(\omega = 0) = \frac{1}{\mathrm{R_t}} + \frac{1}{R_L} + \mathrm{R}_s \tag{9}$$

$$\mathrm{R}_P = Z(\omega = 0) = R_s + R_t \tag{10}$$

As shown in Fig. 2, the spectrum of the cigarette butts extracts intensive inhibitors in HCl solution with N80 steel appear to similar form including a semicircular dispersing capacitive loop in high frequency region and a little inductive arc in low frequency region. The diameter size order of the four depressed capacitive semicircle is $CuCl_2$ > $CrCl_2$ > $NiCl_2$ > $CoCl_2$, this indicates that the corrosion degree order is $CoCl_2$ > $NiCl_2$ > $CrCl_2$ > $CuCl_2$.

In Table 2, the R_p value order is $CuCl_2$ > $CrCl_2$ > $NiCl_2$ > $CoCl_2$ > cigarette butts water extracts > blank, which indicates the best corrosion inhibitive effect order also is $CuCl_2$ > $CrCl_2$ > $NiCl_2$ > $CoCl_2$ > cigarette butts extracts. The corrosion inhibitive effects of the four cigarette butts extracts inhibitors are all more excellent than cigarette butts extracts. And this is consistent with weight loss and polarization results.

EN Results

In order to expound the EN results of cigarette butts extracts copper complex, the current and potential noise time series spectra are presented in Fig. 3. The potential and current time series noises in Fig. 3 present oscillations with some superimposed transients [19]. The amplitude degree order of current time series noises is blank > cigarette butts water extracts > $CoCl_2$ > $NiCl_2$ > $CrCl_2$ > $CuCl_2$, which suggests that the corrosion of blank is the most serious and the last is $CuCl_2$ intensifiers. The potential amplitude degree order is just opposite.

The most important step of EN measure is the determination of the noise resistance (R_n), which is defined as the ratio of the standard deviations of the potential noise (σ_E) and coupling current fluctuations (σ_I) [20–22]:

$$\mathrm{R}_n = \frac{\sigma_E}{\sigma_I} \tag{11}$$

The corrosion rate is related to R_n, the less R_n, the greater corrosion rate. Another time domain data analysis is the localization index (LI), which is defined as the ratio of the standard deviations of current fluctuations (σ_I) and the root mean square of current (I_{rms}) [20–22]:

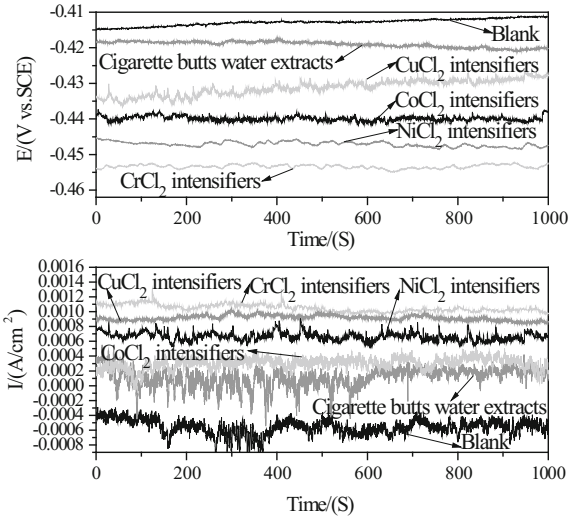

Fig. 3 The current and potential noise time series spectrum of N80 steel in 15% HCl with 5% cigarette butts extracts and its intensive inhibitors at 90 °C

$$\mathrm{LI} = \frac{\sigma_{\mathrm{I}}}{\mathrm{I}_{rms}} \tag{12}$$

The LI value close to 1 indicates the pitting corrosion happened, the LI value between 0.1 and 1 represents the pitting corrosion threatened, the LI close to 0 or lower than 0.1 indicates in the passivation or occurring uniform corrosion. The time domain analysis results of cigarette butts extracts and its intensifiers in 15% HCl solution with N80 steel are shown in Table 3. From Table 3, the R_n value order is blank < cigarette butts water extracts < $CoCl_2$ < $NiCl_2$ < $CrCl_2$ < $CuCl_2$, the LI value order is blank > cigarette butts water extracts > $CoCl_2$ > $NiCl_2$ > $CrCl_2$ > $CuCl_2$. Moreover, the LI values of the intensive inhibitors are all lower than 0.1, the LI value of cigarette butts water extracts is 0.12 fell into 0.1–1 region and greater than intensive

Table 3 The current and potential noise time series results of 5% cigarette butts water extracts and its intensive inhibitors in 15% HCl with N80 steel at 90 °C

Inhibitors with the same concentration of 5% (wt%)		Time domain analysis			
		σ_E (V)	σ_I (A)	R_n (Ω cm^2)	LI
Blank		5.18×10^{-4}	1.01×10^{-4}	5.13	0.18
Cigarette butts water extracts		6.59×10^{-4}	2.12×10^{-5}	31.08	0.12
Cigarette butts extracts intensive inhibitors	$CoCl_2$	6.88×10^{-4}	1.93×10^{-5}	35.65	0.062
	$NiCl_2$	8.10×10^{-4}	1.64×10^{-5}	49.39	0.025
	$CrCl_2$	9.44×10^{-4}	1.37×10^{-5}	68.91	0.019
	$CuCl_2$	1.12×10^{-3}	1.03×10^{-5}	108.74	0.011

inhibitors, which suggests that the N80 steel in 15% HCl solution with cigarette butts extracts is threatened to occur localization corrosion, and the corrosion inhibition effects of intensive inhibitors are all more excellent than cigarette butts extracts. This is in agreement with weight loss, polarization and impedance results.

SEM

The SEM photographs of N80 steel in 15% HCl in the absence and presence of 5% cigarette butts water extracts and its intensive inhibitors at 90 °C are shown in Fig. 4. From Fig. 4, it can clearly see that, the corrosion degree order of N80 steel is blank > cigarette butts water extracts > $CoCl_2$ > $NiCl_2$ > $CrCl_2$ > $CuCl_2$. This is in agreement with weight loss and electrochemical results.

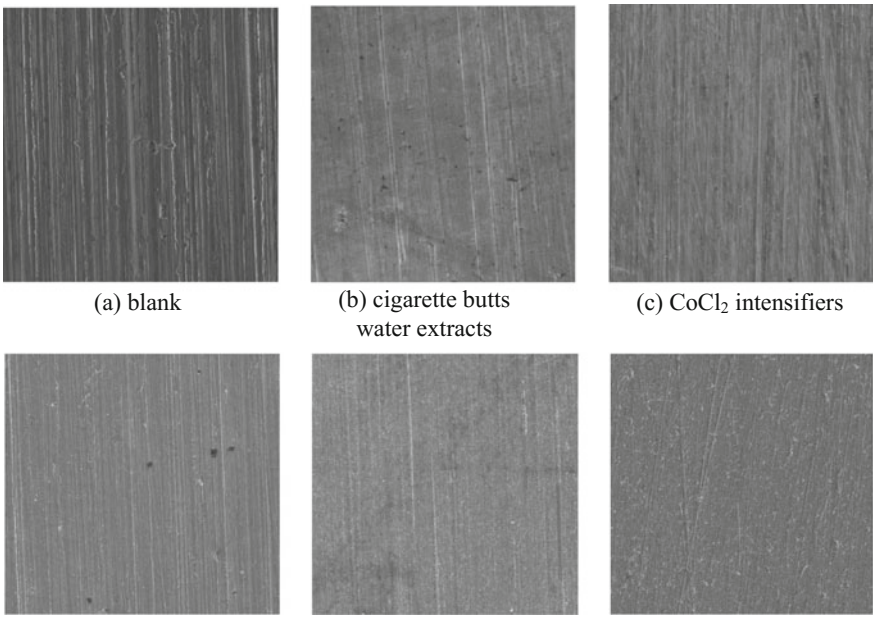

(a) blank (b) cigarette butts water extracts (c) $CoCl_2$ intensifiers

(d) $NiCl_2$ intensifiers (e) $CrCl_2$ intensifiers (f) $CuCl_2$ intensifiers

Fig. 4 The scanning electron microscopy photographs of N80 steel in 15% HCl with cigarette butts water extracts and its intensive inhibitors at 90 °C (magnification times, ×200)

Conclusion

The corrosion inhibitive effect of different metal chlorides intensifiers in cigarette butts extracts are compared in 15% (wt%) hydrochloric acid at 90 °C with N80 steel. Weight loss, polarization, impedance and electrochemical noise results are all shown that the corrosion inhibitive effect order of inhibitors is the corrosion attack degree order of N80 steel is $CuCl_2$ > $CrCl_2$ > $NiCl_2$ > $CoCl_2$ > cigarette butts water extracts > blank. Four metal chlorides all act as synergistic agents. One of the most significant synergism is cuprous chloride; its inhibition efficiency reached 94.2 with 5% dosage. The scanning electron microscope also shows that the $CuCl_2$ synergistic cigarette inhibitor specimen has smooth surface and almost no corrosion.

References

1. J. Zhao, N.S. Zhang, C.T. Qu, X.M. Wu, J.T. Zhang, X. Zhang, Cigarette butts and their application in corrosion inhibition for N80 steel at 90 °C in a hydrochloric acid solution. Ind. Eng. Chem. Res. **49**, 3986–3991 (2010)
2. A. Cizek, H. Tex, U.S. Patent 4,997,040 (1991)
3. S.V. Lamaka, B. Vaghefinazari, Di Mei, R.P. Petrauskas, M.L. Zheludkevich, Comprehensive screening of Mg corrosion inhibitors. Corros. Sci. **128**, 224–240 (2017)
4. I.B. Obot, N.K. Ankah, A.A. Sorour, Z.M. Gasem, K. Haruna, 8-Hydroxyquinoline as an alternative green and sustainable acidizing oilfield corrosion inhibitor. Sustain. Mater. Technol. **14**, 1–10 (2017)
5. C. Zea, R. Barranco-García, J. Alcántara, J. Simancas, D. de la Fuente, pH-dependent release of environmentally friendly corrosion inhibitor from mesoporous silica nanoreservoirs. Micropor. Mesopor. Mat. **255**, 166–173 (2018)
6. S. Varvara, R. Bostan, O. Bobis, L. Găină, R.M. Souto, Propolis as a green corrosion inhibitor for bronze in weakly acidic solution. Appl. Surf. Sci. **426**, 1100–1112 (2017)
7. E. Naveen, B. Vijaya Ramnath, C. Elanchezhian, S.S. Mohamed Nazirudeen, Influence of organic corrosion inhibitors on pickling corrosion behaviour of sinter-forged C45 steel and 2% Cu alloyed C45 steel. J. Alloy. Compd. **695**, 3299–3309 (2017)
8. F.E.T Heakal, A.E. Elkholy, Gemini surfactants as corrosion inhibitors for carbon steel. J. Mol. Liq. **230**, 395–407 (2017)
9. Z. Mahidashti, T. Shahrabi, B. Ramezanzadeh, The role of post-treatment of an ecofriendly cerium nanostructure Conversion coating by green corrosion inhibitor on the adhesion and corrosion protection properties of the epoxy coating. Prog. Org. Coat. **114**, 19–32 (2018)
10. C. Verma, E.E. Ebenso, M.A. Quraishi, Ionic liquids as green and sustainable corrosion inhibitors for metals and alloys: An overview. J. Mol. Liq. **233**, 403–414 (2017)
11. H. Hassannejad, A. Nouri, Sunflower seed hull extract as a novel green corrosion inhibitor for mild steel in HCl solution. J. Mol. Liq. **254**, 377–382 (2018)
12. A.S. Fazayel, M. Khorasani, A.A. Sarabi, The effect of functionalized polycarboxylate structures as corrosion inhibitors in a simulated concrete pore solution. Appl. Surf. Sci. **441**, 895–913 (2018)
13. A. Jmiai, B. El Ibrahimi, A. Tara, S. El Issami, L. Bazzi, Alginate biopolymer as green corrosion inhibitor for copper in 1 M hydrochloric acid: Experimental and theoretical approaches. J. Mol. Struct. **1157**, 408–417 (2018)

14. G. Babaladimath, B. Vishalakshi, S.T. Nandibewoor, Electrical conducting xanthan Gum-graft-polyaniline as corrosion inhibitor for aluminum in hydrochloric acid environment. Mater. Chem. Phys. **205**, 171–179 (2018)
15. M.A. Deyab, Efficiency of cationic surfactant as microbial corrosion inhibitor for carbon steel in oilfield saline water. J. Mol. Liq. **255**, 550–555 (2018)
16. A.A. Olajire, Corrosion inhibition of offshore oil and gas production facilities using organic compound inhibitors—A review. J. Mol. Liq. **248**, 775–808 (2017)
17. S.E. Kaskah, M. Pfeiffer, H. Klock, H. Bergen, C.B. Fischer, Surface protection of low carbon steel with N-acyl sarcosine derivatives as green corrosion inhibitors. Surf. Inter. **9**, 70–78 (2017)
18. M. Izadi, T. Shahrabi, B. Ramezanzadeh, Electrochemical investigations of the corrosion resistance of a hybrid sol–gel film containing green corrosion inhibitor-encapsulated nanocontainers. J. Taiwan Inst. Chem. E. **81**, 356–372 (2017)
19. M. Whelan, K. Barton, J. Cassidy, J. Colreavy, B. Duffy, Corrosion inhibitors for anodised aluminium. Surf. Coat. Technol. **227**, 75–83 (2013)
20. E. Salehi, R. Naderi, B. Ramezanzadeh, Improvement in the protective performance of epoxy ester coating through inclusion of an effective hybrid green corrosion inhibitive pigment. J. Taiwan Inst. Chem. E. **81**, 391–405 (2017)
21. M. Abd El-Raouf, E.A. Khamis, M.T.H. Abou Kana, N.A. Negm, Electrochemical and quantum chemical evaluation of new bis(coumarins) derivatives as corrosion inhibitors for carbon steel corrosion in 0.5 M H_2SO_4. J. Mol. Liq. **255**, 341–353 (2018)
22. N. Gartner, T. Kosec, A. Legat, The efficiency of a corrosion inhibitor on steel in a simulated concrete environment. Mater. Chem. Phys. **184**, 31–40 (2016)

Prospect and Latest Development of Pipeline Integrity Management in China

Shaohua Dong, Yinuo Chen and Zongqi Liu

Abstract China's pipeline industry has established a relatively complete technical system of pipeline integrity to solve the major security problems of detections and diagnosis of oil and gas pipeline, which effectively protect the intrinsic safety of pipeline. However, in recent two years, with the development of new materials, big data, cloud computing and other technology, the pipeline whose steel grade is above X80 has been developed successfully, and hydrogen-containing gas pipeline has been put into use. However, there are new technical problems in pipeline industry to be solved, and therefore it is necessary: (1) to gradually establish a big data management architecture model suitable for the pipeline system to study the fusion processing of big data, efficient algorithm and modeling technology, and provide big data decision support for pipeline energy control, disaster management and risk control, (2) to study the failure behavior of hydrogen-induced cracking of pipeline whose steel grade is above X80, find out its failure mechanism, analyze the difference of failure behavior between pipeline whose steel grade is above X80 and pipeline whose steel grade is lower, and finally form a set of integrity evaluation method of pipeline whose steel grade is above X80 in hydrogen-containing environment, (3) to study the reflection of the signal law of electromagnetic control array and piezoelectric ultrasound when they detect cracks and defects, in order to develop defect reflection signal data processing system, and finally develop the crack detection equipment of pipeline whose steel grade is above X80. In this paper the prospect and latest development of pipeline integrity management in China is reviewed.

Keywords Integrity management · Big data · Hydrogen induced cracking Crack detection

S. Dong · Y. Chen (✉) · Z. Liu
Pipeline Technology and Safety Research Center at China,
University of Petroleum-Beijing, Beijing 102249, China
e-mail: nora_chenyn@163.com

© Springer Nature Singapore Pte Ltd. 2018

Y. Han (ed.), *Advances in Materials Processing*, Lecture Notes in Mechanical Engineering, https://doi.org/10.1007/978-981-13-0107-0_111

Introduction

Pipeline integrity management and control technology originated in the 1970s, when a large number of long distance oil and gas pipeline built by Europe and the United States and other industrial developed countries after World War II has entered the old age, frequent accidents resulted in huge economic losses and casualties, greatly reduced the profitability of the pipeline company, and also seriously affected and restricted the normal production of upstream oil (gas) field.

The United States firstly began to draw lessons from the risk analysis techniques in economics and other industrial sectors to evaluate the risk of oil and gas pipelines, in order to minimize the incidence of oil and gas pipelines, to extend the service life of the major trunk pipelines as much as possible, and allocate limited pipeline maintenance costs reasonably. After several decades of development and application, many countries have gradually established a pipeline safety assessment and integrity management system and a variety of effective evaluation methods.

Development Overview of Pipeline Integrity Management

Foreign Research Progress

In 1968, the United States enacted the first legislation on pipeline safety named the Natural Gas Pipeline Safety Act, which issued The Pipeline Safety Improvement Act (PSIA) in 2002, and in Chap. 14 of PSIA, it is expressly required that the pipeline operator to implement the pipeline integrity management plan in the High Consequence Area (HCA). Based on the PSIA Act, the US Department of Transportation has issued recommended rules for the safety management of gas pipelines and dangerous liquid pipelines in CFR49 Part 192 and CFR49 Part 195. In 2006, the United States promulgated [1] "Pipeline Inspection, Protection, Enforcement and Safety Act", which provided legal protection for pipeline integrity management and corrosion control. On February 3, 2011, the US Senate to the Senate Business Committee submitted the motion named "Pipeline Safety Improvement Law of 2011", and was approved. In 2012, Obama signed the "Pipeline Transport Safety Improvement Act."

In Canada, [2] The National Bureau of Energy (NEB) has developed landline regulations for Canadian provinces, which explicitly require "each company should develop a pipeline integrity management procedure". The Canadian Standards Association (CSA) has developed a pipeline standard CSZ662-2003, "Design, Construction, Operation and Maintenance of the Oil and Gas Pipeline System", which clearly states that the operating company should develop and implement a pipeline integrity management procedure.

At present, pipeline companies of The United States, Europe, Canada, Mexico and other pipeline industry developed countries have implemented an integrated

management strategy for oil and gas pipelines, which has achieved significant economic benefits and improved the intrinsic safety of pipeline system.

Domestic Research Progress

In China, Shanxi-Beijing natural gas pipeline developed a system document in 2001, which put the Shanxi-Beijing pipeline integrity management procedures documents and operating documents into the HSE system. In 2002–2003, Advantica company of the United Kingdom modified the oil pipeline detector for natural gas pipeline of China Petroleum Pipeline Bureau, and completed the internal detection of 1000 km high pressure and large diameter natural gas pipeline of Shanxi-Beijing line for the first time.

In March 2004, at the China Petroleum Pipeline Management and Technology Exchange Conference, Yao Wei published technical exchange papers named "Promote the integrity of management, ensure the safety of the pipeline," which attracted the attention of many participants. The same year in July, the project named "Shanxi-Beijing pipeline integrity management model and application research" won the first prize of State Administration of Work Safety Production Science and Technology Achievement Award. In 2005, "Shanxi and Beijing pipeline integrity technology and application" won the first prize in scientific and technological progress of PetroChina Gas Company; the same year, PII's high-definition detection technology was introduced, and the first application on the gas storage pipeline line GangQing line 711 mm was successful, the British wave of ultrasonic wave detection technology was also introduced and it was promoted in the country. In the same year, China Petroleum Science and Technology Center also began to carry out integrity management research. In September 2006, at the International Conference on IPC Pipeline in Canada, the theme report of "Best Practice of Shanxi-Beijing Pipeline Integrity Management" was published. In 2007, TNO-RISCURVE, ANSYS, ABQUS and other pipe mechanics analysis method were introduced. In 2009, a pipeline safety and material testing laboratories was established, and obtained CNAS certificate of National Certification and Accreditation Board. In 2015, the pipeline company's entire life cycle of asset integrity (risk) control manual was formed. And the China Petroleum Pipeline Company led GB32167-2015 Oil and Gas Pipeline Integrity Management Regulations issued, marking the integrity of the pipeline management to become the technical regulations that managers must follow.

Advances in Pipeline Integrity Management

At present, the integrity management system has been established. The system was formed of four aspects: the pipeline line integrity technology, station facilities integrity technology, oil and gas reservoir security technology, integrity system platform technology, and strived to full coverage [3]. At the same time, oil and gas pipelines integrity management practices have also been established. The specification is intended to promote the intrinsic safety of the pipeline industry. It specifies the contents, methods and requirements of oil and gas pipeline integrity management, including data collection and integration, high consequence area identification, risk assessment, integrity evaluation, risk reduction and maintenance, and efficiency evaluation. The specification applies to GB50251 or GB50253 designed to transport onshore steel pipe of oil and gas medium, but not applicable to the station process pipeline [4].

Pipeline integrity management technology has the following landmark progress.

Pipeline Integrity Assessment Theory System

The system of pipeline integrity evaluation theory system has been established, pipeline hydrogen induced cracking, weld, plane defects, volume defects, pipeline damage assessment of different theoretical methods have also been established. The relevant personnel has studied a variety of online and offline pipeline assessment technology, putting forward the hydrogen induced cracking fracture criteria, establishing the H2S pipeline safety evaluation model and failure assessment map, and solving the problem of detachment of pipeline integrity evaluation theory and production [5]. The pipeline failure assessment method based on stress and strain double criterion was established for the first time, the fractal expansion mechanism of hydrogen—induced cracking and brittle hardening of tubes was found, the failure model and the assessment chart were reconstructed, the failure probability model of pipeline under uncertainty was established based on stress-intensity interference theory. New theories and new methods have improved the accuracy of the assessment by 10% (Table 1).

Table 1 Comparison of old and new technology (pipeline integrity assessment)

Contrast project	The original technology	The project technology
Failure judgment	Stress determination criteria	Stress, strain double judgment criterion
Pipe fracture criterion	Fatigue fracture model	Fatigue + environment fracture fractal fracture model
Failure probability model	Deterministic probability distribution	Fracture distribution based on uncertainty probability
The accuracy of the decision (%)	80	90

The software package of V3.0 (Oil & Gas Pipeline Integrity Super Assessment System V3.0) is established, which is suitable for the evaluation of the applicability of oil and gas pipeline structure. It has good interface and good calculation precision. The software package includes 6 modules, API 579 software module, BS7910 module, pipeline hydrogen induced cracking and life prediction module, weld evaluation module, ASME/Restreng/DNV corrosion evaluation module, internal detection data alignment and evaluation module.

Pipeline Three-Axis High-Definition Magnetic Leakage Detection Device

China Petroleum has developed a series devices of Pipeline three-axis high-definition magnetic leakage detection, the sensor used XYZ three-dimensional distribution instead of the traditional uniaxial distribution, the new integrated curing coupling sensor and all-digital three-dimensional magnetic flux leakage signal acquisition system was developed, a series of detectors (POI) was formed. The detection threshold (POI) increased by 10–90%, and the detection of the depth of the defect threshold increased from 20% of the wall thickness to 5% of the wall thickness (international test indicators) [6] (Table 2).

Table 2 Comparison of old and new technology (leakage detection device)

Performance	Types		
	The original technology		Three-axis high-definition detection technology
	Standard definition detection technology	High-resolution detection technology	
Minimum axial sampling distance	Analog record	≥ 2 mm	2 mm
Minimum return detection pitch (mm)	40–150	8–17	4–12
Can detect the minimum defect depth (wt%)	20	10	5
Depth dimension measurement accuracy (wt%)	±15	±10	±5 – 10
Credibility level (%)	80	80	85
Detection result confirmation degree POI (%)	85	85	95

Multi-channel High-Precision Deformation Detection Device and Pipeline Strain Monitoring System

A multi-channel high-precision deformation detection device and pipeline strain monitoring system was invented, high-precision angular displacement sensor, anti-shake probe swing device and topology algorithm instead of the original straight displacement sensor and simulation algorithm was adopted, positioning accuracy was improved. Vibrating wire high precision anti-jamming sensor was used to monitor f high-risk pipeline strain accurately. The accuracy of the acquisition is ±10 microstrain [7], which realizes the automatic control and remote maintenance of the pipeline strain data acquisition strategy (Table 3).

The pipeline geology disaster monitoring system was developed, the acceleration sensing technology was developed, the time domain algorithm model was established, the tube large displacement continuous monitoring was firstly realized, and the pipeline monitoring network based on the Internet of Things was formed (Fig. 1).

Risk Assessment and Control of Pipeline Level Upgrade

According to the stress-intensity interference theory, the probability distribution model of pipeline stress and intensity is proposed, and the regional level is upgraded. The probability distribution law of pipeline stress and intensity is put forward based on the stress-intensity interference theory, and the semi-quantitative risk assessment model and software of pipeline failure probability were established, and the corresponding index system and control measures were put forward (Table 4).

Based on the statistical data of population distribution in urban areas of China, the acceptable risk probability of domestic gas pipeline regional grading was put forward. Based on the theory of stress-intensity interference, a quantitative analysis method of failure probability of regional upgrading pipeline was proposed.

Table 3 Comparison of old and new technology (pipeline strain monitoring system)

Contrast project	Foreign original technology	The project is highly accurate monitoring technology
Monitoring parameters	Strain, earth pressure	Strain, temperature, displacement, earth pressure
Sensor type	Strain gauge, barometer	Strain gauges, barometer, accelerometer
Displacement range	Indirect measurement 0–0.5 m	Accelerometer direct measurement 0–10 m
Monitoring accuracy (με)	±20	±10

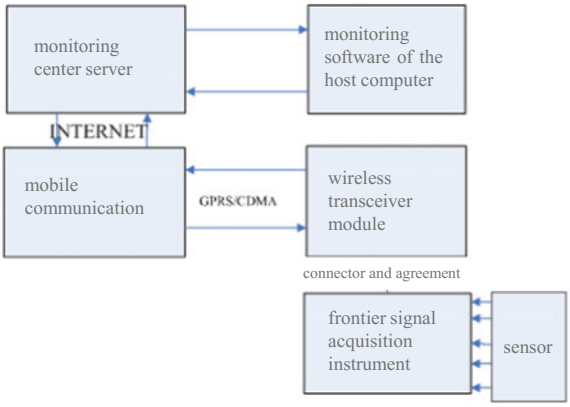

Fig. 1 Schematic diagram of the principle of acceleration sensing technology

Table 4 Comparison of old and new technology (risk assessment)

Contrast project	Domestic and foreign original technology	This project
Target failure probability	Not presented by region level	According to the regional level, put forward quantitative indicators
Risk assessment model of regional level change	No research	The semi-quantitative model of regional level risk assessment is proposed
The establishment of index system	No research	The study gives the regional grading index system

The influence of uncertainty on pipeline failure probability was quantified, the quantitative evaluation of regional upgrading of gas pipeline was put forward, and the risk control measures were put forward and evaluation software was developed (Fig. 2; Table 5).

Station Security Technology

Based on the support vector machine (SVM) model, acoustic emission theory and modern sensing and signal processing technology, the dual-channel natural gas pipeline ball valve leakage detection device and method are developed, and the minimum detectable inner leakage flow reaches 0.04 m^3/h in.; Compressor group combined neural network adaptive fault diagnosis method and hybrid fault early warning model were proposed to improve the compressor group fault diagnosis discovery rate of more than 15% [8]. Compressor vibration monitoring and

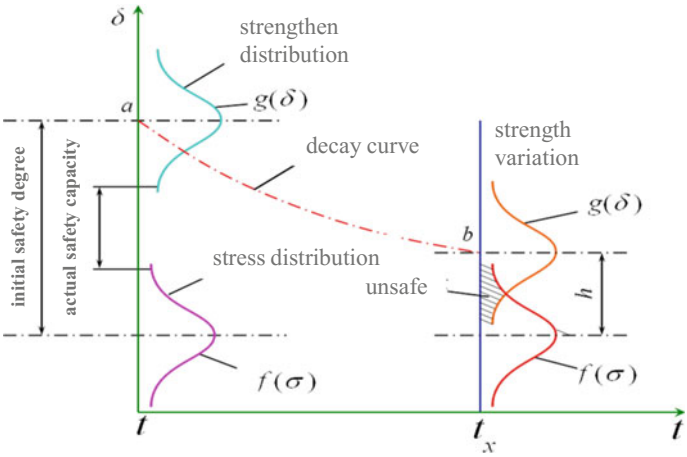

Fig. 2 Pipeline stress intensity distribution curve

Table 5 Research results of regional grade and population density failure probability

Regional level	Failure probability value	The project is highly accurate monitoring technology
1	10^{-3}	75
2	10^{-4}	500
3	10^{-5}	1000
4	10^{-6}	2000

diagnostic management platform was formed, and it can be real-time monitoring of compressor unit operation (Table 6).

Natural gas station ultrasonic guided wave detection database was created. Pipeline single ring, double ring and double station test and other detection technology methods are optimized, the situation of the buried pipeline and the section through the wall was studied, high water level, high clay, the test of asphalt coating line and other problems were solved.

The sound signal acquisition and processing system, which is suitable for the characteristics of natural gas pipeline, was developed. The corresponding signal analysis and processing software was developed. The natural gas pipeline ball valve leakage detection system integrated modern sensing technology, signal processing analysis technology was developed, and ball valve leakage detection problem was solved.

The minimum single-valve detection time is <10 Min; the minimum detectable internal leakage flow rate is: 0.04 m^3/hr in. (or 0.66 L/Min in.); the minimum detection flow meets the petroleum industry API-6D standard. The equipment is shown in Fig. 3.

Table 6 Comparison of old and new technology (station security technology)

Contrast project	Foreign original technology	The project is highly accurate monitoring technology
Ball valve leakage detection accuracy	Can't be quantified and positioned	Can be quantitatively positioned, ±10, 0.04 m^3/h in.
Ball valve internal leakage data extraction mode	Audio	Audio, wavelet transform, support vector machine SVM
Compressor fault diagnosis	Acceleration signal threshold warning	Neural network adaptive identification, coupled hybrid fault early warning
Compressor failure detection rate (%)	70	85

Fig. 3 Valves to be tested and testing equipment

An implicit feature extraction technique that suppresses boundary oscillation, eliminates frequency aliasing and signal denoising is invented, that is, the early weak fault detection and diagnosis technology of large dynamic group, which realizes the extraction of weak features and the diagnosis of early faults (Fig. 4).

As shown in Figs. 5 and 6, the traditional method is characterized by no rubbing effect, and the characteristic of the project method can be used to extract the rubbing characteristics.

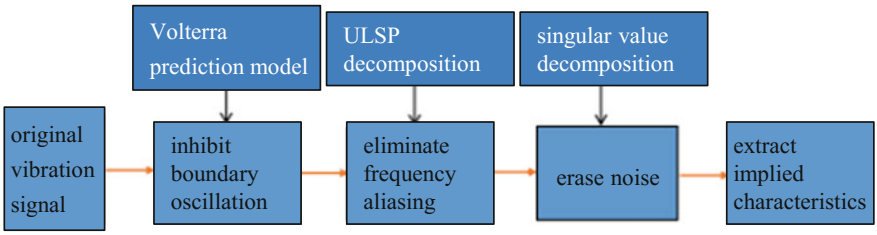

Fig. 4 Large dynamic group early weak fault detection and diagnosis technology schematic diagram

Fig. 5 Traditional method feature extraction effect map

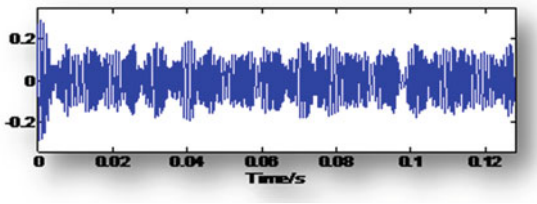

Fig. 6 Traditional method feature extraction effect map in a certain project

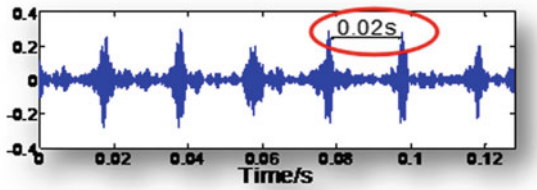

Pipeline Corrosion Control

The mechanism of black dust composition analysis was established to analyze the chemical composition of corrosion products. The mechanism of H_2S, CO_2 and microbial corrosion was studied. A physical model was established to characterize the corrosion rate of pipe wall with the change of iron element concentration. A fungicide for inhibiting the corrosion of microbial sulfur bacteria, iron bacteria and sulfate-reducing bacteria in natural gas pipeline, simulating the migration characteristics of black dust in the tube, and developing a jet pigtilizer with good application effect. So that the amount of dust reduced by 90% [9]. The Ion chromatograph and X-ray single crystal surface detector is shown in Fig. 7.

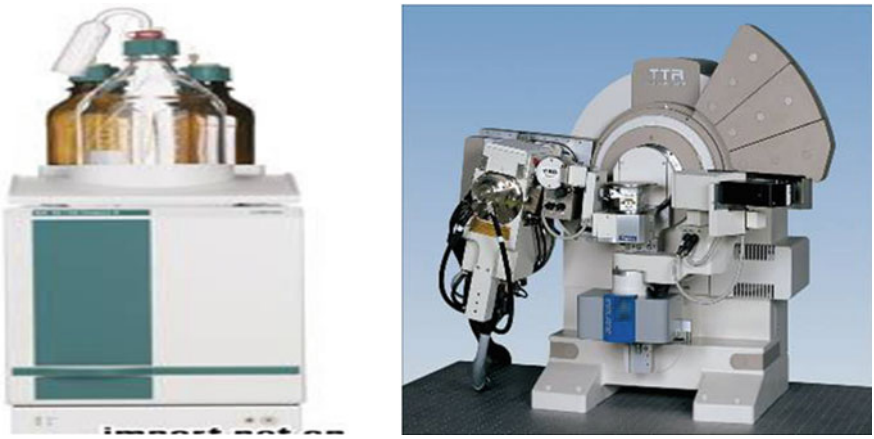

Fig. 7 Ion chromatograph and X-ray single crystal surface detector

Gas Storage Security Technology

In the aspect of gas storage safety and security technology, the technical system of gas storage integrity management system was established (Fig. 8), and the technical system of risk assessment of underground gas storage of salt hole type and dry oil and gas reservoir was systematically studied. The risk assessment of the gas storage and the safety assessment of the injection wells, casing and cement rings were formed, and the gas storage risk assessment software was developed and the corresponding risk control measures were put forward.

Integrity Management Information Platform Technology

PetroChina developed the PIS system, established a pipeline data dictionary and built a digital pipeline emergency decision support GIS system to achieve the emergency situation in the pipeline data timely recall and to meet the emergency command information query analysis needs. Output of one-button emergency management plan document can achieve the transformation and association of pipeline basic information and completion information. Which complete the pipeline geographic information based database, pipeline operation and maintenance dynamic database.

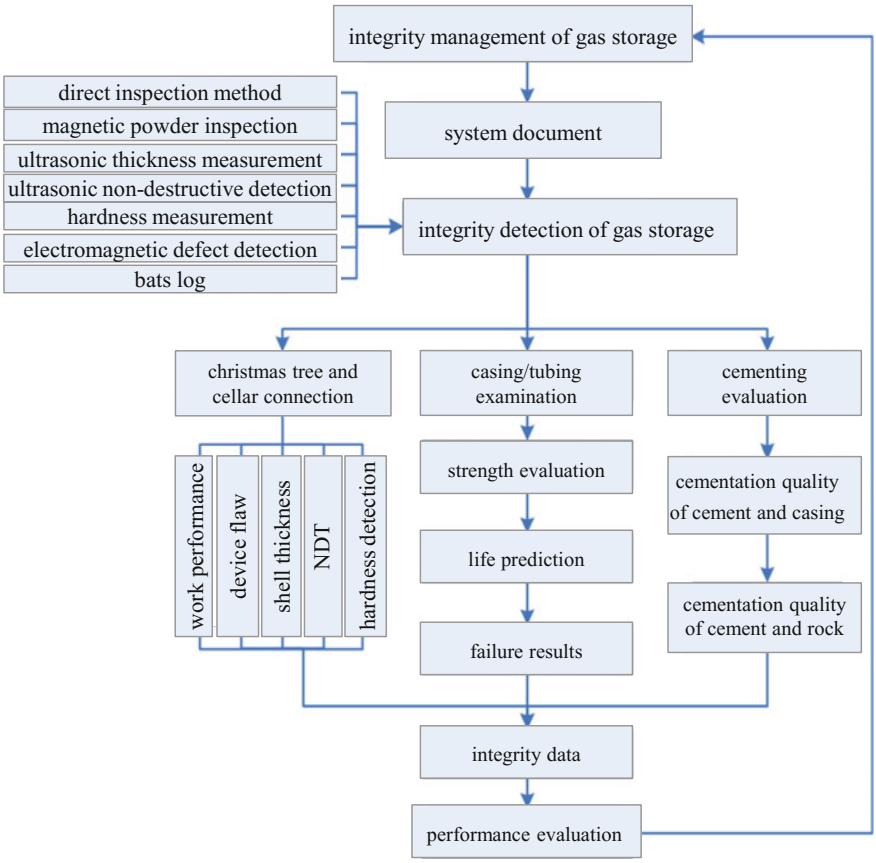

Fig. 8 Gas storage integrity management process

Development of Big Data Technology Industry

Since 2014, China University of Petroleum (Beijing) Pipeline Technology Research Center is committed to the development of the whole life cycle database and management system, and work with PetroChina, Sinopec, CNOOC, and other units to study full life Cycle intelligent pipe network system, which achieved important results.

Quality Analysis of Pipeline Data Based on Big Data Analysis

The internal test data or the center line measurement data was integrated into the center line, and was one by one corresponded, according to the corresponding

logical relationship between the mileage, and the completion of the corresponding data pipe correspondence, the difference between the completion of data and internal testing data was found, the quality of the situation was determined.

Alignment technology of weld, valve, elbow characteristics, all the pipe data and a few obvious characteristics should be corresponded one to one to find the plots which clearly deviate from the center line and finally to determine the accuracy of its characteristics.

Research on Third Party Damage Early Warning Technology Based on Large Position Data

Third-party damage is an important risk to the pipeline. According to statistics, from 2001 to 2015, the domestic pipeline accident due to third-party damage accounted for 30% of the total ~40% of the total; 1984–1992, the pipeline accident in the European countries due to third-party damage accounted for % of the total; 2010–2016, the United States occurred a total of 702 pipeline leakage incidents, of which 177 is due to third-party damage (third-party excavation or external force) caused, accounting for 25.21% of the total.

Location data has become the current used to perceive the laws of human community activities, analysis of geographical conditions and the construction of intelligent city of the important strategic resources [10]. Through the analysis of the location of big data, from the simple positioning data we can derive the human's social attributes and the relationship between environment, thus form a kind of intelligent, socialized application.

The processing steps of the big data are: (1) Preprocessing. (2) Local location data feature extraction. (3) Dimension reduction analysis of big data. (4) Feature association and collaborative mining.

Technology of Geological Disaster Flood Forecast Based on Big Data

The digital river basin model is established by summarizing the characteristics of different geomorphological sites, different sub—processes and different slope—ditch units. Digital river network can store simulation unit, characterize basin topology, auxiliary parallel computing. According to the meteorological forecast or measured rainfall data of Europe, North America, the United Kingdom and China, combined with the parallel computing function of the digital watershed model, the flow of the river is simulated and calculated. Then the surface factor based on the

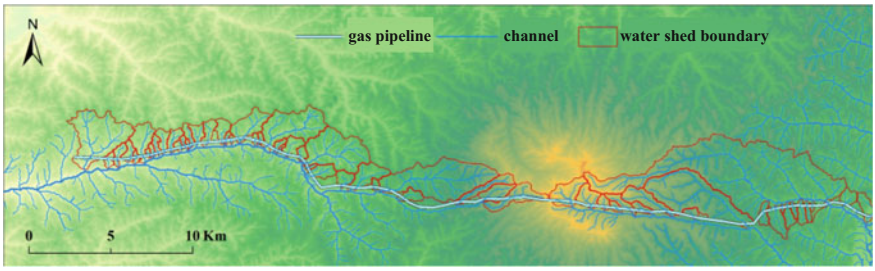

Fig. 9 Static evaluation of flood risk in Linxian pipeline

catchment area and the linear factor based on the river are uniformly mapped to the linear object of the gas pipe segment, so as to carry out the static risk assessment of the pipeline (Fig. 9).

Leakage, Early Warning Signal Time Series Model-Data Mining

As the time series data and static data has a great difference, so its clustering analysis has a lot of complexity. Time series data clustering methods are as following: original data-based clustering; feature-based clustering; model-based clustering.

Big Data Analysis Model in Pipeline Detection

The length of the national pipe network has reached 125,000 km, the detection data has reached thousands of TB level, so the analysis of the detection data is significant. Many researchers have analyzed the data management of the internal detection, but only analyze the causality of the data, but not related to the issue of related issues. Considering the comprehensive analysis of the non-causal factors in the detection data, engineering quality and corrosion area is also important [11, 12]. Therefore, the framework of internal data management based on big data environment is constructed, as shown in the following figure.

Through the detection of big data, we can analyze the following problems: the basic quality of the national pipeline construction, the overall situation of the national pipeline corrosion, the evolution and development of the national pipeline operation risk, pipeline cathodic protection and corrosion of high incidence areas, pipeline welding quality and fill The quality of the situation, in order to achieve multi-round detection and evaluation of the correct comparison of data (Fig. 10).

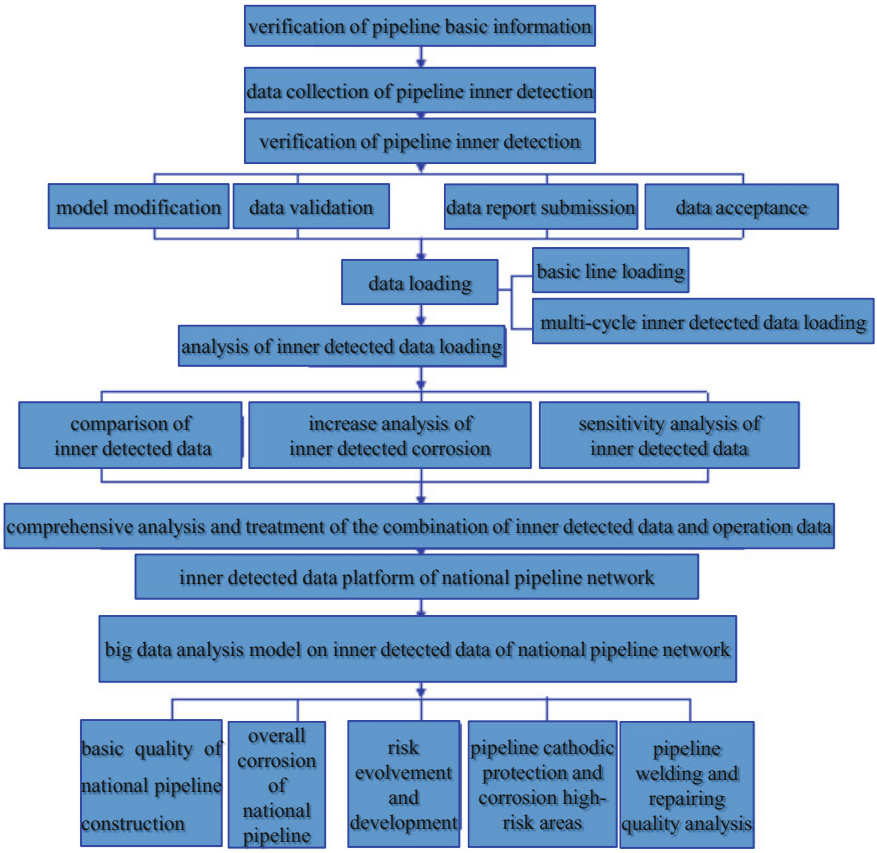

Fig. 10 Internal data management model for big data environment

Analysis of Big Data of Pipeline Weld

Weld is one of the important characteristics of the pipeline, its quality directly affects the safety of the pipeline. The poor quality of the welding caused a lot of accidents. The accidents which caused by the quality of welds are as following: the pipeline hit the mouth; weld radiographs failed with hidden defect; welded radiographs are not corresponding to welds [13]. big data analysis can find weld defects or implied problems, thus to find the whole position of the film.

X-ray based weld images can be used for feature extraction and automatic identification of defects. Firstly, two kinds of image enhancement algorithms are compared with the method of mean filtering and median filtering. The histogram equalization method is used to image enhancement, and the iterative threshold image segmentation algorithm is used to segment the weld area and the feature extraction and feature selection of weld defects are carried out. Finally, the SVM

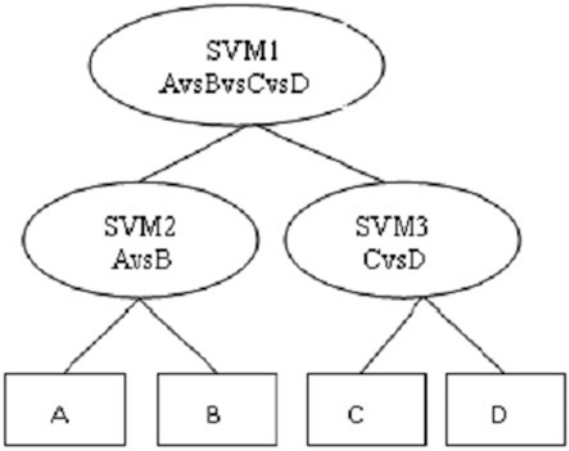

Fig. 11 Schematic diagram of the binary tree SVM algorithm for weld defect classification

classifier based on binary tree is used to classify and identify weld defects [14, 15], and filter the possible defect characteristics such as crack, non-penetration, non-fusion, Stomata, spherical slag and strip slag (Fig. 11).

In the figure above, A is not fused, B is not penetrated, C is the pore, and D is the inclusion. Through the description above, the most efficient SVM structure is obtained.

Pipe Corrosion Risk Data Model—Cluster Analysis Model

In terms of the performance of the K-means algorithm, it can not guarantee that the global optimal solution must be obtained. The accuracy of the final solution depends largely on the initialized grouping. As the algorithm is very fast, therefore, the commonly used method is to run the k average algorithm, select the optimal solution. One of its drawbacks is that the number of groups k is an input parameter, and an inappropriate k may return poor results [16]. In addition, the algorithm assumes that the mean square error is the best parameter to calculate the group's divergence. The factors related to the corrosion area of the pipeline include the low-lying area, the pipeline material and the manufacturing, the internal oil and gas medium, the stray current region, the atmospheric acid rain area, the lightning area, the anticorrosive structure, the epoxy bonding force, the inner corrosion area. The pressure fluctuation area, the downstream of the compressor station 32 km, the temperature is higher than 38 °C, the pipe age is more than 10 years, the rock wool insulation, dry and wet alternately, the beach area, Cl^- and Na^+ is rich, the internal H_2S, the temperature is too low Non-related factors include pipe diameter, X80 pipe, pressure, flow, inspection, geographical conditions, construction, construction, and so on. [17] The non-related factors include pipe diameter, X80 pipe, pressure, flow, inspection, geographical conditions, engineering construction,

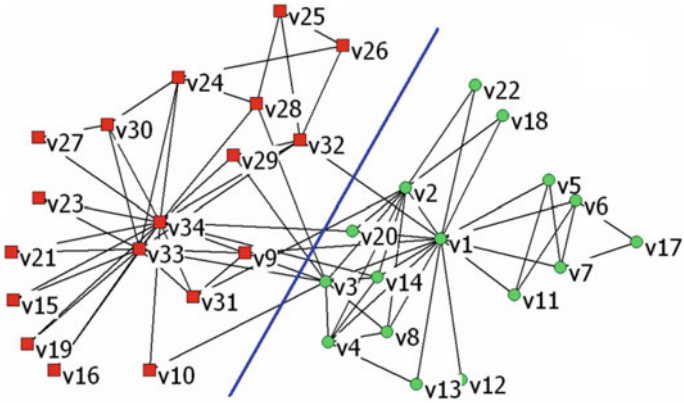

Fig. 12 Topological relationship between the relevant factors of pipeline corrosion zone and non-direct factors

Fig. 13 Relationship between corrosion factors and sensitivity

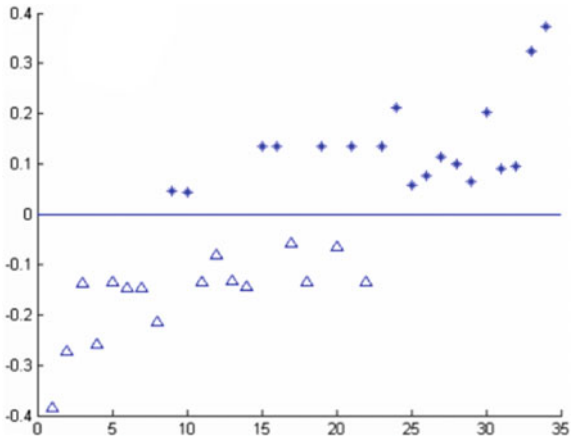

third-party damage, cross-construction, test piles, warning belt, elevation, thunderstorms, floods, geological landslides, change lines, internal testing, atmospheric environment, fiber optic cable, external testing, human environment, construction units. However, when the corrosion direct and non-direct factors are intertwined, it may produce different degrees of influence. Therefore, from the K-means algorithm to the "nuclear clustering and spectral clustering" analysis of pipeline corrosion (Fig. 12), and the correlation between the corrosion resistance of the pipeline and the corrosion sensitivity is obtained by the clustering algorithm (Fig. 13). In the pipeline operation process, the dry and wet alternating, corrosive environment, stray current interference pipe section of the external corrosion should be strengthened management.

Pipeline Emergency Decision-Making and Support Based on Big Data

The emergency data includes emergency planning database, detection plan database, defect disposal plan database, historical risk data, equipment data, historical accident data, aerial remote sensing data, pipeline equipment data, basic geographic data, process flow chart data, station model Data and so on. According to the corresponding emergency basic data, emergency decision support system can be established.

When the accident occurs, the system can be the city government information center and from the public security. Fire, earthquake, weather, the scene and other important information can be sent to the Civil Defense Information Center, the system can classify, decide and processed the image information and related data information that the department collected for the decision-making command staff quickly grasp the disaster, analysis and decision-making command [18]. And the system can automatically calculate the evacuation range, safety radius, automatic output contingency plans, emergency treatment programs, etc., through the repair of materials and repair team routing optimization, to achieve one-button emergency response program output. Output data include: pipeline basic information, Scope of impact, emergency facilities, population distribution, best routing, emergency response programs [19, 20].

Summary

(1) The integrity management of oil and gas pipelines is bound to follow the direction of the development of safety management in the whole life cycle. The key lies in the data integration and accuracy control. The key of the management platform is to analyze the history, present and future trend of equipment and facilities.
(2) The integrity evaluation, risk prediction analysis and big data decision support of pipeline network structure will be an important development direction of life cycle management in oil and gas field (reservoir).
(3) To build a life cycle intelligent management platform of big data, the most important part is functional applications, and the decision support is focused on how to build data model.
(4) It is suggested that big data analysis should focus on the key issues such as solving the problems of material, structure and failure, and solving the key issues such as safety, quality, energy consumption and operation which restrict the development of oil and gas pipeline industry. The establishment of big data centers for oil and gas pipelines will be the core element of the problems.

(5) It is suggested that the integrity evaluation method of X80 pipeline in hydrogen environment with crack defects should be formed, the operation control parameters of hydrogen concentration should be proposed, and the data processing system of the defect reflection signal should be developed to form the crack and defect display method, and finally develop steel crack detection equipment for pipeline whose steel grade is above X80.

Acknowledgements The authors gratefully acknowledge the financial support from the National Key R&D Program of China (No. 2017YFC0805800).

References

1. K. Wang, Application progress of overseas oil and gas pipeline integrity management. Liaoning Chem. Ind. **45**(02), 221–222, 225 (2016)
2. L.J. Wang, Q. Li, J.Y. Liang, Long-distance pipeline within the test data comparison of the status quo and development trends at home and abroad. Oil Gas Storage Transp. **34**, 233–236 (2015)
3. S.H. Dong, Z.P. Yang, The latest development of global oil and gas pipeline integrity technology and management—development countermeasures of pipeline integrity management in China. Oil Gas Storage Transp. **26**, 1–17 (2007)
4. J. Qin, Hao D. Hao, J.S. Song, Analysis and application of oil and gas pipeline integrity management system. Pipeline Technol. Equip. **3**, 7–8 (2011)
5. S.H. Dong, *Pipeline Integrity Management Technology And Practice* (Beijing, 2015), pp. 19–31
6. Q.S. Feng, H.L. Zhang, Advantages of three-axial high-resolution magnetic flux leakage inspection technology and its application status. Oil Gas Storage Transp. **35**(10), 1050–1054 (2016)
7. G.S. Bai, Y.J. Zhang, Series of high-resolution pipeline deformation inspecting tools. Oil Forum. **33**(01), 51–54 (2014)
8. Z.L. Li, H.F. Zhang, Acoustic emission mechanism and testing of leakage in natural gas pipeline ball valve. J. Vibr. Meas. Diagn. **37**(03), 525–531, 630 (2017)
9. Y.F. Liu, Q.P. Li, Research progress and development trend of by-pass pigging. Pipeline Tech. Equip. **02**, 41–43, 46 (2016)
10. Z.X. Song, S.X. Fang, Xie J.L. Xie, Fatigue damage based on stress intensity interference model. J. Beijing Jiaotong Univ. **37**, 52–56 (2013)
11. W. Zhang, P. Feng, J.Y. Yuan, Research progress of missing data processing methods. Chin. J. Hosp. Adm. **19**, 301–304 (2012)
12. L. Guo, F.X. Xu, L.J. Zhou, Pipeline integrity system data integration and application. Oil Gas Storage Transp. **33**, 593–598 (2014)
13. T. Wang, H. Yang, Current status and prospect of inline inspection technologies. Oil Gas Storage Transp. **34**(07), 694–698 (2015)
14. X.X. Lin, Y.X. Li, X. Zhou, Big data environment pipeline management data management. Oil Gas Storage Transp. **34**, 349–353 (2015)
15. Y. Huang, Y.Y. Cheng, Y. Ren, Study on feature extraction of image defects based on X-ray weld. Electron. Testing **7**, 30–33 (2012)
16. S.H. Dong, Y. An, Data analysis model for pipeline system and its application based on big data. Oil Gas Storage Transp. **34**(10), 1027–1032 (2015)
17. W.W. Xiao, C.L. Song, Risk analysis on surface gathering and transportation pipeline corrosion and perforation in oilfields. Oil-Gas Field Surf. Eng. **36**(04), 81–85 (2017)

18. Z.Y. Jiang, Z.L. Li, Y.H. Zhang, Pipeline weld digital ray DR detection technology research. Chem. Ind. **43**, 427–429 (2014)
19. Y.T. Zhou, S.H. Dong, Q.L. Dong, Emergency decision support system based on integrity management. Oil Gas Storage Transp. **34**, 1280–1283 (2015)
20. S.H. Dong, H.W. Zhang, Based on big data of the whole life cycle intelligent pipe network solution. Oil Gas Storage Transp. **1**, 28–36 (2017)

Sulfate Reducting Bacteria Corrosion Component Study of N80 Steel in Simulating Oilfield Produced Water

Wenwen Song, Juantao Zhang, Xunji Li, Bin Li, Fagen Li and Anqing Fu

Abstract Sulfate reducting bacteria (SRB) is isolated from practical oilfield produced water and added to the oilfield produced simulating water to investigate the corrosion component of SRB on N80 steel. Oilfield produced simulating water was prepared to four mediums in order to research SRB corrosion component. Weight loss results showed that the corrosion rate component contributed by SRB was 0.0093 mm/a, which accounts for 7.93% of the total corrosion rate of oilfield produced simulating water. Polarization results indicated that the SRB corrosion mainly increased cathode reaction rate and produced cathode depolarization. And the surface of N80 steel in four mediums all present pitting corrosion.

Keywords Sulfate reducting bacteria · Corrosion component · N80 steel

Introduction

In oilfield produced water, many factors are associated with corrosion of metals, including sulfate, carbonate, iron of chlorine, bacteria, sulfur, and so on. Among them, sulfate reducing bacteria (SRB) are recognized as the major group in oil/gas well corrosion. They can form bio-films, producing hydrogen sulfide, accelerating iron corrosion and affecting electrochemical processes. The SRB is thought to be responsible for >75% of the corrosion in productive oil well sand for >50% of the failures of buried pipelines and cables [1, 2]. Since 1934 SRB have been implicated in pitting corrosion of ferrous metals and their alloys, many researches are focus on the aquatic and terrestrial habitats of SRB, varying in nutrient content, temperature, pressure and pH values, under anoxic and oxygenated conditions [3–6]. However,

W. Song · X. Li · B. Li
Tarim Oilfield Company, Petro China, Korla 841000, Xinjiang, China

J. Zhang (✉) · F. Li · A. Fu
State Key Laboratory for Performance and Structure Safety of Petroleum Tubular Goods and Equipment Materials, Xi'an 710065, China
e-mail: zhangjuantao@cnpc.com.cn

© Springer Nature Singapore Pte Ltd. 2018

Y. Han (ed.), *Advances in Materials Processing*, Lecture Notes in Mechanical Engineering, https://doi.org/10.1007/978-981-13-0107-0_112

there is no report on the SRB corrosion component. Moreover, in oilfield nothing can compete with the structure properties, low cost and versatility of N80 steel used as oil casing. So, in this study, the SRB is isolated from practical oilfield produced water and added to the oilfield produced simulating water to investigate the corrosion component of SRB on N80 steel.

Experimental

SRB Isolation

The fresh oilfield produced water is extracted from oil well and added to API (American Petroleum Institute) defined SRB culture medium with 5% (wt%) inoculum concentration. After culturing 7 days, taking 0.1 mL mass bred SRB solution to solid culture medium for purification. Undergoing six times purification the SRB could be added into oilfield produced simulating water to investigate the corrosion component on N80 steel. Synchronously, the number of SRB in practical oilfield produced water is calculated by MPN (Most Probable Number) method during isolating process.

Materials

The tested material is N80 oil tube steel discs manufactured by CNPC Baoji Petroleum Steel Pipe Co. LTD with the chemical composition of C 0.30, Mn 1.38, Si 0.25, S 0.003, P 0.003, Mo 0.021, Cu 0.0036 and Fe the rest. Before the corrosion test, the surfaces of the sample are mechanically polished by grit sand-paper progressively up to 1200# (# stand for the mesh number), rinsed with alcohol and then stove-dried.

The aggressive medium is oilfield produced simulating water with constituents shown in Table 1. In order to investigate the corrosion component of SRB, the oilfield produced simulating water is prepared to four solutions: (1) primary oilfield produced simulating water; (2) sterile oilfield produced simulating water; (3) sterile oilfield produced simulating water + SRB nutritive medium; (4) sterile oilfield produced simulating water + SRB nutritive medium +SRB. Solution (1) can test the total corrosion rate of oilfield produced simulating water; solution (2) wants to keep the impacts of the other factors except SRB on total corrosion rate; solution (3) is used to indicate the corrosion performance of SRB nutritive medium; if SRB nutritive medium has no corrosion, the SRB corrosion component can be obtained by using corrosion rate of solution (4) minus corrosion rate of solution (2).

Table 1 Constituents of oilfield produced simulating water

$Na^{+}+K^{+}$ (mg/L)	Ca^{2+} (mg/L)	Mg^{2+} (mg/L)	HCO_3^{-} (mg/L)	SO_4^{2-} (mg/L)	Cl^{-} (mg/L)	S^{2-} (mg/L)	Fe^{2+} (mg/L)©	Total dissolved solid (mg/L)	pH	SRB count/mL	Temperature (°C)
8174.1	199.6	88.0	2840.5	199.6	11,416.5	8.9	1.2	45,858.8	6.8	10^3	45

Results and Discussion

SRB Isolation

The growth curve and morphology tested by transmission electron microscope (TEM) of SRB are shown in Fig. 1. From Fig. 1, the growth peak is about at 48 h and the SRB belongs to bacillus without flagellum. So, the weight loss testing time is designed as 5 days and the polarization is carried out after N80 steel specimen immersing in aggressive medium for 3 days.

Weight Loss and Polarization

Table 2 shows weight loss results and polarization parameters of N80 steel in four medium of oilfield produced simulating water. Figure 2 is the polarization curve of N80 steel in four medium of oilfield produced simulating water. It can be seen from Table 2 and Fig. 2, the SRB nutritive medium almost brings no corrosion rate, and the corrosion rate component contributed by SRB is 0.0093 mm/a, which accounts for 7.93% of the total corrosion rate of oilfield produced simulating water. In polarization curves, the cathode slopes of solutions (2–4) respectively are −190.762, −190.883 and −191.795 mV, and the anode slopes of solutions (2–4) respectively are 41.132, 41.167 and 41.207 mV. When adding SRB, the anode slope has almost not changed but the cathode slope increases obviously. It indicates that the SRB corrosion mainly increases cathode reaction rate and produces cathode depolarization.

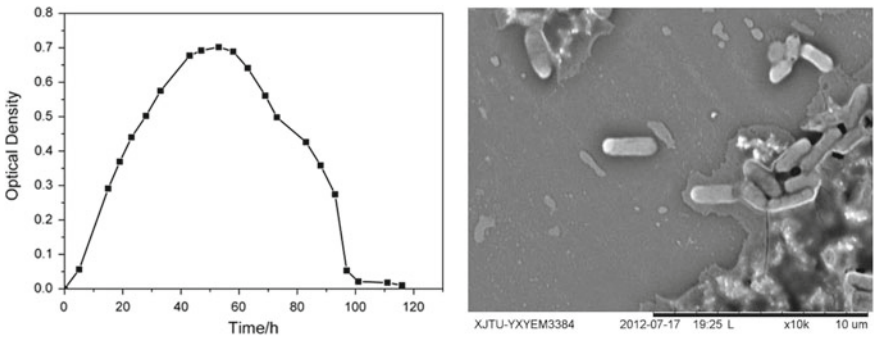

(a) growth curve (b) morphology

Fig. 1 Growth curve and morphology of SRB

Table 2 Weight loss results and polarization parameters of N80 steel in four medium of oilfield produced simulating water

Solutions	Weight loss corrosion rate (mm a^{-1})	Polarization parameters				
		Corrosion potential (mV)	Corrosion current (mA cm^{-2})	Cathode slope (mV)	Anode slope (mV)	Corrosion rate (mm a^{-1})
(1)	0.1329	−749.62	11.586	−193.809	41.903	6.736
(2)	0.1173	−721.59	11.071	−190.762	41.132	6.024
(3)	0.1162	−691.24	11.083	−190.883	41.167	6.081
(4)	0.1216	−727.07	11.312	−191.795	41.207	6.521
SRB corrosion component	0.0093	–	–	–	–	0.497
SRB corrosion component percentage	7.93%	–	–	–	–	7.38%

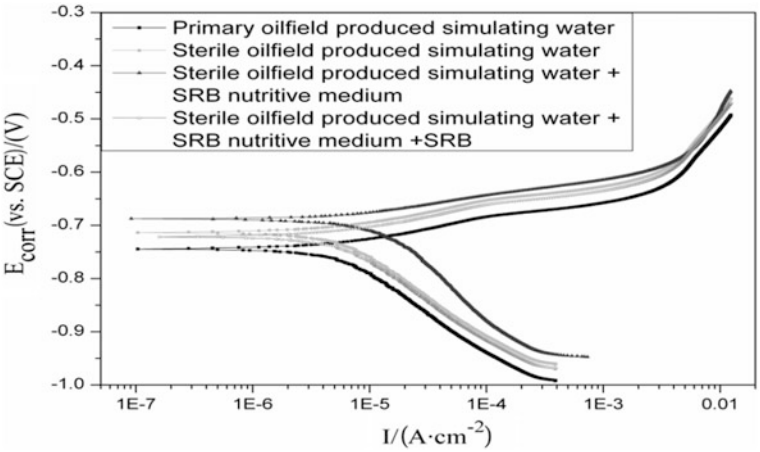

Fig. 2 Polarization curve of N80 steel in four medium of oilfield produced simulating water

Corrosion Morphology

Figure 3 is scanning electron microscope (SEM) photos and energy dispersive spectrometer (EDS) of N80 steel in four medium of oilfield produced simulating water. From Fig. 3, the corrosion of N80 steel in four medium of oilfield produced simulating water all present pitting corrosion with main corrosion product of iron oxide.

Conclusion

The SRB is isolated from practical oilfield produced water and added to the oilfield produced simulating water to investigate the corrosion component of SRB on N80 steel. Weight loss results show that the SRB nutritive medium almost brings no corrosion rate, and the corrosion rate component contributed by SRB is 0.0093 mm/a, which accounts for 7.93% of the total corrosion rate of oilfield produced simulating water. Polarization results indicate that the SRB corrosion mainly increases cathode reaction rate and produces cathode depolarization. Scanning electron microscope photos and energy dispersive spectrometer results illustrate the corrosion of N80 steel in four medium of oilfield produced simulating water all present pitting corrosion with the main corrosion product of iron oxide.

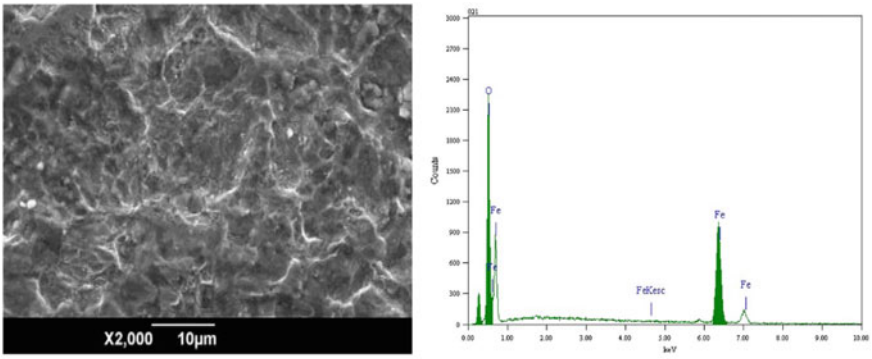

(a) primary oilfield produced simulating water

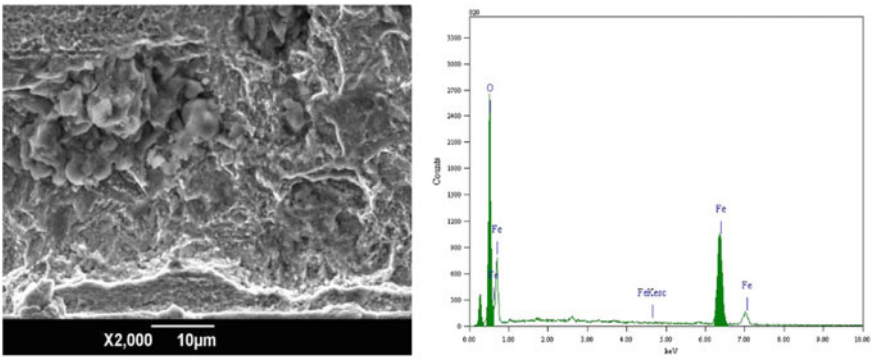

(b) sterile oilfield produced simulating water

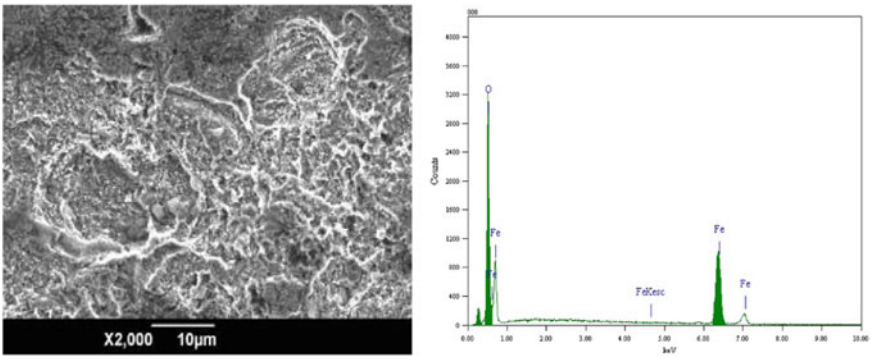

(c) sterile oilfield produced simulating water + SRB nutritive medium

Fig. 3 Scanning electron microscope photos and energy dispersive spectrometer of N80 steel in four medium of oilfield produced simulating water

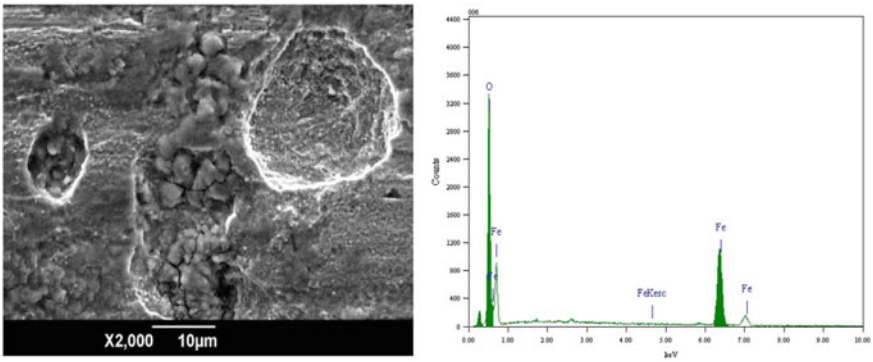

(d) sterile oilfield produced simulating water + SRB nutritive medium +SRB.

Fig. 3 (continued)

References

1. S. Lata, C. Sharma, A.K. Singh, Microbial influenced corrosion by thermophilic bacteria. Cent. Eur. J. Eng. **2**, 113–122 (2012)
2. X.J. Zhao, P. Wang, G.H. Lan, Study on the identification and bio-corrosion behavior of one anaerobic thermophilic bacterium isolated from dagang oil field. Afr. J. Microbiol. Res. **6**, 6218–6223 (2012)
3. I.B. Beech, Sulfate-reducing bacteria in biofilms on metallic materials and corrosion. Microbiol. Today **30**, 115–117 (2003)
4. E. Valencia-Cantero, E. Martínez-Romero, J.J. Pena-Cabriales, The corrosion effects of sulfate-and ferric-reducing bacterial consortia on steel. Geomicrobiol. J. **20**, 157–170 (2003)
5. X.D. Zhao, J.Z. Duan, B.R. Hou, Effect of sulfate-reducing bacteria on corrosion behavior of mild steel in sea mud. J. Mater. Sci. Technol. **23**, 323–328 (2007)
6. J. Starosvetsky, D. Starosvetsky, R. Armon, Identification of microbiologically influenced corrosion (MIC) in industrial equipment failures. Eng. Fail. Anal. **14**, 1500–1511 (2007)

Application of Grain Boundary Diffusion Method into High-Throughput Synthesis Materials Chip for Sintered Nd–Fe–B Magnets

Xing Yu, Guang Feng, Yifei Zhu, Lei Zhao, Yunhai Jia and Haizhou Wang

Abstract Grain boundary diffusion method is usually applied on the sintered Nd–Fe–B magnets via surface attachment of compounds by Dy or Tb or other heavy rare earth elements. These elements could penetrate into the magnet through the grain boundary under the diffusion treatment at high temperatures above the melting point of the Nd-rich magnet phase. In this investigation the surface attachment method, the diffusion condition, the depth distribution of the diffusion element and the microstructure of the magnet were investigated. On the basis of the results and discussion, it is proposed that the sintered Nd–Fe–B magnets can be utilized to synthesize gradient changing materials chip by a heat treatment process in a single sample. The reasons are that that during the grain boundary diffusion process, there are in parallel the diffusion process of heavy rare earth elements at the grain boundary and the diffusion and substitution process within the main phase grains. The difference of the diffusion rates between the two processes can be adjusted by changing the temperature and time of the diffusion treatment. The thickness, type and combination of the rare earth/non rare earth element compounds attached to the sample surface can be decided accordingly. Finally, the micro-region units at different depth are along the diffusion direction exhibit gradient or different composition-structure-properties, hence the aim to achieve high-throughput synthesis the Nd–Fe–B materials chip by the grain boundary diffusion method could be realized.

Keywords Sintered Nd–Fe–B · Grain boundary diffusion · High-throughput synthesis · Materials chip

X. Yu (✉) · G. Feng · Y. Zhu · L. Zhao · Y. Jia · H. Wang
Beijing Advanced Innovation Center of Materials Genome Engineering, Beijing 100081, China
e-mail: yuxing_email@163.com

X. Yu · G. Feng · Y. Zhu · L. Zhao · Y. Jia · H. Wang
Central Iron and Steel Research Institute, Beijing 100081, China

X. Yu · G. Feng · Y. Zhu · L. Zhao · Y. Jia · H. Wang
Beijing Key Laboratory of Metal Materials Characterization, Beijing 100081, China

© Springer Nature Singapore Pte Ltd. 2018

Y. Han (ed.), *Advances in Materials Processing*, Lecture Notes in Mechanical Engineering, https://doi.org/10.1007/978-981-13-0107-0_113

Introduction

Sintered Nd–Fe–B magnets have been widely applied in the motors of hybrid electric vehicles and electric vehicles owing to their outstanding magnetic properties [1]. However, their undesirable thermal stability is still a major concern in some practical applications such as high-temperature motors. To enhance the coercivity of the Nd–Fe–B magnets, the substitution of Dy for Nd is an effective way due to the much higher magneto crystalline anisotropy field (HA) of $Dy_2Fe_{14}B$ phase than that of $Nd_2Fe_{14}B$ [2]. Too much addition of Dy, Tb and other heavy rare earth elements, which form antiferromagnetic coupling with Fe, results in Nd–Fe–B magnet magnetization product (or remanence) decreased. At the same time, too much use of rare earth elements results in increased production costs. Recently, people have developed grain boundary diffusion technology, Dy, Tb and other heavy rare earth elements from the sintered Nd–Fe–B magnet surface along the grain boundary diffusion into the magnet internal. Compared with the traditional technology, grain boundary diffusion technology can use a small amount of heavy rare earth greatly to improve magnet coercivity, while magnet remanence is almost no change [3]. Since the heavy rare earth element diffuses not only along the grain boundary to the inside of the magnet but also from the grain boundary to the inside of the grains, the diffusion process can result in gradient or different component-structure-properties at different micro-region units of magnet. Therefore, this paper proposes that grain boundary diffusion technique can be used for designing high-throughput synthesis of sintered Nd–Fe–B chip. There have great significance for the rapid synthesizing and screening of magnet target micro-unit.

Summarization of Grain Boundary Diffusion Method for Sintered Nd–Fe–B

Grain boundary diffusion method is to attach the heavy rare earth compounds on the surface of the sintered Nd–Fe–B magnets and diffuse into the magnet at the high temperature process. Usually the high temperature of diffusion treatment is above the rich neodymium melting point, and the heavy rare earth elements can penetrate into the magnet through the grain boundary, as shown in Fig. 1 [4].

Compared with Pr, Nd and other light rare earth elements, Dy, Tb and other heavy rare earth elements are more likely to form RE–Fe–B compounds [5]. During the subsequent diffusion process, the heavy rare earth elements diffuse from the grain boundary to the interior of the $Nd_2Fe_{14}B$ main phase grains, and the highly enriched rare earth $(Nd,RE)_2Fe_{14}B$ (RE = Dy, Tb) shell is formed in the grain boundary Nd-rich phase and the main grain outer edge region, as shown in Fig. 2 [4]. In grain boundary diffusion process, the Nd-rich phase has melted into a liquid phase at high temperature, so that the diffusion rate of Dy and Tb at grain boundary

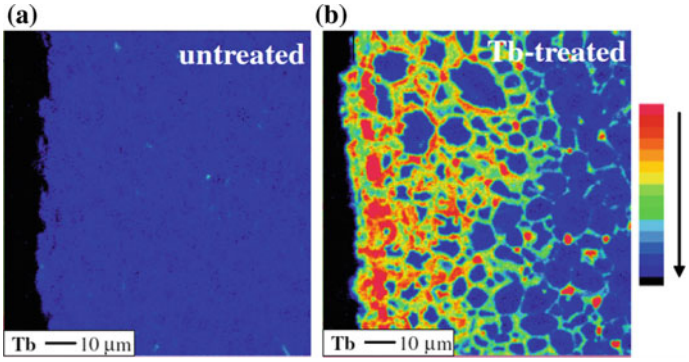

Fig. 1 EPMA images of **a** untreated magnet and **b** treated magnet by grain boundary diffusion

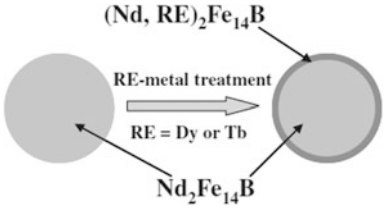

Fig. 2 Schematic illustration for the $Nd_2Fe_{14}B$ grains of Dy- or Tb-metal-treated magnets

is much larger than that in the main grain. As the diffusion rates between the two processes is different, Dy and Tb can be distributed only in the outermost region of the main grain to avoid excessive Nd in the main grain element replaced by adjusting the temperature and time of the diffusion process.

The coercivity of magnet can be greatly improved by the grain boundary diffusion treatment, while the remanence remains substantially unchanged, as shown in Fig. 3 [6]. The coercivity (μ0Hc) was enhanced from 1.31 to 2.04 T by GBDP, while the remanent magnetization (μ0Mr) decreased slightly from 1.44 to 1.42 T.

Although heavy rare earth elements are mainly Dy and Tb in grain boundary diffusion, the chemical states of heavy rare earth elements in attachment process are completely different depending on the surface attachment method. Since the standard free enthalpy of formation of the oxides of Dy and Tb is quite low, only rare earth oxides or rare earth fluorides can maintain their original state in the atmospheric environment. Therefore, heavy rare earth compounds coated on the magnets are mostly oxides and fluorides. Many researchers have extensively studied grain boundary diffusion techniques [4, 6–9], which are classified into four categories according to surface attachment: surface coating (or electrophoresis), magnet surface sputtering heavy rare earths, evaporation and direct landfill. The grain boundary diffusion treatment temperature is usually above the melting point of the Nd-rich phase, so that the Nd-rich phase in the grain boundary is melted into the liquid phase to ensure that the heavy rare earth elements such as Dy and Tb can

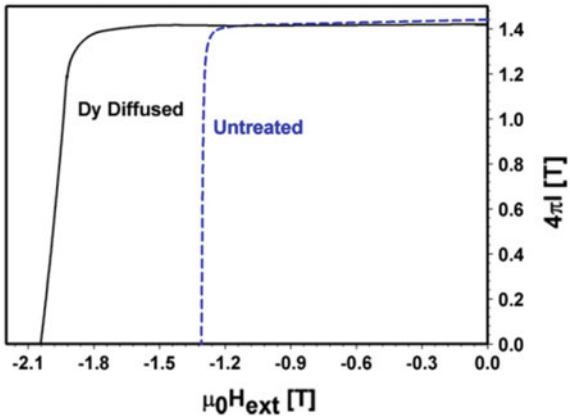

Fig. 3 Demagnetization curves of untreated and GBDP samples

penetrate into magnet through the grain boundary the magnet. At the same time, the main grains are in solid state, and the diffusion and substitution speed of heavy rare earth elements in the main grain are reduced by controlling the treatment temperature of grain boundary diffusion. According to the relevant literature [7–12], the diffusion temperature is controlled in the range of 700–950 °C, the diffusion time is 2–10 h, and the sample thickness is between 2 and 10 mm.

Distribution of Heavy Rare Earth Elements in Grain Boundary Diffusion

In grain boundary diffusion process, the heavy rare earth elements of surface attachment penetrate the inside of magnet from the surface of sintered Nd–Fe–B magnets at high temperatures. When the temperature is increased above 600 °C, the chemical properties of the Nd in Nd-rich region of the magnet internal grain boundary and the edge of the main grain are active. According to the literature reported that Nd and Dy_2O_3 can be replaced by Dy and Nd_2O_3 producing by reaction at high temperatures [13]. Although the heavy rare earth elements mainly diffuse along the grain boundary phase of the molten state, the diffusion process is easily blocked and the diffusion depth is limited as the diffusion process is takes place in the sintered magnet. The concentration of heavy rare earth elements is gradually reduced from the surface to the internal, and is attenuated gradient distribution [14], as shown in Fig. 4. The graph shows the depth profiles of the Nd and Dy concentrations after Dy diffusion treatment at 900 °C for 6 h, and each data point is obtained from the WDX measurement in a Dy-rich shell.

As heavy rare earth diffusion and concentration gradually reduced, increase degree of magnet coercivity will decline. Figures 5 and 6 respectively show the

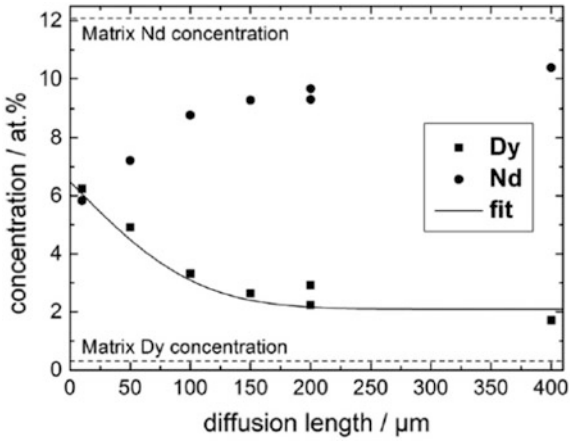

Fig. 4 Depth profiles of the Nd and Dy concentration after Dy diffusion treatment

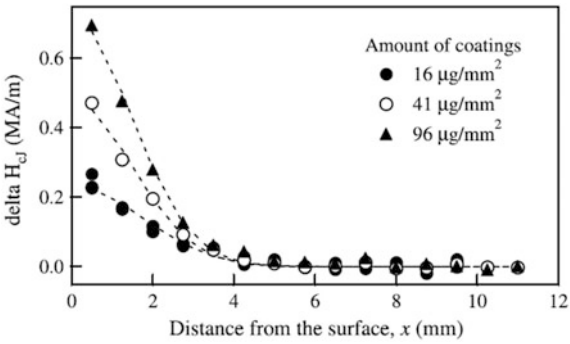

Fig. 5 Coercivity decrease with the depth of magnet under different surface coating conditions

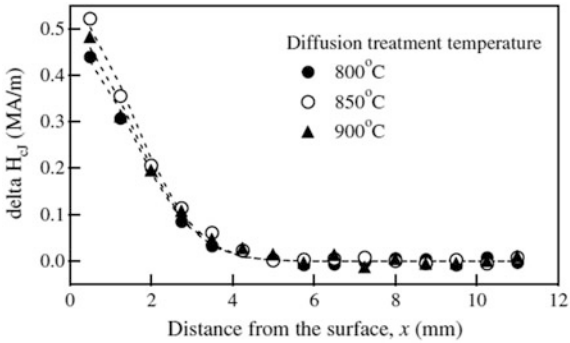

Fig. 6 Coercivity decrease with the depth of magnet under different diffusion temperature conditions

relationship between the increase in coercivity and the depth of the magnet under different surface coating and different diffusion temperature conditions [15].

The grain boundary diffusion distance of magnet is affected by different diffusing elements, the surface attachment mode, and so on. It can be further increased by the

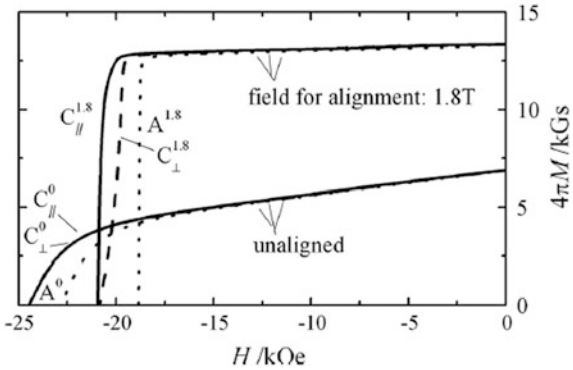

Fig. 7 Demagnetization curves of unaligned and aligned magnets after diffusion treatment

suitable surface attachment method of heavy rare earth. If the grain boundary diffusion treatment is carried out by vapor deposition method [3], the coercivity of 5.5 mm thick magnet can be improved by 580 kA/m. At the same time, many other factors affect the diffusion effect of heavy rare earth. The removal of the oxide layer by acid pickling on the surface of the magnet will play a significant role in enhancing the penetration effect of the dysprosium. The magnet coercivity of grain boundary diffusion treatment is higher in the state of un-ageing than in the state of ageing [16].

The osmotic effect of grain boundary diffusion is anisotropic in the orientation and non-orientation directions, as shown in Fig. 7 [17]. The dysprosium alloy powder was coated on the entire surface of the sample, the sample end face in the orientation direction, and the sample lateral end face. It is found that the squareness of magnet demagnetization curve varies with the diffusion direction, and the diffusion anisotropy is due to the distribution of Nd-rich phase in the grain boundary after orientating.

The grain boundary diffusion of DyH_2 was carried out in Nd–Fe–B matrix with none-Dy, Dy content of 1% and DyF_3. Analysis results of their magnetic properties and structure found that the diffusion effect of DyF_3 adding in matrix is the best [18], as shown in Fig. 8. It is considered that the fluorine can inhibit the formation of Nd–Dy–O at grain boundary in the diffusion process, and it can improve the grain boundary diffusion effect.

Grain Microstructures After Grain Boundary Diffusion

Sintered Nd–Fe–B magnets are polycrystalline composite permanent magnet materials. It mainly includes $Nd_2Fe_{14}B$ phase (volume fraction of about 80–85%), rich Nd phase (volume fraction of about 5–20%) and rich B phase (volume fraction of about 0–8%). $Nd_2Fe_{14}B$ phase is the main phase, showing polygonal grain distribution. The Nd-rich phase is distributed along the grain boundary or at the

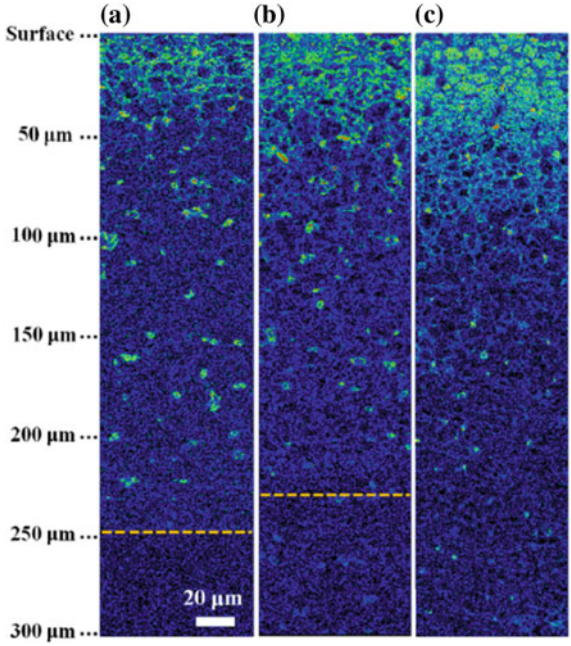

Fig. 8 Low-magnification cross-sectional EPMA Dy mapping images of the **a** DyH_2 dip-coated Dy-free magnet, **b** DyH_2 dip-coated F-magnet (1.0 wt% Dy) and **c** DyH_2 dip-coated F-magnet (1.0 wt% Dy)

grain boundary intersection, showing a thin layer a thin layer. Only a small amount of Nd-rich phases exist in the grains. Few B-rich phase in large or small particles exist in the grain boundary, grain boundary intersection or grain inside. Sintered Nd–Fe–B magnets may also contain Nd oxides, α-Fe phases, holes and so on.

The Dy is significantly enriched at the grain boundary in magnet after treating by grain boundary diffusion. The thickness of Dy-rich layer is very thin (about 10^{-2}–10^{-1} μm), as shown in Fig. 9 [19]. In contrast, the distribution of Dy in magnet synthesized by the two-phase alloy powder sintering method is relatively uniform.

The microstructure of the sintered Nd–Fe–B magnets was observed by transmission electron microscopy. Nd–Fe–B magnets without Dy have discontinuous Nd-rich phase in grain boundary, and Nd–Fe–B magnets adding Dy have formed a continuous, uniform and about 4.4 nm thickness Nd-rich layer in the grain boundary, as shown in Fig. 10 [3]. The excess Nd precipitates at the grain boundary and forms a Nd-rich phase because Dy substitutes for Nd in the $Nd_2Fe_{14}B$ phase.

According to study, it is not a simple solid-state diffusion process that Dy diffuses into the main phase. In the high temperature process, the Nd-rich phase in grain boundary and the outer edge of main phase near the grain boundary will become molten state, and mix with the diffused Dy from the external. During the subsequent solidification process, the $(Dy, Nd)_2Fe_{14}B$ shell is preferentially

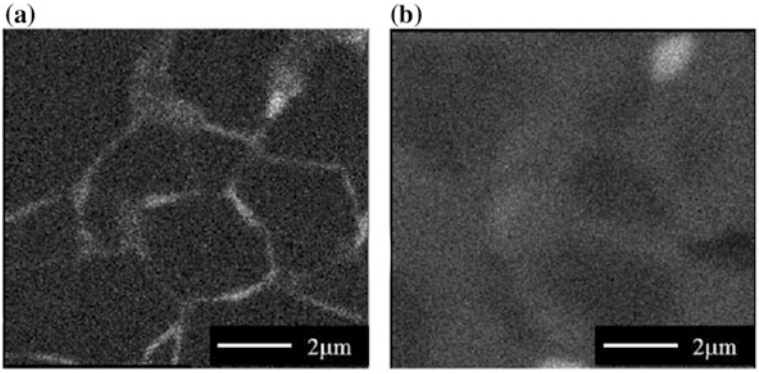

Fig. 9 Dy compositional images taken from magnets produced by **a** grain boundary diffusion process and **b** binary alloy method

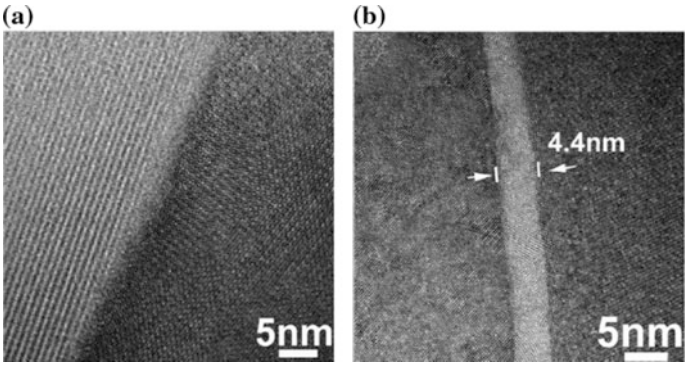

Fig. 10 HRTEM image of the grain boundary of **a** untreated magnet, **b** Dy diffusion processed magnet

solidified at the main phase edge [20]. Using the EBSD, the orientation relationship between the Dy shell near the grain boundary and the $Nd_2Fe_{14}B$ main grain have been analyzed, and it is deduced that the Dy-rich shell is formed by coagulation in the periphery of the original grains [5, 13]. The coercivity of the grain boundary diffusing magnet can be greatly improved because of the enhancement of intergranular de-coupling interaction of Nd-rich phase at grain boundary and the increase of the anisotropy field in the main grain. It is explained by the nucleation field theory that the formation of the antiferromagnetic nucleus is effectively suppressed as the anisotropy field of the transition zone in the main phase is effectively increased [6].

High-Throughput Synthesis of Sintered Nd–Fe–B Chips

The high-throughput synthesis process of sintered Nd–Fe–B chip mainly includes heat treatment chamber processing, split sampling, ultrasonic washing, grinding, polishing, pickling, surface coating and grain boundary diffusion heat treatment.

As shown in Fig. 11, the heat treatment chamber and the corresponding upper cover are machined according to the designed dimensions. The heat treatment chamber and the cover are cleaned with ultrasonic cleaning and dried in the air. At the same time, the grain boundary diffusion samples are cut according to the design size. Depending on the study needs, the magnets are cut into two types of samples: parallel and perpendicular to the C axis.

This paper presents that the heat treatment chamber design can be very convenient for sample assembly, heavy rare earth coating on sample surface. The size of the chamber and the number of sample holes can be designed according to the number of treatment samples, so it can meet the need for high throughput synthesis. After sealing the top cover, the magnet sample and the coated heavy rare earth are isolated from the outside, and it is easy to carry the sample and reduce the demand of the processing furnace.

The magnets are sequentially polished with the sandpaper of 400, 800 and 1000 Cw to have a silver-white glossy surface. The magnet surface need to ensure smooth and level after grinding. The grinded magnets are cleaned with ultrasonic to remove the stained dirt. The magnets were pickled with HNO_3 at a concentration of 5 wt%, And after etching, these metal debris, scratches, cracks and many fine pores were etched away to expose a uniform surface.

As shown in Fig. 12, the heavy rare earth oxide (such as Dy_2O_3) powder and anhydrous ethanol by 2:1 (mass ratio) are mixed evenly for the magnet surface coating; The Nd–Fe–B magnet after cutting, washing and pickling is placed in the cleaned heat treatment chamber, and then the magnet surface is uniformly coated

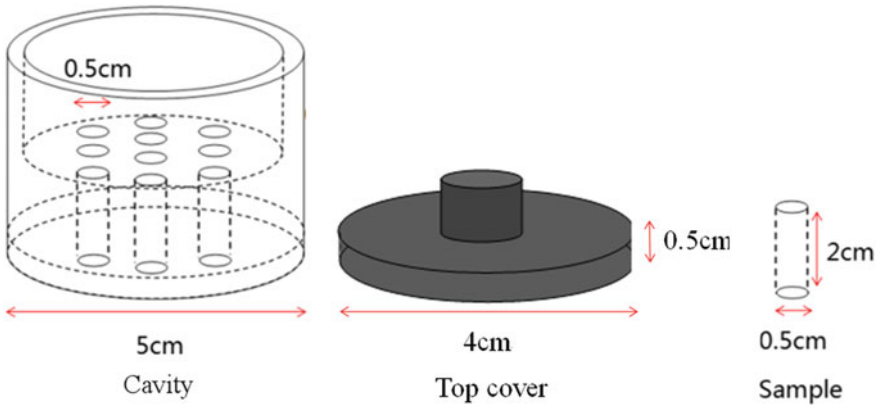

Fig. 11 Schematic diagram of heat treatment chamber and grain boundary diffusion sample

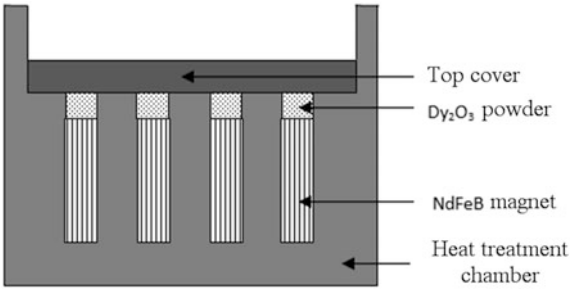

Fig. 12 Diagram of grain boundary diffusion treatment sample assembly and surface heavy rare earth coating

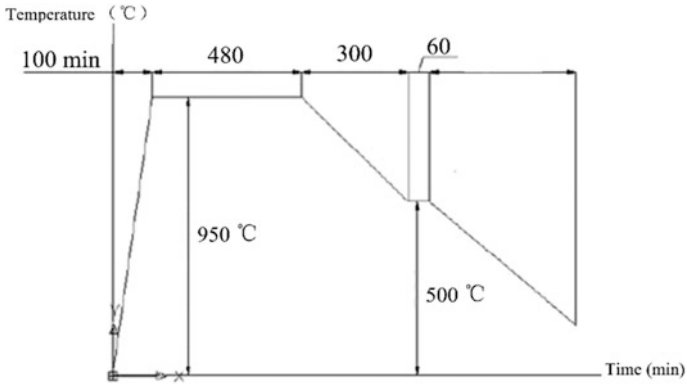

Fig. 13 Heating curve of 950 °C/8 h Dy diffusion and 500 °C/1 h ageing condition

with a certain thickness Dy2O3 powder (particle size less than 5 μm). Coated power need compacting, air-drying, and sealing with cover. In order to study the effect of various rare earth elements/non-rare earth elements on the distribution of composition—structure—property of magnet, the type, composition and thickness of the coated compounds can be changed flexibly.

As shown in Fig. 13, the coated Nd–Fe–B magnets are in turn treated at 950 °C for 8 h, aged at 500 °C for 1 h and cooled in the furnace. After heat treatment, the magnets are processed into suitable size according to the experiment requirements, and polished with sandpaper to ensure smooth and level.

In order to realize the high-throughput synthesis of the sintered Nd–Fe–B chip, it is necessary to obtain the magnet with the change of the gradient at surface and different depth position along the diffusion direction. Therefore, the selected condition is different from the grain boundary diffusion to improve the magnet coercivity. High-throughput synthesis conditions of grain boundary diffusion should be selected for higher diffusion temperatures and longer processing times. Diffusion

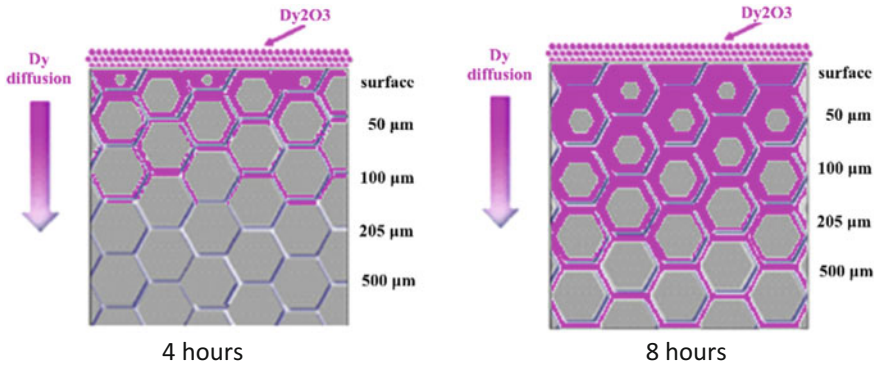

Fig. 14 Diagram of high-throughput synthesis of grain boundary diffusion

temperature is not only higher than the melting point of Nd-rich phase, but also to avoid main grain melting and growth. Increasing the diffusion time ensures that the heavy rare earth elements in the surface have diffused into the interior of main phase grains, while the heavy rare earth elements diffuse along the grain boundary into the deeper magnets to obtain the sintered Nd–Fe–B chip samples, as shown in Fig. 14.

Conclusion

Based on the study of grain boundary diffusion for sintered Nd–Fe–B, the distribution of heavy rare earth elements in the grain boundary diffusion direction and the microstructure of the magnets after grain boundary diffusion treatment is discussed respectively. A heat treatment chamber was designed to facilitate the heavy rare earth coating on surface and the sample heat treatment to meet the needs of high-throughput synthesis. By selecting the higher diffusion temperature and longer processing time than the condition for increasing coercivity, the high-throughput synthesis of the graded Nd–Fe–B materials chip is achieved in a sample by a heat treatment.

Acknowledgements This research was supported by the National Key Research and Development Program of China (No. 2016YFB0700203).

References

1. M. Sagawa, S. Fujimura, N. Togawa et al., New material for permanent magnets on a base neodymium and iron. J. Appl. Phys. **55**, 2083–2087 (1984)
2. S. Hirosawa, Y. Matsuura, H. Yamamoto et al., Magnetization and magnetic anisotropy of $R_2Fe_{14}B$ measured on single crystals. J. Appl. Phys. **59**, 873–879 (1986)

3. H. Sepehriamin, T. Ohkubo, K. Hono, Grain boundary structure and chemistry of Dy-diffusion processed Nd–Fe–B sintered magnets. J. Appl. Phys. **107**, 873-264 (2010)
4. D. Li, S. Suzuki, T. Kawasaki et al., Grain interface modification and magnetic properties of Nd-Fe-B sintered magnets. Jpn. J. Appl. Phys. **47**, 7876–7878 (2008)
5. U.M.R. Seelam, T. Ohkubo, T. Abe et al., Faceted shell structure in grain boundary diffusion-processed sintered Nd–Fe–B magnets. J. Alloy. Compd. **617**, 884–892 (2014)
6. H. Sepehri-Amin, T. Ohkubo, K. Hono, The mechanism of coercivity enhancement by the grain boundary diffusion process of Nd–Fe–B sintered magnets. Acta Mater. **61**, 1982–1990 (2013)
7. D. Li, M. Nishimoto, S. Suzuki et al., Coercivity enhancement of Nd-Fe-B sintered magnets by grain boundary modification via reduction-diffusion process. Mater. Sci. Eng. **1**, 012020 (2009)
8. A.G. Popov, D.Y. Vasilenko, T.Z. Puzanova et al., Effect of diffusion annealing on the hysteretic properties of sintered Nd-Fe-B magnets. Phys. Met. Metall. **111**, 471–478 (2011)
9. M. Soderžnik, K.Ž. Rožman, S. Kobe et al., The grain-boundary diffusion process in Nd–Fe–B sintered magnets based on the electrophoretic deposition of DyF3. Intermetallics **23**, 158–162 (2012)
10. Z. Samardžija, P. Mcguiness, M. Soderžnik et al., Microstructural and compositional characterization of terbium-doped Nd-Fe-B sintered magnets. Mater. Charact. **67**, 27–33 (2012)
11. M. Komuro, Y. Satsu, H. Suzuki, Increase of coercivity and composition distribution in fluoride-diffused NdFeB sintered magnets treated by fluoride solutions. IEEE Trans. Magn. **46**, 3831–3833 (2010)
12. H. Suzuki, Y. Satsu, M. Komuro, Magnetic properties of a Nd–Fe–B sintered magnet with Dy segregation. J. Appl. Phys. **105**, 07A734–07A734-3 (2009)
13. X. Sun, X. Bao, X. Gao et al., Effect of dysprosium addition by pack cementation on magnetic properties and microstructure of Nd-Fe-B sintered magnets. J. Chin. Rare Earth Soc. **27**, 86–91 (2009)
14. K. Löewe, C. Brombacher, M. Katter et al., Temperature-dependent Dy diffusion processes in Nd–Fe–B permanent magnets. Acta Mater. **83**, 248–255 (2015)
15. H. Nakamura, K. Hirota, T. Ohashi et al., Coercivity distributions in Nd-Fe-B sintered magnets produced by the grain boundary diffusion process. J. Phys. D Appl. Phys. **44**, 064003 (2011)
16. X. Fang, *Effects of Grain Boundary Structure and Chemistry on the Coercivity of NdFeB Materials*. (Shanghai Jiao Tong University, 2011)
17. E. Niu, Z.A. Chen, X.Z. Ye et al., Anisotropy of grain boundary diffusion in sintered Nd-Fe-B magnet. Appl. Phys. Lett. **104**, 2909–2911 (2014)
18. T.H. Kim, S.R. Lee, H.J. Kim et al., Simultaneous application of Dy-X, (X = F or H) powder doping and dip-coating processes to Nd–Fe–B sintered magnets. Acta Mater. **93**, 95–104 (2015)
19. K. Hirota, H. Nakamura, T. Minowa et al., Coercivity enhancement by the grain boundary diffusion process to Nd–Fe–B sintered magnets. IEEE Trans. Magn. **42**, 2909–2911 (2006)
20. N. Oono, M. Sagawa, R. Kasada et al., Production of thick high-performance sintered neodymium magnets by grain boundary diffusion treatment with dysprosium–nickel–aluminum alloy. J. Magn. Magn. Mater. **323**, 297–300 (2011)

Structures and Properties of Near-Rapidly Solidified Fe–12Mn–9Al–1.2C Dual-Phase Lightweight Steel Containing 3 wt% Ni

Jianlei Zhang, Wei He, Yang Yang, Yunhu Zhang, Lian Duan, Zhiping Luo, Changjiang Song and Qijie Zhai

Abstract Fe–Mn–Al–C lightweight steel possesses not only excellent comprehensive mechanical properties, but also a low density, which is attractive to the automotive industry. In the present paper, an austenite stabilizer Ni element which usually increases the austenite content was added and its effects on the structure and mechanical properties of a near-rapidly solidified Fe–12Mn–9Al–1.2C dual-phase lightweight steel strip were studied. It was found that the addition of 3% Ni did not show the potential to increase the austenite content or enhance the mechanical properties of Fe–12Mn–9Al–1.2C dual-phase lightweight steel strip. Moreover, the addition of 3% Ni deteriorated the thermal stability of Fe–12Mn–9Al–1.2C steel. In the strip with the addition of Ni, the formed metastable austenite almost fully transformed into ferrite + κ-carbide at a lower annealing temperature.

J. Zhang · W. He · Y. Yang · Y. Zhang · L. Duan · C. Song (✉) · Q. Zhai
State Key Laboratory of Advanced Special Steel, Shanghai Key Laboratory of Advanced Ferrometallurgy and School of Materials Science and Engineering, Shanghai University, Shanghai 200072, China
e-mail: riversxiao@163.com

J. Zhang
e-mail: puyangborui@163.com

W. He
e-mail: hwlj09290603@163.com

Y. Yang
e-mail: 18068889681@163.com

Y. Zhang
e-mail: zhangyunhu.zyh@163.com

L. Duan
e-mail: 1216766146@qq.com

Q. Zhai
e-mail: qjzhai@shu.edu.cn

Z. Luo
Department of Chemistry and Physics,
Fayetteville State University, Fayetteville, NC 28301, USA
e-mail: zluo@uncfsu.edu

© Springer Nature Singapore Pte Ltd. 2018

Y. Han (ed.), *Advances in Materials Processing*, Lecture Notes in Mechanical Engineering, https://doi.org/10.1007/978-981-13-0107-0_114

The formation process of constituent phase in this near-rapidly solidified dual-phase lightweight steel was analyzed. The related results suggested that the constituent phases of the near-rapidly solidified dual-phase lightweight steel depended on the liquid/solid transition, which was controlled by both thermodynamics and kinetics factors.

Keywords Near-rapid solidification · Mechanical property · Microstructure
Dual-phase lightweight steel · Ni element

Introduction

Due to high demands in energy saving and gas emission reduction, reducing the weight of automobiles is of commercial importance [1–5]. Fe–Mn–Al–C steel has attracted much attention in the automotive industry because of its high strength, good ductility and low density [1, 6, 7]. In addition, the constituent Al not only reduces the density, but also improves the oxidation and corrosion resistance of this low-density steel [8–11]. However, if the content of Al is too high, the plasticity and Young's modulus of this material are deteriorated because the content of ferrite is significantly increased [4, 12–14]. The Mn element can stabilize the austenite to achieve good properties [15]. However, the high content of Mn leads to a hard production after the casting, adding high costs to the material processing [16].

Ni is an austenite stabilizer, which usually promotes the formation of austenite in the steel effectively [17–21]. It was found that the addition of Ni significantly increased the strength due to the formation of a FeAl-type brittle and hard intermetallic compound (B2), while the ductility could be retained [17]. Therefore, in the present study, the Ni element is selected to investigate its influence on the structure and mechanical properties of Fe–12Mn–9Al–1.2C dual-phase lightweight steel, whose Mn content is less than the previously investigated Fe–16.1Mn–9.6Al–0.86C–4.9Ni steel [17].

In our previous work [12], the Fe–20Mn–9Al–0.75C steel strip prepared by near-rapid solidification contained a fraction of 82 vol.% austenite. The resulted ultimate tensile strength (UTS), total elongation (TE) and the product of tensile strength and elongation were found to be 951 MPa, 46% and 43.7 GPa%, respectively [12]. Compared to the lightweight steel with similar composition prepared by a traditional process by Hwang et al. [22], the near-rapidly solidified Fe–20Mn–9Al–0.75C dual-phase lightweight steel without any additional treatment had even better mechanical properties. Problems appeared in the traditional method could be avoided by the near-rapid solidification. The high-strength lightweight steel with excellent performance can be produced directly, indicating that the near-rapid solidification is a feasible approach to produce the advanced high-strength lightweight steel. Hence, in this work, the near-rapid solidification process was applied to prepare the Fe–12Mn–9Al–1.2C dual-phase lightweight steel to test the effect of Ni element.

Experimental Procedures

The Fe–12Mn–9Al–1.2C with 3% Ni (mass percentage in the whole text unless otherwise marked) and a reference steel strip without Ni were prepared by centrifugal casting in a near-rapid solidification manner. On the account of high volatility of Mn in Fe–Mn–Al–C light steel, cold-crucible levitation melting method was firstly used to prepare the original ingot rather than using arc melting method. The prepared ingot was re-melted by an induction coil furnace under argon atmosphere, and the sample liquid flowed into a copper mold rotated at the speed of 600 r/min to obtain steel strips with size in 80 mm × 60 mm × 2.5 mm. This method could improve the filling ability of the molten metal by using a centrifugal force, compared with suction casting or spray casting methods. Therefore, larger and high-quality steel strips could be obtained. Finally, the solidified strips were annealed at 400 or 600 °C for 3 h, respectively, in a tubular vacuum annealing furnace.

The composition of the samples was measured by an Inductively Coupled Plasma-Optical Emission Spectrometer (ICP, PERKINE 7300DV) and Carbon Sulfur Analyzer (TC-436). The volume fraction of ferrite was determined by Fischer-scope Ferrite (FMP30). The measured composition of the sample was listed in Table 1. The microstructure was characterized by an Optical Microscope (OM, Zeiss AXIO IMAGER A2M) and a Scanning Electron Microscope (SEM, Phenom Pro) after mechanical polishing and chemical etching of the sample. The etching solutions was composed of 3.3 vol.% nitric acid, 3.3 vol.% acetic acid and 0.1 vol.% hydrofluoric acid and the etching time was 1 s. The phases in the samples were analyzed by an X-ray Diffractometer (XRD, Rigaku D/max-2200, Cu target operated at 40 kV and 40 mA), with a scanning range of 30–100° and scanning speed of 2°/min in a continuous scanning mode. The tensile test was carried out at room temperature by using an MTS Criterion 44 Mechanical Property Tester at a frequency of 100 Hz with a strain rate of $2.5 \times 10^{-4}\ s^{-1}$. The gauge dimension of the tensile specimens was 20 mm × 4 mm × 1 mm.

Results and Discussion

Structure and Properties

XRD patterns from the Fe–12Mn–9Al–1.2C dual-phase lightweight steel as-cast strips with 3% Ni and without Ni are shown in Fig. 1. It is found that there are

Table 1 Measured composition of samples (wt%)

Sample	Mn	Al	C	Ni	Fe
With 3 wt% Ni	10.52	8.46	1.23	2.82	Bal.
Without Ni	11.75	9.12	1.23	0	Bal.

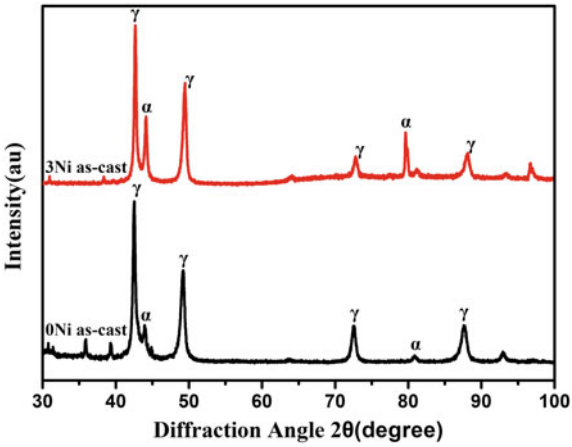

Fig. 1 XRD patterns of as-cast Fe–12Mn–9Al–1.2C strips with 3% Ni (top) and without Ni (bottom) prepared by near-rapid solidification

ferrite and austenite dual phases in the as-cast strips. The intensity of diffraction peaks of the austenite almost remains the same after the addition of 3% Ni. This fact indicates that the addition of 3% Ni does not show the potential to increase the quantity of the austenite phase. Quantitative measurement of the austenite fractions by Fischer-scope Ferrite gives 81.2 and 85.1 vol.% in Fe–12Mn–9Al–1.2C steel strips with 3% Ni and without Ni, respectively. In fact, the addition of Ni slightly decreased the austenite content, which is consistent with the XRD results.

Figure 2 presents the OM morphologies of Fe–12Mn–9Al–1.2C strips with 3% Ni and without Ni prepared by near-rapid solidification. It is observed that the irregular ferrite phase is randomly distributed in the austenite matrix. Furthermore, it is observed that the reference sample has a higher austenite fraction, indicating

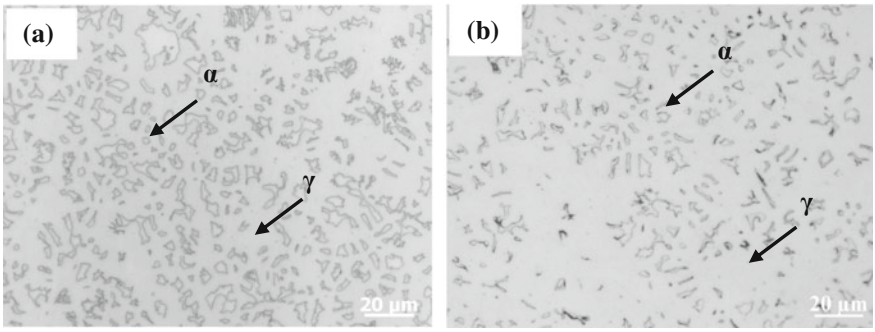

Fig. 2 Optical morphology of strips of Fe–12Mn–9Al–1.2C with 3% Ni and without Ni: **a** with 3% Ni; **b** without Ni

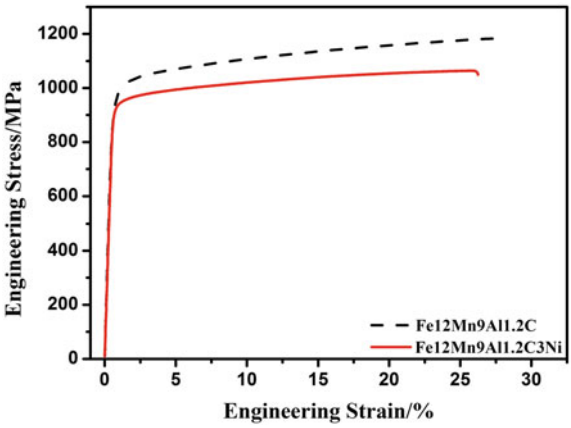

Fig. 3 Stress-strain curves of Fe–12Mn–9Al–1.2C strips with 3% Ni and without Ni

that the content of ferrite slightly increases after 3% Ni addition, which is consistent with the results obtained by XRD and Fischer-scope Ferrite.

The stress-strain curves of Fe–12Mn–9Al–1.2C strips with 3% Ni and without Ni are plotted in Fig. 3. It is found that the addition of 3% Ni does not improve the ultimate tensile strength (UTS) or total elongation (TE) of as-cast Fe–12Mn–9Al–1.2C steel strip at room temperature. Instead, the tensile strength is slightly decreased.

Thermal Stability Analysis of Strips

Figure 4 shows the XRD patterns of the near-rapidly solidified Fe–12Mn–9Al–1.2C dual-phase lightweight steel strip with 3% Ni at different annealing

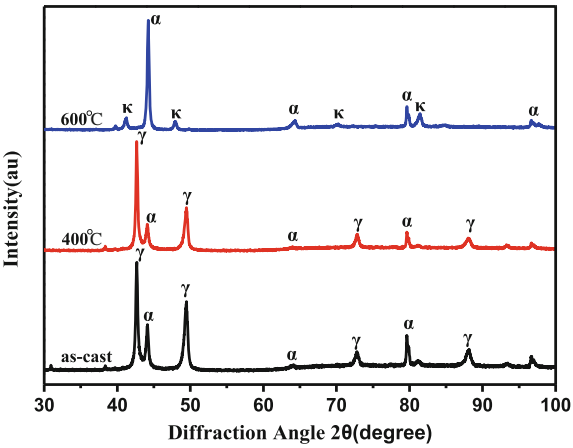

Fig. 4 XRD patterns of near-rapidly solidified Fe–12Mn–9Al–1.2C strips containing 3% Ni at the different annealing temperatures

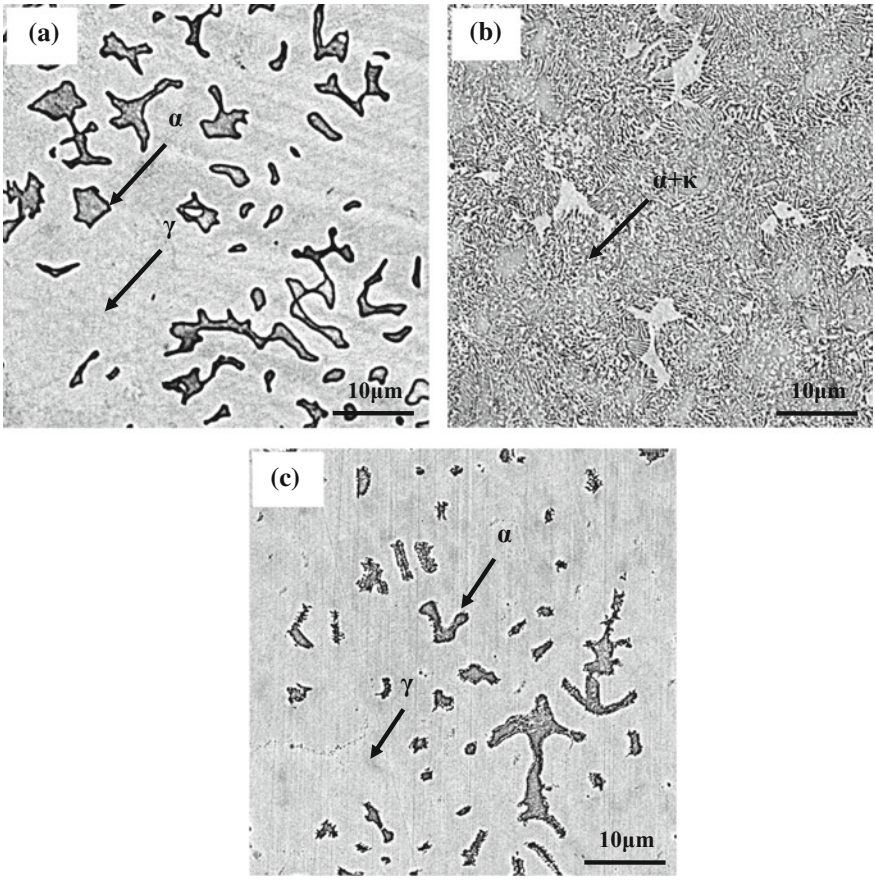

Fig. 5 SEM images of Fe–12Mn–9Al–1.2C. **a** With 3% Ni annealed at 400 °C; **b** with 3% Ni annealed at 600 °C; **c** without Ni annealed at 600 °C

temperatures. Compared with the as-cast strip, no evident changes in the diffraction peaks are observed after annealing at 400 °C. However, after annealing at 600 °C, the characteristic peaks from the austenite disappear, while the ferrite peaks significantly intensify and the peaks of κ-carbides appear, indicating that an eutectoid reaction austenite → ferrite + κ-carbide occurs. Compared with the as-cast strip, the dominant constituent phases of the steel strips are ferrite + κ-carbides, and ferrite content significantly increases to about 85.2 vol.% according to a quantitative analysis from XRD.

Figure 5 shows the SEM micrographs of the Fe–12Mn–9Al–1.2C strips with 3% Ni and without Ni after annealing. The structure of Fe–12Mn–9Al–1.2C with 3% Ni does not change clearly after annealing at 400 °C. The ferrite uniformly distributes in the austenitic matrix, which is similar to the as-cast OM photographs in Fig. 2a. Ferrite shape is slender, and its width is less than 5 μm which is slightly

narrower than that of as-cast strip according to the micrographs. Moreover the ferrite edge becomes round and smooth. However, after annealing at 600 °C, the constituent phases transform from ferrite + austenite to ferrite + κ-carbides, which is a typical eutectoid structure. It indicts that eutectoid reaction has occurred sufficiently. However, the structure of Fe–12Mn–9Al–1.2C strip without Ni after annealing at 600 °C is still composed of ferrite and austenite dual phases, which is similar to the structure of Fe–12Mn–9Al–1.2C with 3% Ni after annealing at 400 °C. It is evident that the addition of 3% Ni causes the occurrence of eutectoid reaction of metastable austenite at a lower annealing temperature.

It can be concluded that the addition of 3% Ni has a significant effect on the thermal stability of the phase in the near-rapidly solidified Fe–12Mn–9Al–1.2C strips. The addition of Ni facilitates the transition from metastable austenite into ferrite + κ-carbides at a lower anneal temperature; or in other words, it promotes the occurrence of eutectoid reaction. Zhu et al. [23] also found that addition of Ni had remarkable effect to the thermal stability of V-Ni microalloyed TRIP (Transformation-Induced Plasticity) steels.

Discussion

In order to understand the effect of 3% Ni on phase transition of Fe–12Mn–9Al–1.2C dual-phase lightweight steel prepared by near-rapid solidification, the phase transition process of this steel at 600–1600 °C was calculated by JMatPro software, as shown in Fig. 6.

From the phase transition shown in Fig. 6, it is found that the addition of 3% Ni does not influence the phase transition route of the Fe–12Mn–9Al–1.2C, as they are both the classical ferrite-austenite model, namely $L \rightarrow L + \delta \rightarrow L + \delta + \gamma \rightarrow \delta + \gamma \rightarrow \delta + \alpha + \gamma + \kappa \rightarrow \delta + \alpha + \kappa$. Below 600 °C, the stable phases of the Fe–12Mn–9Al–1.2C with 3% Ni and without Ni steel below 600 °C are ferrite

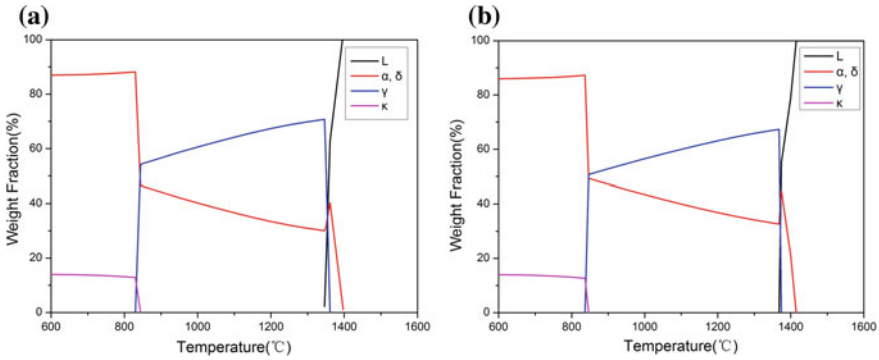

Fig. 6 Phase transitions of Fe–12Mn–9Al–1.2C steel strips: **a** with 3% Ni; **b** without Ni

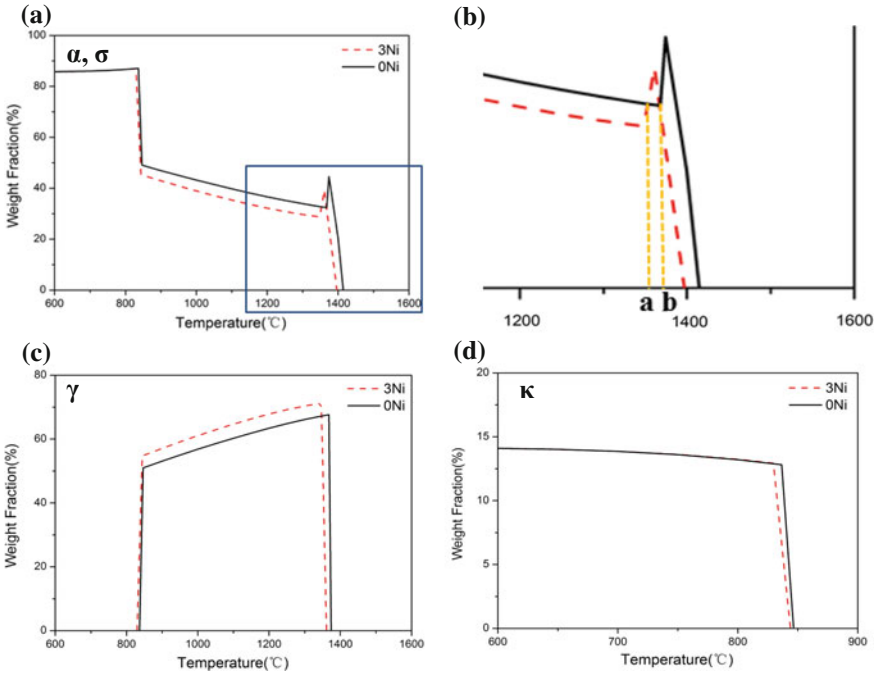

Fig. 7 Effect of 3% Ni on the phase fractions of Fe–12Mn–9Al–1.2C

and κ-carbides. In our experiment, the cooling rate of strips is very high which almost completely inhibits the occurrence of the eutectoid reaction. Therefore, the metastable austenite is retained finally at the room temperature.

To further analyze the phase transitions of Fe–12Mn–9Al–1.2C steel strips after addition of 3% Ni, the phase fraction is computed in the temperature range from 600 °C to 1600 °C, as shown in Fig. 7.

It is found that the addition of 3% Ni increases the austenite content in the temperature range from 830 to 1350 °C. In addition, both the appearance and disappearance (i.e. appearance of α + κ-carbides or eutectoid reaction) temperatures of austenite slightly decrease with the Ni addition, while the addition of 3% Ni decreases the ferrite content in the temperature range from 830 to 1350 °C. Therefore, the austenite does not exist in Fe–12Mn–9Al–1.2C steel either with 3% Ni or without Ni at room temperature, if the cooling rate is very slow.

Based on the above analysis, the content of the metastable austenite in the Fe–12Mn–9Al–1.2C strips with 3% Ni and without Ni should be related to the cooling rate, i.e. kinetics of phase transitions. In our experiments, the thin steel strips rapidly solidify in the copper mould with a cooling rate of about 10^3 K/s, which leads to a higher undercooling by near-rapid solidification. The resulted solidification temperature may stay in the temperature range of a and b, as indicated in the Fig. 7b.

In this temperature range, the amount of solidified ferrite in the sample with the addition of Ni is higher than that without Ni. Meanwhile, on the account of the fact that the cooling rate is so fast, the produced ferrite content still remains when the strip is rapidly cooled to room temperature. Therefore the ferrite content of the steel with 3 wt% Ni is slightly higher than that without Ni at room temperature.

In the present experiment, any new phase is not obtained after the addition of 3% Ni, and the constituent phases are still ferrite and metastable austenite at room temperature. The eutectoid reaction is suppressed because no κ-carbide is clearly found in Fe–12Mn–9Al–1.2C steel strips with 3% Ni or without Ni. Hence, the constituent phases achieved in Fe–12Mn–9Al–1.2C steel strips with 3% Ni or without Ni should be formed above the eutectoid reaction temperature. As shown in Fig. 7, it is known that the maximum content of austenite above eutectoid reaction temperature is about 70 wt% (or 69.44 vol.%), but the metastable austenite contents in both strips are more than 80 vol.%. More austenite is formed from liquid, due to the high cooling rate of the strips during the solid/liquid transition at the high temperature. Hence, although 3% Ni slightly increases the content of austenite (about 4.4 wt%) above the eutectoid reaction temperature, the content of metastable austenite mainly depends on the liquid/solid transition of each phase in the near-rapidly solidified strip. It can be concluded that not only the thermodynamics but also kinetics plays an important role in the formation of the constituent phases.

Conclusions

The present paper investigates the effect of Ni element on the structure and properties in Fe–12Mn–9Al–1.2C dual-phase lightweight steel strip prepared by a near-rapid solidification method. The experimental results show that the phases in the strip with addition of 3 wt% Ni consist of ferrite and metastable austenite. The ferrite is in an irregular granular morphology and randomly distributes in the austenite matrix. The same structure is observed in the reference strip without Ni element. However, although Ni is an austenite stabilizer, the addition of 3 wt% Ni causes a slight decrease in metastable austenite content. Moreover, the addition of 3 wt% Ni reduces the thermal stability of metastable austenite, as Ni element facilitates the occurrence of transition from metastable austenite to ferrite + κ-carbides at a lower annealing temperature. The related analysis suggests that the constituent phases of dual-phase steel strips prepared by near-rapid solidification condition depend on liquid/solid transition, which is controlled by not only the thermodynamics but also kinetics.

Acknowledgements This work was financially supported by the National Natural Science Foundation of China (No. 51574162) and Joint Fund of Iron and Steel Research (No. U1660103). The authors would like to express sincere thanks for the support staff at the Instrumental Analysis & Research Center at Shanghai University and the Center for Advanced Solidification Technology.

References

1. D.W. Suh, N.J. Kim, Low-density steels. Scr. Mater. **68**(6), 337–338 (2013)
2. J. Hirsch, Recent development in aluminium for automotive applications. Trans. Nonferrous Met. Soc. China **24**(7), 1995–2002 (2014)
3. L. Zhang, R. Song, C. Zhao et al., Work hardening behavior involving the substructural evolution of an austenite–ferrite Fe–Mn–Al–C steel. Mater. Sci. Eng., A **640**, 225–234 (2015)
4. Y. Sutou, N. Kamiya, R. Umino et al., High-strength Fe–20Mn–Al–C-based alloys with low density. ISIJ Int. **50**(6), 893–899 (2010)
5. I. Zuazo, B. Hallstedt, B. Lindahl et al., Low-density steels: complex metallurgy for automotive applications. JOM **66**(9), 1747–1758 (2014)
6. H. Kim, D.W. Suh, N.J. Kim, Fe–Al–Mn–C low-density structural alloys: a review on the microstructures and mechanical properties. Sci. Technol. Adv. Mater. **14**(1), 014205 (2013)
7. J. Krajnik, K. Wojciechowski, B. Perzyna et al., Tensile deformation of a low density Fe–27Mn–12Al–0.8C duplex steel in association with ordered phases at ambient temperature. Mater. Sci. Eng., A **586**(6), 276–283 (2013)
8. C.J. Wang, J.W. Lee, T.H. Twu, Corrosion behaviors of low carbon steel, SUS310 and Fe–Mn–Al alloy with hot-dipped aluminum coatings in NaCl-induced hot corrosion. Surf. Coat. Technol. **163–164**(02), 37–43 (2003)
9. W.J. Lu, X.F. Zhang, R.S. Qin, κ-carbide hardening in a low-density high-Al high-Mn multiphase steel. Mater. Lett. **138**, 96–99 (2015)
10. C.J. Wang, Y.C. Chang, NaCl-induced hot corrosion of Fe–Mn–Al–C alloys. Mater. Chem. Phys. **76**(2), 151–161 (2002)
11. C.F. Huang, K.L. Ou, C.S. Chen et al., Research of phase transformation on Fe–8.7Al–28.3Mn–1C–5.5Cr alloy. J. Alloy. Compd. **488**(1), 246–249 (2009)
12. L. Liu, C. Li, Y. Yang et al., A simple method to produce austenite-based low-density Fe–20Mn–9Al–0.75C steel by a near-rapid solidification process. Mater. Sci. Eng., A **679**, 282–291 (2016)
13. C.C. Wu, J.S. Chou, T.F. Liu, Phase transformation in an Fe-10.1Al-28.6Mn-0.46C alloy. Metall. Mater. Trans. A **22**(10), 2265–2276 (1991)
14. R. Rana, C. Liu, Effects of ceramic particles and composition on elastic modulus of low density steels for automotive applications. Can. Metall. Q. **53**(3), 300–316 (2014)
15. C.Y. Chao, C.H. Liu, Effects of Mn contents on the microstructure and mechanical properties of the Fe-10Al-xMn-1.0C alloy. Mater. Trans. **43**(10), 2635–2642 (2002)
16. Y.Y. Wang, X. Sun, Y.D. Wang et al., Effects of Mn content on the deformation behavior of Fe–Mn–Al–C TWIP steels—a computational study. J. Eng. Mater. Technol. **137**(2), 021001 (2015)
17. S.H. Kim, H. Kim, N.J. Kim, Brittle intermetallic compound makes ultrastrong low-density steel with large ductility. Nature **518**(7537), 77–79 (2015)
18. J.I. Kim, C.K. Syn, J.W. Morris, Microstructural sources of toughness in QLT-Treated 5.5Ni cryogenic steel. Metall. Trans. A **14**(1), 93–103 (1983)
19. B. Fultz, J.W. Morris, A Mössbauer spectrometry study of the mechanical transformation of precipitated austenite in 6Ni steel. Metall. Mater. Trans. A **16**(1), 173–177 (1985)
20. H.J. Kim, Y.H. Kim, J.W. Morris, Thermal mechanisms of grain and packet refinement in a lath martensitic steel. ISIJ Int. **38**(11), 1277–1285 (2007)
21. M. Niikura, J.W. Morris, Thermal processing of ferritic 5Mn steel for toughness at cryogenic temperatures. Metall. Trans. A **11**(9), 1531–1540 (1980)
22. S.W. Hwang, J.H. Ji, E.G. Lee, K.-T. Park, Tensile deformation of a duplex Fe–20Mn–9Al–0.6C steel having the reduced specific weight. Mater. Sci. Eng., A **528**(15), 5196–5203 (2011)
23. N. Zhu, Q. Wu, Y. He et al., Effect of Ni on the stability of retained austenite and mechanical properties for TRIP steels containing vanadium. Steel Res. Int. **85**(2), 143–154 (2013)

Constitutive Model of Wrought Superalloy GH4066 in Hot Deformation Process

Yanju Wang, Jiaying Jiang, Chonglin Jia, Xingwu Li and Yongjun Guan

Abstract To clarify the high temperature flow stress behavior and microstructures evolution of the wrought superalloy GH4066, the thermal simulation compression tests were conducted at the temperatures of 800, 900, 1000, 1100 and 1150 °C with the strain rate of 0.0003, 0.001, 0.01, 0.1, 1 and 10 s^{-1} on Gleeble-3800. The test results were used to construct the constitutive model of the superalloy based on the Arrhenius equation modified with the hyperbolic sine form. According to the test results, the dynamic recrystallization happened during the hot compression deformation process. The influence of temperature and strain rate on the dynamic recrystallization was analyzed in this paper, and the results were verified through the metallographic test. The comparison between the experimental and the predicted flow stress showed that the established constitutive model could well reflect the material properties of the superalloy.

Keywords Wrought superalloy · GH4066 · Hot deformation · Material model Dynamic recrystallization

Introduction

Superalloy turbine discs are the key hot end parts of the rotating components for an aircraft engine. As the demand of the aircraft engine with high performance, high reliability, long life and large scale, the performance of the turbine discs should bear higher work temperature and have more excellent mechanical properties [1–5]. The new nickel-based superalloy called GH4066 has been investigated as a potential

Y. Wang (✉) · C. Jia · X. Li · Y. Guan
Aviation Engine Corporation of China, Beijing Institute of Aeronautical Materials, Beijing 100095, China
e-mail: wyjbiam@163.com

J. Jiang
Department of Mechanical Engineering, Imperical College London, London SW7 2AZ, UK

© Springer Nature Singapore Pte Ltd. 2018

Y. Han (ed.), *Advances in Materials Processing*, Lecture Notes in Mechanical Engineering, https://doi.org/10.1007/978-981-13-0107-0_115

constructive material used for turbine discs. The characteristic of this material is very alike the American alloy Rene65, which is based on the optimization of Rene88DT alloy. The comprehensive performance of the new superalloy has reached a fairly high level of the powder metallurgy material so that it can meet the requirement of the hot working conditions of the engine. By aside, the casting process can be used to make large size turbine discs of this material, which will reduce the product cost and have great economic significance. Therefore, the new material GH4066 is expected to become the preferred material for the hot end rotating parts of the advanced aero engine [6–12].

As known, flow stress is a key factor to measure the permanent deformation resistance ability of the metal, which can determine the plastic deformation performance of the material. In metal-forming process, parameters as the temperature, strain rate and strain are all have relationships with the flow stress. In order to establish precise relationships among the three parameters and to investigate their influence on the flow stress and microstructure, tests are usually performed at different deformation conditions. In combination with the finite-element methods and these relationships, it make possible to know the metal forming process and optimize the process parameters [13–15]. At present, study on the hot deformation behavior of the new nickel-based superalloy GH4066 is very poor. In order to achieve the objective of getting the products with high quality and knowing the forming process, the most important step is to establish a constitutive equation describing the evolution of flow stress under specified conditions. However, It is a relatively complex task to establish constitutive equation of the material. Under hot deformation condition, flow stress is determined by the factors of work hardening and dynamic softening, including the dynamic recovery and dynamic recrystallization. In order to establish the constitutive model not only conforms to the micro-mechanism of metal deformation, but also can describe the flow stress of the macroscopic experiment, many scholars have done a lot of research work [16–18]. Based on the hot compression test of the GH4066 material, the hot deformation behavior under different deformation conditions has been studied, and the constitutive model of the material based on the Arrhenius equation has been established in this paper, that can provide the theoretical basis for optimizing the parameters of the deformation process.

Material and Experimental Procedures

First, a piece of vertical section disk was cut from an annealed and hot isostatic pressed GH4066 ingot. The typical chemical composition of the material is Ni–0.03C–16.0Cr–13.0Co–1.0Fe–3.7Ti–2.1Al–0.7Nb–4.0Mo–4.0W (mass fraction, %). A series of cylindrical specimens with the diameter of 8 mm and the hight of 12 mm, shown in Fig. 1, were sliced from the disk by an electrical discharge machine. The typical grain feature is shown in Fig. 2 and the initial grain size of the specimen is about 44.9 μm. The flow stress test was performed on a Gleeble-3800

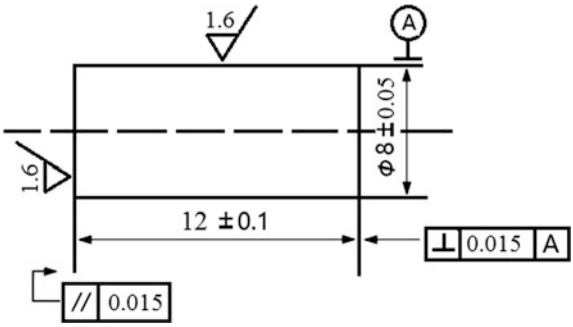

Fig. 1 The drawing of the sample size

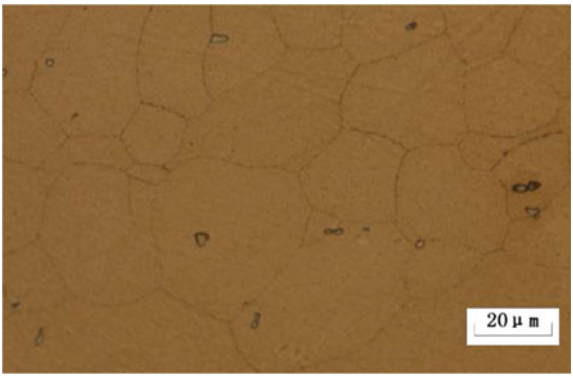

Fig. 2 Microstructure of the sample

system and the compression axial direction is along the axial of ingot. Both the ends of each specimen were mechanically polished and the graphite foil lubricant was employed for lubrication. The compression process was performed in the vacuum environment to prevent oxidation.

In order to ensure the homogenization of the original grain structure, the specimens were heated to 1200 °C at a heating rate of 20 °C/s at first, then two minutes holding and cooled to 800, 900, 1000, 1100, and 1150 °C respectively. The stress and strain values were measured at different deformation rates (0.0003, 0.001, 0.01, 0.1, 1, 10 s^{-1}, respectively) with a maximum deformation of 60%. The repeated tests were performed under similar condition, the height and diameter of the specimen before and after the test were recorded. After the test, the specimens were sectioned into two parts along the CA direction to observe the microstructure.

Results and Discussion

Figure 3 shows the measured true stress-strain curves of the wrought superalloy GH4066 under different deformation conditions. As the figure shown, the flow stress of the material is sensitive to both strain rate and deformation temperature. The flow stress value decreases significantly with the deformation temperature increasing, especially in the temperature range from 800 to 1000 °C, but it is not so obvious in the high temperature range from 1100 to 1150 °C. As the test results, the true stress increases significantly with the strain rate at the same deformation temperature. In the initial stage of the forming process, the stress abruptly increases due to the dominance of work hardening. With the increase in strain, the stress acquires steady-state due to the equilibrium established between work hardening and work softening.

The flow stress of the material is mainly related to the deformation temperature, strain rate and the extent of distortion. Known from the metallurgy theory, there are two typical thermal stress-strain curves in the process of hot deformation, the dynamic recovery and dynamic recrystallization. For the first type, the flow stress increases to a certain peak value, and then tends to be stable. And for the other, it increases to the peak value with the strain increasing but then decreased gradually to a steady state value. As the test result, the soften mechanism of GH4066 is dynamic recrystallization. It can be seen from Fig. 3 that there are three factors which can affect the dynamic recrystallization of the wrought superalloy, the deformation temperature, the deformation rate and the distortion extent. The higher

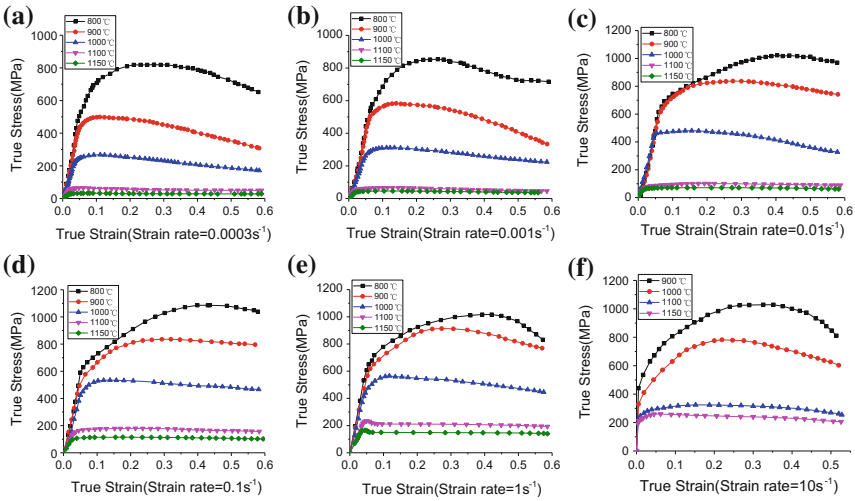

Fig. 3 True stress-strain curves under different deformation conditions, as **a** strain rate is 0.0003 s^{-1}, **b** strain rate is 0.001 s^{-1}, **c** strain rate is 0.01 s^{-1}, **d** strain rate is 0.1 s^{-1}, **e** strain rate is 1 s^{-1}, **f** strain rate is 10 S^{-1}

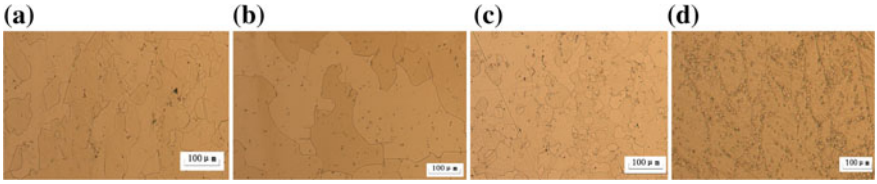

Fig. 4 Microstructure of the material under different deformation conditions, as **a** the deformation temperature is 800 °C and the strain rate is 1 s^{-1}; **b** it is 900 °C and 1 s^{-1}, **c** it is 1100 °C and 0.1 s^{-1}, **d** it is 1150 °C and 0.1 s^{-1}

the deformation temperature and the slower the deformation rate, the more prone to recrystallization, as there will be sufficient time for recrystallization. When the deformation strain reaches to a critical value, the dislocation density will reach to the critical value correspondingly and the dynamic recrystallization will occur. Figure 4 shows the microstructure of the material under different deformation conditions. In Fig. 4a, the deformation temperature is 800 °C and the strain rate is 1 s^{-1}. In Fig. 4b, it is 900 °C and 1 s^{-1}, and in Fig. 4c, it is 1100 °C and 0.1 s^{-1}. In Fig. 4d, it is 1150 °C and 0.1 s^{-1}. It can be seen that the grains of the material were grown up with the deformation temperature increasing from 800 to 900 °C when the strain rate is 1 s^{-1}. The grains were obviously refined as the strain rate decreases to 0.1 s^{-1} and the deformation temperature increases from 900 to 1100 °C. Therefore, the higher the deformation temperature and the lower the strain rate, the more likely to recrystallization. The recrystallized grains are mainly produced and grown up at the grain boundary when the deformation temperature increases to 1150 °C as the strain rate was 0.1 s^{-1}.

Constitutive Equation Modeling

Based on the true stress-strain data obtained by the thermal simulation test, the real peak stress data at the corresponding strain rate and temperature are used to establish the constitutive equation of the material. The comparative analysis between the real peak stress and steady stress under different deformation conditions is shown in Fig. 5. It is obvious that the peak stress value is decreased with the deformation temperature, and increased with the strain rate.

In hot deformation process, the relationship between the flow stress and the strain rate can be expressed as [19]:

$$\dot{\varepsilon} = f(\sigma)\exp[-Q/(RT)] \tag{1}$$

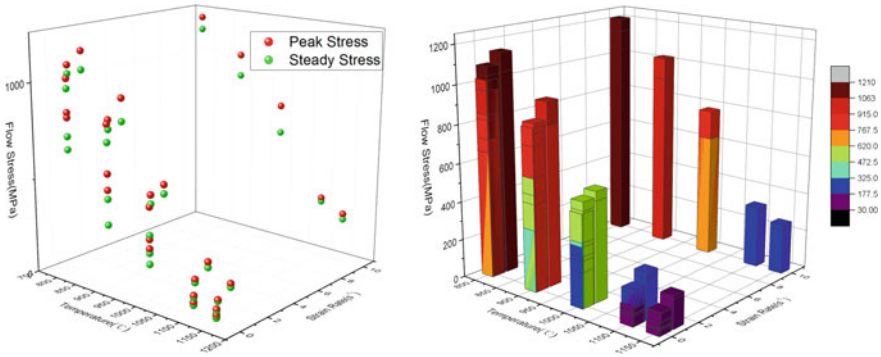

Fig. 5 Comparison between the real peak stress and steady stress under different deformation conditions

At low stress level:

$$f(\sigma) = A_1\sigma^{n1} \text{ If } \alpha\sigma < 0.8 \tag{2}$$

At high stress level:

$$f(\sigma) = A_2\exp(\beta\sigma) \text{ If } \alpha\sigma > 1.2 \tag{3}$$

where A_1, A_2, β are all temperature independent material constants, $\beta = \alpha n_1$;

SELLARS and TEGART suggested that the relationship between the flow stress and the strain rate can be expressed by the hyperbolic sine-modified Arrhenius equation at all stress levels, as shown in the following [20, 21]:

$$\dot{\varepsilon} = A[\sinh(\alpha\sigma)]^n \exp[-Q/(RT)] \tag{4}$$

where, $\dot{\varepsilon}$—strain rate/s^{-1}; Q—the heat activation energy, n/J/mol; σ—the flow stress/MPa; n—the stress exponent; α—the stress level factor, $\alpha = \beta/n$; T—the absolute temperature/K; R—the gas constant, R = 8.314 J/mol K; A—the structural factor; Q, A, n, α are all temperature independent material constants.

In a phenomenological approach, the flow stress is expressed in terms of the hyperbolic law in an Arrhenius-type equation, shown as the Eq. (5). The strain rate is controlled by the heat activation energy in hot deformation process, and the effect of temperature and strain rate on the deformation is represented by Zener and Hollomon by introducing the parameter Z [22].

$$Z = \dot{\varepsilon}\exp(Q/RT) = A[\sinh(\alpha\sigma)]^n \tag{5}$$

Based on the Arrhenius constitutive equation, the relationship between the undetermined coefficients and the equivalent strain is considered, that is, the

relationship between the parameters of Q, A, n, a and the equivalent strain is established to consider the equivalent strain versus flow stress impact.

Substituting Eq. (2) into Eq. (1), the Eq. (6) is obtained as following:

$$\dot{\varepsilon} = \mathrm{A}_1 \sigma^{\mathrm{n}_1} \exp[-Q/(RT)] \tag{6}$$

Take the logarithm for Eq. (6), the Eq. (7) is obtained shown as following:

$$\ln \dot{\varepsilon} = \ln A_1 + n_1 \ln \sigma - Q/(RT) \tag{7}$$

At the specified deformation temperature, T, R, Q, A_1 are all constants. Seeking partial alignment and finishing the Eq. (7), we get Eq. (8) as following:

$$\mathrm{n}_1 = \frac{\partial \ln \dot{\varepsilon}}{\partial \ln \sigma} \tag{8}$$

Substituting Eq. (3) into Eq. (1), Eq. (9) is obtained as following:

$$\dot{\varepsilon} = \mathrm{A}_2 \exp(\beta\sigma) \exp[-Q/(RT)] \tag{9}$$

At the specified deformation temperature, T, R, Q, A_2 are all constants. Seeking partial alignment and finishing the Eq. (9), we get Eq. (10) as following:

$$\beta = \frac{\partial \ln \dot{\varepsilon}}{\partial \sigma} = \alpha n_1 \tag{10}$$

The heat activation energy has relationship with the deformation ability of the material in hot deformation process. It is an important mechanical performance parameter that mainly related to the deformation temperature and strain rate. The dislocation slip ability is strengthened with the heat distortion temperature increasing. Sometimes, the dynamic recrystallization can occur since it can reduce the activation energy required for the material deformation. The dislocation density of the material will increase along with the deformation rate increasing, so that the sliding resistance of the movable dislocation will increase, thus the deformation energy of the material will be improved. The Z-H parameter method is used to calculate the activation energy Q in this paper.

Take the logarithm for Eq. (4), Eq. (11) is obtained as following:

$$\ln \dot{\varepsilon} = \ln A + n \ln[\sinh(\alpha\sigma)] - Q/(RT) \tag{11}$$

Subsequently, the substitution of the corresponding values in Fig. 5 into Eq. (11) gives the relationship between the flow stress and strain rate, as shown in Figs. 6, 7, 8 and 9. According to Eq. (11), when the strain rate is constant, $\ln[\sinh(\alpha\sigma)]$ and T^{-1} has a linear relationship and the slop is Q/(Rn), as shown in Fig. 8. When the temperature is constant, $\ln \dot{\varepsilon}$ and $\ln[\sinh(\alpha\sigma)]$ has a linear

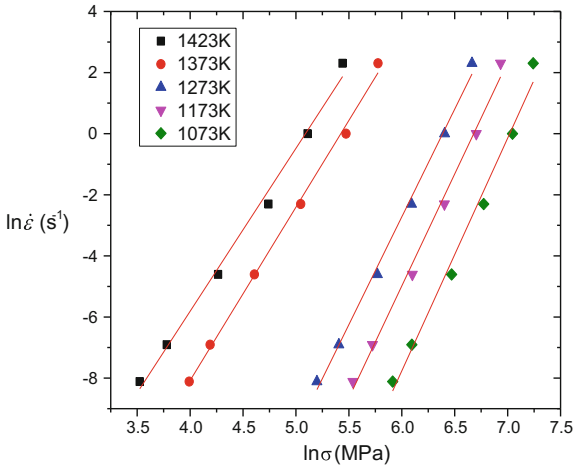

Fig. 6 Seeking for the slope of $(\ln\dot{\varepsilon} - \ln\sigma)$

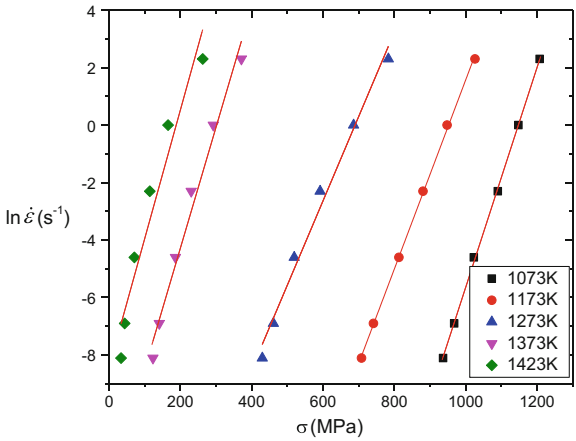

Fig. 7 Seeking for the slope of $(\ln\dot{\varepsilon} - \sigma)$

relationship and the slop is n, as shown in Fig. 9. Therefore, the heat activation energy Q can be calculated by Eq. (12).

$$Q = R\left\{\frac{\partial \ln[\sinh(\alpha\sigma)]}{\partial(1/T)}\right\}_{\dot{\varepsilon}}\left\{\frac{\partial \ln\dot{\varepsilon}}{\partial \ln[\sinh(\alpha\sigma)]}\right\}_{T} \tag{12}$$

According to Eqs. (8), (10), (12) and the Figs. 6, 7, 8 and 9, The value of n_1, β and n can be obtained from the slope of the linear fitting plots. The parameter Q can be obtained by the product of the slope $(\ln[\sinh(\alpha\sigma)] - (1/T))$ and $(\ln\dot{\varepsilon} - \ln[\sinh(\alpha\sigma)])$, as showing in Figs. 8 and 9.

According to Eq. (11), the Eq. (13) can be obtained, and the value of lnA can be calculated, the average value of A is evaluated as 9.90638E + 31 s^{-1}.

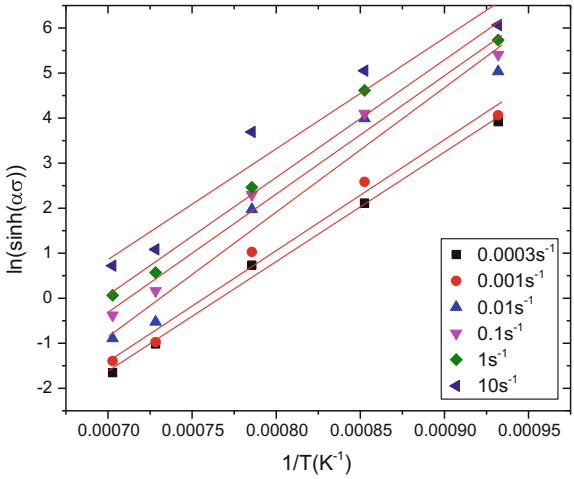

Fig. 8 Seeking for the slope of $(\ln[\sinh(\alpha\sigma)] - (1/T))$

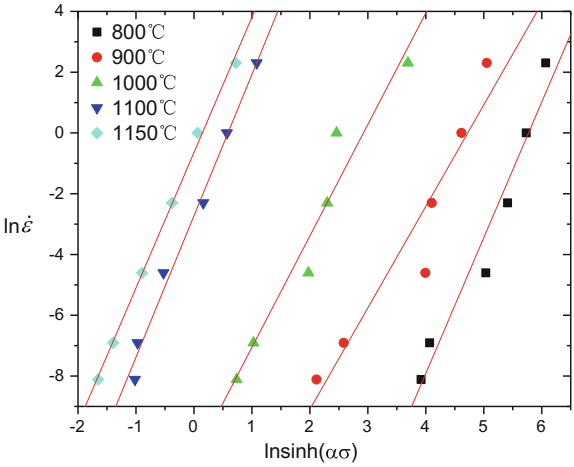

Fig. 9 Seeking for the slope of $(\ln\dot{\varepsilon} - \ln[\sinh(\alpha\sigma)])$

$$\ln A = \ln\dot{\varepsilon} + Q/(RT) - n\ln[\sinh(\alpha\sigma)] \tag{13}$$

Based on the above calculation results, the constitutive model of the material is established shown as the following equations:

$$\dot{\varepsilon} = 9.91 \times 10^{31}[\sinh(0.0056 \times \sigma)]^{4.1173}\exp(-105418.57/T) \tag{14}$$

$$Z = \dot{\varepsilon}\exp(876450/RT) \tag{15}$$

In order to predict the flow stress of the material in hot deformation process, the above model can be transformed into Eq. (16).

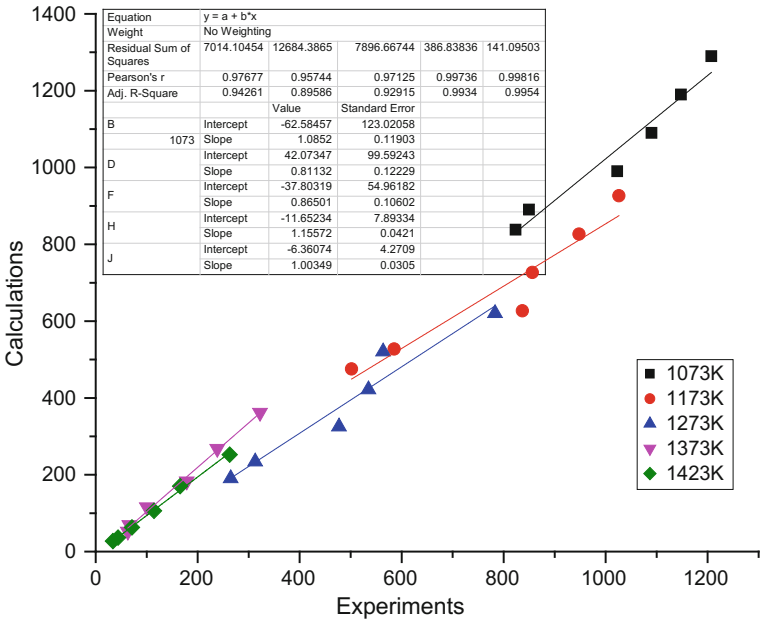

Fig. 10 Comparison between the experimental and calculated results

$$\begin{aligned}\sigma &= \frac{1}{\alpha}\ln\left\{\left(\frac{Z}{A}\right)^{1/n} + \left[\left(\frac{Z}{A}\right)^{2/n} + 1\right]^{1/2}\right\} \\ &= 178.57 \times \ln\left\{\left(\frac{Z}{9.91 \times 10^{31}}\right)^{0.243} + \left[\left(\frac{Z}{9.91 \times 10^{31}}\right)^{0.486} + 1\right]^{\frac{1}{2}}\right\}\end{aligned} \tag{16}$$

The stress values at different strain rates and temperature can be calculated according to Eqs. (15) and (16). Figure 10 shows the comparison between the experiment value and the calculated results by this model. The slops of (calculation values–experimental values) are all near 1 under different deformation conditions. The mean error of the stress value prediction for the flow stress of the material is −7.5%. Therefore, the model can be used to describe the constitutive characteristics of the material.

Summary

(1) During the hot deformation process the Flow stress of the wrought superalloy GH4066 increases with the strain rate and decreases with the deformation temperature. And this is quite obviously in the lower deformation temperature

range. During the hot deformation process the dynamic recrystallization occurs. The lower the rate of the deformation is, the more easily to recrystallize.

(2) Based on the Arrhenius hyperbolic sine equation and the thermal simulation test data, the constitutive equation of the material is established, and the basic parameters and the heat activation energy in the equation are obtained by fitting the experimental data.

(3) Error analysis shows that the constitutive model of GH4066 is in good agreement with the experimental results and can be used to describe the constitutive relation of this material.

Acknowledgements This work is sponsored by the Aviation Engine Corporation of China, Beijing Institute of Aeronautical Materials. Donation of follow-on batches of specimens by BIAM and the Test by Mechanical Engineering Department of Imperial College London is gratefully acknowledged.

References

1. J.C. Williams, E.A. Starke, Acta Mater. **51**, 5775 (2003)
2. R.F. Decker, JOM **58**(9), 32 (2006)
3. C.T. Sims, N.S. Stoloff, W.C. Hagel, *Superalloys II-High Temperature Materials for Aerospace and Industrial Power* (wiley, New York, 1987), p. 32
4. C.X. Shi, Z.Y. Zhong, Acta Metall. Sin. **33**, 1 (1997)
5. M.J. Donachie, S.J. Donachie, *Superalloys: A Technical Guide* (ASM International, Ohio, 2002), p. 120
6. B.J. Zhang, G.P. Zhao, Acta Metall. Sin. **51**, 10 (2015)
7. J.L.W. Carter, M.W. Kuper, M.D. Uchic, M.J. Mills, Mater. Sci. Eng. **A605**, 127 (2014)
8. J. Tiley, G.B. Viswanathan, R. Srinivasan, R. Banerjee, D.M. Dimiduk, H.L. Fraser, Acta Mater. **57**, 2538 (2009)
9. R. Radis, M. Schaffer, M. Albu, G. Kothleitner, P. Polt, E. Kozeschnik, Acta Mater. **57**, 5739 (2009)
10. J. MacSleyne, M.D. Uchic, J.P. Simmons, M.D. Graef, Acta Mater. **57**, 6251 (2009)
11. K.O. Findley, A. Saxena, Metall. Mater. Trans. **37A**, 1469 (2005)
12. R.C. Reed, *The Superalloys: Fundamentals and Applications* (Cambridge University Press, Cambridge, 2006), p. 236
13. Z.Y Zhao, *Metal Plastic Deformation and Rolling Theory* (Metallurgical Industry Press, Beijing, 1980)
14. H.T. Yang, S.Y. Wang, H.Q. Li et al., J. Plast. Eng. **12**(6), 38 (2015)
15. H. Takuda, T. Morishita, T. Kinoshita, J. Mater. Process. Technol. **164–165**, 1258 (2005)
16. Y.C. Lin, D.X. Wen, Y.C. Huang et al., A unified physically based constitutive model for describing strain hardening effect and dynamic recovery behavior of a Ni-based superalloy. J. Mater. Res. **30**(24), 3784–3794 (2015)
17. M. Yaguchi, M. Yamamoto, T. Ogata, A viscoplastic constitutive model for nickel-base superalloy, part 1: kinematic hardening rule of anisotropic dynamic recovery. Int. J. Plast. **18** (8), 1083–1109 (2002)
18. L.L. Bao, J.X. Dong, S.Q. Zhao et al., Structure and mechanical properties of a new high structure stability nickel-based superalloy. Rare Metal Mater. Eng. **34**, 54–57 (2005)
19. Y.C. Lin, D.X. Wen, J. Deng et al., Constitutive models for high-temperature flow behaviors of a Ni-based superalloy. Mater. Des. **59**(9), 115–123 (2014)

20. C.M. Sellars, W.J. Mctegart, On the mechanism of hot deformation. Acta Metall. **14**(9), 1136–1138 (1966)
21. G.A. Nourollahi, M. Farahani, A. Babakhani et al., Compressive deformation behavior modeling of AZ31 magnesium alloy at elevated temperature considering the strain effect. Mater. Res. **16**(6), 1309–1314 (2013)
22. Y.C. Lin, M.S. Chen, J. Zhong, Effect of temperature and strain rate on the compressive deformation behavior of 42CrMo steel. J. Mater. Process. Technol. **205**(1–3), 308–315 (2008)

Gradient Speed Control Method to Reduce the Residual Stress on a Turbine Disk in Forging Process

Yanju Wang, Jiaying Jiang, Yong Zhang, Yongjun Guan and Xingwu Li

Abstract The distribution of the residual stress on the turbine disk is affected by the forging process. The residual stress will reduce fatigue life of the turbine disk and increase the assemble error to meet the production. And the process parameters such as forging speed, forging temperature and friction will all affect the residual stress. In order to reduce the residual stress and improve the service life of the turbine disk, the relationship between the forging speed and residual stress on the turbine disk in the forging process was studied in this paper. By the combination of numerical simulation method and the forging process test, the numerical model of the forging process for the superalloy turbine disk was established, and the relationship between the residual stress distribution and forging speed was analyzed and calculated. Based on this, a gradient speed control method for reducing residual stress of the turbine disk was proposed. The calculation results showed that the gradient speed controlling in the forging process of the turbine disk effectively reduced the residual stress, decreased the usage and fee of the energy, and improved the service life of the turbine disk. According to the geometrical characteristics of the turbine disk, the gradient forging speed range was designed and optimized in this research. The results show that the residual stress of the turbine disk can be greatly reduced by the optimized gradient speed control method, which is a feasible way to reduce the residual stress of the superalloy turbine disks in the forging process.

Keywords Gradient speed control · Turbine disk · Residual stress Forging process · Deformation

Y. Wang (✉) · Y. Zhang · Y. Guan · X. Li
Aviation Engine Corporation of China, Beijing Instititute of Aeronautical Materials, Beijing 100095, China
e-mail: wyjbiam@163.com

J. Jiang
Department of Mechanical Engineering, Imperical College London, London SW7 2AZ, UK

© Springer Nature Singapore Pte Ltd. 2018

Y. Han (ed.), *Advances in Materials Processing*, Lecture Notes in Mechanical Engineering, https://doi.org/10.1007/978-981-13-0107-0_116

Introduction

For the commercial engine, the safety, reliability and durability requirements are significantly higher than the military aircraft, and these properties are mainly dependent on the core components as turbine disks and blades, so it is quite necessary to use advanced materials and strict manufacturing process to prepare the above key parts. Turbine discs are the key hot end components in the engine which service in abominable environment with high temperatures, high pressures, and withstand complex alternating loads [1–3]. IN718 alloy (GH4169 in domestic) is a niobium and molybdenum precipitation hardening nickel-based superalloy. At 650 °C and below, this material has good performance with high strength, good fatigue properties and high temperature creep and oxidation resistance, so it has been commonly used to manufacture the engine sealing discs and turbine disks. In foreign, the usage of IN718 superalloy accounted for about 30–50% of the total on the advanced aircraft engine, while 50% of the turbine disks on verification engine was made by IN718 alloy [4, 5]. In the manufacturing process for IN718 alloy turbine disks, the internal temperature distribution or the deformation are both non-uniform, so there will be residual stress on the turbine disks, which will reduce the fatigue properties of the components, and even lead to deformation defect. That will have a significant impact on the safety, reliability, durability and service life of the commercial aviation engine [6–8]. Therefore, it is very important to study the method of reducing the residual stress and get effective measures to improve the service life of IN718 alloy turbine disk.

In this paper, the residual stress on IN718 turbine discs was analyzed through the numerical simulation method. The stress, strain and thermal field distribution on the turbine disks were analyzed based on the flow behavior of the material in the forging process. By the calculation, some important information as the distribution of the internal heat or stress parameters on the disks, the load-stroke/energy-stroke relationships, the mold stress and etc. were all obtained. Otherwise, the whole residual stress distribution, and the strain distribution of each stage during the forging process were obtained. Based on this, the gradient speed control method is proposed to optimize the forging parameters and reduce the residual stress. That will be a reference for setting the residual stress test standard and the reduction control law.

Simulation of the Forging Process for the Turbine Disks

Figure 1 shows the sectional drawing of the turbine disc and the 3D model of the forging dies. As shown in Fig. 1a below, the diameter of the turbine disk is 311 mm. Taking all those factors into consideration as the forming dimension, the geometric characteristics and volume of the turbine disk, the geometrical characteristics of the upper and lower forging dies are designed, as shown in Fig.1b.

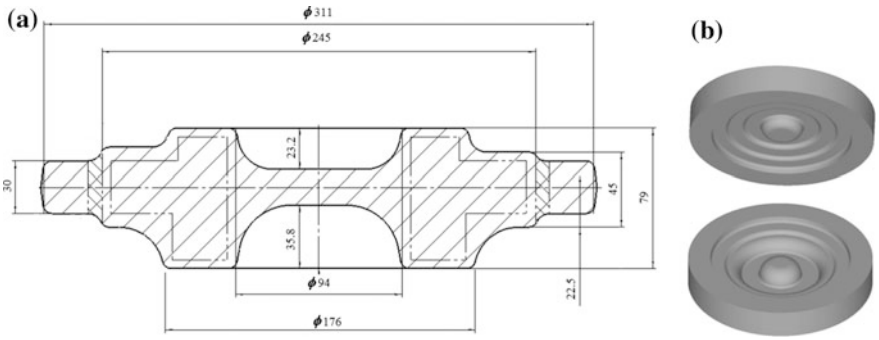

Fig. 1 Sectional drawing of the turbine disc and the 3D model of the forging dies

The numerical simulation of the forging process was carried out in Deform2D since the center symmetrical geometric character of the forging mold and turbine disk. Therefore, one half of the turbine disk and the forging die were selected for the analysis. The initial blank of the turbine disk is a cylindrical one with the initial isothermal forging temperature 1010 °C, and the initial mold temperature is 930 °C, special lubricants is used between the mold and the blank. By geometric model creation and meshing, the numerical geometric model was established. In assemble processing, the blank material was settled as a plastic body, while the mold is rigid, they were contacted by definition in the model. As shown in Fig. 2, the blank adopts 8920 quadrilateral surface elements, and the grid re-division and adaptive features were defined for those meshes. In the material character definition, the turbine plate is selected as IN718, and its thermal conductivity, thermal diffusivity, specific heat capacity, linear expansion coefficient, elasticity, oxidation rate and other related parameters were all defined. In the model; the heat exchange and movement boundary conditions were all set according to the real forging process parameters. As a result, the distribution characteristics of the residual stress on the turbine disk under different forging speed conditions could be calculated by this numerical simulation model.

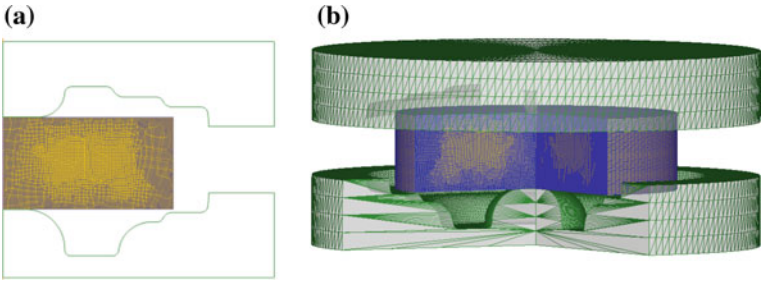

Fig. 2 Geometric model and meshing for the turbine disk

Forging Process Analysis

Figure 3 shows the distribution of the residual stress on the blank during the hot forging process as the forging speed is set to a constant with 0.5 mm/s. Obviously, the residual stress value on the turbine blank was increasing with the deformation, especially in the area where the blank is in contact with the mold because of friction and the area in the mold cavity with larger curvature. The existence of residual stress will affect the dimensional stability, the fatigue resistance, the stress corrosion resistance and the static mechanical properties of the turbine disk. Therefore, it is necessary to control the residual stress by the optimization of the manufacturing process parameters.

Figure 4 shows the distribution of the residual stress on the blank after the forging process as the forging speed is 0.5 mm/s. As a result, the distribution of the residual stress is relatively uniform on the turbine disk except for the contact area between the blank and dies.

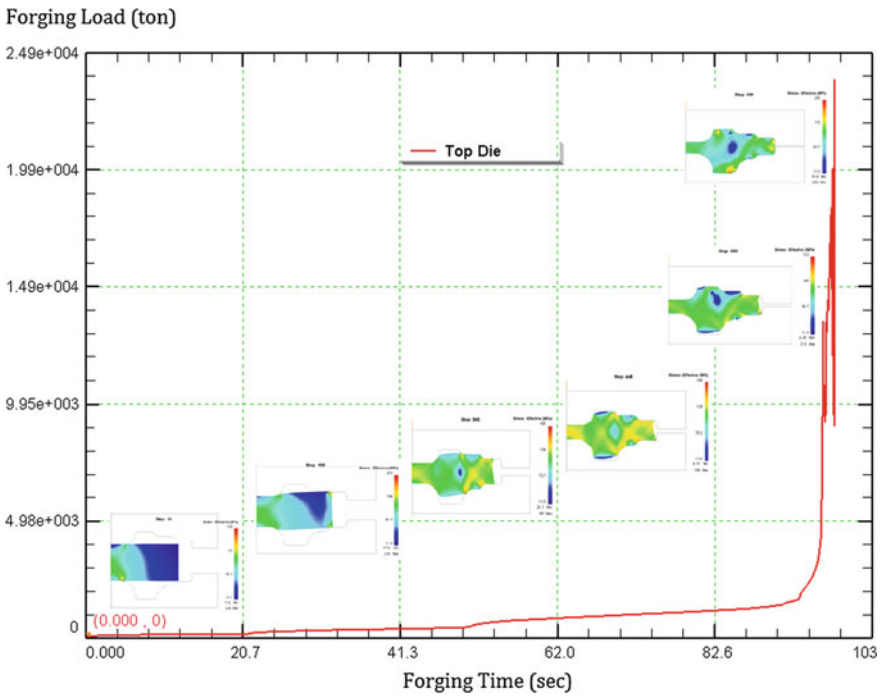

Fig. 3 Distribution of the residual stress on the blank during the hot forging process (forging speed is 0.5 mm/s)

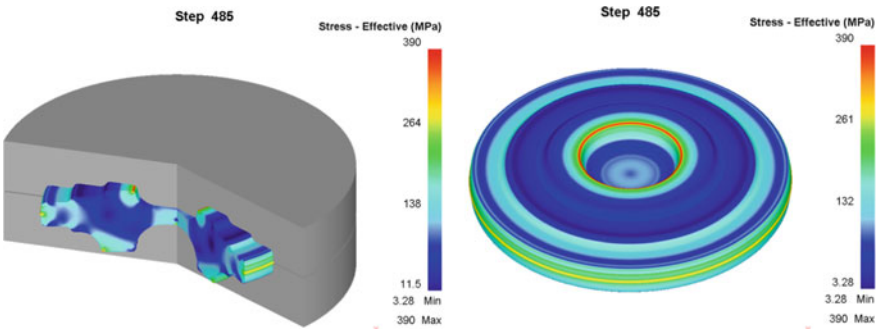

Fig. 4 Distribution of the residual stress on the blank after the forging process

Relationship Between the Gradient Velocity and Residual Stress

As known for a metal forming process, the strain, strain rate and temperature are the main factors to effect the flow stress [9, 10]. And in the forging process, the strain rate will be changed along with the forging speed, so as the residual stress distribution on the turbine disk. Figure 5 shows the residual stress distribution on the turbine disk as the forging speed is 0.5 mm/s and 1 mm/s especially when the forging process is finished. At the same forging time step, the residual stress distribution is quite different along with the forging speeds. By increasing the forging speed, the strain rate was improved in the deformation process, which can accelerate the production of dynamic softening of the material, therefore, the residual stress value on the turbine disk was significantly reduced at the end of the forging process. Otherwise, the forging load was increased from 24,000 to 32,000 ton along with the forging speed increasing. For the intention of reducing the residual stress

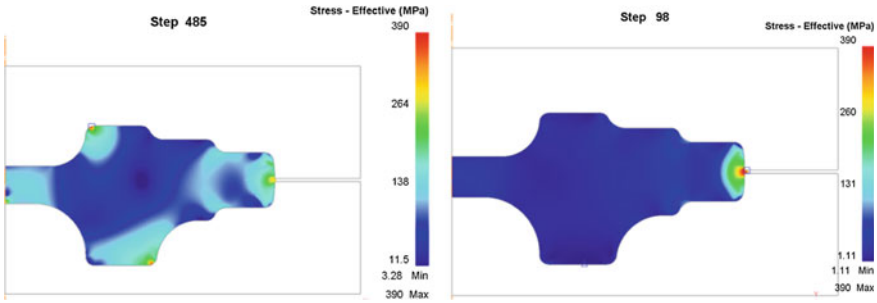

(a) 0.5mm/s (b) 1mm/s

Fig. 5 Residual stress distribution on the turbine disk with different forging speed (0.5 and 1 mm/s)

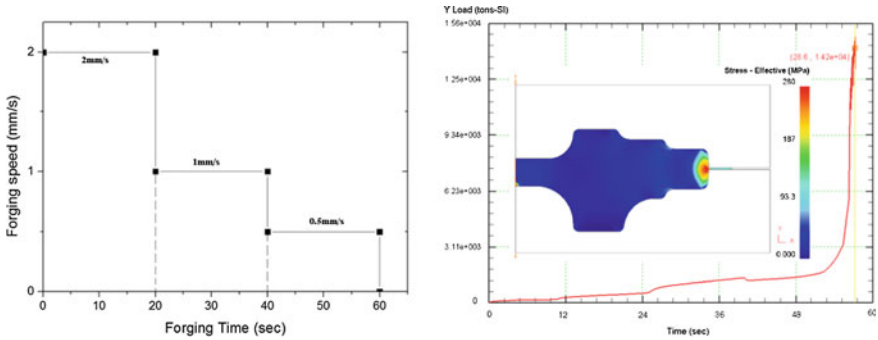

(a) The Gradient Speed (b) Residual Stress on the disk

Fig. 6 Calculation and analysis of gradient speed and residual stress

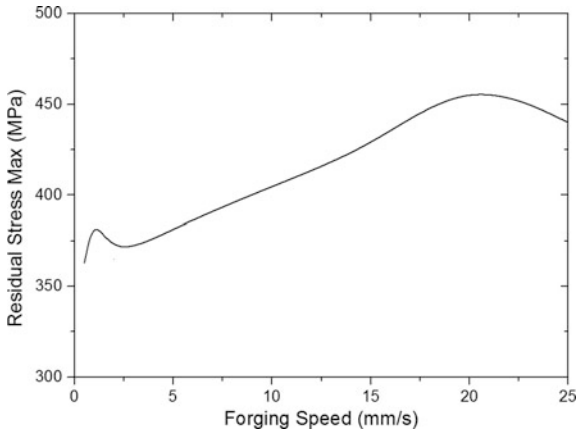

Fig. 7 Relationship between the forging speed and the maximum value of residual stress

but not making the forging load increased dramatically, a gradient velocity control method was presented in this paper.

Figure 6a shows the gradient forging speed of the turbine disk during the forging process. Figure 6b shows the final residual stress distribution on the turbine disk after the forging process with this gradient forging speed Fig. 6a. By comparing with Fig. 5, the maximum residual stress value is reduced by 28.2%, and the maximum load value is reduced by more than 50%. The relationship between the forging speed and the maximum value of the residual stress is shown in Fig. 7. As a result, the optimal gradient forging velocity is given as: [0, 20 s] 2 mm/s, [20, 40 s] 1 mm/s, [40, 60 s] 0.5 mm/s. And this conclusion will be further confirmed by designing a process test.

Summary

The forging process parameters of the turbine disk will directly affect the distribution of the residual stress on the turbine disk. One of the most important influencing factors is the forging speed. The numerical simulation method can be used to analyze the distribution of the residual stress on the turbine disks with different forging speeds. As a result, the influence relationship between the residual stress and forging speed can be concluded. Based on this, the gradient velocity control method is proposed to reduce the residual stress, and the optimal interval of the forging speed is given by this research.

References

1. H. Feng, *Study on the Durability of Critical Parts of Aviation Turbine Engine* (Harbin Engineering University, 2015)
2. R.C. Benn, J.M. Davidson, K.R. Andryszak, Turbine blade superalloy I (1987)
3. S. Farahany, M. Aghaie-Khafri, A. Ourdjini et al., Influence of heat treatment on properties of hot isostatically pressed turbine blade superalloy IN738. Adv. Mater. Res. **264–265**, 502–507 (2011)
4. H.Y. Zhang, S.H. Zhang, Z.X. Li et al., Hot die forging process optimization of superalloy IN718 turbine disc using processing map and finite element method. Proc. Inst. Mech. Eng. Part B J. Eng. Manuf. **224**(1), 103–110 (2010)
5. N. Nayan, N.P. Gurao, S.V.S.N. Murty et al., Microstructure and micro-texture evolution during large strain deformation of Inconel alloy IN718. Mater. Charact. **110**, 236–241 (2015)
6. L.F. Zhao, L.I. Xing-Dong, L.I. Hui et al., Measurement of residual stress of nickel-base directionally crystallized superalloy blade in gas turbines. Therm. Turbine (2016)
7. M.N. James, D.G. Hattingh, D. Asquith et al., Applications of residual stress in combatting fatigue and fracture. Procedia Struct. Integrity **2**, 11–25 (2016)
8. A.G. Youtsos, *Residual Stress and its Effects on Fatigue and Fracture* (Springer, Netherlands, 2006)
9. Y. Liu, Y. Ning, X. Yang et al., Effect of temperature and strain rate on the workability of FGH4096 superalloy in hot deformation. Mater. Des. **95**, 669–676 (2016)
10. Y. Liu, Z. Yin, J. Luo et al., The constitutive relationship and processing map of hot deformation in A100 steel. High Temp. Mater. Process. (London) **35**(4), 399–405 (2016)

Microstructure Evolution in Solidified Al–Si Hypereutectic Alloys Under the Impact of an Electric Current Pulse

Yunhu Zhang, ZhiShuai Xu, Honggang Zhong, Chen Xiangru, Changjiang Song and Qijie Zhai

Abstract Investigating the structure evolution of silicon phase in Al–Si alloys in the extra energy field is of high importance to understand and control the growth behavior of faceting phases. The present paper focuses on the influence of an electric current pulse (ECP) on the structure of directionally solidified Al–20.5 wt% Si hypereutectic alloy. Experimental results showed that ECP had a great impact on the structures of silicon phase. The interconnected, porous primary silicon structure was observed in the initial growth period, accompanied by a small quantity of eutectic silicon directly growing from the primary silicon. In the following growth period, it was surprisingly found that the numerous complex regular silicon and eutectic silicon structures appear instead of the primary silicon. On the other hand, the reference sample without ECP showeds that the structures were composed of several coarse plate-like primary silicon and eutectic structures. The variation of silicon structures indicated that the solidification behavior of faceting phases was remarkably modified by ECP, which may be due to the forced melt flow generated by the electromagnetic force.

Y. Zhang (✉) · Z. Xu · H. Zhong · C. Xiangru · C. Song · Q. Zhai
State Key Laboratory of Advanced Special Steel, Shanghai Key Laboratory of Advanced Ferrometallurgy, School of Materials Science and Engineering, Shanghai University, Shanghai 200072, China
e-mail: zhangyunhu.zyh@163.com

Z. Xu
e-mail: xzsshu@163.com

H. Zhong
e-mail: hgzhong@shu.edu.cn

C. Xiangru
e-mail: cxr16@shu.edu.cn

C. Song
e-mail: riversxiao@shu.edu.cn

Q. Zhai
e-mail: qjzhai@shu.edu.cn

© Springer Nature Singapore Pte Ltd. 2018

Y. Han (ed.), *Advances in Materials Processing*, Lecture Notes in Mechanical Engineering, https://doi.org/10.1007/978-981-13-0107-0_117

Keywords Al–Si alloy · Structure evolution · Solidification · Electric current pulse

Introduction

Al alloys are widely utilized in the automotive and aerospace industries [1–3]. As one of the most important cast Al alloys, Al–Si alloys have been intensively investigated owing to the high strength over weight ratio, high fatigue strength, good wear resistance, low thermal expansion, good castability and machinability [4]. Therefore, great efforts have been performed to modify the structure of silicon phase in Al–Si alloys [5–8].

In recent decades, the interest in applying electric current pulse (ECP) in the solidification process of alloys is dramatically increasing because the remarkable grain refinement is achieved in the solidified alloys [9–14]. Meanwhile, it is found that the microstructure morphology can be largely modified by ECP [12–16]. In particular, it has been recognized that ECP has the capability to modify the morphology of silicon phase in the Al–Si alloys [13, 14].

Since the solidification experiments with ECP are usually carried out in the traditionally casting mold, the growth behavior of alloys is really difficult to understand due to the complex solidification process. Hence, the directional solidification is used because of the controllable temperature gradient and growth velocity [17–22]. However, it is unfortunate that most of those studies focus on the growth of non-faceting phases. The knowledge about the faceting phase (silicon) growth in electric field remains insufficient and fragmentary. The present paper is devote to showing the structure evolution of silicon phase in directionally solidified Al–Si hypereutectic alloy to gain more insights into the growth behavior of faceting phase under the application of ECP.

Experimental

The Al–20.5 wt%Si hypereutectic alloy (nominal composition) was prepared by melting pure Al (99.9 wt%) and Si (99.9 wt%). The molten alloy was filled into an Ø4 mm quartz tube and cooled in ambient air. Then, the preparatory sample was put into an alumina crucible (420 mm in length and 4 mm in inner-diameter), and placed in a Bridgman furnace. After that, the furnace was heated up to 1173 K, and then held 20 min to completely remelt the sample. In the final step, the tube was pulled downwards at a speed of 4 μm/s. Meanwhile, a damping electric current pulse is initiated. The applied electric current intensity, frequency and pulse length were 400 A, 200 Hz and 0.5 ms, namely. Details of the experimental setup and the waveform of ECP were described in references [22].

Directionally solidified samples were cut along the longitudinal and transverse sections for metallographic examination. Selected sections were ground on the SiC paper and then polished from 6 to 1 μm gradually. The as-polished samples were directly examined using optical microscopy. Additionally, scanning electron microscopy (SEM) was used to characterize structures of the samples. The specimens for SEM examination were etched by 20 wt% NaOH solution for 2 min at 80°C. The area percentage of the primary Si and the complex regular structure (CRS) were measured by using the software package ANALYSIS FIVE (Olympus Europe, Hamburg).

Results and Discussion

Primary Silicon Structure

Figure 1 displays the solidified structure in the longitudinal section of samples solidified at the growth length of 1, 2 and 4 cm, respectively. As shown in Fig. 1a, the reference sample without the application of ECP presents several really coarse, isolated, plate-like primary silicon structures at both of the growth length of 1, 2 and 4 cm. On the other hand, the application of ECP generates a significant modification of the primary silicon structure. Figure 1b presents an interconnected, porous primary silicon structure at the growth length of 1 cm. However, only a small quantity of sporadic primary silicon is observed in sections of sample solidified at the growth length of 2 and 4 cm.

The area rate of primary silicon in the transversal sections of samples with and without applied ECP is listed in Table 1. The quantity of primary silicon in sample without ECP keeps the same scale of 30% at both of growth length 1, 2 and 4 cm. On the other hand, it is surprisingly found that the area rate of primary silicon in sample at the growth length of 1 cm is as high as 82.6% under the influence of ECP. Conversely, only the area rate of 0.7 and 2.1% are observed at the growth length of 2 and 4 cm, respectively.

The growth mechanism of the coarse, plate-like primary silicon is classified as the twin plane re-entrant angle growth (TPRE) [6], which is controlled by the solute diffusion in the melt. The formation of the interconnected, porous primary silicon indicates that the continuous growth may be initiated in the sample with ECP. It has been proved that a strong fluid flow is generated by ECP on account of the concentrated electromagnetic force beneath the electrodes [23]. In here considered configuration, the primary silicon phase are firstly participated in the mushy zone, leading to a non-homogeneous distribution of electric currents as well as the concentration of electromagnetic force, consequently generating a forced flow [24].

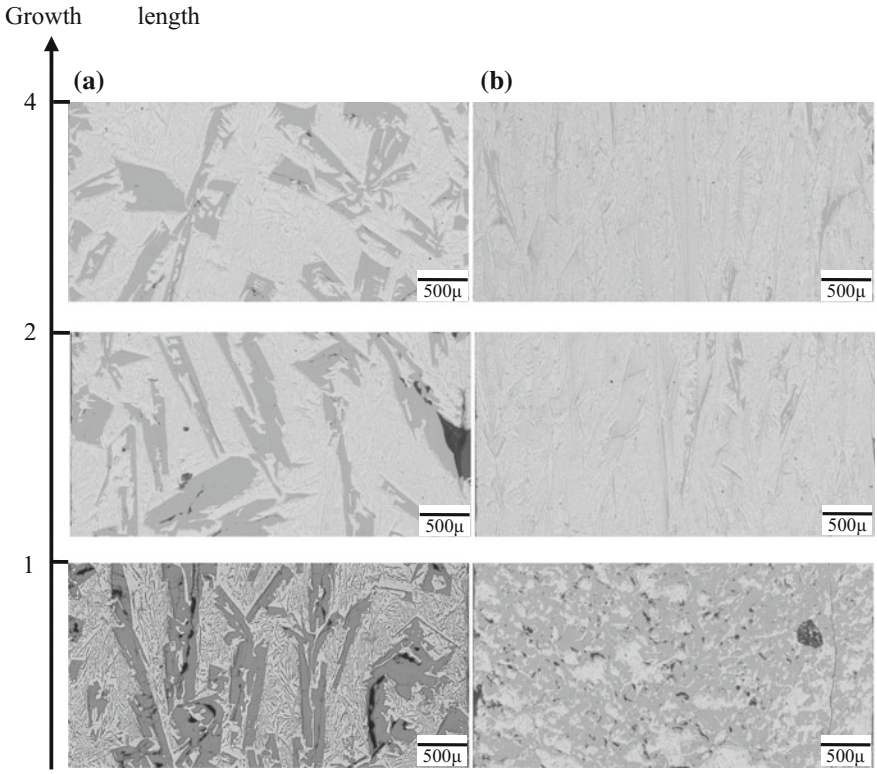

Fig. 1 Solidified structure in longitudinal section of Al–20.5 wt%Si alloy along the growth direction: **a** without ECP, **b** with ECP

Table 1 Area percentage of the primary silicon (A_{QS}) and CRS (A_{CRS}) in the transversal section (%)

	Without ECP			With ECP		
	1 cm	2 cm	4 cm	1 cm	2 cm	4 cm
A_{QS}	35.1	35.7	25.8	82.6	0.7	2.1
A_{CRS}	–	–	0.4	–	9.9	9.2

The depletion zone (Al-rich) surrounding the primary silicon can be replaced efficiently by the Si-rich melt to promote the growth of primary silicon under the influence of forced flow. Furthermore, it means that the growth behavior of primary silicon may be changed from TPRE to the continuous growth due to the sufficient support of the solute.

Eutectic Silicon and Complex Regular Structure

Figure 2 displays the transversal microstructures of the samples at the growth length of 1, 2 and 4 cm, respectively. The reference microstructure in the sample without ECP at the growth length of 1 cm is shown in Fig. 2a. It is observed that a large number of fine flake eutectic Si enwrap the coarse primary silicon. However, in the sample with ECP shown in Fig. 2d, the growth of eutectic is almost completely suppressed. Only sporadic, short flake eutectic silicon directly grows from the primary silicon. Subsequently, as the growth length increasing, the microstructure in the sample without ECP at the growth length of 2 and 4 cm (see Figs. 2b, c) keeps the same tendency in comparison with the structure at 1 cm (see Fig. 2a). As for the sample with ECP, the complex regular structure (CRS) is observed surprisingly, mixing with a significant number of flake eutectic silicon at the growth length of 2 and 4 cm (see Figs. 2e, f). The single CRS is comprised of a spine and regularly distributed lamellae, as shown in Fig. 3. As a result of the peculiar structure, the hardness in CRS is at least 30% higher than the eutectic structure [25]. The measured area percentage of CRS is above 9% (see Table 1), which is even higher than that in Al–Si eutectic alloy at the same growth velocity of 4 μm/s [22].

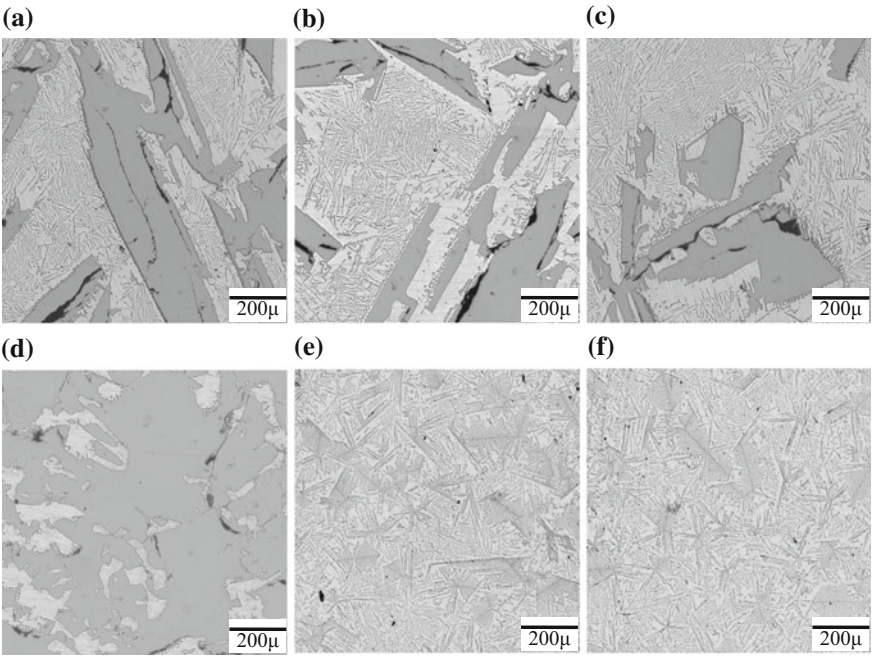

Fig. 2 Transversal microstructures of Al–20.5 wt%Si alloy under the influence of ECP: without ECP **a** 1 cm, **b** 2 cm, **c** 4 cm, with ECP **d** 1 cm, **e** 2 cm, **f** 4 cm

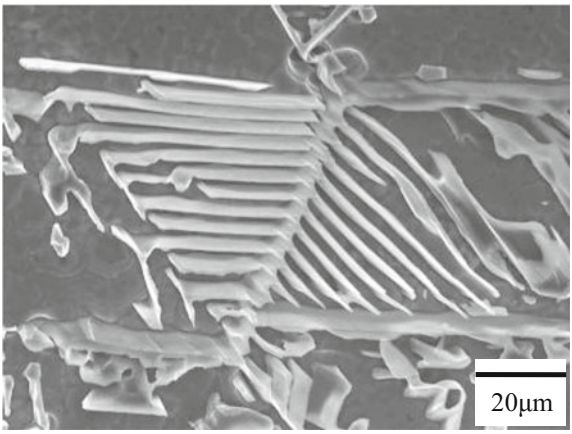

Fig. 3 SEM image of a single complex regular structure

Two phenomena may contribute to the occurrence of CRS. One is that the formation of CRS is promoted under the application of ECP, although CRS perform the same growth behavior in the samples with and without ECP [22]. The other one is that the composition of melt at the growth length of 2 cm reduces dramatically as a result of the aggregation of primary silicon at the initial growth period. According to the literature, CRS is appeared in the directionally solidified Al–Si alloys with a composition range of 12.6–17 wt% at the low growth velocity in the order of 10 μm/s [6].

Conclusions

The structure evolution of silicon in the directionally solidified Al–Si hypereutectic alloy has been investigated under the influence of ECP. The experimental results show that the ECP generate an interconnected, porous primary silicon structure during the initial growth. In the following growth, the complex regular structure mixing with eutectic structure forms. In comparison to the reference samples without ECP, only several coarse plate-like primary silicon and eutectic structures are observed.

Acknowledgements The authors gratefully acknowledge the financial supports from the Shanghai Sailing Program (Grant no. 17YF1405600), National Natural Science Foundation of China (Grant no. 51704192, 51320105003), Science and Technology Commission of Shanghai Municipality (Grant no. 14DZ2261200).

References

1. A. Heinz, A. Haszler, C. Keidel, S. Moldenhauer, R. Benedictus, W. Miller, Recent development in aluminium alloys for aerospace applications. Mater. Sci. Eng., A **280**, 102–107 (2000)
2. W. Miller, L. Zhuang, J. Bottema, A.J. Wittebrood, P. De Smet, A. Haszler, A. Vieregge, Recent development in aluminium alloys for the automotive industry. Mater. Sci. Eng., A **280**, 37–49 (2000)
3. T. Dursun, C. Soutis, Recent developments in advanced aircraft aluminium alloys. Mater. Des. **56**, 862–871 (2014)
4. H. Ye, An overview of the development of Al–Si–alloy based material for engine applications. J. Mater. Eng. Perform. **12**, 288–297 (2003)
5. K. Kobayashi, L. Hogan, The crystal growth of silicon in Al–Si alloys. J. Mater. Sci. **20**, 1961–1975 (1985)
6. O. Atasoy, F. Yilmaz, R. Elliott, Growth structures in aluminium-silicon alloys I. The coupled zone. J Cryst Growth **66**, 137–146 (1984)
7. S. Lu, A. Hellawell, Growth mechanisms of silicon in Al–Si alloys. J. Cryst. Growth **73**, 316–328 (1985)
8. S.D. McDonald, K. Nogita, A.K. Dahle, Eutectic nucleation in Al–Si alloys. Acta Mater. **52**, 4273–4280 (2004)
9. X. Liao, Q. Zhai, J. Luo, W. Chen, Y. Gong, Refining mechanism of the electric current pulse on the solidification structure of pure aluminum. Acta Mater. **55**, 3103–3109 (2007)
10. J. Li, J. Ma, Y. Gao, Q. Zhai, Research on solidification structure refinement of pure aluminum by electric current pulse with parallel electrodes. Mater. Sci. Eng., A **490**, 452–456 (2008)
11. J. Ma, J. Li, Y. Gao, Q. Zhai, Grain refinement of pure Al with different electric current pulse modes. Mater. Lett. **63**, 142–144 (2009)
12. M. Nakada, Y. Shiohara, M.C. Flemings, Modification of solidification structures by pulse electric discharging. ISIJ Int. **30**, 27–33 (1990)
13. H. Ding, Y. Zhang, S. Jiang, R. Chen, Z. Zhao, J. Guo, D. Xu, H. Fu, Influences of pulse electric current treatment on solidification microstructures and mechanical properties of Al–Si piston alloys. China foundry **6**, 24–31 (2009)
14. C. Ban, Y. Han, Q. Ba, J. Cui, Influence of pulse electric current on solidification structures of Al–Si alloys. Mater. Sci. Forum **546**, 723–728 (2007)
15. J. Zhu, T. Wang, F. Cao, W. Huang, H. Fu, Z. Chen, Real time observation of equiaxed growth of Sn–Pb alloy under an applied direct current by synchrotron microradiography. Mater. Lett. **89**, 137–139 (2012)
16. T. Wang, J. Xu, T. Xiao, H. Xie, J. Li, T. Li, Z. Cao, Evolution of dendrite morphology of a binary alloy under an applied electric current: an in situ observation. Phys. Rev. E **81**, 042601 (2010)
17. L.N. Brush, R.N. Grugel, The effect of an electric current on rod-eutectic solidification in Sn–0.9 wt.% Cu alloys. Mater. Sci. Eng. A, **238**, 176–181 (1997)
18. X. Liao, Q. Zhai, C. Song, W. Chen, Y. Gong, Effects of electric current pulse on stability of solid/liquid interface of Al–4.5 wt%Cu alloy during directional solidification. Mater. Sci. Eng. A, **466**, 56–60 (2007)
19. C. Song, Y. Guo, Y. Zhang, H. Zheng, M. Yan, Q. Han, Q. Zhai, Effect of currents on the microstructure of directionally solidified Al–4.5 wt%Cu alloy. J. Cryst. Growth **324**, 235–242 (2011)
20. F. Li, L.L. Regel, W.R. Wilcox, The influence of electric current pulses on the microstructure of the MnBi/Bi eutectic. J. Cryst. Growth **223**, 251–264 (2001)
21. X. Feng, Y. Yang, Numerical modeling of crystal growth of a nickel-based superalloy with applied direct current. J. Cryst. Growth **334**, 170–176 (2011)

22. Y. Zhang, C. Song, L. Zhu, H. Zheng, H. Zhong, Q. Han, Q. Zhai, Influence of electric-current pulse treatment on the formation of regular eutectic morphology in an Al–Si eutectic alloy. Metall. Mater. Trans. B **42**, 604–611 (2011)
23. D. Räbiger, Y. Zhang, V. Galindo, S. Franke, B. Willers, S. Eckert, The relevance of melt convection to grain refinement in Al–Si alloys solidified under the impact of electric currents. Acta Mater. **79**, 327–338 (2014)
24. Y. Zhang, X. Miao, Z. Shen, Q. Han, C. Song, Q. Zhai, Macro segregation formation mechanism of the primary silicon phase in directionally solidified Al–Si hypereutectic alloys under the impact of electric currents. Acta Mater. **97**, 357–366 (2015)
25. F. Yilmaz, Structure and properties of directionally solidified Al–Si hypereutectic alloys. Mater. Sci. Eng., A **124**, L1–L5 (1990)

First-Principles Calculations, Thermodynamic Calculations and Kinetic Calculations of Ultra High Strength Aluminum Alloys of Al–Zn–Mg–Cu–Zr

Jinsan Wang, Jinxin Zang and Xiang Xiao

Abstract The research for next generation of ultra high strength aluminum alloys is focused on materials of Al–Zn–Mg–Cu–Zr. In the present paper, the Al–Zn–Mg–Cu–Zr multi-component system was studied and the formation enthalpy of strengthening precipitate η′, the phase diagram of Al–Zn–Mg–Cu–Zr, the TTT diagram and the CCT diagram calculated by using the methods of First-principles calculations, thermodynamic calculations and kinetic calculations. Based on calculated results, a set of compositions and hot process parameters including temperature zones of hot processes and critical cooling rate of solution treatment are obtained. The calculated results provide primary guidance to developing Al–Zn–Mg–Cu–Zr ultra high strength aluminum alloys.

Keywords First-principles calculations · Thermodynamic · Kinetic Al–Zn–Mg–Cu–Zr · Phase diagram

Introduction

Ultra high strength aluminum alloy is the main structure material in aviation and spaceflight industry [1–3]. In the designing of this alloy, some of the most important factors and attributes to be considered are chemical composition and

J. Wang (✉) · J. Zang
Beijing Institute of Aeronautical Materials, Beijing 100095
People's Republic of China
e-mail: wjsbiam@163.com

J. Zang
e-mail: apple_zjx@163.com

X. Xiao
Suzhou Research Institute for Nonferrous Metals, Suzhou 215026
People's Republic of China
e-mail: xiaoxiang_zhl@163.com

© Springer Nature Singapore Pte Ltd. 2018

Y. Han (ed.), *Advances in Materials Processing*, Lecture Notes in Mechanical Engineering, https://doi.org/10.1007/978-981-13-0107-0_118

processing parameters and the resulting effects of the microstructure on mechanical properties [4–6]. Various efforts have been undertaken to develop a better understanding among the above-mentioned attributes to acquire a combination of high specific strength and good fracture toughness [7–9].

Many studies are undertaken to analyze the properties of ultra high strength aluminum alloys [10, 11]. These alloys are composed of the elements Zn, Mg, Cu and Zr mainly [12–14]. The Zn, Mg and Cu form precipitates following solution heat treatment and aging [15, 16]. The strength and toughness of the alloys depend on these precipitate highly. The representative sequence for precipitation of the strengthening precipitates in ultra high strength aluminum alloys is as follows: The super saturated solid solution → GP zones → η′ → η. GP zones precipitates to form are coherent with the parent matrix. These act as heterogeneous nucleation sites for more stable precipitates of η′ and η (MgZn2) phase leading to the dissolution of metastable GP zones. GP zones are coherent while η′ is semicoherent and η is incoherent. η′ and η phase can also form directly during quenching and aging. Maximum strengthening has been found for the peak-aged condition that consists of primarily η′ phase.

First-principles calculations are particularly useful for obtaining the energetics of the stable and metastable precipitates [17, 18]. The calculated results can improve the thermodynamic database lack of reliability since it has no enough experimental data [19]. Thermodynamic calculations can be used to acquire the phase diagrams and thermochemistry propertied of related alloy systems by building corresponding thermodynamic model [20, 21]. According to above method, the phase diagrams are calculated in actual multi-component alloys. Kinetic calculations [22] can be coupled with the thermodynamic descriptions to predict precipitation of the second phase and the cooling rate. In the present paper, the formation enthalpy of metastable phase η′ is obtained by First-principles calculations. Based on the calculated data, the mass fractions of η′ and phase diagram in different compositions of Al–Zn–Mg–Cu–Zr systems are acquired by thermodynamic calculations. Thus a set of compositions and the temperature zones of heat processes can be ascertained. According to these, the TTT (time-temperature-transformation) and CCT (continuous-cooling-transformation) diagram are calculated by kinetic method.

Methodology

The first-principles calculations are used to gain the formation enthalpy of the metastable precipitate η′. The scalar relativistic all-electron Blöchl's projector augmented-wave (PAW) [23, 24] method within the generalized gradient approximation (GGA) is adopted, as implemented in the highly-efficient Vienna ab initio simulation package (VASP) [25, 26]. For the GGA exchange-correlation function, the Perdew–Burke–Ernzerhof parameterization (PBE) [27–29] is employed. A plane-wave energy cutoff is held constant as 400 eV for the $A_xB_yC_z$ compounds (A = Mg, B = Zn, C = Al, and x, y and z are the stoichiometric numbers of the

elements A, B and C respectively in the related compound), and Brillouin zone integrations are performed using Monkhorst-Pack [30, 31] K-point meshes (12 × 12 × 12 in the present work). The total energy is converged numerically to less than 1×10^{-6} eV/unit with respect to electronic, ionic and unit cell degrees of freedom. All calculations are performed using the "high" setting within VASP to avoid wrap-around errors.

The formation enthalpy of the η′ phase is calculated by the following equation:

$$\Delta H\left(A_xB_yC_z\right) = E_{total}\left(A_xB_yC_z\right) - xE_{total}(A) - yE_{total}(B) - zE_{total}(C) \qquad (1)$$

where $E_{total}(A_xB_yC_z)$, $E_{total}(A)$, $E_{total}(B)$ and $E_{total}(C)$ are the calculated total energies (per atom at T = 0 K) of the intermetallic compound $A_xB_yC_z$, pure A, pure B and pure C, respectively.

The CALPHAD [32, 33] (Computer Coupling of Phase Diagrams and Thermochemistry) approach which aims at developing models to achieve thermodynamic calculations may be used effectively to develop a satisfactory extrapolation of the relevant phase diagrams. The Pandat [34] software is created using the CALPHAD methodology, and uses extensive thermodynamic databases of assessed systems to calculate the Gibbs free energies of all possible phases present in the alloy systems. The PanAl database [35] and thermodynamic description of η′ phase available in First-principles calculations contain the relevant thermodynamic information on the present Al–Zn–Mg–Cu–Zr muti-component system.

The metastable phase η′ is treated as the stoichiometric compound $A_xB_yC_z$, since no noticeable homogeneity ranges are reported for these compounds. Meanwhile, due to lack of the heat capacities of these phases, the Gibbs free energy per mole of atoms is expressed for each of the intermetallic compounds, according to the Neumann–Kopp rule:

$$G_m^{A_xB_yC_z} = \frac{x}{x+y+z}{}^0G_A^{\mathrm{SER}} + \frac{y}{x+y+z}{}^0G_B^{\mathrm{SER}} + \frac{z}{x+y+z}{}^0G_C^{\mathrm{SER}} + a + bT \qquad (2)$$

where, x and y and z are the stoichiometric coefficients of the compound $A_xB_yC_z$; ${}^0G_A^{\mathrm{SER}}$, ${}^0G_B^{\mathrm{SER}}$ and ${}^0G_C^{\mathrm{SER}}$ are the molar Gibbs free energies for the pure components A, B and C in their Standard Element Reference (SER) states, Fcc for Al, Hcp for Zn and Hcp for Mg. The parameter a is the formation enthalpy of η′ phase, and it can be calculated by First-principles calculations in the present work. And the parameter b is set to zero since the formation entropy of η′ phase is neglected.

The JMatPro (Java-based materials properties) software [36] was developed to augment to kinetic calculations by incorporating various theoretical materials models and properties databases. The TTT and CCT diagrams are calculated by using JMatPro software. The calculations are based on Johnson–Mehl–Avrami model [37] where critical input as driving forces and compositions of the precipitating phases:

$$f = 1 - \exp(-kt^n) \tag{3}$$

where f and t are volume fraction of phase and time respectively; n and k are the empirical coefficients which are fitted with experimental data.

Results and Discussion

First-Principles Calculations

The η′ phase is a well-studied metastable phase. η′ is commonly assumed to have the composition MgZn2, in analogy with the stable phase η. In fact the crystal structure of η′ is more complex. Auld and Cousland [38] deduced a structure model of η′ with an approximate composition Mg4Zn13Al2. And at present the research results support the validity of the Auld and Cousland model for η′. So this model is adopted in present work. The crystal structure of η′ is shown in Fig. 1.

By the first-principles method, the formation enthalpy of metastable phase η′ is calculated to be −8637 J/mol atom^{-1}. Thus the calculated data of η′ is adopted in present work during the thermodynamic calculations of Al–Zn–Mg–Cu–Zr muti-component system.

Thermodynamic Calculations

Based on the result of first-principles calculations and the PanAl database of Pandat software, the phase diagrams of Al–Zn–Mg–Cu–Zr muti-component systems are calculated. Using the calculation results and the compositions of 7085 aluminum alloy (Table 1), a set of compositions and the temperature zones of heat processes are obtained.

The mass fractions of η′ in different compositions of Mg and Zn are illustrated in Fig. 2. It can be seen that the mass fractions of η′ add with the increase of the contents of element Zn when the contents of element Mg are unchangeable. Moreover the mass fractions of η′ have peak values with the assured content of element Zn and the variable content of element Mg. It is remarkable that the mass fractions of η′ reduce rapidly when the contents of Mg locate in the right of peak values. Therefore it is the best method for choosing the contents of Mg located in the left of peak values when the ultra high strength alloys are designed. To obtain the more strengthening precipitate η′, the content of Zn is set to 8 wt%. Relatively the selected content of Mg is lower than 2 wt% from Fig. 2.

According to above work, the phase diagram of Al–Zn–Mg system is shown in Fig. 3 when the content of Mg is from 1.2 to 2.6 wt%. From the figure, the T phase

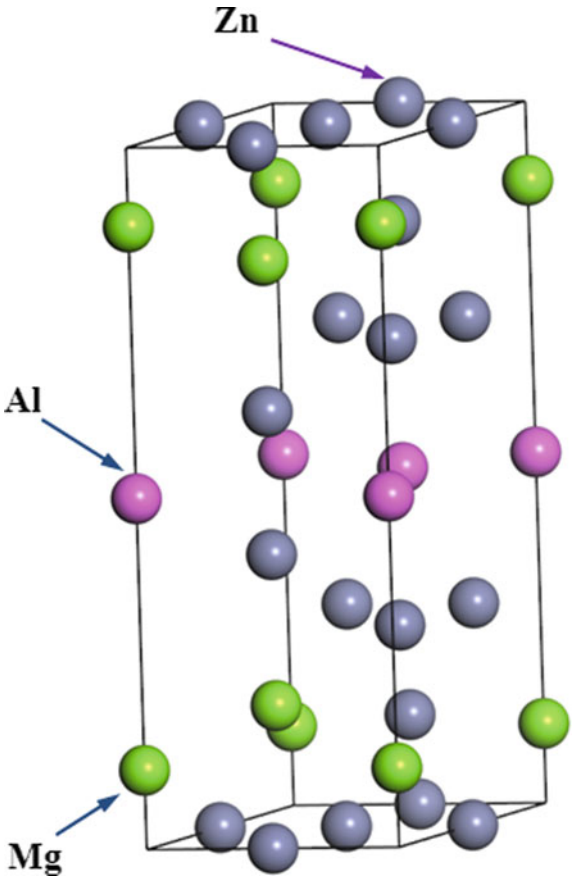

Fig. 1 Crystal structure of metastable phase η′

Table 1 Compositions of 7085 aluminum alloy (wt%)

	Zn	Mg	Cu	Zr	Al
7085	7–8	1.2–1.8	1.3–2	0.08–0.15	Bal.

will be found when the content of Mg is higher than 1.7 and the temperature is higher than 25 °C. To eliminate the harmful phase T, the content of Mg is set to 1.7 wt%.

In situation of 8 wt% Zn and 1.7 wt% Mg, the phase diagram of Al–Zn–Mg–Cu is calculated and illustrated in Fig. 4 when the content of Cu is from 1.3 to 2.6 wt%. It can be seen that the S phase will generate when the content of Cu is

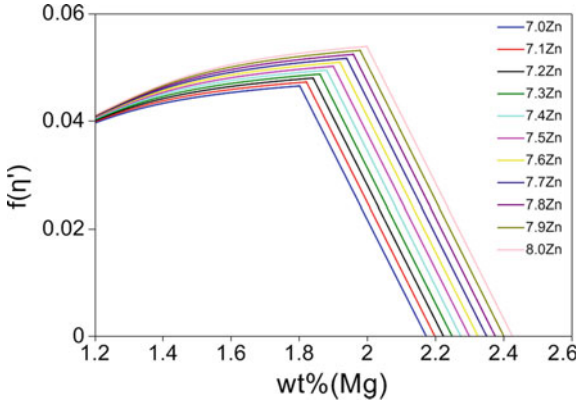

Fig. 2 Calculated mass fractions of η′ in different compositions of Mg and Zn

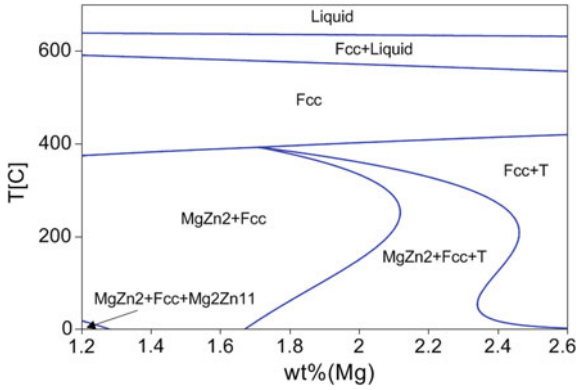

Fig. 3 Calculated phase diagram of Al–Zn–Mg system

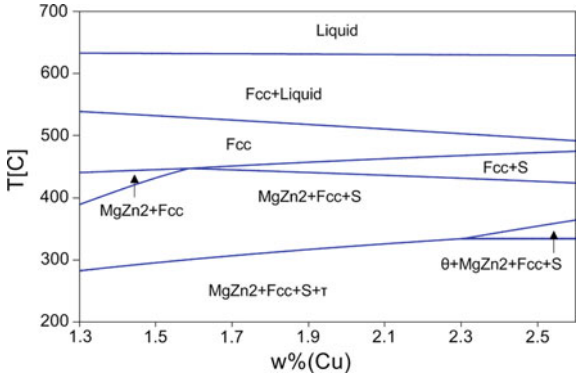

Fig. 4 Calculated phase diagram of Al–Zn–Mg–Cu system

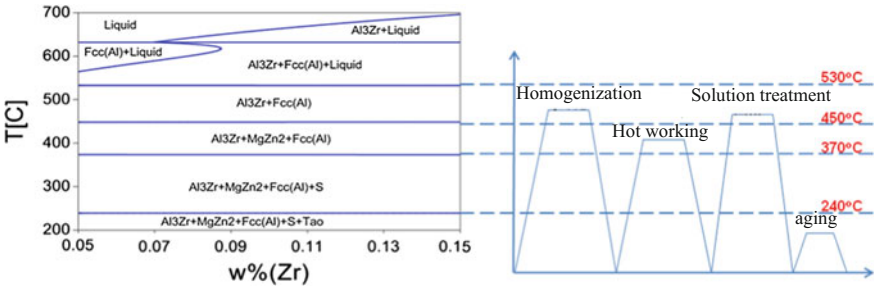

Fig. 5 Calculated phase diagram of Al–Zn–Mg–Cu–Zr system and the temperature zones of hot processes

higher than 1.6 wt% in 450 °C. To decrease the mass fraction of S phase, the content of Cu is set to 1.6 wt%.

The content of Zr is about 0.1 wt% through experience. Moreover, according to above mentioned compositions of Zn, Mg and Cu, the phase diagram of Al–Zn–Mg–Cu–Zr muti-component system is calculated and shown in Fig. 5 when the content of Zr is from 0.05 to 0.15 wt%. Also the temperature zones of hot processes are illustrated in Fig. 5 from the phase diagram of Al–Zn–Mg–Cu–Zr system. The temperature zone of homogenization, hot working and solution treatment is in the range of 450–530, 370–450 and 450–530 °C respectively. And the temperature zone of aging is slower than 240 °C.

Kinetic Calculations

Based on the compositions of Al8Zn1.7Mg1.6Cu0.1Zr, the TTT and CCT diagrams are calculated and illustrated in Figs. 6 and 7. Specifically, the phase transformation curves of Al2Cu, Al2CuMg, MgZn2, T and Meta-MgZn2 are acquired. It can be seen that the curves of Meta-MgZn2 precipitate locate on the far left in these two figures. Therefore, the Meta-MgZn2 (η′) precipitates firstly in the procedure of isothermal transformation and continuous cooling. In order to keep the strength of alloy, the precipitation of second phase should be avoided as much as possible in the procedure of heat treatment. That means the two curves (including cooling curve and Meta-MgZn2 formation curve) do not intersect. So the enough fast cooling rate is essential when we design the process parameters of solution treatment. According to this principle, the value of cooling rate is better than 30 °C/s to eliminate precipitate in solution treatment.

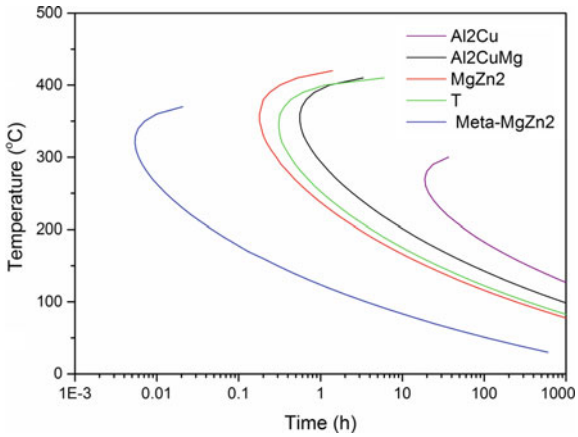

Fig. 6 Calculated TTT diagram in Al–Zn–Mg–Cu–Zr alloy

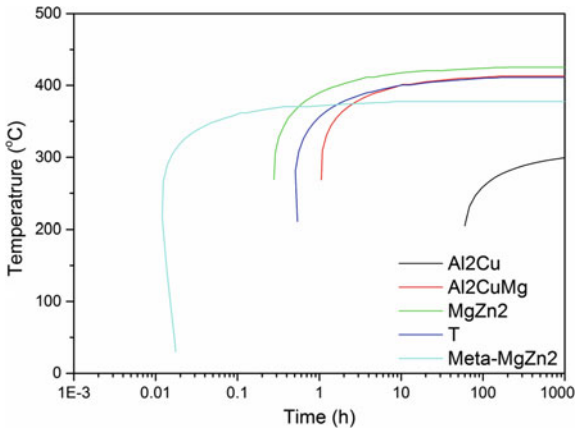

Fig. 7 Calculated CCT diagram in Al–Zn–Mg–Cu–Zr alloy

Conclusions

In the present paper, the Al–Zn–Mg–Cu–Zr system for ultra high strength aluminum alloys is developed by the method of first-principles calculations, thermodynamic calculation and kinetic calculations. The formation enthalpy of metastable strengthening precipitate η′ is obtained by First-principles calculations to assist thermodynamic calculations. Furthermore the mass fraction of η′ and phase diagrams of Al–Zn–Mg–Cu–Zr muti-component systems are acquired by thermodynamic calculations. Based on the results, a set of compositions and the temperature zones of hot processes are calculated. Thus the TTT and CCT diagrams are gained by kinetic calculations in these compositions. And the critical cooling rate of solution treatment is evaluated by using CCT diagram.

Acknowledgements This work was supported by Defense Industrial Technology Development Program (JCKY2016205C009).

References

1. D.A. Lukasak, R.M. Hart, Strong aluminum alloy shaves airframe weight. Adv. Mater. Process. **140**, 46–49 (1991)
2. K.H. Chen, H.W. Liu, Z. Zhang, The improvement of constituent dissolution and mechanical properties of 7055 aluminum alloy by stepped heat treatments. J. Mater. Process. Technol. **142**, 190–196 (2003)
3. L.P. Huang, K.H. Chen, S. Li, Influence of high-temperature pre-precipitation on local corrosion behaviors of Al–Zn–Mg alloy. Scripta Mater. **56**, 305–308 (2007)
4. C.P. Ferrer, M.G. Koul, B.J. Connolly, Improvements in strength and stress corrosion cracking properties in aluminum alloy 7075 via low-temperature retrogression and re-aging heat treatments. Corrosion **59**, 520–528 (2003)
5. J.F. Li, Z. Peng, C.X. Li, Mechanical properties, corrosion behaviors and microstructures of 7075 aluminium alloy with various aging treatments. T. Nonferr. Metal. Soc. **18**, 755–762 (2008)
6. K.H. Chen, H.C. Fang, Z. Zhang, Effect of Yb, Cr and Zr additions on recrystallization and corrosion resistance of Al–Zn–Mg–Cu alloys. Mater. Sci. Eng., A **497**, 426–431 (2008)
7. H. Tanaka, H. Esaki, K. Yamada, Mechanical properties of 7475 based aluminum alloy sheets with fine subgrain structures. J. Jpn. Inst. Light Met. **52**, 553–558 (2002)
8. H. Yoshida, Y. Baba, The role of zirconium to improve strength and stress-corrosion resistance of Al–Zn–Mg and Al–Zn–Mg–Cu alloys. Trans. Jpn. Inst. Met. **23**, 620–630 (1982)
9. Y.D. He, X.M. Zhang, J.H. You, Effect of minor Sc and Zr on microstructure and mechanical properties of Al–Zn–Mg–Cu alloy. T. Nonferr. Metal. Soc. **16**, 1228–1235 (2006)
10. K. Ural, A study of optimization of heat-treatment conditions in retrogressions and reageing treatment of 7075-T6 aluminum alloy. J. Mater. Sci. Lett. **13**, 383–385 (1994)
11. S. Chayong, H.V. Atkinson, R. Kapranos, Multistep induction heating regimes for thixoforming 7075 aluminum alloy. Mater. Sci. Technol. **20**, 490–496 (2004)
12. I.J. Polmear, A trace element effect in alloys based on the Aluminium–Zinc–Magnesium system. Nature **186**, 303–304 (1960)
13. I.J. Polmear, The ageing characteristics of complex Al–Zn–Mg alloys distinctive effects of copper and silver on the ageing mechanism. J. Inst. Met. **89**, 51–59 (1960)
14. S. Kikuchi, H. Yamazaki, T. Otsuka, J. Mater. Process. Technol. **38**, 689–701 (1993)
15. H.C. Fang, K.H. Chen, X. Chen, X, Effect of Cr, Yb and Zr additions on localized corrosion of Al–Zn–Mg–Cu alloy. Corros. Sci. **51**, 2872–2877 (2009)
16. R. Ayer, J.Y. Koo, J.W. Steeds, Microanalytical study of the heterogeneous phases in commercial Al–Zn–Mg–Cu alloys. Metall. Trans. A **16**, 1925–1936 (1985)
17. C. Ravi, C. Wolverton, First-principles study of crystal structures and stability of Al–Mg–Si–Cu precipitates. Acta Mater. **52**, 4213–4217 (2004)
18. C. Wolverton, Crystal structure and stability of complex precipitate phases in Al–Cu–Mg–Si and Al–Zn–Mg alloys. Acta Mater. **49**, 3129–3142 (2001)
19. D.D. Zhan, L.C. Zhou, Y. Kong, Structure and thermodynamics of the key precipitated phases in the Al–Mg–Si alloys from first-principles calculations. JMS **46**, 7839–7849 (2011)
20. J.L. Meijering, Retrograde solubility curves especially in alloy solid solutions. Philips Res. Rep. **3**, 281–302 (1948)
21. L. Kaufman, H. Bernstein, Computer calculation of phase diagrams, New York, 1970. (Academic Press, 1970), pp. 85–88

22. N. Saunders, X. Li, A.P. Miodownik, J.-Ph. Schillé, Materials Design Approaches and Experiences (TMS, Warrendale, 2001)
23. P.E. Blochl, Projector augmented-wave method. Phys. Rev. B **17953**, 50–51 (1994)
24. G. Kresse, J. Joubert, From ultrasoft pseudopotentials to the projector augmented-wave method. Phys. Rev. B **1758**, 59–60 (1999)
25. G. Kresse, J. Furthmuller, Efficient iterative schemes for ab initio totalenergy calculations using a plane-wave basis set. Phys. Rev. B **11169**, 54–55 (1996)
26. G. Kresse, J. Furthmuller, Efficiency of ab-initio total energy calculations for metals and semiconductors using a plane-wave basis set. Comput. Mater. Sci. **15**, 6–7 (1996)
27. J.P. Perdew, K. Burke, M. Ernzerhof, Phys. Rev. Lett. **77**, 3865 (1996)
28. J.P. Perdew, K. Burke, M. Ernzerhof, Generalized gradient approximation made simple. Phys. Rev. Lett. **78**, 1936 (1997)
29. J.P. Perdew, K. Burke, M. Ernzerhof, Perdew, Burke and Ernzerhof reply. Phys. Rev. Lett. **80**, 889–890 (1998)
30. H.J. Monkhorst, J.D. Pack, Special points for Brillouin-zone integrations. Phys. Rev. B **5188**, 13–14 (1976)
31. M. Methfessel, A.T. Paxton, High-precision sampling for Brillouin-zone integration in metals. Phys. Rev. B **3616**, 40–41 (1989)
32. A.T. Dinsdale, SGTE data for pure elements. CALPHAD **15**, 317–425 (1991)
33. O. Redlich, A.T. Kister, Algebraic representation of thermodynamic properties and the classification of solutions. Ind. Eng. Chem. **40**, 345–348 (1948)
34. Information on http://www.computherm.com
35. H.W.L. Phillips, Equilibrium diagrams of aluminum alloy systems. The Aluminum Development Association, Information Bulletin 25, London, pp. 105–108 (1961)
36. N. Saunders, Z. Guo, X. Li, A.P. Miodownik, J.P. Schille, Using JMatPro to model materials properties and behavior. JOM **55**, 60–65 (2003)
37. X. Li, A.P. Miodownik, N. Saunders, Modelling of materials properties in duplex stainless steels. Mater. Sci. Technol. **18**, 861–868 (2002)
38. J.H. Auld, S.M. Cousland, The structure of the metastable η′ phase in Al–Zn–Mg alloys. J. Australian Inst. Met. **19**, 194–195 (1974)

Thermodynamic Description of the Al–Mg–Y System

Kaiming Cheng, Jixue Zhou, Jingrui Zhao, Shouqiu Tang and Yuansheng Yang

Abstract The Al–Mg–Y system was critically assessed by means of the CALPHAD technique. The solution phases of liquid, face-centered cubic (FCC), body-centered cubic (BCC) and hexagonal close-packed (HCP) were modeled with Redlich–Kister equation. The thermodynamic models of compounds $Al_{12}Mg_{17}$, $Al_{30}Mg_{23}$ and Al_3Mg_2 in the Al–Mg system, AlY_2, Al_2Y_3, AlY and Al_3Y in the Al–Y system, as well as $Mg_{24}Y_5$ in the Mg–Y system were kept consistent with that of the corresponding binary systems. In order to reproduce the ternary solid solubility of previously determined isothermal section at 400 °C, an identical formula of $(Al,Mg,Y)_2(Al,Mg,Y)$ was used to model Al_2Y phase in the Al–Y system and Mg_2Y in the Mg–Y system. The ordered part of BCC phase, i.e. the BCC_B2 phase, was treated with a thermodynamic model of $(Al,Mg,Y)_{0.5}(Al,Mg,Y)_{0.5}(Va)_3$. The ternary phase of Al_4MgY was described as linear compound with sub-lattice model. On the basis of the optimized thermodynamic parameters of Al–Mg, Al–Y and Mg–Y systems in literature, the Al–Mg–Y system was optimized in present work. The currently calculated isothermal sections at 400 and 800 °C, as well as the liquidus surface projection agree well with the previous experimental data.

Keywords Thermodynamic modeling · Al–Mg–Y alloy · Phase relation

Introduction

Magnesium–aluminium (Mg–Al) based alloys are widely used because of the low density, high strength-to-weight ratio, specific rigidity, satisfactory salt-spray corrosion resistance and good ductility [1]. Addition of rear-earth (RE) elements

K. Cheng (✉) · J. Zhou · J. Zhao · S. Tang
Shandong Key Laboratory for High Strength Lightweight Metallic Materials, Advanced Materials Institute, Shandong Academy of Sciences, Jinan 250014, China
e-mail: chengkaimingtry@gmail.com; chengkm@sdas.org

Y. Yang
Institute of Metal Research, Chinese Academy of Sciences, Shenyang 110016, China

© Springer Nature Singapore Pte Ltd. 2018

Y. Han (ed.), *Advances in Materials Processing*, Lecture Notes in Mechanical Engineering, https://doi.org/10.1007/978-981-13-0107-0_119

(RE = La, Ce, Pr, Nd, Sm, Gd, Tb, Dy, Ho, Er, Tm, Lu, Y, and Sc) in Mg–Al alloys can improve the creep resistance and strength at elevated temperatures due to the precipitation of intermetallic phases (such as $Al_{11}RE_3$ and Al_2RE phases). Meanwhile, RE elements can suppress the formation of the detrimental $Mg_{17}Al_{12}$ phase in the interdendritic or grain boundary region [2]. Recently, it has also been reported that magnesium alloys with heavy RE elements, such as Mg–10Y [3], Mg–10Gd [4] and Mg–10Gd–3Y [5] alloys, can be significantly grain refined by minor addition of Al, where the precipitation of Al_2Y intermetallic compound during solidification can enhance the heterogeneous nucleation.

Understanding of the nature of precipitating phases, precipitation sequences and relative amounts of secondary phases in the ternary Al–Mg–RE systems requires information on thermodynamic properties and phase diagram. So, a self-consistent thermodynamic database is of great importance. Combination of the experimental investigation with thermodynamic calculation is a powerful strategy to investigate the phase equilibria in multi-component systems, which has been successfully applied to study plenty of Al–Mg–RE alloys systems [6–12]. For the Al–Mg–Y system, it was first extrapolated based on critical thermodynamic description of the Al–Y and Mg–Y sub-binary systems [13], in which no ternary solid solubility was considered. Then, thermodynamic assessment of the Al–Mg–Y system was performed by [14] considering previous experimental data, but the calculated isothermal section exhibits different phase relation from that of the literature.

The partial isothermal sections between 500 and 300 °C for the Al–Mg–Y system was first investigated by Drits et al. [15]. Then, Zar et al. [16] determined an isothermal section at 400 °C and reported the existence of a ternary compound Al_4MgY. Their work showed that this ternary compound is a congruent compound melt at around 750 °C with a certain primary solidification region in the liquidus projection drawn based on the experimental data. Later on, Odi et al. [17] constructed an isothermal section for the entire composition range at 400 °C, which confirmed the ternary compound Al_4MgY and extensive solubility of the third component in Al_2Y, MgY, and Mg_2Y binary compounds. In present work, the Al–Mg–Y system was optimized by means of the CALPHAD method on the basis of these experimental data in literature.

Thermodynamic Descriptions

Solution Phases

In the Al–Mg–Y system, there are four solution phases: liquid, face-centered cubic (FCC), body-centered cubic (BCC) and hexagonal close-packed (HCP). Their molar Gibbs energies are described by the following expression:

$$G_m^\phi = x_{\mathrm{Al}} G_{\mathrm{Al}}^\phi + x_{\mathrm{Mg}} G_{\mathrm{Mg}}^\phi + x_{\mathrm{Y}} G_{\mathrm{Y}}^\phi + RT\left(x_{\mathrm{Al}} \ln x_{\mathrm{Al}} + x_{\mathrm{Mg}} \ln x_{\mathrm{Mg}} + x_{\mathrm{Y}} \ln x_{\mathrm{Y}}\right) + {}^E G_m^\phi \tag{1}$$

where R is the gas constant, x_{Al}, x_{Mg} and x_{Y} are mole fraction of Al, Mg and Y, respectively; ${}^E G_m^\phi$ is the excess Gibbs energy, expressed by the Redlich–Kister polynomial,

$$\begin{aligned} {}^E G_m^\phi = {} & x_{\mathrm{Al}} x_{\mathrm{Mg}} \sum_j {}^j L_{\mathrm{Al,Mg}}^\phi \left(x_{\mathrm{Al}} - x_{\mathrm{Mg}}\right)^j + x_{\mathrm{Mg}} x_{\mathrm{Y}} \sum_j {}^j L_{\mathrm{Mg,Y}}^\phi \left(x_{\mathrm{Mg}} - x_{\mathrm{Y}}\right)^j \\ & + x_{\mathrm{Al}} x_{\mathrm{Y}} \sum_j {}^j L_{\mathrm{Al,Y}}^\phi \left(x_{\mathrm{Al}} - x_{\mathrm{Y}}\right)^j + x_{\mathrm{Al}} x_{\mathrm{Mg}} x_{\mathrm{Y}} {}^j L_{\mathrm{Al,Mg,Y}}^\phi \end{aligned} \tag{2}$$

where ${}^j L_{\mathrm{Al,Mg}}^\phi$, ${}^j L_{\mathrm{Mg,Y}}^\phi$ and ${}^j L_{\mathrm{Al,Y}}^\phi$ are the binary interaction parameters, which are from Refs. [18–20]. ${}^j L_{\mathrm{Al,Mg,Y}}^\phi$ is the ternary interaction parameter expressed as:

$$L_{\mathrm{Al,Mg,Y}}^\phi = x_{\mathrm{Al}} {}^0 L_{\mathrm{Al,Mg,Y}}^\phi + x_{\mathrm{Mg}} {}^1 L_{\mathrm{Al,Mg,Y}}^\phi + x_{\mathrm{Y}} {}^2 L_{\mathrm{Al,Mg,Y}}^\phi \tag{3}$$

where ${}^j L_{\mathrm{Al,Mg,Y}}^\phi = a_j + b_j T$, a_j and b_j are the parameters to be optimized in this work.

Intermetallic Compounds

The binary compounds in the Al–Mg–Y system can be classified as two types according to the solubility of the third component. The compounds $Al_{12}Mg_{17}$, $Al_{30}Mg_{23}$ and Al_3Mg_2 in the Al–Mg system, AlY_2, Al_2Y_3, AlY and Al_3Y in the Al–Y system, as well as $Mg_{24}Y_5$ in the Mg–Y system belong to the compounds that have no ternary solid solubility, and the thermodynamic models are kept consistent with that of the corresponding binary systems. In order to reproduce the ternary solid solubility, a two-sublattice model [21, 22] of $(Al,Mg,Y)_2(Al,Mg,Y)$ was used to model Al_2Y phase in the Al–Y system and Mg_2Y in the Mg–Y system. The Gibbs energy per mole of the formula unit Al_2Y is given by the following expression:

$$
\begin{aligned}
G^{Al_2Y} = {} & y'_{Al}y''_{Al}G^{Al_2Y}_{Al:Al} + y'_{Al}y''_{Mg}G^{Al_2Y}_{Al:Mg} + y'_{Al}y''_{Y}G^{Al_2Y}_{Al:Y} + y'_{Mg}y''_{Al}G^{Al_2Y}_{Mg:Al} \\
& + y'_{Mg}y''_{Mg}G^{Al_2Y}_{Mg:Mg} + y'_{Mg}y''_{Y}G^{Al_2Y}_{Mg:Y} + y'_{Y}y''_{Al}G^{Al_2Y}_{Y:Al} + y'_{Y}y''_{Mg}G^{Al_2Y}_{Y:Mg} \\
& + y'_{Y}y''_{Y}G^{Al_2Y}_{Y:Y} + 2RT\left(y'_{Al}\ln y'_{Al} + y'_{Mg}\ln y'_{Mg} + y'_{Y}\ln y'_{Y}\right) \\
& + RT\left(y''_{Al}\ln y''_{Al} + y''_{Mg}\ln y''_{Mg} + y''_{Y}\ln y''_{Y}\right) \\
& + y'_{Al}\left[\begin{array}{l} y''_{Al}y''_{Mg}\sum_i {}^iL^{Al_2Y}_{Al:Al,Mg}\left(y''_{Al}-y''_{Mg}\right)^i + y''_{Al}y''_{Y}\sum_i {}^iL^{Al_2Y}_{Al:Al,Y}\left(y''_{Al}-y''_{Y}\right)^i \\ \qquad + y''_{Mg}y''_{Y}\sum_i {}^iL^{Al_2Y}_{Al:Mg,Y}\left(y''_{Mg}-y''_{Y}\right)^i + y''_{Al}y''_{Mg}y''_{Y}L^{Al_2Y}_{Al:Al,Mg,Y} \end{array}\right] \\
& + y'_{Mg}\left[\begin{array}{l} y''_{Al}y''_{Mg}\sum_i {}^iL^{Al_2Y}_{MgAl,Mg}\left(y''_{Al}-y''_{Mg}\right)^i + y''_{Al}y''_{Y}\sum_i {}^iL^{Al_2Y}_{Mg:Al,Y}\left(y''_{Al}-y''_{Y}\right)^i \\ \qquad + y''_{Mg}y''_{Y}\sum_i {}^iL^{Al_2Y}_{Mg:Mg,Y}\left(y''_{Mg}-y''_{Y}\right)^i + y''_{Al}y''_{Mg}y''_{Y}L^{Al_2Y}_{Mg:Al,Mg,Y} \end{array}\right] \\
& + y'_{Y}\left[\begin{array}{l} y''_{Al}y''_{Mg}\sum_i {}^iL^{Al_2Y}_{Y:Al,Mg}\left(y''_{Al}-y''_{Mg}\right)^i + y''_{Al}y''_{Y}\sum_i {}^iL^{Al_2Y}_{Y:Al,Y}\left(y''_{Al}-y''_{Y}\right)^i \\ \qquad + y''_{Mg}y''_{Y}\sum_i {}^iL^{Al_2Y}_{Y:Mg,Y}\left(y''_{Mg}-y''_{Y}\right)^i + y''_{Al}y''_{Mg}y''_{Y}L^{Al_2Y}_{Y:Al,Mg,Y} \end{array}\right] \\
& + y''_{Al}\left[\begin{array}{l} y'_{Al}y'_{Mg}\sum_i {}^iL^{Al_2Y}_{Al,Mg:Al}\left(y'_{Al}-y'_{Mg}\right)^i + y'_{Al}y'_{Y}\sum_i {}^iL^{Al_2Y}_{Al,Y:Al}\left(y'_{Al}-y'_{Y}\right)^i \\ \qquad + y'_{Mg}y'_{Y}\sum_i {}^iL^{Al_2Y}_{Mg,Y:Al}\left(y'_{Mg}-y'_{Y}\right)^i + y'_{Al}y'_{Mg}y'_{Y}L^{Al_2Y}_{Al,Mg,Y:Al} \end{array}\right] \\
& + y''_{Mg}\left[\begin{array}{l} y'_{Al}y'_{Mg}\sum_i {}^iL^{Al_2Y}_{Al,Mg:Mg}\left(y'_{Al}-y'_{Mg}\right)^i + y'_{Al}y'_{Y}\sum_i {}^iL^{Al_2Y}_{Al,Y:Mg}\left(y'_{Al}-y'_{Y}\right)^i \\ \qquad + y'_{Mg}y'_{Y}\sum_i {}^iL^{Al_2Y}_{Mg,Y:Mg}\left(y'_{Mg}-y'_{Y}\right)^i + y'_{Al}y'_{Mg}y'_{Y}L^{Al_2Y}_{Al,Mg,Y:Mg} \end{array}\right] \\
& + y''_{Y}\left[\begin{array}{l} y'_{Al}y'_{Mg}\sum_i {}^iL^{Al_2Y}_{Al,Mg:Y}\left(y'_{Al}-y'_{Mg}\right)^i + y'_{Al}y'_{Y}\sum_i {}^iL^{Al_2Y}_{Al,Y:Y}\left(y'_{Al}-y'_{Y}\right)^i \\ \qquad + y'_{Mg}y'_{Y}\sum_i {}^iL^{Al_2Y}_{Mg,Y:Y}\left(y'_{Mg}-y'_{Y}\right)^i + y'_{Al}y'_{Mg}y'_{Y}L^{Al_2Y}_{Al,Mg,Y:Y} \end{array}\right]
\end{aligned}
\tag{4}
$$

where y'_* and y''_* are the site fractions of Al, Mg or Y in the first and second sublattices, respectively. $G^{Al_2Y}_{*:*}$ represents the Gibbs energy of the compound Al_2Y when the first and second sublattices are occupied by only one element Al, Mg or Y, which are related to the enthalpies of pure Al, Mg and Y in their reference state. $L^{Al_2Y}_{*:*}$ represents the *j*th interaction parameters between the elements in the first and

the second sublattices. Due to the identical sublattice model, the expression of Gibbs energy per mole of the formula unit Mg_2Y is similar to Eq. 4. However, it should be mentioned that the Al_2Y and Mg_2Y are not described with the same set of thermodynamic parameters since they are Laves phases with cF4–$MgCu_2$ and hP12–$MgZn_2$ structure, respectively.

The intermetallic compound MgY with an ordered BCC_B2 structure was described in the thermodynamic model of $(Al,Mg,Y)_{0.5}(Al,Mg,Y)_{0.5}(Va)_3$, and its Gibbs energy per mole formula unit is given by the following expression:

$$G_m^{\mathrm{MgY}} = G_m^{\mathrm{dis}}(x_i) + G_m^{\mathrm{ord}}\left(y_i', y_i''\right) - G_m^{\mathrm{ord}}(x_i) \tag{5}$$

where the mole fraction x_i and the site fractions y_i' y'' are related according to $x_i = 0.5y_i' + 0.5y_i''$. The first term $G_m^{\mathrm{dis}}(x_i)$ is molar Gibbs energy of the disordered BCC phase. $G_m^{\mathrm{ord}}\left(y_i', y_i''\right)$ is calculated using Eq. 6 below, then $G_m^{\mathrm{ord}}(x_i)$ is calculated using the same model parameters but replacing y_i' and y'' with mole fraction x_i in Eq. 6. When the phase becomes disordered, i.e. $x_i = y_i' = y_i''$, the contributions from the ordering, i.e. $G_m^{\mathrm{ord}}\left(y_i', y_i''\right) - G_m^{\mathrm{ord}}(x_i)$, will be cancelled and only the first term $G_m^{\mathrm{dis}}(x_i)$ gives a contribution to the Gibbs energy.

$$\begin{aligned}
G_m^{\mathrm{ord}} = {} & y_{\mathrm{Al}}'y_{\mathrm{Al}}''G_{\mathrm{Al:Al}}^{\mathrm{MgY}} + y_{\mathrm{Al}}'y_{\mathrm{Mg}}''G_{\mathrm{Al:Mg}}^{\mathrm{MgY}} + y_{\mathrm{Al}}'y_{\mathrm{Y}}''G_{\mathrm{Al:Y}}^{\mathrm{MgY}} + y_{\mathrm{Mg}}'y_{\mathrm{Al}}''G_{\mathrm{Mg:Al}}^{\mathrm{MgY}} \\
& + y_{\mathrm{Mg}}'y_{\mathrm{Mg}}''G_{\mathrm{Mg:Mg}}^{\mathrm{MgY}} + y_{\mathrm{Mg}}'y_{\mathrm{Y}}''G_{\mathrm{Mg:Y}}^{\mathrm{MgY}} + y_{\mathrm{Y}}'y_{\mathrm{Al}}''G_{\mathrm{Y:Al}}^{\mathrm{MgY}} + y_{\mathrm{Y}}'y_{\mathrm{Mg}}''G_{\mathrm{Y:Mg}}^{\mathrm{MgY}} \\
& + y_{\mathrm{Y}}'y_{\mathrm{Y}}''G_{\mathrm{Y:Y}}^{\mathrm{MgY}} + 0.5RT\left(y_{\mathrm{Al}}'\ln y_{\mathrm{Al}}' + y_{\mathrm{Mg}}'\ln y_{\mathrm{Mg}}' + y_{\mathrm{Y}}'\ln y_{\mathrm{Y}}'\right) \\
& + 0.5RT\left(y_{\mathrm{Al}}''\ln y_{\mathrm{Al}}'' + y_{\mathrm{Mg}}''\ln y_{\mathrm{Mg}}'' + y_{\mathrm{Y}}''\ln y_{\mathrm{Y}}''\right) \\
& + y_{\mathrm{Al}}'\left[\begin{array}{l} y_{\mathrm{Al}}''y_{\mathrm{Mg}}''\sum_i {}^iL_{\mathrm{Al:Al,Mg}}^{\mathrm{MgY}}\left(y_{\mathrm{Al}}'' - y_{\mathrm{Mg}}''\right)^i + y_{\mathrm{Al}}''y_{\mathrm{Y}}''\sum_i {}^iL_{\mathrm{Al:Al,Y}}^{\mathrm{MgY}}\left(y_{\mathrm{Al}}'' - y_{\mathrm{Y}}''\right)^i \\ \qquad + y_{\mathrm{Mg}}''y_{\mathrm{Y}}''\sum_i {}^iL_{\mathrm{Al:Mg,Y}}^{\mathrm{MgY}}\left(y_{\mathrm{Mg}}'' - y_{\mathrm{Y}}''\right)^i + y_{\mathrm{Al}}''y_{\mathrm{Mg}}''y_{\mathrm{Y}}''L_{\mathrm{Al:Al,Mg,Y}}^{\mathrm{MgY}} \end{array}\right] \\
& + y_{\mathrm{Mg}}'\left[\begin{array}{l} y_{\mathrm{Al}}''y_{\mathrm{Mg}}''\sum_i {}^iL_{\mathrm{MgAl,Mg}}^{\mathrm{MgY}}\left(y_{\mathrm{Al}}'' - y_{\mathrm{Mg}}''\right)^i + y_{\mathrm{Al}}''y_{\mathrm{Y}}''\sum_i {}^iL_{\mathrm{Mg:Al,Y}}^{\mathrm{MgY}}\left(y_{\mathrm{Al}}'' - y_{\mathrm{Y}}''\right)^i \\ \qquad + y_{\mathrm{Mg}}''y_{\mathrm{Y}}''\sum_i {}^iL_{\mathrm{Mg:Mg,Y}}^{\mathrm{MgY}}\left(y_{\mathrm{Mg}}'' - y_{\mathrm{Y}}''\right)^i + y_{\mathrm{Al}}''y_{\mathrm{Mg}}''y_{\mathrm{Y}}''L_{\mathrm{Mg:Al,Mg,Y}}^{\mathrm{MgY}} \end{array}\right]
\end{aligned}$$

$$
\begin{aligned}
&+ y'_{\mathrm{Y}} \left[\begin{array}{l} y''_{\mathrm{Al}} y''_{\mathrm{Mg}} \sum_i {}^{i}L^{\mathrm{MgY}}_{\mathrm{Y:Al,Mg}} \left(y''_{\mathrm{Al}} - y''_{\mathrm{Mg}} \right)^{i} + y''_{\mathrm{Al}} y''_{\mathrm{Y}} \sum_i {}^{i}L^{\mathrm{MgY}}_{\mathrm{Y:Al,Y}} \left(y''_{\mathrm{Al}} - y''_{\mathrm{Y}} \right)^{i} \\ \qquad + y''_{\mathrm{Mg}} y''_{\mathrm{Y}} \sum_i {}^{i}L^{\mathrm{MgY}}_{\mathrm{Y:Mg,Y}} \left(y''_{\mathrm{Mg}} - y''_{\mathrm{Y}} \right)^{i} + y''_{\mathrm{Al}} y''_{\mathrm{Mg}} y''_{\mathrm{Y}} L^{\mathrm{MgY}}_{\mathrm{Y:Al,Mg,Y}} \end{array} \right] \\
&+ y''_{\mathrm{Al}} \left[\begin{array}{l} y'_{\mathrm{Al}} y'_{\mathrm{Mg}} \sum_i {}^{i}L^{\mathrm{MgY}}_{\mathrm{Al,Mg:Al}} \left(y'_{\mathrm{Al}} - y'_{\mathrm{Mg}} \right)^{i} + y'_{\mathrm{Al}} y'_{\mathrm{Y}} \sum_i {}^{i}L^{\mathrm{MgY}}_{\mathrm{Al,Y:Al}} \left(y'_{\mathrm{Al}} - y'_{\mathrm{Y}} \right)^{i} \\ \qquad + y'_{\mathrm{Mg}} y'_{\mathrm{Y}} \sum_i {}^{i}L^{\mathrm{MgY}}_{\mathrm{Mg,Y:Al}} \left(y'_{\mathrm{Mg}} - y'_{\mathrm{Y}} \right)^{i} + y'_{\mathrm{Al}} y'_{\mathrm{Mg}} y'_{\mathrm{Y}} L^{\mathrm{MgY}}_{\mathrm{Al,Mg,Y:Al}} \end{array} \right] \\
&+ y''_{\mathrm{Mg}} \left[\begin{array}{l} y'_{\mathrm{Al}} y'_{\mathrm{Mg}} \sum_i {}^{i}L^{\mathrm{MgY}}_{\mathrm{Al,Mg:Mg}} \left(y'_{\mathrm{Al}} - y'_{\mathrm{Mg}} \right)^{i} + y'_{\mathrm{Al}} y'_{\mathrm{Y}} \sum_i {}^{i}L^{\mathrm{MgY}}_{\mathrm{Al,Y:Mg}} \left(y'_{\mathrm{Al}} - y'_{\mathrm{Y}} \right)^{i} \\ \qquad + y'_{\mathrm{Mg}} y'_{\mathrm{Y}} \sum_i {}^{i}L^{\mathrm{MgY}}_{\mathrm{Mg,Y:Mg}} \left(y'_{\mathrm{Mg}} - y'_{\mathrm{Y}} \right)^{i} + y'_{\mathrm{Al}} y'_{\mathrm{Mg}} y'_{\mathrm{Y}} L^{\mathrm{MgY}}_{\mathrm{Al,Mg,Y:Mg}} \end{array} \right] \\
&+ y''_{\mathrm{Y}} \left[\begin{array}{l} y'_{\mathrm{Al}} y'_{\mathrm{Mg}} \sum_i {}^{i}L^{\mathrm{MgY}}_{\mathrm{Al,Mg:Y}} \left(y'_{\mathrm{Al}} - y'_{\mathrm{Mg}} \right)^{i} + y'_{\mathrm{Al}} y'_{\mathrm{Y}} \sum_i {}^{i}L^{\mathrm{MgY}}_{\mathrm{Al,Y:Y}} \left(y'_{\mathrm{Al}} - y'_{\mathrm{Y}} \right)^{i} \\ \qquad + y'_{\mathrm{Mg}} y'_{\mathrm{Y}} \sum_i {}^{i}L^{\mathrm{MgY}}_{\mathrm{Mg,Y:Y}} \left(y'_{\mathrm{Mg}} - y'_{\mathrm{Y}} \right)^{i} + y'_{\mathrm{Al}} y'_{\mathrm{Mg}} y'_{\mathrm{Y}} L^{\mathrm{MgY}}_{\mathrm{Al,Mg,Y:Y}} \end{array} \right]
\end{aligned}
\tag{6}
$$

The ternary phase of Al_4MgY was described as linear compound using sublattice model. The Gibbs energy per mole of the formula unit Al_4MgY is given by the following expression:

$$
G^{\mathrm{Al_4MgY}} - 4H^{\mathrm{SER}}_{\mathrm{Al}} - H^{\mathrm{SER}}_{\mathrm{Mg}} - H^{\mathrm{SER}}_{\mathrm{Y}} = 4G^{\mathrm{FCC}}_{\mathrm{Al}} + G^{\mathrm{HCP}}_{\mathrm{Mg}} + G^{\mathrm{HCP}}_{\mathrm{Y}} + L^{\mathrm{Al_4MgY}}_{\mathrm{Al:Mg:Y}} \tag{7}
$$

where $L^{\mathrm{Al_4MgY}}_{\mathrm{Al:Mg:Y}} = a + bT$, a and b are the coefficients to be evaluated.

Optimization Procedure

The optimization was carried out by means of the module PARROT of the thermodynamic software Thermo–Calc [23], which can handle various kinds of experimental data. The program works by minimizing a squared error sum where each of the selected values is given a certain weight. The weight is chosen by personal judgment, and changed by trial and error during the work until most of the selected experimental information is reproduced within the expected uncertainty limits.

The thermodynamic model parameters for the Al–Mg–Y system were optimized on the basis of the experimental information available in the literature [17]. A general rule for the selection of the adjustable parameters is that only those

coefficients that are determined by the experimental values should be adjusted [24]. If there are insufficient experimental data to adjust the particular parameter, a reasonable estimate should be given, or its value should be constrained to the others.

The thermodynamic descriptions of the liquid phase, as well as of the FCC, BCC and HCP phases, were obtained by a combination of the corresponding Gibbs energy functions from the assessments of the binary systems using Muggianu interpolation of binary excess terms [25]. The interaction parameters ${}^{0}L^{\phi}_{\mathrm{Al,Mg,Y}}$, ${}^{1}L^{\phi}_{\mathrm{Al,Mg,Y}}$ and ${}^{2}L^{\phi}_{\mathrm{Al,Mg,Y}}$ were taken from the three binary systems assessed by our work. The ternary interaction parameters were fixed to zero as a result of lack of information regarding the solidification behavior and the homogeneity ranges of ternary solution phases. For the compounds in the ternary Al–Mg–Y system, the parameters $G^{\mathrm{Al_2Y}}_{\mathrm{Mg:Y}}$, $G^{\mathrm{Al_2Y}}_{\mathrm{Y:Mg}}$, $G^{\mathrm{Mg_2Y}}_{\mathrm{Al:Y}}$, $G^{\mathrm{Mg_2Y}}_{\mathrm{Y:Al}}$, $G^{\mathrm{MgY}}_{\mathrm{Al:Y}}$, $G^{\mathrm{MgY}}_{\mathrm{Y:Al}}$, ${}^{0}L^{\mathrm{MgY}}_{\mathrm{Al,Mg:Y}}$ and ${}^{0}L^{\mathrm{MgY}}_{\mathrm{Y:Al,Mg}}$ were optimized according to the experimental information on the compounds in the Al–Mg–Y ternary system. The thermodynamic parameters of the binary compounds in Al–Mg, Al–Y and Mg–Y binary systems came from Saunders [18], Liu et al. [19] and Guo et al. [20], respectively.

Results and Discussion

The isothermal section of the Al–Mg–Y system calculated at 400 °C based on the present thermodynamic description is shown in Fig. 1 compared with the experimental data [17]. It can be seen that the current calculation results can reasonably reproduce the solid solubility of the binary intermetallic compounds of Al_2Y, MgY and Mg_2Y. The experimentally determined two-phase and three-phase regions are well described, indicating a good agreement on the phase relation at this temperature with the reported experimental data. The present calculation result shows better reproduction of the phase relation as well as ternary solid solubility of the intermetallic compounds than previous assessments [13, 14]. The ternary phase of Al_4MgY can be detected to be stable at this temperature in the Al-rich corner, resulting in a satisfactory description of the phase relation in this composition region. Though the current calculation can describe the large solid solution range of Al_2Y phase reported in [17], the recent developed Mg–10Y alloy with minor addition of Al suggests very small solubility of Mg in Al_2Y phase [3]. The as-cast state of the Mg–10Y–*x*Al may weaken the solid solubility of Mg, but new experimental investigation is still needed to validate the composition range of Al_2Y at certain temperature in the annealed state.

In Fig. 2, the isothermal section of the Al–Mg–Y system calculated at 800 °C is presented for discussion. It can be seen that all the binary intermetallic compounds in the Al–Y system remains stable at this temperature. In the Mg–Y system, only MgY phase exists and shows a solid solubility, while all the intermetallic phases

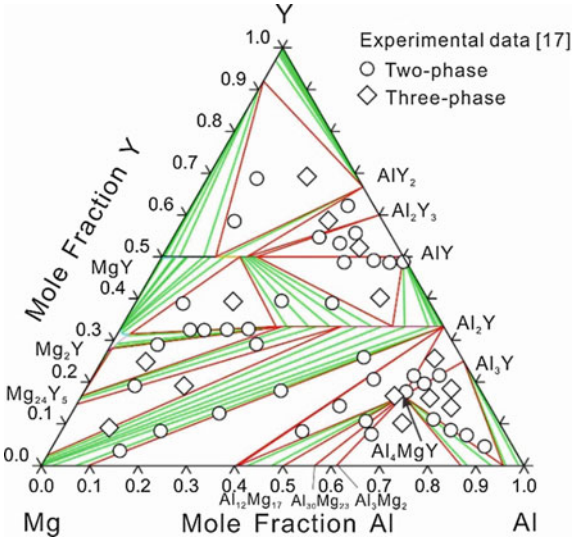

Fig. 1 Calculated isothermal section of the Al–Mg–Y system at 400 °C based on the present thermodynamic description compared with the experimental data [17]. The green tie-lines and red triangles represent the two-phase and three-phase regions calculated based on current thermodynamic description, respectively. The experimentally determined two-phase and three-phase data points are respectively marked as open circle and open diamond

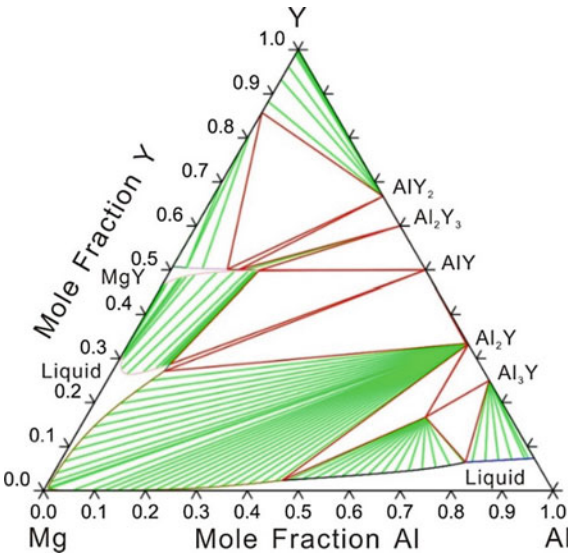

Fig. 2 Isothermal section of the Al–Mg–Y system calculated at 800 °C. The green tie-lines and red triangles represent the two-phase and three-phase regions calculated based on current thermodynamic description, respectively

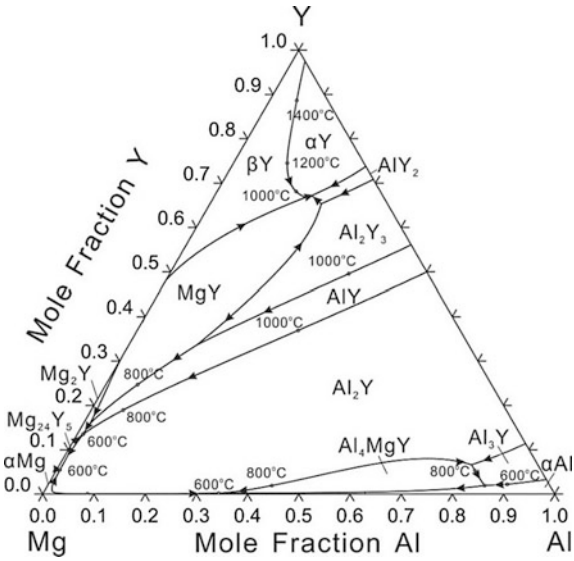

Fig. 3 The calculated liquidus projection of the Al–Mg–Y system

melts at 800 °C. It is noteworthy that the ternary Al_4MgY phase, which should exhibit congruent melting behavior, remains stable at this temperature. Liquid phase begins to appear on the Al-rich corner and the Mg–Y side at this temperature.

The liquidus projection of the Al–Mg–Y system is presented in Fig. 3. On the Al–Mg side in Fig. 3, we can detect that the formation of the primary Al–Mg intermetallic compounds is dramatically suppressed with the addition of Y. With the formation of compounds having high thermal stability, such as Al_2Y, Al_4MgY or Al_3Y, the creep resistance and strength of the alloys at elevated temperatures can be improved as stated in [2]. It is obvious that the Al_2Y primary phase region extends from Al–Y side deeply to the Mg-rich corner, this correspondents to the case when small amount of Al is added to the Mg–10Y alloy to gain well refined microstructure as reported in [3]. The congruent melting of the Al_4MgY phase determined in [16] can also be seen in the currently calculated liquidus projection, but the predicted temperature is higher than 800 °C. Further experimental investigations are necessary in this region to obtain the accurate melting temperature for the Al_4MgY phase.

Summary

The phase relations and thermodynamic description in the Al–Mg–Y system were critically evaluated from the experimental information available in the literatures. A set of self-consistent thermodynamic parameters describing the Gibbs energy of each individual phase as a function of composition and temperature were derived.

Thought further experimental investigation is still needed to obtain more accurate phase diagram information, such as the solid solubility of Mg in the Al_2Y phase and the congruent melting temperature of the Al_4MgY phase, one can already make various calculations of practical interest using the current thermodynamic description.

Acknowledgements The authors are grateful for the financial support from the National Key Research and Development Program of China (No. 2016YFB0701202 and No. 2016YFB0301105), the Natural Science Foundation of Shandong province (ZR2017BEM022) and the Youth Foundation of Shandong Academy of Sciences (2014QN024).

References

1. Z. Yang, J.P. Li, J.X. Zhang, G.W. Lorimer, J. Robson, Acta Metall. Sin. (Engl. Lett.) **21**, 313–328 (2008)
2. G. Pettersen, H. Westengen, R. Hoier, O. Lohne, Mater. Sci. Eng., A **207**, 115–120 (1996)
3. D. Qiu, M.X. Zhang, J.A. Taylor, P.M. Kelly, Acta Mater. **57**, 3052–3059 (2009)
4. J.C. Dai, M.A. Easton, S.M. Zhu, G.H. Wu, W.J. Ding, J. Mater. Res. **27**, 2790–2797 (2012)
5. J.C. Dai, S.M. Zhu, M.A. Easton, M.X. Zhang, D. Qiu, G.H. Wu, W.C. Liu, W.J. Ding, Mater. Sci. Eng., A **576**, 298–305 (2013)
6. A. Pisch, R. Schmid-Fetzer, G. Cacciamani, P. Riani, A. Saccone, R. Ferro, Z. Metallkd. **89,** 474–477 (1998)
7. G. Cacciamani, P. Riani, G. Borzone, N. Parodi, A. Saccone, R. Ferro, A. Pisch, R. Schmid-Fetzer, Intermetallics **7**, 101–108 (1999)
8. J. Gröbner, R. Schmid-Fetzer, A. Pisch, G. Cacciamani, P. Riani, R. Ferro, Z. Metallkde. **90**, 872–880 (1999)
9. J. Gröbne, D. Kevorkov, R. Schmid-Fetzer, Z. Metallkd. **92**, 2–7 (2001)
10. S. De Negri, A. Saccone, G. Cacciamani, R. Ferro, Intermetallics **11**, 1125–1134 (2003)
11. G. Cacciamani, S. De Negri, A. Saccone, R. Ferro, Intermetallics **11**, 1135–1151 (2003)
12. L.L. Jin, D. Kevorkov, M. Medraj, P. Chatrand, J. Chem. Thermodynamics. **58**, 166–195 (2013)
13. S. Al Shakhshir, M. Medraj, J. Phase Equilb. Diffus. **27**, 231–244 (2006)
14. X.J. Liu, C.P. Wang, M.Z. Wen, X. Chen, F.S. Pan, Rare Met. **25**, 441–447 (2006)
15. M.E. Drits, E.M. Padezhnova, T.V. Dobatkina, Russ. Metall. **3**, 197–201 (1979)
16. O.S. Zarechnyuk, M.E. Drits, R.M. Rykhal, V.V. Kinzhibalo, Russ. Metall. **5**, 214–217 (1980)
17. K.O. Odinev, I.N. Ganiev, V.V. Kinzhibalo, K.K. Kurbanov, Tsvetn. Metall. **4**, 75–77 (1989)
18. N. Saunders, CALPHAD **14**, 61–70 (1990)
19. S.H. Liu, Y. Du, H.L. Chen, CALPHAD **30**, 334–340 (2006)
20. C.P. Guo, Z.M. Du, C.R. Li, CALPHAD **31**, 75–88 (2007)
21. M. Hillert, L.I. Staffansson, Acta Chem. Scand. **24**, 3618–3626 (1970)
22. B. Sundman, J. Agren, J. Phys. Chem. Solids **42**, 297–301 (1981)
23. B. Sundman, B. Jansson, J.-O. Andersson, CALPHAD **9**, 153–190 (1985)
24. G.J. Shiflet, J.K. Lee, H.I. Aaronson, CALPHAD **3**, 129–137 (1979)
25. Y.M. Muggianu, M. Gambino, J.-P. Bros, J. Chim. Phys. **72**, 83–88 (1975)

Finite Element Simulation of Hot Spinning for GH4169 Superalloy Thin-Walled Shell

Bangqi Yin, Degui Liu, Xiangyi Xue, Yang Wu, Hongchao Kou and Jinshan Li

Abstract GH4169 superalloy is widely used in aviation, aerospace and other fields due to its high strength, good creep resistance and comprehensive fatigue performance and so on. Spinning which possesses good flexibility and low cost is an economic and rapid forming method for thin-walled parts of revolution, so it is quite suitable for the forming of the GH4169 superalloy thin-walled shell in this paper. Based on the finite element method, the hot spinning finite element (FE) model of GH4169 superalloy thin-walled shell was established in the present work, and the influences of process parameters such as roller feed rate and roller working radius on the forming process were investigated and these process parameters were optimized. The results show that excessive roller feed rate will lead to stress concentration at the place where the roller is in contact with the blank sheet during the forming process, and that too large or too small radius of roller fillet may cause great strain difference between the inner and outer surface of the blank. An ideal combination of process parameters is obtained with the roller feed rate of 1.33 mm/r, and the radius of roller fillet of 20 mm.

B. Yin (✉) · X. Xue · Y. Wu · H. Kou · J. Li
State Key Laboratory of Solidification Processing, Northwestern Polytechnical University, Xi'an 710072, China
e-mail: ybq358@163.com

X. Xue
e-mail: xuexy@nwpu.edu.cn

Y. Wu
e-mail: 709700642@qq.com

H. Kou
e-mail: hchkou@nwpu.edu.cn

J. Li
e-mail: ljsh@nwpu.edu.cn

D. Liu
Aeronautical Key Laboratory of Plastic Forming Technology, Beijing Aeronautical Manufacturing Technology Research Institute, Beijing 100024, China
e-mail: 15910321681@163.com

© Springer Nature Singapore Pte Ltd. 2018

Y. Han (ed.), *Advances in Materials Processing*, Lecture Notes in Mechanical Engineering, https://doi.org/10.1007/978-981-13-0107-0_120

Keywords GH4169 superalloy · Hot spinning · Process parameters
Finite element simulation

Introduction

GH4169 superalloy is widely used in gas turbines, modern aero engines and high-temperature applications [1–4] due to its excellent high-temperature strength, good heat corrosion resistance, comprehensive fatigue performance and fracture toughness and so on [5–8]. Spinning is an advanced continuous and local metal forming process, where a rotating blank is progressively shaped over a mandrel to produce rotationally symmetrical shapes [9]. Compared with other processing method, spinning has many advantages such as high quality, high precision, high efficiency and low cost [10–13]. Therefore, it is quite suitable for the forming of GH4169 superalloy components. However, the deformation of the GH4169 alloy is difficult to control at room temperature due to its high deformation resistance, which tends to generate rupture at the beginning of spinning and fracture on the edge of workpiece. Therefore, it is very important to develop a hot-spinning technology for production of GH4169 superalloy products.

Nowadays, although a large number of works have been carried out on the theoretical study and finite element simulation analysis of spinning [14–16], the related researches are still inadequate. Marghmaleki et al. [17] established the three-dimensional finite element model of the annular aluminum sheet spinning and studied the thermal effect of spinning process by explicit finite element method. Also, Li et al. [18] established a thermo-mechanical coupled three-dimensional elastic-plastic finite element model of thin-walled titanium alloy shell based on ABAQUS/Explicit platform and the flame boundary condition was applied. In the aspect of hot spinning simulation of superalloys, Sun et al. [19] established a thermo-mechanical coupled three-dimensional elastoplastic finite element model of the hot spinning of Ni–Cr–W–Mo alloy curved generatrix profile and studied the distributions of temperature fields, stress fields and strain fields in spinning process. Han et al. [20] established the three-dimensional thermo-mechanical elastic-plastic model of thin-walled titanium alloy shell by using the commercial finite element software ABAQUS, and the influence of process parameters such as preheating temperature and the deviation ratio on the temperature gradient and fittability were studied.

In the present work, a three-dimensional coupled thermal-mechanical finite element model of hot spinning for GH4169 superalloy thin-walled shell was established based on the finite element software. The influence of roller feed rate and roller working radius were investigated.

The Finite Element Simulation of Hot Spinning

Establishment of the FE Model

The hot spinning of GH4169 superalloy thin-walled shell is a complicated process with material nonlinearity, geometrical nonlinearity and boundary nonlinearity, thus making it difficult to control. Considering the difficulty and accuracy of spinning, some necessary simplications are carried out in this paper:

(1) The central part of the blank is set as a hollow area;
(2) The area of line contact between rollers and blank is very small, so the heat exchange between roller and workpiece is neglected;
(3) The influence of gravity and inertia force is ignored in the calculation;
(4) The external heat source is not taken into consideration.

Based on the discussion above, a 3D elastic-plastic coupled thermal-mechanical FE model for the hot spinning of thin-walled shell is established using the finite element software, as shown in Fig. 1. A blank is tied to a mandrel, making the blank and mandrel rotate synchronously. Meanwhile, the axial and radial feeding is achieved by the moving track of the roller. In this FE model, the contact between the material and tools is simulated with the penalty contact method. Besides, the friction on the contact surfaces applies the Coulomb friction model and remains unchanged during the hot spinning.

Prior to spinning, the mandrel was preheated to prevent a sharp drop in the temperature of blank when it reaches the mandrel in the first place. Heat flux on a surface caused by convection and radiation to the environment, and heat generation resulting from frictional sliding and plastic straining during the spinning were taken into consideration. Besides, a gap thermal conduction has been applied to simulate the heat exchange between workpiece and mandrel since it is a complicated combination of thermal conductions of the contact point, gap substance, and radiation.

Since hot spinning is a complicated dynamic contact process, and sensitivity of the linear element to the mesh distortion is less than that of the quadratic element,

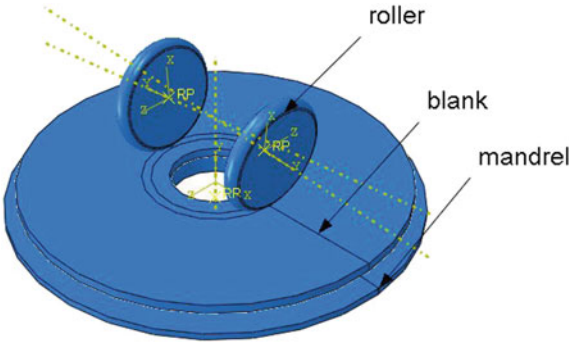

Fig. 1 Diagram of FE model for hot spinning

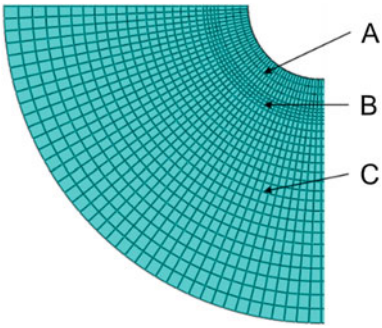

Fig. 2 The finite element distribution of blank

the linear element is employed in the paper. In this model, all components are set as deformable parts. For the blank, 3D 8-noded hexahedral elements with linear reduction integration were applied. Meanwhile, the adaptive meshing technology is adopted to avoid severe mesh distortion caused by larger inhomogeneous plastic deformation during the process. The blank is meshed into 12, 960 elements and there is 3 layers in the thickness direction. As is shown in Fig. 2, the blank is divided into 3 parts. The undeformed region at center of the blank (A zone) is discretized with uniform hexahedral elements. There is severe deformation in the fillet transition region (B zone), and the mesh is refined in this area. The mesh size in the main forming area (C zone) decreases gradually from end to center of the blank. For the rollers and the mandrel, they are meshed with 3D 8-noded hexahedral elements.

Some Necessary Parameters for FE Modeling

In the present work, the material of the blank is GH4169 alloy. The true stress-strain curves are shown in Fig. 3, and its physical properties at high temperature are endowed with the same parameters as Ni-base superalloy with similar composition, as shown in Table 1. The material of the mandrel is defined as 3Cr2W8V.

It is assumed that the roller temperature is 60 °C, and the environment temperature is 20 °C. The basic simulation parameters of hot spinning and the values of the variable parameters are listed in Tables 2 and 3, respectively. In simulations, when the influencing laws of some one parameter on the deformation characteristics of hot spinning are studied, the values of other parameters are endowed with the basic ones.

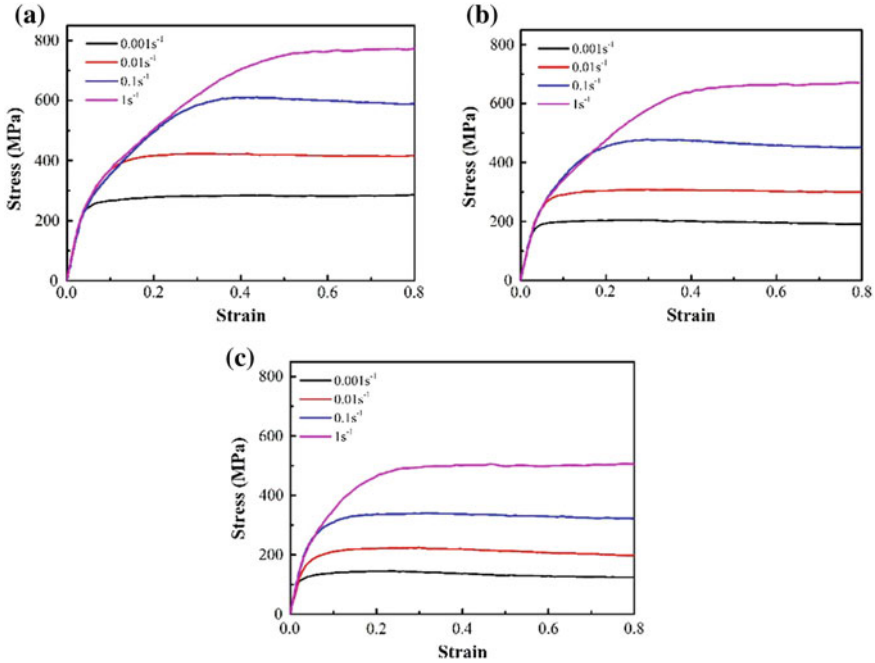

Fig. 3 True stress-strain curves of GH4169 superalloy at different deformation conditions **a** 900 °C; **b** 950 °C; **c** 1000 °C

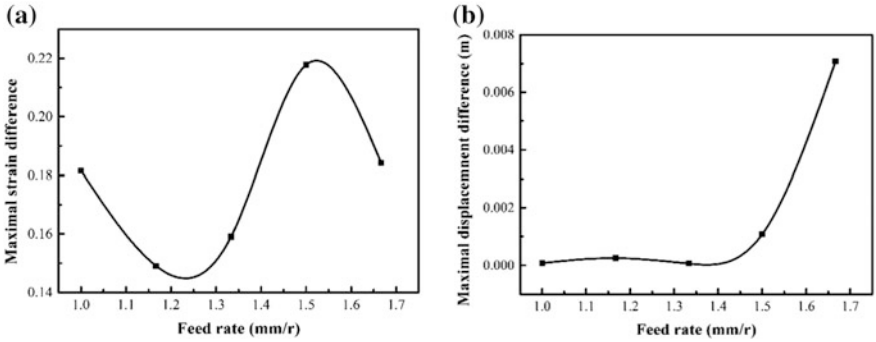

Fig. 4 Effects of roller feed rate on strain difference (**a**) and displacement difference (**b**)

Table 1 Material parameters of GH4169 alloy

Parameter	Value										
T [°C]	100	200	300	400	500	600	700	800	900	1000	1100
E [GPa]	207	202	196	190	184	177	171	164	157	150	143
c [J kg^{-1} °C^{-1}]	419	436	449	466	474	486	574	596	609	618	626
λ [W m^{-1} °C^{-1}]	10.4	12.4	14.4	16.3	18.4	20.4	22.4	24.3	26.3	28.4	30.4
α [10^{-6} °C^{-1}]	11.8	12.4	12.8	13.2	13.6	14.1	14.7	15.2	15.7	16.1	16.6

Table 2 Basic simulation parameters of hot spinning

Parameter	Value
Initial diameter of disk blank [mm]	860
Initial thickness of disk blank [mm]	20
Diameter of roller [mm]	260
Roller working radius [mm]	20
Blank temperature [°C]	950
Half cone angle of mandrel [°]	85
Rotation speed of mandrel [r min^{-1}]	120
Friction coefficient between disk blank and roller	0.01
Feed rate of roller [mm r^{-}]	1.33
Contact heat transfer coefficient [W/(m^2 °C)]	1650 [19]
Heat transfer coefficient between blank and mandrel [W/(m^2 °C)]	18.5 [19]
Radiation coefficient of blank [W/(m^2 °C)]	0.65 [19]
Heat transfer coefficient between mandrel and environment [W/(m^2 °C)]	20 [19]
Radiation coefficient of mandrel [W/(m^2 °C)]	0.8 [19]

Table 3 Parameter values for the FEM simulation

Parameter	Value
Roller feed rate [mm r^{-1}]	1, 1.167, 1.33, 1.5, 1.667
Roller working radius [mm]	12, 15, 20, 25, 30

Result and Discussion

The Influence of Process Parameters on Spinning

In the present work, the influences of roller feed rate and roller working radius on the forming process are analyzed. In the process of spinning, strain concentrates mainly on fillet of mandrel and may cause fracture of workpiece. Therefore, the difference in strain of two tracks on the inside and outside surfaces of the blank is

used as a measure of the crack trend. The wrinkle trend is an important quality index of the spun part, and the maximal displacement difference between two adjacent nodes at the edge of the blank is defined as the index qualifying the wrinkle trend.

Effects of Roller Feed Rate on Spinning

The effects of roller feed rate on the strain difference and displacement difference are shown in Fig. 4. From Fig. 4a, it can be seen that with the increase of roller feed rate, the maximal strain difference between two sides of the blank decreases firstly and increases later and then decreases again. During the process of spinning, the deformation area of place where roller and blank contact each other is a spiral band. When the roller feed rate is a relative smaller value, the overlap of spiral band results in the inhomogeneous circumferential flow of material, which causes poor fittability of spun part and great strain difference. If the value of roller feed rate is too large, the overlap part is small and the spinning force is large, resulting in a great strain difference between inside surface and outside surface. As is shown in Fig. 4b, the roller feed rate has a neglectable effect on the maximal displacement at the edge of the blank with roller feed rate ranging from 1 to 1.4 mm/r. When the feed rate is larger than 1.4 mm/r, the maximal displacement rises greatly with the increase of feed rate. These effects can explained by the unstable plastic deformation process and metal accumulation ahead of the forming roller when deformation degree or velocity is too large. Besides, the friction causes the temperature on contact point between forming roller and spun parts rising a lot due to large deformation velocity. This high-temperature and pressure condition will lead to a change in the deformation state of local zone.

Effects of Roller Working Radius on Spinning

Figure 5 shows the effects of roller working radius on strain difference and displacement difference. Figure 5a illustrates that, the strain difference is a relatively large value and increases slightly when the roller working radius increases from 12 to 15 mm, and then it decreases at first then increases again with the increase of roller working radius. If the roller working radius is too small, the cutting phenomenon occurs easily and will result in large local strain at the contact point. Meanwhile, too large roller working radius can lead to larger spinning force, which may cause the strain at outside surface increasing a lot and the strain difference increasing accordingly. Figure 5b indicates that the maximal displacement difference decreases firstly and then increases with the increase of roller working radius. When the roller working radius is a relative smaller value, the cutting phenomenon may lead to the excessive wall thickness reduction and wrinkle in the forming

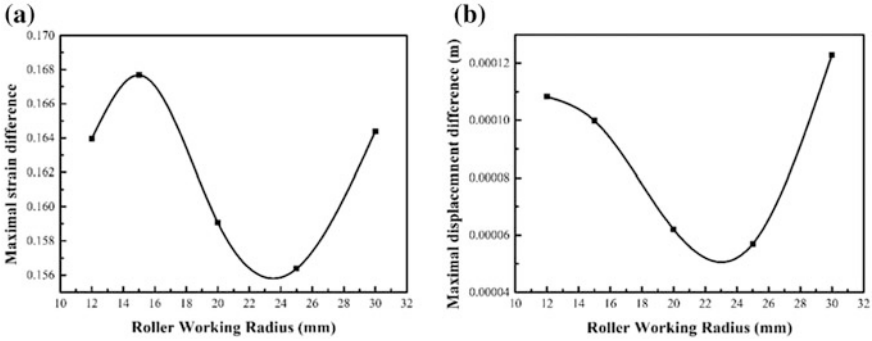

Fig. 5 Effects of roller working radius on strain difference (**a**) and displacement difference (**b**)

process. With the increase of roller working radius, the cutting phenomenon tends to disappear and the displacement difference decreases. While if the roller working radius increases to a critical value, the increase of roller working radius makes it difficult for material to flow along the axial direction and thus resulting in the spun parts wrinkling at the outside surface, especially at the edge of the blank.

Determination of Processing Parameters and Multipass Spinning Simulation Results

According to the discussion above, a comparison of spinning quality of different processing parameters is shown in Table 4. Considering spinning quality as well as forming efficiency, a preferable combination of processing parameters is gained in this paper: the roller feed rate is 1.33 mm/r, and the roller working radius is 20 mm. In the present work, the movement of the roller adopt a track of straight line, and the first spinning pass and adjacent spinning pass both employ the angle of 5°. The diagram of spinning angle is shown in Fig. 6.

With the selected processing parameters and spinning angle, a relatively satisfactory results of hot spinning is obtained, as shown in Fig. 7. From the figure below, it can be clearly seen that as the spinning pass continues to increase, the stress distribution comes to being more inhomogeneous and the phenomenon of

Table 4 Comparison of spinning quality with different processing parameters

Parameter	Strain difference	Displacement difference
Roller feed rate [mm r^{-1}]	1.167 < 1.33 < 1< 1.667 < 1.5	1.33 < 1< 1.167 < 1.5 < 1.667
Roller working radius [mm]	25 < 20 < 30 < 12 < 15	25 < 20 < 15 < 12 < 30

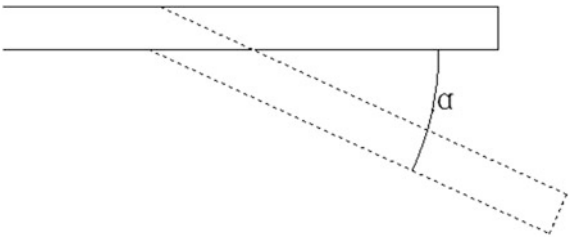

Fig. 6 Diagram of spinning angle

stress concentration becomes more obvious. This may be caused by the residual stresses after every spinning pass. Because of the nonuniform plastic deformation, residual stresses occur in spun parts, which may have great effects on the stress distribution of the forming parts on the next pass. Besides, the distribution of the wall thickness distribution is more uneven with the increase of spinning pass. This effect can be explained by the accumulation of uneven deformation at each spinning pass. After each pass, there appear more and more wrinkles on the surface of the blank. During the hot spinning, the uneven surface changes the contact state between roller and blank, thus making a great difference on the quality of the spun parts.

As the hot spinning is a continuous local plastic deformation process, it is difficult to control the shape, size and accuracy of forming parts, and wrinkles and cracks caused by uneven deformation are easy to occur in actual processing. In order to gain a better understanding of the quality of the spun parts, the simulation for the last pass of the hot spinning is selected as the analysis object in this paper, as shown in Fig. 8. From the figure below, it can be seen that there are stress concentration phenomenon in many places of spinning parts during the simulation, especially where the roller contacts the blank, which may cause cracks in the actual spinning parts. This may be caused by the free spring back of the blank. The degree of springback increases near the mouth of the blank, which makes the blank produce an outward bending effect, thus leading to large radial compressive stresses on the surface. Besides, it is obvious that there exist over thinning and material accumulation near the end of the blank, which causes a lot of wrinkles at the edge of the spun parts. On the one hand, the gap of the spinning is relatively small, which will increase the deformation degree of the material. As the deformation resistance increases, more and more metals flow to the front of the roller, thus the phenomenon of material accumulation occurs. On the other hand, the depth at which the roller presses into the blank increases, which causes the area of place where the roller contact the blank increasing and the spinning force rising up.

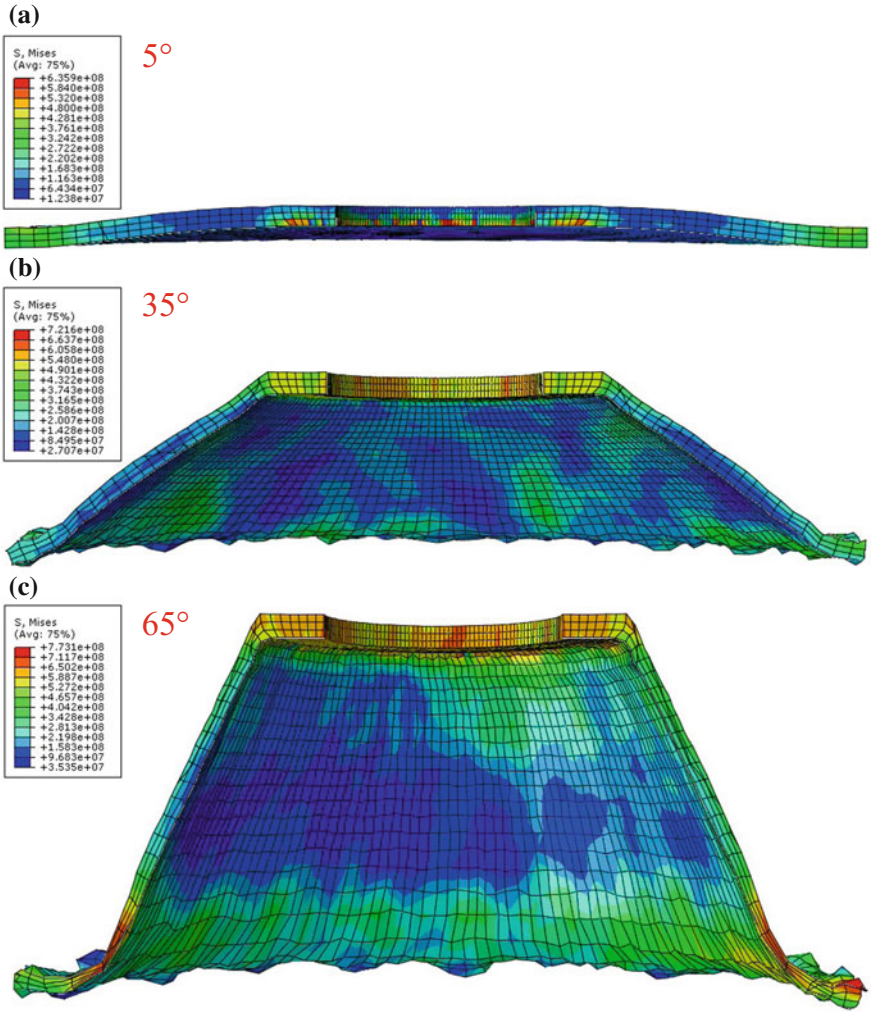

Fig. 7 Multipass spinning simulation results

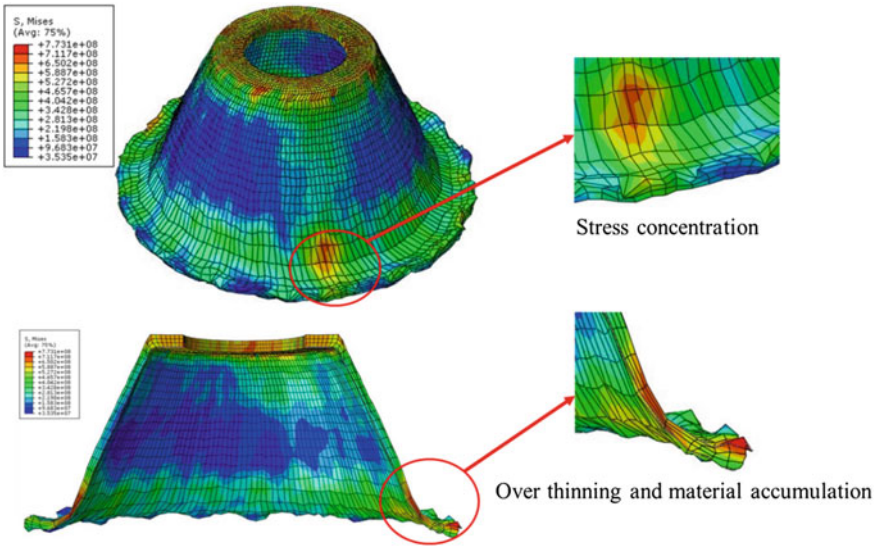

Fig. 8 Some defects occurred during the hot spinning simulation

Conclusions

In this paper, a 3D elastic-plastic coupled thermal-mechanical FE model for the hot spinning of thin-walled shell was established using the finite element software. The influences of process parameters such as roller feed rate and roller working radius on the forming process were investigated and these process parameters were optimized. The conclusions are as follows:

(1) With the increase of roller feed rate, the strain difference decreases firstly and increases later then decreases again. Meanwhile, the displacement difference has little change at first, then there is a sharp increase after the roller feed rate reaches a critical value. An appropriate range of roller feed rate is between 1.167 mm/r and 1.33 mm/r.
(2) When the roller working radius increases, the strain difference increases firstly and decreases later then increases again. Simultaneously the displacement difference decreases firstly and then increases. A suitable range of roller working radius is from 20 to 25 mm.
(3) A satisfactory combination of processing parameters is gained in this paper: the roller feed rate is 1.33 mm/r, and the roller working radius is 20 mm. Through the analysis of the final spun parts in the simulation, it is found that there is stress concentration phenomenon in the place where the skirt and the main body meets each other and the fillet transition area of the blank, and it is clear that over thinning and material accumulation exists near the end of the blank.

Acknowledgements This work was supported by the Program of Introducing Talents of Discipline to Universities ("111" Project, No. B08040).

References

1. X. Yang, W. Li, J. Li et al., FEM analysis of temperature distribution and experimental study of microstructure evolution in friction interface of GH4169 superalloy. Mater. Design **84**, 133–143 (2015)
2. G. Chen, Y. Zhang, D.K. Xu et al., Low cycle fatigue and creep-fatigue interaction behavior of nickel-base superalloy GH4169 at elevated temperature of 650 °C. Mat. Sci. Eng. A **655**, 175–182 (2016)
3. N.Y. Ye, M. Cheng, S.H. Zhang et al., Effect of δ phase on mechanical properties of GH4169 alloy at room temperature. J. Iron. Steel Res. Int. **22**, 752–756 (2015)
4. J.H. Du, X.D. Lu, Q. Deng et al., Progress in the research and manufacture of GH4169 alloy. J. Iron. Steel Res. Int. **22**, 657–663 (2015)
5. X. Yang, W. Li, Y. Feng et al., Physical simulation of interfacial microstructure evolution for hot compression bonding behavior in linear friction welded joints of GH4169 superalloy. Mater. Design **104**, 436–452 (2016)
6. P. Lv, X. Sun, J. Cai et al., Microstructure and high temperature oxidation resistance of nickel based alloy GH4169 irradiated by high current pulsed electron beam. Surf. Coat. Tech. **309**, 401–409 (2017)
7. B.S. Lu, L.G. Wang, Y. Huang, Effect of deformation rate on interfacial heat transfer coefficient in the superalloy GH4169 hot forging process. Appl. Therm. Eng. **108**, 516–524 (2016)
8. Y. Ning, M.W. Fu, X. Chen, Hot deformation behavior of GH4169 superalloy associated with stick δ phase dissolution during isothermal compression process. Mat. Sci. Eng. A **540**, 164–173 (2012)
9. F. Ma, H. Yang, M. Zhan, Plastic deformation behaviors and their application in power spinning process of conical parts with transverse inner rib. J. Mater. Process. Tech. **210**, 180–189 (2010)
10. L. Huang, H. Yang, M. Zhan et al., Numerical simulation of influence of material parameters on splitting spinning of aluminum alloy. T. Nonferr. Metal. Soc. **18**, 674–681 (2008)
11. W. Xu, X. Zhao, H. Ma et al., Influence of roller distribution modes on spinning force during tube spinning. Int. J. Mech. Sci. **113**, 10–25 (2016)
12. L. Huang, R. Zeng, X. Zhang et al., Study on plastic deformation behavior of hot splitting spinning of TA15 titanium alloy. Mater. Design **58**, 465–474 (2014)
13. M. Zhan, X. Wang, H. Long, Mechanism of grain refinement of aluminium alloy in shear spinning under different deviation ratios. Mater. Design **108**, 207–216 (2016)
14. L. Wang, H. Long, Investigation of material deformation in multi-pass conventional metal spinning. Mater. Design **32**, 2891–2899 (2011)
15. M. Zhan, H. Yang, J.H. Zhang et al., 3D FEM analysis of influence of roller feed rate on forming force and quality of cone spinning. J. Mater. Process. Tech. **187**, 486–491 (2007)
16. L. Wang, H. Long, Roller path design by tool compensation in multi-pass conventional spinning. Mater. Design **46**, 645–653 (2013)

17. I.S. Marghmaleki, Y.T. Beni, A.R. Noghrehabadi et al., Finite element simulation of thermomechanical spinning process. Proc. Eng. **10**, 3769–3774 (2011)
18. H. Li, M. Zhan, H. Yang et al., Coupled thermal-mechanical fem analysis of power spinning of titanium alloy thin-walled shell. Chin. J. Mech. Eng. **44**, 187–193 (2008). (in Chinese)
19. L.L. Sun, H.C. Kou, R. Hu et al., FEM numerical simulation of first-pass heat spinning for Ni–Cr–W–Mo superalloy workpiece with curvilinear shape. J. Plast. Eng. **17**, 33–38 (2010). (in Chinese)
20. D. Han, M. Zhan, H. Yang, Deformation mechanism of TA15 shells in hot shear spinning under various load conditions. Rare Metal Mat. Eng. **42**, 243–248 (2013)

First-Principles Study of Au-Doping Effects in $Hg_{1-x}Cd_xTe$ (x = 0.25, 0.5, 0.75)

Xueli Sun, Dechun Li, Zhaogen Zhong, Shengzhi Zhao, Kejian Yang, Xiangyang Li, Reng Wang and Ji Liu

Abstract First-principles calculations based on density functional theory have been performed for the structural and electronic properties of Au-doped mercury cadmium telluride (MCT, $Hg_{1-x}Cd_xTe$), using the state-of-the-art computational method with the Heyd-Scus-eria-Ernzerh (HSE) of hybrid functional to correct the band gap. Structural relaxations, charge densities, electron localization functions (ELFs), density of states (DOSs) and band structures were obtained to reveal dopant stability and doping efficiency. The bonding characteristics between Au and host atoms were discussed by analysing charge densities and ELFs. The influence of Cd composition on the electronic structure of Au-doped $Hg_{1-x}Cd_xTe$ (x = 0.25, 0.5, 0.75) was also analysed by the calculated DOSs and band structures. It is found that $Hg_{0.75}Cd_{0.25}Te$ and $Hg_{0.5}Cd_{0.5}Te$ are more suitable for the p-type doping than

X. Sun · Z. Zhong
Naval Aviation University, Yantai 264001, Shandong, China
e-mail: snow0530@126.com

Z. Zhong
e-mail: zhongzhaogen@163.com

D. Li (✉) · S. Zhao · K. Yang · J. Liu
School of Information Science and Engineering, Shandong University, Jinan 250100, China
e-mail: dechun@sdu.edu.cn

S. Zhao
e-mail: Shengzhi_zhao@sdu.edu.cn

K. Yang
e-mail: k.j.yang@sdu.edu.cn

J. Liu
e-mail: liuji60@sdu.edu.cn

X. Li · R. Wang
Shanghai Institute of Technical Physics, Chinese Academy of Sciences, Shanghai 200083, China
e-mail: lixy@mail.sitp.ac.cn

R. Wang
e-mail: tiaoqi1980@163.com

© Springer Nature Singapore Pte Ltd. 2018

Y. Han (ed.), *Advances in Materials Processing*, Lecture Notes in Mechanical Engineering, https://doi.org/10.1007/978-981-13-0107-0_121

$Hg_{0.25}Cd_{0.75}Te$. Meanwhile, for both $Hg_{1-x}Cd_xTe$ and Au-doped $Hg_{1-x}Cd_xTe$, the linear relationships between band gaps and Cd composition are presented.

Keywords $Hg_{1-x}Cd_xTe$ · First-principles · Hybrid functional · Au doping Electronic structures

Introduction

In recent years, infrared technique is desirable for many potential applications in military, medical treatment, metallurgy, chemical industry, aerospace, etc. [1]. Many different materials have been developed to meet the requirements of infrared detection, such as lead sulphide, indium arsenide, Lithium tantalite and $Hg_{1-x}Cd_xTe$ [2, 3]. Among these materials, MCT is the most important and versatile material for detector applications over the entire IR range, due to its advantages like lower concentration of the intrinsic carrier, lower surface state density, smaller dielectric constant and larger optical absorption coefficient [4]. On the other hand, the performance of infrared detectors is still limited by the electrical properties, size and uniformity parameter of materials [5]. Therefore, in order to further improve the performance of MCT-based infrared detector, precisely controllable doping has been studied for decades to replace the native acceptor doping. N-type doping of $Hg_{1-x}Cd_xTe$ is achieved easily by indium in situ substituting mercury, whose carrier concentration can be obtained above 1018 cm^{-3} [6]. However, well-controlled p-type doping is still one of the most serious bottlenecks in MCT-based detector technology currently. As is known to all, there are mainly two kinds of p-type $Hg_{1-x}Cd_xTe$. The undoped p-type MCT is dominated by the presence of mercury vacancies, which acts as a trap center limiting the minority-carrier lifetime [7–9]. For doped p-type material, the group-I elements are found to substitute on metal sites while group V elements substitute on Te sites [10]. The group V impurities, especially arsenic in $Hg_{1-x}Cd_xTe$, can provide a shallow accepter level, which show a complicated amphoteric behaviour, and require high temperature p-type activation. However, the high temperature process is unacceptable for II–VI heterostructures [11–13]. Considering the group I impurities, lithium, copper and silver are all fast diffuser and undesirable for p-type dopant of $Hg_{1-x}Cd_xTe$ [14, 15].

In recent years, Au is currently favoured as an acceptor in II–VI heterostructures [16]. Experimental results have indicated that gold is a good p-type dopant in MCT grown by liquid phased epitaxy (LPE), molencular beam epitaxy (MBE) and vapour phase epitaxy (VPE) [17–19]. Au-doped $Hg_{1-x}Cd_xTe$ has been investigated with first- principles calculations, which indicated that the gold impurity not only maintains a relative stable bonding with the host atom, but also behaves as an acceptor and produce a shallow energy level in $Hg_{1-x}Cd_xTe$ [20]. However, the effects of in situ gold dopant on the electronic structure of $Hg_{1-x}Cd_xTe$ still await comprehensive investigations, especially the bonding mechanism and band

structure. The influence of the Cd composition on the electronic structure of Au-doped $Hg_{1-x}Cd_xTe$ has also not been reported so far.

In general, density functional theory (DFT) using the local density approximation (LDA) or the generalized gradient approximation (GGA) often severely underestimates the band gap (Eg), so it is much better to apply a hybrid functional to correct the band gap underestimation in the first-principles calculations [21–23]. In this paper, by first-principles calculations based on DFT as implemented in the Vienna ab initio simulation package (VASP) code with a modified HSE hybrid exchange-correlation functional, band structures and density of states are calculated. Besides, the ELF of undoped $Hg_{1-x}Cd_xTe$ and Au-doped $Hg_{1-x}Cd_xTe$ are obtained, and the influence of the mole fraction of Cd on the electronic structure of $Hg_{1-x}Cd_xTe$ and Au-doped $Hg_{1-x}Cd_xTe$ has also been studied.

Models and Methods

It is well known that, $Hg_{1-x}Cd_xTe$ is a pseudobinary alloy, which means two type of cations occupy the cation sites randomly. The disorder may have some effects on the electronic properties of the doped MCT. In order to simplify the calculation procedure, we only choose the perfect quasi-zinc-blende crystal structure as the basis of the primitive cell. We have considered a $2 \times 2 \times 2$ supercell of 64 atoms consisting of eight $Hg_{1-x}Cd_xTe$ unit cells in quasi-zinc-blende crystal structure, in which Hg (0.5, 0.5, 0.5) atoms were replaced by Au atom. By the well-known Vegard's law, the relationship between lattice parameters and Cd composition of MCT can be expressed as [24]:

$$a = 6.46136 + 0.019999x \tag{1}$$

The lattice parameters of $Hg_{0.75}Cd_{0.25}Te$, $Hg_{0.5}Cd_{0.5}Te$, and $Hg_{0.25}Cd_{0.75}Te$ are 6.466, 6.471, and 6.476, respectively. All calculations were performed by using VASP with projector-augmented wave (PAW) for the interaction between electrons and ions, and Perdew-Burke-Ernzerh (PBE)-based HSE functional for the exchange-correlation. The cutoff energy for the plane-wave expansion was set to 500 eV. Hybrid functional mixes about 17% nonlocal Hartree-Fock exchange with 87% semilocal exchange, and the HSE screening parameter is set to a value of 0.2 $Å^{-1}$. Brillouin-zone integration is performed on the Monkhorst-Pack scheme with a $2 \times 2 \times 2$ mesh. A small Gaussian broadening $\sigma = 0.05$ eV was applied so that the peaks of the defect cannot merge with the band continuum for the calculations of density of states (DOS). In the calculations of band structure, k-point meshes were replaced by high symmetry point, which was set manually according to the Brillouin zone path. In addition, all structures were fully optimized until the force on each atom is smaller than 0.03 eV/Å. All the results were obtained on the basis of the convergences.

Results and Discussion

Atomic Relaxations

The existence of Au impurity in MCT induces structural relaxations of host atoms and modifies the electronic structure of the system. The calculated radial relaxations of the nearest-neighbor (Te_1) and the next-nearest-neighbor (Hg_2 or Cd_2) atoms around the in situ Au impurity are shown in Table 1. The positive and negative signs denote outward relaxation and inward relaxation, respectively. The subscript is the number of the atomic shells around Au. The results indicate that Te_1 anions and Hg_2 (Cd_2) cations around the in situ impurity Au relax inward. The covalent radii difference between dopant cation Au and host atoms Hg (the covalent radii are 1.34 and 1.49 Å for Au and Hg, respectively) causes the shortening of the bond lengths. And the inward relaxations of Te_1 atoms around impurity are induced by the strong bonds between Au and host atoms. On the other hand, the inward relaxation of Te_1 cations is larger than that of Hg_2 (Cd_2) cations. The reason for the phenomena is also connect with the strong bond between Au atom and Te atom. The relationship between the inward radial relaxation which is represent by DR/A and relaxation ratio of the Te_1 atoms and the mole fraction of Au-doped MCT are shown in Fig. 1. Obviously, with Cd composition increasing, the inward relaxations of the Te atoms become smaller due to the strong bond between Cd and Te atom.

Bonding Mechanism

To find out the reason of Te_1 atoms inward relaxation in Au-doped MCT, the valance charge and the difference of valence charge density have been calculated. The difference of valence charge density is obtained by the subtraction between total valence charge density of Au-doped MCT and total valence charge density of undoped MCT, which represents the charge redistribution when atoms are brought together to form the crystal. The difference of charge density and the valence charge density (2D) in the (101) plane for Au-doped $Hg_{1-x}Cd_xTe$ is shown in Figs. 2 and 3, respectively.

Table 1 The relaxation results of Au-doped $Hg_{1-x}Cd_xTe$

X		Au–Te_1	Au–Cd_2	Au–Hg_2	Au–Te_2
0.25	Change [Å]	−0.1053	−0.03406	−0.0403	−0.0041
	Change ratio [%]	3.76	0.74	0.88	0.07
0.5	Change [Å]	−0.1033	−0.03506	−0.0422	−0.0064
	Change ratio [%]	3.7	0.77	0.92	0.12
0.75	Change [Å]	−0.0995	−0.0359		−0.0061
	Change ratio [%]	3.5	0.78		0.11

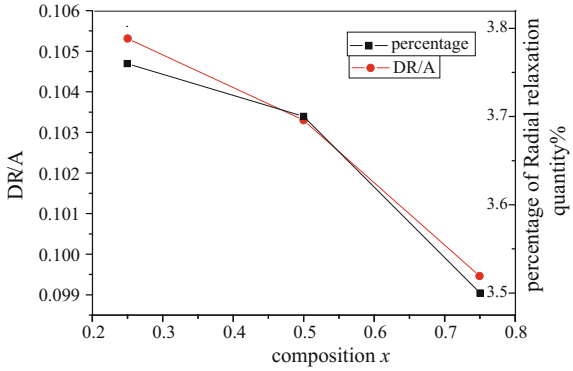

Fig. 1 Relationship between the inward radial relaxations and relaxation ratio of the Te_1 atoms and the mole fraction of MCT

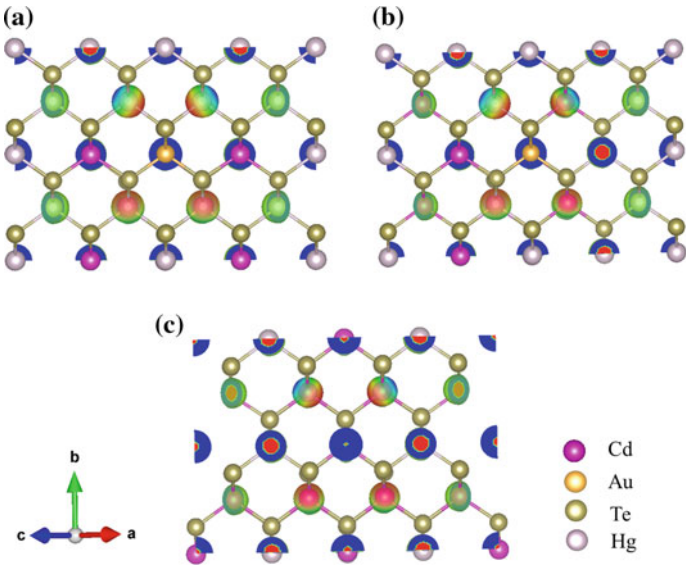

Fig. 2 Relationship between the inward radial relaxations and relaxation ratio of the Te_1 atoms and the mole fraction of MCT

In Fig. 2, the presence of charge (the blue part) around Au atom indicates that Au has stronger ability to attract electrons than that of the substituted Hg atom. Thus, we can infer that the bond of Te–Au is stronger than that of Te–Hg. Additionally, the presence of charge around Cd atoms implies that the electron attraction of Cd atoms become easier than that of undoped $Hg_{1-x}Cd_xTe$. Namely, the bond of Cd–Te in Au-doped $Hg_{1-x}Cd_xTe$ is stronger than that in undoped

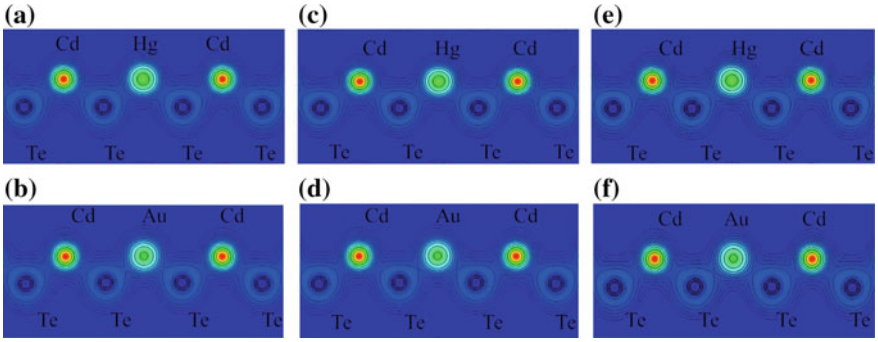

Fig. 3 The valence charge density (2D) in the (101) plane for **a** undoped $Hg_{0.75}Cd_{0.25}Te$, **b** Au-doped $Hg_{0.75}Cd_{0.25}Te$, **c** undoped $Hg_{0.25}Cd_{0.75}Te$, **d** Au-doped $Hg_{0.75}Cd_{0.25}Te$, **e** undoped $Hg_{0.5}Cd_{0.5}Te$ and **f** Au-doped $Hg_{0.25}Cd_{0.75}Te$

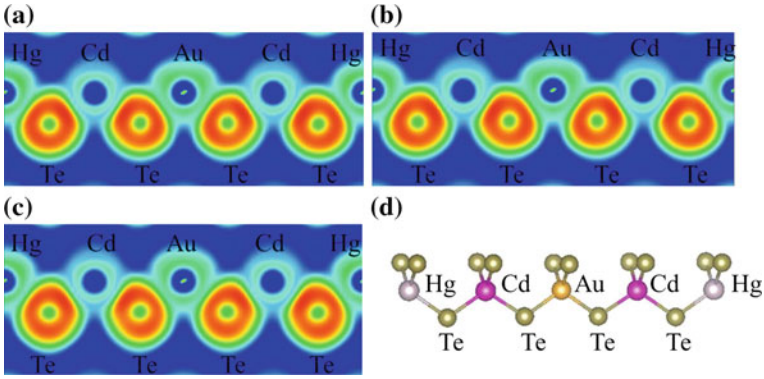

Fig. 4 ELF in the (101) plane for **a** Au-doped $Hg_{0.75}Cd_{0.25}Te$, **b** Au-doped $Hg_{0.5}Cd_{0.5}Te$ and **c** Au-doped $Hg_{0.25}Cd_{0.75}Te$. **d** Local structure around Au impurity

$Hg_{1-x}Cd_xTe$. The strong bonds of both Au–Hg and Cd–Te in $Hg_{1-x}Cd_xTe$ can guarantee the stability of doping behaviour.

From Fig. 3d–f, the electron accumulation between Au and Te in Au-doped MCT shows that the Au–Te bonds are stronger than the substituted Hg–Te bonds. It indicates a relatively stable structure after Au in situ substituting Hg. The result was in good agreement with the conclusion of the difference of charge density. As it can be seen from Fig. 3d–f, the electron accumulation along Au–Te decreases gradually with the increase of Cd composition, which means that Au–Te bonds weaken with the increase of Cd composition. In addition to the smaller gold radius, the strong bonding also results in the host atoms inward relaxation.

As it is shown in Fig. 4, we calculated the ELF to analyse the bonding characteristics [25–27]. In Fig. 4a, the value of ELF is about 0.85 between Au and Te, indicating the polar covalent bonding between them. In addition, the ELF value

around Hg atoms and Cd atoms is 0.85 and 0.87, respectively, clearly implying the polar covalent bonding between Hg(Cd) and Te. The bonding characteristics of Au–Te are similar with that of Hg–Te according to the results. ELF value of Au–Te is less than that of Cd–Te, which indicates that Au–Te bond is weaker than Cd–Te bond. The results in Fig. 4b, c are analogous to Fig. 4a. For Fig. 4b, c, the ELF values of Au–Hg bonds are 0.84 and 0.82, respectively. ELF value between Te and Au shows a weakening tendency with the increase of Cd composition. The results accords with the conclusion of Te atoms inward relaxation and valence charge density. In summary, more relatively stable structure after Au in situ substituting Hg for MCT with lower Cd composition.

Band Structures and Densities of States

To find out the reason of Te1 atoms inward relaxation in Au-doped MCT, the valance charge and the difference of valence charge density have been calculated. The difference of valence charge density is obtained by the subtraction between total valence charge density of Au-doped MCT and total valence charge density of undoped MCT, which represents the charge redistribution when atoms are brought together to form the crystal. The difference of charge density and the valence charge density (2D) in the (101) plane for Au-doped $Hg_{1-x}Cd_xTe$ is shown in Figs. 2 and 3, respectively.

According to the results of Bonding mechanism, Au-doped $Hg_{0.75}Cd_{0.25}Te$ is considered to be more stable than Au-doped $Hg_{0.5}Cd_{0.5}Te$ and Au-doped $Hg_{0.25}Cd_{0.75}Te$. Thus, $Hg_{0.75}Cd_{0.25}Te$ is chosen to discuss the change of Band structure and DOS. The Band structure and DOS of undoped $Hg_{0.75}Cd_{0.25}Te$ and Au-doped $Hg_{0.75}Cd_{0.25}Te$ are presented in Fig. 5. Fermi level is set to zero. Obviously, the conduction band minimum and valence band maximum in Fig. 5a, c are both located at Γ point, which means that undoped $Hg_{0.75}Cd_{0.25}Te$ and Au-doped $Hg_{0.75}Cd_{0.25}Te$ have direct band gaps. It can be obtained that the band gap of $Hg_{0.75}Cd_{0.25}Te$ is 0.163 eV, which is in good agreement with the experimental value. Compared with $Hg_{0.75}Cd_{0.25}Te$, the band gap of Au-doped $Hg_{0.75}Cd_{0.25}Te$ in Fig. 5c reduced significantly, which is 0.13 eV. It can be seen from Fig. 5a, c that the band structure of Au-doped $Hg_{0.75}Cd_{0.25}Te$ is more intensive than that of $Hg_{0.75}Cd_{0.25}Te$. From the Fig. 5c, three defect bands emerge upon the top of valence band (the red lines), and the Fermi level shifts downward into valence band (−0.5 to 0.38 eV). The in situ gold is dominant acceptor.

The origin of these impurity states can be explored by using the partial density of states (PDOS), as shown in Fig. 6. From the total DOS of Au-doped $Hg_{0.75}Cd_{0.25}Te$ shown in Fig. 6b, it can be clearly seen that the impurity states mixing together the valence band (−0.5 to 0.38 eV), which result in the promotion of the valence band. The Fermi level extends into the valence band maximum (VBM) and the Au impurity act as a shallow acceptor. Figure 6c–f show that the states around the Fermi level mainly come from Au-p, Au-d and Te-p states after Au in situ

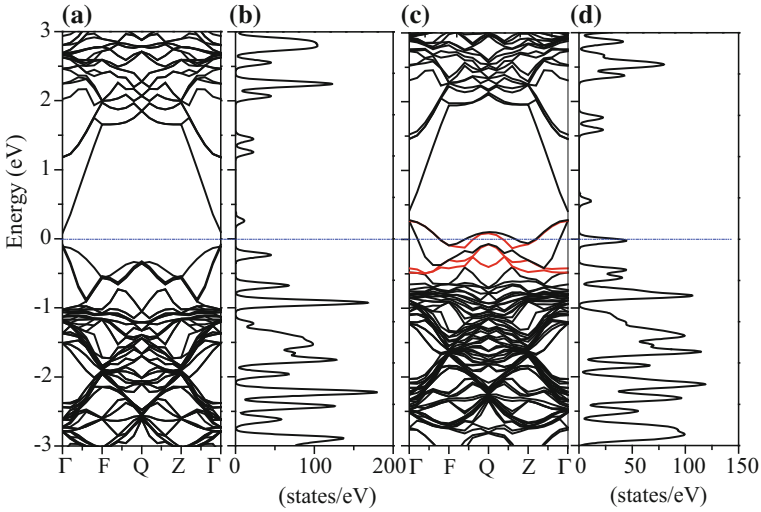

Fig. 5 **a** Band structure of undoped $Hg_{0.75}Cd_{0.25}Te$, **b** total DOS of undoped $Hg_{0.75}Cd_{0.25}Te$, **c** band structure of Au-doped $Hg_{0.75}Cd_{0.25}Te$ and **d** total DOS of Au-doped $Hg_{0.75}Cd_{0.25}Te$

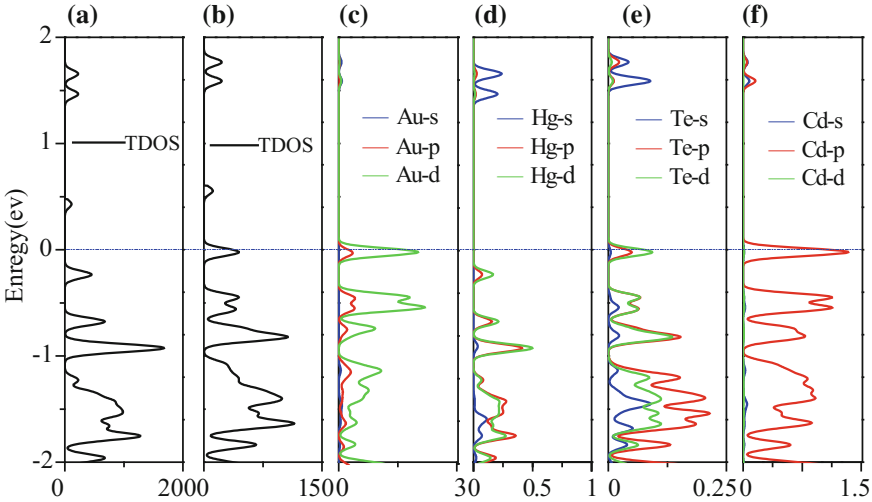

Fig. 6 Total DOS of **a** undoped $Hg_{0.75}Cd_{0.25}Te$ and **b** Au-doped $Hg_{0.75}Cd_{0.25}Te$. Partial DOSs of **c** Au, **d** Hg, **e** Cd and **f** Te in Au-doped $Hg_{0.75}Cd_{0.25}Te$

substituting Hg. That is to say, these impurity states for the Au doped system produced by the hybridization among Au-p, Au-d and Te-p state.

The band structures of undoped $Hg_{1-x}Cd_xTe$ and Au-doped $Hg_{1-x}Cd_xTe$ with different Cd compositions are shown in Fig. 7. The band structures of

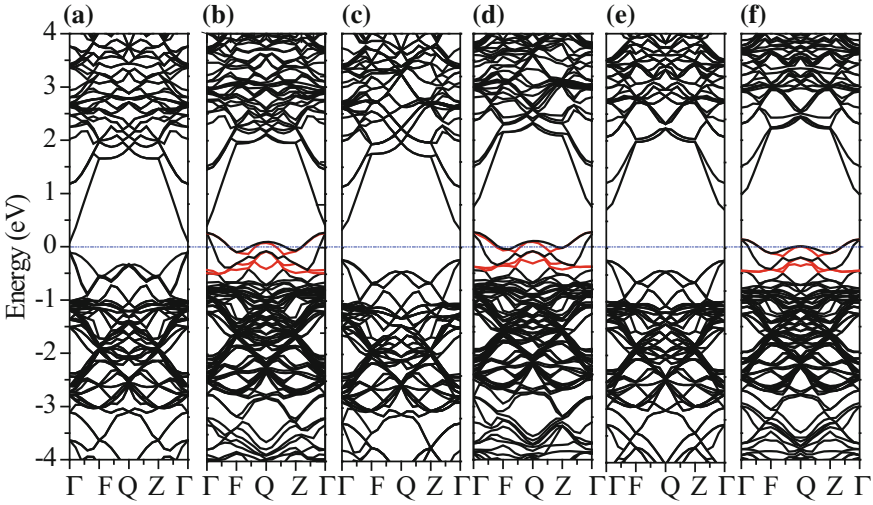

Fig. 7 The band structures of **a** undoped $Hg_{0.75}Cd_{0.25}Te$, **b** Au-doped $Hg_{0.75}Cd_{0.25}Te$, **c** undoped $Hg_{0.5}Cd_{0.5}Te$, **d** Au-doped $Hg_{0.5}Cd_{0.5}Te$, **e** undoped $Hg_{0.25}Cd_{0.75}Te$ and **f** Au-doped $Hg_{0.25}Cd_{0.75}Te$

Au-doped $Hg_{1-x}Cd_xTe$ ($x = 0.5$, $x = 0.75$) have similar features with Au-doped $Hg_{0.75}Cd_{0.25}Te$. The band structures of Au-doped $Hg_{1-x}Cd_xTe$ are more intensive than that of $Hg_{1-x}Cd_xTe$. Besides, three impurity energy levels emerge upon the top of valence band (the red lines). In addition, the Fermi level extends into the VBM due to the hybridization between impurity energy levels and the energy levels near VBM. Au atoms act as an acceptor. The VBM of $Hg_{0.75}Cd_{0.25}Te$ and $Hg_{0.5}Cd_{0.5}Te$ are rose by about 0.27 eV, and the value of $Hg_{0.25}Cd_{0.75}Te$ is about 0.14 eV. It indicates a more obvious promotion of VBM of $Hg_{0.75}Cd_{0.25}Te$ and $Hg_{0.5}Cd_{0.5}Te$ than that of $Hg_{0.25}Cd_{0.75}Te$. So it is more suitable for $Hg_{0.75}Cd_{0.25}Te$ and $Hg_{0.5}Cd_{0.5}Te$ to realize the p-type doping.

As is known to all, the relationship between the band gap and Cd composition (or the temperature) is very important to $Hg_{1-x}Cd_xTe$ materials. Here, we just study the impact of Cd composition on the band gap, when $T = 0$ K. $Hg_{1-x}Cd_xTe$ materials are narrow gap semiconductor who has a tunable band gap with Cd composition. A number of expressions approximating Eg (x, T) are available at present. The most widely used expression is due to Laureti et al. [28], which can be expressed as

$$\begin{aligned} E_g = &-0.303(1-x) + 1.606x - 0.132x(1-x) + [6.3(1-x) \\ &- 3.25x - 5.29x(1-x)]10^{-4}T^2/[11(1-x) + 18.7x + T](\text{eV}) \end{aligned} \tag{2}$$

where Eg is in electron Volt and T is in Kelvin.

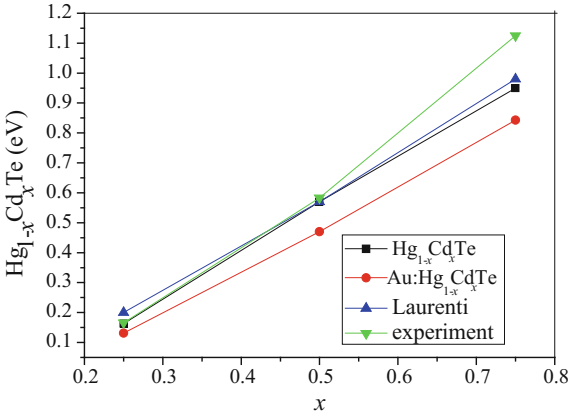

Fig. 8 Band gaps of $Hg_{1-x}Cd_xTe$ and Au-doped $Hg_{1-x}Cd_xTe$ with different x

The band gap versus Cd composition is plotted in Fig. 8. The band gaps of undoped MCT have been calculated to be 0.163, 0.57 and 0.95 eV, respectively. It can be found that the relationship between perfect band gap and Cd composition can be described by a linear equation, $Eg = 1.574x - 0.226$ (the black square line), for x ranging from 0 to 1. Based on the linear equation, the band gap of HgTe is −0.23 eV when the $x = 0$, whose experiment value is between 0 and −0.3 eV. While in the case of $x = 1$, the band gap of CdTe is 1.35 eV, whose experiment value is 1.58 eV. The band gaps of Au-doped $Hg_{1-x}Cd_xTe$ have been calculated to be 0.131, 0.47 and 0.843 eV, respectively. The change trend of band gaps is similar with the undoped $Hg_{1-x}Cd_xTe$ case, that the band gap (the red circle line) increases with Cd composition decrease. According to the results, the linear equation of band gaps of Au-doped $Hg_{1-x}Cd_xTe$ has been fitted, $Eg = 1.42x - 0.231$. The band gap energy tunability results in IR detector applications that span the entire IR range. It will be very convenient that we can fabricate the MCT detectors working in a certain wavelength by select the doped MCT with a corresponding Cd component. The band gaps we have obtained are well consistent with not only the theoretical values which are calculated by Eq. (2) (the blue uptriangle line) but also the experimental values (the green downtriangle line), as is shown in Fig. 8. It indicates that the results we have calculated are very reliable.

Summary

In summary, the effects of gold impurity on structural and electronic properties of $Hg_{1-x}Cd_xTe$ have been systematically studied based on the first-principles calculations. The results indicate that the gold impurity maintains a relatively strong bond with the host atom. It is also found that the Te atoms inward relaxation and the Au–Te bonds show a weakening trend with the increase of Cd composition. The calculated DOSs and band structures imply that the in situ Au impurity behaves as

an acceptor and produces three impurity energy levels above VBM. It is also found that $Hg_{0.75}Cd_{0.25}Te$ and $Hg_{0.5}Cd_{0.5}Te$ are more suitable for the p-type doping than $Hg_{0.25}Cd_{0.75}Te$. Meanwhile, for both MCT and Au-doped MCT, the linear relationships between band gaps and Cd composition are presented.

Acknowledgements Project supported by National Natural Science Foundation of major research projects China (91538201), Taishan Scholar Engineering under Special Funding (ts201511020), National Science Foundation of China (61575109, 21173134, 21473103), Natural Science Foundation of Shandong Province (ZR2014FM035), and Open project of Infrared Imaging Materials and Devices Laboratory of Chinese Academy of Sciences (IIMDKFJJ-14-07).

References

1. A. Rogalski, Toward third generation HgCdTe infrared detectors. J. Alloy. Compd. **371**, 53–57 (2004)
2. R. Rehm, M. Walther, J. Fleißner, J. Schmitz, J. Ziegler, W. Cabanski, R. Breiter, Bispectral thermal imaging with quantum-well infrared photodetectors and InAs/GaSb type II superlattices. Proc. SPIE. **6206**, 62060Y (2006)
3. A. Rogalski, Material considerations for third generation infrared photon detectors. Infrared Phys. Technol. **50**, 240–252 (2007)
4. A. Rogalski, HgCdTe infrared detector material: history, status and outlook. Rep. Prog. Phy. **62**, 2267–2336 (2005)
5. J. Bajaj, J.M. Arias, M. Zandian, J.G. Pasko, L.J. Kozlowski, R.E. De Wames, W.E. Tennant, Molecular beam epitaxial HgCdTe material characteristics and device performance: reproducibility status. J. Electron. Mater. **24**, 1076–1607 (1995)
6. S.K. Ghandhi, N.R. Taskar, K.K. Parat, Indium doping of n-type HgCdTe layers grown by organometallic vapor phase epitaxy. Appl. Phys. Lett. **57**, 252 (1990)
7. L.Z. Sun, X. Chen, Y.L. Sun, Relaxations and bonding mechanism in Hg1 − xCdxTe with mercury vacancy defect: first-principles study. Phys. Rev. B **73**, 195206 (2006)
8. M.A. Berding, A. Sher, A.B. Chen, Vacancy formation and extraction energies in semiconductor compounds and alloys. J. Appl. Phys. **68**, 5064–5076 (1990)
9. M.A. Berding, M. van Schilfgaarde, A. She, First-principles calculation of native defect densities in Hg0.8Cd0.2Te. Phys. Rev. B **50**, 1519 (1994)
10. H.R. Vydyanath, J.A. Ellsworth, C.M. Devaney, Electrical Activity, mode of incorporation and distribution coefficient of group V elements in Hgl−xCdxTe grown from tellurium rich liquid phase epitxial growth solutions. J. Electron. Mater. **16**, 13–25 (1987)
11. C.H. Grein, J.W. Garland, S. Sivananthan, P.S. Wijewarnasuriya, F. Aqariden, M. Fuchs, Arsenic incorporation in MBE grown Hg1−xCdxTe. J. Electron. Mater. **28**, 789–792 (1999)
12. S. H. Wei, S.B. Zhang, Chemical trends of defect formation and doping limit in II–VI semiconductors: the case of CdTe. Phys. Rev. **B66** (2002)
13. S. Sivananthan, P.S. Wijewarnauriya, F. Awariden, Mode of arsenic incorporation in HgCdTe grown by MBE. J. Electron. Mater. **26**, 621–624 (1997)
14. D.J. Friedman, G.P. Carey, C.K. Shih, Diffusion of Ag and Hg at the Ag/(Hg, Cd)Te interface. Appl. Phys. Lett. **48**, 44–46 (1986)
15. H.D. Shih, M.A. Kinch, F. Aaariden, P.K. Liao, H.F. Schaake, V. Nathan, Development of gold-doped $Hg_{0.79}Cd_{0.21}Te$ for very-long-wavelength infrared detectors. Appl. Phys. Lett. **82**, 4157–4159 (2003)
16. A.J. Ciani, S. Ogut, I.P. Batra, Concentrations of native and gold defects in HgCdTe from first principles calculations. J. Electron. Mater. **33** (2004)

17. A. Singh, A.K. Shukla., S. Jain, B.S. Yadav, R. Pal, Electrial characeriatics of electroless gold contacts on p-type $Hg_{1-x}Cd_xTe$. Mater. Sci. Semicond. Process. **26**, 294–300 (2014)
18. F. Aqariden, H.D. Shih, M.A. Kinch, H.F. Schaake, Electrical properties of low-arsenic-doped HgCdTe grown by molecular beam epitaxy. Appl. Phys. Lett. **78** (2001)
19. M.C. Chen, R.A. Schiebel, Observation of a deep level in p-type Hg0.78Cd0.22Te with high dislocation density. J. Appl. Phys. **71**, 5269–5271 (1992)
20. J.L. Han, L.Z. Sun, X.D. Qu, Y.P. Chen, J.X. Zhong, Electronic properties of the Au impurity in $Hg_{0.\ 75}Cd_{0.\ 25}Te$: first-principles study. Phys. Rev. B **404**, 131–137 (2009)
21. D.C. Li, M. Yang, Y.Q. Cai, S.Z. Zhao, Y.P. Feng, First principles study of the ternary complex model of EL2 defect in GaAs saturable absorber. Opt. Express **20**, 6258 (2012)
22. D.C. Li, M. Yang, Y.Q. Cai, S.Z. Zhao, Y.P. Feng, First-principles study of the effect of BiGa heteroantisites in GaAs:Bi alloy. Comp. Mater. Sci. **63**, 178–181 (2012)
23. D.C. Li, M. Yang, Y.Q. Cai, S.Z. Zhao, Y.P. Feng, First principles study of Bismuth alloying effects in GaAs saturable absorber. Opt. Express **20**, 11574–11580 (2012)
24. Q.X. Wang, J.R. Yang, T. Sun, Y.F. Wei, W.Z. Fang, L. He, Relationship between lattice parameters and compositions of molecular beam epitaxial $Hg_{1-x}Cd_xTe$ films. Acta Phys. Sin. **54**, 3726–3733 (2005)
25. A. Savin, O. Jepsen, J. Flad, O.K. Andersen, H. Preuss, H.G. Schnering, Electron localization in solid-state structures of the elements: the diamond structure. Int. Ed. Engl. **31**, 187–188 (1992)
26. J. Lento, J.L. Mozos, R.M. Nieminen, Charged point defects in semiconductors and the supercell approximation. J. Phys. Condens. Matter **14**, 2637–2645 (2002)
27. S.I. Simak, U. Haussermann, I.A. Abrikosov, O. Eriksson, J.M. Wills, S. Lidin, B. Johansson, Stability of the anomalous large-void CoSn structure. Phys. Rev. Lett. **79**, 1333–1336 (1997)
28. J.P. Laurenti, J. Camassel, A. Bouhemadou, Temperature dependence of the fundamental absorption edge of mercury cadmium telluride. J. Appl. Phys. **67**, 6454–6460 (1990)

Preparation and Numerical Simulation of Structural Parameters of Ni–Fe Bimetallic Porous Anode Support for Solid Oxide Fuel Cells

Xin Gu, Jie Yu, Wenhui Ma, Guoqiang Lv, Dingwen Kang and Guangjie Xie

Abstract Optimization of preparation conditions for Ni–Fe bimetallic porous anode-supported planar solid oxide fuel cells was carried out. Experimental and literature data were used to build a 3D model of an anode-supported solid oxide fuel cell. A parametric study was carried out to determine the influence of various design parameters on performance. Some operating variables, such as thickness and porosity, were changed to observe their effects on the cell performance. Increased thickness had an adverse influence on the performance of the cell, but an increase in porosity improved performance.

Keywords Solid oxide fuel cells · Chemical reaction · Thickness Porosity

X. Gu · J. Yu (✉) · W. Ma · G. Lv · D. Kang · G. Xie
Faculty of Materials and Metallurgical Engineering, Kunming University of Science and Technology, Kunming 650093, China
e-mail: kgyujie@163.com

X. Gu
e-mail: 872101202@qq.com

W. Ma
e-mail: mwhsilicon@126.com

G. Lv
e-mail: 397393808@qq.com

D. Kang
e-mail: 2511396810@qq.com

G. Xie
e-mail: 196679139@qq.com

W. Ma · G. Lv
State Key Laboratory of Complex Nonferrous Metal Resources Cleaning Utilization in Yunnan Province, The National Engineering Laboratory for Vacuum Metallurgy, Kunming 650093, China

© Springer Nature Singapore Pte Ltd. 2018

Y. Han (ed.), *Advances in Materials Processing*, Lecture Notes in Mechanical Engineering, https://doi.org/10.1007/978-981-13-0107-0_122

Introduction

The electrodes of the SOFC play a crucial role in determining the fuel cell's main transport processes and reactions [1], so the design of SOFC electrodes is critical. Many electrochemical physical phenomena occur at the same time, directly influencing the working conditions and the properties of SOFC electrodes. Dong et al. [2] constructed a micro model and optimized structures for an anode-supported SOFC. They found that electrochemical reactions and mass transport depend on the particle size and the thickness of functional layers. Some studies have been conducted to optimize microstructural materials [3–6]. The study by Li [5] showed that the combination effect of electrodes can increase the exchange current density and reduce open polarization resistance. They used SSM55 ($Sm_{0.5}Sr_{0.5}MnO_3$) material in YSZ (yttria-stabilized zirconia) scaffold to improve the distribution uniformity and connectivity of nanoparticles. Jumlat [6] studied material optimization using GDC (gadolinium-doped ceria) and NiO as anodic material, then used starch as the pore former. This design achieved increased performance at operating temperatures (600, 550, and 500 °C) and the maximum power density was 48.62 mW/cm^2 at 600 °C. To improve the electrochemical properties of cells, some studies considered the characteristic parameters of the microstructure. Costamagna [7] used an analytical model to improve the electrode conductivity, cell polarization, ohm effect, and the thicknesses of the electrode to maximize the current density of the cell. These studies showed that microstructure optimization has a clear effect on cell performance, especially the output voltage and output current density. Bhattacharya [8] optimized the porosity of the electrode, the effective diffusivity, and the rate of chemical reactions in the microstructure of a SOFC. The results showed that optimized design and operating conditions can increase the cell performance of an anode-supported tubular cell by using an isothermal model [9]. The optimal distribution of porosity and electrode pore size were obtained by using GA (genetic algorithm) for microstructure optimization [10]. Microstructure design using COMSOL Multiphysics 3.5a was conducted by Shi [10, 11] to maximize the average current density under certain voltage.

Many efforts have exploited anode-supported SOFC models [12–18]. In a macrography model, the electrode is modeled as a porous structure of purely electron-conducting particles, and electrochemical reactions occur only at the electrolyte/electrode interface, and the reaction zone layers act as the boundary of the interface [12, 13, 15–18]. However, electrochemical reactions actually occur in interfaces and electrodes [19]. Therefore, to enhance the predictive power of single SOFC designs, the electrode reaction should be considered. The purpose of this study was to establish a mathematical model of a planar anode-supported SOFC, considering all the correlative electrochemical, physical, and chemical processes in anode support layer. Then, the model was applied to analyze the influence of thickness and porosity on performance of the anode-supported SOFC.

Table 1 Porosity of Ni–Fe alloy anode substrate

Sample	Pore former (wt%)	Sintering temperature (°C)	Reduction temperature (°C)	Porosity
NF0	6	1450	700	0.2881
NF10	6	1450	700	0.2812
NF30	6	1450	700	0.2179
NF10	8	1450	700	0.2412
NF10	6	1400	700	0.2780
NF10	6	1450	650	0.3009

Experimental

Ni–Fe alloy anode substrate were prepared by reducing the as-sintered NiO–Fe_2O_3 composites containing 0, 10, or 30 wt% of Fe_2O_3, designated NF0, NF10, and NF30, respectively. The $NiCl_2$ and $FeCl_3$ powder were mixed in water at 80 °C. After adding excessive NaOH, the mixture was stirred for 2 h and then filtered 5 times to separate the precipitate. After being completely dried, the material was sintered at 600 °C in air for 3 h. The sintered NiO–Fe_2O_3 and corn starch powders were completely mixed by mill and then pressed into slices. Disc specimens were pressed at 10 MPa, followed by sintering at 1450 °C in air for 4 h. After reduction in H_2 at 700 °C for 2 h, the porous Ni–Fe alloy anode substrate was obtained.

The porosity of the substrate was measured by the Archimedes method. Table 1 lists the porosity of all the samples in distinct states. The reduced sample's had porosity between 0.2179 and 0.3009. The porosity of the Ni–Fe sample was lower than that without Fe addition. The samples sintered at high temperature exhibited larger porosity, and the sample had the greatest porosity when sintered at 1450 °C. Some cracks and bending were observed with sintering and reducing temperatures of 1500 and 750 °C, respectively.

Methodology

Model Formulation

The study used a three-dimensional model of an anode-supported SOFC composite Ni–Fe bimetallic porous anode support and LSGM ($La_{0.9}Sr_{0.1}Ga_{0.8}Mg_{0.2}O_{3-\delta}$) electrolyte. Figure 1 shows the diagram of a planar anode-supported SOFC.

Table 2 shows the dimensions of the SOFC model. This model consists of different reaction layers to define the electrochemical reactions at the boundary of electrolyte-electrode.

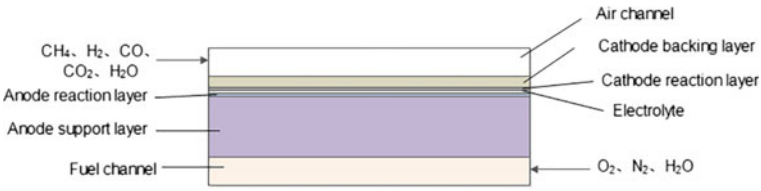

Fig. 1 Schematic of the SOFC

Table 2 SOFC dimensions (mm)

Cell length	10	Anode support layer height	1
Cell width	1	Anode reaction layer height	0.05
Fuel channel height	0.5	Cathode reaction layer height	0.05
Air channel height	0.5	Cathode backing layer height	0.2
Channel width	0.5	Electrolyte height	0.05

COMSOL was used to build the model. The model consists of a mass conservation equation, a momentum conservation equation, a charge conservation equation, and an energy conservation equation.

Physical Parameters

The fuel cell with a temperature of 600 °C, an anode inlet speed of 0.5 m/s, and a cathode inlet speed of 6.5 m/s was simulated. The fuel composition used in the simulation is shown in Table 3.

The physical and electrochemical parameters used in the model are listed in Table 4.

Table 3 The fuel composition

Species	Mole fraction
CH_4	0.171
H_2	0.284
H_2O	0.473
CO	0.028
CO_2	0.044

Table 4 Physical properties

Operating temperature, T(°C)	600
Total pressure, P (atm)	1
Resistivity of electron-conducting particles in anode, $\rho_{el}(\Omega m)$	$\rho_{el,a} = 2.98 \times 10^{-5} \exp\left(-\frac{1332}{T}\right)$
Resistivity of electron-conducting particles in cathode, $\rho_{el}(\Omega m)$	$\rho_{el,c} = 8.11 \times 10^{-5} \exp\left(\frac{600}{T}\right)$
Resistivity of ion-conducting particles in electrolyte, $\rho_{io}(\Omega m)$	$\sigma_{io,c} = 10 \exp\left(\frac{1}{1273} - \frac{1}{T}\right)$
Anode support layer's porosity, ε	0.3
Anode support layer's tortuosity, τ	3.5
Anode reacting layer's porosity, ε	0.25
Anode reacting layer's tortuosity, τ	3
Anode support layer's surface area per unit volume, $A_v(m^2/m^3)$	8.31942×10^5
Anode reacting layer's surface area per unit volume, $A_v(m^2/m^3)$	6.693171×10^6
Cathode reacting layer's porosity, ε	0.3
Cathode backing layer's porosity, ε	0.35
Cathode reacting layer's tortuosity, τ	3
Cathode backing layer's tortuosity, τ	3.5
Cathode reacting layer's surface area per unit volume, $A_v(m^2/m^3)$	2.6×10^6
cathode backing layer's surface area per unit volume, $A_v(m^2/m^3)$	1.08×10^5

Momentum Transfer Process

Taking into account the open flow fields in the cell and the steady state and compressible flow conditions, the continuity and Navier-Stokes equations were used. The Brinkman equation was applied.

$$\frac{\rho}{\varepsilon}\left[(u \cdot \nabla)\frac{u}{\varepsilon}\right] = \nabla \cdot \left\{-pI + \frac{\mu}{\varepsilon}\left[\nabla u + (\nabla u)^T - \frac{2\mu}{3\varepsilon}(u \cdot \nabla)I\right]\right\} - \left(\mu K^{-1} + \beta_F|u| + \frac{Q_{br}}{\varepsilon^2}\right)u + F \quad (1)$$

where K and ε are the permeability and porosity of porous electrodes, respectively, ρ is the fluid density, μ is the dynamic viscosity of fluid, u is the gas velocity, and p is the pressure.

Mass Transfer Process

The mass transport equation included the calculation of the Maxwell-Stefan diffusion coefficient matrix, which simulates the fuel cell flow fields and the steady state material transport in electrodes. To obtain more realistic calculation results, the dusty gas model is used [20].

$$D_{ij} = \frac{3.198 \times 10^{-8} T^{1.75} \left(\frac{1}{M_i} + \frac{1}{M_j}\right)^{\frac{1}{2}}}{p\left(v_i^{\frac{1}{3}} + v_j^{\frac{1}{3}}\right)^2} \tag{2}$$

$$D_{ij}^{eff} = \frac{\varepsilon}{\tau}\left(\frac{1}{D_{ij}^{MS}} + \frac{1}{D_i^{KN}}\right)^{-1} \tag{3}$$

$$D_i^{KN} = \frac{2}{3} r_g \sqrt{\frac{8RT}{\pi M_i}} \tag{4}$$

where D_{ij} is the Maxwell-Stefan diffusion coefficient, D_{ij}^{eff} is the effective diffusion coefficient, D_i^{KN} is the Knudsen diffusion coefficient of species i, and τ and ε are the tortuosity and porosity of the porous layers, respectively. M_i is the molecular weight of species I and r_g is the radius of the pore.

Heat Transfer Process

Heat transfer in gas flow fields was described using the following forms of the energy equation. Based on a ideal gas mixture, the specific heat of the liquid mixture was determined as a function of temperature.

To determine the thermal conductivity of the fluid mixtures, the method of Wassiljewa was used with the Mason modifications proposed by Todd [20, 21]. In the electrode, an improved energy equation was used.

$$\rho_{eff} c_{p,eff} V \nabla T = \nabla\left(k_{eff} \nabla T\right) + S_T \tag{5}$$

$$c_{p,eff} = \varepsilon c_{p,f} + (1 - \varepsilon) c_{p,s} \tag{6}$$

$$k_{eff} = \varepsilon k_f + (1 - \varepsilon) k_s \tag{7}$$

where, $c_{p,eff}$ and k_{eff} are the effective specific heat capacity and effective thermal conductivity of the backing layers, respectively. $c_{p,f}$ is the heat capacity of fluid mixture in substrate layers, $c_{p,s}$ is the heat capacity of the solid phase of substrate

layers, k_f is the thermal conductivity of fluid mixture in substrate layers, and k_s is the thermal conductivity of the solid phase of substrate layers.

Chemical Reactions Process

The fuel composition was hydrogen and carbon monoxide. Therefore, the main reactions considered were the methane reforming reaction and the water gas shift reaction.

$$CH_4 + H_2O \leftrightarrow 3H_2 + CO \qquad \Delta H298 = 206 \text{ KJ/mole} \tag{8}$$

$$CO + H_2O \leftrightarrow H_2 + CO_2 \qquad \Delta H298 = -41.1 \text{ KJ/mole} \tag{9}$$

The chemical reaction rates for the aforementioned reactions are given as [18, 22, 23]:

$$R_r = A_a\left[0.0636T^2 \exp\left(-\frac{27063}{T}\right)C_{CH_4}C_{H_2O} - 3.7 \times 10^{-23}T^4 \exp\left(-\frac{232.78}{T}\right)C_{CO}C_{H_2}^3\right] \tag{10}$$

$$R_s = \varepsilon\left[1.199T^2 \exp\left(-\frac{12509}{T}\right)C_{CO}C_{H_2O} - 67.7T^2 \exp\left(-\frac{16909}{T}\right)C_{CO_2}C_{H_2}\right] \tag{11}$$

where R_r and R_s are chemical reaction rates for the methane reforming and water gas shift reactions, respectively. A_a is the surface area per unit volume.

The rate of production/consumption of various species in the anode support layer can be expressed as follows:

$$S_{CH_4} = -R_r \tag{12}$$

$$S_{H_2} = 3R_r + R_s \tag{13}$$

$$S_{H_2O} = -R_r - R_s \tag{14}$$

$$S_{CO} = R_r - R_s \tag{15}$$

$$S_{CO_2} = R_s \tag{16}$$

Electrochemical Reaction Process

The electrochemical reaction includes the oxidation of carbon monoxide and hydrogen, and the reduction of oxygen.

$$CO + O^{2-} \rightarrow CO_2 + 2e^- \tag{17}$$

$$H_2 + O^{2-} \rightarrow H_2O + 2e^- \tag{18}$$

$$O_2 + 4e^- \rightarrow 2O^{2-} \tag{19}$$

Figure 2 shows the working principle of the anode, including the chemical reactions of the anode support layer and the electrochemical reactions of the anode function layer.

The ion and charge transport in SOFC were simulated by a distributed charge transfer method. Table 5 shows a summary of the charge transfer equation.

Effective electronic conductivities and effective ionic conductivities in the reaction layers were determined as follows:

$$\sigma_{el}^{eff} = \left(\frac{1-\varepsilon}{\tau}\right)\sigma_{el}V_{eff} \tag{20}$$

$$\sigma_{io}^{eff} = \left(\frac{1-\varepsilon}{\tau}\right)\sigma_{io}V_{eff} \tag{21}$$

where V_{eff} is the volume fraction of electrically-conducting particles in the reaction layers, and σ_{el} and σ_{io} are the conductivities of pure electronic and ionic conducting materials, respectively. The electrochemical reactions are described in Butler-Volmer.

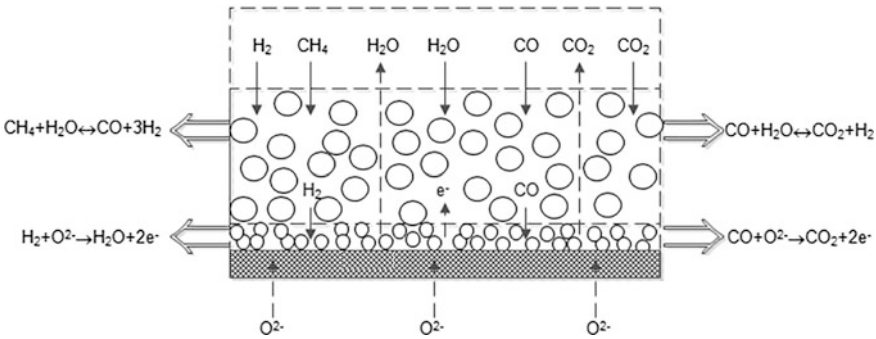

Fig. 2 Anode work schematic

Table 5 The charge transfer equation

Anode support layer	$\nabla \cdot \left(-\sigma_{el,a}^{eff} \nabla \phi_{el}\right) = 0$
Cathode backing layer	$\nabla \cdot \left(-\sigma_{el,c}^{eff} \nabla \phi_{el}\right) = 0$
Anode reacting layer	$\nabla \cdot \left(-\sigma_{el,a}^{eff} \nabla \phi_{el}\right) = -I_a A_v$
	$\nabla \cdot \left(-\sigma_{io,a}^{eff} \nabla \phi_{io}\right) = I_a A_v$
Cathode reacting layer	$\nabla \cdot \left(-\sigma_{el,c}^{eff} \nabla \phi_{el}\right) = I_c A_v$
	$\nabla \cdot \left(-\sigma_{io,c}^{eff} \nabla \phi_{io}\right) = -I_c A_v$
Electrolyte	$\nabla \cdot (-\sigma_{io} \nabla \phi_{io}) = 0$

$$I_{H_2} = I_{O,H_2}\left[C_R \exp\left(\frac{\alpha nF\eta_{act,H_2}}{RT}\right) - C_O \exp\left(-\frac{(1-\alpha)nF\eta_{act,H_2}}{RT}\right)\right] \tag{22}$$

$$I_{CO} = I_{O,CO}\left[C_R \exp\left(\frac{\alpha nF\eta_{act,CO}}{RT}\right) - C_O \exp\left(-\frac{(1-\alpha)nF\eta_{act,CO}}{RT}\right)\right] \tag{23}$$

$$I_{O_2} = I_{O,O_2}\left[C_R \exp\left(\frac{\alpha nF\eta_{act,O_2}}{RT}\right) - C_O \exp\left(-\frac{(1-\alpha)nF\eta_{act,O_2}}{RT}\right)\right] \tag{24}$$

where $I_{O,H2}$, $I_{O,CO}$ and $I_{O,O2}$ are the exchange current densities for H_2, CO oxidation, and O_2 reduction reactions, respectively. C_R and C_O are dimensionless expressions, describing the dependence on the reduced and oxidized species in the reaction, α is the charge transfer coefficient, with a value between 0 and 1, n is the number of electrons involved in the electrochemical reaction, and η is the activation overpotential [24], defined as:

$$\eta_{act,H_2} = \phi_{el,a} - \phi_{io,a} - E_{H_2}^{rev} \tag{25}$$

$$\eta_{act,CO} = \phi_{el,a} - \phi_{io,a} - E_{CO}^{rev} \tag{26}$$

$$\eta_{act,O_2} = \phi_{el,c} - \phi_{io,c} - E_{O_2}^{rev} \tag{27}$$

The E_i^{rev} in Eqs. 25–27 is the equilibrium potential, and is defined as:

$$E_{H_2}^{rev} = \frac{RT}{2F}\ln\left(\frac{p_{H_2}^0 p_{H_2O}}{p_{H_2O}^0 p_{H_2}}\right) \tag{28}$$

$$E_{CO}^{rev} = \frac{RT}{2F}\ln\left(\frac{p_{CO}^0 p_{CO_2}}{p_{CO_2}^0 p_{CO}}\right) \tag{29}$$

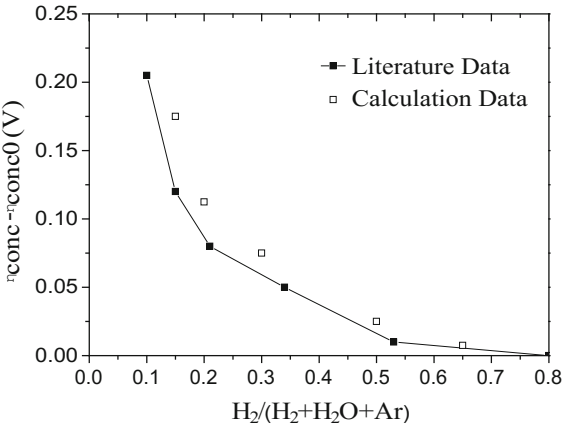

Fig. 3 Comparison with literature data

$$E_{O_2}^{rev} = \frac{RT}{4F} \ln\left(\frac{p_{O_2}}{p_{O_2}^0}\right) \tag{30}$$

Model Validation Analysis

The concentration overpotential data calculated by numerical simulation are compared with the literature [25] data (Fig. 3). The abscissa represents the change in reactant concentration, and the ordinates represent the difference value between the actual and reference concentration overpotential. The concentration overpotential of the reference was measured for a mole fraction of hydrogen in the system equal to 0.8 and in the absence of argon gas. The curves are superimposable, affirming the validity of the model.

Results and Discussion

The thickness of the anode support layer is one of the important parameters determining the performance of SOFC, as shown in Fig. 4a. Increasing the thickness of the anode support layer can increase the ohmic overpotential and can increase the migration of carbon monoxide and hydrogen to the reaction layer.

Figure 4b shows that when the thickness of the anode support layer was 0.1 mm, the maximum power density was 0.5777 W/cm^2. When the thickness of the anode support layer increased from 0.1 to 1.5 mm, the maximum power density was reduced by 15%. Thus, the thin anode support layer can reduce the concentration polarization.

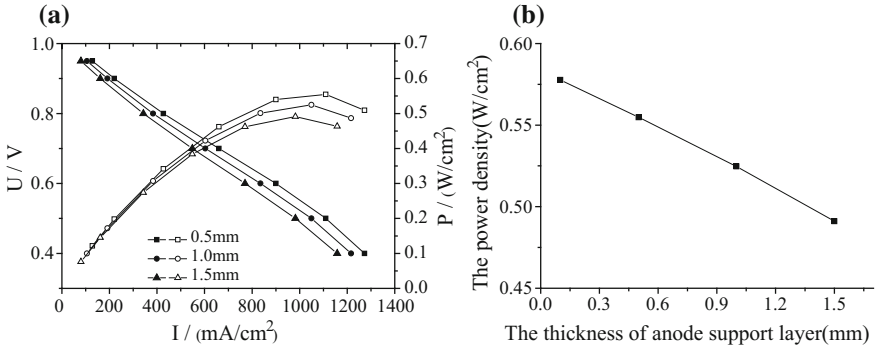

Fig. 4 **a** I–V and power density curve of the anode-supported SOFC with different thickness; **b** Relationship between the power density and anode thickness

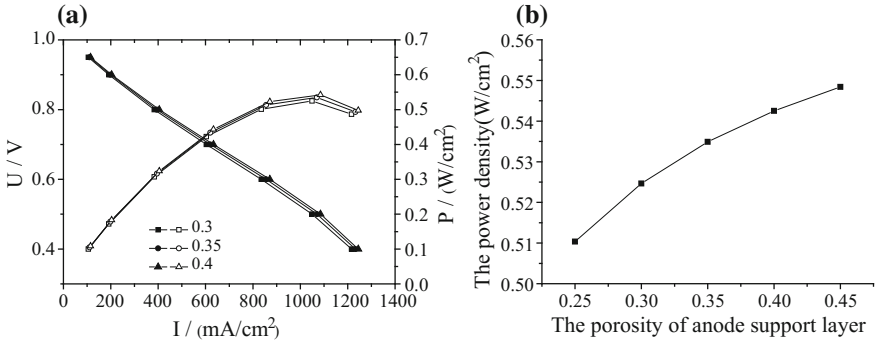

Fig. 5 **a** I–V and power density curve of the anode-supported SOFC with different porosity; **b** Relationship between the power density and anode porosity

Figure 5a shows the effect of porosity on the cell performance of SOFC. Increasing the porosity of the anode support layer can improve the performance of SOFC. This is because mass transfer resistance decreases when the porosity of anode support layer increases. However, the performance did not improve significantly when the porosity of anode support layer increased from 0.3 to 0.4.

The data in Fig. 5b shows that when the porosity of anode support layer was 0.45, the maximum power density was 0.5484 W/cm^2. When the porosity of anode support layer increased from 0.25 to 0.45, the maximum power density increased by 7.5%, indicating that an anode support layer with large porosity will reduce the concentration polarization.

Conclusions

The porosity is improved by increasing the sintering temperature and reducing the reduction temperature. When the sintering temperature exceeds 1450 °C or the reduction temperature is below 700 °C, the sample exhibites cracking and bending.

Increasing porosity improves the performance and reduces the mass transfer resistance, but the cell performance cannot be improved significantly when the porosity of anode support layer increases from 0.3 to 0.4.

Increasing the thickness reduces the rate of chemical reactions and then reduces the chemical reaction space. Because the anode support layer needs to support the entire cell, the thickness of the anode support layer shall not be too thin, and 0.5–1 mm is appropriate.

Acknowledgements The work was supported by the Science and Technology Project of Yunnan Province (No. 2016FB080), the National Natural Science Foundation of China (No. 51764028) and the Science and Technology Program of Yunnan Province (No. 2015RD016).

References

1. P.R. Shearing, Q. Cai, J.I. Golbert, Microstructural analysis of a solid oxide fuel cell anode using focused ion beam techniques coupled with electrochemical simulation. J. Power Sources **195**, 4804–4810 (2010)
2. H.J. Dong, H.N. Jin, C.J. Kim, Microstructural optimization of anode-supported solid oxide fuel cells by a comprehensive microscale model. J. Electrochem. Soc. **153**, A406–A417 (2006)
3. O. Vasylyev, M. Brychevskyi, Y. Brodnikovskyi, The structural optimization of ceramic fuel cells. Univ. J. Chem. **4**, 31–54 (2016)
4. T. Abdullah, L. Liu, Simulation-based microstructural optimization of solid oxide fuel cell for low temperature operation. Int. J. Hydrogen Energy **41**, 13632–13643 (2016)
5. W. Li, C. Xiong, Q. Zhang, Electrochim. Acta **190**, 531–537 (2016)
6. A.L. Jumlat, P. Sathish, Optimizing anode microstructure of intermediate temperature solid oxide fuel cell based on gadolinium doped ceria. Dev. Renew. Energy Technol. 1–4 (2014)
7. P. Costamagna, P. Costa, E. Arato, Some more considerations on the optimization of cermet solid oxide fuel cell electrodes. Electrochim. Acta **43**, 967–972 (1998)
8. D. Bhattacharyya, R. Rengaswamy, Transport, sensitivity, and dimensional optimization studies of a tubular Solid Oxide Fuel Cell. J. Power Sources **190**, 499–510 (2009)
9. D. Bhattacharyya, R. Rengaswamy, C.Y. Finnerty, Isothermal models for anode-supported tubular solid oxide fuel cells. Chem. Eng. Sci. **62**, 4250–4267 (2007)
10. J. Shi, X. Xue, Optimization design of electrodes for anode-supported solid oxide fuel cells via genetic algorithm. J. Electrochem. Soc. **158**, B143–B151 (2010)
11. J. Shi, X. Xue, Microstructure optimization designs for anode-supported planar solid oxide fuel cells. J. Fuel Cell Sci. Technol. **8**, 061006 (2011)
12. P. Aguiar, C.S. Adjiman, N.P. Brandon, Anode-supported intermediate temperature direct internal reforming solid oxide fuel cell. I: model-based steady-state performance. J. Power Sources **138**, 120–136 (2004)
13. J.W. Kim, A.V. Virkar, K.Z. Fung, Polarization effects in intermediate temperature anode-supported solid oxide fuel cells. J. Electrochem. Soc. **146**, 69–78 (1999)

14. H.N. Jin, H.J. Dong, A comprehensive micro-scale model for transport and reaction in intermediate temperature solid oxide fuel cells. Electrochim. Acta **51**, 3446–3460 (2006)
15. B. Sunden, Analysis of chemically reacting transport phenomena in an anode duct of intermediate temperature SOFCs. J. Fuel Cell Sci. Technol. **3**, 89–98 (2006)
16. J. Yuan, B. Sunden, Analysis of intermediate temperature solid oxide fuel cell transport processes and performances. J. Heat Transf. **127**, 1380–1390 (2005)
17. T. Ackmann, L.G.J.D. Haart, W. Lehnert, Modeling of mass and heat transport in plannar substrate type SOFCs. J. Electrochem. Soc. **150**, A783–A789 (2003)
18. W. Lehnert, J. Meusinger, F. Thom, Modelling of gas transport phenomena in SOFC anodes. J. Power Sources **87**, 57–63 (2000)
19. M.M. Hussain, X. Li, I. Dincer, J. Power Sources **189**, 916–928 (2009)
20. B. Todd, J.B. Young, Thermodynamic and transport properties of gases for use in solid oxide fuel cell modelling. J. Power Sources **110**, 186–200 (2002)
21. B.E. Poling, J.M. Prausnitz, J.P. O'Connell, *The Properties of Gases and Liquids*, fifth edn. (The McGraw-Hill Companies, New York, 2000)
22. J.M. Klein, Y. Bultel, S. Georges, Modeling of a SOFC fuelled by methane: from direct internal reforming to gradual internal reforming. Chem. Eng. Sci. **62**, 1636–1649 (2007)
23. K. Hou, R. Hughes, The kinetics of methane steam reforming over a Ni/α-Al2O catalyst. Chem. Eng. J. **82**, 311–328 (2001)
24. R. Suwanwarangkul, E. Croiset, E. Entchev, Experimental and modeling study of solid oxide fuel cell operating with syngas fuel. J. Power Sources **161**, 308–322 (2006)
25. R. Suwanwarangkul, E. Croiset, M.W. Fowler, Performance comparison of Fick's Dusty-Gas and Stefan-Maxwell Models to predict the concentration overpotential of a SOFC anode. J. Power Sources **122**, 9–18 (2003)

Thermodynamic Calculation of Phase Diagrams for the Rare Earth Binary Alloys: RE–Nd (RE = La, Ce, Pr, Y) Systems

Kaicheng Yang, Lei Xu, Maohua Rong, Qingrong Yao and Jiang Wang

Abstract In this work, the experimental data of phase equilibria of the RE–Nd (RE = La, Ce, Pr, Y) binary systems in the published literature were investigated firstly, and then the RE–Nd (RE = La, Ce, Pr, Y) binary systems were calculated using the CALPHAD method. The calculation results were compared with the experiment data. The phase diagrams of RE–Nd (RE = La, Ce, Pr, Y) systems could provides important information for the design of novel Nd–Fe–B-based permanent magnets with rare earth elements.

Keywords RE–Nd binary systems · Thermodynamic · CALPHAD Phase diagram

Introduction

The Nd–Fe–B alloy is the most excellent magnetic properties of permanent magnets in the world. In order to use reasonably the rare earth resources, many researchers aim to use cheaper light rare earth elements (La, Ce, Pr, Y) to replace heavy rare earth elements in Nd–Fe–B alloy to reduce the costs of magnets [1–7]. Thus, it is necessary to understand the effect of light rare earth elements (La, Ce, Pr, Y) on microstructure and magnetic properties of Nd–Fe–B permanent magnets. Phase equilibria and thermodynamic information of the related RE–Nd–Fe–B systems are indispensable.

K. Yang · L. Xu · M. Rong (✉) · Q. Yao · J. Wang
School of Material Science and Engineering & Guangxi Key Laboratory of Information Materials, Guilin University of Electronic Technology, Guilin 541004, China
e-mail: rongmh124@guet.edu.cn

Q. Yao
e-mail: qingry96@guet.edu.cn

J. Wang
e-mail: waj124@guet.edu.cn

© Springer Nature Singapore Pte Ltd. 2018

Y. Han (ed.), *Advances in Materials Processing*, Lecture Notes in Mechanical Engineering, https://doi.org/10.1007/978-981-13-0107-0_123

As the sub-binary systems of the multi-component RE–Nd–Fe–B (RE = La, Ce, Pr, Y) systems, the phase relation and thermodynamic properties of RE–Nd (RE = La, Ce, Pr, Y) systems are of great importance for the heat treatment method and foundry technology of RE–Nd–Fe–B alloy. Thus, the phase relation and thermodynamic properties in the RE–Nd (RE = La, Ce, Pr, Y) binary systems were investigated firstly in this work and then thermodynamic calculations of these binary systems were carried out using the CALPHAD method based on the experimental data in the literature.

Thermodynamic Models

There are no phase diagram and thermodynamic data about Y–Nd system. This system was no considered in this work. Thus, we chose the Y–La and Y–Ce systems rather than Y–Nd system, because Y–La and Y–Ce system have phase diagram data, they are also important sub-binary systems for RE–Nd–Fe–B system. According to the experimental information in the literature, there are no intermetallic compounds in the La–Nd, Ce–Nd, Pr–Nd and Y–Ce binary systems. The Gibbs energy of solid solution phase (ϕ = liquid, fcc, bcc, hcp, dhcp) are described by the following expressions, Eqs. 1–3 and 7–10 are given from the reported in Ref. [25]:

$$G_{\mathrm{m}}^{\varphi} = \sum_{\mathrm{i}=RE1,RE2} {}^{0}G_{\mathrm{i}}^{\varphi} x_{\mathrm{i}} + RT \sum_{\mathrm{i}=RE1,RE2} x_{\mathrm{i}} \ln x_{\mathrm{i}} + x_{RE1} x_{RE2} \sum_{\mathrm{m}=0}^{\mathrm{n}} {}^{\mathrm{m}}L_{RE1,RE2}^{\varphi} (x_{RE1} - x_{RE2})^{\mathrm{m}} \tag{1}$$

$${}^{0}G_{\mathrm{i}}^{\varphi}(T) = a + bT + cT \ln T + dT^2 + eT^3 + fT^{-1} + gT^7 + hT^{-9} \tag{2}$$

$${}^{\mathrm{m}}L_{RE1,RE2}^{\Phi} = A_{\mathrm{m}} + B_{\mathrm{m}} T \tag{3}$$

in which ${}^{0}G_{\mathrm{i}}^{\varphi}(T)$ is the Gibbs energy of pure elements and is taken from PURE database [8]. x_{i} is the mole fraction of the element i and R is the gas constant. ${}^{\mathrm{m}}L_{RE1,RE2}^{\varphi}$ is the interaction parameter. T is temperature. A_{m} and B_{m} are to be assessed parameters. Due to lack of experimental data, all the solid solution phases were assumed to ideal mixing in the La–Nd, Ce–Nd and Pr–Nd systems.

Note that the lattice stabilities of dhcp-Ce, fcc-Y and fcc-Nd are not available in the PURE database [8]. In this work, they are taken from the data reported in Ref. [9, 10] as:

$${}^{0}G_{Ce}^{dhcp} = -190 + 0.56886T + {}^{0}G_{Ce}^{fcc} \tag{4}$$

$${}^{0}G_{Ce}^{hcp} = -14708.0 + 13.1890T \tag{5}$$

$$ {}^{0}G_{Y}^{fcc} = {}^{0}G_{Y}^{hcp} + 6000 \tag{6} $$

Intermetallic Compounds

Due to the homogeneity range, the intermetallic compounds, LaY were treated using two sublattice model with the formula $(La, Y)_1(Y)_1$. And the Gibbs energy of the intermetallic compound LaY can be expressed as follows:

$$ \begin{aligned} G_m^{LaY} &= y'_{La} y''_Y G_{La:Y}^{LaY} + y'_Y y''_Y G_{Y:Y}^{LaY} + RT(y'_{La} \ln y'_{La} + y'_Y \ln y'_Y) \\ &+ RT(y''_{La} \ln y''_{La} + y''_Y \ln y''_Y) + y'_{La} y'_Y y''_Y L_{La,Y:Y}^{LaY} \end{aligned} \tag{7} $$

$$ G_{La:Y}^{LaY} = {}^{0}G_{La}^{dhcp} + {}^{0}G_{Y}^{hcp} + A_1 + B_1 T \tag{8} $$

$$ G_{Y:Y}^{LaY} = 2^{0}G_{Y}^{hcp} + 6000 \tag{9} $$

$$ L_{La,Y:Y}^{LaY} = A_2 + B_2 T \tag{10} $$

Thermodynamic Calculation

Thermodynamic model parameters of phases in the Y–La and Y–Ce binary systems were optimized by Du [25] and Meng [18]. We calculated the thermodynamic properties of these systems based on their optimized parameters. The La–Nd, Ce–Nd and Pr–Nd systems were assumed to ideal model. The calculated results were compared with the experimental data in the following section.

La–Nd System

Peterson [11] studied the solid solution phase in the La–Nd phase diagram. All phase equilibria are drawn by dashed lines due to lack of experimental data. Wu [12] reported the solubility of Nd in β-La is about 35 at.% and that of La in α-Nd is about 40 at.%. Yoshiyuki et al. [13] measured the activities of La–Nd alloy at 1400 °C. Figure 1a is the calculated La–Nd phase diagram in this work. The calculated temperature of the invariant reaction is about 773 °C. Figure 1b is the calculated activities of La–Nd system at 1400°C with the experimental data [12]. The calculation results show the difference compared with the experimental data [12, 13]. The experimental data show the La–Nd system is different from ideal

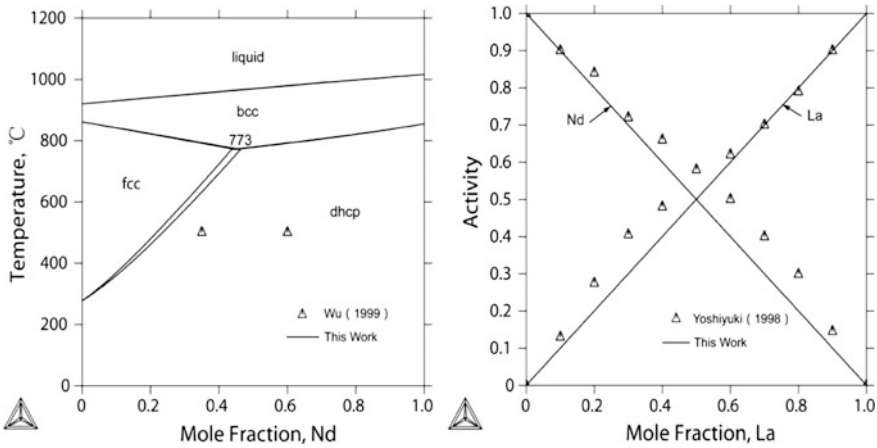

Fig. 1 The calculated La–Nd binary phase diagram **a** and the activities of La and Nd in liquid La–Nd alloys at 1400 °C **b** with the experimental data [12, 13]

behavior although this system is composed of light-light rare earth elements. There are no more experimental data, and considering the experimental uncertainties in the reported literature, we still accept this calculation result.

Ce–Nd System

Speight [14] and Hachimi [15] studied the solid solution phases in the Ce–Nd binary system, Gschneidner et al. [16] predicted the Ce–Nd phase diagram according to the experimental results of them, all phase equilibria are drawn by dashed lines. Keiser [17] measured the composition of phase boundary of the two-phase (dhcp + fcc) region using diffusion couples annealed at difference temperature, but the experimental data would be unreliable due to the limited annealed time. Cacciamani et al. [9] assumed ideal mixing in all the solid and liquid phases of the Ce–Nd binary system and calculated the Ce–Nd phase diagram. Figure 2 is the calculated Ce–Nd phase diagram in this work with the experimental data [14]. It can be seen that the invariant reaction at 700°C. The transformation temperature of dhcp(Ce) → bcc(Ce) is not consistent with each other because the lattice stabilities of the dhcp structure of Ce are different.

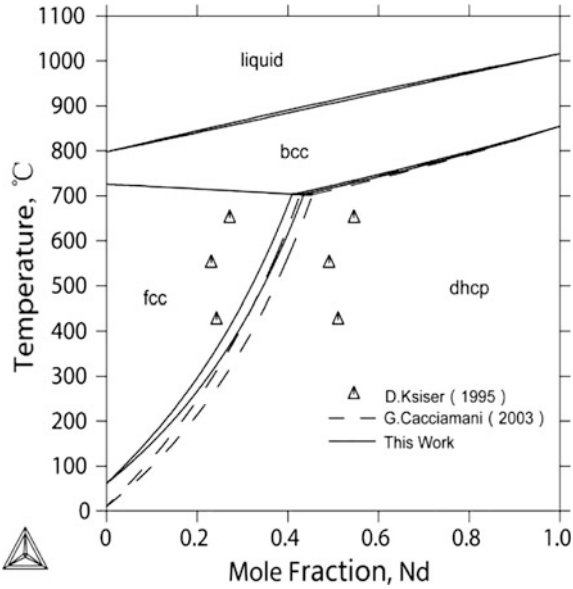

Fig. 2 The calculated Ce–Nd binary phase diagram with the experimental data [14]

Pr–Nd System

Markova [19] and Terekhova [20] studied the Pr–Nd binary phase diagram using thermal analysis, metallography, X-ray diffraction and hardness measurements. Their experimental results show that there are three solution phase, e.g. liquid, bcc and dhcp. Lundin et al. [21] measured the activities of Pr–Nd liquid alloy at 1400 °C. Shiflet et al. [22] calculated the Pr–Nd phase diagram. Figure 3a is the calculated Pr–Nd binary system in this work with the calculated results [22]. Figure 3b is the calculated activities of Pr and Nd at 1400 °C with the experimental data [20]. The calculated results are in good agreement with the experimental data [21].

Y–La System

The Y–La binary phase diagram was studied experimentally by Spedding [23], and redrawn by Gschneidner [24]. Figure 4a is the comparison of the calculated Y–La binary phase diagram with the experimental data [23]. Figure 4b is the calculated enthalpy of mixing of liquid Y–La alloys. The enthalpy of formation of intermetallic compounds at 298 K and the activities of La and Y in liquid Y–La at 1800 K were calculated as shown in Fig. 5, respectively.

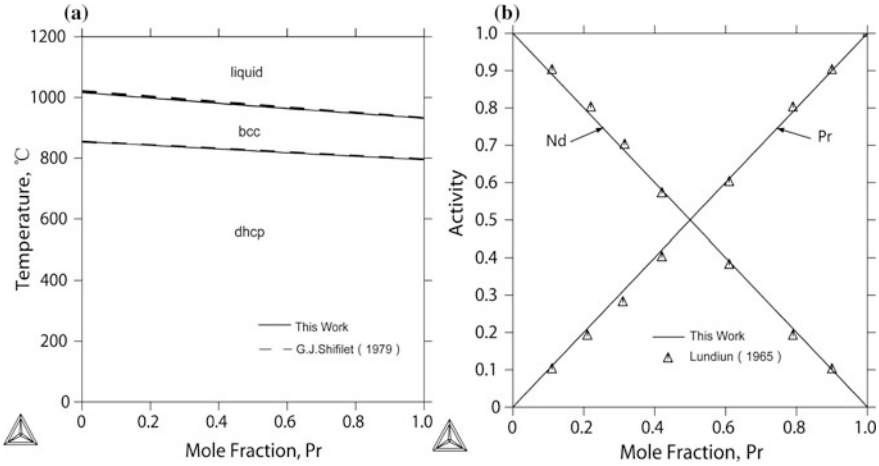

Fig. 3 The calculated Pr–Nd binary phase diagram **a** and the activities of Pr and Nd in liquid Pr–Nd alloys at 1400 °C **b** with the experiment data [21]

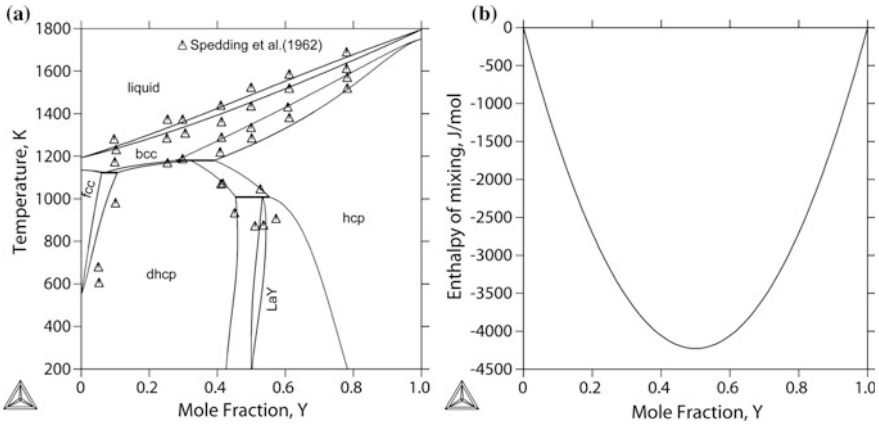

Fig. 4 The calculated Y–La binary phase diagram (**a**) with the experimental data [23] and the enthalpy of mixing of liquid Y–La alloys (**b**)

Y–Ce System

Flandorfer et al. [26] determined the Y–Ce phase diagram by differential thermal analysis and X-ray diffraction, obtained most composition of phase boundary of this system. They indicated that the Ce_2Y is a metastable phase. According to the experimental data of Flandorfer, the eutectic reaction at about 978 K and the peritectic reaction at about 1053 K. Figure 6a is the comparison of the calculated Y–Ce phase diagram with the experimental data [26]. Figure 6b is the calculated

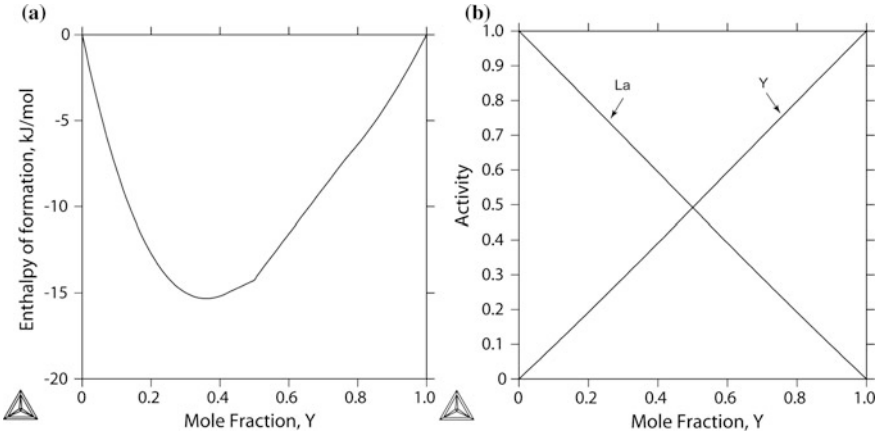

Fig. 5 The calculated the enthalpy of formation of intermetallic compounds at 298 K (**a**) and the activities of La and Y in liquid Y–La alloys at 1800 K (**b**)

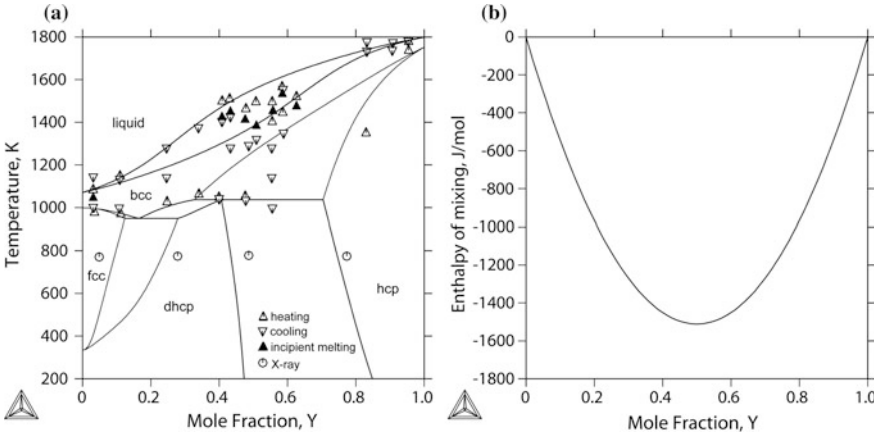

Fig. 6 The calculated Y–Ce binary phase diagram (**a**) with the experimental data [26] and the enthalpy of mixing of liquid Y–Ce alloys (**b**)

enthalpies of mixing of liquid Y–Ce alloys. The activities of Ce and Y in liquid Y–Ce alloys at 1800 K and the enthalpy of formation of intermetallic compounds at 298 K were calculated as shown in Fig. 7.

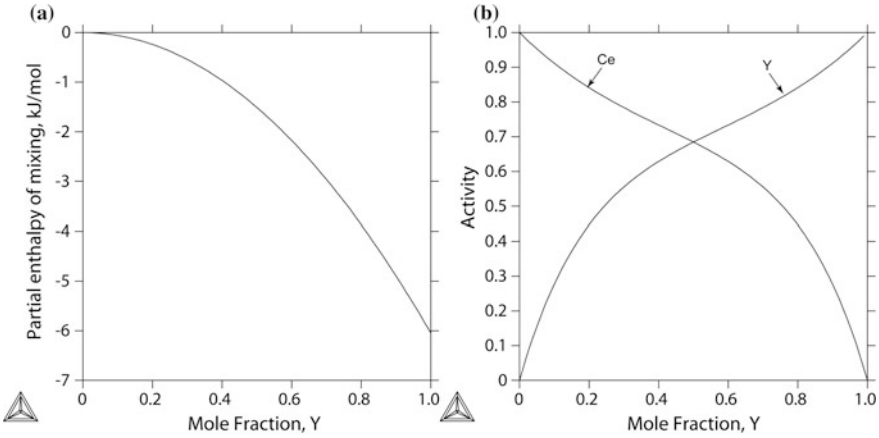

Fig. 7 The calculated the partial molar of mixing of Ce **a** and the activities of Ce and Y **b** in liquid Y–Ce alloys at 1800 K

Conclusions

The phase relation of La–Nd, Ce–Nd and Pr–Nd and thermodynamic properties of Y–La and Y–Ce were calculated using CALPHAD method in this work. The calculation results of most systems are consistent well with experimental data. In addition, the ideal model used in La–Nd binary system can not reproduce the experimental data, more detailed experimental studies are required to better determine phase equilibria in the La–Nd system, such work is outside the scope of this investigation.

Acknowledgements This work was supported financially by the National Key Research and Development Program of China (2016YFB0700901), the National Basic Foundation of China (2014CB643703), the National Natural Science Foundation of China (51761008, 51461013) and the Guangxi Natural Science Foundation (2016GXNSFDA380015, 2016GXNSFGA380001).

References

1. Z. Qiao, S. Pan, J. Xiong, J. Magn. Magn. Mater. **423**, 197–202 (2017)
2. M. Kuru, O. Sahin, S. Ozarslan, J. Alloy. Compd. **694**, 726–732 (2017)
3. M. Pousthomis, C. Garnero, C.G. Marcelot, J. Magn. Magn. Mater. **424**, 304–313 (2017)
4. K. Pei, X. Zhang, M. Lin, J. Magn. Magn. Mater. **398**, 96–100 (2016)
5. M. Hussain, J. Liu, L.Z. Zhao, J. Magn. Magn. Mater. **399**, 26–31 (2016)
6. Z. Li, W. Liu, S. Zha, J. Magn. Magn. Mater. **393**, 551–554 (2015)
7. Z. Li, W. Liu, S. Zha, J. Rare Earth **33**, 961–964 (2015)
8. A.T. Dinsdale, CALPHAD **15**, 317–425 (1991)
9. G. Cacciamani, A.M. Cardinale, G. Borzone, R. Ferro, CALPHAD **27**, 227–233 (2003)

10. Y. Wang, S. Curtarolo, C. Jiang, R. Arroyave, T. Wang, G. Ceder, L.Q. Chen, Z.K. Liu, CALPHAD **28**, 79–90 (2004)
11. T.S. Peterson, S. Legvold, K.A. Gschneidner, T.W. Tang, J.O. Moorman, J. Appl. Phys. **49**, 20–21 (1987)
12. S. Wu, L. Zhang, L. Zeng, Y. Zuang, J. Alloy. Compd. **291**, 220–221 (1999)
13. Y. Shoji, T. Matsui, J. Nucl. Mater. **254**, 9–13 (1998)
14. J.D. Speight, I.R. Harris, G.V. Raynor, J. Alloy. Compd. **15**, 317–318 (1968)
15. O. Hachimi, S. Hayun, A. Venkert, M.P. Dariel, J. Alloy. Compd. **427**, 104–109 (2007)
16. K.A. Gschneidner, F.W. Calderwood, Bull. Alloy Phase Diagrams **3**, 90–91 (1982)
17. D. Keiser, Scripta Mater. **33**, 959–965 (1995)
18. F.G. Meng, L.B. Liu, H.S. Liu, Z.P. Jin, CALPHAD **30**, 323–325 (2006)
19. I.A. Markova, V.F. Terekhova, E.M. Savitskii, Zhur. Neorg. Khim. **8**, 1041–1042 (1998)
20. V.F. Terekhova, Met. Sci. Heat Treat. **5**, 465–471 (1963)
21. C.E. Lundin, A.S. Yamamoto, J.F. Nachman, Acta Metall. **13**, 148–149 (1965)
22. G.J. Shiflet, J.K. Lee, H.I. Asronson, CALPHAD **3**, 129–130 (1979)
23. F.H. Spedding, R.M. Valletta, A.H. Daane, Trans. ASM. **55**, 483–485 (1962)
24. K.A. Gschneidner Jr., F.W. Calderwood, Bull. Alloy Phase Diagrams **3**, 94–96 (1982)
25. Z. Du, C. Guo, C. Li, W. Zhang, Int. J. Mater. Res. **25**, 492–500 (2006)
26. H. Flandorfer, M. Giovanni, A. Saccone, P. Rogl, R. Ferro, Met. Mater. Trans. A **28**, 265–275 (1997)

Erratum to: Effect of Process Parameters on the Interface Microstructure and Thickness of Silver Cladding Copper Wires Prepared by Core-Cladding Continuous Casting

Feng Yi, Xuefeng Liu and Yue Pan

Erratum to:
Chapter "Effect of Process Parameters on the Interface Microstructure and Thickness of Silver Cladding Copper Wires Prepared by Core-Cladding Continuous Casting" in: Y. Han (ed.), *Advances in Materials Processing*, Lecture Notes in MechanicalEngineering, https://doi.org/10.1007/978-981-13-0107-0_20

The original version of the book was inadvertently published with incorrect temperature ranges in chapter "Effect of Process Parameters on the Interface Microstructure and Thickness of Silver Cladding Copper Wires Prepared by Core-Cladding Continuous Casting", which have to be now corrected. The erratum chapter and the book have been updated with the changes.

The updated online version of this chapter can be found at
https://doi.org/10.1007/978-981-13-0107-0_20

© Springer Nature Singapore Pte Ltd. 2018

Y. Han (ed.), *Advances in Materials Processing*, Lecture Notes in Mechanical Engineering, https://doi.org/10.1007/978-981-13-0107-0_124